ORGANISATION EUROPÉENNE POUR LA RECHERCHE NUCLÉAIRE

CERN EUROPEAN ORGANIZATION FOR NUCLEAR RESEARCH

HEAVY QUARKONIUM PHYSICS

QWG Conveners

N. Brambilla
M. Krämer
R. Mussa
A. Vairo

HEAVY QUARKONIUM PHYSICS

Authors: *QWG & Topic conveners*: N. Brambilla[42], M. Krämer[16], R. Mussa[26], A. Vairo[42,36];
Topic Conveners: G. Bali[19], G. T. Bodwin[1], E. Braaten[45], E. Eichten[17], S. Eidelman[6], S. Godfrey[7],
A. Hoang[43], M. Jamin[44], D. Kharzeev[5], M. P. Lombardo[24], C. Lourenço[11], A. B. Meyer[20],
V. Papadimitriou[17,58], C. Patrignani[25], M. Rosati[28], M. A. Sanchis-Lozano[62], H. Satz[4], J. Soto[2];
Contributors: D. Z. Besson[30], D. Bettoni[23], A. Böhrer[55], S. Boogert[37], C.-H. Chang[9,29], P. Cooper[17],
P. Crochet[13], S. Datta[4], C. Davies[19], A. Deandrea[39], R. Faustov[53], T. Ferguson[8], R. Galik[14],
F. A. Harris[21], O. Iouchtchenko[11], O. Kaczmarek[4], F. Karsch[4], M. Kienzle[18], V. V. Kiselev[54],
S. R. Klein[33], P. Kroll[64], A. Kronfeld[17], Y.-P. Kuang[61], V. Laporta[3], J. Lee[32], A. Leibovich[49],
J. P. Ma[29], P. Mackenzie[17], L. Maiani[50], M. L. Mangano[11], A. Meyer[17], X. H. Mo[22],
C. Morningstar[8], A. Nairz[11], J. Napolitano[51], S. Olsen[21], A. Penin[31], P. Petreczky[52], F. Piccinini[47],
A. Pineda[2], A. D. Polosa[3,10], L. Ramello[48], R. Rapp[57], J. -M. Richard[12], V. Riquer[11], S. Ricciardi[38],
E. Robutti[25], O. Schneider[34], E. Scomparin[60], J. Simone[17], T. Skwarnicki[56] G. Stancari[17,23],
I. W. Stewart[41], Yu. Sumino[59], T. Teubner[35], J. Tseng[46], R. Vogt[15,33], P. Wang[22], B. Yabsley[63],
C. Z. Yuan[22], F. Zantow[4], Z. G. Zhao[40], A. Zieminski[27]

[1] HEP Division, Argonne National Laboratory, Argonne, Illinois, USA
[2] Universitat de Barcelona, Barcelona, Catalonia, Spain
[3] Università di Bari and INFN Bari, Italy
[4] Facultät für Physik, Universität Bielefeld, Germany
[5] Brookhaven National Laboratory, Upton, New York, USA
[6] Budker Institute, Novosibirsk, Russia
[7] Carleton University, Ottawa, Canada
[8] Carnegie Mellon University, Pittsburgh, Pennsylvania, USA
[9] CCAST (World Laboratory), Beijing, China
[10] Centro Studi e Ricerche "E. Fermi", Roma, Italy
[11] CERN, Geneva, Switzerland
[12] CNRS-IN2P3-Universite Joseph Fourier, Grenoble, France
[13] CNRS-IN2P3, France
[14] Cornell University, Ithaca, New York, USA
[15] University of California, Davis, California, USA
[16] School of Physics, The University of Edinburgh, Edinburgh, United Kingdom;
   now at Institut für Theoretische Physik E, RWTH Aachen, Aachen, Germany
[17] Fermi National Accelerator Laboratory, Batavia, Illinois, USA
[18] Geneva University, Geneva, Switzerland

[19] Glasgow University, Glasgow, United Kingdom
[20] Institut für Experimentalphysik, Universität Hamburg, Hamburg, Germany
[21] Hawaii University, Honolulu, USA
[22] Institute of High Energy Physics, Chinese Academy of Sciences, Beijing, China
[23] INFN, Ferrara, Italy
[24] INFN, Frascati, Italy
[25] INFN, Genova, Italy
[26] INFN, Torino, Italy
[27] Indiana University, Bloomington, Indiana, USA
[28] Iowa State University, Ames, Iowa, USA
[29] Institute of Theoretical Physics, Chinese Academy of Sciences, Beijing, China
[30] University of Kansas, Lawrence, USA
[31] Institut für Theoretische Teilchenphysik, Universität Karlsruhe, Karlsruhe, Germany
[32] Department of Physics, Korea University, Seoul, Korea
[33] Laurence Berkeley National Laboratory, Berkeley, California, USA
[34] Ecole Polytechnique Fédérale de Lausanne, Lausanne, Switzerland
[35] University of Liverpool, United Kingdom
[36] CFIF, Instituto Superior Tecnico, Lisbon, Portugal
[37] University College London, London, United Kingdom
[38] Univ. of London, Royal Holloway, United Kingdom
[39] Université de Lyon 1, Villeurbanne, France
[40] Univ. of Michigan, Ann Arbor, Michigan, USA
[41] Massachusetts Institute of Technology, Cambridge, USA
[42] Università di Milano & INFN Milano, Italy
[43] Max-Planck-Institut für Physik, Munich, Germany
[44] Physik-Department, TU München, Garching, Germany
[45] Ohio State University, Columbus, Ohio, USA
[46] Oxford University, Oxford, United Kingdom
[47] Università di Pavia & INFN Pavia, Italy
[48] Università del Piemonte Orientale, Alessandria, Italy
[49] University of Pittsburgh, Pittsburgh, Pennsylvania, USA
[50] Università di Roma "La Sapienza" & INFN Roma, Italy
[51] RPI, Troy, New York, USA
[52] Physics Department and RIKEN-BNL, Brookhaven National Laboratory, Upton, New York, USA
[53] Russian Academy of Science, Scientific Council for Cybernetics, Moscow, Russia
[54] Russian State Research Center "Institute for High Energy Physics", Protvino, Moscow Region, Russia
[55] Siegen University, Siegen, Germany
[56] Syracuse University, Syracuse, New York, USA
[57] Texas A& M University, Texas, USA
[58] Texas Tech University, Lubbock, Texas, USA
[59] Tohoku University, Tohoku, Japan
[60] Università di Torino & INFN, Torino, Italy
[61] Tsinghua University, Beijing, People's Republic of China
[62] Instituto de Física Corpuscular (IFIC) and Departamento de Física Teórica, Centro Mixto Universidad de Valencia-CSIC, Valencia, Spain
[63] Virginia Tech University, Virginia, USA
[64] Universität Wuppertal, Wuppertal, Germany

ABSTRACT

This report is the result of the collaboration and research effort of the Quarkonium Working Group over the last three years. It provides a comprehensive overview of the state of the art in heavy-quarkonium theory and experiment, covering quarkonium spectroscopy, decay, and production; the determination of QCD parameters from quarkonium observables; quarkonia in media; and the effects on quarkonia of physics beyond the Standard Model. An introduction to common theoretical and experimental tools is included. Future opportunities for research in quarkonium physics are also discussed.

FOREWORD

As the community of high-energy physicists impatiently awaits the startup of the LHC and the opening of the new energy frontier, it is very welcome news that so much challenging and exciting data are constantly being produced in the field of quarkonium physics. The proliferation of puzzling measurements has led over the past several years to new challenges for the theorists, requiring the introduction of new ideas, and providing new probes for the understanding of QCD at its deeper levels.

Ten years ago, reports by the CDF Collaboration signalled the end of an era in quarkonium physics, but at the same time opened new windows on this field, which contributed so much to the development of QCD. The observation of the top quark with a mass of about 175 GeV closed all hopes of including toponium in the family of clean and useful quarkonium states. In parallel, the observation of an excess in charmonium production by orders of magnitude over what was predicted in the then available theoretical models gave birth to the modern theoretical understanding of charmonium production. Since then, in addition to successful explanations, a large set of puzzles kept being generated by data obtained at the Tevatron, at HERA, and in low-energy e^+e^- colliders: the apparent violation of universality emerging when comparing data from the hadron and the ep colliders, the poor agreement (at the limit of inconsistency!) between the predictions for the polarization of the J/ψ produced in hadronic collisions and the actual data, the excess of double charmonium production first observed by Belle. The solution to these puzzles still remains to be found, as new data keep pouring in.

But the surprises and advances have not been limited to the complex issue of the production mechanisms. The spectroscopy of quarkonium has also received challenging inputs from the observation of new narrow states, whose understanding requires an added dose of sophistication in the theory, together perhaps with the need for inclusion of more exotic patterns of bound states (hybrids, molecules, tetraquarks). Progress in lattice calculations and effective field theories has turned quarkonium physics into a powerful tool to measure the mass of the heavy quarks and the strength of the QCD coupling, providing accuracies comparable to or better than those allowed by any other technique. The properties of production and absorption of quarkonium in a nuclear medium are beginning to provide quantitative inputs for the study of QCD at high density and temperature, giving a unique experimental test bed for analytical and lattice studies.

The interplay of solid theoretical work and of accurate and versatile experimental techniques has brought quarkonium physics to a renaissance, with a flourishing of activity second only to the golden age which followed the discovery of charmonium almost 30 years ago. The appearance of this CERN Report, which documents the state of the art through the contributions of the leaders in the field, represents therefore a timely and much needed publication. The inclusion of both the theoretical and experimental perspectives leads to a precious resource for the active researcher, as well as for the young newcomers to the field.

I am happy to praise the organizers of the Quarkonium Working Group, the conveners and all the participants, who have worked so hard over the past couple of years to produce this Report, which will provide an essential guide to this ever-exciting area of research for years to come.

<div align="center">

Michelangelo Mangano
CERN PH Department

</div>

On the eve of the startup of the LHC and the search for new physics beyond the Standard Model at energy scales of several TeV, there is still a sector of the Standard Model that evades our control: the sector of strongly interacting particles, i.e. quarks and gluons. We believe we have the field theory that describes strong interaction, QCD, but we are not yet able to extract from it in a controlled way a great part of the hadron properties. These same hadron properties obviously play a relevant role in many searches for new physics and new phenomena, CP violation being a strong case in hand. At the LHC hadron processes will again take the stage. It is, therefore, relevant to get hold of the strong sector of the Standard Model. For several reasons heavy quarkonium offers a unique opportunity in this direction. Quarkonium systems may be crucially important to improve our understanding of QCD. They probe all the energy regimes of QCD, from the hard region, where an expansion in the coupling constant is possible, to the low-energy region, where nonperturbative effects dominate. Heavy-quark–antiquark bound states are thus an ideal, and to some extent, unique laboratory where our understanding of nonperturbative QCD and its interplay with perturbative QCD may be tested in a controlled framework.

Moreover, in the last few years a wealth of new experimental results have become available. The diversity, quantity and accuracy of the data currently being collected is impressive and includes:

– data on quarkonium formation from BES at BEPC, E835 at Fermilab, KEDR (upgraded) at VEPP-4M, and CLEO III at CESR;
– clean samples of charmonia produced in B-decays, in photon–photon fusion and in initial-state radiation from the B-meson factory experiments BaBar at SLAC and Belle at KEK, including the unexpected observation of associated $(c\bar{c})(c\bar{c})$ production;
– heavy quarkonia production from gluon–gluon fusion in $p\bar{p}$ annihilations at 2 TeV from the CDF and D0 experiments at Fermilab, including the first observation of B_c candidates;
– charmonia production in photon–gluon fusion from the ZEUS and H1 experiments at DESY;
– charmonia production in heavy-ion collisions from the PHENIX and STAR experiments at RHIC, and the NA60 experiment at CERN.

These experiments may operate as heavy quarkonium factories, producing quarkonium states in large amounts. If properly analysed and interpreted, the data can lead to surprising results and major progress in our understanding of QCD. This is exemplified by the very recent discovery of a new unexpected narrow charmonium state, temporarily labelled $X(3872)$, which was announced by the Belle Collaboration at the Lepton–Photon Conference 2003 and confirmed within a month by the CDF Collaboration at Fermilab, during the 2nd QWG Workshop.

In the near future, even larger data samples are expected from the CLEO-c and BES III upgraded experiments, while the B factories, the Fermilab Tevatron, and the DESY experiments will continue to supply valuable data for several years. New facilities will become operational (LHC at CERN, Panda at GSI, much-higher-luminosity B factories at KEK and SLAC, a Linear Collider, etc.) offering fantastic challenges and opportunities, which we must start facing today. Considerable efforts are also being made to study deconfined quark matter, at SPS, RHIC and LHC energies, for which heavy quarkonium is among the most crucial probes. The complexity of these studies requires a close communication and the exchange of ideas between experts in quarkonium physics and heavy-ion collisions.

Effective field theories, such as Nonrelativistic QCD (NRQCD), provide new tools and definite predictions concerning, for instance, heavy-quarkonium production and decays. New effective field theories for heavy quarkonium, as potential NRQCD (pNRQCD) and velocity NRQCD (vNRQCD), have recently been developed and are producing a wealth of new results. The lattice implementation of such effective theories has been partially carried out and many more results with drastically reduced systematic uncertainties are expected in the near future. The progress in the understanding of non-relativistic effective field theories makes it possible to go beyond phenomenological models and, for

the first time, face the possibility of providing a unified description of all aspects of heavy-quarkonium physics. This allows us to use quarkonium as a benchmark for our understanding of QCD, for the precise determination of relevant Standard Model parameters (e.g., heavy quark masses, α_s), and for new physics searches.

It is crucial, now, to ensure an efficient communication between experimentalists and theorists, within the broad quarkonium physics community. This has been the main motivation for the creation of an international research collaboration, the Quarkonium Working Group, which constitutes the support platform of this CERN Report (see also `http://www.qwg.to.infn.it`)

The aim of the QWG is essentially twofold. First, to guarantee an intense and efficient exchange of results and ideas between experimentalists and theorists, now that many new measurements are becoming available. Second, to overcome the dispersal of the research in this field and jointly study the different approaches and techniques, by establishing new collaborations and improving existing ones. The concrete goals are:

– to achieve a better understanding of the dynamics of the strong interaction and of strongly coupled theories, using quarkonium systems;
– to gain detailed knowledge of the physics of confinement/deconfinement;
– to improve the determination of the fundamental parameters of the Standard Model and constrain the allowed parameter space for new physics;
– to identify missing experimental information required to improve our understanding of QCD, and to identify theoretical calculations needed for the interpretation of current and future experiments;
– to make this information available to people working in related fields.

This CERN Report presents the state of the art in heavy-quarkonium physics at the end of 2004 and is a first step to achieving the goals of the QWG. The Report includes experimental and theoretical results by different approaches and different communities (high-energy, perturbative, lattice, nuclear, etc.) in a common language. The progress in the field and the impact of such progress on other areas are presented, open problems and outstanding puzzles are discussed, and the future opportunities of this field are outlined.

Given the richness of the physics involved in the project, the research goals have been pursued by specifying seven main topics organized by theoretical and experimental topic conveners:

– Quarkonium spectroscopy [Conveners: G. Bali, N. Brambilla, J. Soto (TH); R. Mussa (EXP)];
– Quarkonium decays [Conveners: E. Eichten, A. Vairo (TH); C. Patrignani (EXP)];
– Quarkonium production [Conveners: G. Bodwin, E. Braaten, M. Krämer (TH); A. B. Meyer, V. Papadimitriou (EXP)];
– Precision determination of Standard Model parameters [Conveners: A. Hoang, M. Jamin (TH); S. Eidelman (EXP)];
– Quarkonium in media [Conveners: D. Kharzeev, M. P. Lombardo, H. Satz (TH); C. Lourenço, M. Rosati (EXP)];
– Beyond the Standard Model [Convener: M. A. Sanchis-Lozano (TH)];
– Future opportunities [Conveners: S. Godfrey, M. A. Sanchis-Lozano (TH)].

The Quarkonium Working Group was initiated in 2002 by Nora Brambilla, Roberto Mussa and Antonio Vairo, who were, shortly afterwards, joined by Armin Böhrer and Michael Krämer as the QWG conveners team. Most of the topic conveners listed above belong to the initial group of people who supported the QWG and contributed to its research programme. The CERN TH Division and CERN, and especially Michelangelo Mangano, have played an important role in the history of the QWG, by hosting the first QWG meeting and by supporting the enterprise of compiling the CERN Report.

The QWG has organized three international meetings, which were held at CERN (2002), Fermilab (2003) and IHEP Beijing (2004). Approximately 250 theoretical and experimental physicists participated

in the meetings. The organizers, participants, and supporting institutions are listed below. The third meeting was preceded by the first QWG graduate school organized at the ITP Beijing with about 100 participating graduate students.

We would like to express here our sincerest thanks to all those who have contributed to this enterprise and made this document possible, in particular the topic conveners and the organizers and participants of the three QWG meetings. We also gratefully acknowledge the support from the institutions that hosted the QWG meetings. Finally, we would like to express our deepest thanks to Armin Böhrer who was of key relevance at the start of the QWG by producing and hosting in Siegen the first QWG Web page, designing the QWG logo, participating in the organization of the first two QWG workshops, and supporting in all ways the development of the QWG. We also thank E. Berger, D. Kharzeev and A. Zieminski for having been topical conveners of a topical section later absorbed by other ones.

As of September 2004, Vaia Papadimitriou joined the QWG conveners team. As of December 2004, Aldo Deandrea and Xiaoyan Shen agreed to join the topical conveners team.

The Quarkonium Working Group has very quickly coalesced into an active, international community of physicists working and collaborating on quarkonium physics, QCD, and the related impact on the Standard Model and physics beyond the Standard Model. Given the continuous flux of data and the order-of-magnitude(s) improvement in the statistical analysis coming and expected to come from present and future accelerator experiments, this promises to remain a very rich research area for several years to come. To fully benefit from it, we believe it is important that the community of physicists working in the field maintains a common area of discussion, transcending individual experimental and theoretical collaborations. It is our hope that this CERN Report will provide a basis for such future developments.

<div align="center">

The QWG Conveners
Nora Brambilla, Michael Krämer, Roberto Mussa, Antonio Vairo

</div>

1st International Workshop on Heavy Quarkonium

CERN, 8–10 November 2002

`http://www.qwg.to.infn.it/WS-nov02/index.html`

Organizing Committee: A. Böhrer, N. Brambilla, O. Iouchtchenko, M. Kienzle, M. Krämer, C. Lourenço, M. L. Mangano, R. Mussa, T. Teubner, A. Vairo

Speakers: G. Bali, E. L. Berger, G. Bodwin, A. Böhrer, E. Braaten, N. Brambilla, H. Castilia-Valdez, C. Davies, A. Deandrea, E. Eichten, S. Eidelman, R. Faustov, T. Ferguson, M. Graham, S. Godfrey, F. A. Harris, A. Hoang, O. Iouchtchenko, F. Karsch, V. V. Kiselev, B. Kniehl, M. Krämer, M.-P. Lombardo, C. Lourenço, J. P. Ma, M. L. Mangano, A. Meyer, R. Mussa, S. Necco, V. Papadimitriou, A. Penin, K. Peters, P. Petreczky, A. Pich, A. Pineda, A. Polleri, M. Rosati, M. A. Sanchis-Lozano, H. Satz, J. Simone, G. Stancari, I. W. Stewart, Y. Sumino, T. Teubner, J. Tseng, A. Vairo, R. Waldi, B. Yabsley

Supported by the CERN TH Division

Agenda and slides available at `http://www.qwg.to.infn.it/WS-nov02/WSagenda.html`
List of participants available on website.

2nd International Workshop on Heavy Quarkonium

Fermilab, 20–22 September 2003

`http://www.qwg.to.infn.it/WS-sep03/index.html`

Organizing Committee: G. Bodwin, A. Böhrer, N. Brambilla, E. Eichten, V. Jain, M. Krämer, R. Mussa, V. Papadimitriou, S. Pordes, A. Vairo

Speakers: J. Appel, G. Bali, G. Bauer, D. Bettoni, E. Braaten, N. Brambilla, K. T. Chao, P. Cooper, A. Deandrea, E. Eichten, A. El-Khadra, J. Erler, R. Faustov, T. Ferguson, S. Fleming, R. Galik, S. Godfrey, Y. Gotra, Z. J. Guo, F. A. Harris, T. Hatsuda, A. Hoang, J. Huang, U. Husemann, V. Jain, M. Jamin, S. Kelly, D. Kharzeev, S. R. Klein, J. Lee, A. Leibovich, P. Mackenzie, A. B. Meyer, C. Morningstar, H. Muramatsu, R. Mussa, A. Nairz, J. Napolitano, V. Papadimitriou, C. Patrignani, J. C. Peng, P. Petreczky, S. Pordes, J. W. Qiu, R. Rapp, S. Ricciardi, J-M. Richard, E. Robutti, M. Rosati, M. A. Sanchis-Lozano, H. Sato, X. Shen, J. Simone, R. Spighi, L. Stanco, R. Thews, T. Umeda, A. Vairo, R. Vogt, M. Voloshin, C. Y. Wong, W. Xie, B. Yabsley, C. Z. Yuan, G. Zanderighi, Z.G. Zhao

Supported by Fermilab

Agenda and slides available at `http://www.qwg.to.infn.it/WS-sep03/WSagenda.html`
List of participants available on website.

3rd International Workshop on Heavy Quarkonium

IHEP Beijing, 12–15 October 2004

`http://www.qwg.to.infn.it/WS-oct04/index.html`

Organizing Committee: N. Brambilla, K. T. Chao, A. Deandrea, M. Krämer, Y. P. Kuang, W. G. Li, J. P. Ma, R. Mussa, V. Papadimitriou, C. F. Qiao, X. Y. Shen, A. Vairo, C. Z. Yuan

Speakers: G. Bali, S. Baranov, D. Bernard, G. Bodwin, E. Braaten, N. Brambilla, R. Brugnera, C.-H. Chang, K.-T. Chao, H.-S. Chen, Y.-Q. Chen, C.-H. Ching, A. Deandrea, E. Eichten, G. Feild, C. Gao, M. Garcia-Perez, Z. Guo, L. Han, B. Heltsley, P. Ko, J. Lee, T. Lee, Z. Liu, J.-P. Ma, T. Mehen, R. Mussa, S. L. Olsen, C. Patrignani, K. Peters, P. Petreczky, O. Philipsen, A. Pineda, C.-F. Qiao, M. Rosati, G. Rong, M. A. Sanchis-Lozano, X. Y. Shen, J. Soto, Y. Sumino, A. Tomaradze, A. Vairo, J. X. Wang, P. Wang, Y. L. Wang, Z. Wang, C. Y. Wong, J. L. Wu, B. Zhang, D. Zhang, S.-L. Zhu, N. Zhou

Supported by the Chinese Center for Advanced Science and Technology (CCAST), the Institute of Theoretical Physics (ITP), Beijing, the Institute of High Energy Physics (IHEP), Beijing, the Nature Science Foundation of China (NSFC), Peking University, and Tshinghua University

Agenda and slides available at `http://www.qwg.to.infn.it/WS-oct04/WSagenda.html`
List of participants available on the website.

1st International School of the QWG

Topical Seminar School on Heavy Quarkonia at Accelerators: New Theoretical Tools and Experimental Techniques
ITP, Beijing, 8–11 October 2004

`http://www.qwg.to.infn.it/TS-oct04/index.html`

Organizing Committee: N. Brambilla, K. T. Chao, M. Krämer, Y. P. Kuang, W. G. Li, J. P. Ma, M. L. Mangano, R. Mussa, V. Papadimitriou, C. F. Qiao, X. Y. Shen, A. Vairo, C. Z. Yuan

Lecturers:

G. Bodwin:	*Introduction to NRQCD and quarkonium production*;
G. Bali:	*Quarkonium and Exotics*;
N. Brambilla:	*Introduction to pNRQCD, quarkonium spectroscopy and decays*;
B. Heltsley:	*Crystal Calorimetry in modern particle physics detectors*;
M. Laine:	*Introduction to quarkonium at high temperatures*;
R. Mussa:	*Angular Distributions in Helicity Formalism*;
S. Nikitin:	*Resonant depolarization technique for high precision mass measurement at e^+e^- storage rings*;
C. Patrignani:	*How an experimental measure (quarkonium) enters the data particle*;
M. Rosati:	*Quarkonium and Heavy Ion Experiments*;
J. Soto:	*Introduction to EFTs. Renormalization Group in NRQCD and pNRQCD; SCET and heavy quarkonium.*

Supported by the Chinese Center for Advanced Science and Technology (CCAST), the Institute of Theoretical Physics (ITP), Beijing, the Institute of High Energy Physics (IHEP), Beijing, the Nature Science Foundation of China (NSFC), Peking University, and Tshinghua University

Sponsored by CERN and Fermilab

Agenda and slides available at `http://www.qwg.to.infn.it/TS-oct04/TSAgenda.html`

CONTENTS

Chapter 1

COMMON THEORETICAL TOOLS

Authors: G. Bali, N. Brambilla, J. Soto, A.Vairo

1 QCD[1]

Quantum Chromodynamics (QCD) [1] is the sector of the Standard Model (SM) which is relevant for the strong interactions. It is obtained from the full SM by setting the weak and electromagnetic coupling constants to zero and freezing the scalar doublet to its vacuum expectation value. What remains is a Yang–Mills (YM) theory with local gauge group $SU(3)$ (colour) vectorially coupled to six Dirac fields (quarks) of different masses (flavours). The vector fields in the YM Lagrangian (gluons) live in the adjoint representation and transform like connections under the local gauge group whereas the quark fields live in the fundamental representation and transform covariantly. The QCD Lagrangian reads

$$\mathcal{L}_{\mathrm{QCD}} = -\frac{1}{4}F^a_{\mu\nu}F^{a\,\mu\nu} + \sum_{\{q\}} \bar{q}\left(i\gamma^\mu D_\mu - m_q\right)q\,, \tag{1.1}$$

where $\{q\} = u, d, s, c, b, t$, $F^a_{\mu\nu} = \partial_\mu A^a_\nu - \partial_\nu A^a_\mu + g f^{abc} A^b_\mu A^c_\nu$, $D_\mu = \partial_\mu - i T^a A^a_\mu$. f^{abc} are the $SU(3)$ structure constants and T^a form a basis of the fundamental representation of the $SU(3)$ algebra. When coupled to electromagnetism, gluons behave as neutral particles whereas u, c and t quarks have charges $+2/3$ and d, s and b quarks have charges $-1/3$.

The main properties of QCD follow:

- It is Poincaré, parity, time reversal and (hence) charge conjugation invariant. It is in addition invariant under $U(1)^6$ which implies individual flavour conservation.
- Being a non-Abelian gauge theory, the physical spectrum consists of colour singlet states only. The simplest of these states have the quantum numbers of quark–antiquark pairs (mesons) or of three quarks (baryons), although other possibilities are not excluded.
- The QCD effective coupling constant $\alpha_{\mathrm{s}}(q)$ decreases as the momentum transfer scale q increases (asymptotic freedom) [2,3]. This allows to make perturbative calculations in α_{s} at high energies.
- At low energies it develops an intrinsic scale (mass gap), usually referred as Λ_{QCD}, which provides the main contribution to the masses of most hadrons. At scales $q \sim \Lambda_{\mathrm{QCD}}$, $\alpha_{\mathrm{s}}(q) \sim 1$ and perturbation theory cannot be used. Investigations must be carried out using nonperturbative techniques, the best established of which is lattice QCD.
  Quarks are conventionally divided into light $m_q \ll \Lambda_{\mathrm{QCD}}$, $q = u, d, s$ and heavy $m_Q \gg \Lambda_{\mathrm{QCD}}$, $Q = c, b, t$

$$m_u = 1.5 \div 4.0\,\mathrm{MeV}\,, \quad m_d = 4 \div 8\,\mathrm{MeV}\,, \quad m_s = 80 \div 130\,\mathrm{MeV}\,,$$
$$\tag{1.2}$$
$$m_c = 1.15 \div 1.35\,\mathrm{GeV}\,, \quad m_b = 4.1 \div 4.4\,\mathrm{GeV}\,, \quad m_t = 174.3 \pm 5.1\,\mathrm{GeV}\,.$$

These are $\overline{\mathrm{MS}}$ masses at scale 2 GeV, m_c and m_b for the light quarks, charm and bottom respectively. All values are taken from [4]. The extraction of the values of the heavy quark masses will be discussed in Chapter 6.

---

[1] Author: J. Soto

- If light quark masses are neglected, the $U(1)^3$ flavour conservation symmetry of the QCD Lagrangian in this sector is enlarged to a $U(3) \otimes U(3)$ group. The axial $U(1)$ subgroup is explicitly broken by quantum effects (axial anomaly). The vector $U(1)$ subgroup provides light flavour conservation. The remaining $SU(3) \otimes SU(3)$ subgroup, known as chiral symmetry group, turns out to be spontaneously broken down to the diagonal $SU(3)$ (flavour symmetry). This produces eight Goldstone bosons, which, upon taking into account the explicit breaking of the symmetry due to the non-zero quark masses, acquire masses that are much smaller than Λ_{QCD}.

- Hadrons containing heavy quarks have masses of the order of m_Q rather than of the order Λ_{QCD}. They enjoy particular kinematical features that allow for specific theoretical treatments. The study of hadrons containing two heavy quarks is the aim of this report.

2 EFFECTIVE FIELD THEORIES[2]

From the point of view of QCD the description of hadrons containing two heavy quarks is a rather challenging problem, which adds to the complications of the bound state in field theory those coming from a nonperturbative low-energy dynamics. A proper relativistic treatment of the bound state based on the Bethe–Salpeter equation [5] has proved difficult. Perturbative calculations have turned out unpractical at higher order and the method has been abandoned in recent QED calculations. Moreover, the entanglement of all energy modes in a fully relativistic treatment is more an obstacle than an advantage for the factorization of physical quantities into high-energy perturbative and low energy nonperturbative contributions. Partial semirelativistic reductions and models have been often adopted to overcome these difficulties at the price to introduce uncontrolled approximations and lose contact with QCD. The fully relativistic dynamics can, in principle, be treated without approximations in lattice gauge theories. This is in perspective the best founded and most promising approach. As we will detail in the following, it is not without difficulties at the present for heavy quarkonium.

A nonrelativistic treatment of the heavy quarkonium dynamics, which is suggested by the large mass of the heavy quarks, has clear advantages. The velocity of the quarks in the bound state provides a small parameter in which the dynamical scales may be hierarchically ordered and the QCD amplitudes systematically expanded. Factorization formulas become easier to achieve. A priori we do not know if a nonrelativistic description will work well enough for all heavy quarkonium systems in nature. For instance, the charm quark may not be heavy enough. The fact that most of the theoretical predictions presented in the report are based on such a nonrelativistic assumption and the success of most of them may be seen as a support to the assumption.

On the example of positronium in QED, a nonrelativistic bound state is characterized by at least three scales: the scale of the mass m (called hard), the scale of the momentum transfer $p \sim mv$ (soft) and the scale of the kinetic energy of the quark and antiquark in the centre-of-mass frame $E \sim p^2/m \sim mv^2$ (ultrasoft). The scales mv and mv^2 are dynamically generated, v is the heavy-quark velocity in the centre-of-mass frame. In a nonrelativistic system: $v \ll 1$, and the above scales are hierarchically ordered: $m \gg mv \gg mv^2$. In perturbation theory $v \sim \alpha_{\mathrm{s}}$. Feynman diagrams will get contributions from all momentum regions associated with the scales. Since these momentum regions depend on α_{s} each Feynman diagram contributes to a given observable with a series in α_{s} and a non trivial counting. For energy scales close to Λ_{QCD} perturbation theory breaks down and one has to rely on nonperturbative methods. The wide span of energy scales involved makes also a lattice calculation in full QCD extremely challenging since one needs a space–time grid that is large compared to the largest length of the problem, $1/mv^2$, and a lattice spacing that is small compared to the smallest one, $1/m$. To simulate, for instance, a $b\bar{b}$ state where $m/mv^2 \sim 10$, one needs lattices as large as 100^4, which are beyond present computing capabilities [6] (see also the next sections of the chapter).

We may, however, also take advantage of the existence of a hierarchy of scales by substituting QCD with simpler but equivalent Effective Field Theories (EFTs). EFTs have become increasingly popular

---

[2]Authors: N. Brambilla, A. Vairo

in particle physics during the last decades. They provide a realization of Wilson renormalization group ideas and fully exploit the properties of local quantum field theories. An EFT is a quantum field theory with the following properties: a) it contains the relevant degrees of freedom to describe phenomena that occur in certain limited range of energies and momenta and b) it contains an intrinsic energy scale Λ that sets the limit of applicability of the EFT. The Lagrangian of an EFT is organized in operators of increasing dimension, hence, an EFT is in general non-renormalizable in the usual sense. In spite of this, it can be made finite to any finite order in $1/\Lambda$ by renormalizing (matching) the constants (matching coefficients) in front of the operators in the Lagrangian until that order. This means that one needs more renormalization conditions when the order in $1/\Lambda$ is increased. However, even if the only way of fixing the constants would be by means of experimental data, this would reduce but not spoil the predictive power of the EFT. If the data are abundant, the constants can be fit once for ever and used later on to make predictions on new experiments.

The prototype of EFT for heavy quarks is the Heavy Quark Effective Theory (HQET), which is the EFT of QCD suitable to describe systems with only one heavy quark [7]. These systems are characterized by two energy scales: m and Λ_{QCD}. HQET is obtained by integrating out the scale m and built as a systematic expansion in powers of Λ_{QCD}/m. As discussed above, bound states made of two heavy quarks are characterized by more scales. Integrating out only the scale m, which for heavy quarks can be done perturbatively, leads to an EFT, Nonrelativistic QCD (NRQCD) [6, 8, 9], that still contains the lower scales as dynamical degrees of freedom. Disentangling the remaining scales is relevant both technically, since it enables perturbative calculations otherwise quite complicate, and more fundamentally, since it allows to factorize nonperturbative contributions into the expectation values or matrix elements of few operators. These may be eventually evaluated on the lattice, extracted from the data or calculated in QCD vacuum models. In the last few years, the problem of systematically treating these remaining dynamical scales in an effective theory framework has been addressed by several groups and has now reached a solid level of understanding (a list of references to the original literature can be found in [10–12]). In one approach an additional effective theory (pNRQCD) very close to a quantum-mechanical description of the bound system, containing only the heavy quarkonium field and ultrasoft degrees of freedom, is matched to NRQCD [13–15]. An alternative approach, formulated only for the weak coupling case $mv^2 \gg \Lambda_{\mathrm{QCD}}$, does not involve matching from NRQCD, but instead matches a different effective theory (vNRQCD) to full QCD directly at the hard scale [16–18].

In the next section we will give a brief general introduction to NRQCD, since this is the framework for many applications reviewed in this report. More specific presentations of NRQCD can be found in Chapter 3, Section 2.2, Chapter 4, Section 3.1 and Chapter 5, Section 1.1. NRQCD on the lattice will be presented mainly in the following Section 3.2.3 and in Chapter 3, Section 2.1. In Chapter 4, Section 4.2 a short presentation of SCET, an EFT suited to describe collinear fields interacting with soft degrees of freedom, in combination with NRQCD may be found.

2.1 Nonrelativistic QCD

NRQCD is obtained by integrating out modes of energy and momentum m from QCD Green functions describing heavy quark–antiquark pairs. It is characterized by an ultraviolet (UV) cut-off $\nu_{NR} = \{\nu_p, \nu_s\}$ that satisfies $E, p, \Lambda_{\mathrm{QCD}} \ll \nu_{NR} \ll m$; ν_p is the UV cut-off of the relative three-momentum of the heavy quark and antiquark; ν_s is the UV cut-off of the energy of the heavy quark and antiquark, and of the four-momenta of the gluons and light quarks. NRQCD is, therefore, designated to describe the dynamics of heavy quark–antiquark pairs (not necessarily of the same flavour) at energy scales in the centre-of-mass frame much smaller than their masses. At these energies quark–antiquark pairs cannot be created so it is enough to use Pauli spinors for both the heavy quark and the heavy antiquark degrees of freedom. Other degrees of freedom of the theory are gluons and light quarks of four momentum smaller than ν_s.

The high-energy modes that have been integrated out have a relevant effect on the low-energy physics. This effect is not lost, but encoded into the matching coefficients c and new local interactions of the NRQCD Lagrangian. In principle, there are infinite such terms to be included, in practice only few of

them are needed. Each operator can be counted in v. The velocity v and α_s (in the matching coefficients) are the two small expansion parameters of NRQCD. If we aim at an accuracy of order $(\alpha_s^k \, v^n)$ we have to keep in the Lagrangian only terms and matching coefficients that contribute up to that order to the physical observable under study. The couplings m, g, c are determined by the requirement that NRQCD reproduces the results of QCD up to order $(\alpha_s^k \, v^n)$.

If the quark and antiquark have the same flavour, they can annihilate into hard gluons. In NRQCD their effect is encoded in the imaginary parts of the four-fermion matching coefficients (denoted by f in the following). Their role in the description of heavy quarkonium annihilations in NRQCD will be discussed in Chapter 4.

In general, at each matching step the non-analytic behaviour in the scale that is integrated out becomes explicit in the matching coefficients. Since in this case we are integrating out the mass, it becomes an explicit parameter in the expansion in powers of $1/m$ in the Lagrangian, while the dependence in $\ln(m/\nu)$ is encoded into the matching coefficients.

Up to field redefinitions the NRQCD Lagrangian for one heavy flavour of mass m and n_f massless quarks at $\mathcal{O}(1/m^2)$, but including the kinetic energy term $\mathbf{D}^4/(8m^3)$, reads [8, 9, 19–21]:

$$\mathcal{L}_{\text{NRQCD}} = \mathcal{L}_g + \mathcal{L}_l + \mathcal{L}_\psi + \mathcal{L}_\chi + \mathcal{L}_{\psi\chi}, \tag{1.3}$$

$$\mathcal{L}_g = -\frac{1}{4}F^{\mu\nu a}F^a_{\mu\nu} + c_1^g \frac{1}{4m^2}g f_{abc}F^a_{\mu\nu}F^{\mu\,b}{}_\alpha F^{\nu\alpha\,c}, \tag{1.4}$$

$$\mathcal{L}_l = \sum_{i=1}^{n_f}\bar{q}_i i\slashed{D}q_i + c_1^{ll}\frac{g^2}{8m^2}\sum_{i,j=1}^{n_f}\bar{q}_iT^a\gamma^\mu q_i\,\bar{q}_jT^a\gamma_\mu q_j + c_2^{ll}\frac{g^2}{8m^2}\sum_{i,j=1}^{n_f}\bar{q}_iT^a\gamma^\mu\gamma_5 q_i\,\bar{q}_jT^a\gamma_\mu\gamma_5 q_j$$

$$+c_3^{ll}\frac{g^2}{8m^2}\sum_{i,j=1}^{n_f}\bar{q}_i\gamma^\mu q_i\,\bar{q}_j\gamma_\mu q_j + c_4^{ll}\frac{g^2}{8m^2}\sum_{i,j=1}^{n_f}\bar{q}_i\gamma^\mu\gamma_5 q_i\,\bar{q}_j\gamma_\mu\gamma_5 q_j, \tag{1.5}$$

$$\mathcal{L}_\psi = \psi^\dagger\Bigg\{iD_0 + c_2\frac{\mathbf{D}^2}{2m} + c_4\frac{\mathbf{D}^4}{8m^3} + c_F g\frac{\boldsymbol{\sigma}\cdot\mathbf{B}}{2m}$$

$$+c_D g\frac{\mathbf{D}\cdot\mathbf{E}-\mathbf{E}\cdot\mathbf{D}}{8m^2} + ic_S g\frac{\boldsymbol{\sigma}\cdot(\mathbf{D}\times\mathbf{E}-\mathbf{E}\times\mathbf{D})}{8m^2}\Bigg\}\psi$$

$$+c_1^{hl}\frac{g^2}{8m^2}\sum_{i=1}^{n_f}\psi^\dagger T^a\psi\,\bar{q}_i\gamma_0 T^a q_i + c_2^{hl}\frac{g^2}{8m^2}\sum_{i=1}^{n_f}\psi^\dagger\gamma^\mu\gamma_5 T^a\psi\,\bar{q}_i\gamma_\mu\gamma_5 T^a q_i$$

$$+c_3^{hl}\frac{g^2}{8m^2}\sum_{i=1}^{n_f}\psi^\dagger\psi\,\bar{q}_i\gamma_0 q_i + c_4^{hl}\frac{g^2}{8m^2}\sum_{i=1}^{n_f}\psi^\dagger\gamma^\mu\gamma_5\psi\,\bar{q}_i\gamma_\mu\gamma_5 q_i, \tag{1.6}$$

$$\mathcal{L}_\chi = \text{c.c. of } \mathcal{L}_\psi, \tag{1.7}$$

$$\mathcal{L}_{\psi\chi} = \frac{f_1(^1S_0)}{m^2}O_1(^1S_0) + \frac{f_1(^3S_1)}{m^2}O_1(^3S_1) + \frac{f_8(^1S_0)}{m^2}O_8(^1S_0) + \frac{f_8(^3S_1)}{m^2}O_8(^3S_1), \tag{1.8}$$

$$O_1(^1S_0) = \psi^\dagger\chi\,\chi^\dagger\psi, \qquad O_1(^3S_1) = \psi^\dagger\boldsymbol{\sigma}\chi\,\chi^\dagger\boldsymbol{\sigma}\psi,$$
$$O_8(^1S_0) = \psi^\dagger T^a\chi\,\chi^\dagger T^a\psi, \qquad O_8(^3S_1) = \psi^\dagger T^a\boldsymbol{\sigma}\chi\,\chi^\dagger T^a\boldsymbol{\sigma}\psi,$$

where ψ is the Pauli spinor that annihilates the quark, χ is the Pauli spinor that creates the antiquark, $iD_0 = i\partial_0 - gA_0^a T^a$, $i\mathbf{D} = i\boldsymbol{\nabla} + g\mathbf{A}^a T^a$, $\mathbf{E}^i = F^{i0\,a}T^a$, $\mathbf{B}^i = -\epsilon_{ijk}F^{jk\,a}T^a/2$ and c.c. stands for charge conjugate. The allowed operators in the Lagrangian are constrained by the symmetries of QCD. However, due to the particular kinematical region we are focusing, Lorentz invariance is not linearly

realized in the heavy quark sector. In practice, Lorentz invariance is realized through the existence of relations between the matching coefficients, e.g., $c_2 = c_4 = 1$, $c_S = 2c_F - 1$ [19, 22–26].

The matching coefficients may be calculated in perturbation theory. For the heavy quark (anti-quark) bilinear sector as well as for the purely gluonic sector up to $\mathcal{O}(1/m^2)$ the matching coefficients have been obtained at one loop in [19]. The complete LL running of these coefficients in the basis of operators (1.4)–(1.6) has been calculated in [20, 21][3]. For c_F a NLL evaluation can be found in [28]. In the four heavy fermion sector the matching coefficients f of the $1/m^2$ operators have been obtained at one loop in [29]. As discussed above, in this sector the matching coefficients have a non-zero imaginary part. Due to their relevance in heavy quarkonium decay processes, the calculation of corrections of higher order in α_s has a long history [9, 30–36]. We summarize it in Section 3.1.1 of Chapter 4. An updated list of imaginary parts of four fermion matching coefficients may be found in [37].

Since several scales remain dynamical in NRQCD, it is not possible to give a homogeneous power counting for each operator without extra assumptions, i.e., the power counting in v is not unambiguous. To obtain a better defined power counting one should go to EFTs of lower energy. It should be noticed that the importance of a given operator for a practical calculation does not depend only on its size, but also on the leading power of α_s of the corresponding matching coefficient.

Finally, since modes of energy m have been removed from the Lagrangian, NRQCD lattice simulations may use lattices that are coarser by about a factor $1/v^4$ (~ 100 in the $b\bar{b}$ case) than those needed by full QCD [6]. We will come back to this in Section 3.2.3.

2.2 Lower energy EFTs

Effective field theories suited to describe the low energy modes of the heavy quarkonium dynamics that will be used in this report are pNRQCD and vNRQCD. Here we will not give details on these EFTs since specific introductions to pNRQCD can be found in Chapter 3, Section 2.2.1 and Chapter 4, Section 3.1.3, and to vNRQCD in Chapter 6, Section 5. For detailed recent reviews on effective field theories for heavy quarkonium we refer the reader to [10] and [11], which are mainly devoted to pNRQCD and vNRQCD respectively.

What we want to point out here is that in all these EFTs objects like potentials show up. For short range (or weakly coupled) quarkonia the potentials may be built order by order in perturbation theory. At higher order the pure potential picture breaks down and the interaction of the heavy quark fields with the low-energy gluons has to be taken into account (see the pNRQCD Lagrangian of Chapter 3, Eq. (3.9) and the vNRQCD Lagrangian of Chapter 6, Eqs. (6.20) and (6.21)). For long range (or strongly coupled) quarkonia the potentials are nonperturbative objects that may be expressed in terms of gluon fields expectation values. Noteworthy, the pNRQCD Lagrangian in the strong coupling regime reduces exactly, under some circumstances, to the simple case of a heavy quarkonium field interacting with a potential (see Chapter 3, Eq.(3.11)).

The potential picture that emerges from these EFTs is quite different from the one of traditional potential models and superior. Not only the potential is derived from QCD, but higher-order corrections can be systematically included without being plagued by divergences or *ad hoc* cut-offs; these are absorbed in the renormalization procedure of the EFT. Nevertheless, traditional potential models, which so much have contributed to the early understanding of the heavy quarkonium properties, may be still useful and will often appear in the report. First, a potential model can be seen, in absence of competitive lattice data, as a specific *ansatz* on the form of the low-energy QCD dynamics encoded in the potential defined by an EFT. Second, potential models still provide the only available tool to describe physical systems for which a suitable EFT has not been built yet. This is, for instance, the case of systems coupled to open flavour channels.

---

[3]After correcting a few misprints in the anomalous dimension matrix [27], the results of [21] agree with those of Ref. [20].

3 LATTICE INTRODUCTION[4]

Low energy nonperturbative QCD can either be modelled or simulated on the Lattice. Lattice gauge theory methods are particularly powerful in heavy quark physics when combined with effective field theories (EFTs). Lattice QCD input significantly increases the predictive power of EFTs as more and more low energy parameters can be calculated reliably directly from QCD and less fits to experimental data are required for this purpose. Past lattice QCD results were often obtained within the quenched approximation (neglecting sea quarks) or with unrealistically heavy up and down quarks and $n_f = 2$, rather than $n_f = 2 + 1$. At present these limitations are gradually being removed.

We shall only describe general aspects of lattice gauge theory simulations. Recent reviews of different aspects of Lattice QCD can for instance be found in Refs. [38–48]. Several books [49–54] on the subject have been written and the summary talks of the yearly proceedings of lattice conferences (see Ref. [55] for the most recent ones) provide an overview of the field. Ref. [56] contains collections of early papers.

Obviously there are infinitely many gauge invariant ways to discretize the continuum QCD action. We will summarise and define the actions most commonly used and address limitations of the method, before we discuss extrapolations and sources of systematic errors.

3.1 General aspects

Lattice simulations rely on stochastic (Monte Carlo) methods. Hence all results inevitably carry statistical errors which however are no problem of principle as they can be made arbitrarily small on (arbitrarily) big computers or by means of algorithmic and methodological improvements. In order to carry out path integral quantisation in a mathematically sound ways, the discretisation of space–time appears necessary. This also enables us to map continuous problems onto a finite computer. Discretisation, i.e., for instance replacing derivatives $\partial_t \phi(t)$ by $[\phi(t + a) - \phi(t - a)]/(2a)$ with "lattice spacing" a and, in this example, lattice "errors" of $\mathcal{O}(a^2)$, inevitably carries the smell of *inexactness*. We stress however that the very nature of QCD itself requires us to introduce an ultra-violet regulator and, as we shall see below, lattice discretisation is one possible choice. Continuum results are then obtained by removing the regulator, $a \to 0$.

Observables are calculated ("measured") taking their expectation values in the path integral approach: this amounts to calculating averages over all possible "configurations" of gauge fields on the lattice, weighted with the respective exponent of the action. In simulations with sea quarks, producing these configurations is costly and the ILDG [57] (International Lattice Data Grid) is due to be set up, with the aim of standardising formats of organising and labelling such lattice data, in a way that allows for easy distributed storage, retrieval and sharing of such deposits among different lattice groups.

The typical observables are n-point Green functions. In order to determine a hadronic rest mass one has to construct an operator with the respective quantum numbers: spin J, parity P, charge conjugation C, isospin, flavour content etc. This is then projected onto zero momentum and the 2-point Green function calculated, creating the particle at time 0 and destroying it at time t. For large t this will then decay exponentially, $\propto \exp(-mt)$, with m being the ground state mass within the channel in question. There exist numerous "wave functions" with the right quantum numbers, some with better and some with inferior overlap to the physical ground state. It is a refined art to identify spatial "smearing" or "fuzzing" functions that maximise this overlap and allow to extract the mass at moderate t-values, where the signal still dominates over the statistical noise. The multi-exponential t-dependence of Green functions complicates the identification of excited states, i.e., sub-leading or sub-sub-leading exponents. By working with very precise data, realising a variational multi-state basis of test wave functions [58], and employing sophisticated fitting techniques [59, 60], it has however in some cases become possible to calculate moderately low lying radial excitations.

---

[4]Author: G. Bali

Lattice QCD is formulated in Euclidean space time: in the continuum, this amounts to replacing Lorentz boosts and $O(3)$ rotational symmetry by $O(4)$ rotations. The reason for this is that a real (and bounded) action is required to allow for a probabilistic interpretation of the path integral measure and computer simulation. As an analytical continuation to Minkowski space time of a finite number of finite-precision data points is impossible, the predictive power is confined to quantities that have a Euclidean space time interpretation such as masses and matrix elements.

Lattice discretisation unavoidably breaks rotational $O(4)$ invariance, on the scale of the lattice spacing a. As the continuum limit $a \to 0$ is approached, any fixed physical correlation length ξ will become much larger than the lattice spacing. Provided the interaction ranges that appear within the action are localised in space time, all physics will become independent of the underlying discretisation and a universal continuum limit will be reached, in which $O(4)$ invariance is restored. Asymptotic freedom implies that such a continuum limit is approached as the lattice coupling constant, $g \to 0$.

Replacing $O(4)$ invariance by its hypercubic subgroup means that in particular higher spin states are hard to identify. For instance $J = 4$ cannot easily be distinguished from $J = 0$ on a hypercubic lattice. At finite lattice spacing a, only discrete translations in space and imaginary time are possible. This results in the maximum modulus of Euclidean four-momentum components of π/a, providing the required ultraviolet regularisation. Although an infrared cut-off is not necessary in principle, on a finite computer only a finite number of lattice points can be realised. Typically toroidal boundary conditions are taken in all directions for the gauge fields while fermions, being Grassmann-valued fields, are antiperiodic in time. This results in quantisation of momentum components in steps of $2\pi/(La)$ where L denotes the number of lattice points along the dimension in question: not all momenta can be realised and this leads to kinematic constraints when it comes to calculating decay matrix elements or to extracting a particle mass from a dispersion relation.

The temporal extent aL_τ of the lattice can also be interpreted as an inverse temperature (see e.g., Ref. [61]) and in this case QCD matter at high temperature can be simulated. There are some subtleties related to this approach. For instance the limit of infinite Euclidean time cannot be taken anymore. Details of thermal field theory are discussed in Chapter 7.

While the lattice regulator inevitably violates Poincaré invariance it preserves gauge invariance and most global symmetries of QCD. The exception was chiral symmetry which, one had to hope, would become restored in the continuum limit. However, within the past 10 years, formulations of chiral lattice fermions [62, 63] have evolved that implement an exact lattice chiral symmetry, which in the continuum limit corresponds to the continuum chiral symmetry. These are known as overlap fermions or domain wall fermions (which in some sense are a special case of the former) and in some literature (somewhat inaccurately) as Ginsparg–Wilson fermions since the lattice-Dirac operator used obeys the so-called Ginsparg–Wilson relation [64]. We shall refer to these implementations as chiral fermions.

At presently available light quark masses chiral fermions are typically two orders of magnitude more expensive to simulate than traditional formulations. As the quark mass is decreased chiral fermions become more competitive. Obvious advantages of chiral formulations are the applicability of chiral perturbation theory also at finite lattice spacing and a more continuum-like mixing between many lattice operators. With respect to quarkonia in which both valence quarks are heavy these new developments are at present of limited significance as light quark mass effects are usually sub-leading.

Lattice QCD is a *first principles* approach. No parameters apart from those that are inherent to QCD, i.e., strong coupling constant at a certain scale and quark masses, have to be introduced. In order to fix these $n_f + 1$ parameters $n_f + 1$ low energy quantities are matched to their experimental values. In simulations of quarkonia the lattice spacing $a(\beta, m_i)$, that corresponds to given values of the inverse lattice strong coupling, $\beta = 6/g^2$ and lattice quark masses m_i, is frequently obtained by matching to spin-averaged experimental level splittings. In simulations with un-realistic sea quark content one might hope that this increases the reliability of other predictions as the systematics are partly correlated. With realistic sea quark content the predictive power with respect to quarkonium physics can be enhanced by

using independent input such as the experimental proton mass m_p or the pion decay constant, f_π, instead. A scale that cannot directly be accessed by experiment but which owes its popularity to the accuracy and ease with which it can be calculated is the Sommer scale r_0 [65], implicitly defined through,

$$r^2 \left. \frac{dV(r)}{dr} \right|_{r=r_0} = 1.65 \,, \tag{1.9}$$

where $V(r)$ denotes the static quark–antiquark potential and the numerical value on the right hand side is adjusted such that fits of the bottomonium spectrum to phenomenological or lattice potentials yield $r_0 \approx 0.5$ fm. r_0 is also well-defined in the theory with sea quarks and its model dependence is much smaller than that of the string tension. Within the quenched approximation scale uncertainties cannot be avoided anyway and hence such model dependence is admissible. In simulations with sea quarks this is different but r_0 still provides a convenient reference scale, that can be used to relate different lattice results with each other.

3.2   Actions and finite a effects

We shall discuss the gauge and heavy quark actions that are usually employed. In simulations with sea quarks, in addition a light quark action needs to be specified.

Results from lattice simulations are inevitably obtained at a finite lattice spacing a. Ideally, they are then extrapolated to the physically relevant (and universal) continuum limit $a \rightarrow 0$. Within the quenched approximation, such extrapolations have become the standard while in simulations with light sea quarks a sufficient variation of the lattice spacing is often still prohibitively expensive in terms of computer time. The leading order a behaviour depends on the choice of the discretisation.

One can follow Symanzik [66] and use a continuum effective field theory to show that the cutoff effects have the form $a^n(\ln \Lambda a)^m$, where Λ denotes a low energy scale of the order of a few hundred MeV and $m \geq 0$. The leading power is usually (see below) $n = 1$ or 2 and within this leading term, $m = 0$. By changing the discretisation, the leading terms can be reduced or eliminated. This strategy is called "improvement", and it is used to hasten the approach to the continuum limit.

In a classical mechanical system improvement is straightforward. However, even in this case there exists a break-even point at which further improvement becomes computationally more expensive than the equivalent reduction of the lattice spacing, due to the exploding number of terms and interaction range. Typically this point is reached around $n \approx 5$. In a quantum field theory the situation is more complex. In QCD the (Wilson) coefficients of improvement terms obtain quantum corrections which can be obtained perturbatively as a power series in the strong coupling constant g^2, in a suitable scheme. Following an effective field theory philosophy, such calculations can be done and the size of next order corrections estimated. However, at sufficiently small a any $c_1 g^{2n}(a)a + c_2 a^2$ expression will be dominated by the first term that, in this example, is proportional to a. To eliminate such terms the coefficient has to be determined nonperturbatively. Otherwise little is gained in a continuum limit extrapolation, other than a reduction of the slope of the leading order term. At a given finite a value there is however still some gain from improvement as the results will be more continuum-like. Examples for a systematic nonperturbative improvement programme exist [67].

In the lattice literature often the word "scaling" is meant to imply that an effective continuum limit is reached: within the "scaling region" mass ratios appear to be independent of a, within statistical errors. If a is reduced even further, eventually one will encounter "asymptotic scaling", i.e., lattice masses $a(g)m$ will depend on the coupling g^2 in the way expected from the perturbative two-loop β function. It is quite clear by now that "asymptotic scaling" in terms of the bare lattice coupling might never be achieved on large lattices. However, asymptotic scaling has been verified for a particular choice of the coupling, as a function of the linear extent of tiny lattices, see e.g., Ref. [68].

3.2.1 Gauge actions

In lattice simulations, $SU(3)$ group elements $U_{x,\mu}$ are typically represented as complex 3×3 matrices that live on directed links connecting a lattice site x with the neighbouring site $x + a\hat{\mu}$. Traces of products of such "link variables" or "links" along closed paths (Wilson loops) are gauge invariant. The simplest non-trivial such example is a 1×1 square, an elementary "plaquette". The lattice action should preserve gauge invariance which means that it can be expressed as a sum over such loops. Fermion fields ψ_x and $\bar{\psi}_x$ are living on the lattice sites and a quark can be "transported" from site $x + a\hat{\mu}$ to site x by means of a left multiplication with $U_{x,\mu}$: the combination $\bar{\psi}_x U_{x,\mu} \psi_{x+a\hat{\mu}}$ is gauge invariant.

The simplest gauge action is the so-called Wilson action [69], which is proportional to the trace of the sum over all elementary plaquettes:

$$S_W = -\beta \sum_{x,\mu>\nu} \operatorname{Re} \operatorname{tr} \Pi_{x,\mu,\nu}, \tag{1.10}$$

where x runs over all lattice sites and $\Pi_{x,\mu\nu} = U_{x,\mu} U_{x+a\hat{\mu},\nu} U^\dagger_{x+a\hat{\nu},\mu} U^\dagger_{x,\nu}$. Up to an irrelevant constant the Wilson action agrees with the Euclidean continuum action to $\mathcal{O}(a^2)$:

$$S_{\text{YM}} = \int d^4x \, \frac{1}{4g^2} \sum_{a=1}^{8} F^a_{\mu\nu}(x) F^a_{\mu\nu}(x) = S_W + \text{const.} + \mathcal{O}(a^2), \tag{1.11}$$

where we identify $\beta = 6/g^2$. Asymptotic freedom tells us that $a \to 0$ as $\beta \to \infty$. In simulations without sea quarks it has been established that $\beta = 6$ corresponds to a lattice spacing $a \approx 0.1 \, \text{fm} \approx (2 \, \text{GeV})^{-1}$. With sea quarks (using the same gluonic action) the same lattice spacing will be obtained at a somewhat smaller β-value as the running of $a(g)$ with the coupling g will be somewhat slower. As mentioned above, perturbation theory in terms of the lattice coupling g^2 is not yet reliable around $g^2 \approx 1$, to describe the running of $a(g^2)$ (asymptotic scaling).

The $\mathcal{O}(a^2)$ artifacts within Eq. (1.11) can be replaced by $\mathcal{O}(a^4)$ lattice corrections, by adding two paths consisting of six links, for instance a 1×2 rectangle and a "chair". The result is known as the Symanzik–Weisz action [70] and the coefficients of the individual terms have been calculated to one loop [$\mathcal{O}(g^2)$] accuracy [71]. At tree level, only the coefficient of the rectangle assumes a non-trivial value. One (somewhat arbitrary) choice in the space of actions is the Iwasaki-action [72], again the sum of plaquette and rectangle, but with the relative weight fixed to a constant, originally motivated by demanding invariance of physical mass ratios under numerical renormalisation group transformations, within a certain β window. In addition to simulations with these gauge actions [73–75], there have also been simulations employing a combination of the plaquette in the fundamental and in its adjoint representation [74] as well as simulations on anisotropic lattices, using an anisotropic Wilson action [76–78] or anisotropic variants of actions including Symanzik–Weisz style terms [79].

The main motivation for adding such extra terms to the action is to achieve a more continuum-like behaviour already at finite lattice spacing. It also turns out that simulations with chiral fermions benefit from such a choice which implies a "smoother" gauge field background.

In order to achieve full $\mathcal{O}(a^2)$ improvement the coefficients of the extra terms would have to be determined nonperturbatively, for instance by imposing continuum relations: in the pure gauge theory example above one could impose rotational invariance of the static quark potential at two distances, e.g., $V(3,0,0) = V(2,2,1), V(5,0,0) = V(3,4,0)$ to fix the two coefficients, or use dispersion relations of glueballs or torelons. This is laboursome and in general the fermions will not be nonperturbatively improved beyond $\mathcal{O}(a^2)$ anyway. So in practice, only approximate improvement has been implemented, either by using the perturbative coefficients at a given order or by employing a so-called "tadpole" improvement prescription.

The latter is motivated by two observations. The first one is that short-distance lattice quantities differ considerably from their continuum counterparts, even at lattice spacings at which one would, based

on the $\overline{\text{MS}}$ scheme continuum experience, assume perturbation theory to be valid. For instance around $a^{-1} = 2\,\text{GeV}$ the numerical value for the plaquette with Wilson action reads $\square = \frac{1}{3}\langle \text{tr}\,\Pi \rangle \approx 0.6$ while at $g = 0$ this should obviously be normalised to *one*. This is closely related to the breaking of continuum rotational symmetry on the scale of a lattice spacing a. Parisi [80] hypothesized that such ultra-violet effects could largely be factored out and put into commuting pre-factors. This mean-field improvement amounts to dividing links that appear within lattice operators by constant factors, e.g., $u_0 = \square^{1/4}$. An independent observation is that lattice perturbation theory, whose convergence behaviour in terms of the lattice coupling g^2 is well known to be quite bad, differs from continuum perturbation theory largely by a class of lattice-specific tadpole diagrams which are numerically large. By normalising everything with respect to other "measured" observables like u_0 these contributions cancel at one loop order and one might hope that tadpole dominance and cancellation approximately generalises to higher orders as well [81].

Finally, there is the idea of (classically) "perfect" actions [82]. If one found an action that lies right on top of a renormalisation group trajectory then, independent of the lattice spacing a, one would obtain continuum results. Such actions can be identified by demanding independence of physical results under a change of the underlying scale. An action that contains a finite set of couplings is suggested and these are then optimised with respect to such constraints. In practice, one can of course at best construct an action that is close to such a trajectory in which case decreasing the lattice spacing still helps to reduce deviations of the nearly perfect action from a real renormalisation group trajectory which one attempts to approximate. An example of such an (approximately) perfect action and its construction can be found in Ref. [83].

3.2.2 Light quark actions

The Dirac action is bi-linear in the quark fields. In the language of perturbation theory this amounts to the non-existence of vertices containing an odd number of quark fields. This means that the quark part of a lattice calculation can to some extent be separated from the gauge field evaluation: the gluon fields contain all information of the QCD vacuum, including sea quark loops, provided these are unquenched (see below). Hadronic n-point functions can be obtained from contractions of colour fields, Γ-matrices and quark-propagators, calculated on this gluonic background.

We denote a discretisation of the continuum Euclidean Dirac operator $[D_\mu \gamma_\mu + m_i]$ as $M_i[U]$. Each quark flavour i now contributes a factor,

$$S_{f_i} = (\bar{\psi}, M_i[U]\psi), \tag{1.12}$$

to the action, where the scalar product $(\cdot, \cdot)$ is over all $V = L^3 l_\tau$ sites of Euclidean space time, colour and Dirac-spinor index. Note that M_i depends on the gauge fields U. Components of M_i^{-1} correspond to quark propagators. Often it is sufficient to calculate propagators that originate from only one source point. In this case only one space–time row of the otherwise $12V \times 12V$ matrix M_i^{-1} needs to be calculated. As the non-diagonal contributions to the Dirac operator all originate from a first order co-variant derivative, M_i will be a sparse matrix with non-vanishing elements only in the vicinity of the (space time) diagonal. This tremendously helps to reduce the computational task. Quark propagators can be contracted into hadronic Green functions, expectation values (over gauge configurations) of which will decay with the mass in question in the limit of large Euclidean times.

One complication arises from the fermions as these are represented by anti-commuting Grassmann numbers. Realising these directly on a computer implies a factorial (with the number of lattice points) complexity [84] but fortunately they can be integrated out analytically as,

$$\int [d\psi][d\bar{\psi}] e^{(\bar{\psi}, M_i[U]\psi)} = \det M_i[U] = \int [d\phi][d\phi^+] e^{(\phi^+, M_i^{-1}[U]\phi)}, \tag{1.13}$$

where ϕ and ϕ^+ are auxiliary Boson (pseudo-fermion) fields. The price one pays is that calculating $\det M_i[U]$ (or M_i^{-1}) involves effective interactions over several lattice sites. This renders simulations containing sea quark effects two to three orders of magnitude more expensive than using the quenched (or valence quark) approximation, $\det M_i[U] = \mathrm{const.}$.

As one would expect ratios of light hadron masses from lattice simulations of quenched QCD have been found to be inconsistent with the observed spectrum [85]. However, the differences are typically smaller than 10 %, suggesting that the quenched approximation has some predictive power if cautiously consumed. Apart from the obvious shortcomings like a stable $\Upsilon(4S)$, the consequences of violating unitarity at light quark mass can become dramatic in some channels [86]. Roughly speaking as the axial anomaly does not exist in quenched QCD the η' will be a surplus light Goldstone Boson or, more precisely, a ghost particle. The impact of this can be investigated in quenched chiral perturbation theory.

Ultimately, one needs to include sea quarks and there are three classes of light quark actions: staggered, Wilson-type, and chiral.

After trivially rescaling the quark fields, $\psi_x \to a^{-3/2}\psi_x, \bar{\psi} \to a^{-3/2}\bar{\psi}_x$, to allow for a representation as dimensionless numbers, a naïve discretisation of the Dirac action would read,

$$S_N = \sum_x \left\{ ma\bar{\psi}_x\psi_x + \frac{1}{2}\sum_\mu \gamma_\mu\bar{\psi}_x \left[U_{x,\mu}\psi_{x+a\hat{\mu}} - U^\dagger_{x-a\hat{\mu},\mu}\psi_{x-a\hat{\mu}} \right] \right\}. \tag{1.14}$$

This action corresponds to the continuum action, up to $\mathcal{O}(a^2)$ terms, however, it turns out that it corresponds to 16 mass-degenerate species of Dirac fermions in the continuum limit, rather than to one: the famous fermion-doubling problem [89, 90]. In the lattice literature these species are now often called tastes, instead of flavours, to emphasize that they are unphysical.

It has been noted however that by means of a unitary transformation, the naïve action can be diagonalised in spinor-space, into four identical non-interacting terms, each corresponding to four continuum tastes. The result is the so-called Kogut–Susskind (KS) action [91], in which 16 spin-taste components are distributed within a 2^4 hypercube, a construction that is known in the continuum as Kähler fermions. The advantage is that one taste of KS fermions corresponds to $n_f = 4$ continuum tastes rather than $n_f = 16$. Another nice feature is that even at finite lattice spacing one of the 15 ($n_f^2 - 1$) pions will become exactly massless as $m \to 0$. The price that one pays is strong spin-taste mixing at finite lattice spacing and large coefficients accompanying the leading $\mathcal{O}(a^2)$ lattice artifacts. KS-type fermions are referred to as "staggered" and there are improved versions of them, most notably the Naik action [92], the AsqTad [93] (a squared tadpole improved) action and HYP actions [94, 95] (in which parallel transporters are smeared "iteratively" within hypercubes). The latter two choices notably reduce the tastes mixing interactions.

In order to bring down $n_f = 4$ to $n_f = 1$, as required to achieve $n_f = 2 + 1$, sometimes the determinant within Eq. (1.13) is replaced by its fourth positive root [96, 97]. It can be shown that within perturbation theory this indeed corresponds to replacing the n_f-factors accompanying sea quark loops by $n_f/4$. However, some caution is in place. The operator $\sqrt{M}$ is non-local [98] and if its non-locality altered $\sqrt{\det M} = \det\sqrt{M}$, universality could be lost in the continuum limit. One might argue that A is not the only operator with the property $\det A = \sqrt{\det M}$ but also in the Schwinger model there exist some discouraging results for the behaviour of the topological winding number at small quark masses [99]. Moreover, the valence quark action automatically differs from the one used for the sea quarks as each taste of sea quarks will correspond to 4 tastes of valence quarks [100].

Nonetheless, large scale simulations with this action are pursued at present as the computational costs of going to light sea quark masses appear much smaller than with other actions. Moreover, as long as the sea quark masses are not too small, this approximation to QCD is not completely wrong and in fact likely to be more realistic than quenched QCD. Indeed, in quarkonium physics where light quark

mass effects are sub-leading, first results appear very encouraging [97]. There also exist first theoretical attempts of constructing a local representation of the $n_F < 4$ staggered action [101, 102].

Another "solution" to the fermion doubling problem are Wilson fermions [90]: the lattice analogue of the term, $-\frac{1}{2}aD_\mu D_\mu$, is added to the M of Eq. (1.14). This increases the masses of the 15 doublers by amounts that are proportional to a^{-1}, removing the unwanted modes. Like in the case of staggered fermions the chiral symmetry that QCD classically enjoys at $m = 0$ is explicitly broken at any finite lattice spacing a. In addition, one encounters additive mass renormalisation and a rather awkward eigenvalue spectrum of the lattice Dirac operator as well as $\mathcal{O}(a)$ lattice terms. The latter can be removed by adding yet another counterterm to M: $\propto -ic_{sw}\sigma_{\mu\nu}F_{\mu\nu}$. The resulting action is known as the Sheikholeslami–Wohlert (SW) or clover action [103]. The c_{sw} coefficient is known to one loop [$\mathcal{O}(g^2)$] in perturbation theory [103, 104] but has also been determined nonperturbatively in quenched QCD with Wilson gauge action [67], in $n_f = 2$ QCD with Wilson [105] and $n_f = 3$ QCD with Iwasaki gauge actions [106]. Another variant is the FLIC (fat link irrelevant clover) action [107]. Finally, there exists twisted mass QCD [108], in which an imaginary mass term is introduced into the Wilson action. Unfortunately, in this case there will be mixing between parity partners within Green functions, something that one also encounters in staggered formulations. However, the changed eigenvalue spectrum of M renders smaller quark masses accessible. Moreover, in the case of a purely imaginary renormalized mass parameter, $\mathcal{O}(a)$ improvement holds.

Finally, formulations of chiral lattice fermions exist. These are automatically $\mathcal{O}(a)$ improved and do not suffer from the fermion doubling problem. Realisations of these fall into three categories: overlap fermions, based on the Neuberger action [62], domain wall fermions, which live on a five-dimensional lattice and become chiral as the size of the fifth dimension is sent to infinity [63] and perfect actions [82, 87, 88]. As always there is no free lunch and at presently accessible sea quark masses these formulations are around two orders of magnitude more expensive than the "traditional" quark actions, described above. For this reason, these formulations have not yet been applied to quarkonia (although one quenched study with "chiral" charm quarks exists [109]) but in the future as algorithmic and hardware development will reduce costs, gauge configurations with chiral sea quarks will become increasingly available, in particular also because at lighter quark masses chiral fermions will become more competitive.

3.2.3 Heavy quark actions

To a very good approximation bottom quarks can be neglected from the sea as their presence will only affect the theory at very short distances. This is also true for charm quarks but, depending on the phenomenology one is interested in, to a somewhat lesser extent. In principle nothing speaks against employing the same quark actions as above to the heavy quark sector as well. With a naive treatment of cutoff effects, lattice corrections $\propto (ma)^n$ arise. This suggests that to make contact with the continuum limit, the condition $m < a^{-1}$ has to apply: as m becomes large the lattice spacing has to be made finer and finer, the number of lattice points larger and larger and computational costs will explode, if not for charm then certainly for bottom.

One possible way out would be to introduce an anisotropy, $\xi = a_\sigma/a_\tau$ with a temporal lattice spacing $a_\tau \ll m^{-1}$ while the spatial lattice spacing can be kept coarser. An obvious application of anisotropic actions is finite temperature physics [110] but an anisotropy has also been employed successfully in investigations of pure gauge theories [79, 111] as well as in charmonium physics [76, 78]. Obviously, the anisotropy of the gauge action has to be matched to that of the light quark and heavy quark actions, in order to obtain a sensible continuum limit. This matching certainly becomes very expensive when sea quarks are included and even more so in the presence of improvement terms.

Another starting point are effective field theories, in particular NRQCD which relies on a power counting in terms of the relative heavy quark velocity, v. In addition, EFTs automatically provide the framework for factorisation of physical processes into nonperturbative low energy QCD and perturba-

tive high energy QCD contributions. The fermionic part of the $\mathcal{O}(v^4)$ Euclidean continuum NRQCD Lagrange density with quark fields ψ and antiquark fields χ reads [6, 8],

$$\mathcal{L} = -\psi^\dagger \left[D_4 + H\right] \psi - \chi^\dagger [D_4 - H^\dagger]\chi + \mathcal{L}_{\psi\chi}, \tag{1.15}$$

with

$$
\begin{aligned}
H &=& m + \delta m - c_2 \frac{\mathbf{D}^2}{2m} - c_F \frac{g\boldsymbol{\sigma} \cdot \mathbf{B}}{2m} - c_4 \frac{(\mathbf{D}^2)^2}{8m^3} \\
&-& ic_D \frac{g(\mathbf{D} \cdot \mathbf{E} - \mathbf{E} \cdot \mathbf{D})}{8m^2} + c_S \frac{g\boldsymbol{\sigma} \cdot (\mathbf{D} \times \mathbf{E} - \mathbf{E} \times \mathbf{D})}{8m^2} + \cdots,
\end{aligned}
\tag{1.16}
$$

where the matching coefficients $c_i(m/\mu, g^2) = 1 + \mathcal{O}(g^2)$, $\delta m = \mathcal{O}(g^2)$ are functions of the matching scale μ and coupling g^2. In the continuum $c_2 = c_4 = 1$, however, this is in general different on the lattice, where rotational invariance is broken and to $\mathcal{O}(v^4)$ an additional term $\propto a^2 \sum_i D_i^4/m$ appears. There are many obvious ways of discretising the above equation on the lattice and often the published expressions involve "tadpole" improvement factors $u_0 = 1 + \mathcal{O}(g^2)$. On a lattice with infinite temporal extent it is possible to use a discretisation of the above Hamiltonian within the kernel of a time-symmetric evolution equation [112] such that fields at time $t + a$ can be computed entirely from fields at time t (and vice versa). This turns the computation of propagators particularly economical. In reality, computations are performed on a finite torus but as long as propagators fall off sufficiently fast in Euclidean time, the resulting error of this approximation will be small.

In addition there are the four-fermion interaction terms $\mathcal{L}_{\psi\chi}$ which (in the case of flavour singlet quarkonia) are accompanied by factors $\propto \alpha_s$ and have to be considered at $\mathcal{O}(v^4)$. In principle it is known how to do this in lattice simulations [112]. For the B_c system, where annihilation is not possible, there will be further suppression of these terms by an additional factor α_s. Finally, due to integrating out heavy quark loops, two new purely gluonic operators are encountered [19, 29], accompanied by factors $1/m^2$. This "unquenching" of the heavy quark can in principle easily be implemented in lattice simulations too. However, this is obviously an effect, less important than achieving a realistic light flavour sea quark content.

Starting from a latticized NRQCD action there are in principle different ways to calculate quark propagators. Usually the full fermionic matrix that appears within a lattice discretisation of Eq. (1.16) is inverted, as described above, exploiting a Hamiltonian evolution equation. As an alternative one could also analytically expand the Green functions of interest in powers of $1/m$ and calculate the resulting coefficients individually. It is worthwhile to mention that in the continuum the expression "HQET" refers to heavy-light systems and "NRQCD" to quarkonia. In the lattice literature however, NRQCD is used for both, heavy-heavy and heavy-light system, indicating that the propagator is obtained as the inverse of the lattice NRQCD quark matrix. The term HQET implies an expansion of heavy quark propagators about the static limit. As these are somewhat smeared out in space, NRQCD propagators can be determined more accurately than HQET ones, however, with the invention of new "fat" static quark actions [94] that reduce δm within Eq. (1.16) above this has recently changed.

The m/μ dependence of the matching coefficients c_i has been calculated in the $\overline{\mathrm{MS}}$ scheme to various orders in perturbation theory but so far no result on the ma dependence exists in lattice schemes. This seems to be changing, however [113]. Such corrections are important as in the Coulomb-limit, in which NRQCD power counting rules are formulated, $\alpha_s = \mathcal{O}(v)$. The difference δm between kinetic and rest mass can be determined nonperturbatively from the Υ dispersion relation.

The Fermilab method [114] constitutes a hybrid between heavy quark and light quark methods. It is based on an expansion in terms of the lattice spacing, starting from the Wilson quark action that encompasses the correct heavy quark symmetry. For $ma \ll 1$ this is equivalent to the Symanzik-improvement programme, the lowest order correction resembling the SW/clover term. However, at $ma > 1$ the result is interpreted in terms of the heavy quark terms that one obtains from a $1/m$ expansion. Evidently, the

light-quark clover term has the same structure as the $\sigma \cdot \mathbf{B}$ fine structure interaction, in particular on anisotropic lattices, where the difference can be attributed to the matching coefficients.

An extension of the Fermilab method is an effective field theory framework for describing discretization effects [115]. This theory lumps all discretization effects into short-distance coefficients of the NRQCD/HQET effective Lagrangian. Compared to the continuum HQET or NRQCD, the coefficients now depend on both short distances, m_Q^{-1} and a. This theory is also a natural extension of Symanzik's theory of cutoff effects into the regime $m_Q a \not\ll 1$ [116]. The theory of heavy-quark cutoff effects is not limited to the Fermilab method and can be used to compare the relative size of cutoff effects in various ways of discretising the heavy-quark action [117].

Finally, it is possible to solve NRQCD on the lattice by computing static propagators with field strength insertions, in the spirit of the $1/m$ HQET expansion. This can either be done on the level of quarkonium Green functions (an approach that so far has never been attempted) or within the framework of static potentials and relativistic corrections derived from NRQCD [15, 118]. When constructing Green functions one has to keep the power counting in mind as well as the fact that the lowest order NRQCD Lagrangian goes beyond the static limit as the kinetic term is required. It is also possible to put pNRQCD [14] onto the lattice. In the limit $\Lambda < mv^2$ quarkonia are represented as colour singlet or colour octet states, propagating in the QCD vacuum [119]. This condition is only met for would-be toponium and to some extent for the lowest lying bottomonium states. However, this approach is conceptionally interesting and reduces the number of relevant decay matrix elements.

3.3 Extrapolations

In lattice simulations there are in general three kinds of effects: finite volume effects, lattice artifacts and errors due to wrong light quark masses. Within NRQCD there are additional error sources due to the truncation of the effective field theory at a fixed order in the velocity v and determination of matching coefficients to a given accuracy in α_{s}. In addition to these controlled errors there are error sources that are not controlled by a small parameter like quenching or the use of ill-defined light quark actions. The statistical analysis of lattice data is not trivial but we shall not discuss the possible errors, caveats and pitfalls here as this would be too technical.

Due to the confinement phenomenon and screening of colour, finite size effects are usually quite benign and — once the lattice is sufficiently large — fall off at least like $1/(La)^3$. Because of this it is often sufficient to repeat simulations on 2-3 different volumes to check if finite size effects can be resolved within statistical errors, rather than to attempt proper infinite volume extrapolations. Obviously, higher lying states and charmonia are spatially more extended than lower lying states and bottomonia. In simulations with sea quarks the lattice size has to be large, compared to the pion mass. For instance the condition $La > 4/m_\pi$ yields $La > 5.7$ fm at physical pion mass. There are no large-volume lattice results as yet obtained at such light quark masses. To disentangle possible finite volume from other systematic effects, sequences of lattice simulations at different lattice spacings are often obtained at a volume that is fixed in physical units.

The power n of the dominant finite lattice spacing effect $\mathcal{O}(a^n)$ is in general known and can be fitted to lattice data if sufficient leverage in a is provided. In the context of "improvement" (to a given order of perturbation theory or *ad hoc*) sometimes the coefficient of the leading order term is small since it is suppressed by powers of g^2 such that the sub-leading term has to be accounted for as well. Within the context of effective field theories one cannot extrapolate to the continuum limit as the lattice spacing provides the cut-off scale but one can check independence of the results with respect to variations of a. Once the ma dependences of the short range matching coefficients are determined, the scaling should improve. A notable exception is the Fermilab action which has a continuum limit. However, the functional form in the cross-over region between $ma > 1$ and $ma < 1$ is not as simple as $a^n (\ln a)^m$.

As computer power is limited, lattice sea quark masses are typically not much smaller than the strange quark mass but with the so-called AsqTad "$n_f = 2 + 1$" action values $m \approx 0.2\, m_s$ have been reported [97]. Lattice results have to be chirally extrapolated to the physical limit. Chiral corrections to quarkonium mass splittings are to leading order proportional to m_π^2 [120]. While within present-day lattice calculations of light hadronic quantities as well as of B and D physics, such finite mass effects are frequently the dominant source of systematic error, in the case of quarkonia, the dependence appears to be much milder, due to the absence of a light valence quark content.

If effective field theories are realised or simulations are only available at very few lattice spacings cut-off effects can be estimated by power counting rules and/or by varying the action(s). In the absence of fully unquenched results, some experience can be gained by comparing to experiment, on the likely effect of implementing a wrong number of sea quarks but this error source is not controllable from *first principles*. A real *ab initio* study must go beyond the valence quark approximation.

REFERENCES

[1] H. Fritzsch, M. Gell-Mann and H. Leutwyler, Phys. Lett. B **47**, 365 (1973).

[2] D. J. Gross and F. Wilczek, Phys. Rev. Lett. **30**, 1343 (1973).

[3] H. D. Politzer, Phys. Rev. Lett. **30**, 1346 (1973).

[4] S. Eidelman *et al.* [Particle Data Group Collaboration], Phys. Lett. B **592**, 1 (2004).

[5] E. E. Salpeter and H. A. Bethe, Phys. Rev. **84**, 1232 (1951).

[6] B. A. Thacker and G. P. Lepage, Phys. Rev. D **43**, 196 (1991).

[7] N. Isgur and M. B. Wise, Phys. Lett. **B237**, 527 (1990); M. Neubert, Phys. Rept. **245**, 259 (1994) [arXiv:hep-ph/9306320].

[8] W. E. Caswell and G. P. Lepage, Phys. Lett. B **167**, 437 (1986).

[9] G. T. Bodwin, E. Braaten and G. P. Lepage, Phys. Rev. D **51**, 1125 (1995) [Erratum-ibid. D **55**, 5853 (1997)] [arXiv:hep-ph/9407339].

[10] N. Brambilla, A. Pineda, J. Soto and A. Vairo, arXiv:hep-ph/0410047.

[11] A. H. Hoang, arXiv:hep-ph/0204299.

[12] N. Brambilla, arXiv:hep-ph/0012026; A. Pineda, Nucl. Phys. Proc. Suppl. **93**, 188 (2001) [arXiv:hep-ph/0008327].

[13] A. Pineda and J. Soto, Nucl. Phys. Proc. Suppl. **64**, 428 (1998) [arXiv:hep-ph/9707481].

[14] N. Brambilla, A. Pineda, J. Soto and A. Vairo, Nucl. Phys. B **566**, 275 (2000) [arXiv:hep-ph/9907240].

[15] A. Pineda and A. Vairo, Phys. Rev. D **63**, 054007 (2001) [Erratum-ibid. D **64**, 039902 (2001)] [arXiv:hep-ph/0009145]; N. Brambilla, A. Pineda, J. Soto and A. Vairo, Phys. Rev. D **63**, 014023 (2001) [arXiv:hep-ph/0002250].

[16] M. E. Luke, A. V. Manohar and I. Z. Rothstein, Phys. Rev. D **61**, 074025 (2000) [arXiv:hep-ph/9910209].

[17] A. V. Manohar and I. W. Stewart, Phys. Rev. D **62**, 014033 (2000) [arXiv:hep-ph/9912226].

[18] A. H. Hoang and I. W. Stewart, Phys. Rev. D **67**, 114020 (2003) [arXiv:hep-ph/0209340].

[19] A. V. Manohar, Phys. Rev. D **56**, 230 (1997) [arXiv:hep-ph/9701294].

[20] C. W. Bauer and A. V. Manohar, Phys. Rev. D **57**, 337 (1998) [arXiv:hep-ph/9708306].

[21] B. Blok, J. G. Korner, D. Pirjol and J. C. Rojas, Nucl. Phys. B **496**, 358 (1997) [arXiv:hep-ph/9607233].

[22] M. E. Luke and A. V. Manohar, Phys. Lett. B **286**, 348 (1992) [arXiv:hep-ph/9205228].

[23] Y. Q. Chen, Phys. Lett. B **317**, 421 (1993).

[24] R. Sundrum, Phys. Rev. D **57**, 331 (1998) [arXiv:hep-ph/9704256].

[25] M. Finkemeier, H. Georgi and M. McIrvin, Phys. Rev. D **55**, 6933 (1997) [arXiv:hep-ph/9701243].

[26] N. Brambilla, D. Gromes and A. Vairo, Phys. Lett. B **576**, 314 (2003) [arXiv:hep-ph/0306107].

[27] D. Pirjol, private communication.

[28] G. Amoros, M. Beneke and M. Neubert, Phys. Lett. B **401**, 81 (1997) [arXiv:hep-ph/9701375].

[29] A. Pineda and J. Soto, Phys. Rev. D **58**, 114011 (1998) [arXiv:hep-ph/9802365].

[30] A. Petrelli, M. Cacciari, M. Greco, F. Maltoni and M. L. Mangano, Nucl. Phys. B **514**, 245 (1998) [arXiv:hep-ph/9707223].

[31] R. Barbieri, M. Caffo, R. Gatto and E. Remiddi, Phys. Lett. B **95**, 93 (1980); Nucl. Phys. B **192**, 61 (1981).

[32] P. B. Mackenzie and G. P. Lepage, Phys. Rev. Lett. **47**, 1244 (1981).

[33] F. Maltoni, *Quarkonium phenomenology*, PhD thesis (Univ. of Pisa, 1999) [http://www.fis.uniroma3.it/~maltoni/thesis.ps].

[34] A. Czarnecki and K. Melnikov, Phys. Rev. Lett. **80**, 2531 (1998) [arXiv:hep-ph/9712222].

[35] M. Beneke, A. Signer and V. A. Smirnov, Phys. Rev. Lett. **80**, 2535 (1998) [arXiv:hep-ph/9712302].

[36] R. Barbieri, G. Curci, E. d'Emilio and E. Remiddi, Nucl. Phys. B **154**, 535 (1979); K. Hagiwara, C. B. Kim and T. Yoshino, Nucl. Phys. B **177**, 461 (1981).

[37] A. Vairo, Mod. Phys. Lett. A **19**, 253 (2004) [arXiv:hep-ph/0311303].

[38] G. S. Bali, "QCD forces and heavy quark bound states," Phys. Rept. **343**, 1 (2001) [arXiv:hep-ph/0001312].

[39] M. Creutz, "Aspects of chiral symmetry and the lattice," Rev. Mod. Phys. **73**, 119 (2001) [arXiv:hep-lat/0007032]; "The early days of lattice gauge theory," AIP Conf. Proc. **690**, 52 (2003) [arXiv:hep-lat/0306024].

[40] C. Davies, "Lattice QCD," arXiv:hep-ph/0205181.

[41] T. DeGrand, Int. J. Mod. Phys. A **19**, 1337 (2004) [arXiv:hep-ph/0312241].

[42] M. Di Pierro, "From Monte Carlo integration to lattice quantum chromodynamics: An introduction," arXiv:hep-lat/0009001.

[43] R. Gupta, "Introduction to lattice QCD," arXiv:hep-lat/9807028.

[44] R. Kenway, "Lattice QCD Results And Prospects," Int. J. Mod. Phys. A **18S1** (2003) 1; "Lattice field theory," arXiv:hep-ph/0010219.

[45] A. S. Kronfeld, "Uses of effective field theory in lattice QCD," arXiv:hep-lat/0205021.

[46] M. Lüscher, "Lattice QCD: From quark confinement to asymptotic freedom," Annales Henri Poincare **4**, S197 (2003) [arXiv:hep-ph/0211220]; "Advanced lattice QCD," arXiv:hep-lat/9802029.

[47] C. McNeile, "Heavy quarks on the lattice," arXiv:hep-lat/0210026; "Meson and baryon spectroscopy on a lattice," arXiv:hep-lat/0307027.

[48] G. Münster and M. Walzl, "Lattice gauge theory: A short primer," arXiv:hep-lat/0012005.

[49] E. Seiler, "Gauge Theories As A Problem Of Constructive Quantum Field Theory And Statistical Mechanics," Springer Lecture Notes in Physics **159**, 1 (1982).

[50] M. Creutz, "Quarks, Gluons And Lattices," Cambridge University Press (1982).

[51] C. Itzykson and J. M. Drouffe, "Statistical Field Theory. Vol. 1: From Brownian Motion To Renormalization And Lattice Gauge Theory," Cambridge University Press (1989).

[52] H. J. Rothe, "Lattice Gauge Theories: An Introduction," World Scientific Singapore (1992).

[53] I. Montvay and G. Münster, "Quantum Fields On A Lattice," Cambridge University Press (1994).

[54] J. Smit, "Introduction To Quantum Fields On A Lattice: A Robust Mate," Cambridge University Press (2002).

[55] R. Edwards, J. Negele and D. Richards, "Lattice Field Theory. Proceedings, 20th International Symposium, Lattice 2002, Cambridge, USA, June 24-29, 2002," Nucl. Phys. B, Proc. Suppl. 119 (2003); M. Müller-Preussker *et al.*, "Lattice Field Theory. Proceedings, 19th International Symposium, Lattice 2001, Berlin, Germany, August 19-24, 2001," Nucl. Phys. B, Proc. Suppl. 106 (2002)

[56] C. Rebbi, "Lattice Gauge Theories And Monte Carlo Simulations," World Scientific Singapore (1983); M. Creutz, "Quantum Fields on the computer," World Scientific Singapore (1992).

[57] A. C. Irving, R. D. Kenway, C. M. Maynard and T. Yoshie, Nucl. Phys. Proc. Suppl. **129**, 159 (2004) [arXiv:hep-lat/0309029].

[58] C. Michael and M. Teper, Nucl. Phys. B **314**, 347 (1989).

[59] C. Michael and A. McKerrell, Phys. Rev. D **51**, 3745 (1995) [arXiv:hep-lat/9412087]; C. Michael, Phys. Rev. D **49**, 2616 (1994) [arXiv:hep-lat/9310026].

[60] G. P. Lepage, B. Clark, C. T. H. Davies, K. Hornbostel, P. B. Mackenzie, C. Morningstar and H. Trottier, Nucl. Phys. Proc. Suppl. **106**, 12 (2002) [arXiv:hep-lat/0110175].

[61] J. I. Kapusta, "Finite Temperature Field Theory," Cambridge University Press (1989).

[62] H. Neuberger, Phys. Lett. B **417**, 141 (1998) [arXiv:hep-lat/9707022]; Phys. Lett. B **427**, 353 (1998) [arXiv:hep-lat/9801031]; R. Narayanan, Phys. Rev. D **58**, 097501 (1998) [arXiv:hep-lat/9802018].

[63] D. B. Kaplan, Phys. Lett. B **288**, 342 (1992) [arXiv:hep-lat/9206013]; Y. Shamir, Nucl. Phys. B **406**, 90 (1993) [arXiv:hep-lat/9303005].

[64] P. H. Ginsparg and K. G. Wilson, Phys. Rev. D **25**, 2649 (1982).

[65] R. Sommer, Nucl. Phys. B **411**, 839 (1994) [arXiv:hep-lat/9310022].

[66] K. Symanzik, Nucl. Phys. B **226**, 187 (1983).

[67] M. Lüscher, S. Sint, R. Sommer, P. Weisz and U. Wolff, Nucl. Phys. B **491**, 323 (1997) [arXiv:hep-lat/9609035].

[68] S. Capitani, M. Lüscher, R. Sommer and H. Wittig [ALPHA Collaboration], Nucl. Phys. B **544**, 669 (1999) [arXiv:hep-lat/9810063].

[69] K. G. Wilson, Phys. Rev. D **10**, 2445 (1974).

[70] P. Weisz, Nucl. Phys. B **212**, 1 (1983).

[71] P. Weisz and R. Wohlert, Nucl. Phys. B **236**, 397 (1984) [Erratum-ibid. B **247**, 544 (1984)].

[72] Y. Iwasaki and T. Yoshie, Phys. Lett. B **143**, 449 (1984); Phys. Lett. B **125**, 201 (1983).

[73] S. Necco, Nucl. Phys. B **683**, 137 (2004) [arXiv:hep-lat/0309017].

[74] C. Michael and M. Teper, Nucl. Phys. B **305**, 453 (1988).

[75] A. Ali Khan *et al.* [CP-PACS Collaboration], Phys. Rev. D **65**, 054505 (2002) [Erratum-ibid. D **67**, 059901 (2003)] [arXiv:hep-lat/0105015].

[76] P. Chen, Phys. Rev. D **64**, 034509 (2001) [arXiv:hep-lat/0006019].

[77] G. S. Bali, Phys. Rev. D **62**, 114503 (2000) [arXiv:hep-lat/0006022].

[78] M. Okamoto *et al.* [CP-PACS Collaboration], Phys. Rev. D **65**, 094508 (2002) [arXiv:hep-lat/0112020].

[79] C. J. Morningstar and M. J. Peardon, Phys. Rev. D **60**, 034509 (1999) [arXiv:hep-lat/9901004].

[80] G. Parisi, in "Proc. of the 20th Int. Conf. on High Energy Physics", Madison, Jul 17-23, 1980, eds. L. Durand and L.G. Pondrom, (American Inst. of Physics, New York, 1981).

[81] G. P. Lepage and P. B. Mackenzie, Phys. Rev. D **48**, 2250 (1993) [arXiv:hep-lat/9209022].

[82] P. Hasenfratz and F. Niedermayer, Nucl. Phys. B **414**, 785 (1994) [arXiv:hep-lat/9308004].

[83] F. Niedermayer, P. Rufenacht and U. Wenger, Nucl. Phys. B **597**, 413 (2001) [arXiv:hep-lat/0007007].

[84] M. Creutz, Phys. Rev. Lett. **81**, 3555 (1998) [arXiv:hep-lat/9806037].

[85] S. Aoki *et al.* [CP-PACS Collaboration], Phys. Rev. D **67**, 034503 (2003) [arXiv:hep-lat/0206009].

[86] W. A. Bardeen, A. Duncan, E. Eichten, N. Isgur and H. Thacker, Phys. Rev. D **65**, 014509 (2002) [arXiv:hep-lat/0106008].

[87] P. Hasenfratz, S. Hauswirth, K. Holland, T. Jorg, F. Niedermayer and U. Wenger, Int. J. Mod. Phys. C **12**, 691 (2001) [arXiv:hep-lat/0003013].

[88] C. Gattringer *et al.* [BGR Collaboration], Nucl. Phys. B **677**, 3 (2004) [arXiv:hep-lat/0307013].

[89] H. B. Nielsen and M. Ninomiya, Nucl. Phys. B **185**, 20 (1981) [Erratum-ibid. B **195**, 541 (1982)].

[90] K. Wilson, in *New Phenomena in Subnuclear Physics*, Erice 1975, ed. A. Zichichi, Plenum Press, New York (1977).

[91] L. Susskind, in *Weak and Electromagnetic Interactions At High Energies*, Les Houches 1976, North Holland, Amsterdam (1977); Phys. Rev. D **16**, 3031 (1977).

[92] S. Naik, Nucl. Phys. B **316**, 238 (1989).

[93] G. P. Lepage, Phys. Rev. D **59**, 074502 (1999) [arXiv:hep-lat/9809157].

[94] A. Hasenfratz and F. Knechtli, Phys. Rev. D **64**, 034504 (2001) [arXiv:hep-lat/0103029].

[95] E. Follana, Q. Mason, C. Davies, K. Hornbostel, P. Lepage and H. Trottier [HPQCD Collaboration], Nucl. Phys. Proc. Suppl. **129**, 447 (2004) [arXiv:hep-lat/0311004].

[96] K. M. Bitar *et al.*, Phys. Rev. D **46**, 2169 (1992) [arXiv:hep-lat/9204008].

[97] C. T. H. Davies *et al.* [HPQCD Collaboration], Phys. Rev. Lett. **92**, 022001 (2004) [arXiv:hep-lat/0304004].

[98] B. Bunk, M. Della Morte, K. Jansen and F. Knechtli, arXiv:hep-lat/0403022.

[99] S. Dürr and C. Hoelbling, Phys. Rev. D **69**, 034503 (2004) [arXiv:hep-lat/0311002].

[100] C. Aubin and C. Bernard, Phys. Rev. D **68**, 034014 (2003) [arXiv:hep-lat/0304014].

[101] F. Maresca and M. Peardon, arXiv:hep-lat/0411029.

[102] D. H. Adams, arXiv:hep-lat/0411030.

[103] B. Sheikholeslami and R. Wohlert, Nucl. Phys. B **259**, 572 (1985).

[104] S. Aoki, R. Frezzotti and P. Weisz, Nucl. Phys. B **540**, 501 (1999) [arXiv:hep-lat/9808007].

[105] K. Jansen and R. Sommer [ALPHA collaboration], Nucl. Phys. B **530**, 185 (1998) [Erratum-ibid. B **643**, 517 (2002)] [arXiv:hep-lat/9803017].

[106] S. Aoki *et al.* [CP-PACS Collaboration], Nucl. Phys. Proc. Suppl. **119**, 433 (2003) [arXiv:hep-lat/0211034].

[107] J. M. Zanotti *et al.* [CSSM Lattice Collaboration], Phys. Rev. D **65**, 074507 (2002) [arXiv:hep-lat/0110216].

[108] R. Frezzotti, P. A. Grassi, S. Sint and P. Weisz [Alpha collaboration], JHEP **0108**, 058 (2001) [arXiv:hep-lat/0101001].

[109] S. Tamhankar *et al.*, arXiv:hep-lat/0409128.

[110] S. Datta, F. Karsch, P. Petreczky and I. Wetzorke, Phys. Rev. D **69**, 094507 (2004) [arXiv:hep-lat/0312037].

[111] K. J. Juge, J. Kuti and C. Morningstar, arXiv:hep-lat/0401032.

[112] G. P. Lepage, L. Magnea, C. Nakhleh, U. Magnea and K. Hornbostel, Phys. Rev. D **46**, 4052 (1992) [arXiv:hep-lat/9205007].

[113] H. D. Trottier, Nucl. Phys. Proc. Suppl. **129**, 142 (2004) [arXiv:hep-lat/0310044].

[114] A. X. El-Khadra, A. S. Kronfeld and P. B. Mackenzie, Phys. Rev. D **55**, 3933 (1997) [arXiv:hep-lat/9604004].

[115] A. S. Kronfeld, Phys. Rev. D **62**, 014505 (2000) [arXiv:hep-lat/0002008].

[116] J. Harada *et al.*, Phys. Rev. D **65**, 094513 (2002) [arXiv:hep-lat/0112044]; Phys. Rev. D **65**,

094514 (2002) [arXiv:hep-lat/0112045].

[117] A. S. Kronfeld, Nucl. Phys. Proc. Suppl. **129**, 46 (2004) [arXiv:hep-lat/0310063].

[118] G. S. Bali, K. Schilling and A. Wachter, Phys. Rev. D **56**, 2566 (1997) [arXiv:hep-lat/9703019].

[119] G. S. Bali and A. Pineda, Phys. Rev. D **69**, 094001 (2004) [arXiv:hep-ph/0310130].

[120] B. Grinstein and I. Z. Rothstein, Phys. Lett. B **385**, 265 (1996) [arXiv:hep-ph/9605260].

Chapter 2

COMMON EXPERIMENTAL TOOLS

Convener: R. Mussa

Authors: A. Böhrer, S. Eidelman, T. Ferguson, R. Galik, F. A. Harris, M. Kienzle, A. B. Meyer, A. Meyer, X. H. Mo, V. Papadimitriou, E. Robutti, G. Stancari, P. Wang, B. Yabsley, C. Z. Yuan

1 OVERVIEW[1]

This chapter aims to provide an overview of the experimental facilities which are contributing to provide the wealth of data on heavy quarkonia during the current decade. The experiments can be sorted in 7 broad classes, according to the accelerator which is being used. The world laboratory on heavy quarkonium can count on dedicated experiments working in the most important HEP facilities, such as:

- Three τ-charm factories, described in Section 2: **BES**, which provided record samples of J/ψ's and ψ''s in the last years, and will run a new intensive program at these energies from 2006 on (BES III), **CLEO**, which after 25 years of running at $\Upsilon(nS)$ energies is presently involved in a 3 years program (CLEO-c) across open charm threshold, but also **KEDR** which, exploiting the polarimeter in the VEPP-4 collider, has recently provided high precision measurements of J/ψ and ψ' masses;

- Three B-factories: after CLEO, **BaBar** and **Belle**, described in Section 3, have proved to have a large physics potential also as charmonium factories, through a rich variety of reactions (B decays to charmonium, $\gamma\gamma$, ISR, double $c\bar{c}$), and can easily be exploited to study bottomonium physics;

- One $\bar{p}p$ charmonium factory: the Antiproton Accumulator of the Tevatron, at Fermilab, was exploited by the **E835** experiment, described in Section 4, to scan all known narrow charmonium states in formation from $p\bar{p}$ annihilation.

In these last years, clean record samples of all the narrow vector resonances have been accumulated. Table 2.1 shows the record samples of charmonia produced (or formed) in:

- one B-factory (via B decays, $\gamma\gamma$, radiative return) with 250 fb^{-1} (such quantity is continuously increasing at present);
- the highest statistics runs recently done by the τ-charm factory BES (58 M $J\psi$'s and 14 M $\psi(2S)$)
- the data samples formed in the $p\bar{p}$ charmonium experiment E835

In 2003, CLEO III accumulated the largest data samples of $\Upsilon(1,2,3S)$ states: 29 M, 9 M, 6 M respectively. If the production of Υ states may now stop for a while, the available samples on charmonium are expected to boost in the future years, not only as a result of the steady growth in data from B-factories, but mainly from the dedicated efforts of the CLEO-c project, which aims to take 1 billion J/ψ's in 2006, and the BES III upgrade, from 2007 on. Another $p\bar{p}$ charmonium factory is going to start data taking at GSI in the next decade.

---

[1]Author: R. Mussa

Table 2.1: This table summarizes the numbers of charmonium states produced or formed , not necessarily detected, in the B-factories, τ-charm factories and in $p\bar{p}$.

Particle	$\psi(2S)$	$\eta_c(2S)$	χ_{c2}	χ_{c1}	χ_{c0}	J/ψ	$\eta_c(1s)$
B decays	0.8M	0.4M	0.3M	0.9M	0.75M	2.5M	0.75M
$\gamma\gamma$	–	1.6M	1M	–	1.2M	–	8.0 M
ISR	4M	–	–	–	–	9M	–
$\psi(2S)$ decays	14M	?	0.9M	1.2M	1.2M	8.1M	39K
J/ψ decays	–	–	–	–	–	58M	0.14 M
$p\bar{p}$	2.8M	?	1M	1M	1.2M	0.8M	7M

Beside the dedicated experiments, many other facilities provide not just valuable information on the mechanisms of heavy quarkonium production, but have nonetheless a high chance to discover new states:

– A Z-factory: the four LEP experiments, described in Section 5, studied heavy quarkonium production in $\gamma\gamma$ fusion.

– 2 Hadron Colliders, described in Section 6: Tevatron, where **CDF** and **D0** can investigate the production mechanisms of prompt heavy quarkonium at high energy and RHIC, where Star and Phenix can search in heavy quarkonium suppression the signature of deconfined quark–gluon plasma.

– 1 ep Collider: HERA, described in Section 7, where the experiments **H1** and **ZEUS** can study charmonium photoproduction, and **HERA-B** studies charmonium production in pA interactions.

The list of available sources of new data is far from complete: other Fixed Target Experiments, such as NA50, NA60, study charmonium production in pN, NN interactions.

At the end of the chapter, a set of appendices give details on some of the experimental techniques which are widely employed in this field, for the determination of narrow resonance parameters such as masses, widths and branching ratios. These appendices aim to focus on some of systematic limits that the present generation of high statistics experiments is likely to reach, and give insights on the future challenges in this field:

– Appendix 8.1 explains the physical principle of resonant depolarization, which provides the absolute energy calibration of the narrow vector states of charmonium and bottomonium.

– Results from all e^+e^- scanning experiments crucially depend on the subtraction of radiative corrections on the initial state: a detailed and comprehensive review of the analytical expression which connects the experimental excitation curve to physical quantities such as partial widths and branching ratios is given in Appendix 8.2.

– Scanning techniques using $p\bar{p}$ annihilations are less affected by radiative corrections; the physical limits of the stochastic cooling on antiproton beams are reviewed in Appendix 8.3.

– Appendix 8.4 reviews the available software tools to calculate the luminosity in $\gamma\gamma$ fusion experiments, an issue which may become relevant as we hope to measure $\gamma\gamma$ widths with accuracies better than 10% with the current high statistics samples from B-factories.

– Recent evidences both in e^+e^- and $p\bar{p}$ formation experiments have shown that the interference between continuum and resonant amplitudes can be observed in the charmonium system and may soon lead to a better understanding of some experimental puzzles, and therefore to a substantial reduction on systematic errors on branching fractions. This issue is addressed in Appendix 8.5.

2 τ-CHARM FACTORIES

2.1 BES[2]

BES is a conventional solenoidal magnet detector that is described in detail in Ref. [1]; BES II is the upgraded version of the BES detector, which is described in Ref. [2] and shown in Fig. 2.1. In BES II, a 12-layer vertex chamber (VC) surrounding the 1.2 mm thick beryllium beam pipe provides trigger and track coordinate information. A forty-layer main drift chamber (MDC), located radially outside the VC, provides trajectory and energy loss (dE/dx) information for charged tracks over 85% of the total solid angle. The momentum resolution is $\sigma_p/p = 0.017\sqrt{1 + p^2}$ (p in GeV/c), and the dE/dx resolution for hadron tracks is $\sim 8\%$. An array of 48 scintillation counters surrounding the MDC measures the time-of-flight (TOF) of charged tracks with a resolution of ~ 200 ps for hadrons. Radially outside the TOF system is a 12 radiation length, lead–gas barrel shower counter (BSC), operating in self-quenching streamer mode. This measures the energies of electrons and photons over $\sim 80\%$ of the total solid angle with an energy resolution of $\sigma_E/E = 22\%/\sqrt{E}$ (E in GeV). Surrounding the BSC is a solenoidal magnet that provides a 0.4 Tesla magnetic field over the tracking volume of the detector. Outside of the solenoidal coil is an iron flux return that is instrumented with three double layers of counters that identify muons of momentum greater than 0.5 GeV/c. The BES II parameters are summarized in Table 2.2, and a summary of the BES data sets is given in Table 2.3.
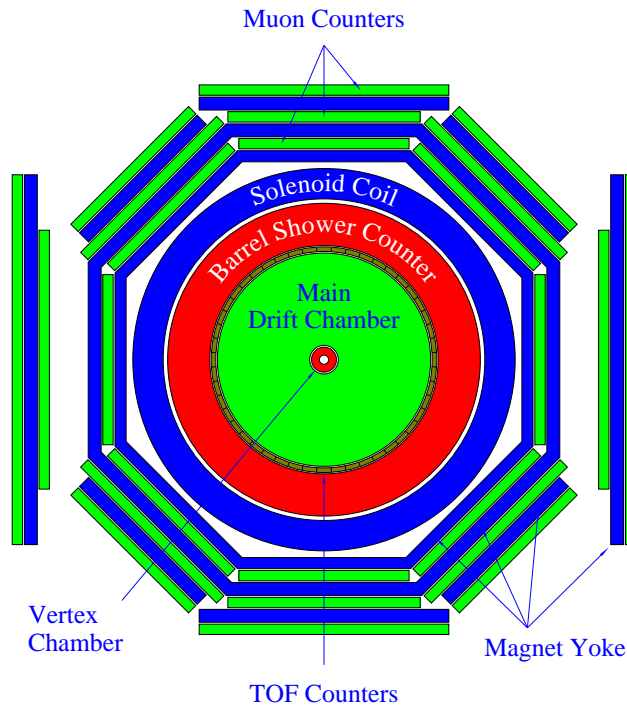
End view of the BES detector

Fig. 2.1: End view of BES (BES II) detector.

2.2 The CLEO detector[3]

2.2.1 *The CLEO III and CLEO-c detectors*

In the twenty-five year history of the CLEO Collaboration there had been a succession of detector upgrades that led from CLEO I to CLEO I.5 to CLEO II [3] to CLEO II.V. In preparation for its last running

---

[2]Author: F. A. Harris
[3]Author: R. Galik

Table 2.2: Summary of BES II detector parameters.

Detector	Major parameter	BES II
VC	$\sigma_{xy}(\mu m)$	100
MDC	$\sigma_{xy}(\mu m)$	190–220
	$\Delta p/p$ (%)	$1.7\sqrt{1+p^2}$
	$\sigma_{dE/dx}$ (%)	8.4
TOF	σ_T (ps)	200
	L_{atten} (m)	$3.5-5.5$
BSC	$\Delta E/\sqrt{E}$ (%)	22%
	σ_z(cm)	2.3
μ counter	σ_z(cm)	5.5
DAQ	dead time (ms)	8

Table 2.3: Summary of BES data sets.

Detector	Physics	E_{CM} (GeV)	Sample
BES I	J/ψ	3.097	7.8×10^6
	m_τ	3.55 scan	5 pb^{-1}
	D_s, D	4.03	22.3 pb^{-1}
	$\psi(2S)$	3.686	3.8×10^6
BES II	R–scan	2–5 scan	6 + 85 points
	$\psi(2S)$-scan	~ 3.686	24 points
	J/ψ	3.097	58×10^6
	$\psi(3770)$ para.	$\psi(3770)$ scan	
	$\psi(2S)$	3.686	14×10^6
	$\psi(3770)$	~ 3.770	~ 27 pb^{-1}
	continuum	3.65	6.4 pb^{-1}

at the $\Upsilon(4S)$[4] there was a large scale modification, primarily aimed at bringing the hadron identification capabilities up to the same high level as the tracking and electromagnetic calorimetry. This configuration, described below, was called CLEO III. All of the $b\bar{b}$ resonance data ($\Upsilon(1S)$, $\Upsilon(2S)$, $\Upsilon(3S)$) and the $\Upsilon(5S)$ running of 2002–3 were taken with this CLEO III configuration. A conference proceeding on the commissioning and initial performance evaluation of CLEO III has been published [4].

The transition to running in the $c\bar{c}$ region called for rethinking the optimization of various components, particularly tracking, in that the magnetic field would be lowered from 1.5 T to 1.0T to accommodate CESR having to handle the solenoid compensation of such "soft" beams. A thorough study was completed and available as a Laboratory preprint [5], often referred to as the "CLEO-c Yellow Book". The modifications are described below and the cut-away view of the detector is shown in Fig. 2.2

2.2.2 CLEO III

As noted above the thrust of the upgrade to CLEO III was to greatly enhance hadronic particle identification without sacrificing the excellent charged particle tracking and electromagnetic calorimetry of

---

[4]The last such $B\bar{B}$ running was in June 2001.

2230104-002
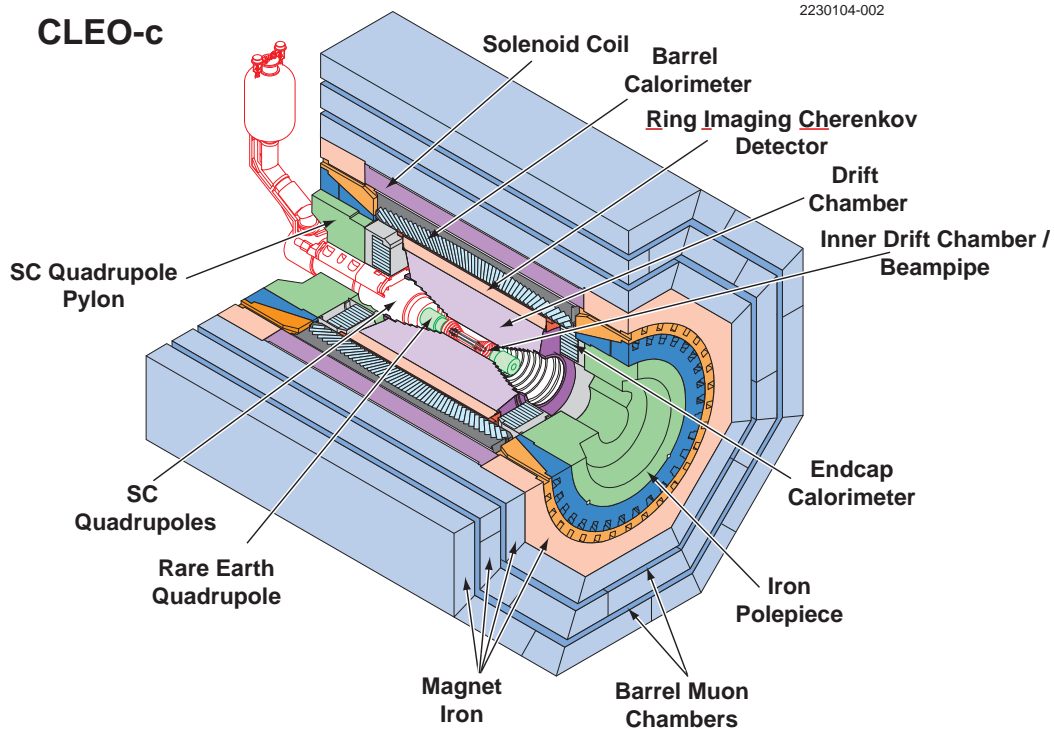
Fig. 2.2: CLEO-c.

CLEO II [3]. CLEO chose to accomplish this with a **ring-imaging Cherenkov (RICH) detector** which has an active region of 81% of 4π, matching that of the barrel calorimeter. Details of the construction and performance have been published [6]; a summary follows.

The RICH construction has LiF radiators of thickness 1cm followed by a nitrogen-filled expansion volume of 16 cm. The Cherenkov photons then pass through a CaF_2 window into the photo-sensitive gas, for which a mixture of triethylamine (TEA) and methane (CH_4) is used. Readout is done on the 250,000 cathode pads that sense the avalanche of electrons liberated in the TEA–CH_4 and accelerated to anode wires. To minimize effects of total internal reflection the LiF radiators in the central region, i.e., nearest the interaction region (IR), have a sawtooth pattern cut on their outer surface.

From Bhabha scattering calibrations, the single photon angular resolution ranges from 13 (nearest the IR) to 19 mrad (furtherest from the IR). The number of *detected* photons averages 12 in the central, sawtooth region and 11 in the outer, flat radiator regions. This leads to a Cherenkov angle determination of resolution better than 5 mrad, except at the very outer edges along the beam direction, in good agreement with simulations of the device.

As always, the performance is a trade-off between fake-rate (mis-ID) and efficiency. Charged kaons and pions in the decay of a D meson in the chain $D^* \to D\pi \to (K\pi)\pi$ can be identified using kinematics. Such a sample shows that below $p = 2\text{GeV}/c$ even 90% efficiency for kaon identification has less than a 2% fake-rate for pions. At $p = 2.6\text{GeV}/c$, the kinematic limit for B decay, 80% efficiency still has only a fake-rate of 8%. These identification capabilities are enhanced by using dE/dx in the drift chamber (described next). The ultimate efficiency/fake performance is very specific to the decay channel of interest.

The RICH takes up some 15 cm in radius more than the previous scintillator system from CLEO II. This meant a new **drift chamber** was to be built that would have the same momentum resolution as that of CLEO II but with reduced radius, spanning 12–82 cm from the beam line. Again, a detailed document has been published [7], of which a summary follows.

Accomplishing this meant minimizing mass (use of a helium based gas, namely 60%He–40%C_3H_8; thin inner support cylinder, 0.12% radiation lengths; aluminum field wires with gold-plating), carefully monitoring hole and wire positions, and paying close attention to field wire geometry. The innermost 16 layers are axial while the outer 31 layers are stereo with sequential superlayers (of four layers each) alternating in the sign of the stereo angle. Both the axial and stereo sections participate in the CLEO III trigger. The end plates consist of a highly tapered assembly for the axial layers (allowing full tracking coverage over 93% of the solid angle) and a slightly conical outer section that minimizes end plate mass (greatly improving the energy resolution of the end cap CsI electromagnetic calorimeter). The outer cylinder is instrumented with cathode strips for additional z measurements.

Spatial resolution within the cells is parametrized by two Gaussians with the narrower constrained to have 80% of the fitted area. Averaged over the full cell this narrow component is 88 μm with the middle of the cell being as good as 65 μm. Some figures of merit from 5 GeV/c Bhabha tracks are a momentum resolution of 55 MeV/c , a z resolution of 1.2 mm from the cathodes and of 1.5 mm from the stereo anodes, and dE/dx resolution of 5.0%, which means K/π separation to 700 MeV/c of hadron momentum. All measures of performance are beyond the design specifications.

To provide extremely accurate track position measurements in both the azimuthal and z coordinates, CLEO had installed a three layer, double sided **silicon vertex detector** [8] which was the distinguishing feature of CLEO II.V. For CLEO III this was upgraded to a four layer device [9] with the smallest radius being 2.5 cm. While the z readout sides performed well throughout the lifetime of CLEO III the $r - \phi$ side quickly showed declining efficiency, in unusual patterns, that has never been explained. This led us to rethink this innermost tracker with the advent of CESR-c (see below).

The other hardware components of CLEO III were the same as for CLEO II. The ∼8000 CsI crystals of the **electromagnetic calorimeter** still perform very well; the endcap regions were re-stacked to allow for better focusing quadrupoles and greatly benefited from the reduced material in the drift chamber endplate. The **muon system** was unchanged as was the **superconducting solenoid** with the exception of some reshaping of the endcap pole pieces. The magnetic field for all the Υ region running was 1.5 T. The **trigger** and **data acquisition** systems were totally revamped for CLEO III, allowing CLEO to be extremely efficient and redundant for even low multiplicity events and have minimal dead time up to read out rates of 1 kHz.

2.2.3   CLEO-c

Very few changes were needed in preparing for the transition to CLEO-c data collection in the $c\bar{c}$ region. Both the average multiplicity and average momenta of charged tracks are lower, so particle identification via the RICH and dE/dx becomes even better than at CLEO III energies. The lowered magnetic field strength of 1.0T means recalibration of the drift chamber, but actually improves the ability to trigger on and find low momentum tracks. The muon chambers become less useful for identifying leptons from the interaction region in that such muons range out in the iron; however, the chambers are still a useful veto of cosmic rays. The CsI calorimeter routinely identifies showers down to 70 MeV, so it needed no modification, other than changing the thresholds in its trigger hardware to accommodate lowered energies of Bhabha scattering events.

The premature aging of the CLEO III silicon meant that we had to either replace it or substitute a small wire chamber. The CLEO-c program does not have the stringent vertexing requirements of CLEO III (the D mesons are at rest in CLEO-c!). Further, track reconstruction is optimized by having fewer scattering surfaces. After detailed studies of mass reconstruction and other figures of merit, it was decided to build a six-layer stereo chamber with similar design as the main drift chamber. In this case the *outer* skin is very thin (∼ 0.1% of a radiation length), so that this small chamber and the larger one look as much as possible like a single volume of gas. The stereo wires (strung at 10–15 degrees) are needed to get z information for low-momentum tracks that do not reach beyond the axial layers of the main chamber.

This new wire chamber has been installed, calibrated, commissioned and fully integrated into CLEO hardware and software; it is highly efficient and has a very low noise occupancy. The first CLEO-c data uses this new device in its track fitting algorithms, although work continues in areas such as calibration and alignment to optimize its contributions to tracking.

2.3 KEDR[5]

The KEDR detector described in detail elsewhere [67] is shown in Fig. 2.3.
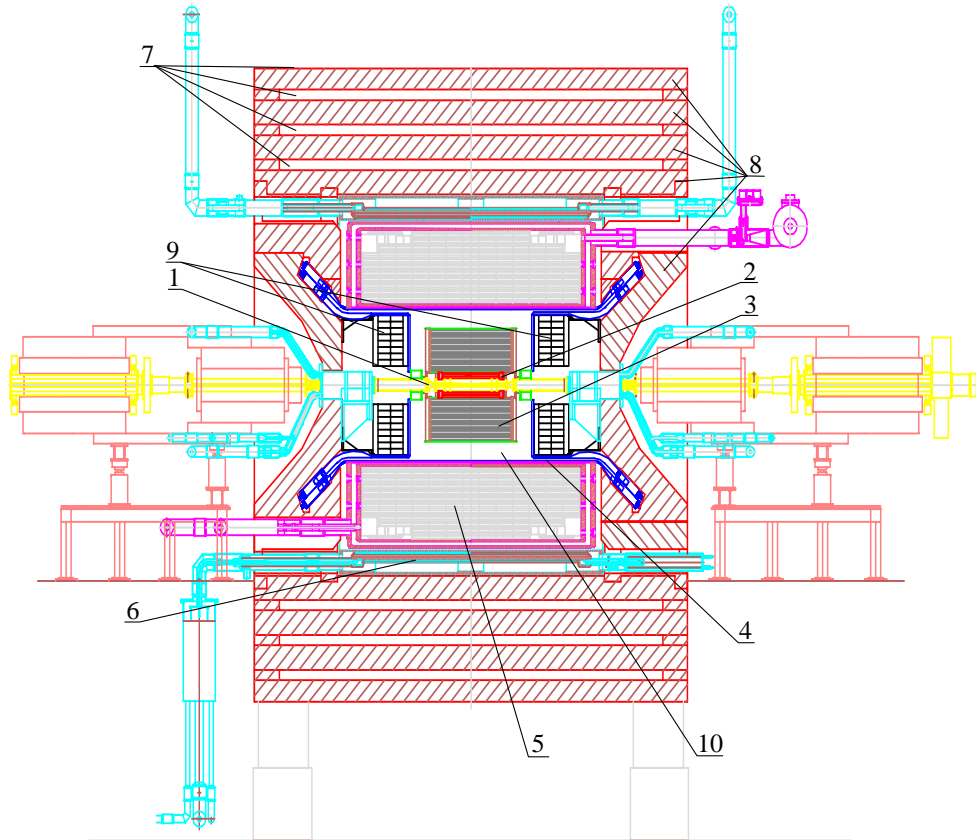
Fig. 2.3: Layout of the KEDR detector: 1 – beam pipe, 2 – vertex detector, 3 – drift chamber, 4 – TOF scintillation counters, 5 – LKr barrel calorimeter, 6 – superconducting coil, 7 – muon tubes, 8 – magnet yoke, 9 – CsI endcap calorimeter, 10 – Aerogel Cherenkov counters

It consists of the vertex detector, the drift chamber, the time-of-flight system of scintillation counters, the particle identification system based on the aerogel Cherenkov counters, the calorimeter (the liquid krypton in the barrel part and the CsI crystals in the end caps) and the muon tube system inside and outside of the magnet yoke. In this experiment the magnetic field was off and the liquid krypton calorimeter as well as aerogel counters were out of operation.

The detection efficiency, determined by the visible peak height and the table value of the leptonic width, is about 0.25 for the J/ψ ($\sim 20 \cdot 10^3$ events) and about 0.28 for the ψ' ($\sim 6 \cdot 10^3$ events).

Luminosity was measured by events of Bhabha scattering detected in the end-cap CsI calorimeter.

---

[5]Author: S. Eidelman

3 B-FACTORIES

3.1 BaBar[6]

BaBar is a general-purpose detector, located at the only interaction point of the electron and positron beams of the PEP-II asymmetric collider at the Stanford Linear Accelerator Center. Although its design has been optimized for the study of time-dependent CP asymmetries in the decay of neutral B mesons, it is well suited for the study of a broad range of physics channels of interest, taking profit from the large samples of data made available by the high luminosity.
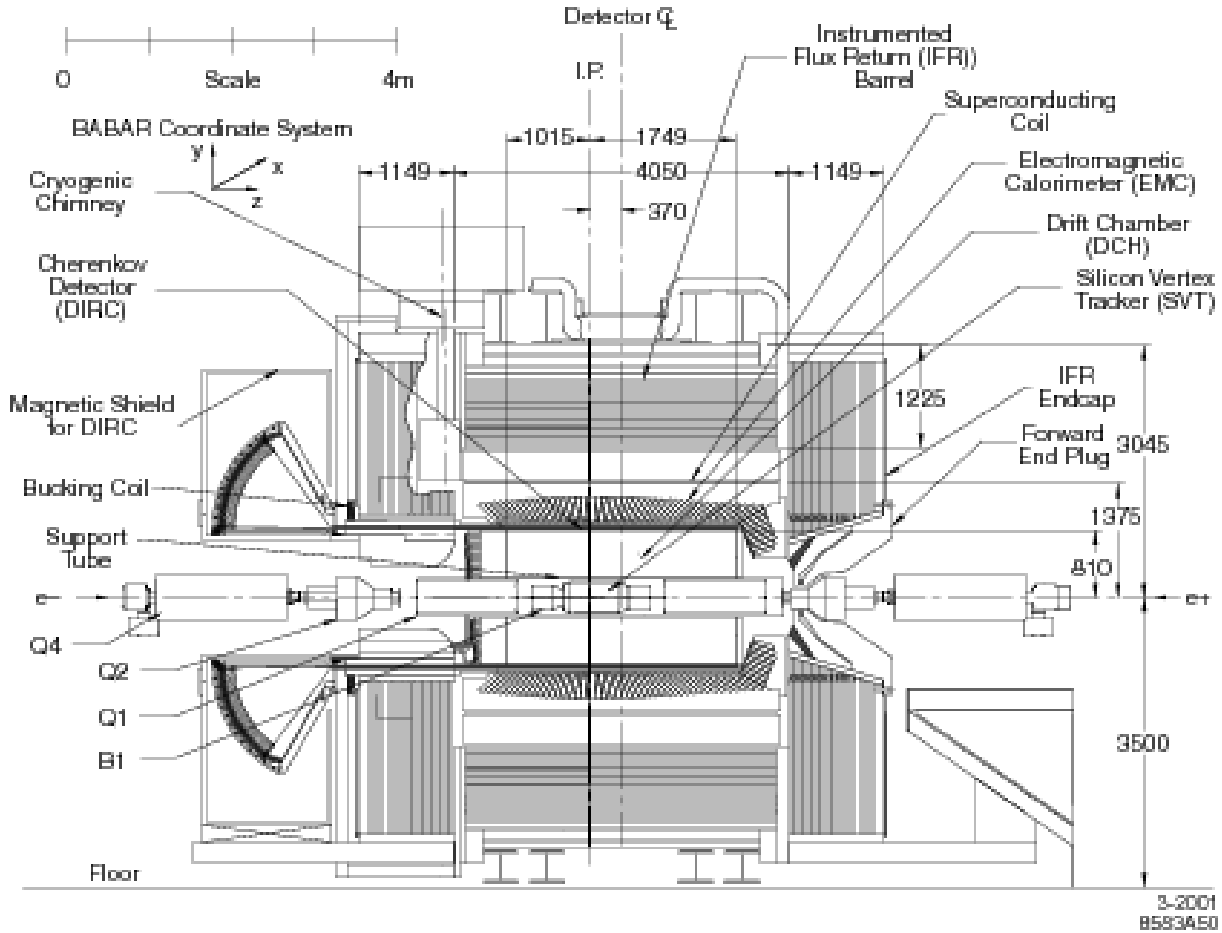
Fig. 2.4: BaBar detector longitudinal section.

The PEP-II B-factory operates at an energy of 10.58 GeV, equal to the mass of the $\Upsilon(4S)$ meson; the colliding electron and positron beams have an energy of 9 and 3.1 GeV, respectively, corresponding to a Lorentz boost of the centre of mass of $\beta = 0.55$. The maximum instantaneous luminosity now exceeds 9×10^{33} cm^{-2}s^{-1}, well above the design value of 3×10^{33} cm^{-2}s^{-1}. The peak cross-section for formation of the $\Upsilon(4S)$ (which then decays exclusively to B^+B^- or $B^0\overline{B}^0$) is about 1 nb; at the same energy, the total cross-section for $e^+e^- \to q\bar{q}$ ($q = u,d,s,c$) is about 3 nb: in particular, $\sigma(e^+e^- \to c\bar{c}) \approx 1.3$ nb. Of particular interest for the study of charmonium states are also events where the effective e^+e^- energy is lowered by the initial emission of a photon (*Initial State Radiation*, or ISR), and $\gamma\gamma$ fusion processes, where the two photons are radiated by the colliding beams: both of them occur at substantial rates in the energy range of the charmonium spectrum.

A longitudinal section and an end view of the BaBar detector are shown in Fig. 2.4 and Fig. 2.5.

---

[6]Author: E. Robutti

respectively. The structure is that typical of full-coverage detectors at collider machines, except for a slight asymmetry in z, with a larger acceptance in the positive direction of the electron beam ("forward"), which reflects the asymmetry in the beam energies.
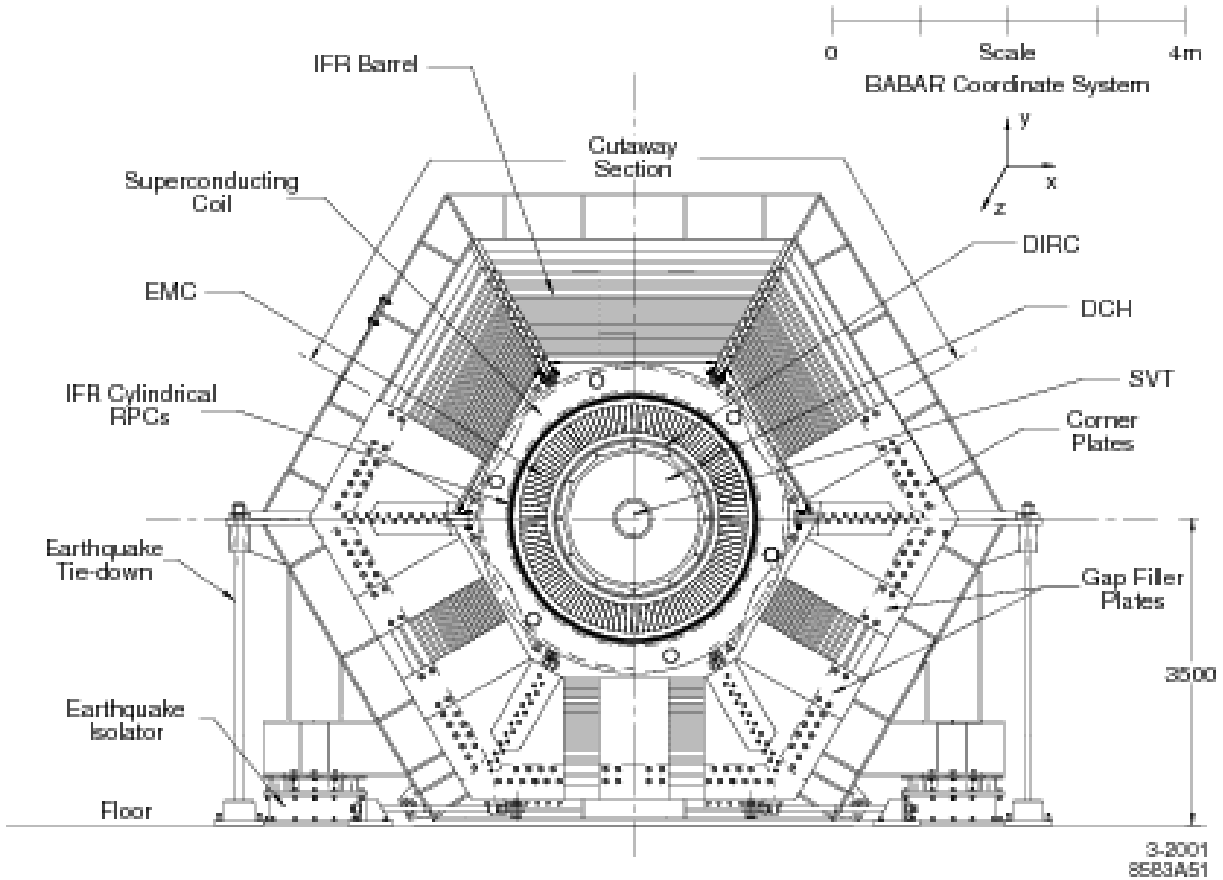
Fig. 2.5: BaBar detector end view.

The inner part of the apparatus is surrounded by a superconducting solenoid providing the 1.5 T magnetic field used for the measurement of particle charges and momenta. It includes the tracking, particle identification and electromagnetic calorimetry systems.

The tracking system is composed of a *Silicon Vertex Tracker* (SVT) and a *Drift CHamber* (DCH). The SVT is a five-layer, double-sided silicon strip detector, which is used for precision measurements of the primary and secondary decay vertices, as well as a stand-alone tracking device for particles with low transverse momentum ($50 - 120$ MeV/c). The DCH is a 40-layer cylindrical drift chamber with a helium–isobutane mixture as the sensitive gas, and is the primary device used for the measurement of particle momenta; it is also used for the reconstruction of secondary vertices outside the outer radius of the SVT. Both detectors provide redundant dE/dx samplings for particle identification of charged hadrons with momenta below ~ 700 MeV/c.

The tracking reconstruction efficiency exceeds 95% for tracks with transverse momentum above 200 MeV/c. The resolution for the track impact parameters is about 25 and 40 μm in the transverse plane and along the detector axis, respectively. The momentum resolution is well described by the linear relation: $\sigma_{p_t}/p_t \simeq 0.45\% + 0.13\% \cdot p_t(\text{GeV}/c)$. The dE/dx resolution at 1 GeV/c is about 7.5%.

Separation of pions and kaons at momenta above 500 MeV/c is provided by the DIRC (*Detector of Internally Reflected Cherenkov light*). This is a novel kind of ring-imaging Cherenkov detector, in which Cherenkov light is produced in bars of fused silica and transported by total internal reflection, preserving

Table 2.4: Overview of the coverage, segmentation, and performance of the BaBar detector systems. The notation (C), (F), and (B) refers to the central barrel, forward and backward components of the system, respectively. The detector coverage in the laboratory frame is specified in terms of the polar angles θ_1 (forward) and θ_2 (backward). Performance numbers are quoted for $1 \ \mathrm{GeV}/c^2$ particles, except where noted.

System	θ_1 (θ_2)	No. Channels	ADC (bits)	TDC (ns)	No. Layers	Segmentation	Performance
SVT	20.1° (–29.8°)	150K	4	–	5	50–100 $\mu m \ r - \phi$ 100–200 μm z	$\sigma_{d_0} = 55 \ \mu$m $\sigma_{z_0} = 65 \ \mu$m
DCH	17.2° (–27.4°)	7,104	8	2	40	6–8 mm drift distance	$\sigma_\phi = 1$ mrad $\sigma_{tan\lambda} = 0.001$ $\sigma_{p_T}/p_T = 0.47\%$ $\sigma(dE/dx) = 7.5\%$
DIRC	25.5° (–38.6°)	10,752	–	0.5		35×17 mm^2 ($r\Delta\phi \times \Delta r$) 144 bars	$\sigma_{\theta_C} = 2.5$mrad per track
EMC(C)	27.1° (–39.2°)	2×5760	17–18	–		47×47 mm^2 5760 cystals	$\sigma_E/E = 3.0\%$ $\sigma_\phi = 3.9$ mrad
EMC(F)	15.8° (27.1°)	2×820				820 crystals	$\sigma_\theta = 3.9$ mrad
IFR(C)	47° (–57°)	22K+2K	1	0.5	19+2	20–38 mm	90% $\mu^\pm$ eff. 6–8% $\pi^\pm$ mis-id
IFR(F)	20° (47°)	14.5K			18	28–38 mm	(loose selection, 1.5–3.0 GeV/c^2)
IFR(B)	–57° (–26°)	14.5K			18	28–38 mm	

the angle of emission, to a water tank viewed by an array of photomulpliers tubes. The pion–kaon separation obtained after association of signals to the tracks ranges from about 10σ at $1 \ \mathrm{GeV}/c$ to about 3σ at $4 \ \mathrm{GeV}/c$.

The *ElectroMagnetic Calorimeter* (EMC) is a finely segmented array of CsI(Tl) crystals with projective geometry. Its energy resolution is well described by the relation $\sigma_E/E \simeq 2.3\% \cdot E(\mathrm{GeV})^{-1/4} \oplus 1.9\%$; the angular resolution ranges from about 12 mrad at low energies to about 3 mrad at high energies; the width of the reconstructed π^0 mass peak is about $7 \ \mathrm{MeV}/c^2$.

Outside the superconducting coil is the detector for muons and neutral hadrons, called *Instrumented Flux Return* (IFR): the iron return yoke of the magnet is segmented into layers of increasing thickness from the inside to the outside, interspersed with Resistive Plate Chambers as the active elements. Muons are identified by criteria exploiting the deepest penetration of their tracks into the iron: a typical efficiency for a selector was about 90% in the momentum range $1.5 < p < 3 \ \mathrm{GeV}/c$ with a pion fake rate for pions of about 6–8%. The RPC have suffered a loss of efficiency since the beginning of operation, causing a small degradation in the performance of muon selectors. In the barrel section of the IFR, they will be substituted by Limited Streamer Tubes, starting from Summer 2004.

Table 2.4 summarizes parameters and performances of the different subsystems composing the BaBar detector.

The trigger system includes a first hardware level, L1, collecting information from the DCH, EMC and IFR, and a software level, L3, selecting events for different classes of processes of physics interest. Output rates are currently around 3 kHz for L1 and 120 Hz for L3. The combined efficiency exceeds 99.9% for $B\overline{B}$ events, and is about 99%, 96% and 92% for $c\bar{c}$, uds and $\tau\tau$ events.

3.2 Belle[7]

The purpose of the Belle experiment is to study time-dependent CP asymmetries in the decay of B-mesons, such as $B^0 \to J/\psi\, K_S^0$, $\pi^+\pi^-$, and ϕK_S^0. The experiment is therefore designed to provide boosted $B^0\overline{B}^0$ pairs, allowing decay-time differences to be measured as differences in B-meson decay position; vertex resolution of order $50\,\mu$m, to measure those decay positions; and high-acceptance tracking and electromagnetic calorimetry, to measure the decay products. Efficient electron and muon identification are required to reconstruct the J/ψ, and kaon/pion separation is required to distinguish kaons (e.g., for B-meson flavour tagging) and pions (e.g., for separation of $B^0 \to \pi^+\pi^-$ from $K^+\pi^-$ decays). Detection of K_L^0 mesons is also desirable, to allow measurement of $B^0 \to J/\psi\, K_L^0$ and ϕK_L^0 modes as a complement to $J/\psi\, K_S^0$ and ϕK_S^0.
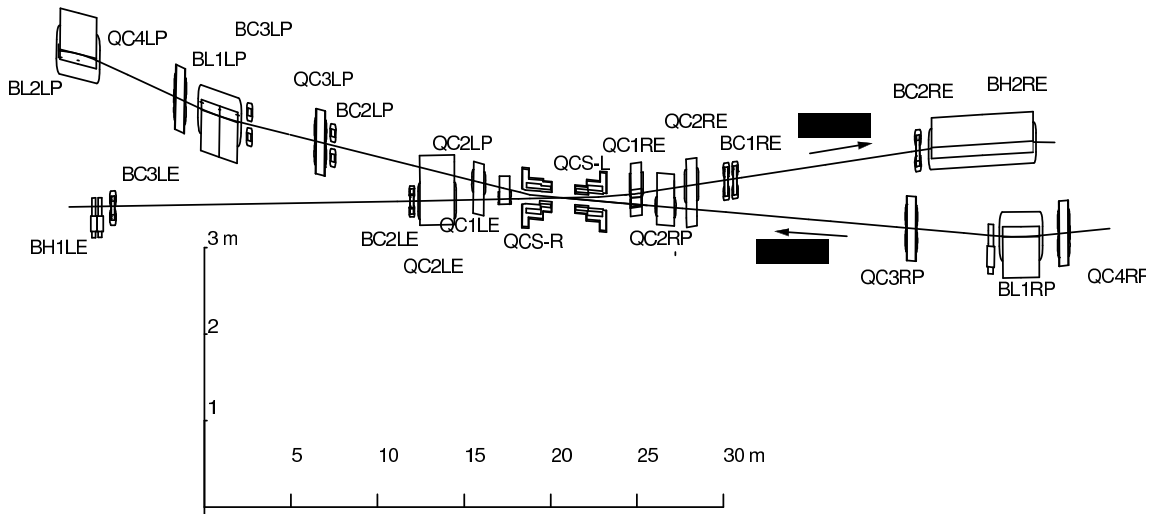
Fig. 2.6: Layout of the KEKB interaction region.

Belle is therefore suited to a wide range of other physics analyses, particularly in the $e^+e^- \to c\bar{c}$ continuum, and in the production and decay of charmonium states. The experiment has an active programme of study in both of these fields.

The detector is located at the interaction point of the KEKB e^+e^- collider [10] at K.E.K. in Tsukuba, Japan. KEKB consists of an injection linear accelerator and two storage rings 3 km in circumference, with asymmetric energies: 8 GeV for electrons and 3.5 GeV for positrons. The e^+e^- centre-of-mass system has an energy at the $\Upsilon(4S)$ resonance and a Lorentz boost of $\beta\gamma = 0.425$. The interaction region is shown in Fig. 2.6: the lower-energy positron beam is aligned with the axis of the Belle detector, and the higher-energy electron beam crosses it at an angle of 22 mrad. This arrangement allows a dense fill pattern without parasitic collisions, and also eliminates the need for separation bend magnets. KEKB's luminosity is the world's highest, exceeding the $10^{34}\,\mathrm{cm}^{-2}\mathrm{s}^{-1}$ design value: with the introduction of continuous beam injection, a record luminosity of $13.9 \times 10^{33}\,\mathrm{cm}^{-2}\mathrm{s}^{-1}$ was achieved in June 2004; further improvements are foreseen with the introduction of crab cavities.

The Belle detector [11], shown in side view in Fig. 2.7, is built into a 1.5 Tesla superconducting solenoid magnet of 1.7 metre radius. (Compensating solenoids and final-focus quadrupole magnets can also be seen on the beamline, inside the main solenoid volume.) The design is that of a classic barrel spectrometer, but with an asymmetry along the beam axis to provide roughly uniform acceptance in the e^+e^- centre-of-mass.

---

[7]Author: B. Yabsley
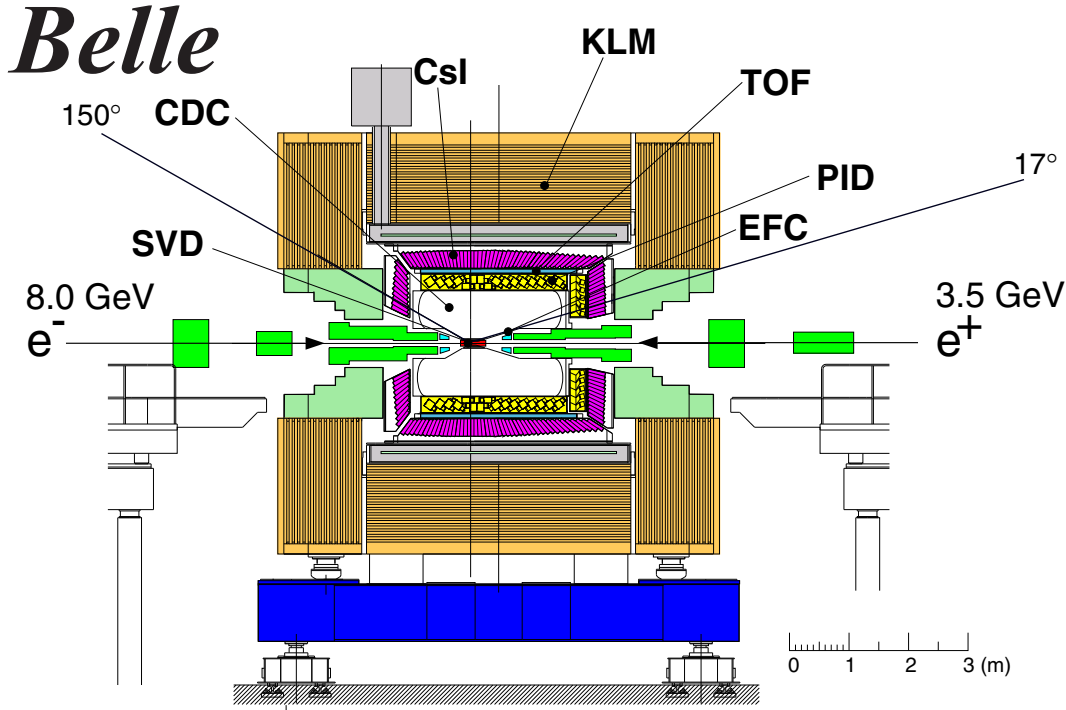
Fig. 2.7: Side view of the Belle detector.

Precision tracking and vertex measurements are provided by a central drift chamber (CDC) and a silicon vertex detector (SVD). The CDC is a small-cell cylindrical drift chamber with 50 layers of anode wires including 18 layers of stereo wires. A low-Z gas mixture (He (50%) and C_2H_6 (50%)) is used to minimize multiple Coulomb scattering, ensuring good momentum resolution for low momentum particles. The tracking acceptance is $17° < \theta < 150°$, where the laboratory polar angle θ is measured with respect to the (negative of the) positron beam axis. The SVD consists of double-sided silicon strip detectors arranged in a barrel, covering 86% of the solid angle. Three layers at radii of 3.0, 4.5 and 6.0 cm surround the beam-pipe, a double-wall beryllium cylinder of 2.3 cm radius and 1 mm thickness. The strip pitches are $42\,\mu$m in the the z (beam-axis) coordinate and $25\,\mu$m for the azimuthal coordinate $r\phi$; in each view, a pair of neighbouring strips is ganged together for readout. The impact parameter resolution for reconstructed tracks is measured as a function of the track momentum p (measured in GeV/c) to be $\sigma_{xy} = [19 \oplus 50/(p\beta\sin^{3/2}\theta)]\,\mu$m and $\sigma_z = [36 \oplus 42/(p\beta\sin^{5/2}\theta)]\,\mu$m. The momentum resolution of the combined tracking system is $\sigma_{p_t}/p_t = (0.30/\beta \oplus 0.19p_t)\%$, where p_t is the transverse momentum in GeV/c.

The subdetectors used in kaon/pion separation are shown in Fig. 2.8: the CDC, a barrel arrangement of time-of-flight counters (TOF), and an array of aerogel Cherenkov counters (ACC). The CDC measures energy loss for charged particles with a resolution of $\sigma(dE/dx) = 6.9\%$ for minimum-ionizing pions. The TOF consists of 128 plastic scintillators viewed on both ends by fine-mesh photo-multipliers that operate stably in the 1.5 T magnetic field. Their time resolution is 95 ps (rms) for minimum-ionizing particles, providing three standard deviation (3σ) $K^{\pm}/\pi^{\pm}$ separation below 1.0 GeV/c, and 2σ up to 1.5 GeV/c. The ACC consists of 1188 aerogel blocks with refractive indices between 1.01 and 1.03 (see Fig. 2.8) depending on the polar angle. Fine-mesh photo-multipliers detect the Cherenkov light: the effective number of photoelectrons is ~ 6 for $\beta = 1$ particles. Information from the three subdetectors is combined into likelihoods $\mathcal{L}_K$, $\mathcal{L}_\pi$ etc. for various particle identification hypotheses, and likelihood ratios such as $\mathcal{R}_{K/\pi} = \mathcal{L}_K/(\mathcal{L}_K + \mathcal{L}_\pi)$ are used as discriminators. A typical selection with $\mathcal{R}_{K/\pi} > 0.6$ retains about 90% of the charged kaons with a charged pion misidentification rate of about 6%.
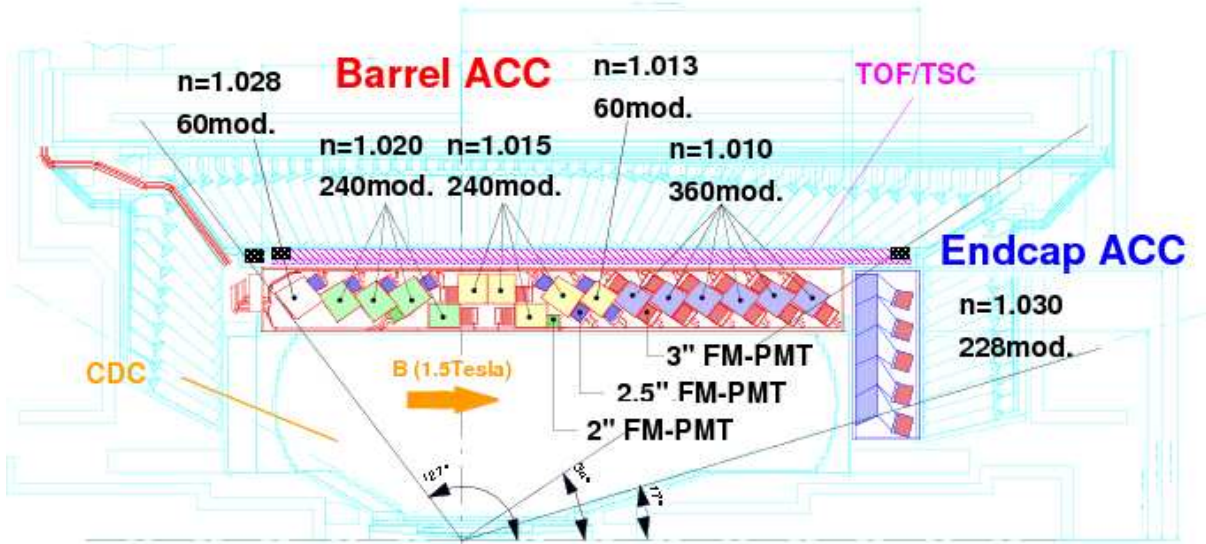
Fig. 2.8: Half-section of the inner region of the Belle detector, showing the layout of the subdetectors used in kaon/pion separation.

Photons and other neutrals are reconstructed in a CsI(Tl) calorimeter consisting of 8736 crystal blocks in a projective geometry, 16.1 radiation lengths deep, covering the same angular region as the CDC. The energy resolution is 1.8% for photons above 3 GeV. Electron identification is based on a combination of dE/dx measurements in the CDC, the response of the ACC, the position and shape of the electromagnetic shower, and the ratio of the cluster energy to the particle momentum. The electron identification efficiency is determined from two-photon $e^+e^- \rightarrow e^+e^-e^+e^-$ processes to be more than 90% for $p > 1.0\,\mathrm{GeV}/c$. The hadron misidentification probability, determined using tagged pions from inclusive $K_S^0 \rightarrow \pi^+\pi^-$ decays, is below 0.5%.

Outside the solenoid, the flux return is instrumented to provide a K_L^0 and muon detector (KLM). The active volume consists of 14 layers of iron absorber (4.7 cm thick) alternating with resistive plate counters (RPCs), covering polar angles $20° < \theta < 155°$. The overall muon identification efficiency, determined by using a two-photon process $e^+e^- \rightarrow e^+e^-\mu^+\mu^-$ and simulated muons embedded in $B\overline{B}$ candidate events, is greater than 90% for tracks with $p > 1\,\mathrm{GeV}/c$ detected in the CDC. The corresponding pion misidentification probability, determined using $K_S^0 \rightarrow \pi^+\pi^-$ decays, is less than 2%.

The Belle trigger and event selection are essentially open for hadronic events, with over 99% efficiency for $B\overline{B}$ and somewhat less for $e^+e^-\rightarrow c\bar{c}$ and light-quark continuum processes. Analysis of such events is performed using a common hadronic event skim; special provision is made to retain events with a J/ψ or $\psi(2S)$ candidate but otherwise low multiplicity. Tau-pair and two-photon $(e^+e^-\rightarrow e^+e^-\gamma\gamma\rightarrow e^+e^-X)$ events are studied using dedicated triggers and data skims.

$154\,\mathrm{fb}^{-1}$ of data were taken in the configuration described above. An upgrade in summer 2003 replaced the SVD and the innermost drift-chamber layers with a four-layer silicon detector covering the same range in polar angle as the CDC. The beam-pipe radius was reduced to 1.5 cm and the inner SVD layer to 2.0 cm, placing the first reconstructed hit of each track closer to the interaction point. Position resolution is similar to that of the original SVD, with strip pitches of $75\,\mu\mathrm{m}$ (z) and $50\,\mu\mathrm{m}$ ($r\phi$); every strip is read out. A further $124\,\mathrm{fb}^{-1}$ has been collected in this configuration through the middle of June

2004. Possible future upgrades to the particle identification system, and further upgrades to the vertexing, are currently under study.

4 $\bar{p}p$ CHARM FACTORIES[8]

4.1 E835

The E835 experiment was located in the Fermilab Antiproton Accumulator, where a stochastically cooled ($\Delta p/p \sim 10^{-4}$) beam intersects an internal jet target of molecular hydrogen. The $\bar{p}$ beam was injected in the Accumulator with an energy of 8.9 GeV and decelerated to the 3.7–6.4 GeV energy range, to form the charmonium states. Stochastic cooling allowed to reduce RMS spreads on $\sqrt{s}$ to less than 250 keV. The E835 experiment was the continuation of the E760 experiment, that took data in years 1990–91, at a typical instantaneous luminosity $\mathcal{L} \sim 0.5 \cdot 10^{31}$. The E760/E835 detector, described in detail in [12], was a non-magnetic cylindrical spectrometer with full azimuthal coverage and polar angle acceptance from 2 to 70 degrees in the lab frame. It consisted of a lead-glass EM calorimeter divided into a barrel and a forward section. The inner part of the barrel was instrumented with a multicell threshold Čerenkov counter, triggering hodoscopes and charged tracking chambers. The plastic scintillator hodoscopes and the Čerenkov were used for triggering: pulse heights from these devices allow to identify electrons/positrons and to distinguish them singly from electron–positron pairs due to γ conversions and to π^0 Dalitz decays.

The E835 detector was a major upgrade of the E760 detector:

– The variable target density allowed to keep a constant instantaneous luminosity ($\mathcal{L} \sim 2 \cdot 10^{31}$) throughout each stack.

– In order to withstand the $\sim$3 MHz interaction rate, all detector channels were instrumented with multi-hit TDCs.

– The inner tracking detector, a proportional multiwire drift chamber, was replaced by an increased number of straw tubes and scintillating fibers, which were used for measuring the polar angle θ and providing trigger information based on this coordinate.

The calorimeter had an energy resolution $\sigma_E/E = 0.014 + 0.06/\sqrt{E(\text{GeV})}$ and an angular resolution (r.m.s.) of 11 mrad in ϕ and 6 mrad in θ. The angular resolution of the inner tracking system was 11 mrad in ϕ, whereas in θ it varies from 3 mrad at small angles to 11 mrad at large angles, dominated by size of the interaction region, and by multiple scattering at lower momenta.

Table 2.5: Integrated luminosities $\mathcal{L}dt$ (in pb^{-1}) taken by E760, E835-I, E835-II

State	Decay Channels	E760	E835-I	E835-II
η_c	$\gamma\gamma$	2.76	17.7	–
J/ψ	e^+e^-	0.63	1.69	–
χ_{c0}	$J/\psi\gamma, \gamma\gamma, 2\pi^0, 2\eta$	–	2.57	32.8
χ_{c1}	$J/\psi\gamma$	1.03	7.26	6.3
$h_c(1P)$ search	$J/\psi\pi^0, \eta_c\gamma$	15.9	46.9	50.5
χ_{c2}	$J/\psi\gamma, \gamma\gamma$	1.16	12.4	1.1
$\eta_c(2S)$ search	$\gamma\gamma$	6.36	35.0	–
ψ'	$e^+e^-, \chi_{cJ}\gamma, J/\psi\pi^0,$			
	$J/\psi\pi^+\pi^-, J/\psi\pi^0\pi^0, J/\psi\eta$	1.47	11.8	15.0
above	J/ψ+X	–	2.6	7.5

---

[8]Author: R. Mussa

E835 EQUIPMENT LAYOUT (Y2K)
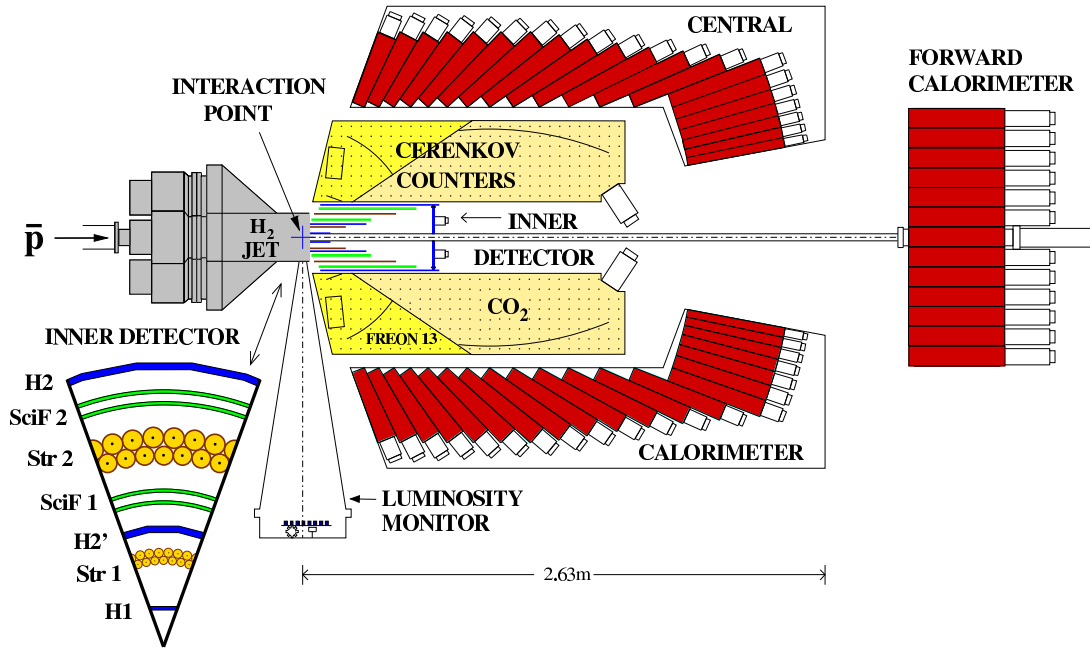
Fig. 2.9: The E835 detector in year 2000.

Table 2.5 summarizes the data taken by the two experiments, subdivided in energy regions. The h_c search region extends from 3523 to 3529 MeV/c^2, i.e., 6 MeV/c^2 around the centre of gravity of P states (located at 3525.3). The $\eta_c(2S)$ was searched between 3575 and 3660 MeV/c^2. Experiment E835 took data in 1996–7 (phase I) and 2000 (phase II). During the long shutdown between the two runs, substantial changes in the Antiproton Source allowed to smoothly scan the χ_{c0} region but prevented to take new data down to J/ψ and η_c energies.

5 EXPERIMENTS AT LEP[9]

At four of the eight straight sections of the LEP e$^+$e$^-$-collider at CERN [13] four collaborations have installed their detectors: ALEPH [14], DELPHI [15], L3 [16], and OPAL [17]. The design of the detectors is guided by the physics of interest. The detectors consist of several subdetectors each dedicated to special aspects of the final state under investigation.

The main physics goal at LEP is the test of the Standard Model. The mass and width of the Z boson are being measured to a high precision. The couplings of the leptons and quarks to γ/Z are investigated. Special emphasis is put on the study of τ-decays. The τ-polarization gives a good insight into the couplings. The high production probability of the heavy flavours, charm and bottom, allows for investigations of effects, such as branching ratios, hadron masses, time dependent mixing etc. Indirect information on the top mass is extracted and the influence from the Higgs mass is studied. Direct Higgs-search is one of the most important topics in the new physics area. Supersymmetric particles, if they exist in the accessible range, should not be able to escape detection. The strong interaction, with confinement and asymptotic freedom still not understood, is to be investigated. The perturbative part (e.g., α_s-determination) and the non-perturbative part, fragmentation and particle production, guided the design of the detectors as well.

---

[9]Authors: A. Böhrer, M. Kienzle

In addition, the general features of the detectors have to keep the systematic uncertainties for their measurements very small to profit from the excellent energy calibration of LEP and to efficiently use the high event statistics.

All LEP detectors have therefore in common, a good hermiticity as well as a good efficiency. The total (hadronic) energy has to be measured as completely as possible. The total absorption guarantees that all particles except neutrinos are seen. Muons also deposit only a small fraction of their energy, but are detected in special muon chambers and by their characteristic signature in the hadron calorimeter. Care for efficient detection and identification of leptons is taken. In general particle identification is provided. Good two-track resolution is possible inside jets of hadrons; energy loss measurements on more than hundred samplings, high granularity of the calorimeters are needed. High precision tracking and vertexing of secondary vertices guaranties good detection and momentum resolution for charged particles, even in the case when they do not come from the primary interaction point.

The trigger system ensures that all events of interest are seen with low background. The triggers of the four LEP detectors have a high redundancy. For example, hadronic events are found when the energy exceeds a few GeV in the electromagnetic calorimeter (total energy trigger), or two tracks are seen together with energy deposition in the hadron calorimeter, which exceeds the energy expected for a minimum ionizing particle (μ-trigger). The efficiency for hadronic events is $\geq 99.99\%$ with an uncertainty of 0.01%.

These requirements lead to four LEP detector designs with a similar general outline, while the detectors differ in their details (see Table 2.6, [18]). The detectors show a cylindrical symmetry around the beam pipe. In the forward direction, calorimeters are installed for the measurement of the luminosity with high precision. The main body has closest to the beam pipe a vertex detector mounted, with precision measurements of the hits from tracks crossing; a general tracking system, which may consist of separate tracking devices; an electromagnetic calorimeter for measuring electrons and photons; a coil of a magnet in order to bend charged particles for the momentum measurement in the tracking devices; a hadron calorimeter for hadronic showers absorbing strong interacting particle, but passed by muons; the latter are detected in the muon chambers, surrounding the experiments.

In the following all four detectors will be described. The ALEPH detector will be presented in some detail. For the other three detectors, special aspects relevant for the subject of this paper are discussed.

5.1 ALEPH detector

The ALEPH detector (Fig. 2.10) [14] shows the typical cylindrical symmetry around the beam pipe. The interaction point of the electron and positron beams is at the centre of the detector. The tracking chambers and the electromagnetic calorimeter are immersed in a solenoidal magnetic field of $1.5\,\mathrm{T}$ produced by the superconducting coil (with a length of $6.4\,\mathrm{m}$ and a diameter of $5.3\,\mathrm{m}$). Outside the coil the hadron calorimeter is used as return yoke.

The beam pipe inside ALEPH, with a length of $5.5\,\mathrm{m}$ extends between the two 'low-β' quadrupoles, which focuses the electron and positron beams onto the interaction point. The tube is made of $1.5\,\mathrm{mm}$ thick aluminium, with an inner diameter of $106\,\mathrm{mm}$. The central part ($760\,\mathrm{mm}$ length), however, is made of beryllium, $1.1\,\mathrm{mm}$ thick.

Closest to the interaction point, the silicon vertex detector (VDET) is installed. It consists of two concentric rings with average radius $6.5\,\mathrm{cm}$ and $11.3\,\mathrm{cm}$. The inner layers has 9 silicon wafers in azimuth, the outer layer has 15 wafers; both layers are four wafers ($5.12 \times 5.12 \times 0.03\,\mathrm{cm}^3$) long in z-direction. The arrangement in azimuth is such that the wafers overlap by 5%. This allows an internal relative alignment with tracks passing through adjacent wafers. The point resolution in the $r - \phi$ and $r - z$ view is $12\,\mu\mathrm{m}$. The hit association of VDET hits to tracks extrapolated from the TPC is found by Monte Carlo to be 98% for tracks in hadronic events with two vertex hits in the acceptance of the vertex detector: $|\cos\theta| < 0.85$.

Table 2.6: Characteristics of the four LEP experiments [14]– [18].

	ALEPH	DELPHI	L3	OPAL
B-field	1.5T	1.2T	0.5T	0.435T
Si VTX	2 layers	3 layers	2 layers	2 layers
	$R\phi\,z$	$R\phi\,z$	$R\phi\,z$	$R\phi\,z$
r=0.1m	$12\mu, 12\mu$	$9\mu, 7.6\mu$		$5\mu, 13\mu$
inner tr.	8pts,150μ,5cm	24pts,100μ	TEC+z.chb	159pts
r=0.3m	drift ch.	jet ch. $R\phi$		135μ,6cm
main tr.	TPC, 1atm	TPC, 1atm	37 pts, 30 to 70 μ	JET 4 atm
detector				
dE/dx	4.6%	5.5%	BGO e.m. cal	3.5%
			4% at 200 MeV	
r=1.1m		RICH,1cmC_6F_{14}	HCAL 60 U plates	
		gas C_5F_{12}	$55\%/\sqrt{E}$	
r=1.8	ECAL 21.5X_0	OD 5pts,150μ	filter 1λ,5pts	z chb 6x300μ
	$18\%/\sqrt{E}$,3sp	HPC 18X_0	support pipe	coil 1.7X_0
r=2.2	coil 1.6X_0	$33\%/\sqrt{E}$,9sp	muon chb	lead glass 20X_0
		coil 2X_0	3sets	$5\%/\sqrt{E}$
r=2.9	HCAL 1.2mFe	HCAL 1.2mFe	lever arm2.7m	HCAL 1mFe
	muon chb	muon chb		muon chb
	2 layers	2 layers		4 layers
r=5.7	lever arm 0.5m	lever arm .3/.6m	coil	lever arm .7m
Lumi.	calorimeter	calorimeter	wire ch.	calorimeter
forward	tungsten/silicon	lead/scint.	BGO+prop.	tube ch.
	24–58mrad	29–185mrad	25–70mrad	58–120mrad

Fig. 2.10: ALEPH detector [14].

Around the vertex detector the inner tracking chamber (ITC) is built with the same polar geometrical acceptance as the vertex detector. This conventional cylindrical drift chamber is filled with 80% argon and 20% carbon dioxide with ethanol. The chamber provides eight measurements in $r - \phi$ in a radial range between $16\,\mathrm{cm}$ and $26\,\mathrm{cm}$, with the wires stretched in z-direction and arranged in eight concentric layers of hexagonal drift cells. In $r - \phi$ the position of hits is measured to $150\,\mu\mathrm{m}$; in z the position is obtained by the measurements of the difference of the arrival time of the pulses at both ends of the $2\,\mathrm{m}$ long wires. The precision reached is $5\,\mathrm{cm}$. However, only the $r - \phi$ measurements are used for the tracking; the information of z can be used for track association with the tracks reconstructed in the TPC. An important aspect of the ITC is that it is the only tracker used for the trigger.

The time projection chamber (TPC) serves as the main tracking chamber in ALEPH. In a volume extending in radius from $0.3\,\mathrm{m}$ to $1.8\,\mathrm{m}$, with a length of $4.4\,\mathrm{m}$ up to 21 space points are measured. The ionization charge is recorded in proportional wire chambers at both ends of the drift volume, reading out cathode pads arranged in 21 concentric circles; up to 338 $\mathrm{d}E/\mathrm{d}x$ samples are used for particle identification. The z coordinate of the hits in the TPC is calculated from the drift time of the electrons collected. For this, the magnet field, electric field both pointing in horizontal direction (and their distortions), and the drift velocity must be known perfectly. These quantities are determined from a measured magnetic field map, by laser calibration and study of reconstructed tracks and their vertices. The resolution is found in $r - \phi$ as $173\,\mu\mathrm{m}$ and in z as $740\,\mu\mathrm{m}$.

In hadronic events, 98.6% of the tracks are reconstructed, when they cross at least four out of 21 pad rows, $|\cos\theta| < 0.966$. The momentum resolution has been determined with di-muon events. The transverse momentum resolution $\sigma(1/p_t)$ is 1.2×10^{-3} (p_t in GeV/c) for the TPC alone; including ITC an VDET the resolution is $\sigma(p_t)/p_t = 0.0006 \cdot p_t \oplus 0.005$ (p_t in GeV/c); $\oplus$ implies that the two errors are added in quadrature.

The TPC is surrounded by the electromagnetic calorimeter (ECAL), which consists of a barrel part and two endcaps, in order to measure electromagnetic energy in an angular range $|\cos\theta| < 0.98$. With its fine segmentation in projective towers of approximately $3\,\mathrm{cm}$ by $3\,\mathrm{cm}$, i.e., $0.9°$ by $0.9°$, the angular resolution is $\sigma_{\theta,\phi} = 2.5/\sqrt{E} + 0.25$ (E in GeV; $\sigma_{\theta,\phi}$ in mrad). The towers are read out in three segments in depth called storeys of 4, 9, and 9 radiation lengths. This lead-proportional tube chamber has an energy resolution for electromagnetic showers of $\sigma_E/E = 0.18/\sqrt{E} + 0.009$ (E in GeV).

The outer shell used as return yoke, is the hadron calorimeter (HCAL). It is made from iron plates of $5\,\mathrm{cm}$ thickness, interleaved with 22 layers of plastic streamer tubes and one layer of tubes in front. The towers are arranged in projective direction to the primary vertex with a solid angle of $3.7°$ by $3.7°$, corresponding to 4×4 of the electromagnetic calorimeter towers. Both the cathode pads defining the towers (pads of different tubes forming one tower are connected galvanically within one storey) and wires in the $1\,\mathrm{cm}$ wide tubes are read out. The latter are used for muon identification and as a trigger. The energy resolution can be parameterized $\sigma_E/E = 0.85/\sqrt{E}$ (E in GeV). In addition, two double layers of streamer tubes are installed around the hadron calorimeter outside the magnetic field and serve as muon detectors.

5.2 DELPHI detector

The layout of the DELPHI detector [15] is shown in Fig. 2.11. The subdetectors are arranged in a cylinder symmetrical arrangement with only the hadron calorimeter and the muon chambers being outside the superconducting coil. The vertex detector closest to the beam pipe is made of silicon wafers. It provides measurements in three layers with information in both z- and $r - \phi$-direction. The single hit resolution is found to be $9\,\mu\mathrm{m}$ and $7.6\,\mu\mathrm{m}$. The vertex detector is surrounded by the inner detector (ID) of a jet-chamber geometry with five multi wire proportional chambers (MWPC) layers. The main tracking device is a Time Projection Chamber (TPC) measuring up to 16 space points per track. Together with the outer detector (OD) with 5 layers of drift tubes the four tracking chambers provide a momentum resolution of $\sigma(p)/p = 0.0006 \cdot p$ (p in GeV/c).
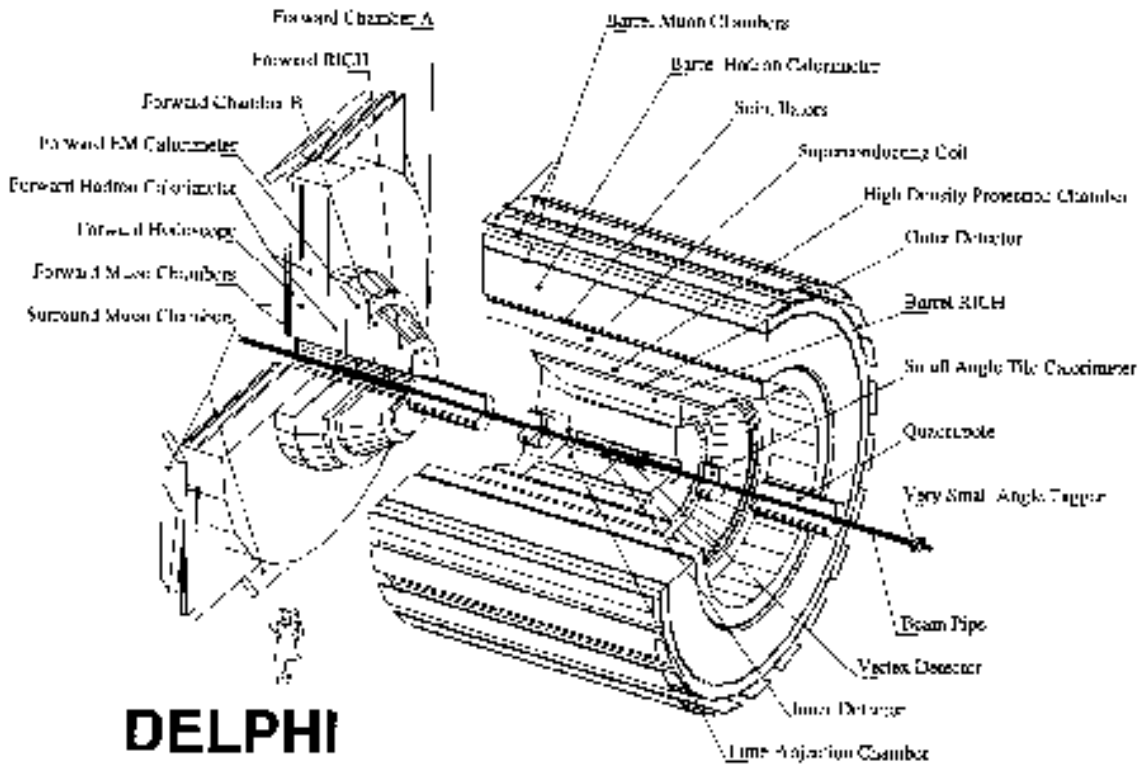
Fig. 2.11: DELPHI detector [15].

A specialty of the DELPHI detector is the Ring Imaging Cherenkov detector (RICH) enclosed by the outer detector. The particle identification in the RICH complements the identification with dE/dx in the TPC. The DELPHI collaboration has chosen to use a gas and a liquid RICH (C_5F_{12} and C_6F_{14}), having two different refractive indices. While the dE/dx measurement is most powerful in the momentum range below $1\,\text{GeV}/c$, the liquid radiator allows for particle identification from $0.7\,\text{GeV}/c$ to $8\,\text{GeV}/c$ and the gaseous radiator from $2.5\,\text{GeV}/c$ to $25\,\text{GeV}/c$, with angular resolution between $1.2\,\text{mrad}$ and $5.2\,\text{mrad}$.

The high density projection chamber (HPC) consists of layers of TPCs, which are separated by lead wires. These wires separate the drift cells and provide the drift field, but also serve as converter material for the electromagnetically interacting particles. The energy deposits on the pads are monitored with π^0's, where one decay photon converted in the material *in front of* the HPC and the momentum is precisely measured: with the π^0 mass as a constraint, the energy resolution is measured to $\sigma(E)/E = 0.33/\sqrt{E} \oplus 0.043$ (E in GeV).

Outside the magnet coil a layer of scintillators is installed, mainly for trigger purposes. The hadron calorimeter (HCAL) made from iron interleaved with limited streamer tubes, serves as return yoke and muon filter, as well. Muon identification is supported by additional muon chambers. The resolution of the HCAL is $\sigma(E)/E = 1.12/\sqrt{E} \oplus 0.21$ (E in GeV).

5.3 L3 detector

The subdetectors in the detector of the L3 collaboration (Fig. 2.12) [16] are mounted inside a support tube with a diameter of $4.45\,\mathrm{m}$ with the exception of the muon detection system. The muon chambers are only surrounded by a very large low field air magnet $(0.5\,\mathrm{T})$. The coil has an inner diameter of $11.9\,\mathrm{m}$. The size of the magnet allows a long lever arm for the muon momentum measurement. This requires a high precision alignment and monitoring of these chambers.
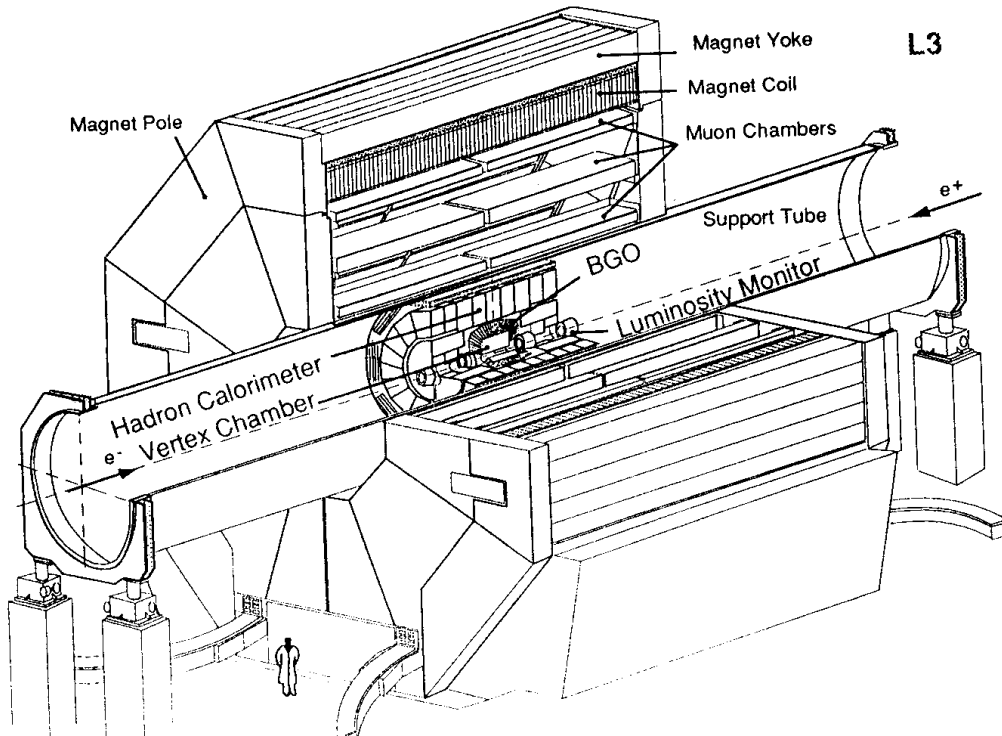
Fig. 2.12: L3 detector [16].

The tracking system consists of a silicon vertex detector and a central track detector. The latter is a Time Expansion Chamber (TEC) providing 37 points on standard wires for the $r - \phi$ measurement; in addition 14 wires resolving left-right ambiguities. The z coordinate is measured on 11 wires by charge division. The surrounding two cylindrical proportional chambers are designed to provide a good z measurement. With a total lever arm of $0.32\,\mathrm{m}$ the momentum resolution is $\sigma(p_t)/p_t^2 = 0.0206 \pm 0.0006$ (p_t in GeV/c).

Muons in $\mathrm{e^+e^-} \rightarrow \mu^+\mu^-$ are measured with the high precision of $\sigma(p)/p \approx 2.5\%$, with the long lever arm to the muon chambers. Apart from the muon detection, special emphasis was put on a high precision measurement for electromagnetic showers. They are measured in a crystal calorimeter read out by photomultipliers. The crystals of bismuth germanium oxide (BGO) have a shape of a truncated pyramid, $24\,\mathrm{cm}$ long and of $2 \times 2\,\mathrm{cm}^2$ at the inner and $3 \times 3\,\mathrm{cm}^2$ at the outer end. The energy resolution varies from 5% at $100\,\mathrm{MeV}$ to 1.4% at high energy.

A layer of scintillation counters is used for time-of-flight measurement. Besides its trigger task, it efficiently rejects cosmic shower events. A uranium calorimeter with proportional wire chambers measures hadronic showers and absorbs most particles except muons. Around this calorimeter a muon filter is mounted, made of brass plates interleaved with five layers of proportional tubes.

5.4 OPAL detector

The OPAL detector (Fig. 2.13) [17] comprises a tracking system inside a solenoidal magnet of $0.435\,\text{T}$, which consists of a vertex detector a jet-chamber and a z-chamber. The new vertex detector of OPAL with two concentric layers of silicon wafers is placed at radii of $6.1\,\text{cm}$ and $7.5\,\text{cm}$. The single hit resolution in $r - \phi$ is $5\,\mu\text{m}$, in z $13\,\mu\text{m}$. The main tracking with the jet-chamber provides up to 159 space points ($\sigma_{r\phi} = 135\,\mu\text{m}$, $\sigma_z = 6\,\text{cm}$) per track. It allows good particle identification with the energy ionization loss $\mathrm{d}E/\mathrm{d}x$. The z-direction of tracks is substantially improved with information from the z-chambers, which are made of modules of drift chambers with 6 staggered anodes strung in ϕ-direction. The momentum resolution is measured to $\sigma_p/p^2 = 0.0022\,\text{GeV}^{-1}$.
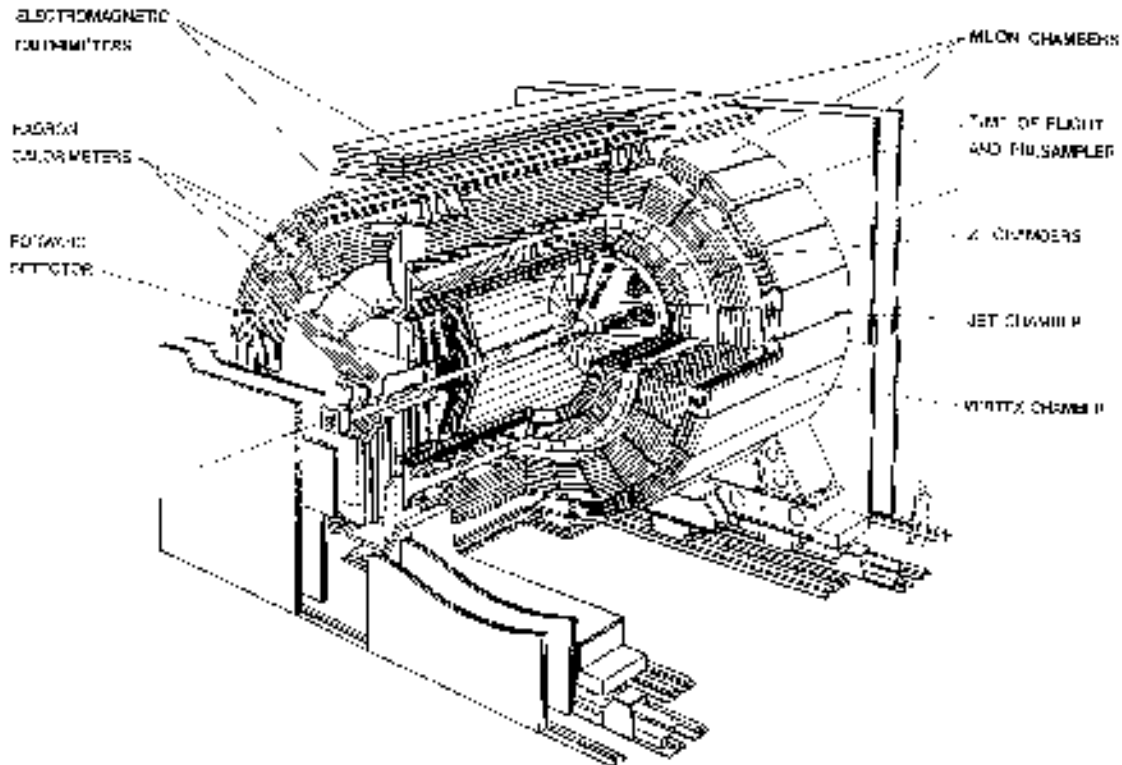
Fig. 2.13: OPAL detector [17].

A time-of-flight system, consisting of scintillation counters, allows particle identification in the momentum range from $0.6\,\text{GeV}/c$ to $2.5\,\text{GeV}/c$. It is used for triggering and for cosmic shower rejection.

Electromagnetic showers are measured with an assembly of lead glass blocks, with $10 \times 10\,\text{cm}^2$ and $37\,\text{cm}$ in depth, read out with photomultipliers. The energy resolution is about $\sigma(E)/E = 0.05/\sqrt{E}$ (E in GeV), when combined with a presampler mounted in front of the calorimeter. Hadrons are measured with nine chambers, limited streamer tubes, interleaved with eight layers of iron plates, where the hadrons may shower. Muons are detected in addition in four layers of drift chambers, the muon chambers.

6 EXPERIMENTS AT HADRON COLLIDERS

6.1 CDF in Run II[10]

The CDF Run II detector [19], in operation since 2001, is an azimuthally and forward-backward symmetric apparatus designed to study $p\bar{p}$ collisions at the Tevatron. It is a general purpose solenoidal detector which combines precision charged particle tracking with fast projective calorimetry and fine grained muon detection. Tracking systems are contained in a superconducting solenoid, 1.5 m in radius and 4.8 m in length, which generates a 1.4 T magnetic field parallel to the beam axis. Calorimetry and muon systems are all outside the solenoid. The main features of the detector systems are summarized below.

The tracking system consists of a silicon microstrip system [20] and of an open-cell wire drift chamber [21] that surrounds the silicon. The silicon microstrip detector consists of seven layers (eight layers for $1.0 < |\eta| < 2.0$) in a barrel geometry that extends from a radius of $r = 1.5$ cm from the beam line to $r = 28$ cm. The layer closest to the beam pipe is a radiation-hard, single sided detector called Layer 00 which employs LHC designs for sensors supporting high-bias voltages. This enables signal-to-noise performance even after extreme radiation doses. The remaining seven layers are radiation-hard, double sided detectors. The first five layers after Layer 00 comprise the SVXII system and the two outer layers comprise the ISL system. This entire system allows track reconstruction in three dimensions. The impact parameter resolution of the combination of SVXII and ISL is 40 μm including a 30 μm contribution from the beamline. The z_0 resolution of the SVXII and ISL is 70 μm. The 3.1 m long cylindrical drift chamber (COT) covers the radial range from 40 to 137 cm and provides 96 measurement layers, organized into alternating axial and $\pm 2°$ stereo superlayers. The COT provides coverage for $|\eta| \leq 1$. The hit position resolution is approximately 140 μm and the momentum resolution $\sigma(p_T)/p_T^2 = 0.0015$ (GeV/c)$^{-1}$. The COT provides in addition dE/dx information for the tracks.

A Time-of-Flight (TOF) detector [22], based on plastic scintillators and fine-mesh photomultipliers is installed in a few centimeters clearance just outside the COT. The TOF resolution is ≈ 100 ps and it provides at least two standard deviation separation between $K^\pm$ and $\pi^\pm$ for momenta $p < 1.6$ GeV/c.

Segmented electromagnetic and hadronic sampling calorimeters surround the tracking system and measure the energy flow of interacting particles in the pseudo-rapidity range $|\eta| < 3.64$. The central calorimeters (and the endwall hadronic calorimeter) cover the pseudorapidity range $|\eta| < 1.1(1.3)$. The central electromagnetic calorimeter [23] (CEM) uses lead sheets interspersed with polystyrene scintillator as the active medium and employs phototube readout. Its energy resolution is $13.5\%/\sqrt{E_T} \oplus 2\%$. The central hadronic calorimeter [24] (CHA) uses steel absorber interspersed with acrylic scintillator as the active medium. Its energy resolution is $75\%/\sqrt{E_T} \oplus 3\%$. The plug calorimeters cover the pseudorapidity region $1.1 < |\eta| < 3.64$. They are sampling scintillator calorimeters which are read out with plastic fibers and phototubes. The energy resolution of the plug electromagnetic calorimeter [25] is $16\%/\sqrt{E} \oplus 1\%$. The energy resolution of the plug hadronic calorimeter is $74\%/\sqrt{E} \oplus 4\%$.

The muon system resides beyond the calorimetry. Four layers of planar drift chambers (CMU) detect muons with $p_T > 1.4$ GeV/c which penetrate the five absorption lengths of calorimeter steel. An additional four layers of planar drift chambers (CMP) instrument 0.6 m of steel outside the magnet return yoke and detect muons with $p_T > 2.0$ GeV/c. The CMU and CMP chambers each provide coverage in the pseudo-rapidity range $|\eta| < 0.6$. The Intermediate MUon detectors (IMU) are covering the region $1.0 < |\eta| < 1.5$.

The beam luminosity is determined by using gas Cherenkov counters located in the $3.7 < |\eta| < 4.7$ region which measure the average number of inelastic $p\bar{p}$ collisions per bunch crossing [26].

The trigger and data acquisition systems are designed to accommodate the high rates and large data volume of Run II. Based on preliminary information from tracking, calorimetry, and muon systems, the output of the first level of the trigger is used to limit the rate for accepted events to ≈ 18 kHz at

---

[10]Author: V. Papadimitriou

the luminosity range of 3–7 10^{31} $cm^{-2}s^{-1}$. At the next trigger stage, with more refined information and additional tracking information from the silicon detector, the rate is reduced further to ≈ 300 Hz. The third and final level of the trigger, with access to the complete event information, uses software algorithms and a computing farm, and reduces the output rate to ≈ 75 Hz, which is written to permanent storage.

The CDF Run I and Run 0 detector, which operated in the time period 1987–1996, is described elsewhere [27]. Major differences for Run II include: the replacement of the central tracking system; the replacement of a gas sampling calorimeter in the plug-forward region with a scintillating tile calorimeter; preshower detectors; extension of the muon coverage, a TOF detector and upgrades of trigger, readout electronics, and data acquisition systems.

6.2   DO detector in Run II[11]

The DO Run II detector, in operation since 2001, is made of the following main elements. The central tracking system consists of a silicon microstrip tracker (SMT) and a central fiber tracker (CFT), both located within a 2 T superconducting solenoidal magnet [28]. The SMT has $\approx 800,000$ individual strips, with typical pitch of $50 - 80$ μm, and a design optimized for tracking and vertexing capability at $|\eta| < 3$. The system has a six-barrel longitudinal structure, each with a set of four layers arranged axially around the beam pipe, and interspersed with 16 radial disks. The CFT has eight thin coaxial barrels, each supporting two doublets of overlapping scintillating fibers of 0.835 mm diameter, one doublet being parallel to the collision axis, and the other alternating by $\pm 3^\circ$ relative to the axis. Light signals are transferred via clear light fibers to solid-state photon counters (VLPC) that have $\approx 80\%$ quantum efficiency.

Central and forward preshower detectors located just outside of the superconducting coil (in front of the calorimetry) are constructed of several layers of extruded triangular scintillator strips that are read out using wavelength-shifting fibers and VLPCs. The next layer of detection involves three liquid-argon/uranium calorimeters: a central section (CC) covering $|\eta|$ up to ≈ 1, and two end calorimeters (EC) extending coverage to $|\eta| \approx 4$, all housed in separate cryostats [29]. In addition to the preshower detectors, scintillators between the CC and EC cryostats provide sampling of developing showers at $1.1 < |\eta| < 1.4$.

The muon system resides beyond the calorimetry, and consists of a layer of tracking detectors and scintillation trigger counters before 1.8 T toroids, followed by two more similar layers after the toroids. Tracking at $|\eta| < 1$ relies on 10 cm wide drift tubes [29], while 1 cm mini drift tubes are used at $1 < |\eta| < 2$.

Luminosity is measured using plastic scintillator arrays located in front of the EC cryostats, covering $2.7 < |\eta| < 4.4$. A forward-proton detector, situated in the Tevatron tunnel on either side of the interaction region, consists of a total of 18 Roman pots used for measuring high-momentum charged-particle trajectories close to the incident beam directions.

The trigger and data acquisition systems are designed to accommodate the large luminosity of Run II. Based on preliminary information from tracking, calorimetry, and muon systems, the output of the first level of the trigger is used to limit the rate for accepted events to ≈ 1.5 kHz. At the next trigger stage, with more refined information, the rate is reduced further to ≈ 800 Hz. The third and final level of the trigger, with access to the complete event information, uses software algorithms and a computing farm, and reduces the output rate to ≈ 50 Hz, which is written to permanent storage.

The DO Run I detector is described elsewhere [29]. Major differences for Run II include: the replacement of the central tracking system, optimized for the absence of a central magnetic field, by a magnetic tracking system; preshower detectors; and upgrades of trigger, readout electronics, and data acquisition systems.

---

[11]Author: Arnd Meyer

7 EXPERIMENTS AT HERA[12]

The electron positron storage ring HERA (Fig. 2.14) at the DESY laboratory in Hamburg collides 27.5 GeV electrons or positrons with 920 GeV protons[13]. The storage ring has a circumference of $6.4\,km$ and consists of two separate accelerators with a maximum of 180 colliding bunches each, providing a bunch crossing rate of 10 MHz. Four experiments are situated at HERA. The two collider experiments H1 and ZEUS have been in operation since 1992. In 1995 the HERMES experiment started data taking using the polarized electron beam on a fixed polarized gas target [30]. The HERA-B proton proton fixed target experiment was operated between 1998 and 2003. HERA-B makes use of the proton beam halo using a wire target and is described in Section 7.3.
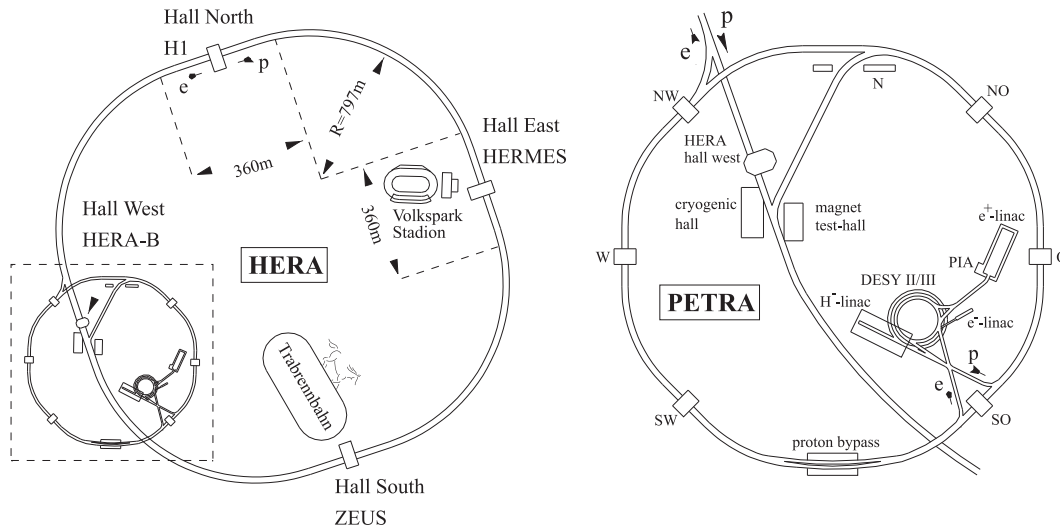
Fig. 2.14: The HERA collider with the four experiments H1, ZEUS, HERMES and HERA-B on the left and its pre-accelerators on the right.

The H1 and ZEUS detectors are typical multi-purpose collider experiments. A schematic view of the ZEUS detector is shown in Fig. 2.15. The physics programs comprise the full spectrum of QCD studies, measurements of the proton structure functions and exclusive hadronic final states, as well as electroweak physics and searches for new physics phenomena [31]. With an ep centre-of-mass energy of 320 GeV the HERA collider experiments H1 and ZEUS are close to the present energy frontier for accelerator based experiments. Only the Tevatron experiments CDF and D0 (described in section 6) have access to higher centre-of-mass energies. Events in deep inelastic ep scattering have been measured down to values of x as low as $\sim 10^{-6}$ and up to values of Q^2 of $30,000$ GeV^2. In QCD, measurements of exclusive final states comprise jet physics, heavy flavour production, processes in hard and soft diffraction and hadron spectroscopy.

In the years between 1992 and 2000 the collider experiments H1 and ZEUS collected an integrated luminosity of 100 pb^{-1} each. The bulk data were taken in the years 1996 through 2000. In the years 2001/2 a major luminosity upgrade was put in place. The interaction points were equipped with new focusing magnets which allow for substantially increased specific luminosities. Since 2003/4 the HERA collider is running and an integrated luminosity of 700 pb^{-1} is expected to be produced for each of the two experiments [32].

The designs of the H1 and ZEUS detectors were chosen to be somewhat complementary, with emphasis on the reconstruction of the scattered electron in the case of H1 and on the precise calorimetric measurement of the hadronic final states in the case of ZEUS. Both experiments are capable of

---

[12]Author: Andreas B. Meyer
[13]Until 1998 the proton energy was 820 GeV.
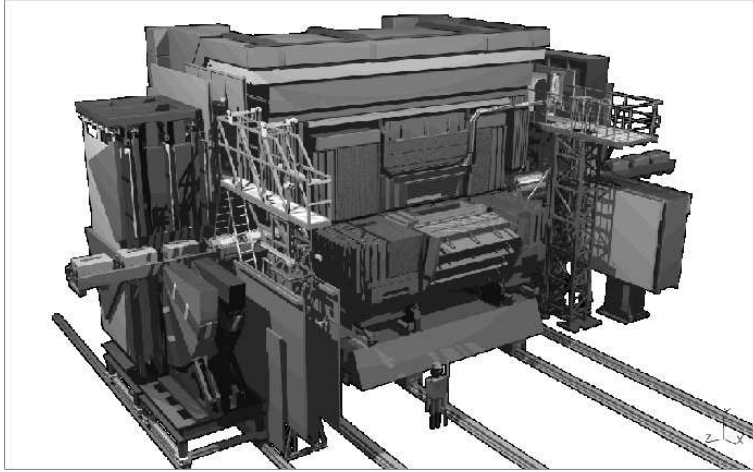
Fig. 2.15: Schematic view of the ZEUS Detector.

the triggering and reconstruction of charmonium and bottomonium events down to very low transverse momenta $p_{t,\psi} \sim 0$. A candidate charmonium event is displayed in figure 2.16. In the following the experiments are described in detail, emphasizing those components that are most relevant for the triggering and reconstruction of quarkonium events with two decay leptons in the final state.

7.1 H1

The design of the 2800 ton H1 detector [33], schematically shown in Fig. 2.16, emphasizes charged particle tracking in the central region as well as high calorimetric resolution for electromagnetic energy depositions.

The primary components of the H1 tracking system are two coaxial cylindrical jet-type drift chambers (CJC) covering the polar angle region between $15°$ and $165°$. The two chambers consist of 30 (60) drift cells respectively with 24 (32) sense wires strung parallel to the beam axis. The sense wires are read out at both ends, and the z-coordinate is measured by charge division with a resolution of $\sigma_z = 22\,\mathrm{mm}$. The spatial resolution of the CJC in the $r\varphi$ plane is $\sigma_{r\varphi} = 170\,\mu\mathrm{m}$. The momentum resolution in the coordinate transverse to the 1.2 Tesla solenoidal field of $\sigma(p_T)/p_T = 0.01\,p_T[\mathrm{GeV}] \oplus 0.015$. The magnetic field is produced by a 5 m long superconducting solenoid of 5.8 m in diameter which encloses the calorimeter. Two further inner drift chambers and two multiwire proportional chambers (MWPC), serve to measure the longitudinal track coordinates and to provide trigger information. The Forward Tracking Detectors cover a polar angular range between $5°$ and $30°$. The system consists of three super-modules composed of three planar drift chambers, a multiwire proportional chamber, a transition radiator and a radial drift chamber. The MWPCs serve for trigger purposes and complement the polar angular coverage of the central proportional chambers.

The H1 main calorimeter employs a fine-grain liquid argon (LAr) sandwich structure in the barrel and forward (proton-beam) region (with angular range from $4°$ to $155°$ in polar angle). In the backward region (with angular range from $155°$ to $177.5°$) a lead/scintillating-fiber calorimeter [34] provides an excellent energy resolution of $\sigma(E)/E = 0.07/\sqrt{E[\mathrm{GeV}]} \oplus 0.01$, and a time resolution better than 1 ns. The electromagnetic section of the liquid argon calorimeter uses lead plates as absorber material. In the hadronic section (which provide a depth of 4 to 6 nuclear interaction lengths) steel plates are used. Both sections are segmented transversely in cells of 4×4 cm^2 in cross-section and are further segmented in longitudinal shower direction. In total there are 31,000 electromagnetic and 14,000 hadronic readout channels. The electromagnetic LAr calorimeter achieves an energy resolution of
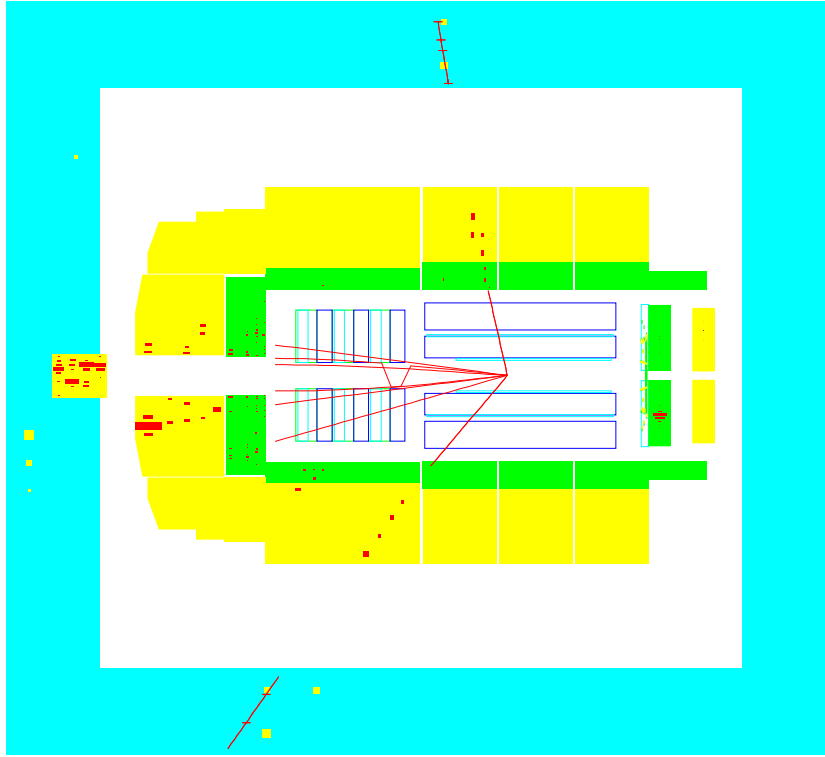
Fig. 2.16: Display of a charmonium event candidate in the H1 Detector.

$\sigma(E)/E = 0.12/\sqrt{E[\mathrm{GeV}]} \oplus 0.01$. The high degree of segmentation allows for a distinction between hadronic and electromagnetic energy depositions in the offline reconstruction, resulting in a hadronic energy resolution of $\sigma(E)/E = 0.55/\sqrt{E[\mathrm{GeV}]} \oplus 0.01$.

Muons are identified as minimum ionizing particles in both the calorimeters and in the magnetic field iron return yoke surrounding the magnetic coil. The iron system is instrumented with 16 layers of limited-streamer tubes of 1 cm^2 cell size. Altogether the muon system consists of 100k channels. Up to five out of 16 layers are used for triggering. In order to provide a two-dimensional measurement five of the 16 layers are equipped in addition with strip electrodes glued perpendicular to the sense wire direction.

The H1 trigger and readout system consists of four levels of hardware and software filtering. The triggering of charmonium event candidates relies on track pattern recognition in the central jet chambers and timing information in the MWPC. For the detection of the scattered electron calorimeter triggers are used. For the muon decay channel coincidences of hits in the same sector of the instrumented iron (in different layers) are required at the first trigger level.

7.2 ZEUS

The ZEUS detector [35, 36] makes use of a 700 ton compensating uranium sampling calorimeter, with equal sampling fractions for electromagnetic and hadronic shower components. The calorimeter is made up of layers of 2.6 mm SCSN-38 scintillator and 3.3 mm stainless-steel-clad depleted-uranium plates. One layer corresponds to 1.0 radiation length (X_0) and 0.04 interaction lengths. This choice of layer thicknesses results in a sampling fraction of 4% for electromagnetic and hadronic shower components, and hence compensation, and 7% for minimum-ionizing particles. The compensation results in a very good hadronic energy resolution of $\sigma(E)/E = 0.35/\sqrt{E[\mathrm{GeV}]} \oplus 0.02$. The resolution for electromagnetic showers is $\sigma(E)/E = 0.18/\sqrt{E[\mathrm{GeV}]} \oplus 0.01$.

The ZEUS solenoidal coil of diameter 1.9 m and length 2.6 m provides a 1.43 T magnetic field for the charged-particle tracking volume. The tracking system consists of a central wire chamber covering the polar angular region from $15°$ to $164°$, a forward planar tracking detector from $8°$ to $28°$ and a second planar tracking chamber in the backward direction, covering the region from $158°$ to $170°$. The momentum resolution attained is $\sigma(p_T)/p_T = 0.005\,p_T \oplus 0.015$ and a track is extrapolated to the calorimeter face with a transverse resolution of about 3 mm. Ionization measurements from the central tracking chamber also serve to identify electron–positron pairs from J/ψ decays.

The muon system is constructed of limited streamer tubes inside and outside of the magnetic return yoke, covering the region in polar angle from $10°$ to $171°$. Hits in the inner chambers provide muon triggers for J/ψ decays.

The ZEUS trigger algorithm is primarily calorimeter-based, exploiting the excellent time resolution of the calorimeter, while that of H1 emphasizes tracking algorithms for reconstruction of the interaction vertex. The shaping, sampling, and pipelining algorithm of the readout developed for the ZEUS calorimeter and used in modified form for the silicon and presampler systems permits the reconstruction of shower times with respect to the bunch crossings with a resolution of better than 1 ns, providing essential rejection against upstream beam–gas interactions, as well as allowing 5 μs for the calculations of the calorimeter trigger processor. For the triggering of the charmonium production channels a muon track candidate in the central drift chamber with one or more hits in the muon chambers can be validated by energy in the calorimeter above a threshold of 460 MeV.

7.3   HERA-B

The fixed target experiment HERA-B is located at the HERA storage ring at DESY (see Section 7), The data taking took place in the years between 2000 and 2003. At HERA-B, wire targets are inserted into the halo of the 920 GeV HERA proton beam to spawn inelastic pA collisions in which charmonium and other heavy flavour states are produced. The pN ($N = p, n$) centre-of-mass energy is $\sqrt{s} = 41.6$ GeV. A side view of the HERA-B spectrometer is shown in Fig. 2.17. A detailed description of the apparatus is given in Ref. [37–39].

The wire target [40] consists of two wire stations, each containing four target wires of different materials. A servo system automatically steers the target wires during the data taking in order to maintain a constant interaction rate. The spectrometer has a geometrical coverage from 15 mrad to 220 mrad in the horizontal plane and from 15 mrad to 160 mrad in the vertical plane. The instrumentation emphasises vertexing, tracking and particle identification. The silicon vertex detector system [41] is realized by a system of 20 Roman pots containing seven planar stations (four stereo views) of double-sided silicon micro-strip detectors which are operated in a vacuum vessel at 10 to 15 mm distance from the proton beam. An additional station is mounted immediately behind the 3 mm thick Aluminium window of the vacuum vessel. The tracker is divided into a fine grained inner tracker using micro-strip gas chambers with gas electron multipliers and a large area outer tracker consisting of honeycomb drift cells with wire pitches between 5 mm near and 10 mm [42–44]. Particle identification is performed by a Ring Imaging Cherenkov hodoscope [45, 46], an electromagnetic calorimeter [47] and a muon detector [48, 49]. The calorimeter is divided into three radial parts with decreasing granularities. The muon system consists of four tracking stations. It is built from gas-pixel chambers in the radially innermost region and from proportional tube chambers, some with segmented cathodes (pads), everywhere else.

The detector components used for charmonium analyses include the tracking and vertex detectors, the calorimeter and the muon system. A complex trigger and read-out chain [50] allows for a reduction of an initial interaction rate of several MHz to a final output rate of order 100 Hz. A dedicated J/ψ-trigger is based on the selection of $\mu^+\mu^-$ and e^+e^- pairs and subsequent reconstruction of invariant masses.
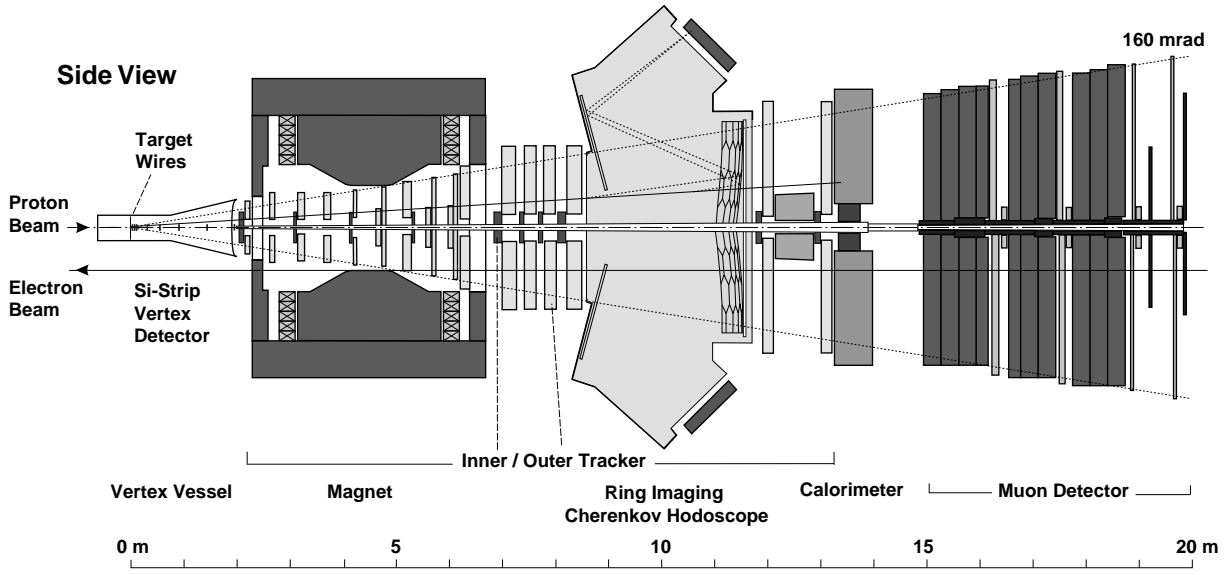
Fig. 2.17: Side view of the HERA-B Spectrometer.

8 APPENDICES

8.1 Resonant depolarization for absolute mass measurements[14]

Electrons and positrons in storage rings can become polarized due to emission of synchrotron radiation according to the Sokolov–Ternov effect [54]. The spins of the polarized electrons precess around the vertical guiding magnetic field with the precession frequency Ω, which in the plane orbit approximation is directly related to the particle energy E and the beam revolution frequency ω:

$$\Omega/\omega = 1 + \gamma \cdot \mu'/\mu_0 = 1 + \nu \,, \tag{2.1}$$

where $\gamma = E/m_{\mathrm{e}}$, m_{e} is the electron mass, μ' and μ_0 are the anomalous and normal parts of the electron magnetic moment. The ν is a spin tune, which represents the spin precession frequency in the coordinate basis related to the particle velocity vector.

The precession frequency can be determined using the *resonant depolarization*. To this end one needs a polarized beam in the storage ring which is affected by the external electromagnetic field with the frequency Ω_D given by the relation

$$\Omega \pm \Omega_D = \omega \cdot n \tag{2.2}$$

with any integer n (for VEPP-4M in the $J/\psi(1S)$ region $n = 3$).

The precession frequency is measured at the moment of the polarization destruction detected by the *polarimeter*, while the *depolarizer* frequency is being scanned. The process of forced depolarization is relatively slow compared to the period of the synchrotron oscillations of the particle energy. This allows to determine the average spin tune $\langle \nu \rangle$ and corresponding average energy of the particles $\langle E \rangle$ with higher accuracy than the beam energy spread σ_{E}.

Formula (2.1) gives the value of γ averaged over the beam revolution time. Thus, for a symmetric machine, it corresponds to the energy in the interaction point.

The method described has been developed in Novosibirsk and first applied to the ϕ meson mass measurement at the VEPP-2M storage ring [55]. Later it was successfully used to measure masses of

---

[14]Author: S. Eidelman

the ψ- [51] and Υ-meson family [56–58], see also Ref. [59], in which the values of the masses were rescaled to take into account the change of the electron mass value. The relative mass accuracy achieved in these experiments was $1 \cdot 10^{-5}$ for the Υ-family and $3 \cdot 10^{-5}$ for the ψ-family. The resonant depolarization experiments on bottomonium masses were also performed with the CUSB detector at CESR [60] ($\Upsilon(1S)$) and with the ARGUS detector at DORIS [61] ($\Upsilon(2S)$). The accuracy of the $J/\psi(1S)$ meson mass measurement was improved in the Fermilab $p\bar{p}$-experiment E760 [62] to $1.2 \cdot 10^{-5}$ using the $\psi(2S)$ mass value from Ref. [51]. The resonant depolarization method was also successfully applied to the high precision measurement of the Z-boson mass at LEP [63]. The comprehensive review of this technique and its application to particle mass measurements can be found in [64].

8.2 e^+e^- scanning, radiative corrections[15]

8.2.1 Introduction

The measurement of the mass and total width of 1^{--} resonances by e^+e^- colliding experiments is done by scanning the resonance curve and fitting the data with the theoretical cross-section as a function of these parameters. The e^+e^- partial width is also determined from this fitting, i.e., Γ_{ee} is measured as the coupling of the resonance to the incoming e^+e^-, instead of decaying process; while most other decay modes are measured as branching ratios by dividing the number of the observed events decaying into this mode by the total number of resonance events. Such fitting requires precise calculation of initial state radiative corrections. This is done by the structure function approach [69–71]. It yields the accuracy of 0.1%. In this scheme, the radiatively corrected cross-section is expressed as

$$\sigma(s) = \int_0^{1-s_m/s} dx\, \tilde{\sigma}(s(1-x))F(x,s), \qquad (2.3)$$

where $\sqrt{s}$ is the C.M. energy of the colliding beam, $\sqrt{s_m}$ is the cut-off of the invariant mass in the event selection, and

$$\tilde{\sigma}(s) = \frac{\sigma_B(s)}{|1 - \Pi(s)|^2}. \qquad (2.4)$$

with $\sigma_B(s)$ the Born order cross-section and $\Pi(s)$ the vacuum polarization. In Eq. (2.3)

$$F(x,s) = \beta x^{\beta-1} \delta^{V+S} + \delta^H, \qquad (2.5)$$

with

$$\beta = \frac{2\alpha}{\pi}\left(\ln\frac{s}{m_e^2} - 1\right), \qquad (2.6)$$

$$\delta^{V+S} = 1 + \frac{3}{4}\beta + \frac{\alpha}{\pi}\left(\frac{\pi^2}{3} - \frac{1}{2}\right) + \beta^2\left(\frac{9}{32} - \frac{\pi^2}{12}\right), \qquad (2.7)$$

$$\delta^H = -\beta\left(1 - \frac{x}{2}\right)$$
$$+ \frac{1}{8}\beta^2\left[4(2-x)\ln\frac{1}{x} - \frac{1+3(1-x)^2}{x}\ln(1-x) - 6 + x\right]. \qquad (2.8)$$

Here the conversion of bremsstrahlung photons to real e^+e^- pairs is included in the cross-section which is the usual experimental situation. Thus there is cancellation between the contributions of virtual and real e^+e^- pairs in the leading term [71].

---

[15]Author: P. Wang

Since this note discusses resonances, like ψ' and ψ''. so $\sigma_B(s)$ is expressed by Breit–Wigner formula. For narrow resonances, like J/ψ and ψ', it is

$$\sigma_B(s) = \frac{12\pi\Gamma_{ee}^0\Gamma_f}{(s - M^2)^2 + \Gamma^2 M^2}, \tag{2.9}$$

where M and Γ are the mass and total width of the resonance; Γ_{ee}^0 and Γ_f are the partial widths to the e^+e^- mode and to the final state respectively. Usually to measure M, Γ and Γ_{ee}, f is inclusive hadrons. Here Γ_{ee}^0 describes the coupling strength of the resonance to e^+e^- through a virtual photon. For example, in potential model, Γ_{ee}^0 is related to the wave function at the origin $\psi(0)$ in the way

$$\Gamma_{ee}^0 = \frac{4\alpha^2 Q_q^2 |\psi(0)|^2}{M^2} \tag{2.10}$$

where Q_q is the charge carried by the quark in the quarkonium and α is the QED fine structure constant. Since the decay of a quarkonium 1^{--} state to e^+e^- pair is through a virtual photon, there is always vacuum polarization associated with this process. So the experimentally measured e^+e^- partial width, denoted explicitly as Γ_{ee}^{exp}, is related to Γ_{ee}^0 by the expression

$$\Gamma_{ee}^{exp} = \frac{\Gamma_{ee}^0}{|1 - \Pi(M^2)|^2}. \tag{2.11}$$

Particle Data Group adopts the convention of Ref [73] that Γ_{ee} means Γ_{ee}^{exp}. The radiatively corrected resonance cross-section is

$$\sigma_{res}(s) = \int_0^1 dx\, F(x, s) \frac{12\pi\Gamma_{ee}^{exp}\Gamma_f}{(s - M^2)^2 + \Gamma^2 M^2}. \tag{2.12}$$

For resonances, as long as $\sqrt{s} - \sqrt{s_m} \gg \Gamma$, the integral of Eq. (2.12) is insensitive to $\sqrt{s_m}$, because the Breit-Wigner formula behaves like a δ function. One can put the upper limit of integral to 1.

8.2.2 *Analytical expression*

For the practical purpose of fitting, the expression of radiative corrected resonance cross-section in Eq. (2.12) is integrated analytically [74]. To get the best accuracy, one rewrites $F(x, s)$ in Eq. (2.5) in terms of a series expansion:

$$
\begin{aligned}
F(x, s) &= \beta x^{\beta-1}\left[1 + \frac{3}{4}\beta + \frac{\alpha}{\pi}\left(\frac{\pi^2}{3} - \frac{1}{2}\right) + \beta^2\left(\frac{9}{32} - \frac{\pi^2}{12}\right)\right] \\
&\quad + x^\beta\left(-\beta - \frac{\beta^2}{4}\right) + x^{\beta+1}\left(\frac{\beta}{2} - \frac{3}{8}\beta^2\right) + O(x^{\beta+2}\beta^2) \\
&= \beta x^{\beta-1}\delta^{V+S} + \delta^H,
\end{aligned}
\tag{2.13}
$$

with

$$\delta^H = x^\beta\left(-\beta - \frac{\beta^2}{4}\right) + x^{\beta+1}\left(\frac{\beta}{2} - \frac{3}{8}\beta^2\right). \tag{2.14}$$

Notice that here the omitted terms start from $x^{\beta+2}\beta^2$, while the three terms which are kept all have β term in their coefficients. Equation (2.13) differs from Eq. (2.5) in the δ^H term. Their equivalence can be verified if one writes $x^\beta = 1 + \beta \ln x$, $x^{\beta+1} = x + \beta x \ln x$ and $\ln(1 - x) = -x - x^2/2 + \dots$.

With $F(x, s)$ in the form of Eq.(2.13), the radiatively corrected resonance cross-section of Eq. (2.12) can be expressed as

$$
\begin{aligned}
\sigma_{res}(s) \quad = \quad & \frac{12\pi\Gamma_{ee}\Gamma_f}{s^2}\{\delta^{V+S}[a^{\beta-2}\Phi(\cos\theta, \beta) \\
& +\beta(\frac{1}{\beta-2} + \frac{2(s-M^2)}{(\beta-3)s} + \frac{3(s-M^2)^2 - M^2\Gamma^2}{(\beta-4)s^2})] \\
& -\beta(1+\frac{\beta}{4})[\frac{1}{1+\beta}a^{\beta-1}\Phi(\cos\theta, \beta+1) \\
& +\frac{1}{\beta-1} + \frac{2(s-M^2)}{(\beta-2)s} + \frac{3(s-M^2)^2 - M^2\Gamma^2}{(\beta-3)s^2}] \\
& +(\frac{\beta}{2} - \frac{3}{8}\beta^2)[\frac{1}{2}\ln\frac{1+2a\cos\theta+a^2}{a^2} \\
& -\cot\theta(\arctan\frac{1+a\cos\theta}{a\sin\theta} - \frac{\pi}{2}+\theta)]\},
\end{aligned}
\tag{2.15}
$$

with

$$
\Phi(\cos\theta, \nu) \quad \equiv \quad \frac{\pi\nu\sin[(1-\nu)\theta]}{\sin\theta \ \sin\pi\nu}; \tag{2.16}
$$

$$
a^2 \quad = \quad \left(1 - \frac{M^2}{s}\right)^2 + \frac{M^2\Gamma^2}{s^2}; \tag{2.17}
$$

$$
\cos\theta \quad = \quad \frac{1}{a}\left(\frac{M^2}{s} - 1\right). \tag{2.18}
$$

8.2.3 *Narrow resonances*

Below the open charm or bottom threshold, the resonances are narrow with widths from tens to hundreds KeV, while the beam energy resolution of e^+e^- colliders is of the order of MeV. If the resonance width is comparable or smaller than the beam energy resolution, the observed resonance cross-section is the cross-section by Eq. (2.15) folded with the beam energy resolution function $G(W, W')$. Also in the observed cross-section, there is always a continuum part from direct virtual photon annihilation which is usually treated as $1/s$ dependence. So the experimentally observed cross-section is

$$
\sigma_{obs}(W) \quad = \quad \frac{R}{s} + \int_0^\infty G(W, W')\sigma_{res}(W')dW'. \tag{2.19}
$$

In the above, R is a fitting parameter and $G(W, W')$ is usually taken as a Gaussian function:

$$
G(W, W') \quad = \quad \frac{1}{\sqrt{2\pi}\Delta}\exp\left[-\frac{(W-W')^2}{2\Delta^2}\right], \tag{2.20}
$$

with Δ the standard deviation of the Gaussian distribution.

In the fitting of the experimental data with the theoretical curve, M, Γ, Γ_{ee}, R and Δ are obtained.

8.2.4 *$\mu^+\mu^-$ final state*

Usually the $\mu^+\mu^-$ curve is also fitted, to extract $\Gamma_{\mu\mu}$. The fitting of inclusive hadron can be combined with the $\mu^+\mu^-$ curve to obtain M, Γ, Γ_{ee}, $\Gamma_{\mu\mu}$, R and Δ. Here unlike for an inclusive hadronic final

state, the continuum $\mu^+\mu^-$ cross-section is calculated by QED [79], and the interference between virtual photon and the resonance must be included. The cross-section of $e^+e^- \to \mu^+\mu^-$ at Born order is

$$\sigma_B(s) = \frac{4\pi\alpha^2}{3s}[1 + 2ReB(s) + |B(s)|^2] \tag{2.21}$$

where

$$B(s) = \frac{3s\Gamma_{ee}/M\alpha}{(s - M^2) + iM\Gamma}. \tag{2.22}$$

With radiative correction, it can be expressed as

$$\sigma_{\mu^+\mu^-}(s) = \frac{1}{|1 - \Pi(s)|^2}\left\{\frac{4\pi\alpha^2}{3s}\left[1 + \frac{\beta}{2}\left(2\ln x_f - \ln(1 - x_f) + \frac{3}{2} - x_f\right) + \frac{\alpha}{\pi}\left(\frac{\pi^2}{3} - \frac{1}{2}\right)\right]\right.$$

$$+ C_1\delta^{V+S}\left[a^{\beta-2}\Phi(\cos\theta, \beta) + \beta\left(\frac{x_f^{\beta-2}}{\beta - 2} + \frac{x_f^{\beta-3}}{\beta - 3}R_2 + \frac{x_f^{\beta-4}}{\beta - 4}R_3\right)\right]$$

$$+ \left[-\beta\delta^{V+S}C_2 + \left(-\beta - \frac{\beta^2}{4}\right)C_1\right]\left[\frac{a^{\beta-1}}{1 + \beta}\Phi(\cos\theta, \beta + 1) + \frac{x_f^{\beta-1}}{\beta - 1} + \frac{x_f^{\beta-2}}{\beta - 2}R_2 + \frac{x_f^{\beta-3}}{\beta - 3}R_3\right]$$

$$+ \left[\left(\beta + \frac{\beta^2}{4}\right)C_2 + \left(\frac{\beta}{2} - \frac{3}{8}\beta^2\right)C_1\right]\left[\frac{1}{2}\ln\frac{x_f^2 + 2ax_f\cos\theta + a^2}{a^2}\right.$$

$$\left.\left. - \cot\theta\left(\tan^{-1}\frac{x_f + a\cos\theta}{a\sin\theta} - \frac{\pi}{2} + \theta\right)\right]\right\} \tag{2.23}$$

where

$$C_1 = [8\pi\alpha\frac{\sqrt{\Gamma_e^0\Gamma_\mu^0}}{M}(s - M^2) + 12\pi(\frac{\Gamma_e^0\Gamma_\mu^0}{M^2})s]/s^2,$$

$$C_2 = [8\pi\alpha\frac{\sqrt{\Gamma_e^0\Gamma_\mu^0}}{M} + 12\pi(\frac{\Gamma_e^0\Gamma_\mu^0}{M^2})]/s,$$

$$R_2 = \frac{2(s - M^2)}{s} = -2a\cos\theta \tag{2.24}$$

$$R_3 = a^2(4\cos^2\theta - 1)$$

$$x_f = 1 - \frac{s_m}{s}.$$

$\Phi(\cos\theta, \nu)$, a and θ are defined previously in Eq. (2.16),(2.17) and (2.18). Here unlike the resonance term, the continuum term depends on the invariant mass cut $\sqrt{s_m}$ in the $\mu^+\mu^-$ event selection. Also $\Gamma_{\mu\mu}$ is defined similar to Γ_{ee}, in the way

$$\Gamma_{\mu\mu} \equiv \Gamma_{\mu\mu}^{exp} = \frac{\Gamma_{\mu\mu}^0}{|1 - \Pi(M_{res}^2)|^2}. \tag{2.25}$$

For μ pair final state, unlike the inclusive hadrons, the vacuum polarization cannot be absorbed into the definition of Γ_{ee} in all terms, so it must be calculated explicitly. The leptonic part of $\Pi(s)$ is well known. (For example, in Ref [77], although there the definition of $\Pi(s)$ has a minus sign relative to the more common convention used here.) The hadronic part was first calculated in Ref [78], and a more recent treatment is found in Ref [80].

For narrow resonances, the μ pair cross-section also need to be folded with the beam energy resolution function.

8.2.5 Very narrow resonances

For the narrow resonances with $\Gamma \ll \Delta$, (e.g., Γ is an order of magnitude smaller than Δ), then Eq. (2.19) is insensitive to Γ, the fitting becomes impractical. In such case, the area method [72, 75] can be used to extract

$$(Area)_0 = \frac{6\pi^2 \Gamma_{ee} \Gamma_f}{M^2 \Gamma},$$ (2.26)

together with M, R and Δ from the fitting. Here the final state f is inclusive hadrons. This method requires additional information on the leptonic branching ratio $\mathcal{B}(l^+l^-)$, which is obtained from counting the μ pair events on top of the resonance. With the assumption that $\mathcal{B}(e^+e^-) = \mathcal{B}(\mu^+\mu^-)$ and $\Gamma_{had} = \Gamma(1 - 2\mathcal{B}(l^+l^-))$(If the resonance is above the τ production threshold, $\Gamma_{had} = \Gamma(1 - 3\mathcal{B}(l^+l^-))$. A phase space correction is needed for $\psi(2S)$, for it is close to the τ threshold.), Γ and Γ_{ee} can be solved from $(Area)_0$ and $\mathcal{B}(l^+l^-)$.

Both of the original papers on the area method in Ref. [72] and [75] mistreated radiative correction. This was pointed out later on by Ref [73]. For the convenience of the readers, here the complete formulae of area method are presented.

The experimentally observed cross-section is

$$\sigma_{obs}(W) = \frac{R}{s} + (Area)_0 \delta^{V+S} Gr(W - M),$$ (2.27)

where δ^{V+S} is defined in Eq. (2.7), and the radiatively corrected Gaussian function

$$Gr(w) = \left(\frac{2\Delta}{W}\right)^\beta \frac{1}{\Delta} F(\frac{w}{\Delta}, \beta).$$ (2.28)

The function $F(z, \beta)$ is approximated [75] as

$$
\begin{aligned}
F(z, \beta) \approx & \frac{\Gamma(1 + \beta)}{\sqrt{2\pi}} e^{-z^2/2} \left[0.31 - \frac{0.73z}{\sqrt{1 + \left(\frac{z}{1+1.37\beta}\right)^2}} + z^2 \right]^{-\beta/2} \\
& + \theta(z)\beta z^\beta \left(\frac{z^{2.18}}{1 + z^{3.18}} \right) \\
& \times \left\{ 1 + \frac{(1 - \beta)(2 - \beta)/2}{\left[\left(z - \frac{46}{z^2+21}\right)^2 + 2.44 + 1.5\beta \right]} \right\},
\end{aligned}
$$ (2.29)

where $\Gamma(1 + \beta)$ is the Gamma function and $\theta(z)$ is the step function. Notice that to derive Eq. (2.27), δ^H term in Eq. (2.5) is neglected, and the Breit–Wigner is approximated as a δ function compared with Δ. These limit the accuracy of the results.

For large positive or negative z, there are asymptotic expansions of $F(z, \beta)$ [75], which are useful to calculate the resonance cross-sections away from the peak, e.g., radiative tails.

8.2.6 Resonance near threshold

$\psi(3770)$ and $\Upsilon(4S)$ are near the threshold of $D\bar{D}$ or $B\bar{B}$ production. They decay predominantly into $D\bar{D}$ or $B\bar{B}$. The line shape is cut off at the threshold. In the radiative correction expressed by the integral of Eq. (2.3), the cut off $\sqrt{s_m} = 2m_P$, with m_P the mass of the pseudoscalar meson (D^0 or $B^\pm$)

produced at the threshold. (If the resonance is well above the threshold, i.e., $\sqrt{s} - 2m_P \gg \Gamma$, the integral is not sensitive to the upper limit.) The line shape of the resonances is

$$\sigma_{res}(s) = \frac{R}{s} + \int_0^{1-4M_P^2/s} dx \, F(x,s) \frac{12\pi\Gamma_{ee}^{exp}\Gamma_f}{(s-M^2)^2 + \Gamma^2 M^2}. \tag{2.30}$$

In the above, the first term is the continuum cross-section due to direct virtual photon annihilation. This term could be greater than the resonance itself. For example, for $\psi(3770)$, the continuum cross-section is 13nb; while the radiatively corrected resonance cross-section is about 8nb.

8.2.7 The energy dependent width

Above the open charm or bottom threshold, the resonances are wide, usually over 10MeV. For such wide resonances, the energy dependence of its width need to be considered. Such dependence cannot be derived from first principle, and the formula is model dependent. For example, in the MARK III scan of $\psi(3770)$, it is in the form:

$$\Gamma(E) \propto \frac{p_{D^0}^3}{1 + (rp_{D^0})^2} + \frac{p_{D^\pm}^3}{1 + (rp_{D^\pm})^2} \tag{2.31}$$

and the width listed by PDG is defined as

$$\Gamma_{\psi''} = \Gamma(E = M_{\psi''}) \tag{2.32}$$

In the above, p_{D^0} and $p_{D^\pm}$ are the momentum of D^0 and $D^\pm$ produced. r is a free parameter. Usually the fitting is not sensitive to r. So in Eq. (2.30),

$$\Gamma(E) = \frac{\Gamma_{\psi''}\left(\frac{p_{D^0}^3}{1+(rp_{D^0})^2} + \frac{p_{D^\pm}^3}{1+(rp_{D^\pm})^2}\right)}{\frac{(p^0)_{D^0}^3}{1+(rp_{D^0}^0)^2} + \frac{(p^0)_{D^\pm}^3}{1+(rp_{D^\pm}^0)^2}} \tag{2.33}$$

where

$$p_{D^0} = \frac{1}{2}\sqrt{E^2 - 4m_{D^0}^2}; \tag{2.34}$$

$$p_{D^\pm} = \frac{1}{2}\sqrt{E^2 - 4m_{D^\pm}^2}; \tag{2.35}$$

$$p_{D^0}^0 = \frac{1}{2}\sqrt{M^2 - 4m_{D^0}^2}; \tag{2.36}$$

and

$$p_{D^\pm}^0 = \frac{1}{2}\sqrt{M^2 - 4m_{D^\pm}^2} \tag{2.37}$$

The width of $\Upsilon(4S)$ and the states above are expressed similarly.

The Breit–Wigner with the energy dependent width cannot be integrated analytically with $F(x,s)$. In the fitting, the cross-section is numerically integrated. On the other hand, for these wide resonances, usually the finite beam energy spread can be neglected.

8.2.8 The shift and scale down of the maximum height

With the radiative correction, the maximum height of the resonance is shifted from the mass of the resonance M to [76]

$$M + \Delta\sqrt{s}_{max} \tag{2.38}$$

where

$$\Delta\sqrt{s}_{max} \approx \frac{\beta\pi}{8}\Gamma \tag{2.39}$$

and the maximum height of the resonant peak is reduced by a factor [76]

$$\rho \approx \left(\frac{\Gamma}{M} \right)^{\beta} \delta^{V+S};$$
(2.40)

where β and δ^{V+S} are defined in Eq. (2.6) and (2.7). For the narrow resonances, the shift of the maximum height due to radiative correction is small, due to the narrow widths. On the other hand, the finite beam resolution also shifts the maximum height of the observed resonance shape. It is roughly at the order of one-tenth of Δ. This needs to be taken into account in the precision measurements of the branching ratios.

8.3 $\bar{p}p$ scanning techniques and limits[16]

8.3.1 Introduction

The $\bar{p}p$ formation technique, where the antiproton beam annihilates with a hydrogen target, has been thoroughly exploited to scan all known charmonium states, overcoming the limitations of the e^+e^-, which can actually form only vector states. A successful program was carried out at CERN's ISR by R704 [82, 83] and at the Fermilab Antiproton Source by E760 [84–86] and E835 [87–90]. All detectors used so far were non-magnetic. Experiment PANDA at the future GSI facility also includes a program of charmonium studies [91] and will be the first provided with a magnetic field.

Many aspects of antiproton beam conditioning for charmonium studies are discussed in Ref. [92]. The antiproton beam energy is scanned across the resonance in steps appropriate for the width of the resonance under study. The observed cross-section is given by $\sigma_{obs}(W = \sqrt{s}) = \sigma_{cont} + \int_0^\infty G(W, W')$ $\sigma_{BW}(W')\, dW'$. The mass, width and peak cross-section $\sigma_{BW}(M_R)$ are determined by the number of observed events, after deconvoluting the beam energy spectrum $G(W, W')$ and subtracting the continuum cross-section σ_{cont} from the observed cross-section $\sigma_{obs}(W = \sqrt{s}) = \sigma_{cont} + \int_0^\infty G(W, W')\, \sigma_{BW}(W')$ dW'. They are not directly influenced by the detector resolution.

For instance, Fig. 2.18 shows a 16-point scan of the ψ' resonance. The bottom plot shows the normalized beam energy distributions as the beam was decelerated. The top plot indicates the measured cross-sections (red circles) compared with the best predictions (green triangles) from a maximum-likelihood fit to the convolution of the beam distributions (bottom plot) with a Breit–Wigner resonance curve (solid line).

An important role is played by the beam energy distribution. This function can be measured from the Schottky revolution frequency spectrum, the bunching radiofrequency, the orbit length of particles in the rf bucket and the slip factor of the machine [86, 93]. The only quantity that needs external input is the orbit length. It needs to be calibrated with the scan of a narrow resonance whose mass is well known. Typically, the ψ' is chosen, because the absolute value of its mass is measured with extreme accuracy (25 keV) by the resonant depolarization method in e^+e^- [94, 95], described in Section (8.1). Using the ψ' for calibration, the other masses are determined with an uncertainty ≤ 200 keV. The main contribution to the uncertainty comes from the orbit length: its value is obtained by comparison of the reference orbit with the beam-position monitor readings during the scan of the resonance under study.

8.3.2 Signal extraction in hadronic annihilations

The rate of charmonium formation formed depends on the coupling between the initial state and the resonance. In e^+e^- annihilation, the couplings of e^+e^- to both J/ψ and $\Upsilon(1S)$ are of the order of 10^{-2}. The branching fractions $\bar{p}p \rightarrow c\bar{c}$ are of the order of 10^{-4}–10^{-3} for charmonium, but probably much smaller for bottomonium: $\approx 10^{-7}$ is the theoretical prediction [96], and $< 5 \times 10^{-4}$ is the experimental upper limit for $\bar{p}p \rightarrow \Upsilon(1S)$ [97]. The relatively low intensity of antiproton beams is partially compensated by

---

[16]Author: G. Stancari
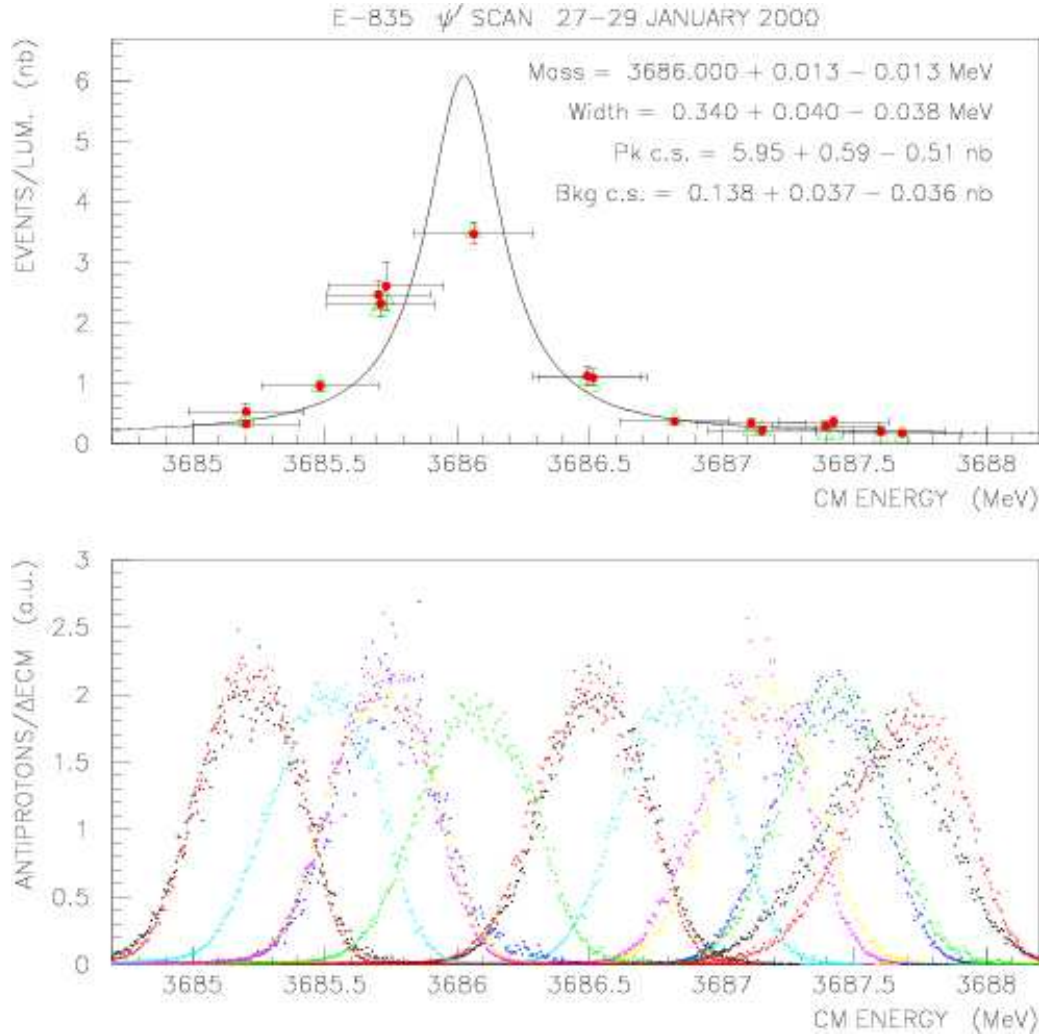
Fig. 2.18: (colour) Resonance scan at the $\psi(2S)$.

the availability of jet targets; typical luminosities were 2×10^{31} cm^{-2}s^{-1} for E835; at GSI, an increase of a factor 10 is expected.

Formation cross-sections for charmonium states in $p\bar{p}$ annihilations range between 10 and 10^3 nb, but only a small fraction can be detected. In antiproton–proton annihilations, the limiting factor is the large total cross-section (70 mb). This implies that a clean charmonium signal (pb–nb) can be extracted only by identifying its inclusive or exclusive electromagnetic decays to a high-invariant-mass e^+e^- or $\gamma\gamma$ pair, such as $\bar{p}p \to \chi_c \to J/\psi + X \to e^+e^- + X$.

Hadronic channels such as $\pi^0\pi^0$ and $\eta\eta$ have recently been investigated. Using data taken in 2000, E835 has provided the first evidence [98] of a charmonium signal exploiting the interference between resonance and continuum at the χ_{c0} energy.

8.3.3 Limits on energy and width resolution

A small beam energy spread is desirable because it reduces the uncertainty on the mass by sharpening the resonance peak. However, efforts to make the beam much narrower than the resonance are obviously not necessary. For antiproton beams, the minimum attainable momentum spread is determined by longitudinal stability (Keil–Schnell criterion [99]) rather than stochastic cooling power. Typically,

with a beam current $I = 50$ mA, one can achieve a momentum spread $\sigma_p/p = 10^{-4}$, which translates to $\sigma_{\sqrt{s}} = 0.2$ MeV in the centre-of-momentum frame. As the beam intensity increases, the minimum attainable momentum spread increases as $\sqrt{I}$. In e^+e^- machines there is no need for stochastic cooling, but the energy spread is dominated by initial state radiation: $\sigma_{\sqrt{s}} = 1$ MeV at the J/ψ, $\sigma_{\sqrt{s}} = 4$ MeV at the $\Upsilon(1S)$.

8.4 Luminosity of photon photon scattering[17]

The cross-section for a $\gamma\gamma$ process is related to the cross-section at the e^+e^- level, which is measured in the laboratory, by the formula

$$d\sigma(e^+e^- \to e^+e^-X) = \sigma(\gamma_1\gamma_2 \to X)\frac{d^2n_1}{dz_1dP_1^2}\frac{d^2n_2}{dz_2dP_2^2}dz_1dz_2dP_1^2dP_2^2 \tag{2.41}$$

where z_i is the scaled photon energy in the laboratory frame and P_i^2 is the photon mass. This is the equivalent photon approximation (EPA) [100] where the longitudinal polarization component as well as the mass of the incoming photons are neglected in $\sigma(\gamma\gamma \to X)$. The P_i^2 integration can be carried out to give the photon "density" in the $e^{\pm}$ (the photon flux)

$$f_{\gamma/e}(z, P_{min}, P_{max}) = \int_{P_{min}^2}^{P_{max}^2} \frac{d^2n}{dzdP^2}dP^2 =$$

$$= \frac{\alpha}{2\pi}\left[\frac{1 + (1-z)^2}{z}\ln\frac{P_{max}^2}{P_{min}^2} - 2m_e^2z\left(\frac{1}{P_{min}^2} - \frac{1}{P_{max}^2}\right)\right]. \tag{2.42}$$

For untagged experiments (the scattered $e^{\pm}$ are undetected) P_{min} is the kinematic limit:

$$P_{min}^2 = \frac{m_e^2z^2}{1-z} \tag{2.43}$$

and $P_{max} \simeq E_{beam}$.

For resonance production, Eq.(2.41) simplifies since one of the z_i integrations can be performed with the constraint $z_1z_2 = \tau = M^2/s_{e^+e^-}$ where M is the resonance mass. It is then customary to define luminosity functions:

$$\frac{d\mathcal{L}}{dM} = \frac{2\tau}{M}\int dz_1dz_2 f_{\gamma/e}(z_1)f_{\gamma/e}(z_2)\delta(z_1z_2 - \tau) \tag{2.44}$$

so that

$$d\sigma(e^+e^- \to e^+e^-X) = \int M\frac{d\mathcal{L}}{dM}\sigma(\gamma\gamma \to X). \tag{2.45}$$

This luminosity curve makes it easy to determine the counting rate for resonance production knowing the width of the resonance in the $\gamma\gamma$ channel.

The most accurate Monte Carlo computation of two-photon production in e^+e^- collisions is the program GALUGA [101] widely used to extract the luminosity function and the photon structure function in various kinematical regions.

---

[17]Author: M. Kienzle

8.5 Interference with continuum in e^+e^- experiments[18]

8.5.1 Introduction

It is well known that the e^+e^- experiments have lots of advantages in the study of the charmonium physics: large cross-section, small background, and well-determined initial state (both four-momentum and quantum numbers). However, there is an inevitable amplitude — the continuum amplitude

$$e^+e^- \rightarrow \gamma^* \rightarrow hadrons$$

accompanied with the production of the resonances. This amplitude does not go through the resonance, but in general it can produce the same final hadronic states as charmonia do. This amplitude has been overlooked in many previous studies.

8.5.2 Experimentally observed cross-section

We know that J/ψ and $\psi(3686)$ (shortened as ψ') decay into light hadrons through three-gluon and one-photon annihilation of which the amplitudes are denoted by a_{3g} and a_γ respectively. This is also true for $\psi(3770)$ (shortened as ψ'') in its OZI suppressed decay into light hadrons. In general, for the resonance $\mathcal{R}$ ($\mathcal{R} = J/\psi$, ψ' or ψ''), the cross-section at the Born order is expressed as

$$\sigma_B(s) = \frac{4\pi s \alpha^2}{3}|a_{3g} + a_\gamma|^2 \,, \tag{2.46}$$

where $\sqrt{s}$ is the C.M. energy, α is the fine structure constant. If the J/ψ, ψ' or ψ'' is produced in e^+e^- collision, the process

$$e^+e^- \rightarrow \gamma^* \rightarrow hadrons \tag{2.47}$$

could produce the same final hadronic states as charmonium decays do [102]. We denote its amplitude by a_c, then the cross-section becomes

$$\sigma'_B(s) = \frac{4\pi s \alpha^2}{3}|a_{3g} + a_\gamma + a_c|^2 \,. \tag{2.48}$$

So what truly contribute to the experimentally measured cross-section are three classes of Feynman diagrams, i.e., the three-gluon decays, the one-photon decays, and the one-photon continuum process, as illustrated in Fig. 2.19. To analyze the experimental results, we must take into account three amplitudes and two relative phases.
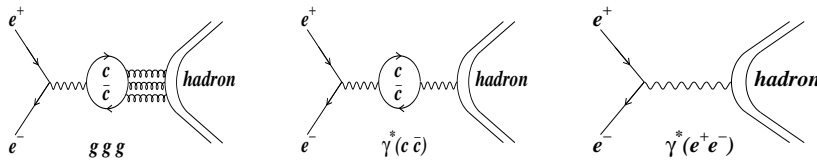
Fig. 2.19: The Feynman diagrams of $e^+e^- \rightarrow light\ hadrons$ at charmonium resonance. From left to right are of three-gluon annihilation, of one-photon annihilation and of one-photon continuum.

For an exclusive mode, a_c can be expressed by

$$a_c(s) = \frac{\mathcal{F}(s)}{s}e^{i\phi'} \,, \tag{2.49}$$

---

[18]Authors: C.Z. Yuan, P. Wang, X. H. Mo

Table 2.7: Estimated amplitudes at J/ψ, ψ' and ψ'' peaks

$\sqrt{s}$	$m_{J/\psi}$	$m_{\psi'}$	$m_{\psi''}$
$|a_{3g}(m_{\mathcal{R}}^2)|^2 \propto$	70% $\sigma_B^{J/\psi}$	19% $\sigma_B^{\psi'}$	$\sim 1\%$ $\sigma_B^{\psi''}$
$|a_{\gamma}(m_{\mathcal{R}}^2)|^2 \propto$	13% $\sigma_B^{J/\psi}$	1.6% $\sigma_B^{\psi'}$	$2.5 \times 10^{-5}\sigma_B^{\psi''}$
$|a_c(m_{\mathcal{R}}^2)|^2 \propto$	20 nb	14 nb	14 nb

where ϕ' is the phase relative to a_{3g}; $\mathcal{F}(s)$ depends on the individual mode, and for simplicity, the phase space factor is incorporated into $|\mathcal{F}(s)|^2$. The one-photon annihilation amplitude can be written as

$$a_{\gamma}(s) = \frac{3\Gamma_{ee}\mathcal{F}(s)/(\alpha\sqrt{s})}{s - m_{\mathcal{R}}^2 + im_{\mathcal{R}}\Gamma_t}e^{i\phi} \ , \tag{2.50}$$

where $m_{\mathcal{R}}$ and Γ_t are the mass and the total width of $\mathcal{R}$, Γ_{ee} is the partial width to e^+e^-, ϕ is the phase relative to a_{3g}. The strong decay amplitude a_{3g} is defined by $\mathcal{C} \equiv |a_{3g}/a_{\gamma}|$, which is the relative strength to a_{γ}, so

$$a_{3g}(s) = \mathcal{C} \cdot \frac{3\Gamma_{ee}\mathcal{F}(s)/(\alpha\sqrt{s})}{s - m_{\mathcal{R}}^2 + im_{\mathcal{R}}\Gamma_t} \ . \tag{2.51}$$

For resonances, $\mathcal{C}$ can be taken as a constant.

In principle, a_{3g}, a_{γ} and a_c depend on individual exclusive mode both in absolute values and in relative strength. In this note, for illustrative purpose, following assumptions are used for an exclusive hadronic mode: $\mathcal{F}(s)$ is replaced by $\sqrt{R(s)}$, where $R(s)$ is the ratio of the inclusive hadronic cross-section to the $\mu^+\mu^-$ cross-section measured at nearby energy [103]; in Eq. (2.51),

$$\mathcal{C} = \sqrt{\frac{B(\mathcal{R} \to ggg \to hadrons)}{B(\mathcal{R} \to \gamma^* \to hadrons)}} \ . \tag{2.52}$$

Here $B(\mathcal{R} \to \gamma^* \to hadrons) = B_{\mu^+\mu^-}R(s)$, where $B_{\mu^+\mu^-}$ is the $\mu^+\mu^-$ branching ratio; while $B(\mathcal{R} \to ggg \to hadrons)$ is calculated as following: we first estimate the branching ratio of $B(\mathcal{R} \to \gamma gg) + B(\mathcal{R} \to ggg)$ by subtracting the lepton pairs, $\gamma^* \to hadrons$, and the modes with charmonium production from the total branching ratio (100%). Then using pQCD result [104] $B(\mathcal{R} \to \gamma gg)/B(\mathcal{R} \to ggg) \approx 6\%$ we obtain $B(\mathcal{R} \to ggg \to hadrons)$. Table 2.7 lists all the estimations used as inputs in the calculations, where $\sigma_B^{\mathcal{R}}$ is the total resonance cross-section of Born order at $s = m_{\mathcal{R}}^2$ obtained from

$$\sigma_0^{\mathcal{R}}(s) = \frac{12\pi\Gamma_{ee}\Gamma_t}{(s - m_{\mathcal{R}}^2)^2 + m_{\mathcal{R}}^2\Gamma_t^2} \ . \tag{2.53}$$

The cross-section by e^+e^- collision incorporating radiative correction on the Born order is expressed by [105]

$$\sigma_{r.c.}(s) = \int_0^{x_m} dx F(x,s)\frac{\sigma_0(s(1-x))}{|1 - \Pi(s(1-x))|^2} \ , \tag{2.54}$$

where σ_0 is σ_B or σ_B' by Eq. (2.46) or (2.48), $F(x,s)$ has been calculated in Ref. [105] and $\Pi(s)$ is the vacuum polarization factor [106]; the upper limit of the integration $x_m = 1 - s_m/s$ where $\sqrt{s_m}$ is the experimentally required minimum invariant mass of the final state f after losing energy to multi-photon emission. In this note, we assume that $\sqrt{s_m}$ equals to 90% of the resonance mass, i.e., $x_m = 0.2$.

For narrow resonances like J/ψ and ψ', one should consider the energy spread function of e^+e^- colliders:

$$G(\sqrt{s}, \sqrt{s'}) = \frac{1}{\sqrt{2\pi}\Delta} e^{-\frac{(\sqrt{s}-\sqrt{s'})^2}{2\Delta^2}}, \tag{2.55}$$

where Δ describes the C.M. energy spread of the accelerator, $\sqrt{s}$ and $\sqrt{s'}$ are the nominal and actual C. M. energy respectively. Then the experimentally measured cross-section

$$\sigma_{exp}(s) = \int_0^\infty \sigma_{r.c.}(s') G(\sqrt{s}, \sqrt{s'}) d\sqrt{s'} . \tag{2.56}$$

The radiative correction reduces the maximum cross-sections of J/ψ, ψ' and ψ'' by 52%, 49% and 29% respectively. The energy spread further reduces the cross-sections of J/ψ and ψ' by an order of magnitude. The radiative correction and energy spread also shift the maximum height of the resonance peak to above the resonance mass. Take ψ' as an example, from Eq. (2.53), $\sigma_B^{\psi'} = 7887$ nb at ψ' mass; substitute $\sigma_0(s)$ in Eq. (2.54) by $\sigma_0^{\mathcal{R}}(s)$ in Eq. (2.53), $\sigma_{r.c.}$ reaches the maximum of 4046 nb at $\sqrt{s} = m_{\psi'} + 9$ keV; with the energy spread $\Delta = 1.3$ MeV at BES/BEPC, combining Eqs. (2.53−2.56), σ_{exp} reaches the maximum of 640 nb at $\sqrt{s} = m_{\psi'} + 0.14$ MeV. Similarly, at J/ψ, with BES/BEPC energy spread $\Delta = 1.0$ MeV, the maximum of σ_{exp} is 2988 nb. At CESRc [5], the maximum of σ_{exp} at J/ψ is 1270 nb ($\Delta = 2.5$ MeV), and at ψ', it is 250 nb ($\Delta = 3.6$ MeV). In this note, we calculate σ_{exp} at the energies which yield the maximum inclusive hadronic cross-sections.

To measure an exclusive mode in e^+e^- experiment, the contribution of the continuum part should be subtracted from the experimentally measured σ'_{exp} to get the physical quantity σ_{exp}, where σ_{exp} and σ'_{exp} indicate the experimental cross-sections calculated from Eqs.(2.54−2.56) with the substitution of σ_B and σ'_B from Eqs. (2.46) and (2.48) respectively for σ_0 in Eq. (2.54). Up to now, most of the measurements did not include this contribution and $\sigma'_{exp} = \sigma_{exp}$ is assumed at least at J/ψ and ψ'. As a consequence, the theoretical analyses are based on pure contribution from the resonance; on the other hand, the experiments actually measure quantities with the contribution of the continuum amplitude included.

We display the effect from the continuum amplitude and corresponding phase for J/ψ, ψ' and ψ'' respectively. To do this, we calculate the ratio

$$k(s) \equiv \frac{\sigma'_{exp}(s) - \sigma_{exp}(s)}{\sigma'_{exp}(s)} \tag{2.57}$$

as a function of ϕ and ϕ', as shown in Fig. 2.20a for ψ' at $\sqrt{s} = m_{\psi'} + 0.14$ MeV for $\Delta = 1.3$ MeV. It can be seen that for certain values of the two phases, k deviates from 0, or equivalently the ratio $\sigma'_{exp}/\sigma_{exp}$ deviates from 1, which demonstrates that the continuum amplitude is non-negligible. By assuming there is no extra phase between a_γ and a_c (i.e., set $\phi = \phi'$), we also work out the k values for different ratios of $|a_{3g}|$ to $|a_\gamma|$, as shown in Fig. 2.20b: line 3 corresponds to the numbers listed in Table 2.7, line 1 is for pure electromagnetic decay channels, and others are chosen to cover the other possibilities of the ratio $|a_{3g}|$ to $|a_\gamma|$.

8.5.3 *Dependence on experimental conditions*

Here we emphasize the dependence of the observed cross-section in e^+e^- collision on the experimental conditions. The most crucial ones are the accelerator energy spread and the beam energy setting for the narrow resonances like J/ψ and ψ'.

Figure 2.21 depicts the expected cross-sections of inclusive hadrons and $\mu^+\mu^-$ pairs at ψ' in an experimental setting under BEPC/BES condition. Two arrows in the figure denote the different positions of the maximum heights of the cross-sections. The height is reduced and the position of the peak is
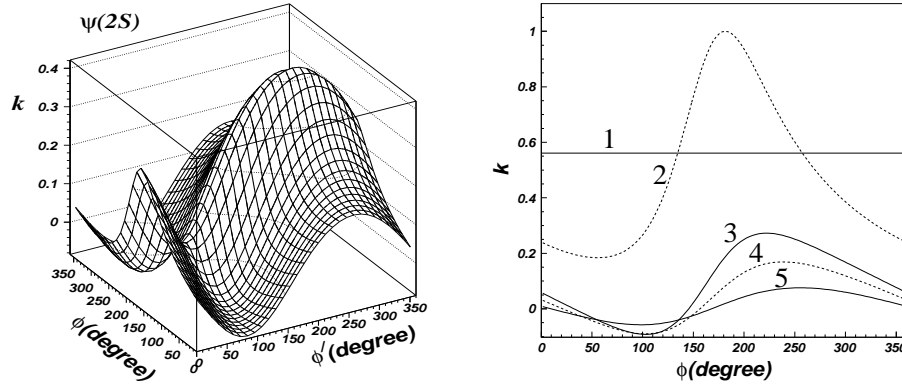
Fig. 2.20: Left: k as a function of ϕ and ϕ' for ψ', with input from Table 2.7. Right: k as a function of ϕ ($\phi = \phi'$) for different ratios of $|a_{3g}|$ to $|a_\gamma|$: line 1 to 5 for $a_{3g} = 0$, $|a_{3g}| = |a_\gamma|$, $|a_{3g}| = 3.4|a_\gamma|$, $|a_{3g}| = 5|a_\gamma|$ and $|a_{3g}| = 10|a_\gamma|$, respectively.

shifted due to the radiative correction and the energy spread of the collider. However, the energy smear hardly affects the continuum part of the cross-section. The $\mu^+\mu^-$ channel is further affected by the interference between resonance and continuum amplitude. As a consequence, the relative contribution of the resonance and the continuum varies as the energy changes. In actual experiments, data are naturally taken at the energy which yields the maximum inclusive hadronic cross-section. This energy does not coincide with the maximum cross-section of each exclusive mode. So it is important to know the beam spread and beam energy precisely, which are needed in the delicate task to subtract the contribution from a_c.

It is worth noting that in principle if a_c is not considered correctly, different experiments will give different results for the same quantity, like the exclusive branching ratio of the resonance, due to the dependence on beam energy spread and beam energy setting. The results will also be different for different kinds of experiments, such as production of J/ψ and ψ' in $p\bar{p}$ annihilation, or in B meson decays. This is especially important since the beam spreads of different accelerators are much different [107] and charmonium results are expected from B-factories.

8.5.4   Implications to charmonium physics

With the non-resonance virtual photon amplitude taking into account in the analysis of the data from e^+e^- experiments, some important conclusions in the charmonium physics could be changed. In this section, we discuss the ψ', ψ'' and J/ψ decays.

In the pure electromagnetic decays of ψ', like $\pi^+\pi^-$ or $\omega\pi^0$, depending on the energy resolution of the e^+e^- collider, a large fraction (e.g., about 60% for $\Delta = 1.3$ MeV) of the observed cross-section is due to non-resonance continuum contribution. With the subtraction of this contribution, the electromagnetic form factors (e.g., $\pi^+\pi^-$ and $\omega\pi^0$) are changed substantially [108].

It has been known from experimental data that in two-body J/ψ decays, the relative phase between the strong amplitude a_{3g} and electromagnetic (EM) amplitude a_γ is orthogonal for the decay modes 1^+0^- ($90°$) [109], 1^-0^- ($(106 \pm 10)°$) [107, 110, 111], 0^-0^- ($(89.6 \pm 9.9)°$) [107, 111, 112], 1^-1^- ($(138 \pm 37)°$) [107] and $N\overline{N}$ ($(89 \pm 15)°$) [111, 113]. It was argued that this large phase follows from the orthogonality of three-gluon and one-photon virtual processes [114]. But at first glance, the $\psi' \to 1^-0^-$ data does not seem to support the extension of such orthogonality to ψ' decays. Here very small branching fractions are reported for $\rho\pi$ and $K^{*+}K^-$ modes (at $\mathcal{O}(10^{-5})$) while much larger branching fraction for $K^{*0}\overline{K^0}$ mode (at $\mathcal{O}(10^{-4})$) [115, 116]. Since the amplitudes of these three decay
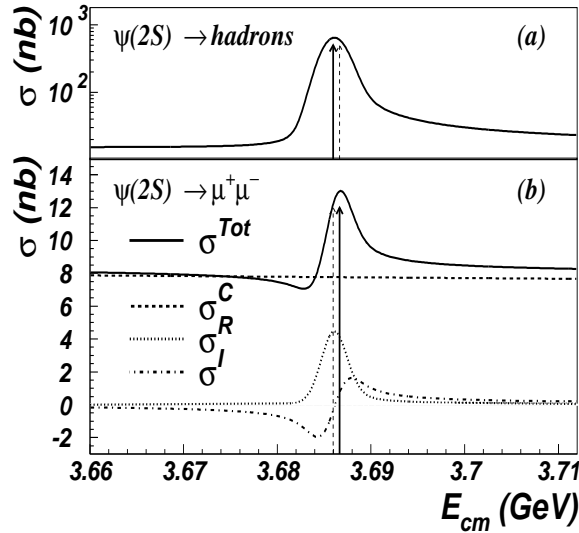
Fig. 2.21: Cross-sections in the vicinity of ψ' for inclusive hadrons (a) and $\mu^+\mu^-$ (b) final states. The solid line with arrow indicates the peak position and the dashed line with arrow the position of the other peak. In (b), dashed line for QED continuum (σ^C), dotted line for resonance (σ^R), dash dotted line for interference(σ^I), and solid line for total cross-section(σ^{Tot}).

modes are expressed as [117]

$$
\begin{aligned}
A_{\rho\pi} &= a_{3g} + a_\gamma, \\
A_{K^{*+}K^-} &= a_{3g} + \epsilon + a_\gamma, \\
A_{K^{*0}\overline{K^0}} &= a_{3g} + \epsilon - 2a_\gamma,
\end{aligned}
\tag{2.58}
$$

with ϵ a SU(3) breaking parameter, it suggests cancellation between a_{3g} and a_γ in $A_{\rho\pi}$ and $A_{K^{*+}K^-}$. This means the phase between a_{3g} and a_γ is around $180°$. But since the available data are from e^+e^- experiments, the amplitude a_c must be included. To explain the data, Eq. (2.58) should be replaced by:

$$
\begin{aligned}
A_{\rho\pi} &= a_{3g} + a_\gamma + a_c, \\
A_{K^{*+}K^-} &= a_{3g} + \epsilon + a_\gamma + a_c, \\
A_{K^{*0}\overline{K^0}} &= a_{3g} + \epsilon - 2(a_\gamma + a_c),
\end{aligned}
\tag{2.59}
$$

Instead of cancellation between a_{3g} and a_γ in $A_{\rho\pi}$ and $A_{K^{*+}K^-}$, the observed cross-sections could be due to the destructive interference between a_{3g} and a_c for these two modes. On the other hand, the interference between these two amplitudes is constructive for $K^{*0}\overline{K^0}$. Such interference pattern happens if the phase between a_{3g} and a_γ is $-90°$, because on top of the resonance, the phase between a_γ and a_c is $-90°$. This means that the orthogonality between a_{3g} and a_γ observed in J/ψ decays holds true in $\psi' \to 1^-0^-$ decays, and it has a negative sign [118]. Similarly, with the amplitude a_c included, from the measured $\psi' \to \pi^+\pi^-$, K^+K^- and $K^0_S K^0_L$ [119], we know that in $\psi' \to 0^-0^-$ decays, the phase between a_{3g} and a_γ is either $(-82 \pm 29)°$ or $(121 \pm 27)°$ [120].

In the OZI suppressed ψ'' decays, MARK III set an upper limit of $\rho\pi$ production cross-section by e^+e^- collision at this resonance to be less than 6.3 pb [121]. On the other hand, CLEO measured $e^+e^- \to \rho\pi$ cross-section at 3.67 GeV to be $(8.3^{+1.7}_{-1.4} \pm 1.2)$ pb. Scaled down to 3.770 GeV according to $1/s^2$, we expect the non-resonance cross-section of $e^+e^- \to \gamma^* \to \rho\pi$ to be (7.5 ± 1.8) pb, which is already greater than the upper limit at the ψ'' peak. We reach the conclusions [122]: (i) there must be destructive interference between the ψ'' resonance and the non-resonance virtual photon amplitudes, i.e., the phase between the strong and EM amplitude is around $-90°$; (ii) the $\mathcal{B}(\psi'' \to \rho\pi)$ is roughly at $(6 \sim 7) \times 10^{-4}$. This branching fraction coincides with the prediction by $2S - 1D$ mixing scenario

which was proposed by Rosner to explain the small $\rho\pi$ branching fraction in ψ' decays [123]. (In the original work of Ref. [123], this branching fraction is 4.1×10^{-4}. But with the new measurement of $J/\psi \to \rho\pi$ by BES [124], it becomes larger.) So with the amplitude a_c being taken into account, we find that this scenario is supported by experimental data. One important prediction of this scenario is that the ψ'' could have a large charmless decay branching fraction (more than 10%) [125]. In the search of the exclusive charmless decays, the interference effect is important, although there are some modes which do not couple with virtual photon, like $K_S^0 K_L^0$ which is purely from ψ'' decays and is clean in such search [126].

In this way, the correct treatment of the amplitude a_c enables us to reach two important conclusions in charmonium physics: (i) the orthogonality between a_{3g} and a_γ can be extended from J/ψ decays to ψ' and OZI suppressed ψ'' decays and the sign of the phase must be negative; (ii) $\mathcal{B}(\psi'' \to \rho\pi)$ is consistent with the $2S - 1D$ mixing scenario which is proposed to solve the $\rho\pi$ puzzle in J/ψ and ψ' decays.

As for J/ψ, the interference between the amplitude a_c and the resonance is at the order of a few percent at most. It is smaller than the statistical and systematic uncertainties of current measurements. Nevertheless, for future high precision experiments such as CLEO-c [5] and BES III [127], when the accuracy reaches a few per mille or even smaller level, it should be taken into account.

8.5.5 *Summary and perspective*

In summary, the continuum amplitude a_c, by itself or through interference with the resonance, could contribute significantly to the observed cross-sections in e^+e^- experiments on charmonium physics. Its treatment depends sensitively on the experimental details, which has not been fully addressed in both e^+e^- experiments and theoretical analyses. In principle, any experimental measurement should subtract the contribution of the continuum amplitude to get the physical quantity related to the resonance. Unfortunately, up to now, most of the experiments just neglect this contribution and the measured quantities are assumed to be purely from resonance decays for almost all the channels studied, or just subtract the continuum contribution incoherently without considering the interference effect, at least at J/ψ and ψ'. This potentially leaves a huge gap between theory and experiments: the quantities which the experiments provide are not exactly what the theory wants to understand.

The effect of the continuum amplitude in the physics analyses are extensively examined in a series of papers published recently [108, 118, 120, 122, 128, 129]: it modifies the measurements of the $\pi^+\pi^-$ and $\omega\pi^0$ form factors at ψ' significantly; it changes the fitting of the relative phase between the strong and electromagnetic decay amplitudes of ψ', it sheds light on the understanding of the "$\rho\pi$ puzzle", and it decreases the observed $\rho\pi$ cross-section near the ψ'' resonance peak to a much smaller level than the expectation from either pure continuum contribution or estimation of the ψ'' non-$D\overline{D}$ decays. The recent large J/ψ and ψ' samples [130] make these studies important due to the improved statistical precision.

The effect of this continuum amplitude will become more significant in the coming high luminosity experiments, such as CLEOc [5] and BES III [127], in this energy region. To achieve high precision to match the high statistics, the cross-section of each mode in the vicinity of the resonance should be measured. This implies an energy scan near the resonance peak at a few energy points with considerably large statistics to allow a reasonable subtraction of the continuum contribution via a fit to the line shape of the resonance.

The above argument also applies to the bottomonium states in the study of their exclusive hadronic decays, where the maximum cross-sections of the resonances are even smaller than those of the charmonium states.

REFERENCES

[1] J. Z. Bai. *et al.* (BES Collab.), Nucl. Instr. Meth. A **344**, 319 (1994).

[2] J. Z. Bai. *et al.* (BES Collab.), Nucl. Instr. Meth. A **458**, 627 (2001).

[3] Y. Kubota *et al.*, Nucl. Instr. Meth. A **320**, 66 (1992).

[4] G. Viehhauser, Nucl. Instr. Meth. A **462**, 146 (2001).

[5] R. A. Briere, *et al.*, "CLEO-c and CESR-c: A New Frontier of Weak and Strong Interactions", CLNS 01/1742 (2001).

[6] M. Artuso *et al.*, Nucl. Instrum. Meth. A **502**, 91 (2003) [arXiv:hep-ex/0209009].

[7] D. Peterson *et al.*, Nucl. Instr. Meth. A **478**, 142 (2002).

[8] T. S. Hill, Nucl. Instr. Meth. A **418**, 32 (1998).

[9] J. Fast *et al.*, Nucl. Instr. Meth. A **435**, 9 (1999).

[10] S. Kurokawa and E. Kikutani, Nucl. Instr. Meth. A **499**,1 (2003).

[11] A. Abashian *et al*, Nucl. Instrum. Meth. A **479**, 117 (2002).

[12] G. Garzoglio *et al.*, Nucl. Instrum. Meth. A **519**, 558 (2004).

[13] LEP design report, CERN–LEP/84–01 (1984).

[14] D. Decamp *et al.* (ALEPH Collab.), Nucl. Instr. Meth. A **294**, 121 (1990);
D. Buskulic *et al..* (ALEPH Collab.), Nucl. Instr. Meth. A **360**, 481 (1995);
ALEPH Handbook, Ed.: C. Bowdery, ISBN 92–9083–072–7 (1995).

[15] P. Aarnio *et al.* (DELPHI Collab.), Nucl. Instr. Meth. A **303**, 233 (1991);
(DELPHI Collab.), Contribution to the 28th International Conference on High Energy Physics, Brussels (July 1995), EPS764;
CERN preprint CERN–PPE–95–194 (1995)

[16] B. Adeva *et al.* (L3 Collab.), Nucl. Instr. Meth. A **289**, 35 (1990);
O. Adriani *et al.* (L3 Collab.), Phys. Rep. **236**, 1 (1993);
F. Beissel *et al.*, Nucl. Instr. Meth. A **332**, 33 (1993);
B. Acciarri *et al.* (L3 Collab.), Nucl. Instr. Meth. A **351**, 300 (1994).

[17] K. Ahmet *et al.* (OPAL Collab.), Nucl. Instr. Meth. A **305**, 275 (1991);
P.P. Allport *et al.* (OPAL Collab.), Nucl. Instr. Meth. A **324**, 34 (1993);
P.P. Allport *et al.* (OPAL Collab.), Nucl. Instr. Meth. A **346**, 476 (1993).

[18] A. Böhrer, Phys. Rep. **291**, 107 (1997).

[19] CDF II Collaboration, FERMILAB–PUB–96/390–E (1996).

[20] A. Sill *et al*, Nucl. Instrum. Meth. A **447**, 1 (2000).

[21] T. Affolder *et al*, Nucl. Instrum. Meth. A **42586**, 249 (2004).

[22] D. Acosta *et al*, Nucl. Instrum. Meth. A **518**, 605 (2004).

[23] L. Balka *et al*, Nucl. Instrum. Meth. A **267**, 272 (1988).

[24] S. Bertolucci *et al*, Nucl. Instrum. Meth. A **267**, 301 (1988).

[25] Y. Seiya *et al*, Nucl. Instrum. Meth. A **480**, 524 (2002).

[26] D. Acosta *et al*, Nucl. Instrum. Meth. A **461**, 540 (2001).

[27] F. Abe *et al.*, Nucl. Instrum. Methods Phys. Res. A **271**, 387 (1985).

[28] V. Abazov *et al.*, to be submitted to Nucl. Instrum. Methods Phys. Res. A, and T. LeCompte and H.T. Diehl, "The CDF and D0 Upgrades for Run II", Ann. Rev. Nucl. Part. Sci. **50**, 71 (2000)

[29] S. Abachi *et al.*, Nucl. Instrum. Methods Phys. Res. A **338**, 185 (1994)

[30] K. Ackerstaff *et al.* [HERMES Collaboration], Nucl. Instrum. Meth. A **417**, 230 (1998) [arXiv:hep-ex/9806008].

[31] H1 and ZEUS publications are listed at http://www-h1.desy.de/publications/H1publication.short_list.html and http://www-zeus.desy.de/zeus_papers/zeus_papers.html

[32] G. Ingelman, A. De Roeck and R. Klanner, DESY–96–235.

[33] I. Abt *et al.* [H1 Collaboration], Nucl. Instrum. Meth. A **386**, 310 and 348 (1997).

[34] T. Nicholls *et al.* [H1 SPACAL Group Collaboration], Nucl. Instrum. Meth. A **374**, 149 (1996).

[35] M. Derrick *et al.* [ZEUS Collaboration], Phys. Lett. B **293**, 465 (1992).

[36] ZEUS Collaboration, U.Holm (ed.), *The ZEUS Detector* Status Report (unpublished), DESY 1993, available on http://www-zeus.desy.de/bluebook/bluebook.html

[37] E. Hartouni *et al.* , HERA–B Design Report, DESY–PRC–95–01 (1995).

[38] C. Padilla [HERA–B Collaboration], Nucl. Instrum. Meth. A **446**, 176 (2000).

[39] The HERA–B Collaboration, HERA–B Status Report, DESY–PRC–00–04 (2000).

[40] K. Ehret, Nucl. Instrum. Meth. A **446**, 190 (2000).

[41] C. Bauer *et al.*, Nucl. Instrum. Meth. A **453**, 103 (2000).

[42] T. Zeuner [HERA–B Collaboration], Nucl. Instrum. Meth. A **446**, 324 (2000).

[43] C. Pruneau, S. Gavin and S. Voloshin, Phys. Rev. C **66**, 044904 (2002) [arXiv:nucl–ex/0204011].

[44] M. Capeans, Nucl. Instrum. Meth. A **446**, 317 (2000).

[45] J. Pyrlik [HERA–B RICH Collaboration], Nucl. Instrum. Meth. A **446**, 299 (2000).

[46] I. Arino *et al.*, Nucl. Instrum. Meth. A **453**, 289 (2000).

[47] A. Zoccoli [HERA–B Collaboration], Nucl. Instrum. Meth. A **446**, 246 (2000);
G. Avoni *et al.* , Proc. of the IX Conf. on Calorimetry in Particle Physics, Annecy, France, Oct. 9–14, 2000, Calorimetry in High energy physics, (2001) 777.

[48] M. Buchler *et al.*, IEEE Trans. Nucl. Sci. **46**, 126 (1999) [arXiv:physics/9812018].

[49] A. Arefev *et al.*, IEEE Trans. Nucl. Sci. **48**, 1059 (2001).

[50] J. M. Hernández *et al.*, Nucl. Science Symp. Conf. Record, 2000 IEEE, vol.**2** 12/116 (2000).

[51] A.A. Zholents *et al.*, Phys. Lett. B **96**, 214 (1980).

[52] J.Z. Bai *et al.*, Phys. Rev. Lett. **69**, 3021 (1992).

[53] V.M. Aulchenko *et al.*, Phys. Lett. B **573**, 63 (2003).

[54] A.A. Sokolov and I.M. Ternov, Sov. Phys. Dokl. **18**, 1203 (1964).

[55] A.D. Bukin *et al.*, in: Vth Int. Symposium on High Energy Physics and Elementary Particle Physics, Warsaw, 1975, p.138.

[56] A.S. Artamonov *et al.*, Phys. Lett. B **118**, 225 (1982).

[57] A.S. Artamonov *et al.*, Phys. Lett. B **173**, 272 (1984).

[58] S.E. Baru *et al.*, Z. Phys. C **56**, 547 (1992).

[59] A.S. Artamonov *et al.*, Phys. Lett. B **474**, 427 (2000).

[60] W.W. MacKay *et al.*, Phys. Rev. D **29**, 2483 (1984).

[61] D.P. Barber *et al.*, Phys. Lett. B **135**, 498 (1984).

[62] T.A. Armstrong *et al.*, Phys. Rev. D **47**, 772 (1993).

[63] R. Assmann *et al.*, Eur. Phys. J. C **6**, 187 (1999).

[64] A.N. Skrinsky and Yu.M. Shatunov, Sov. Phys. Usp. **32**, 548 (1989).

[65] C. Bernardini *et al.*, Phys. Rev. Lett. **10**, 407 (1963).

[66] V.E. Blinov *et al.*, Nucl. Instr. Meth. A **494**, 81 (2002).

[67] V.V. Anashin *et al.*, Nucl. Instr. Meth. A **478**, 420 (2002).

[68] K. Hagiwara *et al.* [Particle Data Group Collaboration], Phys. Rev. D **66**, 010001 (2002).

[69] E. A. Kuraev and V. S. Fadin, Yad. Fiz. **41**, 733 (1985) [Sov. J. Nucl. Phys. **41**, 466 (1985)].

[70] G. Altarelli and G. Martinelli, CERN **86–02**, 47 (1986); O. Nicrosini and L. Trentadue, Phys. Lett. B **196**, 551 (1987).

[71] F. A. Berends, G. Burgers and W. L. Neerven, Nucl. Phys. B **297**, 429 (1988); *ibid.* **304**, 921 (1988).

[72] Y. S. Tsai, SLAC–PUB–3129 (1983).

[73] P. Alexander *et al.*, Nucl. Phys. B **320**, 45 (1989).

[74] R.N. Cahn, Phys. Rev. D **36**, 2666 (1987).

[75] J. D. Jackson and D. L. Scharre, Nucl. Instrum. Meth. **128**, 13 (1975).

[76] F.A. Berends *et al.*, in Proceedings of the Workshop on Z Physics at LEP, v.1, (1989) page 89, edited by G.Altarelli, R.Kleiss and C.Verzegnassi.

[77] F.A. Berends, K.J.F. Gaemers and R. Gastmans, Nucl. Phys. B **57**, 381 (1973).

[78] F.A. Berends and G.L. Komen, Phys. Lett. B **63**, 432 (1976).

[79] F.A. Berends and R. Kliess, Nucl. Phys. B **177**, 237 (1980).

[80] P. Ruiz–Femenia and A. Pich, Phys. Rev. D **64**, 053001 (2001) [arXiv:hep-ph/0103259].

[81] G. S. Abrams *et al.*, Phys. Rev. D **21**, 2716 (1980).

[82] C. Baglin *et al.*, Phys. Lett. B **171**, 135 (1986).

[83] C. Baglin *et al.*, Phys. Lett. B **187**, 191 (1987).

[84] T. A. Armstrong *et al.*, Phys. Rev. Lett. **68**, 1468 (1992).

[85] T. A. Armstrong *et al.*, Phys. Rev. Lett. **69**, 2337 (1992).

[86] T. A. Armstrong *et al.*, Phys. Rev. D **47**, 772 (1993).

[87] M. Ambrogiani *et al.*, Phys. Rev. Lett. **83**, 2902 (1999).

[88] S. Bagnasco *et al.*, Phys. Lett. B **533**, 237 (2002).

[89] M. Ambrogiani *et al.*, Phys. Lett. B **566**, 45 (2003).

[90] M. Andreotti *et al.*, Phys. Rev. Lett. **91**, 091801 (2003).

[91] W. F. Henning (ed.), An International Accelerator Facility for Beams of Ions and Antiprotons, Conceptual Design Report, Gesellschaft für Schwerionenforschung, Darmstadt (Germany), November 2001, `www.gsi.de/GSI-Future/cdr`.

[92] D. P. McGinnis, G. Stancari, S. J. Werkema, Nucl. Instrum. Methods A **506**, 205 (2003).

[93] S. J. Werkema, Precision measurements of the Accumulator beam energy, P–Bar Note 633, Fermilab, February 2000, `www-bdnew.fnal.gov/pbar/documents/pbarnotes/pdf_files/pb633.pdf`.

[94] A. S. Artamonov *et al.*, Phys. Lett B **474**, 427 (2000).

[95] V. M. Aulchenko *et al.* [KEDR Collaboration], Phys. Lett. B **573**, 63 (2003) [arXiv:hep-ex/0306050].

[96] V. L. Chernyak and A. R. Zhitnitsky, Phys. Rep. **112**, 175 (1984).

[97] S. E. Baru *et al.*, Phys. Rep. **267**, 71 (1996).

[98] M. Andreotti *et al.* [Fermilab E835 Collaboration], Phys. Rev. Lett. **91**, 091801 (2003) [arXiv:hep-ex/0308055].

[99] E. Keil and W. Schnell, CERN–ISR–TH–RF/69–48, July 1969.

[100] V.M. Budnev *et al.*, Phys. Rep. **15**, 181 (1975).

[101] G. A. Schuler, Comput. Phys. Commun. **108**, 279 (1998); /afs/cern.ch/user/s/schulerg/public/galuga2.

[102] S. Rudaz, Phys. Rev. D **14**, 298 (1976).

[103] J. Z. Bai *et al.*, Phys. Rev. Lett. **84**, 594 (2000); J. Z. Bai *et al.*, Phys. Rev. Lett. **88**, 101802 (2002).

[104] W. Kwong, Phys. Rev. D **37**, 3210 (1988).

[105] E. A. Kuraev and V. S. Fadin, Sov. J. Nucl. Phys. **41**, 466 (1985); G. Altarelli and G. Martinelli, CERN **86–02**, 47 (1986); O. Nicrosini and L. Trentadue, Phys. Lett. B **196**, 551 (1987); F. A. Berends, G. Burgers and W. L. Neerven, Nucl. Phys. B **297**, 429 (1988); *ibid.* **304**, 921 (1988).

[106] F. A. Berends, K. J. F.Gaemers and R. Gastmans, Nucl. Phys. B **57**, 381 (1973); F. A. Berends and G. J. Komen, Phys. Lett. B **63**, 432 (1976).

[107] L. Köpke and N. Wermes, Phys. Rep. **174**, 67 (1989).

[108] P. Wang, X. H. Mo and C. Z. Yuan, Phys. Lett. B **557**, 192 (2003).

[109] M. Suzuki, Phys. Rev. D **63**, 054021 (2001).

[110] R. M. Baltrusaitis *et al.*, Phys. Rev. D **32**, 2883 (1985); D. Coffman *et al.*, Phys. Rev. D **38**, 2695 (1988); J. Jousset *et al.*, Phys. Rev. D **41**, 1389 (1990); A. Bramon, R. Escribano and M. D. Scadron, Phys. Lett. B **403**, 339 (1997); M. Suzuki, Phys. Rev. D **58**, 111504 (1998); N. N. Achasov and V. V. Gubin, Phys. Rev. D **61**, 117504 (2000).

[111] G. López Castro *et al.*, in CAM–94, Cancum, Mexico, edited by A. Zepeda, AIP Conf. Proc. **342** (AIP, New York, 1995), p.441.

[112] M. Suzuki, Phys. Rev. D **60**, 051501 (1999).

[113] A. Antonelli, Phys. Lett. B **301**, 317 (1993); R. Baldini, C. Bini and E. Luppi, Phys. Lett. B **404**, 362 (1997); R. Baldini, *et al.* Phys. Lett. B **444**, 111 (1998).

[114] J. M. Gérard and J. Weyers, Phys. Lett. B **462**, 324 (1999).

[115] M. Ablikim *et al.* [BES Collaboration], arXiv:hep-ex/0408047; arXiv:hep-ex/0407037.

[116] N. E. Adam *et al.* [CLEO Collaboration], arXiv:hep-ex/0407028.

[117] H. E. Haber and J. Perrier, Phys. Rev. D **32**, 2961 (1985).

[118] P. Wang, C. Z. Yuan, X. H. Mo, Phys. Rev. D **69**, 057502 (2004).

[119] J. Z. Bai *et al.*, Phys. Rev. Lett. **92**, 052001 (2004).

[120] C. Z. Yuan, P. Wang, X. H. Mo, Phys. Lett. B **567**, 73 (2003).

[121] Yanong Zhu, Ph. D. thesis, California Institute of Technology, 1988, Caltech Report No. CALT–68–1513; W. A. Majid, Ph. D. thesis, University of Illinois, 1993, UMI–94–11071–mc.

[122] P. Wang, C. Z. Yuan and X. H. Mo, Phys. Lett. B **574**, 41 (2003).

[123] J. L. Rosner, Phys. Rev. D **64**, 094002 (2001).

[124] M. Ablikim *et al.*, Phys. Rev. D **70**, 012005 (2004).

[125] P. Wang, C. Z. Yuan and X. H. Mo, arXiv:hep-ph/0410300.

[126] P. Wang, C. Z. Yuan and X. H. Mo, Phys. Rev. D **70**, 077505 (2004).

[127] H. S. Chen, "BEPCII/BES III project", talk at ICHEP 2002, Amsterdam, Holland, July 24–31, 2002.

[128] P. Wang, C. Z. Yuan and X. H. Mo, HEP & NP **27**, 456 (2003) [arXiv:hep-ex/0210062].

[129] P. Wang, C. Z. Yuan, X. H. Mo and D. H. Zhang, Phys. Lett. B **593**, 89 (2004).

[130] F. A. Harris, "Recent ψ' and η_c Results from BES", report at ICHEP 2002, Amsterdam, Holland, July 24–31, 2002.

Chapter 3

SPECTROSCOPY

Conveners: G. Bali, N. Brambilla, R. Mussa, J. Soto

Authors: G. Bali, D. Besson, A. Böhrer, N. Brambilla, P. Cooper, C. Davies, E. Eichten, S. Eidelman, R. Faustov, T. Ferguson, R. Galik, S. Godfrey, A. Kronfeld, P. Mackenzie, C. Morningstar, R. Mussa, V. Papadimitriou, A. Pineda, S. Ricciardi, J. -M. Richard, E. Robutti, J. Simone, T. Skwarnicki, J. Soto, G. Stancari, Yu. Sumino, J. Tseng, B. Yabsley, Z. Zhao

1   THEORY INTRODUCTION[1]

Most theorists agree that QCD alone should describe the spectroscopy of heavy quarkonium. Nevertheless, there are important difficulties to do so in practise. One can roughly distinguish between two approaches: the phenomenological and the theoretical one.

The phenomenological approach attempts to model what are believed to be the features of QCD relevant to heavy quarkonium with the aim to produce concrete results which can be directly confirmed or falsified by experiment and may guide experimental searches. The theoretical approach tries to describe heavy quarkonium with QCD based calculations and/or approximations.

The basic tools of the phenomenological approach are potential models, both non-relativistic and relativistic. The use of non-relativistic potential models is justified by the fact that the bottom and, to a lesser extent, the charm masses are large in comparison to Λ_{QCD}, the typical hadronic scale. Hence a quantum mechanical description of the system based on two heavy quarks interacting through a suitable potential appears reasonable. The potential is usually chosen in a way that at short distances coincides with the weak coupling QCD one-gluon exchange Coulomb potential and in the long range it incorporates confinement, for instance, by including a linearly rising potential. Since relativistic effects appear to be sizable for some states, mostly in charmonium, models incorporating some relativistic kinematics are also being used. Different models of quark confinement may result in different classes of relativistic corrections. For states close to and beyond the two heavy-light meson threshold, the potential models have to be complemented with these extra degrees of freedom in order to account for possible mixing effects. Hybrid states which are expected from QCD should also be incorporated by hand. The phenomenological approaches will be described in Section 3.

The theoretical approach aims at obtaining the spectrum of heavy quarkonium from QCD. This is in principle more complicated than obtaining masses of light mesonic states since an additional large scale m, the mass of the heavy quark, enters the calculation. If we assume that m is much larger than any other scale in the system, in particular Λ_{QCD}, the heavy quark and antiquark are expected to move slowly about each other at a relative velocity $v \ll 1$. The system becomes non-relativistic and hence splittings between states with the same quantum numbers are expected to be of size $\sim mv^2$ whereas hyperfine splittings are of order $\sim mv^4$, if one proceeds by analogy to QED bound states (where $v \sim \alpha$). If $v^2 \sim 0.1$, as expected in ground state bottomonium, a direct (lattice) QCD calculation requires a precision significantly better than 10 % to detect spin-averaged masses and of more than 1 % to resolve fine structure splittings. Moreover, all these scales have to be resolved on one and the same lattice, necessitating many lattice points. This is to be compared with light quarkonium where the splittings are a leading order effect. Consequently, calculating the heavy quarkonium spectrum from lattice QCD

---

[1]Author: J. Soto

requires a tremendous computational effort, which in some cases can be somewhat ameliorated with the introduction of anisotropic lattices, as discussed in Section 2.1.

Alternatively, it may be advisable to exploit the fact that m is large and v small before attempting the computation. This is most efficiently done using non relativistic effective field theories. The effective theory which takes into account that m is much larger than the remaining scales in the system is NRQCD [1–3]. Since $m \gg \Lambda_{QCD}$, NRQCD can be made equivalent to QCD at any desired order in $1/m$ and $\alpha_s(m) \ll 1$ by enforcing suitable matrix elements to be equal at that order in both theories. One may then attempt a lattice calculation from NRQCD. What one gains now is that the spin independent splittings are a leading order effect rather than a v^2 one and the hyperfine splittings a v^2 correction (rather than v^4). See Section 2.2.1 for a detailed discussion of these calculations.

NRQCD, however, does not fully exploit the fact that v is small. In particular, gluons of energy $\sim mv$, the typical relative three-momentum of the heavy quarks, are still explicit degrees of freedom in NRQCD whereas they can never be produced at energies $\sim mv^2$. For lower lying states the scale mv corresponds both to the typical momentum transfer k (inverse size of the system) and to the typical relative three-momentum p. It is then convenient to introduce a further effective theory where degrees of freedom of energy $\sim k$ are integrated out. This EFT is called pNRQCD [4, 5], see Section 2.3. The degrees of freedom of pNRQCD depend on the interplay of the scales k, $E \sim mv^2$ and Λ_{QCD}. The weak and strong coupling regimes are discussed respectively in Section 2.3.1 and 2.3.2. A related EFT for the weak coupling regime, called vNRQCD [6], will be discussed in Chapter 6 (Standard Model). Sum rules are also discussed in the same chapter in relation to the calculation of the lowest energy levels in the spectrum.

The distribution of the theory contributions is as follows. We begin with the theoretical approach and use the EFT philosophy as an organizing principle. We shall arrange the contributions according to the number of hypothesis that are done in order to obtain them from QCD. Hence, we shall start by contributions which rely on QCD only. Next we will discuss contributions which may be embraced by NRQCD, and finally contributions which may be embraced by pNRQCD. We would like to emphasize that, if the relevant hypothesis are fulfilled, (i) NRQCD and pNRQCD are equivalent to QCD, and (ii) each of these EFTs allows to factorize a relevant scale, which further simplifies calculations. All the states can in principle be studied from QCD, the main tool being lattice techniques. In practise, however, a number of limitations exists, which are described in Section 2.1. Except for very high excitations (particularly in charmonium) for which relativistic effects become important, these states can also be studied from NRQCD, the main tool being again lattice techniques, see Section 2.2. States below and not too close to open flavour threshold can also be studied using pNRQCD. A few of these, including the $\Upsilon(1S)$ and $\eta_b(1S)$, can be studied by means of analytical weak coupling techniques (Section 2.3.1). The remaining ones can be studied using pNRQCD in the strong coupling regime (Section 2.3.2), which needs as an input nonperturbative potentials to be calculated on the lattice. We continue next with the phenomenological approach, which mainly consist of a description of potential models (Section 3.1) and of approaches to open flavour thresholds (Section 3.3). The former provide good phenomenological descriptions for the states below open flavour threshold whereas the latter are important for a good description of excitations close or above the open flavour threshold, in particular of the recently discovered $X(3872)$ charmonium state. An effort has been made to link potential models to the theoretical approach. Double (and triple) heavy baryons are also discussed both in the theoretical (Sections 2.2.3, 2.3.4) and phenomenological approach (Section 3.4.2).

2 THEORETICAL APPROACH

2.1 Direct lattice QCD calculation[2]

2.1.1 Methods

(For an introduction to general QCD lattice methods cf. Chapter 1.) When simulating quarks with a mass m on a lattice with lattice spacing a, one will inevitably encounter ma [or $(ma)^2$] corrections, which are of order one, unless $m \ll a^{-1}$. The Fermilab group [7] have argued in favour of a re-interpretation of the clover action, suggesting that physical results can be obtained even for masses as large as $ma \approx 1$, see also Section 2.2.1 below. However, still one would either want to extrapolate such results to the continuum limit or at least put them into the context of an effective field theory with two large scales, in this case m and a^{-1}. If interpreted as an EFT, higher order terms have to be added and the matching coefficients to QCD have to be determined to sufficiently high order in perturbation theory, to reduce and estimate remaining systematic uncertainties.

In the quenched approximation, the condition $ma \ll 1$ can be realized for charm quarks; however, at present bottom quarks are still somewhat at the borderline of what is possible. One approach to tackle this problem is to introduce an anisotropy, with a temporal lattice spacing a_τ smaller than the spatial lattice spacing $a_\sigma = \xi a_\tau$, with parameter $\xi > 1$. The spatial lattice extent $L_\sigma a_\sigma$ has to be large enough to accommodate the quarkonium state (whose size is of order $r \simeq (mv)^{-1}$). With a sufficiently large a_σ this is possible, keeping the number of points L_σ limited, while the temporal lattice spacing can be chosen to be smaller than the quarkonium mass in question, $a_\tau < M^{-1}$, at relative ease. This means that anisotropic simulations are naively cheaper by a factor ξ^3, compared to the isotropic analogue with a lattice spacing $a = a_\tau$.

While at tree level the lattice spacing errors are indeed of $\mathcal{O}[(ma_\tau)^n]$, one loop corrections mean that there will still be $\mathcal{O}[\alpha_s(ma_\sigma)^n]$ terms present: only to the extent to which $\alpha_s \xi^n$ is small, the leading order lattice effects can be regarded as $\mathcal{O}[(ma_\tau)^n]$. Furthermore, the anisotropy parameter ξ has to be determined consistently for the quark and gluon contributions to the QCD action. Within the quenched approximation this problem factorizes: one can first "measure" the gauge anisotropy by determining the decay of purely gluonic spatial and temporal correlation functions. Subsequently, one can adjust the Fermionic anisotropy accordingly. This fine-tuning does not come for free, in particular if the number of adjustable parameters is larger than two. Consequently, no consistent nonperturbative $\mathcal{O}(a)$ improvement programme has been carried through so far, for non-trivial anisotropies. While there might be a net gain from using anisotropy techniques in the quenched approximation, the parameter tuning becomes much more delicate and costly once light sea quarks are included. In this case the numerical matching of the anisotropy for light Fermions cannot be disentangled from the gluonic one anymore.

2.1.2 Results with relativistic heavy quarks

We will first review results on the quenched bottomonium spectrum, before discussing charmonia in the quenched approximation, on anisotropic as well as on isotropic lattices and with sea quarks.

Only one bottomonium study with relativistic action has been performed so far [8], employing lattices with anisotropies $\xi = 4$ and $\xi = 5$, in the quenched approximation. In this case, the inverse lattice spacing, a_τ^{-1} was varied from 4.5 GeV up to about 10.5 GeV. The lattice extents were typically of size $L_\sigma a_\sigma \approx 1$ fm, however, they were not kept constant when varying a_τ such that finite size effects are hard to disentangle. The spatial lattice sizes are also dangerously close to the inverse confinement–deconfinement phase transition temperature (cf. Chapter 7). After using the $1^1P_1 - 1^3S_1$ splitting (identifying the 1^1P_1 mass with the spin averaged experimental $1\overline{^3P}$ states) to set the lattice spacing and the 1^3S_1 to adjust the b quark mass, qualitative agreement with the spin-averaged experimental spectrum is observed.

---

[2]Author: G. Bali

Table 3.1: Charmonium results in the quenched approximation [9–12], where the scale is such that $r_0^{-1} = 394$ MeV. The purely statistical errors do not reflect the uncertainty in r_0, or due to quenching. All values are in units of MeV. Glueball masses [13–15] are included for comparison. The last three lines refer to spin-exotic (non-quark model) quantum numbers.

J^{PC}	state	CP–PACS	Columbia	QCD-TARO	experiment	glueballs
0^{-+}	η_c	3013 (1)	3014 (4)	3010 (4)	2980(1)	2500(40)
	η_c'	3739(46)	3707(20)		3654(10)	3500(60)
1^{--}	J/ψ	3085 (1)	3084 (4)	3087 (4)	3097	
	$\psi(2S)$	3777(40)	3780(43)		3686	3700(50)
1^{+-}	h_c	3474(10)	3474(20)	3528(25)	$m(1^3\overline{P})=3525$	2830(30)
	h_c'	4053(95)	3886(92)		—	
0^{++}	χ_{c0}	3408	3413(10)	3474(15)	3415(1)	1720(30)
	χ_{c0}'	4008(122)	4080(75)		—	2540(120)
1^{++}	χ_{c1}	3472 (9)	3462(15)	3524(16)	3511	
	χ_{c1}'	4067(105)	4010(70)		—	
2^{++}	χ_{c2}	3503(24)	3488(11)		3556	2300(25)
	χ_{c2}'	4030(180)			—	
2^{-+}	1^1D_2		3763(22)		—	2975(30)
					—	3740(40)
2^{--}	1^3D_2		3704(33)		$X(3872)$???	3780(40)
3^{--}	1^3D_3		3822(25)		—	3960(90)
3^{+-}	1^1F_3		4224(74)		—	3410(40)
3^{++}	1^3F_3		4222(140)		—	3540(40)
0^{+-}	H_0		4714(260)		—	4560(70)
1^{-+}	H_1		4366(64)		—	
2^{+-}	H_2		4845(220)		—	3980(50)

For the $1^3S_1 - 1^1S_1$ splitting, where one might hope finite size effects to largely cancel, the authors obtain the continuum extrapolated value of 59 ± 20 MeV. To leading order in pQCD, this splitting is expected to be proportional to the wave function density at the origin, multiplied by $\alpha_s(\mu)$. Adjusting the lattice spacing from spin-averaged splittings amounts to matching the quenched lattice coupling to the phenomenological one at a low energy scale $\ll \mu$. In the quenched approximation $\alpha_s(\mu)$ approaches zero faster as μ is increased and hence $\alpha_s(\mu)$ will be underestimated: the quoted fine structure splitting represents a lower limit on the phenomenological one. Indeed, the analogous result for the charmonium case underestimates the known experimental number by a factor 1.25–1.5, when setting the scale in a similar way [9, 10].

Both, the Columbia group [11, 12] as well as the CP–PACS Collaboration [9] have studied the charmonium spectrum on anisotropic lattices. The same anisotropic clover quark action was used as for the bottomonium study discussed above, where the leading order lattice artefacts are expected to be of $\mathcal{O}(\alpha_s a_\tau)$ and $\mathcal{O}(a_\tau^2)$. The CP–PACS Collaboration studied the anisotropy, $\xi = 3$, on a set of four inverse lattice spacings a_σ^{-1}, ranging from about 1 up to 2.8 GeV, on spatial volumes $(1.6\,\text{fm})^3$. The Columbia group simulated four lattice spacings ranging from about 0.8 up to 2 GeV at anisotropy $\xi = 2$. They were able to vary their volume from 1.5 up to 3.3 fm and found finite volume effects to be below their statistical resolution.

We display the respective continuum-limit extrapolated results in Table 3.1. We also include results from the QCD–TARO collaboration [10], with $\xi = 1$. The quark mass is set such that the spin averaged $1\overline{S}$ state corresponds to 3067.6 MeV. (Note that the present phenomenological value is slightly higher than this.) For comparison we convert the Columbia results into units of $r_0^{-1} = 394$ MeV. This
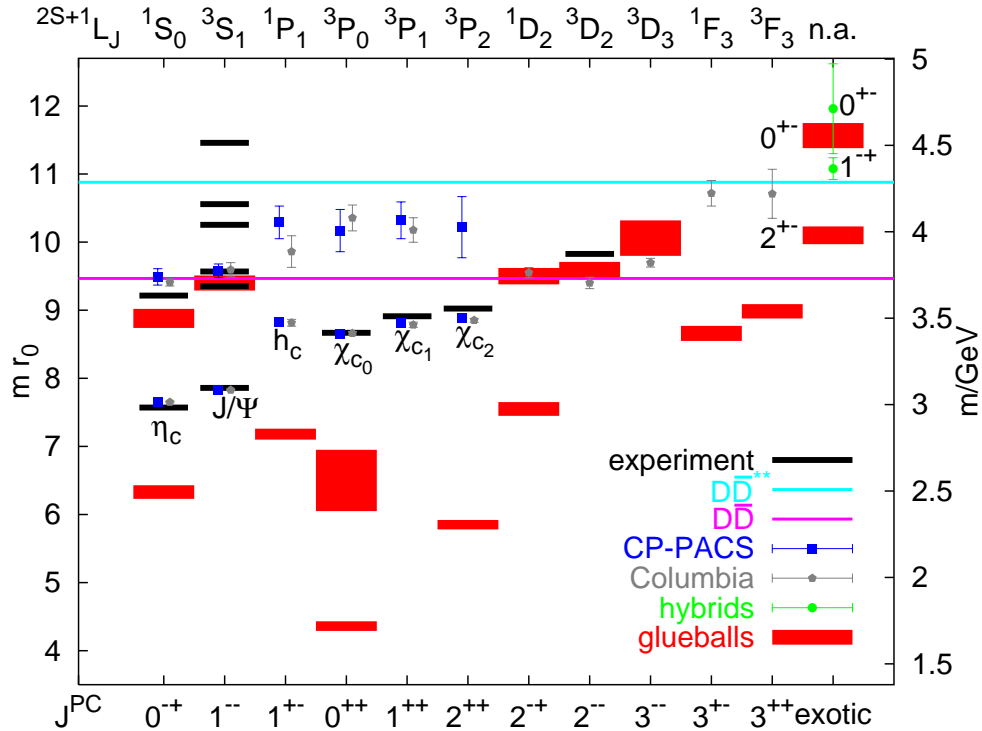
Fig. 3.1: The quenched charmonium spectrum (CP–PACS [9], Columbia [11, 12]), glueballs [13–15] and spin-exotic $c\bar{c}$-glue hybrids [12], overlayed with the experimental spectrum.

scale is implicitly defined through the static potential [16], $dV(r)/dr|_{r=r_0} = 1.65$. It cannot directly be obtained in experiment. However, r_0/a is easily and very precisely calculable in lattice simulations. In the quenched approximation we have to assume a scale error on spin averaged splittings of at least 10 %, on top of the errors displayed in the Table. We also include glueball masses [13–15] into the table. The last three lines incorporate spin-exotic J^{PC} assignments ($c\bar{c}g$ hybrid mesons).

The anisotropic results are also displayed in Fig. 3.1, borrowed from Ref. [17], where we plot the new $X(3872)$ state at $J^{PC} = 2^{--}$, however, this assignment is somewhat arbitrary. As can be seen, where overlap exists, the results from the three collaborations employing three different anisotropies are consistent with each other. All S- and P-wave fine structure splittings are underestimated, which is expected in the quenched approximation. The Columbia group [12] reported that the state created by the $J = 1$ D-wave operator rapidly converged towards the mass of the vector S-wave ground state. The same was observed in the case of the 2^{++} F-wave with respect to the χ_{c_2} ground state: this indicates that the charm quark mass is too light for L to be a good quantum number.

That the charm mass is not particularly heavy, in comparison to typical scales of gluonic excitations, can also be seen from the overlap between the glueball and charmonium spectra. Once sea quarks are switched on, these glueballs will become unstable. However, the presence of a background of such excitations might very well affect spectrum and decays in some channels. For instance the dominant decay of a vector charmonium is into gluons, and it is quite conceivable that such a channel should also couple to would-be glueballs.

When performing the Wick contractions of propagators of flavour singlet states like charmonia, two contributions arise: a connected one, with quark and antiquark propagating alongside each other, and a disconnected (OZI suppressed) one, with annihilation and creation diagrams of $c\bar{c}$. In all charmonium simulations that have been performed so far, with two notable exceptions [18, 19], the disconnected diagram has been neglected. It is well known that OZI processes play a role within the light pseudoscalar

and scalar sectors. This has also been extensively studied on the lattice [20,21]. In the case of charmonia, in particular for S and D waves, substantial corrections due to mixing with intermediate gluonic states are a possibility, even within the quenched approximation. For states that are close to threshold, in addition mixing with two-meson states will occur, once sea quarks are included.

Charmonia have also been studied on isotropic lattices, within the quenched approximation [10, 18, 19, 22, 23], and with sea quarks [24]. The QCD–TARO collaboration [10] worked at tiny lattice spacings, ranging from about 2 GeV down to 5 GeV. The results are consistent with those obtained by the Columbia group [12] and by CP–PACS [9], but the use of an $\mathcal{O}(a)$ improved action allowed for a very well controlled continuum limit extrapolation. The quenched value, within the OZI approximation and using $r_0^{-1} = 394$ MeV to set the scale, is 77(2)(6) MeV, with all remaining systematic errors quoted. This value would increase by 15 % if the scale was set from the $1\overline{^3P} - 1\overline{S}$, still short of the experimental 117 MeV.

In an exploratory study, in which for the first time the diagram that contains disconnected quark loops has been included, McNeile and Michael [18] find evidence that while the position of the ground state vector state appears to be largely unaffected, the pseudoscalar mass is reduced by an amount of the order of 20 MeV with respect to the non-flavour singlet reference value. One explanation might be the background of glueballs, c.f. Fig. 3.1. A more recent study by QCD–TARO [19] confirms that the vector state remains largely unaffected. They rule out an increase of the pseudoscalar mass, however, a decrease by an amount of up to 20 MeV would not contradict their data.

First studies [24] utilizing the AsqTad staggered light quark action and approximating $2 + 1$ flavours of sea quarks by taking roots of the Fermionic determinant have been performed. The light quark mass was varied down to about $m_s/6$. The $\mathcal{O}(\alpha_s a)$ clover action, in the Fermilab heavy quark interpretation [7] was used. Extrapolating to physical sea quark mass, a hyperfine structure splitting of 97(2) MeV is obtained, see also Section 2.2.1 below. This is an increase of almost 40 %, over their quenched reference value. At least the latter would have been somewhat smaller if normalized with respect to r_0 rather than to the $\Upsilon' - \Upsilon$ splitting. However, OZI diagrams have been neglected and neither is the lattice spacing dependence resolved as yet. Clearly, a precision study of the charmonium spectrum requires not only sea quarks but also flavour singlet diagrams to be included.

2.2   NRQCD

NRQCD takes advantage that the masses of the charm and bottom quarks are much larger than Λ_{QCD} in order to build an EFT which is equivalent to QCD at any desired order in $1/m$ and $\alpha_s(m)$. Starting from NRQCD two approaches may be followed for spectrum computations: direct lattice calculations (Section 2.2.1) or further integration of the soft scale (the scale of the momentum transfer) to arrive at an EFT in which only the ultrasoft degrees of freedom remain dynamical, pNRQCD (Section 2.3). An introduction to NRQCD is given in Chapter 1, see also Refs. [25–27] for some introduction to the nonrelativistic EFT formulation. An introduction to lattice methods (quenched and unquenched) has been given in Chapter 1.

2.2.1   *Lattice NRQCD calculations with light sea quarks*[3]

The use of non-relativistic effective field theories permits the computer to handle only scales appropriate to the physics of the non-relativistic bound states without having to spend a lot of computer power on the large scale associated with the heavy quark mass which is irrelevant to the bound state dynamics. This makes the calculations more tractable so that many more hadron correlators can be calculated for better statistical precision. We will focus our discussion on the most recent calculations obtained within this approach, which include light sea quarks.

---

[3]Authors: C. Davies, A. Kronfeld, P. Mackenzie, J. Simone

On the lattice, heavy quark effects and discretisation effects are intertwined. One can treat them together by introducing an effective Lagrangian [28, 45]

$$\mathcal{L} = - \psi^\dagger \left[\delta m + D_4 - \frac{\boldsymbol{D}^2}{2m} - \frac{c_4^{\text{lat}}}{8m^3} \left(\boldsymbol{D}^2 \right)^2 - \frac{w_1^{\text{lat}} a^2}{6m} \sum_i D_i^4 - \frac{c_D^{\text{lat}}}{8m^2} \left(\boldsymbol{D} \cdot g\boldsymbol{E} - g\boldsymbol{E} \cdot \boldsymbol{D} \right) \right.$$

$$\left. - \frac{c_S^{\text{lat}}}{8m^2} i\boldsymbol{\sigma} \cdot \left(\boldsymbol{D} \times g\boldsymbol{E} + g\boldsymbol{E} \times \boldsymbol{D} \right) - \frac{c_F^{\text{lat}}}{2m} \boldsymbol{\sigma} \cdot g\boldsymbol{B} \right] \psi + \cdots, \qquad (3.1)$$

similar to the standard (continuum) NRQCD Lagrangian, but note that the derivative operators are 'improved' on the lattice to remove leading errors arising from the lattice spacing. See also the Section 3.2.3 "Heavy Quark Actions" in Chapter 1. We have omitted the term $\psi^\dagger m\psi$.

Compared to the NRQCD description of continuum QCD, an unimportant difference is the Euclidean metric (D_4 instead of $-iD_0$). Also, unlike in dimensional regularization, in lattice regularization the mass shift δm will in general be non-zero. However, this cancels from mass differences and decay amplitudes. Moreover, it can be determined nonperturbatively from the Υ dispersion relation. Obviously, terms accompanied by w_i are lattice specific. The essential difference is that the matching scale is provided by the lattice spacing: the short-distance coefficients c_i^{lat}, w_i^{lat} and δm depend on am and on the details of the chosen discretisation. The matching of c_i^{lat} and w_i^{lat} is carried out to some accuracy in α_s. From Eq. (3.1) one sees that the most important matching condition is to identify the kinetic mass m with the heavy quark mass in the lattice scheme, and then tune the higher-dimension interactions.

One area of lattice QCD which has remained problematic is the handling of light quarks on the lattice. This is now being addressed successfully and is critical to obtaining precision results of use to experiment. In particular the problem is how to include the dynamical (sea) $u/d/s$ quark pairs that appear as a result of energy fluctuations in the vacuum. We can often safely ignore $c/b/t$ quarks in the vacuum because they are so heavy, but we know that light quark pairs have significant effects, for example in screening the running of the gauge coupling and in generating Zweig-allowed decay modes for unstable mesons.

Many calculations in the past have used the "quenched approximation," attempting to compensate sea quark effects by *ad hoc* shifts in the bare coupling and (valence) quark masses. The results then suffer from errors as large as 10–30%. The error of the quenched approximation is not really quantifiable and this is reflected by a lack of internal consistency when different kinds of hadrons are used to fix the bare parameters. This ambiguity plagues the lattice QCD literature.

The MILC Collaboration recently have produced ensembles of gluon field configurations which include 2 degenerate light sea quarks (u, d) and a heavier one (s) [30]. They rely on fast supercomputers and a new discretisation of the quark action: the improved staggered formalism [31]. At quark masses small enough for reliable chiral extrapolations, staggered Fermions appear much faster than any other formulation of lattice Fermions. However, each flavour of staggered quarks is included in the sea by taking the fourth root of the staggered determinant and there are still theoretical issues to be resolved about this. Taking the u and d masses the same makes the lattice calculation much faster and leads to negligible errors in isospin-averaged quantities. The sea s quark mass is chosen to be approximately correct based on earlier studies (in fact the subsequent analysis shows that it was slightly high and further ensembles are now being made with a lower value). The sea u and d quarks take a range of masses down as low as a sixth of the (real) m_s. Ensembles are available at two different values of the lattice spacing, 0.12 fm and 0.09 fm, and the spatial lattice volume is $(2.5\text{ fm})^3$, reasonably large. Analysis of hadronic quantities on these ensembles has been done by the MILC and HPQCD collaborations [29].

There are 5 bare parameters of QCD relevant to this analysis: α_s, $m_{u/d}$, m_s, m_c and m_b. Changing the bare α_s changes the lattice spacing. It is important to fix these parameters with the masses of "gold-plated" hadrons, i.e., hadrons which are well below their strong decay thresholds. Such hadrons are well-defined experimentally and theoretically and should be accurately calculable in lattice QCD.
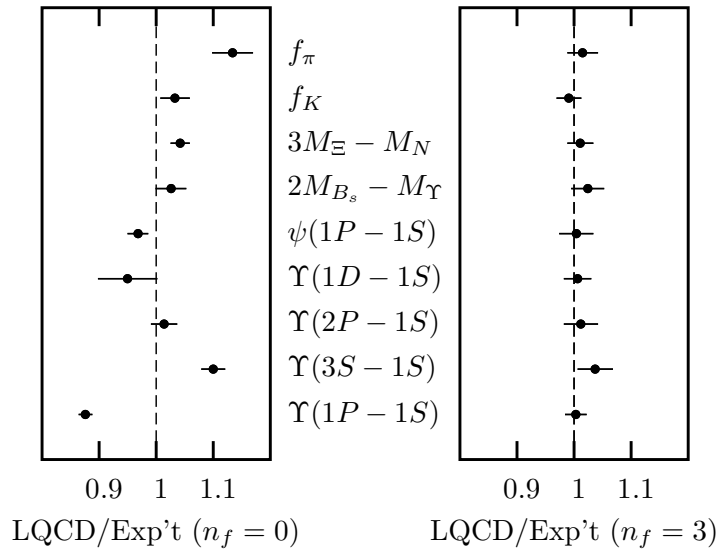
Fig. 3.2: Lattice QCD results divided by experiment for a range of "gold-plated" quantities which cover the full range of hadronic physics [29]. The unquenched calculations on the right show agreement with experiment across the board, whereas the quenched approximation on the left yields systematic errors of $\mathcal{O}(10\%)$.

Using them to fix parameters will then not introduce unnecessary additional systematic errors into lattice results for other quantities. This has not always been done in past lattice calculations, particularly in the quenched approximation. It becomes an important issue when lattice QCD is to be used as a precision calculational tool. We use the radial excitation energy in the Υ system (i.e., the mass splitting between the Υ' and the Υ) to fix the lattice spacing. This is a good quantity to use because it is very insensitive to all quark masses, including the b quark mass (experimental values for this splitting are very similar for charmonium and bottomonium) and so it can be determined without a complicated iterative tuning process. m_π, m_K, m_{D_s} and m_Υ are used to fix the quark masses. Thus, quarkonium turns out to be a central part in this study.

Once the Lagrangian parameters are set, we can focus on the calculation of other gold-plated masses and decay constants. If QCD is correct and lattice QCD is to work it must reproduce the experimental results for these quantities precisely. Figure 3.2 shows that this indeed works for the unquenched calculations with u, d and s quarks in the vacuum. A range of gold-plated hadrons are chosen which range from decay constants for light hadrons through heavy-light masses to heavy quarkonium. This tests QCD in different regimes in which the sources of systematic error are very different and stresses the point that QCD predicts a huge range of physics with a small set of parameters.

Refs. [24, 32–34] give more details on the quantities shown in Fig. 3.2. Here we concentrate on the spectrum of bottomonium and charmonium states, using, respectively, lattice NRQCD [35] and the Fermilab method for heavy quarks [7]. We include a brief discussion of the B_c mass, including the status of an ongoing unquenched calculation using the MILC ensembles.

Υ results with NRQCD

Figure 3.3(a) shows the radial and orbital splittings [33] in the $b\bar{b}$ (Υ) system for the quenched approximation ($n_f = 0$) and with the dynamical MILC configurations with 3 flavours of sea quarks. We use the standard lattice NRQCD effective theory for the valence b quarks [35], which takes advantage of the non-relativistic nature of the bound states. The lattice NRQCD action used here is accurate through v^4 where v is the velocity of the b quark in its bound state. It also includes corrections to remove discretisation errors at $\mathcal{O}(p^2 a^2 v^2) \sim \mathcal{O}(v^4)$, but does not include $\mathcal{O}(\alpha_s v^4)$ corrections to the coefficients c_i and

(a)

(b)
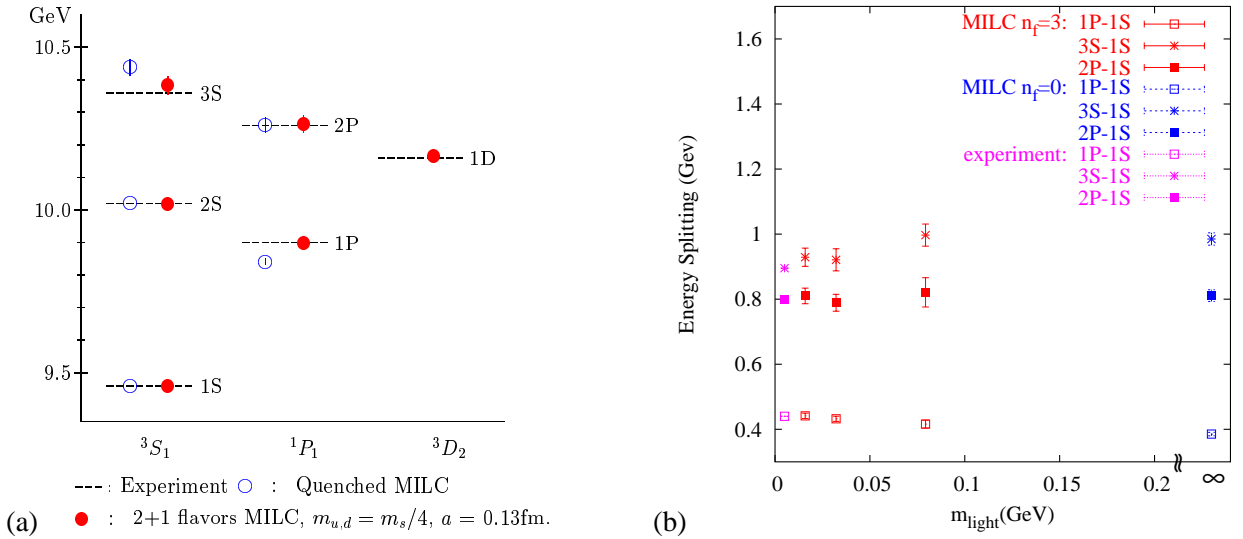
Fig. 3.3: Radial and orbital splittings in the Υ system from lattice QCD, using the $\Upsilon' - \Upsilon$ splitting and the Υ mass to fix the lattice spacing and the b-quark mass [33]. (a) Comparison of the quenched approximation (open circles) and QCD with u, d and s sea quarks (filled) circles. Note that the 1S and 2S levels are used to fix the b quark mass and lattice spacing respectively so are not predictions. (b) Dependence of the splittings as a function of the of the bare sea u/d quark mass.

w_i in Eq. (3.1), which are subleading. This means that spin-independent splittings, such as radial and orbital excitations, are simulated through next-to-leading-order in the velocity expansion and should be accurate to around 1%. Thus, these splittings provide a very accurate test not only of lattice QCD, but also of the effective-field theory framework. At present, the fine structure in the spectrum is only correct through leading-order [which is $\mathcal{O}(v^4)$ in this case] and more work must be done to bring this to the same level and allow tests against, for example, the splittings between the different χ_b states [33]. This is in progress. Systematic uncertainties due to such truncations have for instance been estimated in Ref. [36], based on lattice potentials.

The Υ system is a good one for looking at the effects of sea quarks because we expect it to be relatively insensitive to sea quark masses. The momentum transfer inside an Υ is larger than any of the u, d or s masses and so we expect the radial and orbital splittings to simply count the number of sea quarks once they are reasonably light. Figure 3.3(b) shows this to be true — the splittings are independent of the sea u/d quark mass in the region we are working in. Chiral extrapolation in the u/d quark mass is immaterial in this case. Therefore, the left-most lattice points in Fig. 3.3(b) are the ones used in Figs. 3.2 and 3.3(a).

ψ results with the Fermilab method

Figure 3.4 shows the spectrum of charmonium states below the $D\overline{D}$ threshold [24]. In this plot the lattice spacing was fixed from the $\Upsilon' - \Upsilon$ splitting (as above), and the c quark mass was tuned to get the D_s mass correct. Therefore, these results are obtained directly from QCD without adjusting any free parameters. For Fig. 3.4(a), the zero of energy has been moved to the spin-averaged mass $\bar{m}_\psi = \frac{1}{4} m_{\eta_c} + \frac{3}{4} m_{J/\psi}$.

These results are obtained using the Fermilab method [7] for the charmed quark. In this method one starts with Wilson Fermions, but the discretisation effects are controlled and understood using non-relativistic field theories, as in Eq. (3.1). The non-relativistic interpretation also has implications for how the action is improved. In the notation of Eq. (3.1) the chromomagnetic interaction is adjusted so that c_F^{lat} is correct at tree level. However, at higher order, there are $O[(m_c a)^2] \sim 10\%$ and $\mathcal{O}(\alpha_s)$ errors and
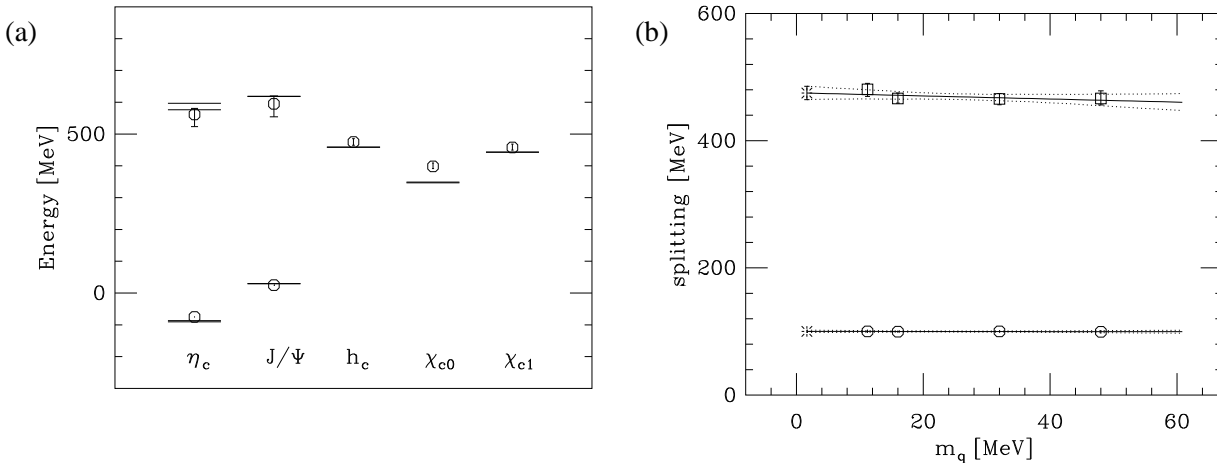
Fig. 3.4: Radial and orbital splittings in the charmonium system from lattice QCD with 3 light sea quarks, fixing the lattice spacing from the $\Upsilon' - \Upsilon$ splitting (as above), and the c quark mass from the D_s mass [24]. (a) Spectrum; (b) dependence on the sea quark mass.

some sign of these is seen in the mismatch with experiment of the hyperfine splitting in Fig. 3.4(a). In the past such discrepancies were masked by quenching errors, whereas now they can be resolved. Note that OZI violating contributions [18, 19] are also neglected currently. They are expected to be small but a decrease of up to 20 MeV in m_{η_c} is not ruled out.

The Fermilab action can be systematically improved, and the theoretical work needed is in progress. The most important new features are a one-loop calculation of the chromomagnetic coupling [37], and a systematic enumeration of all operators needed for improvement through v^6 [38].

B_c ground state

In 1998 the lowest-lying bound state of $\bar{b}c$ quarkonium was observed in semi-leptonic decays [39], yielding a mass of $m_{B_c} = 6.4 \pm 0.4$ GeV. A more precise measurement with hadronic decays is expected to come soon from Run II of the Tevatron, cf. Section 9. For lattice QCD, the B_c is a 'gold-plated' hadron and we have the opportunity to predict its mass ahead of experiment. Here we report on a preliminary lattice calculation, building on the progress detailed above. In previous quenched calculations accurate result could not be provided, due to the inconsistency of this approach described above.

The method used in the present study was developed in a quenched calculation [40], and follows almost immediately from Eq. (3.1). As long as one may use the effective Lagrangian to describe the charmed and bottom quarks on the lattice, the meson mass satisfies [28],

$$M_{1B_c} = m_{\bar{b}} + m_c + B_{B_c}, \tag{3.2}$$

where B_{B_c} is the binding energy of the B_c meson. The accuracy of the binding energy depends on how well the coefficients c_i^{lat} have been adjusted. The scheme- and scale-dependent quark masses cancel from the relation [40],

$$M_{1B_c} - \tfrac{1}{2}\left[M_{1\psi} + M_{1\Upsilon}\right] = B_{B_c} - \tfrac{1}{2}\left[B_\psi + B_\Upsilon\right]. \tag{3.3}$$

Note that within potential models flavour independence implies that this combination is small and positive [41, 42]. One can now predict the B_c mass by adding back the experimental $\tfrac{1}{2}\left[M_\psi + M_\Upsilon\right]$. A variant of this technique is to use the D_s and B_s masses instead of (half the) quarkonium masses.

An unquenched lattice calculation has recently been carried out [43, 44], using the MILC ensembles discussed above. Analyses at two light sea quark masses and two values of the lattice spacing show

a consistent picture, as expected. Using the quarkonium baseline, Allison *et al.* find [43]

$$M_{B_c} = 6304 \pm 4 \pm 11^{+18}_{-0} \text{ MeV}, \tag{3.4}$$

where the uncertainties are, respectively, from statistics (after chiral extrapolation), tuning of the heavy-quark masses, and heavy-quark discretization effects. The last is estimated from the mismatch of operators of order v^4 in the effective Lagrangian and are dominated by the relativistic correction $(\boldsymbol{D}^2)^2$. The estimate is guided by potential models (and is the only change from earlier conference reports [44]). The overall errors are so small because the lattice calculation has been set up to focus on the binding-energy difference, and raw uncertainties of several percent have been leveraged to the sub-percent level for the mass itself.

This result can be checked with the heavy-light baseline, $M_{B_c} = M_{D_s} + M_{B_s} + [B_{B_c} - (B_{D_s} + B_{B_s})]$, with somewhat larger uncertainties. Allison *et al.* find [43]

$$M_{B_c} = 6243 \pm 30 \pm 11^{+37}_{-0} \text{ MeV}. \tag{3.5}$$

The systematic uncertainties are larger with the heavy-light baseline because there is less cancellation between the B_c quarkonium and the heavy-light D_s and B_s.

The dominant uncertainties can be reduced by choosing more highly-improved actions in lattice gauge theory, or by reducing the lattice spacing, as discussed in Ref. [43].

2.2.2   Heavy hybrids on the lattice[4]

QCD suggests the existence of mesonic states in which the valence quark-antiquark pair is bound by an *excited* gluon field. A natural starting point in the quest to understand such states is the heavy quark sector. The vastly different characteristics of the slow massive heavy quarks and the fast massless gluons suggest that such systems may be amenable to a Born–Oppenheimer treatment, similar to diatomic molecules. The slowly moving heavy quarks correspond to the nuclei in diatomic molecules, whereas the fast gluon and light-quark fields correspond to the electrons. At leading order, the gluons and light quarks provide adiabatic potentials $V_{Q\bar{Q}}(r)$, where r is the quark–antiquark separation, and the behavior of the heavy quarks is described by solving the Schrödinger equation separately for each $V_{Q\bar{Q}}(r)$. The Born–Oppenheimer approximation provides a clear and unambiguous picture of conventional and hybrid mesons: conventional mesons arise from the lowest-lying adiabatic potential, whereas hybrid mesons arise from the excited-state potentials.

The first step in a Born–Oppenheimer treatment of heavy quark mesons is determining the gluonic terms $V_{Q\bar{Q}}(r)$. Since familiar Feynman diagram techniques fail and the Schwinger–Dyson equations are intractable, the path integrals needed to determine $V_{Q\bar{Q}}(r)$ are estimated using Markov-chain Monte Carlo methods (Lattice QCD simulations). The spectrum of gluonic excitations in the presence of a static quark–antiquark pair has been accurately determined in lattice simulations [46, 47] which make use of anisotropic lattices, improved actions, and large sets of operators with correlation matrix techniques. These gluonic $V_{Q\bar{Q}}(r)$ levels may be classified by the magnitude Λ of the projection of the total angular momentum $\mathbf{J}_g$ of the gluon field onto the molecular axis, and by $\eta = \pm 1$, the symmetry under charge conjugation combined with spatial inversion about the midpoint between the quark and the antiquark. States with $\Lambda = 0, 1, 2, \ldots$ are denoted by $\Sigma, \Pi, \Delta, \ldots$, respectively. States which are even (odd) under the above-mentioned CP operation are denoted by the subscripts g (u). An additional $\pm$ superscript for the Σ states refers to even or odd symmetry under a reflection in a plane containing the molecular axis.

In the leading Born–Oppenheimer approximation, one replaces the covariant Laplacian $\boldsymbol{D}^2$ by an ordinary Laplacian $\boldsymbol{\nabla}^2$. The error that one makes is equivalent to $1/M_Q$ and $1/M_Q^2$ corrections [48] to $V_{Q\bar{Q}}$ that go beyond the LBO and are suppressed by a factor v^2, using perturbative NRQCD power

---

[4]Author: C. Morningstar
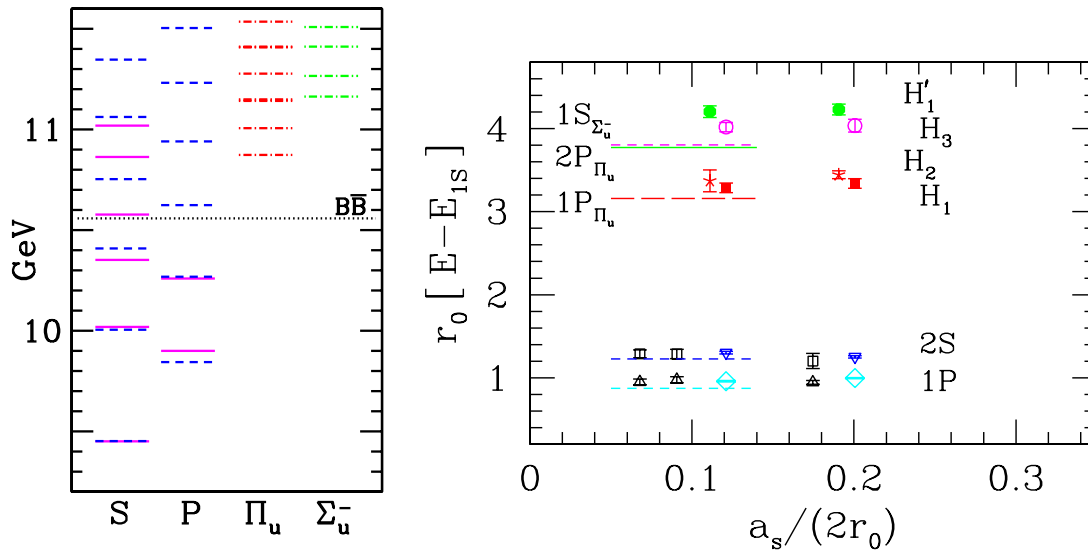
Fig. 3.5: (Left) The spectrum of conventional and hybrid heavy-quark mesons in the leading Born–Oppenheimer approximation and neglecting light quarks (from Ref. [46]). Conventional S and P states are shown, as well as hybrids based on the Π_u and Σ_u^- adiabatic surfaces. Solid lines indicate spin-averaged experimental measurements. (Right) Simulation results from Ref. [46] for two conventional and four hybrid bottomonium level splittings (in terms of $r_0^{-1} = 450$ MeV and with respect to the $1S$ state) against the lattice spacing a_s. Predictions from the leading Born–Oppenheimer calculation, shown as horizontal lines, reproduce all of the simulation results to within 10 %, strongly supporting the validity of a Born–Oppenheimer picture for such systems at leading order. Results from Ref. [49] using an NRQCD action with higher-order relativistic corrections are shown as hollow boxes and hollow upright triangles.

counting rules. The spin interactions of the heavy quarks are also neglected, and one solves the radial Schrödinger equation:

$$-\frac{1}{2\mu}\frac{d^2u(r)}{dr^2} + \left\{ \frac{\langle \boldsymbol{L}_{Q\bar{Q}}^2 \rangle}{2\mu r^2} + V_{Q\bar{Q}}(r) \right\} u(r) = E\, u(r), \tag{3.6}$$

where $u(r)$ is the radial wavefunction of the quark–antiquark pair and μ denotes the reduced mass. The expectation value in the centrifugal term is given in the adiabatic approximation by

$$\langle \boldsymbol{L}_{Q\bar{Q}}^2 \rangle = L(L+1) - 2\Lambda^2 + \langle \boldsymbol{J}_g^2 \rangle, \tag{3.7}$$

where $\langle \boldsymbol{J}_g^2 \rangle = 0$ for the Σ_g^+ level and $\langle \boldsymbol{J}_g^2 \rangle = 2$ for the Π_u and Σ_u^- levels.

The leading-order Born–Oppenheimer spectrum of conventional $\bar{b}b$ and hybrid $\bar{b}gb$ states (in the absence of light quarks) obtained from the above procedure is shown in Fig. 3.5. Below the $\overline{B}B$ threshold, the Born–Oppenheimer results agree well with the spin-averaged experimental measurements of bottomonium states (any small discrepancies essentially disappear once light quark loops are included). Above the threshold, agreement with experiment is lost, suggesting significant corrections either from mixing and other higher-order effects or (more likely) from light sea quark effects.

The validity of the Born–Oppenheimer picture relies on the smallness of mixing between states based on different $V_{Q\bar{Q}}(r)$. In addition, relativistic (including spin) corrections and radiation of colour neutral objects such as glueballs and mesons are neglected. In Ref. [46] the LBO level splittings have been compared with those determined from meson simulations using a non-relativistic (NRQCD) heavy-quark action. The NRQCD action included only a covariant temporal derivative and the leading covariant

kinetic energy operator; quark spin and D^4 terms were neglected. Differences between the two results originate from both different $\mathcal{O}(1/M_Q)$ terms [48] and from the automatic inclusion of mixing effects between different adiabatic surfaces within the NRQCD simulations. Naively one might expect the former effect to be of $\mathcal{O}(v^2) \approx 10$ %. The level splittings (in terms of the hadronic scale r_0 and with respect to the $1S$ state) of the conventional $2S$ and $1P$ states and four hybrid states were compared (see Fig. 3.5) and indeed found to agree within 10%, strongly supporting the validity of the leading Born–Oppenheimer picture, at least in the absence of light sea quarks and spin-effects.

A very recent study [50] has demonstrated that the Υ ground state carries little admixture from hybrids, supporting the LBO, at least in the sector that is governed by the ground state potential. Using lowest-order lattice NRQCD to create heavy-quark propagators, a basis of unperturbed S-wave and $|1H\rangle$ hybrid states was formed. The $c_F \boldsymbol{\sigma} \cdot \boldsymbol{B}/2M_Q$ spin interaction was then applied at an intermediate time slice to compute the mixings between such states due to this interaction in the quenched approximation. Diagonalizing the resulting two-state Hamiltonian then yielded the admixtures of hybrid configuration in the Υ and η_b. For a reasonable range of c_F values, the following results were obtained: $\langle 1H|\Upsilon\rangle \approx 0.076-0.11$ and $\langle 1H|\eta_b\rangle \approx 0.13-0.19$. Hence, hybrid mixings due to quark spin effects in bottomonium are very small. Even in charmonium, the mixings were found not to be large: $\langle 1H|J/\Psi\rangle \approx 0.18 - 0.25$ and $\langle 1H|\eta_c\rangle \approx 0.29 - 0.4$. Investigations of the mixing of hybrid states with radially excited standard quarkonium states which are energetically closer and spatially more extended are certainly an exciting avenue of future research.

In the absence of light quark loops, one obtains a very dense spectrum of mesonic states since the $V_{Q\bar{Q}}(r)$ potentials increase indefinitely with r. However, the inclusion of light quark loops changes the $V_{Q\bar{Q}}(r)$ potentials. First, there are slight corrections at small r, and these corrections remove the small discrepancies of the leading Born–Oppenheimer predictions with experiment below the $B\overline{B}$ threshold seen in Fig. 3.5. For large r, the inclusion of light quark loops drastically changes the behavior of the $V_{Q\bar{Q}}(r)$ potentials: instead of increasing indefinitely, these potentials eventually level off at a separation above 1 fm when the static quark–antiquark pair, joined by gluonic flux, can undergo fission into $(Q\bar{q})(\bar{Q}q)$, where q is a light quark and Q is a heavy quark. Clearly, such potentials cannot support the populous set of states shown in Fig. 3.5; the formation of bound states and resonances substantially extending over 1 fm in diameter seems unlikely. A complete open-channel calculation taking the effects of including the light quarks correctly into account has not yet been done, but unquenched lattice simulations [51] show that the Σ_g^+ and Π_u potentials change very little for separations below 1 fm when sea quarks are included. This makes it conceivable that a handful of low-lying states whose wavefunctions do not extend appreciably beyond 1 fm in diameter may exist as well-defined resonances in nature.

In addition to such direct threshold effects there is the possibility of transitions between different adiabatic surfaces, mediated by radiation of pions and other light mesons or pairs of light mesons. A first lattice study of such effects has been performed by McNeile and Collaborators [52].

A recent quenched calculation [8] of bottomonium hybrids using a relativistic heavy-quark action on anisotropic lattices confirms the predictions of the Born–Oppenheimer approximation, but admittedly, the uncertainties in the simulation results are large. These calculations used a Symanzik-improved anisotropic gauge action and an improved Fermion clover action. Quenched results on Charmonium hybrids obtained by employing a relativistic quark actions [12] can be found in Fig. 3.1 and Table 3.1 in Section 2.1. The dominant decay channel for the lightest (1^{-+}) hybrid would be into a D and a $\overline{D}^{**}$ should it be heavier than the respective threshold, and radiation of a light pseudoscalar or scalar state if lighter.

A determination of the spectrum properly taking into account effects from light quarks is still needed. Taking the Born–Oppenheimer approximation beyond leading order is also a project for future work. Monte Carlo computations of relevant matrix elements involving the gauge field can not only facilitate the evaluation of higher-order terms in the Born–Oppenheimer expansion, but also provide valuable information on the production and decays of these novel states.

2.2.3 *QQq baryons on the lattice*[5]

While recent lattice results from several groups on three quark static potentials exist [53–57], no such potentials have been calculated for the situation containing two static sources at distance r, accompanied by a light quark, as yet. However, two groups have directly studied the situation for $Q = c$, within the quenched approximation, one employing the so-called D234 improved Wilson type action [58] as well as NRQCD [59] on anisotropic lattices and the UKQCD Collaboration employing the relativistic clover charm quark action [60].

In the NRQCD study [59] two lattice spacings, $a \approx 0.15\,\text{fm}, 0.22\,\text{fm}$ and four light quark masses have been realized and bbq, ccq as well as bqq and cqq baryons studied. No finite volume checks were performed and radiative corrections to the NRQCD matching coefficients ignored. In the UKQCD study [60] only one lattice spacing $a \approx 0.08$ fm and one volume, $La \approx 2$ fm were realized. The light quark masses scattered around the strange quark mass and both, singly and doubly charmed baryons were studied. All studies yield consistent results. The values quoted by UKQCD are [60],

$$\Xi_{cc} = 3549(13)(19)(92)\,\text{MeV} \quad , \quad \Omega_{cc} = 3663(12)(17)(95)\,\text{MeV}$$
$$\Xi_{cc}^* = 3641(18)(08)(95)\,\text{MeV} \quad , \quad \Omega_{cc}^* = 3734(14)(08)(97)\,\text{MeV}. \tag{3.8}$$

The first errors are statistical, the second encapsulate uncertainties in the chiral extrapolations and fit ranges. The third error represents the uncontrolled systematics: finite a effects, finite volume effects and quenching, estimated by comparing the lattice Λ_c mass to the experimental result.

2.3 pNRQCD[6]

From the various dynamical scales that play a role in the heavy quarkonium systems, namely m, mv, mv^2 and Λ_{QCD}, only the hard scale m has been factorized in NRQCD and becomes explicit in its Lagrangian. Only the fact that $m \gg mv, mv^2, \Lambda_{\text{QCD}}$ is exploited but no use is made of the scale separation, $mv \gg mv^2$. A higher degree of simplification is achieved by building another effective theory, where degrees of freedom of order $\sim mv$ are integrated out as well, i.e., an EFT where only the ultrasoft degrees of freedom (with energies $\sim mv^2$) remain dynamical. In this way a big simplification is obtained and analytic calculations of the spectrum become feasible, at least in some dynamical regimes, at variance with NRQCD where the spectrum can only be obtained in a model independent way by Lattice calculation. pNRQCD [4, 5] takes advantadge of the fact that for many non-relativistic systems the scale associated to the size of the system $k \sim mv$ is much larger than the binding energy $E \sim mv^2$. Therefore it is possible to integrate out the scale of the momentum transfer k in a way such that pNRQCD is equivalent to NRQCD at any desired order in E/k, k/m and $\alpha_{\text{s}}(\mu)$. Two dynamical situations may occur here: (1) k is much larger than Λ_{QCD}, (2) k is of the order of Λ_{QCD}. In the first case the matching from NRQCD to pNRQCD may be performed in perturbation theory, expanding in terms of α_{s}. In the second situation, the matching has to be nonperturbative, i.e., no expansion in α_{s} is allowed. We will refer to these two limits as the weak and strong coupling regimes. Recalling that $k \sim r^{-1} \sim mv$, these two situations correspond to systems with inverse typical radius smaller or bigger than Λ_{QCD}, or systems respectively dominated by the short range or long range (with respect to the confinement radius) physics. We will consider these two situations in the following two subsections.

2.3.1 *Weak coupling regime*[7]

When $k \gg E >\sim \Lambda_{\text{QCD}}$, we are in the perturbative matching regime ($v \sim \alpha_{\text{s}}(m\alpha_{\text{s}})$). The scale $r \sim 1/(mv)$ is integrated out and the pNRQCD Lagrangian consists of a singlet and an octet wave function field interacting with respective potentials and coupled to ultrasoft gluons. The effective degrees

---

[5]Author: G. Bali

[6]Authors: N. Brambilla, J. Soto

[7]Authors: N. Brambilla, J. Soto

of freedom are: $Q\bar{Q}$ states (decomposed into a singlet and an octet wave function under colour trans-formations) with energy of order of the next relevant scale, $\Lambda_{\rm QCD}$, mv^2 and momentum $\mathbf{p}$ of order mv, plus ultrasoft gluons $A_\mu(\mathbf{R}, t)$ with energy and momentum of order $\Lambda_{\rm QCD}$, mv^2. All the gluon fields are multipole expanded (i.e., expanded in r). The Lagrangian is then an expansion in the small quantities p/m, $1/(rm)$ and $\mathcal{O}(\Lambda_{\rm QCD}, mv^2) \times r$.

The pNRQCD Lagrangian is given at the next to leading order (NLO) in the multipole expansion by [5] (in the centre-of-mass system):

$$\mathcal{L}_{\rm pNRQCD} = {\rm Tr}\left\{ {\rm S}^\dagger \left(i\partial_0 - \frac{\mathbf{p}^2}{m} - V_s(r) - \sum_{n\geq 1} \frac{V_s^{(n)}}{m^n} \right) {\rm S} + {\rm O}^\dagger \left(iD_0 - \frac{\mathbf{p}^2}{m} - V_o(r) - \sum_{n\geq 1} \frac{V_o^{(n)}}{m^n} \right) {\rm O} \right\}$$

$$+ gV_A(r){\rm Tr}\left\{ {\rm O}^\dagger \mathbf{r} \cdot \mathbf{E}\, {\rm S} + {\rm S}^\dagger \mathbf{r} \cdot \mathbf{E}\, {\rm O} \right\} + g\frac{V_B(r)}{2}{\rm Tr}\left\{ {\rm O}^\dagger \mathbf{r} \cdot \mathbf{E}\, {\rm O} + {\rm O}^\dagger {\rm O}\mathbf{r} \cdot \mathbf{E} \right\} - \frac{1}{4}F_{\mu\nu}^a F^{\mu\nu a}. \qquad (3.9)$$

The $V_{s,o}^{(n)}, V_A, V_B$ are potentials, which play the role of matching coefficients and contain the non-analytical dependence in r, to be calculated in the matching between NRQCD and pNRQCD. Poincaré invariance imposes relations among these matching coefficients [61]. To leading order in the multipole expansion, the singlet sector of the Lagrangian gives rise to equations of motion of the Schrödinger type. The other terms in Eq. (3.9) contain (apart from the Yang–Mills Lagrangian) retardation (or non-potential) effects that start at the NLO in the multipole expansion. At this order the non-potential effects come from the singlet-octet and octet-octet interactions mediated by an ultrasoft chromoelectric field.

Recalling that $r \sim 1/(mv)$ and that the operators count like the next relevant scale, $\mathcal{O}(mv^2, \Lambda_{\rm QCD})$, to the power of the dimension, it follows that each term in the pNRQCD Lagrangian has a definite power counting. As a consequence of this power counting the interaction of quarks with ultrasoft gluons is suppressed in the Lagrangian by a factor v (by gv if $mv^2 \gg \Lambda_{\rm QCD}$) with respect to the LO.

The various potentials in Eq. (3.9) have been calculated at different orders in the perturbative matching. V_s is known to two loops $[\mathcal{O}(\alpha_s^3)]$ [62, 63] as well as the leading log of the three loop contribution [64]. V_o is known to two loops (see York Schröder, private communications in Ref. [65]). $V_s^{(1)}$ is known to two loops [67] and $V_s^{(2)}$ to one loop [68]. V_A and V_B are known at tree level [5] (and are independent of r) and have no logs at one loop [70].

Note that the static limit of pNRQCD ($m \to \infty$) results in a nontrivial theory (unlike in pNRQED), since both singlet and octet fields remain dynamical and interact through ultrasoft gluons. The static energy of two infinitely heavy sources $V_{QCD}(r)$, which will be discussed below, can be obtained for small r. In fact, the coefficient of the infrared logarithmic contribution to $V_{QCD}(r)$ first pointed out in Ref. [71] was calculated using the static pNRQCD Lagrangian [64].

Given the Lagrangian in Eq. (3.9) it is possible to calculate the quarkonium energy levels. Contributions to the spectrum originate both in quantum mechanical perturbation theory and in the dynamics of ultrasoft gluons. The latter contributions contain nonperturbative effects and this will be discussed in the corresponding section below.

The static QCD potential[8]

For decades, the static QCD potential $V_{\rm QCD}(r)$, formally defined from an expectation value of the Wilson loop, has been widely studied for the purpose of elucidating the nature of the interaction between heavy quark and antiquark. The potential at short distances can be computed by perturbative QCD, whereas its long distance shape can be computed by lattice simulations. (See Sections 2.3.2 and 2.3.3 for lattice computations.)

---

[8]Author: Yu. Sumino

Computations of $V_{\mathrm{QCD}}(r)$ in perturbative QCD have a long history. The 1-loop and 2-loop corrections were computed in Refs. [72–74] and [62, 63, 75–78], respectively. The logarithmic correction at 3-loops originating from the ultrasoft scale was first pointed out in Ref. [71] and computed in Refs. [64, 79]. A renormalization-group (RG) improvement of $V_{\mathrm{QCD}}(r)$ at next-to-next-to-leading log (NNLL) was performed in Ref. [70].[9]

Since the discovery [83–85] of the cancellation of $\mathcal{O}(\Lambda_{\mathrm{QCD}})$ renormalons between $V_{\mathrm{QCD}}(r)$ and twice the quark pole mass[10], the convergence of the perturbative series improved drastically and much more accurate perturbative predictions of the potential shape became available. This feature indicates the validity of the renormalon dominance picture for the QCD potential and pole mass. According to this picture, a perturbative uncertainty of $V_{\mathrm{QCD}}(r)$, after cancelling the $\mathcal{O}(\Lambda_{\mathrm{QCD}})$ renormalon, is estimated to be $\mathcal{O}(\Lambda_{\mathrm{QCD}}^3 r^2)$ at $r \ll \Lambda_{\mathrm{QCD}}^{-1}$ [87].

An OPE of $V_{\mathrm{QCD}}(r)$ was developed within the pNRQCD framework [5]. In this framework, residual renormalons, starting from $\mathcal{O}(\Lambda_{\mathrm{QCD}}^3 r^2)$, are absorbed into the matrix element of a non-local operator (non-local gluon condensate). Then, in the multipole expansion at $r \ll \Lambda_{\mathrm{QCD}}^{-1}$, the leading nonperturbative contribution to the potential becomes $\mathcal{O}(\Lambda_{\mathrm{QCD}}^3 r^2)$ [5].

Several studies [78, 88–91] showed that perturbative predictions for $V_{\mathrm{QCD}}(r)$ agree well with phenomenological potentials (determined from heavy quarkonium spectroscopy) and lattice calculations of $V_{\mathrm{QCD}}(r)$, once the $\mathcal{O}(\Lambda_{\mathrm{QCD}})$ renormalon is accounted for. Ref. [92] showed that also a Borel resummation of the perturbative series yields a potential shape in agreement with lattice results if the $\mathcal{O}(\Lambda_{\mathrm{QCD}})$ renormalon is properly treated. In fact the agreement holds within the expected $\mathcal{O}(\Lambda_{\mathrm{QCD}}^3 r^2)$ uncertainty.[11] These observations further support the validity of renormalon dominance and of the OPE for $V_{\mathrm{QCD}}(r)$.

Qualitatively, the perturbative QCD potential becomes steeper than the Coulomb potential as r increases (once the $\mathcal{O}(\Lambda_{\mathrm{QCD}})$ renormalon is cancelled). This feature can be understood, within perturbative QCD, as an effect of the *running* of the strong coupling constant [88, 89, 93].

Using a scale-fixing prescription based on the renormalon dominance picture, it was shown analytically [94] that the perturbative QCD potential approaches a "Coulomb+linear" form at large orders, up to an $\mathcal{O}(\Lambda_{\mathrm{QCD}}^3 r^2)$ uncertainty. The "Coulomb+linear" potential can be computed systematically as more terms of perturbative series are included via RG; up to NNLL, it shows a convergence towards lattice results.

Heavy quarkonium spectra [12]

In recent years, perturbative computations of the heavy quarkonium spectrum (an expansion in α_{s} and $\ln \alpha_{\mathrm{s}}$) have enjoyed a significant development. A full computation of the spectrum up to $\mathcal{O}(\alpha_{\mathrm{s}}^4 m)$ was performed in Refs. [98, 99]. The spectra up to the same order for the system with unequal heavy quark masses and with non-zero quark mass in internal loops were computed, respectively, in Refs. [95, 97] and [77, 95]. Perturbative computations at higher orders were made possible by the advent of effective field theories such as pNRQCD [4, 5] or vNRQCD [6] and by the threshold expansion technique [100]. The $\mathcal{O}(\alpha_{\mathrm{s}}^5 m \ln \alpha_{\mathrm{s}})$ term originating from the ultrasoft scale was computed in Refs. [64, 69, 79]. Ref. [101, 102] resummed the $\alpha_{\mathrm{s}}^4 m (\alpha_{\mathrm{s}} \ln \alpha_{\mathrm{s}})^n$ terms. The full Hamiltonian at the next-to-next-to-next-to-leading order was computed in Ref. [68]. Except for the 3-loop non-logarithmic term of the perturbative QCD potential,[13] the energy levels of the $1S$ states were computed up to $\mathcal{O}(\alpha_{\mathrm{s}}^5 m)$ from this Hamiltonian [103]. The fine splittings have been calculated at NLO order $\mathcal{O}(\alpha_{\mathrm{s}}^5 m)$ in [104].

---

[9]There are estimates of higher-order corrections to the perturbative QCD potential in various methods [80–82].

[10]For similar work inside HQET see [86].

[11]This is true only in the range of r where the respective perturbative predictions are stable. All perturbative predictions become uncontrolled beyond certain distances, typically around $r \sim \Lambda_{\mathrm{QCD}}^{-1}$.

[12]Author: Yu. Sumino

[13]Estimates of the 3-loop correction to the QCD potential have been given in various methods [80–82].

In the meantime, the discovery of the renormalon cancellation in the quarkonium spectrum [83–85] led to a drastic improvement of the convergence of the perturbative expansion of the energy levels. (See Chapter 6 for precise determinations of the heavy quark masses, as important applications.) In Refs. [93, 95] the whole structure of the bottomonium spectrum up to $\mathcal{O}(\alpha_s^4 m)$ was predicted taking into account the cancellation of the $\mathcal{O}(\Lambda_{\mathrm{QCD}})$ renormalons, and a good agreement with the experimental data was found for the gross structure of the spectrum. (Only the states below the threshold for strong decays were considered.) The consistency of the perturbative predictions with the experimental data seems to indicate that, for bottomonium, the momentum scale of the system is larger than Λ_{QCD}, i.e., $mv \gg \Lambda_{\mathrm{QCD}}$, up to some of the $n = 3$ states. This is, however, in apparent conflict with the fact that the leading nonperturbative effects scale as a power ≥ 4 of the principal quantum number (see *Nonperturbative effects* below) and, hence, are expected to be very important for any excited state.

Subsequently, in Refs. [96, 106] a specific formalism based on perturbative QCD was developed: using the static QCD potential computed in Ref. [78] and taking into account the cancellation of the $\mathcal{O}(\Lambda_{\mathrm{QCD}})$ renormalons, the Schrödinger equation was solved numerically to determine the zeroth-order quarkonium wave function; all the corrections up to $\mathcal{O}(\alpha_s^5 m)$ for the fine and hyperfine splittings have been included. Good agreements were found between the computed and the observed fine and hyperfine splittings of the bottomonium and charmonium spectra, in addition to the gross structure of the bottomonium spectrum[14].

In Table 3.2 particularly impressing is the result for the perturbative calculation of the B_c mass, that, with finite charm mass effects included, is equal to $6307 \pm 17 \mathrm{GeV}$ and is in complete agreement, inside errors and with small errors, with lattice NRQCD unquenched result given in Eq. (4).

These analyses have shown that the perturbative predictions of the spectra agree with the corresponding experimental data within the estimated perturbative uncertainties, and that the size of nonperturbative contributions is compatible with the size of perturbative uncertainties.

Although uncertainties of the perturbative predictions for the individual energy levels grow rapidly for higher excited states, level spacings among them have smaller uncertainties, since the errors of the individual levels are correlated. In particular, uncertainties of the fine and hyperfine splittings are suppressed due to further cancellation of renormalons. These features enabled sensible comparisons of the level structures including the excited states.

In predicting the spectrum, pNRQCD is a useful tool not only for fully perturbative computations but also for factorizing short-distance contributions into matching coefficients (perturbatively computable) and nonperturbative contributions into matrix elements of operators [5, 48]. This will be discussed in *Nonperturbative effects* below.

The Renormalization group in heavy quarkonium spectroscopy [15]

In recent years, there has been a growing interest to perform renormalization group analysis in heavy quarkonium [6, 70, 101, 102, 107, 108, 110–117]. In many cases this interest has been driven by the lack of convergence and strong scale dependence one finds in the fixed (NNLO) analysis performed for sum rules and t–$\bar{t}$ production near threshold (see Chapter 6). This problem has turned out to be highly non-trivial. We will focus here on computations related with spectroscopy.

The heavy quarkonium spectrum is known with NNLL accuracy [101, 102]. These expressions have not yet been used for phenomenological analysis of single heavy quarkonium states either in bottomonium and charmonium systems. It would be very interesting to see their effects on the spectra.

The hyperfine splitting of the heavy quarkonium spectrum is known with LL [113, 114] and NLL accuracy for the bottomonium and charmonium spectrum [107] and also for the B_c spectrum [108]. For

---

[14]For technical reasons a linear extrapolation of the potential at $r > 4.5 \mathrm{~GeV}^{-1}$ was introduced in Ref. [96]. This artefact was eliminated in Ref. [106], in which it was also shown that effects caused by the linear extrapolation of the potential were minor.

[15]Author: A. Pineda

Table 3.2: Predicted masses of $b\bar{b}$, $c\bar{c}$ and $b\bar{c}$ states in perturbative QCD-based, renormalon-subtracted computations. BSV01 (and BV00) is the full perturbative computation up to $\mathcal{O}(\alpha_s^4 m)$ without non-zero charm-mass corrections; BSV02 is the full perturbative computation up to $\mathcal{O}(\alpha_s^4 m)$ including non-zero charm-mass corrections; RS03 is based on a specific scheme and specific reorganization of perturbative series, incorporates full corrections up to $\mathcal{O}(\alpha_s^4 m)$ in the individual levels and full corrections up to $\mathcal{O}(\alpha_s^5 m)$ in the fine splittings, includes non-zero charm-mass corrections. Errors shown in brackets represent $\sqrt{\delta_{\alpha_s}^2 + \delta_{\text{h.o.}}^2}$ (BSV01,BV00) and $\sqrt{\delta_{\alpha_s}^2 + \delta_{\text{h.o.}}^2 + \delta_{m_c}^2}$ (BSV02), respectively, where δ_{α_s} originates from the error of $\alpha_s(M_Z)$, $\delta_{\text{h.o.}}$ is the error due to higher-order corrections, and δ_{m_c} is the error in the finite charm mass corrections. The errors do not include non-perturbative contributions estimates. Numbers without errors are those without explicit or reliable error estimates in the corresponding works.

State	expt	BSV01 [93]	BSV02 [95]	RS03 [96]	BV00 [97]
$b\bar{b}$ states					
1^3S_1	9460	9460	9460	9460	
1^3P_2	9913	9916(59)	10012(89)	9956	
1^3P_1	9893	9904(67)	10004(86)	9938	
1^3P_0	9860	9905(56)	9995(83)	9915	
2^3S_2	10023	9966(68)	10084(102)	10032	
2^3P_2	10269		10578(258)	10270	
2^3P_1	10255		10564(247)	10260	
2^3P_0	10232	10268	10548(239)	10246	
3^3S_1	10355	10327(208)	10645(298)	10315	
$c\bar{c}$ states					
1^3S_1	3097	3097			
1^1S_0	2980(2)	3056			
$b\bar{c}$ states					
1^1S_0	6400(400)	6324(22)	6307(17)		6326 (29)

Table 3.3: Predicted fine and hyperfine splittings (in MeV) of $b\bar{b}$ and $c\bar{c}$ states in perturbative QCD-based, renormalon-subtracted computations. $^3P_{\rm cog}$ denotes the centre of gravity of the triplet P-wave states. PT88 extracts the matrix elements of $\mathcal{O}(1/m^2)$ operators from the experimental values for the fine splittings, instead of computing them from perturbative QCD. BSV01 is the full perturbative computation up to $\mathcal{O}(\alpha_{\rm s}^4 m)$ without non-zero charm-mass corrections. BSV02 is the full perturbative computation up to $\mathcal{O}(\alpha_{\rm s}^4 m)$ including non-zero charm-mass corrections; RS03 and RS04 are based on specific schemes and specific reorganization of perturbative series, incorporate full corrections up to $\mathcal{O}(\alpha_{\rm s}^5 m)$ in the splittings, and include non-zero charm-mass corrections. KPPSS03 and PPSS04 are the full NNLL computation [up to order $\alpha_{\rm s}^5 m \times (\alpha_{\rm s}\ln\alpha_{\rm s})^n)$] without non-zero charm-mass corrections. Errors are shown in brackets when explicit and reliable estimates are given in the respective works. The errors do not include nonperturbative contributions estimates except in KPPSS03 and PPSS04 where they were roughly estimated using the multipole expansion.

Level splitting	expt	PT88 [105]	BSV01 [93]	BSV02 [95]	RS03 [96]	RS04 [106]	KPPSS03 [107]	PPSS04 [108]
$b\bar{b}$ states								
$1^3P_2 - 1^3P_1$	20		12	8	18(10)			
$1^3P_1 - 1^3P_0$	33		-1	9	23(10)			
$2^3P_2 - 2^3P_1$	13			16	11(10)			
$2^3P_1 - 2^3P_0$	23			14	14(10)			
$1^3S_1 - 1^1S_0$						44(11)	$39(11)^{+9}_{-8}$	
$2^3S_1 - 2^1S_0$						21(8)		
$3^3S_1 - 3^1S_0$						12(9)		
$1^3P_{\rm cog} - 1^1P_1$			-0.5			$-0.4(0.2)$		
$2^3P_{\rm cog} - 2^1P_1$			-0.4			$-0.2(0.1)$		
$c\bar{c}$ states								
$1^3P_2 - 1^3P_1$	46					43(24)		
$1^3P_1 - 1^3P_0$	95					56(34)		
$1^3S_1 - 1^1S_0$	118(1)					88(26)	104	
$2^3S_1 - 2^1S_0$	32(10)					38(36)		
$1^3P_{\rm cog} - 1^1P_1$	-0.9		-1.4			$-0.8(0.8)$		
$b\bar{c}$ states								
$1^3S_1 - 1^1S_0$								$65(24)^{+19}_{-16}$

those observables a phenomenological analysis has been performed. The predictions can be found in Table 3.3. The general trend is that the introduction of these effects improves the agreement with experiment (when experimental data are available). In particular, the resummation of logarithms brings the perturbative prediction of the hyperfine splitting of charmonium significantly closer to the experimental figure if compared with a NLO computation. It is then possible to give predictions for the hyperfine splitting of the ground state of bottomonium, and in particular for the $\eta_b(1S)$ mass, as well as for the hyperfine splitting of the B_c ground state. In these computations a threshold mass was used (equivalent to the pole mass at this order). In any case, it should also be mentioned that the use of the $\overline{\text{MS}}$ mass may give a NLO value for the charmonium hyperfine splitting in agreement with experiment [109].

As a final remark, for the bottomonium, charmonium and B_c spectrum, one should be careful, since the ultrasoft scale may run up to very low scales. On the other hand the general dependence on the renormalization scale appears to be the same no matter whether we talk of toponium, bottomonium or charmonium. This may point to the fact that the same physics holds for all of them.

Nonperturbative effects[16]

Given the Lagrangian in Eq. (3.9) it is possible to calculate the full quarkonium energy levels at order $m\alpha_s^5$ [68, 69, 79]. At this order the energy E_n of the level n receives contributions both from standard quantum mechanics perturbation theory and from the singlet-octet interaction (retardation effect) through ultrasoft gluons. The latter reads

$$\delta E_n|_{us} = -i\frac{g^2}{3N_c}\int_0^\infty dt \, \langle n|\mathbf{r}e^{it(E_n^{(0)}-h_o)}\mathbf{r}|n\rangle \, \langle \mathbf{E}(t)\,\mathbf{E}(0)\rangle(\mu). \tag{3.10}$$

being $E_n^{(0)}$ and h_o the binding energy and the octet Hamiltonian respectively, at leading order. When we assume that the chromoelectric fields have a typical scale $\sim \Lambda_{\text{QCD}}$, the expression (3.10) allows to discuss the nature of the leading nonperturbative contributions. Thus the integral in (3.10) is a convolution of two objects: the exponential with a typical scale mv^2 and the chromoelectric correlator with a typical scale Λ_{QCD}. Depending on the relative size of the two scales three different situations occur:

– if $mv^2 \gg \Lambda_{\text{QCD}}$, the correlator reduces to the local gluon condensate and one recovers the result of Refs. [119, 120], which is proportional to the sixth power of the principal quantum number. The NLO nonperturbative contribution has been evaluated in Ref. [122]. Note, however, that in this case the dominant contribution to the nonlocal chromoelectric correlator corresponds to fluctuations of order mv^2, which can be calculated perturbatively [69, 79].

– if $mv^2 \ll \Lambda_{\text{QCD}}$, the exponential can be expanded and one obtains a quadratic short range nonperturbative potential [5, 123]. This potential absorbs the residual renormalons contained in the fully perturbative computations [5]. For a Coulombic system, its expectation value grows as the fourth power of the principal quantum number.

– if $mv^2 \sim \Lambda_{\text{QCD}}$, no expansion can be performed and the nonlocal condensate has to be kept. Its expectation value grows as the fourth power of the principal quantum number [69].

Hence, both nonperturbative potentials and (non-potential) local condensates are obtained from pNRQCD in the weak coupling regime for different kinematical limits, see also [124].

2.3.2   *Strong coupling regime*[17]

When $k > \sim \Lambda_{\text{QCD}} \gg E$, the pNRQCD Lagrangian consist of a singlet wave function field interacting with a potential and with pseudo-Goldstone bosons [5]. The dynamics of the singlet field S is described by the following Lagrangian (here, we do not specialize to the centre-of-mass system) [48, 125]

$$\mathcal{L}_{\text{pNRQCD}} = \text{Tr}\left\{ S^\dagger\left(i\partial_0 - \frac{\mathbf{p}_1^2}{2m_1} - \frac{\mathbf{p}_2^2}{2m_2} - V(\mathbf{x}_1, \mathbf{x}_2, \mathbf{p}_1, \mathbf{p}_2)\right)S\right\} \tag{3.11}$$

---

[16]Authors: N. Brambilla, J. Soto

[17]Authors: N. Brambilla, J. Soto

The dynamics of the pseudo-Goldstone boson is given by the Chiral Lagrangian [126]. The coupling of pseudo-Goldston bosons with the singlet field has not been worked out yet. If we ignore this coupling, we recover in Eq. (3.11) the structure of non-relativistic potential models [48, 125]. If we assume that V is analytical in $1/m$, the structure of the potential up to order $1/m^2$ is

$$V(\mathbf{x}_1, \mathbf{x}_2, \mathbf{p}_1, \mathbf{p}_2) = V^{(0)}(r) + \frac{V^{(1,0)}(r)}{m_1} + \frac{V^{(0,1)}(r)}{m_2} + \frac{V^{(2,0)}}{m_1^2} + \frac{V^{(0,2)}}{m_2^2} + \frac{V^{(1,1)}}{m_1 m_2}, \qquad (3.12)$$

$$V^{(2,0)} = \frac{1}{2}\left\{\mathbf{p}_1^2, V_{\mathbf{p}^2}^{(2,0)}(r)\right\} + \frac{V_{\mathbf{L}^2}^{(2,0)}(r)}{r^2}\mathbf{L}_1^2 + V_r^{(2,0)}(r) + V_{LS}^{(2,0)}(r)\mathbf{L}_1 \cdot \mathbf{S}_1, \qquad (3.13)$$

$$V^{(0,2)} = \frac{1}{2}\left\{\mathbf{p}_2^2, V_{\mathbf{p}^2}^{(0,2)}(r)\right\} + \frac{V_{\mathbf{L}^2}^{(0,2)}(r)}{r^2}\mathbf{L}_2^2 + V_r^{(0,2)}(r) - V_{LS}^{(0,2)}(r)\mathbf{L}_2 \cdot \mathbf{S}_2, \qquad (3.14)$$

$$V^{(1,1)} = -\frac{1}{2}\left\{\mathbf{p}_1 \cdot \mathbf{p}_2, V_{\mathbf{p}^2}^{(1,1)}(r)\right\} - \frac{V_{\mathbf{L}^2}^{(1,1)}(r)}{2r^2}(\mathbf{L}_1 \cdot \mathbf{L}_2 + \mathbf{L}_2 \cdot \mathbf{L}_1) + V_r^{(1,1)}(r)$$
$$+V_{L_1 S_2}^{(1,1)}(r)\mathbf{L}_1 \cdot \mathbf{S}_2 - V_{L_2 S_1}^{(1,1)}(r)\mathbf{L}_2 \cdot \mathbf{S}_1 + V_{S^2}^{(1,1)}(r)\mathbf{S}_1 \cdot \mathbf{S}_2 + V_{S_{12}}^{(1,1)}(r)\mathbf{S}_{12}(\hat{\mathbf{r}}), \qquad (3.15)$$

where $r = |\mathbf{r}|$, $\mathbf{r} = \mathbf{x}_1 - \mathbf{x}_2$, $\mathbf{L}_j \equiv \mathbf{r} \times \mathbf{p}_j$ and $\mathbf{S}_{12}(\hat{\mathbf{r}}) \equiv 12\hat{\mathbf{r}} \cdot \mathbf{S}_1\, \hat{\mathbf{r}} \cdot \mathbf{S}_2 - 4\mathbf{S}_1 \cdot \mathbf{S}_2$. The requisite of Poincaré invariance imposes well defined relations among the spin-dependent and velocity dependent potentials above [127–129]. If one further assumes that the matching to NRQCD can be done in the $1/m$ expansion, the explicit form of the potentials can be obtained in terms of Wilson loop operators [48, 128–133]. We display here some of them for illustration (for the form of all the potentials see [48]). For the static potential we have

$$V^{(0)}(r) = \lim_{T \to \infty} \frac{i}{T} \ln\langle W \rangle, \qquad (3.16)$$

for the potential at order $1/m$

$$V_s^{(1,0)}(r) = \lim_{T \to \infty} -\frac{g^2}{4T}\int_{-T/2}^{T/2}dt \int_{-T/2}^{T/2}dt'|t - t'|\langle\!\langle \mathbf{E}(t) \cdot \mathbf{E}(t')\rangle\!\rangle_c. \qquad (3.17)$$

At the order $1/m^2$ we display a potential contributing to the spin-dependent (precisely the spin–orbit) relativistic corrections

$$V_{LS}^{(2,0)}(r) = \frac{c_F^{(1)}}{2r^2}i\mathbf{r} \cdot \lim_{T \to \infty} \frac{1}{T}\int_{-T/2}^{T/2}dt \int_{-T/2}^{T/2}dt''\,(t - t'')\,\langle\!\langle g\mathbf{B}(\mathbf{x}_1, t'') \times g\mathbf{E}(\mathbf{x}_1, t)\rangle\!\rangle$$
$$+\frac{c_S^{(1)}}{2r^2}\mathbf{r} \cdot (\boldsymbol{\nabla}_r V^{(0)}), \qquad (3.18)$$

and a potential contributing to the spin-independent velocity dependent relativistic corrections

$$V_{\mathbf{p}^2}^{(2,0)}(r) = \frac{i}{4}\hat{\mathbf{r}}^i\hat{\mathbf{r}}^j \lim_{T \to \infty} \frac{1}{T}\int_{-T/2}^{T/2}dt \int_{-T/2}^{T/2}dt''\,(t - t'')^2\,\langle\!\langle g\mathbf{E}^i(\mathbf{x}_1, t'')\, g\mathbf{E}^j(\mathbf{x}_1, t)\rangle\!\rangle_c. \qquad (3.19)$$

The angular brackets $\langle\ldots\rangle$ stand for the average value over the Yang–Mills action, W for the rectangular static Wilson loop of extension $r \times T$ (the time runs from $-T/2$ to $T/2$, the space coordinate from $\mathbf{x}_1$ to $\mathbf{x}_2$):

$$W \equiv \mathrm{P}\exp\left\{-ig \oint_{r \times T} dz^\mu A_\mu(z)\right\}, \qquad dz^\mu A_\mu \equiv dz^0 A_0 - d\mathbf{z} \cdot \mathbf{A}, \qquad (3.20)$$

and $\langle\!\langle\ldots\rangle\!\rangle \equiv \langle\ldots W\rangle/\langle W\rangle$; P is the path-ordering operator. Moreover, we define the connected Wilson loop with $O_1(t_1)$, $O_2(t_2)$ and $O_3(t_3)$ operator insertions by:

$$\langle\!\langle O_1(t_1)O_2(t_2)\rangle\!\rangle_c = \langle\!\langle O_1(t_1)O_2(t_2)\rangle\!\rangle - \langle\!\langle O_1(t_1)\rangle\!\rangle\langle\!\langle O_2(t_2)\rangle\!\rangle. \qquad (3.21)$$

The operators $\mathbf{E}^i = F_{0i}$ and $\mathbf{B}^i = \epsilon^{ijk}F^{jk}/2$ ($F_{\mu\nu} = \partial_\mu A_\nu - \partial_\nu A_\mu + ig[A_\mu, A_\nu]$) are the chromoelectric and chromomagnetic field respectively.

Notice that the final result for the potentials (static and relativistic corrections) appears factorized in a part containing the high energy dynamics (and calculable in perturbation theory) which is inherited from the NRQCD matching coefficients (the c_j, d_j, cf. Section 2.1 on NRQCD in Chapter 1), and a part containing the low energy dynamics given in terms of Wilson loops and chromo-electric and chromo-magnetic insertions in the Wilson loop [48]. The inclusion of NRQCD matching coefficients solved the inconsistency between perturbative one-loop calculations and the Wilson loop approach which arose in the past [132, 134]. The low energy contributions can be calculated on the lattice [135, 136] or estimated in QCD vacuum models [134, 137].

Almost all the potentials given in Eq. (3.15) were evaluated on the lattice in Refs. [135, 136], but this is not so for the potentials of order $1/m$, $V^{(1,0)}$, $V^{(0,1)}$. It would be very interesting to have such an evaluation (the perturbative one exist at two loops [67]) since, phenomenologically, they have not been considered up to now. In general, it would be very interesting to have updated and more precise lattice calculations of all the potentials. We recall that these lattice calculations have also a definite impact on the study of the properties of the QCD vacuum in presence of heavy sources. So far the lattice data for the spin-dependent and spin-independent potentials are consistent with a flux-tube picture, while it is only for the spin-dependent terms that the so called scalar confinement is consistent with the lattice data [48, 134, 138].

It has recently been shown [139] that the assumption that V is analytic in $1/m$ is not correct. New non-analytic terms arise due to the three-momentum scale $\sqrt{m\Lambda_{\text{QCD}}}$. These terms can be incorporated into local potentials ($\delta^3(\mathbf{r})$ and derivatives of it) and scale as half-integer powers of $1/m$. Moreover, it is possible to factorize these effects in a model independent way and compute them within a systematic expansion in some small parameters. In any case, the corrections to the spectrum coming from these non-analytical terms are subleading with respect to the terms given in Eq. (3.12).

We emphasize that, in this regime, non-relativistic potential models, as the ones discussed in Section 3 are demonstrated to be EFTs of QCD, provided that the potentials used there are compatible with the ones extracted from QCD (and the interaction with pseudo-Goldstone bosons neglected). It is a matter of debate, however, which states in bottomonium and charmonium should be considered as belonging to this regime. On one hand the mass should be sufficiently lower than the heavy-light meson pair threshold to justify the omission of higher Fock state effects. On the other hand if the states are too low in mass then the perturbative matching regime of Section 2.3.1 will apply and the problem can be further simplified.

Since the potentials are defined in an effective field theory framework they are not plagued by the inconsistency typically emerging in higher order calculations in potential models. It is well known that at second order in quantum mechanical perturbation theory the spin dependent terms result in a contribution which is as large as the leading order one. This is due to the fact that the resulting expression becomes ill-defined. Regulating it requires to introduce a cut-off (or dimensional regularization). A large cut-off gives rise to a linear and to a logarithmic divergence. These divergences can be renormalized by redefining the coupling constant of a delta potential [140]. This is a mere reflection of the fact that when one matches QCD to NRQCD, one expands the energy and three momentum. This induces infrared divergences in the matching coefficients. For quarkonium this happens in the calculation of a matching coefficient of a four Fermion operator at two loops. If one uses a consistent regularization scheme both for the QCD-NRQCD matching calculation and the quantum mechanical calculation in pNRQCD, the divergences exactly cancel and, at the end of the day, a totally consistent scale independent result is obtained (for a QED example see Refs. [141, 142]). Notice that an EFT framework is crucial to understand this second order calculation and to render the result meaningful.
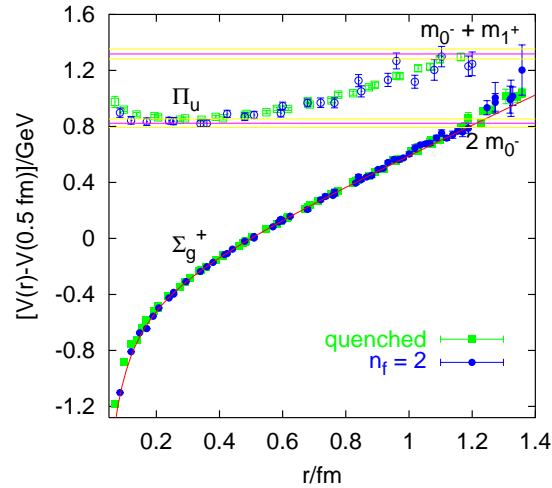
Fig. 3.6: The singlet static energy (quenched and unquenched data) from Ref. [51], see also [143]

2.3.3 The QCD static spectrum and mechanism of confinement[18]

The spectrum of gluons in the presence of a static quark–antiquark pair has been extensively studied with high precision using lattice simulations. Such studies involve the calculation of large sets of Wilson loops with a variety of different spatial paths. Projections onto states of definite symmetries are done, and the resulting energies are related to the static quark–antiquark potential and the static hybrids potentials. With accurate results, such calculations provide an ideal testing ground for models of the QCD confinement mechanism.

The singlet static energy

The singlet static energy is the singlet static potential $V_s^{(0)}$.

In the plot3.6, we report simulation results both with and without light quark–antiquark pair creation. Such pair creation only slightly modifies the energies for separations below 1 fm, but dramatically affects the results around 1.2 fm, at a distance which is too large with respect to the typical heavy quarkonium radius to be relevant for heavy quarkonium spectroscopy. At finite temperature, the so-called string breaking occurs at a smaller distance (cf. corresponding Section in Chapter 7, *Media*).

One can study possible nonperturbative effects in the static potential at short distances. As it has already been mentioned in the "static QCD potential" subsection, the proper treatment of the renormalon effects has made possible the agreement of perturbation theory with lattice simulations (and potential models) [78, 88–92]. Here we would like to quantify this agreement assigning errors to this comparison. In particular, we would like to discern whether a linear potential with the usual slope could be added to perturbation theory. In order to do so we follow here the analysis of Ref. [90, 144], where the potential is computed within perturbation theory in the Renormalon Subtracted scheme defined in Ref. [81]. The comparison with lattice simulations [145] in Fig. 3.7 shows that nonperturbative effects should be small and compatible with zero, since perturbation theory is able to explain lattice data within errors. The systematic and statistical errors of the lattice points are very small (smaller than the size of the points). Therefore, the main sources of uncertainty of our (perturbative) evaluation come from the uncertainty in the value of $\Lambda_{\overline{MS}}$ ($\pm 0.48\, r_0^{-1}$) obtained from the lattice [146] and from the uncertainty in higher orders in perturbation theory. We show our results in Fig. 3.7. The inner band reflects the uncertainty in $\Lambda_{\overline{MS}}$ whereas the outer band is meant to estimate the uncertainty due to higher orders in perturbation theory. We estimate the error due to perturbation theory by the difference between the NNLO and NNNLO evaluation. The usual confining potential, $\delta V = \sigma r$, goes with a slope $\sigma = 0.21 \text{GeV}^2$. In lattice units

---

[18]Authors: N. Brambilla, C. Morningstar, A. Pineda
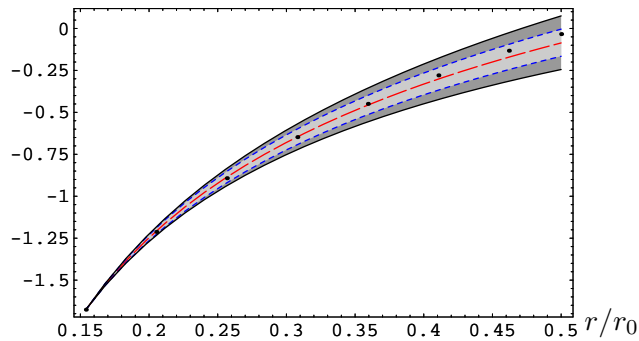
Fig. 3.7: Plot of $r_0(V_{\rm RS}(r) - V_{\rm RS}(r') + E_{latt.}(r'))$ versus r at three loops (estimate) plus the leading single ultrasoft log (dashed line) compared with the lattice simulations [145] $E_{latt.}(r)$. For the scale of $\alpha_s(\nu)$, we set $\nu = 1/0.15399\, r_0^{-1}$. $\nu_{us} = 2.5\, r_0^{-1}$ and $r' = 0.15399\, r_0$. The inner and outer band are meant to estimate the errors in $\Lambda_{\overline{\rm MS}}$ and perturbative. For further details see the main text.

we take: $\sigma = 1.35\, r_0^{-2}$. The introduction of a linear potential at short distances with such slope is not consistent with lattice simulations. This is even so after the errors considered in Fig. 3.7 have been included.

At larger distances, $r \gg \Lambda_{\rm QCD}$, $V_s^{(0)}$ grows linearly, with the string tension $\sigma = 0.21 {\rm GeV}^2$. Such a linear growth of the energy is often taken as evidence that the gluon field forms a flux tube whose dynamics can be described by an effective string theory. However, it should be pointed out that a linearly growing potential does not necessarily imply string formation; for example, the spherical bag model also predicts a linearly rising potential for moderate r. It has been shown [147] that the formation of a string-like flux tube implies a characteristic and universal $-\frac{\pi}{12r}$ correction to the ground-state energy, deriving from the zero-point energy of the transverse string vibration. Recent high precision simulations [148] (cf. also [149]) show that the coefficient of the $1/r$ correction differs from $-\pi/12$ by 12%. The authors of Ref. [148] introduce an *ad hoc* end-effect term with a fit parameter b to the effective string action to explain this significant difference. However, in a more recent paper [150], these authors show that an open-closed string duality relation requires $b = 0$. Furthermore, a simple resonance model was used in Refs. [151, 152] to show that the Casimir energy expected from a string description could be reproduced in a model in which string formation was not a good description, concluding that no firm theoretical foundation for discovering string formation from high precision ground state properties below the 1 fm scale currently exists.

Excitations of the static energy

The spectrum of gluons in the presence of a static quark–antiquark pair provides valuable clues about the nonperturbative dynamics of QCD. Adopting the viewpoint that the nature of the confining gluon field is best revealed in its excitation spectrum, in Ref. [47], recent advances in lattice simulation technology, including anisotropic lattices, improved gauge actions, and large sets of creation operators, were employed to investigate the static energies of gluonic excitations between static quarks (hybrid static energies).

In NRQCD (as in QCD) the gluonic excitations between static quarks have the same symmetries of a diatomic molecule plus charge conjugation. In the centre-of-mass system these correspond to the symmetry group $D_{\infty h}$ (substituting the parity generator by CP). The mass eigenstates are classified in terms of the angular momentum along the quark–antiquark axes ($|L_z| = 0, 1, 2, \ldots$ which traditionally are labelled as $\Sigma, \Pi, \Delta, \ldots$), CP (even, g, or odd, u), and the reflection properties with respect to a plane passing through the quark–antiquark axes (even, $+$, or odd, $-$). Only the Σ states are not degenerate with respect to the reflection symmetry, see also Section 2.2.2. In Fig. 3.8 we display lattice results of
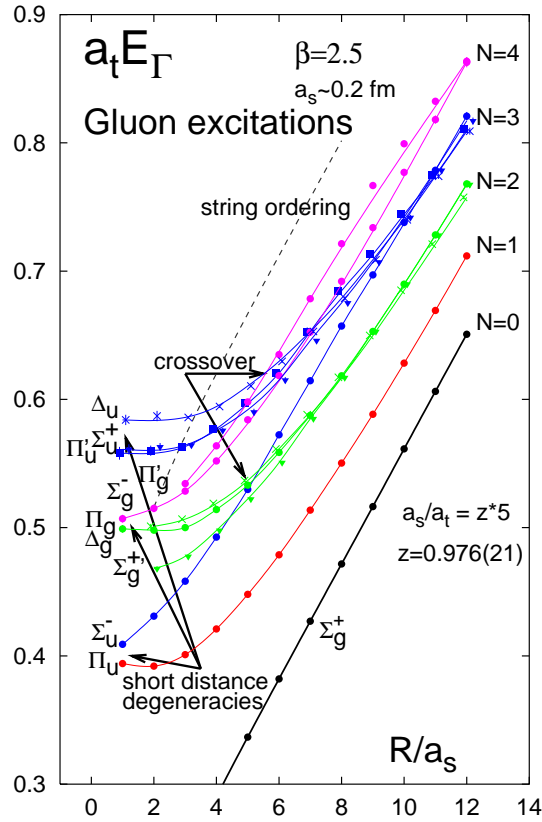
Fig. 3.8: The spectrum of gluonic excitations in the presence of a static quark–antiquark pair separated by a distance R in 4-dimensional $SU(3)$ gauge theory (from Ref. [47]). Results are from one simulation for lattice spacing $a_s \sim 0.2$ fm using an improved action on a $(10^2 \times 30) \times 60$ anisotropic lattice with coupling $\beta = 2.5$ and bare aspect ratio $\xi = 5$. At large distances, *all* levels without exception are consistent with the expectations from an effective string theory description. A dramatic level rearrangement is observed in the crossover region between $0.5 - 2.0$ fm. The dashed line marks a lower bound for the onset of mixing effects with glueball states.

the hybrid static energies V_H obtained from Wilson loops with operators of the appropriate symmetry inserted at the end points.

$D_{\infty h}$ is a subgroup of the rotational symmetry group $O(3)$ times charge conjugation. In the short-range limit, $r \ll \Lambda_{\mathrm{QCD}}$, the hybrid energies approach so-called gluelump levels that can be classified according to the usual $O(3)$ J^{PC}. The corresponding operators can be explicitly constructed using pNRQCD in the static limit [5]. In the case of pure gluodynamics, the spectrum then consists of static energies which depend on $\mathbf{r}$. The energy units are provided by the only other scale in the problem, Λ_{QCD}. The gluelumps operators are of the type $\mathrm{Tr}\{OH\}$, where $\mathrm{O} = O^a T^a$ corresponds to a quark–antiquark state in the adjoint representation (the octet) and $H = H^a T^a$ is a gluonic operator. By matching the QCD static hybrid operators into pNRQCD, we get the static energies (also called hybrids static potentials) V_H of the gluelumps. At leading order in the multipole expansion, they read [5]

$$V_H(r) = V_o(r) + \frac{1}{T_g^H}, \tag{3.22}$$

being T_g^H the correlation time of the corresponding gluelump correlator $\langle H^a(t)\phi(t,0)_{ab}^{\mathrm{adj}} H^b(0)\rangle^{\mathrm{non-pert.}}$ $\simeq h\, e^{-it/T_g^H}$. The lattice data confirm that (in the region in which decay into glueball channels is not yet possible) all the V_H behave like $V_o^{(0)} = \frac{\alpha_{\mathrm{s}}}{6r}$ for $r{\to}0$ cf. Fig. 3.8 and Ref. [65]. The constant T_g^H depends on the gluelump operator H, its inverse corresponds to the mass of the gluelump H. Note that

T_g^H are scheme and scale dependent. pNRQCD, in which r is integrated out, predicts the short-range degeneracies,

$$\Sigma_g^{+\,\prime} \sim \Pi_g\,; \qquad \Sigma_g^- \sim \Pi_g' \sim \Delta_g\,; \quad \Sigma_u^- \sim \Pi_u\,; \qquad \Sigma_u^+ \sim \Pi_u' \sim \Delta_u\,. \qquad (3.23)$$

This is confirmed by the lattice data, cf. Fig. 3.8. Similar observations have also been previously made in the lattice theory in Ref. [153]. It is interesting to notice that the hierarchy of the states, as displayed in Fig. 3.8, is reflected in the dimensionality of the operators of pNRQCD [5, 65].

By using only **E** and **B** fields and keeping only the lowest-dimensional representation we may identify the operator H for the short-range hybrids called $\Sigma_g^{+\,\prime}$ (and Π_g) with $\mathbf{r} \cdot \mathbf{E}$ (and $\mathbf{r} \times \mathbf{E}$) and the operator H for the short-range hybrids called Σ_u^- (and Π_u) with $\mathbf{r} \cdot \mathbf{B}$ (and $\mathbf{r} \times \mathbf{B}$). Hence, the corresponding static energies for small r are

$$V_{\Sigma_g^{+\,\prime},\Pi_g}(r) = V_o(r) + \frac{1}{T_g^E}, \qquad\qquad V_{\Sigma_u^-,\Pi_u}(r) = V_o(r) + \frac{1}{T_g^B}.$$

The lattice results of Ref. [47] show that, in the short range, $V_{\Sigma_g^{+\,\prime},\Pi_g}(r) > V_{\Sigma_u^-,\Pi_u}(r)$. This supports the sum-rule prediction [154] that the pseudovector hybrid lies lower than the vector one, i.e., $T_g^E < T_g^B$ and the lattice evaluations of Refs. [65, 153]. In this way, in the short-distance limit, we can relate the behavior of the energies for the gluonic excitations between static quarks with the large time behavior of gluonic correlators. We can extract results for gauge invariant two-point gluon field strength correlators (which are also the relevant nonperturbative objects in the stochastic vacuum model [137]) $\langle 0|F_{\mu\nu}^a(t)\phi(t,0)_{ab}^{\mathrm{adj}}F_{\mu\nu}^b(0)|0\rangle$, ϕ being the adjoint string. One can parameterize these correlators in terms of two scalar functions: $\langle 0|\mathbf{E}^a(t)\phi(t,0)_{ab}^{\mathrm{adj}}\mathbf{E}^b(0)|0\rangle$ and $\langle 0|\mathbf{B}^a(t)\phi(t,0)_{ab}^{\mathrm{adj}}\mathbf{B}^b(0)|0\rangle$ with correlations lengths: $T^E = 1/\Lambda_E$ and $T^B = 1/\Lambda_B$, respectively. Note that while differences between gluelump masses Λ_H are universal the absolute normalization is scheme- and scale-dependent [65].

The matching of pNRQCD to ($n_f = 0$) QCD has been performed in the static limit to $\mathcal{O}(\alpha_\mathrm{s}^3)$ in the lattice scheme and the (scheme- and scale-dependent) gluelump masses $\Lambda_H = 1/T_g^H$ have been determined both, in the continuum limit from short distance energy levels and at finite lattice spacing from the gluelump spectrum [65]. Perfect agreement between these two determinations was found. It would be highly desirable to have lattice determinations at even shorter distances to further increase the precision of such determinations, however, such calculations are rather challenging due to the need to properly treat lower-lying glueball scattering states.

The behaviour of the hybrid static energies for large r provides further valuable information on the mechanism of confinement. The linearly rising ground-state energy is *not* conclusive evidence of string formation [138]. Computations of the gluon action density surrounding a static quark–antiquark pair in $SU(2)$ gauge theory also hint at flux tube formation [155]. Complementary information come from the study of the static energies of the gluonic excitations between static quarks. A treatment of the gluon field in terms of the collective degrees of freedom associated with the position of the long flux might then be sufficient for reproducing the long-wavelength physics. If true, one then hopes that the oscillating flux can be well described in terms of an effective string theory [66]. In such a case, the lowest-lying excitations are expected to be the Goldstone modes associated with the spontaneously broken transverse translational symmetry. These modes are a universal feature of any low-energy description of the effective QCD string and have energy separations above the ground state given by multiples of π/R. A well-defined pattern of degeneracies and level orderings among the different symmetry channels form a very distinctive signature of the onset of the Goldstone modes for the effective QCD string.

The spectrum of more than a dozen levels shown in Fig. 3.8 provides strong evidence that the gluon field can be well approximated by an effective string theory for large separations R. For separations above 2 fm, the levels agree *without exception* with the ordering and degeneracies expected from an effective string theory. The gaps agree well with $N\pi/R$, but a fine structure remains, offering the possibility

to obtain details of the effective QCD string action in future higher precision simulations. For small $R < 2$ fm, the level orderings and degeneracies are not consistent with the expectations from an effective string description, and the gaps differ appreciably from $N\pi/R$ with $N = 1, 2, 3, \ldots$. Such deviations, as large as 50% or more, cannot be considered mere corrections, making the applicability of an effective string description problematical. Between 0.5 to 2 fm, a dramatic level rearrangement occurs.

Non-universal details of the underlying string description for large separations, such as higher order interactions and their couplings, are encoded in the fine structure of the spectrum at large separations. It is hoped that near future simulations will have sufficient precision to be able to differentiate between such corrections. In the meantime, the excitation spectrum in other space–time dimensions and other gauge theories, such as $SU(2)$ and $Z(2)$, are being explored [149, 156].

2.3.4 pNRQCD for QQQ and QQq baryons [19]

In the case of a bound state formed by three heavy quarks, still a hierarchy of physical scales similar to the quarkonium case exists. Consequently, starting from a NRQCD description for each heavy quark, it is possible to integrate out the scale of the momentum transfer $\simeq mv$ and write the pNRQCD Lagrangian for heavy baryons [157, 158]. Similarly to before two different dynamical situations may occur: the momentum transfer is much larger than Λ_{QCD}, or it is of order Λ_{QCD}. In the first case the matching is perturbative and the Lagrangian is similar to Eq. (3.9) with more degrees of freedom for the quark part: two octets, one singlet and one decuplet (as it comes from the colour decomposition of $3\times3\times3$) [157]. In the second case the matching is nonperturbative and the Lagrangian is similar to Eq.(3.11) with only the three quark singlet as degree of freedom. The (matching) potentials are nonperturbative objects and their precise expression in terms of static Wilson loop and (chromo)electric and (chromo)magnetic insertions in static Wilson loops can be calculated [157]. Experimental data for baryons composed by three quarks are not existing at the moment, however lattice calculation of the three quark potential exist [53–55].

Baryons made by two heavy quarks and a light quark QQq combine the slow motion of the heavy quark with the fast motion of the light quark. Thus a treatment combining in two steps an effective field theory for the QQ interaction and an effective field theory for the QQ degrees of freedom with the light quark is the most appropriate one. The interest of these states is also related to the fact that the SELEX experiment recently announced the discovery of four doubly charmed baryon states. This will be discussed in more detail in Section 3.4.2. The non relativistic motion of the two heavy quarks is similar to quarkonium while the light quark is moving relativistically around the slowly moving QQ. Since the QQ is in a colour antitriplet state, in the heavy quark limit the system is similar to a $\bar{Q}q$ system. However, the situation is much more interesting because if one constructs first the EFT for the two heavy quarks more degrees of freedom enter and depending on the dynamical situation of the physical system, these degrees of freedom may or may not have a role. In particular if we work under the condition that the momentum transfer between the two heavy quarks is smaller than Λ_{QCD}, then we can construct a pNRQCD Lagrangian of the type Eq. (3.9) with a triplet and a sextet as QQ degrees of freedom [157]. Such degrees of freedom, would also be relevant for the study of double charmonia production [159].

2.4 Thresholds effects (EFT) [20]

For states for which $k \sim E \sim \Lambda_{\mathrm{QCD}}$, namely close or beyond threshold, one has to stay at the NRQCD level. It is still an open question whether one can build a suitable EFT to study mixing and threshold effects.

For a confining potential (e.g., harmonic oscillator), however, the typical momentum transfer k decreases with the principal quantum number whereas both the typical relative three-momentum p and the binding energies increase. For some principal quantum number n, the binding energy will become com-

---

[19]Author: N. Brambilla
[20]Authors: N. Brambilla, J. Soto

parable to the momentum transfer and hence $k \geq E$ will not hold anymore. For these states pNRQCD is not a good effective theory anymore (it may still remain a successful model). This is expected to happen for states close to or higher than the heavy-light meson pair threshold. There is no EFT beyond NRQCD available for this regime at the moment. Notice also that for some n the typical three momentum will become comparable to m and hence relativistic effects will not be small and NRQCD will not be a good EFT anymore. This is expected to happen for states much higher than the heavy-light meson pair threshold. Relativistic quark models like the ones discussed in Section 3 are probably unavoidable for this situation although it is not known at the moment how to link them to QCD.

3 PHENOMENOLOGICAL APPROACH[21]

From the discovery of charmonium states [160–162], QCD motivated potential models have played an important role in understanding quarkonium spectroscopy [163–166]. The initial models describing charmonium spectroscopy, using a QCD motivated Coulomb plus linear confining potential with colour magnetic spin dependent interactions, have held up quite well. This approach also provides a useful framework for refining our understanding of QCD and guidance towards progress in quarkonium physics. The discovery of the Υ family of meson [167] was quickly recognized as a $b\bar{b}$ bound state whose spectroscopy was well described by the potential model picture used to describe the charmonium system.

In this section we give an overview of potential models of quarkonium spectroscopy [168]. Most models [169–180] have common ingredients. Almost all such models are based on some variant of the Coulomb plus linear potential confining potential expected from QCD. Quark potential models typically include one-gluon exchange and most models also include the running constant of QCD, $\alpha_{\mathrm{s}}(Q^2)$. Finally, relativistic effects are often included at some level [169–183]. At the minimum, all models we consider include the spin-dependent effects that one would expect from one-gluon-exchange, analogous to the Breit–Fermi interaction in QED, plus a relativistic spin–orbit Thomas precession term expected of an object with spin (the quark or antiquark) moving in a central potential. Potential models have been reasonably successful in describing most known mesons. Although cracks have recently appeared [187, 188] these point to the need for including physics effects that have hitherto been neglected such as coupled channel effects [188].

In the next section we will give a brief introduction to quark potential models and attempt to describe the differences between models. The subject is roughly thirty years old and a large literature on the subject exists. It is impossible to cover all variants and we will almost totally neglect the considerable work that brought us to where we are today. We apologise to all those whose work we do not properly cite and hope they understand. In the next sections we compare the predictions of some models with experiment for the $c\bar{c}$, $b\bar{b}$ and $c\bar{b}$ mesons and point out variations in predictions and how they arise from the underlying model.

3.1 Potential models[22]

Quarkonium potential models typically take the form of a Schrödinger like equation:

$$[T + V]\Psi = E\Psi \tag{3.24}$$

where T represents the kinetic energy term and V the potential energy term. We lump into these approaches the Bethe–Salpeter equation (e.g., Ref. [182, 184]) and quasi-potential approaches (e.g., Ref. [173]).

---

[21]Author: S. Godfrey
[22]Author: S. Godfrey

Different approaches have been used for the kinetic energy term ranging from the non-relativistic Schrödinger equation to relativistic kinetic energy [171, 179, 189]

$$T = \sqrt{p^2 + m_Q^2} + \sqrt{p^2 + m_{\bar{Q}}^2} \tag{3.25}$$

in the spinless Salpeter equation.

3.1.1 The potential

The quark–antiquark potential is typically motivated by the properties expected from QCD [48, 128–134] and while there are differences, most recent potentials show strong similarities. It is worth pointing out that in the early days of quarkonium spectroscopy this was not obvious and much effort was expended in fitting different functional forms of the potential to the observed quarkonium masses. In the end, the shape of the potentials converged to a form that one might expect from the asymptotic limits of QCD and which has been qualitatively verified by Lattice QCD calculations [135] of the expression of the potentials obtained in the Wilson loop [128–134] and in the EFT [48] approach. This is a great success of quarkonium phenomenology.

To derive the quarkonium potential we start with QCD where the gluons couple to quarks and to each other. The quark–gluon interaction is similar to the electron–photon interaction in quantum electrodynamics with the Born term for the qq or $q\bar{q}$ interaction at short distance being the familiar $1/r$ form. In contrast with QED the gluon self-coupling results in a slow decrease of the effective coupling strength at short distance. In terms of the Fourier conjugate momentum the lowest order QCD corrections to $\alpha_s = g_s^2/4\pi$ can be parametrized as

$$\alpha_s(Q^2) = \frac{12\pi}{(33 - 2n_f)\ln(Q^2/\Lambda^2)} \tag{3.26}$$

where n_f is the number of Fermion flavours with mass below Q, and $\Lambda \sim \Lambda_{\mathrm{QCD}}$ is the characteristic scale of QCD measured to be ~ 200 MeV. At short distances one-gluon-exchange leads to the Coulomb like potential

$$V(r) = -\frac{4}{3}\frac{\alpha_s(r)}{r} \tag{3.27}$$

for a $q\bar{q}$ pair bound in a colour singlet where the factor of $4/3$ arises from the SU(3) colour factors. At short distances one-gluon-exchange becomes weaker than a simple Coulomb interaction.

At momentum scales smaller than Λ_{QCD} which corresponds to a distance of roughly 1 fm, α_s blows up and one-gluon-exchange is no longer a good representation of the $q\bar{q}$ potential. The qualitative picture is that the chromoelectric lines of force bunch together into a *flux tube* which leads to a distance-independent force or a potential

$$V(r) = \sigma r. \tag{3.28}$$

This has been validated by Lattice QCD calculations. Phenomenologically, every recent model which we will consider has found $\sigma \sim 0.18$ GeV^2.

Numerous variations of the resulting Coulomb plus linear potential exist in the literature. Some of the better known ones are the Cornell potential [170], Richardson's potential [190], and the Buchmüller Tye potential [191]. Overall, the spin-independent features of quarkonium spectroscopy are well described by the potentials just described.

Let us also mention that heavy quark mass corrections to the (static) central (spin and velocity independent) potential exist, although they have not yet been taken into account in potential models applications so far. They correspond to $V_r^{(1,0)}$, $V_r^{(2,0)}$ and $V_r^{(1,1)}$ in Section 2.3.2. Their expressions in perturbation theory are known [48, 68]. Part of $V_r^{(2,0)}$ and $V_r^{(1,1)}$ was included in the phenomenological application to the spectrum in Refs. [128, 129, 135, 185].

3.1.2 Spin-dependent potentials

Spin dependent multiplet splittings are an important test of the details of quarkonium models. In particular, the nature of spin dependent potentials are decided by the Lorentz nature of the confining potentials [129, 131, 138, 186]. While there is general consensus that the short distance one-gluon-exchange piece is Lorentz vector and the linear confining piece is Lorentz scalar this is by no means universal and other possibilities are vigorously advocated. Gromes described how to obtain the spin-dependent potentials given the Lorentz structure of the interaction [129] and one can also use the prescription given in Berestetskij, Lifschitz and Pitaevskij [192]. Simply put, one can obtain the form of the spin dependent interaction by Fourier transforming the on-shell $q\bar{q}$ scattering amplitude:

$$M = [\bar{u}(p'_f)\Gamma u(p'_i)] \ V(Q^2) \ [\bar{u}(p_f)\Gamma u(p_i)] \tag{3.29}$$

where the Γ matrices give the Lorentz structure of the interaction and $V(Q^2)$ is the Fourier transform of the spin-independent potential. For example, for a Lorentz-vector interaction $\Gamma = \gamma^\mu$ and for a Lorentz-scalar interaction $\Gamma = I$. In principle other forms are possible with each giving rise to characteristic spin-dependent interactions. These can be found by expanding the scattering amplitude to order $(v/c)^2$ which corresponds to an expansion in inverse powers of quark masses. In the early years of quarkonium phenomenology they were all tried and it was found that the Lorentz-vector one-gluon-exchange plus Lorentz scalar linear confining potential gave the best agreement with experiment [23]. Note that the form of the full QCD potential at order $1/m^2$ [48, 128, 130–133] has now been obtained in the EFT (cf. Section 2.3.2), and while the spin-dependent nonperturbative potential may correspond to a scalar interaction in the language used above, the velocity-dependent potentials do not fit such a picture. The effective kernel is thus not a simple scalar, precisely the dependence both on the momentum and on the Lorentz structure is more involved than a pure convolution (i.e., only depending on the momentum transfer) scalar structure [48, 134, 138, 186]. However, the spin dependency is well approximated by a scalar interaction for phenomenological applications. The QCD spin-dependent potentials are explicitly given in Section 2.3.2. A complete calculation of the spin structure of the spectrum using the full expression given in Section 2.3.2 does not yet exist.

To lowest order in $(v/c)^2$ the Lorentz-vector one-gluon-exchange gives rise to terms familiar from one-photon exchange in atomic physics. The colour contact interaction, which in the language of Section 2.3.2 corresponds to taking $V_{S^2}^{(1,1)}(r)$ at leading order in perturbation theory,

$$H_{q\bar{q}}^{cont} = \frac{32\pi}{9} \frac{\alpha_s(r)}{m_q m_{\bar{q}}} \mathbf{S}_q \cdot \mathbf{S}_{\bar{q}} \delta^3(\mathbf{r}) \tag{3.30}$$

gives rise to, for example the $J/\psi - \eta_c$ splitting. The colour tensor interaction, which in the language of Section 2.3.2 corresponds to taking $V_{\mathbf{S}_{12}}^{(1,1)}(r)$ at leading order in perturbation theory,

$$H_{q\bar{q}}^{ten} = \frac{4}{3} \frac{\alpha_s(r)}{m_q m_{\bar{q}}} \frac{1}{r^3} \left[\frac{3\,\mathbf{S}_q \cdot \mathbf{r}\,\mathbf{S}_{\bar{q}} \cdot \mathbf{r}}{r^2} - \mathbf{S}_q \cdot \mathbf{S}_{\bar{q}} \right] \tag{3.31}$$

contributes to splitting of $L \neq 0$ spin triplet multiplets like the χ_{cJ} and χ_{bJ} multiplets. The final spin dependent term is the spin orbit interaction which has two contributions. The first piece arises from the colour-magnetic one-gluon-exchange while the second piece is the Thomas precession term which is a relativistic effect for an object with spin moving in a central potential

$$H_{q\bar{q}}^{s.o.} = H_{q\bar{q}}^{s.o.(cm)} + H_{q\bar{q}}^{s.o.(tp)}. \tag{3.32}$$

The colour magnetic piece arising from one-gluon exchange is given by:

$$H_{q\bar{q}}^{s.o.(cm)} = \frac{4}{3} \frac{\alpha_s(r)}{r^3} \left(\frac{\mathbf{S}_q}{m_q m_{\bar{q}}} + \frac{\mathbf{S}_{\bar{q}}}{m_q m_{\bar{q}}} + \frac{\mathbf{S}_q}{m_q^2} + \frac{\mathbf{S}_{\bar{q}}}{m_{\bar{q}}^2} \right) \cdot \mathbf{L} \tag{3.33}$$

---

[23] Although other forms are still advocated. See Ebert *et al.* [173, 193].

and the Thomas precession term is given by

$$H_{q\bar{q}}^{s.o.(tp)} = -\frac{1}{2r}\frac{\partial H_{q\bar{q}}^{conf}}{\partial r}\left(\frac{\mathbf{S}_q}{m_q^2} + \frac{\mathbf{S}_{\bar{q}}}{m_{\bar{q}}^2}\right)\cdot\mathbf{L} \tag{3.34}$$

which includes a contribution from both the short distance $1/r$ piece and the linear Lorentz-scalar confining potential. In the language of Section 2.3.2, both terms in (3.32) are obtained by taking $V_{LS}^{(1,1)}$ at leading order in perturbation theory and using the Gromes relation for $V_{LS}^{(2,0)}$. In these formulae $\alpha_{\rm s}(r)$ is the running coupling constant of QCD.

For mesons consisting of quarks with different flavours such as the B_c meson, charge conjugation is no longer a good quantum number so states with different total spins but with the same total angular momentum, like the $^3P_1 - ^1P_1$ and $^3D_2 - ^1D_2$ pairs (i. e. $J = L$ for $L \geq 1$) can mix via the spin–orbit interaction or some other mechanism. Equations (3.33) and (3.34) can be rewritten to explicitly give the antisymmetric spin–orbit mixing term:

$$H_{s.o.}^- = +\frac{1}{4}\left(\frac{4}{3}\frac{\alpha_{\rm s}}{r^3} - \frac{k}{r}\right)\left(\frac{1}{m_Q^2} - \frac{1}{m_{\bar{Q}}^2}\right)\mathbf{S}_- \cdot \mathbf{L} \tag{3.35}$$

where $\mathbf{S}_- = \mathbf{S}_Q - \mathbf{S}_{\bar{Q}}$. Consequently, the physical the physical $J = L$ ($J \geq 1$) states are linear combinations of ^3L_J and ^1L_J states which we describe by the following mixing:

$$\begin{aligned} L' &= ^1L_J\cos\theta_{nL} + ^3L_J\sin\theta_{nL} \\ L &= -^1L_J\sin\theta_{nL} + ^3L_J\cos\theta_{nL} \end{aligned} \tag{3.36}$$

where L designates the relative angular momentum of the $Q\bar{Q}$ pair and the subscript is the total angular momentum of the $Q\bar{Q}$ which is equal to L. Our notation implicitly implies $L - S$ coupling between the quark spins and the relative angular momentum. In the limit in which only one quark mass is heavy, $m_Q\rightarrow\infty$, and the other one is light the states can be described by the total angular momentum of the light quark which is subsequently coupled to the spin of the heavy quark. This limit gives rise to two doublets, one with $j = 1/2$ and the other $j = 3/2$ and corresponds to two physically independent mixing angles $\theta = -\tan^{-1}(\sqrt{2}) \simeq -54.7°$ and $\theta = \tan^{-1}(1/\sqrt{2}) \simeq 35.3°$ [194, 195]. Some authors prefer to use the $j - j$ basis [196] but we will follow the $L - S$ eigenstates convention implied in the spin–orbit terms given above and include the LS mixing as a perturbation. It is straightforward to transform between the $L - S$ basis and the $j - j$ basis. We note that radiative transitions are particularly sensitive to the $^3L_L - ^1L_L$ mixing angle with the predictions from the different models giving radically different results. We also note that the definition of the mixing angles are fraught with ambiguities. For example, charge conjugating $c\bar{b}$ into $b\bar{c}$ flips the sign of the angle and the phase convention depends on the order of coupling $\mathbf{L}$, $\mathbf{S}_Q$ and $\mathbf{S}_{\bar{Q}}$ [195].

3.1.3 Relativistic corrections

The Hamiltonian with the spin-dependent terms as written above is actually inconsistent as it stands as the terms more singular than r^{-2} are illegal operators in the Schrödinger equation. This is resolved by returning to the full scattering amplitude which has the effect of smearing the coordinate $\mathbf{r}$ out over distances of the order of the inverse quark mass and the strengths of the various potentials become dependent on the momentum of the interacting quarks. The smearing of the potentials has the consequence of taming the singularities. Alternatively, if one regards this Hamiltonian in the spirit of effective field theories, these singular operators are subleading in any reasonable power counting, and hence they must be treated as a perturbation. They may need regularization (smearing) at higher orders of perturbation theory, which introduces a scale dependence. This scale dependence cancels against the one of higher order NRQCD matching coefficients, see Section 2.3.2,

From this starting point different authors [169–180] diverge in how they incorporate further relativistic corrections. For example, Godfrey and Isgur (GI) [171] use the full relativistic scattering amplitude as the starting point but do not take it literally and instead parameterize the various relativistic effects. The relativistic smearing is described by a quark form factor and momentum dependent corrections are parametrized in a form that is in keeping with the generalities, if not the details, of the $q\bar{q}$ scattering amplitude. The reasoning is that the scattering amplitudes are for free Dirac Fermions while quarks inside a hadron are strongly interacting and will have off-mass-shell behavior. In addition, in field theory the Schrödinger equation arises in the $q\bar{q}$ sector of Fock space by integrating over more complex components of Fock space such as $|q\bar{q}g\rangle$. This integration will introduce additional momentum dependence in the $q\bar{q}$ potential not reflected in eq. (3.29). There are other deficiencies that arise from taking eq. (3.29) literally. Thus, GI use the full scattering amplitude as a framework on which to build a semiquantitative model of relativistic effects. While they acknowledge that this procedure is not entirely satisfactory they argue that it enables them to successfully describe all mesons, from the lightest to the heaviest, in a unified framework.

In contrast, the more recent work by Ebert, Faustov and Galkin performs an expansion in powers of velocity, including all relativistic corrections of order v^2/c^2, including retardation effects and one-loop radiative corrections [173, 193]. Ebert *et al* use a quasipotential approach in which the quasipotential operator of the quark–antiquark interaction is constructed with the help of the off-mass-shell scattering amplitude. The expression they derived to describe the spin-independent and spin-dependent corrections are rather lengthy and we refer the reader to their papers [173, 193, 197]. They found that relativistic effects are important, particularly in radiative transitions (which are outside the scope of this section).

While the GI calculation [171] assumed a short distance Lorentz-vector interaction and a Lorentz-scalar confining potential Ebert *et al* [173, 193] employ a mixture of long-range vector and scalar linear confining potentials. The effective long-range vector vertex includes an anomalous chromomagnetic moment of the quark, κ. The fitted value for κ results in the vanishing of the long-range magnetic contribution to the potential so that the long range confining potential is effectively Lorentz scalar.

In both cases taking the non-relativistic limit recovers eqns. (3.30–3.34). Despite differences in the details of the various approaches most recent calculations are in fairly good agreement.

3.1.4 *Charm mass corrections to the bottomonium mass spectrum*[24]

For the calculation of the bottomonium mass spectrum it is necessary to take into account additional corrections due to the non-zero mass of the charm quark [75, 95, 198, 199]. The one-loop correction to the one-gluon exchange part of the static $Q\bar{Q}$ potential in QCD due to the finite c quark mass is given by [75, 200]

$$\Delta V_{m_c}(r) = -\frac{4}{9}\frac{\alpha_s^2(\mu)}{\pi r}\left[\ln(\sqrt{a_0}m_c r) + \gamma_E + E_1(\sqrt{a_0}m_c r)\right], \qquad E_1(x) = \int_x^\infty e^{-t}\frac{dt}{t} \qquad (3.37)$$

where $\gamma_E \cong 0.5772$ is the Euler constant and $a_0 \cong 5.2$. Averaging of $\Delta V_{m_c}(r)$ over solutions of the relativistic wave equation with the Cornell and Coulomb potentials yields the bottomonium mass shifts presented in Table 3.4.

The Table 3.4 shows that for a fixed value of α_s the averaging with and without confining potential substantially differ especially for the excited states. For growing $n = n_r + L + 1$ the values of $\langle\Delta V_{m_c}\rangle$ slowly decrease for Cornell potential whereas for the Coulomb potential with a fixed value of α_s they fall rapidly. The bottomonium mass spectrum with the account of the finite charm mass corrections was obtained in Refs. [95, 173]

---

[24]Author: R. Faustov

Table 3.4: Charm mass corrections to the bottomonium masses (in MeV).

State	$1S$	$1P$	$2S$	$1D$	$2P$	$3S$
$\langle \Delta V_{m_c} \rangle_{\text{Cornell}}^{\alpha_{\text{s}}=0.22}$ [200]	-12	-9.3	-8.7	-7.6	-7.5	-7.2
$\langle \Delta V_{m_c} \rangle_{\text{Coul}}^{\alpha_{\text{s}}=0.22}$	-9.5	-4.2	-3.8	-2.3	-2.2	-2.1
$\langle \Delta V_{m_c} \rangle_{\text{Coul}}^{\alpha_{\text{s}}=0.3}$	-20.7	-9.7	-8.8	-5.5	-5.2	-4.9
$\langle \Delta V_{m_c} \rangle_{\text{Coul}}$ [95]	-14.3	-22.1	-21.9		-49	-40.5
$\alpha_{\text{s}}(\mu)$	0.277	0.437	0.452		0.733	0.698

3.1.5 Coupled-channel effects

An important ingredient that has not received the attention it deserves but which has been brought to the forefront by some spectacular recent failures of quark models are coupled channel effects. As the mass of a quarkonium state approaches the threshold for decay to pairs of flavoured mesons, contributions from virtual loops of the flavoured meson channels are expected to make important contributions to masses and other meson properties [169, 170, 201]. These coupled channel effects are expected to shift masses from naive quark model predictions and to alter decay and production properties due to higher order Fock-space components present in the wavefunctions. These may account for the discrepancies between quark model predictions and those of the recently discovered and $X(3872)$ properties [187, 188]. There has been very little work on this important subject since the original Cornell model [169, 170] and it is an important topic that needs to be addressed [188]. For the charmonium example the present situation is discussed in Section 3.3.

3.2 Comparison of models with experiment[25]

3.2.1 Bottomonium

We start with the $b\bar{b}$ system as it has the most states observed of any of the heavy quarkonium systems (see Table 3.5). This is due to the fact that threshold for the Zweig allowed decay to $B\overline{B}$ lies above the $3S$ state. The $J^{PC} = 1^{--}$ n^3S_1 states are copiously produced in e^+e^- annihilation and can decay via $E1$ transitions to the 1^3P_J and 2^3P_J multiplets. The masses of the χ_b states provide valuable tests of the spin-dependence of the various models. In particular, the splittings of the ^3P_J masses are determined by the spin–orbit and tensor terms which are sensitive to the presence of vector and scalar interactions. The Lorentz vector one-gluon-exchange plus Lorentz scalar linear confinement gives a good description of the data (as long as no velocity dependent corrections are included [185, 202].

A test of potential models is their ability to predict as yet unseen properties correctly. Most potential models predict that the lowest D-wave centre of gravity is around 10.16 GeV. Although details of the multiplet splittings differ most models predict that the splittings are smaller than in the P-wave states. Thus, the observation of these states represents an important test of potential models.

Recently the CLEO collaboration has observed the first D-wave $b\bar{b}$ state in the cascade $\Upsilon(3S)\rightarrow \chi_b'\gamma\rightarrow^3D_J\gamma\gamma\rightarrow\chi_b\gamma\gamma\gamma\rightarrow\Upsilon(1S)\gamma\gamma\gamma\gamma$ [203]. Due to expected transition probabilities (essentially reliable Clebsch factors) it is believed that the observed state is the $J = 2$, 1^3D_2 state. This is an important observation as it is able to distinguish among the various models [204]. Unfortunately this programme at CLEO is completed and it is not clear when there will be another opportunity to search for more of the missing states.

So far no spin singlet $b\bar{b}$ state has been observed. The mass splittings between the singlet and triplet states is a key test of the applicability of perturbative quantum chromodynamics to the $b\bar{b}$ system and is a useful check of lattice QCD results. The η_b (n^1S_0) states can be produced via M1 radiative

---

[25]Authors:S. Godfrey

Table 3.5: Predicted and observed masses of $b\bar{b}$ states.

State	expt	GI85 [171]	FU91 [175]	EQ94 [196]	GJ96 [179]	EFG03 [173]	ZVR95 [180]
1^3S_1	9460	9465	9459	9464	9460	9460	9460
1^1S_0		9402	9413	9377	9408	9400	9410
1^3P_2	9913	9897	9911	9886	9914	9913	9890
1^3P_1	9893	9876	9893	9864	9893	9892	9870
1^3P_0	9860	9847	9865	9834	9862	9863	9850
1^1P_1		9882	9900	9873	9901	9901	9880
2^3S_1	10023	10003	10015	10007	10016	10023	10020
2^1S_0		9976	9992	9963	9991	9993	10000
1^3D_3		10155	10172	10130		10162	10150
1^3D_2	10162	10147	10166	10126		10158	10150
1^3D_1		10138	10158	10120		10153	10140
1^1D_2		10148	10167	10127		10158	10150
2^3P_2	10269	10261	10269	10242	10270	10268	10280
2^3P_1	10255	10246	10256	10224	10254	10255	10260
2^3P_0	10232	10226	10234	10199	10229	10234	10240
2^1P_1		10250	10261	10231	10259	10261	10270
3^3S_1	10355	10354	10356	10339	10358	10355	10390
3^1S_0		10336	10338	10298	10338	10328	10370

transitions from the Υ (n^3S_1) states, either unhindered or hindered, and via E1 radiative transitions from the n^1P_1 states [205]. In the latter case, the decay chain would be $\Upsilon(3S) \rightarrow h_b(^1P_1)\pi\pi$ followed by $h_b \rightarrow \eta_b \gamma$. The decay chain $\Upsilon(3S) \rightarrow h_b + \pi^0 \rightarrow \eta_b + \pi^0 + \gamma$ is also possible [206]. We note that there does not appear to be a consensus in the literature on the relative importance of the two $\Upsilon \rightarrow h_b$ hadronic transitions. The decay chains proceeding via an intermediate h_b would also be a means of observing the h_b state. A recent run by CLEO did not lead to reports of the observation of the η_b state although the limits straddles the range of predictions. There is also the possibility that the η_b can be observed by the Tevatron and LHC experiments.

3.2.2 Charmonium

The discovery of the J/ψ and ψ' states revolutionized our understanding of hadron spectrocopy by demonstrating that they could be well described by potential models with the qualitative features expected from QCD (see Table 3.6).

The spin triplet $^3S_1$ states are produced copiously in e^+e^- annihilation and the ^3P_J states are produced via E1 radiative transitions. The χ_0 ($^3P_0$), χ_1 ($^3P_1$) and χ_2 ($^3P_2$) $c\bar{c}$ states were first discovered in radiative decays from the 2^3S_1 level (the $\psi(3685)$). The χ states themselves undergo radiative transitions to the J/ψ with measured partial widths in reasonable agreement with theoretical predictions once relativistic effects are taken into account.

The singlet states have been far more elusive. The 1^1S_0 state has been known for some time, seen in magnetic dipole (M1) transitions from both the J/ψ and ψ'. In contrast, a strong claim for observation of the 2^1S_0 state has only occurred recently, first with its observation in the decay $B \rightarrow K\eta_c'$, $\eta_c' \rightarrow K_s K^+\pi^-$ by the Belle Collaboration [207] and its subsequent observation by Belle in the mass

spectrum recoiling against J/ψ in e^+e^- annihilation [208] and by CLEO [209] and Babar [210] in $\gamma\gamma$ collisions. While the mass measurement by Belle was higher than expected by most quark potential models, the current world average [245] is in reasonable agreement with theory.

One place the models disagree is in the mass of the 1^1P_1 state relative to the 1^3P_J cog [206]. However, the $^1P_1$ state has yet to be confirmed. The $1^3P_{cog} - 1^1P_1$ splitting is dependent on the Lorentz structure of the interquark potentials and relativistic corrections so that the h_c mass measurement is an important test of perturbative QCD and more phenomenological quark potential models which have a large variation of predictions. The decay chain $\psi' \to h_c + \pi^0 \to \eta_c + \pi^0 + \gamma$ has been discussed as a possible mode of discovery of the h_c [206]. Optimistically, one might hope that the current CLEO run will see evidence for the h_c in this cascade.

The charmonium D-wave states are predicted to lie above $D\overline{D}$ threshold. The $\psi(3770)$ is associated with the 1^3D_1 state. It's leptonic width is larger than expected for a pure D state which is probably due to mixing with the 2^3S_1 state induced by tensor mixing or coupled channel effects. The 1^3D_3, 1^3D_2, and 1^1D_2 are predicted to lie close in mass to the $\psi(3770)$. A $J^P = 2^-$ state cannot decay to two 0^- particles so the 1^3D_2 and $^1D_2$ cannot decay to $D\overline{D}$ and are expected to lie below the $D^*\overline{D}$ threshold. They are therefore expected to be narrow with prominent transitions to lower $c\bar{c}$ states. While there is no such conservation law for the 1^3D_3 state, recent calculations indicate that it should also be relatively narrow, $\mathcal{O}(\text{MeV})$, due to the angular momentum barrier [187, 188]. It is therefore possible that all $c\bar{c}$ D-wave states will be observed. A $c\bar{c}$ state has recently been observed in B decay, the $X(3872)$ [211]. It's mass is higher than expected by quark models which has led to considerable speculation about whether it is a conventional $c\bar{c}$ state or a $D\bar{D}^*$ molecule [212]. A number of tests have been proposed to sort this out [187, 188] and experimental analysis is in progress. Observation of the η_{c2} and $\psi_{(2,3)}$ states would constrain spin-dependent interactions and provide insights into the importance of coupled channel effects in the charm threshold region.

Table 3.6: Predicted and observed masses of $c\bar{c}$ states (in MeV).

State	Expt	GI85 [171]	EQ94 [196]	FU91 [175]	GJ96 [179]	EFG03 [173]	ZVR95 [180]
1^3S_1	3096.87 ± 0.04	3098	3097	3104	3097	3096	3100
1^1S_0	2979.8 ± 1.8	2975	2980	2987	2979	2979	3000
1^3P_2	3556.18 ± 0.13	3550	3507	3557	3557	3556	3540
1^3P_1	3510.51 ± 0.12	3510	3486	3513	3511	3510	3500
1^3P_0	3415.0 ± 0.8	3445	3436	3404	3415	3424	3440
1^1P_1		3517	3493	3529	3526	3526	3510
2^3S_1	3685.96 ± 0.09	3676	3686	3670	3686	3686	3730
2^1S_0	3654 ± 10	3623	3608	3584	3618	3588	3670
1^3D_3		3849		3884		3815	3830
1^3D_2		3838		3871		3813	3820
1^3D_1	3769.9 ± 2.5	3819		3840		3798	3800
1^1D_2		3837		3872		3811	3820
2^3P_2		3979				3972	4020
2^3P_1		3953				3929	3990
2^3P_0		3916				3854	3940
2^1P_1		3956				3945	3990
3^3S_1		4100				4088	4180
3^1S_0		4064				3991	4130
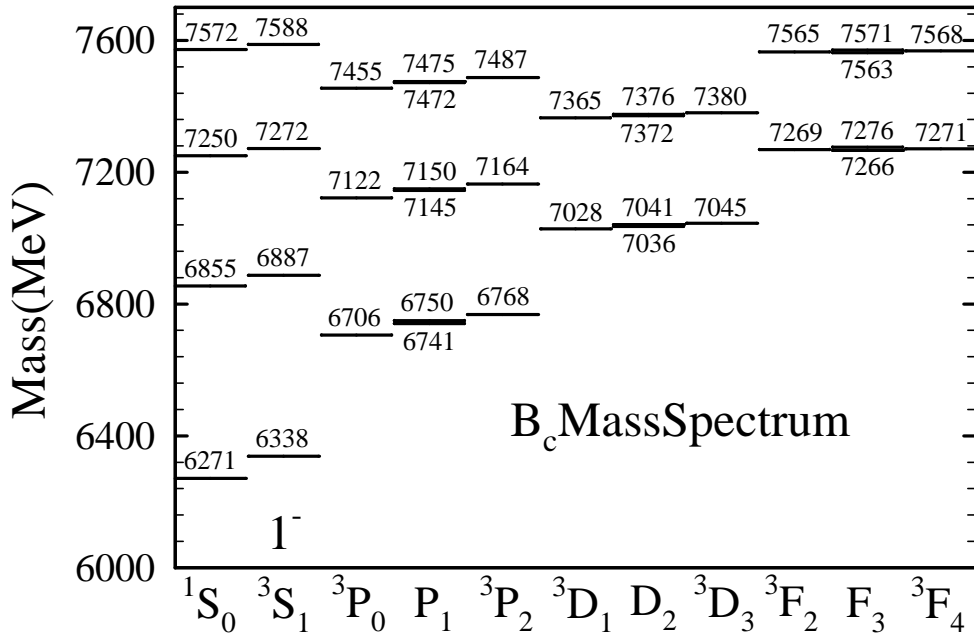
Fig. 3.9: B_c spectrum.

3.2.3 B_c mesons

The B_c mesons provide a unique window into heavy quark dynamics. Although they are intermediate to the charmonium and bottomonium systems the properties of B_c mesons are a special case in quarkonium spectroscopy as they are the only quarkonia consisting of heavy quarks with different flavours. Because they carry flavour they cannot annihilate into gluons so are more stable and excited B_c states lying below BD (and BD^* or B^*D) threshold can only undergo radiative or hadronic transitions to the ground state pseudoscalar which then decays weakly. This results in a rich spectroscopy of narrow radial and orbital excitations (Fig. 3.9 and Table 3.7) [171, 173, 174, 176, 179, 180, 182, 196, 213–216]. which are more stable than their charmonium and bottomonium analogues. The hadronic transitions emitting two charged pions should offer a good opportunity to reconstruct the excited B_c state.

The discovery of the B_c meson by the Collider Detector at Fermilab (CDF) Collaboration [217] in $p\bar{p}$ collisions at $\sqrt{s} = 1.8$ TeV has demonstrated the possibility of the experimental study of this system and has stimulated considerable interest in B_c spectroscopy. Calculations of B_c cross-sections at hadron colliders predict that large samples of B_c states should be produced at the Tevatron and at the LHC opening up this new spectroscopy. It should therefore be possible to start exploring $c\bar{b}$ spectroscopy at the Tevatron, producing $1P$ and $2S$ states and possibly even the D-wave states in sufficient numbers to be observed. At the LHC, with its higher luminosity, the D-wave $c\bar{b}$ states should be produced in a sizable number so that the LHC should allow the study of the spectroscopy and decay of B_c mesons.

3.3 Coupling to open-charm channels[26]

3.3.1 Theoretical models

Near the threshold for open heavy flavour pair production, there are significant nonperturbative contributions from light quark pairs to the masses, wavefunctions and decay properties of physical $Q\bar{Q}$ states. QCD sum rules [218, 219] have been used to obtain some results [220–222] and lattice QCD calculations extended into the flavour-threshold region [223] should eventually give a firm basis for predictions.

---

[26]Authors: E. Eichten

Table 3.7: Predicted B_c masses and spin–orbit mixing angles (in MeV).

State	GI85 [171]	EFG03 [173]	FU99 [176]	GKLT94 [174]	EQ94 [196]	GJ96 [179]	ZVR95 [180]	Lattice
1^3S_1	6338	6332	6341	6317	6337	6308	6340	6321 ± 30
1^1S_0	6271	6270	6286	6253	6264	6247	6260	$6280 \pm 30 \pm 190$
1^3P_2	6768	6762	6772	6743	6747	6773	6760	6783 ± 30
$1P_1'$	6750	6749	6760	6729	6730	6757	6740	6765 ± 30
$1P_1$	6741	6734	6737	6717	6736	6738	6730	6743 ± 30
1^3P_0	6706	6699	6701	6683	6700	6689	6680	6727 ± 30
θ_{1P}	22.4°	20.4°	28.5°	17.1°	$\sim 2°$	25.6°		$33.4 \pm 1.5°$
2^3S_1	6887	6881	6914	6902	6899	6886	6900	6990 ± 80
2^1S_0	6855	6835	6882	6867	6856	6853	6850	6960 ± 80
2^3P_2	7164	7156		7134	7153		7160	
$2P_1'$	7150	7145		7124	7135		7150	
$2P_1$	7145	7126		7113	7142		7140	
2^3P_0	7122	7091		7088	7108		7100	
θ_{2P}	18.9°	23.0°		21.8°	17°			
3^3S_1	7272	7235			7280		7280	
3^1S_0	7250	7193			7244		7240	
1^3D_3	7045	7081	7032	7007	7005		7040	
$1D_2'$	7036	7079	7028	7016	7012		7030	
$1D_2$	7041	7077	7028	7001	7009		7020	
1^3D_1	7028	7072	7019	7008	7012		7010	
θ_{1D}	44.5°	-35.9°			34.4°			
1^3F_4	7271						7250	
$1F_3'$	7266						7250	
$1F_3$	7276						7240	
1^3F_2	7269						7240	
θ_{1F}	41.4°							

However, at present a more phenomenological approach is required to provide a detailed description of these effects.

The effects of light quark pairs near open heavy flavour threshold can be described by coupling the potential model $Q\bar{Q}$ states to nearby physical multibody states. In this threshold picture, the strong interactions are broken into sectors defined by the number of valence quarks. This separation is reminiscent of the Tamm–Dancoff approximation [224]. The dynamics of the $Q\bar{Q}$ states (with no valence light quarks, q) is described by the interaction $\mathcal{H}_0$. Nonrelativistic potential models are normally used to determine the properties of the resulting bound states in this sector. In this framework excitations of the gluonic degrees of freedom would also be contained the spectrum of $\mathcal{H}_0$.

The two meson sector $Q\bar{q} + q\bar{Q}$ are described by the Hamiltonian $\mathcal{H}_2$. In the simplest picture, $\mathcal{H}_2$ is assumed to be described the low-lying spectrum of two free heavy-light mesons. The physical situation is more complex. At large separation between two mesons the interactions are dominated t-channel pion exchanges. For states very near threshold such as the X(3872) charmonium state such pion exchange in attractive channels might have significant effects on properties of the physical states [225]. At somewhat shorter distances, more complicated interactions exist and new bound states might arise, e.g., molecular states [226, 227].

Our command of quantum chromodynamics is inadequate to derive a realistic description of the interactions, $\mathcal{H}_I$, that communicate between the $Q\bar{Q}$ and $Q\bar{q}+q\bar{Q}$ sectors. Two simple phenomenological models have been used to describe this coupling: the Cornell coupled-channel model (CCC) and the vacuum quark pair creation model (QPC).

The Cornell coupled-channel model for light quark pair creation [169] generalizes the Cornell $Q\bar{Q}$ model [170] without introducing new parameters, writing the interaction Hamiltonian as

$$\mathcal{H}_I = \frac{3}{8} \sum_a \int \; : \rho_a(\mathbf{r})V(\mathbf{r} - \mathbf{r}')\rho_a(\mathbf{r}') : d^3r\, d^3r' \; , \tag{3.38}$$

where V is the quarkonium potential and $\rho_a(\mathbf{r}) = \frac{1}{2}\psi^\dagger(\mathbf{r})\lambda_a\psi(\mathbf{r})$ is the colour current density, with ψ the quark field operator and λ_a the octet of SU(3) matrices. To generate the relevant interactions, ψ is expanded in creation and annihilation operators (for up, down, strange and heavy quarks), but transitions from two mesons to three mesons and all transitions that violate the Zweig rule are omitted. It is a good approximation to neglect all effects of the Coulomb piece of the potential in Eq. (3.38). It was shown that this simple model coupling charmonium to charmed-meson decay channels gives a qualitative understanding of the structures observed above threshold while maintaining the successes of the single-channel $c\bar{c}$ analysis below threshold [170].

The characteristic of the CCC model is the use of the time component of a long-range vector interaction between the heavy quarks colour densities rather than the Lorentz scalar confining interaction.

The vacuum quark pair creation model (QPC). This model was developed by Le Yaouanc *et. al.* [228–230] based on an earlier idea of Micu [231] that the light quark pair is produced from the vacuum with vacuum quantum numbers $\mathrm{J^{PC}} = 0^{++}$. The model is also referred to as the $^3\mathrm{P}_0$ model. The form of the interaction Hamiltonian is

$$\mathcal{H}_I = \gamma \int \bar{\psi}\psi(\mathbf{r})d^3r \tag{3.39}$$

The constant γ is a free parameter of the model. This model has been applied to the light meson states [232, 233]. It was first applied above charm threshold by the Orsay group [234].

The main theoretical weakness of the QPC model is its failure to reproduce the vanishing of the pair production amplitudes for a static $Q\bar{Q}$ source at zero spatial separation. The flux tube breaking model [235, 236] somewhat addresses this weakness. It has the same basic interaction as the QPC model (Eq. 3.39) but the integration is only over a region near a "string" between the Q and $\bar{Q}$ positions. This region is defined by a upper bound on the shortest distance between the pair creation point and the string. Detailed applications of QPC models to the quarkonium systems are presently under investigation [237].

There have been attempts to compare the various models for quark pair creation [185, 238, 239]. At present the most studied system is the open charm threshold region and we will focus on that system below. However, the same threshold effects are present in the $b\bar{b}$ states near $B\overline{B}$ threshold and $c\bar{b}$ states near $D\overline{B}$ threshold. A detailed comparison of the scaling behaviour between different heavy quark systems would provide valuable insight into the correct form for the coupling to light-quark pairs.

3.3.2 Mass shifts

The mass ω of the quarkonium state ψ in the presence of coupling to decay channels is given by:

$$[\mathcal{H}_0 + \mathcal{H}_2 + \mathcal{H}_I]\psi = \omega\psi. \tag{3.40}$$

Above threshold ω has both a real (mass) and imaginary part (width).

The basic coupled-channel interaction $\mathcal{H}_I$ (Eq. (3.38) or Eq. (3.39)) appearing in Eq. (3.40) is independent of the heavy quarks spin, but the hyperfine splittings of D and D^*, D_s and D_s^*, induce

Table 3.8: Charmonium spectrum, including the influence of open-charm channels. All masses are in MeV. The penultimate column holds an estimate of the spin splitting due to tensor and spin–orbit forces in a single-channel potential model. The last column gives the spin splitting induced by communication with open-charm states, for an initially unsplit multiplet. From [188].

State	Mass	Centroid	Splitting (Potential)	Splitting (Induced)
1^1S_0	2 979.9	3 067.6	-90.5	$+2.8$
1^3S_1	3 096.9		$+30.2$	-0.9
1^3P_0	3 415.3		-114.9	$+5.9$
1^3P_1	3 510.5	3 525.3	-11.6	-2.0
1^1P_1	3 525.3		$+1.5$	$+0.5$
1^3P_2	3 556.2		$+31.9$	-0.3
2^1S_0	3 637.7	3 673.9	-50.4	$+15.7$
2^3S_1	3 686.0		$+16.8$	-5.2
1^3D_1	3 769.9		-40	-39.9
1^3D_2	3 830.6	(3 815)	0	-2.7
1^1D_2	3 838.0		0	$+4.2$
1^3D_3	3 868.3		$+20$	$+19.0$
2^3P_0	3 931.9		-90	$+10$
2^3P_1	4 007.5	3 968	-8	$+28.4$
2^1P_1	3 968.0		0	-11.9
2^3P_2	3 966.5		$+25$	-33.1

spin-dependent forces that affect the charmonium states. These spin-dependent forces give rise to S–D mixing that contributes to the $\psi(3770)$ electronic width, for example, and are a source of additional spin splitting.

The masses resulting from a full coupled channel analysis [188] in the CCC model are shown in the second column of Table 3.8. The parameters of the potential model sector, $\mathcal{H}_0$, must be readjusted to fit the physical masses, ω, to the observed experimental values. To compute the induced splittings, the bare centroid of the spin-triplet states is adjusted so that the physical centroid, after inclusion of coupled-channel effects, matches the value in the middle column of Table 3.8. The centroid for the 1D masses is determined by pegging the observed mass of the $1^3D_1 \psi(3770)$. For the 2P levels, the bare centroid is adjusted so that the 2^1P_1 level lies at the centroid of a potential-model calculation. The assumed spin splittings in the single-channel potential model are shown in the penultimate column and the induced coupled channel spin splittings for initially unsplit multiplets are presented in the rightmost column of Table 3.8. The shifts induced in the low-lying 1S and 1P levels are small. For the other known states in the 2S and 1D families, coupled-channel effects are noticeable and interesting.

In a simple potential picture, the $\eta_c(2S)$ level lies below the $\psi(2S)$ by the hyperfine splitting given by

$$M(\psi(2S)) - M(\eta_c(2S)) = \frac{|\psi(2S)(0)|^2}{|\psi(0)|^2}[M(\psi) - M(\eta_c)] . \tag{3.41}$$

Using the observed 1S hyperfine splitting, $M(\psi) - M(\eta_c) = 117$ MeV, one would find $M(\psi(2S)) - M(\eta_c(2S)) = 67$ MeV, which is larger than the observed 48.3 ± 4.4 MeV, as is typical for potential-model calculations.

One important result of coupling the open-charm threshold is that the ψ' receives a downward shift of the nearby $D\overline{D}$, that the η_c' does not get, as this state does not couple to $D\overline{D}$. This is implicitly present in the early Cornell papers [170], but the shift of spin singlets states was not explicitly calculated. The effect was first mentioned by Martin and Richard [240, 241], who calculated the size of the effect. Recent papers using the CCC model interaction [188, 242] have confirmed this behaviour. In fact, the 2S induced shifts in Table 3.8 draw ψ' and η_c' closer by 20.9 MeV, substantially improving the agreement between theory and experiment. This suggests that the ψ'–η_c' splitting reflects the influence of virtual decay channels.

If the observed $X(3872)$ is a charmonium state, it is most naturally interpreted as the 1^3D_2 or 1^3D_3 level [187, 188]; if not, both these states remain to be observed and the dynamics of $\mathcal{H}_2$ is significantly richer. As shown in Table 3.8, the coupling to open-charm channels increases the 1^3D_2–1^3D_1 splitting by about 20 MeV, but does not fully account for the observed 102 MeV separation between $X(3872)$ and $\psi(3770)$. However the position of the 3^{--} 1^3D_3 level turns out to be very close to 3872 MeV.

3.3.3 Mixing and physical state properties

The physical states are not pure potential-model eigenstates but include components with two virtual (real above threshold) open flavour meson states. Separating the physical state (ψ) into $Q\bar{Q}$ (ψ_0) and two meson components (ψ_2), the resulting separation $\mathcal{H}$ by sector leads to an effective Hamiltonian for the ψ_0 sector given by:

$$\left[\mathcal{H}_0 + \mathcal{H}_I^\dagger \frac{1}{\omega - \mathcal{H}_2 + i\epsilon}\mathcal{H}_I\right]\psi_0 = \omega\psi_0 \tag{3.42}$$

Table 3.9: Charmonium content of states near flavour threshold. The wave function ψ takes account of mixing induced through open charm–anticharm channels. Unmixed potential-model eigenstates are denoted by $|n^{2s+1}L_J\rangle$. The coefficient of the dominant eigenstate is chosen real and positive. The 1S, 1P, 2S, and 1^3D_1 states are evaluated at their physical masses. The remaining 1D states are considered at the masses in Table 3.8. $\mathcal{Z}_{c\bar{c}}$ represents the ($c\bar{c}$) probability fraction of each state.

State	Major Components	$\mathcal{Z}_{c\bar{c}}$
$\psi(1^1S_0)$	$0.986\lvert1^1S_0\rangle - 0.042\lvert2^1S_0\rangle - 0.008\lvert3^1S_0\rangle$	0.974
$\psi(1^3S_1)$	$0.983\lvert1^3S_1\rangle - 0.050\lvert2^3S_1\rangle - 0.009\lvert3^3S_1\rangle$	0.968
$\psi(1^3P_0)$	$0.919\lvert1^3P_0\rangle - 0.067\lvert2^3P_0\rangle - 0.014\lvert3^3P_0\rangle$	0.850
$\psi(1^3P_1)$	$0.914\lvert1^3P_1\rangle - 0.075\lvert2^3P_1\rangle - 0.015\lvert3^3P_1\rangle$	0.841
$\psi(1^1P_1)$	$0.918\lvert1^1P_1\rangle - 0.077\lvert2^1P_1\rangle - 0.015\lvert3^1P_1\rangle$	0.845
$\psi(1^3P_2)$	$0.920\lvert1^3P_2\rangle - 0.080\lvert2^3P_2\rangle - 0.015\lvert3^3P_2\rangle - 0.002\lvert1^3F_2\rangle$	0.854
$\psi(2^1S_0)$	$0.087\lvert1^1S_0\rangle + 0.883\lvert2^1S_0\rangle - 0.060\lvert3^1S_0\rangle - 0.016\lvert4^1S_0\rangle$	0.791
$\psi(2^3S_1)$	$0.103\lvert1^3S_1\rangle + 0.838\lvert2^3S_1\rangle - 0.085\lvert3^3S_1\rangle - 0.017\lvert4^3S_1\rangle$ $+0.040\lvert1^3D_1\rangle - 0.008\lvert2^3D_1\rangle$	0.723
$\psi(1^3D_1)$	$0.694\lvert1^3D_1\rangle + 0.097\,e^{0.935i\pi}\lvert2^3D_1\rangle + 0.008\,e^{-0.668i\pi}\lvert3^3D_1\rangle$ $+0.013\,e^{0.742i\pi}\lvert1^3S_1\rangle + 0.168\,e^{0.805i\pi}\lvert2^3S_1\rangle + 0.014\,e^{0.866i\pi}\lvert3^3S_1\rangle$ $+0.012\,e^{-0.229i\pi}\lvert4^3S_1\rangle$	0.520
$\psi(1^3D_2)$	$0.754\lvert1^3D_2\rangle - 0.084\lvert2^3D_2\rangle - 0.011\lvert3^3D_2\rangle$	0.576
$\psi(1^1D_2)$	$0.770\lvert1^1D_2\rangle - 0.083\lvert2^1D_2\rangle - 0.012\lvert3^1D_2\rangle$	0.600
$\psi(1^3D_3)$	$0.812\lvert1^3D_3\rangle + 0.086\,e^{0.990i\pi}\lvert2^3D_3\rangle + 0.013\,e^{-0.969i\pi}\lvert3^3D_3\rangle$ $+0.007\,e^{0.980i\pi}\lvert4^3D_3\rangle + 0.016\,e^{0.848i\pi}\lvert1^3G_3\rangle$	0.667

Solving Eq. (3.42) in the $Q\bar{Q}$ sector determines the mixing between the potential model states and

coupling to decay channels. This approach has been described in detail [170] for the CCC model with $\mathcal{H}_I$ (Eq. 3.38). An effective Hamiltonian approach has also been considered in the QPC model [201].

The results for the low-lying $c\bar{c}$ states is shown in Table 3.9 for the CCC model. The overall probability for the physical state to be in the $c\bar{c}$ sector, denoted $\mathcal{Z}_{c\bar{c}}$, decreases as open charm threshold is approached. For states above threshold the mixing coefficients become complex. These mixing effects contribute to observed S–D mixing as well as modifying radiative transition rates [243, 244]. A more detailed discussion of these effects appear in the Decay section.

3.3.4 Zweig-allowed strong decays

Once the mass of a resonance is given, the coupled-channel formalism yields reasonable predictions for the other resonance properties. Eichten, Lane and Quigg [188] have estimated the strong decay rates within the CCC model for all the charmonium levels that populate the threshold region between $2M_D$ and $2M_{D*}$. For 1^3D_1 state $\psi''(3770)$, which lies some 40Mev above charm threshold, they obtain $\Gamma(\psi''(3770) \to D\overline{D}) = 20.1$ MeV, to be compared with the PDG's fitted value of 23.6 ± 2.7 MeV [245]. The natural-parity 1^3D_3 state can decay into $D\overline{D}$, but its F-wave decay is suppressed by the centrifugal barrier factor. The partial width is only 0.77 MeV at a mass of 3868 MeV and the 1^3D_3 may be discovered as a narrow $D\overline{D}$ resonance up to a mass of about 4000 MeV.

Barnes and Godfrey [187] have estimated the decays of several of the charmonium states into open charm, using the $^3P_0$ model. Their estimates of open-charm partial decay widths into $D\overline{D}$ are 42.8 MeV for the 1^3D_1 state and 3.6 MeV for a 1^3D_3 state at a mass of 3868 MeV. They did not carry out a coupled-channel analysis which makes a direct comparison of models more difficult. Detailed comparisons (e.g., Ackleh, Barnes and Swanson [238]) between various light quark pair creation models are highly desirable.

Estimates for decay widths of the 1^{--} charmonium states above open-charm threshold in the $^3P_0$ model have recently been reported by Barnes [237]. The comparison with experimentally extracted values is shown in Table 3.10. Along with the current PDG values for the total widths of $c\bar{c}$ resonances, a reanalysis by Seth [246] of the existing experimental data is also shown in Table 3.10.

The resonance decay widths are determined from fitting measurements of ΔR in e^+e^- annihilation to a model for each resonance including radiative corrections. This whole procedure is complicated by its dependence on the resonance shape, i.e., the expected non Breit–Wigner nature of the partial widths for radially excited resonances. It may be more useful for theorists to produce a model of ΔR for direct comparison with data. Greater resolving power between models is possible if the contribution from each individual open heavy flavour final state is separately reported.

For the CCC model, the structure of $\Delta R(b\bar{b})$ in the threshold region was studied in the original Cornell group works [169, 170] and later extended to the $\Delta R(b\bar{b})$ in the threshold region [247]. The structure of $\Delta R(c\bar{c})$ and $\Delta R(b\bar{b})$ has also been studied in QPC models [248]. There are also some attempts to compare the different models [249, 250].

Experiments can also search for additional narrow charmonium states in neutral combinations of charmed mesons and anticharmed mesons. The most likely candidates correspond to the 1^3D_3, 2^3P_2, and 1^3F_4 levels [188, 242, 251]. These detailed analyses of the $c\bar{c}$ system can be extended to the $b\bar{b}$ system, where it may be possible to see discrete threshold-region states in direct hadronic production.

3.4 QQq states and molecules[27]

3.4.1 Doubly charmed baryons

The earliest studies on QQq baryons were based on the flavour group SU(4)$_F$, as an extension of SU(3))$_F$. After the discovery of hidden and naked charm, some classic papers were written on hadrons with charm, including a section on (ccq) states [252, 253].

---

[27]Author: J. M. Richard

Table 3.10: Open-charm strong decay modes of the 1^{--} states. Experimental widths from the PDG [245] and a recent analysis of Seth [246]. The theoretical widths using the QPC model [237] and the CCC model [188] are shown. For the $\psi(4159)$ some S wave plus P wave charmed meson two body channels are also open.

| State | Mode | Γ_{EXP} (MeV) | | Γ_{THEORY} (MeV) | |
		PDG	Seth	QPC Model	CCC model
$\psi(3770)$ ($^3\mathrm{D}_1$)	DD			42.8	20.1
	total	23.6 ± 2.7		42.8	20.1
$\psi(4040)$ ($3\,^3\mathrm{S}_1$)	DD			0.1	
	DD*			33.	
	$\mathrm{D}_s\mathrm{D}_s$			8.	
	D*D*			33.	
	total	52 ± 10	88 ± 5	74.	
$\psi(4159)$ ($2\,^3\mathrm{D}_1$)	DD			16.	
	DD*			0.4	
	D*D*			35.	
	$\mathrm{D}_s\mathrm{D}_s$			8.	
	total	78 ± 20	107 ± 8	73.	
$\psi(4415)$ ($4\,^3\mathrm{S}_1$)	DD			0.4	
	DD*			2.3	
	D*D*			16.	
	$\mathrm{D}_s\mathrm{D}_s$			1.3	
	$\mathrm{D}_s\mathrm{D}_s^*$			2.6	
	$\mathrm{D}_s^*\mathrm{D}_s^*$			0.7	
	total	43 ± 15	119 ± 15		

Now, our ideas on flavour symmetry have evolved. The conventional SU$(n)_{\mathrm{F}}$ approach, with elegant mass formulae, is replaced by *flavour independence*. The potential between two quarks is generated by their colour, and flavour enters only in recoil corrections through the quark mass, mainly for describing the fine and hyperfine structure.

Flavour independence was the main guide line of the detailed studies of (QQq) baryons made in the 80's and later [254, 255, 258–263]: the dynamics tuned for mesons, light baryons and single-charm baryons was tentatively extrapolated to the (QQq) sector. More papers came after the recent findings at SELEX (cf. the experimental part of this chapter), for instance Ref. [264], where a link is made with double-charm exotics, to be discussed shortly.

To study confinement, (QQq) baryons are perhaps the most interesting of ordinary hadrons, as they combine two extreme regimes in a single bag:

1. the slow relative motion of two heavy quarks, as in charmonium,

2. the fast motion of a light quark. Remember that the electron moves faster in hydrogen than in positronium. Similarly, a light quark is likely more relativistic in heavy-light hadrons than in light mesons.

In the (QQq) wave function, the average QQ separation is smaller than the Qq one. This leads to envisage approximations. One of them consists of replacing the full three-body calculation by a two-step procedure where one first calculates the QQ mass, by solving a two-body problem, and then estimates the $QQ - q$ mass by solving another two-body problem. The second step is rather safe. The finite-size corrections are small. For instance, they cancel out exactly for the harmonic oscillator. As for the first step, one should be aware that the QQ potential is *effective*, since it contains both the direct QQ

interaction and a contribution from the light quark. For instance, in the harmonic oscillator model, 1/3 of the QQ interaction comes from the light quark, and neglecting this term results into an underestimation of energies and spacings by a factor $\sqrt{3/2}$. Another limitation to the quark–diquark picture, is that the diquark is not frozen. The first excitations of QQq occur inside the diquark. So one should recalculate the properties of the diquark for each level.

Another way to take advantage of the large mass ratio M/m is to use the Born–Oppenheimer approximation, as done, e.g., by Fleck and Richard [254]. For a given QQ separation r_{12}, the two-centre problem is solved for the light quark, with proper reduced mass. The ground-state energy $E_0(r_{12})$, supplemented by the direct QQ interaction, provides the adiabatic potential V_{QQ}. Solving the 2-body problem with this potential gives the first levels. The adiabatic potential built out of the second "electronic" energy $E_1(r_{12})$ leads to a second series of levels. This is very similar to the spectroscopy of H_2^+ in atomic physics.

Within explicit potential models, the Born–Oppenheimer approximation can be checked against an accurate solution of the 3-body problem, using for instance a systematic hyperspherical expansion. The approximation is excellent for (bbq) and (ccq), with $q = u$, d or s, or even for (ssu) or (ssd) [254, 265].

In Ref. [254], (ccq) masses were estimated from a specific variant of the bag model, already used for charmed mesons. The results turn out to be rather sensitive to details such as centre-of-mass corrections, value of the bag constant, etc. Other bag-model calculations have been performed [266].

Potential models, on the other hand, tend to give very stable results, when the parameters are varied while maintaining a reasonable fit of lighter hadrons. One typically obtains:

- a ground-state near or slightly above $3.6\,\text{GeV}$ for the (ccu) or (ccd) ground state,
- a hyperfine splitting of about $80\,\text{MeV}$ between the spin 3/2 and spin 1/2 states,
- the first orbital excitation about $300\,\text{MeV}$ above the ground-state,
- the first (ccs) state near $3.7\,\text{GeV}$

Note that models tuned to (cqq) or lighter baryons might underestimate the short-range QQ attraction. If models are adjusted to $(c\bar{c})$ spectroscopy, there is an ambiguity on how to translate it to cc. The usual recipe stating that

$$V_{QQ} = \frac{1}{2} V_{Q\bar{Q}} \,, \tag{3.43}$$

implies pairwise forces mediated by colour-octet exchanges. Small, non-confining, colour-singlet exchanges, as well as three-body forces might complicate the issue.

Most existing calculations are of rather exploratory nature, since made when double charm was considered as science fiction, or far future. Meanwhile, the art of QCD has made significant progress. One could retain from simple potential models that the Born–Oppenheimer approximation provides an adequate framework. The effective QQ potential could be estimated from relativistic models or from lattice calculations, similar to those of the $Q\bar{Q}$ potential or the effective QQ potential in exotic $(QQ\bar{q}\bar{q})$ mesons, to be discussed shortly. It is hoped that the new experimental results will stimulate such calculations.

The literature already contains approaches somewhat more ambitious than simple bag or non-relativistic potential models: relativistic models [267], QCD sum rules [258], string picture [261], etc. The lattice QCD approach is presented in Section 2.2.3 and the EFT one is presented in Section 2.4

The appearance of the $D_{s,J}^*$ state not very far above the ground state D_s of meson with flavour content $(c\bar{s})$ has stimulated several studies on the dynamics of light quarks in a static colour field. In Ref. [268], it is suggested that the same phenomenon will occur for double-charm baryons. On this respect the doubling of states in the preliminary data by SELEX is of particular interest.

3.4.2 Exotic mesons with double charm

The physics of multiquarks, though it benefits from a dramatic revival since the tentative discovery of a light pentaquark, remains penalized by the confusion about baryonium states in the late 70's and early 80's. This is actually a difficult field, where speculations about confinement mechanisms should be combined with delicate few-body calculations.

The H dibaryon [269], and the heavy pentaquark P proposed independently by Lipkin [270] and the Grenoble group [271], owe their tentative stability to chromomagnetic forces, schematically [253]

$$H_{cm} = -C \sum_{i<j} \frac{\boldsymbol{\sigma}_i \cdot \boldsymbol{\sigma}_j \, \tilde{\lambda}_i \cdot \tilde{\lambda}_j}{m_i m_j} \delta^{(3)}(\mathbf{r}_{ij}) \, , \qquad (3.44)$$

or its bag model analogue [272], that describes the observed hyperfine splittings such as $\Delta - N$ or $J/\Psi - \eta_c$. The astute observation by Jaffe [269] is that this operator provides a binding $(ssuudd) - 2(sud) \sim -150\,\mathrm{MeV}$ to the $H = (ssuudd)$ dibaryon with spin and isospin $J = I = 0$. This estimate, however, relies on SU(3)$_\mathrm{F}$ flavour symmetry and $\langle \delta^{(3)}(\mathbf{r}_{ij}) \rangle$ being independent of (i,j) pair and borrowed from the wave function of ordinary baryons. Relaxing these hypotheses, and introducing kinetic energy and spin-independent forces in the 6-body Hamiltonian, and a realistic estimate of short-range correlations, usually spoils the stability of H [273–275]. The existence of H is nowadays controversial. It has been searched in many experiments, without success so far. For instance, the doubly-strange hypernucleus $_{\Lambda\Lambda}^{6}\mathrm{He}$ is not observed to decay into $H + \alpha$ [276].

If the calculation made for the H is repeated in the limit where $m(Q) \to \infty$, the same binding $(\bar{Q}qqqq) - (\bar{Q}q) - (qqq) \sim -150\,\mathrm{MeV}$ is obtained for the pentaquark $(\bar{Q}qqqq)$, $qqqq$ being in a SU(3)$_\mathrm{F}$ triplet [270, 271]. All corrections, again, tend to weaken this binding [275, 277] so it is not completely sure that the actual pentaquark is stable. See, also, [278].

After the tentative discovery of a light pentaquark state at about 1.53 GeV, with flavour content $(uudd\bar{s})$, and possible partners with strangeness $S = -2$, many authors have revisited the possibility of stable or metastable pentaquarks with heavy antiflavour. See, for instance Refs. [279–284]. In the light pentaquark, the binding is achieved by the chiral dynamics of light quarks. A forerunner in this field was Stancu [285], who proposed positive-parity pentaquarks with a heavy antiquark in a simple potential model where the chromomagnetic interaction is replaced by a short-range spin-flavour interaction which looks like the exchange of Goldstone bosons between quarks.

In short, there are still many open issues for the H dibaryon, the pentaquarks, as well as for possible light scalar mesons made out of two quarks and two antiquarks. This is, however, more of the domain of light-quark spectroscopy.

More than twenty years ago, another mechanism for multiquark binding was proposed. It was pointed out that current confining potentials applied to a $(QQ\bar{q}\bar{q})$ system put its mass below the dissociation threshold into $(Q\bar{q}) + (Q\bar{q})$, provided the mass ratio $m(Q)/m(q)$ is large enough [286]. This *chromoelectric* binding was studied by several authors, in the context of flavour-independent potentials [264, 287–295] [296, 297] (see, also, [298, 299]), with a remarkable convergence towards the same conclusion. This somewhat contrasts with the confusion in other sectors of multiquark spectroscopy.

Let us consider, indeed, the limit of a purely flavour-independent potential V for $(QQ\bar{q}\bar{q})$. The situation becomes similar to that of exotic four-body molecules (M^+, M^+, m^-, m^-), all of them using the very same Coulomb potential when M and m are varied. The hydrogen molecule with $M \gg m$ is much more stable than the positronium molecule Ps$_2$ with $M = m$. If one decomposes the 4-body Hamiltonian as

$$\mathcal{H}_4 = \left[\frac{M^{-1} + m^{-1}}{4} \left(\mathbf{p}_1^2 + \mathbf{p}_2^2 + \mathbf{p}_3^2 + \mathbf{p}_4^2 \right) + V \right] + \frac{M^{-1} - m^{-1}}{4} \left(\mathbf{p}_1^2 + \mathbf{p}_2^2 - \mathbf{p}_3^2 - \mathbf{p}_4^2 \right) \, , \quad (3.45)$$

the first term, even under charge conjugation, corresponds to a rescaled equal-mass system with *the same threshold* as $\mathcal{H}_4$. The second term, which breaks charge conjugation, improves the energy of $\mathcal{H}_4$ (one

can applies the variational principle to $\mathcal{H}_4$ using the symmetric ground state of the first term as a trial wave function). In the molecular case, the second term changes the marginally bound Ps_2 (or rescaled copy) into the deeply bound H_2. In quark models, an unbound $(qq\bar{q}\bar{q})$ becomes a stable $(QQ\bar{q}\bar{q})$.

The effective QQ potential has been estimated by Rosina et al. [294] in the framework of empirical potential models, and by Mihaly et al. [296] and Michael et al. (UKQCD) [297], who used lattice simulations of QCD. The question is obviously: is the c quark heavy enough to make $(cc\bar{q}\bar{q})$ bound when $q = u$ or d? At this point, the answer is usually negative, most authors stating that b is required to bind $(QQ\bar{q}\bar{q})$ below its $(Q\bar{q}) + (Q\bar{q})$ threshold.

There is, however, another mechanism: pion-exchange or, more generally, nuclear-like forces between hadrons containing light quarks or antiquarks. This effect was studied by several authors, in particular Törnqvist [300, 301], Manohar and Wise [302], and Ericson and Karl [303]. In particular a D and D^* can exchange a pion, this inducing an attractive potential. It is weaker than in the nucleon–nucleon case, but what matters for a potential $gV(r)$ to bind, is the product gm of the strength g and reduced mass m. It is found that (DD^*) is close to be bound, while binding is better established for (BB^*). The result depends on how sharply the long-range potential is empirically regularised at short distances.

A lattice calculation such as those of Refs. [296, 297] contains in principle all effects. In practice, the pion is unphysically heavy such that long-range forces are perhaps not entirely included. Explicit quark models such as [294] make specific assumptions about interquark forces, but do not account for pion exchange. In our opinion, a proper combination of long- and short-range forces should lead to bind (DD^*), since each component is almost sufficient by itself. This is presently under active study.

There is a further possibility to build exotic, multicharmed systems. If the interaction between two charmed mesons is slightly too weak to lead to a bound state (this is presumably the case for (DD), since pion exchange does not contribute here), it is likely that the very same meson–meson interaction binds three or more mesons. This is known as the phenomenon of "Boromean" binding.

For instance, in atomic physics, neither two ^{3}He atoms nor a ^{3}He atom and a ^{4}He atom can form a binary molecule, even at vanishing temperature, but it is found that ^{3}He^{3}He^{4}He is bound [304]. Similarly, in nuclear physics, the isotope ^{6}He is stable against evaporating two neutrons, or any other dissociation process, while ^{5}He is unstable. In a 3-body picture, this means that (α, n, n) is stable, while neither (α, n) nor (n, n) have a stable bound state. In short, binding three constituents is easier than two.

3.5 Quarkonium hybrids[28]

The existence of gluonic excitations in the hadron spectrum is one of the most important unanswered questions in hadron physics. Hybrid mesons form one such class which consists of a $q\bar{q}$ with an excited gluonic degree of freedom. Their spectroscopy are discussed extensively in this Chapter. Recent observations of charmonium states in exclusive B-meson decays [207, 305–309] suggest that charmonium hybrid mesons (ψ_g) [310] with mass ~ 4 GeV may be produced in B-decay via $c\bar{c}$ colour octet operators [311, 312]. Some of these states are likely to be narrow with clean signatures to $J/\psi\pi^+\pi^-$ and $J/\psi\gamma$ final states. The unambiguous discovery of such a state would herald an important breakthrough in hadronic physics, and indeed, in our understanding of Quantum Chromodynamics, the theory of the strong interactions. In this section we give a brief overview of charmonium hybrid properties and and suggest search strategies for charmonium hybrids at existing B-factories [313].

3.5.1 Spectroscopy

Lattice gauge theory and hadron models predict a rich spectroscopy of charmonium hybrid mesons [12, 23, 235, 310, 314–319]. For example, the flux tube model predicts 8 low lying hybrid states in the 4 to

---

[28]Author: S. Godfrey

4.2 GeV mass region with $J^{PC} = 0^{\pm\mp}$, $1^{\pm\mp}$, $2^{\pm\mp}$, and $1^{\pm\pm}$. Of these states the 0^{+-}, 1^{-+}, and 2^{+-} have exotic quantum numbers; quantum numbers not consistent with the constituent quark model. The flux-tube model predicts $M(\psi_g) \simeq 4 - 4.2$ GeV [314, 315]; lattice QCD predictions for the $J^{PC} = 1^{-+}$ state range from 4.04 GeV to 4.4 GeV [23, 317] with a recent quenched lattice QCD calculation [12] finding $M(1^{-+}) = 4.428 \pm 0.041$ GeV. These results have the 1^{-+} lying in the vicinity of the $D^{**}D$ threshold of 4.287 GeV. There is the tantalising possibility that the 1^{-+} could lie below $D^{**}D$ threshold and therefore be relatively narrow.

3.5.2 Decays

There are three important decay modes for charmonium hybrids: (i) the Zweig allowed fall-apart mode $\psi_g \rightarrow D^{(*,**)}\bar{D}^{(*,**)}$ [320–322]; (ii) the cascade to conventional $c\bar{c}$ states, of the type $\psi_g \rightarrow (c\bar{c})(gg) \rightarrow (c\bar{c})$ +(light hadrons) and $\psi_g \rightarrow (c\bar{c}) + \gamma$ [323]; (iii) decays to light hadrons via intermediate gluons, $\psi_g \rightarrow (ng)$ $\rightarrow$ light hadrons, analogous to $J/\psi \rightarrow$ light hadrons and $\eta_c \rightarrow$ light hadrons. Each mode plays a unique role. ψ_g hybrids with exotic J^{PC} quantum numbers offer the most unambiguous signal since they do not mix with conventional quarkonia.

3.5.2.1 (i) Decays to $D^{(*)}D^{(*)}$: In addition to J^{PC} selection rules (for example, 2^{-+} and 2^{--} decay to $D\bar{D}$ are forbidden by parity and the exotic hybrid $\psi_g(0^{+-})$ decays to $D^{(*)}D^{(*)}$ final states are forbidden by P and/or C conservation) a general feature of most models of hybrid meson decay is that decays to two mesons with the same spatial wave function are suppressed [324]. The dominant coupling of charmonium hybrids is to excited states, in particular $D^{(*)}(L = 0) + D^{**}(L = 1)$ states for which the threshold is ~ 4.3 GeV. This is at the kinematic limit for most mass predictions so that decays into the preferred $D^{(*)}D^{**}$ states are expected to be significantly suppressed if not outright kinematically forbidden. A refined version of the Isgur Kokoski Paton flux model [320] predicts partial widths of 0.3– 1.5 MeV depending on the J^{PC} of the hybrid [322]. These widths are quite narrow for charmonia of such high mass. If the hybrid masses are above D^{**} threshold then the total widths increase to 4–40 MeV for 4.4 GeV charmonium hybrids which are still relatively narrow for hadron states of such high mass. The challenge is to identify decay modes that can be reconstructed by experiment.

3.5.2.2 (ii) Decays to $(c\bar{c})$ + (light hadrons): The $\psi_g \rightarrow (c\bar{c})$ + (light hadrons) mode offers the cleanest signature for ψ_g observation if its branching ratio is large enough. In addition, a small total width also offers the possibility that the radiative branching ratios into J/ψ, η_c, χ_{cJ}, and h_c could be significant and offer a clean signal for the detection of these states.

For masses below DD^{**} threshold the cascade decays $\psi_g \rightarrow (\psi, \eta_c, \ldots) + (gg)$ and annihilation decays $\psi_g(C = +) \rightarrow (gg) \rightarrow$ light hadrons will dominate. If the masses of exotic J^{PC} states are above DD^{**} threshold their widths are also expected to be relatively narrow for states of such high mass, in which case cascades to conventional $c\bar{c}$ states transitions of the type $\psi_g \rightarrow (\psi, \psi')$+(light hadrons) should have significant branching ratios [323] making them important signals to look for in ψ_g searches. In the Kuang–Yan formalism [325] the matrix elements for hadronic transitions between conventional quarkonia are related to hybrid-conventional quarkonium hadronic transitions. A not unreasonable assumption is that the partial widths for the decays $\psi_g(1^{-+}) \rightarrow \eta_c + (\pi\pi, \eta, \eta')$ and $\psi_g(0^{+-}, 2^{+-}) \rightarrow J/\psi + (\pi\pi, \eta, \eta')$ will be similar in magnitude to $(c\bar{c}) \rightarrow \pi\pi J/\psi$ and $(c\bar{c}) \rightarrow \eta J/\psi$, of $\mathcal{O}(10 - 100)$ keV.

Estimates of radiative transitions involving hybrids with light quarks [326, 327] found that the $E1$ transitions between hybrid and conventional states to be comparable in magnitude to transitions between conventional mesons. While neither calculation can be applied directly to $c\bar{c}$ one might take this to suggest that the partial widths for $\psi_g(1^{-+}) \rightarrow \gamma + (J/\psi, h_c)$ and $\psi_g(0^{+-}, 2^{+-}) \rightarrow \gamma + (\eta_c, \chi_{cJ})$ are the same order of magnitude as transitions between conventional charmonium states. However, a recent flux-tube model calculations by Close and Dudek [327] found that the $\Delta S = 0$ E1 transitions to hybrids

only occur for charged particles, and hence would vanish for $c\bar{c}$. The $\Delta S = 1$ M1 transitions can occur, but are non-leading and less well defined. Estimates [327] for their widths are $\mathcal{O}(1 - 100)$ keV. Clearly, given our general lack of understanding of radiative transitions involving hybrids, the measurement of these transitions, $\psi_g \rightarrow (c\bar{c})\gamma$, has important implications for model builders.

3.5.2.3 **(iii) Decays to light hadrons:** Decays of the type $\psi_g \rightarrow$ light hadrons offer the interesting possibility of producing light exotic mesons. Estimates of annihilation widths to light hadrons will be order of magnitude guesses at best due to uncertainties in wavefunction effects and QCD corrections. We estimate the annihilation widths $\Gamma[\psi_g(C = -)\rightarrow$ light hadrons] and $\Gamma[c\bar{c}(C = +)\rightarrow$ light hadrons] by comparing them to $\Gamma(\psi' \rightarrow$ light hadrons) and $\Gamma(\eta_c' \rightarrow$ light hadrons). The light hadron production rate from $\psi_g(C = -)$ decays is suppressed by one power of α_s with respect to $\psi_g(C = +)$ decays. This very naive assumption gives $\Gamma[\psi_g(C = -)\rightarrow$ light hadrons] $\sim \mathcal{O}(100)$ keV and $\Gamma[c\bar{c}(C = +)\rightarrow$ light hadrons] $\sim \mathcal{O}(10)$ MeV [328]. These widths could be smaller because the $q\bar{q}$ pair in hybrids is expected to be separated by a distance of order $1/\Lambda_{QCD}$ resulting in a smaller annihilation rate than the S-wave ψ' and η_c' states.

3.5.3 Hybrid production

Recent developments in both theory and experiment lead us to expect that charmonium hybrids will be produced in B decays. The partial widths for $B \rightarrow c\bar{c} + X$, with $c\bar{c}$ representing specific final states such as $J/\psi, \psi', \chi_{c0}, \chi_{c1}, \chi_{c2}, {}^3D_2, {}^1D_2$ etc., have been calculated in the NRQCD formalism [3,329–333] which factorizes the decay mechanism into short (hard) and nonperturbative (soft) contributions. The hard contributions are fairly well understood but the soft contributions, included as colour singlet and colour octet matrix elements, have model dependent uncertainties. Insofar as hybrid $c\bar{c}$ wavefunctions have a non-trivial colour representation they can be produced via a colour octet intermediate state. Chiladze *et al.* [312] estimated the branching ratio $\mathcal{B}[B \rightarrow \psi_g(0^{+-}) + X] \sim 10^{-3}$ for $M \sim 4$ GeV (though recent quenched lattice calculations suggest $M(0^{+-}) = 4.70 \pm 0.17$ GeV, and hence will be inaccessible). Close *et al.* [311] estimate a similar branching ratio to 1^{-+} and argued that if $M_g < 4.7$ GeV, the total branching ratio to ψ_g for all J^{PC} could be $\mathcal{B}[\psi_g(\text{all } J^{PC}) + X] \sim \mathcal{O}(1\%)$. Thus, using two different approaches for estimating $\mathcal{B}[B \rightarrow \psi_g + X]$ both Chiladze *et al.* [312] and Close *et al.* [311] obtain similar results. Both calculations estimate $\mathcal{B}$'s of $\mathcal{O}(0.1 - 1\%)$ which are comparable to the $\mathcal{B}$'s for conventional $c\bar{c}$ states.

3.5.4 Experimental signatures

The decays discussed above lead to a number of possible signals: $\psi_g \rightarrow D^{(*)}D^{(*,**)}$, $\psi_g(0^{+-}, 2^{+-}) \rightarrow J/\psi + (\pi^+\pi^-, \eta, \eta')$, $\psi_g(1^{-+}) \rightarrow \eta_c + (\pi^+\pi^-, \eta, \eta')$, $\psi_g \rightarrow (c\bar{c})\gamma$, and $\psi_g \rightarrow$ light hadrons. Of the possible decay modes, $\psi_g \rightarrow J/\psi\pi^+\pi^-$, $\psi_g \rightarrow J/\psi\eta$, and $\psi_g \rightarrow (c\bar{c})\gamma$ give distinctive and easily reconstructed signals. In the former case, the subsequent decay, $J/\psi \rightarrow e^+e^-$ and $\mu^+\mu^-$ offers a clean tag for the event so that searches for peaks in the invariant mass distributions $M(e^+e^-\pi^-\pi^+) - M(e^+e^-)$ is a promising search strategy for hybrids. Both the 0^{+-} and 2^{+-} should decay via the $\psi_g \rightarrow J/\psi\pi\pi$ cascade. For the ψ_g lying below DD^{**} threshold combining estimates of $\mathcal{B}(B \rightarrow \psi_g + X) \simeq 10^{-3}$ and $\mathcal{B}[\psi_g(2^{+-}) \rightarrow J/\psi\pi^+\pi^-] \simeq 0.2$ with the PDG value of $\mathcal{B}(\psi \rightarrow \ell^+\ell^-) = 11.81\%$ and the Babar detection efficiency we estimate that for 100 fb^{-1} of integrated luminosity each experiment should observe roughly 50 events. If the 2^{+-} lies above the DD^{**} threshold the $\mathcal{B}$ for $2^{+-} \rightarrow J/\psi\pi\pi$ decreases significantly to 2.6×10^{-2} lowering the expected number to about 6 events. Similarly, for the 0^{+-} hybrid we estimate roughly 1200 events if it lies below threshold but only 5 events once the DD^{**} decay modes open up.

The 1^{-+} state is expected to be the lightest exotic $c\bar{c}$ hybrid [12, 23] and therefore the most likely to lie below DD^{**} threshold. However, in this case the cascade goes to $\eta_c\pi\pi$, a more difficult final state to reconstruct. Estimates of the relevant partial widths are $\mathcal{B}(B \rightarrow \psi_g + X) \simeq 10^{-3}$ and

$\mathcal{B}(\psi_g(1^{-+}{\to}\eta_c\pi^+\pi^-) \simeq 9 \times 10^{-3}$. The Babar collaboration studied the decay $B{\to}\eta_c K$ by observing the η_c in $KK\pi$ and $KKKK$ final states. Combining the PDG values for the $\mathcal{B}$'s to these final states with the Babar detection efficiencies of roughly 15% and 11% respectively we estimate that for 100 fb^{-1} each experiment should observe roughly 10 events. If the 1^{-+} lies above the DD^{**} threshold, the $\mathcal{B}$ for $1^{-+}{\to}\pi\pi\eta_c$ decreases to 3×10^{-3} lowering the expected number to about 3 events.

The radiative transition, $\psi_g(1^{-+}){\to}\gamma J/\psi$, also has a distinct signal if it has a significant branching ratio. The conservative value of $\Gamma(\psi_g(1^{-+}){\to}\gamma J/\psi) \simeq 1$ keV, yields a rather small $\mathcal{B}$ for this transition. On the other hand, a monochramatic photon offers a clean tag with a high efficiency. One could look for peaks in $M(\mu^+\mu^-\gamma) - M(\mu^+\mu^-)$. Babar observed χ_{c1} and χ_{c2} this way [307] obtaining $\simeq 394$ χ_{c1}'s and $\simeq 1100$ χ_{c2}'s with a 20.3 fb^{-1} data sample and an efficiency of about 20 % for the $J/\psi\gamma$ final state [307]. So although the rate may be too small to observe, given the potential payoff, it is probably worth the effort to perform this search.

Experiments might also look for charmonium hybrids in invariant mass distributions of light hadrons. For example, Belle observed the χ_{c0} by looking at the invariant mass distributions from the decays $\chi_{c0}{\to}\pi^+\pi^-$ and $\chi_{c0}{\to}K^+K^-$ [306]. They found efficiencies of 21% for $\chi_{c0}{\to}\pi^+\pi^-$ and 12.9% for $\chi_{c0}{\to}K^+K^-$, obtaining ~ 16 events in the former case and ~ 9 in the latter.

The decay to charmed mesons also needs to be studied. Because there are more particles in the final state it will be more difficult to reconstruct the charmonium hybrid. On the other hand, with sufficient statistics these channels will be important for measuring the ψ_g quantum numbers and distinguishing their properties from conventional $c\bar{c}$ states.

3.5.5 Summary and future opportunities

The fundamental problem with all the estimates given above is that they are based on models that have not been tested against experiment. Observing a charmonium hybrid and measuring its properties is necessary to test these calculations. It may be that the models are correct but it is also possible that they have totally missed the mark.

Establishing the existence of mesons with explicit gluonic degrees of freedom is one of the most important challenges in strong interaction physics. As demonstrated by the discovery of the $\eta_c(2S)$ in B decay, B decays offer a promising approach to discovering charmonium hybrid mesons. We have focused on how to search for these states in B-decay. Other possibilities are 1^{--} hybrids produced in e^+e^- annihilation. These would likely mix with conventional vector quarkonium states so that it would be very difficult to distinguish them from conventional states. And recently the Belle collaboration observed the η_c' in double charm production in e^+e^- collisions. Part of the GSI upgrade is to study and search for charmonium states in $p\bar{p}$ annihilation. It is quite possible that hybrids can be studied once the PANDA project comes to fruition. While there is no question that the estimates for the various partial widths are crude, the essential point is that these states are expected to be relatively narrow and that distinctive final states are likely to have observable branching ratios. Given how much we can learn by finding these states we strongly advocate that some effort be devoted to their searches. In the long term, with the various facilities mentioned above, we should be able to open up and study an exciting new spectroscopy.

4   INTRODUCTION TO EXPERIMENTAL SPECTROSCOPY[29]

The experimental spectroscopy review is made of four Sections on charmonia and bottomonia, followed by a Section on B_c, and one on the ccq systems. The paragraphs follow a hyerarchical structure, based on the precision reached in the knowledge of the parameters of these states. Therefore we start from the vector states (ψ's and Υ's), which were first discovered, have the narrowest widths, and are easiest to produce and detect. At present, with the resonant depolarization technique, it is possible to know these

---

[29]Author: R. Mussa

masses with absolute precision between 10 and 100 keV, and these states are widely used as calibration tools for HEP detectors.

Section 6 scans through triplet P-wave states (known as χ_c's and χ_b's), which were discovered from radiative transitions of upper vector excitations. χ_c's could not be precisely studied before the 90's, when direct access to the formation of these states in $\bar{p}p$ annihilations allowed to reach 100–200 keV precisions on their masses, and $\approx 10\%$ resolution of their total widths. The first two Sections allow to realize that the S and P wave states of both ortho-charmonium and -bottomonium constitute a very solid, well established system of resonant states. These narrow resonances can be detected with very small or negligible experimental background and have reached the mature stage, from a barely spectroscopical point of view.

In contrast, all S=0 states are a very active field of research for spectroscopy. The best known among those, $\eta_c(1S)$ (described in Section 7.1) despite being produced with a wide variety of techniques, has still an uncertainty above 1 MeV on the measured mass, and a rapid progress is expected to happen in the next few years. Same can be said of the recently re-discovered $\eta_c(2S)$, described in Section 7.1 which greatly benefits from the advent of the new generation of B-factories. The hyperfine splitting on charmonium S states is then approaching maturity. On the other side, the large amount of data taken by CLEO at $\Upsilon(1, 2, 3S)$ energies did not yield so far to the discovery of η_b states. A comprehensive review of these searches, also performed at LEP experiments and CDF, is then given in Section 7.2. The elusive singlet P state of charmonium, named h_c, has been extensively searched by the $p\bar{p}$ experiments, resulting in inconclusive evidences; its saga is described in Section 7.3. With the advent of B-factories, its search has regained interest.

Being right across the first open charm threshold, charmonium D-wave multiplets still lack a complete understanding, while the first evidence of bottomonium D state comes from the recent CLEO III run at $\Upsilon(3S)$, described in Section 6.3. The phenomenology of all the other vector orbital excitations is still quite unclear as the different thresholds open up: R scans between 3.7 and 4.7 GeV are reviewed in Section 8.1. Further studies on these states have regained priority after the discovery of the narrow state X(3872), seen by Belle, and confirmed by BaBar, CDF and D0. An overview on the experimental evidences of this resonance, as well as the current experimental attempts to clarify its nature and its quantum numbers, is given separately in Section 8.2. Despite its most likely interpretation as one of the two above mentioned D states, other possible assignments of this resonance, extensively described in the theory chapter, span from orbital excitations of P wave states to molecular charmonia, opening a wide number of possible searches in this energy region.

Another field of research which can bloom in the next years, mostly thanks to large samples of B states taken at the Tevatron as well as HERA-B, is the study of the B_c. Despite the weak decay of its ground state may accomunate this object to the heavy light mesons, the mass of its two components suggests that the spectrum of its excited states can be quite similar to the one of charmonium and bottomonium. The experimental evidence of the ground state of such system and the searches for its excitations are described in Section 9.

The last Section is devoted to another class of bound states which share a set of similarities with the heavy quarkonia. The evidence of the doubly charmed baryons claimed by Fermilab experiment E781 is still rather weak and is described in Section 10; further searches, possibly by the B-factories, are needed before speculating on their phenomenology.

5 HIGH PRECISION MEASUREMENTS OF VECTOR STATE MASSES AND WIDTHS

5.1 Charmonia[30]

The first precise measurement of the $J/\psi(1S)$ and $\psi(2S)$ meson masses [334] set the mass scale in the range around 3 GeV which provided a base for the accurate determination of the charmonium state

---

[30]Author:S. Eidelman
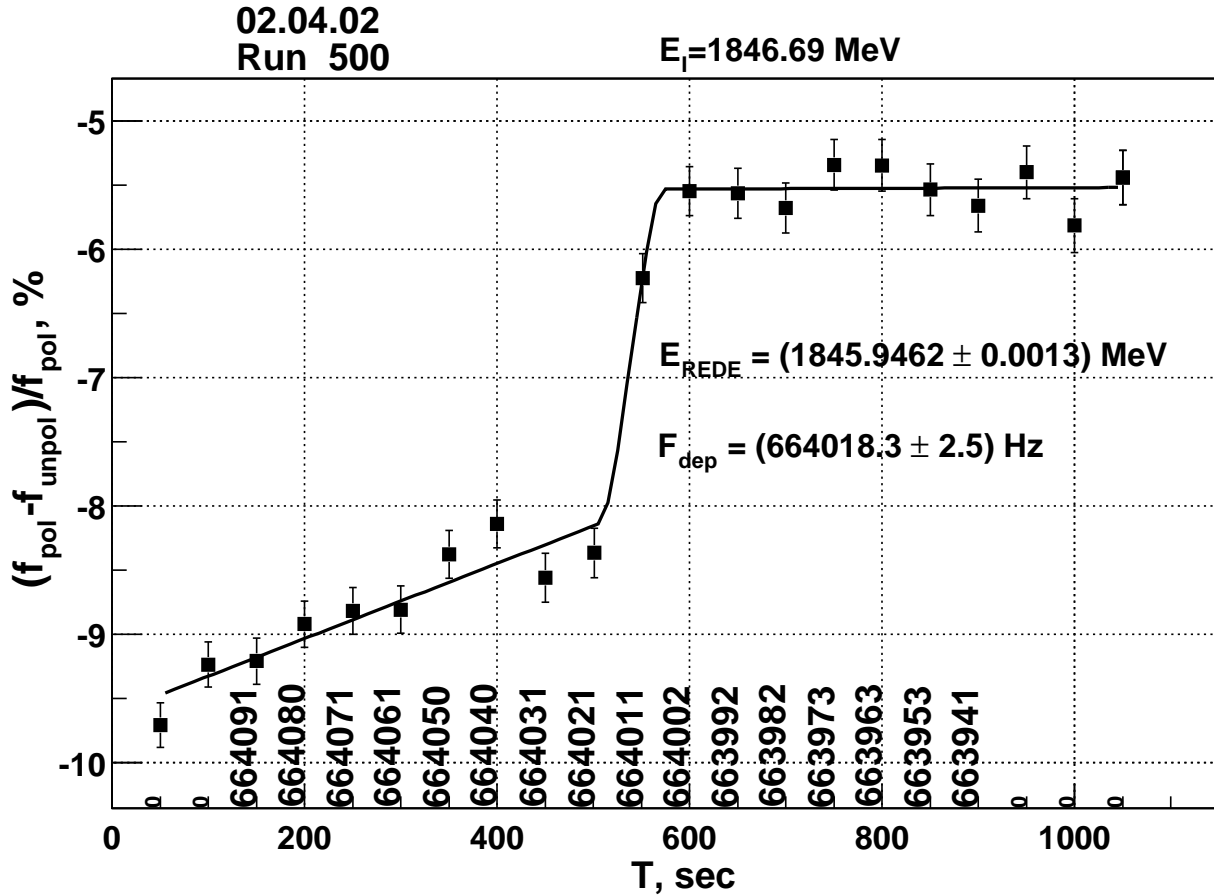
Fig. 3.10: The variation of the coincidence rate ratio for the polarized and unpolarized beams.

location. The method of resonant depolarization, described in Appendix 8.1 of Chapter 2, has been developed in Novosibirsk and first applied to the ϕ meson mass measurement at the VEPP-2M storage ring [339]. Later it was successfully used to measure masses of the ψ- [334] and Υ-meson family [340, 342, 343], see also Ref. [344], in which the values of the masses were rescaled to take into account the change of the electron mass value. The accuracy of the $J/\psi(1S)$ meson mass measurement was later improved in the Fermilab $p\bar{p}$-experiment E760 [347] to $1.2 \cdot 10^{-5}$ using the $\psi(2S)$ mass value from Ref. [334]. The new high precision measurement [337] of the J/ψ and ψ' meson masses has been performed at the collider VEPP-4M using the KEDR detector [352]. The polarimeter unit was installed in the technical straight section of VEPP-4M and consisted of the polarimeter — two scintillation counters detecting electron pairs of the intrabeam scattering whose rate is spin-dependent (Touschek effect [350]) and the TEM wave-based depolarizer [351]. The characteristic jump in the relative rate of scattered electrons at the moment of resonant depolarization is $3 \div 3.5\%$ with the statistical error of 0.3–0.4% for the beam polarization degree higher than 50%. Typical behavior of the rate ratio is shown in Fig. 3.10.

The characteristic uncertainty of the beam energy calibration due to the depolarization procedure is 1.5 keV.

The first part of the experiment consisted of three scans of the $J/\psi(1S)$ region (the integrated luminosity ≈ 40 nb^{-1}, the beam energy spread $\sigma_E \approx 0.6$ MeV) and three scans of the $\psi(2S)$ region (the integrated luminosity ≈ 76 nb^{-1}, $\sigma_E \approx 0.9$ MeV). Then the betatron and synchrotron dumping decrements of VEPP-4M were rearranged to reduce the energy spread down to 0.45 MeV and the fourth scan of $J/\psi(1S)$ was performed (the integrated luminosity is ≈ 10 nb^{-1}). The goal of this was the verification of systematic errors connected with the collider operating mode and the beam energy spread.

The beam polarization time in the VEPP-4M ring is about 100 hours at the $J/\psi(1S)$-energy. For the energy calibration runs, the beam spent the time sufficient for the polarization in the booster ring VEPP-3 (2.5 hours at $J/\psi(1S)$ and about 1 hour at $\psi(2S)$) and was injected to VEPP-4M without essential loss of the polarization degree.

During the scan the data were acquired at seven energies around the resonance peak. Before data acquisition, the beam energy calibration was made at point 1 to fix the current energy scale. At points 2–6 the calibrations before and after data taking were performed with the opposite direction of the depolarizer frequency scan. The point 7 requires no energy calibration.

On completion of the scan the VEPP-4M magnetization cycle was performed and the whole procedure was repeated. The energy dependence of the resonance cross-section was fitted taking into account the interference with continuum and radiative corrections. The results obtained can be presented in the form

$$M_{J/\psi(1S)} - M_{J/\psi(1S)}^{PDG} = \;\; 47 \pm 10 \pm 7 \, \text{keV},$$

$$M_{\psi(2S)} \;\; - \;\; M_{\psi(2S)}^{PDG} = 151 \pm 25 \pm 9 \, \text{keV},$$

demonstrating the agreement with the world average values taking into account their uncertainties of ± 40 keV and ± 90 keV, respectively [245]. The following mass values have been obtained:

$$M_{J/\psi(1S)} = 3096.917 \pm 0.010 \pm 0.007 \, \text{MeV},$$

$$M_{\psi(2S)} = 3686.111 \pm 0.025 \pm 0.009 \, \text{MeV}.$$

The relative measurement accuracy reached $4 \cdot 10^{-6}$ for the $J/\psi(1S)$, $7 \cdot 10^{-6}$ for the $\psi(2S)$ and is approximately 3 times better than that of the previous precise experiments in [334] and [347].

The new result for the mass difference is

$$M_{\psi(2S)} - M_{J/\psi(1S)} = 589.194 \pm 0.027 \pm 0.011 \, \text{MeV}.$$

Substantial improvement in the beam energy accuracy obtained by the presented experiment sets a new standard of the mass scale in the charmonium range.

5.2   Bottomonia[31]

Development of the resonant depolarization method suggested and first realized in Novosibirsk [339,353] also allowed high precision measurements of the resonance masses in the Υ family. The MD-1 group in Novosibirsk carried out three independent measurements of the $\Upsilon(1S)$ mass [340, 342, 343, 354]. The $\Upsilon(1S)$ mass was also measured by the CUSB collaboration in Cornell [345]. Their result was by 0.63 ± 0.17 MeV or 3.8σ lower than that of MD-1. The reasons of this discrepancy are not clear, however, when the MD-1 group performed a fit of the CUSB results using the Novosibirsk procedure (in particular, it included a new method or calculating radiative corrections according to [355] instead of the older approach of Ref. [356]), the difference between the two results decreased to 0.32 ± 0.17 MeV or 1.9σ only.

The mass of the $\Upsilon(2S)$ meson was measured by the MD-1 group in Novosibirsk [342, 354] and two groups in DESY — ARGUS and Crystal Ball [346]. Both groups in DESY obtained the mass value consistent with that in Novosibirsk, the average being 0.5 ± 0.8 MeV lower than that of MD-1.

The mass of the $\Upsilon(3S)$ meson was measured by the MD-1 group only [342, 354]. As in the case of the $\Upsilon(2S)$ meson, a systematic error of the measurement was less than 0.2 MeV, much smaller than the statistical one.

---

[31]Author: S. Eidelman

Finally, in 2000 all the results on the mass of the ψ [334,357] and Υ [340,342,343,354,354] family resonances were updated [344] to take into account a more precise value of the electron mass [358, 359] (for the ψ family an additional correction has been made to take into account the new way of calculating radiative corrections [355]). In Table 3.11 we summarize the information on these experiments presenting for each detector the number of energy points and the energy range studied, the integrated luminosity and the final value of the mass. The results after the update mentioned above are shown in parentheses.

Table 3.11: Mass Measurements in the Υ Meson Family

Resonance	Collider	N of Points $\sqrt{s}$, MeV	Detector Reference	$\int$ Ldt, pb^{-1}	Mass, MeV
$\Upsilon(1S)$	VEPP-4	43 9420–9490	MD-1 [343] ([344])	2.0	$9460.59 \pm 0.09 \pm 0.05$ $(9460.51 \pm 0.09 \pm 0.05)$
	CESR	13 9446–9472	CUSB [345]	0.285	$9459.97 \pm 0.11 \pm 0.07$
$\Upsilon(2S)$	VEPP-4	37 9980–10075	MD-1 [354] ([344])	0.6	10023.6 ± 0.5 (10023.5 ± 0.5)
	DORIS	13 9960–10040	ARGUS [346] Cr. Ball [346] Average [346]	2.0 2.0	10023.43 ± 0.45 10022.8 ± 0.5 $10023.1 \pm 0.4 \pm 0.5$
$\Upsilon(3S)$	VEPP-4	35 10310–10410	MD-1 [354] ([344])	1.25	10355.3 ± 0.5 (10355.2 ± 0.5)

6 SPIN AVERAGED AND FINE SPLITTINGS

6.1 Charmonium P states: COG and fine splittings[32]

The most precise determinations of mass and width come from the study of charmonium spectroscopy by direct formation of $\bar{c}c$ states in $\bar{p}p$ annihilation at the Fermilab Antiproton Source (experiments E760 and E835). The E760 collaboration measured the resonance parameters of the χ_{c1} and χ_{c2} [360].

For both E760 and E835-I, the transition energy of the Antiproton Accumulator was close enough to the χ_{c0} mass to prevent stable running with large stacks in this energy region. Nevertheless, a few stacks were decelerated to the χ_{c0} region at the end of Run I, yielding an unexpectedly high rate of $J/\psi\gamma$ events. The Accumulator underwent a major upgrade between 1997 and 2000, shifting the transition energy [362] and allowing a smooth running at the χ_{c0}, with substantial increase in statistics [361], and a better control of systematics.

A new measurement of the χ_{c1} parameters was made in year 2000, with roughly 15 times more statistics than the predecessor experiment E760. The χ_{c2} parameters were also remeasured with statistics comparable to those of experiment E760. This report includes the new results, in publication, not yet included in the PDG.

The effect of scanning a narrow resonance with a beam of comparable width is show in Fig. 3.11, where the excitation curve for one scan at the χ_{c1} is compared with the deconvoluted Breit Wigner shape and the measured beam energy profiles for each point.

In mass and width measurements, the systematic error comes from uncertainties on auxiliary variables measured concurrently to data taking (changes in beam orbit length, efficiency and luminosity at each energy point), as well as the absolute calibration of the beam energy. The absolute calibration of the beam energy is deduced from the absolute calibration of the orbit length, done using $\psi(2S)$ scans, and

---

[32]Authors: R. Mussa, G. Stancari
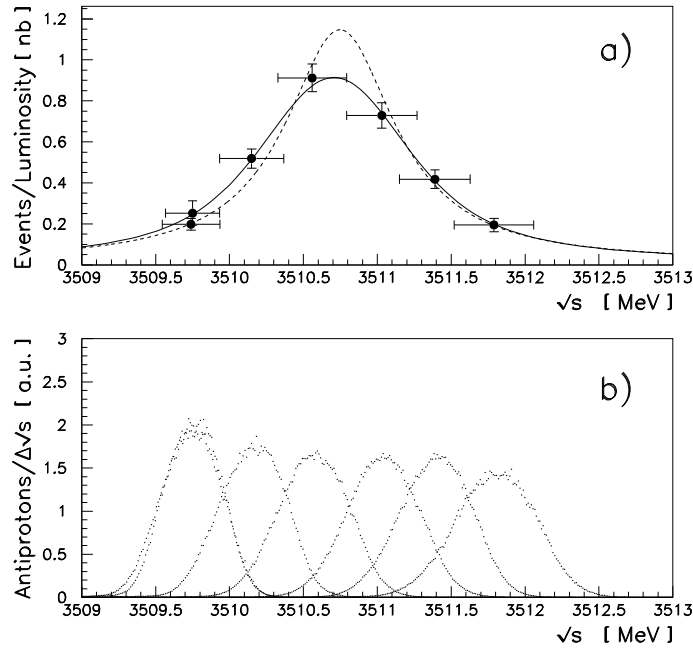
Fig. 3.11: Measured cross-section at each data point, excitation curve (full line) and deconvoluted resonance curve (dotted line) for one scan at the χ_{c1} ; plotted in the lower part of the figure are the beam energy profiles corresponding to each data point

assuming 3686.000 for the mass of this state. The more precise determination recently done at VEPP-4, documented in the previous section, implies a systematic shift (up) of 70, 83, 89 keV of the $\chi_{c0,1,2}$ measurements respectively. The systematic error on χ_c masses from $\psi(2S)$ mass determination reduces then to 16,19,20 keV respectively, and is now negligible if compared to the other sources, which are uncorrelated when we merge different scans. The impact of radiative corrections to account for proton bremsstrahlung is still well below other systematic errors; it was estimated using the expression:

$$\sigma_{BW}^{rad}(\beta, s) = \beta \int_0^{\frac{\sqrt{s}}{2}} \frac{dk}{k} \left(\frac{2k}{\sqrt{s}} \right)^\beta \sigma_{BW}(s - 2k\sqrt{s})$$

with

$$\begin{aligned}
\beta &= \frac{2\alpha}{\pi} \times \left(\frac{s - 2m_p^2}{\sqrt{s(s - 4m_p^2)}} \times \ln \frac{s + \sqrt{s(s - 4m_p^2)}}{s - \sqrt{s(s - 4m_p^2)}} - 1 \right) \\
&= 6.7 \times 10^{-3}(\chi_{c0}), \quad 7.0 \times 10^{-3}(\chi_{c1}), \quad 7.2 \times 10^{-3}(\chi_{c2}).
\end{aligned}$$

Systematic shifts on masses are $\Delta m(\chi_{c0,1,2}) = -0.06, -0.01, -0.02 \, \text{MeV}/c^2$; the shifts on total widths are $\Delta\Gamma/\Gamma \approx -1\%$ for all χ_c states.

E835 could also measure the χ_{c0} excitation curve in the $p\bar{p} \to \pi^0\pi^0$ channel, exploiting the amplification due to interference with continuum. The measurement is compatible with result obtained in $\psi\gamma$ and of course has correlated systematic errors.

A measurement of mass [365] and width [366] with accuracy almost comparable to the one obtained in $p\bar{p}$ annihilations was made by BES on the χ_{c0}, exploiting the sample of 3.8M ψ' decays to various decay channels. There are not yet mass and width measurements of χ_c states from the 14M ψ' sample. Table 3.12 summarizes the most accurate results on masses and widths at present. Statistical

Table 3.12: Parameters of χ_c states from E760, E835, and BES

R	Expt.	Mass(MeV/c^2)	Γ(MeV)	Ref.
χ_{c0}				
	BES	3414.1±0.6±0.8	14.3±2.0±3.0	[365]
	E835	3415.4±0.4±0.2	9.9±1.0±0.1	[361]
	E835	3414.7±0.7±0.2	8.6±1.7±0.1	[363]
	PDG 2004	3415.19±0.34	10.1±0.8	[245]
χ_{c1}				
	E760	3510.61±0.10±0.02	0.88±0.11±0.08	[360]
	PDG 2004	3510.59±0.10	0.91±0.13	[245]
	E835	3510.725±0.065±0.018	0.88±0.06±0.09	[364]
χ_{c2}				
	E760	3556.24±0.07±0.12	1.98±0.17±0.07	[360]
	PDG 2004	3556.26±0.11	2.11±0.16	[245]
	E835	3556.10±0.09±0.17	1.93±0.19±0.09	[364]

errors on $\chi_{c1,2}$ masses are obtained from gaussian sums of errors from event statistics and errors from orbit length measurements; the latter are dominant, therefore future improvements will require to push fractional errors on orbit lengths below 10^{-6}. In the case of χ_{c0} there is still room for improvement: ten times more statistics at the χ_{c0} in a $p\bar{p}$ annihilation experiment could take errors on masses down to 200 keV, and on widths down to 3%. To reach a comparable level on narrow χ_b states is very challenging, and will require new ideas.

It is finally possible to present the results on P states by calculating the spin independent (M_{COG}), spin–orbit (h_{LS}) and tensor (h_T) terms of the $c\bar{c}$ Hamiltonian. All values are summarized in Table 3.13.

Table 3.13: Fine splittings between χ_c states

	$c\bar{c}(n=1)$
M_{COG} (in MeV)	
$\Delta M_{21} = M(\chi_{c2}) - M(\chi_{c1})$ (in MeV)	45.6±0.2
$\Delta M_{10} = M(\chi_{c1}) - M(\chi_{c0})$ (in MeV)	95.3±0.4
$\rho(\chi) = \Delta M_{21}/\Delta M_{10}$	0.470±0.003
h_T (in MeV)	10.06±0.06
h_{LS} (in MeV)	34.80±0.09

6.2 Bottomonium P states: COG and Fine splittings[33]

After discovery of the $\Upsilon(1S)$, $\Upsilon(2S)$ and $\Upsilon(3S)$ resonances at the fixed target pN experiment at Fermilab in 1997 [367] the first two were observed a year later at the e^+e^- storage ring DORIS at DESY [368]. Since DORIS energy reach was stretched well beyond its design, the $\Upsilon(3S)$ could not be reached. The

---

[33]Author: T. Skwarnicki

limited statistics and limited photon detection capabilities of the detectors prevented observation of the $\chi_{bJ}(1P)$ states via E1 photon transitions from $\Upsilon(2S)$ at that time. Energy range of another e^+e^- storage ring, CESR at Cornell University, was extended high enough to reach the $\Upsilon(3S)$ in 1982. The CUSB detector at CESR had sufficient photon detection resolution in NaI(Tl)/Lead-glass calorimeter to discover the three $\chi_{bJ}(2P)$ states in inclusive photon spectrum in $\Upsilon(3S)$ decays [369]. The $J=1$ and $J=2$ states were also observed in two-photon cascade, $\Upsilon(3S) \to \gamma\chi_{bJ}(2P)$, $\chi_{bJ}(2P)\to\gamma\Upsilon(nS)$ ($n=1,2$), followed by $\Upsilon(nS)\to l^+l^-$, where l^+l^- stands for e^+e^- or $\mu^+\mu^-$ [370]. The latter "exclusive" approach eliminates all photon backgrounds from π^0s copiously produced in hadronic decays of $b\bar{b}$ states, but results in low signal statistics. In fact, the $J=0$ is very difficult to observe this way since it has larger gluonic annihilation width, which suppresses branching ratios for radiative transitions. A year later the CUSB experiment produced similar evidence for $\chi_{bJ}(1P)$ states in the $\Upsilon(2S)$ data [371]. The $J=2$ and $J=1$ states were also observed by the CLEO experiment in inclusive photon spectrum, with photons reconstructed in the tracking system after conversion to e^+e^- pairs at the beam-pipe [372].

Meanwhile DORIS accumulated more data at the $\Upsilon(2S)$ resonance with two new detectors: magnetic spectrometer ARGUS, and NaI(Tl)-calorimeter Crystal Ball, which previously explored photon spectroscopy in charmonium at SPEAR. The Crystal Ball confirmed the CUSB results on the $\chi_{bJ}(1P)$ states [373], though the $J=0$ photon line was observed at a different energy, soon confirmed by ARGUS via photon conversion technique [374]. Analysis of angular correlation in $\gamma\gamma l^+l^-$ by Crystal Ball established spin assignment to the observed $\chi_{b2}(1P)$ and $\chi_{b1}(1P)$ states [375]. Next round of improvements in experimental results came about a decade later from the CESR upgraded to higher luminosity and upgraded CUSB and CLEO experiments. The CUSB-II detector was equipped with compact BGO calorimeter. The CLEO II collaboration built large CsI(Tl) calorimeter which was put inside the superconductive magnet. Both experiments improved the results on $\chi_{bJ}(2P)$ states, with the increased $\Upsilon(3S)$ data size [376].

A few years later the CLEO II experiments took a short $\Upsilon(2S)$ run. Even though the number of $\Upsilon(2S)$ resonance decays was not much larger than in the previous measurements, the results on $\chi_{bJ}(1P)$ states were substantially improved [377] thanks to much larger photon detection efficiency of well-segmented CLEO II calorimeter.

CESR continued to improve its luminosity via the storage ring upgrades. Its running time was exclusively devoted to B-meson physics with data taken at the $\Upsilon(4S)$ resonance. The CLEO tracking and particle identification systems were replaced, while the CsI(Tl) calorimeter was preserved. After the B physics program at CESR had ended, the CLEO III detector accumulated large samples at the narrow $\Upsilon(nS)$ resonances. Number of collected $\Upsilon(2S)$ and $\Upsilon(3S)$ resonant decays was increased by an order of magnitude. Analysis of inclusive photon spectra has been recently completed [378]. Photon lines due to $\Upsilon(2S)\to\gamma\chi_{bJ}(1P)$ and $\Upsilon(3S)\to\gamma\chi_{bJ}(2P)$ observed in inclusive photon spectrum are shown in Fig. 3.12 and Fig. 3.13 respectively. Determination of energies of these photon lines is limited by the systematic error in calibration of the calorimeter. The latter was improved in CLEO III by analysis of the $\psi(2S)$ photon spectrum obtained with the same detector [379]. Since the photon energies in $\psi(2S)\to\gamma\chi_{cJ}(1P)$ transitions are precisely know from the scans of the resonant cross-sections in e^+e^- ($\psi(2S)$) or $\bar{p}p$ (χ_{cJ}) collisions, the $\psi(2S)$ photon lines were turned into the calibration points.

Comparisons of the photon energies for $\Upsilon(2S)\to\gamma\chi_{bJ}(1P)$ and $\Upsilon(3S)\to\gamma\chi_{bJ}(2P)$ determined in various experiments, together with the world average values, are shown in Fig. 3.14 and Fig. 3.15 respectively. The masses of the $\chi_{bJ}(1P)$ ($\chi_{bJ}(2P)$) states can be calculated from these photon energies and the masses of $\Upsilon(2S)$ ($\Upsilon(3S)$). The errors on the latter are significant, thus the errors on the masses of the $\chi_{bJ}(nP)$ states are strongly correlated between different values of J. These need to be properly taken into account when calculating the centre-of-gravity mass and fine-splitting parameters. The results are tabulated in Table 3.14.
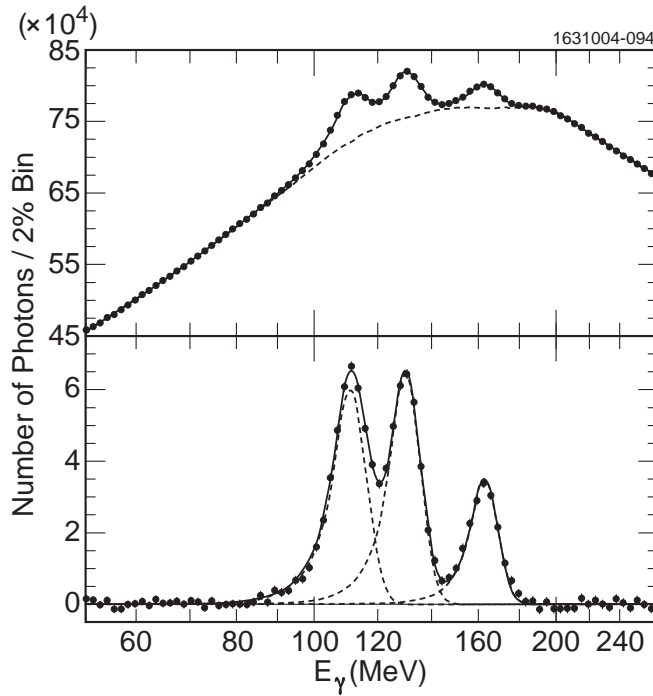
Fig. 3.12: Fit to the $\Upsilon(2S) \to \gamma\chi_{bJ}(1P)$ $(J = 2, 1, 0)$ photon lines in the CLEO III data. The points represent the data (top plot). Statistical errors on the data are smaller than the point size. The solid line represents the fit. The dashed line represents total fitted background. The background subtracted data (points with error bars) are shown at the bottom. The solid line represents the fitted photon lines together. The dashed lines show individual photon lines.
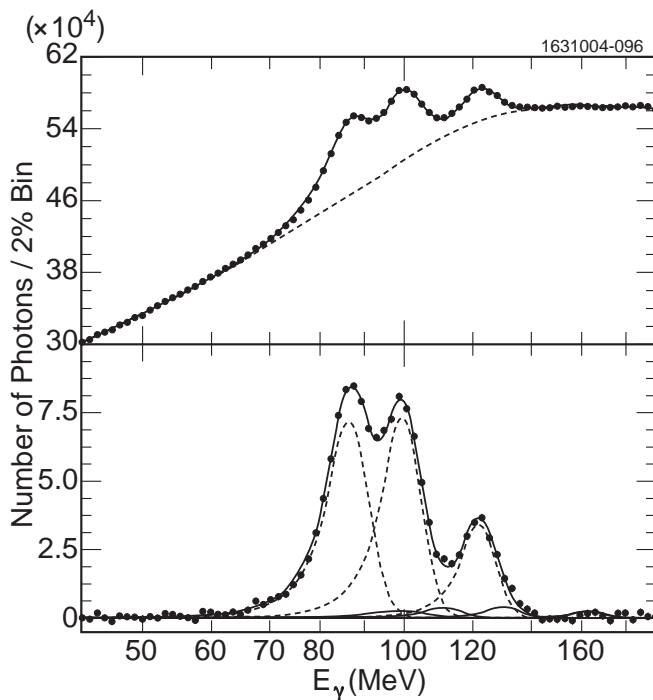
Fig. 3.13: Fit to the $\Upsilon(3S) \to \gamma\chi_{bJ}(2P)$ $(J = 2, 1, 0)$ photon lines in the CLEO III data. See caption of Fig. 3.12 for the description. Small solid-line peaks in the bottom plot show the $\chi_{bJ}(2P) \to \gamma\Upsilon(1D)$ and $\Upsilon(2S) \to \gamma\chi_{bJ}(1P)$ contributions.

Average: (110.4 ± 0.3) MeV
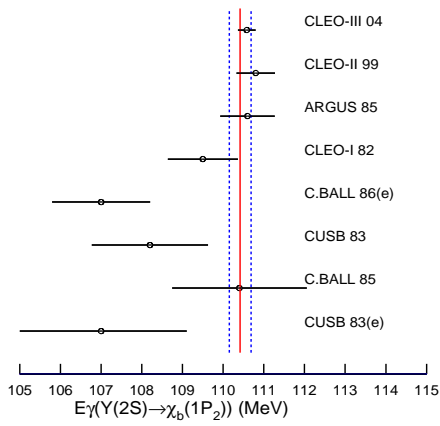
Average: (129.6 ± 0.3) MeV
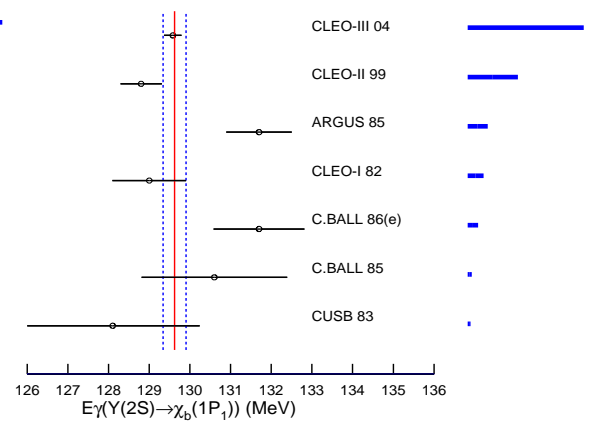
Average: (162.4 ± 0.4) MeV
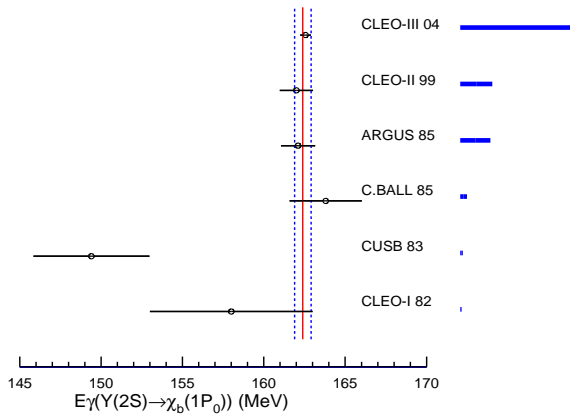
Fig. 3.14: Measurements of the photon energies in $\Upsilon(2S) \rightarrow \gamma \chi_{bJ}(1P)$. The vertical bars indicate the world average value (solid) and its error (dashed). These are also listed on top. The thick horizontal bars to the right of the name of the experiment give the relative weight of each experiment into the average value. Photon energy measurements from analyses of exclusive $\gamma\gamma l^+ l^-$ events are indicated with an "(e)" after the date of the publication.

Average: (86.1 ± 0.2) MeV
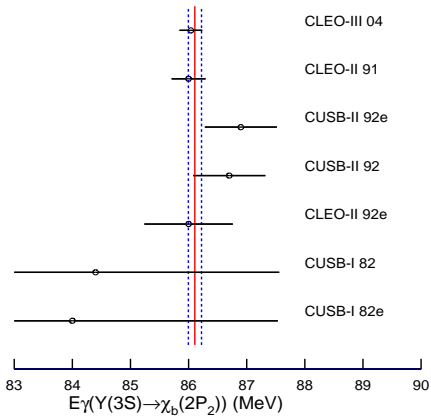
Average: (99.3 ± 0.2) MeV
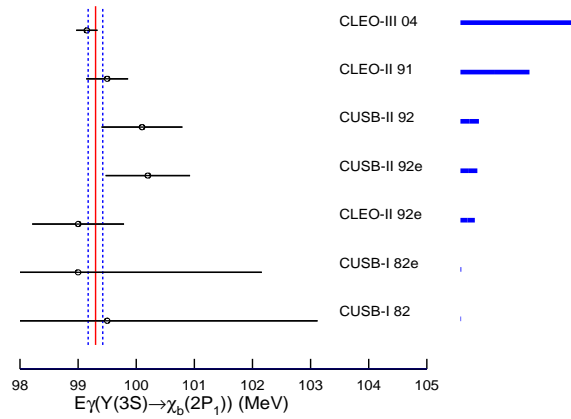
Average: (121.9 ± 0.4) MeV
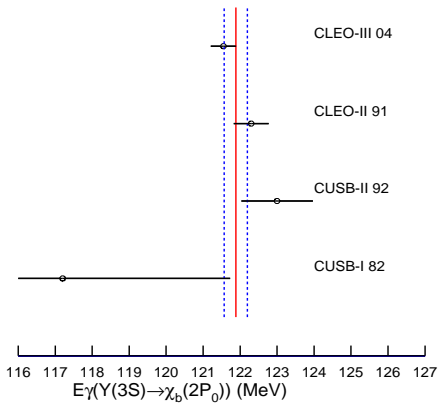
Fig. 3.15: Measurements of the photon energies in $\Upsilon(3S) \to \gamma\chi_{bJ}(2P)$. The vertical bars indicate the world average value (solid) and its error (dashed). These are also listed on top. The thick horizontal bars to the right of the name of the experiment give the relative weight of each experiment into the average value. Photon energy measurements from analyses of exclusive $\gamma\gamma l^+l^-$ events are indicated with an "(e)" after the date of the publication.

Table 3.14: Masses and fine splittings for the $\chi_b(nP)$ states obtained from the world average values. The values of ρ given in brackets come from the CLEO III measurements [378] and have smaller errors than the world average values since cancellations in the systematic errors of photon energies for different J values are properly considered.

	$b\bar{b}(n=1)$
$M(\chi_{b2})$	9912.2±0.4 (in MeV)
$M(\chi_{b1})$	9892.8±0.4 (in MeV)
$M(\chi_{b0})$	9859.5±0.5 (in MeV)
M_{COG}	9899.9±0.4 (in MeV)
$\Delta M_{21} = M(\chi_{b2}) - M(\chi_{b1})$ (in MeV)	19.4±0.4
$\Delta M_{10} = M(\chi_{b1}) - M(\chi_{b0})$ (in MeV)	33.3±0.5
$\rho(\chi) = \Delta M_{21}/\Delta M_{10}$	0.584±0.016 (0.574±0.012)
h_T (in MeV)	3.27±0.08
h_{LS} (in MeV)	13.64±0.14
	$b\bar{b}(n=2)$
$M(\chi_{b2})$	10268.7±0.5 (in MeV)
$M(\chi_{b1})$	10255.4±0.5 (in MeV)
$M(\chi_{b0})$	10232.6±0.6 (in MeV)
M_{COG}	10260.3±0.5 (in MeV)
$\Delta M_{21} = M(\chi_{b2}) - M(\chi_{b1})$ (in MeV)	13.3±0.3
$\Delta M_{10} = M(\chi_{b1}) - M(\chi_{b0})$ (in MeV)	22.8±0.4
$\rho(\chi) = \Delta M_{21}/\Delta M_{10}$	0.583±0.020 (0.584±0.014)
h_T (in MeV)	2.25±0.07
h_{LS} (in MeV)	9.35±0.12

6.3 Bottomonium D states[34]

The lowest radial excitations of the D states in charmonium have masses above the the $D\bar{D}$ meson threshold. The lightest member of the spin-triplet is a vector state. It is identified with the $\psi(3770)$ state, which is a third $c\bar{c}$ resonance observed in the e^+e^- cross-section. Unlike the $J/\psi(1S)$ and the $\psi(2S)$ resonances, the $\psi(3770)$ is broad because it decays to $D\bar{D}$ meson pairs. Since, the coupling of the D state to e^+e^- is expected to be small, its large e^+e^- cross-section is attributed to a significant mixing between the $2S$ and $1D$ $J^{PC} = 1^{--}$ states. Whether the narrow $X(3872)$ state is one of the other members of the $1D$ family is a subject of intense disputes. The $J=2$ states (the spin triplet and the spin singlet) are narrow below the $D\bar{D}^*$ threshold, since they can't decay to $D\bar{D}$. The $J=3$ state can decay to $D\bar{D}$ but, perhaps, its width is sufficiently suppressed by the angular momentum barrier [187]. In all scenarios, masses of all $1D$ states must be strongly affected by the proximity of open-flavour thresholds via coupled channel effects.

In contrast, the $1D$ states of bottomonium are well below the open-flavour threshold, thus their masses are easier to predict theoretically. Unfortunately, the mixing of the $2S$ and $1D$ $J^{PC} = 1^{--}$ states is expected to be small for bottomonium. Not surprisingly, the $J=1$ $1D$ $b\bar{b}$ state has not been observed in e^+e^- collisions. The spin-triplet states are accessible from the $\Upsilon(3S)$ resonance by two subsequent E1 photon transitions via intermediate $\chi_{bJ}(2P)$ states. Energies of photons in the $\chi_{bJ}(2P) \rightarrow \gamma\Upsilon(1D)$ transitions fall in the same range as the dominant $\Upsilon(3S) \rightarrow \gamma\chi_{bJ}(2P)$ photon lines. Therefore, they cannot be resolved in the inclusive photon spectrum. Two-photon coincidence is of not much help, since the photon background from π^0 decays is very large in $\Upsilon(3S)$ decays. Nevertheless, the $\Upsilon(1D)$ states have been discovered by CLEO III in the $\Upsilon(3S)$ decays [380]. The photon backgrounds are removed

---

[34]Author:T. Skwarnicki
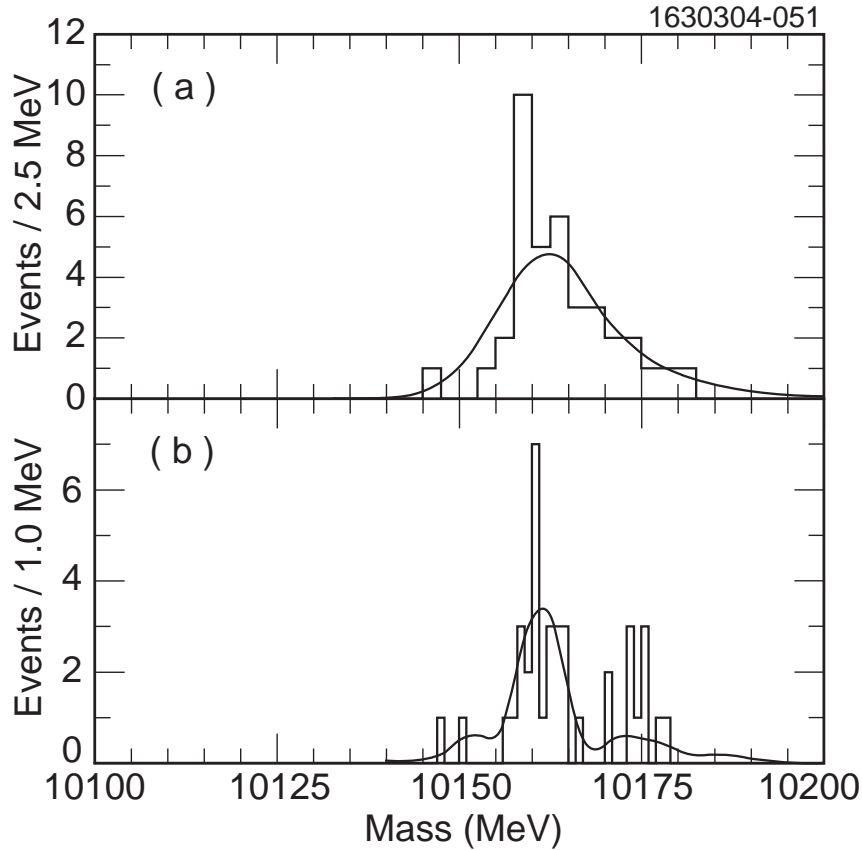
Fig. 3.16: Distributions of the measured $\Upsilon(1D)$ mass in the CLEO III data [380] using (a) the recoil mass against the two lowest energy photons, (b) the fit implementing the $\chi_{bJ'}(2P)$, $\chi_{bJ}(1P)$, $\Upsilon(1S)$ mass constraints. The results of fits for a single $\Upsilon(1D)$ state are superimposed. The mass-constraint method produces satellite peaks because of ambiguities in J' and J values.

by using the "exclusive" approach (see the previous section), in which the three additional decays are required, $\Upsilon(1D) \rightarrow \gamma\chi_{bJ}(1P)$, $\chi_{bJ}(1P) \rightarrow \gamma\Upsilon(1S)$, $\Upsilon(1S) \rightarrow l^+l^-$. Since the product branching ratio for these five subsequent decays is rather small [204, 381], the large CLEO III sample of the $\Upsilon(3S)$ resonances was essential for this measurement. After suppression of the $\Upsilon(3S) \rightarrow \pi^0\pi^0\Upsilon(1S)$ and 4-photon cascades via the $\chi_{bJ}(2P)$, $\Upsilon(2S)$, $\chi_{bJ}(1P)$ states 38 $1D$ candidates are observed in the CLEO III data. The mass of the $1D$ state is estimated by two different techniques, as shown in Fig. 3.16. In both cases, the mass distribution appears to be dominated by production of just one state. The theoretical and experimental clues point to the $J = 2$ assignment. The mass of the $\Upsilon_2(1D)$ state is measured by CLEO III to be: $(10161.1 \pm 0.6 \pm 1.6)$ MeV.

Masses of the other bottomonium $1D$ states remain unknown. However, the fine structure of the $1D$ spin-triplet is predicted to be small. All potential model calculations predict the $\Upsilon_2(1D)$ mass to be between 0.5 and 1.0 MeV lower than the centre-of-gravity (c.o.g.) mass for this triplet [204]. Adding this theoretical input, CLEO obtains (10162 ± 2) MeV for the c.o.g. mass, where they assigned an additional uncertainty of 1 MeV to the correction for the 1^3D_2-c.o.g. mass difference.

The CLEO III also looked for $\Upsilon(1D) \rightarrow \pi^+\pi^-\Upsilon(1S)$ and $\Upsilon(1D) \rightarrow \eta\Upsilon(1S)$ transitions. No evidence for such decays was found and upper limited were set [380]. The upper limit on $\Upsilon(1D) \rightarrow \pi^+\pi^-\Upsilon(1S)$ rules out rather large width for this transition predicted by the Kuang–Yan model [325, 382].
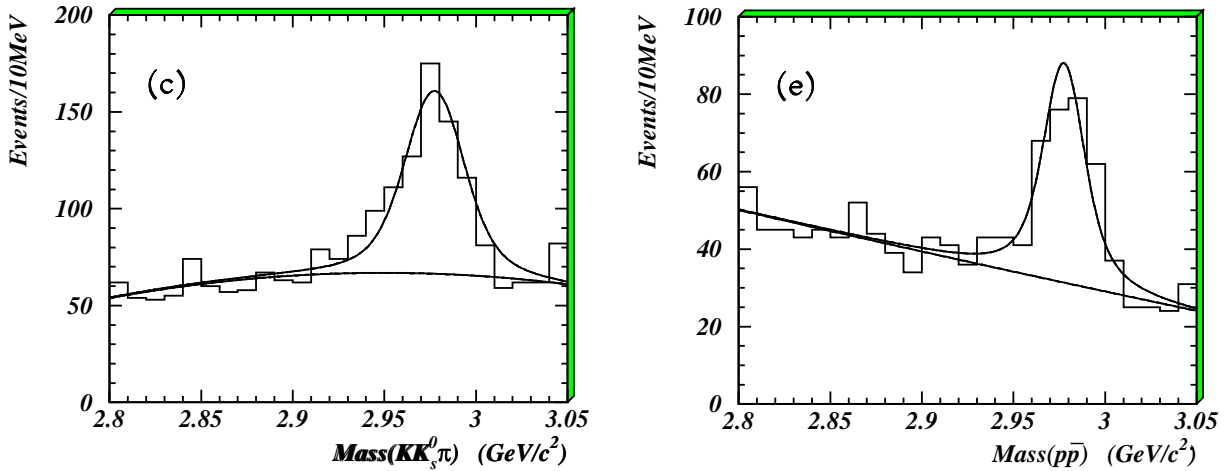
Fig. 3.17: Invariant mass distributions for $K_S^0 K^\pm \pi^\mp$(left) and $p\bar{p}$(right) events from BES

7 HYPERFINE SPLITTINGS

7.1 $\eta_c(1, 2S)$: comparison of all measurements[35]

Despite the large variety of available data on the $\eta_c(1S)$, the precise determination of its mass and width is still an open problem. It is likely that unexpected systematic errors be present in some of these measurements. It is worth to compare the subsets of measurements of masses and widths of the η_c done with the same reaction, before comparing the large variety of techniques which allowed to measure this state, each one with its own dominant systematic error. The two states share most of the decay channels, therefore the same analysis is usually applied to extract their signal.

7.1.1 $\eta_c(1S)$ in J/ψ and ψ' decays

The η_c parameters have been extracted from the radiative transitions of J/ψ and ψ' by a large number of experiments: while Crystal Ball (and more recently CLEO-c) studied the inclusive photon spectrum, Mark II and III, DM2, BES studied the invariant mass distributions of decay products in reactions with 2 or 4 charged tracks and 0 to 2 neutral pions. The samples taken in the 80's and early 90's were recently overwhelmed by the 58 M BES sample. Table 3.15 summarizes the mass and width measurements done in the past 20 years. The η_c peak is observed in the invariant mass of the following decay modes: $K_S^0 K^\pm \pi^\mp$, $\pi^+\pi^-\pi^+\pi^-$, $\pi^+\pi^- K^+K^-$, $K^+K^-K^+K^-$, $p\bar{p}$. Figure 3.17 shows two of these distributions.

Table 3.15: The world largest samples of J/ψ and ψ' used for the determination of the η_c mass and width.

Expt.	MarkIII	DM2	BES I	BES II
year	1986	1991	2000	2003
Mass(MeV/c^2)	2980.2±1.6	2974.4±1.9	2976.3±2.3±1.2	2977.5±1.0±1.2
Width(MeV)	$10.1^{+33.0}_{-8.2}$	–	11.0±8.1±4.1	17.0±3.7±7.4
Sample	2.7MJ/ψ	8.6MJ/ψ	3.8Mψ'+7.8MJ/ψ	58MJ/ψ

---

[35]Authors: R. Galik, R. Mussa, S. Ricciardi
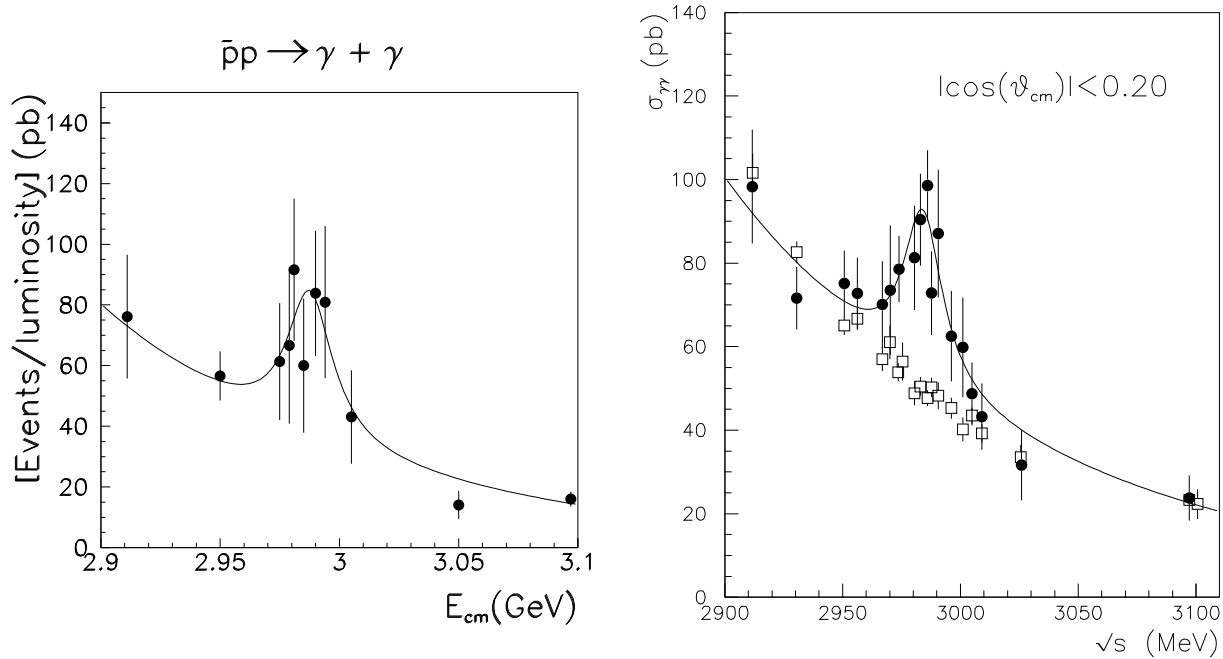
Fig. 3.18: Cross-section (black dots) observed by E760 (left) and E835(right) for the reaction $p\bar{p}{\rightarrow}\gamma\gamma$ in the region with $\cos\theta_{CM} <$0.25(E760), 0.2(E835). The blank squares show the expected feed-down from $\pi^0\pi^0$, $\pi^0\gamma$.

A cut on the kinematic fit to the exclusive hypothesis (referred as J/ψ veto) is applied, to reject direct J/ψ decays to the same channels, or feed-down from other decay channels, such as $(\omega, \phi)\pi\pi$, ωK^+K^-, $\gamma K_S^0 K_S^0$. The systematic errors on mass determination come mostly from the mass scale calibration (0.8 MeV/c^2, calculated by comparing K_S^0, ϕ and even χ_c masses with PDG values) and from the J/ψ veto. The J/ψ veto is also the dominant source of systematics on the total width determination: 5.6 out of $7.4\,\text{MeV}/c^2$.

7.1.2 η_c(1S) in $p\bar{p}$ annihilations

The η_c was investigated in $p\bar{p}$ annihilation only in the $\gamma\gamma$ channel, which is affected by a substantial feeddown from the continuum reactions $\pi^0\pi^0$ and $\pi^0\gamma$: both reactions are sharply forward-backward peaked. The number of 'signal' events is 12 in R704, 45 in E760 and 190 in E835, which respectively took 0.7,3.6,17.7 pb^{-1} of data in the η_c mass region. It is worth to stress the fact that an increasing amount of integrated luminosity was taken away from the peak , in order to better understand the size and nature of the non resonant background. The experiment E835 can discriminate a π^0 from a single photon with 96.8% efficiency: this reduces the feed-down to 0.1%$\sigma_{\pi^0\pi^0}$+ 3.2% $\sigma_{\pi^0\gamma}$ at $\sqrt{s} = 2984\,\text{MeV}/c^2$.

The very small sample taken by R704 in the resonant region ends up with a remarkably small result on the η_c width: all this is based on the *ansatz* to have a small background. Such hypothesis was strongly disconfirmed by E760, therefore the R704 result is affected by a very large hidden systematic error. The statement is even stronger, if we take into account that the R704 fiducial region was extended up to $cos(\theta_{cm,\pi^0}) = 0.35$, where the feeddown dominates, and the detector did not have full azimuthal coverage (thus introducing an even larger feeddown).

E835 precisely measured the $\pi^0\gamma$ and $\pi^0\pi^0$ cross-section: the feeddown from these reactions can account for most of the background. E835 could not exclude the existence of a residual tiny $\gamma\gamma$ continuum, which can in principle interfere with the resonant reaction, but is not large enough to shift the mass peak beyond the statistical error. Figure 3.18, on the right, shows both signal and feed-down

cross-section observed in E835. A power law dependence on energy was assumed for the background, in the fits. The choice of background parametrization and of the fiducial region for the signal are the dominant sources of systematic error, which amounts to 1 MeV/c^2 on the mass and 2 MeV on the width. A comparative summary of $p\bar{p}$ measurements on $\eta_c(1S)$ parameters can be found in Table 3.16.

Table 3.16: Comparison of E760 and E835 results.

Expt.	E760	E835
Ldt (pb^{-1})	3.6	17.7
$m(\eta_c)$(MeV/c^2)	2988.3 ± 3.3	2984.1 ± 2.1 ± 1.0
$\Gamma(\eta_c)$ (MeV/c^2)	$23.9^{+12.6}_{-7.1}$	$20.4^{+7.7}_{-6.7} \pm 2.0$

E760 and E835 also searched for the $\eta_c(2S)$ state in the energy range $3575 \,\text{MeV}/c^2 < \sqrt{s} < 3660 \,\text{MeV}/c^2$, putting a 90% CL upper limit at $\simeq 0.4$ eV on $\mathcal{B}(\eta_c(2S){\to}p\bar{p}) \times \Gamma(\eta_c(2S){\to}\gamma\gamma)$.

7.1.3 η_c(1,2S) in B decays

In the last years, the B-factories have exploited the B meson decays to charmonium as a new powerful tool for the measurement of the η_c mass [393], as well as for the discovery of $\eta_c(2S)$ and the measurement of its mass. Exclusive decays of both B^0 and B$^+$ mesons were detected with the η_c reconstructed in the $K^0_S K^{\mp}\pi^{\pm}$, $K^+ K^-\pi^0$, $K^{*0}K^{\mp}\pi^{\pm}$, $\bar{p}p$ decay channels. Exploiting common decay modes, it was possible to measure the mass difference between J/ψ and η_c, Fig. 3.19 (left) shows the invariant mass distribution of decay products from $B \to K + X$ in the 2.75–3.2 GeV/c^2 region: J/ψ and η_c peaks are clearly visible. Fitting the distribution with a Breit–Wigner convoluted with a MonteCarlo generated resolution function, it was possible to extract a value of 2979.6±2.3±1.6 MeV/c^2 for the mass , and a total width of 29±8±6 MeV (from a sample of 182±25 events, out of 31.3 M $B\bar{B}$ pairs). The systematic errors include the effect of varying the bin size as well as the shape of background, and the difference between data and MC generated detector resolutions.

The $K^0_S K^{\mp}\pi^{\pm}$ final state is an ideal place to look for the $\eta_c(2S)$, a state which was awaiting confirmation since its first and only observation by Crystal Ball in the inclusive photon spectrum from $\psi\,'$ decays. In 2002, the Belle collaboration reported the evidence of $\eta_c(2S)$ production via the exclusive processes $B^+{\to}K^+\eta_c(2S)$ and $B^0{\to}K^0_S\eta_c(2S)$. Given the suppression of the $\psi\,'{\to}K_S K^{\pm}\pi^{\mp}$ decay, contamination from the process $B{\to}K\psi\,'$ is estimated to be negligible. The first evidence [207] of the $\eta_c(2S)$ came from a sample of 44.8M$B\bar{B}$ pairs, using the exclusive channel $B{\to}K(K^0_S K^-\pi^+)$. A likelihood function based on the angle between the B candidate and the e^+e^- axis, and on the transverse momenta of the other tracks with the respect to the B candidate thrust axis, was used to suppress any background from continuum processes. Given a good B candidate, the feeddown from $B{\to}D(D_s) + X$ was reduced by cutting at $|M_{K\pi} - M_D| > 10\,\text{MeV}/c^2$ and $|M_{K_S K^+} - M_{D_s}| > 10\,\text{MeV}/c^2$; the feeddown from $B{\to}K^* + X$ was reduced by cutting at $|M_{K\pi} - M_{K^*}| > 50\,\text{MeV}/c^2$, as the $\eta_c(nS){\to}KK^*$ component is expected to be suppressed by the angular momentum barrier. The mass for the $\eta_c(2S)$ was measured to be 3654±6±8 MeV/c^2, with systematic error coming mostly from the choice of binning. A 90%C.L. upper limit on the width at 55 MeV was given.

7.1.4 η_c(1S) in $\gamma\gamma$ fusion

The e^+e^- collider detectors collecting data in the $\Upsilon(4S)$ region (CLEO, BaBar, BELLE) have good "reach" to produce $C = +1$ charmonium states through two-photon fusion. These are states such as
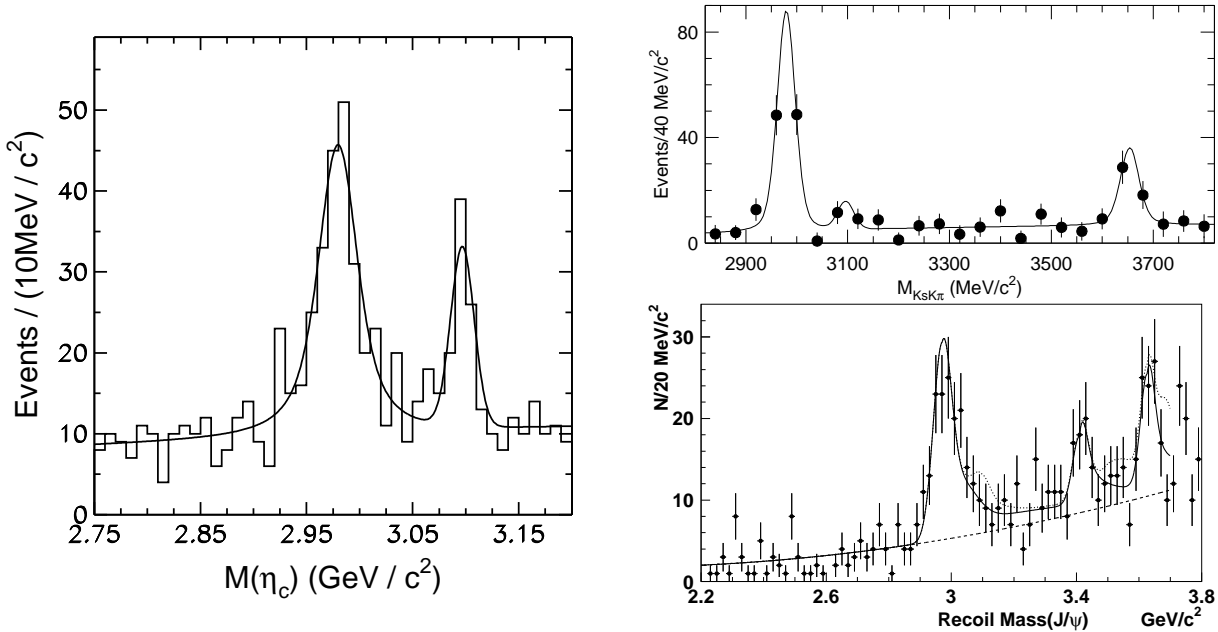
Fig. 3.19: On the left: distribution of reconstructed B decays to $\eta_c(1S)$ and J/ψ, in the common final state $K_S^0 K^{\mp} \pi^{\pm}$, from refs. [393]. On the right: Belle observed the $\eta_c(2S)$ both in B decays (top, from ref. [207]) and in double $c\bar{c}$ (bottom, from ref. [394]).

the η_c and χ_c which are not produced directly in the e^+e^- annihilation process. Such $\gamma\gamma$ interactions strongly peak at low q^2 so that the scattered lepton are not detected ("untagged" events) and the photons are approximately real. For instance, in CLEO the active detector elements go to within $22°$ of the beam axis, or $|\cos\theta| < 0.93$; this means that untagged events all have photons with Q^2 less than roughly 1 GeV^2, and usually *much* less.[36] Both CLEO and BaBar have thus recently studied the reactions:

$$\gamma\gamma \rightarrow (\eta_c/\eta_c') \rightarrow K_S^0 K^{\pm} \pi^{\mp} .$$

The η_c is known to be coupled to two photons ($\mathcal{B}(\eta_c \rightarrow \gamma\gamma) \sim 5 \cdot 10^{-4}$). An estimate of the two-photon production rate of $\eta_c(2S)$ suggests that also the radial excitation could be identified in the current e^+e^- B-factory [395]. The regions of the detector acceptance occupied by such $\gamma\gamma$ fusion reactions and the competing initial state radiation (ISR for short, also called "radiative return") processes are quite dissimilar for a symmetric collider experiment such as CLEO and the asymmetric B-factories. Given this and the differing sources of systematic uncertainties, the BaBar and CLEO results are rather independent.

The CLEO analysis used ≈ 14 fb^{-1} and ≈ 13 fb^{-1} of data taken with the CLEO II and CLEO III detectors, respectively, mostly near the $\Upsilon(4S)$ resonance. The particle identification systems and tracking chambers in these two configurations are quite different, so these can be considered truly independent experiments. The preliminary results were first shown at the April 2003 APS meeting and submitted [387] to the EPS meeting of that summer; final results have recently been submitted for publication [388]. The BaBar collaboration has both preliminary [210] and final results [389], based on a sample of data corresponding to an integrated luminosity of about 90 fb^{-1}. In the CLEO analysis, these events are characterized by lots of missing energy and momentum, but very little transverse momentum (p_T) of the hadronic system and very little excess energy in the detectors. The selection criteria included that $p_T < 0.6$ GeV$/c$, that there were no additional charged tracks, and that the unassociated energy in the electromagnetic calorimeter was less than 200 MeV (300 MeV) for CLEO II (CLEO III). The CLEO mass spectra are shown in Fig. 3.20(a,b) , clearly indicating evidence for both the η_c and η_c'. Fits to

---

[36]The one published *tagged* CLEO analysis started at $Q^2 = 1.5$GeV^2.

these spectra (polynomial backgrounds, Breit–Wigner line shapes, double-Gaussian detector resolution functions) yielded the results shown in Table 3.18.

In the BaBar analysis, events are selected by requiring four charged particles with total transverse momentum $p_T < 0.5$ GeV/c and total energy in the laboratory frame $E_{tot} < 9$ GeV, in order to suppress $e^+e^- \to q\bar{q}$ events. One track is required to be identified as a kaon and pairs of oppositely charged tracks are used to reconstruct $K_S^0 \to \pi^+\pi^-$ decays. The $K_S^0 K^+\pi^-$ vertex is fitted, with the K_S^0 mass constrained to the world average value.

Figure 3.20 (c) shows the resulting $K_S^0 K^+\pi^-$ invariant mass spectrum. The presence of a peak at the J/ψ mass is due to ISR events, where a photon is emitted in the initial state, and a backward-going J/ψ is produced, its decay products falling into the detector acceptance because of the Lorentz boost of the centre of mass. A fit to this distribution with a sum of a smooth background shape, a Gaussian function for the J/ψ peak and the convolution of a non-relativistic Breit–Wigner shape with a Gaussian resolution function for the η_c peak, gives: $m(J/\psi) - m(\eta_c) = (114.4 \pm 1.1)$ MeV/c^2, $m(J/\psi) = (3093.6 \pm 0.8)$ MeV/c^2, $\Gamma(\eta_c) = (34.3 \pm 2.3$ MeV/$c^2)$, $\sigma(J/\psi) = (7.6 \pm 0.8)$ MeV/c^2. The numbers of η_c and J/ψ events are respectively 2547 ± 90 and 358 ± 33.

The results from B-factories can be compared in Table 3.19.

For CLEO, the three major sources of systematic uncertainty in the masses of these singlets are (i) comparisons of masses of the K_S^0 (in $\pi^+\pi^-$), the D^0 (in $K_S^0\pi^+\pi^-$), and the D^+ (in $K^+\pi^+\pi^-$) between CLEO data and the Particle Data Group compilations, (ii) dependences on fitting shapes used for background and for signal, and (iii) the observed shifts between mass values used as input to the Monte Carlo simulations and the mass values reconstructed. In obtaining the widths of these mesons, the dominant source of possible bias is the shape assumed for the background.

In BaBar, the η_c mass resolution $\sigma(\eta_c)$ is constrained by the close J/ψ peak; the small difference (0.8 MeV/c^2) observed between $\sigma(J/\psi)$ and $\sigma(\eta_c)$ in the simulation is taken into account in the fit to data. The simulation is also used to check for possible bias in the fitted masses. The η_c and J/ψ mass peaks are shifted by the same amount (1.1 MeV/c^2) in the simulation, therefore the bias does not affect the mass difference. The systematic error on the mass accounts for an uncertainty on $m(J/\psi) - m(\eta_c)$ due to the background subtraction, and for an uncertainty associated to the different angular distributions of the J/ψ and the η_c. The systematic error on the width is dominated by the uncertainty in the background-subtraction and in the mass resolution.

7.1.5 Overview on all results

Table 3.20 and Figs. 3.21 and 3.22 summarize the results of an attempt to fit the mass of the $\eta_c(1S)$ by using (a) all measurements quoted in this review, (b) only measurements published in the last 5 years, and results from (c) $\psi(1, 2S)$ decays, (d) $p\bar{p}$ annihilation, (e) B-factories. The only *rationale* for dataset (b) is to exclude samples that were superseded by new data taken by the same experiment. A scale factor S was applied on the σ's whenever the confidence level of the χ^2 obtained from the fits was below 10%. The results are then compared with the values found in PDG 2004. The B-factories have been arbitrarily grouped together, despite they use different techniques.

Despite the substantial improvement in statistics, and the new ways to explore the $\eta_c(nS)$ states which came from the B-factories, a discrepancy between results obtained by different techniques remains. The increase in statistics has been surely beneficial in understanding systematic effects. Nonetheless, crosschecks between all different measurement techniques will be even more vital in the future, when statistic errors will be further reduced. Hopefully both asymmetric B-factories will be able to do internal crosschecks of the results from $\gamma\gamma$ fusion and from B-decays. CLEO-c will be able to crosscheck the $\gamma\gamma$ measurement by CLEO III with one from $\psi(1, 2S)$ decays.
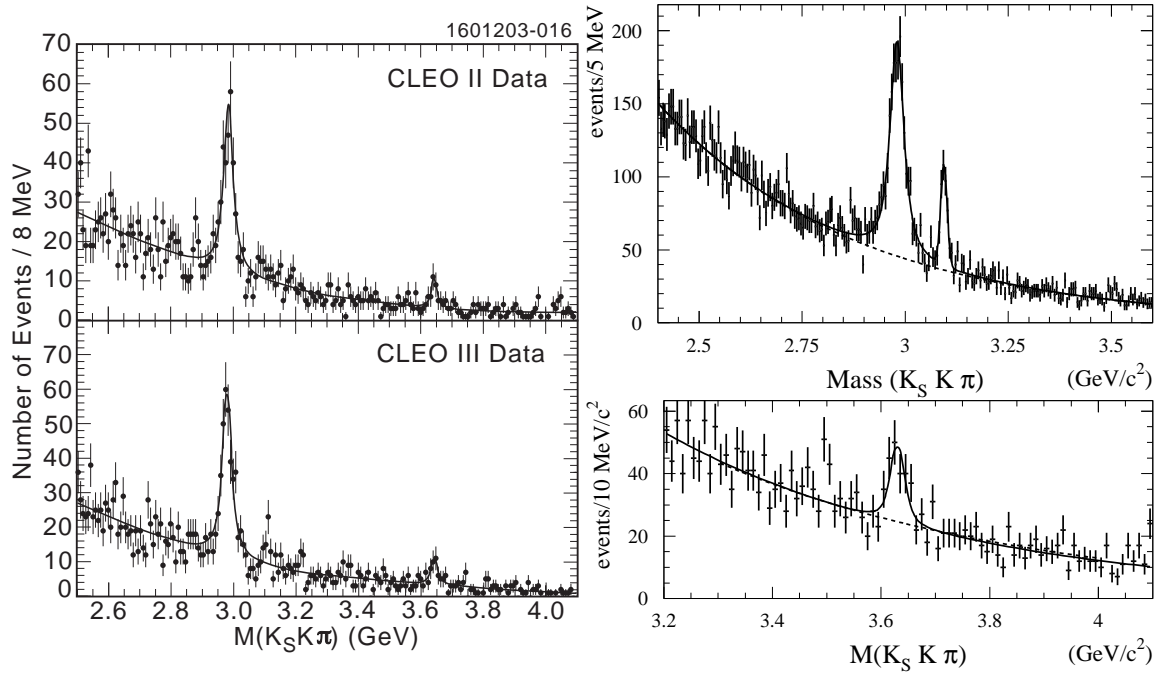
Fig. 3.20: Invariant mass distributions for $K_S^0 K^{\pm}\pi^{\mp}$ events from (a) CLEO II, (b) CLEO III; from BaBarin the (c) η_c (and J/ψ) region and (d) $\eta_c(2S)$region. The results from the fit are superimposed.
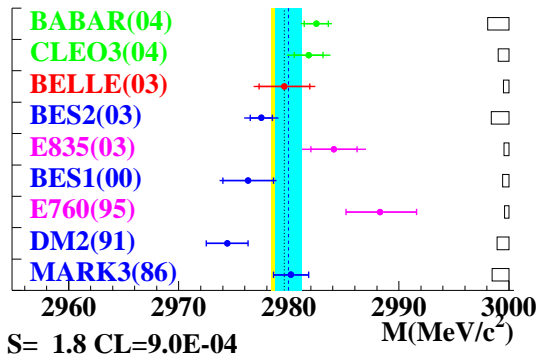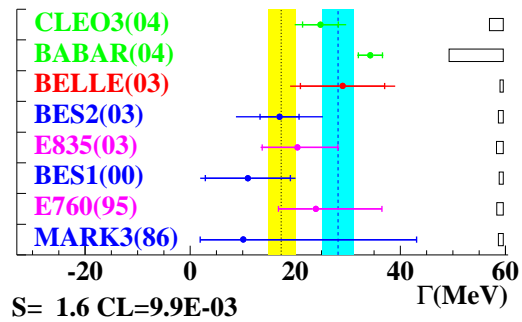
Fig. 3.21: Mass and width fits for $\eta_c(1S)$
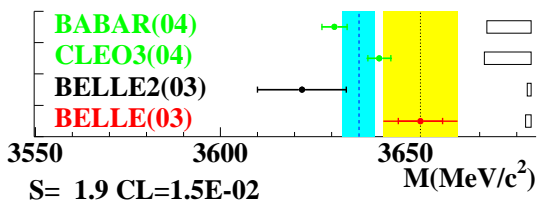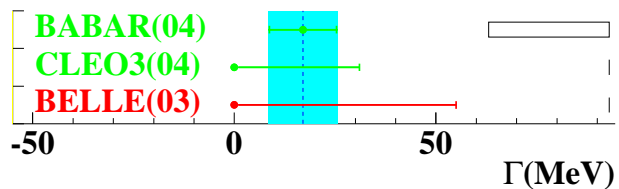
Fig. 3.22: Mass and width fits for $\eta_c(2S)$

Table 3.17: Various theoretical estimates for the mass splitting $\Delta m = m(\Upsilon) - m(\eta_b)$.

	Δm [MeV/c^2]			Ref
lattice NRQCD	19	–	100	[53, 406–410]
lattice potential	60	–	110	[411]
pQCD	36	–	55	[93, 412]
$1/m$ expansion	34	–	114	[413]
potential model	57	–	141	[414] [415–418]

Table 3.18: Summary of the results for η_c and η_c' for both CLEO II and CLEO III data sets. The errors shown are statistical only.

	CLEO II		CLEO III	
	η_c	η_c'	η_c	η_c'
Yield (events)	282±30	28^{+13}_{-10}	310 ±29	33^{+14}_{-11}
Mass (MeV)	2984.2±2.0	3642.4±4.4	2980.0±1.7	3643.4±4.3
Width (MeV)	24.7±5.1	3.9±18.0	24.8±4.5	8.4 ±17.1
significance	15.1σ	4.4σ	17.0σ	4.8σ
$R(\eta_c'/\eta_c)$	0.17±0.07		0.19±0.08	

Table 3.19: Comparison of CLEO, BaBar and Belle results.

Expt.	CLEO	BaBar	Belle
Ldt(fb^{-1})	13+14	90	29.1 [393], 31.3 [207]
$m(\eta_c)$(MeV/c^2)	2981.8 ±1.3 ±1.5	2982.5 ±1.1 ±0.9	2979.6 ±2.3 ±1.6 [393]
$\Gamma(\eta_c)$ (MeV)	24.8 ±3.4 ±3.5	34.3 ±2.3 ±0.9	29 ±8 ±6 [393]
$m(\eta_c(2S))$(MeV/c^2)	3642.9 ±3.1 ±1.5	3630.8 ±3.4 ±1.0	3654 ±6 ±8 [207]
$\Gamma(\eta_c(2S))$ (MeV)	<31 (90%CL)	17.0 ±8.3 ±2.5	<55 (90%CL) [207]

Table 3.20: Fits of all η_c mass measurements

Dataset	Mass(MeV/c^2)	S	C.L.
(a) ALL	2980.0 ±1.2	1.82	0.09%
(b) ALL after 1999	2980.4 ±1.2	1.44	6.6%
(c) $\psi(1, 2S)$ decays	2977.5 ±0.9	1(1.38)	13%
(d) $p\bar{p}$	2984.5 ±1.6	1(1.05)	33%
(e) B-factories	2981.9 ±1.1	1(0.65)	65%
PDG 2004	2979.6 ±1.2	1.7	0.1%

7.2 η_b(nS) and h_b(nP): searches[37]

Over twenty-five years after the discovery of the $\Upsilon(1S)$, no pseudoscalar $b\bar{b}$ states have been conclusively uncovered. In recent years, the search has been conducted at CLEO, LEP, and CDF, using both inclusive and exclusive methods.

The inclusive CLEO search [399] identifies distinctive single photons with its high-resolution CsI electromagnetic calorimeter. These photons are signatures of Υ radiative decays, in this case $\Upsilon(3S) \rightarrow \eta_b\gamma$, $\Upsilon(2S) \rightarrow \eta_b\gamma$, $\Upsilon(3S) \rightarrow \eta_b'\gamma$, and $\Upsilon(3S) \rightarrow h_b\pi^0$ or $h_b\pi^+\pi^-$ followed by $h_b \rightarrow \eta_b\gamma$. Godfrey and Rosner have pointed out that these hindered M1 transitions could have observable branching ratios, in spite of their small associated matrix elements, because of their large phase space [204].

No evidence of a signal for any of the above modes has been seen in the total 2.4 fb^{-1} of data taken at the $\Upsilon(2S)$ and $\Upsilon(3S)$ resonances between 2001 and 2002, corresponding to roughly six million decays of each resonance. Figure 3.23 shows the resulting 90% C.L. upper limits on the branching fractions. Several of the theoretical predictions shown can be ruled out.

It has been shown that with the full data samples of LEP 2, the $\eta_b(1S)$ might be detected in two-photon events [404,405]. The η_b is fully reconstructed with four, six, or eight charged decay products and possibly a π^0. In the expected mass range, for which estimates are listed in Table 3.17, the corresponding invariant mass distribution is rapidly decreasing, and the background from τ pairs can be kept small.

Table 3.21 summarizes the results for ALEPH, L3, and DELPHI. The search by ALEPH [419] in an 800 MeV/c^2 window turned up one candidate, shown in Fig. 3.24, with an excellent mass resolution of 30 MeV/c^2 at a mass of 9.30 ± 0.03 GeV/c^2. The signal expectation is about 1.6 events over one background event.

Table 3.21: 95% C.L. upper limits on the η_b two-photon partial width times branching ratio into various hadronic states from searches at LEP.

Expt	final state	$\Gamma_{\gamma\gamma} \times \mathcal{B}$ (keV)	Ref
ALEPH	4 charged	< 0.048	[419]
	6 charged	< 0.132	[419]
L3	$K^+K^-\pi^0$	< 2.83	[420]
	4 charged	< 0.21	[420]
	4 charged π^0	< 0.50	[420]
	6 charged	< 0.33	[420]
	6 charged π^0	< 5.50	[420]
	$\pi^+\pi^-\eta'$	< 3.00	[420]
DELPHI	4 charged	< 0.093	[421]
	6 charged	< 0.270	[421]
	8 charged	< 0.780	[421]

L3 has reported an analysis, considered close to final, in six decay modes [420]. Six candidates are found, compatible with an expected background of 2.5 events. The mass measurement is dominated by the detector resolution of about 300 MeV/c^2.

Recently, DELPHI has also reported preliminary results [421]. A total of seven candidates are found in a search window of 400 MeV/c^2. The expected background level is 5.5 events, and the mass resolution roughly 120 MeV/c^2.

---

[37]Authors: A. Böhrer, T. Ferguson, J. Tseng
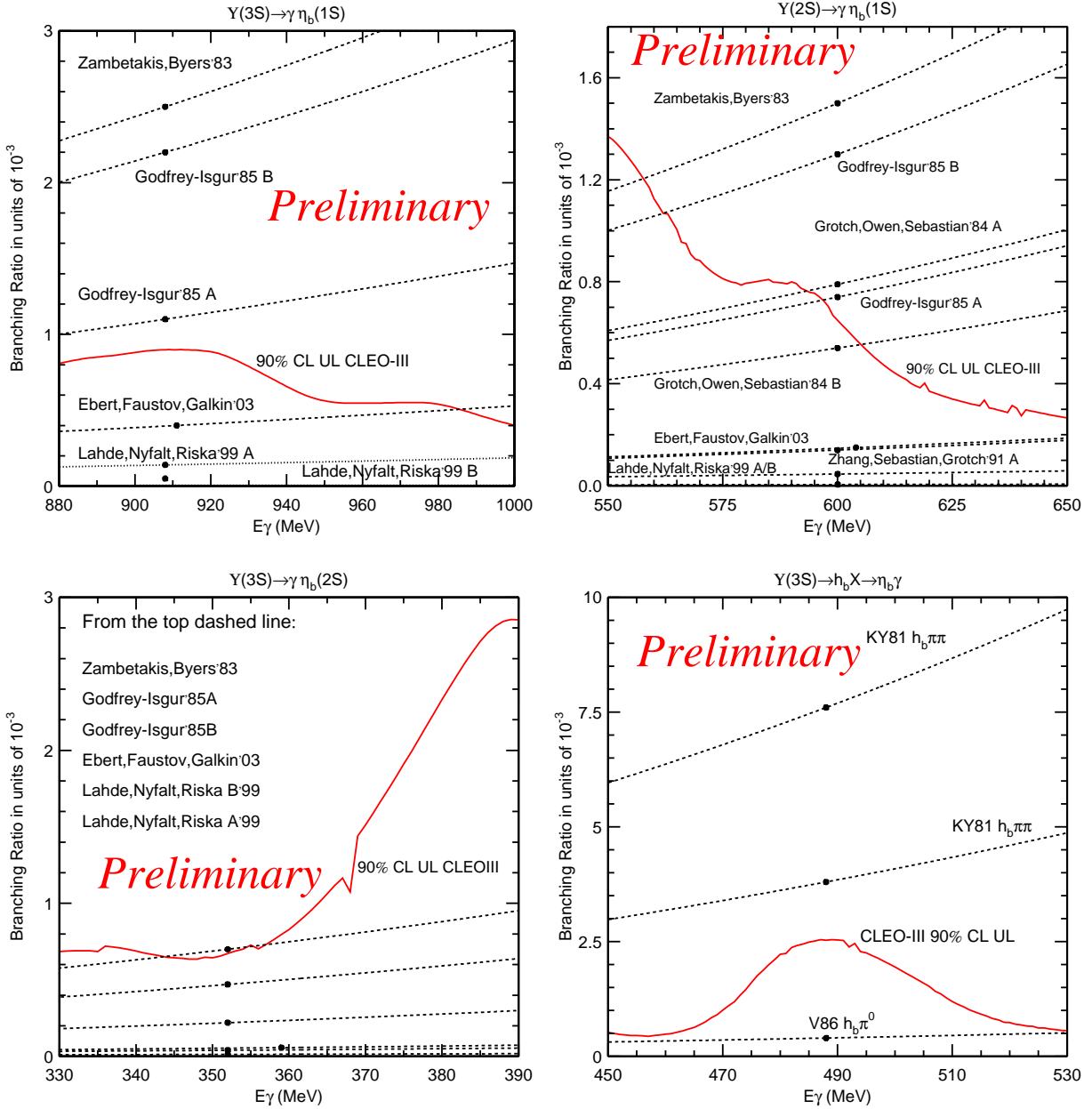
Fig. 3.23: CLEO 90% C.L. upper limits on $\mathcal{B}(\Upsilon(3S) \to \eta_b\gamma)$ (top left), $\mathcal{B}(\Upsilon(2S) \to \eta_b\gamma)$ (top right), $\mathcal{B}(\Upsilon(3S) \to \eta_b'\gamma)$ (bottom left), and $\mathcal{B}(\Upsilon(3S) \to h_b\pi^0, h_b\pi^+\pi^-) \times \mathcal{B}(h_b \to \eta_b\gamma)$ (bottom right) as a function of the photon energy E_γ, along with various theoretical predictions [206, 400–403].

Fig. 3.24: $\eta_b \to K^0_S K^- \pi^+ \pi^+ \pi^-$ candidate at ALEPH, with a reconstructed mass of 9.30 ± 0.03 GeV/c^2.
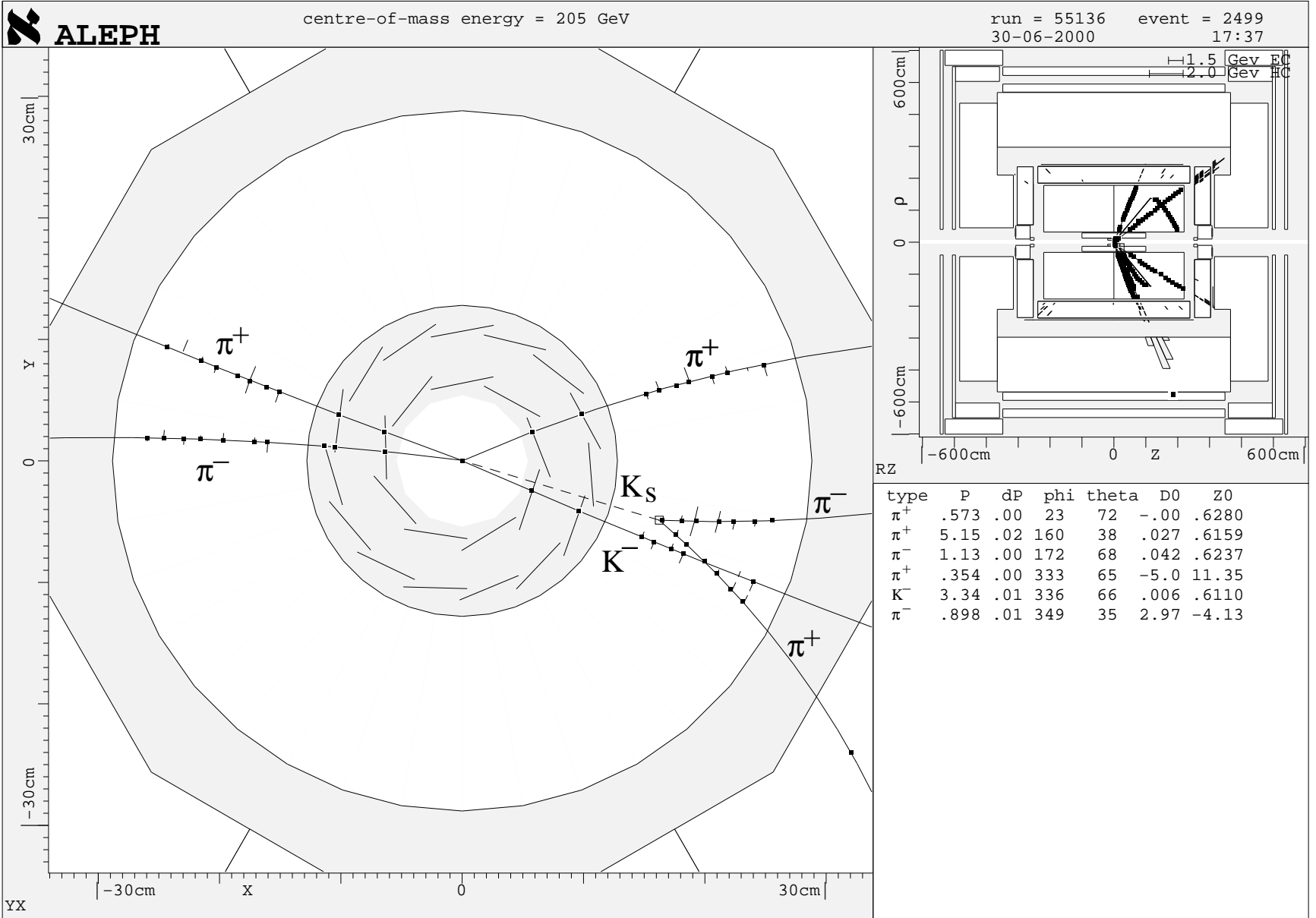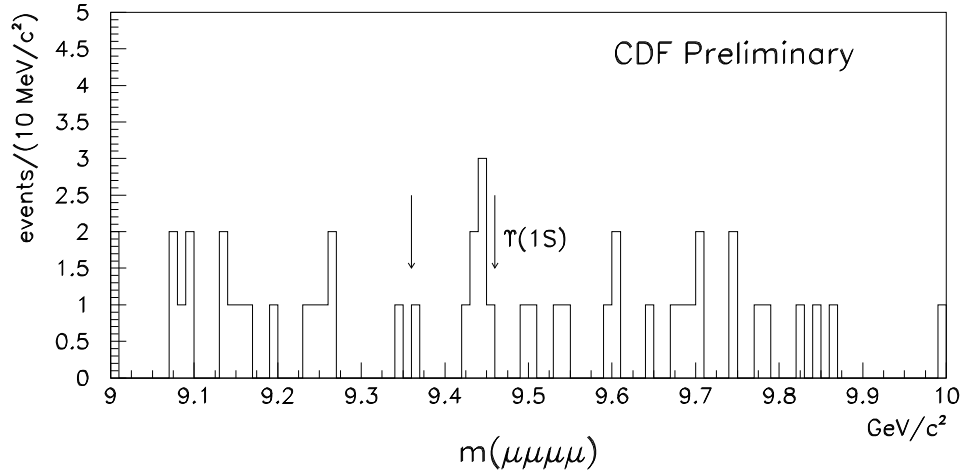
Fig. 3.25: The 4-muon invariant mass distribution from $J/\psi J/\psi$ events in CDF Run 1 data. The search window, the upper side of which is the world-averaged $\Upsilon(1S)$ mass [245], is marked by arrows.

CDF has searched for the exclusive decay $\eta_b \to J/\psi J/\psi$, where both J/ψ's decay to muon pairs, in the full 1992–96 "Run 1" data sample of about 100 pb^{-1} [422]. The mass spectrum is shown in Fig. 3.25; in this region, the mass resolution is about 10 MeV/c^2. A small cluster of seven events can be seen, where 1.8 events are expected from background. The statistical significance of the cluster is estimated to be 2.2σ. A simple fit to the mass distribution gives $9445 \pm 6(stat)$ MeV/c^2 as the mass of the cluster, where the error is only statistical. The mass difference relative to $\Upsilon(1S)$ is well to the low side of the theoretical expectation. If this cluster is due to η_b decay, then the product of its production cross-section and decay branching fractions is near the upper end of expectations [423].

The existence of the η_b is a solid prediction of the quark model, and its mass one of the most tractable to calculate. Both its existence and mass remain, for the present time, open questions. Some data at completed experiments remain to be published, however, while Run 2 is well underway at the Fermilab Tevatron.

7.3 h_c: searches[38]

The search of the singlet state of P wave charmonium (dubbed $h_c(1P)$) poses a unique experimental challenge for a variety of reasons:

- it cannot be resonantly produced in e^+e^- annihilation;
- it cannot be reached via E1 radiative transitions from ψ'; C-parity conservation forbids the transition from a 1^{--} to a 1^{+-} state.
- its production in ψ' hadronic decays to $h_c(1P)\pi^0$ is isospin violating and has a small phase space available (if $M_{h_c(1P)} = M_{COG}$, $p_{\pi^0} = 86$ MeV/c; the two Doppler broadened photons will have and energy between 30 and 100 MeV in the ψ' rest frame. In e^+e^- machines, the sensitivity on slow pions is not just affected by the physical backgrounds from other ψ' decays, but also by the large combinatorial background with low energy uncorrelated photons from the beam.
- its production in B decays via the intermediate state $\eta_c(2S)$, which can decay radiatively (E1) to $h_c(1P)$, is suppressed by the large hadronic width of the $\eta_c(2S)$.
- its detection in the $J/\psi\pi^0$ decay mode, from ψ' and B decays, as well as in hadroproduction, is shadowed by the more copious decay $\chi_{c1,2} \to \gamma J/\psi$, with an extra photon accidentally matching

---

[38] Authors: R. Mussa, D. Besson
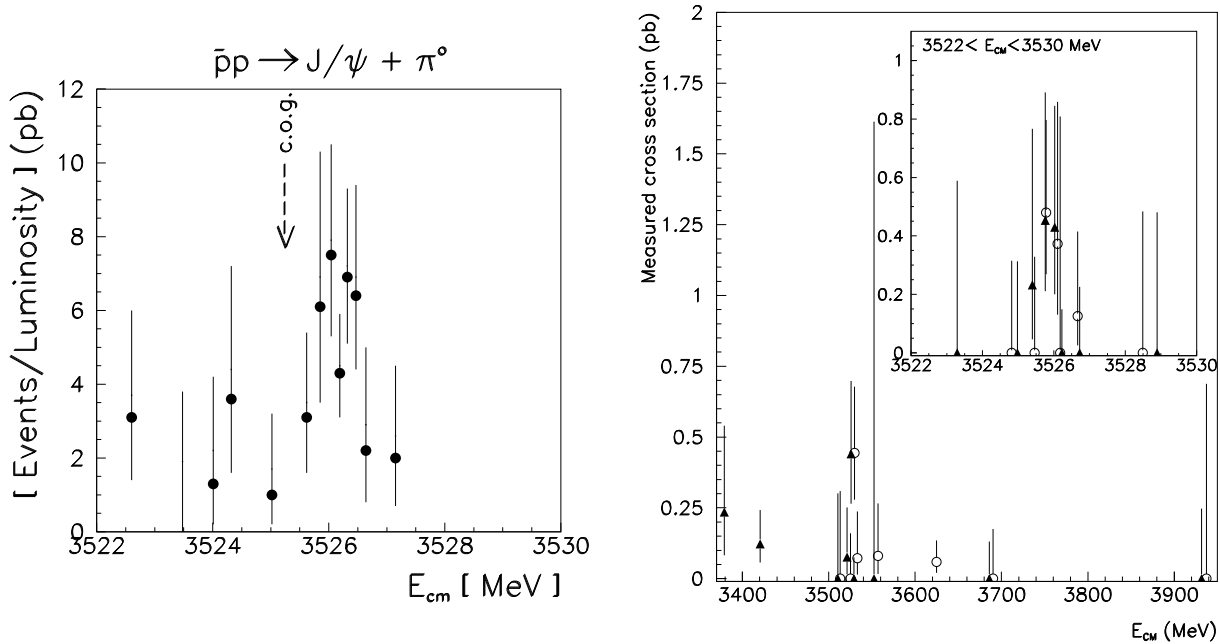
Fig. 3.26: Cross-section (black dots) observed by E760(left) for the reaction $p\bar{p}\to J/\psi\pi^0$ in the COG region; E835 could not confirm this evidence and observed the hint on the right in the $\gamma\eta_c\to 3\gamma$ channel.

the π^0 mass; this is also the most likely explanation of the signal seen in $J/\psi\pi^0$ by experiment E705, in 300 GeV/c $\pi^{\pm}$ and proton interactions on a lithium target [426].

– its formation in $p\bar{p}$ annihilation *may* be suppressed by helicity selection rule, but the same rule would forbid χ_{c0} and η_c formation , against the experimental evidence.

– its production in exclusive B decays *may* be suppressed as $\mathcal{B}(B\to\chi_{c0}K)$; if such selection mechanism does not apply, a search of $h_c(1P)$ via its E1 decay to η_c may soon give positive results.

Such elusive state was extensively searched for in formation from $p\bar{p}$ annihilations: searching for a resonance which has a width expected to be between the ψ and χ_{c1} but with an expected $\mathcal{B}$ to detectable EM decay channels of interests which is 100 to 1000 times weaker than the radiative decay of χ_{c1}, i.e., expected cross-sections between 1 and 10 picobarns. Experiment R704 at CERN [424] observed the signal:

$$\Gamma(h_c(1P)\to p\bar{p}) \times \mathcal{B}(h_c(1P)\to J/\psi + X) \times \mathcal{B}(J/\psi\to e^+e^-) = 0.14^{+0.15}_{-0.06} \text{ eV}$$

at a nominal mass of 3525.4±0.8±0.5 , which should be shifted down 0.8 MeV/c^2 after comparing the χ_c measurements done by the two experiments.

Experiment E760 at Fermilab [425] observed the signal:

$$\Gamma(h_c(1P)\to p\bar{p}) \times \mathcal{B}(h_c(1P)\to J/\psi + \pi^0) \times \mathcal{B}(J/\psi\to e^+e^-) = 0.010 \pm 0.003 \text{ eV}$$

at a nominal mass of 3526.2 ± 0.15, and did not see events in the channels $J/\psi\pi^+\pi^-, J/\psi\pi^0\pi^0$ E760 also determined a level of continuum for the inclusive reaction which was consistent with the one observed by R704.

In channels with such low statistics, a large amount of integrated luminosity taken to precisely quantify the background level is crucial. Such an issue was taken very seriously in E760, and even more in E835. To complicate the experimental situation, the signal observed by E760 is expected to be comparable to the $J/\psi\pi^0$ continuum, as predicted in reference [427], from soft pion radiation. It is hard to predict how interference between the resonant and continuum amplitude can distort the lineshape.

E835 took 6 times more data with respect to E760, to confirm the observation of $h_c(1P)$ and possibly measure the width as well as its decay ratios to other channels:the probably dominant decay mode to $\eta_c\gamma$ was studied, relying upon the rare η_c decays to $\gamma\gamma$. The first data set, 50 pb^{-1} taken in 1996, proved lately to be affected by an anomaly in the beam positioning system, which prevented to determine the absolute energy calibration of the machine better than 200 KeV. A second data taking period in year 2000 allowed to accumulate a comparable sample of data, but with 150 KeV resolution on the CM energy determination.

The E835 experiment, despite the 6 times larger statistics, could not confirm the $J/\psi\pi^0$ evidence observed by E760. On the other side, a hint of a signal is observed in the 3γ channel [428] Very tight cuts were applied in order to reject hadronic backgrounds from reactions with two neutral mesons in the final state. In the 3γ Dalitz plot, invariant masses of all pairs were requested to be above 1 GeV/c^2, to reject backgrounds from $\pi^0, \eta, \eta', \omega$. As the recoil photon angular distribution is expected to behave as $\sin\theta_{CM}^2$ on the resonance, a cut at $\cos\theta_{CM} < 0.5$ was imposed. This allowed to suppress most of the two meson background, which is prevalently forward-backward peaked. 13 events out of 29 pb^{-1} are observed in a $\delta M = 0.5\,\mathrm{MeV}/c^2$ wide bin between 3.5257 and 3.5262 MeV/c^2, while 3 events are observed in the remaining data between the χ_{c1} and the χ_{c2} (87 pb^{-1}). The statistical significance of the excess is between 1 and 3×10^{-3}, with different hypotheses on the resonance width. If the excess is not a statistical fluctuation, assuming a total width of 0.5 MeV, it is possible to measure $\Gamma(h_c\to p\bar{p})\mathcal{B}(h_c\to\eta_c\gamma) = 10.4\pm 3.7 \pm 3.4\,\mathrm{eV}$, where the systematic error comes from the statistical error on $\mathcal{B}(\eta_c\to\gamma\gamma)$), at a mass $M(h_c) = 3525.8 \pm 0.2 \pm 0.2\,\mathrm{MeV}/c^2$. The CLEO Collaboration has preliminary evidence [429] for the spin singlet h_c (1^1P_1) in looking at $\sim 3\times10^6$ decays of the $\psi'(3686)$. This state is seen in two independent analyses, both of which use the decay chain $\psi'\to\pi^0 h_c$ followed by $h_c\to\gamma\eta_c$: one analysis is *in*clusive and the other uses six dominant *ex*clusive decays of the η_c.

The inclusive analysis shows an enhancement at over 3σ significance at a mass of $3524.4 \pm 0.7_{stat}$ MeV. The systematic uncertainty is ~ 1 MeV. The left plot in Fig. 3.27 shows the fit of the data to the resolution function from Monte Carlo simulation and an "ARGUS" background shape.

Shown in the right panel of that figure is the exclusive analysis, with a statistical significance of $\sim 5\sigma$. The figure shows the data with, again, a fit to an ARGUS background and detector resolution function. Also shown are the events from the sideband of the invariant mass spectrum of the η_c reconstruction and the spectrum from a ψ' Monte Carlo simulation that does not include the h_c decay chain. Further checks on backgrounds peaking in the signal region are under way. The mass from the exclusive analysis is $3524.4 \pm 0.9_{stat}$ Mev, with systematic studies ongoing. All of these CLEO results on the h_c are considered preliminary. As a final remark, we can comment that the 20 years old search for this state is not over yet, and its evidence is still weak. It is therefore necessary to (a) consolidate the evidence for such a state from either B or $\psi(2S)$ decays , (b) to measure its mass at better than 1–2 MeV, (c) to prove its coupling to $p\bar{p}$, before planning to precisely measure its mass, total width and partial widths in formation from $p\bar{p}$ annihilations.

8 STATES CLOSE TO OPEN FLAVOUR THRESHOLDS

8.1 R values between 3.7 and 5 GeV[39]

The R value to be discussed in this section is one of the most fundamental quantities in particle physics that is defined as,

$$R = \frac{\sigma(e^+e^- \to hadrons)}{\sigma(e^+e^- \to \mu^+\mu^-)} \tag{3.46}$$

R value is expected to be constant so long as the centre-of-mass (c.m.) energy E_{cm} does not overlap with resonances or the threshold of production of a new quark flavour. A thorough review of R

---

[39]Author: Z. Zhao
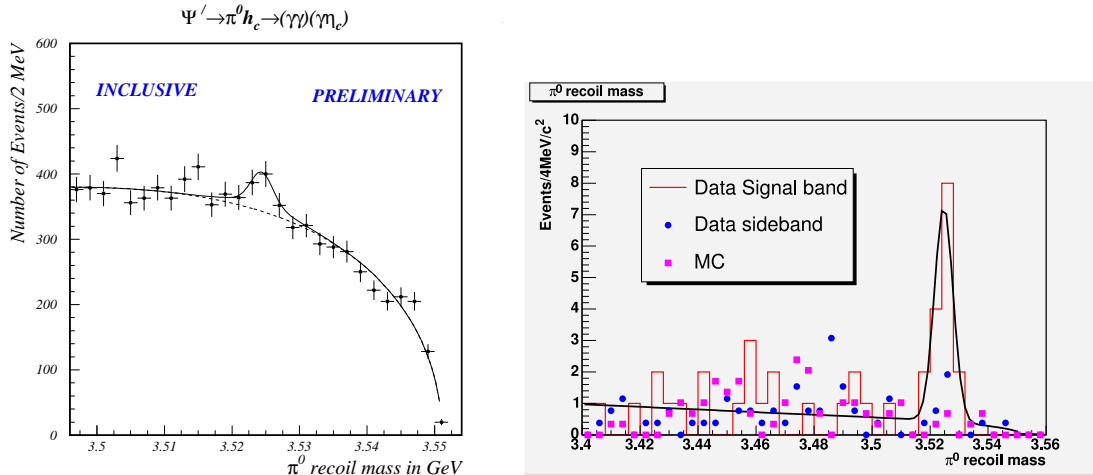
Fig. 3.27: The preliminary evidence from CLEO for the h_c singlet. On the left is the recoil mass spectrum against the π^0 in the *in*clusive analysis that only uses that pion and the photon in the $E1$ decay $h_c \rightarrow \gamma\eta_c$. To the right is the same variable for the *ex*clusive analysis in which six of the dominant η_c decay modes are used. In both cases the fits are to an ARGUS background and a resolution function from Monte Carlo studies. The exclusive plot also shows data events from the η_c sideband region and Monte Carlo simulation events of other ψ' decays.

measurements on the full energy range can be found in Chapter 6, while this subsection focuses on its complex structure in the energy region between 3.7 GeV and 5 GeV.

The most striking feature of the R values below 5 GeV is the complex structure in the energy region between 3.7 GeV and 4.5 GeV. Besides the resonance of $\psi(3770)$, broad resonance like structures peaking at around 4.04, 4.1 and 4.41 GeV have not been well understood in terms of their components and decay channels. These resonances near the charm threshold were observed more than 20 years ago [439–445, 447]. Table 3.22 lists the resonance parameters reported by these experiments.

8.1.1 PLUTO measurement between 3.1 and 4.8 GeV

The PLUTO Collaboration measured R values with the magnetic detector PLUTO at the e^+e^- storage ring DORIS between 3.1 and 4.8 GeV c.m. energy. A superconducting coil procedures a 2T magnetic field parallel to the beam axis. Inside coil there are 14 cylindrical proportional wire chambers and two lead converter, a 2 mm converter at radius 37.5 cm and a 9 mm converter at radius 59.4 cm. Two or more charged tracks are triggered and selected as hadronic event candidates. The background from beam–gas interaction and cosmic ray events is subtracted using the distribution of reconstructed event vertices alone the beam direction. Monte Carlo events are generated according to isotropic phase space to determine the detection efficiency for the hadronic events. An external luminosity monitor system is employed to observe the beam luminosity. The uncertainty of the luminosity measurement is about $\pm 5\%$. The systematic error in R values is estimated to be about 12%. PLUTO results agree with those of the SLAC–LBL group within systematic errors, but is about 10–15% lower than those of SLAC–LBL on the narrow J/ψ resonance and higher energies. However, the agreement on the energy dependence and the structure of the R values is quite good. The accuracy of PLUTO's measurement is limited by systematic error, which amount to almost one unit in R in the broad resonance region. The resonance parameters of the broad resonances cannot be determined with such a limited accuracy and energy points.

8.1.2 DASP measurement between 3.6 and 5.2 GeV

DASP Collaboration measured R values at c.m. energy between 3.6 and 5.2 GeV with a non magnetic inner detector of the double arm spectrometer DASP, which has similar trigger and detection efficiencies

Table 3.22: Resonance parameters measured for the broad structures between 3.7 and 4.5 GeV

Resonance	Experiment	Mass(MeV)	Γ_{tot}(MeV)	Γ_{ee}(eV)
$\psi(3770)$	MARK I	3772 ± 6	28 ± 8	345 ± 85
	DELCO	3770 ± 6	24 ± 5	180 ± 60
	MARK II	3764 ± 5	24 ± 5	276 ± 50
	BES([456])	3772.7 ± 1.6	24.4 ± 4.3	190 ± 25
$\psi(4040)$	DASP	4040 ± 10	52 ± 10	750 ± 150
	BES([456])	4050.4 ± 4.3	98.5 ± 12.8	1030 ± 110
	BES([246])	4040 ± 1	89 ± 6	911 ± 130
	CB([246])	4037 ± 2	85 ± 10	880 ± 110
$\psi(4160)$	DASP	4159 ± 20	78 ± 20	770 ± 230
	BES([456])	4166.5 ± 6.1	55.9 ± 12.3	370 ± 81
	BES([246])	4155 ± 5	107 ± 16	840 ± 130
	CB([246])	4151 ± 4	107 ± 10	830 ± 80
$\psi(4415)$	DASP	4417 ± 10	66 ± 15	490 ± 130
	MARK I	4414 ± 7	33 ± 10	440 ± 140
	BES([456])	4429.4 ± 8.5	86.0 ± 20.9	390 ± 74
	BES([246])	4429 ± 9	118 ± 35	640 ± 230
	CB([246])	4425 ± 6	119 ± 16	720 ± 110

for photon and charged particles. The inner detector of DASP is mounted between the two magnet arms of DASP. It is azimuthally divided into eight sectors, six of which consist of scintillation counters, proportional chambers, lead scintillator sandwiches and tube chambers, and the remaining two facing the magnet aperture, have only scintillation counter and proportional chambers. Tracks are recorded over solid angle of 62% for photon and 76% of 4π for charged particles. DASP collected a total integrated luminosity of 7500 nb^{-1}, which was determined by small angle Bhabha scattering measured by four identical hodoscopes with an uncertainty of 5%. The additional normalization uncertainty is estimated to be 15%. The uncertainties of the detection efficiencies for the hadronic events is about 12%. Three peaks centred around 4.04, 4.16 and 4.42 are observed. The data are insufficient to resolve structures between 3.7 and 4.5 GeV. By making a simplifying assumption that the cross-section can be described by an incoherent sum of Breit–Wigner resonances and a non resonant background, DASP reported resonance parameters as listed in Table 3.22.

8.1.3 *SLAC–LBL measurement between 2.6 and 7.8 GeV*

SLAC–LBL group did a R scan with MARK I at SPEAR which operated at c.m. energy between 2.6 and 7.8 GeV with peak luminosity between 10^{29} and 10^{31} cm^{-2} sec^{-1}. MARK I was a general purpose collider detector of the first generation. Its solenoidal magnet provide a near uniform magnetic field of 3891 ± 1 G over a volume 3.6 m long and 3.3 m in diameter. A pipe counter consisting of four hemicylindrical plastic counters surrounding the vacuum pipe were used to reduce the trigger rate of cosmic ray. Two sets of proportional wire chambers on the outside of the pipe counters had spacial resolution of 700 μm. Four modules of concertric cylindrical wire spark chambers were the main tracking elements of the detector, which gave a spacial resolution in the azimuthal direction of 340 μm, 1.0 and 0.5 cm for the 2^0 and 4^0 stereo gaps, respectively. Outside the spark chamber was an array of 48 plastic scintillation counters with a width of 20 cm each. The time-of-flight for this system was about 480 psec. An array of 24 shower counters made of five layers, each consisting of 0.64 cm of pilot F scintillator and 0.64 cm of lead. The energy resolution measured with Bhabha events was $\Delta E/E = 35\%/\sqrt{E}$. The

muon-identification spark chamber, the end-cap spark chamber, and the photon-detection capabilities of the shower counters were not used in this analysis. The R values and the corresponding resonance parameters in the energy region between 3.4 and 5.5 GeV is plotted together with those from PLUTO and DASP in Fig. 3.28 (right).

MARK I studied exclusive decay channels on the resonance at 4040 MeV and reported [446] $PsPs : PsV : VV = 0.05 \pm 0.03 : 1 : 32 \pm 12$, where Ps represents D meson and V stands for D^* meson. These early results stimulated a variety of theoretical interpretations.

8.1.4 BES measurement between 2 to 5 GeV

BES Collaboration has done a R scan with updated Beijing Spectrometer (BES II) at Beijing Electron–Positron Collider(BEPC).

The trigger efficiencies, measured by comparing the responses to different trigger requirements in R scan data and special runs taken at the J/ψ resonance, are determined to be 99.96%, 99.33% and 99.76% for Bhabha, dimuon and hadronic events, respectively.

BES's measurement first selects charged tracks, then hadronic events with charged tracks equal and greater than two. The number of hadronic events and the beam-associated background level are determined by fitting the distribution of event vertices along the beam direction with a Gaussian for real hadronic events and a polynomial of degree two for the background.

The subtraction of the beam-associated backgrounds is cross checked by applying the same hadronic event selection criteria to separated-beam data.

A new Monte Carlo event generator called LUARLW is developed together with LUND group for the determination of detection efficiencies of the hadronic events [450]. LUARLW removes the extreme-high-energy approximations used in JETSET's string fragmentation algorithm. The final states simulated in LUARLW are exclusive in contrast to JETSET, where they are inclusive. In addition, LUARLW uses fewer free parameters in the fragmentation function than JETSET. Above 3.77 GeV, the production of charmed mesons is included in the generator according to the Eichten Model [451, 452].

Different schemes for the radiative corrections were compared [355, 453–455]. Below charm threshold the four different schemes agree with each other to within 1%. Above charm threshold, where resonances are important, the agreement is within 1 to 3%. The formalism of Ref. [455] is used in our calculation, and differences between it and the schemes described in Ref. [355] are included in the systematic errors. In the calculation of the radiative correction above charm threshold, where the resonances are broad and where the total width of the resonance is related to the energy, we take the interference between resonances into account. The integrated luminosity is determined to a precision of 2–3% from the number of large-angle Bhabha events selectedusing only the BSC energy deposition. Figure 3.28 (right) shows the BES R scan results between 3.6 and 4.6 GeV.

Previously, BES Collaboration measured cross-section for charm meson production, using 22.3 pb^{-1} of e^+e^- data collected with BES I at $\sqrt{S}$=4.03 and 15 pb^{-1} at 4.14 GeV [460]. The charmed mesons used in this measurement are D^0 and D^+, of which the number of signal events are selected by fitting the inclusive $K^-\pi^+$ and $K^-\pi + \pi^+$ invariant mass distribution with Gaussian as signal plus a third order of polynomial background. Taking into account the detection efficiency, the correction of initial state radiation, and quote the corresponding braching ratio from PDG1998, BES reported their results as shown in Table 3.23, together with that predicted by the coupled channel model.

8.1.5 Remarks and prospects

DASP data agree with those of PLUTO resonabl well in shape but exceed their cross-sections by about half a unit in R above 4 GeV. In magnitude DASP's data are in closer agreement with those of SLAC–
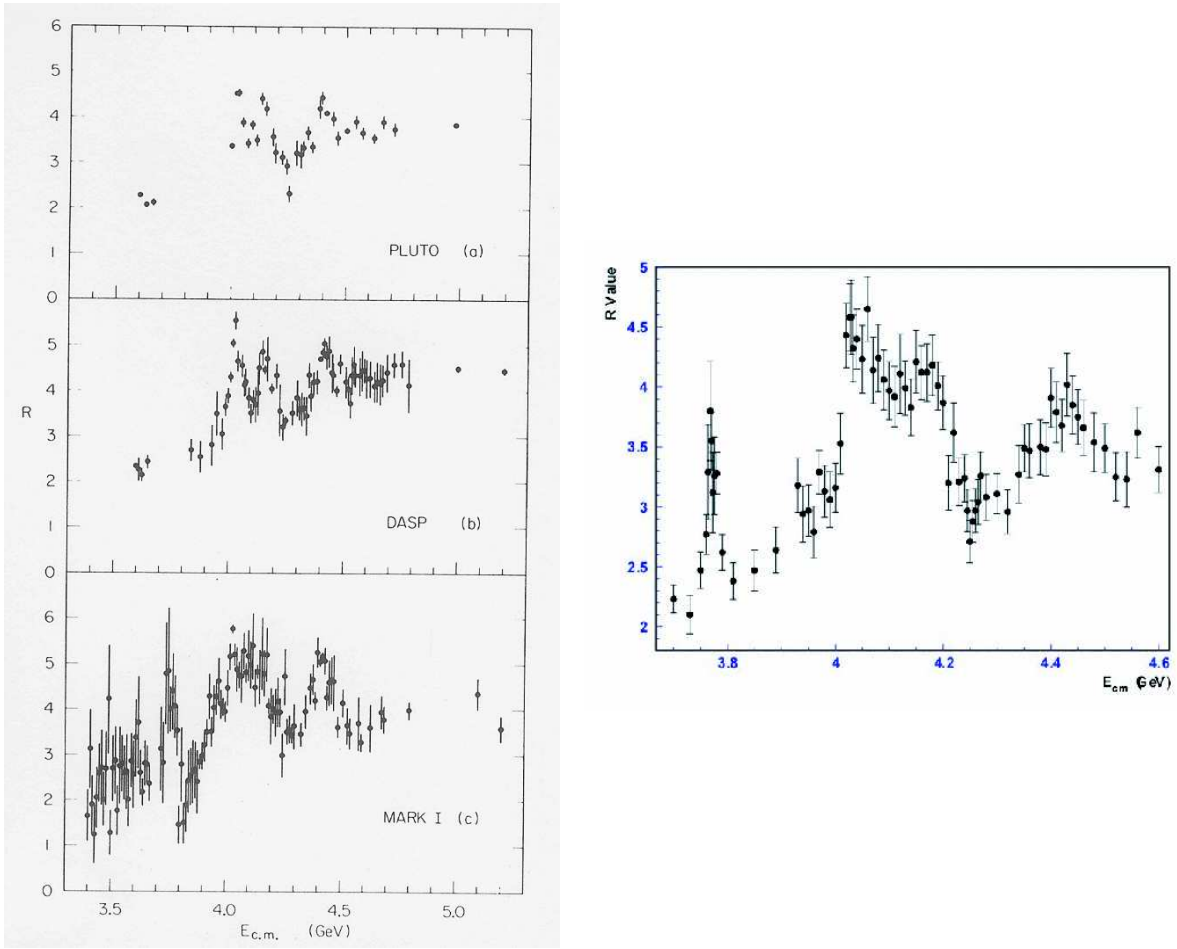
Fig. 3.28: R Values between 3.7 and 5 GeV from PLUTO, DASP and MARKI (left), and BES (right) experiments.

Table 3.23: Comparison of tree level cross-section measurement of BES with predictions of the coupled channel model. experimental D_s cross-section is taken from early work.

$\sqrt{s}$=4.03 GeV	Experiment	Coupled channel model
$\sigma_{D^0}+\sigma_{\bar{D}^0}$	19.9±0.6±2.3 nb	18.2 nb
$\sigma_{D^+}+\sigma_{D^-}$	6.5±0.2±0.8 nb	6.0 nb
$\sigma_{D_s^+}+\sigma_{D_s^-}$	0.81±0.16±0.27 nb	11.6 nb
σ_{charm}	13.6±0.3 ±1.5 nb	12.9 nb
$\sqrt{s}$=4.14 GeV	Experiment	Coupled channel model
$\sigma_{D^0} + \sigma_{\bar{D}^0}$	9.3±2.1±1.1 nb	15.1 nb
$\sigma_{D^+} + \sigma_{D^-}$	1.9±0.9±0.2 nb	4.5 nb
$\sigma_{D_s^+} + \sigma_{D_s^-}$	1.64± 0.39± 0.42 nb	1.85 nb
σ_{charm}	6.4±1.2±0.7 nb	10.7 nb

LBL but show some difference in the finer details of the energy dependence. For example, SLAC–LBL data didn't resolve the structure at 4.16 GeV. The total width measured by SLAC–LBL is smaller than that of DASP measurement. Despite of these discrepances, the difference observed among the three experiments are within the systmatic errors quoted.
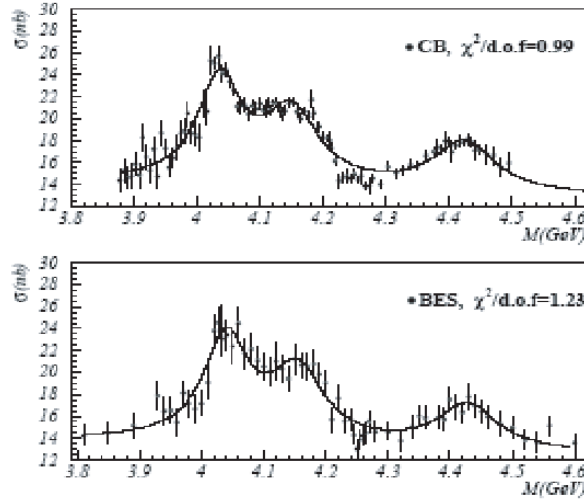
Fig. 3.29: Refit the R data of CB and BES II.

BES's R scan is done with a newer generation detector and e^+e^- collider as compared with the previous measurements, and has about 80 points in the energy region from 3.7 to 5 GeV. Because of this fine scan in this energy region that contributes most to the precision evaluation of $\alpha_{QED}(M_Z)$.

BES also fitted resonances as a Breit–Wigner shape with different continue background and takes into account the energy-dependence of resonance width and the coherence of the resonance [457]. BES's preliminary results are consistent with those of previous measurements for the peak positions at 3.77, 4.04, 4.16 and 4.42 GeV, and show larger Γ_{tot} of the resonances at 4.04 and 4.42 GeV and smaller Γ_{ee} of the resonaces at 3.77 and 4.16 GeV.

Fitting BES's R data between 3.7 and 4.6 GeV (75 data points) with Breit–Wigner resonances and none resonant background based on perturbative QCD [456], one obtain resonance parameters as listed in Table 3.22. The results from this fit has similar conclusion as the one from BES's, except that Γ_{tot} is no longer larger than the other measurements of the resonance at 4.42 GeV.

Recently, Kamal K. Seth refitted resonance parameters of the higher vector states of charmonium with existing R data [246]. Three Breit–Wigner resonances plus background that is parametrized with a linear function. He shows that the Crystal Ball (CB) and BES measurements are in excellent agreement. The analysis of the CB and BES data leads to consistent resonance parameters for the three vector resonances above the $D\bar{D}$ threshold. The masses of the three resonances determined by him in general agree with PDG, but have much smaller errors. However, the total widths of these three resonances determined by this work are about 67%, 37% and 179% larger than those adopted by PDG. The corresponding electron widths determined by this work are 23%, 8% and 51% larger with about a factor of 2 less errors. Figure 3.29 shows the fits to CB and BES data.

A factor of 2 to 3 reduction in uncertainty in the energy region of 3–5 GeV significantly improved the experimental situation, providing an opportunity to directly test QCD sum role where the notion of quark–hadron duality (QHD) plays a dominant role [456], and evaluate charm quark mass via experimental data to a precision below 10%. However, BES's data is still not enough, in terms of both statistics and systematic error restriction, to provide a clear picture of the broad resonance structures. To fully understand the complicated structures at the energies between 3.7 and 4.5 GeV, one needs to:

– perform the R scan with smaller energy steps and higher statistic in the entire energy region to a precision around 2–3%.
– collect data at the peak positions with high enough statistics to study the exclusive decay channels of the resonances.
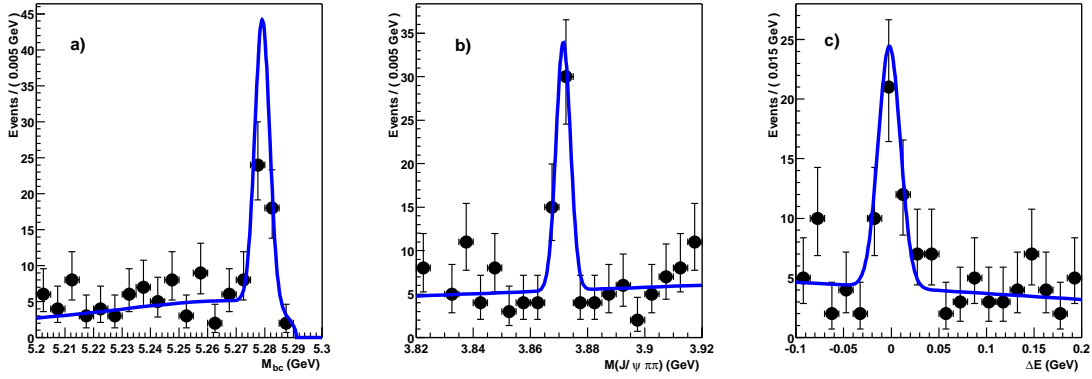
Fig. 3.30: From the Belle discovery paper [211]: projections of the data (points with error bars) and the results of an unbinned maximum likelihood fit (solid curve) for the $X(3872) \to \pi^+ \pi^- J/\psi$ signal region. The variables (a) beam-constrained mass $M_{bc} = \sqrt{E_{\text{beam}}^2 - p_B^2}$, (b) invariant mass $M_{\pi^+\pi^- J/\psi}$, and (c) energy difference $\Delta E = E_B - E_{\text{beam}}$, are those used in the fit; E_B and p_B are the energy and momentum of the $B^\pm \to K^\pm \pi^+ \pi^- J/\psi$ candidate, and E_{beam} the energy of either $e^\pm$ beam, in the $e^+ e^-$ centre-of-mass system.

These could be the important physics topics for CLEO-c at CESR-c and BES III at BEPC II [458, 459]. Both CLEO-c and BES III may have the ability to clarify the ambiguity that has been bothering physicists for over 20 years.

8.2 X(3872): discovery and interpretations[40]

The $X(3872)$ is a narrow state decaying into $\pi^+ \pi^- J/\psi$, with a mass $M_X \sim 3872\,\text{MeV}$. Given the observed final state and the observed mass, in the charmonium region, it is natural to assume that the $X(3872)$ is itself a charmonium state. It has however proved difficult to identify the $X(3872)$ with any of the expected narrow $c\bar{c}$ mesons, leading to suggestions that it may be a more exotic particle. In this section, we briefly review the discovery and known properties of the $X(3872)$, and the difficulties they create for its interpretation.

8.2.1 Discovery, confirmation, and properties

The $X(3872)$ was discovered by the Belle collaboration in a study of $B^\pm \to K^\pm \pi^+ \pi^- J/\psi$ decays [211]. In addition to the well-known ψ', a second peak was seen in the $M(\pi^+ \pi^- J/\psi)$ distribution; the results of an unbinned maximum likelihood fit to the $X(3872)$ signal region in M, and two other variables which peak in the case of $B^\pm \to K^\pm \pi^+ \pi^- J/\psi$ decay, are shown in Fig. 3.30. A yield of 35.7 ± 6.8 events was observed, with high significance (10.3σ), and the width of the mass peak was found to be consistent with the detector resolution. As the measured mass is well above the $D\overline{D}$ open charm threshold, the narrow width implies that decays to $D\overline{D}$ are forbidden; Belle [461] reports $\Gamma(X(3872) \to D\overline{D})/\Gamma(X(3872) \to \pi^+\pi^- J/\psi) < 7$ (90% CL), to be compared with a corresponding value > 160 for the $\psi(3770)$ [462]. Comparing decays via the $X(3872)$ to those via the ψ', Belle finds a considerable production rate in B decays, with product branching ratio

$$\frac{\mathcal{B}(B^+ \to K^+ X(3872)) \times \mathcal{B}(X(3872) \to \pi^+ \pi^- J/\psi)}{\mathcal{B}(B^+ \to K^+ \psi') \times \mathcal{B}(\psi' \to \pi^+ \pi^- J/\psi)} = 0.063 \pm 0.012\,(\text{stat}) \pm 0.007\,(\text{syst}). \quad (3.47)$$

The observation has been confirmed in inclusive $p\overline{p}$ collisions by CDF [463] and D0 [464], as shown in Fig. 3.31, and in exclusive B meson decays by BaBar [465], shown in Fig. 3.32. The observed masses

---

[40]Author: B. Yabsley
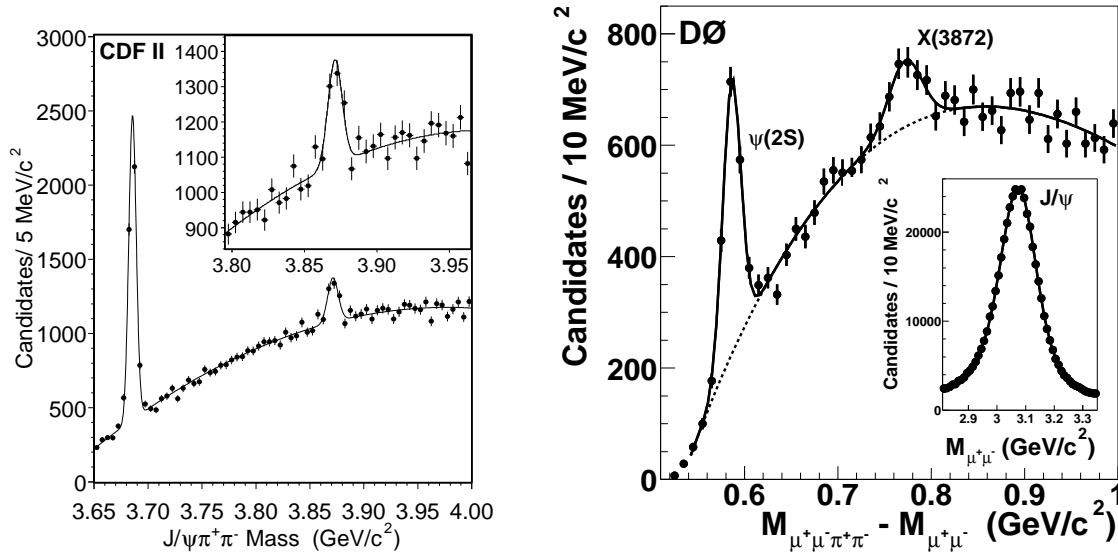
Fig. 3.31: Confirmation of the $X(3872)$ in inclusive $p\overline{p}$ collisions by CDF [463] (left) and D0 [464] (right). In each case peaks due to ψ' and $X(3872)\rightarrow\pi^+\pi^- J/\psi$ can be clearly seen; the insets show (left) an enlargement of the $X(3872)$ region and (right) the mass distribution for the $J/\psi\rightarrow\mu^+\mu^-$ candidates used in the analysis.

are consistent, with a weighted average value

$$M_X = (3871.9 \pm 0.5)\,\text{MeV} \tag{3.48}$$

across the four experiments [211,463–465]. Each of CDF, D0, and BaBar likewise find a width consistent with the detector resolution; the only limit is that inferred by Belle [211],

$$\Gamma_X < 2.3\,\text{MeV (90\% CL)}. \tag{3.49}$$

Belle finds a $M(\pi^+\pi^-)$ distribution concentrated at the kinematic boundary [211], coinciding with the ρ mass (Fig. 3.33). This is confirmed by CDF [463], who find little signal with $M(\pi^+\pi^-) < 500\,\text{MeV}$; BaBar report that their statistics are too small to allow a clear conclusion, but do not exclude a concentration at the boundary [465].

8.2.2 *Decay modes and interpretation of the $X(3872)$*

The Belle collaboration has performed searches for various decay modes [211, 466] and an angular distribution study [466], to compare $X(3872)$ properties with those of predicted, but so far unseen, charmonium states. They restrict their attention to states with

1. expected masses [401] within 200 MeV of $M_X \simeq 3872\,\text{MeV}$;
2. unnatural quantum numbers $J^P = 0^-$, 1^+, 2^-, ... since decays to $D\overline{D}$ are not seen; and
3. spin angular momentum $J < 3$, since the state is seen in exclusive $B\rightarrow K X(3872)$ production with a significant rate, making high J unlikely (*cf.* $B^+\rightarrow K^+\chi_{c2}$, still not observed, and $B^+\rightarrow K^+\chi_{c0}$ and $K^+\chi_{c1}$ with branching fractions $(6 \sim 7) \times 10^{-4}$).

The 1^3D_3 state, ψ_3, is also studied following suggestions [187,188] that the rate for $\psi_3\rightarrow D\overline{D}$, suppressed by an $L = 3$ angular momentum barrier, may be low.

The search therefore includes the $C = -1$ states ψ_2, h'_c, and ψ_3, and the $C = +1$ states η_{c2}, χ'_{c1}, and η''_c. The observation of decays to $\pi^+\pi^- J/\psi$ favors $C = -1$, for which this mode is isospin-conserving; this would imply $\Gamma(X\rightarrow\pi^0\pi^0 J/\psi) \simeq \frac{1}{2}\Gamma(X\rightarrow\pi^+\pi^- J/\psi)$. On the other hand, the observed
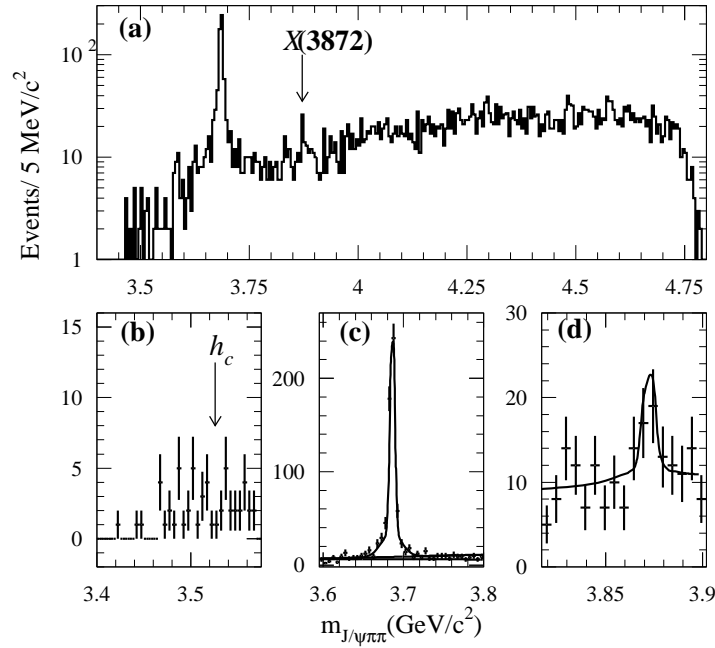
Fig. 3.32: Confirmation of the $X(3872)$ in $B^{\pm} \to K^{\pm} \pi^{+} \pi^{-} J/\psi$ decay from BaBar [465]. Distributions of the $\pi^{+}\pi^{-}J/\psi$ invariant mass are shown for B candidates in (a) the B-signal region, together with expanded views of the (b) h_c, (c) $\psi(2S)$, and (d) $X(3872)$ mass regions. In (c) and (d), the results of an unbinned maximum likelihood fit to the data are superimposed as a solid curve.
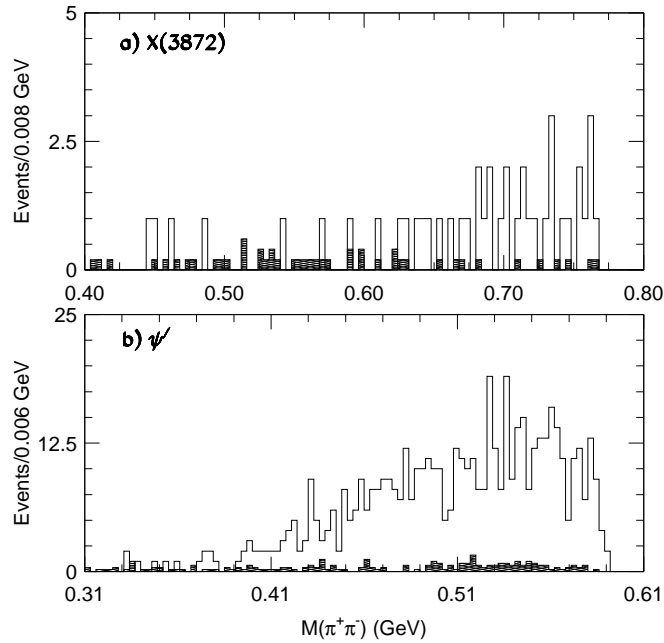
Fig. 3.33: From [211]: $M(\pi^{+}\pi^{-})$ distribution for events in the (a) $M(\pi^{+}\pi^{-}J/\psi) = 3872\,\text{MeV}$ signal region and (b) the ψ' region in Belle data. The shaded histograms are sideband data normalized to the signal-box area. Note the different horizontal scales.
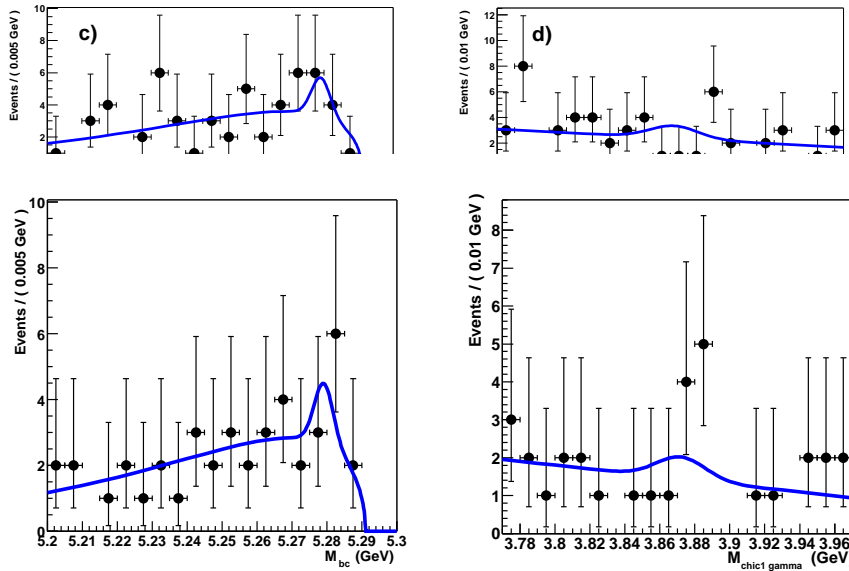
Fig. 3.34: (Upper plots) Signal band projections for the beam-constrained (B-candidate) mass M_{bc}, and charmonium candidate mass $M_{\gamma\chi_{c1}}$, in the Belle search for decays $B^+\to K^+X(3872)$, $X\to\gamma\chi_{c1}$ [211]; the results of an unbinned maximum likelihood fit are superimposed. The signal yield, $3.7\pm3.7\pm2.2$, is consistent with zero. (Lower plots) Similar distributions in the search for decays to $\gamma\chi_{c2}$ [466]; the fitted yield is $2.9\pm3.0\pm1.5$ events.

concentration of events at $M(\pi^+\pi^-)\approx m_\rho$ suggests that the decay may proceed via $X(3872)\to\rho J/\psi$, an isospin-violating process; this requires $C=+1$ and forbids the decay to $\pi^0\pi^0 J/\psi$. A study of the $\pi^0\pi^0 J/\psi$ final state is therefore important.

8.2.3   Searches for radiative decays

If the $X(3872)$ is identified with the 1^3D_2 (ψ_2) state, the decay to $\gamma\chi_{c1}$ is an allowed E1 transition with a large partial width, calculated to be $\Gamma(X\to\gamma\chi_{c1})\simeq210\,\mathrm{keV}$ in potential models, taking coupled channel effects into account [187, 188]. Similarly, the partial width for 1^3D_3 (ψ_3)$\to\gamma\chi_{c2}$ is calculated to be $\sim300\,\mathrm{keV}$. This is to be compared to the partial width for $\psi_{2,3}\to\pi^+\pi^- J/\psi$, expected to be equal to the $\psi(3770)$ partial width for both states. Ref. [466] conservatively assumes $\Gamma(\psi(3770)\to\pi^+\pi^- J/\psi)<130\,\mathrm{keV}$, leading to predictions $\Gamma(X\to\gamma\chi_{cJ})/\Gamma(X\to\pi^+\pi^- J/\psi)>1.6$ for $\psi_2\to\gamma\chi_{c1}$ and >2.3 for $\psi_3\to\gamma\chi_{c2}$ respectively. Belle has performed searches for $X(3872)$ decays to these final states (see Fig. 3.34), setting upper limits on the branching ratios (at 90% CL) of 0.89 for $\gamma\chi_{c1}$ [211], and 1.1 for $\gamma\chi_{c2}$ [466], below these expectations. Other considerations disfavor these states. If the X is the ψ_2, its separation from the $\psi(3770)$, $\Delta M=102\,\mathrm{MeV}$, is larger than present theory can accomodate [188]. The ψ_3 mass is expected to be similar. Production $B^+\to K^+\psi_3$ is also expected to be suppressed relative to other $K^+(c\bar{c})$ decays, due to the high spin $J=3$, whereas the data implies a comparable rate if $X(3872)=\psi_3$ [466].

Another radiative decay search, for $X(3872)\to\gamma J/\psi$, tests the $X(3872)=2^3P_1$ (χ'_{c1}) assignment [466]. The partial width $\Gamma(\chi'_{c1}\to\gamma J/\psi)$, for $M_{\chi'_{c1}}=3872\,\mathrm{MeV}$, is expected to be 11 KeV in the potential model [187], possibly reduced by coupled channel effects [188]. To estimate the partial width for the isospin-violating process $\chi'_{c1}\to\pi^+\pi^- J/\psi$, we take the isospin-violating hadronic charmonium transition $\psi'\to\pi^0 J/\psi$, with $\Gamma\simeq0.3\,\mathrm{keV}$: the ratio $\Gamma(X\to\gamma J/\psi)/\Gamma(X\to\pi^+\pi^- J/\psi)$ should then be $\mathcal{O}(10)$. The Belle search places an upper limit of 0.40 (90% CL) on this ratio, inconsistent with the expected value. The χ'_{c1} mass is predicted [187, 188] to be $3930\sim3990\,\mathrm{MeV}$ or greater, likewise inconsistent with the $X(3872)$.
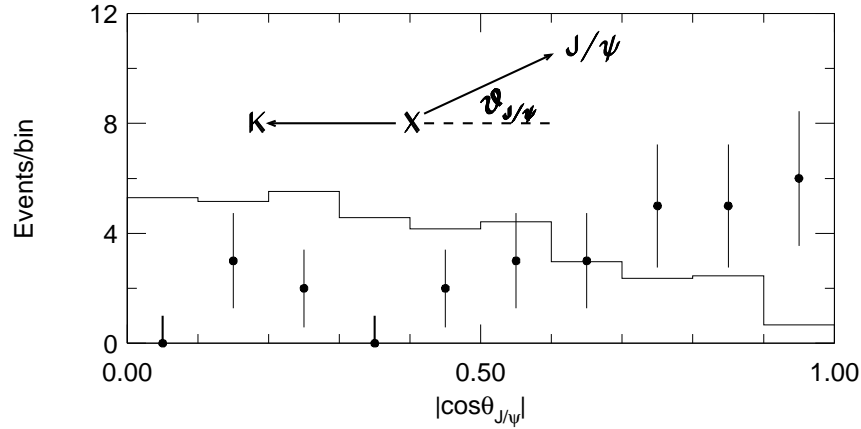
Fig. 3.35: From [466]: $|\cos^2 \theta_{J/\psi}|$ distribution for $X(3872)\to\pi^+\pi^- J/\psi$ events in the data (points with error bars), and assuming $J^{PC} = 1^{+-}$ in the Monte Carlo (histogram); background events, determined using sidebands, are included in the Monte Carlo.

8.2.4 *Studies of angular distributions*

The $X(3872)$ will be produced polarized in the reaction $B^\pm \to K^\pm X(3872)$ for any spin $J_X > 0$, as both the initial state B and the accompanying K mesons are spin zero. Angular distributions of the final state particles can therefore distinguish between different quantum number assignments J^{PC} for the $X(3872)$. If the X is the h_c', with $J^{PC} = 1^{+-}$, decays should be distributed as $(1 - \cos^2 \theta_{J/\psi})\mathrm{d}\cos\theta_{J/\psi}$ [467], where $\theta_{J/\psi}$ is the angle between the J/ψ and the negative of the K momentum vectors in the $X(3872)$ rest frame. In the Belle study [466], the data tend to peak near $\cos\theta_{J/\psi} = 1$, where the 1^{+-} expectation is zero; both the data and expectation are shown in Fig. 3.35. The poor fit to the data ($\chi^2/dof = 75/9$) rules out any 1^{+-} assignment for the $X(3872)$, including the h_c'; this state in any case has an expected mass well above 3872 MeV. Further angular studies of other modes are foreseen.

8.2.5 *Other searches*

If $X(3872) = 1^1D_2$ (η_{c2}), the isospin conserving transition $\eta_{c2}\to\pi^+\pi^-\eta_c$ should be much more common than $\eta_{c2}\to\pi^+\pi^- J/\psi$, which is isospin violating; the branching fraction $\mathcal{B}(X\to\pi^+\pi^- J/\psi)$ would be $\mathcal{O}(1\%)$ or less, implying a large $B\to KX(3872)$ rate. This seems unlikely but can be tested by searching for the $X(3872)\to\pi^+\pi^-\eta_c$ decay.

Similar considerations apply if $X(3872) = \eta_c''$: the branching fraction to $\pi^+\pi^- J/\psi$ should be small, although in this case (with the η_c'' below open charm threshold) the dominant decay would be into two gluons, less convenient for a search. Assuming that such a state would have a similar width to the η_c (17 ± 3 MeV) [245], which also predominantly decay via two gluons, it is already disfavored by the 2.3 MeV upper limit on the $X(3872)$ width. Given $M_{\psi(3S)} = (4040 \pm 10)$ MeV, $M_{\eta_c''} = 3872$ MeV also implies a large $\psi(3S) - \eta_c''$ mass splitting, ~ 168 MeV, contrary to the expectation that the splitting will decrease with increasing radial quantum number (*cf.* $M_{\psi'} - M_{\eta_c'} = 48$ MeV [391] and $M_\psi - M_{\eta_c} = 117$ MeV) [245].

8.2.6 *Summary*

The status of the six candidates considered by Belle [466] is summarized in Table 3.24: some are already excluded by the data, and none is a natural candidate. Significant further information is expected once searches for other decays become available; the search for $X(3872)\to\pi^0\pi^0 J/\psi$ is particularly important. Already however the lack of a natural charmonium candidate that fits the data suggests two possibilities: (1) that the theory used to predict charmonium properties is flawed, or (2) that the $X(3872)$ is not a

Table 3.24: From [466]: Some properties of candidate charmonium states for the $X(3872)$, and a summary of the comparison with data. Mass predictions are taken from [401], and width predictions computed from [187], using a 3872 MeV mass value; the predicted width for the η_c'' is taken to be the same as the η_c width. Masses and widths are shown in MeV.

state	alias	J^{PC}	M_{pred}	Γ_{pred}	comment
1^3D_2	ψ_2	2^{--}	3838	0.7	Mass wrong; $\Gamma_{\gamma\chi_{c1}}$ too small
2^1P_1	h_c'	1^{+-}	3953	1.6	Ruled out by $\lvert\cos\theta_{J/\psi}\rvert$ distribution
1^3D_3	ψ_3	3^{--}	3849	4.8	M, Γ wrong; $\Gamma_{\gamma\chi_{c2}}$ too small; J too high
1^1D_2	η_{c2}	2^{-+}	3837	0.9	$\mathcal{B}(\pi^+\pi^- J/\psi)$ expected to be very small
2^3P_1	χ_{c1}'	1^{++}	3956	1.7	$\Gamma_{\gamma J/\psi}$ too small
3^1S_0	η_c''	0^{-+}	4060	~ 20	Mass and width are wrong

conventional $(c\bar{c})$ state. As the $X(3872)$ mass is very close to the $M_{D^0} + M_{D^{*0}}$ threshold, a $D\overline{D}^*$ bound state is a natural candidate [212, 467–472].

9 THE OBSERVATION OF THE B_c MESON AT CDF AND D0[41]

The CDF Collaboration has observed the ground state of the bottom-charm meson $B_c^\pm$ via the decay mode $B_c^\pm \to J/\psi l^\pm \nu$ and measured its mass, lifetime and production cross-section [39, 473]. The measurement was done at the Tevatron, in Run I, at $\sqrt{(s)} = 1.8$ TeV. Figure 3.36a shows the mass spectra for the combined $J/\psi e$ and $J/\psi \mu$ candidate samples, the combined backgrounds, and the fitted contribution from the $B_c^\pm \to J/\psi l^\pm \nu$ decay. The fitted number of B_c events is $20.4^{+6.2}_{-5.5}$, out of which $12.0^{+3.8}_{-3.2}$ come for the electron sample and $8.4^{+2.7}_{-2.4}$ from the muon sample. A fit to the same distribution with background alone was rejected at the level of 4.8 standard deviations. The $B_c^\pm$ mass was measured to be equal to $6.40\pm0.39(\mathrm{stat.})\pm0.13(\mathrm{syst.})$ GeV/c^2.

A measure of the time between production and decay of a $B_c^\pm$ meson is

$$ct^* \equiv \frac{M(J/\psi l) \cdot L_{xy}(J/\psi l)}{\lvert p_T(J/\psi l)\rvert} \tag{3.50}$$

where L_{xy} is the distance between the beam centroid and the decay point of the $B_c^\pm$ candidate in the transverse plane and projected along the $J/\psi l$ direction, and $p_T(J/\psi l)$ is the tri-lepton transverse momentum. Figure 3.36b shows the ct^* distribution for the data, the signal and the background distributions. The mean proper decay length $c\tau$ and hence the lifetime τ of the $B_c^\pm$ meson was obtained from the above distribution. It was determined that $c\tau = 137^{+53}_{-49}(\mathrm{stat.})\pm9(\mathrm{syst.})$ μm or $\tau = 0.46^{+0.18}_{-0.16}(\mathrm{stat.})\pm0.03(\mathrm{syst.})$ ps.

Recently [474] the D0 collaboration has reported the observation of a B_c signal in the decay mode $B_c^\pm \to J/\psi \mu^\pm \nu$, from a sample of 210 pb^{-1} of data taken during Run II, at $\sqrt{s} = 1.96$ TeV. The dimuon coming from J/ψ was required to be within 0.25 from the J/ψ mass, and a third muon track was required to come from the same vertex. The analysis yielded $95\pm12\pm11$ events, at a mass $M(B_c^\pm) = 5.95^{+0.14}_{-0.13}(\mathrm{stat.})\pm0.34(\mathrm{syst.})$ GeV/c^2. The lifetime was calculated to be $\tau(B_c^\pm) = 0.448^{+0.123}_{-0.096}$ (stat.) $\pm0.121(\mathrm{syst.})$ ps. Fitted mass and lifetime are found to be uncorrelated. Figure 3.37(left) shows the invariant mass and pseudo-proper time distributions of the events. The analysis accounts for the possible contribution from $B_c \to \psi(2S)\mu^\pm \nu$ on the inclusive sample. As shown in Fig. 3.37(right), it is estimated that about 15 events are due to this component, and the systematic errors are obtained by

---

[41]Author: V. Papadimitriou
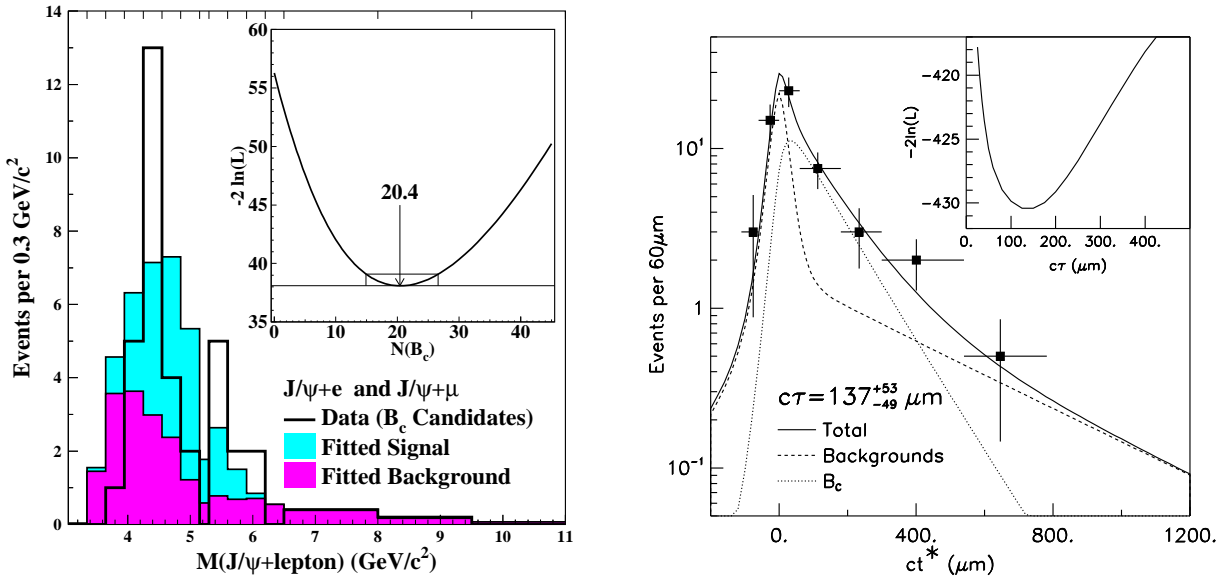
Fig. 3.36: On the left, (a) the histogram of the $J/\psi l$ mass that compares the signal and background contributions determined in the likelihood fit to the combined data for $J/\psi e$ and $J/\psi \mu$. The mass bins, indicated by tick marks at the top, vary in width. The total $B_c^{\pm}$ contribution is $20.4^{+6.2}_{-5.5}$ events. The inset shows the behavior of the log-likelihood function $-2Ln(L)$ vs the number of B_c mesons. On the right, (b) the distribution in ct^* for the combined $J/\psi e$ and $J/\psi \mu$ data along with the fitted curve and contributions to it from signal and background. The inset shows the log-likelihood function vs $c\tau$ for the B_c meson.

varying this contribution from 0 to 30 events. In the near future, the mass uncertainty can be improved to better than 5(50) MeV/c^2 by CDF(D0) by using hadronic exclusive decay channels.

10   EVIDENCE FOR DOUBLY CHARMED BARYONS AT SELEX[42]

The addition of the charmed quark to the (uds) triplet extends the flavour symmetry of the baryon octet and decuplet from SU(3) to SU(4). There is strong experimental evidence for all the predicted baryon states which contain zero or one valence charmed quark [245]. We review here the first experimental evidence for one of the six predicted baryon states which contain two valence charmed quarks, the doubly charmed baryons. There have been many predictions of the masses and other properties of these states [475–478]. The properties of doubly charmed baryons provide a new window into the structure of baryonic matter.

10.1   The SELEX experiment

The SELEX experiment uses the Fermilab 600 GeV/c charged hyperon beam to produce charm particles in a set of thin foil targets of Cu or diamond. The three-stage magnetic spectrometer is shown elsewhere [479, 481]. The most important features are: (a) the high-precision, highly redundant, silicon vertex detector that provides an average proper time resolution of 20 fs for single-charm particle decays, (b) a 10 m long Ring-Imaging Cherenkov (RICH) detector that separates π from K up to 165 GeV/c [480], and (c) a high-resolution tracking system that has momentum resolution of $\sigma_P/P < 1\%$ for a 200 GeV/c reconstructed Λ_c^+.

The experiment selected charm candidate events using an online secondary vertex algorithm which required full track reconstruction for measured fast tracks. An event was written to tape if all the fast

[42]Author:P. Cooper
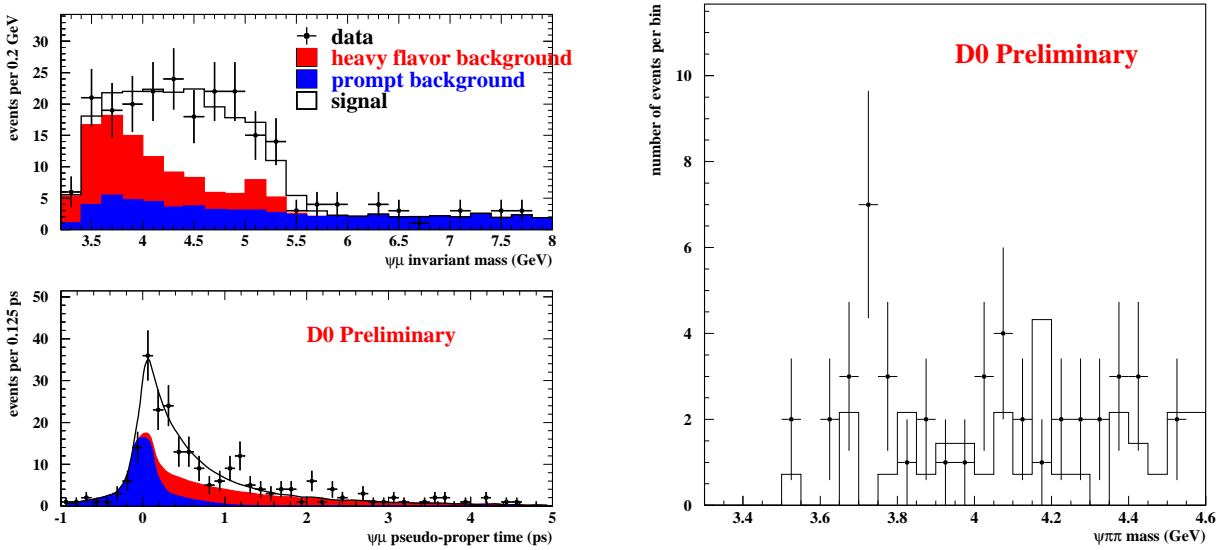
Fig. 3.37: The $J/\psi\mu$ invariant mass (top left) and pseudo-proper time distributions (bottom left) of the $B_c \rightarrow J/\psi\mu X$ candidates (points with error bars) from D0. The signal MonteCarlo events, generated with a mass of 5.95 GeV/c^2, as well as the most likely background sources are shown as solid histograms. The right plot shows the $J/\psi\pi^+\pi^-$ invariant mass of $J/\psi\pi^+\pi^-\mu X$ events that have M($J/\psi\pi^+\pi^-\mu$) between 4 and 6 GeV/c^2. The background (solid histogram) is estimated from events outside this mass range.

tracks in the event were inconsistent with having come from a single primary vertex. This filter passed 1/8 of all interaction triggers and had about 50% efficiency for otherwise accepted charm decays. The experiment recorded data from 15.2×10^9 inelastic interactions and wrote 1×10^9 events to tape using both positive and negative beams. 67% of events were induced by Σ^-, 13% by π^-, and 18% by protons.

10.2 Search strategy

A Cabibbo-allowed decay of a doubly charmed baryon must have a net positive charge and contain a charmed quark, a strange quark and a baryon. We chose to search for decay modes like $\Xi_{cc}^+ \rightarrow \Lambda_c^+ K^- \pi^+$ with an intermediate $K^-\pi^+$ secondary vertex between the primary vertex and the Λ_c^+ vertex and $\Xi_{cc}^+ \rightarrow pD^+K^-$ with an intermediate pK^- secondary vertex between the primary vertex and the D^+ .

Events were analyzed for evidence of a secondary vertex composed of an opposite-signed pair between the primary and the single charm decay point. We used all tracks not assigned to the single charm candidate in the search. The new secondary vertex had to have an acceptable fit χ^2 and a separation of at least 1σ from the new primary. These cuts were developed and fixed in previous searches for short-lived single-charm baryon states. We have applied them here without change. As a background check we also kept wrong-sign combinations in which the mass assignments are reversed.

10.3 $\Xi_{cc}^+ \rightarrow \Lambda_c^+ K^- \pi^+$ Search results and significance

The signal and wrong-sign backgrounds are shown in Fig. 3.38. There is a obvious peak at a mass of 3519 ± 2MeV/c^2. The number of events in the signal region shown is 22 events. We estimate the number of expected background events in the signal region from the sidebands as 6.1 ± 0.5 events. This determination has a (Gaussian) statistical uncertainty, solely from counting statistics. The single-bin significance of this signal is the excess in the signal region divided by the total uncertainty in the background estimate: $15.9/\sqrt{6.1 + 0.5^2} = 6.3\sigma$. The Poisson probability of observing at least this excess, including the Gaussian uncertainty in the background, is 1.0×10^{-6}. The overall probability of
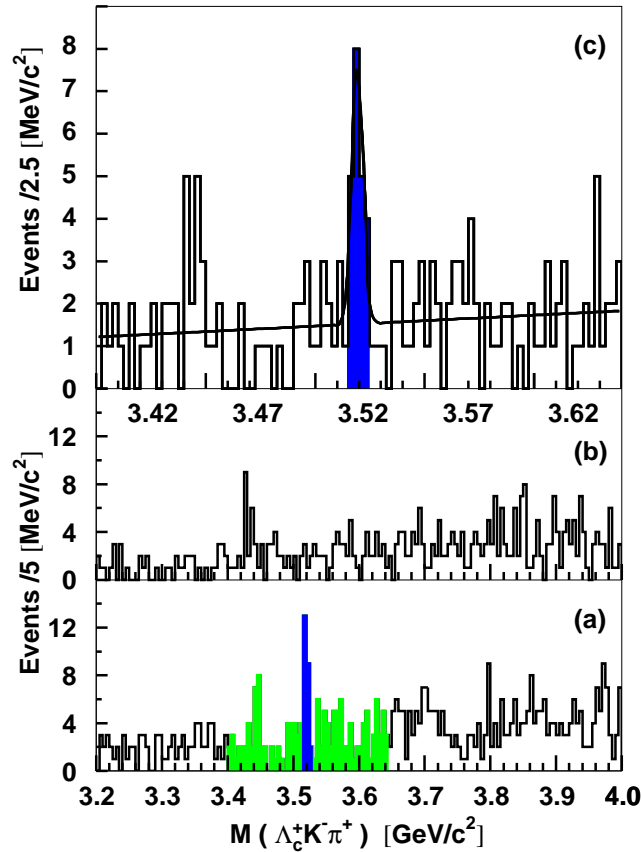
Fig. 3.38: (a) The $\Lambda_c^+ K^- \pi^+$ mass distribution in 5 MeV/c^2 bins. The shaded region 3.400–3.640 GeV/c^2 contains the signal peak and is shown in more detail in (c). (b) The wrong-sign combination $\Lambda_c^+ K^+ \pi^-$ mass distribution in 5 MeV/c^2 bins. (c) The signal (shaded) region (22 events) and sideband mass regions with 162 total events in 2.5 MeV/c^2 bins. The fit is a Gaussian plus linear background.

observing an excess at least as large as the one we see anywhere in the search interval is 1.1×10^{-4}. This result is published in reference [481].

10.4 $\Xi_{cc}^+ \to p D^+ K^-$ search

After the discovery and publication of the $\Xi_{cc}^+ \to \Lambda_c^+ K^- \pi^+$ signal we sought to confirm the discovery in another decay mode which was likely to have a significant branching ratio. Obvious choices were $\Xi_c^+ \pi^+ \pi^-$ and $\Xi_{cc}^+ \to p D^+ K^-$. Since the SELEX D^+ signal is large and well studied we began with it.

A similar analysis technique [482] resulted in the signal and wrong-sign background shown in Fig. 3.39. In this new decay mode we observe an excess of 5.4 events over an expected background of 1.6 ± 0.35 events. The Poisson probability that a background fluctuation can produce the apparent signal is less than 1.5×10^{-5}. The observed mass of this state is 3518 ± 3 MeV/c^2, consistent with the published result. Averaging the two results gives a mass of 3518.7 ± 1.7 MeV/c^2. The observation of this new weak decay mode confirms the previous suggestion that this state is a double charm baryon. The relative branching ratio $\Gamma(\Xi_{cc}^+ \to p D^+ K^-)/\Gamma(\Xi_{cc}^+ \to \Lambda_c^+ K^- \pi^+) = 0.078 \pm 0.045$.

The lifetime of this state in both decay modes is very short; less than 33 fs at 90% confidence. The properties of these two signals are consistent with each other. SELEX reports an independent confirmation of the double charm baryon Ξ_{cc}^+, previously seen in the $\Xi_{cc}^+ \to \Lambda_c^+ K^- \pi^+$ decay mode, via the observation of its decay $\Xi_{cc}^+ \to p D^+ K^-$.
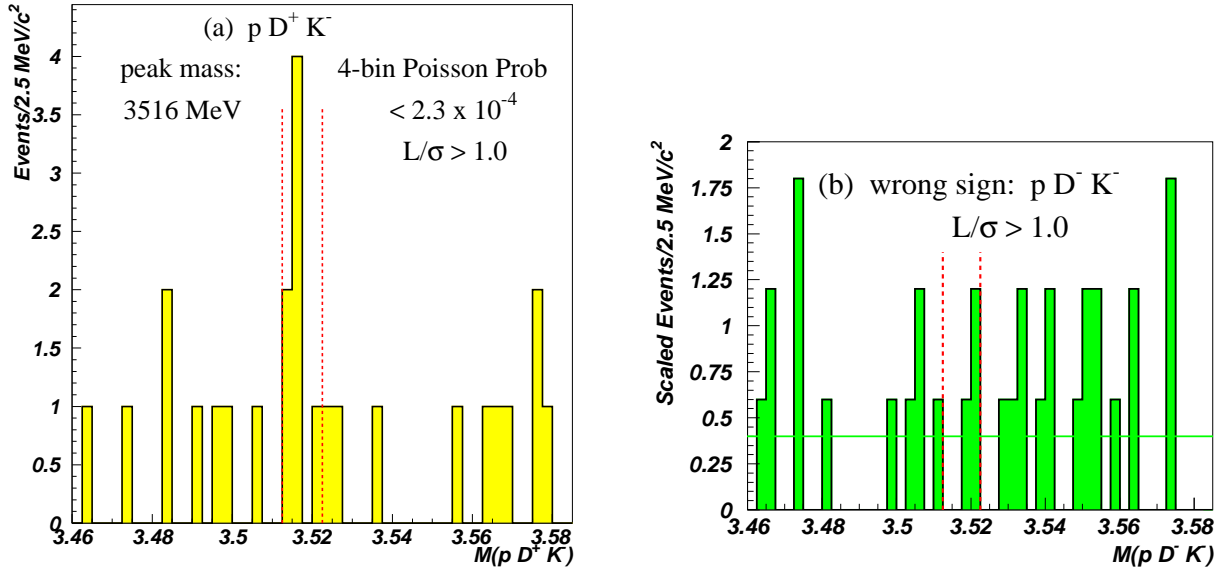
Fig. 3.39: (a) $\Xi_{cc}^+ \to pD^+K^-$ mass distribution for right-sign mass combinations. (b) Wrong-sign events with a D^-K^+, scaled by 0.6. The line shows a maximum likelihood fit to occupancy.

10.5 Conclusions

The $\Xi_{cc}^+(ccd)$ doubly charmed baryon has now been observed by SELEX in two decay modes at a mass of $3518.7 \pm 1.7 \; \mathrm{MeV}/c^2$ with a lifetime less than 33 fs at 90% confidence. Analysis continues with SELEX data to searchfor additional decays modes for this state and to search for the two other doubly-charmed baryons ground states expected: $\Xi_{cc}^{++}(ccu)$ and $\Omega_{cc}^+(ccs)$.

11 SUMMARY AND OUTLOOK[43]

It took few years , after the discovery of the J/ψ, to sketch the spectroscopical pattern of the narrow ortocharmonium and ortobottomonium states: the experimental determination of such energy levels is extremely good, all states are know with precisions better than 1 MeV. On the other side, the experimental history of spin singlet states has started to clear up only in the recent years, but open puzzles remain:

- the total width of the $\eta_c(1S)$ (the ground state of charmonium) is as large as the one of the $\psi(3770)$, which can decay to open charm:
- after 16 years, the real $\eta_c(2S)$ has been observed, disconfirming an evidence by Crystal Ball that misled theory calculations on hyperfine splittings for more than a decade.
- two compatible evidences of the h_c state have been found in the last year, and may bring to an end the saga of the spin singlet P state; a concrete strategy to consolidate this observation is now needed.
- none of the 5 spin singlet states in the bottomonium system has been found yet; given the absence of scheduled running time on narrow Υ states in the near future, it is necessary to elaborate smarter search strategies to spot these states at asymmetric B-factories or hadron colliders .

The quest to complete the experimental spectra is now extending to the higher excitations:

- the search for narrow D-states resulted in the discovery of the $\Upsilon(1D)$ states in CLEO III, and to the observation of the intriguing X(3872) meson by Belle; while the bottomonium state falls well in the expected pattern, there is a wide variety of speculations on the nature of the X(3872).

---

[43] Authors: G. Bali, N. Brambilla, R. Mussa, J. Soto

– the need to achieve a deeper understanding of the region just above open charm threshold, together with the improvement of the experimental tools, will allow to disentangle each single contribution to the R ratio, hopefully clarifying the puzzles opened by the pioneering studies of Mark II.

As we have seen in this chapter the application of EFTs of QCD to heavy quarkonium has considerably increased our understanding of these systems from a fundamental point of view. NRQCD has allowed, on the one hand, for efficient lattice calculations of the masses of the bottomonium and charmonium states below open heavy flavour threshold. On the other hand, it has paved the way to pNRQCD, which provides, in the strong coupling regime, a rigorous link from QCD to potential models for states below open heavy flavour threshold. In the weak coupling regime, pNRQCD has allowed to carry out higher-order calculations and to implement renormalization group resummations and renormalon subtractions in a systematic way. This regime appears to be applicable at least for the $\Upsilon(1S)$ and $\eta_b(1S)$. Interestingly, as discussed in Section 2.3.1 (Tables 3.2 and 3.3) even some excited states can be reproduced in perturbation theory (inside the errors of the perturbative series).

The most challenging theoretical problem at present is the description of states above open heavy flavour threshold. The recent discovery of $X(3872)$ has made clear that potential models suffer from large systematic uncertainties in this region and that the inclusion of, at least, heavy-light meson degrees of freedom is necessary. Although NRQCD holds in this region, extracting information from it on the lattice is not simple, since besides heavy quarkonium, heavy-light meson pairs and hybrid states populate it. It would be important to develop theoretical tools in order to bring current phenomenological approaches into QCD based ones.

In order to stimulate progress in heavy quarkonium spectroscopy, we shall try to pose a number of questions, and try to provide what we believe to be reasonable answers to them, from the theory and experimental point of view.

• **Q.** What does theory need from experiment?

A1(*TH:*) Discovery and good mass measurements of the missing states below open heavy flavour threshold.

A1(*EXP:*) Concerning triplet S and P states of neutral heavy quarkonia, experimental measurements are mature and ahead of theory. Concerning the singlet S and P states, charmonia are under very active investigation at present, and probably will be nailed down to less than .5 MeV/c^2 in the near future, with an active cooperation amid experimental groups. In bottomonium, the situation looks less promising: only Tevatron experiments have currently some chance to detect the missing (narrow?) states, while CLEO III searches turned out no plausible candidates, and showed that more luminosity is needed at $\Upsilon(1, 2, 3S)$, but none of the active B-factories is planning to shift out of $\Upsilon(4S)$.

The experimental study of the spectrum of the charged heavy quarkonium, the B_c, has not started yet. The ground state has been seen by CDF and confirmed by D0, but via its semileptonic decay, which yield still very wide uncertainties on the mass (0.4 GeV/c^2). The experimental search for an exclusive, non leptonic mode is under way and will allow to know this state with accuracies better than 5 MeV/c^2 in the near future. Beyond this, most experimental efforts will be focused on finding the dominant decay modes of the ground state. The search for the B_c^*, which decays dominantly to B_c via M1 radiation of a soft photon , will be extremely challenging for current Tevatron experiments, due to the high combinatorial background and to the low efficiency on low energy photons. Same can be said for the P states , which are expected to decay to $B_c^{(*)}$ via dipion emission. It is hard to predict whether the hadronic B-factories, BTEV and LHCB, will be able to contribute to these spectroscopical studies. The issue should be discussed in Chapter 9.

A2(*TH:*) Thorough analysis of the region above open heavy flavour threshold in search for quarkonium states, hybrid states, molecules and other exotica.

A2(*EXP:*) The BES II R scan and the surprises from the asymmetric B-factories (X(3872) and double $c\bar{c}$ production) have ignited new experimental and theoretical interest in this physics region. The CLEO-c running at $\psi(3770)$ and above $D_s\bar{D}_s$ threshold has a very large physics potential for heavy quarkonium studies. At the same time, B factories can benefit from a large variety of techniques to identify new charmonium states: (a) inclusive ones , such as J/ψ and ψ' recoil in double $c\bar{c}$, or K recoil in tagged B decays; (b) exclusive ones , such as $B\to(\psi,\eta_c)XK^{(*)}$ (for narrower states), $B\to D^{(*)}\bar{D}^{(*)}K^{(*)}$ (for wider states).

Some discovery potential is to be expected also from hadron colliders, where the large, very clean samples of D mesons can be used as starting point to search for peaks in $D\bar{D}$ invariant mass combinations.

- **Q.** What does experiments need from theory?

A1(*EXP:*) In spectroscopy, two are the crucial issues in the search of missing states: (a) a good understanding of the production/formation mechanisms; (b) a comprehensive set of decay channels, with solid predictions on the partial widths. The two issues are related between each other, and to the hot topics of the next chapter.

There is NOT an infinite number of ways to produce charmonium, less for bottomonium, much less for B_c: these couplings deserve a higher level of understanding, both theoretically and experimentally. This is much more important, when we do want to understand whether we can get some deeper insight from the non observation of a missing state. It must be noticed that most production mechanisms are not fully understood, and/or lead to wrong predictions.

A limited set of processes, then, deserve deeper theoretical understanding:

- M1 hindered radiative transitions: relativistic corrections are dominant in these processes that are the main gateways to η_b's.

- isospin violating hadronic transitions: it is now very important to establish a physical relation between $\psi(2S)\to h_c\pi^0$ and $h_c\to J/\psi\pi^0$. This can help clarifying the consistency between the two (still weak) evidences.

- factorization in B decays: exclusive B decays to K+$c\bar{c}$ were expected to yield $0^{-+},1^{--},1^{++}$ charmonia, and, in smaller quantities, $0^{++},2^{++}$. The prediction holds for the second, but χ_{c0}'s are produced as copiously as χ_{c1}'s . The understanding of the effective selection rules can help to set limits on the h_c production, and to find the possible quantum numbers of the X(3872) meson.

- coupling to exclusive $p\bar{p}$: helicity selection rule in perturbative QCD forbids the formation of η_c, χ_{c0}, h_c from $p\bar{p}$ annihilations; no suppression is observed in the first two cases, and the third is under active investigation. It is auspicable that recent developments in NRQCD can help to explain the $p\bar{p}$ coupling and make testable predictions on the coupling to $\eta_c(2S)$ and X(3872).

- the double $c\bar{c}$ selection rules are not yet clear: so far only scalars and pseudoscalars were observed recoiling against the J/ψ . This process has already allowed an indipendent confirmation of the $\eta_c(2S)$ observation. By understanding the dynamics, one can converge more rapidly on the determination of the quantum numbers of any bump that shows up in the J/ψ recoil spectrum.

Within theory one may ask the following questions:

- **Q.** What does the phenomenological approach need from the theoretical one?

A $*$ That the theory clearly points out the most relevant feautures that should be implemented in phenomenological models.

- **Q.** What does the theoretical approach need from the phenomenological one?

A $*$ To point out shortcomings in models which are relevant to experimental observations.

Within the theoretical approach:

• **Q.** What does EFTs need from lattice?

∗ Calculation of the correlators which parameterize nonperturbative effects in the weak coupling regime of pNRQCD.

∗ Calculation of the various potentials which enter pNRQCD in the strong coupling regime.

• **Q.** What does lattice need from EFT?

∗ Calculation of the NRQCD matching coefficients in lattice regularizations.

∗ Chiral extrapolations.

Let us next describe the future development which are desirable within each particular approach.

From the side of the EFT the priority "to-do" list is:
– Develop a suitable EFT for the region above open heavy flavour threshold.
– Include the effects of virtual pions. Pions should be included in the strong coupling regime of pNRQCD as ultrasoft degrees of freedom and their effect on the spectrum should be investigated.
– A systematic investigation of the structure of the renormalon subtractions in NRQCD matching coefficients and in the perturbative potentials.

For what concerns lattice calculations the priority practical lattice "to-do list" is:
– Further investigations of sea quark effects, in particular on charmonia and also in bottomonia, including charm mass effects.
– Calculation of threshold effects in charmonia and bottomonia, first using lattice potentials, then a multichannel analysis in lattice NRQCD/QCD.
– Further investigations of OZI suppressed contributions, in particular in the PS charm-sector.
– Mixing of charmonia and would-be glueballs.
– Doubly charmed baryons.
– QQq potentials.

From the side of phenomenological models the wish list includes:
– The major deficiency of these models is that they only include the $q\bar{q}$ components of the Fock space expansion and totally neglect higher Fock space components which can be included as coupled channel effects. These are expected to be most prominent for states close to threshold.

From the side of experiments we need:
– to clarify the nature of the X(3872) state, fully exploiting the four running experiments that see this state.
– to strengthen the h_c evidence , by asking for an active collaboration between experiments , in order to intensify the checks which certify the compatibility between the two recent evidences.
– to support further cross checks on the systematic errors on the masses of pseudoscalar charmonia: both BaBar and Belle should already have a large sample of $\gamma\gamma\rightarrow\eta_c(1, 2S)$, to measure with high precision both states.
– to search for doubly charmed baryons in asymmetric B-factories, as well as at the Tevatron.
– to measure, at CLEO-c, the coupling of the $\psi(3770)$ and the $\Upsilon(1, 2, 3S)$ states to $p\bar{p}$, to quantify the perspectives to study charmonium at open charm threshold and bottomonium with antiproton beams.
– to support further η_b searches at the Tevatron, and to strengthen the physics case for further running at narrow bottomonium energies.

REFERENCES

[1] W. E. Caswell and G. P. Lepage, Phys. Lett. B **167**, 437 (1986).

[2] B. A. Thacker and G. P. Lepage, Phys. Rev. D **43**, 196 (1991).

[3] G. T. Bodwin, E. Braaten and G. P. Lepage, Phys. Rev. D **51**, 1125 (1995) [Erratum-ibid. D **55**, 5853 (1997)] [arXiv:hep-ph/9407339].

[4] A. Pineda and J. Soto, Nucl. Phys. Proc. Suppl. **64**, 428 (1998) [arXiv:hep-ph/9707481].

[5] N. Brambilla, A. Pineda, J. Soto and A. Vairo, Nucl. Phys. B **566**, 275 (2000) [arXiv:hep-ph/9907240].

[6] M. E. Luke, A. V. Manohar and I. Z. Rothstein, Phys. Rev. D **61**, 074025 (2000) [arXiv:hep-ph/9910209].

[7] A. X. El-Khadra, A. S. Kronfeld and P. B. Mackenzie, Phys. Rev. D **55**, 3933 (1997) [arXiv:hep-lat/9604004].

[8] X. Liao and T. Manke, Phys. Rev. D **65**, 074508 (2002) [arXiv:hep-lat/0111049].

[9] M. Okamoto *et al.* [CP-PACS Collaboration], Phys. Rev. D **65**, 094508 (2002) [arXiv:hep-lat/0112020].

[10] S. Choe *et al.* [QCD-TARO Collaboration], JHEP **0308**, 022 (2003) [arXiv:hep-lat/0307004].

[11] P. Chen, Phys. Rev. D **64**, 034509 (2001) [arXiv:hep-lat/0006019].

[12] X. Liao and T. Manke, arXiv:hep-lat/0210030.

[13] C. J. Morningstar and M. J. Peardon, Phys. Rev. D **60**, 034509 (1999) [arXiv:hep-lat/9901004].

[14] B. Lucini and M. Teper, JHEP **0106**, 050 (2001) [arXiv:hep-lat/0103027].

[15] G. S. Bali, K. Schilling, A. Hulsebos, A. C. Irving, C. Michael and P. W. Stephenson [UKQCD Collaboration], Phys. Lett. B **309**, 378 (1993) [arXiv:hep-lat/9304012].

[16] R. Sommer, Nucl. Phys. B **411**, 839 (1994) [arXiv:hep-lat/9310022].

[17] G. S. Bali, Eur. Phys. J. A **19**, 1 (2004) [arXiv:hep-lat/0308015].

[18] C. McNeile and C. Michael [UKQCD Collaboration], Phys. Rev. D **70**, 034506 (2004) [arXiv:hep-lat/0402012].

[19] P. de Forcrand *et al.* [QCD-TARO Collaboration], JHEP **0408**, 004 (2004) [arXiv:hep-lat/0404016].

[20] C. McNeile, C. Michael and K. J. Sharkey [UKQCD Collaboration], Phys. Rev. D **65**, 014508 (2002) [arXiv:hep-lat/0107003].

[21] T. Struckmann *et al.* [TχL Collaboration], Phys. Rev. D **63**, 074503 (2001) [arXiv:hep-lat/0010005].

[22] P. Boyle [UKQCD Collaboration], arXiv:hep-lat/9903017; P. Boyle [UKQCD Collaboration], Nucl. Phys. Proc. Suppl. **63**, 314 (1998) [arXiv:hep-lat/9710036].

[23] C. W. Bernard *et al.* [MILC Collaboration], Phys. Rev. D **56**, 7039 (1997) [arXiv:hep-lat/9707008].

[24] M. di Pierro *et al.*, Nucl. Phys. Proc. Suppl. **129**, 340 (2004) [arXiv:hep-lat/0310042]; M. Di Pierro *et al.*, Nucl. Phys. Proc. Suppl. **119**, 586 (2003) [arXiv:hep-lat/0210051]; A. X. El-Khadra, S. Gottlieb, A. S. Kronfeld, P. B. Mackenzie and J. N. Simone, Nucl. Phys. Proc. Suppl. **83**, 283 (2000).

[25] N. Brambilla, arXiv:hep-ph/0012026; A. Pineda, Nucl. Phys. Proc. Suppl. **93**, 188 (2001) [arXiv:hep-ph/0008327]; A. H. Hoang, arXiv:hep-ph/0204299.

[26] B. Grinstein, Int. J. Mod. Phys. A **15**, 461 (2000) [arXiv:hep-ph/9811264]; A. V. Manohar and I. W. Stewart, Nucl. Phys. Proc. Suppl. **94**, 130 (2001) [AIP Conf. Proc. **618**, 381 (2002)] [arXiv:hep-lat/0012002].

[27] N. Brambilla, A. Pineda, J. Soto and A. Vairo, arXiv:hep-ph/0410047.

[28] A. S. Kronfeld, Phys. Rev. D **62**, 014505 (2000) [arXiv:hep-lat/0002008].

[29] C. T. H. Davies *et al.* [HPQCD, Fermilab Lattice, MILC, and UKQCD Collaborations], Phys. Rev. Lett. **92**, 022001 (2004) [arXiv:hep-lat/0304004].

[30] C. W. Bernard *et al.*, Phys. Rev. D **64**, 054506 (2001) [arXiv:hep-lat/0104002].

[31] G. P. Lepage, Phys. Rev. D **59**, 074502 (1999) [arXiv:hep-lat/9809157].

[32] S. A. Gottlieb, Nucl. Phys. Proc. Suppl. **128**, 72 (2004) [Nucl. Phys. Proc. Suppl. **129**, 17 (2004)] [arXiv:hep-lat/0310041].

[33] A. Gray *et al.* [HPQCD collaboration], Nucl. Phys. Proc. Suppl. **119**, 592 (2003) [arXiv:hep-lat/0209022]. C. Davies *et al.*, Nucl. Phys. Proc. Suppl. **119**, 595 (2003) [arXiv:hep-lat/0209122].

[34] C. Aubin *et al.* [MILC Collaboration], Nucl. Phys. Proc. Suppl. **129**, 227 (2004) [arXiv:hep-lat/0309088].

[35] G. P. Lepage *et al.*, Phys. Rev. D **46**, 4052 (1992) [arXiv:hep-lat/9205007]; C. T. H. Davies *et al.*, Phys. Rev. D **50**, 6963 (1994) [arXiv:hep-lat/9406017].

[36] G. S. Bali and P. Boyle, Phys. Rev. D **59**, 114504 (1999) [arXiv:hep-lat/9809180].

[37] M. A. Nobes and H. D. Trottier, Nucl. Phys. Proc. Suppl. **129**, 355 (2004) [arXiv:hep-lat/0309086].

[38] M. B. Oktay, A. X. El-Khadra, A. S. Kronfeld, P. B. Mackenzie and J. N. Simone, Nucl. Phys. Proc. Suppl. **119**, 464 (2003) [arXiv:hep-lat/0209150]; M. B. Oktay, A. X. El-Khadra, A. S. Kronfeld and P. B. Mackenzie, Nucl. Phys. Proc. Suppl. **129**, 349 (2004) [arXiv:hep-lat/0310016].

[39] F. Abe *et al.* [CDF Collaboration], Phys. Rev. Lett. **81**, 2432 (1998) [arXiv:hep-ex/9805034].

[40] H. P. Shanahan, P. Boyle, C. T. H. Davies and H. Newton [UKQCD Collaboration], Phys. Lett. B **453**, 289 (1999) [arXiv:hep-lat/9902025].

[41] R. A. Bertlmann and A. Martin, Nucl. Phys. B **168**, 111 (1980).

[42] S. Nussinov and M. A. Lampert, Phys. Rept. **362**, 193 (2002) [arXiv:hep-ph/9911532].

[43] I. F. Allison, C. T. H. Davies, A. Gray, A. S. Kronfeld, P. B. Mackenzie and J. N. Simone [HPQCD, Fermilab Lattice, and UKQCD Collaborations], arXiv:hep-lat/0411027.

[44] I. F. Allison *et al.* [HPQCD, Fermilab Lattice, and UKQCD Collaborations], arXiv:hep-lat/0409090.

[45] A. S. Kronfeld, Nucl. Phys. Proc. Suppl. **129** (2004) 46 [arXiv:hep-lat/0310063].

[46] K. J. Juge, J. Kuti and C. J. Morningstar, Phys. Rev. Lett. **82**, 4400 (1999) [arXiv:hep-ph/9902336].

[47] K. J. Juge, J. Kuti and C. Morningstar, Phys. Rev. Lett. **90**, 161601 (2003) [arXiv:hep-lat/0207004].

[48] N. Brambilla, A. Pineda, J. Soto and A. Vairo, Phys. Rev. D **63**, 014023 (2001) [arXiv:hep-ph/0002250]; A. Pineda and A. Vairo, Phys. Rev. D **63**, 054007 (2001) [Erratum-ibid. D **64**, 039902 (2001)] [arXiv:hep-ph/0009145].

[49] C. T. H. Davies, K. Hornbostel, G. P. Lepage, A. Lidsey, P. McCallum, J. Shigemitsu and J. H. Sloan [UKQCD Collaboration], Phys. Rev. D **58**, 054505 (1998) [arXiv:hep-lat/9802024].

[50] T. Burch and D. Toussaint [MILC Collaboration], Phys. Rev. D **68**, 094504 (2003) [arXiv:hep-lat/0305008].

[51] G. S. Bali *et al.* [TχL Collaboration], Phys. Rev. D **62**, 054503 (2000) [arXiv:hep-lat/0003012].

[52] C. McNeile, C. Michael and P. Pennanen [UKQCD Collaboration], Phys. Rev. D **65**, 094505 (2002) [arXiv:hep-lat/0201006].

[53] G. S. Bali, Phys. Rept. **343**, 1 (2001) [arXiv:hep-ph/0001312].

[54] C. Alexandrou, P. De Forcrand and A. Tsapalis, Phys. Rev. D **65**, 054503 (2002) [arXiv:hep-lat/0107006]; C. Alexandrou, P. de Forcrand and O. Jahn, Nucl. Phys. Proc. Suppl. **119**, 667 (2003) [arXiv:hep-lat/0209062].

[55] T. T. Takahashi, H. Suganuma, Y. Nemoto and H. Matsufuru, Phys. Rev. D **65**, 114509 (2002) [arXiv:hep-lat/0204011]; H. Suganuma, T. T. Takahashi and H. Ichie, arXiv:hep-lat/0312031.

[56] F. Okiharu and R. M. Woloshyn, Nucl. Phys. Proc. Suppl. **129-130**, 745 (2004) [arXiv:hep-lat/0310007].

[57] V. G. Bornyakov *et al.* [DIK Collaboration], Phys. Rev. D **70**, 054506 (2004) [arXiv:hep-lat/0401026].

[58] R. Lewis, N. Mathur and R. M. Woloshyn, Phys. Rev. D **64**, 094509 (2001) [arXiv:hep-ph/0107037].

[59] N. Mathur, R. Lewis and R. M. Woloshyn, Phys. Rev. D **66**, 014502 (2002) [arXiv:hep-ph/0203253].

[60] J. M. Flynn, F. Mescia and A. S. B. Tariq [UKQCD Collaboration], JHEP **0307**, 066 (2003) [arXiv:hep-lat/0307025].

[61] N. Brambilla, D. Gromes and A. Vairo, Phys. Lett. B **576**, 314 (2003) [arXiv:hep-ph/0306107].

[62] Y. Schröder, Phys. Lett. B **447**, 321 (1999) [arXiv:hep-ph/9812205].

[63] M. Peter, Phys. Rev. Lett. **78**, 602 (1997) [arXiv:hep-ph/9610209].

[64] N. Brambilla, A. Pineda, J. Soto and A. Vairo, Phys. Rev. D **60**, 091502 (1999) [arXiv:hep-ph/9903355].

[65] G. S. Bali and A. Pineda, Phys. Rev. D **69**, 094001 (2004) [arXiv:hep-ph/0310130].

[66] M. Baker and R. Steinke, Phys. Rev. D **63**, 094013 (2001) [arXiv:hep-ph/0006069]; M. Baker and R. Steinke, Phys. Rev. D **65**, 094042 (2002) [arXiv:hep-th/0201169].

[67] B. A. Kniehl, A. A. Penin, M. Steinhauser and V. A. Smirnov, Phys. Rev. D **65** (2002) 091503 [arXiv:hep-ph/0106135].

[68] B. A. Kniehl, A. A. Penin, V. A. Smirnov and M. Steinhauser, Nucl. Phys. B **635**, 357 (2002) [arXiv:hep-ph/0203166].

[69] N. Brambilla, A. Pineda, J. Soto and A. Vairo, Phys. Lett. B **470**, 215 (1999) [arXiv:hep-ph/9910238].

[70] A. Pineda and J. Soto, Phys. Lett. B **495**, 323 (2000) [arXiv:hep-ph/0007197].

[71] T. Appelquist, M. Dine and I. J. Muzinich, Phys. Rev. D **17**, 2074 (1978).

[72] T. Appelquist, M. Dine and I. J. Muzinich, Phys. Lett. B **69**, 231 (1977).

[73] W. Fischler, Nucl. Phys. B **129**, 157 (1977).

[74] A. Billoire, Phys. Lett. B **92**, 343 (1980).

[75] M. Melles, Phys. Rev. D **62**, 074019 (2000) [arXiv:hep-ph/0001295].

[76] M. Melles, Nucl. Phys. Proc. Suppl. **96**, 472 (2001) [arXiv:hep-ph/0009085].

[77] A. H. Hoang, arXiv:hep-ph/0008102.

[78] S. Recksiegel and Y. Sumino, Phys. Rev. D **65**, 054018 (2002) [arXiv:hep-ph/0109122].

[79] B. A. Kniehl and A. A. Penin, Nucl. Phys. B **563**, 200 (1999) [arXiv:hep-ph/9907489].

[80] F. A. Chishtie and V. Elias, Phys. Lett. B **521**, 434 (2001) [arXiv:hep-ph/0107052].

[81] A. Pineda, JHEP **0106**, 022 (2001) [arXiv:hep-ph/0105008].

[82] G. Cvetic, J. Phys. G **30**, 863 (2004) [arXiv:hep-ph/0309262].

[83] A. Pineda, Ph.D. Thesis, Barcelona 1998.

[84] A. H. Hoang, M. C. Smith, T. Stelzer and S. Willenbrock, Phys. Rev. D **59**, 114014 (1999) [arXiv:hep-ph/9804227].

[85] M. Beneke, Phys. Lett. B **434**, 115 (1998) [arXiv:hep-ph/9804241].

[86] I. I. Y. Bigi, M. A. Shifman, N. G. Uraltsev and A. I. Vainshtein, Phys. Rev. D **50**, 2234 (1994) [arXiv:hep-ph/9402360]; M. Beneke, Phys. Lett. B **344**, 341 (1995) [arXiv:hep-ph/9408380];

M. Beneke and V. M. Braun, the Nucl. Phys. B **426**, 301 (1994) [arXiv:hep-ph/9402364]; M. Neubert and C. T. Sachrajda, Nucl. Phys. B **438**, 235 (1995) [arXiv:hep-ph/9407394]; G. Martinelli and C. T. Sachrajda, Nucl. Phys. B **478**, 660 (1996) [arXiv:hep-ph/9605336].

[87] U. Aglietti and Z. Ligeti, Phys. Lett. B **364**, 75 (1995) [arXiv:hep-ph/9503209].

[88] Y. Sumino, Phys. Rev. D **65**, 054003 (2002) [arXiv:hep-ph/0104259].

[89] S. Necco and R. Sommer, Phys. Lett. B **523**, 135 (2001) [arXiv:hep-ph/0109093].

[90] A. Pineda, J. Phys. G **29**, 371 (2003) [arXiv:hep-ph/0208031].

[91] S. Recksiegel and Y. Sumino, Eur. Phys. J. C **31**, 187 (2003) [arXiv:hep-ph/0212389].

[92] T. Lee, Phys. Rev. D **67**, 014020 (2003) [arXiv:hep-ph/0210032].

[93] N. Brambilla, Y. Sumino and A. Vairo, Phys. Lett. B **513**, 381 (2001) [arXiv:hep-ph/0101305].

[94] Y. Sumino, Phys. Lett. B **571**, 173 (2003) [arXiv:hep-ph/0303120].

[95] N. Brambilla, Y. Sumino and A. Vairo, Phys. Rev. D **65**, 034001 (2002) [arXiv:hep-ph/0108084].

[96] S. Recksiegel and Y. Sumino, Phys. Rev. D **67**, 014004 (2003) [arXiv:hep-ph/0207005].

[97] N. Brambilla and A. Vairo, Phys. Rev. D **62**, 094019 (2000) [arXiv:hep-ph/0002075].

[98] A. Pineda and F. J. Yndurain, Phys. Rev. D **58**, 094022 (1998) [arXiv:hep-ph/9711287].

[99] S. Titard and F. J. Yndurain, Phys. Rev. D **51**, 6348 (1995) [arXiv:hep-ph/9403400].

[100] M. Beneke and V. A. Smirnov, Nucl. Phys. B **522**, 321 (1998) [arXiv:hep-ph/9711391].

[101] A. Pineda, Phys. Rev. D **65**, 074007 (2002) [arXiv:hep-ph/0109117].

[102] A. H. Hoang and I. W. Stewart, Phys. Rev. D **67**, 114020 (2003) [arXiv:hep-ph/0209340].

[103] A. A. Penin and M. Steinhauser, Phys. Lett. B **538**, 335 (2002) [arXiv:hep-ph/0204290].

[104] N. Brambilla and A. Vairo, arXiv:hep-ph/0411156.

[105] J. Pantaleone and S. H. H. Tye, Phys. Rev. D **37**, 3337 (1988).

[106] S. Recksiegel and Y. Sumino, Phys. Lett. B **578**, 369 (2004) [arXiv:hep-ph/0305178].

[107] B. A. Kniehl, A. A. Penin, A. Pineda, V. A. Smirnov and M. Steinhauser, Phys. Rev. Lett. **92**, 242001 (2004) [arXiv:hep-ph/0312086].

[108] A. A. Penin, A. Pineda, V. A. Smirnov and M. Steinhauser, Phys. Lett. B **593**, 124 (2004) [arXiv:hep-ph/0403080].

[109] A. Vairo, IFUM-816-FT.

[110] A. V. Manohar and I. W. Stewart, Phys. Rev. D **62**, 014033 (2000) [arXiv:hep-ph/9912226].

[111] A. V. Manohar and I. W. Stewart, Phys. Rev. D **63**, 054004 (2001) [arXiv:hep-ph/0003107].

[112] A. H. Hoang, A. V. Manohar, I. W. Stewart and T. Teubner, Phys. Rev. Lett. **86**, 1951 (2001) [arXiv:hep-ph/0011254]; Phys. Rev. D **65**, 014014 (2002) [arXiv:hep-ph/0107144].

[113] A. H. Hoang, A. V. Manohar and I. W. Stewart, Phys. Rev. D **64**, 014033 (2001) [arXiv:hep-ph/0102257].

[114] A. Pineda, Phys. Rev. D **66**, 054022 (2002) [arXiv:hep-ph/0110216].

[115] A. H. Hoang, Phys. Rev. D **69**, 034009 (2004) [arXiv:hep-ph/0307376].

[116] A. Pineda, Acta Phys. Polon. B **34**, 5295 (2003) [arXiv:hep-ph/0404225].

[117] A. A. Penin, A. Pineda, V. A. Smirnov and M. Steinhauser, arXiv:hep-ph/0406175.

[118] A. Pineda, Acta Phys. Polon. B **34**, 5295 (2003) [arXiv:hep-ph/0404225].

[119] M. B. Voloshin, Nucl. Phys. B **154**, 365 (1979).

[120] H. Leutwyler, Phys. Lett. B **98**, 447 (1981).

[121] Y. Kiyo and Y. Sumino, Phys. Lett. B **535**, 145 (2002) [arXiv:hep-ph/0110277].

[122] A. Pineda, Nucl. Phys. B **494**, 213 (1997) [arXiv:hep-ph/9611388].

[123] I. I. Balitsky, Nucl. Phys. B **254**, 166 (1985).

[124] N. Brambilla, eConf **C030614**, 029 (2003) [arXiv:hep-ph/0312142].

[125] N. Brambilla, D. Eiras, A. Pineda, J. Soto and A. Vairo, Phys. Rev. D **67**, 034018 (2003) [arXiv:hep-ph/0208019]; N. Brambilla, D. Eiras, A. Pineda, J. Soto and A. Vairo, Phys. Rev. Lett. **88**, 012003 (2002) [arXiv:hep-ph/0109130].

[126] J. Gasser and H. Leutwyler, Annals Phys. **158** (1984) 142; Nucl. Phys. B **250** (1985) 465.

[127] N. Brambilla, D. Gromes and A. Vairo, Phys. Rev. D **64**, 076010 (2001) [arXiv:hep-ph/0104068].

[128] A. Barchielli, N. Brambilla and G. M. Prosperi, Nuovo Cim. A **103**, 59 (1990).

[129] D. Gromes, Z. Phys. C **26**, 401 (1984).

[130] K. G. Wilson, Phys. Rev. D **10**, 2445 (1974); L. Susskind, in Les Houches, Session XXIX, ed. R. Balian and C.H. Llewellyn Smith (North-Holland Publishing Company, Amsterdam, 1977).

[131] E. Eichten and F. Feinberg, Phys. Rev. D **23**, 2724 (1981).

[132] Y. Q. Chen, Y. P. Kuang and R. J. Oakes, Phys. Rev. D **52**, 264 (1995) [arXiv:hep-ph/9406287].

[133] M. E. Peskin, in Proc. 11th SLAC Institute, SLAC Report No. 207, 151, ed. P. Mc Donough (1983); A. Barchielli, E. Montaldi and G. M. Prosperi, Nucl. Phys. B **296**, 625 (1988) [Erratum *ibid.* B **303**, 752 (1988)]; N. Brambilla, P. Consoli and G. M. Prosperi, Phys. Rev. D **50**, 5878 (1994) [arXiv:hep-th/9401051]; A. P. Szczepaniak and E. S. Swanson, Phys. Rev. D **55**, 1578 (1997) [arXiv:hep-ph/9609525]; F. Jugeau and H. Sazdjian, Nucl. Phys. B **670**, 221 (2003) [arXiv:hep-ph/0305021].

[134] N. Brambilla and A. Vairo, arXiv:hep-ph/9904330; F. J. Yndurain, arXiv:hep-ph/9910399.

[135] G. S. Bali, K. Schilling and A. Wachter, Phys. Rev. D **56**, 2566 (1997) [arXiv:hep-lat/9703019].

[136] G. S. Bali, N. Brambilla and A. Vairo, Phys. Lett. B **421**, 265 (1998) [arXiv:hep-lat/9709079].

[137] M. Baker, N. Brambilla, H. G. Dosch and A. Vairo, Phys. Rev. D **58**, 034010 (1998) [arXiv:hep-ph/9802273]; N. Brambilla and A. Vairo, arXiv:hep-ph/0004192; N. Brambilla and A. Vairo, Phys. Rev. D **55**, 3974 (1997) [arXiv:hep-ph/9606344]; M. Baker, J. S. Ball, N. Brambilla, G. M. Prosperi and F. Zachariasen, Phys. Rev. D **54**, 2829 (1996) [arXiv:hep-ph/9602419]; M. Baker, J. S. Ball, N. Brambilla and A. Vairo, Phys. Lett. B **389**, 577 (1996) [arXiv:hep-ph/9609233]; M. Baker, J. S. Ball and F. Zachariasen, Phys. Rev. D **56**, 4400 (1997) [arXiv:hep-ph/9705207]; H. G. Dosch and Y. A. Simonov, Phys. Lett. B **205**, 339 (1988); M. Schiestl and H. G. Dosch, Phys. Lett. B **209**, 85 (1988); Y. A. Simonov, Nucl. Phys. B **324**, 67 (1989).

[138] N. Brambilla, arXiv:hep-ph/9809263; N. Brambilla, G. M. Prosperi and A. Vairo, Phys. Lett. B **362**, 113 (1995) [arXiv:hep-ph/9507300].

[139] N. Brambilla, A. Pineda, J. Soto and A. Vairo, Phys. Lett. B **580**, 60 (2004) [arXiv:hep-ph/0307159].

[140] G. P. Lepage, arXiv:nucl-th/9706029.

[141] A. Czarnecki, K. Melnikov and A. Yelkhovsky, Phys. Rev. A **59**, 4316 (1999) [arXiv:hep-ph/9901394].

[142] A. Czarnecki, K. Melnikov and A. Yelkhovsky, Phys. Rev. Lett. **82**, 311 (1999) [arXiv:hep-ph/9809341].

[143] B. Bolder *et al.*, Phys. Rev. D **63**, 074504 (2001) [arXiv:hep-lat/0005018].

[144] A. Pineda, arXiv:hep-ph/0310135.

[145] S. Necco and R. Sommer, Nucl. Phys. B **622**, 328 (2002) [arXiv:hep-lat/0108008].

[146] S. Capitani, M. Lüscher, R. Sommer and H. Wittig [ALPHA Collaboration], Nucl. Phys. B **544**, 669 (1999) [arXiv:hep-lat/9810063].

[147] M. Lüscher, K. Symanzik and P. Weisz, Nucl. Phys. B **173**, 365 (1980).

[148] M. Lüscher and P. Weisz, JHEP **0207**, 049 (2002) [arXiv:hep-lat/0207003].

[149] M. Caselle, M. Pepe and A. Rago, JHEP **0410**, 005 (2004) [arXiv:hep-lat/0406008].

[150] M. Luscher and P. Weisz, JHEP **0407**, 014 (2004) [arXiv:hep-th/0406205].

[151] K. J. Juge, J. Kuti, C. Morningstar, Nucl. Phys. (Proc. Suppl.) **129**, 686 (2004) [arXiv:hep-lat/0310039].

[152] K. J. Juge, J. Kuti, C. Morningstar, [arXiv:hep-lat/0401032].

[153] M. Foster and C. Michael [UKQCD Collaboration], Phys. Rev. D **59**, 094509 (1999) [arXiv:hep-lat/9811010].

[154] H. G. Dosch, M. Eidemuller and M. Jamin, Phys. Lett. B **452**, 379 (1999) [arXiv:hep-ph/9812417].

[155] G. S. Bali, K. Schilling and C. Schlichter, Phys. Rev. D **51**, 5165 (1995) [arXiv:hep-lat/9409005].

[156] K. J. Juge, J. Kuti, C. Morningstar, [arXiv:hep-lat/0312019].

[157] N. Brambilla, T. Rösch, A. Vairo "QCD Effective Lagrangians for Heavy Baryons" IFUM-808-FT; T. Rösch, Diploma thesis, Heidelberg 2003.

[158] J. Soto, arXiv:hep-ph/0301138.

[159] J. P. Ma and Z. G. Si, Phys. Lett. B **568**, 135 (2003) [arXiv:hep-ph/0305079].

[160] J. J. Aubert *et al.*, Phys. Rev. Lett. **33**, 1404 (1974).

[161] J. E. Augustin *et al.*, Phys. Rev. Lett. **33**, 1406 (1974).

[162] G. S. Abrams *et al.*, Phys. Rev. Lett. **33**, 1453 (1974).

[163] T. Appelquist and H. D. Politzer, Phys. Rev. Lett. **34**, 43 (1975).

[164] A. De Rujula and S. L. Glashow, Phys. Rev. Lett. **34**, 46 (1975).

[165] T. Appelquist, A. De Rujula, H. D. Politzer and S. L. Glashow, Phys. Rev. Lett. **34**, 365 (1975).

[166] E. Eichten, K. Gottfried, T. Kinoshita, J. B. Kogut, K. D. Lane and T. M. Yan, Phys. Rev. Lett. **34**, 369 (1975) [Erratum-ibid. **36**, 1276 (1976)].

[167] S. W. Herb *et al.*, Phys. Rev. Lett. **39**, 252 (1977); W. R. Innes *et al.*, Phys. Rev. Lett. **39**, 1240 (1977) [Erratum-ibid. **39**, 1640 (1977)].

[168] Some earlier reviews on this subject are: V. A. Novikov, L. B. Okun, M. A. Shifman, A. I. Vainshtein, M. B. Voloshin and V. I. Zakharov, Phys. Rept. **41**, 1 (1978); W. Kwong, J. L. Rosner and C. Quigg, Ann. Rev. Nucl. Part. Sci. **37**, 325 (1987); W. Lucha, F. F. Schoberl and D. Gromes, Phys. Rept. **200**, 127 (1991).

[169] E. Eichten, K. Gottfried, T. Kinoshita, K. D. Lane and T. M. Yan, Phys. Rev. Lett. **36**, 500 (1976).

[170] E. Eichten, K. Gottfried, T. Kinoshita, K. D. Lane and T. M. Yan, Phys. Rev. D **17**, 3090 (1978) [Erratum-ibid. D **21**, 313 (1980)]; Phys. Rev. D **21**, 203 (1980).

[171] S. Godfrey and N. Isgur, Phys. Rev. D **32**, 189 (1985).

[172] D. P. Stanley and D. Robson, Phys. Rev. D **21** (1980) 3180.

[173] D. Ebert, R.N. Faustov and V.O. Galkin, Phys. Rev. D **67**, 014027 (2003) [hep-ph/0210381].

[174] S.S. Gershtein, V. V. Kiselev, A. K. Likhoded and A. V. Tkabladze, Phys. Rev. D **51**, 3613 (1995) [arXiv:hep-ph/9406339].

[175] L. P. Fulcher, Phys. Rev. D **44**, 2079 (1991).

[176] L. P. Fulcher, Phys. Rev. D **60**, 074006 (1999) [arXiv:hep-ph/9806444].

[177] L. P. Fulcher, Phys. Rev. D **50**, 447 (1994).

[178] S. N. Gupta, J. M. Johnson, W. W. Repko and C. J. I. Suchyta, Phys. Rev. D **49**, 1551 (1994) [arXiv:hep-ph/9312205].

[179] S. N. Gupta and J. M. Johnson, Phys. Rev. D **53**, 312 (1996) [arXiv:hep-ph/9511267].

[180] J. Zeng, J. W. Van Orden and W. Roberts, Phys. Rev. D **52**, 5229 (1995) [arXiv:hep-ph/9412269].

[181] F. J. Llanes-Estrada, S. R. Cotanch, A. P. Szczepaniak and E. S. Swanson, Phys. Rev. C **70**, 035202 (2004) [arXiv:hep-ph/0402253]; F. J. Llanes-Estrada and S. R. Cotanch, Nucl. Phys. A **697**, 303 (2002) [arXiv:hep-ph/0101078].

[182] M. Baldicchi and G. M. Prosperi, Phys. Rev. D **66**, 074008 (2002) [arXiv:hep-ph/0202172]; M. Baldicchi and G. M. Prosperi, Phys. Rev. D **62**, 114024 (2000) [arXiv:hep-ph/0008017]; P. Maris and C. D. Roberts, Int. J. Mod. Phys. E **12**, 297 (2003) [arXiv:nucl-th/0301049]; N. Brambilla and A. Vairo, Phys. Rev. D **56**, 1445 (1997) [arXiv:hep-ph/9703378]; N. Brambilla and A. Vairo, Phys. Lett. B **407**, 167 (1997) [arXiv:hep-ph/9703377]. N. Brambilla, E. Montaldi and G. M. Prosperi, Phys. Rev. D **54**, 3506 (1996) [arXiv:hep-ph/9504229];

[183] T. J. Allen, T. Coleman, M. G. Olsson and S. Veseli, Phys. Rev. D **67**, 054016 (2003) [arXiv:hep-ph/0207141]; T. J. Allen, M. G. Olsson and S. Veseli, Phys. Rev. D **62**, 094021 (2000) [arXiv:hep-ph/0001227].

[184] C. D. Roberts, Lect. Notes Phys. **647**, 149 (2004) [arXiv:nucl-th/0304050].

[185] N. Brambilla and G. M. Prosperi, Phys. Lett. B **236**, 69 (1990).

[186] N. Brambilla, Nuovo Cim. A **105**, 949 (1992); N. Brambilla and G. M. Prosperi, Phys. Rev. D **46**, 1096 (1992) [Erratum-ibid. D **46**, 4105 (1992)].

[187] T. Barnes and S. Godfrey, Phys. Rev. D **69**, 054008 (2004) [arXiv:hep-ph/0311162].

[188] E. J. Eichten, K. Lane and C. Quigg, Phys. Rev. D **69**, 094019 (2004) [arXiv:hep-ph/0401210].

[189] S. Jacobs, M. G. Olsson and C. I. Suchyta, Phys. Rev. D **33**, 3338 (1986) [Erratum-ibid. D **34**, 3536 (1986)].

[190] J. L. Richardson, Phys. Lett. B **82**, 272 (1979).

[191] W. Buchmüller and S. H. H. Tye, Phys. Rev. D **24**, 132 (1981).

[192] V. B. Berestetskij, E. M. Lifschitz, and L. P. Pitaevskij, *Relativistic Quantum Theory*, (Oxford, New York, Pergamon Press 1971) pp 280-286.

[193] D. Ebert, R. N. Faustov and V. O. Galkin, Phys. Rev. D **62**, 034014 (2000) [arXiv:hep-ph/9911283].

[194] S. Godfrey and R. Kokoski, Phys. Rev. D **43**, 1679 (1991).

[195] This is discussed in more detail in Appendix A of T. Barnes, N. Black and P. R. Page, Phys. Rev. D **68**, 054014 (2003) [arXiv:nucl-th/0208072].

[196] E.J.Eichten and C.Quigg, Phys. Rev. D **49**, 5845 (1994) [hep-ph/9402210].

[197] S. N. Gupta and S. F. Radford, Phys. Rev. D **24** (1981) 2309; Phys. Rev. D **25** (1982) 3430; S. N. Gupta, S. F. Radford and W. W. Repko, Phys. Rev. D **26**, 3305 (1982); J. Pantaleone, S. H. H. Tye and Y. J. Ng, Phys. Rev. D **33**, 777 (1986).

[198] A. H. Hoang and A. V. Manohar, Phys. Lett. B **483**, 94 (2000) [arXiv:hep-ph/9911461].

[199] D. Eiras and J. Soto, Phys. Lett. B **491**, 101 (2000) [arXiv:hep-ph/0005066].

[200] D. Ebert, R. N. Faustov and V. O. Galkin, Phys. Rev. D **66**, 037501 (2002) [ar2002rbXiv:hep-ph/0204204].

[201] N. Isgur, Phys. Rev. D **60**, 054013 (1999) [arXiv:nucl-th/9901032].

[202] T. Barnes and G. I. Ghandour, Phys. Lett. B **118**, 411 (1982).

[203] S. E. Csorna *et al.* [CLEO Collaboration], arXiv:hep-ex/0207060.

[204] S. Godfrey and J. L. Rosner, Phys. Rev. D **64**, 097501 (2001) [Erratum-ibid. D **66**, 059902 (2002)] [arXiv:hep-ph/0105273].

[205] S. Godfrey and J. L. Rosner, Phys. Rev. D **64**, 074011 (2001) [Erratum-ibid. D **65**, 039901 (2002)] [arXiv:hep-ph/0104253].

[206] S. Godfrey and J. L. Rosner, Phys. Rev. D **66**, 014012 (2002) [arXiv:hep-ph/0205255].

[207] S. K. Choi *et al.* [BELLE collaboration], Phys. Rev. Lett. **89**, 102001 (2002) [Erratum-ibid. **89**, 129901 (2002)] [arXiv:hep-ex/0206002].

[208] K. Abe *et al.* [Belle Collaboration], Phys. Rev. Lett. **89**, 142001 (2002) [arXiv:hep-ex/0205104].

[209] J. Ernst *et al.* (CLEO), CLEO-CONF-03-05, hep-ex/0306060.

[210] G. Wagner [BABAR Collaboration], arXiv:hep-ex/0305083.

[211] S. K. Choi *et al.* [Belle Collaboration], Phys. Rev. Lett. **91**, 262001 (2003) [arXiv:hep-ex/0309032].

[212] E. S. Swanson, Phys. Lett. B **598**, 197 (2004) [arXiv:hep-ph/0406080]; E. Braaten, M. Kusunoki and S. Nussinov, Phys. Rev. Lett. **93**, 162001 (2004) [arXiv:hep-ph/0404161].

[213] Y. Q. Chen and Y. P. Kuang, Phys. Rev. D **46**, 1165 (1992) [Erratum-ibid. D **47**, 350 (1993)]; S. M. Ikhdair and R. Sever, Int. J. Mod. Phys. A **19**, 1771 (2004) [arXiv:hep-ph/0310295].

[214] S. S. Gershtein, V. V. Kiselev, A. K. Likhoded and A. V. Tkabladze, Phys. Usp. **38**, 1 (1995) [Usp. Fiz. Nauk **165**, 3 (1995)] [arXiv:hep-ph/9504319].

[215] I. P. Gouz, V. V. Kiselev, A. K. Likhoded, V. I. Romanovsky and O. P. Yushchenko, arXiv:hep-ph/0211432.

[216] S. Godfrey, arXiv:hep-ph/0406228.

[217] F. Abe *et al.* [CDF Collaboration], Phys. Rev. D **58**, 112004 (1998) [arXiv:hep-ex/9804014].

[218] V. A. Novikov, L. B. Okun, M. A. Shifman, A. I. Vainshtein, M. B. Voloshin and V. I. Zakharov, Phys. Rev. Lett. **38**, 626 (1977) [Erratum-ibid. **38**, 791 (1977)].

[219] M. B. Voloshin, Sov. J. Nucl. Phys. **36**, 143 (1982) [Yad. Fiz. **36**, 247 (1982)].

[220] Y. I. Azimov, Y. L. Dokshitzer and V. A. Khoze, Sov. J. Nucl. Phys. **36**, 878 (1982) [Yad. Fiz. **36**, 1510 (1982)].

[221] M. B. Voloshin and Y. M. Zaitsev, Sov. Phys. Usp. **30**, 553 (1987) [Usp. Fiz. Nauk **152**, 361 (1987)].

[222] V. V. Kiselev, Mod. Phys. Lett. A **10**, 2113 (1995) [arXiv:hep-ph/9401339].

[223] G. S. Bali, T. Duessel, T. Lippert, H. Neff, Z. Prkacin and K. Schilling, arXiv:hep-lat/0409137; T. Lippert *et al.* (SESAM Collaboration) talk given at Lattice 2004, Fermilab, June 2004, to appear in the Proceedings.

[224] I. Tamm, J. Phys. (Moscow) **9**, 449 (1945); S. M. Dancoff, Phys. Rev. **78**, 382 (1950).

[225] E. Braaten and M. Kusunoki, Phys. Rev. D **69**, 074005 (2004) [arXiv:hep-ph/0311147].

[226] A. De Rujula, H. Georgi and S. L. Glashow, Phys. Rev. Lett. **38**, 317 (1977).

[227] A. De Rujula and R. L. Jaffe, MIT-CTP-658 *Presented at 5th Int. Conf. on Meson Spectroscopy, Boston, Mass., Apr 29-30, 1977*

[228] A. Le Yaouanc, L. Oliver, O. Pene and J. C. Raynal, Phys. Rev. D **8**, 2223 (1973).

[229] A. Le Yaouanc, L. Oliver, O. Pene and J. C. Raynal, Phys. Rev. D **9**, 1415 (1974).

[230] A. Le Yaouanc, L. Oliver, O. Pene and J. C. Raynal, Phys. Rev. D **12**, 2137 (1975) [Erratum-ibid. D **13**, 1519 (1976)].

[231] L. Micu, Nucl. Phys. B **10**, 521 (1969).

[232] T. Barnes, F. E. Close, P. R. Page and E. S. Swanson, Phys. Rev. D **55**, 4157 (1997) [arXiv:hep-ph/9609339].

[233] S. Godfrey and J. Napolitano, Rev. Mod. Phys. **71**, 1411 (1999) [arXiv:hep-ph/9811410].

[234] A. Le Yaouanc, L. Oliver, O. Pene and J. C. Raynal, Phys. Lett. B **71**, 397 (1977).

[235] N. Isgur and J. Paton, Phys. Rev. D **31**, 2910 (1985).

[236] R. Kokoski and N. Isgur, Phys. Rev. D **35**, 907 (1987).

[237] T. Barnes, arXiv:hep-ph/0406327.

[238] E. S. Ackleh, T. Barnes and E. S. Swanson, Phys. Rev. D **54**, 6811 (1996) [arXiv:hep-ph/9604355].

[239] Y. A. Simonov, Phys. Atom. Nucl. **66**, 2045 (2003) [Yad. Fiz. **66**, 2095 (2003)] [arXiv:hep-ph/0211410].

[240] A. Martin and J. M. Richard, Phys. Lett. B **115**, 323 (1982).

[241] A. Martin and J. M. Richard, CERN Cour. **43N3**, 17 (2003).

[242] E. J. Eichten, K. Lane and C. Quigg, Phys. Rev. Lett. **89**, 162002 (2002) [arXiv:hep-ph/0206018].

[243] J. L. Rosner, Phys. Rev. D **64**, 094002 (2001) [arXiv:hep-ph/0105327].

[244] J. L. Rosner, arXiv:hep-ph/0405196.

[245] S. Eidelman *et al.* [Particle Data Group Collaboration], Phys. Lett. B **592**, 1 (2004).

[246] K. K. Seth, arXiv:hep-ex/0405007.

[247] E. Eichten, Phys. Rev. D **22**, 1819 (1980).

[248] K. Heikkila, S. Ono and N. A. Tornqvist, Phys. Rev. D **29**, 110 (1984) [Erratum-ibid. D **29**, 2136 (1984)].

[249] N. Byers and E. Eichten, UCLA/89/TEP/56 *in Proc. of Europhysics Conf. on High Energy Physics, Madrid, Spain, Sep 6-13, 1989.*

[250] N. Byers, arXiv:hep-ph/9412292.

[251] C. Quigg, arXiv:hep-ph/0403187.

[252] M. K. Gaillard, B. W. Lee and J. L. Rosner, Rev. Mod. Phys. **47**, 277 (1975).

[253] A. De Rujula, H. Georgi and S. L. Glashow, Phys. Rev. D **12**, 147 (1975).

[254] S. Fleck and J. M. Richard, Prog. Theor. Phys. **82**, 760 (1989).

[255] S. Fleck and J. M. Richard, Part. World **1**, 67 (1990).

[256] M. J. Savage and M. B. Wise, Phys. Lett. B **248**, 177 (1990).

[257] M. J. Savage and R. P. Springer, Int. J. Mod. Phys. A **6**, 1701 (1991).

[258] E. Bagan, H. G. Dosch, P. Gosdzinsky, S. Narison and J. M. Richard, Z. Phys. C **64**, 57 (1994) [arXiv:hep-ph/9403208].

[259] R. Roncaglia, D. B. Lichtenberg and E. Predazzi, Phys. Rev. D **52**, 1722 (1995) [arXiv:hep-ph/9502251].

[260] B. Silvestre-Brac, Few Body Syst. **20**, 1 (1996).

[261] S. S. Gershtein, V. V. Kiselev, A. K. Likhoded and A. I. Onishchenko, Phys. Rev. D **62**, 054021 (2000).

[262] V. V. Kiselev and A. E. Kovalsky, Phys. Rev. D **64**, 014002 (2001) [arXiv:hep-ph/0005019].

[263] S. P. Tong, Y. B. Ding, X. H. Guo, H. Y. Jin, X. Q. Li, P. N. Shen and R. Zhang, Phys. Rev. D **62**, 054024 (2000) [arXiv:hep-ph/9910259].

[264] B. A. Gelman and S. Nussinov, Phys. Lett. B **551**, 296 (2003) [arXiv:hep-ph/0209095].

[265] J. M. Richard, Phys. Rept. **212**, 1 (1992).

[266] W. Ponce, Phys. Rev. D **19**, 2197 (1979).

[267] D. Ebert, R. N. Faustov, V. O. Galkin and A. P. Martynenko, Phys. Rev. D **66**, 014008 (2002) [arXiv:hep-ph/0201217].

[268] W. A. Bardeen, E. J. Eichten and C. T. Hill, Phys. Rev. D **68**, 054024 (2003) [arXiv:hep-ph/0305049].

[269] R. L. Jaffe, Phys. Rev. Lett. **38**, 195 (1977) [Erratum-ibid. **38**, 617 (1977)].

[270] H. J. Lipkin, Phys. Lett. B **195**, 484 (1987).

[271] C. Gignoux, B. Silvestre-Brac and J. M. Richard, Phys. Lett. B **193**, 323 (1987).

[272] A. Chodos, R. L. Jaffe, K. Johnson, C. B. Thorn and V. F. Weisskopf, Phys. Rev. D **9**, 3471 (1974).

[273] J. L. Rosner, Phys. Rev. D **33**, 2043 (1986).

[274] G. Karl and P. Zenczykowski, Phys. Rev. D **36**, 2079 (1987).

[275] S. Fleck, C. Gignoux, J. M. Richard and B. Silvestre-Brac, Phys. Lett. B **220**, 616 (1989).

[276] A. Gal, Nucl. Phys. A **721**, 945 (2003) [arXiv:nucl-th/0211070].

[277] G. Karl and P. Zenczykowski, Phys. Rev. D **36**, 3520 (1987).

[278] J. Leandri and B. Silvestre-Brac, Phys. Rev. D **40**, 2340 (1989).

[279] R. L. Jaffe and F. Wilczek, Phys. Rev. Lett. **91**, 232003 (2003) [arXiv:hep-ph/0307341].

[280] I. W. Stewart, M. E. Wessling and M. B. Wise, Phys. Lett. B **590**, 185 (2004) [arXiv:hep-ph/0402076].

[281] Y. R. Liu, A. Zhang, P. Z. Huang, W. Z. Deng, X. L. Chen and S. L. Zhu, Phys. Rev. D **70**, 094045 (2004) [arXiv:hep-ph/0404123].

[282] S. L. Zhu, Int. J. Mod. Phys. **LA19**, 3439 (2004) [arXiv:hep-ph/0406204].

[283] M. Oka, Prog. Theor. Phys. **112**, 1 (2004) [arXiv:hep-ph/0406211].

[284] J. Pochodzalla, arXiv:hep-ex/0406077.

[285] F. Stancu, Phys. Rev. D **58**, 111501 (1998) [arXiv:hep-ph/9803442].

[286] J. P. Ader, J. M. Richard and P. Taxil, Phys. Rev. D **25**, 2370 (1982).

[287] L. Heller and J. A. Tjon, Phys. Rev. D **32**, 755 (1985).

[288] L. Heller and J. A. Tjon, Phys. Rev. D **35**, 969 (1987).

[289] J. Carlson, L. Heller and J. A. Tjon, Phys. Rev. D **37**, 744 (1988).

[290] S. Zouzou, B. Silvestre-Brac, C. Gignoux and J. M. Richard, Z. Phys. C **30**, 457 (1986).

[291] H. J. Lipkin, Phys. Lett. B **172**, 242 (1986).

[292] D. M. Brink and F. Stancu, Phys. Rev. D **49**, 4665 (1994).

[293] D. M. Brink and F. Stancu, Phys. Rev. D **57**, 6778 (1998).

[294] D. Janc and M. Rosina, Few Body Syst. **31**, 1 (2001) [arXiv:hep-ph/0007024].

[295] D. Janc, M. Rosina, D. Treleani and A. Del Fabbro, Few Body Syst. Suppl. **14**, 25 (2003) [arXiv:hep-ph/0301115].

[296] A. Mihaly, H. R. Fiebig, H. Markum and K. Rabitsch, Phys. Rev. D **55**, 3077 (1997).

[297] C. Michael and P. Pennanen [UKQCD Collaboration], Phys. Rev. D **60**, 054012 (1999) [arXiv:hep-lat/9901007]; P. Pennanen, C. Michael and A. M. Green [UKQCD Collaboration], Nucl. Phys. Proc. Suppl. **83**, 200 (2000) [arXiv:hep-lat/9908032].

[298] A. M. Green and P. Pennanen, Phys. Lett. B **426**, 243 (1998) [arXiv:hep-lat/9709124].

[299] A. M. Green and P. Pennanen, Phys. Rev. C **57**, 3384 (1998) [arXiv:hep-lat/9804003].

[300] N. A. Törnqvist, Phys. Rev. Lett. **67**, 556 (1991).

[301] N. A. Törnqvist, Z. Phys. C **61**, 525 (1994) [arXiv:hep-ph/9310247].

[302] A. V. Manohar and M. B. Wise, Nucl. Phys. B **399**, 17 (1993) [arXiv:hep-ph/9212236].

[303] T. E. O. Ericson and G. Karl, Phys. Lett. B **309**, 426 (1993).

[304] D. Bressanini, G. Morosi, L. Bertini and M. Mella, Few-Body Syst. **31**, 199 (2002).

[305] CLEO Collaboration, R. Balest *et al.*, Phys. Rev. D **52**, 2661 (1995).

[306] Belle Collaboration (K. Abe *et al.*), Phys. Rev. Lett. **88**, 031802 (2002).

[307] BABAR Collaboration, (B. Aubert *et al.*), Phys. Rev. D **67**, 032002 (2003) [hep-ex/0207097]. See also Phys. Rev. Lett. **90**, 091801 (2003).

[308] BABAR Collaboration (B. Aubert *et al.*), Phys. Rev. D **65**, 032001 (2002).

[309] BABAR Collaboration (B. Aubert *et al.*), hep-ex/0203040.

[310] R. C. Giles and S.-H. H. Tye, Phys. Rev. D **16**, 1079 (1977).

[311] F. E. Close, I. Dunietz, P. R. Page, S. Veseli and H. Yamamoto, Phys. Rev. D **57**, 5653 (1998).

[312] G. Chiladze, A. F. Falk and A. A. Petrov, Phys. Rev. D **58**, 034013 (1998).

[313] A detailed account with more complete references is given by F. E. Close and S. Godfrey, Phys. Lett. B **574**, 210 (2003) [arXiv:hep-ph/0305285].

[314] J. Merlin and J. Paton, Phys. Rev. D **35**, 1668 (1987).

[315] T. Barnes, F. E. Close and E. S. Swanson, Phys. Rev. D **52**, 5242 (1995) [arXiv:hep-ph/9501405].

[316] T. Barnes, Nucl. Phys. B **158**, 171 (1979); P. Hasenfratz, R. Horgan, J. Kuti, and J. Richard, Phys. Lett. B **95**, 299 (1980); T. Barnes and F. E. Close, Phys. Lett. B **116**, 365 (1982); M. Chanowitz and S. Sharpe, Nucl. Phys. B **222**, 211 (1983); T. Barnes, F. E. Close and F. de Viron, Nucl. Phys. B **224**, 241 (1983); M. Flensberg, C. Peterson, and L. Skold, Z. Phys. C **22**, 293 (1984).

[317] S. Perantonis and C. Michael, Nucl. Phys. B **347**, 854 (1990); L. A. Griffiths, C. Michael and P. E. Rakow, Phys. Lett. B **129**, 351 (1983).

[318] K. J. Juge, J. Kuti and C. J. Morningstar, arXiv:hep-ph/9711451; Nucl. Phys. Proc. Suppl. **63**, 326 (1998) [arXiv:hep-lat/9709131].

[319] D. Horn and J. Mandula, Phys. Rev. D **17**, 898 (1978). Y. S. Kalashnikova and Y. B. Yufryakov, Phys. Atom. Nucl. **60**, 307 (1997) [Yad. Fiz. **60N2**, 374 (1997)] [arXiv:hep-ph/9510357].

[320] N. Isgur, R. Kokoski and J. Paton, Why They Are Missing And Where To Find Them," Phys. Rev. Lett. **54**, 869 (1985).

[321] F. E. Close and P. R. Page, Nucl. Phys. B **443**, 233 (1995) [arXiv:hep-ph/9411301].

[322] P. R. Page, E. S. Swanson and A. P. Szczepaniak, Phys. Rev. D **59**, 034016 (1999) [arXiv:hep-ph/9808346]. E. S. Swanson and A. P. Szczepaniak, Phys. Rev. D **56**, 5692 (1997) [arXiv:hep-ph/9704434].

[323] F. E. Close, Phys. Lett. B **342**, 369 (1995) [arXiv:hep-ph/9409203].

[324] P. R. Page, Phys. Lett. B **402**, 183 (1997) [arXiv:hep-ph/9611375].

[325] Y. P. Kuang and T. M. Yan, Phys. Rev. D **24**, 2874 (1981).

[326] F. E. Close and P. R. Page, Phys. Rev. D **52**, 1706 (1995) [arXiv:hep-ph/9412301].

[327] F. E. Close and J. J. Dudek, Phys. Rev. Lett. **91**, 142001 (2003) [arXiv:hep-ph/0304243].

[328] An estimate of the $\Gamma(\eta'_c \rightarrow \text{light hadrons})$ is given by S. Godfrey and J. L. Rosner, Phys. Rev. D **66**, 014012 (2002).

[329] G. T. Bodwin, E. Braaten, T. C. Yuan, and G. P. Lepage, Phys. Rev. D **46**, R3703 (1992).

[330] M. Beneke, F. Maltoni and I. Z. Rothstein, Phys. Rev. D **59**, 054003 (1999) [arXiv:hep-ph/9808360].

[331] P. Ko, J. Lee and H. S. Song, Phys. Rev. D **53**, 1409 (1996) [arXiv:hep-ph/9510202]; P. Ko, Phys. Rev. D **52**, 3108 (1995).

[332] F. Yuan, C. F. Qiao and K. T. Chao, Phys. Rev. D **56**, 329 (1997) [arXiv:hep-ph/9701250].

[333] P. w. Ko, J. Lee and H. S. Song, Phys. Lett. B **395**, 107 (1997) [arXiv:hep-ph/9701235].

[334] A. A. Zholents *et al.*, Phys. Lett. B **96**, 214 (1980).

[335] J. Z. Bai *et al.* [BES Collaboration], Phys. Rev. Lett. **69**, 3021 (1992).

[336] V.M. Aulchenko et al., Phys. Lett. B573 (2003) 63.

[337] V. M. Aulchenko *et al.* [KEDR Collaboration], Phys. Lett. B **573**, 63 (2003) [arXiv:hep-ex/0306050].

[338] A. A. Sokolov and I. M. Ternov, Phys. Dokl. **8**, 1203 (1964).

[339] A. D. Bukin *et al.*, in: Vth Int. Symposium on High Energy Physics and Elementary Particle Physics, Warsaw, 1975, p.138.

[340] A. S. Artamonov *et al.*, Phys. Lett. B **118**, 225 (1982).

[341] A. S. Artamonov *et al.*, Phys. Lett. B **173**, 272 (1984).

[342] A. S. Artamonov *et al.*, Phys. Lett. B **137**, 272 (1984).

[343] S. E. Baru *et al.*, Z. Phys. C **56**, 547 (1992).

[344] A. S. Artamonov *et al.* [OLYA Collaboration], Phys. Lett. B **474**, 427 (2000) [arXiv:hep-ex/0001040].

[345] W. W. MacKay *et al.* [CUSB Collaboration], Phys. Rev. D **29**, 2483 (1984).

[346] D. P. Barber *et al.* [ARGUS Collaboration], Phys. Lett. B **135**, 498 (1984).

[347] T. A. Armstrong *et al.* [E760 Collaboration], Phys. Rev. D **47**, 772 (1993).

[348] R. Assmann *et al.*, Eur. Phys. J. C **6**, 187 (1999).

[349] A. N. Skrinsky and Y. M. Shatunov, Sov. Phys. Usp. **32**, 548 (1989) [Usp. Fiz. Nauk **158**, 315 (1989)].

[350] C. Bernardini *et al.*, Phys. Rev. Lett. **10**, 407 (1963).

[351] V. E. Blinov *et al.*, Nucl. Instrum. Meth. A **494**, 81 (2002).

[352] V. V. Anashin *et al.*, Nucl. Instrum. Meth. A **478**, 420 (2002).

[353] Y. S. Derbenev, A. M. Kondratenko, S. I. Serednyakov, A. N. Skrinsky, G. M. Tumaikin and Y. M. Shatunov, Part. Accel. **10**, 177 (1980).

[354] S. E. Baru *et al.*, Z. Phys. C **30**, 551 (1986) [Erratum-ibid. C **32**, 622 (1986)].

[355] E. A. Kuraev and V. S. Fadin, Sov. J. Nucl. Phys. **41**, 466 (1985) [Yad. Fiz. **41**, 733 (1985)].

[356] J. D. Jackson and D. L. Scharre, Nucl. Instrum. Meth. **128**, 13 (1975).

[357] A. A. Zholents *et al.*, Yad. Fiz. **34**, 1471 (1981).

[358] E. R. Cohen and B. N. Taylor, J. Phys. Chem. Ref. Data **2**, 664 (1973).

[359] E. R. Cohen and B. N. Taylor, Rev. Mod. Phys. **59**, 1121 (1987) [Europhys. News **18**, 65 (1987)].

[360] T. A. Armstrong *et al.* [E760 Collaboration], Nucl. Phys. B **373**, 35 (1992).

[361] S. Bagnasco *et al.* [Fermilab E835 Collaboration], Phys. Lett. B **533**, 237 (2002).

[362] D. P. McGinnis, G. Stancari, S. J. Werkema, Nucl. Instrum. Methods A **506**, 205 (2003).

[363] M. Andreotti *et al.* [Fermilab E835 Collaboration], Phys. Rev. Lett. **91**, 091801 (2003) [arXiv:hep-ex/0308055].

[364] M. Andreotti *et al.* [Fermilab E835 Collaboration], in preparation.

[365] J. Z. Bai *et al.* [BES Collaboration], Phys. Rev. D **60**, 072001 (1999) [arXiv:hep-ex/9812016].

[366] J. Z. Bai *et al.* [BES Collaboration], Phys. Rev. Lett. **81**, 3091 (1998) [arXiv:hep-ex/9807001].

[367] S. W. Herb *et al.* [E288], Phys. Rev. Lett. **39**, 252 (1977); W. R. Innes *et al.* [E288], Phys. Rev. Lett. **39**, 1240 (1977); *erratum* **39**, 1640 (1977).

[368] C. Berger *et al.* [PLUTO], Phys. Lett. B**76**, 243 (1978); C. W. Darden *et al.* [DASP], Phys. Lett. B**76**, 246 (1978); J. K. Bienlein *et al.* [LENA], Phys. Lett. B**78**, 360 (1978).

[369] K. Han *et al.* [CUSB], Phys. Rev. Lett. **49**, 1612 (1982).

[370] G. Eigen *et al.* [CUSB], Phys. Rev. Lett. **49**, 1616 (1982).

[371] C. Klopfenstein *et al.* [CUSB], Phys. Rev. Lett. **51**, 160 (1983); F. Pauss *et al.* [CUSB], Phys. Lett. B **130**, 439 (1983).

[372] P. Haas *et al.*[CLEO], Phys. Rev. Lett. **52**, 799 (1984).

[373] R. Nernst *et al.* [Crystal Ball], Phys. Rev. Lett. **54**, 2195 (1985); W. S. Walk *et al.* [Crystal Ball], Phys. Rev. D **34**, 2611 (1986).

[374] H. Albrecht *et al.*[ARGUS], Phys. Lett. B **160**, 331 (1985).

[375] T. Skwarnicki *et al.* [Crystal Ball], Phys. Rev. Lett. **58**, 972 (1987).

[376] R. Morrison *et al.* [CLEO-II], Phys. Rev. Lett. **67**, 1696 (1991); U. Heintz *et al.* [CUSB-II], Phys. Rev. D **46** 1928 (1992); G. Crawford *et al.* [CLEO-II], Phys. Lett. B **294**, 139 (1992).

[377] K. W. Edwards *et al.* [CLEO Collaboration], Phys. Rev. D **59**, 032003 (1999) [arXiv:hep-ex/9803010].

[378] M. Artuso *et al.* [CLEOIII], CLNS 04/1897, CLEO 04-16 (2004), *submitted to PRL*.

[379] S. B. Athar *et al.* [CLEO Collaboration], arXiv:hep-ex/0408133.

[380] G. Bonvicini *et al.* [CLEO Collaboration], Phys. Rev. D **70**, 032001 (2004) [arXiv:hep-

ex/0404021].

[381] W. Kwong and J. L. Rosner, Phys. Rev. D **38**, 279 (1988).

[382] J. L. Rosner, Phys. Rev. D **67**, 097504 (2003) [arXiv:hep-ph/0302122].

[383] J. Z. Bai *et al.* [BES Collaboration], Phys. Rev. D **62**, 072001 (2000) [arXiv:hep-ex/0002006].

[384] D. Bisello *et al.* [DM2 collaboration], Nucl. Phys. B **350**, 1 (1991).

[385] Z. Bai *et al.* [MARK-III Collaboration], Phys. Rev. Lett. **65**, 1309 (1990).

[386] R. M. Baltrusaitis *et al.* [Mark-III Collaboration], Phys. Rev. D **33**, 629 (1986).

[387] J. Ernst *et al.*, [CLEO Collaboration], arXiv:hep-ex/0306060. Contributed to Europhysics Conference, July, 2003, Aachen, Germany;

[388] D. M. Asner *et al.* [CLEO Collaboration], Phys. Rev. Lett. **92**, 142001 (2004) [arXiv:hep-ex/0312058].

[389] B. Aubert *et al.* [BABAR Collaboration], arXiv:hep-ex/0311038.

[390] Edwards *et al.*, Phys. Rev. Lett. **48**, 70 (1982).

[391] T. Skwarnicki, Int. J. Mod. Phys. A **19**, 1030 (2004) [arXiv:hep-ph/0311243].

[392] B. Aubert *et al.* [BABAR Collaboration], Nucl. Instrum. Meth. A **479**, 1 (2002) [arXiv:hep-ex/0105044].

[393] F. Fang *et al.* [Belle Collaboration], Phys. Rev. Lett. **90** (2003) 071801 [arXiv:hep-ex/0208047].

[394] K. Abe *et al.* [Belle Collaboration], arXiv:hep-ex/0306015.

[395] T. Barnes, T. E. Browder and S. F. Tuan, Phys. Lett. B **385**, 391 (1996) [arXiv:hep-ph/9605278].

[396] B. Aubert *et al.* [BABAR Collaboration], Phys. Rev. D **70**, 011101 (2004) [arXiv:hep-ex/0403007].

[397] H. C. Huang *et al.* [Belle Collaboration], Phys. Rev. Lett. **91**, 241802 (2003).

[398] J. Z. Bai *et al.* [BES Collaboration], Phys. Lett. B **578**, 16 (2004) [arXiv:hep-ex/0308073].

[399] S. B. Athar *et al.* [CLEO Collaboration], arXiv:hep-ex/0408133.

[400] V. Zambetakis and N. Byers, Phys. Rev. D **28**, 2908 (1983).

[401] S. Godfrey and N. Isgur, Phys. Rev. D **32**, 189 (1985).

[402] T. A. Lahde, C. J. Nyfalt and D. O. Riska, Nucl. Phys. A **645**, 587 (1999) [arXiv:hep-ph/9808438].

[403] D. Ebert, R. N. Faustov and V. O. Galkin, Phys. Rev. D **67**, 014027 (2003) [arXiv:hep-ph/0210381].

[404] A. Boehrer, arXiv:hep-ex/0106020.

[405] A. Boehrer, arXiv:hep-ex/0305029.

[406] A. X. El-Khadra, arXiv:hep-ph/9508266.

[407] L. Marcantonio, P. Boyle, C. T. H. Davies, J. Hein and J. Shigemitsu [UKQCD Collaboration], Nucl. Phys. Proc. Suppl. **94**, 363 (2001) [arXiv:hep-lat/0011053].

[408] C. T. H. Davies, private communication, as cited in [419].

[409] A. Spitz *et al.* [TXL Collaboration], Phys. Rev. D **60**, 074502 (1999) [arXiv:hep-lat/9906009].

[410] T. Manke *et al.* [CP-PACS Collaboration], Phys. Rev. D **62**, 114508 (2000) [arXiv:hep-lat/0005022].

[411] G. S. Bali, K. Schilling and A. Wachter, Phys. Rev. D **56**, 2566 (1997) [arXiv:hep-lat/9703019].

[412] N. Brambilla, private communication, as cited in [419].

[413] S. Narison, Phys. Lett. B **387**, 162 (1996) [arXiv:hep-ph/9512348].

[414] J. L. Rosner, in S. J. Lindenbaum, ed., *Experimental Meson Spectroscopy - 1983*, AIP Conference Proceedings No. 113 (New York: AIP, 1984), p. 46.

[415] T. Barnes, F. E. Close, private communication, as cited in [419].

[416] T. Barnes, arXiv:hep-ph/0103142.

[417] E. J. Eichten and C. Quigg, Phys. Rev. D **49**, 5845 (1994) [arXiv:hep-ph/9402210].

[418] D. Ebert, R. N. Faustov and V. O. Galkin, arXiv:hep-ph/0006186.

[419] A. Heister *et al.* [ALEPH Collaboration], Phys. Lett. B **530**, 56 (2002) [arXiv:hep-ex/0202011].

[420] M. Levtchenko [L3 Collaboration], Nucl. Phys. Proc. Suppl. **126**, 260 (2004).

[421] A. Sokolov, Nucl. Phys. Proc. Suppl. **126**, 266 (2004).

[422] J. Tseng [CDF collaboration], FERMILAB-CONF-02-348-E *Presented at 5th International Conference on Quark Confinement and the Hadron Spectrum, Gargnano, Brescia, Italy, 10-14 Sep 2002*

[423] E. Braaten, S. Fleming and A. K. Leibovich, Phys. Rev. D **63**, 094006 (2001) [arXiv:hep-ph/0008091].

[424] C. Baglin *et al.* [R704 Collaboration], Phys. Lett. B **171**, 135 (1986).

[425] T. A. Armstrong *et al.*, Phys. Rev. Lett. **69**, 2337 (1992).

[426] L. Antoniazzi *et al.* [E705 Collaboration], Phys. Rev. D **50**, 4258 (1994).

[427] M. K. Gaillard, L. Maiani and R. Petronzio, Phys. Lett. B **110**, 489 (1982).

[428] C. Patrignani [for the E835 collaboration], arXiv:hep-ex/0410085.

[429] A. Tomaradze [for the CLEO collaboration], arXiv:hep-ex/0410090.

[430] B. Pietrzyk, "Fit of Standard Model: results on $\alpha_{QED}(M_Z)$ and influence on m_H", Proceeding of "Workshop on Hadron Cross-Section at Low Energies", Pisa, Italy, October 8-10, 2003.

[431] F. Jegerlehner, arXiv:hep-ph/0312372.

[432] B. Lee Roberts, "Results and Prospects on the Measurement of g-2", Proceeding of "Workshop on Hadron Cross-Section at Low Energies", Pisa, Italy, October 8-10, 2003.

[433] M. Davier, "Hadronic contrubition to a_μ", Proceeding of "Workshop on Hadron Cross-Section at Low Energies", Pisa, Italy, October 8-10, 2003.

[434] M. Steinhauser, "The Impact of $\sigma(e^+e^- \to hadron)$ Measurement on the Parameters of Standard Model", Proceeding of "Workshop on Hadron Cross-Section at Low Energies", Pisa, Italy, October 8-10, 2003.

[435] R. R. Akhmetshin *et al.* [CMD-2 Collaboration], Phys. Lett. B **527**, 161 (2002) [arXiv:hep-ex/0112031].

[436] R. R. Akhmetshin *et al.* [CMD-2 Collaboration], Phys. Lett. B **578**, 285 (2004) [arXiv:hep-ex/0308008].

[437] J. Z. Bai *et al.* [BES Collaboration], Phys. Rev. Lett. **84**, 594 (2000) [arXiv:hep-ex/9908046].

[438] J. Z. Bai *et al.* [BES Collaboration], Phys. Rev. Lett. **88**, 101802 (2002) [arXiv:hep-ex/0102003].

[439] J. Burmester *et al.* [PLUTO Collaboration], Phys. Lett. B **66**, 395 (1977).

[440] R. Brandelik *et al.* [DASP Collaboration], Phys. Lett. B **76**, 361 (1978).

[441] J. Siegrist *et al.*, Phys. Rev. Lett. **36**, 700 (1976).

[442] P. A. Rapidis *et al.*, Phys. Rev. Lett. **39**, 526 (1977) [Erratum-ibid. **39**, 974 (1977)].

[443] I. Peruzzi *et al.*, Phys. Rev. Lett. **39**, 1301 (1977).

[444] J. Siegrist *et al.*, "Hadron Production By E+ E- Annihilation At Center-Of-Mass Energies Between Phys. Rev. D **26**, 969 (1982).

[445] G. S. Abrams *et al.*, Phys. Rev. D **21**, 2716 (1980).

[446] G. Goldhaber *et al.*, Phys. Lett. B **69**, 503 (1977).

[447] W. Bacino *et al.*, Phys. Rev. Lett. **40**, 671 (1978).

[448] A. Osterheld *et al.*, SLAC-PUB-4160.

[449] J. Z. Bai *et al.* [BES Collaboration], Nucl. Instrum. Meth. A **458**, 627 (2001).

[450] B. Andersson and H. m. Hu, arXiv:hep-ph/9910285.

[451] E. Eichten, K. Gottfried, T. Kinoshita, K. D. Lane and T. M. Yan, Phys. Rev. D **21**, 203 (1980).

[452] J. C. Chen, G. S. Huang, X. R. Qi, D. H. Zhang and Y. S. Zhu, Phys. Rev. D **62**, 034003 (2000).

[453] F. A. Berends and R. Kleiss, Nucl. Phys. B **178**, 141 (1981).

[454] G. Bonneau and F. Martin, Nucl. Phys. B **27**, 381 (1971).

[455] C. Edwards *et al.*, SLAC-PUB-5160.

[456] M. Eidemuller, J. Phys. G **29**, 1153 (2003) [arXiv:hep-ph/0210247].

[457] G. S. Huang *et al*, "Resonance parameters between $3.7 - 5.0$ GeV from BES data", BES analysis Memo.

[458] D. G. Cassel, "CLEOC and CESR-C: A new frontier of weak and strong interaction", Proceeding of LP2001, 23-28, July 2001, Rome, Italy.

[459] H. S. Chen, "BES III and BEPCII Project", Proceeding of ICHEP2002, 24-31, July 2002, Amsterdam, Holland.

[460] Z. Bai *et al.* [BES Collaboration], Phys. Rev. D **62**, 012002 (2000) [arXiv:hep-ex/9910016].

[461] K. Abe *et al.* [Belle Collaboration], Phys. Rev. Lett. **93**, 051803 (2004) [arXiv:hep-ex/0307061].

[462] J. Z. Bai *et al.* [BES Collaboration], arXiv:hep-ex/0307028.

[463] D. Acosta *et al.* [CDF II Collaboration], Phys. Rev. Lett. **93**, 072001 (2004) [arXiv:hep-ex/0312021].

[464] V. M. Abazov *et al.* [D0 Collaboration], Phys. Rev. Lett. **93**, 162002 (2004) [arXiv:hep-ex/0405004].

[465] B. Aubert *et al.* [BABAR Collaboration], arXiv:hep-ex/0406022.

[466] S. L. Olsen [Belle Collaboration], arXiv:hep-ex/0407033.

[467] S. Pakvasa and M. Suzuki, Phys. Lett. B **579**, 67 (2004) [arXiv:hep-ph/0309294].

[468] M. B. Voloshin, Phys. Lett. B **579**, 316 (2004) [arXiv:hep-ph/0309307].

[469] N. A. Tornqvist, Phys. Lett. B **590**, 209 (2004) [arXiv:hep-ph/0402237].

[470] F. E. Close and P. R. Page, Phys. Lett. B **578**, 119 (2004) [arXiv:hep-ph/0309253].

[471] C. Y. Wong, Phys. Rev. C **69**, 055202 (2004) [arXiv:hep-ph/0311088].

[472] E. Braaten and M. Kusunoki, Phys. Rev. D **69**, 114012 (2004) [arXiv:hep-ph/0402177].

[473] F. Abe *et al.* [CDF Collaboration], Phys. Rev. D **58**, 112004 (1998) [arXiv:hep-ex/9804014].

[474] D0 Collaboration, D0 note 4539-CONF.

[475] A. De Rujula, H. Georgi and S. L. Glashow, Phys. Rev. D **12**, 147 (1975).

[476] M. J. Savage and M. B. Wise, Phys. Lett. B **248**, 177 (1990).

[477] J. G. Korner, M. Kramer and D. Pirjol, Prog. Part. Nucl. Phys. **33**, 787 (1994).

[478] K. Anikeev *et al.*, arXiv:hep-ph/0201071, see references [111-124].

[479] M. Mattson, Ph.D. thesis (Carnegie Mellon University, 2002).

[480] J. Engelfried *et al.*, Nucl. Instrum. Meth. A **431**, 53 (1999).

[481] M. Mattson *et al.* [SELEX Collaboration], Phys. Rev. Lett. **89**, 112001 (2002) [arXiv:hep-ex/0208014].

[482] A. Ocherashvili *et al.* [SELEX Collaboration], arXiv:hep-ex/0406033.

Chapter 4

DECAY

Conveners: E. Eichten, C. Patrignani, A. Vairo

Authors: D. Z. Besson, E. Braaten, A. Deandrea, E. Eichten, T. Ferguson, F. A. Harris, V. V. Kiselev, P. Kroll, Y.- P. Kuang, A. Leibovich, S. L. Olsen, C. Patrignani, A. Vairo

1 INTRODUCTION[1]

The study of decay observables has witnessed in the last years a remarkable progress. New experimental measurements, mainly coming from Belle, BES, CLEO and E835 have improved existing data on inclusive (Section 3 and 4), electromagnetic (Section 3) and several exclusive (Section 5) decay channels as well as on several electromagnetic (Section 6) and hadronic (Section 7) transition amplitudes. In some cases the new data have not only led to a reduction of the uncertainties but also to significant shifts in the central values. Also the error analysis of several correlated measurements has evolved and improved our determination of quarkonium branching fractions (Section 2). New data have also led to the discovery of new states. These have been mainly discussed in Chapter 3.

From a theoretical point of view several heavy quarkonium decay observables may be studied nowadays in the framework of effective field theories of QCD. These have been introduced in Chapters 1 and 3. In some cases, like inclusive and electromagnetic decay widths, factorization of high and low energy contributions has been achieved rigorously. In some others, where more degrees of freedom, apart from the heavy-quarkonium state, are entangled and the problem becomes quite complicated, models are still used to some extent and factorization formulas, if there are, are on a less solid ground. There is room there for new theoretical developments. High energy contributions can be calculated in perturbation theory. Low energy matrix elements, which may include, among others, heavy quarkonium wave functions, colour-octet matrix elements, correlators, overlap integrals in radiative transitions, multipole gluon emission factors, can be determined either by suitable fitting of the data or on the lattice or by means of potential models. They typically set the precision of the theoretical determinations.

In each of the following sections we will have a first part where the theoretical framework is reviewed and the basic formalism set up and a second part that summarizes the phenomenological applications and presents the experimental status. In the last section of the chapter, Section 8, we will discuss decay modes of the B_c. There are no data available yet (apart from the lifetime), but B_c will be copiously produced at future hadron colliders. This system, differently from bottomonium and charmonium, decays only weakly. Therefore, it opens in quarkonium physics a window to some of the electroweak parameters of the Standard Model.

The outline of the chapter is the following. We will start in Section 2 by making some general remarks on the determination of quarkonium branching ratios from experiments. In Section 3 we will discuss inclusive and electromagnetic decay widths, in Section 4 Υ inclusive radiative decays, in Section 5 exclusive decays, in Section 6 radiative and in Section 7 hadronic transitions. Finally, Section 8 will be devoted to the decays of the B_c.

---

[1]Author: A. Vairo

2 BRANCHING RATIO MEASUREMENTS[2]

The measurement of branching ratios (or partial widths) $\mathcal{B}$ is deceptively simple: the total number of events observed in a given final state $N^{\mathrm{obs}}_{Q\bar{Q}\to f}$ is proportional to the total number of events produced $N^{\mathrm{prod}}_{Q\bar{Q}}$ for that particular resonance:

$$N^{\mathrm{obs}}_{Q\bar{Q}\to \mathrm{f}} = \mathrm{eff} \times N^{\mathrm{prod}}_{Q\bar{Q}} \times \mathcal{B}(Q\bar{Q}\to \mathrm{f}), \tag{4.1}$$

$N^{\mathrm{prod}}_{Q\bar{Q}}$ in turn needs to be measured by counting some specific events. In most cases, depending on the process under study and the analysis strategy, $N^{\mathrm{prod}}_{Q\bar{Q}}$ is calculated from the number of events observed in a given "reference" final state $N^{\mathrm{obs}}_{Q\bar{Q}\to \mathrm{Ref}}$:

$$N^{\mathrm{prod}}_{Q\bar{Q}} = \frac{N^{\mathrm{obs}}_{Q\bar{Q}\to \mathrm{Ref}}}{\mathrm{eff}'\ \mathcal{B}_{\mathrm{Ref}}}.$$

The reported value of $\mathcal{B}(Q\bar{Q}\to \mathrm{f})$ will therefore use $\mathcal{B}_{\mathrm{Ref}}$ as reported by some previous experiment:

$$\mathcal{B}(Q\bar{Q}\to \mathrm{f}) = \frac{N^{\mathrm{obs}}_{Q\bar{Q}\to \mathrm{f}}}{N^{\mathrm{obs}}_{Q\bar{Q}\to \mathrm{Ref}}}\ \frac{\mathrm{eff}'}{\mathrm{eff}}\ \mathcal{B}_{\mathrm{Ref}}. \tag{4.2}$$

As discussed in [1], there are a number of potentially dangerous consequences in this procedure. First of all different experiments might use the same reference mode, so their values of $\mathcal{B}$ are not independent. Even worse, the $\mathcal{B}(Q\bar{Q}\to \mathrm{f})$ reported in Eq. (4.2) will also be (hiddenly) correlated to the normalization Ref' chosen by the previous experiment(s) where $\mathcal{B}_{\mathrm{Ref}}$ had been measured, and ultimately may depend on some other branching ratio $\mathcal{B}'_{\mathrm{Ref}'}$. Such hidden correlations are hard to identify and can have pernicious consequences on the evaluation of $\mathcal{B}'$ based on independent measurements from different experiments.

For precision determination of branching ratios or partial widths, it is important to know the normalization used in each measurement and to quote explicitly the quantity that is indeed directly measured by each experiment

$$\frac{\mathcal{B}(Q\bar{Q}\to \mathrm{f})}{\mathcal{B}_{\mathrm{Ref}}} = \frac{N^{\mathrm{obs}}_{Q\bar{Q}\to \mathrm{f}}}{N^{\mathrm{obs}}_{Q\bar{Q}\to \mathrm{Ref}}}\ \frac{\mathrm{eff}'}{\mathrm{eff}}, \tag{4.3}$$

i.e., the ratio or product of branching ratios (even of different particles), which is most directly related to the event yield. Many experiments could also provide measurements of ratios of branching ratios

$$R_{\mathcal{B}}(f/f') = \frac{\mathcal{B}(Q\bar{Q}\to \mathrm{f})}{\mathcal{B}(Q\bar{Q}\to \mathrm{f}')}, \tag{4.4}$$

which do not depend on the normalization, and where usually also a number of other systematics cancel.

With the increased statistical precision that is to be expected in the next few years, it will become increasingly important for an appropriate branching ratio and partial width evaluation that individual measurements are reported according to Eq. (4.3) and whenever possible also as in Eq. (4.4). In order to perform the best estimate based on a set of measurements from different experiments, it might also become important to take into account the systematic errors that are common to all measurements performed by the same experiment. An appropriate choice of a set of independent measurements of (4.3) and (4.4) from each experiment is likely the best option for a global fit to quarkonium branching ratios. A comparison of $R_{\mathcal{B}}(f/f')$ that could be directly measured by virtually all experiments, could also

---

[2]Author: C. Patrignani

help understand possible systematic effects, which are going to be the limiting factor on branching ratio determinations.

Here, we briefly outline the experimental techniques and analysis strategies adopted to determine these branching ratios with emphasis on the corresponding possible normalization choices, as a necessary ingredient to understand possible mutual dependencies and constraints.

2.1 Branching ratios measured in e^+e^- formation experiments

e^+e^- formation experiments are undoubtedly the most important tool to investigate charmonium and bottomonium branching ratios by a variety of techniques. In these experiments the n^3S_1 quarkonium states can be directly formed and the $\mathcal{B}(n^3S_1{\to}f)$ are determined either normalizing to a specific decay mode, i.e., providing a direct measurement of $\dfrac{\mathcal{B}(n^3S_1{\to}f)}{\mathcal{B}(n^3S_1{\to}\text{Norm})}$, or measuring the number of n^3S_1 by performing a scan of the resonance.

The usual choice for the normalization channel is the inclusive hadronic decay mode, which is close to 100% for all resonances, i.e., it provides to a good approximation an absolute normalization. However, it requires subtraction of the non resonant hadronic cross-section whose yield (at the given running condition) must be calculated taking into account the interference with the resonance. When the total number of events is determined by a scan of the resonance (which also provides measurements of Γ_{tot}, $\mathcal{B}_{\ell\ell}$ and $\mathcal{B}_{\text{hadr}}$), there is in principle a possible correlation of the branching ratio to the values for these quantities that is likely small if the scan has many points, but should not be overlooked. As stressed in Chapter 2, Section 8.5, interference with the continuum for any specific final state might introduce sizeable corrections. A measurement of the ratio $R_{\mathcal{B}}(f/\text{Norm})$ across the formation energy of the resonance is needed to understand the interference and its impact on branching ratios.

All other states are studied in hadronic or radiative decays, and the number of events produced for each state must be determined using the appropriate n^3S_1 branching ratio:

$$N^{\text{prod}}_{n'3P_J} = N^{\text{prod}}_{n^3S_1} \times \mathcal{B}(n^3S_1{\to}\gamma\, n'^3P_J), \tag{4.5}$$

$$N^{\text{prod}}_{n'1S_0} = N^{\text{prod}}_{n^3S_1} \times \mathcal{B}(n^3S_1{\to}\gamma\, n'^1S_0). \tag{4.6}$$

Thus, for ^3P_J and $^1S_0$ states these experiments can only directly measure the ratios $R_{\mathcal{B}}(f/f')$ and the following combinations of branching ratios:

$$\frac{\mathcal{B}(n^3S_1{\to}\gamma\, n'^3P_J)}{\mathcal{B}(n^3S_1{\to}\text{Norm})}\,\mathcal{B}(n^3P_J{\to}f), \tag{4.7}$$

$$\frac{\mathcal{B}(n^3S_1{\to}\gamma\, n'^1S_0)}{\mathcal{B}(n^3S_1{\to}\text{Norm})}\,\mathcal{B}(n'^1S_0{\to}f). \tag{4.8}$$

On the other hand, since the $\mathcal{B}(\psi(2S){\to}J/\psi\pi^+\pi^-)$ is reasonably large, and the events can be easily selected by just reconstructing the $\pi^+\pi^-$ recoiling against the J/ψ, absolute measurements of J/ψ branching ratios have been obtained based on "tagged" J/ψ samples:

$$\mathcal{B}(J/\psi{\to}f) = \frac{eff_{\pi^+\pi^- X}}{eff_{\pi^+\pi^- f}}\frac{N^{\text{obs}}(\psi'{\to}(\pi^+\pi^-)_{\text{recoil}}f)}{N^{\text{obs}}(\psi'{\to}(\pi^+\pi^-)_{\text{recoil}} X)}. \tag{4.9}$$

From the experimental point of view this is a particularly clean measurement, since the efficiency ratio can be determined with high precision. With the increased CLEO III samples, it would be interesting to fully exploit the possibility of using "tagged" $\Upsilon(2S)$ and $\Upsilon(3S)$ samples to perform absolute $\Upsilon(1S)$ and $\Upsilon(2S)$ branching ratios determinations.

Radiative decay branching ratios (e.g., direct $1^{--}{\to}\gamma\, X$ and $1^{--}{\to}\gamma\, X{\to}\gamma\gamma X'$) have also been directly measured.

In all cases, photon candidates that are likely to originate from π^0 are not considered (π^0 veto), and the efficiency correction relies on Monte Carlo, and ultimately on the event generator used to model the particle multiplicities, and the angular and momentum distributions.

Despite efforts to tune JETSET [2] fragmentation parameters to reproduce specific classes of inclusive events (e.g., hadronic events in the continuum [3] below $D\bar{D}$ threshold or J/ψ, $\psi(2S)$ decays [4]), there are simply not enough experimentally measured χ_c, χ_b, η_c, η_b decays to light hadrons (*l.h.*) to compare these models with. That could eventually become a limiting systematic to these measurements.

2.2 Branching ratios and partial widths measured in $p\bar{p}$ formation experiments

In these experiments [5] a scan of the resonance allows direct measurements of mass, total width and $\mathcal{B}(p\bar{p})\mathcal{B}_{\rm f}$ for all charmonium resonances.[3] For resonances whose natural width is comparable or smaller than the beam width ($\mathcal{O}(700\,{\rm MeV})$ for E760 and E835), the product $\mathcal{B}(p\bar{p})\mathcal{B}_{\rm f}$ is highly correlated to the total width, and the quantity $\Gamma(p\bar{p})\mathcal{B}_{\rm f}$ is more precisely determined. By detecting the resonance formation in more than one final state, the ratio of branching ratios $R_{\mathcal{B}}(f/f')$ can be determined independently from the total width and $\mathcal{B}(p\bar{p})$, in general with small systematic errors since the final state is fully reconstructed, and the angular distribution only depends on a limited number of decay and formation amplitudes. Interference effects with the continuum could affect the measurement of $\mathcal{B}(p\bar{p})\mathcal{B}_{\rm f}$ and $R_{\mathcal{B}}(f/f')$, but as in e^+e^- experiments, their relevance could be estimated by a measurement of $R_{\mathcal{B}}(f/f')$ across the formation energy of the resonance. Unfortunately, only a few highly characteristic final states of charmonium (e^+e^-, $J/\psi\,X$, $\gamma\gamma$) can be detected by these experiments, because of the large hadronic non-resonant cross-section.

Recently, a pioneering study of $p\bar{p}\to\pi^0\pi^0$ [6] and $\eta\eta$ differential cross-sections at the χ_{c0} formation energy has shown that also selected exclusive two-body hadronic decays can be successfully measured. The interference with the continuum could be successfully exploited by the next generation of $p\bar{p}$ annihilation experiments to extend the knowledge of χ_c and η_c branching ratios to baryons or light hadrons.

2.3 Branching ratios and partial widths measured in two-photon reactions

The number of events observed for a specific final state is proportional to $\Gamma_{\gamma\gamma}\mathcal{B}_{\rm f}\times\mathcal{L}_{\gamma\gamma}$, where the effective two-photon luminosity function $\mathcal{L}_{\gamma\gamma}$ (see Chapter 2, Section 8.4) is calculated by all experiments using the same formalism (even if not all using the same generator). The only directly measurable quantity is

$$\Gamma_{\gamma\gamma}\mathcal{B}_{\rm f}, \tag{4.10}$$

or (if more than one final state is detected) $R_{\mathcal{B}}(f/f')$. The theoretical uncertainties in $\mathcal{L}_{\gamma\gamma}$ are largely common to all experiments and that should be taken into account for future high statistics measurements. It might be worth mentioning here that the values reported in the past by different experiments for the $\Gamma_{\gamma\gamma}$, derived from their measurement of (4.10), are not independent and they are not always easily comparable since some of them are obtained by a weighted average of many decay modes, which are individually poorly known.

2.4 Branching ratios and partial widths measured by radiative return (ISR)

Because of initial state radiation (ISR, also referred to as hard photon emission or radiative return), e^+e^- colliders are effectively at the same time (asymmetric) colliders for all $\sqrt{s}$ energies below nominal collision energy. The effective luminosity (and therefore event yields) can be sizeable [7] and can be determined quite accurately by counting $\mu\mu\gamma$ events, for which precise expressions (and event generators

---

[3]The $p\bar{p}$ branching ratios of bottomonium states are likely 3 orders of magnitudes smaller than for charmonium, and only when a measurement will be available, it will be possible to judge on the feasibility of such experiments.

based on them) are commonly available. The major advantage of this technique is that $e^+e^-\to X$ can be measured simultaneously and under uniform detector conditions over a broad range of $\sqrt{s}$. And they "come for free" at any of the e^+e^- factories, which are expected to collect large data samples.

The main interest is the measurement of R, but for any exclusive final state those experiments could obtain a direct measurement of $\Gamma_{e^+e^-}\mathcal{B}_{\mathrm{f}}$ for any resonance whose mass is lower than the collision energy, and, again by detecting more than one final state, $R_\mathcal{B}(f/f')$. To date only BES [8] and BaBar [9] have used this technique to measure $\Gamma(\psi'\to e^+e^-)\mathcal{B}(\psi'\to J/\psi\pi\pi)$ and $\Gamma(J/\psi\to e^+e^-)\mathcal{B}(J/\psi\to\mu^+\mu^-)$ respectively. Measurements of $\Gamma_{e^+e^-}\mathcal{B}_{l^+l^-}$ would provide important constraints on both the total width and $\Gamma_{e^+e^-}$ for all 1^{--} states, providing at the same time an important cross check for possible systematic errors.

2.5 Branching ratios measured in B decays

Asymmetric B factories focused originally on exclusive B decays to final states involving a $c\bar{c}$ as the cleanest modes to study CP violation.

With the impressive amount of data collected so far (more than $500\,\mathrm{fb}^{-1}$ as of summer 2004 adding Belle and BaBar) and $\mathcal{B}(B\to c\bar{c}X)$ of order 10^{-3}, both experiments are collecting larger and larger samples of exclusive B decays to charmonia, and they are obviously interested in reconstructing them into as many different final states as possible. The same is true for D0 and CDF, since the preliminary reconstruction of highly characteristic exclusive charmonium (and bottomonium) final states is needed for other analyses.

For charmonium the quantity directly measured by these experiments is

$$\mathcal{B}(B\to c\bar{c}X)\times\mathcal{B}(c\bar{c}\to\mathrm{f}), \tag{4.11}$$

and again from the number of fully reconstructed events into different final states these experiments can directly measure $R_\mathcal{B}(f/f')$ for a variety of final states and for virtually all quarkonium states. Even if the precision might not always compete with other techniques, the wide range of possible $R_\mathcal{B}(f/f')$ measurements, with likely different sources of systematic errors, would certainly be important in evaluating quarkonium branching ratios, in particular for those states (χ_Q and η_Q) whose branching ratios are largely unknown.

2.6 Indirect determinations as a tool to investigate systematic effects

The possibilities offered by the mutual constraints posed by measurements of different products or ratios of branching ratios have so far been only partially exploited.

The first advantage is that branching ratios measured by different techniques have different sources of systematic errors, and the comparison can provide insight on how to nail them down. The current best estimate for $\mathcal{B}(\chi_{c2}\to\gamma J/\psi)$ [10] is largely determined by measurements of $\Gamma(\chi_{c2}\to p\bar{p})\mathcal{B}(\chi_{c2}\to\gamma J/\psi)$, $\Gamma(\chi_{c2}\to\gamma\gamma)\mathcal{B}(\chi_{c2}\to\gamma J/\psi)$ and $\mathcal{B}(\chi_{c2}\to\gamma\gamma)/\mathcal{B}(\chi_{c2}\to\gamma J/\psi)$, to the point that these measurements indirectly constrain the estimate of $\mathcal{B}(\psi'\to\gamma\chi_{c2})$ to a value significantly lower than the world average of direct measurements, since the product $\mathcal{B}(\psi'\to\gamma\chi_{c2})\mathcal{B}(\chi_{c2}\to\gamma J/\psi)$ has been measured with high precision.[4]

The other advantage is that measurements of different product and ratios of branching ratios pose constraints on their values: for χ_{c0} at present the partial widths $\Gamma_{\gamma\gamma}$ and $\Gamma_{\gamma J/\psi}$ are known to $\approx 10\%$ [10], even if none of the many measurements more or less directly related to these quantities (Γ, $\Gamma_{\gamma\gamma}\mathcal{B}_{4\pi}$, $\Gamma_{\gamma\gamma}/\Gamma_{\gamma J/\psi}$, $\Gamma_{\gamma J/\psi}\mathcal{B}_{p\bar{p}}$, $\mathcal{B}(\psi'\to\gamma\chi_{c0})$, $\mathcal{B}(\psi'\to\gamma\chi_{c0})\mathcal{B}_{p\bar{p}}$, $\mathcal{B}(\psi'\to\gamma\chi_{c0})\mathcal{B}_{\gamma J/\psi}$ and others) is individually known much better than that.

---

[4]New more precise measurements of $\mathcal{B}(\psi'\to\gamma\chi_{c2})$ might in turn provide constraints for $\mathcal{B}(\psi'\to\gamma\chi_{c2})\mathcal{B}(\chi_{c2}\to\gamma J/\psi)$

The proposed next generation of $p\bar{p}$ experiments with extended PID ability could provide invaluable information by measuring $p\bar{p}\rightarrow p\bar{p}$ differential cross-section at the η_c (and possibly at the χ_{c0}). This would provide a direct measurement of $\mathcal{B}(c\bar{c}\rightarrow p\bar{p})$, indirectly constraining the radiative J/ψ (and ψ') M1 transitions from the well measured $\mathcal{B}(J/\psi\rightarrow\gamma\eta_c\rightarrow\gamma p\bar{p})$. Since at present the $\approx 30\%$ uncertainty in $\mathcal{B}(J/\psi\rightarrow\gamma\eta_c)$ is the major source of uncertainty in all η_c branching ratios, this will also directly affect all η_c branching ratios.

With the increased statistics available at B factories it might soon become possible to determine at least some of the $\mathcal{B}(B\rightarrow c\bar{c}\,l.h.)$ branching ratios without explicitly reconstructing the charmonium. In this case, simultaneous measurements of the same B decay mode in exclusive final states $\mathcal{B}(B\rightarrow c\bar{c}\,l.h.)\mathcal{B}(c\bar{c}\rightarrow\mathrm{f})$ would allow B factories to directly measure $\mathcal{B}(c\bar{c}\rightarrow\mathrm{f})$ from Eq. (4.11). Considering that the photon in $\psi(2S)\rightarrow\gamma\eta_c(2S)$ is very soft and that this inclusive radiative transition will likely be difficult to measure for both CLEO-c and BES III, this might well be the best way of determining the $\eta_c(2S)$ branching ratios, and indirectly determining the partial width for the M1 $\psi(2S)\rightarrow\gamma\eta_c(2S)$ transition itself.

3 ELECTROMAGNETIC AND INCLUSIVE DECAYS INTO LIGHT PARTICLES[5]

3.1 Theoretical framework

The main dynamical mechanism of heavy-quarkonium decay into light particles is quark–antiquark annihilation. Since this happens at a scale $2m$ (m is the heavy quark mass), which is perturbative, the heavy quarks annihilate into the minimal number of gluons allowed by colour conservation and charge conjugation. The gluons subsequently create light quark–antiquark pairs that form the final state hadrons: $Q\bar{Q}\rightarrow ng^{*}\rightarrow m(q\bar{q})$. Values of n are given for various quarkonia in Table 4.1; for comparison the minimal number of photons into which a $Q\bar{Q}$ pair can annihilate is also listed. Experimentally this fact is reflected by the narrow width of the heavy quarkonia decays into hadronic channels in a mass region where strong decays typically have widths of hundreds of MeV. As an example let us consider the J/ψ decay into light hadrons. Following [11], this process is regarded as the decay into three real gluons. The calculation of this width leads to the result

$$\Gamma(J/\psi\rightarrow l.h.) \;=\; \frac{10}{81}\frac{\pi^2-9}{\pi e_c^2}\frac{\alpha_{\mathrm{s}}^3}{\alpha_{\mathrm{em}}^2}\,\Gamma(J/\psi\rightarrow e^+e^-) = 205\ \mathrm{keV}\left(\frac{\alpha_{\mathrm{s}}}{0.3}\right)^3. \tag{4.12}$$

Although this value is somewhat larger than the experimental one it explains the narrowness of the hadronic decays of the quarkonia. Corrections like relativistic, α_{s} or colour-octet ones, may lead to a better agreement with experiment. A systematic way to include these corrections is provided by nonrelativistic effective field theories of QCD.

In an effective field theory language[6], at scales lower than m heavy-quarkonium annihilation is resolved as a contact interaction. This is described at the Lagrangian level by four-fermion operators whose matching coefficients develop an imaginary part. Consequently, the annihilation width of a heavy quarkonium state $|H\rangle$ into light particles may be written as

$$\Gamma(H \rightarrow light\ particles) = 2\,\mathrm{Im}\,\langle H|\mathcal{L}_{\psi\chi}|H\rangle, \tag{4.13}$$

where $\mathcal{L}_{\psi\chi}$ is given by Eq. (1.8) of Chapter 1 up to four-fermion operators of dimension 6. The low-energy dynamics is encoded in the matrix elements of the four-fermion operators evaluated on the heavy-quarkonium state. If one assumes that only heavy-quarkonium states with quark-antiquark in a colour-singlet configuration can exist, then only colour-singlet four-fermion operators contribute and the matrix elements reduce to heavy-quarkonium wave functions (or derivatives of them) calculated at the origin.

---

[5]Authors: T. Ferguson, C. Patrignani, A. Vairo
[6]We refer to Chapter 1 for a basic introduction to effective field theories and NRQCD.

Table 4.1: Quantum numbers of quarkonium states and the minimal number of virtual gluons and photons into which they can annihilate. The subscript d refers to a gluonic colour-singlet state that is totally symmetric under permutations of the gluons.

	$^{2S+1}L_J$	$I^G(J^{PC})$	gluons	photons
η_c, η_b	$^1S_0$	$0^+(0^{-+})$	2g	2γ
J/ψ, $\Upsilon(1S)$	$^3S_1$	$0^-(1^{--})$	$(3g)_d$	γ
h_c, h_b	$^1P_1$	$0^-(1^{+-})$	$(3g)_d$	3γ
χ_{c0}, χ_{b0}	$^3P_0$	$0^+(0^{++})$	2g	2γ
χ_{c1}, χ_{b1}	$^3P_1$	$0^+(1^{++})$	2g	2γ
χ_{c2}, χ_{b2}	$^3P_2$	$0^+(2^{++})$	2g	2γ

This assumption is known as the "colour-singlet model". Explicit calculations show that at higher order the colour-singlet matching coefficients develop infrared divergences (for P waves this happens at NLO [12]). In the colour-singlet model, these do not cancel in the expression of the decay widths. It has been the first success of NRQCD [13, 14] to show that the Fock space of a heavy-quarkonium state may contain a small component of quark–antiquark in a colour-octet configuration, bound with some gluonic degrees of freedom (the component is small because operators coupling transverse gluons with quarks are suppressed by powers of $v \ll 1$, v being the heavy-quark velocity in the centre-of-mass frame), that due to this component, matrix elements of colour-octet four-fermion operators contribute and that exactly these contributions absorb the infrared divergences of the colour-singlet matching coefficients in the decay widths, giving rise to finite results [14, 15]. NRQCD is now the standard framework to study heavy-quarkonium inclusive decays.

The NRQCD factorization formulas are obtained by separating contributions coming from degrees of freedom of energy m from those coming from degrees of freedom of lower energy. In the case of heavy-quarkonium decay widths, they have been rigorously proved [14]. High-energy contributions are encoded into the imaginary parts of the four-fermion matching coefficients, $f, g_{1,8,ee,\gamma\gamma,...}(^{2S+1}L_J)$ and are ordered in powers of α_s (coefficients labeled with ee, $\gamma\gamma$, ... refer to pure electromagnetic decays into e^+e^-, $\gamma\gamma$, ...). Low-energy contributions are encoded into the matrix elements of the four-fermion operators on the heavy-quarkonium states $|H\rangle$ ($\langle \ldots \rangle_H \equiv \langle H| \ldots |H\rangle$). These are, in general, nonperturbative objects, which can scale as powers of Λ_{QCD}, mv, mv^2, ... (i.e., of the low-energy dynamical scales of NRQCD). Therefore, matrix elements of higher dimensionality are suppressed by powers of v or Λ_{QCD}/m. Including up to four-fermion operators of dimension 8, the NRQCD factorization formulas for inclusive decay widths of heavy quarkonia into light hadrons, which follow from Eq. (4.13), read [14, 15]:

$$
\begin{aligned}
\Gamma(V_Q(nS) \to l.h.) = \frac{2}{m^2} \bigg(&\operatorname{Im} f_1(^3S_1) \langle O_1(^3S_1) \rangle_{V_Q(nS)} \\
&+ \operatorname{Im} f_8(^3S_1) \langle O_8(^3S_1) \rangle_{V_Q(nS)} + \operatorname{Im} f_8(^1S_0) \langle O_8(^1S_0) \rangle_{V_Q(nS)} \\
&+ \operatorname{Im} g_1(^3S_1) \frac{\langle \mathcal{P}_1(^3S_1) \rangle_{V_Q(nS)}}{m^2} + \operatorname{Im} f_8(^3P_0) \frac{\langle O_8(^3P_0) \rangle_{V_Q(nS)}}{m^2} \\
&+ \operatorname{Im} f_8(^3P_1) \frac{\langle O_8(^3P_1) \rangle_{V_Q(nS)}}{m^2} + \operatorname{Im} f_8(^3P_2) \frac{\langle O_8(^3P_2) \rangle_{V_Q(nS)}}{m^2} \bigg), \quad (4.14)
\end{aligned}
$$

$$\Gamma(P_Q(nS) \to l.h.) = \frac{2}{m^2} \left(\mathrm{Im}\, f_1(^1S_0) \, \langle O_1(^1S_0) \rangle_{P_Q(nS)} \right.$$

$$+ \mathrm{Im}\, f_8(^1S_0) \, \langle O_8(^1S_0) \rangle_{P_Q(nS)} + \mathrm{Im}\, f_8(^3S_1) \, \langle O_8(^3S_1) \rangle_{P_Q(nS)}$$

$$\left. + \mathrm{Im}\, g_1(^1S_0) \frac{\langle \mathcal{P}_1(^1S_0) \rangle_{P_Q(nS)}}{m^2} + \mathrm{Im}\, f_8(^1P_1) \frac{\langle O_8(^1P_1) \rangle_{P_Q(nS)}}{m^2} \right), \quad (4.15)$$

$$\Gamma(\chi_Q(nJS) \to l.h.) = \frac{2}{m^2} \left(\mathrm{Im}\, f_1(^{2S+1}P_J) \frac{\langle O_1(^{2S+1}P_J) \rangle_{\chi_Q(nJS)}}{m^2} \right.$$

$$\left. + \mathrm{Im}\, f_8(^{2S+1}S_S) \, \langle O_8(^1S_0) \rangle_{\chi_Q(nJS)} \right). \tag{4.16}$$

At the same order the electromagnetic decay widths are given by:

$$\Gamma(V_Q(nS) \to e^+ e^-) = \frac{2}{m^2} \left(\mathrm{Im}\, f_{ee}(^3S_1) \, \langle O_{\mathrm{EM}}(^3S_1) \rangle_{V_Q(nS)} \right.$$

$$\left. + \mathrm{Im}\, g_{ee}(^3S_1) \frac{\langle \mathcal{P}_{\mathrm{EM}}(^3S_1) \rangle_{V_Q(nS)}}{m^2} \right), \tag{4.17}$$

$$\Gamma(P_Q(nS) \to \gamma\gamma) = \frac{2}{m^2} \left(\mathrm{Im}\, f_{\gamma\gamma}(^1S_0) \, \langle O_{\mathrm{EM}}(^1S_0) \rangle_{P_Q(nS)} \right.$$

$$\left. + \mathrm{Im}\, g_{\gamma\gamma}(^1S_0) \frac{\langle \mathcal{P}_{\mathrm{EM}}(^1S_0) \rangle_{P_Q(nS)}}{m^2} \right), \tag{4.18}$$

$$\Gamma(\chi_Q(nJ1) \to \gamma\gamma) = 2\, \mathrm{Im}\, f_{\gamma\gamma}(^3P_J) \frac{\langle O_{\mathrm{EM}}(^3P_J) \rangle_{\chi_Q(nJ1)}}{m^4}, \quad J = 0, 2. \tag{4.19}$$

The symbols V_Q and P_Q indicate respectively the vector and pseudoscalar S-wave heavy quarkonium and the symbol χ_Q the generic P-wave quarkonium (the states $\chi_Q(n10)$ and $\chi_Q(nJ1)$ are usually called $h_Q((n-1)P)$ and $\chi_{QJ}((n-1)P)$, respectively).

The operators $O, \mathcal{P}_{1,8,\mathrm{EM}}(^{2S+1}L_J)$ are the dimension 6 and 8 four-fermion operators of the NR-QCD Lagrangian. They are classified by their transformation properties under colour as singlets (1) and octets (8), and under spin (S), orbital (L) and total angular momentum (J). The operators with the subscript EM are the colour-singlet operators projected on the QCD vacuum. The explicit expressions of the operators can be found in [14] (or listed in Appendix A of [16]). The dimension 6 operators are also given in Eq. (1.8) of Chapter 1.

In general different power countings are possible at the level of NRQCD, due to the fact that different scales (mv, Λ_{QCD}, mv^2, $\sqrt{m\Lambda_{\mathrm{QCD}}}$, ...) are still dynamically entangled [17, 18]. Likely different power countings will apply to different physical systems. Therefore, the relative importance of the different matrix elements that appear in Eqs. (4.14)–(4.19) may change in going from lower to higher quarkonium states and from bottomonium to charmonium. Whatever the power counting is, the pseudoscalar and vector state decay widths are dominated by the colour-singlet matrix elements, which contribute at order mv^3. The hadronic P-state decay widths have two contributions (the colour-singlet and colour-octet matrix elements), which contribute at the same order mv^5, if we assume that a fraction v of the P-state wave function projects onto the colour-octet operator.

Since NRQCD is an expansion in two small parameters (α_s and v), progress comes typically from (1) improving the perturbative series of the matching coefficients either by fixed order calculations or by resumming large contributions (large logs or large contributions associated to renormalon singularities);

(2) improving the knowledge of the NRQCD matrix elements either by direct evaluation, which may be obtained by fitting the experimental data, by lattice calculations, and by models, or by exploiting the hierarchy of scales still entangled in NRQCD and constructing EFTs of lower energy.

3.1.1 The perturbative expansion

The imaginary parts of the four-fermion matching coefficients have been calculated over the last twenty years to different levels of precision. Up to order α_s^3 the imaginary parts of $f_8(^1S_0)$, $f_1(^3P_1)$, and $f_8(^3P_J)$ can be found in [19], the imaginary parts of $f_8(^3S_1)$, $f_8(^1P_1)$ in [20] and the imaginary part of $f_1(^1S_0)$ in [19,21]. Two different determinations of $f_1(^3P_0)$ and $f_1(^3P_2)$ exist at NLO in [19] and [22]. The imaginary part of $f_1(^3S_1)$ has been calculated (numerically) up to order α_s^4 in [23]. The imaginary part of $g_1(^3S_1)$ at order α_s^3 can be found in [24], the imaginary part of $g_1(^1S_0)$ at order α_s^2 in [14]. Where the electromagnetic coefficients are concerned, the imaginary part of $f_{ee}(^3S_1)$ has been calculated up to order $\alpha^2\alpha_s^2$ in [25, 26], the imaginary parts of $f_{\gamma\gamma}(^1S_0)$ and $f_{\gamma\gamma}(^3P_{0,2})$ up to order $\alpha^2\alpha_s$ can be found in [19, 27] and $g_{ee}(^3S_1)$ and $g_{\gamma\gamma}(^1S_0)$ up to order α^2 in [14]. A complete list of the above matching coefficients at our present level of knowledge can be found in Appendix A of [28]. The LL running for the imaginary parts of the matching coefficients of the four-fermion NRQCD operators of dimension 6 and 8 have been obtained in [16] and can be read there in Appendix C. The tree-level matching of dimension 9 and 10 S-wave operators can be found in [29]. The tree-level matching of dimension 9 and 10 electromagnetic P-wave operators can be found in [30].

The convergence of the perturbative series of the four-fermion matching coefficients is often poor. While the large two-loop contribution of $\mathrm{Im}\, f_{ee}(^3S_1)$ seems to be related, at least in the bottomonium case, to the factorization scale and, therefore, may be put presumably under control via renormalization group improvement techniques [26,31], large corrections appearing in other S-wave decay channels have been ascribed to renormalon-type contributions [32]. There is no such study so far for P-wave decays.

3.1.2 The relativistic expansion

The NRQCD matrix elements may be fitted to the experimental decay data [33–35] or calculated on the lattice [36, 37]. The matrix elements of colour-singlet operators can be linked at leading order to the Schrödinger wave functions at the origin [14][7] and, hence, may be evaluated by means of potential models [38] or potentials calculated on the lattice [39]. In [34] by fitting to the charmonium P-wave decay data it was obtained that $\langle O_1(^1P_1)\rangle_{h_c(1P)} \approx 8.1 \times 10^{-2}$ GeV^5 and $\langle O_8(^1S_0)\rangle_{h_c(1P)} \approx 5.3 \times 10^{-3}$ GeV^3 in the $\overline{\mathrm{MS}}$ scheme and at the factorization scale of 1.5 Gev. In the quenched lattice simulation of [37] it was obtained that $\langle O_1(^1S_0)\rangle_{\eta_c(1S)} \approx 0.33$ GeV^3, $\langle O_1(^1P_1)\rangle_{h_c(1P)} \approx 8.0 \times 10^{-2}$ GeV^5 and $\langle O_8(^1S_0)\rangle_{h_c(1P)} \approx 4.7 \times 10^{-3}$ GeV^3 in the $\overline{\mathrm{MS}}$ scheme and at the factorization scale of 1.3 Gev. In the lattice simulation of [36] and in the three light-quark flavours extrapolation limit it was obtained that $\langle O_1(^1S_0)\rangle_{\eta_b(1S)} \approx 4.1$ GeV^3, $\langle O_1(^1P_1)\rangle_{h_b(1P)} \approx 3.3$ GeV^5 and $\langle O_8(^1S_0)\rangle_{h_b(1P)} \approx 5.9 \times 10^{-3}$ GeV^3 in the $\overline{\mathrm{MS}}$ scheme and at the factorization scale of 4.3 GeV.

It has been discussed in [30] and [29], that higher-order operators, not included in the formulas (4.14)–(4.19), even if parametrically suppressed, may turn out to give sizable contributions to the decay widths. This may be the case, in particular, for charmonium, where $v^2 \sim 0.3$, so that relativistic corrections are large, and for P-wave decays where the above formulas provide, indeed, only the leading-order contribution in the velocity expansion. In fact it was pointed out in [30] (see also [40]) that if no special cancellations among the matrix elements occur, then the order v^2 relativistic corrections to the electromagnetic decays $\chi_{c0}{\rightarrow}\gamma\gamma$ and $\chi_{c2}{\rightarrow}\gamma\gamma$ may be as large as the leading terms.

In [24, 34] it was also noted that the numerical relevance of higher-order matrix elements may be enhanced by their multiplying matching coefficients. This is, indeed, the case for the decay width of S-wave vector states, where the matching coefficients multiplying the colour-octet matrix elements (with

---

[7]This statement acquires a precise meaning only in the context of pNRQCD, see Section 3.1.3.

the only exception of $\mathrm{Im}f_8(^3P_1)$) are enhanced by α_{s} with respect to the coefficient $\mathrm{Im}f_1(^3S_1)$ of the leading colour-singlet matrix element.

In the bottomonium system, 14 S- and P-wave states lie below the open flavour threshold ($\Upsilon(nS)$ and $\eta_b(nS)$ with $n = 1, 2, 3$; $h_b(nP)$ and $\chi_{bJ}(nP)$ with $n = 1, 2$ and $J = 0, 1, 2$) and in the charmonium system 8 ($\psi(nS)$ and $\eta_c(nS)$ with $n = 1, 2$; $h_c(1P)$ and $\chi_{cJ}(1P)$ with $J = 0, 1, 2$). For these states Eqs. (4.14)–(4.19) describe the decay widths into light hadrons and into photons or e^+e^- in terms of 46 NRQCD matrix elements (40 for the S-wave decays and 6 for the P-wave decays), assuming the most conservative power counting. More matrix elements are needed if higher-order operators are included.

3.1.3 pNRQCD

The number of nonperturbative parameters may be reduced by integrating out from NRQCD degrees of freedom with energy lower than m, since each degree of freedom that is integrated out leads to a new factorization. Eventually, one ends up with pNRQCD [41, 42], where only degrees of freedom of energy mv^2 are left dynamical. In the context of pNRQCD, the NRQCD four-fermion matrix elements can be written either as convolutions of Coulomb amplitudes with non-local correlators (in the dynamical situation $mv^2 \gtrsim \Lambda_{\mathrm{QCD}}$) or as products of wave functions at the origin by non-local correlators (in the dynamical situation $mv^2 \ll \Lambda_{\mathrm{QCD}}$).

The first situation may be the relevant one at least for the bottomonium ground state [42–44]. In the limiting case $mv^2 \gg \Lambda_{\mathrm{QCD}}$, the correlators reduce to local condensates and explicit formulas have been worked out in [45, 46]. Concerning the perturbative calculation of the electromagnetic decay widths, the NLL renormalization group improved expression can be found in [47] and has been used in a phenomenological analysis in [48]. The perturbative wave functions at the origin at NNLO order can be found in [49]. Recently, a full NNLL analysis has been carried out in [31]; the authors predict $\Gamma(\eta_b \to \gamma\gamma)/\Gamma(\Upsilon(1S) \to e^+e^-) = 0.502 \pm 0.068 \pm 0.014$, where the first error is an estimate of the theoretical uncertainty and the second reflects the uncertainty in α_{s}. We also mention that there exists a determination of $\Gamma(\Upsilon(2S) \to e^+e^-)/\Gamma(\Upsilon(1S) \to e^+e^-)$ in lattice NRQCD with 2+1 flavours of dynamical quarks [50]. The calculated ratio is still far from the experimental result, although the unqueching has considerably reduced the discrepancy.

The last situation is expected to be the relevant one for most of the existing excited heavy-quarkonium states (with the possible exception of the lowest bottomonium states) and has been studied in [16, 51, 52]. However, a general consensus on the above assignments of heavy-quarkonium states to dynamical regions has not been reached yet (see also Chapter 3).

At leading order in the v and Λ_{QCD}/m expansion, the colour-singlet matrix elements can be expressed in terms of the wave functions at the origin only [14, 16]:

$$\langle O_1(^3S_1)\rangle_{V_Q(nS)} = \langle O_1(^1S_0)\rangle_{P_Q(nS)} = \langle O_{\mathrm{EM}}(^3S_1)\rangle_{V_Q(nS)}$$

$$= \langle O_{\mathrm{EM}}(^1S_0)\rangle_{P_Q(nS)} = C_A \frac{|R_{n0}^{(0)}(0)|^2}{2\pi}, \tag{4.20}$$

$$\langle O_1(^{2S+1}P_J)\rangle_{\chi_Q(nJS)} = \langle O_{\mathrm{EM}}(^{2S+1}P_J)\rangle_{\chi_Q(nJS)} = \frac{3}{2}\frac{C_A}{\pi}|R_{n1}^{(0)\prime}(0)|^2, \tag{4.21}$$

where $R_{n\ell}^{(0)}$ is the zeroth-order radial part of the heavy-quarkonium wave function, obtained from the pNRQCD Hamiltonian [18, 53] and $C_A = N_c = 3$.

In the situation $mv^2 \ll \Lambda_{\mathrm{QCD}}$ there are no dynamical gluons at energies of order mv^2. Under the conditions that: (a) all higher gluonic excitations between the two heavy quarks develop a mass gap of order Λ_{QCD}, (b) threshold effects are small, and (c) contributions coming from virtual pairs of quark–antiquark with three-momentum of order $\sqrt{m\Lambda_{\mathrm{QCD}}}$ are subleading,[8] the NRQCD colour-octet matrix

---

[8]Condition (b) may be problematic for the $\psi(2S)$, whose mass is very close to the $D\bar{D}$ production threshold.

elements relevant for Eqs. (4.14)–(4.19) can be written at leading order in the v and Λ_{QCD}/m expansion as [16, 51]:

$$\langle O_8(^3S_1)\rangle_{V_Q(nS)} = \langle O_8(^1S_0)\rangle_{P_Q(nS)} = C_A \frac{|R_{n0}^{(0)}(0)|^2}{2\pi}\left(-\frac{2(C_A/2 - C_F)\mathcal{E}_3^{(2)}}{3m^2}\right), \quad (4.22)$$

$$\langle O_8(^1S_0)\rangle_{V_Q(nS)} = \frac{\langle O_8(^3S_1)\rangle_{P_Q(nS)}}{3} = C_A\frac{|R_{n0}^{(0)}(0)|^2}{2\pi}\left(-\frac{(C_A/2 - C_F)c_F^2\mathcal{B}_1}{3m^2}\right), \quad (4.23)$$

$$\frac{\langle O_8(^3P_J)\rangle_{V_Q(nS)}}{2J+1} = \frac{\langle O_8(^1P_1)\rangle_{P_Q(nS)}}{9} = C_A\frac{|R_{n0}^{(0)}(0)|^2}{2\pi}\left(-\frac{(C_A/2 - C_F)\mathcal{E}_1}{9}\right), \quad (4.24)$$

$$\langle O_8(^1S_0)\rangle_{\chi_Q(nJS)} = \frac{T_F}{3}\frac{|R_{n1}^{(0)\,\prime}(0)|^2}{\pi m^2}\mathcal{E}_3, \quad (4.25)$$

where c_F stands for the chromomagnetic matching coefficient, which is known at NLL [54], $C_F = (N_c^2 - 1)/(2N_c) = 4/3$ and $T_F = 1/2$. Therefore, at the considered order, the colour-octet matrix elements factorize into the product of the heavy-quarkonium wave function with some chromoelectric and chromomagnetic correlator (Wilson lines connecting the fields are not explicitly shown, but understood):

$$\mathcal{E}_n = \frac{1}{N_c}\int_0^\infty dt\, t^n \langle\mathrm{Tr}(g\mathbf{E}(t)\cdot g\mathbf{E}(0))\rangle, \qquad \mathcal{B}_n = \frac{1}{N_c}\int_0^\infty dt\, t^n\langle\mathrm{Tr}(g\mathbf{B}(t)\cdot g\mathbf{B}(0))\rangle, \quad (4.26)$$

$$\mathcal{E}_3^{(2)} = \frac{1}{4N_c}\int_0^\infty dt_1 \int_0^{t_1} dt_2 \int_0^{t_2} dt_3\,(t_2 - t_3)^3\left\{\langle\mathrm{Tr}(\{g\mathbf{E}(t_1)\cdot, g\mathbf{E}(t_2)\}\{g\mathbf{E}(t_3)\cdot, g\mathbf{E}(0)\})\rangle_c\right.$$
$$\left. - \frac{4}{N_c}\langle\mathrm{Tr}(g\mathbf{E}(t_1)\cdot g\mathbf{E}(t_2))\,\mathrm{Tr}(g\mathbf{E}(t_3)\cdot g\mathbf{E}(0))\rangle_c\right\}, \quad (4.27)$$

where

$$\langle\mathrm{Tr}(g\mathbf{E}(t_1)\cdot g\mathbf{E}(t_2)\,g\mathbf{E}(t_3)\cdot g\mathbf{E}(0))\rangle_c = \langle\mathrm{Tr}(g\mathbf{E}(t_1)\cdot g\mathbf{E}(t_2)\,g\mathbf{E}(t_3)\cdot g\mathbf{E}(0))\rangle$$
$$- \frac{1}{N_c}\langle\mathrm{Tr}(g\mathbf{E}(t_1)\cdot g\mathbf{E}(t_2))\rangle\langle\mathrm{Tr}(g\mathbf{E}(t_3)\cdot g\mathbf{E}(0))\rangle. \quad (4.28)$$

These correlators are universal in the sense that they do not depend on the heavy-quarkonium state and, hence, may be calculated once and for all, either by means of lattice simulations [55], or specific models of the QCD vacuum [56], or extracted from some set of experimental data [51].

Finally, at leading order the matrix elements of the $\mathcal{P}_1$ operators can be written as:

$$\langle\mathcal{P}_1(^3S_1)\rangle_{V_Q(nS)} = \langle\mathcal{P}_1(^1S_0)\rangle_{P_Q(nS)} = \langle\mathcal{P}_{\mathrm{EM}}(^3S_1)\rangle_{V_Q(nS)}$$
$$= \langle\mathcal{P}_{\mathrm{EM}}(^1S_0)\rangle_{P_Q(nS)} = C_A\frac{|R_{n0}^{(0)}(0)|^2}{2\pi}\left(mE_{n0}^{(0)} - \mathcal{E}_1\right), \quad (4.29)$$

where $E_{n0}^{(0)} \simeq M - 2m \sim mv^2$ is the leading-order binding energy. Equation (4.29) reduces to the formula obtained in [24] if the heavy-quarkonium state satisfies also the condition $mv \gg \Lambda_{\mathrm{QCD}}$.

The leading corrections to the above formulas come from quark–antiquark pairs of three momentum of order $\sqrt{m\Lambda_{\mathrm{QCD}}}$. The existence of this degree of freedom in the heavy-quarkonium system has been pointed out in [52], where the leading correction to Eq. (4.20) has been calculated.

The pNRQCD factorization formulas reduce, when applicable, the number of nonperturbative parameters needed to describe heavy-quarkonium decay widths [16]. In particular, using charmonium data to extract $\mathcal{E}_3$, in Ref. [51] it was found $\mathcal{E}_3(1\,\mathrm{GeV}) = 5.3^{+3.5}_{-2.2}$, where the errors account for the experimental uncertainties only. This value has been used to predict P-wave bottomonium inclusive decay widths in [51, 57]. We will come back to this in Section 3.2.4.

3.2 Experimental status

This section is a snapshot of the current status of various experimental results on the electromagnetic and inclusive hadronic decays of heavy-quarkonium states. The results come from the CLEO experiment at CESR, the BES experiment at BEPC and E835 at Fermilab.

3.2.1 Υ widths

Crucial parameters for any heavy-quarkonium state are its total width and its hadronic and three leptonic partial widths. For the three Υ bound states, since their total widths, Γ_{tot}, are much less than the energy spread of the CESR machine (≈ 4 MeV) where they are studied, the procedure is to scan over each resonance measuring the hadronic and $\mu^+\mu^-$ rates. Then we use:

$$\int \sigma_{\text{had}}\, dE_{\text{cm}} \ \propto \ \left(\frac{\Gamma_{ee}\,\Gamma_{\text{had}}}{\Gamma_{\text{tot}}}\right) \quad \text{and} \quad \mathcal{B}_{\mu\mu} \ = \ \frac{\Gamma_{\mu\mu}}{\Gamma_{\text{tot}}}. \tag{4.30}$$

Assuming lepton universality, we have: $\Gamma_{\text{tot}} = \Gamma_{\text{had}} + 3\,\Gamma_{\ell\ell}$. This allows us to solve for the total width and the partial widths into electrons and hadrons:

$$\Gamma_{ee} \ = \ \frac{(\Gamma_{ee}\Gamma_{\text{had}}/\Gamma_{\text{tot}})}{1 - 3\,\mathcal{B}_{\mu\mu}}, \qquad \Gamma_{\text{tot}} = \frac{\Gamma_{ee}}{\mathcal{B}_{\mu\mu}}, \qquad \Gamma_{\text{had}} \ = \ \Gamma_{\text{tot}}(1 - 3\mathcal{B}_{\mu\mu}). \tag{4.31}$$

Once the total width is known, the partial width into $\tau^+\tau^-$ can then be determined from its respective branching ratio. The current experimental status from the 2004 PDG [10] is shown in Table 4.2.

Table 4.2: Present PDG values [10] for the parameters of the Υ states.

Resonance	Γ_{tot} (keV)(% error)	Γ_{ee} (keV)(% error)	$\mathcal{B}_{\mu\mu}$(%)(% error)	$\mathcal{B}_{\tau\tau}$(%)(% error)
Υ(1S)	53.0 ± 1.5 (2.8%)	1.314 ± 0.029 (2.2%)	2.48 ± 0.06 (2.4%)	2.67 ± 0.15 (5.6%)
Υ(2S)	43 ± 6 (14%)	0.576 ± 0.024 (4.2%)	1.31 ± 0.21 (16%)	1.7 ± 1.6 (94%)
Υ(3S)	26.3 ± 3.4 (13%)	$-$	1.81 ± 0.17 (9.4%)	$-$

The PDG does not use the 1984 CLEO measurement of $\Gamma_{ee}(3S) = 0.42 \pm 0.05$ keV because new radiative corrections have now been accepted which were not used in that analysis, thus invalidating the measurement. From the large percentage errors on many of the quantities in the table, it is obvious that there is much room for improvement. To this end, the CLEO III detector devoted a large amount of running at each of the three Υ resonances, as shown in Table 4.3.

Table 4.3: Summary of the CLEO III running at the three Υ bound states.

Resonance	$\int L\, dt$ (fb^{-1})	Number of Decays (M)	Factor Increase Over CLEO!II
Υ(1S)	1.2	29	15
Υ(2S)	0.9	6.0	12
Υ(3S)	1.5	6.5	14

All the results from this running have not yet been finalized, but new measurements of the muonic branching ratios for the 3 bound Υ states have been published [58]. These new measurements are shown in Table 4.4, along with the corresponding new values for the total widths. The new $\Upsilon(2S)$ and $\Upsilon(3S)$

DECAY

Table 4.4: New CLEO measurements [58] of the muonic branching ratios for the 3 Υ states, along with their statistical and systematic errors and the corresponding new values for the total widths.

Resonance	$\mathcal{B}_{\mu\mu}$(%)(% error)	Γ_{tot} (keV)(% error)
Υ(1S)	$2.49 \pm 0.02 \pm 0.07$ (2.8%)	52.8 ± 1.8 (3.4%)
Υ(2S)	$2.03 \pm 0.03 \pm 0.08$ (4.0%)	29.0 ± 1.6 (5.5%)
Υ(3S)	$2.39 \pm 0.07 \pm 0.10$ (5.1%)	20.3 ± 2.1 (10.3%)

muonic branching ratio measurements are substantially higher than previous results, giving correspondingly smaller total widths for these resonances.

From the number of detected hadronic and leptonic events and a knowledge of the CLEO detector performance, estimates of the final statistical and systematic errors for the other resonance parameters can be made. These are shown in Table 4.5. Thus, once the analyses are complete, there will be a tremendous improvement in our knowledge of the basic parameters of the Υ bound-state resonances.

Table 4.5: Expected fractional errors for various quantities from the eventual CLEO III measurements.

Parameter	Statistical Error	Systematic Error	Total Error
$\Gamma_{ee}\Gamma_{\text{had}}/\Gamma_{\text{tot}}$	1%	2.5%	3%
Γ_{ee}	2%	2%	3%
$\mathcal{B}_{\tau\tau}$	2%	3%	4%
Γ_{tot}	2%	3%	4%

3.2.2 J/ψ and $\psi(2S)$ widths

In the last two years the knowledge of both J/ψ and $\psi(2S)$ parameters has improved. In 2002, the BES collaboration reported results [59] from a new scan of the $\psi(2S)$ resonance, corresponding to an integrated luminosity of 1.15 pb^{-1} and 114k $\psi(2S)$ hadronic decays. In 2004 BaBar has presented the first measurement of $\Gamma_{ee}\mathcal{B}_{\mu\mu}$ [9] from ISR production of J/ψ in 88.4 fb^{-1} taken at the $\Upsilon(4S)$ resonance. Table4.6 lists the values of the widths and leptonic branching ratios for J/ψ and $\psi(2S)$ from PDG [10].

Table 4.6: Present PDG values [10] for the parameters of the J/ψ and $\psi(2S)$ states.

Resonance	Γ_{tot} (keV)(% error)	Γ_{ee} (keV)(% error)	$\mathcal{B}_{\mu\mu}$(%)(% error)	$\mathcal{B}_{\tau\tau}$(%)(% error)
J/ψ	91.0 ± 3.2 (3.5%)	$5.40 \pm 0.15 \pm 0.07$ (3.1%)	5.88 ± 0.10 (1.7%)	—
$\psi(2S)$	281 ± 17 (6%)	2.12 ± 0.12 (9%)	0.73 ± 0.08 (11%)	0.28 ± 0.07 (25%)

3.2.3 Two-photon partial widths measurements

Experimental determinations of two-photon partial widths of quarkonia depend on measurements of products and ratios of branching ratios performed by more than one experiment, and the best estimate

is obtained from a global fit to directly measured quantities as it is done by the PDG [10]. When more measurements are available, subsets of measurements may allow a direct extraction of the value for $\Gamma_{\gamma\gamma}$, in general with a larger error than a global fit. But this can be useful both as a cross check for the global fit and to identify which measurements could yield improvements.

The simplest case is the χ_{c2}, where direct measurements of three independent quantities allows one to extract $\Gamma_{\gamma\gamma}$ and $\Gamma_{J/\psi\gamma}$:

$$\Gamma = 2.00 \pm 0.18\,\text{MeV}, \tag{4.32}$$

$$\Gamma_{\gamma\gamma}\mathcal{B}_{J/\psi\gamma} = 121 \pm 13\,\text{eV} , \tag{4.33}$$

and

$$\frac{\mathcal{B}_{\gamma\gamma}}{\mathcal{B}_{J/\psi\gamma}} = (1.02 \pm 0.15) \cdot 10^{-3}, \tag{4.34}$$

where experimental values are world averages [10] except in Eq. (4.34) where we averaged the E835 result with the ratio of $\mathcal{B}_{p\bar{p}}\mathcal{B}_{\gamma\gamma}$ and $\mathcal{B}_{p\bar{p}}\mathcal{B}_{J/\psi\gamma}$ measured by E760 [61, 62]. The product of Eq. (4.32), Eq. (4.33), and Eq. (4.34), yields $\Gamma_{\gamma\gamma} = 0.50 \pm 0.05$ keV, while taking Eq. (4.33) multiplied by Eq. (4.32) and divided by Eq. (4.34), we would obtain $\Gamma_{J/\psi\gamma} = 490 \pm 50$ keV, or $\mathcal{B}_{J/\psi\gamma} = 0.244 \pm 0.024$. The global fit to all measurements [10] (including all other measurements related to $\mathcal{B}_{J/\psi\gamma}$) improves on $\Gamma_{J/\psi\gamma} = 430 \pm 40$ keV and $\mathcal{B}_{J/\psi\gamma} = 0.202 \pm 0.017$, but has almost no effect on $\Gamma_{\gamma\gamma} = 0.52 \pm 0.05$ keV, indicating that the measurements considered above are the only ones relevant to $\Gamma_{\gamma\gamma}$.

The case for χ_{c0} is similar to that of the χ_{c2}, even if apparently more complicated. The world average of total width measurements is [10]

$$\Gamma = 10.2 \pm 0.9\,\text{MeV}. \tag{4.35}$$

There is a measurement of

$$\Gamma_{\gamma\gamma}\mathcal{B}_{2\pi^+2\pi^-} = 75 \pm 13 \pm 8\ \text{eV} \ \ [63], \tag{4.36}$$

and measurements (from a single experiment) of $\mathcal{B}_{p\bar{p}}\mathcal{B}_{\gamma\gamma}$ [64] and $\mathcal{B}_{p\bar{p}}\mathcal{B}_{\pi^0\pi^0}$ [6], from which we can calculate (assuming isospin symmetry) the ratio

$$\frac{\mathcal{B}_{\gamma\gamma}}{\mathcal{B}_{\pi\pi}} = 0.043 \pm 0.011 \ . \tag{4.37}$$

Even if $\mathcal{B}_{\pi\pi}$ and $\mathcal{B}_{2\pi^+2\pi^-}$ are not directly measured, their ratio can be determined from quantities measured by a single experiment (in this case BES [65–67]):

$$\frac{\mathcal{B}_{\pi\pi}}{\mathcal{B}_{2\pi^+2\pi^-}} = 0.47 \pm 0.10 \ . \tag{4.38}$$

This means that we can extract $\Gamma_{\gamma\gamma} = 3.9 \pm 0.8$ keV from the product of the four quantities in Eqs. (4.35), (4.36), (4.37), and (4.38). Notice that including MARK II measurements in the evaluation of Eq. (4.38) would give $\Gamma_{\gamma\gamma} = 3.1 \pm 0.8$. The global fit (which does not include the new measurement of $\mathcal{B}_{p\bar{p}}\mathcal{B}_{\gamma\gamma}$ [64]) yields a significantly more precise value $\Gamma_{\gamma\gamma} = 2.6 \pm 0.5$ keV, indicating that in this case there are other measurements that are relevant, such as $\mathcal{B}(\psi(2S){\to}\gamma\chi_{c0}{\to}3\gamma)$.

The case for $\eta_c(1S)$ and $\eta_c(2S)$ is different. To date these states have been observed in two-photon reactions with direct measurement of

$$\eta_c(1S): \quad \Gamma_{\gamma\gamma}\mathcal{B}_{K\bar{K}\pi} \ = 0.48 \pm 0.06\ \text{keV} , \tag{4.39}$$

$$\eta_c(2S): \quad \Gamma_{\gamma\gamma}\mathcal{B}_{K\bar{K}\pi} \ = 73 \pm 23\ \text{eV} \ [68] . \tag{4.40}$$

The $\eta_c(1S)$ has also been observed in $\bar{p}p$ annihilations with direct measurement of

$$\mathcal{B}_{\gamma\gamma}\mathcal{B}_{p\bar{p}} = (0.26 \pm 0.05) \times 10^{-6}. \tag{4.41}$$

In this case there are no measurements of the ratio of branching ratios between the $\gamma\gamma$ and any other decay mode, so it is necessary to use the values of $\mathcal{B}_{K\bar{K}\pi}$ or $\mathcal{B}_{p\bar{p}}$ that (for $\eta_c(1S)$ only) are determined by

$$\mathcal{B}_X = \frac{\mathcal{B}(J/\psi \rightarrow \gamma\eta_c \rightarrow \gamma X)}{\mathcal{B}(J/\psi \rightarrow \gamma\eta_c)}, \tag{4.42}$$

with precision limited by the $\approx 30\%$ uncertainty in $\mathcal{B}(J/\psi \rightarrow \gamma\eta_c)$ that is to date a common systematic to all two-photon partial widths of $\eta_c(1S)$. Since no measurement is yet available for the $\eta_c(2S)$ branching ratio to $K\bar{K}\pi$, its $\Gamma_{\gamma\gamma}$ cannot be determined.

The most obvious strategy to increase the precision on $\Gamma_{\gamma\gamma}$ is to improve the measurements for quantities used in its determination. But based on the case of χ_{c2} discussed above, a major improvement could be obtained by measuring the pair of quantities $\Gamma_{\gamma\gamma}\mathcal{B}_X$ and $\mathcal{B}_{\gamma\gamma}/\mathcal{B}_X$ for more than one final state X. B factories can reasonably measure to $< 10\%$ precision $\Gamma_{\gamma\gamma}\mathcal{B}_X$ for more than one final state. It is also reasonable that total widths will be more precisely measured in $p\bar{p}$ experiments, thus the question is whether it is possible to measure to better than 10% the ratios $\mathcal{B}_{\gamma\gamma}/\mathcal{B}_X$. How well can BES and CLEO measure $\psi(2S)$ or J/ψ to 3γ? How well can $\bar{p}p \rightarrow \gamma\gamma$ be measured and what are the channels that could be measured in these experiments simultaneously to $\bar{p}p \rightarrow \gamma\gamma$? With a magnetic detector, $p\bar{p} \rightarrow \phi\phi$ is the obvious choice, but interference with two-body non-resonant reactions may offer other opportunities (e.g., $p\bar{p} \rightarrow p\bar{p}$). The goal of $< 5\%$ precision on two-photon widths is not unreasonable.

3.2.4 χ_b widths

Since the $\chi_b(2P_J)$ states are not produced directly in e^+e^- annihilations, their hadronic widths cannot be measured using the same technique as for the S states. However, we can use the fact that the partial width for their photonic E1 transitions to the $\Upsilon(2S)$ state are proportional to a common matrix element squared times a phase space factor of E_γ^3 (see Secs. 6.1.3 and 6.2.2, $E_\gamma = k$). Thus, from measuring the individual photon energies and branching ratios for the decays $\chi_b(2P_J) \rightarrow \Upsilon(2S) + \gamma$, along with the branching ratios for $\chi_b(2P_J) \rightarrow \Upsilon(1S) + \gamma$, we can measure the ratio of the $\chi_b(2P_J)$ hadronic partial widths, $\Gamma(\text{had})$. We first use:

$$\mathcal{B}(2S) = \frac{\Gamma(2S)}{\Gamma(1S) + \Gamma(2S) + \Gamma(\text{had})}, \tag{4.43}$$

where $\mathcal{B}(2S) = \mathcal{B}(\chi_b(2P_J) \rightarrow \Upsilon(2S) + \gamma)$ and $\mathcal{B}(1S) = \mathcal{B}(\chi_b(2P_J) \rightarrow \Upsilon(1S) + \gamma)$ are the two E1 branching ratios, and $\Gamma(2S)$ and $\Gamma(1S)$ are the corresponding partial widths. Then, since $\Gamma(2S)/\Gamma(1S) = \mathcal{B}(2S)/\mathcal{B}(1S)$, we can solve for the hadronic partial width, obtaining:

$$\Gamma(\text{had}) = \Gamma(2S) \left[\frac{1 - \mathcal{B}(1S)}{\mathcal{B}(2S)} - 1 \right]. \tag{4.44}$$

Making the assumption mentioned above that the partial widths for E1 transitions of different J states to the same Υ state should be proportional to a common matrix element squared times E_γ^3, we obtain an expression for the ratio of hadronic partial widths for two different $\chi_b(2P_J)$ states. For example, for $J = 0$ and $J = 2$, we get:

$$\frac{\Gamma_{\text{had}}(2P_0)}{\Gamma_{\text{had}}(2P_2)} = \left(\frac{E_\gamma(2P_0 \rightarrow 2S + \gamma)}{E_\gamma(2P_2 \rightarrow 2S + \gamma)} \right)^3 \left(\frac{\frac{1 - \mathcal{B}(1S)_0}{\mathcal{B}(2S)_0} - 1}{\frac{1 - \mathcal{B}(1S)_2}{\mathcal{B}(2S)_2} - 1} \right), \tag{4.45}$$

where $\mathcal{B}(2S)_0 = \mathcal{B}(\chi_b(2P_0) \rightarrow \Upsilon(2S) + \gamma)$, etc. Using this technique and the E1 branching ratios given in Section 6.2.2, CLEO III finds the ratio of the $J = 0$ to the $J = 2$ hadronic widths to be:

$$\frac{\Gamma_{\text{had}}(2P_0)}{\Gamma_{\text{had}}(2P_2)} = 6.1 \pm 2.8. \tag{4.46}$$

For the $J = 1$ and $J = 2$ states, CLEO III measures:

$$\frac{\Gamma_{\text{had}}(2P_1)}{\Gamma_{\text{had}}(2P_2)} = 0.25 \pm 0.09. \tag{4.47}$$

Since the $J = 1$ state cannot annihilate into two massless gluons, to first order its hadronic width is expected to be suppressed by one order of α_{s} compared to the $J = 2$ state. The measurement confirms this suppression.

As discussed in Section 3.1, at leading order in the heavy-quark velocity expansion, the above ratios depend on a colour-octet matrix element. One can consider the combination

$$\frac{\Gamma_{\text{had}}(2P_0) - \Gamma_{\text{had}}(2P_1)}{\Gamma_{\text{had}}(2P_2) - \Gamma_{\text{had}}(2P_1)}, \tag{4.48}$$

which is completely determined by perturbative QCD [15]. Using (4.46) and (4.47), this ratio is measured by CLEO III to be:

$$\frac{\Gamma_{\text{had}}(2P_0) - \Gamma_{\text{had}}(2P_1)}{\Gamma_{\text{had}}(2P_2) - \Gamma_{\text{had}}(2P_1)} = 7.8 \pm 3.8. \tag{4.49}$$

LO QCD predicts $15/4 = 3.75$ for this ratio, and NLO QCD about 7, which is quite consistent with (4.49). However, the combination (4.48) distinguishes between bottomonium and charmonium only at NNLO, while the ratios (4.46) and (4.47) do so at NLO. A direct determination of these ratios has been done in the framework of pNRQCD, as discussed in Section 3.1.3, using the factorization formula (4.25) and fixing the nonperturbative constant to the value found from charmonium data. The result at NLO is $\Gamma_{\text{had}}(2P_0)/\Gamma_{\text{had}}(2P_2) \simeq 4.0$, consistent with (4.46), and $\Gamma_{\text{had}}(2P_1)/\Gamma_{\text{had}}(2P_2) \simeq 0.50$, which is somewhat larger than (4.47) [51, 57].

CLEO cannot resolve the individual photon lines for the similar decays from the $\Upsilon(3S)$ to the $\chi_b(1P_J)$ states (see Sec. 6.2.2). However, we can use the quite old $\chi_b(1P_J) \to \Upsilon(1S) + \gamma$ branching ratios from the PDG [10] for $J = 1$ and 2 (the $J = 0$ branching ratio is very small, given the large hadronic width of that state). In this case, the ratio of the hadronic widths for the two states can be found from:

$$\frac{\Gamma_{\text{had}}(1P_1)}{\Gamma_{\text{had}}(1P_2)} = \left(\frac{E_\gamma(1P_1 \to 1S + \gamma)}{E_\gamma(1P_2 \to 1S + \gamma)} \right)^3 \left(\frac{\frac{1}{\mathcal{B}(1S)_1} - 1}{\frac{1}{\mathcal{B}(1S)_2} - 1} \right). \tag{4.50}$$

This leads to the result:

$$\frac{\Gamma_{\text{had}}(1P_1)}{\Gamma_{\text{had}}(1P_2)} = 0.46 \pm 0.20, \tag{4.51}$$

showing again the suppression of the $J = 1$ state's hadronic width compared to the $J = 2$, albeit with larger errors in this case.

3.2.5 χ_c widths

The χ_c states are also not directly produced in e^+e^- annihilations. However, in this case an extremely powerful alternative method has been used to measure their masses and total widths. In an experimental technique first pioneered by experiment R704 at CERN, and continued by experiments E760 and E835 at the Fermilab Antiproton Accumulator, a stochastically cooled $\overline{p}$ beam collides with a hydrogen gas jet target. In the subsequent $p\overline{p}$ annihilations, all J^{PC} states can be formed via 2 or 3 gluons. Thus, the P-wave charmonium states are directly accessible. By scanning the proton beam energy over each resonance, the mass and total width of each P state can be measured with extremely high accuracy.

As mentioned in Section 3.2.3, these experiments have also measured products or ratios of branching ratios that help constrain the radiative and $\gamma\gamma$ widths of those states. Table 4.7 shows the current best estimates of the χ_c widths, using data from PDG [10]. E835 is finalizing the analysis of the scans of the χ_{c1} and χ_{c2} resonances [69], with an anticipated precision of $\approx 7\%$ on χ_{c1} and χ_{c2} total widths.

Table 4.7: Widths of χ_c states from PDG [10].

Resonance	Γ_{tot} (MeV)(% error)	$\Gamma(\gamma J/\psi)$ (keV)(% error)	$\Gamma(\gamma\gamma)$(%)(% error)
χ_{c0}	10.1 ± 0.8 (8%)	119 ± 16 (13%)	2.6 ± 0.5 (19%)
χ_{c1}	0.91 ± 0.13 (14%)	290 ± 50 (17%)	—
χ_{c2}	2.11 ± 0.16 (8%)	430 ± 40 (9%)	0.52 ± 0.05 (10%)

In order to show the impact of the new measurements of the χ_c widths, in Table 4.8 we compare the PDG 2000 [70] with the PDG 2004 [10] determinations of different ratios of hadronic and electromagnetic widths (similar ratios have been considered in the previous section for the χ_b case). There have been sizable shifts in some central values and considerable reductions in the errors. In particular, the error on the ratio of the electromagnetic χ_{c0} and χ_{c2} widths has been reduced by about a factor 10, while in all other ratios the errors have been reduced by a factor 2 or 3. The considered ratios of hadronic and electromagnetic widths do not depend at leading order in the velocity expansion (see Eqs. (4.16) and (4.19)) on any nonperturbative parameter. Therefore, they can be calculated in perturbation theory. The last two columns of Table 4.8 show the result of a leading and next-to-leading order calculation respectively. Despite the fact that the convergence is not always very good and that, therefore, the NLO calculation should be taken with some care (see also Section 3.1.1), all data now clearly prefer (and are consistent with) NLO results.

3.2.6 $\Upsilon(1S) \to \gamma + X$ and $\Upsilon(1S) \to X$

There has been much theoretical interest lately in trying to predict the direct photon energy distribution for $\Upsilon(1S) \to \gamma + X$ inclusive decays [71]. See the following section. The last reported measurement was from the CLEO II experiment in 1997 [72], based on 1.4 million $\Upsilon(1S)$ decays. Besides the photon energy spectrum, they measured the ratio:

$$\frac{\Gamma(\gamma gg)}{\Gamma(ggg)} \;=\; (2.75 \;\pm\; 0.04 \;\pm\; 0.15)\,\% \,, \tag{4.52}$$

which allowed a fairly accurate determination of $\Lambda_{\overline{\text{MS}}}$ and α_{s}. Given the small statistical errors in these measurements, it is doubtful that the CLEO III experiment will repeat them using their 29 million $\Upsilon(1S)$ decays. Rather, the emphasis will be on detailed studies of exclusive $\gamma + X$ decays of the $\Upsilon(1S)$, especially the search for possible glueball candidates.

For measurements of the inclusive production of various hadronic particle types from the $\Upsilon(1S)$, one must go back to a 1985 paper by the CLEO I experiment [73], based on only 50k $\Upsilon(1S)$ decays. They measured the average multiplicities and momentum distributions of π, K, ρ, K^*, ϕ, p, Λ and Ξ in $\Upsilon(1S)$ decays and compared them to those from the nearby continuum. The only addition to these results was a 2003 CLEO II measurement [74] of the inclusive η' production from the $\Upsilon(1S)$, based on 1.9 million decays and motivated by the large observed $B \to \eta' + X$ branching ratio.

4   INCLUSIVE RADIATIVE DECAYS[9]

The radiative inclusive decay of heavy quarkonium has been investigated for about a quarter century. Here we will study $\Upsilon \to X\gamma$ decays in particular. The direct radiative decay is calculated by using the operator product expansion, where the operators are the same nonperturbative matrix elements that appear in the inclusive decay to hadrons (see Section 3.1). Thus we obtain an expansion in the velocity, v,

---

[9]Author: A. Leibovich

Table 4.8: Comparison of ratios of χ_{cJ} partial widths. The experimental values PDG 2004 are obtained from the world averages of [10], with the assumption $\Gamma(\chi_{c0}\to l.h.) \approx \Gamma(\chi_{c0}) = 10.1 \pm 0.8$ MeV, $\Gamma(\chi_{c1}\to l.h.) \approx \Gamma(\chi_{c1})[1 - \mathcal{B}(\chi_{c1}\to\gamma J/\psi)] = 0.62 \pm 0.10$ MeV, $\Gamma(\chi_{c2}\to l.h.) \approx \Gamma(\chi_{c2})[1 - \mathcal{B}(\chi_{c2}\to\gamma J/\psi)] = 1.68 \pm 0.15$ MeV. Similarly the experimental values PDG 2000 have been obtained from [70]. The chosen ratios do not depend at leading order in the velocity expansion on octet or singlet matrix elements. The LO and NLO columns refer to a leading and next-to-leading order calculation done at the renormalization scale $2m_c$ with the following choice of parameters: $m_c = 1.5$ Gev and $\alpha_{\rm s}(2m_c) = 0.245$.

Ratio	PDG 2004	PDG 2000	LO	NLO
$\dfrac{\Gamma(\chi_{c0}\to\gamma\gamma)}{\Gamma(\chi_{c2}\to\gamma\gamma)}$	5.1 ± 1.1	13 ± 10	3.75	≈ 5.43
$\dfrac{\Gamma(\chi_{c2}\to l.h.) - \Gamma(\chi_{c1}\to l.h.)}{\Gamma(\chi_{c0}\to\gamma\gamma)}$	410 ± 100	270 ± 200	≈ 347	≈ 383
$\dfrac{\Gamma(\chi_{c0}\to l.h.) - \Gamma(\chi_{c1}\to l.h.)}{\Gamma(\chi_{c0}\to\gamma\gamma)}$	3600 ± 700	3500 ± 2500	≈ 1300	≈ 2781
$\dfrac{\Gamma(\chi_{c0}\to l.h.) - \Gamma(\chi_{c2}\to l.h.)}{\Gamma(\chi_{c2}\to l.h.) - \Gamma(\chi_{c1}\to l.h.)}$	7.9 ± 1.5	12.1 ± 3.2	2.75	≈ 6.63
$\dfrac{\Gamma(\chi_{c0}\to l.h.) - \Gamma(\chi_{c1}\to l.h.)}{\Gamma(\chi_{c2}\to l.h.) - \Gamma(\chi_{c1}\to l.h.)}$	8.9 ± 1.1	13.1 ± 3.3	3.75	≈ 7.63

of the heavy quarks. The rate is written as

$$\frac{1}{\Gamma_0}\frac{d\Gamma^{\rm dir}}{dz} = \sum_n C_n(M,z)\langle\Upsilon|O_n|\Upsilon\rangle, \tag{4.53}$$

where $M = 2m_b$, $z = 2E_\gamma/M$, the $C_n(z,M)$ are short distance Wilson coefficients, calculable in perturbation theory, and the NRQCD matrix elements scale with a certain power in v. The lowest order contribution is the colour-singlet ${}^3S_1$ operator, where the quark–antiquark pair annihilate into a photon and two gluons. Therefore, in the $v\to0$ limit, we obtain the colour-singlet model calculation of Ref. [75]. At higher order in the velocity expansion, there are direct contributions from the colour-octet matrix elements [76]. The decay through a colour-octet matrix element can occur at one lower order in $\alpha_{\rm s}$, with the $b\bar{b}$ decaying to a photon and a single gluon.

However, this calculation is only valid in the intermediate range of photon energies ($0.3 \lesssim z \lesssim 0.7$). For low photon energies, $z \lesssim 0.3$, the major photon production mechanism is fragmentation [76, 77]. At large photon energies, $z \gtrsim 0.7$, the perturbative [76] and nonperturbative expansions [78] both break down.

4.1 Photon fragmentation

The inclusive photon spectrum can be written as a sum of a direct and a fragmentation contribution [77],

$$\frac{d\Gamma}{dz} = \frac{d\Gamma^{\text{dir}}}{dz} + \frac{d\Gamma^{\text{frag}}}{dz}, \tag{4.54}$$

where in the direct term the photon is produced in the hard scattering, and in the fragmentation term the photon fragments from a parton produced in the initial hard scattering. The fragmentation contribution has been well studied in Ref. [76].

Catani and Hautmann pointed out the importance of fragmentation for the photon spectrum in quarkonium decays [77]. The fragmentation rate can be written as

$$\frac{d\Gamma^{\text{frag}}}{dz} = \sum_{a=q,\bar{q},g} \int_z^1 \frac{dx}{x} \frac{d\Gamma_a}{dx} D_{a\gamma}\left(\frac{z}{x}, M\right), \tag{4.55}$$

where the rate to produce parton a, $d\Gamma_a/dx$, is convoluted with the probability that the parton fragments to a photon, $D_{a\gamma}$, with energy fraction z/x. The rate to produce parton a can again be expanded in powers of v [76], with the leading term being the colour-singlet rate for an Υ to decay to three gluons,

$$\frac{d\Gamma_{\text{LO}}^{\text{frag}}}{dz} = \int_z^1 \frac{dx}{x} \frac{d\Gamma_{ggg}}{dx} D_{g\gamma}\left(\frac{z}{x}, M\right). \tag{4.56}$$

At higher orders in v, there are three colour-octet fragmentation contributions, where the photon can fragment off either a quark or a gluon.

The partonic rates must be convoluted with the fragmentation functions, $D_{a\gamma}(z, M)$. The M-dependence of the fragmentation functions can be predicted using perturbative QCD via Altarelli–Parisi evolution equations. However, the solution depends on nonperturbative fragmentation function at some input scale Λ, which must be measured from experiment. This has been done by the ALEPH collaboration for the $D_{q\gamma}$ fragmentation function [79], but the $D_{g\gamma}$ fragmentation function is unknown, so at this point it must be modeled.

4.2 Resumming the large z contribution

The colour-octet contributions to the rate are the first subleading terms in the operator product expansion. Diagrammatically, these contributions occur for the quark–antiquark pair annihilating into a photon back-to-back with a gluon. Thus the $^1S_0$ and $^3P_0$ colour-octet contributions begin as a delta function of $(1 - z)$ [76]. If we look at the integrated rate near the endpoint, the colour-octet contributions are as important as the "leading" colour-singlet piece, in the region $1 - v^2 \lesssim z \leq 1$. Perturbative corrections to the colour-octet contributions have large kinematic logarithms, which destroy the perturbative expansion. The α_s correction to the leading colour-singlet rate was calculated numerically in Ref. [80]. It leads to small corrections over most of phase space; however, in the endpoint region the corrections are of order the leading contribution. Thus both higher orders in v and in α_s are not suppressed in the endpoint region. Both the nonperturbative and perturbative series break down.

This breakdown at large z is due to NRQCD not including collinear degrees of freedom. In the endpoint region, the outgoing gluons are moving back-to-back to the photon, with large energy and small invariant mass (i.e., a collinear jet). The correct effective field theory is a combination of NRQCD for the heavy degrees of freedom and the soft-collinear effective theory (SCET) [81,82] for the light degrees of freedom.

SCET is an effective field theory describing collinear fields interacting with soft degrees of freedom. It is thus the appropriate effective field theory to use when there are energetic particles moving with small invariant mass, such as $\Upsilon \to X\gamma$ in the endpoint region. We therefore use NRQCD to describe the

+ crossed diagram
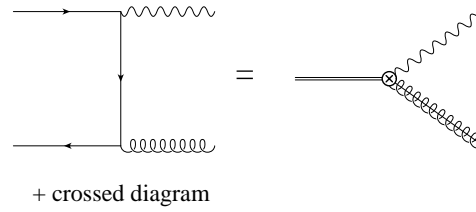
Fig. 4.1: Matching QCD onto NRQCD and SCET. The double lines represents the Υ, while the spring with the line through it represent a collinear gluon.
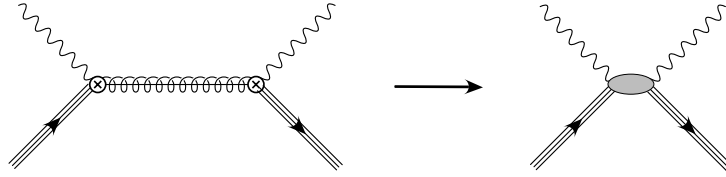
Fig. 4.2: The leading OPE: tree level matching of the time ordered product in the collinear-soft theory to a nonlocal operator in the soft theory.

quarkonium, and SCET to describe the jet of collinear particles. The invariant mass of the jet of particles is $p^2 \sim M_\Upsilon^2 (1-z)$, which is small as $z \to 1$. In SCET there are three mass scales: the hard scale, which for this process is $\mu_h \sim M_\Upsilon$, the collinear scale, which is $\mu_c \sim M_\Upsilon \sqrt{1-z}$, and the ultrasoft scale, $\mu_u \sim M_\Upsilon (1-z)$. These scales are widely separated in the endpoint region. SCET allows us to separate the physics coming from the disparate scales.

To calculate, the QCD process is matched onto operators in SCET and NRQCD. For example, the matching for the colour-octet channel is pictured in Fig. 4.1. Then to resum the kinematic logarithms, we use the renormalization group equations in SCET, by evolving from μ_h to μ_u. So we first renormalize the operators in SCET, and calculate the anomalous dimensions in the usual way. Then by running the SCET operators to the ultrasoft scale, the logarithms of $1-z$ are summed.

The colour-singlet process does not run below the collinear scale. This is because the ultrasoft gluons cannot couple to the colour-singlet jet or the incoming colour-singlet quarkonium. This fact was first pointed out by Hautmann [83]. However, there are still logarithms that are generated between the hard and collinear scales [71, 84]. For the colour-octet processes [85], at the collinear scale μ_c we integrate out collinear modes. Since there are collinear particles in the final state, we first perform an OPE for the inclusive Υ radiative decay rate in the endpoint region, and match onto the large energy effective theory [86]. The result is a nonlocal OPE in which the two currents are separated along a light-like direction. Diagrammatically this is illustrated in Fig. 4.2. This is run to the ultrasoft scale, at which point we are left with a nonperturbative shape function, which describes the movement of the heavy quark–antiquark pair within the meson. This function is precisely what was shown to occur in Ref. [78]. Unfortunately, this nonperturbative function is unknown, and must be modeled.

Before we proceed we need the NRQCD matrix elements. We can extract the colour-singlet matrix elements from the Υ leptonic width. The colour-octet matrix elements are more difficult to determine. NRQCD predicts that the colour-octet matrix elements scale as v^4 compared to the singlet matrix elements. In Ref. [19] it was argued that an extra factor of $1/2N_c$ should be included. By looking at the shape of the resummed colour-octet rates, it appears that these channels would give a contribution an order of magnitude too large compared with the data in the endpoint region if they were even as small as $v^4/2N_c$ times the colour-singlet, as shown in Fig. 4.3, so we will set them to zero. This eliminates two
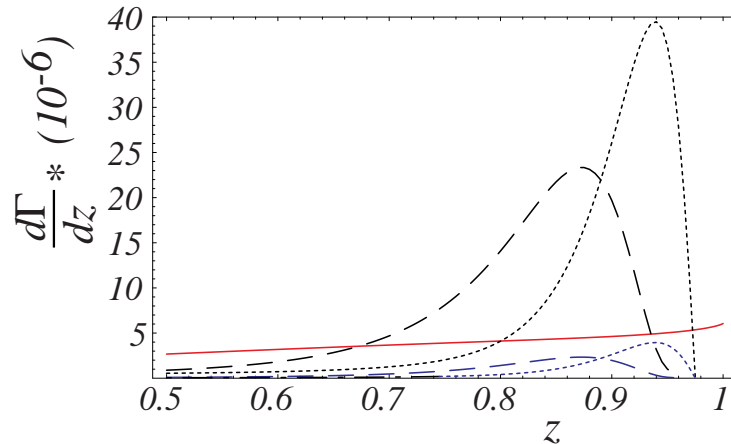
Fig. 4.3: The differential decay spectra in the region $0.5 < z$. The dashed curves are the fully resummed colour-octet result convoluted with a model for the shape function for two choices of the colour-octet matrix elements. The larger curves have the colour-octet matrix elements suppressed by $v^4/10$, while the lower curves have $v^4/100$. In addition we have interpolated the fully resummed result with the next-to-leading order result in the region away from the endpoint. The dotted curves are the next-to-leading result convoluted with the structure function for two choices of the matrix elements. The solid curve is the tree-level colour-singlet contribution.

of the three possible colour-octet matrix elements, leaving the $^3S_1$. It also eliminates the dependence at this order on the unknown shape functions and the largest dependence on the unknown fragmentation function, $D_{g\gamma}$. We set the colour-octet $^3S_1$ matrix element to be v^4 suppressed compared to the colour-singlet matrix element extracted from the leptonic width, where we use $v^2 = 0.08$. This colour colour-octet matrix element does not give a large contribution in the large z region, but is important at low z, due to the fragmentation function $D_{q\gamma}$.

The CLEO collaboration measured the number of photons in inclusive $\Upsilon(1S)$ radiative decays [72]. The data does not remove the efficiency or energy resolution and is the number of photons in the fiducial region, $|\cos\theta| < 0.7$. In order to compare our theoretical prediction to the data, we integrate over the barrel region and convolute with the efficiency that was modeled in the CLEO paper. We do not do a bin-to-bin smearing of our prediction.

In Fig. 4.4 we compare the prediction to the data. The error bars on the data are statistical only. The dashed line is the direct tree-level plus fragmentation result, while the solid curve includes the re-summation of the kinematic logarithms. For these two curves we use the α_s extracted from these data, $\alpha_s(M_\Upsilon) = 0.163$, which corresponds to $\alpha_s(M_Z) = 0.110$ [72]. The shape of the resummed result is much closer to the data than the tree-level curve, though it is not a perfect fit. We also show the resummed plus fragmentation result, using the PDG value of $\alpha_s(M_Z)$, including theoretical uncertainties, denoted by the shaded region. To obtain the darker band, we first varied the choice of m_b between $4.7\ \mathrm{GeV} < m_b < 4.9\ \mathrm{GeV}$ and the value of α_s within the errors given in the PDG, $\alpha_s(M_Z) = 0.1172(20)$ [87]. We also varied the collinear scale, μ_c from $M\sqrt{(1-z)/2} < \mu_c < M\sqrt{2(1-z)}$. Finally, the lighter band also includes the variation, within the errors, of the parameters for the quark to photon fragmentation function extracted by ALEPH [79]. The low z prediction is dominated by the quark to photon fragmentation coming from the colour-octet $^3S_1$ channel. We did not assign any error to the colour-octet $^3S_1$ matrix elements. Since it is unknown, there is a very large uncertainty in the lower part of the prediction that we decided not to show. Recently, colour-octet $^1S_0$ and $^3P_0$ contributions, calculated in the weak-coupling regime, have been included in the analysis [88]. They appear to improve the agreement with the data in the end-point region. Also recently operator mixing between the gluon jet, considered here, and the quark–antiquark jet has been considered in [89].
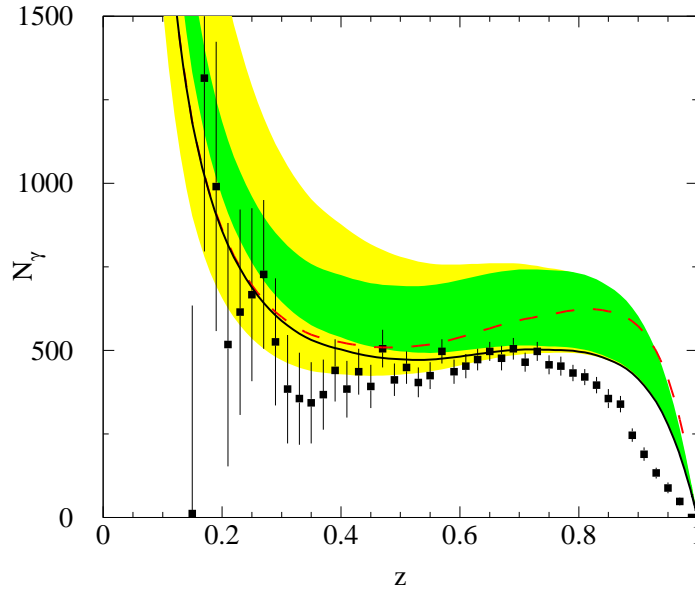
Fig. 4.4: The inclusive photon spectrum, compared with data [72]. The theory predictions are described in the text. The plot is from Ref. [71].

5   EXCLUSIVE DECAYS[10]

Exclusive charmonium decays have been investigated within QCD by many authors, e.g., [90–93]. As already argued at the beginning of Section 3.1 the dominant dynamical mechanism is $c\bar{c}$ annihilation into the minimal number of gluons allowed by symmetries and subsequent creation of light quark–antiquark pairs forming the final state hadrons.

In hard exclusive reactions higher Fock-state contributions are usually suppressed by inverse powers of the hard scale, Q, appearing in the process ($Q \sim m_c$ for exclusive charmonium decays), as compared to the valence Fock-state contributions. Hence, higher Fock-state contributions are expected to be negligible in most cases. It has turned out, however, that higher Fock states of the charmonium play an important role in understanding the production (see Chapter 5) and the inclusive decays of charmonium (see Section 3.1). As shown in [14] the long-distance matrix elements can there be organized into a hierarchy according to their scaling with v, the typical velocity of the c quark in the charmonium. The velocity expansion can also be applied to exclusive charmonium decays [94]. The Fock expansions of the charmonium states start (in the power counting of [14]) as

$$
\begin{aligned}
|J/\psi\rangle &= \underbrace{|c\bar{c}_1(^3S_1)\rangle}_{\mathcal{O}(1)} + \underbrace{|c\bar{c}_8(^3P_J)\,g\rangle}_{\mathcal{O}(v)} + \underbrace{|c\bar{c}_8(^3S_1)\,gg\rangle}_{\mathcal{O}(v^2)} + \dots, \\
|\eta_c\rangle &= \underbrace{|c\bar{c}_1(^1S_0)\rangle}_{\mathcal{O}(1)} + \underbrace{|c\bar{c}_8(^1P_1)\,g\rangle}_{\mathcal{O}(v)} + \underbrace{|c\bar{c}_8(^1S_0)\,gg\rangle}_{\mathcal{O}(v^2)} + \dots, \\
|\chi_{cJ}\rangle &= \underbrace{|c\bar{c}_1(^3P_J)\rangle}_{\mathcal{O}(1)} + \underbrace{|c\bar{c}_8(^3S_1)\,g\rangle}_{\mathcal{O}(v)} + \dots,
\end{aligned}
\tag{4.57}
$$

where the subscripts at the $c\bar{c}$ pair specify whether it is in a colour-singlet (1) or colour-octet (8) state; $\mathcal{O}(1)$, $\mathcal{O}(v)$ and $\mathcal{O}(v^2)$ are the orders to which the corresponding Fock states contribute, once evaluated

---

[10]Author: P. Kroll (with contributions from C. Patrignani)

in a matrix element. The amplitude for a two-body decay of a charmonium state satisfies a factorization formula, which separates the scale m_c from the lower momentum scales. The decay amplitude is then expressed as a convolution of a partonic subprocess amplitude that involves the scale m_c, the charmonium wave function for the initial state that involves scales of order $m_c v$ and lower, and a factor that takes into account the light hadron wave functions for the final state. This factor involves only the scale Λ_{QCD}. In the formal limit of $m_c \rightarrow \infty$ the dominant terms in the factorization formula involve the minimal number of partons in the hard scattering, which is given by the valence quarks of the hadrons participating in the considered process. Terms involving additional partons in the initial state are suppressed by powers of v while terms involving additional partons in the final state are suppressed by powers of $\Lambda_{\mathrm{QCD}}/m_c$. Moreover, in this limit of an asymptotically large charm quark mass, the valence quarks of a light hadron move collinear with it, their transverse quark momenta can be neglected. In this situation the soft parton–hadron transition is described by a leading-twist distribution amplitude, $\Phi(x, \mu_F)$, for finding valence quarks in the hadron, each carrying some fraction x_i of the hadron's momentum and for which the quark helicities sum up to the hadronic one. The distribution amplitudes, which represent light-cone wave functions integrated over transverse momenta up to a factorization scale μ_F of order m_c [91, 92], are the only nonperturbative input required in the calculation of decay amplitudes along these lines. The convolution formula in such a leading-twist calculation of a charmonium decay into a pair of hadrons h_1, h_2 reads

$$M \;=\; \int [dx]_N [dy]_N [d^3 k]_{N'}\, \Phi_1(x, \mu_F)\, \Phi_2(y, \mu_F)\, T_H(x, y, m_c, \mu_F)\, \Psi_c(k)\,, \qquad (4.58)$$

where $x(y)$ represents the set of independent momentum fractions for an N-particle Fock state of a light hadron and Ψ_c is the charmonium wave function for an N'-particle Fock state. k denotes the set of momenta of the particles in that Fock state. Soft and hard physics is separated at the factorization scale μ_F.

The relative strength of various contributions to specific decay processes can be easily estimated. Typical lowest-order Feynman graphs are shown in Fig. 4.5. A P-wave $c\bar{c}$ pair requires a power of the c-quark's relative momentum $\mathbf{k}$ ($k \sim m_c v$) from the hard scattering amplitude, which is to be combined with a $\mathbf{k}$ from the P-wave charmonium spin wave function in a k^2. In contrast to $\mathbf{k}$ itself, a term proportional to k^2 does not lead to a vanishing contribution after the $\mathbf{k}$ integration. Since, for dimensional reasons, $\mathbf{k}$ is to be replaced by $\mathbf{k}/m_c$ the subprocess amplitude involving a P-wave $c\bar{c}$ pair, is of order v. Combining this fact with the Fock-state expansion (4.57), one finds for the amplitude of χ_{cJ} decays into, say, a pairs of pseudoscalar mesons (P) the behaviour

$$M(\chi_{cJ} \rightarrow PP) \;=\; a_1\, \alpha_\mathrm{s}^2 v + a_8\, \alpha_\mathrm{s}^2 \big(v\sqrt{\alpha_\mathrm{s}}\big) + \mathcal{O}(v^2)\,, \qquad (4.59)$$

where the a_i are process-typical constants. For the reaction $J/\psi \rightarrow B\overline{B}$ (B stands for baryon), on the other hand, one has

$$M(J/\psi \rightarrow B\overline{B}) \;=\; \tilde{a}_1\, \alpha_\mathrm{s}^3 + \tilde{a}_8\, \alpha_\mathrm{s}^3 v \big(v\sqrt{\alpha_\mathrm{s}}\big) + \tilde{b}_8\, \alpha_\mathrm{s}^3\, v^2 \alpha_\mathrm{s} + \mathcal{O}(v^3)\,. \qquad (4.60)$$

Or, for the η_c decaying for instance into a scalar (S) and a pseudoscalar meson

$$\mathcal{M}(\eta_c \rightarrow SP) \;=\; \hat{a}_1\, \alpha_\mathrm{s}^2 + \hat{a}_8\, \alpha_\mathrm{s}^2 v \big(v\sqrt{\alpha_\mathrm{s}}\big) + \hat{b}_8\, \alpha_\mathrm{s}^2 (v\sqrt{\alpha_\mathrm{s}})^2 + \mathcal{O}(v^3)\,. \qquad (4.61)$$

Thus, one sees that in the case of the χ_{cJ} the colour-octet contributions $\propto a_8$ are not suppressed by powers of either v or $1/m_c$ as compared to the contributions from the valence Fock states [94]. For charmonium decays $\sqrt{\alpha_\mathrm{s}}$ is large and does not suppress the colour-octet contribution considerably. Hence, the colour-octet contribution, i.e., the next higher Fock state of the charmonium state, has to be included for a consistent analysis of P-wave charmonium decays. The situation is different for J/ψ decays into baryon–antibaryon pairs or $\eta_c \rightarrow SP$: higher Fock state contributions first start at $\mathcal{O}(v^2)$. Moreover, there
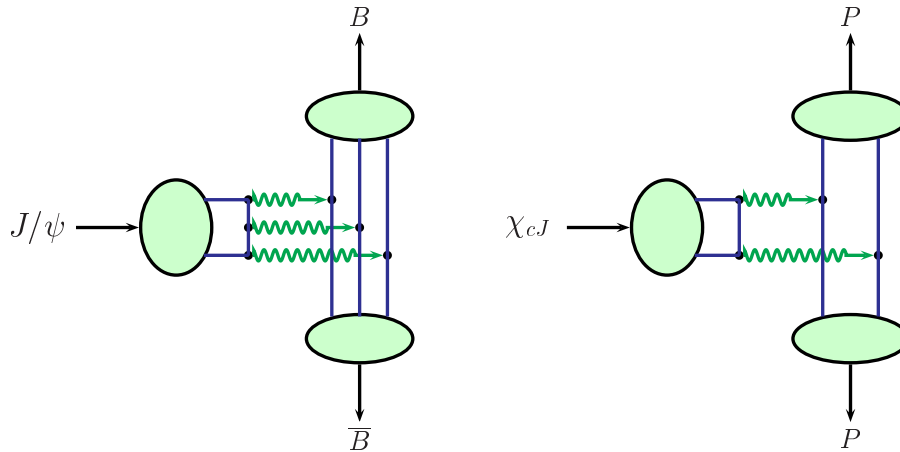
Fig. 4.5: Typical lowest-order Feynman graphs for J/ψ decays into a baryon-antibaryon pair (left) and χ_{cJ} decays into a pair of pseudoscalar mesons (right). The wavy lines represent gluons.

is no obvious enhancement of the corresponding subprocess amplitudes, they appear with at least the same power of α_s as the valence Fock state contributions. Thus, despite of the fact that m_c is not very large and v not small ($v^2 \simeq 0.3$), it seems reasonable to expect small higher Fock-state contributions to the baryonic decays of the J/ψ.

The leading-twist formation of the light hadrons in the final state has implications for their helicity configurations. As a consequence of the vector nature of QCD (and QED) time-like virtual gluons (or photons) create light, (almost) massless quarks and antiquarks in opposite helicity states, see Fig. 4.6. To leading-twist accuracy such partons form the valence quarks of the light hadrons and transfer their helicities to them (see Fig. 4.6). Hence, the total hadronic helicity is zero

$$\lambda_1 + \lambda_2 \;=\; 0\,. \tag{4.62}$$

The conservation of hadronic helicities is a dynamical consequence of QCD (and QED) which holds to leading-twist order. The violation of helicity conservation in a decay process signals the presence of higher-twist, higher Fock state and/or soft, non-factorizable contributions. Such processes (e.g., $J/\psi \to \rho\pi$, $\eta_c \to \rho\rho$) have indeed been observed experimentally with often sizeable branching ratios. For the two-meson channels involving pseudoscalar (P) and vector mesons (V) they are characterized by

$$(-1)^{J_c}\, P_c \neq (-1)^{J_1+J_2}\, P_1 P_2\,, \tag{4.63}$$

where J_i and P_i are the spin and parity of the meson i. The amplitudes for processes of this kind are proportional to the Levi-Civita tensor, ε, which is to be contracted in all possible ways with the available Lorentz vectors, namely the two independent light hadron momenta, p_1 and p_2, and the polarization vectors (or tensors) of the light vector mesons and the charmonium state. As an example let us consider the process $J/\psi \to VP$, for which the amplitude reads

$$\mathcal{M}_{\lambda_V,\lambda_{J/\psi}}(J/\psi \to VP) \;=\; \frac{A}{M_{J/\psi}^2}\, \varepsilon(p_1, p_2, \epsilon^*(\lambda_V), \epsilon(\lambda_{J/\psi}))\,, \tag{4.64}$$

where A is a constant. Now, in the rest frame of the decaying meson, the polarization vector of a helicity zero vector meson can be expressed by a linear combination of the two final state momenta. The number of independent Lorentz vectors is, therefore, insufficient to contract the Levi-Civita tensor with the consequence of a vanishing amplitude for processes involving longitudinally polarized vector mesons.

DECAY
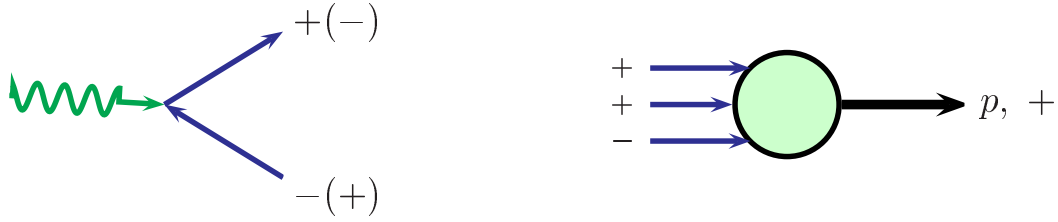
Fig. 4.6: Helicity configurations in the creation of a light $q\bar{q}$ pair (left) and for a leading-twist parton–proton transition (right).

Thus, hadronic helicity conservation (4.62) is violated in $J/\psi \to VP$ decays. By the same argument longitudinally polarized vector mesons are forbidden in the decay $\eta_c \to VV$. Since angular momentum conservation requires the same helicity for both vector mesons, hadronic helicity is not conserved in the case of transversally polarized vector mesons, too. With similar arguments the processes $\chi_{c1}, h_c \to VV$ and $\chi_{c2} \to VP$ are also forbidden to leading twist order. We note that hadronic helicity conservation does also not hold in η_c and χ_{c0} decays into baryon–antibaryon pairs where, in the charmonium rest frame, angular momentum conservation requires $\lambda_B = \lambda_{\bar{B}}$. A systematic investigation of higher-twist contributions to these processes is still lacking despite some attempts of estimating them, for a review see [95]. Recent progress in classifying higher-twist distribution amplitudes and understanding their properties [96, 97] now permits such analyses. The most important question to be answered is whether or not factorization holds for these decays to higher-twist order. It goes without saying that besides higher-twist effects, the leading-twist forbidden channels might be under control of other dynamical mechanisms such as higher Fock state contributions or soft power corrections. In Section 5.1 a variety of such mechanisms will be discussed.

Next, let us consider G-parity and isospin. G-parity or isospin-violating decays are not strictly forbidden since they can proceed through electromagnetic $c\bar{c}$ annihilation and may receive contributions from the isospin-violating part of QCD. The latter contributions, being related to the $u - d$ quark mass difference, seem to be small [92]. G-parity or isospin-violating decays of C-even charmonia (e.g., $\eta_c, \chi_{c1}, \chi_{c2} \to PV$ for non-strange final state mesons) have not been observed experimentally as yet [10]. Proceeding on the assumption that these decays are dominantly mediated by $c\bar{c} \to 2\gamma^* \to PV$, this is understandable. They are suppressed by a factor $(\alpha_{\rm em}/\alpha_{\rm s})^4$ as compared to the G-parity and isospin allowed decays of the C-even charmonia and their decay widths are therefore extremely small. Channels involving strange mesons (e.g., KK^*), are also expected to be strongly suppressed by virtue of U-spin invariance. For J/ψ decays the situation is different. Many G-parity violating (e.g., $\pi^+\pi^-$) or isospin-violating (e.g., $\omega\pi^0$) decays have been observed, the experimental branching ratios being of the order of 10^{-4}–10^{-3} [10]. As compared to G-parity and isospin allowed J/ψ decays they are typically suppressed by factors of about 10^{-2}–10^{-1} in accord with what is expected for an electromagnetic decay mechanism, see Fig. 4.7. An overview over the allowed and forbidden charmonium decays into pseudoscalar and vector mesons is given in Table 4.9.
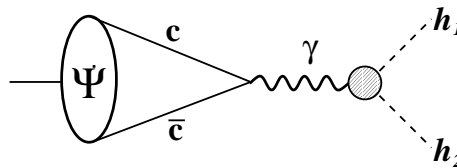
Fig. 4.7: Electromagnetic $\psi(nS)$ decays into pairs of hadrons. The shaded blob indicates a time-like electromagnetic transition form factor.

199

Table 4.9: Charmonium decays into PP, PV and VV meson pairs. The symbols 0, ϵ, $\surd$ denote channels forbidden by angular momentum and parity conservation, forbidden to leading-twist accuracy, and allowed, respectively. The brackets indicate that these channels violate either G-parity or isospin invariance for non-strange mesons.

	PP	PV	VV
η_c	0	$(\surd)$	ϵ
J/ψ	$(\surd)$	ϵ	$(\surd)$
h_c	0	$\surd$	ϵ
χ_{c0}	$\surd$	0	$\surd$
χ_{c1}	0	$(\surd)$	ϵ
χ_{c2}	$\surd$	(ϵ)	$\surd$

All what we have discussed so far holds for exclusive bottomonium decays as well. The situation is even better in this case. Due to the larger mass of the b quark, corrections to the leading-twist QCD results for bottomonium decays are probably reasonably small. Thus, the data on branching ratios can be expected to exhibit the pattern of leading-twist predictions. Exclusive quarkonium decays constitute an interesting laboratory for investigating corrections to the leading-twist lowest-order approach from various sources such as power and higher-twist corrections as well as higher Fock-state contributions. A systematic study of such is still lacking.

5.1 Decays of J/ψ and $\psi(2S)$ into two mesons[11]

The most dramatic unsolved problem in quarkonium physics is probably the ρ–π puzzle. In analyzing the 2-body decays of the J/ψ and $\psi(2S)$ into two light hadrons h_1 and h_2, it is convenient to consider the following quantity:

$$\kappa[h_1 h_2] = \frac{\mathcal{B}(\psi(2S) \to h_1 h_2)}{\mathcal{B}(J/\psi \to h_1 h_2)} \frac{\mathcal{B}(J/\psi \to e^+ e^-)}{\mathcal{B}(\psi(2S) \to e^+ e^-)} \frac{\varrho[J/\psi h_1 h_2]}{\varrho[\psi(2S) h_1 h_2]}, \tag{4.65}$$

where

$$\varrho[H h_1 h_2] = \sqrt{1 - 2(M_{h_1}^2 + M_{h_2}^2)/M_H^2 + (M_{h_1}^2 - M_{h_2}^2)^2/M_H^4}. \tag{4.66}$$

is a phase space factor that depends on the masses of the hadrons H, h_1, and h_2. As will be explained shortly, very simple theoretical considerations lead to the expectation that this quantity should be close to 1 for all light hadrons h_1 and h_2:

$$\kappa[h_1 h_2] = 1. \tag{4.67}$$

This prediction was once referred to as the 12% rule because the experimental value of the ratio of the electronic branching fractions of the $\psi(2S)$ and J/ψ was at one time near 12%. That experimental value is now $15 \pm 2\%$. The last factor in (4.65) is a phase space factor that is close to 1 for hadrons whose masses are much smaller than that of the J/ψ. Thus the prediction (4.67) implies that the ratio of the branching fractions of the $\psi(2S)$ and J/ψ into $h_1 h_2$ should be near 15%. All the baryon–antibaryon decay modes that have been measured are compatible with the prediction (4.67), see Sec. 5.2. Some two-meson decay modes are compatible with this prediction, but there are others for which it is badly violated. The most severe violation that has been observed is in the $\rho\pi$ decay mode. The first hint of this problem was seen by the Mark II collaboration in 1983 [98]. The decay $J/\psi \to \rho\pi$, with a branching fraction of about 1.3%, is the largest 2-body hadronic decay mode of the J/ψ. In contrast, the partial

[11]Author: E. Braaten

width for $\psi(2S)\to\rho\pi$ is so small that this decay was not observed until very recently by the CLEO and BES collaborations [99,100]. The branching fraction is measured to be 0.46 ± 0.09, and the ratio defined in (4.65) is $\kappa[\rho\pi] = 0.028 \pm 0.006$. The dramatic discrepancy between this result and the prediction in Eq. (4.67) is the $\rho - \pi$ puzzle.

We proceed to explain the assumptions underlying the prediction (4.67). Because there is a nonzero amplitude for the J/ψ to be a pure $c\bar{c}$ state, the matrix element for its decay into two light hadrons h_1 and h_2 can be expressed in the form

$$\mathcal{M}(J/\psi\to h_1 h_2) = \int \frac{d^3 p}{(2\pi)^3} \psi_{J/\psi}(\mathbf{p})\mathcal{A}(c(\mathbf{p})\bar{c}(-\mathbf{p})\to h_1 h_2), \tag{4.68}$$

where $\psi_{J/\psi}(\mathbf{p})$ is the momentum-space wave function for the pure $c\bar{c}$ component of the J/ψ. This can be regarded as an exact formula that defines the amplitude $\mathcal{A}(c\bar{c}\to h_1 h_2)$. It relies on the fact that wave functions satisfy integral equations, so even if there are other components of the J/ψ wave function besides $c\bar{c}$, the iteration of the integral equation will eventually produce a pure $c\bar{c}$ state. The annihilation of the $c\bar{c}$ pair produces an intermediate state consisting of partons with momenta of order m_c, which is much larger than either the momentum scale $p \sim m_c v$ for the $c\bar{c}$ wave function of the J/ψ or the scale Λ_{QCD} associated with the wave functions of the light hadrons h_1 and h_2. If the factored expression in (4.68) also corresponds to a separation of small momenta associated with the wave function of J/ψ from small momenta associated with the wave functions of h_1 and h_2, then the amplitude $\mathcal{A}$ in (4.68) should be insensitive to the value of $\mathbf{p}$. It can be approximated by its value at $\mathbf{p} = 0$ up to corrections suppressed by powers of v and Λ_{QCD}/m_c:

$$\mathcal{A}(c(\mathbf{p})\bar{c}(-\mathbf{p})\to h_1 h_2) \approx \mathcal{A}(c(\mathbf{0})\bar{c}(\mathbf{0})\to h_1 h_2). \tag{4.69}$$

With this approximation, the matrix element (4.68) reduces to

$$\mathcal{M}(J/\psi\to h_1 h_2) \approx \psi_{J/\psi}(\mathbf{r} = 0)\mathcal{A}(c(\mathbf{0})\bar{c}(\mathbf{0})\to h_1 h_2), \tag{4.70}$$

where $\psi_{J/\psi}(\mathbf{r})$ is the coordinate-space wave function for the pure $c\bar{c}$ component of J/ψ. The decay rate then has the factored form

$$\Gamma(J/\psi\to h_1 h_2) \approx \left|\psi_{J/\psi}(\mathbf{r} = 0)\right|^2 \left|\mathcal{A}(c(\mathbf{0})\bar{c}(\mathbf{0})\to h_1 h_2)\right|^2 \frac{\varrho[J/\psi h_1 h_2]}{16\pi M_{J/\psi}}. \tag{4.71}$$

The corresponding expression for the decay $\psi(2S)\to h_1 h_2$ differs only in the mass and the wave function factor. These factored expressions apply equally well to decays into $e^+ e^-$. Taking the ratio of decay rates in (4.65), we obtain the prediction $\kappa[h_1 h_2] = 1$ for any light hadrons h_1 and h_2. Any significant deviation of $\kappa[h_1 h_2]$ from 1 indicates a breakdown of the approximation (4.69).

An important reference point for the prediction (4.67) is provided by the (leading twist) asymptotic predictions of perturbative QCD [91, 92]. These predictions are most easily described using a ratio R defined by

$$R_{J/\psi}[h_1 h_2] = \frac{\Gamma(J/\psi\to h_1 h_2)}{\Gamma(J/\psi\to e^+ e^-)}. \tag{4.72}$$

The asymptotic predictions for this ratio depend on the helicities λ_1 and λ_2 of the two hadrons h_1 and h_2. If the hadrons are mesons and the decay proceeds via the annihilation process $c\bar{c}\to ggg$, the prediction for the scaling behavior of the ratio is

$$R_{J/\psi}[h_1(\lambda_1)h_2(\lambda_2)] \sim \frac{\alpha_s^6(m_c)}{\alpha_{\text{em}}^2} \left(\frac{\Lambda_{\text{QCD}}}{m_c}\right)^{4+2|\lambda_1+\lambda_2|}. \tag{4.73}$$

If the decay proceeds via the annihilation process $c\bar{c}\to\gamma^*$, the prefactor $\alpha_s^6/\alpha_{\text{em}}^2$ is replaced by α_s^2. The scaling behavior (4.73) illustrates one of the basic qualitative features of the asymptotic QCD predictions: light hadron helicity conservation. The dominant decay modes are predicted to satisfy the helicity

selection rule (4.62). In the case of the decay $J/\psi \rightarrow \rho\pi$, the helicity of the pion is $\lambda_\pi = 0$ and the helicity of the ρ is constrained by Lorentz invariance to be $\lambda_\rho = \pm 1$. Thus this decay necessarily violates the helicity selection rule, and its rate is predicted to be suppressed by $\Lambda_{\mathrm{QCD}}^2/m_c^2$ relative to modes that are compatible with the helicity selection rule. But $\rho\pi$ is observed to be the largest 2-body decay mode of the J/ψ. This appears to be a clear violation of the asymptotic PQCD predictions. An understanding of the ρ–π puzzle may have important implications for the relevance of asymptotic PQCD to charmonium decays.

The dramatic failure of the prediction (4.67) in some channels indicates a breakdown of the approximation (4.69) for either the J/ψ decay or the $\psi(2S)$ decay or both. The contribution to the amplitude $\mathcal{A}$ from the annihilation of $c\bar{c}$ into 3 hard gluons or a virtual photon should be insensitive to the relative momentum $\mathbf{p}$ of the $c\bar{c}$ pair. The failure of the prediction (4.67) indicates that at least one other dynamical mechanism must be involved. The sensitivity of the amplitude to $\mathbf{p}$ could arise from a fluctuation of the charmonium state into some component of the wave function other than $c\bar{c}$. In a hadronic basis, this fluctuation can be expressed in terms of mixing of the charmonium state with other hadrons. In a parton basis, it can be expressed in terms of $c\bar{c}$ annihilation from a higher Fock state that includes soft gluons.

Many explanations for the $\rho\pi$ puzzle have been proposed. The small upper bound on $\kappa[\rho\pi]$ can be explained either by an enhancement of the rate for $J/\psi \rightarrow \rho\pi$ or by a suppression of the rate for $\psi(2S) \rightarrow \rho\pi$. The enhancement of $J/\psi \rightarrow \rho\pi$ relative to $\psi(2S) \rightarrow \rho\pi$ could occur through mixing of J/ψ with another narrow state that has a much larger branching fraction into $\rho\pi$. One such possibility is

1. mixing of J/ψ with a narrow glueball [101, 102].

Direct searches have failed to reveal any evidence for such a glueball. The suppression of $\psi(2S) \rightarrow \rho\pi$ relative to $J/\psi \rightarrow \rho\pi$ could be explained if the decay is dominated by a particular component of the wave function that is suppressed for $\psi(2S)$ relative to J/ψ. The possibilities include

2. suppression of the $c\bar{c}$ wave function at the origin for a component of $\psi(2S)$ in which the $c\bar{c}$ is in a colour-octet $^3S_1$ state [103],

3. suppression of the $\omega\phi$ component of $\psi(2S)$ [104].

The suppression of $\psi(2S) \rightarrow \rho\pi$ relative to $J/\psi \rightarrow \rho\pi$ could be explained if the amplitude is dominated by two components of the wave function that nearly cancel in the case of $\psi(2S)$ but not for J/ψ. The possibilities include

4. cancellation between $c\bar{c}$ and $D\bar{D}$ components of $\psi(2S)$ [105],

5. cancellation between $c\bar{c}$ and glueball components of $\psi(2S)$ [105],

6. cancellation between S-wave $c\bar{c}$ and D-wave $c\bar{c}$ components of $\psi(2S)$ [106].

This last proposal leads to the very simple and unambiguous prediction that the D-wave charmonium state $\psi(3770)$ should have a branching fraction into $\rho\pi$ of about 4×10^{-4} [106]. A recently proposed explanation for the ρ–π puzzle is a

7. cancellation between the amplitudes for the resonant process $e^+e^- \rightarrow \psi(2S) \rightarrow \rho\pi$ and the direct process $e^+e^- \rightarrow \rho\pi$. See Sec. 2.8.5.

This proposal predicts that the observed suppression of $\psi(2S) \rightarrow \rho\pi$ relative to $J/\psi \rightarrow \rho\pi$ is specific to e^+e^- annihilation and should not occur for other charmonium production processes, such as B-meson decay.

It is reasonable to expect that a definitive solution to the ρ–π puzzle should also explain the deviations of $\kappa[h_1 h_2]$ from the prediction 1 for other hadrons h_1 and h_2. The existing measurements of the branching fractions into two mesons for J/ψ and $\psi(2S)$ are shown in Table 4.10. While many of the values of $\kappa[h_1 h_2]$ are compatible with 1, there are modes other than $\rho\pi$ for which κ is significantly smaller than 1, such as ρa_2, and and there are modes for which κ is significantly greater than 1, such as $K_S^0 K_L^0$.

Table 4.10: Comparison of J/ψ and ψ' branching ratios to VP, PP, PA, VS, VV and VT mesons. Unless specified data are from PDG [10]. Where specified we have included in the averages recent data on $\psi(2S)$ decays from BES [100, 107–109] and CLEO [99], the latter derived from reported ratios of branching ratios using values in PDG [10].

Decay mode h_1h_2	$\mathcal{B}(J/\psi\rightarrow h_1h_2)$ $(\times 10^4)$	$\mathcal{B}(\psi'\rightarrow h_1h_2)$ $(\times 10^4)$	$\kappa[h_1h_2]$ (Eq. 4.65)
$\varrho\pi$	127 ± 9	0.46 ± 0.09 [99] [100]	0.028 ± 0.006
$\omega\pi^0$	4.2 ± 0.6	0.22 ± 0.09 [99] [109]	0.40 ± 0.17
$\varrho\eta$	1.93 ± 0.23	0.23 ± 0.12 [99] [109]	0.9 ± 0.5
$\omega\eta$	15.8 ± 1.6	< 0.11 [108]	< 0.06
$\phi\eta$	6.5 ± 0.7	0.35 ± 0.11 [99] [108]	0.40 ± 0.13
$\varrho\eta'(958)$	1.05 ± 0.18	$0.19^{0.16}_{-0.11} \pm 0.03$ [109]	2.5 ± 0.9
$\omega\eta'(958)$	1.67 ± 0.25	< 0.81 [108]	< 4.3
$\phi\eta'(958)$	3.3 ± 0.4	$0.33 \pm 0.13 \pm 0.07$ [108]	0.71 ± 0.33
$K^*(892)^{\mp}K^{\pm}$	50 ± 4	0.26 ± 0.11 [99] [107]	0.039 ± 0.017
$\bar{K}^*(892)^0K^0$+c.c.	42 ± 4	1.55 ± 0.25 [99] [107]	0.28 ± 0.05
$\pi^+\pi^-$	1.47 ± 0.23	0.8 ± 0.5	4.3 ± 2.7
K^+K^-	2.37 ± 0.31	1.0 ± 0.7	3.2 ± 2.3
$K^0_SK^0_L$	1.46 ± 0.26	0.52 ± 0.07	2.7 ± 0.6
$\pi^{\pm}b_1(1235)^{\mp}$	30 ± 5	3.9 ± 1.6 (incl. [99])	1.0 ± 0.4
$\pi^0b_1(1235)^0$	23 ± 6	$4.0^{+0.9}_{-0.8} \pm 0.6$ [99]	1.3 ± 0.5
$K^{\pm}K_1(1270)^{\mp}$	< 30	10.0 ± 2.8	> 1.7
$K^{\pm}K_1(1400)^{\mp}$	38 ± 14	< 3.1	< 0.8
$\omega f_0(980)\rightarrow\omega\pi\pi$	1.1 ± 0.4		
$\phi f_0(980)\rightarrow\phi\pi\pi$	2.5 ± 0.7	0.60 ± 0.22	1.7 ± 0.8
$\omega f_0(1710)\rightarrow\omega K\bar{K}$	4.8 ± 1.1		
$\phi f_0(1710)\rightarrow\phi K\bar{K}$	3.6 ± 0.6		
$\omega f_1(1420)$	6.8 ± 2.4		
$\phi f_1(1285)$	2.6 ± 0.5		
$\omega f_2(1270)$	43 ± 6	2.1 ± 0.6 [111]	0.34 ± 0.11
$\varrho a_2(1320)$	109 ± 22	2.6 ± 0.9 [111]	0.17 ± 0.07
$K^*(892)^0\bar{K}_2^*(1430)^0$ + c.c.	67 ± 26	1.9 ± 0.5 [111]	0.19 ± 0.09
$\phi f_2'(1525)$	12.3 ± 2.1	0.44 ± 0.16 [111]	0.22 ± 0.09

One clue to the mechanism is how $\kappa[h_1 h_2]$ depends on the J^{PC} quantum numbers for hadrons $h_1 h_2$ with the same flavour quantum numbers as $\rho\pi$. As can be seen in Table 4.10, there also seems to be suppression in the vector-tensor (VT) channel ρa_2, but there seems to be no significant suppression in the axial vector-pseudoscalar (AP) channel $b_1\pi$ or in the pseudoscalar-pseudoscalar (PP) channel $\pi^+\pi^-$. The absence of any suppression in the channel $\pi^+\pi^-$ is to be expected, because it proceeds predominantly through $c\bar{c}$ annihilation into a single photon, and therefore the approximation (4.70) should hold.

Another clue to the suppression mechanism is the pattern of $\kappa[h_1 h_2]$ for different radial excitations of mesons with the same J^{PC} quantum numbers. An example is the AP decay modes $K^\pm K_1^\mp$ for different K_1 resonances. The mode $K^\pm K_1(1400)^\mp$ has been observed in J/ψ decays but not in $\psi(2S)$ decays. The mode $K^\pm K_1(1270)^\mp$ has been observed in $\psi(2S)$ decays but not in J/ψ decays. The lower bound on κ for $K^\pm K_1(1270)^\mp$ is significantly greater than the upper bound on κ for $K^\pm K_1(1400)^\mp$. This demonstrates that whether κ is suppressed or enhanced relative to the prediction (4.67) is not determined solely by the J^{PC} quantum numbers of the mesons.

The suppression pattern in a given channel as a function of the flavour quantum numbers should also provide important clues to the suppression mechanism. The channel for which the most measurements are available is the VP channel. The decay amplitude for $J/\psi \rightarrow VP$ can be resolved into 3 terms with distinct flavour structures:

– a flavour-connected amplitude g with quark structure $(q_i\bar{q}_j)(q_j\bar{q}_i)$,
– a flavour-disconnected amplitude h with quark structure $(q_i\bar{q}_i)(q_j\bar{q}_j)$,
– an electromagnetic amplitude e with quark structure $Q_{ik}(q_i\bar{q}_j)(q_j\bar{q}_k)$ where Q is the light quark charge matrix.

For example, the amplitude for $J/\psi \rightarrow \rho\pi$ is proportional to $g + e$. A quantitative analysis should also take into account SU(3) symmetry breaking from the strange quark mass and $U_A(1)$ symmetry breaking from the triangle anomaly. In the case of J/ψ, there are enough precise measurements of VP decays to completely determine the flavour decomposition of the amplitude [112, 113]. The conclusion is that $|e|$ and $|h|$ are comparable in magnitude and about an order of magnitude smaller than $|g|$.

The analogous flavour decomposition for $\psi(2S) \rightarrow VP$ expresses the decay amplitudes as a linear combination of amplitudes g', h', and e' with distinct flavour structures. The same reasoning that led to the prediction $\kappa[h_1 h_2] = 0$ implies that these amplitudes g', h' and e' should differ from the corresponding amplitudes g_1, h_1 and e for J/ψ by the factor

$$\left(\frac{M_{\psi(2S)}\Gamma(\psi(2S)\rightarrow e^+e^-)}{M_{J/\psi}\Gamma(J/\psi\rightarrow e^+e^-)} \right)^{1/2} \approx 0.70. \tag{4.74}$$

However, the measurement $\kappa[\rho\pi] \approx 0.028$ implies $|g' + e'| \approx 0.12|g + e|$. Since $|g| \gg |e|$, this requires $|g'|$ to be suppressed relative to $0.70|g|$. A mechanism for such a suppression was proposed in Ref. [103]. If g' was so strongly suppressed that it was small compared to $|e'|$, it would make the rate for $\psi(2S)\rightarrow\rho\pi$ comparable to electromagnetic processes such as $\psi(2S)\rightarrow\omega\pi^0$. The stronger suppression of $\psi(2S)\rightarrow\rho\pi$ that is observed requires that g' and e' be comparable in magnitude and to have phases such that there is a further cancellation in the sum $g' + e'$.

The CLEO collaboration has recently presented the first evidence for two-body decays of the $\Upsilon(1S)$ [114]. They observed signals with a statistical significance of greater than 5σ for decays into $\phi f_2'(1525)$ and $\bar{K}K_1(1400)$. The decay of $\Upsilon(1S)$ into $\bar{K}K_1(1270)$ is observed to be suppressed relative to $\bar{K}K_1(1400)$, which is the same pattern observed in J/ψ decays. The CLEO collaboration also set upper limits on other decay modes, the strongest of which is $\mathcal{B}(\Upsilon(1S)\rightarrow\rho\pi) < 4 \times 10^{-6}$.

5.2 Decays of J/ψ and $\psi(2S)$ into baryon–antibaryon

As we already discussed these decays seem to be dominated by hard physics where the charm and anticharm quark annihilate into gluons at short distances. In a leading-order calculation of decay widths

for the $B\overline{B}$ channels contributions from higher charmonium Fock states can be neglected since they only produce $\mathcal{O}(v^2)$ corrections, see Eq. (4.60); contributions from higher baryon Fock states are suppressed by powers of $1/m_c$. For consistency, the masses of the J/ψ and $\psi(2S)$ are to be replaced by $2m_c$ (except in phase space factors) since the energy for the binding of a $c\bar{c}$ pair in a charmonium state is an $\mathcal{O}(v^2)$ effect. The only soft physics information on the charmonium state needed in a calculation to lowest order in v is its decay constant. The corresponding electronic decay widths

$$\Gamma(J/\psi \to e^+ e^-) \;=\; \frac{4\pi}{3} \frac{e_c^2\, \alpha_{\rm em}^2\, f_{J/\psi}^2}{M_{J/\psi}}\,, \tag{4.75}$$

provide their values: $f_{J/\psi} = 409\,\text{MeV}$, $f_{\psi(2S)} = 282\,\text{MeV}$. The other soft physics information required is the leading-twist baryon distribution amplitude. As can be shown [115] the proton is described by one independent distribution amplitude, $\Phi_{123}^p(x)$, to leading-twist accuracy. The set of subscripts $1, 2, 3$ refers to the quark configuration $u_+\, u_-\, d_+$ of a proton with positive helicity. The distribution amplitudes for other valence quark configurations in the proton are obtained by permutations of the subscripts. Since flavour SU(3) is a good symmetry, only mildly broken by quark mass effects, it is reasonable to assume that the other members of the lowest-lying baryon octet are also described by only one independent distribution amplitude, which, up to flavour symmetry breaking effects, is the same as the proton one.

To start with and for orientation, we present the leading-twist result for the width of the decays of transversely polarized J/ψs, as for instance are produced in $e^+ e^-$ annihilations, into proton–antiproton pairs. The width, evaluated from the asymptotic form of the baryon wave function $\Phi_{\rm AS}^B = 120\, x_1\, x_2\, x_3$, reads

$$\Gamma(J/\psi \to p\bar{p}) \;=\; \frac{5^6\, 2^{10}}{3^5}\, \pi^5\, \alpha_{\rm s}(m_c)^6\, \frac{\varrho[J/\psi\, p\bar{p}]}{M_{J/\psi}} \left(\frac{f_{J/\psi}\, f_p^2}{m_c^4} \right)^2 I_{\rm AS}^2\,, \tag{4.76}$$

where

$$I_{\rm AS} \;=\; 6 \int [dx]_3\, [dy]_3\, \frac{x_1 y_3}{[x_1(1-y_1) + (1-x_1)y_1][x_3(1-y_3) + (1-x_3)y_3]}\,. \tag{4.77}$$

The normalization parameter f_p represents the proton's light-cone wave function for zero spatial separation of the quarks. Strictly speaking, it is defined by [116]

$$\frac{f_p(\mu_F)}{8\sqrt{n_c!}}\, \Phi_{123}^p(x, \mu_F) \;=\; \int^{\mu_F} [d^2 k_\perp]_3 \Psi_{123}^p(x, k_\perp)\,, \tag{4.78}$$

with

$$\int [dx]_3 \Phi_{123}^p(x, \mu_F) \;=\; 1\,. \tag{4.79}$$

Both the distribution amplitude and f_p are subject to evolution [116]. A typical value for f_p is $\simeq 6 \times 10^{-3}\,\text{GeV}^2$ [92, 117]. Evaluating the branching ratio from (4.76), (4.77), one obtains

$$\mathcal{B}(J/\psi \to p\bar{p}) \;=\; 1.5 \times 10^{-3} \left(\frac{\alpha_{\rm s}}{0.4} \right)^3 \left(\frac{1.5\,\text{GeV}}{m_c} \right)^7 \left(\frac{f_p}{6 \times 10^{-3}\,\text{GeV}^2} \right)^4\,, \tag{4.80}$$

which is in quite good agreement with experiment, see Table 4.11. The predictions for the branching ratio are more robust than that from the $J/\psi \to p\bar{p}$ decay widths since the total J/ψ width is dominated by the decays into light hadrons. Hence, according to (4.12) and (4.75), the branching ratios approximately scale as $1/m_c^7$ and $\alpha_{\rm s}^3$.

In previous calculations [92, 118] of the $J/\psi \to p\bar{p}$ decay width, distribution amplitudes have been employed that are strongly concentrated in the end-point regions where one of the momentum fractions is small. The use of such distribution amplitudes has been heavily criticized [119]. Due to their properties the bulk of the amplitude for the subprocess $c\bar{c} \to 3g^* \to 3(q\bar{q})$ is accumulated in the soft end-point regions where the use of perturbative QCD is inconsistent. Moreover, such distribution amplitudes lead

to extremely strong contributions to the decay amplitude and require compensation by small values of α_s, typically in the range of 0.2–0.3. Such values are unrealistically small with regard to the characteristic scales available in charmonium decays. For an average gluon virtuality of about $1\,\mathrm{GeV}^2$ one would expect α_s to be rather 0.4.

Recent theoretical [97, 120] and phenomenological [117] studies provide evidence that the proton distribution amplitude is close to the asymptotic form for baryons: the end-point concentrated forms seem to be obsolete. In a recent analysis of the J/ψ and $\psi(2S)$ decays into baryon–antibaryon pairs [121] use is made of the phenomenological proton distribution amplitude proposed in [117]

$$\Phi^{p}_{123}(x,\mu_0) \;=\; \Phi^{B}_{\mathrm{AS}}\,\frac{1}{2}\left(1 + 3x_1\right), \tag{4.81}$$

which is valid at the factorization scale $\mu_0 = 1\,\mathrm{GeV}$. This distribution amplitude goes along with the normalization parameter $f_p(\mu_0) = 6.64 \times 10^{-3}\,\mathrm{GeV}^2$. In [121] the distribution amplitude (4.81) has been suitably generalized to the cases of hyperons and decuplet baryons by allowing for flavour symmetry breaking due to the effect of the strange quark mass. Instead of the collinear approximation as used in [92, 118] or in (4.76), the modified perturbative approach [122] is applied in [121]. In this approach quark transverse momenta are retained and Sudakov suppressions, comprising those gluonic radiative corrections not included in the evolution of the distribution amplitude, are taken into account. The advantage of the modified perturbative approach is the strong suppression of the soft end-point regions where perturbative QCD cannot be applied. If distribution amplitudes close to the asymptotic form are employed the difference between a calculation on the basis of the collinear approximation and one within the modified perturbative approach is, however, not substantial given that the $J/\psi \to B\overline{B}$ amplitude is anyhow not very sensitive to the end-point regions. This is in marked contrast to the case of the proton's electromagnetic form factor [123]. On the other hand, a disadvantage of the modified perturbative approach is that the full baryon light-cone wave function is needed and not just the distribution amplitude. In [121] the transverse momentum dependence of the baryon wave functions has been parameterized by a simple Gaussian

$$\propto \exp\left[-a_B^2 \sum k_{\perp i}^2/x_i\right], \tag{4.82}$$

where a value of $0.75\,\mathrm{GeV}^{-1}$ has been adopted for the transverse size parameter a_B. For the decuplet baryons a somewhat larger value has been used ($0.85\,\mathrm{GeV}^{-1}$). Calculating the subprocess amplitude from the Feynman graphs shown in Fig. 4.5 and working out the convolution of subprocess amplitude and baryon wave functions, one obtains the widths Γ_{3g} for the J/ψ decays into $B\overline{B}$ pairs mediated by the hard annihilation process $c\bar{c} \to 3g^* \to 3(q\bar{q})$. The results are listed and compared to experimental data in Table 4.11. In addition to the three-gluon contribution there is also an isospin symmtetry violating electromagnetic one generated by the subprocess $c\bar{c} \to \gamma^* \to 3(q\bar{q})$, see Fig. 4.7. According to [121] this contribution is probably small, of the order of a few percent only. An important ingredient in this estimate of the size of the electromagnetic contribution is the agreement of the experimental widths for J/ψ decays into $n\bar{n}$ and $p\bar{p}$ within the errors [10]. The contributions from the $c\bar{c} \to g^*g^*\gamma^* \to 3(q\bar{q})$ to the baryon–antibaryon channels amount to less than 1% of the three-gluon contribution and can be neglected.

The widths for the corresponding decays of the $\psi(2S)$ are easily obtained within the perturbative approach by rescaling the J/ψ ones by the ratio of the electronic $\psi(2S)$ and J/ψ decay widths, the 15% rule, i.e., Eq. (4.65) with $\kappa[B\overline{B}] = 1$, holds strictly in the approach put forward in [121]. The results obtained that way are also quoted in Table 4.11. Good agreement between theory and experiment [10] is observed. Predictions of the absolute value of a decay width are subject to many uncertainties, see (4.76) while ratios of any two $B\overline{B}$ decay widths are robust since most of the uncertainties cancel to a large extent. It is to be emphasized that the $\psi(2S)$ and J/ψ decay widths do not scale as $(M_{J/\psi}/M_{\psi(2S)})^8 \simeq 1/4$ as suggested in [91] since the subprocess amplitude in a calculation to lowest order in the charm quark velocity (see (4.60)) has to be calculated with $2m_c$ and not with the bound state mass.

Table 4.11: Results for J/ψ and $\psi(2S)$ branching ratios for $B\overline{B}$ channels in units of 10^{-3} and 10^{-4}, respectively. The three-gluon contributions, taken from [121], are evaluated from $m_c = 1.5$ Gev, and the one-loop α_s with $\Lambda_{\rm QCD} = 210$ MeV. Unless specified data are taken from Ref. [10]. For the $J/\psi \to p\bar{p}$ we have included the recent BES measurement [124] in the average. The theoretical branching ratios are evaluated using $\Gamma(J/\psi) = 91.0 \pm 3.2\,{\rm keV}$ [10].

channel	$p\bar{p}$	$\Sigma^0\overline{\Sigma}^0$	$\Lambda\overline{\Lambda}$	$\Xi^-\overline{\Xi}^+$	$\Delta^{++}\overline{\Delta}^{--}$	$\Sigma^{*-}\overline{\Sigma}^{*+}$
$\mathcal{B}_{3g}(J/\psi)$	1.91	1.24	1.29	0.69	0.72	0.45
$\mathcal{B}_{\rm exp}$ [10]	2.16 ± 0.08	1.27 ± 0.17	1.30 ± 0.12	0.90 ± 0.20	1.10 ± 0.29	1.03 ± 0.13
$\mathcal{B}_{3g}(\psi(2S))$	2.50	1.79	1.79	1.11	1.07	0.80
$\mathcal{B}_{\rm exp}$ [10]	2.07 ± 0.31	1.2 ± 0.6	1.81 ± 0.34	0.94 ± 0.31	1.28 ± 0.35	1.10 ± 0.40

Bottomonium decays into $B\overline{B}$ pairs can be calculated along the same lines. The hard scale is now provided by the b-quark mass. Hence, relativistic and higher-twist corrections are expected to be smaller than in the charmonium case. But, as it turns out, the predicted decay widths for the baryonic channels are very small. Approximately, i.e., ignoring the fact that the $k_\perp$-dependent suppression of the three-gluon contribution is perhaps a bit different in the two cases, one finds the following rescaling formula

$$
\begin{aligned}
\Gamma(\Upsilon \to B\overline{B}) &= \frac{\varrho[\Upsilon B\overline{B}]}{\varrho[J/\psi B\overline{B}]} \frac{\Gamma(\Upsilon \to e^+e^-)}{\Gamma(J/\psi \to e^+e^-)} \\
&\times \left(\frac{e_c}{e_b}\right)^2 \left(\frac{\alpha_s(m_b)}{\alpha_s(m_c)}\right)^6 \left(\frac{m_b}{m_c}\right)^8 \Gamma(J/\psi \to B\overline{B}).
\end{aligned}
\tag{4.83}
$$

Using $m_b = 4.5\,{\rm GeV}$ one obtains, for instance, a value of $0.02\,{\rm eV}$ for the $\Upsilon \to p\bar{p}$ decay width, which value corresponds to a branching ratio of 0.3×10^{-7} well below the present experimental upper bound [10].

It goes without saying that the hard contributions, Γ_{3g}, to the J/ψ and $\psi(2S)$ decays into $B\overline{B}$ pairs respect the helicity sum rule (4.62), i.e., the amplitude for the production of baryon and antibaryon in equal helicities states vanishes. Measurements of the angular distribution in $e^+e^- \to J/\psi,\ \psi(2S) \to B_8\overline{B}_8$

$$
\frac{d\Gamma}{d\cos\vartheta} \propto 1 + \alpha_{B_8} \cos^2 \vartheta,
\tag{4.84}
$$

where B_8 is any member of the lowest-lying baryon octet and ϑ the c.m.s. production angle, allow for a test of this prediction. In the formal limit of an infinitely heavy charm quark $\alpha_{B_8} = 1$ as a consequence of hadronic helicity conservation [91]. The available data [124–128], listed in Table 4.12, tell us that only a fraction of about 10% of the total number of $B_8\overline{B}_8$ pairs are produced with the same helicity of baryon and antibaryon. This observation is in fair agreement with hadronic helicity conservation. The production of $B_8\overline{B}_8$ pairs with equal helicities has been modeled as a constituent quark [129,130] and/or hadron mass effect [131], both the effects are part of the $\mathcal{O}(v^2)$ and higher-twist/power corrections. Also electromagnetic effects in α_B have been investigated. For results we refer to Table 4.12.

5.3 Hadronic two-body decays of the η_c

Such decays of the η_c have been observed in experiment only for the $B\overline{B}$ and VV channels, upper bounds exist for a few others like $a_0(980)\pi$. Decays into PP and PV have not been observed, they are either

Table 4.12: Experimental and theoretical results for the parameter α_{B_8} in $J/\psi, \psi(2S) \to B_8 \overline{B}_8$ as defined in Eq. (4.84). Experimental values obtained averaging data from BES [124], DM2 [125], MARK II [126], E760 [127] and E835 [128].

$\alpha_{B_8}(J/\psi)$	$p\overline{p}$	$\Lambda\overline{\Lambda}$	$\Sigma^0\overline{\Sigma}^0$
Predicted: [131]	0.46	0.32	0.31
[129] (no e.m. corr)	0.69	0.51	0.43
[129] (incl. e.m. corr)	0.70		
Experiment: J/ψ	0.66 ± 0.05	0.65 ± 0.19	0.26 ± 0.30
$\psi(2S)$	0.68 ± 0.14		

strictly forbidden or strongly suppressed, see Table 4.9. As noted at the beginning of this section the $B\overline{B}$ and VV channels are forbidden to leading-twist accuracy since hadronic helicity conservation (4.62) is in conflict with angular momentum conservation for these processes. In contrast to the expectation from the leading-twist approximation the measured branching ratios are rather large (10^{-3}–10^{-2}). We repeat, it is worthwhile to explore the role of higher-twist baryon and vector meson wave functions in the decays of the η_c [96,97].

In [104] a mixing approach for the explanation of these η_c decays has been advocated. As is well-known the $U_A(1)$ anomaly leads to mixing among the pseudoscalar mesons $\eta - \eta' - \eta_c$ [132,133]. This mixing can adequately be treated in the quark-flavour mixing scheme [134] where one starts from the quark-flavour basis and assumes that the basis states and their decay constants follow the same pattern of mixing with common mixing angles. This assumption is supported by an analysis of the $\gamma - \eta$ and $\gamma - \eta'$ transition form factors at large momentum transfer [135]. The quark-flavour basis states are defined by the flavour content of their valence Fock states

$$\eta_q \to (u\bar{u} + d\bar{d})/\sqrt{2}, \qquad \eta_s \to s\bar{s}, \qquad \eta_{c0} \to c\bar{c}. \tag{4.85}$$

The admixture of the light quarks to the η_c, which we need here in this work, is controlled by a mixing angle θ_c [134]

$$|\eta_c\rangle = |\eta_{c0}\rangle - \frac{\theta_c}{\sqrt{1+y^2/2}} \left[|\eta_q\rangle + \frac{y}{\sqrt{2}} |\eta_s\rangle \right]. \tag{4.86}$$

The ratio of the basis decay constants f_q and f_s is denoted by y

$$y = f_q/f_s. \tag{4.87}$$

According to [134], its value amounts to 0.81 while $\theta_c = -1° \pm 0.1°$. The light-quark admixture to the η_c (4.86) is somewhat smaller than estimates given in [132] but slightly larger than quoted in [136]. In combination with the strong vertex $q\bar{q} \to VV$ this small light-quark component of the η_c suffices to account for the VV decays. In the spirit of this dynamical mechanism (see Fig. 4.8) the invariant amplitude, A, for the $\eta_c \to VV$ decays can be parameterized as

$$A(\eta_c \to VV) = C_{VV}^{\text{mix}} \, \sigma_{VV} \, F_{\text{mix}}(s = M_{\eta_c}^2). \tag{4.88}$$

It is related to the decay width by

$$\Gamma(\eta_c \to VV) = \frac{1}{32\pi S_{VV}} \frac{\varrho[\eta_c VV]^3}{M_{\eta_c}} |A(\eta_c \to VV)|^2. \tag{4.89}$$

Table 4.13: Mixing factors as well as experimental and theoretical ratios of decay widths for $\eta_c \to V^0 V^0$. The ratios are quoted with respect to the $\rho^0 \rho^0$ channel ($C_{\rho^0 \rho^0}^{\mathrm{mix}} = 1$). Experimental ratios are calculated taking into account the common systematics.

VV	C_{VV}^{mix}	R_{th}	R_{exp}
$\omega\omega$	1	0.63	< 0.37 [137]
			< 0.75 [138]
$K^{*0}\overline{K}^{*0}$	$(1+y^2)/2$	0.61	0.47 ± 0.09 [138]
			0.55 ± 0.27 [137]
$\phi\phi$	y^2	0.13	0.93 ± 0.33 [137]
			0.35 ± 0.10 [138]
			0.30 ± 0.10 [139]
			0.21 ± 0.14 [140]

The statistical factor for the decay into a pair of identical particles is denoted by S_{VV}. The mixing factor C_{VV}^{mix} embodies the mixing of the η_c with the basis states η_q and η_s (4.86). These factors are quoted in Table 4.13. Flavour symmetry breaking effects in the transitions $\eta_i \to VV$ ($i = q, s$) are absorbed in the factor σ_{VV}. As a simple model for it one may take the square of the vector meson's decay constants as a representative of SU(3) violations in these transitions ($f_\rho = 216\,\mathrm{MeV}$, $f_\omega = 195\,\mathrm{MeV}$, $f_\phi = 237\,\mathrm{MeV}$, $f_{K^*} = 214\,\mathrm{MeV}$). In order to have a dimensionless quantity, f_V^2 is scaled by the squared vector meson mass

$$\sigma_{VV} = \left(\frac{f_V}{M_V} \right)^2 . \tag{4.90}$$

Ratios of decay widths are free of the unknown transition form factor F_{mix}. With respect to the $\rho^0 \rho^0$ channel one finds for the other uncharged vector mesons channels

$$\frac{\Gamma(\eta_c \to V^0 V^0)}{\Gamma(\eta_c \to \rho^0 \rho^0)} = \frac{2}{S_{V^0 V^0}} \left(C_{V^0 V^0}^{\mathrm{mix}} \right)^2 \left(\frac{\sigma_{V^0 V^0}}{\sigma_{\rho^0 \rho^0}} \right)^2 \left(\frac{\varrho[\eta_c V^0 V^0]}{\varrho[\eta_c \rho^0 \rho^0]} \right)^3 . \tag{4.91}$$

The theoretical and experimental results on the ratios are listed in Table 4.13. Reasonable agreement between theory and experiment can be seen although the errors are large. Assuming a monopole behaviour for the transition form factor F_{mix} and fitting its strength to the $\rho\rho$ data, one obtains a value that is in accord with the concept of mixing.
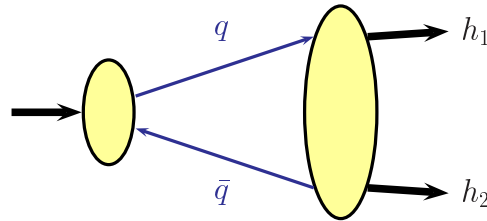

Fig. 4.8: The mixing mechanism for charmonium decays into light hadrons.

The mixing approach can also be applied to the η_c decays into baryon–antibaryon pairs. It seems that at least the $p\bar{p}$ channel for which the decay width has been measured, is also controlled by the mixing mechanism [104].

5.4   The decays of the χ_{cJ} and the role of the colour-octet contribution

The colour-singlet contribution to χ_{cJ} decays into pairs of pseudoscalar or vector mesons is well-known, it has been calculated several times [90, 92, 95]. The convolution of wave functions and hard subprocess amplitudes, which are to be calculated from Feynman graphs as shown in Fig. 4.5, leads to a decay width for the $\pi^+\pi^-$ channel as ($J = 0, 2$)

$$
\begin{aligned}
\Gamma(\chi_{cJ} \to \pi^+ \pi^-) &= 2 \frac{\pi^2}{3^5} \frac{\varrho[\chi_{cJ}\,\pi\pi]}{M_{\chi_{cJ}}} \frac{f_\pi^4}{m_c^7} |R'_{\chi_{cJ}}(0)|^2 \, \alpha_{\rm s}^4(m_c) \\
&\times \left| a_J + b_J \, B_2^\pi(m_c) + c_J \, B_2^\pi(m_c)^2 \right|^2 ,
\end{aligned}
\tag{4.92}
$$

where the parameters a_J, b_J and c_J are analytically calculable real numbers in the leading-twist approximation; they represent the convolution of distribution amplitudes an subprocess amplitude. The parameter a_0, for instance, reads

$$
a_0 = 27\pi^2/2 - 36 .
\tag{4.93}
$$

The representation (4.92) also holds in the modified perturbative approach but the parameters are then complex valued. The constant $B_2^\pi(\mu_0)$ is the first coefficient of the expansion of the leading-twist pion distribution amplitude upon Gegenbauer polynomials $C_n^{3/2}$ [116]

$$
\Phi_\pi = \Phi_{\rm AS}^M \left[1 + \sum_{n=2,4,\cdots} B_n^\pi(\mu_F) \, C_n^{3/2}(2x - 1) \right] ,
\tag{4.94}
$$

where $\Phi_{\rm AS}^M$ is the asymptotic form of a meson distribution amplitude

$$
\Phi_{\rm AS}^M = 6x(1 - x) ,
\tag{4.95}
$$

and

$$
B_n(\mu_F) = \left(\frac{\ln(\mu_F^2/\Lambda_{\rm QCD}^2)}{\ln(\mu_0^2/\Lambda_{\rm QCD}^2)} \right)^{\gamma_n} B_n(\mu_0) .
\tag{4.96}
$$

In Eq. (4.92) terms of order higher than 2 in the expansion are neglected and the factorization scale dependence of the Gegenbauer coefficient B_2 is controlled by $\gamma_2 = -50/81$. As the starting scale of the evolution, μ_0, a value of $1\,{\rm GeV}$ is taken. Finally, $f_\pi\,(= 132\,{\rm MeV})$ is the pion decay constant and $R'_{\chi_{cJ}}(0)\,(= 0.22\,{\rm GeV}^{5/2}$ [33, 141]) denotes the derivative of the nonrelativistic radial $c\bar{c}$ wave functions at the origin (in coordinate space). As usual a normalization factor $f_\pi/(2\sqrt{6})$ is pulled out from the distribution amplitude.

The distribution amplitude of the pion is fairly well-known by now from analyses of the $\pi^0 - \gamma$ transition form factor. It is close to the asymptotic form of a meson distribution amplitude [142]. Deviations from that form are difficult to estimate since they strongly depend on details of the analysis such as whether or not NLO, higher-twist corrections or tranverse degrees of freedom are taken into account [142, 143]. But in any case the Gegenbauer coefficient B_2^π seems to be small in magnitude. Combining the results from different analyses of the $\pi^0 - \gamma$ transition form factor, one may conclude that $|B_2^\pi| \lesssim 0.1$ at $\mu_0 = 1\,{\rm GeV}$. Taking first $B_2^\pi = 0$ in (4.92), one evaluates from (4.92) the branching ratio

$$
\mathcal{B}(\chi_{c0(2)} \to \pi^+\pi^-) \simeq 0.31\,(0.10) \times 10^{-3} \left(\frac{\alpha_{\rm s}}{0.4} \right)^2 \left(\frac{1.5\,{\rm GeV}}{m_c} \right)^3 .
\tag{4.97}
$$

The majority of the widths of the χ_{c0} and χ_{c2} come from decays into light hadrons. The contribution coming from the decay of a colour-singlet $c\bar{c}$ into real gluons is given by [33]

$$
\Gamma(\chi_{cJ} \to l.h.) \propto |R'_{\chi_{cJ}}(0)|^2 \frac{\alpha_{\rm s}^2}{m_c{}^4} .
\tag{4.98}
$$

Therefore, the branching ratios approximately scale as given in (4.97) and not as in (4.92). The $c\bar{c}$ wave function $R'_{\chi_{cJ}}(0)$ almost cancel in the ratio. Otherwise its well-known scaling properties [144] would have to be taken into account as well.

The variation of the branching ratio with the Gegenbauer coefficient B_2^π is displayed in Fig. 4.9. One can conclude that, stretching all parameters (B_2^π, α_s, m_c) to the extreme, the predictions for $\mathcal{B}(\chi_{c0(2)} \to \pi^+\pi^-)$ from the colour-singlet contribution to leading-twist accuracy stay a factor 3–6 below the data. Results of similar magnitude are found within the modified perturbative approach.
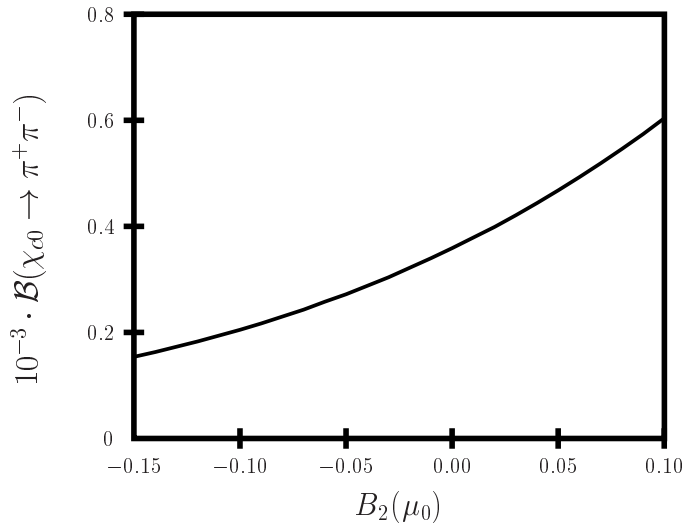
Fig. 4.9: Dependence of the leading-twist colour-singlet contribution to the $\chi_{c0} \to \pi^+\pi^-$ branching ratio on the expansion parameter B_2^π of the pion distribution amplitude at the scale $\mu_0 = 1\,\mathrm{GeV}$. The evolution of B_2^π is evaluated from $\Lambda_{\mathrm{QCD}} = 200\,\mathrm{MeV}$.

Thus, there is obviously room for the colour-octet contributions (see (4.59)), i.e., from the sub-process $c\bar{c}g \to 2(q\bar{q})$. A first attempt to include the colour-octet contribution has been undertaken in [94]. This calculation, performed within the modified perturbative approach [122], is based on a very rough model for the colour-octet χ_{cJ} wave function, the new ingredient of this calculation. Despite this the authors of Ref. [94] were able to show that the combined colour-singlet and -octet contributions are likely large enough to account for the data [10, 66], see Table 4.14. The calculation of the $\chi_{cJ} \to \pi^+\pi^-$ decay width can be generalized to other pseudoscalar meson channels with results of similar quality as for the $\pi\pi$ channels. For the $\eta'\eta'$ channel an additional two-gluon Fock component of the η' is to be taken into account whose leading-twist distribution amplitude has recently been extracted from a NLO analysis of the $\eta - \gamma$ and $\eta' - \gamma$ transition form factor [145, 146]. For the $\eta\eta$ channel the two-gluon contribution is probably negligible.

The colour-singlet contribution to the decays $\chi_{cJ} \to p\bar{p}$ ($J = 1, 2$) has been investigated by many authors [92, 95, 118, 150]. Employing the proton distribution amplitude (4.81) or a similar one, one again finds results that are clearly below experiment, which again signals the lack of the colour-octet contributions. An analysis of the $\chi_{c1(2)}$ decays into the octet and decuplet baryons along the same lines as for the pseudoscalar meson channels [94] has been carried through by Wong [147]. The branching ratios have been evaluated from the baryon wave functions (4.81), (4.82) and the same colour-octet χ_{cJ} wave function as in [94]. Some of the results obtained in [147] are shown and compared to experiment in Table 4.14. As can be seen from the table the results for the $p\bar{p}$ channels are in excellent agreement with experiment while the branching ratios for $\Lambda\overline{\Lambda}$ channels are much smaller than experiment [148] although the errors are large. A peculiar fact has to be noted: the experimental $\Lambda\overline{\Lambda}$ branching ratios are larger than the proton–antiproton ones although there is agreement within two standard deviations.

Table 4.14: Comparison of theoretical and experimental branching ratios for various χ_{cJ} decays into pairs of light hadrons. The theoretical values have been computed within the modified perturbative approach, colour-singlet and -octet contributions are taken into account ($B_2^\pi = B_2^\eta = B_1^K = 0$, $B_2^K = -0.1$, baryon wave functions (4.81), (4.82)). The branching ratios are quoted in units of 10^{-3} for the mesonic channels and 10^{-5} for the baryonic ones. Data taken from [10]. The values listed for $p\bar{p}$ branching rates do not include the most recent values $\left(27.4^{+4.2}_{-4.0} \pm 4.5\right) \cdot 10^{-5}$, $\left(5.7^{+1.7}_{-1.5} \pm 0.9\right) \cdot 10^{-5}$ and $\left(6.9^{+2.5}_{-2.2} \pm 1.1\right) \cdot 10^{-5}$ measured by BES [149] for χ_c0, χ_{c1} and χ_{c2} respectively.

process	theory	experiment
$\mathcal{B}(\chi_{c0}\to\pi^+\pi^-)$	3.0 [94]	4.9 ± 0.6
$\mathcal{B}(\chi_{c2}\to\pi^+\pi^-)$	1.8 [94]	1.77 ± 0.27
$\mathcal{B}(\chi_{c0}\to K^+K^-)$	2.4 [94]	6.0 ± 0.9
$\mathcal{B}(\chi_{c2}\to K^+K^-)$	1.4 [94]	0.94 ± 0.21
$\mathcal{B}(\chi_{c0}\to\eta\,\eta)$	2.0 [94]	2.1 ± 1.1
$\mathcal{B}(\chi_{c2}\to\eta\,\eta)$	1.3 [94]	< 1.5
$\mathcal{B}(\chi_{c0}\to p\,\bar{p})$	$-$	22.4 ± 2.7
$\mathcal{B}(\chi_{c1}\to p\,\bar{p})$	6.4 [147]	7.2 ± 1.3
$\mathcal{B}(\chi_{c2}\to p\,\bar{p})$	7.7 [147]	6.8 ± 0.7
$\mathcal{B}(\chi_{c0}\to\Lambda\overline{\Lambda})$	$-$	47 ± 16
$\mathcal{B}(\chi_{c1}\to\Lambda\overline{\Lambda})$	3.8 [147]	26 ± 12
$\mathcal{B}(\chi_{c2}\to\Lambda\overline{\Lambda})$	3.5 [147]	34 ± 17

The present analyses of the χ_{cJ} decays suffer from the rough treatment of the colour-octet charmonium wave function. As we mentioned before a reanalysis of the decays into the PP and $B\overline{B}$ channels as well as an extension to the VV ones is required. Our knowledge of the colour-octet wave function has been improved recently due to the intense analyses of inclusive processes involving charmonia, e.g., [151]. This new information may be used to ameliorate the analysis of the $\chi_{cJ}\to PP, B\overline{B}$ decays and, perhaps, to reach a satisfactory quantitative understanding of these processes. We finally want to remark that the colour-octet contribution does not only play an important role in the χ_{cJ} decays into PP and $B\overline{B}$ pairs but potentially also in their two-photon decays [30, 33, 152] (see also Section 3).

The leading-twist forbidden $\chi_{c0}\to B\overline{B}$ decays have sizeable experimental branching ratios, see Table 4.14. There is no reliable theoretical interpretation of these decays as yet. The only proposition [153] is the use of a diquark model, a variant of the leading-twist approach in which baryons are viewed as being composed of quarks and quasi-elementary diquarks. With vector diquarks as constituents one may overcome the helicity sum rule (4.62). The diquark model in its present form, however, contends with difficulties. Large momentum transfer data on the Pauli form factor of the proton as well as a helicity correlation parameter for Compton scattering off protons are in severe conflict with predictions from the diquark model.

5.5 Radiative decays of charmonia into light hadrons

First let us consider the process $J/\psi\to\gamma\pi^0$. The apparently leading contribution to it is generated by the subprocess $c\bar{c}\to\gamma\,g^*g^*\to\gamma q\bar{q}$, which, in principle, leads to a decay width of order α_s^4. However, due to the pion's flavour content $\propto u\bar{u} - d\bar{d}$ this contribution exactly cancels to zero in the limit of massless quarks. A VDM contribution $J/\psi\to\rho\pi$ followed by a $\rho - \gamma$ conversion [95] seems to dominate this

process. Indeed, an estimate of the VDM contribution leads to a branching ratio of 3.3×10^{-5}, which compares favorably with the experimental result of $(3.9 \pm 1.3) \times 10^{-5}$ [10]. Analogue estimates of the $\gamma\eta$ and $\gamma\eta'$ branching ratios lead to similar values, about 1×10^{-5}, which fall short of the experimental results by two orders of magnitude. The solution of this discrepancy is a gluonic contribution, which occurs as a consequence of the $U_A(1)$ anomaly; it formally presents a power correction. According to Novikov et al. [154], the photon is emitted by the c quark with a subsequent annihilation of the $c\bar{c}$ pair into lighter quarks through the effect of the anomaly. The creation of the corresponding light quarks is controlled by the gluonic matrix element $\langle 0|\alpha_s G\widetilde{G}|\eta^{(\prime)}\rangle$ where G is the gluon field strength tensor and $\widetilde{G}$ its dual. Photon emission from the light quarks is negligible as can be seen from the smallness of the $\gamma\pi$ width. This mechanism leads to the following width for the radiative J/ψ decay into $\eta^{(\prime)}$ [154]

$$\Gamma(J/\psi\to\gamma\eta^{(\prime)}) \;=\; \frac{2^5}{5^2 3^8}\,\pi e_c^2 \alpha_{\mathrm{em}}^3\,\varrho[J/\psi\gamma\eta^{(\prime)}]\left(\frac{M_{J/\psi}}{m_c^2}\right)^4 \frac{|\langle 0|\frac{\alpha_s}{4\pi}G\widetilde{G}|\eta^{(\prime)}\rangle|^2}{\Gamma(J/\psi\to e^+ e^-)}\,. \tag{4.99}$$

In the quark-flavour mixing scheme the gluonic matrix element for the η is given by [155]

$$\langle 0|\frac{\alpha_s}{4\pi}G\widetilde{G}|\eta\rangle \;=\; -\sin\theta_8\,\sqrt{2+y^2}\,f_q\,a^2\,. \tag{4.100}$$

For the η' matrix element $\sin\theta_8$ is to be replaced by $\cos\theta_8$. The angle θ_8 controls the mixing of the octet decay constants. In [134] the various mixing parameters have been determined; their values amount to:

$$\theta_8 \;=\; -21.2^\circ\,;\quad f_q \;=\; 1.07 f_\pi\,;\quad a^2 \;=\; 0.265\,\mathrm{GeV}^2\,;\quad \phi \;=\; 39.3^\circ\,. \tag{4.101}$$

The latter angle is the mixing angle in the quark-flavour basis. The parameter y has been defined in Eq. (4.87). Evaluating the decay width or rather the branching ratio from these parameter values, one obtains

$$\mathcal{B}(J/\psi\to\gamma\eta) \;=\; 3.7 \times 10^{-4}\left(\frac{1.5\,\mathrm{GeV}}{m_c}\right)^7\,. \tag{4.102}$$

The comparison with the experimental value of $(8.6 \pm 0.8)\cdot 10^{-4}$ [10] reveals that the order of magnitude is correctly predicted. As happens frequently in exclusive charmonium decays the charm-quark mass appears to a high power in the theoretical estimates of branching ratios with the consequence of large uncertainties in the predicted values. With regard to the fact that the total J/ψ decay width is dominated by the decays into light hadrons (4.12), the power of m_c in (4.102) is approximately seven. The mass of the J/ψ appears in (4.99) through a pole saturation of a QCD sum rule [154]; it should not be replaced by $2m_c$.

While the calculation of the individual decay widths is not easy, ratios of the η and η' widths can be reliably predicted from $\eta - \eta'$ mixing. Using the quark-flavour mixing scheme again, one finds from (4.99) and (4.100) the following ratios for radiative J/ψ decays [134]

$$\frac{\mathcal{B}(J/\psi\to\gamma\eta')}{\mathcal{B}(J/\psi\to\gamma\eta)} \;=\; \cot^2\theta_8 \left(\frac{\varrho[J/\psi\gamma\eta']}{\varrho[J/\psi\gamma\eta]}\right)^3\,. \tag{4.103}$$

The extension to the η_c is also possible. With (4.86) one obtains

$$\frac{\mathcal{B}(J/\psi\to\gamma\eta')}{\mathcal{B}(J/\psi\to\gamma\eta_c)} \;=\; \theta_c^2 \cos^2\theta_8 \left(\frac{\varrho[J/\psi\gamma\eta']}{\varrho[J/\psi\gamma\eta_c]}\right)^3\,. \tag{4.104}$$

This approach leads to the following numerical results:

$$\begin{aligned}
\frac{\mathcal{B}(J/\psi\to\gamma\eta')}{\mathcal{B}(J/\psi\to\gamma\eta)} &\;=\; 5.39\,, \qquad \text{Exp}:\; 5.0 \pm 0.6 \;[10]\,, \\[4pt]
\frac{\mathcal{B}(J/\psi\to\gamma\eta')}{\mathcal{B}(J/\psi\to\gamma\eta_c)} &\;=\; 0.48\,, \qquad \text{Exp}:\; 0.33 \pm 0.1 \;[10]\,.
\end{aligned} \tag{4.105}$$

Due to the large uncertainties in the angle θ_c the prediction for the second ratio has an error of about 20%.

It is tempting to extend the anomaly dominance to the case of the radiative Υ decays. One obtains

$$\frac{\mathcal{B}(\Upsilon\to\gamma\eta')}{\mathcal{B}(\Upsilon\to\gamma\eta)} = 6.51, \qquad \frac{\mathcal{B}(\Upsilon\to\gamma\eta')}{\mathcal{B}(\Upsilon\to\gamma\eta_c)} = 3.5 \times 10^{-4}. \tag{4.106}$$

Comparison with experiment is not yet possible, only upper bounds exist for the individual branching ratios. Doubts have, however, been raised by Ma [156] on the validity of this approach for the Υ decays. Generalizing the result for the J/ψ case (4.99) appropriately, one finds a too large branching ratio, namely $\simeq 8.3 \times 10^{-5}$, as compared to the experimental upper limit of $\leq 1.6 \times 10^{-5}$ [10]. The estimate advocated for by Ma, is based on the assumption of scale independence of the gluonic matrix element. With regard to the well separated scales m_c and m_b this assumption is suspicious. Nonetheless, the investigation of the $\Upsilon\to\gamma\eta^{(\prime)}$ decays is to be addressed further. Of interest would also be an investigation of the radiative h_c decays into pseudoscalar mesons. It is likely that these decays are under control of the same dynamical mechanism as the corresponding J/ψ decays. Results analogue to (4.103), (4.104) would then hold. Instead of the decays into pseudoscalar mesons one may also explore radiative quarkonium decays into scalar mesons. As is well-known scalar mesons may have sizeable glue–glue Fock components [157], they may even be glueballs although they likely have sizeable admixtures of light quarks [158, 159]. It would be interesting to unravel the dynamics mediating these decays. For first attempts see for instance [159, 160].

The decays $J/\psi\to\rho\eta^{(\prime)}$ can be treated analogously to the radiative decays. Since in these processes G-parity is not conserved, they proceed through $c\bar{c}\to\gamma^*$. On account of the flavour content of the ρ meson, the $\gamma^*\to\rho\eta^{(\prime)}$ transition only probes the η_q component of the $\eta^{(\prime)}$ if OZI-suppressed contributions are neglected. Hence,

$$\frac{\mathcal{B}(J/\psi\to\rho\eta')}{\mathcal{B}(J/\psi\to\rho\eta)} = \tan^2\phi \left(\frac{\varrho[J/\psi\rho\eta']}{\varrho[J/\psi\rho\eta]}\right)^3, \tag{4.107}$$

the $\rho-\eta_q$ form factor cancels in the ratio. Equation (4.107) leads to 0.52 for the ratio of the decay widths while the experimental value is 0.54 ± 0.21 [10].

Finally, we want to mention the radiative J/ψ decay into a proton–antiproton pair. Recently, an enhancement near $2M_p$ in the invariant mass spectrum of $p\bar{p}$ pairs has been observed while $J/\psi\to\pi^0 p\bar{p}$ behaves regular near the $p\bar{p}$ threshold [161]. The combination of both the results hints at a peculiar behaviour of the $p\bar{p}$ pair in an isospin-zero state. The enhancement observed in $J/\psi\to\gamma p\bar{p}$ parallels similar anomalies near the $p\bar{p}$ threshold. They have been reported by Belle [162] for the decays $B^+\to K^+ p\bar{p}$ and $\overline{B}^0\to D^0 p\bar{p}$. An anomalous threshold behaviour is also seen in the proton's time-like form factor [163], in the charged pion spectrum from $\bar{p}d\to\pi^-\pi^0 p$ and $\pi^+\pi^- n$ reactions [164] and in the real part of the elastic proton–antiproton forward amplitude [165].

Frequently these anomalies have been associated with narrow $p\bar{p}$ bound states. Indeed, an analysis of the BES provides evidence for an S-wave bound state with a mass of $1859^{+3}_{-10}(\text{stat})^{+5}_{-25}(\text{syst})$ MeV and a total width less than 30 MeV [161]. A P-wave bound state instead of an S-wave one cannot be excluded from the BES data. This BES result is very close to findings from an analysis of $\bar{p}d$ reactions [166] (a bound state mass of $1870\,\text{MeV}$ and a width of $10\,\text{MeV}$) and from a proton–antiproton forward dispersion relation [167] (mass: $1852\,\text{MeV}$, width: $35\,\text{MeV}$). In the CERN WA56 experiment [168], on the other hand, a narrow peak (mass $2.02\,\text{GeV}$) has been observed in the $p\bar{p}$ invariant mass spectrum of the reaction $\pi^- p\to p_f\pi^-[p\bar{p}]$ where p_f is a fast forward going proton. Puzzling is, however, the fact that this peak is not seen in $J/\psi\to\gamma p\bar{p}$ [161] while there is no indication of a threshold enhancement in the WA56 measurement. Several authors [169] have pointed out that the dynamics of the low-energy $p\bar{p}$ system such as pion exchange or the physics inherent in the effective range expansion, provides an important contribution to the threshold enhancement. An appealing mechanism has been suggested by Rosner [170]. He assumes that the partonic subprocess in the process $J/\psi\to\gamma p\bar{p}$ is $c\bar{c}\to\gamma gg$ followed

by a nonperturbative $gg \to (p\bar{p})_S$ transition where the subscript indicates a $p\bar{p}$ pair in a resonant S-state. Rosner further assumes that the corresponding B decays, for instance $B^+ \to K^+ p\bar{p}$, receives a substantial contribution associated with the subprocess $\bar{b} \to \bar{s}gg$ and the same nonperturbative $gg \to (p\bar{p})_S$ transition as for $J/\psi \to \gamma p\bar{p}$. Producing an η' through this mechanism instead of the proton–antiproton pair leads to similar contributions except that now a different gluonic matrix element occurs, see (4.99). In ratios of these processes most details cancel and, according to Rosner, one arrives at

$$\frac{\mathcal{B}(B^+ \to K^+(p\bar{p})_S)|_{gg}}{\mathcal{B}(B^+ \to K^+\eta')|_{gg}} = \frac{\varrho[B^+K^+(p\bar{p})_S]}{\varrho[B^+K^+\eta']} \left(\frac{\varrho[J/\psi\gamma\eta']}{\varrho[J/\psi\gamma(p\bar{p})_S]} \right)^3 \frac{\mathcal{B}(J/\psi \to \gamma(p\bar{p})_S)}{\mathcal{B}(J/\psi \to \gamma\eta')} . \qquad (4.108)$$

The gg subscript at the B-meson matrix elements is meant as a hint that there might be other non-negligible contributions to the B decays than those from the subprocess $\bar{b} \to \bar{s}gg$. This mechanism relates the threshold enhancement in $B^+ \to K^+ p\bar{p}$ to that in $J/\psi \to \gamma p\bar{p}$. Using the experimental information on the latter process, Rosner found that this mechanism provides a substantial fraction of the first one. It is to be stressed that the ratio of $B^{+(0)}$ decays into $K^{+(0)}\eta'$ and $K^{+(0)}\eta$ are not in conflict with this interpretation.

6 ELECTROMAGNETIC TRANSITIONS[12]

For quarkonium states, $Q_1\bar{Q}_2$, above the ground state but below threshold for strong decay into a pair of heavy flavoured mesons, electromagnetic transitions are often significant decay modes. In fact, the first charmonium states not directly produced in e^+e^- collisions, the χ_c^J states, were discovered in photonic transitions of the ψ' resonance. Even today, such transitions continue to be used to observe new quarkonium states [171].

6.1 Theoretical framework

6.1.1 Effective Lagrangian

The theory of electromagnetic transitions between these quarkonium states is straightforward. Much of the terminology and techniques are familiar from the study of EM transitions in atomic and nuclear systems. The photon field $\mathbf{A}_{em}^\mu$ couples to charged quarks through the electromagnetic current:

$$j_\mu \equiv \sum_{i=u,d,s} j_\mu^i + \sum_{i=c,b,t} j_\mu^i . \qquad (4.109)$$

The heavy valence quarks (c, b, t) can be described by the usual effective action:

$$\mathcal{L}_{\mathrm{NRQCD}} = \psi^\dagger \left\{ iD_0 + \frac{\mathbf{D}^2}{2m} + c_F \, g \frac{\boldsymbol{\sigma} \cdot \mathbf{B}}{2m} + c_D \, g \frac{[\mathbf{D}\cdot, \mathbf{E}]}{8m^2} + ic_S \, g \frac{\boldsymbol{\sigma} \cdot [\mathbf{D}\times, \mathbf{E}]}{8m^2} + \ldots \right\} \psi , \qquad (4.110)$$

where the $\mathbf{E}$ and $\mathbf{B}$ fields are the chromoelectric and chromomagnetic fields. Corrections to the leading NR behaviour are determined by the expansion in the quark and antiquark velocities. For photon momentum small compared to the heavy quark masses, the form of the EM interaction (in Coulomb gauge) is determined in the same way as the NRQCD action itself [13, 14, 42, 172], the leading order terms are:

$$\mathbf{j} \cdot \mathbf{A}_{em} = e_Q \psi^\dagger \left\{ \frac{\{\mathbf{D}\cdot, \mathbf{A}_{em}\}}{2m} + (1 + \kappa_Q) \frac{\boldsymbol{\sigma} \cdot \mathbf{B}_{em}}{2m} + \ldots \right\} \psi . \qquad (4.111)$$

The first term of Eq. (4.111) produces electric and the second magnetic transitions. The coefficient κ_Q is a possible anomalous magnetic moment for the heavy quark. It is a perturbative quantity at the level

---

[12]Author: E. Eichten

of NRQCD, but may get nonperturbative contributions in going to lower energy effective field theories, once the scale Λ_{QCD} has been integrated out. Since we may assume that potential models are an attempt to mimic such theories, we will interpret in this last way the quantity κ_Q that appears there and will be used in the following.

For quarkonium systems, light quarks (u, d, s) only contribute to internal quark loops, described perturbatively at short distance and as virtual pairs of heavy flavour mesons at large distance. In the SU(3) limit the total contribution from light quarks vanishes since its EM current has no SU(3) singlet part. Hence, to leading order in SU(3) breaking these contributions can be ignored. We return to these corrections in Sec. 6.5.

6.1.2 Transition amplitudes

Within a $\bar{Q}_2 Q_1$ quarkonium system, the electromagnetic transition amplitude is determined by the matrix element of the EM current, $\langle f | j_{\mathrm{em}}^{\mu} | i \rangle$, between an initial quarkonium state, i, and a final state f. Including the emission of a photon of momentum k and polarization ϵ_γ, the general form of the transition amplitude is the sum of two terms

$$\mathcal{M}(i \to f) = [\mathbf{M}^{(1)}(i \to f) + \mathbf{M}^{(2)}(i \to f)] \cdot \epsilon_\gamma(k), \qquad (4.112)$$

where in the term $\mathbf{M}^{(1)}$ the photon is emitted off the quark Q_1 with mass m_1 and charge e_1,

$$\mathbf{M}^{(1)}(i \to f) = \frac{e_1}{2m_1} \int d^3x \langle i | Q_1^{\dagger}(x)(\mathbf{D}, \exp{(i\mathbf{x} \cdot \mathbf{k})} + (1 + \kappa_{Q_1})\boldsymbol{\sigma} \times \mathbf{k} \exp{(i\mathbf{x} \cdot \mathbf{k})})Q_1(x) | f \rangle, \qquad (4.113)$$

and in the corresponding term $\mathbf{M}^{(2)}$ the photon is emitted off the antiquark $\bar{Q}_2$ with mass m_2 and charge $-e_2$.

Electromagnetic transition amplitudes can be computed from first principles in Lattice QCD [173]. Preliminary studies [174] have even included electromagnetic interactions directly into Lattice QCD simulations. However, these transitions for quarkonium systems have not yet been computed. Various relations between transitions also arise from QCD sum rules [175].

Although other calculational models, e.g., using the MIT bag model [176], have been explored, only potential model approaches provide the detailed predictions for the strength of individual transition amplitudes needed to compare with experiments. The remainder of this section will focus on the issues within potential model approaches.

Within nonrelativistic (NR) potential models, a quarkonium state is characterized by a radial quantum number, n, orbital angular momentum, l, total spin, s, and total angular momentum, J. In the NR limit the spin dependence decouples from the spatial dependence. The spatial wave function for a NR state, $\psi(x)$, can be expressed in terms of a radial wave function, $u_{nl}(r)$ and an orbital angular momentum dependence by:

$$\psi(x) = Y_{lm}(\theta, \phi)\frac{u_{nl}(r)}{r}. \qquad (4.114)$$

The spatial dependence of EM transition amplitudes reduces to expectation values of various functions of quark position and momentum between the initial and final state wave functions. Expanding Eq. (4.113) in powers of photon momentum generates the electric and magnetic multipole moments. This is also an expansion in powers of velocity. The leading order transition amplitudes are electric dipole (E1) or magnetic dipole (M1).

6.1.3 Electric transitions

Electric transitions do not change quark spin. The lowest NR order transition is the electric dipole (E1) transition. These transitions have $\Delta l = \pm 1$ and $\Delta s = 0$. To compute the E1 transition amplitudes

$\exp(i\mathbf{x} \cdot \mathbf{k})$ can be replaced by 1 in electric transition term in Eq. (4.113). Separating out the overall centre of mass motion of the system, the quark momentum operator, $i\mathbf{D}/m_Q$, can be replaced by the commutator, $[h, \mathbf{x}]$, of the bound state Hamiltonian, h, with the quark position operator, $\mathbf{x}$. Finally, the Hamiltonian acting on the initial or final state is simply the mass of that state. To leading NR order, this is equal to the momentum of the final photon $k = (M_i^2 - M_f^2)/(2M_i)$. The E1 radiative transition amplitude between initial state $(n^{2s+1}J)$, i, and final state $(n'^{2s'+1}J')$, f, is [177]:

$$\mathbf{M}^e(i \to f)_\mu = \delta_{s,s'}(-1)^{s+J+J'+1+M'}k\sqrt{(2J+1)(2J'+1)(2l+1)(2l'+1)}$$
$$\begin{pmatrix} J' & 1 & J \\ -M' & \mu & M \end{pmatrix} \begin{pmatrix} l' & 1 & l \\ 0 & 0 & 0 \end{pmatrix} \begin{Bmatrix} l & s_a & J \\ J' & 1 & l' \end{Bmatrix} \langle e_Q \rangle \mathcal{E}_{if}, \quad (4.115)$$

where $\langle e_Q \rangle = (e_1 m_2 - e_2 m_1)/(m_1 + m_2)$ and the overlap integral $\mathcal{E}_{if}$ is

$$\mathcal{E}_{if} = \int_0^\infty dr\, u_{n\ell}(r) r u_{n'\ell'}(r). \quad (4.116)$$

If the full photon momentum dependence in Eq. (4.113) is retained (even through this is formally a higher order relativistic corrections); the overlap integral $\mathcal{E}$ for $m_1 = m_2$ and $e_1 = -e_2 = e_Q$ is given by

$$\mathcal{E}_{if} = \frac{3}{k} \int_0^\infty dr\, u_{n\ell}(r) u_{n'\ell'}(r) \left[\frac{kr}{2} j_0\left(\frac{kr}{2}\right) - j_1\left(\frac{kr}{2}\right) \right] + \mathcal{O}(k/m). \quad (4.117)$$

The spin averaged decay rate is given by

$$\Gamma(i \xrightarrow{\text{E1}} f + \gamma) = \frac{4\alpha e_Q^2}{3}(2J'+1)S_{if}^{\text{E}}k^3|\mathcal{E}_{if}|^2, \quad (4.118)$$

where the statistical factor $S_{if}^{\text{E}} = S_{fi}^{\text{E}}$ is

$$S_{if}^{\text{E}} = \max(\ell, \ell') \begin{Bmatrix} J & 1 & J' \\ \ell' & s & \ell \end{Bmatrix}^2. \quad (4.119)$$

6.1.4 Magnetic transitions

Magnetic transitions flip the quark spin. The M1 transitions have $\Delta l = 0$ and the amplitude is given by:

$$\mathbf{M}^m(i \to f)_\mu = \delta_{\ell,\ell'}(-1)^{l+J'+J+l+\mu+M'}3\sqrt{(2J+1)(2J'+1)(2s+1)(2s'+1)}$$
$$\sum_{\nu,\sigma} k_\sigma \begin{pmatrix} 1 & 1 & 1 \\ -\mu & \sigma & \nu \end{pmatrix} \begin{pmatrix} J' & J & 1 \\ -M' & M & \nu \end{pmatrix} \begin{Bmatrix} s & l & J \\ J' & 1 & s' \end{Bmatrix} \begin{Bmatrix} 1 & 1/2 & 1/2 \\ 1/2 & s & s' \end{Bmatrix}$$
$$\left[\frac{e_1}{m_1} + (-1)^{s+s'}\frac{e_2}{m_2} \right] \mathcal{M}_{if}, \quad (4.120)$$

where for equal mass quarks the overlap integral $\mathcal{M}$ is given by

$$\mathcal{M}_{if} = (1 + \kappa_Q) \int_0^\infty dr\, u_{n\ell}(r) u'_{n'\ell}(r) j_0\left(\frac{kr}{2}\right) + \mathcal{O}(k/m). \quad (4.121)$$

The spin-flip radiative transition rate between an initial state $(n^{2s+1}\ell_J)$, i, and a final state $(n'^{2s'+1}S_{J'})$, f, is:

$$\Gamma(i \xrightarrow{\text{M1}} f + \gamma) = \frac{4\alpha e_Q^2}{3m_Q^2}(2J'+1)k^3 S_{if}^{\text{M}}|\mathcal{M}_{if}|^2, \quad (4.122)$$

where the statistical factor $S_{if}^{\text{M}} = S_{fi}^{\text{M}}$ is

$$S_{if}^{\text{M}} = 6(2s+1)(2s'+1) \begin{Bmatrix} J & 1 & J' \\ s' & \ell & s \end{Bmatrix}^2 \begin{Bmatrix} 1 & \frac{1}{2} & \frac{1}{2} \\ \frac{1}{2} & s' & s \end{Bmatrix}^2. \quad (4.123)$$

For $l = 0$ transitions, $S_{if}^{\text{M}} = 1$.

6.1.5 Relativistic corrections

The leading relativistic corrections for electric transitions have been considered by a number of authors [178–186]. A general form was derived by Grotch, Owen and Sebastian [184]. For example, for the equal mass quark–antiquark $\bar{c}c$ and $\bar{b}b$ systems the E1 transition amplitude is $\langle f | \mathbf{X}_0 + \mathbf{X}_1 | i \rangle$,

$$
\begin{aligned}
\mathbf{X}_0 &= e_Q \mathbf{r}, \\
\mathbf{X}_1 &= -i \frac{k e_Q}{2 m_Q} \left(\frac{1}{10} \left(\{ r^2, \mathbf{p} \} - \frac{1}{2} [\mathbf{r}, [\mathbf{r} \cdot, \mathbf{p}]] \right) - \frac{\kappa_Q}{2} (\mathbf{r} \times \mathbf{S}) \right),
\end{aligned}
\tag{4.124}
$$

where κ_Q is the quark anomalous magnetic moment and $\mathbf{p}$ is the relative momentum. The decay rate then has the general form:

$$
\Gamma^{\mathrm{E1}} = \Gamma^{\mathrm{E1}}_{\mathrm{NR}} (1 + R1 + R2 + R3),
\tag{4.125}
$$

where $R1$ are corrections due to the modification of the nonrelativistic wave functions, $R2$ originates from the relativistic modification of the transition operator and $R3$ are the finite size corrections (arising from the plane wave expansion for the emitted photon). For the $1^3P_J \to 1^3S_1$ E1 transition:

$$
\begin{aligned}
R1 &= 2E_1^J + (E_1^J)^2, \\
R2 &= \frac{k \kappa_Q}{2 m_Q} \left[\frac{J(J+1)}{2} - 2 \right], \\
R3 &= -\frac{1}{10} (M_i - M_f)^2 E_2 + \frac{k}{8 m_Q} E_3,
\end{aligned}
\tag{4.126}
$$

where

$$
\begin{aligned}
E_1 &= \frac{\int_0^\infty dr\, r \left[u_{10}^{(0)}(r) u_{11}^{(1)J}(r) + u_{10}^{(1)}(r) u_{11}^{(0)}(r) \right]}{\mathcal{E}_{if}}, \\
E_2 &= \frac{\int_0^\infty dr\, r^3 u_{10}^{(0)}(r) u_{11}^{(0)}(r)}{\mathcal{E}_{if}}, \\
E_3 &= \frac{\int_0^\infty dr\, r \left[u_{10}^{(0)}(r) \left(2r \frac{d}{dr} u_{11}^{(0)}(r) - u_{11}^{(0)}(r) \right) - \left(2r \frac{d}{dr} u_{10}^{(0)}(r) - u_{10}^{(0)}(r) \right) u_{11}^{(0)}(r) \right]}{\mathcal{E}_{if}},
\end{aligned}
\tag{4.127}
$$

and $u^{(1)}(r)$ is the first order relativistic correction to the NR (reduced) radial wave function, $u^{(0)}(r)$.

The corrections for M1 transitions are more complicated and depend explicitly on the structure of the nonrelativistic potential. Assuming that the potential can be decomposed into three terms $V(r) = V_p(r) + (1 - \eta) V_v(r) + \eta V_s(r)$, i.e., a perturbative part $V_p(r)$ and a (nonperturbative) confining part, which is a linear combination of a Lorentz vector $V_v(r)$ and a scalar $V_s(r)$ term, the expression $|\mathcal{M}_{if}|^2$ in Eq. (4.121) is replaced by [183] $|I_1 + I_2 + I_3 + I_4|^2$, where for S wave transitions in $\bar{Q}Q$ systems:

$$
\begin{aligned}
I_1 &= \int_0^\infty dr\, u_{n'0}^{(0)}(r) u_{n0}^{(0)}(r) \left[(1 + \kappa_Q) j_0 \left(\frac{kr}{2} \right) + \frac{k(1 + 2\kappa_Q)}{4 m_Q} \right], \\
I_2 &= \int_0^\infty dr\, u_{n'0}^{(0)}(r) u_{n0}^{(0)}(r) \left[-(1 + \kappa_Q) \frac{\mathbf{p}^2}{2 m_Q^2} - \frac{\mathbf{p}^2}{3 m_Q^2} \right], \\
I_3 &= \int_0^\infty dr\, u_{n'0}^{(0)}(r) u_{n0}^{(0)}(r) \left[\frac{\kappa_Q r}{6 m_Q} \frac{\partial (V_p + (1 - \eta) V_v)}{\partial r} \right], \\
I_4 &= \int_0^\infty dr\, u_{n'0}^{(0)}(r) u_{n0}^{(0)}(r) \left[-\frac{\eta V_s}{m_Q} j_0 \left(\frac{kr}{2} \right) \right].
\end{aligned}
\tag{4.128}
$$
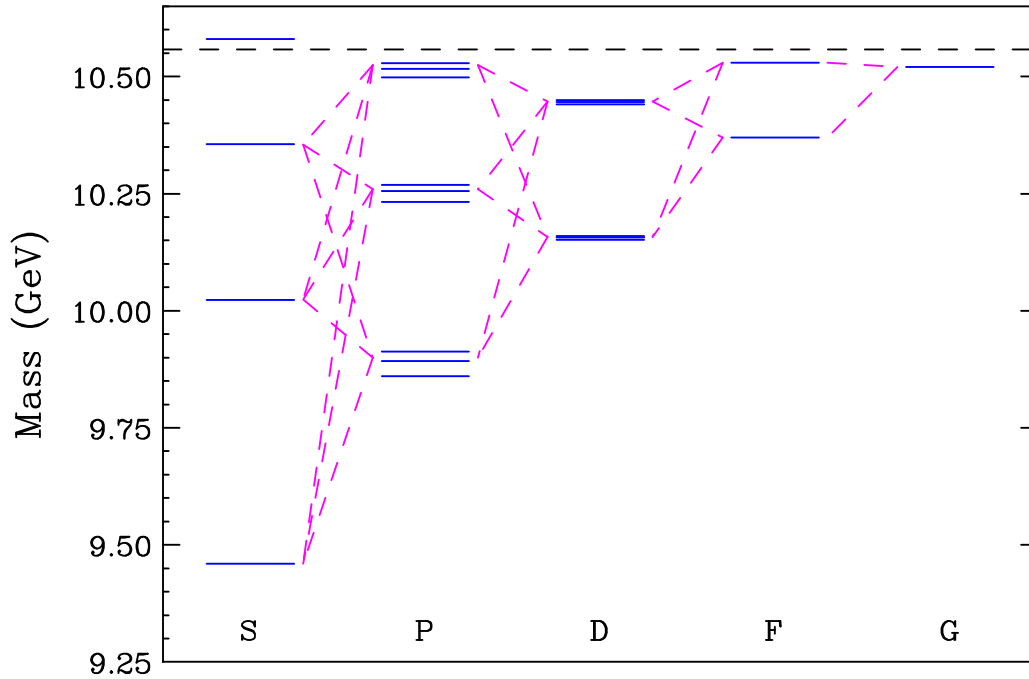
Fig. 4.10: E1 transitions in the narrow spin triplet $\bar{b}b$ states. For each S–P transition indicated there are three individual transitions (one for each P_J state); while for transitions involving any other pair of orbital angular momenta (P–D, D–F, F–G, ...) there are six individual transitions ($\Delta J = 0, \pm 1$).

Further details of these relativistic corrections can been found at the original papers of Feinberg and Sucher [178–180], Zambetakis and Byers [182] and Grotch and Sebastian [183, 184]. General treatments of relativistic corrections for all quarkonium states can be found in recent works [185, 186].

6.2 E1 transitions

Since the discovery of the J/ψ and ψ' resonances in November 1974, E1 transitions have played an important theoretical and experimental role in quarkonium physics. Initial theoretical papers on charmonium [187, 188] predicted the $1P$ states in the $\bar{c}c$ system and suggested that the triplet $1P$ states could be observed through the E1 transitions from the ψ' resonance. In fact, explicit calculations of the $2S \rightarrow 1P$ and $1P \rightarrow 1S$ E1 transition amplitudes $\mathcal{E}_{if}$ by the Cornell group [187] agree within 25% with present experimental values [189].

Today there is a wealth of theoretical predictions and experimental data on E1 transitions. Many E1 transitions have been observed in the $\bar{c}c$, $\bar{b}b$ and more are expected. For example, Fig. 4.10 shows the E1 transitions from narrow spin triplet states in the $\bar{b}b$ system. Transitions occur between two states differing in L by one and J by zero or one; thus for the $\bar{b}b$ system there are a total of 99 E1 transitions, 30 of which are theoretically accessible in e^+e^- collisions from the $\Upsilon(2S)$ and $\Upsilon(3S)$ resonances.

6.2.1 Model predictions

The theoretical models used to calculate the E1 transitions can be classified by the following two considerations: (1) What nonrelativistic potential was used? and (2) Which relativistic corrections (as shown in Eq. (4.125)) were included in the calculations?

An early choice for the potential was the Cornell model [177, 187, 190–192]. Here the exchange interaction was the time component of a vector with a Coulomb short range part $-K/r$ plus a linear r/a^2 long range confining part. The Coulomb part was modified to agree with perturbative QCD at short

Table 4.15: E1 transition rates for low-lying $\bar{c}c$ states. The measured masses are used for observed states. The mass values used for the $^3D_2$, $^1D_2$ and $^3D_3$ states are suggested by the coupled channel calculations of Ref. [207]. The E1 rates are shown for the (NR) model described in the text. The variation of results for $\mathcal{E}_{if}$ with inclusion of relativistic corrections is shown for two models of Ref. [186] with scalar confinement (RA) and a mixture of vector and scalar confining terms (RB).

Transition $i \xrightarrow{\text{E1}} f$		k (MeV)	S^{E}_{if}	$\Gamma(i \to f)$(NR) (keV)	$\mathcal{E}_{if}$(NR) (GeV^{-1})	$\mathcal{E}_{if}$(RA) (GeV^{-1})	$\mathcal{E}_{if}$(RB) (GeV^{-1})
$1^3P_0(3.415)$	$1^3S_1(3.097)$	304	$\frac{1}{9}$	120	1.724	2.121	1.720
$1^3P_1(3.511)$	$1^3S_1(3.097)$	389	$\frac{1}{9}$	241	1.684	1.896	1.767
$1^1P_1(3.526)$	$1^1S_0(2.979)$	504	$\frac{1}{3}$	482	1.615	1.742	1.742
$1^3P_2(3.556)$	$1^3S_1(3.097)$	430	$\frac{1}{9}$	315	1.661	1.596	1.689
$2^3S_1(3.686)$	$1^3P_0(3.415)$	261	$\frac{1}{9}$	47.0	-2.350	-2.296	-1.775
$2^1S_0(3.638)$	$1^1P_1(3.526)$	110	$\frac{1}{3}$	35.1	-2.469	-2.126	-2.126
$2^3S_1(3.686)$	$1^3P_1(3.511)$	171	$\frac{1}{9}$	42.8	-2.432	-2.305	-1.782
$2^3S_1(3.686)$	$1^3P_2(3.556)$	127	$\frac{1}{9}$	30.1	-2.460	-2.362	-1.901
$1^3D_1(3.770)$	$1^3P_0(3.415)$	338	$\frac{2}{9}$	299	2.841	2.718	2.802
$1^3D_1(3.770)$	$1^3P_1(3.511)$	250	$\frac{1}{18}$	99.0	2.957	2.799	2.969
$1^3D_1(3.770)$	$1^3P_2(3.556)$	208	$\frac{1}{450}$	3.88	3.002	3.016	3.348
$1^3D_2(3.831)$	$1^3P_1(3.511)$	307	$\frac{1}{10}$	313	2.886	2.593	2.593
$1^3D_2(3.831)$	$1^3P_2(3.556)$	265	$\frac{1}{50}$	69.5	2.940	2.781	2.991
$1^1D_2(3.838)$	$1^1P_1(3.526)$	299	$\frac{2}{15}$	389	2.896	2.610	2.610
$1^3D_3(3.872)$	$1^3P_2(3.556)$	303	$\frac{2}{25}$	402	2.892	2.508	2.402

distance by Buchmüller and Tye [141, 193]. Other simple forms for the potential, logarithmic [144, 194] and power law [195, 196], were also proposed.

In the NRQCD limit the quark–antiquark interaction is spin independent, but including relativistic corrections introduces dependencies on the Lorentz structure of the potential. Of particular importance is the vector versus scalar nature of the long-range confining interaction. Many modern theoretical calculations assume a long range scalar confining potential [197] or a linear combination of the form $\eta V_S(r) + (1 - \eta)V_V(r)$ [181, 186, 198]. Moxhay and Rosner [199] assumed an additional long range tensor force.

The second consideration is the extent of the inclusion of the relativistic corrections. Some calculations are essentially nonrelativistic. These calculations often include some finite size effects ($R3$ of Eq. (4.125)) by retaining the form for $\mathcal{E}_{if}$ given in Eq. (4.117) [177, 187, 190–192, 200]. Other models also include relativistic corrections to the wave functions ($R1$ of Eq. (4.125)) either perturbatively or nonperturbatively. The relativistic quark model of Godfrey and Isgur [201] is an example in this class. Gupta, Radford and Repko computed the relativistic corrections using only the gluon exchange interactions of QCD perturbation theory [202–204]. Many models include the full relativistic corrections [181, 184, 185, 199, 205, 206].

Differences in theoretical assumptions and experimental input for the various potential model calculations of E1 transitions make it difficult to draw sharp conclusions from the level of agreement of

Table 4.16: E1 transition rates for low-lying spin triplet $\bar{b}b$ states.

Transition $i \xrightarrow{\text{E1}} f$		k (MeV)	S_{if}^{E}	$\Gamma(i \to f)$(NR) (keV)	$\mathcal{E}_{if}$(NR) (GeV^{-1})	$\mathcal{E}_{if}$(RA) (GeV^{-1})	$\mathcal{E}_{if}$(RB) (GeV^{-1})
$1^3P_0(9.860)$	$1^3S_1(9.460)$	392	$\frac{1}{9}$	22.2	1.013	1.205	1.178
$1^3P_1(9.893)$	$1^3S_1(9.460)$	423	$\frac{1}{9}$	27.8	1.010	1.175	1.163
$1^3P_2(9.913)$	$1^3S_1(9.460)$	442	$\frac{1}{9}$	31.6	1.007	1.124	1.137
$2^3S_1(10.023)$	$1^3P_2(9.913)$	110	$\frac{1}{9}$	2.04	-1.597	-1.800	-1.778
$2^3S_1(10.023)$	$1^3P_1(9.893)$	130	$\frac{1}{9}$	2.00	-1.595	-1.781	-1.759
$2^3S_1(10.023)$	$1^3P_0(9.860)$	162	$\frac{1}{9}$	1.29	-1.590	-1.803	-1.781
$1^3D_1(10.151)$	$1^3P_2(9.913)$	236	$\frac{1}{450}$	0.564	1.896	2.104	2.104
$1^3D_1(10.151)$	$1^3P_1(9.893)$	255	$\frac{1}{18}$	10.7	1.890	2.050	2.050
$1^3D_1(10.151)$	$1^3P_0(9.860)$	287	$\frac{2}{9}$	20.1	1.880	2.106	2.106
$1^3D_2(10.157)$	$1^3P_2(9.913)$	241	$\frac{1}{50}$	5.46	1.894	2.048	2.048
$1^3D_2(10.157)$	$1^3P_1(9.893)$	261	$\frac{1}{10}$	20.5	1.888	1.999	1.999
$1^3D_3(10.160)$	$1^3P_2(9.913)$	244	$\frac{2}{25}$	22.6	1.893	1.979	1.979
$2^3P_0(10.232)$	$1^3D_1(10.151)$	81	$\frac{2}{9}$	1.13	-1.723	-1.740	-1.740
$2^3P_0(10.232)$	$2^3S_1(10.023)$	207	$\frac{1}{9}$	9.17	1.697	1.872	1.855
$2^3P_0(10.232)$	$1^3S_1(9.460)$	743	$\frac{1}{9}$	10.9	0.272	0.214	0.239
$2^3P_1(10.255)$	$1^3D_2(10.157)$	98	$\frac{1}{10}$	1.49	-1.720	-1.751	-1.751
$2^3P_1(10.255)$	$1^3D_1(10.151)$	104	$\frac{1}{18}$	0.593	-1.718	-1.721	-1.721
$2^3P_1(10.255)$	$2^3S_1(10.023)$	229	$\frac{1}{9}$	12.4	1.688	1.837	1.831
$2^3P_1(10.255)$	$1^3S_1(9.460)$	764	$\frac{1}{9}$	12.0	0.274	0.228	0.216
$2^3P_2(10.268)$	$1^3D_3(10.160)$	108	$\frac{2}{25}$	2.25	-1.717	-1.763	-1.763
$2^3P_2(10.268)$	$1^3D_2(10.157)$	111	$\frac{1}{50}$	0.434	-1.717	-1.737	-1.737
$2^3P_2(10.268)$	$1^3D_1(10.151)$	117	$\frac{1}{450}$	0.034	-1.715	-1.766	-1.766
$2^3P_2(10.268)$	$2^3S_1(10.023)$	242	$\frac{1}{9}$	14.5	1.682	1.792	1.797
$2^3P_2(10.268)$	$1^3S_1(9.460)$	776	$\frac{1}{9}$	12.7	0.274	0.207	0.218
$3^3S_1(10.355)$	$2^3P_2(10.268)$	86	$\frac{1}{9}$	2.40	-2.493	-2.663	-2.644
$3^3S_1(10.355)$	$2^3P_1(10.255)$	100	$\frac{1}{9}$	2.20	-2.489	-2.607	-2.586
$3^3S_1(10.355)$	$2^3P_0(10.232)$	122	$\frac{1}{9}$	1.35	-2.479	-2.608	-2.582
$3^3S_1(10.355)$	$1^3P_2(9.913)$	433	$\frac{1}{9}$	0.015	0.016	0.063	0.045
$3^3S_1(10.355)$	$1^3P_1(9.893)$	452	$\frac{1}{9}$	0.008	0.011	0.063	0.045
$3^3S_1(10.355)$	$1^3P_0(9.860)$	483	$\frac{1}{9}$	0.001	0.004	0.063	0.045

Table 4.17: E1 transition rates for low-lying spin singlet $\bar{b}b$ states.

Transition $i \xrightarrow{\text{E1}} f$		k (MeV)	S_{if}^{E}	$\Gamma(i \to f)$(NR) (keV)	$\mathcal{E}_{if}$(NR) (GeV^{-1})	$\mathcal{E}_{if}$(RA) (GeV^{-1})	$\mathcal{E}_{if}$(RB) (GeV^{-1})
$1^1P_1(9.900)$	$1^1S_0(9.400)$	487	$\frac{1}{3}$	41.8	1.001	1.149	1.149
$2^1S_0(9.990)$	$1^1P_1(9.900)$	90	$\frac{1}{3}$	1.99	-1.600	-1.743	-1.743
$1^1D_2(10.157)$	$1^1P_1(9.900)$	254	$\frac{2}{15}$	25.3	1.891	2.002	2.002
$2^1P_1(10.260)$	$2^1S_0(9.990)$	266	$\frac{1}{3}$	19.0	1.671	1.817	1.817
$2^1P_1(10.260)$	$1^1D_2(10.157)$	102	$\frac{2}{15}$	2.29	-1.719	-1.782	-1.782
$3^1S_0(10.328)$	$2^1P_1(10.260)$	68	$\frac{1}{3}$	2.10	-2.498	-2.571	-2.571
$3^1S_0(10.328)$	$1^1P_1(9.900)$	419	$\frac{1}{3}$	0.007	0.010	0.064	0.064

a particular model and experimental data. However, it is known that there is usually very little model variation in the NR predictions (lowest order) if the models are fit to the same states [200]. The only exceptions are transitions where the overlap integral $\mathcal{E}_{if}$ exhibits large dynamical cancellations. Therefore, to compare the variations in results due to the inclusion of relativistic corrections from a common base, three models for E1 radiative transitions are presented, which are fit with the same input masses. First a reference Cornell model [191] (NR), with parameters (a and K) adjusted to fit the COG positions of the 1S, 1P and 2S states in each of the $\bar{c}c$ and $\bar{b}b$ systems [208]. Here E1 transitions are computed with $\mathcal{E}_{if}$ given in Eq. (4.117), i.e., with only finite size relativistic corrections included. Second, a recent model by Ebert, Faustov and Galkin [186] with full relativistic corrections in two cases: (RA) $\eta = 1$ (scalar confinement) and (RB) $\eta = -1$ (a fitted mixture of scalar and vector confinement).

The results for $\mathcal{E}_{if}$ are shown for the $\bar{c}c$ narrow states in Table 4.15. The size of the relativistic corrections to $\mathcal{E}_{if}$ shown in Table 4.15 vary as much as $\pm 25\%$. This variation is perfectly consistent with naive expectations for v^2/c^2 corrections. McClary and Byers [181] first emphasized that because of the node in the radial wave function of the 2S state the overlap $\mathcal{E}_{2S,1P}$ is particularly sensitive to relativistic corrections in the $\bar{c}c$ system. The significant leptonic width for the $\Psi(3770)$ resonance implies that there is a sizeable S-D mixing between the 2^3S_1 and 1^3D_1 states. This mixing arises both from the usual relativistic correction terms and coupling to strong decay channels and will affect the $\Psi(3686) \to 1^3P_J$ and $\Psi(3770) \to 1^3P_J$ E1 transitions rates (See Section 6.2.3). For the $1D$ states there may be additional large effects on rates associated with this coupling to nearby strong decay channels. (See Section 6.5.)

Results for narrow $\bar{b}b$ states accessible from the $\Upsilon(3S)$ or $\Upsilon(2S)$ resonances are shown for spin-triplets in Table 4.16 and for the spin-singlets in Table 4.17. The typical size of the relativistic corrections for $\mathcal{E}_{if}$ are approximately half as large as in the corresponding $\bar{c}c$ transition. This is again as expected, since $\langle v^2/c^2 \rangle$ is smaller in the $\bar{b}b$ system. There is a notable exception for the overlap $\mathcal{E}_{3S,1P}$. In the NR limit this overlap is less than 5% of any other S–P overlap. This dynamical accident makes these transition rates very sensitive to the details of wave functions and relativistic corrections, which are *not* well under control theoretically.

Finally, for completeness, radiative transitions involving $\bar{b}b$ states not accessible from the $3S$ states are shown in Table 4.18. Only the NR rates are shown. One observes large dynamical cancellations for the overlap $\mathcal{E}_{3P,1D}$ and to a lesser extent in the overlaps $\mathcal{E}_{3P,1S}$, $\mathcal{E}_{2D,1P}$ and $\mathcal{E}_{3P,2S}$.

Table 4.18: E1 transition rates for the remaining spin triplet $\bar{b}b$ states. For each (n' and ℓ') only the final state J' with the largest rate is shown. The transition rates for spin-singlet $\bar{b}b$ states differ from the corresponding spin triplet rates by the ratio of statistical factors $S^E(s=0)/S^E(s=1)$: 3, 2/3, 9/8 and 16/15 for S–P, P–D, D–F and F–G transitions respectively.

Transition		k	S_{if}^E	$\mathcal{E}_{if}$	$\Gamma(i \to f)$
$i \xrightarrow{\text{E1}} f$		(MeV)		(GeV^{-1})	(keV)
$1^3F_2(10.370)$	$1^3D_1(10.151)$	217	$\frac{3}{25}$	2.681	28.5
$1^3F_3(10.370)$	$1^3D_2(10.157)$	211	$\frac{8}{105}$	2.684	27.8
$1^3F_4(10.370)$	$1^3D_3(10.160)$	208	$\frac{3}{49}$	2.686	30.0
$2^3D_1(10.441)$	$1^3F_2(10.370)$	71	$\frac{3}{25}$	-1.904	0.833
$2^3D_1(10.441)$	$2^3P_0(10.232)$	207	$\frac{2}{9}$	2.487	13.1
$2^3D_1(10.441)$	$1^3P_0(9.860)$	565	$\frac{2}{9}$	0.288	3.60
$2^3D_2(10.446)$	$1^3F_3(10.370)$	76	$\frac{8}{105}$	-1.903	0.907
$2^3D_3(10.450)$	$1^3F_4(10.370)$	80	$\frac{3}{49}$	-1.902	1.09
$2^3D_3(10.450)$	$2^3P_2(10.268)$	180	$\frac{2}{25}$	2.506	15.8
$2^3D_3(10.450)$	$1^3P_2(9.913)$	524	$\frac{2}{25}$	0.278	4.80
$3^3P_0(10.498)$	$2^3D_1(10.441)$	57	$\frac{2}{9}$	-2.584	0.884
$3^3P_0(10.498)$	$3^3S_1(10.355)$	142	$\frac{1}{9}$	2.308	5.47
$3^3P_0(10.498)$	$1^3D_1(10.151)$	341	$\frac{2}{9}$	-0.047	0.063
$3^3P_0(10.498)$	$2^3S_1(10.023)$	464	$\frac{1}{9}$	0.351	4.44
$3^3P_0(10.498)$	$1^3S_1(9.460)$	986	$\frac{1}{9}$	0.137	6.46
$3^3P_1(10.516)$	$2^3D_2(10.446)$	70	$\frac{1}{10}$	-2.579	1.22
$3^3P_1(10.516)$	$3^3S_1(10.355)$	160	$\frac{1}{9}$	2.295	7.71
$3^3P_1(10.516)$	$1^3D_2(10.157)$	353	$\frac{1}{10}$	-0.050	0.060
$3^3P_1(10.516)$	$2^3S_1(10.023)$	481	$\frac{1}{9}$	0.355	5.06
$3^3P_1(10.516)$	$1^3S_1(9.460)$	1003	$\frac{1}{9}$	0.137	6.86
$1^3G_3(10.520)$	$1^3F_2(10.498)$	22	$\frac{4}{49}$	3.812	0.068
$1^3G_4(10.520)$	$1^3F_3(10.498)$	22	$\frac{5}{84}$	3.812	0.069
$1^3G_5(10.520)$	$1^3F_4(10.498)$	22	$\frac{4}{81}$	3.812	0.074
$3^3P_2(10.529)$	$2^3D_3(10.450)$	79	$\frac{2}{25}$	-2.576	1.96
$3^3P_2(10.529)$	$3^3S_1(10.355)$	172	$\frac{1}{9}$	2.284	9.63
$3^3P_2(10.529)$	$1^3D_3(10.160)$	363	$\frac{2}{25}$	-0.053	0.082
$3^3P_2(10.529)$	$2^3S_1(10.023)$	494	$\frac{1}{9}$	0.358	5.54
$3^3P_2(10.529)$	$1^3S_1(9.460)$	1014	$\frac{1}{9}$	0.138	7.16
$2^3F_2(10.530)$	$2^3D_1(10.441)$	89	$\frac{3}{25}$	3.337	3.02
$2^3F_3(10.530)$	$2^3D_2(10.446)$	84	$\frac{8}{105}$	3.340	2.69
$2^3F_4(10.530)$	$2^3D_3(10.450)$	80	$\frac{3}{49}$	3.342	2.62
$2^3F_2(10.530)$	$1^3G_3(10.520)$	10	$\frac{4}{49}$	-2.262	0.003
$2^3F_3(10.530)$	$1^3G_4(10.520)$	10	$\frac{5}{84}$	-2.262	0.003
$2^3F_4(10.530)$	$1^3G_5(10.520)$	10	$\frac{4}{81}$	-2.262	0.003

6.2.2 Comparison with experiment: S and P states[13]

There is now extensive data on electromagnetic transitions among heavy quarkonium states. Figure 4.11 shows the inclusive photon spectra from the $\bar{c}c$ and $\bar{b}b$ 2^3S_1 decays measured with the CLEO detector [209]. This section provides a snapshot of the current status of various S–P transitions. New data come mainly from the CLEO experiment at CESR.

In the NR limit the overlap $\mathcal{E}_{\mathrm{nS,n'P_J}} = |\langle n'P_J|r|nS\rangle|$ is independent of J. Experimentally, it is useful to define averages over J by

$$
\begin{aligned}
\mathcal{E}_{\mathrm{nS,n'P}}(\mathrm{avg}) &= \sqrt{\frac{\mathcal{B}(nS\rightarrow\gamma n'P_J)\,\Gamma_{\mathrm{tot}}(nS)}{D\sum_J(2J+1)E_\gamma(nS\rightarrow n'P_J)^3}} \\
\mathcal{E}_{\mathrm{nP,n'S}}(\mathrm{avg}) &= \sqrt{\frac{\mathcal{B}(nP_J\rightarrow\gamma n'S)\,\Gamma_{\mathrm{tot}}(nP_J)}{D\sum_J E_\gamma(nP_J\rightarrow n'S)^3}}
\end{aligned}
\tag{4.129}
$$

where $D = 4/3\,\alpha\,e_b^2 \mathrm{S}^\mathrm{E}_{^3P_J,^3S_1}$. These quantities reduce to the usual overlaps in the NR limit. In order to see the relativistic corrections (which vary with J) it is also useful to define ratios, $\mathcal{E}_{\mathrm{nS,n'P_J}}/\mathcal{E}_{\mathrm{nS,n'P}}(\mathrm{avg})$. Given the total width of the initial state these overlaps can be determined directly from experimental branching ratios. The experimental results for the $\bar{c}c$ and $\bar{b}b$ states are shown in Table 4.19. These results are extracted from the world average results for $\mathcal{B}(\chi_c(1P_J)\rightarrow\gamma J/\psi)$ and $\mathcal{B}(\psi(2S)\rightarrow\gamma\chi_c(1P_J))$. Also shown are recent results from CLEO-c for $\mathcal{B}(\psi(2S)\rightarrow\gamma\chi_c(1P_J))$ transitions [210]. Results for $\mathcal{B}(\Upsilon(3S)\rightarrow\gamma\chi_b(2P_J))$ and $\mathcal{B}(\Upsilon(2S)\rightarrow\gamma\chi_b(1P_J))$ are taken from Ref. [10]. The E1 transitions show clear evidence of J dependence and, hence, relativisitic corrections in S state transitions. The largest relativistic effects are in the 2^3S_1 to 1^3P_J $\bar{c}c$ transitions.

With their large $\Upsilon(3S)$ data sample and excellent CsI electromagnetic calorimeter, the CLEO III experiment has been able to measure the E1 photon transitions from the $\Upsilon(3S)$ to the $\chi_b(2P_J)$ states, and the subsequent photon decays of those states to the $\Upsilon(2S)$ and $\Upsilon(1S)$. They identify exclusive $\gamma\gamma\ell^+\ell^-$ events, which are consistent with photon transitions through the $\chi_b(2P_J)$ states to the $\Upsilon(2S)$ or $\Upsilon(1S)$, followed by the leptonic decay of the Υ. This provides a very clean signal with little background. Tables 4.20 and 4.21 give a summary of their preliminary results [211] on the product branching ratios, along with comparisons with the previous CLEO II [212] and CUSB [213] measurements. Then, by using the world average values for the $\Upsilon(3S) \rightarrow \chi_b(2P_J) + \gamma$ and Υ leptonic branching ratios, the $\chi_b(2P_J) \rightarrow \Upsilon + \gamma$ branching ratios can be obtained.

For the similar transitions through the $\chi_b(1P_J)$ states: $\Upsilon(3S) \rightarrow \gamma\chi_b(1P_J)$, $\chi_b(1P_J) \rightarrow \gamma\Upsilon(1S)$, the photon lines for the different J states cannot be resolved, due to the finite crystal energy resolution. The J = 0 branching ratio is expected to be small, given the large hadronic width of this state. So CLEO III gives a combined product branching ratio, summed over the J = 1 and J = 2 states. The results are shown in Table 4.22.

We can extract the $|\mathcal{E}_{\mathrm{1P,3S}}|$ matrix element from the photon transitions via the $\chi_b(1P)$ states:

$$
\mathcal{E}_{\mathrm{1P,3S}}(\mathrm{avg}) = \sqrt{\frac{\mathcal{B}(3S\rightarrow\gamma 1P, 1P\rightarrow\gamma 1S)\,\Gamma_{\mathrm{tot}}(3S)}{D\sum_J(2J+1)E_\gamma(1P_J\rightarrow 1S)^3\mathcal{B}(1P_J\rightarrow\gamma 1S)}}.
\tag{4.130}
$$

This formula assumes that the matrix element is spin independent. Taking $\mathcal{B}(3S\rightarrow\gamma 1P, 1P\rightarrow\gamma 1S)$ from Table 4.22 and the world average values for the other quantities from PDG04 [10], we obtain:

$$
\mathcal{E}_{\mathrm{1P,3S}}(\mathrm{avg}) = (0.050 \pm 0.006)\,\mathrm{GeV}^{-1}.
$$

The error here includes the statistical and systematic uncertainties on all quantities added in quadrature. The averaging is only over $J = 1$ and $J = 2$.

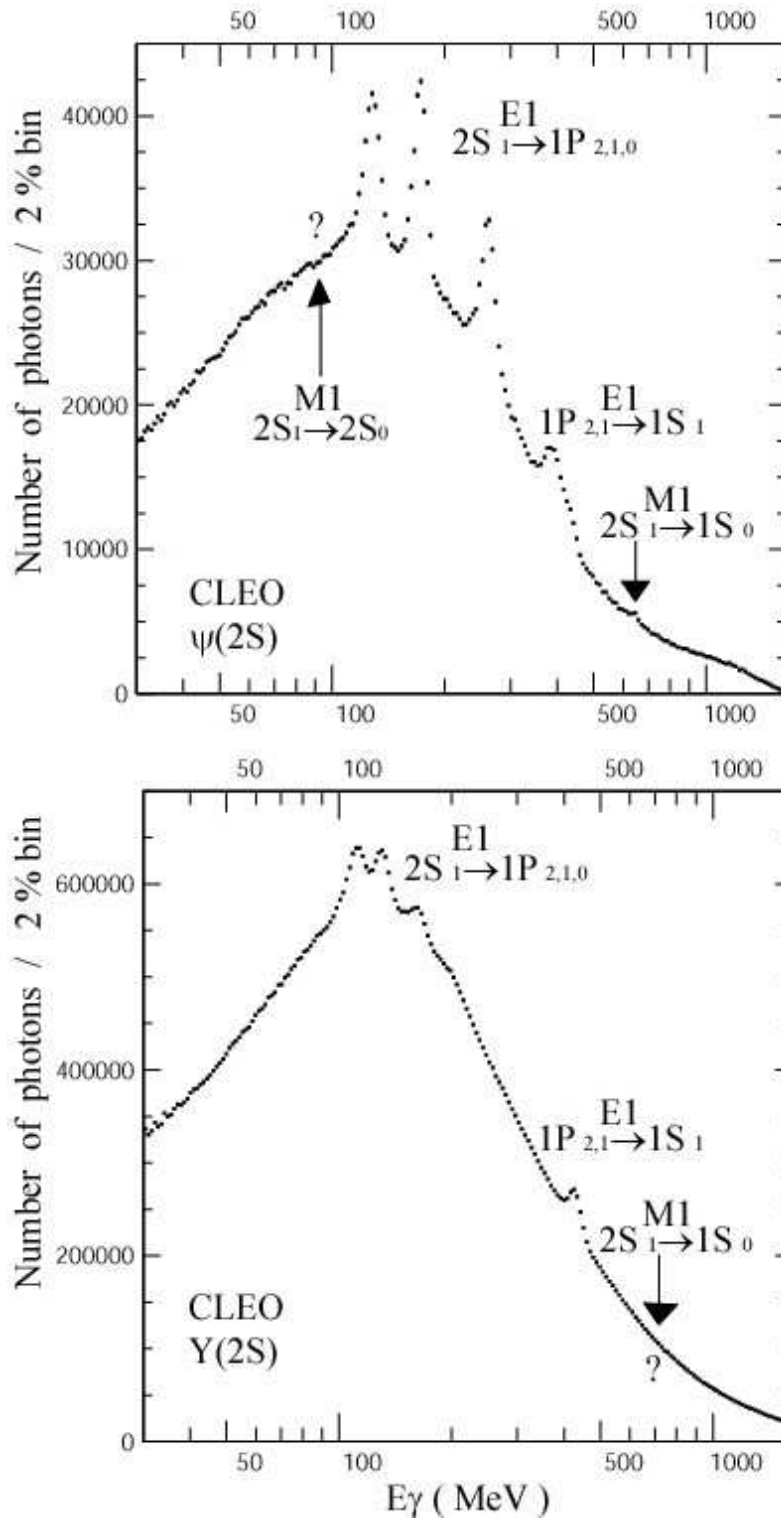[13]Authors: E. Eichten, T. Ferguson

Fig. 4.11: Inclusive photon spectrum from 2^3S_1 decays in the $\bar{c}c$ (top) and $\bar{b}b$ (bottom) systems measured with the CLEO detector. The data correspond to about 1.5M $\psi(2S)$ and 9M $\Upsilon(2S)$ decays. From Skwarnicki [209].

Table 4.19: Measured E1 overlap integrals for S–P transitions. Transition rates use branching ratios and total widths from PDG04 world averages [10] except for second set of values for the $\bar{c}c$ transition $2^3S_1 \rightarrow 1^3P_J$, which uses branching ratios from recent results of CLEO-c [210].

Transition $i \xrightarrow{\text{E1}} f$	$\|\mathcal{E}_{\text{avg}}\|$ (GeV^{-1})	$\mathcal{E}_J/\mathcal{E}_{\text{avg}}$		
		$J = 0$	$J = 1$	$J = 2$
$\bar{c}c$				
1^3P_J 1^3S_1	1.87 ± 0.07	0.92 ± 0.05	0.99 ± 0.06	1.04 ± 0.03
2^3S_1 1^3P_J	1.78 ± 0.07	0.94 ± 0.04	1.01 ± 0.05	1.07 ± 0.05
	1.94 ± 0.07	0.90 ± 0.02	0.97 ± 0.03	1.19 ± 0.04
$\bar{b}b$				
3^3S_1 2^3P_J	2.75 ± 0.21	0.92 ± 0.06	1.06 ± 0.05	1.02 ± 0.06
2^3S_1 1^3P_J	1.94 ± 0.18	0.92 ± 0.06	1.09 ± 0.05	0.98 ± 0.06

Table 4.20: CLEO III preliminary results [211] for $\Upsilon(3S) \rightarrow \gamma \chi_b(2P_J) \rightarrow \gamma\gamma \Upsilon(2S) \rightarrow \gamma\gamma\ell^+\ell^-$, along with comparisons with CLEO II [212] and CUSB [213].

Parameter (units)	Ref.	J = 2	J = 1	J = 0
$\mathcal{B}(\gamma\gamma\ell^+\ell^-)$ (10^{-4})	[211]	$2.73 \pm 0.15 \pm 0.24$	$5.84 \pm 0.17 \pm 0.41$	$0.17 \pm 0.06 \pm 0.02$
	[212]	$2.49 \pm 0.47 \pm 0.31$	$5.11 \pm 0.60 \pm 0.63$	< 0.60
	[213]	$2.74 \pm 0.33 \pm 0.18$	$3.30 \pm 0.33 \pm 0.19$	$0.40 \pm 0.17 \pm 0.03$
$\mathcal{B}(\Upsilon(3S) \rightarrow \gamma\gamma\Upsilon(2S))$ (%)	[211]	$2.20 \pm 0.12 \pm 0.31$	$4.69 \pm 0.14 \pm 0.62$	$0.14 \pm 0.05 \pm 0.02$
$\mathcal{B}(\chi_b(2P_J) \rightarrow \gamma\Upsilon(2S))$ (%)	[211]	$19.3 \pm 1.1 \pm 3.1$	$41.5 \pm 1.2 \pm 5.9$	$2.59 \pm 0.92 \pm 0.51$

Table 4.21: CLEO III preliminary results [211] for $\Upsilon(3S) \rightarrow \gamma \chi_b(2P_J) \rightarrow \gamma\gamma \Upsilon(1S) \rightarrow \gamma\gamma\ell^+\ell^-$, along with comparisons with CLEO II [212] and CUSB [213].

Parameter (units)	Ref.	J = 2	J = 1	J = 0
$\mathcal{B}(\gamma\gamma\ell^+\ell^-)$ (10^{-4})	[211]	$1.93 \pm 0.12 \pm 0.17$	$3.19 \pm 0.13 \pm 0.18$	< 0.16
	[212]	$2.51 \pm 0.47 \pm 0.32$	$3.24 \pm 0.56 \pm 0.41$	< 0.32
	[213]	$1.98 \pm 0.28 \pm 0.12$	$2.34 \pm 0.28 \pm 0.14$	$0.13 \pm 0.10 \pm 0.03$
$\mathcal{B}(\Upsilon(3S) \rightarrow \gamma\gamma\Upsilon(1S))$ (%)	[211]	$0.79 \pm 0.05 \pm 0.07$	$1.31 \pm 0.05 \pm 0.08$	< 0.08
$\mathcal{B}(\chi_b(2P_J) \rightarrow \gamma\Upsilon(1S))$ (%)	[211]	$7.0 \pm 0.4 \pm 0.8$	$11.6 \pm 0.4 \pm 0.9$	< 1.44

Table 4.22: CLEO III preliminary results [211] for $\Upsilon(3S) \rightarrow \gamma \chi_b(1P_J) \rightarrow \gamma\gamma \Upsilon(1S) \rightarrow \gamma\gamma\ell^+\ell^-$, along with comparisons with the CUSB experiment [213]. The values are summed over the J = 1 and J = 2 transitions.

Parameter	Ref.	J = 1 and 2 Combined
$\mathcal{B}(\gamma\gamma\ell^+\ell^-)$ (10^{-4})	[211]	$0.520 \pm 0.054 \pm 0.052$
$\mathcal{B}(\Upsilon(3S) \rightarrow \gamma\gamma\Upsilon(1S))$ (%)	[211]	$0.241 \pm 0.022 \pm 0.021$
	[213]	$0.12 \pm 0.04 \pm 0.01$

Table 4.23: Comparison of average E1 matrix elements and their ratios predicted by different potential models with measurements from $\bar{b}b$ data. "NR" denotes nonrelativistic calculations and "rel" refers to models with relativistic corrections. The first set of model entries are the reference models considered here. The second set is a selection of other models taken from Ref. [211].

	$|\mathcal{E}_{3S,2P}|$		$|\mathcal{E}_{2S,1P}|$		$|\mathcal{E}_{3S,1P}|$		$\dfrac{|\mathcal{E}_{2P,1S}|}{|\mathcal{E}_{2P,2S}|}$	
	GeV^{-1}		GeV^{-1}		GeV^{-1}			
DATA	2.7 ± 0.2		1.9 ± 0.2		0.050 ± 0.006		0.096 ± 0.005	
	World Average				CLEO III [211]			
Model	NR	rel	NR	rel	NR	rel	NR	rel
NR	2.5		1.6		0.014		0.16	
RA		2.6		1.8		0.063		0.12
RB		2.6		1.8		0.045		0.12
Kwong, Rosner [200]	2.7		1.6		0.023		0.13	
Fulcher [214]	2.6		1.6		0.023		0.13	
Büchmuller et al. [141, 193]	2.7		1.6		0.010		0.12	
Moxhay, Rosner [199]	2.7	2.7	1.6	1.6	0.024	0.044	0.13	0.15
Gupta et al. [204]	2.6		1.6		0.040		0.11	
Gupta et al. [202, 203]	2.6		1.6		0.010		0.12	
Fulcher [215]	2.6		1.6		0.018		0.11	
Danghighian et al. [206]	2.8	2.5	1.7	1.3	0.024	0.037	0.13	0.10
McClary, Byers [181]	2.6	2.5	1.7	1.6			0.15	0.13
Eichten et al. [191]	2.6		1.7		0.110		0.15	
Grotch et al. [184]	2.7	2.5	1.7	1.5	0.011	0.061	0.13	0.19

Results for the values of $\mathcal{E}(\mathrm{avg})$ in the $\bar{b}b$ P system are compared to various potential model predictions in Table 4.23. We also include results for $\mathcal{E}_{3S,2P}$ and $\mathcal{E}_{2S,1P}$ from Table 4.19 extracted from the world average results for $\mathcal{B}(\Upsilon(3S)\rightarrow\gamma\chi_b(2P_J))$ and $\mathcal{B}(\Upsilon(2S)\rightarrow\gamma\chi_b(1P_J))$ [10]. While most of the potential models have no trouble reproducing the large matrix elements, $\mathcal{E}_{3S,2P}$, $\mathcal{E}_{2S,1P}$, which show also little model dependence, only a few models predict $\mathcal{E}_{3S,1P}$ in agreement with measurements. Clearly, the latter transition is highly sensitive to the underlying description of $\bar{b}b$ states as discussed above.

The branching ratios given in the Tables 4.20–4.22 can also be used to measure the ratios of various E1 matrix elements, which can then be compared to different potential model predictions. First, the ratio of the matrix elements for the decay of the same $\chi_b(2P_J)$ state to different Υ states can be found using:

$$\frac{\mathcal{E}_{2P_J,1S}}{\mathcal{E}_{2P_J,2S}} = \sqrt{\frac{\mathcal{B}(3S \rightarrow \gamma 2P_J, 2P_J \rightarrow \gamma 1S)}{\mathcal{B}(3S \rightarrow \gamma 2P_J, 2P_J \rightarrow \gamma 2S)} \left(\frac{E_\gamma(2P_J \rightarrow 2S)}{E_\gamma(2P_J \rightarrow 1S)}\right)^3} \tag{4.131}$$

With this method, the following values are obtained:

$$\frac{\mathcal{E}_{2P_2,1S}}{\mathcal{E}_{2P_2,2S}} = 0.105 \pm 0.004 \pm 0.006, \qquad \frac{\mathcal{E}_{2P_1,1S}}{\mathcal{E}_{2P_1,2S}} = 0.087 \pm 0.002 \pm 0.005, \tag{4.132}$$

$$\frac{\mathcal{E}_{2P_2,1S}}{\mathcal{E}_{2P_2,2S}} \Big/ \frac{\mathcal{E}_{2P_1,1S}}{\mathcal{E}_{2P_1,2S}} = 1.21 \pm 0.06, \qquad \frac{\mathcal{E}_{2P_{1,2},1S}}{\mathcal{E}_{2P_{1,2},2S}} = 0.096 \pm 0.002 \pm 0.005. \tag{4.133}$$

To compare to potential model predictions, the last number above is an average over the $J = 1$ and $J = 2$ values. In the nonrelativistic limit, the E1 matrix elements should not depend on J. Since the values

for the J = 1 and J = 2 matrix elements differ by 3.5 standard deviations, there appears to be evidence for relativistic effects in the $\bar{b}b$ system in both the S and P states transitions. Again these results are compared to various potential model predictions in Table 4.23. Predictions for the ratio $|\mathcal{E}_{2P,1S}|/|\mathcal{E}_{2P,2S}|$ are very model dependent, but somewhat higher than the experimental values.

Overall, the comparison of the measured matrix elements and the predictions of various potential models shows that the recent theoretical calculations that incorporate relativistic effects are better at reproducing the data [209, 211].

6.2.3 D states

In the $\bar{c}c$ system, the 1^3D_1 and 1^3D_3 states are above $D\bar{D}$ threshold and have open flavour strong decays. The $J = 2$ states 1^3D_2 and 1^1D_2 are below (or at) the $D^*\bar{D} + D\bar{D}^*$ threshold and are expected to be narrow. In all cases, the coupling to real and virtual strong decay channels is likely to significantly alter the potential model radiative transition rates shown in Table 4.15. (We will discuss this further in Section 6.5 below.) One effect of these couplings is that the $\psi(3770)$ state will not be a pure 1^3D_1 state but will have a sizeable mixing component with the 2^3S_1 state:

$$\psi(3770) = \cos(\phi)|1^3D_1\rangle + \sin(\phi)|2^3S_1\rangle . \tag{4.134}$$

Using the measured leptonic width of the $\psi(3770)$ and resolving a two-fold ambiguity in favor of the value of the mixing angle favored by Cornell coupled channel calculations [191], Rosner finds [106] $\phi = (12 \pm 2)°$. Employing the NR results of Table 4.15, the ratios of E1 transitions to various χ_c states are:

$$\frac{\Gamma(\psi(3770) \to \gamma\chi_{c1})}{\Gamma(\psi(3770) \to \gamma\chi_{c0})} = 1.32 \left(\frac{-\frac{\sqrt{3}}{2} + \tan(\phi)}{\sqrt{3} + \tan(\phi)} \right)^2 ,$$

$$\frac{\Gamma(\psi(3770) \to \gamma\chi_{c2})}{\Gamma(\psi(3770) \to \gamma\chi_{c0})} = 1.30 \left(\frac{\frac{\sqrt{3}}{10} + \tan(\phi)}{\sqrt{3} + \tan(\phi)} \right)^2 . \tag{4.135}$$

Measuring these branching ratios is experimentally challenging. [The only existing data is contained in an unpublished Ph. D. thesis based on MARK III data [216].] CLEO-c may be able to determine some of these branching ratios in the near future.

In the $\bar{b}b$ system CLEO III [171] has presented evidence for the production of $\Upsilon(1D)$ states in the four-photon cascade (see Fig. 4.10), $\Upsilon(3S)\to\gamma\chi_b(2P)$, $\chi_b(2P)\to\gamma\Upsilon(1D)$, $\Upsilon(1D)\to\gamma\chi_b(1P)$, $\chi_b(1P)\to\gamma\Upsilon(1S)$, followed by the $\Upsilon(1S)$ annihilation into e^+e^- or $\mu^+\mu^-$.

In addition to the four-photon cascade via the $\Upsilon(1D)$ states, they observe events with the four-photon cascade via the $\Upsilon(2S)$ state: $\Upsilon(3S) \to \gamma\chi_b(2P)$, $\chi_b(2P) \to \gamma\Upsilon(2S)$, $\Upsilon(2S) \to \gamma\chi_b(1P)$, $\chi_b(1P) \to \gamma\Upsilon(1S)$, $\Upsilon(1S)\to l^+l^-$ The product branching ratio for this entire decay sequence (including $\Upsilon(1S)\to l^+l^-$) is predicted to be $3.84 \cdot 10^{-5}$ [217], thus comparable to the predicted $\Upsilon(1D)$ production rate. In the four-photon cascade via the $\Upsilon(1D)$ the second highest energy photon is due to the third transition, while in these cascades the second highest energy photon is due to the second photon transition (see Fig. 4.10). This allows the discrimination of the $\Upsilon(1D)$ signal from the $\Upsilon(2S)$ background events.

CLEO III [171] finds their data are dominated by the production of one $\Upsilon(1D)$ state consistent with the $J = 2$ assignment and a mass $(10161.1\pm0.6\pm1.6)$ MeV, which is consistent with the predictions from potential models and lattice QCD calculations.

The signal product branching ratio obtained is $\mathcal{B}(\gamma\gamma\gamma\gamma l^+l^-)_{\Upsilon(1D)} = (2.5 \pm 0.5 \pm 0.5) \cdot 10^{-5}$. The first error is statistical, while the second one is systematic. The significance of the signal is 10.2 standard deviations. This branching ratio is consistent with the theoretically estimated rates. Godfrey and Rosner [217], summing over $\Upsilon(1D_{1,2,3})$ contributions, obtained 3.76×10^{-5}; while the predicted rate [200, 217] for the $\Upsilon(1D_2)$ state alone is 2.6×10^{-5}.

Forming the ratio of $\Upsilon(1D)$ to $\Upsilon(2S)$ four-photon cascades would allow the measurement in a fairly model independent way of the estimate of the total width of the $\Upsilon(1D)$ state, if the individual $\Upsilon(2P_J)$ and $\Upsilon(1P_{J'})$ transitions could be resolved.

6.3 M1 transitions

For M1 transitions, the leading order NRQCD prediction for the overlap $\mathcal{M}_{if}$ is independent of the potential model. The spin independence and orthogonality of states guarantee that the spatial overlap matrix is one for states within the same multiplet and zero for allowed transitions between multiplets, which have different radial quantum numbers.

Including relativistic corrections, e.g., finite size corrections, will spoil these exact results and induce a small overlap between states with different radial quantum numbers. Such $n \neq n'$ transitions are denoted hindered.

6.3.1 Model predictions

Within the (NR) model used for the E1 transitions (i.e., a nonrelativistic treatment except for finite size corrections and $\kappa_Q = 0$) the M1 transition rates and overlap matrix elements $\mathcal{M}$ for $\bar{c}c$ and $\bar{b}b$ S states are shown in Table 4.24.

Numerous papers have considered these M1 transitions including full relativistic corrections [182, 184–186, 201, 217, 218]. There are several sources of uncertainty that contribute making M1 transitions particularly complicated to calculate. In addition to the usual issues associated with the form of the long range potential there is the unknown value for the anomalous magnetic moment for the quark (κ_Q). Furthermore, the results depend explicitly on the quark masses and on other details of the potential (see Eqs. 4.128). For the models (RA) and (RB) used for the E1 transitions, $\kappa_Q = -1$. The theoretical uncertainty in the value of κ_Q will eventually be reduced by lattice calculations in quarkonium systems.

6.3.2 Comparison with experiment

M1 transitions have only been observed in the $\bar{c}c$ system. The allowed transitions in the $\bar{c}c$ system below threshold are shown in Fig. 4.12. The transitions within the $1P$ system are tiny (≈ 1 eV). Only the $J/\psi \to \eta_c$ and $\psi' \to \eta_c$ are observed experimentally [10]. For the $\bar{b}b$ system CLEO [219] sees no evidence for the hindered M1 transition $\Upsilon(3S) \to \eta_b(1S)$. The 90% cl upper bound on the branching ratio varies from $4 - 6 \times 10^{-4}$ depending on the mass splitting. For the expected splitting ≈ 910 MeV the bound is 5.3×10^{-4} [219]. This rules out a number of older models [182, 201]. A comparison of the experimental results with a variety of more modern models is shown in Table 4.25. For each model the assumptions for the mixture of scalar and vector confinement and the value of κ_Q is exhibited explicitly. For the model of Lahde [185] the results are also shown without including the exchange term (NEX). This (NEX) piece neglects the time ordering of photon emission and potential interaction, which vanishes in the NR limit. Generally models with a scalar confining interaction and/or a sizable negative anomalous quark magnetic moment are favored.

6.4 Higher order corrections

6.4.1 Higher multipole contributions

In lowest order, only the E1 amplitude contributes to χ_c states radiative transitions. In higher order in v^2/c^2 a M2 amplitude contributes for $J = 1, 2$ and an E3 amplitudes is also possible for the $J = 2$ state. To order v^2/c^2 these M2 and E3 corrections to the dominant E1 term can contribute to angular distributions but cannot contribute to total decay rates. This comes from the orthogonality of terms in the multipole expansion.

Table 4.24: M1 transition rates for S-wave quarkonium states using the NR model described in text. Finite size corrections are included in the calculation of $\mathcal{M}$ (see Eq. (4.121)) and $\kappa_Q = 0$.

Transition $i \xrightarrow{\text{M1}} f$		k (MeV)	$\Gamma(i \to f)$(NR) (eV)	$\mathcal{M}_{if}$(NR)
		$\bar{c}c$		
$1^3S_1(3.097)$	$1^1S_0(2.979)$	115	$1,960$	0.998
$2^3S_1(3.686)$	$2^1S_0(3.638)$	48	140	0.999
$2^1S_0(3.638)$	$1^3S_1(3.097)$	501	538	0.033
$2^3S_1(3.686)$	$1^1S_0(2.979)$	639	926	0.053
		$\bar{b}b$		
$1^3S_1(9.460)$	$1^1S_0(9.400)$	60	8.953	1.000
$2^1S_0(9.990)$	$1^3S_1(9.460)$	516	2.832	0.013
$2^3S_1(10.023)$	$2^1S_0(9.990)$	33	1.509	1.000
$2^3S_1(10.023)$	$1^1S_0(9.400)$	604	2.809	0.018
$3^1S_0(10.328)$	$2^3S_1(10.023)$	300	0.620	0.014
$3^1S_0(10.328)$	$1^3S_1(9.460)$	831	3.757	0.007
$3^3S_1(10.355)$	$3^1S_0(10.328)$	27	0.826	1.000
$3^3S_1(10.355)$	$2^1S_0(9.990)$	359	0.707	0.019
$3^3S_1(10.355)$	$1^1S_0(9.400)$	911	2.435	0.009

Table 4.25: Comparison of M1 transition overlaps with experiment for various models. The transition overlap $I \equiv \frac{M(1^3S_1)}{2m_Q}\mathcal{M}_{if}$ is from nS spin triplet to the n'S spin singlet S states in the $\bar{c}c$ and $\bar{b}b$ systems. The experimental upper bounds are 90% cl.

| Type			Transition $I_{n,n'}$					
Model	parameters		(n,n') [$\bar{c}c$]		(n,n') [$\bar{b}b$]			
	η	κ_Q	$(1,1)$	$(2,1)$	$(1,1)$	$(2,1)$	$(3,1)$	$(3,2)$
Cornell [191]	NR	0	0.84	0.028	0.92	0.017	0.007	0.018
GOS84 [184]	0	0	0.86	0.075	0.88	0.058	–	–
	0	−1	0.58	0.054	0.081	0.007	–	–
	1	0	0.65	0.127	0.91	0.048	–	–
	1	−1	0.39	0.029	0.049	0.021	–	–
EFG02 [186]	0	0	0.84	0.036	0.91	0.018	0.013	0.016
	1	0	1.06	0.027	1.08	0.011	0.009	0.007
	−1	−1	0.62	0.045	0.75	0.025	0.026	0.017
Lahde02 [185]	NEX	0	0.87	0.011	0.92	0.020	0.009	0.016
	1	0	0.67	0.049	0.88	0.032	0.014	0.037
EXP			0.66 ± 0.10	0.042 ± 0.004		< 0.045	< 0.020	< 0.080
Ref			[10]	[10] [210]		[209]	[219]	[209]
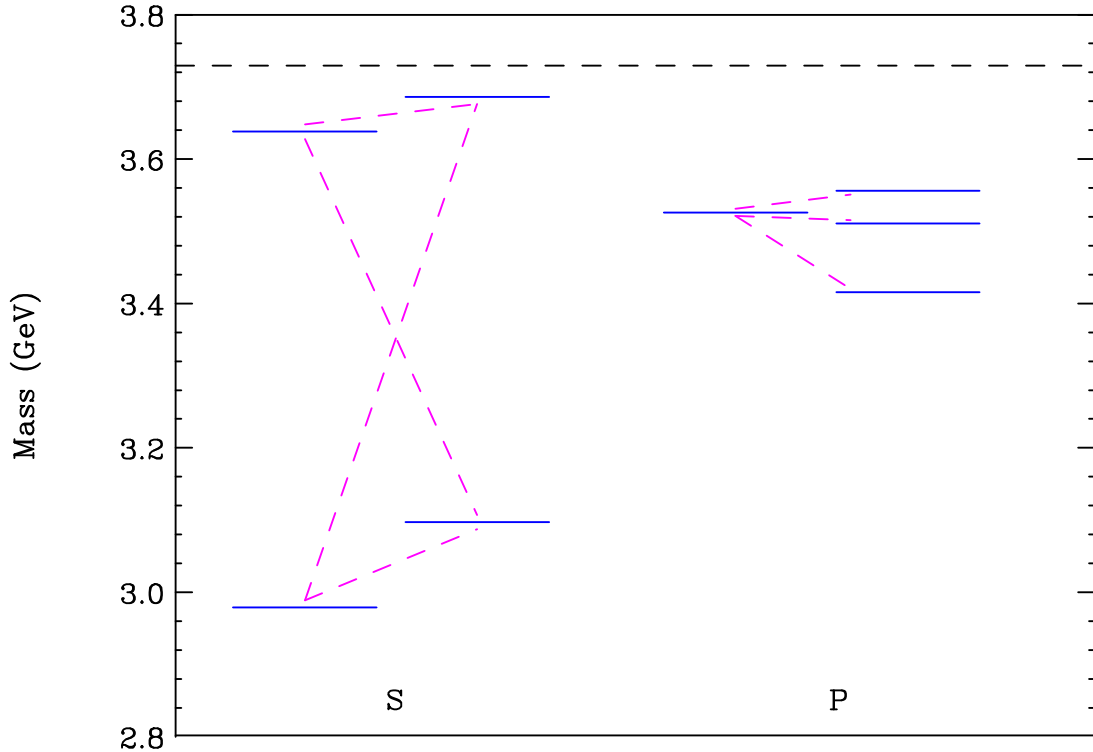
Fig. 4.12: Allowed M1 transitions in the narrow $\bar{c}c$. The $1P$ transition rates are unobservably small ($\approx 1eV$).

It was originally suggested by Karl, Meshkov and Rosner [220] that these corrections can be studied by measuring the angular correlations between the two photons in the transition $\psi\,' \to \chi_c + \gamma \to J/\psi + 2\gamma$. These effects can also be studied for χ_c states directly produced in hadron collisions, B decays or $\bar{p}p$ annihilation by measuring the combined angular distributions of the photon and the l^+l^- pair produced in the subsequent J/ψ decay. The details of these correlations have been calculated by Sebastian, Grotch and Ridener [221].

For the photon transition from a χ_{cJ} state there are $J + 1$ normalized helicity amplitudes, A_ν. Defining $|a| = \sqrt{E1^2 + M2^2 + E3^2}$, $a_1 = E1/|a|$, $a_2 = M2/|a|$ and $a_3 = E3/|a|$ the relation between helicity and multipole amplitudes is:

$$A_\nu = \sum_\ell a_\ell \left(\frac{2\ell + 1}{2J + 1} \right)^{\frac{1}{2}} \langle \ell, 1; 1, \nu - 1 | J, \nu \rangle . \tag{4.136}$$

Allowing for an anomalous magnetic moment κ_c and mixing between the $2S$ and $1D$ states the theoretical predictions for

$$\psi\,' \to \chi_{cJ} + \gamma \quad \text{and} \quad \chi_{cJ} \to J/\psi + \gamma$$

are shown in Table 4.26 along with a comparison with present experimental results. The S–D mixing parameter is $\mathcal{E}_{2S,1P} X = -\tan\phi \, \mathcal{E}_{1D,1P}$ where ϕ is defined in Eq. (4.134). In the notation of Eq. (4.127) the other model dependent parameter is defined by $\mathcal{E}_{1D,1P} Y = \int dr\, r \left(r\frac{du_{12}^{(0)}}{dr} - u_{12}^{(0)} \right) u_{11}^{(0)}$.

As can be seen from Table 4.26 a nonzero E3 amplitude in the $\psi\,' \to \chi_{c2} + \gamma$ decay is evidence for S–D mixing in the $\psi\,'$. Also note that the M2 term is sensitive to a possible anomalous magnetic moment, κ_c, for the charm quark. The recent BES results [223] for the M2 and E3 contributions do not differ significantly from zero. Additional high statistics studies of these angular distributions will

be necessary to determine the size of S–D mixing and shed light on the magnitude of the charm quark magnetic moment.

6.5   Coupling to virtual decay channels

When light quark loops are included in the description of quarkonium systems, the physical quarkonium states are not pure potential-model eigenstates and the effects of coupling to real and virtual heavy-light meson pairs must be included. Our command of quantum chromodynamics is inadequate to derive a realistic description of the interactions that communicate between the $\bar{Q}Q$ and $\bar{Q}q + \bar{q}Q$ sectors. However, the physical picture is that wave functions corresponding to physical states are now linear combinations of potential-model $\bar{Q}Q$ eigenstates plus admixtures of open heavy-flavour-meson pairs. The open heavy-flavour pieces have the spatial structure of bound states of heavy-flavour mesons: they are virtual contributions for states below threshold (see Section 3.3 in Chapter 3 for more details).

Far below heavy flavour threshold, the nonrelativistic potential model is a good approximation to the dynamics of the $\bar{Q}Q$ system. For excited states above the first few levels, the coupling of $\bar{Q}Q$ to heavy-flavour-meson pairs modifies wave functions, masses, and transition rates. In particular, this modifies electromagnetic transition rates considered in the previous subsections. In addition to these contributions, which involved photon coupling to a heavy (anti)quark, the contributions of light quark currents can no longer be neglected. The mass differences among the $\bar{Q}u$, $\bar{Q}d$ and $\bar{Q}s$ mesons, induce large SU(3) symmetry breaking effects. This destroys the cancellation among the light quark EM current contributions.

To compute the E1 radiative transition rates, we must take into account both the standard $(\bar{Q}Q)$ $\rightarrow (\bar{Q}Q)\gamma$ transitions and the transitions between (virtual) decay channels in the initial and final states. This second set of transitions contains light quark contributions for states near threshold. Recently, the effects of configuration mixing on radiative decay rates in the $\bar{c}c$ system were reexamined [207] within the Cornell coupled-channel formalism. A full outline of the calculational procedure appears in Refs. [177, 191]. (In particular, see Section IV.B of Ref. [191].)

Expectations for E1 transition rates among spin-triplet levels are shown in Table 4.27. Both the rates calculated between single-channel potential-model eigenstates (in italics) and the rates that result from the Cornell coupled-channel model are shown, to indicate the influence of the open-charm channels.

The 1^3D_1 transition rates at the mass of $\psi(3770)$ and at the predicted 1^3D_1 centroid, 3815 MeV, are shown. For the $\psi(3770)$, with its total width of about 24 MeV, the $1^3D_1(3770) \rightarrow \chi_{c0}\,\gamma(338)$ transition might someday be observable with a branching fraction of 1%. For the 1^3D_2 and 1^3D_3 levels, the radiative decay rates were calculated at the predicted 1^3D_1 centroid, 3815 MeV, at the mass calculated for the states (3831 MeV and 3868 MeV, respectively), and at the mass of $X(3872)$. The model reproduces the trends of transitions to and from the χ_c states in broad outline. For these low-lying states, the mixing through open-charm channels results in a mild reduction of the rates.

This study was done in the Cornell coupled channel model. It would be useful to do a similarly detailed study of these effects in other models.

6.6 B_c states

Quarkonium systems with unequal quark and antiquark masses, i.e., B_c mesons, are theoretical interesting, but are not easily accessible in e^+e^- collisions. They can be produced in significant numbers in hadron collisions (see Chapter 5, Section 8). CDF has reported the discovery of the ground state B_c meson via its semileptonic weak decay [224]. Theoretical calculations for E1 and M1 radiative transitions have been presented by a number of authors [186, 192, 225, 226] even though the whole excitation spectrum remains to be observed experimentally.

Table 4.26: M2 and E3 multipole amplitudes for radiative transitions involving χ_c states. The values of X and Y are model dependent and are defined in the text. Note $X = 0$ if no S–D mixing.

	$\chi_{cJ} \rightarrow J/\psi + \gamma$		
J	theory [221]	E835 [222]	PDG04 [10]
2	$a_2 \approx -\frac{\sqrt{5}}{3}\frac{k}{4m_c}(1+\kappa_c)$	$-0.093^{+0.039}_{-0.041} \pm 0.006$	-0.13 ± 0.05
2	$a_3 \approx 0$	$0.020^{+0.055}_{-0.044} \pm 0.009$	$0.011^{+0.041}_{-0.033}$
1	$a_2 \approx -\frac{k}{4m_c}(1+\kappa_c)$	$0.002 \pm 0.032 \pm 0.004$	$-0.002^{+0.008}_{-0.017}$
	$\psi' \rightarrow \chi_{cJ} + \gamma$		
J	theory [221]		BES [223]
2	$a_2 \approx -\frac{\sqrt{3}}{2\sqrt{10}}\frac{k}{m_c}[(1+\kappa_c)(1+\frac{\sqrt{2}}{5}X)-i\frac{1}{5}X]/[1-\frac{1}{5\sqrt{2}}X]$		$-0.051^{+0.054}_{-0.036}$
2	$a_3 \approx -\frac{12\sqrt{2}}{175}\frac{k}{m_c}X[1+\frac{3}{8}Y]/[1-\frac{1}{5\sqrt{2}}X]$		$-0.027^{+0.043}_{-0.029}$
1	$a_2 \approx -\frac{k}{4m_c}[(1+\kappa_c)(1+\frac{2\sqrt{2}}{5}X)+i\frac{3}{10}X]/[1+\frac{1}{\sqrt{2}}X]$		

Table 4.27: Calculated and observed rates for E1 radiative transitions among charmonium levels from Ref. [207]. Values in *italics* result if the influence of open-charm channels is not included. Measured rates are shown for comparison. Experimental values are calculated from world averages [10], except for $\mathcal{B}(\psi'\rightarrow\gamma^3P_J)$ whose values are taken from the recent CLEO-c measurement [210].

Transition	k_γ (MeV)	width (keV)	k_γ (MeV)	width (keV)	k_γ (MeV)	width (keV)
	P state					
S state	χ_{c2}		χ_{c1}		χ_{c0}	
J/ψ	429	$300\rightarrow287$	390	$228\rightarrow216$	303	$113\rightarrow107$
[exp]		430 ± 40		290 ± 50		119 ± 16
ψ'	129	$23\rightarrow23$	172	$33\rightarrow32$	261	$36\rightarrow38$
[exp]		25.9 ± 2.1		25.5 ± 2.2		26.2 ± 2.6
	P state					
D state	χ_{c2}		χ_{c1}		χ_{c0}	
$1^3D_1(3770)$	208	$3.2\rightarrow3.9$	251	$183\rightarrow59$	338	$254\rightarrow225$
$1^3D_1(3815)$	250	$5.5\rightarrow6.8$	293	$128\rightarrow120$	379	$344\rightarrow371$
$1^3D_2(3815)$	251	$50\rightarrow40$	293	$230\rightarrow191$		
$1^3D_2(3831)$	266	$59\rightarrow45$	308	$264\rightarrow212$		
$1^3D_2(3872)$	303	$85\rightarrow45$	344	$362\rightarrow207$		
$1^3D_3(3815)$	251	$199\rightarrow179$				
$1^3D_3(3868)$	303	$329\rightarrow286$				
$1^3D_3(3872)$	304	$341\rightarrow299$				

7   HADRONIC TRANSITIONS[14]

7.1   Theoretical approaches

Hadronic transitions (HTs)

$$\Phi_i \rightarrow \Phi_f + h \tag{4.137}$$

are important decay modes of heavy quarkonia [Φ_i, Φ_f and h stand for the initial-, final-state quarkonia and the emitted light hadron(s)]. For instance, the branching ratio of $\psi' \rightarrow J/\psi + \pi + \pi$ is approximately 50%. In the $c\bar{c}$ and $b\bar{b}$ systems, the typical mass difference $M_{\Phi_i} - M_{\Phi_f}$ is around a few hundred MeV, so that the typical momentum of h is low. In the single-channel picture, the light hadron(s) h are converted from the gluons emitted by the heavy quark Q or antiquark $\bar{Q}$ in the transition. The typical momentum of the emitted gluons is too low for perturbative QCD to be reliable. Certain nonperturbative approaches are thus needed for studying HTs. In the following, we briefly review two feasible approaches: namely, the *QCD multipole expansion* (QCDME) and the *Chiral Lagrangian for Heavy Mesons*.

A.   QCD Multipole expansion

Heavy $Q\bar{Q}$ bound states can be calculated by solving the Schrödinger equation with a given potential model. For $c\bar{c}$ and $b\bar{b}$ quarkonia, the typical radius is $a = \sqrt{\langle r^2 \rangle} \sim \mathcal{O}(10^{-1})$ fm. With such a small radius, the idea of QCDME can be applied to the soft gluon emissions in HTs. QCDME is an expansion in powers of $\boldsymbol{x} \cdot \boldsymbol{\nabla}$ operating on the gluon field, where $\boldsymbol{x}$ is the separation between Q and $\bar{Q}$ in the quarkonium. For a gluon with a typical momentum $k \sim$ few hundred MeV, the expansion parameter is actually $ak \sim \mathcal{O}(10^{-1})$, ensuring convergence[15]. Note that the convergence of QCDME does not depend on the value of the QCD coupling constant.

QCDME has been studied by many authors [227–231]. The gauge invariant formulation is given in Ref. [230]. Let $\psi(x)$ and $A_\mu^a(x)$ be the quark and gluon fields. Following Refs. [230, 231], we introduce

$$\Psi(\boldsymbol{x}, t) \equiv U^{-1}(\boldsymbol{x}, t)\psi(x), \quad \frac{\lambda_a}{2} A_\mu^{a\prime}(\boldsymbol{x}, t) \equiv U^{-1}(\boldsymbol{x}, t)\frac{\lambda_a}{2} A_\mu^a(x) U(\boldsymbol{x}, t) - \frac{i}{g_s} U^{-1}(\boldsymbol{x}, t)\partial_\mu U(\boldsymbol{x}, t), \tag{4.138}$$

with

$$U(\boldsymbol{x}, t) = P \exp\left[ig_s \int_{\boldsymbol{X}}^{\boldsymbol{x}} \frac{\lambda_a}{2} \boldsymbol{A}^a(\boldsymbol{x}', t) \cdot d\boldsymbol{x}'\right], \tag{4.139}$$

in which P is the path-ordering operation, the path is along the straight-line connecting the two ends, and $\boldsymbol{X} \equiv (\boldsymbol{x}_1 + \boldsymbol{x}_2)/2$ is the c.o.m. coordinate of Q and $\bar{Q}$. It is shown in Ref. [230] that, in the Lagrangian, $\Psi(\boldsymbol{x}, t)$ serves as the *dressed* (*constituent*) quark field. Now we make the multipole expansion [230]

$$A_0^{a\prime}(\boldsymbol{x}, t) = A_0^{a\prime}(\boldsymbol{X}, t) - (\boldsymbol{x} - \boldsymbol{X}) \cdot \boldsymbol{E}^a(\boldsymbol{f}X, t) + \cdots, \quad \boldsymbol{A}^{a\prime}(\boldsymbol{X}, t) = -\frac{1}{2}(\boldsymbol{x} - \boldsymbol{X}) \times \boldsymbol{B}^a(\boldsymbol{X}, t) + \cdots, \tag{4.140}$$

where $\boldsymbol{E}^a$ and $\boldsymbol{B}^a$ are colour-electric and colour-magnetic fields, respectively. The Hamiltonian is then [230]

$$H_{\text{QCD}}^{\text{eff}} = H_{\text{QCD}}^{(0)} + H_{\text{QCD}}^{(1)}, \tag{4.141}$$

with $H_{\text{QCD}}^{(0)}$ the sum of the kinetic and potential energies of the heavy quarks, and

$$H_{\text{QCD}}^{(1)} = H_1 + H_2, \quad H_1 \equiv Q_a A_0^a(\boldsymbol{X}, t), \quad H_2 \equiv -\boldsymbol{d}_a \cdot \boldsymbol{E}^a(\boldsymbol{X}, \mathbf{t}) - \mathbf{m_a} \cdot \mathbf{B^a}(\boldsymbol{X}, \mathbf{t}) + \cdots, \tag{4.142}$$

in which Q_a, $\boldsymbol{d}_a$, and $\boldsymbol{m}_a$ are the colour charge, colour-electric dipole moment, and colour-magnetic dipole moment of the $Q\bar{Q}$ system, respectively. Equation (4.141) is regarded as an effective Hamiltonian

---

[14] Authors: D. Z. Besson, A. Deandrea, F. A. Harris, Y.-P. Kuang, S. L. Olsen

[15] We know from classical electrodynamics that the coefficient of the $(ak)^l$ term in the multipole expansion contains a factor $\frac{1}{(2l+1)!!}$. Hence the expansion actually works better than what might be expected by simply estimating the size of $(ak)^l$.

[230]. Considering that the heavy quark may have an anomalous magnetic moment, we take g_E and g_M to denote the effective coupling constants for the electric and magnetic multipole gluon emissions (MGE), respectively.

We shall take $H_{\text{QCD}}^{(0)}$ as the zeroth order Hamiltonian, and take $H_{\text{QCD}}^{(1)}$ as a perturbation. This is different from the ordinary perturbation theory since $H_{\text{QCD}}^{(0)}$ is not a free field Hamiltonian. The general formula for the S matrix element in this expansion has been given in Ref. [231], which is

$$\langle f|S|i\rangle = -i2\pi\delta(E_f + \omega_f - E_i)\left\langle f\left|H_2\frac{1}{E_i - H_{\text{QCD}}^{(0)} + i\partial_0 - H_1}\cdots\frac{1}{E_i - H_{\text{QCD}}^{(0)} + i\partial_0 - H_1}H_2\right|i\right\rangle,$$
(4.143)

where ω_f is the energy of the emitted gluons. Explicit evaluations of the S matrix elements in various cases will be presented in Section 7.2.

B. Chiral Lagrangian for heavy mesons

In the effective Lagrangian approach one can construct a heavy meson multiplet field analogous to the one introduced for heavy-light mesons. Symmetry-breaking terms can be easily added to the formalism as we shall see in the following. As in the single heavy quark case, an effective Lagrangian describing the low-momentum interactions of heavy quarkonia with light mesons can be written down. The heavy quarkonium multiplets are described by a simple trace formalism [232]. Parity P and charge conjugation C, which determine selection rules for electromagnetic and hadronic transitions are exactly conserved quantum numbers for quarkonium, together with J. If spin-dependent interactions are neglected, it is natural to describe the spin singlet $m\,^1l_J$ and the spin triplet $m\,^3l_J$ by means of a single multiplet $J(m,l)$. For the case $l = 0$, when the triplet $s = 1$ collapses into a single state with total angular momentum $J = 1$, this is readily realized:

$$J = \frac{(1+\not v)}{2}[H_\mu\gamma^\mu - \eta\gamma_5]\frac{(1-\not v)}{2}\ .$$
(4.144)

Here v^μ denotes the four velocity associated to the multiplet J; H_μ and η are the spin 1 and spin 0 components respectively; the radial quantum number has been omitted. The expressions for the general wave $J^{\mu_1\cdots\mu_l}$ can be found in Appendix C of Ref. [233].

For illustrative purpouses let us start by considering radiative transitions, whose analysis can be easily carried out in terms of the multiplet field introduced above. The Lagrangian for radiative decays is:

$$\mathcal{L} = \sum_{m,n}\delta(m,n)\langle\overline{J}(m)\ J_\mu(n)\rangle v_\nu F^{\mu\nu} + h.c.,$$
(4.145)

where a sum over velocities is understood, $F^{\mu\nu}$ is the electromagnetic tensor, the indices m and n represent the radial quantum numbers, $J(m)$ stands for the multiplet with radial number m and $\delta(m,n)$ is a dimensional parameter (the inverse of a mass), to be fixed from experimental data and which also depends on the heavy flavour. The Lagrangian (4.145) conserves parity and charge conjugation and is invariant under the spin transformation. It reproduces the electric dipole selection rules $\Delta\ell = \pm 1$ and $\Delta s = 0$. It is straightforward to obtain the corresponding radiative widths:

$$\Gamma(^3P_J\to\,^3S_1\gamma) = \frac{\delta^2}{3\pi}k^3\frac{M_{S_1}}{M_{P_J}},$$
(4.146)

$$\Gamma(^3S_1\to\,^3P_J\gamma) = \frac{(2J+1)}{9\pi}\delta^2k^3\frac{M_{S_1}}{M_{P_J}},$$
(4.147)

$$\Gamma(^1P_1\to\,^1S_0\gamma) = \frac{\delta^2}{3\pi}k^3\frac{M_S}{M_P},$$
(4.148)

where k is the photon momentum. Once the radial numbers n and m have been fixed, the Lagrangian (4.145) describes four no spin-flip transitions with a single parameter; this allows three independent predictions. The previous decay widths can be compared with those of the electric transitions of Sec. 6.1.3 and in particular with formula (4.118). The ratio of the masses in the previous widths should be put to one in the nonrelativistic limit and the free parameter δ of the effective Lagrangian encodes the information of the overlap integral of equation (4.116).

The effective heavy-meson description of quarkonium does not seem to present special advantages to describe heavy quarkonium annihilation. In the following we shall concentrate on quarkonium hadronic transitions.

The heavy quark spin symmetry leads to general relations for the differential decay rates in hadronic transitions among quarkonium states that essentially reproduce the results of a QCD double multipole expansion for gluonic emission. Further use of chiral symmetry leads to differential pion decay distributions valid in the soft regime [234, 235]. At the lowest order in the chiral expansion for the emitted pseudoscalars we find a selection rule allowing only for even (odd) number of emitted pseudoscalars for transitions between quarkonium states of orbital angular momenta different by even (odd) units. Such a rule can be violated by higher chiral terms, by chiral breaking, and by terms breaking the heavy quark spin symmetry. Specialization to a number of hadronic transitions reproduces (by elementary tensor construction) the known results from the expansion in gluon multipoles, giving a simple explanation for the vanishing of certain coefficients, which would otherwise be allowed in the chiral expansion. In certain cases, such as for instance $^3P_0 \to {}^3P_2\pi\pi$, $^3P_1 \to {}^3P_2\pi\pi$, or D–S transitions via 2π, the final angular and mass distributions are uniquely predicted from heavy quark spin and the lowest-order chiral expansion.

An important class of hadronic transitions between heavy-quarkonium states is provided by the decays with emission of two pions, for example:

$$\psi' \to J/\psi \, \pi\pi \, . \tag{4.149}$$

To describe these processes one can use the chiral symmetry for the pions and the heavy-quark spin symmetry for the heavy states. The first of these is expected to hold when the pions have small energies. We notice that the velocity superselection rule applies at $q^2 = q_{\max}^2$, when the energy transfer to the pion is maximal. Therefore, we expect these approximations to be valid in the whole energy range only if $q_{\max}^2$ is small.

Nonetheless a number of interesting properties of these transitions can be derived on the basis of the heavy quark symmetry alone. Therefore, before deriving the pion couplings by means of chiral symmetry, we discuss the implications of the heavy quark spin symmetry in hadronic transitions.

As an example, we consider transitions of the type $^3S_1 \to {}^3S_1 + h$ and $^1S_0 \to {}^1S_0 + h$, where h can be light hadrons, photons, etc. By imposing the heavy quark spin symmetry, one is led to describe these processes by an interaction Lagrangian:

$$\mathcal{L}_{SS'} = \langle J' \bar{J} \rangle \Pi_{SS'} + h.c. \ , \tag{4.150}$$

where the dependence upon the pion field is contained in the as-yet-unspecified operator $\Pi_{SS'}$. It is immediate to derive from $\mathcal{L}_{SS'}$ the averaged modulus square matrix elements for the transitions $^3S_1 \to {}^3S_1 + h$ and $^1S_0 \to {}^1S_0 + h$ with an arbitrary fixed number of pions in the light final state h. We obtain:

$$|\mathcal{M}(^3S_1 \to {}^3S_1 + h)|_{\text{av.}}^2 = |\mathcal{M}(^1S_0 \to {}^1S_0 + h)|_{\text{av.}}^2 = 4 M_S M_{S'} |\Pi_{SS',h}|^2, \tag{4.151}$$

where M_S and M_S' are the average masses of the two S-wave multiplets; $\Pi_{SS',h}$ is the appropriate tensor for the emission of the light particles h, to be calculated from the operator $\Pi_{SS'}$. By denoting with $d\Gamma$ the generic differential decay rate, we have:

$$d\Gamma(^3S_1 \to {}^3S_1 + h) = d\Gamma(^1S_0 \to {}^1S_0 + h) \ . \tag{4.152}$$

This is the prototype of a series of relations, which can be derived for hadronic transitions as a consequence of the spin independence of the interaction terms. In all the known cases they coincide with those calculated in the context of a QCD double multipole expansion. We note, however, that we do not even need to specify the nature of the operator Π, which may depend on light fields different from the pseudoscalar mesons (e.g., the photon, or a light hadron, etc), provided that the interaction term we are building is invariant under parity, charge conjugation, and the other symmetries relevant to the transition considered.

A useful symmetry that can be used in processes involving light quarks is the chiral symmetry. It is possible to build up an effective Lagrangian, which allows to study transitions among quarkonium states with emissions of soft light pseudoscalars, considered as the Goldstone bosons of the spontaneously broken chiral symmetry.

The light mesons are described as pseudo-Goldstone bosons, included in the matrix $\Sigma = \xi^2$, where we use the standard notation of chiral perturbation theory. Frequently occurring quantities are the functions of ξ and its derivatives $\mathcal{A}_\mu$ and $\mathcal{V}_\mu$ given by:

$$\mathcal{V}_\mu = \frac{1}{2}\left(\xi^\dagger\partial_\mu\xi + \xi\partial_\mu\xi^\dagger\right) \quad \text{and} \quad \mathcal{A}_\mu = \frac{1}{2}\left(\xi^\dagger\partial_\mu\xi - \xi\partial_\mu\xi^\dagger\right). \tag{4.153}$$

The octet of vector resonances (ρ, etc.) can be introduced as the gauge multiplet associated with the hidden group $SU(3)_H$ (see Ref. [236]), designated as ρ_μ in the following.

By imposing the heavy quark spin symmetry, parity and charge conjugation invariance, and by assuming that the pseudoscalar meson coupling are described by the lowest order (at most two derivatives) chiral invariant operators, we can establish the following selection rules for hadronic transitions:

$$\text{even number of emitted pseudoscalars} \leftrightarrow \Delta l = 0, 2, 4, ...$$
$$\text{odd number of emitted pseudoscalars} \leftrightarrow \Delta l = 1, 3, 5, ... \tag{4.154}$$

In fact the spin independent operator describing $\Delta l = 0, 2, 4, ...$ transitions has charge conjugation $C = +1$. On the other hand, the lowest order, chiral invariant terms with positive charge conjugation are:

$$\langle \mathcal{A}_\mu \mathcal{A}_\nu \rangle, \qquad \langle (\mathcal{V}_\mu - \rho_\mu)(\mathcal{V}_\nu - \rho_\nu) \rangle, \tag{4.155}$$

whose expansion contains an even number of pseudoscalar mesons. Spin independence of the interaction, on the other hand, requires that the $\Delta l = 1, 3, 5, ...$ transitions are described by $C = -1$ operators. At the lowest order we can form just one chiral invariant term with $C = -1$:

$$\langle \mathcal{A}_\mu (\mathcal{V}_\nu - \rho_\nu) \rangle, \tag{4.156}$$

whose expansion contains an odd number (≥ 3) of pseudoscalar mesons.

This selection rule is violated at higher orders of the chiral expansion or by allowing for terms that explicitly break the heavy quark or the chiral symmetries.

To further characterize the hadronic transitions respecting chiral symmetry, we consider below explicit expressions for the most general operators $\Pi_{ll'}$. For simplicity, we limit ourselves to those contributing to two or three pion emissions:

$$\begin{aligned}
\Pi_{SS'} &= A_{SS'}\langle \mathcal{A}_\rho \mathcal{A}^\rho \rangle + B_{SS'}\langle (v \cdot \mathcal{A})^2 \rangle, \\
\Pi^\mu_{PS} &= D_{PS}\, \epsilon^{\mu\nu\rho\sigma} v_\nu \langle \mathcal{A}_\rho (\mathcal{V}_\sigma - \rho_\sigma) \rangle, \\
\Pi^{\mu\nu}_{PP'} &= A_{PP'}\langle \mathcal{A}_\rho \mathcal{A}^\rho \rangle g^{\mu\nu} + B_{PP'}\langle (v \cdot \mathcal{A})^2 \rangle g^{\mu\nu} + C_{PP'}\langle \mathcal{A}^\mu \mathcal{A}^\nu \rangle, \\
\Pi^{\mu\nu}_{DS} &= C_{DS}\langle \mathcal{A}^\mu \mathcal{A}^\nu \rangle.
\end{aligned} \tag{4.157}$$

The constants $A_{ll'}$, $B_{ll'}$, $C_{ll'}$ and $D_{ll'}$ are arbitrary parameters of dimension $(\text{mass})^{-1}$, to be fixed from experiment. One can easily derive amplitudes, decay rates and distributions for the corresponding hadronic transitions.

For instance, the amplitude for the decay (4.149) is given by:

$$\mathcal{M}(^3S_1 \rightarrow ^3S_1 + \pi\pi) = \frac{4i\sqrt{M_S M_{S'}}}{f_\pi^2} \epsilon' \cdot \epsilon^* \left(A_{SS'} p_1 \cdot p_2 + B_{SS'} v \cdot p_1 v \cdot p_2 \right) \tag{4.158}$$

where ϵ and ϵ' are the polarisation vectors of quarkonium states; p_1, p_2 are the momenta of the two pions. It is well known that the use of chiral symmetry arguments leads to a general amplitude for the process in question, which contains a third independent term given by:

$$C_{SS'} \frac{4i\sqrt{M_S M_{S'}}}{f_\pi^2} \left(\epsilon' \cdot p_1 \epsilon^* \cdot p_2 + \epsilon' \cdot p_2 \epsilon^* \cdot p_1 \right) \;. \tag{4.159}$$

In the nonrelativistic limit in QCDME, Yan [230] finds $C_{SS'} = 0$. It is interesting to note that, within the present formalism, this result is an immediate consequence of the chiral and heavy quark spin symmetries. However, these symmetries are not exact and corrections to the symmetry limit are expected.

In the chiral Lagrangian (CL) approach, the $\pi^0 - \eta - \eta'$ mixings can be derived, which should be taken into account in predicting single pseudoscalar meson transitions of heavy quarkonia (cf. Section 7.2). Let us define

$$\hat{m} \equiv \begin{pmatrix} m_u & 0 & 0 \\ 0 & m_d & 0 \\ 0 & 0 & m_s \end{pmatrix}. \tag{4.160}$$

The Lagrangian that gives mass to the pseudoscalar octet (massless in the chiral limit) and causes $\pi^0 - \eta$ mixing is

$$\mathcal{L}_m = \lambda_0 \langle \hat{m}(\Sigma + \Sigma^\dagger) \rangle, \tag{4.161}$$

and that giving rise to the mixing of η' with π^0 and η is

$$\mathcal{L}_{\eta\eta'} = \frac{if_\pi}{4} \tilde{\lambda} \langle \hat{m}(\Sigma - \Sigma^\dagger) \rangle \eta', \tag{4.162}$$

where $\hat{\lambda}$ is a parameter with the dimension of a mass. At first order in the mixing angles the physical states $\tilde{\pi}^0$, $\tilde{\eta}$, and $\tilde{\eta}'$ determined from the above Lagrangians are:

$$\tilde{\pi}^0 = \pi^0 + \epsilon\eta + \epsilon'\eta', \quad \tilde{\eta} = \eta - \epsilon\pi^0 + \theta\eta', \quad \tilde{\eta}' = \eta' - \theta\eta - \epsilon'\pi^0, \tag{4.163}$$

in which the mixing angles are

$$\epsilon = \frac{(m_d - m_u)\sqrt{3}}{4\left(m_s - \frac{m_u + m_d}{2}\right)}, \quad \epsilon' = \frac{\tilde{\lambda}(m_d - m_u)}{\sqrt{2}(m_{\eta'}^2 - m_{\pi^0}^2)}, \quad \theta = \sqrt{\frac{2}{3}} \; \frac{\tilde{\lambda}\left(m_s - \frac{m_u + m_d}{2}\right)}{m_{\eta'}^2 - m_\eta^2}. \tag{4.164}$$

7.2 Predictions for hadronic transitions in the single-channel approach

In this section, we give the predictions for HTs in the single-channel approach. In this approach, the amplitude of HT is diagrammatically shown in Fig. 4.13 in which there are two complicated vertices: namely, the MGE vertex of the heavy quarks and the vertex of hadronization (H) describing the conversion of the emitted gluons into light hadrons. In the following, we shall treat them separately.

Let us first consider the HT processes $n_i^3 S_1 \rightarrow n_f^3 S_1 + \pi + \pi$. To lowest order, these are double electric-dipole transitions (E1E1). The transition amplitude can be obtained from the S matrix element (4.143). After some algebra, we obtain [230, 231, 237]

$$\mathcal{M}_{E1E1} = i\frac{g_E^2}{6} \sum_{KLK'L'} \langle \Phi_f h | \boldsymbol{x} \cdot \boldsymbol{E} | KL \rangle \left\langle KL \left| \frac{1}{E_i - H_{QCD}^{(0)} - iD_0} \right| K'L' \right\rangle \langle K'L' | \boldsymbol{x} \cdot \boldsymbol{E} | \Phi_i \rangle, \tag{4.165}$$
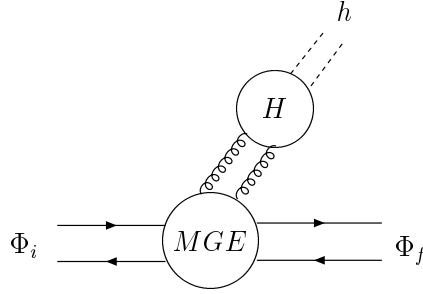
Fig. 4.13: Diagram for a typical hadronic transition in the single-channel QCDME approach.

where $(D_0)_{bc} \equiv \delta_{bc}\partial_0 - g_s f_{abc} A_0^a$, and $|KL\rangle$ is the intermediate state with principal quantum number K and orbital angular momentum L. According to the angular momentum selection rule, $L = L' = 1$. The intermediate states in the HT are the states after the emission of the first gluon and before the emission of the second gluon (cf. Fig. 4.13), i.e., they are states with a gluon and a colour-octet $Q\bar{Q}$. These are the so-called hybrid states. It is difficult to calculate these states from the first principles of QCD. So we shall take a reasonable model for it. The model should *reasonably reflect the main properties of the hybrid states* and should *contain as few free parameters as possible* in order not to affect the predictive power of the theory. The quark confining string (QCS) model [238] satisfies these requirements [16] Explicit calculations with the QCS are given in Ref. [237]; the transition amplitude (4.165) then becomes

$$\mathcal{M}_{E1E1} = i\frac{g_E^2}{6} \sum_{KL} \frac{\langle \Phi_f | x_k | KL \rangle \langle KL | x_l | \Phi_i \rangle}{E_i - E_{KL}} \langle \pi\pi | E_k^a E_l^a | 0 \rangle, \tag{4.166}$$

We see that, in this approach, the transition amplitude contains two factors: namely, the heavy quark MGE factor (the summation) and the H factor $\langle \pi\pi | E_k^a E_l^a | 0 \rangle$. The first factor can be calculated for a given potential model. Let us now consider the second factor. Its scale is the light hadron mass scale, which is very low (highly nonperturbative), and there is, therefore, no currently reliable way of calculating it from the first principles of QCD. Thus we take a phenomenological approach based on PCAC and the soft pion technique in Ref. [240]. From the standard tensor reduction, this H factor can be written as [237]

$$\frac{g_E^2}{6}\langle \pi_\alpha(q_1)\pi_\beta(q_2) | E_k^a E_l^a | 0 \rangle = \frac{\delta_{\alpha\beta}}{\sqrt{(2\omega_1)(2\omega_2)}}\left[C_1 \delta_{kl} q_1^\mu q_{2\mu} + C_2\left(q_{1k}q_{2l} + q_{1l}q_{2k} - \frac{2}{3}\delta_{kl}\boldsymbol{q}_1 \cdot \boldsymbol{q}_2 \right) \right], \tag{4.167}$$

where C_1 and C_2 are two unknown constants. For a given $\pi\pi$ invariant mass $M_{\pi\pi}$, the C_1 term is isotropic (S-wave), while the C_2 term is angular dependent (D-wave). In the nonrelativistic single-channel (NRSC) approach, orbital angular momentum conservation leads to the conclusion that the MGE factor is proportional to δ_{kl}. Thus only the C_1 term contributes to the S-state to S-state transitions[17]. In this case, the $n_i^3 S_1 \rightarrow n_f^3 S_1 + \pi + \pi$ transition rate can be expressed as [237]

$$\Gamma(n_i^3 S_1 \rightarrow n_f^3 S_1 \, \pi \, \pi) = |C_1|^2 G |f_{2010}^{111}|^2, \tag{4.168}$$

where G is a phase-space factor given in Ref. [237] and

$$f_{n_i l_i n_f l_f}^{LP_i P_f} \equiv \sum_K \frac{\int R_f(r) r^{P_f} R_{KL}^*(r) r^2 dr \int R_{KL}^*(r') r'^{P_i} R_i(r') r'^2 dr'}{M_i - E_{KL}}, \tag{4.169}$$

---

[16]Another possible model satisfying the requirements is the MIT bag model for the hybrid states, which can also lead to reasonable predictions [239].

[17]This is consistent with the CL approach in the nonrelativistic limit ($v = 0$) [cf. (4.158)].

Table 4.28: The values of $|C_1|^2$ and the predicted $\pi\pi$ transition rates (in keV) determined for the Υ system using the Cornell model and the BGT model. The corresponding updated experimental values of the transition rates [10] are also listed for comparison. $\pi\pi$ stands for the sum over all the $\pi^+\pi^-$ and $\pi^0\pi^0$ channels.

	Cornell	BGT	Expt.
$|C_1|^2$	83.4×10^{-6}	67.8×10^{-6}	
$\Gamma(\Upsilon' \to \Upsilon\pi\pi)$ (keV)	8.6	7.8	12.0 ± 1.8
$\Gamma(\Upsilon'' \to \Upsilon\pi\pi)$ (keV)	0.44	1.2	1.72 ± 0.35
$\Gamma(\Upsilon'' \to \Upsilon'\pi\pi)$ (keV)	0.78	0.53	1.26 ± 0.40

with R_i, R_f, and R_{KL} the radial wave functions of the initial, final, and intermediate states, respectively.

There is only one overall unknown constant C_1 left in this transition amplitude, which can be determined by taking the well-measured HT rate $\Gamma(\psi' \to J/\psi\pi\pi)$. The updated experimental values are [10]

$$\Gamma_{\text{tot}}(\psi') = 281 \pm 17\,\text{keV}, \quad \mathcal{B}(\psi' \to J/\psi\pi^+\pi^-) = (31.7 \pm 1.1)\%, \quad \mathcal{B}(\psi' \to J/\psi\pi^0\pi^0) = (18.8 \pm 1.2)\%. \tag{4.170}$$

Given these, we can then predict all the S-state to S-state $\pi\pi$ transitions rates in the Υ system. Let us take the Cornell [177, 191] and the Buchmüller–Grunberg–Tye (BGT) [141, 193] potential models as examples to show the extracted $|C_1|$ values and the predicted rates in the Υ system. The results are listed in Table 4.28[18] in which the experimental errors are dominated by the uncertainty of the total width. We see that the BGT model predicted ratios $\Gamma(\Upsilon'' \to \Upsilon\pi\pi)/\Gamma(\Upsilon' \to \Upsilon\pi\pi) \approx 1.2/7.8 = 0.15$ and $\Gamma(\Upsilon'' \to \Upsilon'\pi\pi)/\Gamma(\Upsilon' \to \Upsilon\pi\pi) \approx 0.53/7.8 = 0.07$ are close to the corresponding experimental values 1.72/12.0=0.14 and 1.26/12.0=0.11. However, the predicted absolute partial widths are smaller than the experimental values by roughly a factor of 50–75%. Moreover, when the $M_{\pi\pi}$ distributions are considered, the situation will be more complicated. We shall deal with these issues in Section 7.3.

Note that the phase space factor G in $\Upsilon'' \to \Upsilon\pi\pi$ is much larger than that in $\Upsilon' \to \Upsilon\pi\pi$, $G(\Upsilon'' \to \Upsilon\pi\pi)/\,G(\Upsilon' \to \Upsilon\pi\pi) = 33$ [237]. One may naively expect that $\Gamma(\Upsilon'' \to \Upsilon\pi\pi) > \Gamma(\Upsilon' \to \Upsilon\pi\pi)$. However, we see from Table 4.28 that the measured $\Gamma(\Upsilon'' \to \Upsilon\pi\pi)/\Gamma(\Upsilon' \to \Upsilon\pi\pi) \approx 0.14$. The reason why the predicted ratio is close to the experimental value is that the contributions from various intermediate states to the overlap integrals in the summation in f_{3010}^{111} [cf. (4.169)] *drastically cancel* each other due to the fact that the Υ'' wave function contains two nodes. This is *characteristic* of such intermediate state models (QCS or bag model).

The decays $n_i^3S_1 \to n_f^3S_1 + \eta$ are dominated by E1M2 transitions. We can predict the ratios $R' \equiv \Gamma(\Upsilon' \to \Upsilon\eta)/\Gamma(\psi' \to J/\psi\eta)$ and $R'' \equiv \Gamma(\Upsilon'' \to \Upsilon\eta)/\Gamma(\psi' \to J/\psi\eta)$:

$$R' = \frac{\left(\left| \frac{f_{2010}^{111}(b\bar{b})}{m_b} \right|^2 |\mathbf{q}(b\bar{b})|^3 \right)}{\left(\left| \frac{f_{2010}^{111}(c\bar{c})}{m_c} \right|^2 |\mathbf{q}(c\bar{c})|^3 \right)}, \qquad R'' = \frac{\left(\left| \frac{f_{3010}^{111}(b\bar{b})}{m_b} \right|^2 |\mathbf{q}(b\bar{b})|^3 \right)}{\left(\left| \frac{f_{2010}^{111}(c\bar{c})}{m_c} \right|^2 |\mathbf{q}(c\bar{c})|^3 \right)}, \tag{4.171}$$

where $\mathbf{q}$ is the momentum of η. The BGT model predicts $R' = 0.0025$, $R'' = 0.0013$. Recently BES has obtained an accurate measurement of $\Gamma(\psi' \to J/\psi\eta)$ and $\Gamma(\psi' \to J/\psi\pi^0)$ [241] (see Section 7.6A). With the new BES data and the bounds on $\Gamma(\Upsilon' \to \Upsilon\eta)$ and $\Gamma(\Upsilon'' \to \Upsilon\eta)$ [10], the experimental bounds are $R'|_{\text{exp}} < 0.0098$, $R''|_{\text{exp}} < 0.0065$ [241]. The predictions are consistent with these bounds.

---

[18]The updated results listed in Table reftab:c1ht are roughly larger than those in Ref. [237] by a factor of 1.3 since the updated input data $\Gamma(\psi' \to J/\psi\pi\pi)$ is larger than the old experimental value used in Ref. [237] by the same factor of 1.3.

An interesting prediction in the CL approach is the prediction for the ratio

$$R = \frac{\Gamma(\psi' \to J/\psi\, \pi^0)}{\Gamma(\psi' \to J/\psi\, \eta)}, \tag{4.172}$$

which provides a measure of the light-quark mass ratio $r = (m_d - m_u)/(m_s - (m_u + m_d)/2)$. This belongs to the class of hadronic transitions, which violate heavy quark spin symmetry (HQSS) [235]. For heavy mesons, there are only two types of operators that break HQSS. In the parent's rest frame, the most general spin symmetry breaking term is of the form $\mathbf{a} \cdot \boldsymbol{\sigma}$, where $\boldsymbol{\sigma}$ are the Pauli matrices. In an arbitrary frame one observes that any Γ-matrix sandwiched between two projectors $(1 + \not{v})/2$, or $(1 - \not{v})/2$ can be expressed in terms of $\sigma_{\mu\nu}$ sandwiched between the same projectors:

$$\frac{1 + \not{v}}{2} 1 \frac{1 + \not{v}}{2} = \frac{1 + \not{v}}{2}, \qquad \frac{1 + \not{v}}{2} \gamma_5 \frac{1 + \not{v}}{2} = 0, \qquad \frac{1 + \not{v}}{2} \gamma_\mu \frac{1 + \not{v}}{2} = v_\mu \frac{1 + \not{v}}{2},$$

$$\frac{1 + \not{v}}{2} \gamma_\mu \gamma_5 \frac{1 + \not{v}}{2} = \frac{1}{2} \epsilon_{\mu\nu\alpha\beta} v^\nu \frac{1 + \not{v}}{2} \sigma^{\alpha\beta} \frac{1 + \not{v}}{2}, \frac{1 + \not{v}}{2} \gamma_5 \sigma_{\mu\nu} \frac{1 + \not{v}}{2} = -\frac{i}{2} \epsilon_{\mu\nu\alpha\beta} \frac{1 + \not{v}}{2} \sigma^{\alpha\beta} \frac{1 + \not{v}}{2};$$

there are analogous relations with $(1 + \not{v})/2 \to (1 - \not{v})/2$. We use here $\epsilon_{0123} = +1$. Let us define

$$\sigma_{\mu\nu}^{(\pm)} = \frac{1 \pm \not{v}}{2} \sigma_{\mu\nu} \frac{1 \pm \not{v}}{2}. \tag{4.173}$$

In the parent's rest frame, $\sigma_{\mu\nu}^{(\pm)}$ reduce to Pauli matrices. From the previous identities it follows that the most general spin symmetry breaking terms are of the form $G_1^{\mu\nu} \sigma_{\mu\nu}^{(+)}$, or $G_2^{\mu\nu} \sigma_{\mu\nu}^{(-)}$, with $G_i^{\mu\nu}$ two arbitrary antisymmetric tensors. One expects that any insertion of the operator $\sigma_{\mu\nu}^{(\pm)}$ gives a suppression factor $1/m_Q$.

Using partial conservation of axial-vector current, Ioffe and Shifman [242] give the prediction

$$R = \frac{27}{16} \left[\frac{\mathbf{p}_\pi}{\mathbf{p}_\eta} \right]^3 \left[\frac{m_d - m_u}{m_s - (m_u + m_d)/2} \right]^2. \tag{4.174}$$

The new BES experiment (see Section 7.6A) [241] provides a new precision value of R. With the conventional values of the current quark masses, the prediction of (4.174) is smaller than the BES value by about a factor of 3 [241]. So (4.174) should be regarded as an order of magnitude estimate.

The calculation of R in the CL approach is straightforward. The most general spin breaking Lagrangian for the processes $\psi' \to J/\psi \pi^0, \eta$ is

$$\mathcal{L} = i\epsilon_{\mu\nu\rho\lambda} \left[\langle J' \sigma^{\mu\nu} \bar{J} \rangle - \langle \bar{J} \sigma^{\mu\nu} J' \rangle \right] v^\rho\, \partial^\lambda \left[\frac{iA}{4} \langle \hat{m}(\Sigma - \Sigma^\dagger) \rangle + B\eta' \right] + h.c.. \tag{4.175}$$

The couplings A and B have dimension $(\text{mass})^{-1}$; the B term contributes to the ratio (4.172) via the mixing $\pi^0 - \eta'$ and $\eta - \eta'$. There are no terms with the insertion of two σ terms; the two P and C conserving candidates $\epsilon_{\mu\nu\rho\lambda} \left[\langle J' \sigma^{\mu\tau} \bar{J} \sigma_\tau{}^\nu \rangle + \langle \bar{J} \sigma^{\mu\tau} J' \sigma_\tau{}^\nu \rangle \right] v^\rho \partial^\lambda \langle \hat{m}(\Sigma - \Sigma^\dagger) \rangle$ and $\epsilon_{\mu\nu\rho\lambda} \left[\langle J' \sigma^{\mu\nu} \bar{J} \sigma^{\rho\lambda} \rangle + \langle \bar{J} \sigma^{\mu\nu} J' \sigma^{\rho\lambda} \rangle \right] \langle \hat{m}(\Sigma - \Sigma^\dagger) \rangle$ both vanish.

Using the Lagrangian (4.175) and taking into account the mixings (4.163) and (4.164), we can calculate the ratio (4.172)

$$R = \frac{27}{16} \left[\frac{\mathbf{p}_\pi}{\mathbf{p}_\eta} \right]^3 \left[\frac{m_d - m_u}{m_s - (m_u + m_d)/2} \right]^2 \left[\frac{1 + \dfrac{2B}{3A} \dfrac{\hat{\lambda} f_\pi}{m_{\eta'}^2 - m_{\pi^0}^2}}{1 + \dfrac{B}{A} \dfrac{\hat{\lambda} f_\pi}{m_{\eta'}^2 - m_\eta^2}} \right]^2. \tag{4.176}$$

If we neglect the $\pi^0 - \eta'$ and $\eta - \eta'$ mixings, (4.176) reduces to the simple result (4.174). So far B/A in (4.176) is not determined yet. Taking the $\eta - \eta'$ mixing angle $\theta_P \approx -20°$ [10] and using the new BES data on R [241], one can determine B/A from (4.176): $B/A = -1.42 \pm 0.12$ or -3.11 ± 0.15 [241].

The $\pi\pi$ transitions between P-wave quarkonia, $2^3P_{J_i} \to 1^3P_{J_f} + \pi + \pi$, have been studied in Ref. [237]. The obtained transition rates $\Gamma(2^3P_{J_i} \to 1^3P_{J_f}\pi\pi)$ are of the order of 10^{-1}–10^{-2} keV [237]. The relations between different $\Gamma(2^3P_{J_i} \to 1^3P_{J_f}\pi\pi)$ reflect the symmetry in the E1E1 multipole expansion [230], so that experimental tests of these relations are of special interest.

In the CL approach, the single pseudoscalar meson transitions between heavy quarkonia states such as

$$^3P_{J'} \to {}^3P_J\pi^0 \text{ and } {}^3P_J\eta \qquad (4.177)$$

are chiral-breaking but spin conserving [235], which are important for transitions forbidden in the SU(3) $\times$ SU(3) symmetry limit.

To first order in the chiral breaking mass matrix we consider the quantities:

$$\langle \hat{m}(\Sigma + \Sigma^\dagger) \rangle \text{ and } \langle \hat{m}(\Sigma - \Sigma^\dagger) \rangle. \qquad (4.178)$$

The first quantity is parity even, while the second is parity odd; both have $C = +1$.

The only term spin-conserving and of leading order in the current quark masses contributing to the transition (4.177) is

$$\langle J_\mu \bar{J}_\nu \rangle v_\rho \epsilon^{\mu\nu\rho\sigma} \partial_\sigma \left[\alpha \frac{i f_\pi}{4} \langle \hat{m}(\Sigma - \Sigma^\dagger) \rangle + \beta f_\pi \eta' \right], \qquad (4.179)$$

where α and β are coupling constants of dimensions $(\text{mass})^{-2}$. The direct coupling to η' contributes through the mixing (4.163). The spin symmetry of the heavy sector gives relations among the modulus square matrix elements of the transitions between the two P-wave states. In particular we find that

$$|\mathcal{M}|^2({}^3P_0 \to {}^3P_0\pi) = |\mathcal{M}|^2({}^3P_2 \to {}^3P_0\pi) = 0, \qquad (4.180)$$

and that all non-vanishing matrix elements can be expressed in terms of $^3P_0 \to {}^3P_1\pi$:

$$|\mathcal{M}|^2({}^3P_1 \to {}^3P_1\pi) = \frac{1}{4}|\mathcal{M}|^2({}^3P_0 \to {}^3P_1\pi), \qquad |\mathcal{M}|^2({}^3P_1 \to {}^3P_2\pi) = \frac{5}{12}|\mathcal{M}|^2({}^3P_0 \to {}^3P_1\pi),$$

$$|\mathcal{M}|^2({}^3P_2 \to {}^3P_2\pi) = \frac{3}{4}|\mathcal{M}|^2({}^3P_0 \to {}^3P_1\pi), \qquad |\mathcal{M}|^2({}^1P_1 \to {}^1P_1\pi) = |\mathcal{M}|^2({}^3P_0 \to {}^3P_1\pi), \quad (4.181)$$

where π stays for π^0 or η. The relations (4.181) can be generalized for any spin-conserving transition between $l = 1$ multiplets, leading to the same results as the QCD double multipole expansion [230]. Predictions for widths can be easily obtained from (4.179).

Now we consider the $\pi\pi$ transitions of D-wave quarkonia. Theoretical studies of HTs of D-wave quarkonia have been carried out by several authors in different approaches leading to quite different predictions [237, 243–248]. We briefly review the approach in Refs. [247, 248], and compare the predictions with recent experimental results.

Since the $\psi(3770)$ (or ψ'') lies above the $D\bar{D}$ threshold, it is believed that it decays mainly into $D\bar{D}$ [10]. Experimental observations show that the directly measured $e^+e^- \to \psi(3770)$ cross-section and the $e^+e^- \to \psi(3770) \to D\bar{D}$ cross-section are different [249], suggesting considerable non-$D\bar{D}$ decay modes of $\psi(3770)$. $\psi(3770) \to J/\psi\,\pi\pi$ is one possibility.

If $\psi(3770)$ is regarded as a pure $1D$ state, the predicted leptonic width will be smaller than the experimental value by an order of magnitude. The $\psi(3770)$ is often regarded as a mixture of the $1D$ and $2S$ states [247, 248, 250]: $\psi' = |2S\rangle \cos\theta + |1D\rangle \sin\theta$, $\psi(3770) = -|2S\rangle \sin\theta + |1D\rangle \cos\theta$. θ can be determined by fitting the ratio of the leptonic widths of ψ' and $\psi(3770)$. The determination of θ in

the Cornell potential model [177, 191] and the improved QCD motivated potential model by Chen and Kuang (CK) [251] (which leads to more successful phenomenological results) are: $\theta = -10°$ (Cornell) and $\theta = -12°$ (CK).

The rate of this E1E1 transition is [247]

$$\Gamma(\psi(3770){\to}J/\psi\pi\pi) = |C_1|^2 \left[\sin^2\theta \, G(\psi') \, |f_{2010}^{111}(\psi')|^2 + \frac{4}{15}\left|\frac{C_2}{C_1}\right|^2 \cos^2\theta \, H(\psi'') \, |f_{1210}^{111}(\psi'')|^2 \right].$$
(4.182)

Since there is no available data to determine C_2, we take an approximation to estimate C_2. In Ref. [237], it is assumed that $\langle\pi\pi|E_k^a E_l^a|0\rangle \propto \langle gg|E_k^a E_l^a|0\rangle$, i.e., that the factor describing the conversion of the two gluons into $\pi\pi$ is approximately independent of the pion momenta in the HTs under consideration. In this approximation, we obtain [237]

$$C_2 \approx 3C_1.$$
(4.183)

So it is possible that $C_2/C_1 \sim \mathcal{O}(1)$.

Table 4.29: The predicted transition rate $\Gamma(\psi(3770){\to}J/\psi \ \pi^+\pi^-)$ (in keV) in the Cornell model and the CK model with the updated input data (4.170). The corresponding branching ratios are listed in the brackets using the total width of $\psi(3770)$ given in Ref. [10].

| | $\Gamma(\psi(3770){\to}J/\psi\pi^+\pi^-)$ (keV) | |
	Cornell	CK
$C_2 \approx 3C_1$	139 [$(0.59 \pm 0.07)\%$]	147 [$(0.62 \pm 0.07)\%$]
$C_2 \approx C_1$	26 [$(0.11 \pm 0.01)\%$]	32 [$(0.14 \pm 0.02)\%$]

For comparison, we list the predicted rate $\Gamma(\psi(3770){\to}J/\psi \ \pi^+\pi^-)$ with $C_2/C_1 = 3$ and $C_2/C_1 = 1$ in Table 4.29.[19] Note that S–D mixing only affects a few percent of the rate, so that the rate is essentially $\Gamma(\psi(2D){\to}J/\psi \ \pi^+\pi^-)$.

Recently, BES has measured the rate $\Gamma(\psi(3770){\to}J/\psi + \pi^+ + \pi^-)$ based on 27.7 pb^{-1} data of $\psi(3770)$. The result is $\Gamma(\psi(3770){\to}J/\psi + \pi^+ + \pi^-) = 80 \pm 32 \pm 21$ keV [252] (see Eq. (4.191) in Section 7.6C). Equation (4.182) is in agreement with the central value of the BES result with $C_2/C_1 \approx 2$. Considering the large error in the BES experiment, C_2/C_1 can still be in the range $0.8 \leq C_2/C_1 \leq 2.8$. We expect more precise future measurements to give a better determination of C_2/C_1.

For the Υ system, the state mixings are much smaller [253]. Neglecting such mixings, the predicted rate of $\Upsilon(1^3D_1){\to}\Upsilon\pi\pi$ in the Cornell model with $C_2/C_1 = 3$ was $\Gamma(\Upsilon(1^3D_1){\to}\Upsilon\pi\pi) \approx 24$ keV [237]. Taking the central value $C_2/C_1 \approx 2$ determined from BES data, the prediction is $\Gamma(\Upsilon(1^3D_1){\to}\Upsilon\pi\pi) \approx 11$ keV. Considering the above range of C_2/C_1, we predict 1.8 keV $\leq \Gamma(\Upsilon(1^3D_1) \to \Upsilon\pi\pi) \leq 21$ keV.

HTs are useful processes to investigate the h_c [or $\psi(1^1P_1)$] and h_b [or $\Upsilon(1^1P_1)$] states. h_c and h_b are of special interest since the difference between the mass of the 1^1P_1 state and the centre-of-gravity of the 1^3P_J states gives useful information about the spin-dependent interactions between Q and $\bar{Q}$. The possibilities to detect h_c and h_b at e^+e^- colliders, in $^3S_1{\to}\pi^0 \ ^1P_1$, $^1P_1{\to}\pi\pi \ ^3S_1$, and $^1P_1{\to}\pi^0 \ ^3S_1$ transitions have been studied in Refs. [229, 237, 248, 255, 256]; h_c could also be detected at the B factories [257], depending on the value for the $B{\to}h_c K$ branching ratio. So far, the h_b has not been experimentally found, while the h_c has probably been observed, based on recent preliminary results presented by CLEO [258] and E835 [259]. CLEO has observed significant excess of events in $\psi(2S){\to}\pi^0 h_c{\to}\pi^0\gamma\eta_c$, in both exclusive and inclusive η_c decays. E835 has a significant excess of events

---

[19]The values listed in Table 4.29 are larger than those given in Refs. [247, 248] since the updated input data values are larger.

in $\bar{p}p{\to}h_c{\to}\eta_c\gamma{\to}3\gamma$. The mass of the CLEO and E835 candidates are compatible, and very close to the centre-of-gravity. For more details we refer to Chapter 3.

7.3 Nonrelativistic coupled-channel approach to hadronic transitions

Since a heavy quarkonium Φ lying above the threshold can decay into a pair of heavy flavour mesons $\mathcal{D}\bar{\mathcal{D}}$ [$\mathcal{D}$ stands for D mesons (for $c\bar{c}$) and B mesons (for $b\bar{b}$)], there must exist Φ–$\mathcal{D}$–$\bar{\mathcal{D}}$ couplings as shown in Fig. 4.14.
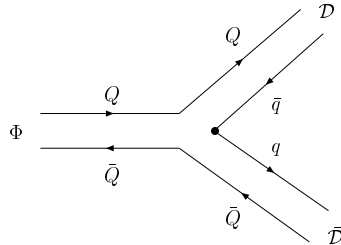
Fig. 4.14: Coupling of the heavy quarkonium Φ to its decay channel $\mathcal{D}\bar{\mathcal{D}}$.

A complete theory should include not only the part describing Φ, but also the part corresponding to the $\mathcal{D}\bar{\mathcal{D}}$ sector as well. Such a theory is the so-called coupled-channel (CC) theory.

It is hard to study the Φ–$\mathcal{D}$–$\bar{\mathcal{D}}$ vertex from the first principles of QCD, since it is the vertex of three bound states. There are various models describing CC effects; the two well-accepted models are the Cornell CC model (CCCM) [177, 191, 260] and the unitary quark model (UQM) [253]. The Φ–$\mathcal{D}$–$\bar{\mathcal{D}}$ vertex in the UQM is taken to be the $^3P_0$ quark-pair-creation (QPC) mechanism [261]. The parameters in the UQM are carefully adjusted so that the model gives a better fit to the $c\bar{c}$ and $b\bar{b}$ spectra, leptonic widths, etc. It is shown that the QPC model gives acceptable results even for OZI-allowed productions of light mesons [261, 262], which is relevant in the calculation of the HT amplitudes in the CC theory.

The formulation of the theory of HTs in the framework of the UQM was given in Ref. [263]. The Feynman diagrams for $n_i^3S_1{\to}n_f^3S_1\pi\pi$ are shown in Fig. 4.15. We see that there are more channels of $\pi\pi$ transitions in this theory than in the single-channel theory. Figures 4.15(a)–4.15(d) are based on the QCDME mechanism; we designate this the MGE part. Figures 4.15(e) and 4.15(f) are based on a new $\pi\pi$ transition mechanism via QPC; we designate this the QPC part. Figure 4.15(a) is similar to Fig. 4.13 but with state mixings, so the single-channel amplitude mentioned in Section 7.2 is only a part of Fig. 4.15(a).

Table 4.30: $\Gamma(\Upsilon'{\to}\Upsilon\pi\pi)$, $\Gamma(\Upsilon''{\to}\Upsilon\pi\pi)$, and $\Gamma(\Upsilon''{\to}\Upsilon'\pi\pi)$ predicted in CC theory, with $\cos\vartheta = -1$ and -0.676, together with the updated experimental values [10]. $\pi\pi$ stands for the sum over all the $\pi^+\pi^-$ and $\pi^0\pi^0$ channels.

	Theory		Expt.
	$\cos\vartheta = -1$	$\cos\vartheta = -0.676$	
$\Gamma(\Upsilon'{\to}\Upsilon\pi\pi)$ (keV)	14	13	12.0 ± 1.8
$\Gamma(\Upsilon''{\to}\Upsilon\pi\pi)$ (keV)	1.1	1.0	1.72 ± 0.35
$\Gamma(\Upsilon''{\to}\Upsilon'\pi\pi)$ (keV)	0.1	0.3	1.26 ± 0.40

Since state mixings and the QPC vertices are all different in the $c\bar{c}$ and the $b\bar{b}$ systems, the predictions for the Υ HT rates by taking the input (4.170) will be different from those in the single-channel
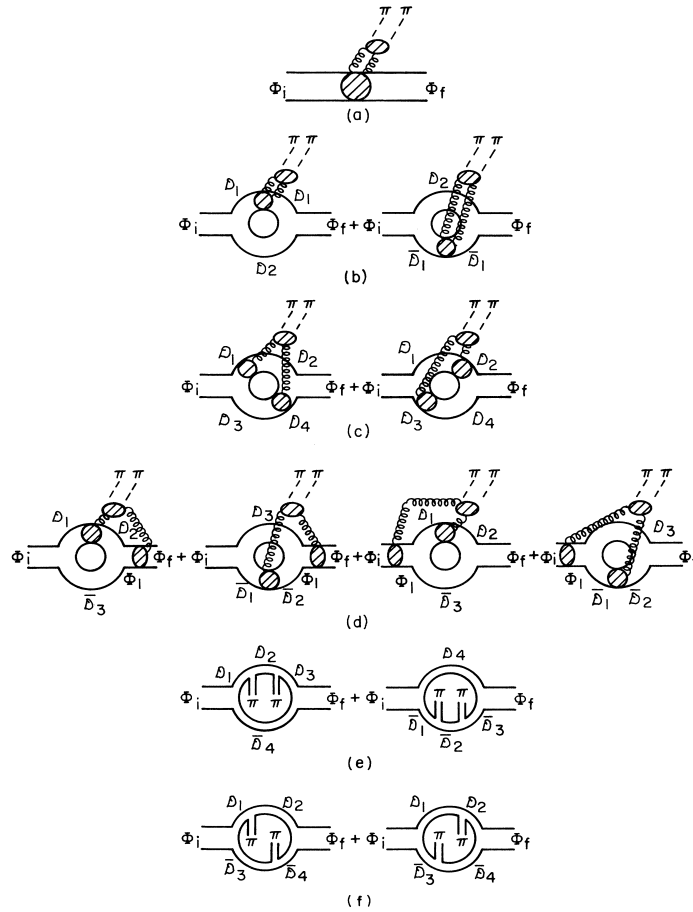
Fig. 4.15: Diagrams for hadronic transitions in the CC approach. Quoted from Ref. [263].

theory. Such predictions were studied in Ref. [263]. Note that for a given QPC model, the QPC part is fixed, while the MGE part still contains an unknown parameter C_1 after taking the approximation $C_2 \approx 3C_1$. Since there is interference between the MGE and the QPC parts, the phase of C_1 is important; explicitly, $C_1 = |C_1|\, e^{i\vartheta}$. The data of the HT rate and $M_{\pi\pi}$ distribution in $\psi' \to J/\psi\,\pi\pi$ can be taken as inputs to determine C_1 and ϑ [263]. Considering the error bars in the $M_{\pi\pi}$ distribution, ϑ is restricted in the range $-1 \leq \cos\vartheta \leq -0.676$ [263]. The predicted transition rates in the Υ system are listed in Table 4.30 together with the experimental results for comparison. We see that the obtained $\Gamma(\Upsilon' \to \Upsilon\pi\pi)$ is in good agreement with the experiment, and the results of $\Gamma(\Upsilon'' \to \Upsilon\pi\pi)$ and $\Gamma(\Upsilon'' \to \Upsilon'\pi\pi)$ are in agreement with the experiment at the level of 2σ and 2.4σ, respectively.

Next we look at the predicted $M_{\pi\pi}$ distributions. It is pointed out in Ref. [265] that there is a tiny difference between the measured $M_{\pi\pi}$ distributions in $\psi' \to J/\psi\pi\pi$ and $\Upsilon' \to \Upsilon\pi\pi$. In the single-channel theory, the formulas for these two $M_{\pi\pi}$ distributions are the same. In the CC theory, once C_1 and ϑ are determined, the $M_{\pi\pi}$ distribution of $\Upsilon' \to \Upsilon\pi\pi$ is uniquely determined. It is shown in Ref. [263] that the prediction fits the experiment [265] very well

However, the situation of the $M_{\pi\pi}$ distributions of $\Upsilon'' \to \Upsilon\pi^+\pi^-$ and $\Upsilon'' \to \Upsilon'\pi^+\pi^-$ are more complicated. Comparison of the CC predictions with the CLEO experiment will be shown in Section 7.5E.

7.4 Application of the QCD multipole expansion to radiative decays of the J/ψ

In the above sections, QCDME is applied to various HTs in which Φ_i and Φ_f are composed of the same heavy quarks. In this case, the dressed (constituent) quark field $\Psi(\mathbf{x}, t)$ needs not actually to be quantized. Now we generalize QCDME theory to processes including changes of heavy quark flavour and heavy quark pair annihilation or creation, for which the quantization of $\Psi(\mathbf{x}, t)$ is needed. This has been studied in Ref. [231] with the electroweak interactions included as well.
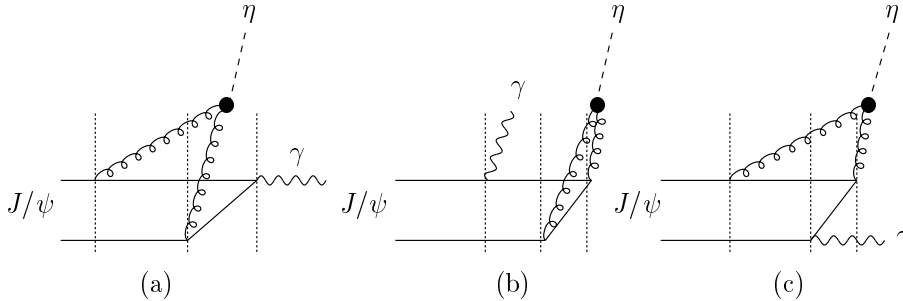

Fig. 4.16: Feynman diagrams for the radiative decay process $J/\psi \rightarrow \gamma + \eta$.

An example of application of such a theory is $J/\psi \rightarrow \gamma\eta$ (see Section 5.5 for a discussion in the framework of Ref. [154]). This process has been studied in the framework of perturbative QCD and the nonrelativistic quark model in Ref. [264], but the predicted rate is significantly smaller than the experimental value. The η momentum in this process is $q_\eta = 1.5$ Gev. If η is converted from two emitted gluons from the heavy quark, the typical gluon momentum is then $k \sim q_\eta/2 \sim 750$ MeV. At this momentum scale perturbative QCD does not work well but QCDME works [231]. The Feynman diagrams for this process in the QCDME approach are shown in Fig. 4.16, in which the intermediate states marked between two vertical dotted lines are all treated as bound states. In this sense this approach is nonperturbative.

Since this process is dominated by E1M2 transition; the transition rate depends on the pseudoscalar nonet mixing angle θ_P. Taking the value $\theta_P \approx -20°$ determined from the $\eta \rightarrow \gamma\gamma$ and $\eta' \rightarrow \gamma\gamma$ rates [10], we obtain [231]

$$\Gamma(J/\psi \rightarrow \gamma\eta) = 0.041 \left(\frac{\alpha_M}{\alpha_E} \right) \text{keV}, \qquad \mathcal{B}(J/\psi \rightarrow \gamma\eta) = (4.7 \pm 0.2) \times 10^{-4} \left(\frac{\alpha_M}{\alpha_E} \right). \qquad (4.184)$$

With the reasonable value $\alpha_M/\alpha_E = 1.8$, the predicted branching ratio can agree with the experimental value $B_{\exp}(J/\psi \rightarrow \gamma\eta) = (8.6 \pm 0.8) \times 10^{-4}$ [10]. To avoid the uncertainties from α_M/α_E and θ_P, we take the ratio of $\Gamma(J/\psi \rightarrow \gamma\eta)$ to another E1M2 transition rate $\Gamma(\psi' \rightarrow J/\psi\eta)$. The theoretical prediction is [231]

$$R_\eta \equiv \frac{\Gamma(J/\psi \rightarrow \gamma\eta)}{\Gamma(\psi' \rightarrow J/\psi\eta)} = 0.012. \qquad (4.185)$$

In R_η, uncertainties in the H factors cancel, so R_η offers a direct test of the MGE mechanism. (4.185) is in agreement with the experimental value $R_\eta|_{\exp} = 0.009 \pm 0.003$ [10] at the 1σ level.

This approach can also be applied to $J/\psi \rightarrow \gamma\eta'$. With $\theta_P \approx -20°$, we obtain

$$R_{\eta'} \equiv \frac{\Gamma(J/\psi \rightarrow \gamma\eta')}{\Gamma(\psi' \rightarrow J/\psi\eta)} = \left| \frac{\mathbf{q}(J/\psi \rightarrow \gamma\eta')}{\mathbf{q}(J/\psi \rightarrow \gamma\eta))} \right|^3 \left| \frac{m_{\eta'}^2(\sqrt{2}\cos\theta_P + \sin\theta_P)}{m_\eta^2(\cos\theta_P - \sqrt{2}\sin\theta_P)} \right|^2 R_\eta = 0.044. \qquad (4.186)$$

This is also in agreement with the experimental value $R_{\eta'}|_{\exp} = 0.044 \pm 0.010$ [10].

We would like to mention that this approach is not suitable for $\Upsilon \rightarrow \gamma\eta$ since the typical gluon momentum in this process is $k \sim q_\eta/2 \sim 2.4$ Gev, appropriate for perturbative QCD, but not for QCDME.
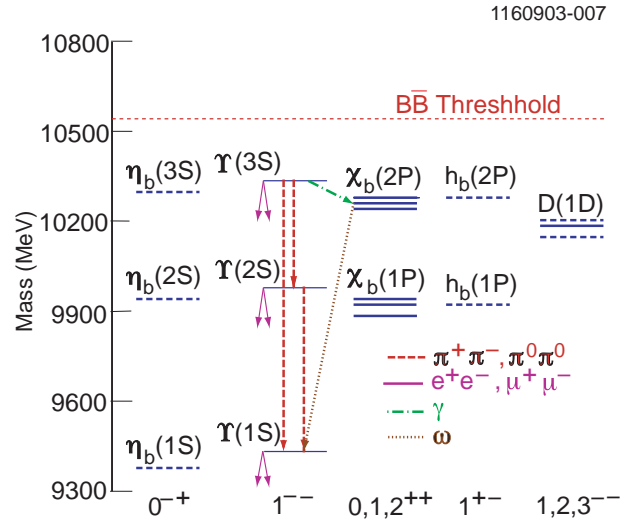
Fig. 4.17: Allowed photon, dipion, and omega transitions allowed within the $b\bar{b}$ system.

7.5   Hadronic transition experiments in the $b\bar{b}$ system

A. Experimental analysis of hadronic transitions — bottomonium

We see from Eq. (4.166) that, in the framework of QCDME, the transition amplitude contains an MGE factor and a H factor. Selection rules, as well as the limited phase space, restrict the possible transitions. A summary of the rich spectroscopy afforded by bottomonia is shown in Fig. 4.17

The principal experimental observables here are the partial widths for the transitions between bottomonia and the Dalitz plot variables: the $\pi\pi$ and $\Upsilon\pi$ invariant mass spectra, and the angular distributions between final-state particles. To measure the transition $\Upsilon'' \to \Upsilon\pi\pi$, for example, in electron–positron annihilation data (where Υ'' is produced at rest, and polarized along the beam axis), one can use the constraint that the Υ energy can be inferred directly from the measurement of the pion four-momenta to calculate the mass recoiling against the dipion system. As with the $\gamma\gamma$ cascades, one differentiates the "exclusive" case in which the Υ decays to a clean, background-free topology, such as $\mu^+\mu^-$ or e^+e^-, from the "inclusive" case in which all events are accepted, and one calculates the mass recoiling against all oppositely-signed dipion pairs. In the former case, one, therefore, selects events consistent with the cascade: $\Upsilon'' \to \Upsilon\pi\pi$, $\Upsilon \to l^+l^-$, allowing one to isolate a very clean sample, but at the expense of lower overall efficiency owing to the small ($\sim 2\%$) dileptonic BR's of the final state Υ's.

B. Branching ratios and partial widths

The CLEO II mass spectra recoiling against charged dipions, for data taken at the Υ' [266], are shown in Figs. 4.18 and 4.19, and illustrate the trade-off between the higher statistical power of the inclusive data sample vs. the better signal-to-noise of the exclusive data sample.[20]

Branching ratios are calculated based directly on the number of events found in each peak. Predictions for the partial widths in the nonrelativistic single-channel and coupled-channel theories are shown in Tables 4.28 and 4.30. In addition to CLEO, the tabulated branching ratios for $\Upsilon' \to \Upsilon\pi\pi$ also include measurements made by the ARGUS [265], CLEO I [267], CUSB-I [268], and Crystal Ball [269] collaborations. The CLEO II collaboration are also able to derive estimates for the transition rates for $\Upsilon'' \to \Upsilon' + X$ by performing a hand scan of the events it reconstructs in $\Upsilon'' \to \Upsilon' + X$, $\Upsilon' \to \Upsilon\pi^+\pi^-$, $\Upsilon \to l^+l^-$, and using the unitarity constraint that the sum of the dipion transitions plus the radiative tran-

---

[20]Because of the poor signal-to-noise ratio, the $\Upsilon'' \to \Upsilon\pi^0\pi^0$ transitions cannot be studied inclusively.
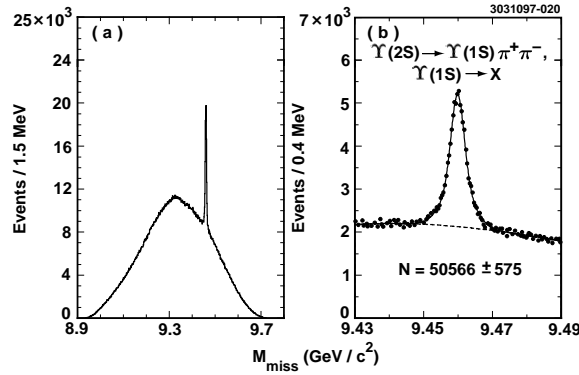
Fig. 4.18: Mass recoiling against two oppositely charged tracks, assumed to be pions, for data taken at the Υ' resonance.
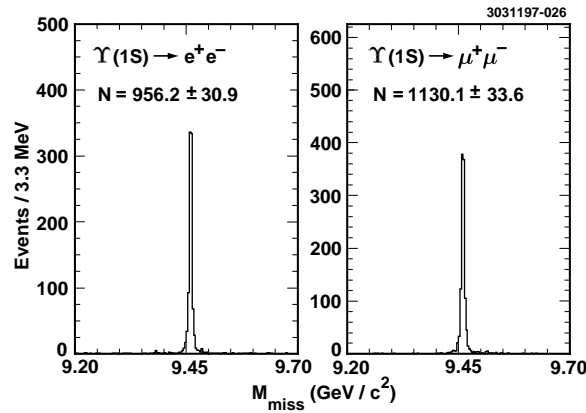

Fig. 4.19: Mass recoiling against two oppositely charged tracks, assumed to be pions, for data taken at the Υ' resonance, with the additional restriction that there be exactly four charged tracks in the event, and that the two most energetic charged tracks be consistent with e^+e^- or $\mu^+\mu^-$.

sitions must saturate the overall $\Upsilon''\rightarrow\Upsilon' + X$ decay rate to determine X. These values have been compiled along with the direct observation of the $\Upsilon''\rightarrow\Upsilon'\pi^0\pi^0$ and $\Upsilon''\rightarrow\Upsilon'\pi^+\pi^-$ transitions. According to isospin symmetry, the $\pi^+\pi^-$ transition rate is expected to be twice that of the $\pi^0\pi^0$ transition, modulo the ratios of available phase space ($\pi^0\pi^0/\pi^+\pi^-$) (1.36 for $\Upsilon''\rightarrow\Upsilon'\pi^0\pi^0$ and 1.02 for $\Upsilon''\rightarrow\Upsilon\pi^0\pi^0$). The measurements to date are generally consistent with this expectation, with the exception of $\Upsilon''\rightarrow\Upsilon'\pi^+\pi^-$. Curiously, despite an inability to match the dipion mass distributions for the $\Upsilon''\rightarrow\Upsilon\pi\pi$ transitions (Secs. 7.2 and 7.3), the QCDME approach gives a better match for this partial width than for $\Upsilon''\rightarrow\Upsilon'\pi\pi$.

C. Angular distributions

In the nonrelativistic limit, orbital angular momentum and spin are separately conserved. The spin of a bottomonium resonance produced at e^+e^- colliders lies along the beam axis. In $\Upsilon(nS)\rightarrow\Upsilon\pi^+\pi^-$, the orbital angular momentum between the pions, or the orbital angular momentum between the dipion system and Υ is a useful observable in addition to the polarization of Υ. Predictions for the populations of the allowed angular momentum states have been made for both the ψ system as well as the Υ system [240,270]. All measurements to date (e.g., by verifying in exclusive events that the angular distribution of the leptons relative to the beam axis follows $dN/d(cos\theta) \sim 1+cos^2\theta$) from ARGUS, CLEO, and CUSB give strong evidence that the daughter Υ is indeed polarized along the beam axis in the dipion transitions, and are consistent with an S-wave decay. The other allowed amplitude is a possible D-wave contribution in the dipion system [cf. Eq. (4.167)]. Convincing evidence for a large D-wave component of the

dipion system has not yet been presented, although it has received some theoretical attention [271–273], and suggestions for non-S-wave anisotropy are found in both the $\Upsilon'' \rightarrow \Upsilon \pi^+ \pi^-$ [266] and $\Upsilon' \rightarrow \Upsilon \pi^+ \pi^-$ data [265, 274], both of which show $\sim 2\sigma$ indications of a D-wave contribution at the few percent level [266]. Mapping out the ratio of D-wave to S-wave amplitudes as a function of dipion mass in the Υ'' system is a project requiring substantially more statistics than have been accumulated to date; expectations are that a D-wave amplitude would be more observable at low values of invariant mass, corresponding to higher energy release in the Υ'' decay. Such an analysis is currently underway at CLEO and should mature within the next year.

D. Single pion transitions

For dipion transitions Yan [230], collaborating with Kuang [237], and their work later extended by Zhou and Kuang [263], estimated the magnitude of the second piece of the product matrix element, the hadronization term of the transition amplitude. An immediate consequence of the multipole approach is the expected suppression of the case $X = \eta$ relative to $X = \pi\pi$. The former system has the wrong quantum numbers for two $E1$ gluons, and proceeds in lowest order as either $E1 \cdot M2$ or $M1 \cdot M1$ in QCDME. Since the mass dependence of the chromomagnetic transitions goes as m^{-4} (m = quark mass), QCDME, therefore predicts that the ratio for $\mathcal{B}(\Upsilon' \rightarrow \Upsilon \eta)/\mathcal{B}(\Upsilon' \rightarrow \Upsilon \pi\pi)$ should be substantially smaller than the ratio $\mathcal{B}(\psi' \rightarrow \psi \eta)/\mathcal{B}(\psi' \rightarrow \psi \pi\pi)$. By contrast, if the ratio of $\pi^+ \pi^-$ to η transitions were governed by phase space alone, the η transition would be about 15% of the $\pi^+ \pi^-$ transition for $\Upsilon' \rightarrow \Upsilon$. The most recent CLEO analysis yielded an upper limit: $\mathcal{B}(\Upsilon' \rightarrow \Upsilon \eta) < 0.0028$, in qualitative agreement with the rule given above.

The isospin-violating decay $\psi(2S) \rightarrow \pi^0 \psi(1S)$ and the M1 transition $\psi(2S) \rightarrow \eta \psi(1S)$ have been observed in the charmonium sector; searches for the corresponding transitions in the bottomonium sector have resulted only in the upper limit: $\Upsilon' \rightarrow \Upsilon \pi^0 < 0.11\%$. The typically poorer energy resolution in neutral particle measurements, coupled with small predicted branching fractions, makes observation of such decays difficult.

E. Dipion mass spectra

The dipion mass spectra are calculated directly from the pion four-momenta. As stated before, the invariant mass spectra are expected to peak at high mass values. This is, in fact, what is observed for the transition $\Upsilon' \rightarrow \Upsilon \pi^+ \pi^-$, as shown in Fig. 4.20, and entirely consistent with an exhaustive study of this process by the ARGUS collaboration [265]. Also shown in Fig. 4.20 are the $\pi^0 \pi^0$ mass spectra for $\Upsilon'' \rightarrow \Upsilon \pi^0 \pi^0$ and $\Upsilon'' \rightarrow \Upsilon' \pi^0 \pi^0$.

The current data show peaking at high mass for the $\Upsilon'' \rightarrow \Upsilon' \pi^+ \pi^-$ and $\Upsilon' \rightarrow \Upsilon \pi\pi$ transitions, consistent with the expectation for S→S transitions (and also consistent with charmonium results). This is the process for which the multipole expansion model, owing to the smallness of the expansion parameter, claims to have the greatest predictive power. However, the $\pi^0 \pi^0$ and $\pi^+ \pi^-$ invariant mass distributions in the $\Upsilon'' \rightarrow \Upsilon \pi^+ \pi^-$ transition show a "double bump" structure that disagrees with the gluon field multipole expansion model as well as with the expectation that the matrix element for a transition with these quantum numbers should approach zero at threshold. This is perhaps an indication that the average value of Q^2 is too large to make predictions reliably using the multipole model. It may also be an indication that a low-mass 0++ scalar (e.g., the σ) may be contributing to the intermediate state.

There have been various attempts to explain the double-peaked shape. Ref. [272,275,276] assumed the existence of a four-quark state Υ_1, which enhances the low-$M_{\pi\pi}$ region. So far such a resonance is not found experimentally. Ref. [277] assumed a large QPC part in the $\Upsilon'' \rightarrow \Upsilon \pi\pi$ amplitude whose interference with the MGE part may form a double-peaked shape. However, the systematic calculation shown in Section 7.3 does not support this assumption. Recently, another attempt considering certain models for a σ meson resonance around 500 MeV in the final state $\pi\pi$ interactions [278, 279] have been
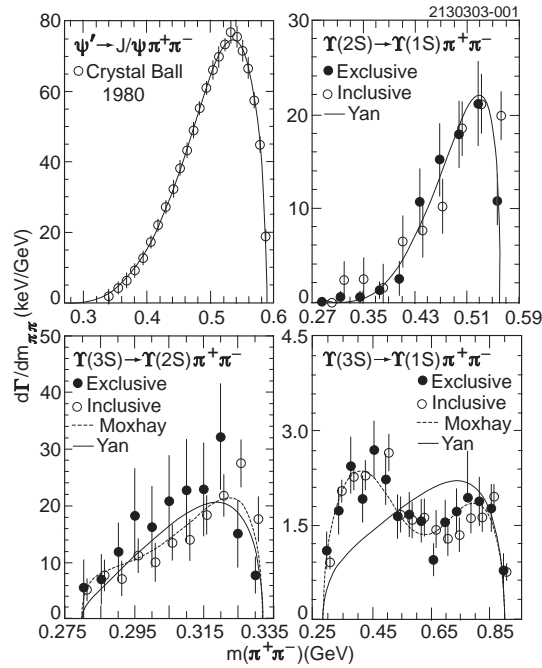
Fig. 4.20: Left: $\pi^+\pi^-$ recoil mass spectra from CLEO II using data taken at the peak of the Υ'' for a) exclusive transitions, and b) inclusive transitions, as indicated [266]. Right: $\pi^0\pi^0$ recoil mass spectrum for exclusives with the indicated cuts on dilepton mass [266].

proposed. By adjusting the free parameters in the models, the CLEO data on the $M_{\pi\pi}$ distributions can be fitted. However, the model need to be tested in other processes. Therefore, the HT $\Upsilon''\rightarrow\Upsilon\pi\pi$ is still an interesting process needing further investigation.

F. Three-pion transitions

With their large Υ'' data sample in hand, the CLEO collaboration is able to probe beyond the now-familiar dipion transitions. Of particular interest are ω-mediated transitions, which have been long-suggested as a possible path to the η_b, via: $\Upsilon''\rightarrow\eta_b\omega$. In QCDME, by colour conservation, this must correspond to three E1 gluon emissions. Although direct decays $\Upsilon''\rightarrow\eta_b\omega$ were not found, CLEO has observed significant production of Υ via $\Upsilon''\rightarrow\chi_b'(2P)\gamma$, $\chi_b'(2P)\rightarrow\Upsilon\omega$, as shown in Figs. 4.21 and 4.22.

What is actually observed are two recoil mass peaks, corresponding to decays from the $\chi_b'(2P)$ (J=2) and (J=1) states. In fact, large partial widths for such decays had been predicted (albeit indirectly) in the original QCDME formulation of Gottfried. As pointed out by Voloshin, since the ω is spin 1, the matrix element should be largely independent of the spin of the parent 2P, consistent with observation. The measured branching fractions ($\mathcal{B}(\chi_b'(J=2)\rightarrow\Upsilon\omega) = (1.0\pm0.3\pm0.1)\%$ and $\mathcal{B}(\chi_b'(J=1)\rightarrow\Upsilon\omega) = (1.6\pm0.3\pm0.24)\%$ are unexpectedly large, given the limited phase space for these decays.

G. Hadronic transitions from the $\Upsilon(4S)$

Observation of hadronic transitions from the $\Upsilon(4S)$, interesting on its own merits, would provide essential information on the $\Upsilon(4S)$ wave function. Since the $\Upsilon(4S)$ resonance is above the threshold for $B\bar{B}$ production, measurement of the dipion transitions, with partial widths a factor 10^{-4} smaller than the dominant strong decays to open bottom, require data samples of order 10^8 $\Upsilon(4S)$ events. The BaBar and Belle experiments now have accumulated samples of 100M $\Upsilon(4S)$ events and may produce the first signals for such dipion transitions soon. CLEO have produced the most recent results on these transitions, resulting only in upper limits: $\Upsilon(4S)\rightarrow\Upsilon'\pi\pi < 0.039\%$; $\Upsilon(4S)\rightarrow\Upsilon\pi\pi < 0.012\%$. Interest in such
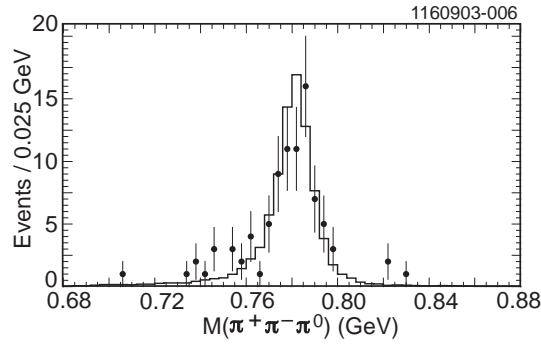
Fig. 4.21: Invariant mass of three pions in events consistent with $\Upsilon'' \to \chi_b' \gamma$; $\chi_b' \to \Upsilon \pi^+ \pi^- \pi^0$.
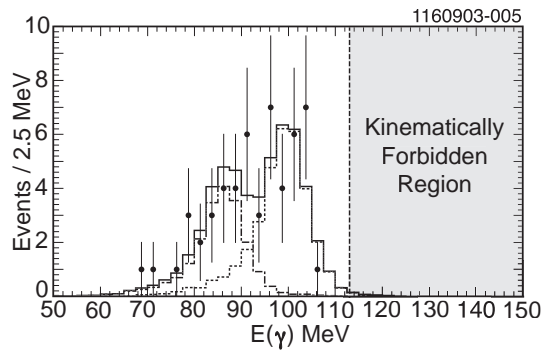

Fig. 4.22: Photon energy distribution for the previous figure's data sample, showing fits to the J=2 and J=1 states. Transitions from the J=0 state are kinematically forbidden (as indicated).

decays has recently been promoted by the BES claim of the corresponding decay in the charmonium sector: $\psi(3770) \to J\psi\pi^+\pi^-$.

H. Unanswered questions

Aside from a first-principles explanation of the dipion mass spectrum in the $\Upsilon'' \to \Upsilon \pi^+ \pi^-$ spectrum (such a three-body decay does not, unfortunately, easily lend itself to lattice gauge techniques), much experimental work remains. Among the dipion transitions one would like to observe are the η transitions between the S states, or one of the two dipion transitions involving the singlet 1^1P_1 state: the isospin-violating decay $\Upsilon'' \to h_b(1^1P_1)\pi^0$, or $\Upsilon'' \to h_b \pi^+ \pi^-$ [21], as well as the dipion transitions between the χ_b states: $\chi_b' \to \chi_b \pi\pi$. Owing to the larger total widths of the χ_b' (J=2 and J=0) states relative to the J=1 state, the first observation of this decay might be expected in the transition between the J=1 states. Transitions at higher order in QCDME, e.g., $\Upsilon'' \to \eta_b \omega$ (E1E1M1 transition), and also HT to the η_b, which is accessible through two routes, each of which involves a radiative and a hadronic transition: either $\Upsilon'' \to h_b(1^1P_1)\pi\pi$; followed by $h_b(1^1P_1) \to \eta_b\gamma$, or $\Upsilon'' \to \chi_b'\gamma$; $\chi_b' \to \eta_b \pi^+\pi^-$, would both help complete our picture of heavy quark spectroscopy (see Chapter 3). Also extremely interesting would be the observation of HTs from the recently discovered triplet D-bottomonia states ($\Upsilon(1^3D_J)$), e.g., $\Upsilon(1^3D_2) \to \Upsilon\pi^+\pi^-$, or $\Upsilon(1^3D_2) \to \Upsilon(1S)\eta$. Currently, only an upper limit exists for the product branching fraction: $\Upsilon'' \to \chi_{b,J=2}'\gamma$, $\chi_{b,J=2}' \to 1^3D$, $1^3D \to \Upsilon\pi\pi$ of 1.1×10^{-4} for the J=2 D-state, and

---

[21]For this $S \to P$ transition, Kuang & Yan predict a dipion mass distribution that peaks at *low* values of invariant mass. This is understood by the following argument: such a transition $1^- \to 0^+1^+$ can only proceed in P wave, which suppresses the high mass region.

2.7×10^{-4}, including all the D-states. A 90% c.l. upper limit is also set for the same decay chain, but with an η rather than dipion transition, of 2.3×10^{-4}.

7.6 Hadronic transition experiments in the $c\bar{c}$ system

Hadron transitions in the charmonium system where there is experimental information include $\pi^+\pi^- \to J/\psi\,\pi^0$, $\pi^+\pi^- \to J/\psi\,\eta$, and $\pi^+\pi^- \to J/\psi\,\pi\pi$. Recently evidence has been presented on $\psi(3770) \to J/\psi\,\pi^+\pi^-$ decays, and very recently, Belle announced the discovery of the $X(3872)$ [280], which is detected via $X(3872) \to J/\psi\,\pi^+\pi^-$, making it another means to study hadronic transitions. Here recent experimental results on $\pi^+\pi^- \to J/\psi\,\pi^0$, $\pi^+\pi^- \to J/\psi\,\eta$, $\pi^+\pi^- \to J/\psi\,\pi\pi$ and $\psi(3770) \to J/\psi\,\pi^+\pi^-$ will be summarized. We will shortly mention the $X(3872) \to J/\psi\,\pi^+\pi^-$ transition, which has been discussed in detail in Chapter 3, Section 8.2.

A. $\pi^+\pi^- \to J/\psi\,\pi^0$, $\pi^+\pi^- \to J/\psi\,\pi^0\,\pi^0$ and $\pi^+\pi^- \to J/\psi\,\eta$

Experimental results for the processes $\psi' \to J/\psi\,\pi^0$ and $J/\psi\,\eta$ are few and were mainly taken in the 1970s and 80s [281–285]. Recently, however, BES, using a sample of $(14.0 \pm 0.6) \times 10^6\ \psi'$ events collected with the BES II detector [286], studied ψ' decaying into $J/\psi(\pi^0, \eta)$, with π^0 and η decaying to two photons, and J/ψ to lepton pairs [241]. Events with two charged tracks identified as an electron pair or muon pair and two or three photon candidates are selected. A five constraint (5C) kinematic fit to the hypothesis $\psi' \to \gamma\gamma l^+l^-$ with the invariant mass of the lepton pair constrained to J/ψ mass is performed, and the fit probability is required to be greater than 0.01.

To remove the huge background from $\psi' \to \gamma\chi_{c1,c2}$ under the $\psi' \to J/\psi\,\pi^0$ signal, the invariant mass of the highest energy gamma and the J/ψ, $M_{\gamma_h, J/\psi}$ is required to be less than 3.49 or greater than $3.58\,\mathrm{Gev/c^2}$. Figure 4.23 shows, after this requirement, the distribution of invariant mass, $M_{\gamma\gamma}$, where the smooth background is due to $\psi(2S) \to \gamma\chi_{c1,2}$ and $J/\psi\,\pi^0\pi^0$. A Breit Wigner with a double Gaussian mass resolution function to describe the π^0 resonance plus a third-order background polynomial is fitted to the data.

In the $\psi' \to J/\psi\,\eta$ channel, the main backgrounds are from $\psi' \to J/\psi\,\pi^0\pi^0$ and $\gamma\chi_{c1,c2}$. By requiring $M_{\gamma_h, J/\psi} < 3.49\,\mathrm{Gev/c^2}$, most background from $\psi' \to \gamma\chi_{c1,c2}$ is removed. The resultant plot shown in Fig. 4.24 shows a clear η signal superimposed on background, mainly from $\psi' \to \pi^0\pi^0 J/\psi$. A fit is made using a Breit–Wigner resonance convoluted with a mass resolution function for the η signal plus a polynomial background, where the width of the η is fixed to its Particle Data Group (PDG) value [10] and the background function is determined from $\psi' \to J/\psi\,\pi^0\pi^0$ Monte Carlo simulated events that satisfy the same criteria as the data.

Table 4.31: Recent BES results on $\psi' \to J/\psi\,\pi^0$ and $\psi' \to J/\psi\,\eta$.

Channel	$J/\psi\,\pi^0$		$J/\psi\,\eta$	
Final state	$\gamma\gamma e^+ e^-$	$\gamma\gamma\mu^+\mu^-$	$\gamma\gamma e^+ e^-$	$\gamma\gamma\mu^+\mu^-$
Number of events	123 ± 18	155 ± 20	2465 ± 101	3290 ± 148
Efficiency (%)	11.21	13.34	26.94	34.07
Sys. error (%)	9.68	8.77	8.54	8.40
Correction factor	0.962	0.974	0.962	0.974
BR (%)	$0.139 \pm 0.020 \pm 0.013$	$0.147 \pm 0.019 \pm 0.013$	$2.91 \pm 0.12 \pm 0.21$	$3.06 \pm 0.14 \pm 0.25$
Combine BR (%)	$0.143 \pm 0.014 \pm 0.013$		$2.98 \pm 0.09 \pm 0.23$	
PDG (%) [10]	0.096 ± 0.021		3.16 ± 0.22	

Using the fitting results and the efficiencies and correction factors for each channel, the branching fractions listed in Table 4.31 are determined. The BES $\mathcal{B}(\psi' \to J/\psi\,\pi^0)$ measurement has improved precision by more than a factor of two compared with other experiments, and the $\psi' \to J/\psi\,\eta$ branching
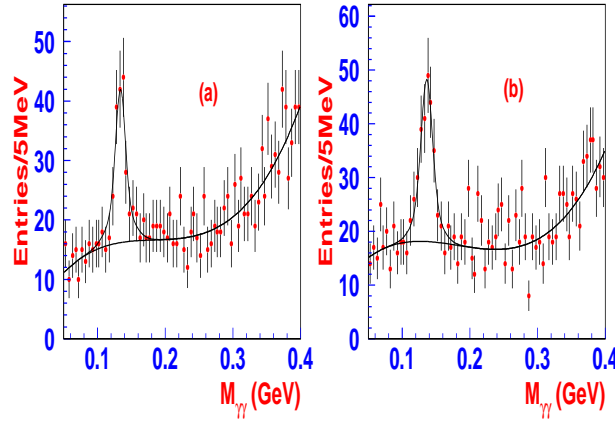
Fig. 4.23: Two-photon invariant mass distribution for candidate $\psi' \to \pi^0 J/\psi$ events for (a) $\gamma\gamma e^+ e^-$ and (b) $\gamma\gamma\mu^+\mu^-$.
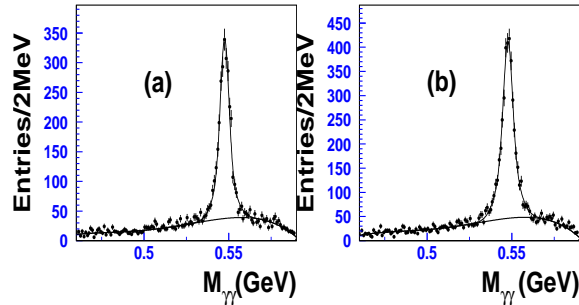

Fig. 4.24: Two-photon invariant mass distribution for candidate $\psi' \to \eta J/\psi$ events for (a) $\gamma\gamma e^+ e^-$ and (b) $\gamma\gamma\mu^+\mu^-$.

fraction is the most accurate single measurement. The BES $\mathcal{B}(\psi' \to J/\psi\ \pi^0)$ agrees better with the Mark II result [284] than with the Crystal Ball result [285]. For the comparison of the BES result with related theoretical predictions, see Section 7.2.

In another recent BES analysis [287], based on a sample of approximately $4 \times 10^6\ \pi^+\pi^-$ events obtained with the BES I detector [288], a different technique is used for measuring branching fractions for the inclusive decay $\pi^+\pi^- \to J/\psi$ anything, and the exclusive processes for the cases where $X = \eta$ and $X = \pi\pi$. Inclusive $\mu^+\mu^-$ pairs are reconstructed, and the number of $\pi^+\pi^- \to J/\psi X$ events is determined from the $J/\psi \to \mu^+\mu^-$ peak in the $\mu^+\mu^-$ invariant mass distribution. The exclusive branching fractions are determined from fits to the distribution of masses recoiling from the J/ψ with Monte Carlo determined distributions for each individual channel.

Selected events are required to have more than one and less than six charged tracks and must have two identified muon tracks with zero net charge. The two muon tracks must satisfy a one constraint kinematic fit to the J/ψ mass. Shown in Fig. 4.25 is the dimuon invariant mass distribution, $m_{\mu\mu}$, for these events. A clear peak at the J/ψ mass is evident above background.

The mass recoiling against the J/ψ candidates, m_X is determined from energy and momentum conservation. In order to distinguish $\psi(2S) \to J/\psi\pi^+\pi^-$ and $\psi(2S) \to J/\psi\pi^0\pi^0$ events, separate m_X histograms are made for events with no additional charged tracks and those with additional charged tracks. To reduce background and improve the quality of the track momentum measurements, events used for this part of the analysis are required to have a kinematic fit $\chi^2 < 7$. The m_X histograms for
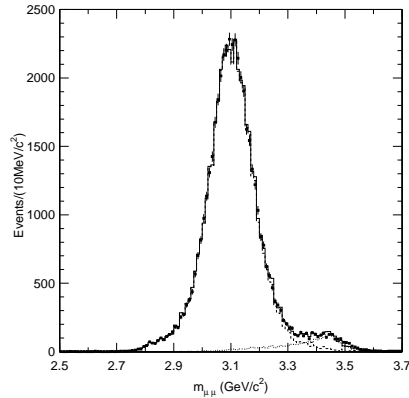
Fig. 4.25: Distribution of dimuon invariant mass, $m_{\mu\mu}$, for events that pass the $J/\psi \rightarrow \mu^+\mu^-$ kinematic fit. Dots with error bars are data. Also shown is the fit (solid histogram) to the distribution with signal (long dashed histogram) and background (short dashed histogram) shapes.

events with and without additional charged tracks, selected according to the above requirements, are shown in Figs. 4.26 and 4.27.

To determine the number of exclusive decays and separate $\psi(2S) \rightarrow J/\psi\pi^0\pi^0$ and $\psi(2S) \rightarrow J/\psi\pi^+\pi^-$ events, m_X histograms for events with and without additional charged tracks, shown in Figs. 4.26 and 4.27, are fit simultaneously. Contributions from the $\psi(2S) \rightarrow \gamma\chi_{c0}, \chi_{c0} \rightarrow \gamma J/\psi$ are expected to be very small [10] and are not included in the fit. The influence of $\pi^+\pi^- \rightarrow J/\psi\pi^0$ is also small, indeed there is no indication of such a component in Fig. 4.26, and this channel is also not included. The m_X distributions for $\psi(2S) \rightarrow \gamma\chi_{c1}, \chi_{c1} \rightarrow \gamma J/\psi$, $\psi(2S) \rightarrow \gamma\chi_{c2}, \chi_{c2} \rightarrow \gamma J/\psi$, and the background are broad and rather similar in shape, as can be seen in Fig. 4.26. Since these are difficult to distinguish, the χ_{c2} to χ_{c1} ratio is constrained using calculated efficiencies and the PDG world average branching fractions for the two processes.

To avoid a number of systematic errors, the channels of interest are normalized to the observed number of $J/\psi\pi^+\pi^-$ events; ratios of the studied branching fractions to that for $\mathcal{B}(\pi^+\pi^- \rightarrow J/\psi\pi^+\pi^-)$ are reported. The advantage of normalizing in this way is that many of the muon selection systematic errors largely cancel, as well as the systematic error due to the χ^2 requirement.

Table 4.32: Final branching ratios and branching fractions. PDG04-exp results are single measurements or averages of measurements, while PDG04-fit are results of their global fit to many experimental measurements. For the value marked with an asterisk, the PDG gives the reciprocal. The BES results in the second half of the table are calculated using the PDG value of $\mathcal{B}_{\pi\pi} = \mathcal{B}(\pi^+\pi^- \rightarrow J/\psi\pi^+\pi^-) = (31.7 \pm 1.1)\%$.

Case	This result	PDG04-exp	PDG04-fit
$\mathcal{B}(J/\psi \text{ anything})/\mathcal{B}_{\pi\pi}$	$1.867 \pm 0.026 \pm 0.055$	2.016 ± 0.150 [289]	$1.821 \pm 0.036^*$
$\mathcal{B}(J/\psi\pi^0\pi^0)/\mathcal{B}_{\pi\pi}$	$0.570 \pm 0.009 \pm 0.026$	$-$	0.59 ± 0.05
$\mathcal{B}(J/\psi\eta)/\mathcal{B}_{\pi\pi}$	$0.098 \pm 0.005 \pm 0.010$	0.091 ± 0.021 [284]	0.100 ± 0.008
$\mathcal{B}(J/\psi \text{ anything})$ (%)	$59.2 \pm 0.8 \pm 2.7$	55 ± 7	57.6 ± 2.0
$\mathcal{B}(J/\psi\pi^0\pi^0)$ (%)	$18.1 \pm 0.3 \pm 1.0$	$-$	18.8 ± 1.2
$\mathcal{B}(J/\psi\eta)$ (%)	$3.11 \pm 0.17 \pm 0.31$	2.9 ± 0.5	3.16 ± 0.22

The final branching fraction ratios and branching fractions are shown in Table 4.32, along with the PDG results, including their experimental averages and global fit results. For the ratio of $\mathcal{B}(\psi(2S)$
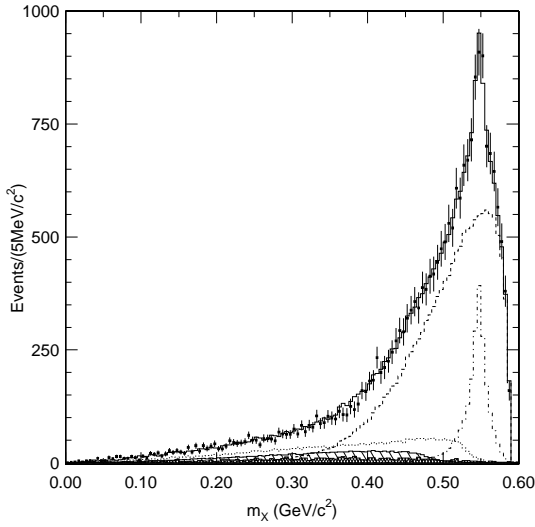
Fig. 4.26: Fit of the m_X distribution events with no additional charged tracks. Shown are the data (points with error bars), the component histograms, and the final fit. For the components, the large, long-dash histogram is $\psi(2S) \to J/\psi\pi\pi$, the narrow, dash–dot histogram is $\psi(2S) \to J/\psi\eta$, the broad, short-dashed histogram is $\pi^+\pi^- \to \gamma\chi_{c1}, \chi_{c1} \to \gamma J/\psi$, the broad, hatched histogram is $\pi^+\pi^- \to \gamma\chi_{c2}, \chi_{c2} \to \gamma J/\psi$, and the lowest cross-hatched histogram is the combined $e^+e^- \to \gamma\mu^+\mu^-$ and $e^+e^- \to \psi(2S), \psi(2S) \to (\gamma)\mu^+\mu^-$ background. The final fit is the solid histogram.
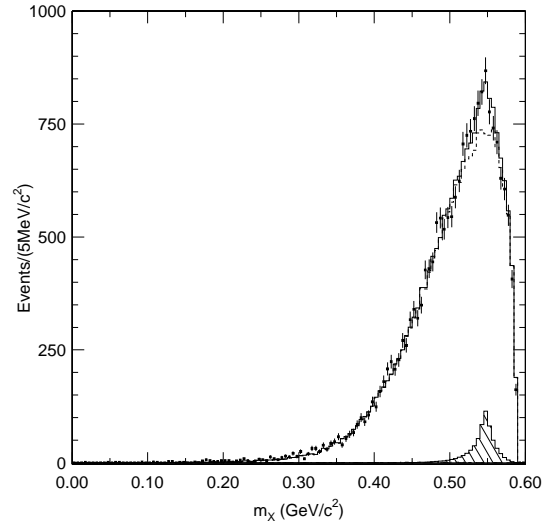
Fig. 4.27: Fit of the m_X distribution for events with any number of additional charged tracks. Shown are the data (points with error bars), the component histograms, and the final fit (solid histogram). The dashed histogram is $\psi(2S) \to J/\psi\pi^+\pi^-$, and the hatched histogram is $\psi(2S) \to J/\psi\eta$. There is very little evidence for $\psi(2S) \to \gamma\chi_{c1/2}, \chi_{c1/2} \to \gamma J/\psi$. This distribution is composed predominantly of $\psi(2S) \to J/\psi\pi^+\pi^-$.

$\to J/\psi\pi^0\pi^0)$ to $\mathcal{B}(\psi(2S) \to J/\psi\pi^+\pi^-)$, the PDG does not use the previous experimental results and gives no average value. For the other branching fraction ratios, only one measurement exists for each, and Table 4.32 lists the single measurements quoted by the PDG. The results for $\mathcal{B}(J/\psi \text{ anything})/\mathcal{B}(\psi(2S) \to J/\psi\pi^+\pi^-)$ and $\mathcal{B}(J/\psi\eta)/\mathcal{B}(\psi(2S) \to J/\psi\pi^+\pi^-)$ have smaller errors than the previous results.

To determine the branching fractions, the ratios are multiplied by the PDG value for $\mathcal{B}(\psi(2S) \to J/\psi\pi^+\pi^-) = (31.7\pm1.1)\%$. The agreement for both the ratios of branching fractions and the calculated branching fractions using the PDG result for $\mathcal{B}(\pi^+\pi^- \to J/\psi\pi^+\pi^-)$ with the PDG fit results is good, and the determination of $\mathcal{B}(J/\psi\eta)$ agrees well with the determination from $\psi(2S) \to \gamma\gamma J/\psi$ decays above.

B. $\pi^+\pi^- \to J/\psi \ \pi^+\pi^-$

The process $\pi^+\pi^- \to J/\psi \ \pi^+\pi^-$, is the largest decay mode of the $\psi(2S)$ [10]. Early investigation of this decay by Mark I [290] found that the $\pi^+\pi^-$ mass distribution was strongly peaked towards higher mass values, in contrast to what was expected from phase space. Further, angular distributions strongly favored S-wave production of $J/\psi \ \pi\pi$, as well as an S-wave decay of the dipion system. The challenge of describing the mass spectrum attracted considerable theoretical interest [227,229,230,237,240,256,291].

The $\pi^+\pi^- \to J/\psi \ \pi\pi$ decay was studied by BES [292], using 22,800 almost background free exclusive $\psi(2S) \to \pi^+\pi^- J/\psi$, $J/\psi \to l^+l^-$ events, where l signifies either e or μ, from a data sample of $3.8 \times 10^6 \ \psi(2S)$ decays.

The angular distributions were fit using the general decay amplitude analysis of Cahn [270]. The decay can be described in terms of partial wave amplitudes, $M_{l,L,S}$, where $\mathbf{l}$ is the $\pi\pi$ angular momentum, $\mathbf{L}$ is J/ψ X ($X \to \pi^+\pi^-$) angular momentum, $\mathbf{S}$ is the channel spin ($\mathbf{S} = \mathbf{s} + \mathbf{l}$), and $\mathbf{s}$ is the spin of the J/ψ. Parity conservation and charge conjugation invariance require both L and l to be even. The partial waves can be truncated after a few terms. Considering only M_{001}, M_{201}, and M_{021} [293]:

$$\frac{d\Gamma}{d\Omega_{J/\psi}} \propto [|M_{001}|^2 + |M_{201}|^2 + \frac{1}{4}|M_{021}|^2(5 - 3\cos^2\theta^*_{J/\psi}) + \frac{1}{\sqrt{2}}\Re\{M_{021}M^*_{001}\}(3\cos^2\theta^*_{J/\psi} - 1)],$$
(4.187)

$$\frac{d\Gamma}{d\Omega_\pi} \propto [|M_{001}|^2 + \frac{1}{4}|M_{201}|^2(5 - 3\cos^2\theta^*_\pi) + |M_{021}|^2 + \frac{1}{\sqrt{2}}\Re\{M_{201}M^*_{001}\}(3\cos^2\theta^*_\pi - 1)], \quad (4.188)$$

$$\frac{d\Gamma}{d\Omega_\mu} \propto [|M_{001}|^2(1 + \cos^2\theta^*_\mu) + \frac{1}{10}(|M_{201}|^2 + |M_{021}|^2)(13 + \cos^2\theta^*_\mu)], \quad (4.189)$$

where $\theta^*_{J/\psi}$ is the polar angle of the J/ψ relative to the beam direction in the lab, θ^*_π is the angle between the momenta of J/ψ and π^+ in the rest frame of the $\pi\pi$ system, and θ^*_μ is the angle between the beam direction and μ^+ in the rest frame of the J/ψ. The $d\Omega$'s are measured in their respective rest frames, and the $M_{l,L,S}$ are functions of $m_{\pi\pi}$.

There are three complex numbers to be obtained. According to Cahn, if the $\psi(2S)$ and J/ψ are regarded as inert, then $M_{l,L,S} = e^{i\delta^0_l(m_{\pi\pi})}|M_{l,L,S}|$, where $\delta^0_l(m_{\pi\pi})$ is the isoscalar phase shift for quantum number l. The phase angles are functions of $m_{\pi\pi}$. Interpolating the S-wave, isoscalar phase shift data found in Ref. [272,294], BES took δ^0_0 to be $\approx 45°$ and $\delta^0_2 \approx 0$. Using these values as input, BES obtained the combined fit to Eqs. (4.187)–(4.189), shown in Fig. 4.28. The fit yields a nonzero result for $|M_{201}|$, indicating that the dipion system contains some D-wave, which is shown by the non-flat angular distribution for $\cos\theta^*_\pi$ seen in Fig. 4.28. On the other hand $|M_{021}|/|M_{001}|$, which measures the amount of D-wave of the J/ψ–X system relative to the S-wave, is consistent with zero, which is indicated by the flat angular distribution for $\cos\theta^*_X$ shown in Fig. 4.28

Observation of a small D-wave contribution is interesting theoretically since, as we have seen in Eqs. (4.180) and (4.168), there is only S-wave contribution in the NRSC approach, i.e.,*the existence of a small D-wave contribution implies that the present NRSC theory should be improved to contain systematic relativistic and coupled-channel contributions.*

The $m_{\pi\pi}$ invariant mass spectrum has been fit with the Novikov–Shifman model and other models, as shown in Fig. 4.29. As can be seen, they give nearly identical fits.

Mannel and Urech have constructed an effective Lagrangian using chiral symmetry arguments to describe the decay of heavy excited S-wave spin-1 quarkonium into a lower S-wave spin-1 state [295]. Using total rates, as well as the invariant mass spectrum from Mark II via ARGUS [265], the parameters of this theory have been obtained. More recently, M. L. Yan *et al.* [296] have pointed out that this model allows D-wave contributions. BES fit the joint $\cos\theta^*_\pi$–$m_{\pi\pi}$ distribution using the amplitude of Mannel and Urech. The results are given in Ref. [292], along with the results from Ref. [295] which are based on ARGUS–Mark II [265].

C. $\psi(3770) \to J/\psi\ \pi^+\pi^-$

BES has reported evidence for $\psi(3770) \to J/\psi\ \pi^+\pi^-$ based on 27.7 pb^{-1} of data taken in the centre-of-mass (c.m.) energy region around 3.773 Gev using the BES II detector [252].

To search for the decay of $\psi(3770) \to J/\psi\ \pi^+\pi^-$, $J/\psi \to e^+e^-$ or $\mu^+\mu^-$, $\mu^+\mu^-\pi^+\pi^-$ and $e^+e^-\pi^+\pi^-$ candidate events are selected. They are required to have four charged tracks with zero total charge. Each track is required to have a good helix fit, to be consistent with originating from the primary
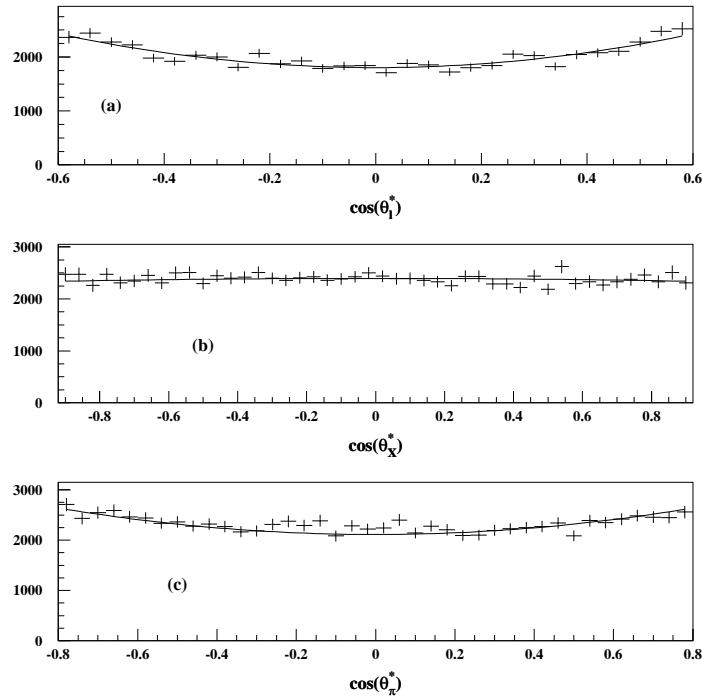
Fig. 4.28: Angular distributions of (a) $\cos\theta_\mu^*$, (b) $\cos\theta_X^*$, and (c) $\cos\theta_\pi^*$. The fit shown uses the partial wave analysis description of Cahn [293].

event vertex, and to satisfy $|\cos\theta| < 0.85$, where θ is the polar angle. Pions and leptons must satisfy particle identification requirements.

In order to reduce background and improve momentum resolution, events are subjected to four-constraint kinematic fits to either the $e^+e^- \to \mu^+\mu^-\pi^+\pi^-$ or the $e^+e^- \to e^+e^-\pi^+\pi^-$ hypothesis. Events with a confidence level greater than 1% are accepted. Figure 4.30(a) shows the dilepton masses determined from the fitted lepton momenta of the accepted events. There are clearly two peaks. The lower mass peak is mostly due to $\psi(3770) \to J/\psi\,\pi^+\pi^-$, while the higher one is produced via radiative return to the peak of the $\psi(2S)$.

A maximum likelihood fit to the mass distribution in Fig. 4.30(a), using a Gaussian function to describe the peak near the J/ψ mass, two Gaussian functions to represent the second peak from radiative return to the $\psi(2S)$ peak, and a polynomial to represent the broad background, yields a signal of 17.8 ± 4.8 events with a significance of $6.2\,\sigma$.

Backgrounds from QED radiative processes with γ conversion, two-photon backgrounds, such as $e^+e^- \to e^+e^-\mu^+\mu^-$ (where the slow muons are misidentified as pions) and $e^+e^- \to e^+e^-\pi^+\pi^-$, and $e^+e^- \to \tau^+\tau^-$, are negligibly small, as are $J/\psi\,\pi^+\pi^-$ events produced in the continuum process, $e^+e^- \to l^+l^-\pi^+\pi^-$. However, there is a contribution from $\psi(2S) \to J/\psi\,\pi^+\pi^-$ that can pass the event selection criteria and yield fitted dilepton masses around 3.097 Gev. This is the main background to $\psi(3770) \to J/\psi\,\pi^+\pi^-$, as shown in Fig. 4.30(b). Here the histogram shows the dilepton mass distribution for $\psi(2S) \to J/\psi\,\pi^+\pi^-$ from a Monte Carlo simulation. The higher peak is due to the radiative return to the $\psi(2S)$ peak, and the lower peak is from the tail of the $\psi(2S)$. The points with error bars show the total contribution from $\psi(2S)$ and $\psi(3770)$ production and decay. From the simulation, it is estimated that $6.0 \pm 0.5 \pm 0.6$ out of 17.8 ± 4.8 events in the peak near 3.1 Gev in Fig. 4.30(a) are due to $\psi(2S) \to J/\psi\,\pi^+\pi^-$, where the first error is statistical and the second one is the systematic error arising from the uncertainty in the $\psi(2S)$ resonance parameters.
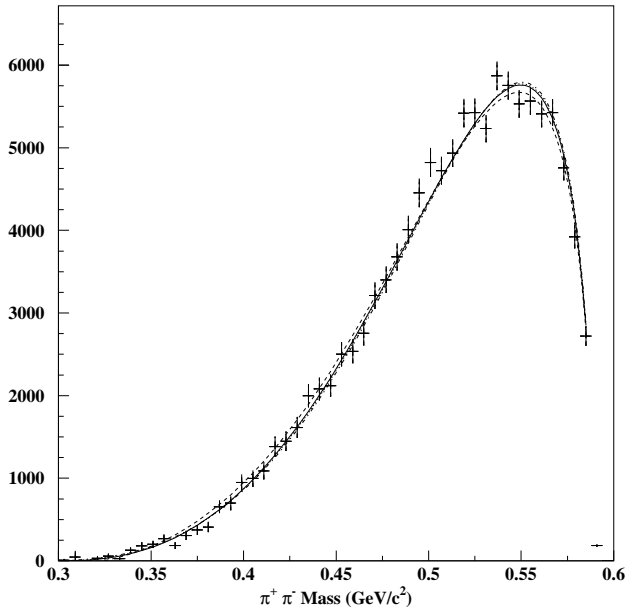
Fig. 4.29: Fits to the $m_{\pi\pi}$ distribution from $\pi^+\pi^- \to$ $\pi^+\pi^- J/\psi$. The points are the data corrected for efficiency, and the curves are the fit results. The smooth curve is the Novikov–Shifman model. The other models, which are described in Ref. [292], give similar results.
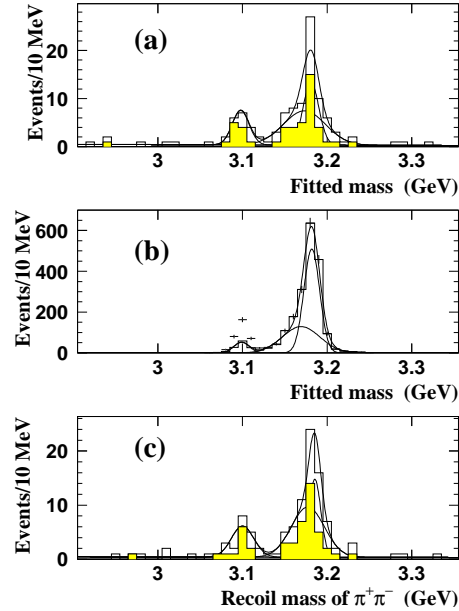
Fig. 4.30: Distributions of dilepton masses for (a) data and (b) Monte Carlo sample for events passing the selection for $\psi(3770) \to \pi^+\pi^- J/\psi$. The hatched histogram in (a) is for $J/\psi \to \mu^+\mu^-$, while the open one is for $J/\psi \to e^+e^-$. The histogram in (b) is for $\psi(2S) \to J/\psi\pi^+\pi^-$, while the points with error bars are the sum of $\psi(3770) \to J/\psi\pi^+\pi^-$ and $\psi(2S) \to J/\psi\pi^+\pi^-$. (c) Distribution of mass recoiling against the $\pi^+\pi^-$ system calculated using measured momenta for events that pass the kinematic fit requirement, where the hatched histogram is for $J/\psi \to \mu^+\mu^-$ and the open one is for $J/\psi \to e^+e^-$.

With the calculated cross-sections for $\psi(3770)$ production at each energy point around 3.773 Gev and the corresponding luminosities, the total number of $\psi(3770)$ events in the data sample is determined to be $N^{\mathrm{prod}}_{\psi(3770)} = (1.85 \pm 0.37) \times 10^5$, where the error is mainly due to the uncertainty in the observed cross-section for $\psi(3770)$ production. The detection efficiency for the decay channel is determined to be $\epsilon_{\psi(3770)\to J/\psi\ \pi^+\pi^-, J/\psi\to l^+l^-} = 0.160 \pm 0.002$, where the error is statistical. Using these numbers and the known branching fractions for $J/\psi \to e^+e^-$ and $\mu^+\mu^-$ [10], the branching fraction for the non-$D\bar{D}$ decay $\psi(3770) \to J/\psi\ \pi^+\pi^-$ is measured to be

$$\mathcal{B}(\psi(3770) \to J/\psi\ \pi^+\pi^-) = (0.34 \pm 0.14 \pm 0.08)\%, \tag{4.190}$$

where the first error is statistical and the second systematic. Using Γ_{tot} from the PDG [10], this branching fraction corresponds to a partial width of

$$\Gamma(\psi(3770) \to J/\psi\ \pi^+\pi^-) = (80 \pm 32 \pm 21)\ \text{keV}. \tag{4.191}$$

The dominant systematic uncertainty is due to the uncertainty in the total number of $\psi(3770)$ produced ($\pm 24\%$). Other systematic uncertainties are due to the efficiency ($\pm 10\%$), the background shape ($\pm 6\%$), and $\psi(2S) \to J/\psi\ \pi^+\pi^-$ background subtraction ($\pm 7\%$).

CLEOc has analyzed a sample of $\psi(3770)$ decays (4.5×10^4) [209]. Although the sample is smaller, they have a larger detection efficiency (37%). They find two events in the signal region, consistent with the estimated background, and set a preliminary upper limit $\mathcal{B}(\psi(3770) \to J/\psi\, \pi^+\pi^-) < 0.26\%$ (90% CL). The result does not confirm the BES result, but is not inconsistent with it either. CLEOc is now analyzing a sample of about 50 pb^{-1}, and the situation should be better understood when this is completed. See Section 7.2 for the comparison of the BES result with the related theoretical prediction.

D. $X(3872) \to J/\psi\, \pi^+\pi^-$

The Belle group has recently reported the observation of the $X(3872)$, a charmonium-like particle with mass 3872.0 ± 0.8 MeV that decays to $J/\psi\, \pi^+\pi^-$ [280]. For a review on the charmonium assignments (and their problems) for the $X(3872)$ we refer to Chapter 3, Section 8.2, and [297].

The $\pi^+\pi^-$ invariant mass distribution for this process, shown in Fig. 3.33(a) in Chapter 3, has a stronger concentration at high mass values than QCDME [230] expectations for D-wave to S-wave transitions, and is also more pronounced than that seen in the S-wave to S-wave $\psi' \to J/\psi\, \pi^+\pi^-$ process, which is shown in Fig. 3.33(b). This concentration at high $\pi^+\pi^-$ masses in $X(3872) \to J/\psi\, \pi^+\pi^-$ has been experimentally confirmed by the CDF experiment [298].

8 DECAYS OF THE B_c[22]

Besides new spectroscopy, production and decay observables, the investigation of the long-lived heavy quarkonium B_c, the pseudoscalar ground state of the $\bar{b}c$ system, provides the possibility to get model-independent information on some electroweak parameters, like the CKM matrix elements, in the heavy quark sector [299, 300]. The first experimental observation of the B_c meson by the CDF collaboration [224, 301] confirmed the theoretical predictions (and postdictions) on its mass, production rate and lifetime [186, 192, 225, 226, 302–309]. Tevatron [310] and LHC [311] will provide in the near future new data with increased statistics, opening the field to full experimental investigation and systematic test of the theory.

Decays of the B_c meson were considered in the pioneering paper by Bjorken of 1986 [312]. A lot of work has been done after that in order to understand long-lived doubly heavy hadrons.[23] Surprisingly, the Bjorken's estimates of total widths and various branching fractions are close to what is evaluated now in a more rigorous way. The B_c properties determined by the strong interactions can be investigated in the framework of effective field theories for heavy quarkonia, i.e., NRQCD [14, 314], potential NRQCD [41, 42] or vNRQCD [315] (see also Chapters 1, 3 and 6). In contrast to the Wilson coefficients, the hadronic matrix elements of operators composed by the effective fields of the nonrelativistic heavy quarks cannot be evaluated in a perturbative manner. So, one has to use nonperturbative methods such as QCD sum rules (SR) [316], operator product expansion (OPE) for inclusive estimates and potential models (PM).

The measured B_c lifetime is equal to

$$\tau[B_c] = 0.46^{+0.18}_{-0.16} \pm 0.03 \text{ ps}, \tag{4.192}$$

which is close to the value expected by Bjorken. The B_c decays were, at first, calculated in PM [317–326]. We do not distinguish here among relativistic and nonrelativistic PM, light-front, Bethe–Salpeter or quasi-potential approaches, calculations with or without confined quark-propagators and so on, because (1) relativistic corrections to the initial and final state heavy quarkonium form factors are suppressed by powers of the heavy quark velocity (at least, by a factor 10); (2) light mesons in the final states are usually factorized, and corrections to the factorization are small; (3) heavy-light mesons in the final states are

---

[22]Author: V. V. Kiselev

[23]Reviews on the physics of B_c meson and doubly heavy baryons can be found in Refs. [186, 192, 225, 226, 302] and [313], respectively. For the doubly heavy baryons see also Chapter 3.

quite accurately described by potential models adjusted to the decays of such mesons. As a consequence the different models agree on most of the decay channels.

The results of PM for the B_c lifetime agree with each others after having been adjusted on the semileptonic decays of the B mesons. The OPE evaluations of inclusive decays give lifetime and widths [305] in agreement with PM, if one sums up the dominant exclusive modes. On the other hand, SR of QCD gave at first semileptonic B_c widths, which were one order of magnitude smaller than those of PM and OPE [327]. The reason was identified in the missing Coulomb resummation [306–308, 319]. At present, all mentioned approaches give close results for the lifetime and decay modes of the B_c if similar sets of parameters are used. Nevertheless, various questions remain open:

- What is the appropriate normalization point of the non-leptonic weak Lagrangian in the B_c decays?
- What are the values of the masses for the c and b quarks that have to be used (see in this respect Chapter 6)?
- What are the implications of the NRQCD symmetries for the B_c form factors?
- How consistent is our understanding of hadronic matrix elements characterizing the B_c decays with the data from other heavy hadrons?

In the following of this section we shortly review the B_c decays by summarizing the theoretical predictions in the different frameworks and discussing how direct experimental measurements can help to answer the above questions.

8.1 B_c lifetime and inclusive decay rates

The B_c decay processes can be divided into three classes [305]:

1) the $\bar{b}$-quark decay with the spectator c quark,

2) the c-quark decay with the spectator $\bar{b}$ quark and

3) the annihilation channel $B_c^+ \rightarrow l^+\nu_l(c\bar{s}, u\bar{s})$, where $l = e, \mu, \tau$.

In the $\bar{b} \rightarrow \bar{c}c\bar{s}$ decays one separates also the Pauli interference with the c quark from the initial state. In accordance with the given classification, the total width is the sum over the partial widths

$$\Gamma(B_c \rightarrow X) = \Gamma(b \rightarrow X) + \Gamma(c \rightarrow X) + \Gamma(\text{ann.}) + \Gamma(\text{PI}). \tag{4.193}$$

We will see that the dominant contribution to the B_c lifetime is expected to be given by the charmed quark decays ($\approx 70\%$), the b-quark decays and the weak annihilation are expected to add about 20% and 10%, respectively, while the Pauli interference term gives a valuable contribution in the $\bar{b} \rightarrow c\bar{c}s$ decays at the level of -1.5%, which we have included in the b-quark decay fraction. The above percentages were obtained in [309]. Somewhat different figures may be obtained in different approaches, e.g., C. H. Chang *et al.* obtain in [305] about 70% for the fraction of c-quark decays, about 22% for the fraction of b-quark decays without Pauli interference, about 17% for the fraction of weak annihilation and about -9% for the fraction of the Pauli interference.

The annihilation width, $\Gamma(\text{ann.})$, can be reliably estimated in the framework of inclusive approaches. Let us consider, for instance, the effective weak interaction Hamiltonian in the quark transition $b \rightarrow c\bar{u}d$:

$$H_{\text{eff}} = \frac{G_F}{2\sqrt{2}}V_{cb}V_{ud}^*\{C_+(\mu)O_+ + C_-(\mu)O_-\}, \tag{4.194}$$

with

$$O_{\pm} = \bar{u}_i\gamma_\nu(1 - \gamma_5)d_i\,\bar{b}_j\gamma^\nu(1 - \gamma_5)c_j \pm \bar{u}_i\gamma_\nu(1 - \gamma_5)d_j\,\bar{b}_i\gamma^\nu(1 - \gamma_5)c_j, \tag{4.195}$$

where i, j are colour indices. The factors $C_\pm(\mu)$ account for the corrections induced by hard gluons to the corresponding four-fermion operators. A review on the evaluation of $C_\pm(\mu)$ can be found in [328]. The normalization condition is given by $C_\pm(m_b) = 1$. A natural choice for μ in decays with given
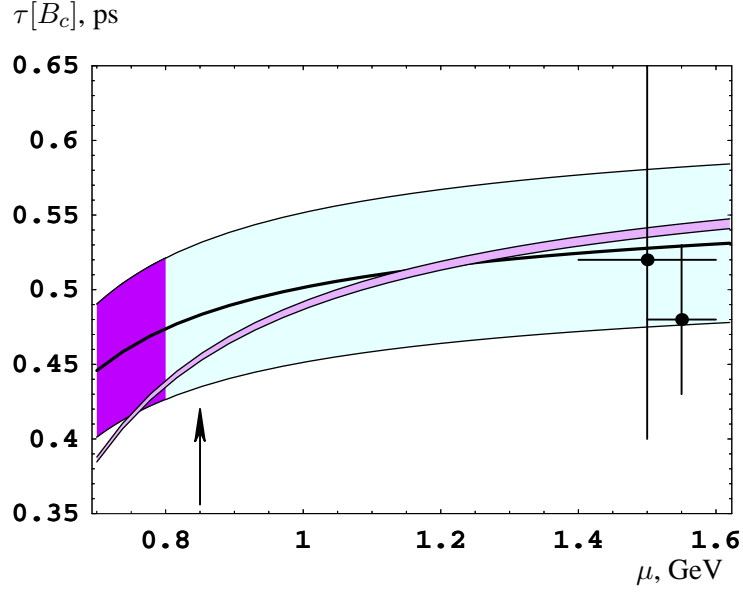
Fig. 4.31: The B_c lifetime calculated in QCD sum rules versus the scale of the hadronic weak Lagrangian in the decay of the charm quark. The wide shaded region, taken from Ref. [308], shows the uncertainty of the semi-inclusive estimates, the dark shaded region is the preferable choice as given by the lifetimes of charmed mesons. The dots represent the values in the OPE approach by M. Beneke and G. Buchalla (left point) and A. Onishchenko (right point) taken from Refs. [305]. The narrow shaded region represents the result of [309] obtained by summing up the exclusive channels with a variation of the hadronic scale in the decays of the $\bar{b}$ in the range of $1 < \mu_b < 5$ Gev. The arrow points to the preferable prescription of $\mu = 0.85$ Gev as discussed in [308].

initial and final hadronic states should correspond to the scale at which the hadronic matrix elements are evaluated. We also define

$$
\begin{aligned}
a_1(\mu) &= \frac{1}{2N_c}\big[C_+(\mu)(N_c+1) + C_-(\mu)(N_c-1)\big], \\
a_2(\mu) &= \frac{1}{2N_c}\big[C_+(\mu)(N_c+1) - C_-(\mu)(N_c-1)\big].
\end{aligned}
\tag{4.196}
$$

Then, we obtain

$$
\Gamma(\text{ann.}) = \sum_{i=\tau,c} \frac{G_F^2}{8\pi}|V_{bc}|^2 f_{B_c}^2 M m_i^2 (1 - m_i^2/m_{Bc}^2)^2 \cdot C_i ,
\tag{4.197}
$$

where $f_{B_c} \approx 400$ MeV (see below), $C_\tau = 1$ for the $\tau^+\nu_\tau$-channel, $C_c = 3|V_{cs}|^2 a_1^2$ for the $c\bar{s}$-channel, and the gluon corrections for the annihilation into hadrons go in the factor $a_1 = 1.22 \pm 0.04$ (see [328]). This estimate of the quark contribution does not depend on a hadronization model, since a large energy release, of the order of the meson mass, takes place. Moreover, one can see that the contributions from light leptons and quarks can be neglected.

As for the non-annihilation decays, in the approach of the OPE for the quark currents of weak decays [305], one takes into account α_s corrections to the free quark decays and uses the quark–hadron duality for the final states. Then one considers the matrix element for the transition operator over the meson state. The latter allows one also to take into account the effects caused by the motion and virtuality of the decaying quark inside the meson because of the interaction with the spectator. In this way the $\bar{b}\rightarrow\bar{c}c\bar{s}$ decay mode turns out to be suppressed almost completely due to the Pauli interference with the charm quark from the initial state. Besides, the c-quark decays with the spectator $\bar{b}$ quark are essentially suppressed in comparison with the free quark decays because of the large binding energy in the initial state.

Table 4.33: Summary of theoretical predictions in various approaches for the branching ratios of the B_c decay modes calculated in the framework of the inclusive OPE approach (see M. Beneke and G. Buchalla in [305]), by summing up the exclusive modes in potential models (for instance, in the model of [318, 319] used in [308]) and according to the semi-inclusive estimates in the sum rules of QCD and NRQCD [307–309].

B_c decay mode	OPE, %	PM, %	SR, %
$\bar{b}{\to}\bar{c}l^+\nu_l$	3.9 ± 1.0	3.7 ± 0.9	2.9 ± 0.3
$\bar{b}{\to}\bar{c}u\bar{d}$	16.2 ± 4.1	16.7 ± 4.2	13.1 ± 1.3
$\sum \bar{b}{\to}\bar{c}$	25.0 ± 6.2	25.0 ± 6.2	19.6 ± 1.9
$c{\to}sl^+\nu_l$	8.5 ± 2.1	10.1 ± 2.5	9.0 ± 0.9
$c{\to}su\bar{d}$	47.3 ± 11.8	45.4 ± 11.4	54.0 ± 5.4
$\sum c{\to}s$	64.3 ± 16.1	65.6 ± 16.4	72.0 ± 7.2
$B_c^+{\to}\tau^+\nu_\tau$	2.9 ± 0.7	2.0 ± 0.5	1.8 ± 0.2
$B_c^+{\to}c\bar{s}$	7.2 ± 1.8	7.2 ± 1.8	6.6 ± 0.7

In an exclusive approach it is necessary to sum up widths of different decay modes calculated in potential models. Considering the semileptonic decays due to the $\bar{b}{\to}\bar{c}l^+\nu_l$ and $c{\to}sl^+\nu_l$ transitions, one finds that the hadronic final states are practically saturated by the lightest $1S$ state in the $(\bar{c}c)$ system, i.e., η_c and J/ψ and the $1S$ states in the $(\bar{b}s)$ system, i.e., B_s and B_s^*. Further, the $\bar{b}{\to}\bar{c}u\bar{d}$ channel, for example, can be calculated through the decay width of $\bar{b}{\to}\bar{c}l^+\nu_l$, taking into account colour factors and hard gluon corrections to the four-quark interaction. It can be also obtained as a sum over the widths of decays to $(u\bar{d})$ bound states.

The results of the calculation of the B_c total width in the inclusive OPE and exclusive PM approaches give values that are consistent with each other, if one takes into account the most significant uncertainty, which is related to the choice of the quark masses (especially of the charm quark):

$$\tau[B_c^+]_{\text{OPE, PM}} = 0.55 \pm 0.15 \text{ ps}. \tag{4.198}$$

So, for instance, M. Beneke and G. Buchalla using OPE [305] give the estimate 0.4–0.7 ps (see Fig. 4.31), which slightly corrects a result by I. Bigi [305]: 0.4 ps. As for the potential approach, despite huge differences in details of exclusive estimates, models usually give a lifetime close to 0.4–0.6 ps, although the estimates strongly depend on the choice of the charm quark mass. We refer to the pioneering paper by M. Lusignoli and M. Masetti [317]. The obtained value agrees with the measured one (4.192). In Table 4.33 the reader may find summarized several theoretical results for inclusive decay channels.

The OPE estimates of inclusive decay rates agree with recent semi-inclusive calculations in the sum rules of QCD and NRQCD [307, 308], where one assumes the saturation of hadronic final states by the ground levels in the $c\bar{c}$ and $\bar{b}s$ systems as well as the factorization that allows to relate the semileptonic and hadronic decay modes. The Coulomb resummation plays an essential role in the B_c decays and removes the disagreement between the estimates in sum rules and OPE. In contrast to OPE, where the basic uncertainty is given by the heavy quark masses, these parameters are fixed by the two-point sum rules for bottomonia and charmonia, so that the accuracy of SR calculations for the total width of the B_c is determined by the choice of the scale μ for the hadronic weak Lagrangian in decays of charmed quarks. We show this dependence in Fig. 4.31, where $m_c/2 < \mu < m_c$. The dark shaded region corresponds to the scales preferred by the data on the charmed meson lifetimes. Choosing the scale in the $c{\to}s$ decays of B_c to be equal to $\mu_{B_c}^2 \approx (0.85 \text{ GeV})^2$, putting $a_1(\mu_{B_c}) = 1.20$ and neglecting the contributions of a nonzero a_2 in the charmed quark decays, in the framework of semi-inclusive sum rule calculations one obtains [308]

$$\tau[B_c]_{\text{SR}} = 0.48 \pm 0.05 \text{ ps}, \tag{4.199}$$

which agrees with the direct sum of exclusive channels presented in the next sections. In Fig. 4.31 we also show the exclusive estimate of the lifetime from Ref. [309].

8.2 Exclusive decays

Typical values for the exclusive decay branching ratios of the B_c, as obtained in QCD SR [308, 309], are shown in Table 4.34 at given values of the factors $a_{1,2}$ and lifetime. The uncertainty of such predictions is about 15%, and the numbers essentially agree with most of the potential models within the theoretical uncertainties of the QCD SR estimates. In square bracket we show the marginal deviations from the central values obtained in some potential models.

In addition to the decay channels with a J/ψ well detectable through its leptonic mode, one could expect significant information on the dynamics of B_c decays coming from channels with a single heavy mesons, if the experimental efficiency is good enough to extract a signal from the cascade decays. Since decays to excited charmonia in the final state (like P waves) [331, 332], radiative leptonic modes [333] and some rare decays [334] are out of reach for the experimental facilities of the nearest future, we do not display them in Table 4.34.

In [309] the $\bar{b}$ decay to the doubly charmed states is predicted to give

$$\mathcal{B}(B_c^+ \to \bar{c}c\,c\bar{s}) \approx 1.39\%. \tag{4.200}$$

Comparing the width with the estimate from the spectator decay [305],

$$\Gamma(B_c^+ \to \bar{c}c\,c\bar{s})\big|_{\text{SR}} \quad \approx \quad 20 \cdot 10^{-15}\,\text{GeV}, \tag{4.201}$$

$$\Gamma(B_c^+ \to \bar{c}c\,c\bar{s})\big|_{\text{spect.}} \quad \approx \quad 90 \times 10^{-15}\,\text{GeV}, \tag{4.202}$$

we see that they differ by a factor of about $1/4.5$. The SR result is in agreement with an estimate in OPE by M. Beneke and G. Buchalla of [305], though the uncertainty is quite large ($\approx 60\%$) due to the mentioned uncertainty in the renormalization point as well as in the charm quark mass.

At present we can say that an accurate direct measurement of the B_c lifetime can provide information on the masses of the c and b quarks and the normalization point of the non-leptonic weak Lagrangian in the B_c decays (the a_1 and a_2 factors). The experimental study of semileptonic decays and the extraction of ratios of form factors can test the spin symmetry of NRQCD and HQET and decrease the uncertainties in the corresponding theoretical evaluation of the quark parameters as well as the hadronic matrix elements. The measurement of branching fractions for semileptonic and non-leptonic modes and their ratios can give information on the values of the factorization parameters, which depend again on the normalization of the non-leptonic weak Lagrangian. The charm quark counting in the B_c decays is related to the overall contribution of b quark decays as well as to the suppression of $\bar{b} \to c\bar{c}\bar{s}$ transitions because of the destructive interference, whose value depends on the nonperturbative parameters (roughly said, the leptonic constant) and on the non-leptonic weak Lagrangian.

8.2.1 Semileptonic decays

The semileptonic decay rates estimated in the QCD sum rules for 3-point correlators [335] are underestimated in [327], because large Coulomb-like corrections were not taken into account. The recent analysis of SR in [306–308] decreased the uncertainty, so that the estimates agree with the calculations in the potential models.

(A) Coulomb resummation

For the heavy quarkonium $\bar{b}c$, where the relative quark velocity is small, Coulomb-like α_{s}/v corrections are important and have to be resummed. It is well known that taking into account these corrections in two-point sum rules numerically enhances the Born value of the spectral density by a factor two or three [316].

Table 4.34: QCD SR predictions [308, 309] for the branching ratios of exclusive B_c^+ decays with the choice of factors: $a_1^c = 1.20$ and $a_2^c = -0.317$ in the non-leptonic decays of the c quark, and $a_1^b = 1.14$ and $a_2^b = -0.20$ in the non-leptonic decays of the $\bar{b}$ quark. The lifetime of the B_c is taken $\tau[B_c] \approx 0.45$ ps. The uncertainty of the widths is estimated to be about 15%. The numbers in square brackets show the marginal values obtained in some potential models [325, 326, 329, 330]. The maximal difference is of one order of magnitude.

Mode	BR, %		Mode	BR, %	
$B_c^+ \to \eta_c e^+\nu$	0.75	[0.5]	$B_c^+ \to \eta_c D_s^{*+}$	0.27	[0.07]
$B_c^+ \to \eta_c \tau^+\nu$	0.23	[0.2]	$B_c^+ \to J/\psi D_s^+$	0.17	[0.05]
$B_c^+ \to \eta_c' e^+\nu$	0.020	[0.05]	$B_c^+ \to J/\psi D_s^{*+}$	0.67	[0.5]
$B_c^+ \to \eta_c' \tau^+\nu$	0.0016	[–]	$B_c^+ \to \eta_c D^+$	0.015	[0.04]
$B_c^+ \to J/\psi e^+\nu$	1.9	[1]	$B_c^+ \to \eta_c D^{*+}$	0.010	[0.002]
$B_c^+ \to J/\psi \tau^+\nu$	0.48	[0.35]	$B_c^+ \to J/\psi D^+$	0.009	[0.002]
$B_c^+ \to \psi' e^+\nu$	0.094	[0.2]	$B_c^+ \to J/\psi D^{*+}$	0.028	[0.014]
$B_c^+ \to \psi' \tau^+\nu$	0.008	[–]	$B_c^+ \to B_s^0 \pi^+$	16.4	[1.6]
$B_c^+ \to D^0 e^+\nu$	0.004	[0.02]	$B_c^+ \to B_s^0 \rho^+$	7.2	[2.4]
$B_c^+ \to D^0 \tau^+\nu$	0.002	[0.08]	$B_c^+ \to B_s^{*0} \pi^+$	6.5	[1.3]
$B_c^+ \to D^{*0} e^+\nu$	0.018	[0.004]	$B_c^+ \to B_s^{*0} \rho^+$	20.2	[11]
$B_c^+ \to D^{*0} \tau^+\nu$	0.008	[0.016]	$B_c^+ \to B_s^0 K^+$	1.06	[0.2]
$B_c^+ \to B_s^0 e^+\nu$	4.03	[1]	$B_c^+ \to B_s^{*0} K^+$	0.37	[0.13]
$B_c^+ \to B_s^{*0} e^+\nu$	5.06	[1.2]	$B_c^+ \to B_s^0 K^{*+}$	–	
$B_c^+ \to B^0 e^+\nu$	0.34	[0.08]	$B_c^+ \to B_s^{*0} K^{*+}$	–	
$B_c^+ \to B^{*0} e^+\nu$	0.58	[0.15]	$B_c^+ \to B^0 \pi^+$	1.06	[0.1]
$B_c^+ \to \eta_c \pi^+$	0.20	[0.12]	$B_c^+ \to B^0 \rho^+$	0.96	[0.2]
$B_c^+ \to \eta_c \rho^+$	0.42	[0.3]	$B_c^+ \to B^{*0} \pi^+$	0.95	[0.08]
$B_c^+ \to J/\psi \pi^+$	0.13	[0.08]	$B_c^+ \to B^{*0} \rho^+$	2.57	[0.6]
$B_c^+ \to J/\psi \rho^+$	0.40	[0.2]	$B_c^+ \to B^0 K^+$	0.07	[0.01]
$B_c^+ \to \eta_c K^+$	0.013	[0.008]	$B_c^+ \to B^0 K^{*+}$	0.015	[0.012]]
$B_c^+ \to \eta_c K^{*+}$	0.020	[0.018]	$B_c^+ \to B^{*0} K^+$	0.055	[0.006]
$B_c^+ \to J/\psi K^+$	0.011	[0.007]	$B_c^+ \to B^{*0} K^{*+}$	0.058	[0.04]
$B_c \to J/\psi K^{*+}$	0.022	[0.016]	$B_c^+ \to B^+ \overline{K^0}$	1.98	[0.18]
$B_c^+ \to D^+ \overline{D}^0$	0.0053	[0.0018]	$B_c^+ \to B^+ \overline{K^{*0}}$	0.43	[0.09]
$B_c^+ \to D^+ \overline{D}^{*0}$	0.0075	[0.002]	$B_c^+ \to B^{*+} \overline{K^0}$	1.60	[0.06]
$B_c^+ \to D^{*+} \overline{D}^0$	0.0049	[0.0009]	$B_c^+ \to B^{*+} \overline{K^{*0}}$	1.67	[0.6]
$B_c^+ \to D^{*+} \overline{D}^{*0}$	0.033	[0.003]	$B_c^+ \to B^+ \pi^0$	0.037	[0.004]
$B_c^+ \to D_s^+ \overline{D}^0$	0.00048	[0.0001]	$B_c^+ \to B^+ \rho^0$	0.034	[0.01]
$B_c^+ \to D_s^+ \overline{D}^{*0}$	0.00071	[0.00012]	$B_c^+ \to B^{*+} \pi^0$	0.033	[0.003]
$B_c^+ \to D_s^{*+} \overline{D}^0$	0.00045	[0.00005]	$B_c^+ \to B^{*+} \rho^0$	0.09	[0.03]
$B_c^+ \to D_s^{*+} \overline{D}^{*0}$	0.0026	[0.0002]	$B_c^+ \to \tau^+ \nu_\tau$	1.6	
$B_c^+ \to \eta_c D_s^+$	0.28	[0.07]	$B_c^+ \to c\bar{s}$	4.9	

(B) Primary modes

In practice, the most important information comes from the ψ mode, since this charmonium is clearly detected in experiments [224, 301]. In addition to the investigation of various form factors and their dependence on the momentum transfer squared, the measurement of the decay to ψ', could answer the question of the reliability of QCD predictions for the decays to excited states. At present, finite energy sum rules predict the width of the $B_c^+ \to \psi' l^+ \nu$ decay in reasonable agreement with potential models if one takes into account an uncertainty of about 50%.

(C) Relations between the form factors

In the limit of infinitely heavy quark masses, the NRQCD and HQET Lagrangians possess spin symmetry. The most familiar implication of such symmetry is the common Isgur–Wise function determining the form factors in the semileptonic decays of single heavy hadrons. In contrast to weak decays with a light spectator quark, the B_c decays to ψ, η_c and $B_s^{(*)}$ involve the heavy spectator, so that the spin symmetry works only at recoil momenta close to zero, where the spectator enters the heavy hadron in the final state with no hard gluon rescattering. Hence, we expect relations between the form factors in the vicinity of zero recoil. The normalization of the form factor is not fixed, as it is in decays of hadrons with a single heavy quark, since the heavy quarkonia wave functions are flavour dependent. In practice, the ratios of form factors, which are fixed at zero recoil, are expected to exhibit a dependence on the momentum transfer squared, which is not significant in actual numerical estimates in the restricted region of the physical phase space. The SR estimates of the form factors show a good agreement with the expectations, whereas the deviations can be traced back to the difference in the q^2 evolution of the form factors from the zero recoil point. This can be neglected within the accuracy of the SR method for the transitions of $B_c \to \bar{c}c$, as shown in [307]. The $1/m_Q$ deviations from the symmetry relations in the decays of $B_c^+ \to B_s^{(*)} e^+ \nu$ are about 10–15%, as found in the QCD sum rules considered in [308]. Form factors for specific decay channels have been considered also in [322, 331].

The combinations of relations derived in [307, 308] reproduce the only equality in [336], which was found for each mode in the strict limit of $v_1 = v_2$ also considered by Sanchis–Lozano in [337].

8.2.2 Leptonic decays

The dominant leptonic decay of the B_c is given by the $\tau \nu_\tau$ mode (see Table 4.33). However, it has a low experimental efficiency of detection because of the hadronic background in the τ decays. Recently, in Refs. [333] the enhancement of muon and electron channels in the radiative modes has been studied. The additional photon removes the helicity suppression for the leptonic decay of pseudoscalar particles, leading to an increase of the muonic mode by about a factor two.

(A) Leptonic constant of B_c

In NRQCD the calculation of the leptonic constant for the heavy quarkonium with two-loop accuracy requires the two-loop matching of the NRQCD currents with the currents in full QCD,

$$J_\nu^{\mathrm{QCD}} = \bar{Q}_1 \gamma_5 \gamma_\nu Q_2, \quad \mathcal{J}_\nu^{\mathrm{NRQCD}} = -\chi^\dagger \psi \, v_\nu, \qquad J_\nu^{\mathrm{QCD}} = \mathcal{K}(\mu_{\mathrm{hard}}; \mu_{\mathrm{fact}}) \, \mathcal{J}_\nu^{\mathrm{NRQCD}}(\mu_{\mathrm{fact}}),$$

where the scale μ_{hard} gives the normalization point for the matching of NRQCD with full QCD, while μ_{fact} denotes the normalization point for the calculations in perturbation theory in NRQCD.

For the pseudoscalar heavy quarkonium composed of heavy quarks with different flavours, the Wilson coefficient $\mathcal{K}$ has been calculated with two-loop accuracy in Refs. [338] and [339]. In NRQCD the current $\mathcal{J}_\nu^{\mathrm{NRQCD}}$ has nonzero anomalous dimension, so that we find

$$\langle 0|\mathcal{J}_\nu^{\mathrm{NRQCD}}(\mu)|\bar{Q}Q\rangle = \mathcal{A}(\mu) \, v_\nu f_{\bar{Q}Q}^{\mathrm{NRQCD}} M_{\bar{Q}Q}, \tag{4.203}$$

where, in terms of nonrelativistic quarks, the leptonic constant for the heavy quarkonium is given by the well-known relation with the wave function at the origin.
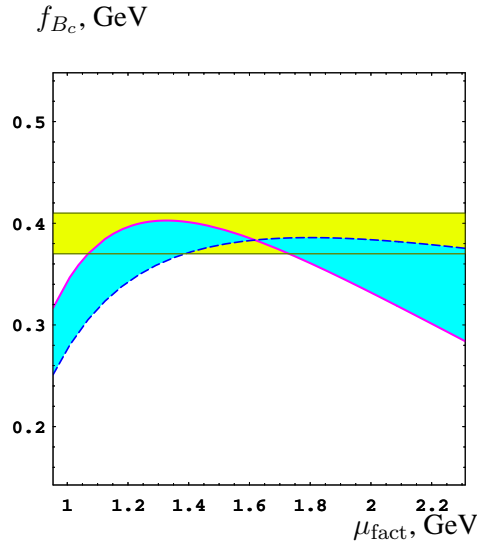
Fig. 4.32: The leptonic constant of the B_c is presented versus the soft scale of normalization. The shaded region restricted by curves corresponds to the change of the hard scale from $\mu_{\text{hard}} = 3$ Gev (the dashed curve) to $\mu_{\text{hard}} = 2$ Gev (the solid curve) with the initial condition for the evolution of the normalization factor $\mathcal{A}(\mu_{\text{fact}})$, $\mathcal{A}(1.2 \text{ GeV}) = 1$ and $\mathcal{A}(1 \text{ GeV}) = 1$ respectively, in the nonrelativistic current matrix element. The horizontal band is the region expected from the QCD sum rules [306,327,340] and scaling relations for the leptonic constants of heavy quarkonia [341]. In the overlap region, the leptonic constant of B_c depends weakly on the parameters.

Following the method described in [342,343], one can estimate the wave function of the $\bar{b}c$ quarkonium using the static potential given in [342]. Details of the calculations can be found in [344]. The result of the calculation of the B_c leptonic constant is shown in Fig. 4.32. The final result of the two-loop calculation is

$$f_{B_c} = 395 \pm 15 \text{ MeV}, \tag{4.204}$$

which is close to an early estimate by S. Capstick and S. Godfrey in [304].

The result on f_{B_c} is in agreement with the scaling relation derived from the quasi-local QCD sum rules [341], which use the regularity in the heavy quarkonium mass spectra, i.e., the fact that the splitting between the quarkonium levels after averaging over the spins of the heavy quarks depends weakly on the quark flavours. So, the scaling law for S-wave quarkonia has the form

$$\frac{f_n^2}{M_n} \left(\frac{M_n}{M_1}\right)^2 \left(\frac{m_1 + m_2}{4\mu_{12}}\right)^2 = \frac{c}{n}, \tag{4.205}$$

where n is the radial quantum number, $m_{1,2}$ the masses of the heavy quarks composing the quarkonium, μ_{12} the reduced mass and c a dimensional constant independent on both the quark flavours and n. The accuracy depends on the heavy quark masses, and is discussed in detail in [341]. The parameter c can be extracted from the known leptonic constants of ψ and Υ.

8.2.3 Non-leptonic modes

With respect to the inclusive non-leptonic widths, which can be estimated in the framework of quark–hadron duality (see Table 4.33), the calculation of exclusive modes usually involves factorization [86, 345], which, as expected, can be quite accurate for the B_c, since the quark–gluon sea is suppressed in the heavy quarkonium. Thus, the important parameters are the factors a_1 and a_2 in the non-leptonic weak Lagrangian, which depend on the normalization point.

The agreement of QCD SR estimates for the non-leptonic decays of the charm quark in the B_c with the values predicted by potential models is rather good for the direct transitions with no permutation of

colour lines, i.e., processes involving the factor a_1 in the non-leptonic amplitude. In contrast, the sum rule predictions are significantly enhanced in comparison with the values calculated in potential models for transitions with colour permutation, i.e., for processes involving the factor a_2 (see Table 4.34). Further, for transitions $\bar{b} \rightarrow c\bar{c}s$ where the interference is significantly involved the size of the interference is about 35–50% of the width evaluated by neglecting interference terms. These estimates are in agreement with the potential models of Refs. [322, 325].

At large recoils as in $B_c^+ \rightarrow \psi\pi^+(\rho^+)$, the spectator picture of transition can be broken by hard gluon exchanges [346]. The spin effects in such decays were studied in [332]. Typically recoil effects are taken into account to some extent in any relativistic approach like [322].

For the widths of non-leptonic c-quark decays the sum rule estimates are typically greater than those of potential models[24]. In this respect we note that the QCD SR calculations are consistent with the inclusive ones. Summing up the calculated exclusive widths, the total width of the B_c meson is shown in Fig. 4.31, which points to a good agreement of the exclusive calculations with those of OPE and semi-inclusive estimates.

Another interesting point is the possibility to extract the factorization parameters a_1 and a_2 in the c-quark decays by measuring the ratios of widths

$$\frac{\Gamma(B_c^+ \rightarrow B^{(*)+}\bar{K}^{(*)0})}{\Gamma(B_c^+ \rightarrow B^{(*)0}K^{(*)+})} = \left|\frac{V_{cs}}{V_{cd}^2}\right|^2 \frac{a_2^2}{a_1^2}, \qquad (4.206)$$

where one should take identical sets of pseudoscalar and vector states in both decays. This procedure can give a test for the factorization approach itself.

The suppressed decays caused by the flavour changing neutral currents were studied in [334].

(A) CP violation in B_c decays

CP violation in B_c decays can be investigated in the same way as in B decays. The expected CP asymmetry of $\mathcal{A}(B_c^\pm \rightarrow J/\psi D^\pm)$ is about 4×10^{-3}, when the corresponding branching ratio is suppressed as 10^{-4} [299]. Therefore, the direct study of CP violation in B_c decays is practically difficult because of the low relative yield of B_c with respect to ordinary B mesons: $\sigma(B_c)/\sigma(B) \sim 10^{-3}$.

As mentioned at the beginning, the B_c meson is expected to be copiously produced in future colliders. In such circumstances a possible challenge is whether one could get an opportunity to extract some information about the CKM unitarity triangle from the B_c in a model independent way. Indeed, there is such an opportunity for the angle γ using the strategy of the reference triangles [352] in the decays of doubly heavy hadrons. This strategy for the study of CP violation in B_c decays was originally proposed by M. Masetti [299], independently investigated by R. Fleischer and D. Wyler [299] and extended to the case of doubly heavy baryons in [353]. Other possibilities include the lepton tagging of B_s in the $B_c^\pm \rightarrow B_s^{(*)}l^\pm\nu$ decays for the study of mixing and CP violation in the B_s sector [354], and a possible transverse polarization of the τ lepton in $B_c \rightarrow \tau\bar{\nu}_\tau\gamma$ [347].

The triangle strategy is based on the direct determination of absolute values for the set of four decays, at least: the decays of the hadron into the tagged D^0 meson, the tagged $\bar{D}^0$ meson, the tagged CP-even state of D^0, and the decay of the anti-hadron into the tagged CP-even state of D^0. To illustrate the point, let us consider the decays

$$B_c^+ \rightarrow D^0 D_s^+ \quad \text{and} \quad B_c^+ \rightarrow \bar{D}^0 D_s^+.$$

The corresponding diagrams with the decay of $\bar{b}$-quark are shown in Figs. 4.33 and 4.34.

The exclusive modes do not have penguin terms at the leading order in the Fermi constant G_F that we consider here. However, the diagram with the weak annihilation of two constituents, i.e., the

---

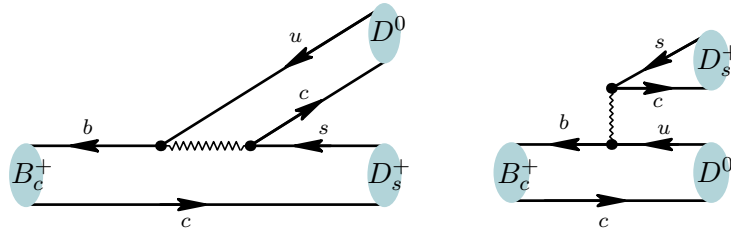[24]See also the recent discussions on the B_c decays in [329, 330, 347–351].

Fig. 4.33: The diagrams of $\bar{b}$-quark decay contributing to the weak transition $B_c^+ \to D^0 D_s^+$.

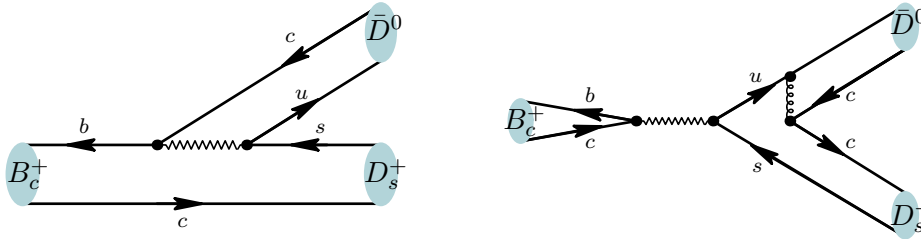Fig. 4.34: The diagrams of $\bar{b}$-quark decay contributing to the weak transition $B_c^+ \to \bar{D}^0 D_s^+$.

charmed quark and beauty antiquark in the B_c^+ meson, can contribute at the next order in α_s as shown in Fig. 4.34 for the given final state. Nevertheless, we see that such diagrams have the same weak-interaction structure as at tree level. The magnitude of the α_s corrections to the absolute values of the corresponding decay widths is discussed in [300]. We expect the sides of the reference-triangles to be of the same order of magnitude, which makes the method an attractive way to extract the angle γ.

The predictions of QCD sum rules for the exclusive decays of B_c are summarized in Table 4.35 at fixed values of $a_{1,2}$ and lifetime. For the sake of completeness and comparison we show the estimates for the channels with the neutral D meson and charged D^+ as well as for the vector states in addition to the pseudoscalar ones.

First, we see that the similar decay modes without the strange quark in the final state can also be used, in principle, for the extraction of γ, however, these channels are more problematic since the sides of the reference-triangles significantly differ from each other[25], so that the measurements have to be extremely accurate to get useful information on the angle, which means that one has to accumulate a huge statistics for the dominant mode.

Second, the decay modes with the vector neutral D meson in the final state are useless for the purpose of the CKM measurement under the discussed approach. However, the modes with the vector charged D^* and D_s^* mesons can be important for the extraction of γ. For instance, one could consider the modes $D^{*+} \to D^0 \pi^+$ and $D^0 \to K^- \pi^+$. The neutral charmed meson should be carefully treated in order to avoid misidentification with the primary one. Otherwise, one could use the mode with the neutral pion, $D^{*+} \to D^+ \pi^0$, whose detection in an experimental facility could be problematic. The same considerations apply to the vector meson D_s^{*+}, whose radiative electromagnetic decay is also problematic for the detection, since the photon could be easily lost. On the other hand, the loss of the photon does not disturb the analysis in the case of fully reconstructed D_s^+ and B_c^+.

In the BTeV [310] and LHCb [311] experiments one expects the B_c production at the level of several billion events. Therefore, one expects 10^4–10^5 decays of B_c in the gold-plated modes under interest.

---

[25]The ratio of widths is basically determined by $|V_{cb}V_{ud}a_2|^2/|V_{ub}V_{cd}a_1|^2 \sim 110$, if we ignore the interference effects.

Table 4.35: QCD SR predictions [300] for the branching ratios of exclusive B_c^+ decays with the choice of factors: $a_1^b = 1.14$ and $a_2^b = -0.20$ in the non-leptonic decays of $\bar{b}$ quark. The lifetime of the B_c is taken $\tau[B_c] \approx 0.45$ ps. For comparison we show in square brackets minimal values estimated in the potential models of [299].

Mode	BR, 10^{-6}		Mode	BR, 10^{-6}	
$B_c^+ \to D^+ \overline{D}^0$	53	[18]	$B_c^+ \to D^+ D^0$	0.32	[0.1]
$B_c^+ \to D^+ \overline{D}^{*0}$	75	[20]	$B_c^+ \to D^+ D^{*0}$	0.28	[0.07]
$B_c^+ \to D^{*+} \overline{D}^0$	49	[9]	$B_c^+ \to D^{*+} D^0$	0.40	[0.4]
$B_c^+ \to D^{*+} \overline{D}^{*0}$	330	[30]	$B_c^+ \to D^{*+} D^{*0}$	1.59	[0.4]
$B_c^+ \to D_s^+ \overline{D}^0$	4.8	[1]	$B_c^+ \to D_s^+ D^0$	6.6	[1.7]
$B_c^+ \to D_s^+ \overline{D}^{*0}$	7.1	[1.2]	$B_c^+ \to D_s^+ D^{*0}$	6.3	[1.3]
$B_c^+ \to D_s^{*+} \overline{D}^0$	4.5	[0.5]	$B_c^+ \to D_s^{*+} D^0$	8.5	[8.1]
$B_c^+ \to D_s^{*+} \overline{D}^{*0}$	26	[2]	$B_c^+ \to D_s^{*+} D^{*0}$	40.4	[6.2]

The experimental challenge is the efficiency of detection. One usually gets a 10% efficiency for the observation of distinct secondary vertices outstanding from the primary vertex of beam interaction. Next, one has to take into account the branching ratios of D_s and D^0 mesons. This efficiency crucially depends on whether one can detect the neutral kaons and pions or not. So, for the D_s meson the corresponding branching ratios grow from 4% (no neutral K and π) to 25%. The same interval for the neutral D^0 is from 11% to 31%. The detection of neutral kaon is necessary for the measurement of decay modes into the CP-odd state D_2 of the neutral D^0 meson, however, one can omit this cross-check channel from the analysis in dealing with the CP-even state D_1. The corresponding intervals of branching ratios reachable by the experiments are from 0.5% to 1.3% for the CP-even state and from 1.5% to 3.8% for the CP-odd state of D^0. A pessimistic estimate for the product of branching ratios is about 2×10^{-4}, which results in 2–20 reconstructed events.

REFERENCES

[1] C. Patrignani, Phys. Rev. D **64**, 034017 (2001) [arXiv:hep-ex/0104003].

[2] T. Sjostrand, "PYTHIA 5.7 and JETSET 7.4: Physics and manual," arXiv:hep-ph/95 08391.

[3] H. m. Hu and A. Tai, in *Proc. of the e^+e^- Physics at Intermediate Energies Conference* ed. Diego Bettoni, eConf **C010430**, T24 (2001) [arXiv:hep-ex/0106017].

[4] J. C. Chen, G. S. Huang, X. R. Qi, D. H. Zhang and Y. S. Zhu, Phys. Rev. D **62**, 034003 (2000).

[5] G. Garzoglio *et al.*, Nucl. Instrum. Meth. A **519**, 558 (2004).

[6] M. Andreotti *et al.* [Fermilab E835 Collaboration], Phys. Rev. Lett. **91**, 091801 (2003) [arXiv:hep-ex/0308055].

[7] M. Benayoun, S. I. Eidelman, V. N. Ivanchenko and Z. K. Silagadze, Mod. Phys. Lett. A **14**, 2605 (1999) [arXiv:hep-ph/9910523].

[8] J. Z. Bai *et al.* [BES Collaboration], Phys. Rev. D **57**, 3854 (1998).

[9] B. Aubert *et al.* [BaBar Collaboration], Phys. Rev. D **69**, 011103 (2004) [arXiv:hep-ex/0310027].

[10] S. Eidelman *et al.* [Particle Data Group Collaboration], Phys. Lett. B **592**, 1 (2004).

[11] T. Appelquist and H. D. Politzer, Phys. Rev. Lett. **34**, 43 (1975).

[12] R. Barbieri, R. Gatto and E. Remiddi, Phys. Lett. B **61**, 465 (1976).

[13] W. E. Caswell and G. P. Lepage, Phys. Lett. B **167**, 437 (1986).

[14] G. T. Bodwin, E. Braaten and G. P. Lepage, Phys. Rev. D **51**, 1125 (1995) [Erratum-ibid. D **55**, 5853 (1997)] [arXiv:hep-ph/9407339].

[15] G. T. Bodwin, E. Braaten and G. P. Lepage, Phys. Rev. D **46**, 1914 (1992) [arXiv:hep-lat/9205006].

[16] N. Brambilla, D. Eiras, A. Pineda, J. Soto and A. Vairo, Phys. Rev. D **67**, 034018 (2003) [arXiv:hep-ph/0208019].

[17] M. Beneke, arXiv:hep-ph/9703429; S. Fleming, I. Z. Rothstein and A. K. Leibovich, Phys. Rev. D **64**, 036002 (2001) [arXiv:hep-ph/0012062].

[18] A. Pineda and A. Vairo, Phys. Rev. D **63**, 054007 (2001) [Erratum-ibid. D **64**, 039902 (2001)] [arXiv:hep-ph/0009145].

[19] A. Petrelli, M. Cacciari, M. Greco, F. Maltoni and M. L. Mangano, Nucl. Phys. B **514**, 245 (1998) [arXiv:hep-ph/9707223].

[20] F. Maltoni, *Quarkonium phenomenology*, PhD thesis (Univ. of Pisa, 1999) [http://www.fis.uni-roma3.it/~maltoni/thesis.ps].

[21] H. W. Huang and K. T. Chao, Phys. Rev. D **54**, 3065 (1996) [Erratum-ibid. D **56**, 7472 (1997 ERRAT,D60,079901.1999)] [arXiv:hep-ph/9601283].

[22] R. Barbieri, M. Caffo, R. Gatto and E. Remiddi, Phys. Lett. B **95**, 93 (1980); Nucl. Phys. B **192**, 61 (1981).

[23] P. B. Mackenzie and G. P. Lepage, Phys. Rev. Lett. **47**, 1244 (1981).

[24] M. Gremm and A. Kapustin, Phys. Lett. B **407**, 323 (1997) [arXiv:hep-ph/9701353].

[25] A. Czarnecki and K. Melnikov, Phys. Rev. Lett. **80**, 2531 (1998) [arXiv:hep-ph/9712222].

[26] M. Beneke, A. Signer and V. A. Smirnov, Phys. Rev. Lett. **80**, 2535 (1998) [arXiv:hep-ph/9712302].

[27] R. Barbieri, G. Curci, E. d'Emilio and E. Remiddi, Nucl. Phys. B **154**, 535 (1979); K. Hagiwara, C. B. Kim and T. Yoshino, Nucl. Phys. B **177**, 461 (1981).

[28] A. Vairo, Mod. Phys. Lett. A **19**, 253 (2004) [arXiv:hep-ph/0311303].

[29] G. T. Bodwin and A. Petrelli, Phys. Rev. D **66**, 094011 (2002) [arXiv:hep-ph/0205210].

[30] J. P. Ma and Q. Wang, Phys. Lett. B **537**, 233 (2002) [arXiv:hep-ph/0203082].

[31] A. A. Penin, A. Pineda, V. A. Smirnov and M. Steinhauser, Nucl. Phys. B **699**, 183 (2004) [arXiv:hep-ph/0406175].

[32] G. T. Bodwin and Y. Q. Chen, Phys. Rev. D **64**, 114008 (2001) [arXiv:hep-ph/0106095]; ibid. D **60**, 054008 (1999) [arXiv:hep-ph/9807492]; E. Braaten and Y. Q. Chen, Phys. Rev. D **57**, 4236 (1998) [Erratum-ibid. D **59**, 079901 (1999)] [arXiv:hep-ph/9710357].

[33] M. L. Mangano and A. Petrelli, Phys. Lett. B **352**, 445 (1995) [arXiv:hep-ph/9503465].

[34] F. Maltoni, arXiv:hep-ph/0007003.

[35] R. Mussa, *talk at the 2nd QWG Workshop, Fermilab, 2003*, http://www.qwg.to.infn.it/WS-sep03/index.html.

[36] G. T. Bodwin, D. K. Sinclair and S. Kim, Phys. Rev. D **65**, 054504 (2002) [arXiv:hep-lat/0107011].

[37] G. T. Bodwin, D. K. Sinclair and S. Kim, Phys. Rev. Lett. **77**, 2376 (1996) [arXiv:hep-lat/9605023].

[38] E. J. Eichten and C. Quigg, Phys. Rev. D **52**, 1726 (1995) [arXiv:hep-ph/9503356].

[39] G. S. Bali, Phys. Rept. **343**, 1 (2001) [arXiv:hep-ph/0001312].

[40] A. Vairo, arXiv:hep-ph/0212271.

[41] A. Pineda and J. Soto, Nucl. Phys. Proc. Suppl. **64**, 428 (1998) [arXiv:hep-ph/9707481].

[42] N. Brambilla, A. Pineda, J. Soto and A. Vairo, Nucl. Phys. B **566**, 275 (2000) [arXiv:hep-ph/9907240].

[43] N. Brambilla, A. Pineda, J. Soto and A. Vairo, Phys. Lett. B **470**, 215 (1999) [arXiv:hep-ph/9910238].

[44] N. Brambilla and A. Vairo, arXiv:hep-ph/0004192.

[45] S. Titard and F. J. Yndurain, Phys. Rev. D **49**, 6007 (1994) [arXiv:hep-ph/9310236]; F. J. Yndurain,

arXiv:hep-ph/0007333.

[46] A. Pineda, Nucl. Phys. B **494**, 213 (1997) [arXiv:hep-ph/9611388].

[47] A. Pineda, Phys. Rev. D **66**, 054022 (2002) [arXiv:hep-ph/0110216].

[48] A. Pineda, Acta Phys. Polon. B **34**, 5295 (2003) [arXiv:hep-ph/0404225].

[49] K. Melnikov and A. Yelkhovsky, Phys. Rev. D **59**, 114009 (1999) [arXiv:hep-ph/9805270]; A. A. Penin and A. A. Pivovarov, "Bottom quark pole mass and |V(cb)| matrix element from R(e+ e- → b Nucl. Phys. B **549**, 217 (1999) [arXiv:hep-ph/9807421].

[50] A. Gray *et al.* [HPQCD collaboration], Nucl. Phys. Proc. Suppl. **119**, 592 (2003) [arXiv:hep-lat/0209022].

[51] N. Brambilla, D. Eiras, A. Pineda, J. Soto and A. Vairo, Phys. Rev. Lett. **88**, 012003 (2002) [arXiv:hep-ph/0109130].

[52] N. Brambilla, A. Pineda, J. Soto and A. Vairo, Phys. Lett. B **580**, 60 (2004) [arXiv:hep-ph/0307159].

[53] N. Brambilla, A. Pineda, J. Soto and A. Vairo, Phys. Rev. D **63**, 014023 (2001) [arXiv:hep-ph/0002250].

[54] G. Amoros, M. Beneke and M. Neubert, Phys. Lett. B **401**, 81 (1997) [arXiv:hep-ph/9701375].

[55] G. S. Bali and A. Pineda, Phys. Rev. D **69**, 094001 (2004) [arXiv:hep-ph/0310130]; M. Foster and C. Michael [UKQCD Collaboration], Phys. Rev. D **59**, 094509 (1999) [arXiv:hep-lat/9811010]; G. S. Bali, N. Brambilla and A. Vairo, Phys. Lett. B **421**, 265 (1998) [arXiv:hep-lat/9709079]; M. D'Elia, A. Di Giacomo and E. Meggiolaro, Phys. Lett. B **408**, 315 (1997) [arXiv:hep-lat/9705032].

[56] A. Di Giacomo, H. G. Dosch, V. I. Shevchenko and Y. A. Simonov, Phys. Rept. **372**, 319 (2002) [arXiv:hep-ph/0007223]; N. Brambilla, arXiv:hep-ph/0012211; M. Baker, N. Brambilla, H. G. Dosch and A. Vairo, Phys. Rev. D **58**, 034010 (1998) [arXiv:hep-ph/9802273].

[57] A. Vairo, Nucl. Phys. Proc. Suppl. **115**, 166 (2003) [arXiv:hep-ph/0205128].

[58] G. S. Adams *et al.* [CLEO Collaboration], submitted to Phys. Rev. Lett. [arXiv:hep-ex/0409027].

[59] J. Z. Bai *et al.* [BES Collaboration], Phys. Lett. B **550**, 24 (2002) [arXiv:hep-ph/0209354].

[60] J. Z. Bai *et al.* [BES Collaboration], Phys. Rev. D **65**, 052004 (2002) [arXiv:hep-ex/0010072].

[61] T. A. Armstrong *et al.* [E760 Collaboration], Nucl. Phys. B **373**, 35 (1992).

[62] T. A. Armstrong *et al.* [E760 Collaboration], Phys. Rev. Lett. **70**, 2988 (1993).

[63] B. I. Eisenstein *et al.* [CLEO Collaboration], Phys. Rev. Lett. **87**, 061801 (2001) [arXiv:hep-ex/0104042].

[64] M. Andreotti *et al.* [Fermilab E835 Collaboration], Phys. Lett. B **584**, 16 (2004).

[65] J. Z. Bai *et al.* [BES Collaboration], Phys. Rev. Lett. **81**, 3091 (1998) [arXiv:hep-ex/9807001].

[66] J. Z. Bai *et al.* [BES Collaboration], Phys. Rev. D **60**, 072001 (1999) [arXiv:hep-ex/9812016].

[67] J. Z. Bai *et al.* [BES Collaboration], Phys. Rev. D **67**, 032004 (2003) [arXiv:hep-ex/0109040].

[68] D. M. Asner *et al.* [CLEO Collaboration], Phys. Rev. Lett. **92**, 142001 (2004) [arXiv:hep-ex/0312058].

[69] S. Bagnasco *et al.* [E835 Collaboration], Phys. Lett. B **553**, 237 (2002); N. Pastrone [E835 Collaboration], arXiv:hep-ex/0306032; R. Mussa, *talk at the 2nd QWG Workshop, Fermilab, 2003*, http://www.qwg.to.infn.it/WS-sep03/index.html.

[70] D. E. Groom *et al.* [Particle Data Group Collaboration], Eur. Phys. J. C **15**, 1 (2000).

[71] S. Fleming and A. K. Leibovich, Phys. Rev. Lett. **90**, 032001 (2003) [arXiv:hep-ph/0211303]; Phys. Rev. D **67**, 074035 (2003) [arXiv:hep-ph/0212094].

[72] B. Nemati *et al.* [CLEO Collaboration], Phys. Rev. D **55**, 5273 (1997) [arXiv:hep-ex/9611020].

[73] S. Behrends *et al.* [CLEO Collaboration], Phys. Rev. D **31**, 2161 (1985).

[74] M. Artuso *et al.* [CLEO Collaboration], Phys. Rev. D **67**, 052003 (2003) [arXiv:hep-ex/0211029].

[75] S. J. Brodsky *et al.*, Phys. Lett. B **73**, 203 (1978); K. Koller and T. Walsh, Nucl. Phys. B **140**, 449 (1978).

[76] F. Maltoni and A. Petrelli, Phys. Rev. D **59**, 074006 (1999) [arXiv:hep-ph/9806455].

[77] S. Catani and F. Hautmann, Nucl. Phys. Proc. Suppl. **39BC**, 359 (1995) [arXiv:hep-ph/9410394].

[78] I. Z. Rothstein and M. B. Wise, Phys. Lett. B **402**, 346 (1997) [arXiv:hep-ph/9701404].

[79] D. Buskulic *et al.* [ALEPH Collaboration], Z. Phys. C **69**, 365 (1996).

[80] M. Kramer, Phys. Rev. D **60**, 111503 (1999) [arXiv:hep-ph/9904416].

[81] C. W. Bauer *et al.*, Phys. Rev. D **63**, 014006 (2001); C. W. Bauer *et al.*, Phys. Rev. D **63**, 114020 (2001).

[82] C. W. Bauer and I. W. Stewart, Phys. Lett. B **516**, 134 (2001) [arXiv:hep-ph/0107001]; C. W. Bauer, D. Pirjol and I. W. Stewart, Phys. Rev. D **65**, 054022 (2002) [arXiv:hep-ph/0109045].

[83] F. Hautmann, Nucl. Phys. B **604**, 391 (2001) [arXiv:hep-ph/0102336].

[84] D. M. Photiadis, Phys. Lett. B **164**, 160 (1985).

[85] C. W. Bauer, C. W. Chiang, S. Fleming, A. K. Leibovich and I. Low, Phys. Rev. D **64**, 114014 (2001) [arXiv:hep-ph/0106316].

[86] M. J. Dugan and B. Grinstein, Phys. Lett. B **255**, 583 (1991).

[87] K. Hagiwara *et al.* [Particle Data Group Collaboration], Phys. Rev. D **66**, 010001 (2002).

[88] X. Garcia i Tormo and J. Soto, Phys. Rev. D **69**, 114006 (2004) [arXiv:hep-ph/0401233]; X. G. i. Tormo, arXiv:hep-ph/0410052.

[89] S. Fleming and A. K. Leibovich, Phys. Rev. D **70**, 094016 (2004) [arXiv:hep-ph/0407259].

[90] A. Duncan and A. H. Mueller, Phys. Lett. B **93**, 119 (1980).

[91] S. J. Brodsky and G. P. Lepage, Phys. Rev. D **24**, 2848 (1981).

[92] V. L. Chernyak and A. R. Zhitnitsky, Nucl. Phys. B **201**, 492 (1982) [Erratum-ibid. B **214**, 547 (1983)].

[93] V. N. Baier and A. G. Grozin, Z. Phys. C **29**, 161 (1985).

[94] J. Bolz, P. Kroll and G. A. Schuler, Phys. Lett. B **392**, 198 (1997) [arXiv:hep-ph/9610265] and Eur. Phys. J. C **2**, 705 (1998) [arXiv:hep-ph/9704378].

[95] V. L. Chernyak and A. R. Zhitnitsky, Phys. Rept. **112**, 173 (1984).

[96] V. M. Braun and I. E. Filyanov, Z. Phys. C **48**, 239 (1990) [Sov. J. Nucl. Phys. **52**, 126 (1990 YAFIA,52,199-213.1990)]; P. Ball, V. M. Braun, Y. Koike and K. Tanaka, Nucl. Phys. B **529**, 323 (1998) [arXiv:hep-ph/9802299]; M. Beneke and T. Feldmann, Nucl. Phys. B **592**, 3 (2001) [arXiv:hep-ph/0008255].

[97] V. Braun, R. J. Fries, N. Mahnke and E. Stein, Nucl. Phys. B **589**, 381 (2000) [Erratum-ibid. B **607**, 433 (2001)] [arXiv:hep-ph/0007279].

[98] M. E. B. Franklin *et al.*, Phys. Rev. Lett. **51**, 963 (1983).

[99] N. E. Adam *et al.* [CLEO Collaboration], Phys. Rev. Lett. **94**, 012005 (2005) [arXiv:hep-ex/0407028].

[100] M. Ablikim *et al.* [BES Collaboration], arXiv:hep-ex/0408047.

[101] W. S. Hou and A. Soni, Phys. Rev. Lett. **50**, 569 (1983).

[102] S. J. Brodsky, G. P. Lepage and S. F. Tuan, Phys. Rev. Lett. **59**, 621 (1987).

[103] Y. Q. Chen and E. Braaten, Phys. Rev. Lett. **80**, 5060 (1998) [arXiv:hep-ph/9801226].

[104] T. Feldmann and P. Kroll, Phys. Rev. D **62**, 074006 (2000) [arXiv:hep-ph/0003096].

[105] M. Suzuki, Phys. Rev. D **63**, 054021 (2001).

[106] J. L. Rosner, Phys. Rev. D **64**, 094002 (2001) [arXiv:hep-ph/0105327].

[107] M. Ablikim *et al.* [BES Collaboration], Phys. Lett. B **614**, 37 (2005) [arXiv:hep-ex/0407037].

[108] M. Ablikim *et al.* [BES Collaboration], Phys. Rev. D **70**, 112003 (2004) [arXiv:hep-ex/0408118].

[109] M. Ablikim *et al.* [the BES Collaboration], Phys. Rev. D **70**, 112007 (2004) [Erratum-ibid. D **71**, 019901 (2005)] [arXiv:hep-ex/0410031].

[110] J. Z. Bai *et al.* [BES Collaboration], Phys. Rev. Lett. **92**, 052001 (2004) [arXiv:hep-ex/0310024]; J. Z. Bai *et al.* [BES Collaboration], Phys. Rev. D **69**, 012003 (2004) [arXiv:hep-ex/0310023].

[111] J. Z. Bai *et al.* [BES Collaboration], Phys. Rev. D **69**, 072001 (2004) [arXiv:hep-ex/0312016].

[112] A. Seiden, H. F. W. Sadrozinski and H. E. Haber, Phys. Rev. D **38**, 824 (1988).

[113] A. Bramon, R. Escribano and M. D. Scadron, Phys. Lett. B **403**, 339 (1997) [arXiv:hep-ph/9703313].

[114] S. A. Dytman [CLEO Collaboration], arXiv:hep-ex/0307035.

[115] Z. Dziembowski, Phys. Rev. D **37**, 768 (1988).

[116] G. P. Lepage and S. J. Brodsky, Phys. Rev. D **22**, 2157 (1980).

[117] J. Bolz and P. Kroll, Z. Phys. A **356**, 327 (1996) [arXiv:hep-ph/9603289].

[118] N. G. Stefanis and M. Bergmann, Phys. Rev. D **47**, 3685 (1993) [arXiv:hep-ph/9211250]; V. L. Chernyak, A. A. Ogloblin and I. R. Zhitnitsky, Z. Phys. C **42**, 583 (1989) [Yad. Fiz. **48**, 1398 (1988 SJNCA,48,889-895.1988)];

[119] N. Isgur and C. H. Llewellyn Smith, Nucl. Phys. B **317**, 526 (1989); A. V. Radyushkin, Nucl. Phys. A **527**, 153C (1991).

[120] V. Y. Petrov and M. V. Polyakov, arXiv:hep-ph/0307077.

[121] J. Bolz and P. Kroll, Eur. Phys. J. C **2**, 545 (1998) [arXiv:hep-ph/9703252].

[122] J. Botts and G. Sterman, Nucl. Phys. B **325**, 62 (1989); H. n. Li and G. Sterman, Nucl. Phys. B **381**, 129 (1992).

[123] J. Bolz, R. Jakob, P. Kroll, M. Bergmann and N. G. Stefanis, Z. Phys. C **66**, 267 (1995) [arXiv:hep-ph/9405340].

[124] J. Z. Bai *et al.* [BES Collaboration], Phys. Lett. B **591**, 42 (2004) [arXiv:hep-ex/0402034].

[125] D. Pallin *et al.* [DM2 Collaboration], Nucl. Phys. B **292**, 653 (1987).

[126] M. W. Eaton *et al.*, Phys. Rev. D **29**, 804 (1984).

[127] T. A. Armstrong *et al.* [E760 Collaboration], Phys. Rev. D **47**, 772 (1993).

[128] Seon-Hee Seo, proceedings of CIPANP 03, New York May, 19-24 2003.

[129] C. Carimalo, Int. J. Mod. Phys. A **2**, 249 (1987).

[130] F. Murgia and M. Melis, Phys. Rev. D **51**, 3487 (1995) [arXiv:hep-ph/9412205]; R. G. Ping, H. C. Chiang and B. S. Zou, Phys. Rev. D **66**, 054020 (2002).

[131] M. Claudson, S. L. Glashow and M. B. Wise, Phys. Rev. D **25**, 1345 (1982).

[132] H. Fritzsch and J. D. Jackson, Phys. Lett. B **66**, 365 (1977).

[133] K. T. Chao, Nucl. Phys. B **317**, 597 (1989).

[134] T. Feldmann, P. Kroll and B. Stech, Phys. Rev. D **58**, 114006 (1998) [arXiv:hep-ph/9802409]; Phys. Lett. B **449**, 339 (1999) [arXiv:hep-ph/9812269].

[135] T. Feldmann and P. Kroll, Eur. Phys. J. C **5**, 327 (1998) [arXiv:hep-ph/9711231].

[136] F. Yuan and K. T. Chao, Phys. Rev. D **56**, 2495 (1997) [arXiv:hep-ph/9706294].

[137] R. M. Baltrusaitis *et al.* [Mark-III Collaboration], Phys. Rev. D **33**, 629 (1986).

[138] D. Bisello *et al.* [DM2 collaboration], Nucl. Phys. B **350**, 1 (1991).

[139] J. Z. Bai *et al.* [BES Collaboration], Phys. Lett. B **578**, 16 (2004) [arXiv:hep-ex/0308073].

[140] H. C. Huang, arXiv:hep-ex/0305068.

[141] W. Buchmüller and S. H. H. Tye, Phys. Rev. D **24**, 132 (1981).

[142] P. Kroll and M. Raulfs, Phys. Lett. B **387**, 848 (1996) [arXiv:hep-ph/9605264]; I. V. Musatov and A. V. Radyushkin, Phys. Rev. D **56**, 2713 (1997) [arXiv:hep-ph/9702443].

[143] M. Diehl, P. Kroll and C. Vogt, Eur. Phys. J. C **22**, 439 (2001) [arXiv:hep-ph/0108220]; A. P. Bakulev, S. V. Mikhailov and N. G. Stefanis, arXiv:hep-ph/0312141.

[144] C. Quigg and J. L. Rosner, Phys. Rept. **56**, 167 (1979).

[145] P. Kroll and K. Passek-Kumericki, Phys. Rev. D **67**, 054017 (2003) [arXiv:hep-ph/0210045].

[146] A. Ali and A. Y. Parkhomenko, Eur. Phys. J. C **30**, 183 (2003) [arXiv:hep-ph/0304278].

[147] S. M. Wong, Nucl. Phys. A **674**, 185 (2000) [arXiv:hep-ph/9903221]; Eur. Phys. J. C **14**, 643 (2000) [arXiv:hep-ph/9903236].

[148] J. Z. Bai *et al.* [BES Collaboration], Phys. Rev. D **67**, 112001 (2003) [arXiv:hep-ex/0304012].

[149] J. Z. Bai *et al.* [BES Collaboration], Phys. Rev. D **69**, 092001 (2004) [arXiv:hep-ex/0401011].

[150] A. Andrikopoulou, Z. Phys. C **22**, 63 (1984); P. H. Damgaard, K. Tsokos and E. L. Berger, Nucl. Phys. B **259**, 285 (1985).

[151] E. Braaten and J. Lee, Phys. Rev. D **67**, 054007 (2003) [arXiv:hep-ph/0211085].

[152] H. W. Huang, C. F. Qiao and K. T. Chao, Phys. Rev. D **54**, 2123 (1996) [arXiv:hep-ph/9601380].

[153] M. Anselmino, R. Cancelliere and F. Murgia, Phys. Rev. D **46**, 5049 (1992).

[154] V. A. Novikov, M. A. Shifman, A. I. Vainshtein and V. I. Zakharov, Nucl. Phys. B **165**, 55 (1980).

[155] T. Feldmann and P. Kroll, Phys. Scripta **T99**, 13 (2002) [arXiv:hep-ph/0201044].

[156] J. P. Ma, Phys. Rev. D **65**, 097506 (2002) [arXiv:hep-ph/0202256].

[157] M. K. Chase, Nucl. Phys. B **174**, 109 (1980); V. N. Baier and A. G. Grozin, Nucl. Phys. B **192**, 476 (1981).

[158] P. Minkowski and W. Ochs, arXiv:hep-ph/0401167.

[159] F. E. Close, G. R. Farrar and Z. p. Li, Phys. Rev. D **55**, 5749 (1997) [arXiv:hep-ph/9610280].

[160] X. G. He, H. Y. Jin and J. P. Ma, Phys. Rev. D **66**, 074015 (2002) [arXiv:hep-ph/0203191].

[161] J. Z. Bai *et al.* [BES Collaboration], Phys. Rev. Lett. **91**, 022001 (2003) [arXiv:hep-ex/0303006].

[162] K. Abe *et al.* [Belle Collaboration], Phys. Rev. Lett. **88**, 181803 (2002) [arXiv:hep-ex/0202017]; Phys. Rev. Lett. **89**, 151802 (2002) [arXiv:hep-ex/0205083].

[163] A. Antonelli *et al.*, Nucl. Phys. B **517**, 3 (1998).

[164] D. Bridges *et al.*, Phys. Lett. B **180**, 313 (1986).

[165] L. Linssen *et al.*, Nucl. Phys. A **469**, 726 (1987); P. Schiavon *et al.*, Nucl. Phys. A **505**, 595 (1989).

[166] O. D. Dalkarov, V. M. Kolybasov, I. S. Shapiro and D. V. Voronov, Phys. Lett. B **392**, 229 (1997).

[167] P. Kroll and W. Schweiger, Nucl. Phys. A **503**, 865 (1989).

[168] A. Ferrer, A. A. Grigorian, V. F. Perepelitsa and P. Sonderegger, Eur. Phys. J. C **10**, 249 (1999).

[169] B. S. Zou and H. C. Chiang, Phys. Rev. D **69**, 034004 (2004) [arXiv:hep-ph/0309273]; B. Kerbikov, A. Stavinsky and V. Fedotov, Phys. Rev. C **69**, 055205 (2004) [arXiv:hep-ph/0402054].

[170] J. L. Rosner, Phys. Rev. D **68**, 014004 (2003) [arXiv:hep-ph/0303079].

[171] G. Bonvicini *et al.* [CLEO Collaboration], Phys. Rev. D **70**, 032001 (2004) [arXiv:hep-ex/0404021].

[172] B. A. Thacker and G. P. Lepage, Phys. Rev. D **43**, 196 (1991).

[173] P. Lepage and C. Davies, Int. J. Mod. Phys. A **19**, 877 (2004); S. A. Gottlieb, Nucl. Phys. Proc. Suppl. **128**, 72 (2004) [Nucl. Phys. Proc. Suppl. **129**, 17 (2004)] [arXiv:hep-lat/0310041] and references therein.

[174] A. Duncan, E. Eichten and H. Thacker, Phys. Rev. Lett. **76**, 3894 (1996) [arXiv:hep-lat/9602005].

[175] P. Colangelo and A. Khodjamirian, arXiv:hep-ph/0010175. See also: A. Y. Khodjamirian, Phys. Lett. B **90**, 460 (1980), Sov. J. Nucl. Phys. **39**, 614 (1984); V. A. Beilin and A. V. Radyushkin,

Nucl. Phys. B **260**, 61 (1985).

[176] J. Baacke, Y. Igarashi and G. Kasperidus, Z. Phys. C **13**, 131 (1982).

[177] E. Eichten, K. Gottfried, T. Kinoshita, K. D. Lane and T. M. Yan, Phys. Rev. D **17**, 3090 (1978) [Erratum-ibid. D **21**, 313 (1980)].

[178] G. Feinberg and J. Sucher, Phys. Rev. Lett. **35**, 1740 (1975).

[179] J. Sucher, Rept. Prog. Phys. **41**, 1781 (1978).

[180] J. S. Kang and J. Sucher, Phys. Rev. D **18**, 2698 (1978).

[181] R. McClary and N. Byers, Phys. Rev. D **28**, 1692 (1983).

[182] V. Zambetakis and N. Byers, Phys. Rev. D **28**, 2908 (1983).

[183] H. Grotch and K. J. Sebastian, Phys. Rev. D **25**, 2944 (1982).

[184] H. Grotch, D. A. Owen and K. J. Sebastian, Phys. Rev. D **30**, 1924 (1984).

[185] T. A. Lahde, Nucl. Phys. **A 714**, 183 (2003) [arXiv:hep-ph/0208110].

[186] D. Ebert, R. N. Faustov and V. O. Galkin, Phys. Rev. D **67**, 014027 (2003) [arXiv:hep-ph/0210381].

[187] E. Eichten, K. Gottfried, T. Kinoshita, J. B. Kogut, K. D. Lane and T. M. Yan, Phys. Rev. Lett. **34**, 369 (1975) [Erratum-ibid. **36**, 1276 (1976)].

[188] T. Appelquist, A. De Rujula, H. D. Politzer and S. L. Glashow, Phys. Rev. Lett. **34**, 365 (1975).

[189] K. Gottfried, CLNS-97-1511 *Talk given at 20th Anniversary Symposium: Twenty Beautiful Years of Bottom Physics, Chicago, IL, 29 Jun - 2 Jul 1997.*

[190] E. Eichten and K. Gottfried, Phys. Lett. B **66**, 286 (1977).

[191] E. Eichten, K. Gottfried, T. Kinoshita, K. D. Lane and T. M. Yan, Phys. Rev. D **21**, 203 (1980).

[192] E. J. Eichten and C. Quigg, Phys. Rev. D **49**, 5845 (1994) [arXiv:hep-ph/9402210].

[193] W. Buchmüller, G. Grunberg and S. H. H. Tye, Phys. Rev. Lett. **45**, 103 (1980) [Erratum-ibid. **45**, 587 (1980)].

[194] C. Quigg and J. L. Rosner, Phys. Rev. D **23**, 2625 (1981).

[195] A. Martin, Phys. Lett. B **93**, 338 (1980).

[196] A. K. Grant, J. L. Rosner and E. Rynes, Phys. Rev. D **47**, 1981 (1993).

[197] W. Buchmüller, Phys. Lett. B **112**, 479 (1982).

[198] D. Pignon and C. A. Piketty, Phys. Lett. **B74**, 108 (1978).

[199] P. Moxhay and J. L. Rosner, Phys. Rev. D **28**, 1132 (1983).

[200] W. Kwong and J. L. Rosner, Phys. Rev. D **38**, 279 (1988).

[201] S. Godfrey and N. Isgur, Phys. Rev. D **32**, 189 (1985).

[202] S. N. Gupta, S. F. Radford and W. W. Repko, Phys. Rev. D **26**, 3305 (1982).

[203] S. N. Gupta, S. F. Radford and W. W. Repko, Phys. Rev. D **30**, 2424 (1984).

[204] S. N. Gupta, S. F. Radford and W. W. Repko, Phys. Rev. D **34**, 201 (1986).

[205] M. Bander, D. Silverman, B. Klima and U. Maor, Phys. Rev. D **29**, 2038 (1984).

[206] F. Daghighian and D. Silverman, Phys. Rev. D **36**, 3401 (1987).

[207] E. J. Eichten, K. Lane and C. Quigg, Phys. Rev. D **69**, 094019 (2004) [arXiv:hep-ph/0401210].

[208] E. J. Eichten, K. Lane and C. Quigg, Phys. Rev. Lett. **89**, 162002 (2002) [arXiv:hep-ph/0206018].

[209] T. Skwarnicki, Int. J. Mod. Phys. A **19**, 1030 (2004) [arXiv:hep-ph/0311243].

[210] S. B. Athar *et al.* [CLEO Collaboration], Phys. Rev. D **70**, 112002 (2004) [arXiv:hep-ex/0408133].

[211] D. Cinabro *et al.* [CLEO Collaboration], arXiv:hep-ex/0207062.

[212] G. D. Crawford *et al.* [CLEO Collaboration], Phys. Lett. B **294**, 139 (1992).

[213] U. Heintz *et al.*, Phys. Rev. D **46**, 1928 (1992).

[214] L. P. Fulcher, Phys. Rev. D **42**, 2337 (1990).

[215] L. P. Fulcher, Phys. Rev. D **39**, 295 (1989).

[216] Y. o. Zhu, Ph. D. Thesis, California Institute of Technology, 1988, Caltech report CALT-68-1513 (unpublished).

[217] S. Godfrey and J. L. Rosner, Phys. Rev. D **65**, 074011 (2001) [Erratum-ibid. D **65**, 039901 (2002)] [arXiv:hep-ph/0104253].

[218] X. Zhang, K. J. Sebastian and H. Grotch, Phys. Rev. D **44**, 1606 (1991).

[219] A. H. Mahmood *et al.* [CLEO Collaboration], arXiv:hep-ex/0207057.

[220] G. Karl, S. Meshkov and J. L. Rosner, Phys. Rev. Lett. **45**, 215 (1980).

[221] K. J. Sebastian, H. Grotch and F. L. Ridener, Phys. Rev. D **45**, 3163 (1992).

[222] M. Ambrogiani *et al.* [E835 Collaboration], Phys. Rev. D **65**, 052002 (2002).

[223] M. Ablikim *et al.* [BES Collaboration], Phys. Rev. D **70**, 092004 (2004) [arXiv:hep-ex/0409034].

[224] F. Abe *et al.* [CDF Collaboration], Phys. Rev. Lett. **81**, 2432 (1998) [arXiv:hep-ex/9805034].

[225] S. S. Gershtein, V. V. Kiselev, A. K. Likhoded and A. V. Tkabladze, Phys. Usp. **38**, 1 (1995) [Usp. Fiz. Nauk **165**, 3 (1995)] [arXiv:hep-ph/9504319].

[226] L. P. Fulcher, Phys. Rev. D **60**, 074006 (1999) [arXiv:hep-ph/9806444].

[227] K. Gottfried, CLNS-376 *Invited paper presented at Int. Symp. on Lepton and Photon Interactions at High Energies, Hamburg, Germany, Aug 25-31, 1977*; Phys. Rev. Lett. **40**, 598 (1978).

[228] G. Bhanot, W. Fischler and S. Rudas, Nucl. Phys. B **155**, 208 (1979); M. E. Peskin, ibid. B **156**, 365 (1979); G. Bhanot and M. E. Peskin, ibid. B **156**, 391 (1979).

[229] M. B. Voloshin, Nucl. Phys. B **154**, 365 (1979); M. B. Voloshin and V. I. Zakharov, Phys. Rev. Lett. **45**, 688 (1980); V. A. Novikov and M. A. Shifman, Z. Phys. C **8**, 43 (1981); M. Shifman, Phys. Rept. **209**, 341 (1991) [Sov. Phys. Usp. **32**, 289 (1989 UFNAA,157,561-598.1989)].

[230] T. M. Yan, Phys. Rev. D **22**, 1652 (1980).

[231] Y.-P. Kuang, Y.-P. Yi and B. Fu, Phys. Rev. D **42**, 2300 (1990).

[232] A. Falk, H. Georgi, B. Grinstein and M.B. Wise, Nucl. Phys. B **343**, 1 (1990).

[233] R. Casalbuoni, A. Deandrea, N. Di Bartolomeo, R. Gatto, F. Feruglio and G. Nardulli, Phys. Rep. **281**, 145 (1997) [arXiv:hep-ph/9605342].

[234] R. Casalbuoni, A. Deandrea, N. Di Bartolomeo, F. Feruglio, R. Gatto and G. Nardulli, Phys. Lett. B **302**, 95 (1993).

[235] R. Casalbuoni, A. Deandrea, N. Di Bartolomeo, R. Gatto, F. Feruglio and G. Nardulli, Phys. Lett. B **309**, 163 (1993) [arXiv:hep-ph/9304280].

[236] M. Bando, T. Kugo and K. Yamawaki, Nucl. Phys. B **259**, 493 (1985); Phys. Rep. **164**, 217 (1988).

[237] Y.-P. Kuang and T.-M. Yan, Phys. Rev. D **24**, 2874 (1981).

[238] S.-H. H. Tye, Phys. Rev. D **13**, 3416 (1976); R.C. Giles and S.-H. H. Tye, Phys. Rev. Lett. **37**, 1175 (1976); Phys. Rev. D **16**, 1079 (77); W. Buchmüller and S.-H. H. Tye, Phys. Rev. Lett. **44**, 850 (1980).

[239] D.-S. Liu and Y.-P. Kuang, Z. Phys. C **37**, 119 (1987); P.-Z. Bi and Y.-M. Shi, Mod. Phys. Lett. A **7**, 3161 (1992).

[240] L. S. Brown and R. N. Cahn, Phys. Rev. Lett. **35**, 1 (1975).

[241] J. Z. Bai *et al.* [BES Collaboration], Phys. Rev. D **70**, 012006 (2004) [arXiv:hep-ex/0403023].

[242] B. L. Ioffe and M. A. Shifman, Phys. Lett. B **95**, 99 (1980).

[243] A. Billoire, R. Lacaze, A. Morel, and H. Navelet, Nucl. Phys. B **155**, 493 (1979).

[244] P. Moxhay, Phys. Rev. D **37**, 2557 (1988).

[245] P. Ko, Phys. Rev. D **47**, 208 (1993).

[246] J. L. Rosner, Phys. Rev. D **67**, 097504 (2003) [arXiv:hep-ph/0302122].

[247] Y.-P. Kuang and T.-M. Yan, Phys. Rev. D **41**, 155 (1990).

[248] Y.-P. Kuang, Phys. Rev. D **65**, 094024 (2002).

[249] R. A. Partridge, CALT-68-1150; R. H. Schindler, SLAC-R-0219; J. Adler, *et al.*, Phys. Rev. Lett. **60**, 89 (1988).

[250] S. Godfrey, Z. Phys. C **31**, 77 (1986).

[251] Y. Q. Chen and Y. P. Kuang, Phys. Rev. D **46**, 1165 (1992) [Erratum-ibid. D **47**, 350 (1993)].

[252] J. Z. Bai *et al.* [BES Collaboration], Phys. Lett. B **605**, 63 (2005) [arXiv:hep-ex/0307028].

[253] K. Heikkilä, S. Ono, and N. A. Törnqvist, Phys. Rev. D **29**, 110 (1984); K. Heikkila, S. Ono and N. A. Tornqvist, Phys. Rev. D **29**, 110 (1984) [Erratum-ibid. D **29**, 2136 (1984)]; S. Ono and N. A. Törnqvist, Z. Phys. C **23**, 59 (1984); N. A. Törnqvist, Phys. Rev. Lett. **53**, 878 (1984); Acta Phys. Polon. B **16**, 503 (1985) [Erratum-ibid. B **16**, 683 (1985)].

[254] A. Tomaradze, *talk at the Hadron 2001 Conference, Protvino, Russia, 2001*.

[255] Crystal Ball Group, Annu. Rev. Nucl. Part. Sci. **33**, 143 (1983).

[256] Y. P. Kuang, S. F. Tuan and T. M. Yan, Phys. Rev. D **37**, 1210 (1988); Y.-P. Kuang, in Proc. Intern. Symp. on Extended Objects and Bound States, March 19-21 (1992), Karuizawa, Japan, eds. O. Hara, S. Ishida, and S. Naka (World Scientific, Singapore,1992).

[257] M. Suzuki, Phys. Rev. D **66**, 037503 (2002) [arXiv:hep-ph/0204043].

[258] A. Tomaradze, *talk at the 3nd QWG Workshop, Beijing, 2004*, http://www.qwg.to.infn.it/WS-oct04/index.html; arXiv:hep-ex/0410090.

[259] C. Patrignani, *talk at the 3nd QWG Workshop, Beijing, 2004*, http://www.qwg.to.infn.it/WS-oct04/index.html; arXiv:hep-ex/0410085.

[260] For example, Ref. [177, 191] and V. E. Zambetakis, "Coupled Channel Mixing Effects And Magnetic Dipole Transitions In Quarkonia. UCLA-86-TEP-2.

[261] A. Le Yaouanc, L. Oliver, O. Pene, and J.-C. Raynal, Phys. Rev. D **8**, 2223 (1973).

[262] M. Chaichian and R. Kogerler, Annals Phys. **124**, 61 (1980).

[263] H.-Y. Zhou and Y.-P. Kuang, Phys. Rev. D **44**, 756 (1991).

[264] J. G. Körner, J. H. Kühn, M. Krammer and H. Schneider, Nucl. Phys. B **229**, 115 (1983).

[265] H. Albrecht *et al.* [ARGUS Collaboration], Z. Phys. C **35**, 283 (1987).

[266] F. Butler *et al.* [CLEO Collaboration], Phys. Rev. D **49**, 40 (1994); I. C. Brock *et al.*, Phys. Rev. D **43**, 1448 (1991).

[267] D. Besson *et al.* [CLEO Collaboration], Phys. Rev. D **30**, 1433 (1984).

[268] V. Fonseca *et al.* [CUSB Collaboration], Nucl. Phys. B **242**, 31 (1984).

[269] D. Gelphman *et al.* [Crystal Ball Collaboration], Phys. Rev. D **32**, 2893 (1985).

[270] R. N. Cahn, Phys. Rev. D **12**, 3559 (1975).

[271] S. Chakravarty and P. Ko, Phys. Rev. D **48**, 1205 (1993).

[272] G. Belanger, T. Degrand and P. Moxhay, Phys. Rev. D **39**, 257 (1989).

[273] D. Morgan and M. R. Pennington, Phys. Rev. D **12**, 1283 (1975).

[274] J. P. Alexander *et al.* [CLEO Collaboration], Phys. Rev. D **58**, 052004 (1998) [arXiv:hep-ex/9802024].

[275] M. B. Voloshin, JETP Lett. **37**, 69 (1983) [Pisma Zh. Eksp. Teor. Fiz. **37**, 58 (1983)]; T. N. Truong, Univeristy of Virginia report (unpublished).

[276] V. V. Anisovich, D. V. Bugg, A. V. Sarantsev and B. S. Zou, Phys. Rev. D **51**, 4619 (1995).

[277] H. J. Lipkin and S. F. Tuan, Phys. Lett. B **206**, 349 (1988); P. Moxhay, Phys. Rev. D **39**, 3497 (1989).

[278] T. Komada, S. Ishida and M. Ishida, Phys. Lett. B **508**, 31 (2001); M. Ishida, S. Ishida, T. Komada and S. I. Matsumoto, Phys. Lett. B **518**, 47 (2001).

[279] M. Uehara, Prog. Theor. Phys. **109**, 265 (2003) [arXiv:hep-ph/0211029].

[280] S. K. Choi *et al.* [Belle Collaboration], Phys. Rev. Lett. **91**, 262001 (2003) [arXiv:hep-ex/0309032].

[281] W. M. Tanenbaum *et al.*, Phys. Rev. Lett. **36**, 402 (1976).

[282] W. Bartel *et al.*, Phys. Lett. B **79**, 492 (1978).

[283] R. Brandelik *et al.* [DASP Collaboration], "Experimental Results On The Decay Sequences Psi-Prime (3685) → Gamma P(C) Nucl. Phys. B **160**, 426 (1979).

[284] T. Himel *et al.*, Phys. Rev. Lett. **44**, 920 (1980).

[285] M. Oreglia *et al.*, Phys. Rev. Lett. **45**, 959 (1980).

[286] J. Z. Bai *et al.* [BES Collaboration], Nucl. Instrum. Meth. A **458**, 627 (2001).

[287] M. Ablikim *et al.* [BES Collaboration], Phys. Rev. D **70**, 012003 (2004) [arXiv:hep-ex/0404020].

[288] J. Z. Bai *et al.* [BES Collaboration], Nucl. Instrum. Meth. A **344**, 319 (1994).

[289] T. A. Armstrong *et al.* [Fermilab E760 Collaboration], Phys. Rev. D **55**, 1153 (1997).

[290] G. Abrams, Proceedings of the 1975 International Symposium on Lepton and Photon Interactions at High Energies, published by the Stanford Linear Accelerator Center, 36 (1975).

[291] M. B. Voloshin, JETP Lett. **21**, 347 (1975) [Pisma Zh. Eksp. Teor. Fiz. **21**, 733 (1975)].

[292] J. Z. Bai *et al.* [BES Collaboration], Phys. Rev. D **62**, 032002 (2000) [arXiv:hep-ex/9909038].

[293] Two of equations in Ref. [270] omitted interference terms. See [292].

[294] T. Ishida, M. Ishida, S. Ishida, K. Takamatsu and T. Tsuru, arXiv:hep-ph/9712230.

[295] T. Mannel and R. Urech, Z. Phys. C **73**, 541 (1997) [arXiv:hep-ph/9510406].

[296] M. L. Yan, Y. Wei and T. L. Zhuang, Eur. Phys. J. C **7**, 61 (1999) [arXiv:hep-ph/9805354].

[297] S. L. Olsen [Belle Collaboration], Int. J. Mod. Phys. A **20**, 240 (2005) [arXiv:hep-ex/0407033].

[298] D. Acosta *et al.* [CDF II Collaboration], Phys. Rev. Lett. **93**, 072001 (2004) [arXiv:hep-ex/0312021].

[299] M. Masetti, Phys. Lett. B **286**, 160 (1992); R. Fleischer and D. Wyler, Phys. Rev. D **62**, 057503 (2000) [arXiv:hep-ph/0004010]; M. A. Ivanov, J. G. Körner and O. N. Pakhomova, Phys. Lett. B **555**, 189 (2003) [arXiv:hep-ph/0212291]; Y. S. Dai and D. S. Du, Eur. Phys. J. C **9**, 557 (1999) [arXiv:hep-ph/9809386]; J. F. Liu and K. T. Chao, Phys. Rev. D **56**, 4133 (1997).

[300] V. V. Kiselev, J. Phys. G **30**, 1445 (2004) [arXiv:hep-ph/0302241].

[301] F. Abe *et al.*, CDF Collaboration, Phys. Rev. **D58**, 112004 (1998).

[302] S. S. Gershtein *et al.*, Sov. J. Nucl. Phys. **48**, 327 (1988), [Yad. Fiz. **48**, 515 (1988)]; V. V. Kiselev, A. K. Likhoded and A. V. Tkabladze, Sov. J. Nucl. Phys. **46**, 535 (1987) [Yad. Fiz. **46**, 934 (1987)]; S. S. Gershtein, A. K. Likhoded and S. R. Slabospitsky, Int. J. Mod. Phys. A **6**, 2309 (1991); S. S. Gershtein *et al.*, Phys. Rev. D **51**, 3613 (1995); A. V. Berezhnoi, V. V. Kiselev, A. K. Likhoded and A. I. Onishchenko, Phys. Atom. Nucl. **60**, 1729 (1997) [Yad. Fiz. **60N10**, (1997)] [arXiv:hep-ph/9703341].

[303] N. Brambilla and A. Vairo, Phys. Rev. D **62**, 094019 (2000) [arXiv:hep-ph/0002075].

[304] S. Capstick and S. Godfrey, Phys. Rev. D **41**, 2856 (1990).

[305] I. I. Y. Bigi, Phys. Lett. B **371**, 105 (1996) [arXiv:hep-ph/9510325]; M. Beneke and G. Buchalla, Phys. Rev. D **53**, 4991 (1996) [arXiv:hep-ph/9601249]; A. I. Onishchenko, arXiv:hep-ph/9912424; C. H. Chang, S. L. Chen, T. F. Feng and X. Q. Li, Commun. Theor. Phys. **35**, 51 (2001); Phys. Rev. D **64**, 014003 (2001) [arXiv:hep-ph/0007162].

[306] V. V. Kiselev and A. V. Tkabladze, Phys. Rev. D **48**, 5208 (1993).

[307] V. V. Kiselev, A. K. Likhoded and A. I. Onishchenko, Nucl. Phys. B **569**, 473 (2000) [arXiv:hep-

ph/9905359].

[308] V. V. Kiselev, A. E. Kovalsky and A. K. Likhoded, Nucl. Phys. B **585**, 353 (2000) [arXiv:hep-ph/0002127]; arXiv:hep-ph/0006104.

[309] V. V. Kiselev, arXiv:hep-ph/0211021.

[310] K. Anikeev *et al.*, arXiv:hep-ph/0201071.

[311] I. P. Gouz, V. V. Kiselev, A. K. Likhoded, V. I. Romanovsky and O. P. Yushchenko, Phys. Atom. Nucl. **67**, 1559 (2004) [Yad. Fiz. **67**, 1581 (2004)] [arXiv:hep-ph/0211432].

[312] J. D. Bjorken, draft report 07/22/86 (1986) [unpublished].

[313] V. V. Kiselev and A. K. Likhoded, Phys. Usp. **45**, 455 (2002) [Usp. Fiz. Nauk **172**, 497 (2002)] [arXiv:hep-ph/0103169]; A. V. Berezhnoi, V. V. Kiselev and A. K. Likhoded, Phys. Atom. Nucl. **59**, 870 (1996) [Yad. Fiz. **59**, 909 (1996)] [arXiv:hep-ph/9507242]; S. P. Baranov, Phys. Rev. D **54**, 3228 (1996); M. A. Doncheski, J. Steegborn and M. L. Stong, Phys. Rev. D **53**, 1247 (1996) [arXiv:hep-ph/9507220]; A. V. Berezhnoi, V. V. Kiselev, A. K. Likhoded and A. I. Onishchenko, Phys. Rev. D **57**, 4385 (1998) [arXiv:hep-ph/9710339]; V. V. Kiselev and A. E. Kovalsky, Phys. Atom. Nucl. **63**, 1640 (2000) [Yad. Fiz. **63**, 1728 (2000)] [arXiv:hep-ph/9908321]; V. V. Braguta, V. V. Kiselev and A. E. Chalov, Phys. Atom. Nucl. **65**, 1537 (2002) [Yad. Fiz. **65**, 1575 (2002)].

[314] T. Mannel and G. A. Schuler, Z. Phys. C **67**, 159 (1995) [arXiv:hep-ph/9410333].

[315] M. E. Luke, A. V. Manohar and I. Z. Rothstein, Phys. Rev. D **61**, 074025 (2000) [arXiv:hep-ph/9910209]; A. V. Manohar and I. W. Stewart, Phys. Rev. D **63**, 054004 (2001) [arXiv:hep-ph/0003107]; A. H. Hoang, A. V. Manohar and I. W. Stewart, Phys. Rev. D **64**, 014033 (2001) [arXiv:hep-ph/0102257].

[316] M. A. Shifman, A. I. Vainshtein and V. I. Zakharov, Nucl. Phys. B **147**, 448 (1979); ibid. 385 (1979); ibid. 519 (1979); V. A. Novikov, L. B. Okun, M. A. Shifman, A. I. Vainshtein, M. B. Voloshin and V. I. Zakharov, Phys. Rept. **41**, 1 (1978); L. J. Reinders, H. Rubinstein and S. Yazaki, Phys. Rept. **127**, 1 (1985).

[317] M. Lusignoli and M. Masetti, Z. Phys. C **51**, 549 (1991).

[318] V. V. Kiselev, Mod. Phys. Lett. A **10**, 1049 (1995) [arXiv:hep-ph/9409348]; V. V. Kiselev, Int. J. Mod. Phys. A **9**, 4987 (1994).

[319] V. V. Kiselev, A. K. Likhoded and A. V. Tkabladze, Phys. Atom. Nucl. **56**, 643 (1993), Yad. Fiz. **56**, 128 (1993).

[320] V. V. Kiselev and A. V. Tkabladze, Yad. Fiz. **48**, 536 (1988); G. R. Jibuti and Sh. M. Esakia, Yad. Fiz. **50**, 1065 (1989), ibid. **51**, 1681 (1990).

[321] A. Abd El-Hady, J. H. Munoz and J. P. Vary, Phys. Rev. D **62**, 014019 (2000) [arXiv:hep-ph/9909406].

[322] C. H. Chang and Y. Q. Chen, Phys. Rev. D **49**, 3399 (1994).

[323] M. A. Ivanov, J. G. Körner and P. Santorelli, Phys. Rev. D **63**, 074010 (2001) [arXiv:hep-ph/0007169].

[324] D. Scora and N. Isgur, Phys. Rev. D **52**, 2783 (1995) [arXiv:hep-ph/9503486].

[325] A. Y. Anisimov, I. M. Narodetsky, C. Semay and B. Silvestre-Brac, Phys. Lett. B **452**, 129 (1999) [arXiv:hep-ph/9812514]; A. Y. Anisimov, P. Y. Kulikov, I. M. Narodetsky and K. A. Ter-Martirosian, Phys. Atom. Nucl. **62**, 1739 (1999) [Yad. Fiz. **62**, 1868 (1999)] [arXiv:hep-ph/9809249].

[326] P. Colangelo and F. De Fazio, Phys. Rev. D **61**, 034012 (2000) [arXiv:hep-ph/9909423].

[327] P. Colangelo, G. Nardulli and N. Paver, Z. Phys. C **57**, 43 (1993); E. Bagan, H. G. Dosch, P. Gosdzinsky, S. Narison and J. M. Richard, Z. Phys. C **64**, 57 (1994) [arXiv:hep-ph/9403208].

[328] G. Buchalla, A. J. Buras and M. E. Lautenbacher, Rev. Mod. Phys. **68** (1996) 1125 [arXiv:hep-ph/9512380].

[329] R. C. Verma and A. Sharma, Phys. Rev. D **65**, 114007 (2002).

[330] D. Ebert, R. N. Faustov and V. O. Galkin, Mod. Phys. Lett. A **17**, 803 (2002) [arXiv:hep-ph/0204167]; Eur. Phys. J. C **32**, 29 (2003) [arXiv:hep-ph/0308149]; Phys. Rev. D **68**, 094020 (2003) [arXiv:hep-ph/0306306].

[331] C. H. Chang, Y. Q. Chen, G. L. Wang and H. S. Zong, Phys. Rev. D **65**, 014017 (2002) [arXiv:hep-ph/0103036]; Commun. Theor. Phys. **35**, 395 (2001) [arXiv:hep-ph/0102150].

[332] O. N. Pakhomova and V. A. Saleev, Phys. Atom. Nucl. **63**, 1999 (2000); Yad. Fiz. **63**, 2091 (2000) [arXiv:hep-ph/9911313]; V. A. Saleev, arXiv:hep-ph/0007352; V. V. Kiselev, O. N. Pakhomova and V. A. Saleev, J. Phys. G **28**, 595 (2002) [arXiv:hep-ph/0110180]; G. Lopez Castro, H. B. Mayorga and J. H. Munoz, J. Phys. G **28**, 2241 (2002) [arXiv:hep-ph/0205273].

[333] G. Chiladze, A. F. Falk and A. A. Petrov, Phys. Rev. D **60**, 034011 (1999) [arXiv:hep-ph/9811405]; C. H. Chang, J. P. Cheng and C. D. Lu, Phys. Lett. B **425**, 166 (1998) [arXiv:hep-ph/9712325]; T. M. Aliev and M. Savci, Phys. Lett. B **434**, 358 (1998) [arXiv:hep-ph/9804407]; J. Phys. G **24**, 2223 (1998) [arXiv:hep-ph/9805239]; P. Colangelo and F. De Fazio, Mod. Phys. Lett. A **14**, 2303 (1999) [arXiv:hep-ph/9904363].

[334] D. S. Du, X. l. Li and Y. d. Yang, Phys. Lett. B **380**, 193 (1996) [arXiv:hep-ph/9603291]; S. Fajfer, S. Prelovsek and P. Singer, Phys. Rev. D **59**, 114003 (1999) [Erratum-ibid. D **64**, 099903 (2001)] [arXiv:hep-ph/9901252]; T. M. Aliev and M. Savci, Phys. Lett. B **480**, 97 (2000) [arXiv:hep-ph/9908203].

[335] P. Ball, M. Beneke and V. M. Braun, Nucl. Phys. B **452**, 563 (1995) [arXiv:hep-ph/9502300]; Phys. Rev. D **52**, 3929 (1995) [arXiv:hep-ph/9503492]; P. Ball, V. M. Braun and H. G. Dosch, Phys. Rev. D **48**, 2110 (1993) [arXiv:hep-ph/9211244]; A. A. Ovchinnikov and V. A. Slobodenyuk, Sov. J. Nucl. Phys. **50**, 891 (1989) [Yad. Fiz. **50**, 1433 (1989)]; Z. Phys. C **44**, 433 (1989).

[336] E. Jenkins, M. E. Luke, A. V. Manohar and M. J. Savage, Nucl. Phys. B **390**, 463 (1993) [arXiv:hep-ph/9204238].

[337] M. A. Sanchis-Lozano, Nucl. Phys. B **440**, 251 (1995) [arXiv:hep-ph/9502359].

[338] E. Braaten and S. Fleming, Phys. Rev. D **52**, 181 (1995) [arXiv:hep-ph/9501296].

[339] A. I. Onishchenko and O. L. Veretin, arXiv:hep-ph/0302132.

[340] S. Narison, Phys. Lett. B **210**, 238 (1988); V. V. Kiselev and A. V. Tkabladze, Sov. J. Nucl. Phys. **50**, 1063 (1989) [Yad. Fiz. **50**, 1714 (1989)]; T. M. Aliev and O. Yilmaz, Nuovo Cim. A **105**, 827 (1992); S. Reinshagen and R. Rückl, CERN-TH-6879-93 *Invited talk at 28th Rencontres de Moriond: QCD and High Energy Hadronic Interactions, Les Arcs, France, 20-27 Mar 1993*; MPI-PH-93-88 *Invited talk at Workshop on Quantum Field Theoretical Aspects of High Energy Physics, Kyffhauser, Germany, Sep 20-24, 1993*; M. Chabab, Phys. Lett. B **325**, 205 (1994); A. I. Onishchenko, arXiv:hep-ph/0005127.

[341] V. V. Kiselev, Phys. Part. Nucl. **31**, 538 (2000) [Fiz. Elem. Chast. Atom. Yadra **31**, 1080 (2000)]; S. S. Gershtein, V. V. Kiselev, A. K. Likhoded, A. V. Tkabladze, A. V. Berezhnoi and A. I. Onishchenko, arXiv:hep-ph/9803433; V. V. Kiselev, Int. J. Mod. Phys. A **11**, 3689 (1996) [arXiv:hep-ph/9504313]; V. V. Kiselev, Nucl. Phys. B **406**, 340 (1993).

[342] V. V. Kiselev, A. E. Kovalsky and A. I. Onishchenko, Phys. Rev. D **64**, 054009 (2001) [arXiv:hep-ph/0005020].

[343] V. V. Kiselev, A. K. Likhoded, O. N. Pakhomova and V. A. Saleev, Phys. Rev. D **65**, 034013 (2002) [arXiv:hep-ph/0105190].

[344] V. V. Kiselev, arXiv:hep-ph/0304017.

[345] M. A. Shifman, Nucl. Phys. B **388**, 346 (1992); B. Blok, M. Shifman, Nucl. Phys. B **389**, 534 (1993).

[346] S. S. Gershtein *et al.*, arXiv:hep-ph/9803433; V. V. Kiselev, Phys. Lett. B **372**, 326 (1996)

[arXiv:hep-ph/9507228]; arXiv:hep-ph/9605451.

[347] C. H. Chang, A. K. Giri, R. Mohanta and G. L. Wang, J. Phys. G **28**, 1403 (2002) [arXiv:hep-ph/0204279].

[348] M. A. Nobes and R. M. Woloshyn, J. Phys. G **26**, 1079 (2000) [arXiv:hep-ph/0005056].

[349] T. Mannel and S. Wolf, Phys. Rev. D **65**, 074012 (2002) [arXiv:hep-ph/0109250].

[350] J. P. Ma and J. S. Xu, Eur. Phys. J. C **24**, 261 (2002); X. G. Wu, C. H. Chang, Y. Q. Chen and Z. Y. Fang, Phys. Rev. D **67**, 094001 (2003) [arXiv:hep-ph/0209125]; C. H. Chang, arXiv:hep-ph/0205112.

[351] A. Faessler, T. Gutsche, M. A. Ivanov, J. G. Korner and V. E. Lyubovitskij, Eur. Phys. J. directC **4**, 18 (2002) [arXiv:hep-ph/0205287]; C. Q. Geng, C. W. Hwang and C. C. Liu, Phys. Rev. D **65**, 094037 (2002) [arXiv:hep-ph/0110376].

[352] M. Gronau and D. Wyler, Phys. Lett. B **265**, 172 (1991).

[353] V. V. Kiselev and O. P. Yushchenko, Phys. Lett. B **568**, 219 (2003) [arXiv:hep-ph/0211382].

[354] C. Quigg, FERMILAB-CONF-93-265-T *Presented at Summer Workshop on B Physics at Hadron Accelerators, Snowmass, Colorado, 21 Jun - 2 Jul 1993*.

Chapter 5

PRODUCTION

Conveners: G.T. Bodwin, E. Braaten, M. Krämer, A.B. Meyer, V. Papadimitriou

Authors: G.T. Bodwin, E. Braaten, C.-H. Chang, M. Krämer, J. Lee, A.B. Meyer, V. Papadimitriou, R. Vogt

1 FORMALISM FOR INCLUSIVE QUARKONIUM PRODUCTION

1.1 NRQCD factorization method

In both heavy-quarkonium annihilation decays and hard-scattering production, large energy–momentum scales appear. The heavy-quark mass m is much larger than Λ_{QCD}, and, in the case of production, the transverse momentum p_T can be much larger than Λ_{QCD} as well. This implies that the associated values of the QCD running coupling constant are much less than one. ($\alpha_s(m_c) \approx 0.25$ and $\alpha_s(m_b) \approx 0.18$.) Therefore, one might hope that it would be possible to calculate the rates for heavy quarkonium decay and production accurately in perturbation theory. However, there are clearly low-momentum, nonperturbative effects associated with the dynamics of the quarkonium bound state that invalidate the direct application of perturbation theory.

In order to make use of perturbative methods, one must first separate the short-distance/high-momentum, perturbative effects from the long-distance/low-momentum, nonperturbative effects — a process which is known as "factorization." One convenient way to carry out this separation is through the use of the effective field theory Nonrelativistic QCD (NRQCD) [1–3]. NRQCD reproduces full QCD accurately at momentum scales of order mv and smaller, where v is the typical heavy-quark velocity in the bound state in the CM frame. ($v^2 \approx 0.3$ for charmonium, and $v^2 \approx 0.1$ for bottomonium.) Virtual processes involving momentum scales of order m and larger can affect the lower-momentum processes, and their effects are taken into account through the short-distance coefficients of the operators that appear in the NRQCD action.

Because $Q\bar{Q}$ production occurs at momentum scales of order m or larger, it manifests itself in NRQCD through contact interactions. As a result, the inclusive cross-section for the direct production of the quarkonium H at large transverse momentum (p_T of order m or larger) in hadron or ep colliders or at large momentum in the CM frame (p^* of order m or larger) in e^+e^- colliders can be written as a sum of products of NRQCD matrix elements and short-distance coefficients:

$$\sigma[H] = \sum_n \sigma_n(\Lambda)\langle \mathcal{O}_n^H(\Lambda)\rangle. \tag{5.1}$$

Here, Λ is the ultraviolet cutoff of the effective theory, the σ_n are short-distance coefficients, and the $\langle \mathcal{O}_n^H \rangle$ are vacuum-expectation values of four-fermion operators in NRQCD. There is a formula analogous to Eq. (5.1) for inclusive quarkonium annihilation rates, except that the vacuum-to-vacuum matrix elements are replaced by quarkonium-to-quarkonium matrix elements [3].

The short-distance coefficients $\sigma_n(\Lambda)$ in (5.1) are essentially the process-dependent partonic cross-sections to make a $Q\bar{Q}$ pair, convolved with parton distributions if there are hadrons in the initial state. The $Q\bar{Q}$ pair can be produced in a colour-singlet state or in a colour-octet state. Its spin state can be singlet or triplet, and it also can have orbital angular momentum. The short-distance coefficients are determined by matching the square of the production amplitude in NRQCD to full QCD. Because the scale of the $Q\bar{Q}$ production is of order m or greater, this matching can be carried out in perturbation theory.

The four-fermion operators in Eq. (5.1) create a $Q\bar{Q}$ pair in the NRQCD vacuum, project it onto a state that in the asymptotic future consists of a heavy quarkonium plus anything, and then annihilate the $Q\bar{Q}$ pair. The vacuum matrix element of such an operator is the probability for a $Q\bar{Q}$ pair to form a quarkonium plus anything. These matrix elements are somewhat analogous to parton fragmentation functions. They contain all of the nonperturbative physics associated with evolution of the $Q\bar{Q}$ pair into a quarkonium state. An important property of the matrix elements, which greatly increases the predictive power of NRQCD, is the fact that they are universal, i.e., process independent.

The colour-singlet and colour-octet four-fermion operators that appear in Eq. (5.1) correspond to the evolution into a colour-singlet quarkonium of a $Q\bar{Q}$ pair created at short distance in a colour-singlet state or a colour-octet state, respectively. In the case of decay, the colour-octet matrix elements have the interpretation of the probability to find the quarkonium in a Fock state consisting of a $Q\bar{Q}$ pair plus some number of gluons. It is a common misconception that colour-octet production proceeds through the production of a higher Fock state of the quarkonium. However, in the leading colour-octet production mechanisms, the gluons that neutralize the colour are not present at the time of the creation of the colour-octet $Q\bar{Q}$ pair, but are emitted during the subsequent hadronization process. The production of the quarkonium through a higher Fock state requires the production of gluons that are nearly collinear to the $Q\bar{Q}$ pair, and it is suppressed by additional powers of v.

NRQCD power-counting rules allow one to organize the sum over operators in Eq. (5.1) as an expansion in powers of v. Through a given order in v, only a finite set of matrix elements contributes. Furthermore, there are simplifying relations between matrix elements, such as the heavy-quark spin symmetry and the vacuum-saturation approximation, that reduce the number of independent matrix elements [3]. Some examples of relations between colour-singlet matrix elements that follow from heavy-quark spin symmetry are

$$\langle \mathcal{O}_1^{J/\psi}(^3S_1) \rangle \;=\; 3\,\langle \mathcal{O}_1^{\eta_c}(^1S_0) \rangle, \tag{5.2}$$
$$\langle \mathcal{O}_1^{\chi_{cJ}}(^3P_J) \rangle \;=\; \tfrac{1}{3}(2J+1)\langle \mathcal{O}_1^{h_c}(^1P_1) \rangle. \tag{5.3}$$

These relations hold up to corrections of order v^2. The prefactors on the right side of Eqs. (5.2)–(5.3) are just ratios of the numbers of spin states. Since the operators in Eqs. (5.2) and (5.3) have the same angular momentum quantum numbers as the $Q\bar{Q}$ pair in the dominant Fock state of the quarkonium, the vacuum-saturation approximation can be used to express the matrix elements in terms of the squares of wave functions or their derivatives at the origin, up to corrections of order v^4. heavy-quark spin symmetry also gives relations between colour-octet matrix elements, such as

$$\langle \mathcal{O}_8^{J/\psi}(^3S_1) \rangle \;=\; 3\,\langle \mathcal{O}_8^{\eta_c}(^1S_0) \rangle, \tag{5.4}$$
$$\langle \mathcal{O}_8^{J/\psi}(^1S_0) \rangle \;=\; \langle \mathcal{O}_8^{\eta_c}(^3S_1) \rangle, \tag{5.5}$$
$$\langle \mathcal{O}_8^{J/\psi}(^3P_J) \rangle \;=\; \tfrac{1}{3}(2J+1)\langle \mathcal{O}_8^{\eta_c}(^1P_1) \rangle, \tag{5.6}$$
$$\langle \mathcal{O}_8^{\chi_{cJ}}(^3S_1) \rangle \;=\; \tfrac{1}{3}(2J+1)\langle \mathcal{O}_8^{h_c}(^1S_0) \rangle. \tag{5.7}$$

These relations hold up to corrections of order v^2. The prefactors on the right side of Eqs. (5.4)–(5.7) are again just ratios of the numbers of spin states. The vacuum-saturation approximation is not applicable to colour-octet matrix elements.

The relative importance of the terms in the factorization formula in Eq. (5.1) is determined not only by the sizes of the matrix elements but also by the sizes of the coefficients σ_n in Eq. (5.1). The size of the coefficient depends on its order in α_s, colour factors, and dimensionless kinematic factors, such as m^2/p_T^2.

The NRQCD factorization approach is sometimes erroneously called the "colour-octet model," because colour-octet terms are expected to dominate in some situations, such as J/ψ production at large p_T in hadron colliders. However, there are also situations in which colour-singlet terms are expected

to dominate, such as J/ψ production in continuum e^+e^- annihilation at the B factories. Moreover, NRQCD factorization is not a model, but a rigorous consequence of QCD in the limit $\Lambda_{\mathrm{QCD}}/m \to 0$.

A specific truncation of the NRQCD expansion in Eq. (5.1) could be called a model, although, unlike most models, it is in principle systematically improvable. In truncating at a given order in v, one can reduce the number of independent matrix elements by making use of approximate relations, such as Eqs. (5.2)–(5.3) and Eqs. (5.4)–(5.7). The simplest truncation of the NRQCD expansion in Eq. (5.1) that is both phenomenologically viable and corresponds to a consistent truncation in v includes four independent NRQCD matrix elements for each S-wave multiplet (one colour-singlet and three colour-octet) and two independent NRQCD matrix elements for each P-wave multiplet (one colour-singlet and one colour-octet). We will refer to this truncation as the standard truncation in v. For the S-wave charmonium multiplet consisting of J/ψ and η_c, one can take the four independent matrix elements to be $\langle \mathcal{O}_1^{J/\psi}(^3S_1)\rangle$, $\langle \mathcal{O}_8^{J/\psi}(^1S_0)\rangle$, $\langle \mathcal{O}_8^{J/\psi}(^3S_1)\rangle$, and $\langle \mathcal{O}_8^{J/\psi}(^3P_0)\rangle$. Their relative orders in v are v^0, v^3, v^4, and v^4, respectively. It is convenient to define the linear combination

$$M_k^H = \langle \mathcal{O}_8^H(^1S_0)\rangle + \frac{k}{m_c^2}\langle \mathcal{O}_8^H(^3P_0)\rangle\,, \tag{5.8}$$

because many observables are sensitive only to the linear combination of these two colour-octet matrix elements corresponding to a specific value of k. These four independent matrix elements can be used to calculate the cross-sections for the η_c and each of the 3 spin states of the J/ψ. Thus, this truncation of NRQCD gives unambiguous predictions for the polarization of the J/ψ. For the P-wave charmonium multiplet consisting of χ_{c0}, χ_{c1}, χ_{c2}, and h_c, we can take the two independent matrix elements to be $\langle \mathcal{O}_1^{\chi_{c0}}(^3P_0)\rangle$ and $\langle \mathcal{O}_8^{\chi_{c0}}(^3S_1)\rangle$. Their orders in v relative to $\langle \mathcal{O}_1^{J/\psi}(^3S_1)\rangle$ are both v^2. These two independent matrix elements can be used to calculate the cross-sections for each of the 12 spin states in the P-wave multiplet. Thus, this truncation of NRQCD gives unambiguous predictions for the polarizations of the χ_{c1}, χ_{c2}, and h_c.

The NRQCD *decay matrix* elements can be calculated in lattice simulations [4–8] or determined from phenomenology. However, it is not yet known how to formulate the calculation of production matrix elements in lattice simulations, and, so, the production matrix elements must be obtained phenomenologically. In general, the production matrix elements are different from the decay matrix elements. The exceptions are the colour-singlet production matrix elements in which the $Q\bar{Q}$ pair has the same quantum numbers as the quarkonium state, such as those in Eqs. (5.2) and (5.3). They can be related to the corresponding decay matrix elements through the vacuum-saturation approximation, up to corrections of relative order v^4 [3]. Phenomenological determinations of the production matrix elements for charmonium states are given in Section 2.1.

The proof of the factorization formula in Eq. (5.1) relies both on NRQCD and on the all-orders perturbative machinery for proving hard-scattering factorization. A detailed proof does not yet exist, but work is in progress [9]. At a large transverse momentum (p_T of order m or larger), corrections to hard-scattering factorization are thought to be of order $(mv)^2/p_T^2$ (not m^2/p_T^2) in the unpolarized case and of order mv/p_T (not m/p_T) in the polarized case. At a small transverse momentum, p_T of order mv or smaller, the presence of soft gluons in the quarkonium binding process makes the application of the standard factorization techniques problematic. It is not known if there is a factorization formula for $d\sigma/dp_T^2$ at small p_T or for $d\sigma/dp_T^2$ integrated over p_T.

In practical calculations of the rates of quarkonium decay and production, a number of significant uncertainties arise. In many instances, the series in α_s and v in the factorization formula in Eq. (5.1) converge slowly, and the uncertainties from their truncation are large — sometimes 100% or larger. In addition, the matrix elements are often poorly determined, either from phenomenology or lattice measurements, and the important linear combinations of matrix elements vary from process to process, making tests of universality difficult. There are also large uncertainties in the heavy-quark masses (approximately

8% for m_c and approximately 2.4% for m_b) that can be very significant for quarkonium rates that are proportional to a large power of the mass.

Many of the largest uncertainties in the theoretical predictions, as well as some of the experimental uncertainties, cancel in the ratios of cross-sections. Examples in charmonium production are the ratio R_ψ of the inclusive cross-sections for $\psi(2S)$ and J/ψ production and the ratio R_{χ_c} of the inclusive cross-sections for χ_{c1} and χ_{c2} production. These ratios are defined by

$$R_\psi = \frac{\sigma[\psi(2S)]}{\sigma[J/\psi]}, \tag{5.9}$$

$$R_{\chi_c} = \frac{\sigma[\chi_{c1}]}{\sigma[\chi_{c2}]}. \tag{5.10}$$

Other useful ratios are the fractions F_H of J/ψ's that come from decays of higher quarkonium states H. The fractions that come from decays of $\psi(2S)$ and from $\chi_c(1P)$ are defined by

$$F_{\psi(2S)} = \mathrm{Br}[\psi(2S) \to J/\psi + X] \frac{\sigma[\psi(2S)]}{\sigma[J/\psi]}, \tag{5.11}$$

$$F_{\chi_c} = \sum_{J=0}^{2} \mathrm{Br}[\chi_{cJ}(1P) \to J/\psi + X] \frac{\sigma[\chi_{cJ}(1P)]}{\sigma[J/\psi]}. \tag{5.12}$$

The $J = 0$ term in (5.12) is usually negligible, because the branching fraction $\mathrm{Br}[\chi_{c0} \to J/\psi \, X]$ is so small. The fraction of J/ψ's that are produced directly can be denoted by $F_{J/\psi}$.

Another set of observables in which many of the uncertainties cancel out consists of polarization variables, which can be defined as ratios of cross-sections for the production of different spin states of the same quarkonium. The angular distribution of the decay products of the quarkonium depends on the spin state of the quarkonium. The polarization of a 1^{--} state, such as the J/ψ, can be measured from the angular distribution of its decays into lepton pairs. Let θ be the angle in the J/ψ rest frame between the positive lepton momentum and the chosen polarization axis. The most convenient choice of polarization axis depends on the process. The differential cross-section has the form

$$\frac{d\sigma}{d(\cos\theta)} \propto 1 + \alpha \cos^2\theta, \tag{5.13}$$

which defines a polarization variable α whose range is $-1 \le \alpha \le +1$. We can define longitudinally and transversely polarized J/ψ's to be ones whose spin components along the polarization axis are 0 and ± 1, respectively. The polarization variable α can then be expressed as $(1 - 3\xi)/(1 + \xi)$, where ξ is the fraction of the J/ψ's that are longitudinally polarized. The value $\alpha = 1$ corresponds to J/ψ with 100% transverse polarization, while $\alpha = -1$ corresponds to J/ψ with 100% longitudinal polarization.

One short-coming of the NRQCD factorization approach is that, at leading order in v, some of the kinematics of production are treated inaccurately. Specifically, the mass of the light hadronic state that forms during the evolution of the $Q\bar{Q}$ pair into the quarkonium state is neglected, and no distinction is made between $2m$ and the quarkonium mass. While the corrections to these approximations are formally of higher order in v, they can be important numerically in the cases of rapidly varying quarkonium-production distributions, such as p_T distributions at the Tevatron and z distributions at the B factories and HERA near the kinematic limit $z = 1$. These effects can be taken into account through the resummation of certain operator matrix elements of higher order in v [10]. The resummation results in universal nonperturbative shape functions that give the probability distributions for a $Q\bar{Q}$ pair with a given set of quantum numbers to evolve into a quarkonium with a given fraction of the pair's momentum. The shape functions could, in principle, be extracted from the data for one process and applied to another process. Effects from resummation of logarithms of $1 - z$ and model shape functions have been calculated for the

process $e^+e^-{\rightarrow}J/\psi + X$ [11]. For shape functions that satisfy the velocity-scaling rules, these effects are comparable in size. It may be possible to use this resummed theoretical prediction to extract the dominant shape function from the Belle and BaBar data for $e^+e^-{\rightarrow}J/\psi + X$ and then use it to make predictions for J/ψ photoproduction near $z = 1$ [12].

1.2 Colour-singlet model

The colour-singlet model (CSM) was first proposed shortly after the discovery of the J/ψ. The initial applications were to η_c and χ_c production through two-gluon fusion [13–16]. Somewhat later, the CSM was applied to the production of J/ψ and η_c in B-meson decays [17–19] and to the production of J/ψ plus a gluon [20–25] through two-gluon fusion and photon–gluon fusion. The CSM was taken seriously until around 1995, when experiments at the Tevatron showed that it under-predicts the cross-section for prompt charmonium production in $p\bar{p}$ collisions by more than an order of magnitude. An extensive review of the colour-singlet model can be found in Ref. [26].

The colour-singlet model can be obtained from the NRQCD factorization formula in Eq. (5.1) by dropping all of the colour-octet terms and all but one of the colour-singlet terms. The term that is retained is the one in which the quantum numbers of the $Q\bar{Q}$ pair are the same as those of the quarkonium. The CSM production matrix elements are related to the corresponding decay matrix elements by the vacuum-saturation approximation, and, so, they can be determined from annihilation decay rates. Thus, the CSM gives absolutely normalized predictions for production cross-sections. The heavy-quark spin symmetry relates the CSM matrix elements of the $4(2L + 1)$ states within an orbital-angular-momentum multiplet with quantum number L. Thus, the CSM also gives nontrivial predictions for polarization.

In the case of an S-wave state, the CSM term in Eq. (5.1) is the one whose matrix element is of leading order in v. However, owing to kinematic factors or factors of α_s in the short-distance coefficients, the CSM term may not be dominant. In the case of a P-wave state or a state of higher orbital angular momentum, the CSM term is only one of the terms whose matrix element is of leading order in v. For these states, the CSM leads to infrared divergences that cancel only when one includes colour-octet terms whose matrix elements are also of leading order in v. Thus, the CSM is theoretically inconsistent for quarkonium states with nonzero orbital angular momentum.

1.3 Colour-evaporation model

The colour evaporation model (CEM) was first proposed in 1977 [27–30] and has enjoyed considerable phenomenological success. In the CEM, the cross-section for a quarkonium state H is some fraction F_H of the cross-section for producing $Q\bar{Q}$ pairs with invariant mass below the $M\bar{M}$ threshold, where M is the lowest mass meson containing the heavy quark Q. (The CEM parameter F_H should not be confused with the fraction of J/ψ's that come from decay of H.) This cross-section has an upper limit on the $Q\bar{Q}$ pair mass but no constraints on the colour or spin of the final state. The $Q\bar{Q}$ pair is assumed to neutralize its colour by interaction with the collision-induced colour field, that is, by "colour evaporation." The Q and the $\bar{Q}$ either combine with light quarks to produce heavy-flavoured hadrons or bind with each other to form quarkonium. If the $Q\bar{Q}$ invariant mass is less than the heavy-meson threshold $2m_M$, then the additional energy that is needed to produce heavy-flavoured hadrons can be obtained from the nonperturbative colour field. Thus, the sum of the fractions F_H over all quarkonium states H can be less than unity. The fractions F_H are assumed to be universal so that, once they are determined by data, they can be used to predict the cross-sections in other processes and in other kinematic regions.

In the CEM at leading order in α_s, the production cross-section for the quarkonium state H in collisions of the light hadrons h_A and h_B is

$$\sigma_{\text{CEM}}^{(\text{LO})}[h_A h_B{\rightarrow}H + X] =$$

$$F_H \sum_{i,j} \int_{4m^2}^{4m_M^2} d\hat{s} \int dx_1 dx_2\, f_i^{h_A}(x_1,\mu)\, f_j^{h_B}(x_2,\mu)\, \hat{\sigma}_{ij}(\hat{s})\, \delta(\hat{s} - x_1 x_2 s)\,, \qquad (5.14)$$

where $ij = q\bar{q}$ or gg, $\hat{s}$ is the square of the partonic centre-of-mass energy, and $\hat{\sigma}_{ij}(\hat{s})$ is the $ij \to Q\bar{Q}$ subprocess cross-section. The leading-order calculation cannot describe the quarkonium p_T distribution, since the p_T of the $Q\bar{Q}$ pair is zero at LO. At NLO in α_s, the subprocesses $ij \to kQ\bar{Q}$, where i, j, and k are light quarks, antiquarks, and gluons, produce $Q\bar{Q}$ pairs with nonzero p_T. Complete NLO calculations of quarkonium production in hadronic collisions using the CEM have been carried out in Refs. [31, 32], using the exclusive $Q\bar{Q}$ production code of Ref. [33] to obtain the $Q\bar{Q}$ pair distributions. The resulting values of the parameters F_H are given in Section 3.3. There are also calculations in the CEM beyond LO that use only a subset of the NLO diagrams [34] and calculations that describe the soft colour interaction within the framework of a Monte Carlo event generator [35]. Calculations beyond LO in the CEM have also been carried out for γp, $\gamma\gamma$ and neutrino–nucleon collisions and for Z^0 decays [36–40]. Apparently, the colour-evaporation model has not been applied to quarkonium production in e^+e^- annihilation.

The most basic prediction of the CEM is that the ratio of the cross-sections for any two quarkonium states should be constant, independent of the process and the kinematic region. Some variations in these ratios have been observed. For example, the ratio of the cross-sections for χ_c and J/ψ are rather different in photoproduction and hadroproduction. Such variations present a serious challenge to the status of the CEM as a quantitative phenomenological model for quarkonium production.

In some papers on the Colour Evaporation Model [34], the collision-induced colour field that neutralizes the colour of the $Q\bar{Q}$ pair is also assumed to randomize its spin. This leads to the prediction that the quarkonium production rate is independent of the quarkonium spin. This prediction is contradicted by measurements of nonzero polarization of the J/ψ, the $\psi(2S)$, and the $\Upsilon(nS)$ in several experiments. The assumption of the randomization of the $Q\bar{Q}$ spin also implies simple spin-counting ratios for the cross-sections for the direct production of quarkonium states in the same orbital-angular-momentum multiplet. For example, the CEM with spin randomization predicts that the direct-production cross-sections for charmonium satisfy $\sigma_{\mathrm{dir}}[\eta_c] : \sigma_{\mathrm{dir}}[J/\psi] = 1 : 3$ and $\sigma_{\mathrm{dir}}[\chi_{c0}] : \sigma_{\mathrm{dir}}[\chi_{c1}] : \sigma_{\mathrm{dir}}[\chi_{c2}] = 1 : 3 : 5$. The inclusive cross-sections need not satisfy these spin-counting relations if there is significant feeddown from decay of higher quarkonium states, as is the case for J/ψ. Deviations from the predicted spin-counting ratio for χ_{c1} to χ_{c2} have been observed. One might conclude that the CEM is ruled out by the observations of nonzero polarization and of deviations from the spin-counting relations. On the other hand, the assumption of the randomization of the $Q\bar{Q}$ spin is really independent of the assumption of colour evaporation. Some proponents of the CEM omit the assumption of spin randomization. Alternatively, since the CEM is just a model, one can simply declare it to apply only to spin-averaged cross-sections. In the remainder of this chapter, when we mention the predictions of the CEM for the relative production rates of quarkonium states that differ only in their spin or total-angular-momentum quantum numbers, we are referring to the version of the CEM that includes the assumption of spin randomization.

There is a simple correspondence between the CEM and the NRQCD factorization approach. The CEM amounts to the assumption that an NRQCD production matrix element $\langle \mathcal{O}_n^H(\Lambda) \rangle$ is proportional to the expectation value of the operator that is obtained by replacing the projector onto the hadronic state H with a projector onto the set of $Q\bar{Q}$ states with invariant mass less than $2m_M$. In addition to an integral over the $Q\bar{Q}$ phase space, the projector contains sums over the $Q\bar{Q}$ spins and colours. The only dependence on the quarkonium H is through a common factor F_H in the proportionality constant for each NRQCD matrix element. Since, in this picture, the probability of forming a specific quarkonium state H is independent of the colour and spin state of the $Q\bar{Q}$ pair, NRQCD matrix elements that differ only by colour and spin quantum numbers are equal up to simple group theory factors. This picture also implies a hierarchy of NRQCD matrix elements according to their orbital-angular-momentum quantum number L. In the integration over the $Q\bar{Q}$ phase space of an NRQCD operator with orbital-angular-momentum quantum number L, the leading term scales as k^{2L+1}, where k is the Q or $\bar{Q}$ momentum in the $Q\bar{Q}$ rest frame. The difference $s_{\max} - 4m^2$ is proportional to k^2. Hence, there is an orbital-angular-momentum suppression factor $[(s_{\max} - 4m^2)/4m^2]^L \sim v^{2L}$ in the matrix elements.[1] That is, the CEM

---

[1]From the perspective of NRQCD, the upper limit $s_{\max} = 4m_M^2$ on the $Q\bar{Q}$ invariant mass that traditionally has been used in the CEM is quite arbitrary. Any choice that satisfies $s_{\max} - 4m_Q^2 \sim 4m_Q^2 v^2$ leads to the same velocity-scaling rules.

implies that S-wave NRQCD matrix elements dominate and that those with orbital-angular-momentum quantum number $L \geq 1$ are suppressed as v^{2L}. One way to test the assumptions of the CEM is to extract the NRQCD matrix elements from data and compare them with the predictions of the CEM.

The qualifier NLO in "the CEM at NLO" is somewhat misleading. As is described in Section 1.4, the NLO cross-section for $Q\bar{Q}$ production that is used in computing the CEM predictions is accurate through order α_s^3, which is next-to-leading order at zero p_T, but leading order at nonzero p_T. This is the same accuracy in α_s as the existing predictions in the NRQCD factorization approach. The NLO $Q\bar{Q}$ p_T distribution is singular at $p_T = 0$, but integrable. The existing NLO calculations in the CEM obtain a smooth p_T distribution at small p_T by using a smearing prescription to mimic the effects of multiple gluon emission. The smearing has a significant effect on the shape of the p_T distribution, except at very large p_T.

1.4 Multiple gluon emission

Multiple gluon emission can be very important for transverse momentum distributions, distributions near kinematic limits, and in situations in which production near threshold is important. For example, a fixed-order perturbative calculation typically gives a transverse momentum distribution $d\sigma/dp_T^2$ for quarkonium that includes terms proportional to $\delta(p_T^2)$ and $1/p_T^2$ that are singular as $p_T \to 0$. (However, the distribution has a well-behaved integral over p_T.) This singular distribution becomes a smooth one when the effects of multiple gluon emission are taken into account to all orders in perturbation theory. Several methods, which we now describe, have been developed to take into account some of these effects.

Resummation methods sum, to all orders in α_s, certain logarithmically enhanced terms that are associated with soft- and collinear-gluon emission. The resummations can be carried out at various levels of precision in the logarithmic enhancements, that is, in leading logarithmic (LL) order, in next-to-leading logarithmic (NLL) order, etc. Resummation can, in principle, be extended to arbitrarily high precision in the logarithmic enhancements. However, in practice, it is seldom carried out beyond LL or NLL accuracy. Generally, logarithms of p_T^2/M^2 have the largest effect on p_T distributions [42], although logarithms of the available partonic energy above threshold (threshold logarithms) and logarithms of s/p_T^2 (small-x logarithms) can also be important for particular processes and kinematic regions[2]. Because arbitrarily soft or collinear gluon emissions are resummed, the resummed expressions depend on nonperturbative functions. This dependence lessens as the mass and transverse momentum scales of the process increase, and it may be insignificant at large masses and/or transverse momenta. Some practical disadvantages of the resummation method are that it has to be reformulated, to some extent, for every process and that it usually does not yield results that are fully differential in all of the kinematic variables. Since resummation calculations retain only soft and collinear logarithmically enhanced terms, they generally do not describe accurately processes in which hard gluons are emitted at large angles — so called "Mercedes events." This situation can be remedied to some extent by combining resummation with exact next-to-leading order (NLO) calculations, which retain all contributions associated with gluon emission at NLO, not just logarithmically enhanced contributions [44].

Parton-shower Monte Carlos share with resummation methods the approach of modeling multiple gluon emission by retaining certain logarithmically enhanced terms in the cross-section. The Monte Carlos take into account a finite, but arbitrarily large, number of gluon emissions. The original implementations of shower Monte Carlo methods, such as ISAJET [45,46], generally treat only the leading collinear logarithmic enhancements correctly, while more recent implementations, such as PYTHIA [47, 48] and HERWIG [49,50] treat both the leading collinear and soft logarithmic enhancements correctly. Generally, the showering processes are cut off so that they do not become so soft or collinear as to be nonperturbative in nature. The showering may then be supplemented with nonperturbative models that describe the hadronization of the partons. A practical advantage of the shower Monte Carlo approach is that it is

---

[2]For a general discussion of resummation techniques for logarithms of p_T^2/M^2 and threshold logarithms, see Ref. [43].

generally applied easily to any Born-level production process. Furthermore, it produces results that are differential in all of the kinematic variables that are associated with the final-state particles. Hence, it lends itself to the application of experimental cuts. As is the case with resummation methods, the shower Monte Carlo approach does not yield an accurate modeling of processes in which hard gluons are emitted at large angles. A partial remedy for this problem is to use shower Monte Carlos in conjunction with exact NLO calculations, rather than LO calculations. Recently, important progress has been made in this direction [51–56]. In contrast with resummation methods, some shower Monte Carlos do not take into account virtual gluon emission. Such shower Monte Carlos do not yield reliable estimates of the total cross-section.

The k_T-*factorization* method is an attempt to take into account initial-state radiation through parton distributions that depend the parton's transverse momentum k_T, as well as on the parton's longitudinal momentum fraction x. It generally gives answers that are very different from those of collinear factorization. The k_T-dependent parton distributions are not very well known phenomenologically, and there are possibly unresolved theoretical issues, such as the universality of the k_T-dependent parton distributions.

The k_T-*smearing* method is a phenomenological model for multiple initial-state radiation. As in the k_T-factorization method, the k_T smearing method makes use of k_T-dependent parton distributions. It is assumed that the distribution factors into the x-dependent PDF's that are defined by collinear factorization and a Gaussian distribution in the transverse momentum k_T. The width $\langle k_T^2 \rangle$ of the Gaussian can be treated as a process-dependent phenomenological parameter. One advantage of this model is that it is easy to implement. On the other hand, while this model may capture some of the crude features of soft- and collinear-gluon emission, it is probably incorrect in detail: resummation methods and shower Monte Carlos yield transverse-momentum distributions that have longer tails than those of a Gaussian distribution. The impact of a parton shower on the quarkonium transverse momentum distribution is, in general, larger than for the Gaussian k_T smearing, and it extends out to larger values of p_T.

1.5 Production in nuclear matter

The existing factorization "theorems" for quarkonium production in hadronic collisions are for cold hadronic matter. These theorems predict that nuclear matter is "transparent" for J/ψ production at large p_T. That is, at large p_T, all of the nuclear effects are contained in the nuclear parton distributions. The corrections to this transparency are of order $(mv)^2/p_T^2$ for unpolarized cross-sections and of order mv/p_T for polarized cross-sections.

The effects of transverse-momentum kicks from multiple elastic collisions between active partons and spectators in the nucleons are among those effects that are suppressed by $(mv)^2/p_T^2$. Nevertheless, these multiple-scattering effects can be important because the production cross-section falls steeply with p_T and because the number of scatterings grows linearly with the length of the path through the nuclear matter. Such elastic interactions can be expressed in terms of eikonal interactions [57] or higher-twist matrix elements [58].

Inelastic scattering of the quarkonium by the nuclear matter is also an effect of higher order in $(mv)^2/p_T^2$. However, it can become dominant when the amount of nuclear matter that is traversed by the quarkonium is sufficiently large. Factorization breaks down when the length L of the quarkonium path in the nucleus satisfies

$$L \gtrsim \frac{\text{Min}(z_Q, z_{\bar{Q}}) P_{\text{onium}}^2}{M_A (k_T^{\text{tot}})^2}, \tag{5.15}$$

where M_A is the mass of the nucleus, z is the parton longitudinal momentum fraction, P_{onium} is the momentum of the quarkonium in the parton CM frame, and k_T^{tot} is the accumulated transverse-momentum "kick" from passage through the nuclear matter. This condition for the break-down of factorization is similar to "target-length condition" in Drell–Yan production [59, 60]. Such a breakdown of factorization

is observed in the Cronin effect at low p_T and in Drell–Yan production at low Q^2, where the cross-section is proportional to the nucleon number raised to a power less than unity.

It is possible that multiple-scattering effects may be larger for colour-octet production than for colour-singlet production. In the case of colour-octet production, the pre-quarkonium $Q\bar{Q}$ system carries a nonzero colour charge and, therefore, has a larger amplitude to exchange soft gluons with spectator partons.

At present, there is no complete, rigorous theory to account for all of the effects of multiple scattering, and we must resort to "QCD-inspired" models. A reasonable requirement for models is that they be constructed so that they are compatible with the factorization result in the large-p_T limit. Many models treat interactions of the pre-quarkonium with the nucleus as on-shell scattering (Glauber scattering). This assumption should be examined carefully, as on-shell scattering is known, from the factorization proofs, not to be a valid approximation in leading order in $(mv)^2/p_T^2$.

2 QUARKONIUM PRODUCTION AT THE TEVATRON

Charmonium and bottomonium are produced copiously in high energy hadron colliders. The present and future hadron colliders include

- the Tevatron, a $p\bar{p}$ collider operating at Fermilab with centre-of-mass energy of 1.8 TeV in Run I and 1.96 TeV in Run II,
- RHIC, a heavy-ion or pp collider operating at Brookhaven with centre-of-mass energy of up to 200 GeV per nucleon–nucleon collision,
- the LHC at CERN, a pp collider under construction at CERN with centre-of-mass energy of 17 TeV.

In this section, we focus on the Tevatron, because it has produced the most extensive and precise data on quarkonium production. The photoproduction of quarkonium at high-energy $p\bar{p}$, pp, and heavy ion colliders is discussed in Chapter 7 of this report.

2.1 Charmonium cross-sections

In high energy collisions, charmonium is produced both through direct production mechanisms and through decays of other hadrons. In the case of charmonium production through B-hadron decays, the charmonium is produced at a secondary vertex, and a vertex detector can be used to identify this contribution to the measured production rate. We refer to the inclusive cross-section for production of a charmonium state with the contribution from B decays removed as the *prompt* cross-section. The prompt cross-section includes both the direct production of the charmonium and its production through decays of higher charmonium states.

In Run I of the Tevatron, the CDF collaboration measured the prompt cross-sections for the production of several charmonium states in $p\bar{p}$ collisions at a centre-of-mass energy of 1.8 TeV [61, 62]. The CDF data for production of direct J/ψ, prompt $\psi(2S)$, and prompt J/ψ from decay of χ_c are shown in Fig. 5.1. In the CDF analysis, prompt J/ψ's that do not come from decays of $\psi(2S)$ or χ_c were assumed to be produced directly.

At non-vanishing transverse momentum, the leading parton processes for producing charmonium ($ij \rightarrow c\bar{c} + k$, where i, j, and k are light quarks, antiquarks, and gluons) occur at order α_s^3. The colour-singlet-model (CSM) predictions are shown as dotted lines in Fig. 5.1. In the top two panels of Fig. 5.1, the more steeply falling dotted lines are the predictions of the CSM at leading order in α_s. The other dotted lines in the top two panels of Fig. 5.1 are contributions of higher order in α_s involving gluon fragmentation. As can be seen in the top panel of Fig. 5.1, the gluon-fragmentation contribution renders the shape of the CSM prediction for direct J/ψ production roughly compatible with the CDF data. However, the normalization is too small by more than an order of magnitude. There is a similar
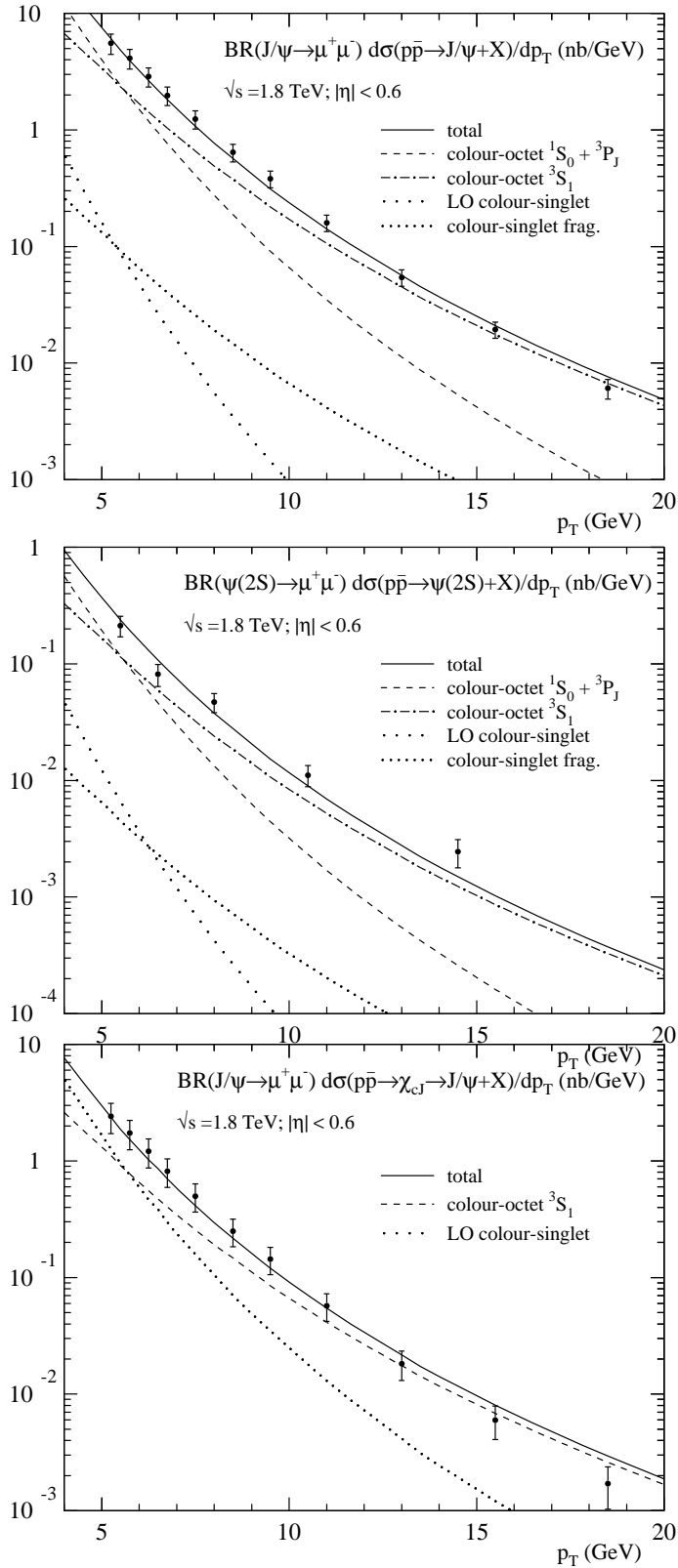
Fig. 5.1: Differential cross-sections for the production of direct J/ψ (top), prompt $\psi(2S)$ (middle), and prompt J/ψ from decay of χ_c (bottom) at the Tevatron as a function of p_T. The data points are CDF measurements from Run I [61, 62]. The dotted curves are the CSM contributions. The solid curves are the NRQCD factorization fits, and the other curves are individual colour-octet contributions to the fits. From Ref. [64].

Table 5.1: NRQCD production matrix elements for charmonium states obtained from the transverse momentum distributions at the Tevatron [64]. The errors quoted are statistical only.

H	$\langle\mathcal{O}_1^H\rangle$	$\langle\mathcal{O}_8^H(^3S_1)\rangle$	$M_{3.5}^H$
J/ψ	$1.16\ \text{GeV}^3$	$(1.19\pm0.14)\times10^{-2}\ \text{GeV}^3$	$(4.54\pm1.11)\times10^{-2}\ \text{GeV}^3$
$\psi(2S)$	$0.76\ \text{GeV}^3$	$(0.50\pm0.06)\times10^{-2}\ \text{GeV}^3$	$(1.89\pm0.46)\times10^{-2}\ \text{GeV}^3$
χ_{c0}	$0.11\ \text{GeV}^5$	$(0.31\pm0.04)\times10^{-2}\ \text{GeV}^3$	

discrepancy in the normalization for prompt $\psi(2S)$ production, as can be seen in the middle panel of Fig. 5.1. In the case of production of prompt J/ψ from decay of χ_c, which is shown in the bottom panel of Fig. 5.1, the discrepancy is less dramatic, but the cross-section is still under-predicted by the CSM. The large discrepancies between the measurements and the CSM predictions for the production cross-section for S-wave charmonium states rules out the CSM as a credible model for quarkonium production.

According to the NRQCD factorization approach, the charmonium production cross-section contains not only the CSM terms, which are absolutely normalized, but also colour-octet terms, whose normalizations are determined by colour-octet matrix elements. In the case of J/ψ and $\psi(2S)$ production, the most important colour-octet matrix elements are $\langle\mathcal{O}_8^H(^3S_1)\rangle$, $\langle\mathcal{O}_8^H(^3P_0)\rangle$, and $\langle\mathcal{O}_8^H(^1S_0)\rangle$. At large p_T, the J/ψ and $\psi(2S)$ cross-sections are dominated by gluon fragmentation into colour-octet $^3S_1$ charm pairs [65], which falls as $d\hat{\sigma}/dp_T^2\sim1/p_T^4$. The colour-octet $^1S_0$ and ^3P_J channels are significant in the region $p_T\lesssim10$ GeV, but fall as $d\hat{\sigma}/dp_T^2\sim1/p_T^6$ and become negligible at large p_t. Because the $^1S_0^{(8)}$ and $^3P_J^{(8)}$ short-distance cross-sections have a similar p_t dependence, the transverse momentum distribution is sensitive only to the linear combination M_k^H defined in (5.8), with $k\approx3$. As can be seen in the top panel of Fig. 5.1, a good fit to the normalization and shape of the direct J/ψ cross-section can be obtained by adjusting $\langle\mathcal{O}_8^{J/\psi}(^3S_1)\rangle$ and $M_{3.5}^{J/\psi}$. As is shown in the middle panel of Fig. 5.1, a similarly good fit to the prompt $\psi(2S)$ cross-section can be obtained by adjusting the corresponding parameters for $\psi(2S)$. In the case of production of the χ_{cJ} states, the most important colour-octet matrix element is $\langle\mathcal{O}_8^H(^3S_1)\rangle$. As can be seen in the bottom panel of Fig. 5.1, the fit to the cross-section for production of prompt J/ψ from decay of χ_c can be improved by adjusting $\langle\mathcal{O}_8^{\chi_{c0}}(^3S_1)\rangle$. Table 5.1 shows the values of the quarkonium matrix elements that are obtained in the fit of Ref. [64, 66]. The colour-singlet matrix elements are taken from the potential-model calculation of Refs. [67, 68]. The colour-octet matrix elements have been extracted from the CDF data [61, 62]. The CTEQ5L parton distribution functions [69] were used, with renormalization and factorization scales $\mu=(p_T^2+4m_c^2)^{1/2}$ and $m_c=1.5$ GeV. The Altarelli–Parisi evolution has been included for the $\langle\mathcal{O}_8^{\chi_{c0}}(^3S_1)\rangle$ fragmentation contribution. See Ref. [66] for further details. The extraction of the various colour-octet matrix elements relies on the differences in their p_T dependences. Smaller experimental error bars could help to resolve the different p_T dependences with greater precision.

The normalization and the shape of the prompt charmonium cross-section at the Tevatron can also be described reasonably well by the colour-evaporation model (CEM). The CEM parameters can be fixed by fitting to the data from pN collisions and by using the measured branching fractions for charmonium decays. The predictions of the CEM at next-to-leading order in α_s (NLO) can be calculated using the NLO parameter sets that are described in Section 3.3. The normalization of the predicted cross-section for prompt J/ψ production is in reasonable agreement with the CDF data from Run I. The shape can be brought into good agreement by adding k_T smearing, with $\langle k_T^2\rangle=2.5$ GeV^2. In Fig. 5.2, the resulting
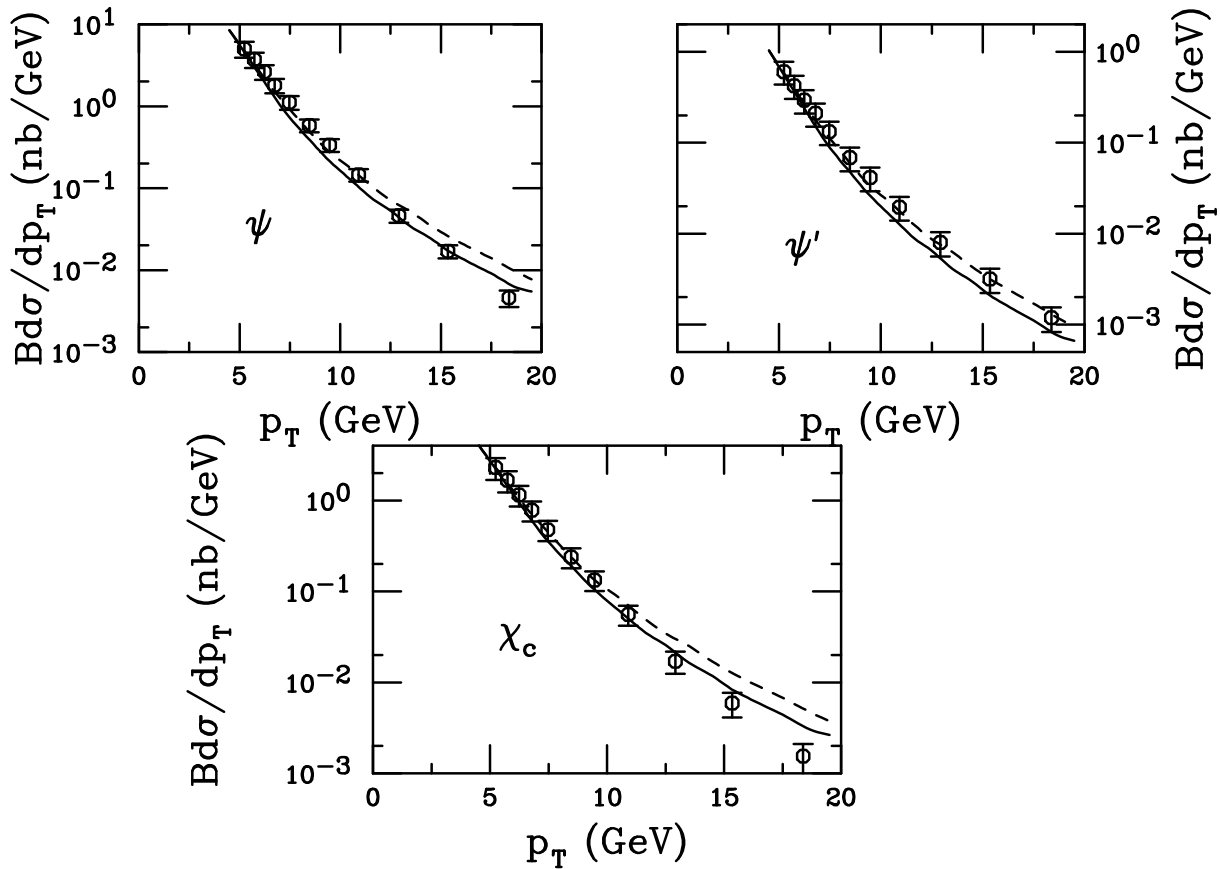
Fig. 5.2: Differential cross-sections for production of direct J/ψ (top left), prompt J/ψ from decays of $\psi(2S)$ (top right), and prompt J/ψ from decays of χ_c (bottom) at the Tevatron as a function of p_T. The data points are the CDF measurements [61, 62]. The dotted and solid curves are the CEM predictions at NLO with $\langle k_T^2 \rangle = 2.5$ GeV^2, using the first and fourth charmonium parameter sets in Table 5.8.

CEM predictions are compared with the CDF charmonium data for production of direct J/ψ, prompt J/ψ from decay of $\psi(2S)$, and prompt J/ψ from decay of χ_c. The predictions are all in good agreement with the CDF data.

In the case of the S-wave production matrix elements, the NRQCD velocity-scaling rules predict that

$$\frac{\langle \mathcal{O}_8 \rangle}{\langle \mathcal{O}_1 \rangle} \sim \frac{v^4}{2N_c}, \tag{5.16}$$

where this estimate includes colour factors that are associated with the expectation values of the NRQCD operators, as advocated by Petrelli *et al.* [70]. As can be seen from Table 5.1, the extracted colour-octet matrix elements are roughly compatible with this estimate [$v^4/(2N_c) \approx 0.015$]. However, a much more stringent test of the theory is to check the universality of the extracted matrix elements in other processes. In the case of the P-wave production matrix elements, the velocity scaling rules yield the estimate

$$\frac{\langle \mathcal{O}_8 \rangle}{\langle \mathcal{O}_1 \rangle / m_c^2} \sim \frac{v^0}{2N_c}. \tag{5.17}$$

The P-wave colour-octet matrix element in Table 5.1 is somewhat smaller than this estimate would suggest. That is also the case for the matrix elements that appear in P-wave quarkonium decays, which have been determined phenomenologically [71] and in lattice calculations [4–8].

In Table 5.2, we show matrix elements for J/ψ production that have been obtained from various other fits to the transverse momentum distribution. We see that there is a large uncertainty that arises from the dependence of the matrix elements on the factorization and renormalization scales, as well as a large dependence on the choice of parton distributions. The extracted values of the colour-octet matrix elements (especially M_k) are very sensitive to the small-p_T behavior of the cross-section and this, in turn, leads to a sensitivity to the behavior of the gluon distribution at small x. Furthermore, the effects of multiple gluon emission are important, and their omission in the fixed-order perturbative calculations leads to overestimates of the sizes of the matrix elements. In Table 5.2, one can see the results of various attempts to estimate the effects of multiple gluon emission. Sanchis–Lozano (S) and Kniehl and Kramer (KK) made use of parton-shower Monte Carlos, while Petrelli (P) and Sridhar, Martin, and Stirling (SMS) employed models containing Gaussian k_T smearing. In addition, Sanchis–Lozano included a resummation of logarithms of p_T^2/m^2. Hägler, Kirschner, Schäfer, Szymanowski, and Teryaev (HKSST) used the k_T-factorization formalism to resum large logarithms in the limit $s \gg 4m_c^2$. (See also the calculations by Yuan and Chao [87, 88].) Similar large dependences on the choices of factorization and renormalization scales, parton distributions, and multiple gluon emission can be seen in the matrix elements that have been extracted from the $\psi(2S)$ and χ_c transverse momentum distributions. See Ref. [64] for details.

Effects of corrections of higher order in α_s are a further uncertainty in the fits to the data in Table 5.2. Such corrections are known to be large in the case of charmonium decays. In the case of charmonium production, a new channel for colour-singlet production, involving t-channel gluon exchange, first appears in order α_s and could yield a large correction. Maltoni and Petrelli [83] have found that real-gluon corrections to colour-singlet $^3S_1$ production give a large contribution. Next-to-leading order (NLO) corrections in α_s for χ_{c0} and χ_{c2} production have been calculated [70], as have NLO corrections for the fragmentation process [89–91]. Large corrections from the resummation of logarithms of p_T^2/m^2 in the fragmentation of partons into quarkonium have also been calculated [80, 92–94].

Similar theoretical uncertainties arise in the extraction of the NRQCD production matrix elements for the $\psi(2S)$ and χ_c states. The statistical uncertainties are larger for $\psi(2S)$ and χ_c production than for J/ψ production. We refer the reader to Ref. [64] for some examples of the NRQCD matrix elements that have been extracted for these states.

The CDF collaboration has measured the fraction of prompt J/ψ's that come from decays of $\psi(2S)$ and $\chi_c(1P)$ states and the fractions that are produced directly [62]. The CDF measurements were made for J/ψ's with transverse momentum $p_T > 4$ GeV and pseudo-rapidity $|\eta| < 0.6$. The fractions, which are defined in Eqs. (5.11) and (5.12), are given in Table 5.3. The fraction of J/ψ's that are directly produced is approximately constant over the range 5 GeV $< p_T <$ 15 GeV. The fraction from decays of $\psi(2S)$ increases from $(7 \pm 2)\%$ at $p_T = 5$ GeV to $(15 \pm 5)\%$ at $p_T = 15$ GeV. The fraction from decays of $\chi_c(1P)$ seems to decrease slowly over this range of p_T. Such variations with p_T are counter to the predictions of the colour-evaporation model.

The CDF collaboration has also measured the ratio of the prompt χ_{c1} and χ_{c2} cross-sections at the Tevatron [95]. The measured value of the ratio R_{χ_c} defined in Eq. (5.10) is

$$R_{\chi_c} = 1.04 \pm 0.29(\text{stat.}) \pm 0.12(\text{sys.}). \tag{5.18}$$

The χ_{c2} and χ_{c1} were observed through their radiative decays into a J/ψ and a photon, which were required to have transverse momenta exceeding 4 GeV and 1 GeV, respectively. The colour-evaporation model predicts that this ratio should be close to the spin-counting ratio $3/5$, since the feeddown from the $\psi(2S)$ is small. The NRQCD factorization fit to the prompt χ_c cross-section in the region $p_T > 5$ GeV implies a ratio of 0.9 ± 0.2 [96]. The CDF result slightly favors the NRQCD factorization prediction.

Charmonium production data from Tevatron Run II have recently become available. Using a 39.7 pb^{-1} data sample from Run II, the CDF Collaboration has measured the inclusive cross-section for J/ψ production and subsequent decay into $\mu^+\mu^-$ [97]. The inclusive cross-section includes both prompt J/ψ's and J/ψ's from decays of b-hadrons. The inclusive differential cross-section as a function of p_T

Table 5.2: J/ψ production matrix elements in units of 10^{-2} GeV^3 [64]. The first error bar is statistical; the second error bar (where present) is obtained by varying the factorization and renormalization scales.

Reference	PDF		$\langle \mathcal{O}_8^{J/\psi}(^3S_1) \rangle$	$M_k^{J/\psi}$	k
LO collinear factorization					
CL [73]	MRS(D0) [74]		0.66 ± 0.21	6.6 ± 1.5	3
BK [66]	CTEQ4L [75]		$1.06 \pm 0.14^{+1.05}_{-0.59}$	$4.38 \pm 1.15^{+1.52}_{-0.74}$	3.5
	GRV-LO(94) [76]		$1.12 \pm 0.14^{+0.99}_{-0.56}$	$3.90 \pm 1.14^{+1.46}_{-1.07}$	
	MRS(R2) [77]		$1.40 \pm 0.22^{+1.35}_{-0.79}$	$10.9 \pm 2.07^{+2.79}_{-1.26}$	
BKL [78]	MRST-LO(98) [79]		0.44 ± 0.07	8.7 ± 0.9	3.4
	CTEQ5L [69]		0.39 ± 0.07	6.6 ± 0.7	
Parton shower radiation					
S [80]	CTEQ2L [81]		0.96 ± 0.15	1.32 ± 0.21	3
	MRS(D0) [74]		0.68 ± 0.16	1.32 ± 0.21	
	GRV-HO(94) [76]		0.92 ± 0.11	0.45 ± 0.09	
KK [82]	CTEQ4M [75]		0.27 ± 0.05	0.57 ± 0.18	3.5
k_T-smearing		$\langle k_T \rangle$[GeV]			
P [83]	CTEQ4M [75]	1	1.5 ± 0.22	8.6 ± 2.1	3.5
		1.5	1.7 ± 0.19	4.5 ± 1.5	
SMS [84]	MRS(D$'_-$) [74]	0.7	1.35 ± 0.30	8.46 ± 1.41	3
		1	1.5 ± 0.29	7.05 ± 1.17	
k_T-factorization					
HKSST1 [85]	KMS [86]		$\approx 0.04 \pm 0.01$	$\approx 6.5 \pm 0.5$	5

Table 5.3: The fractions F_H of prompt J/ψ mesons that are produced by the decay of higher charmonium states H and the fraction $F_{J/\psi}$ that are produced directly.

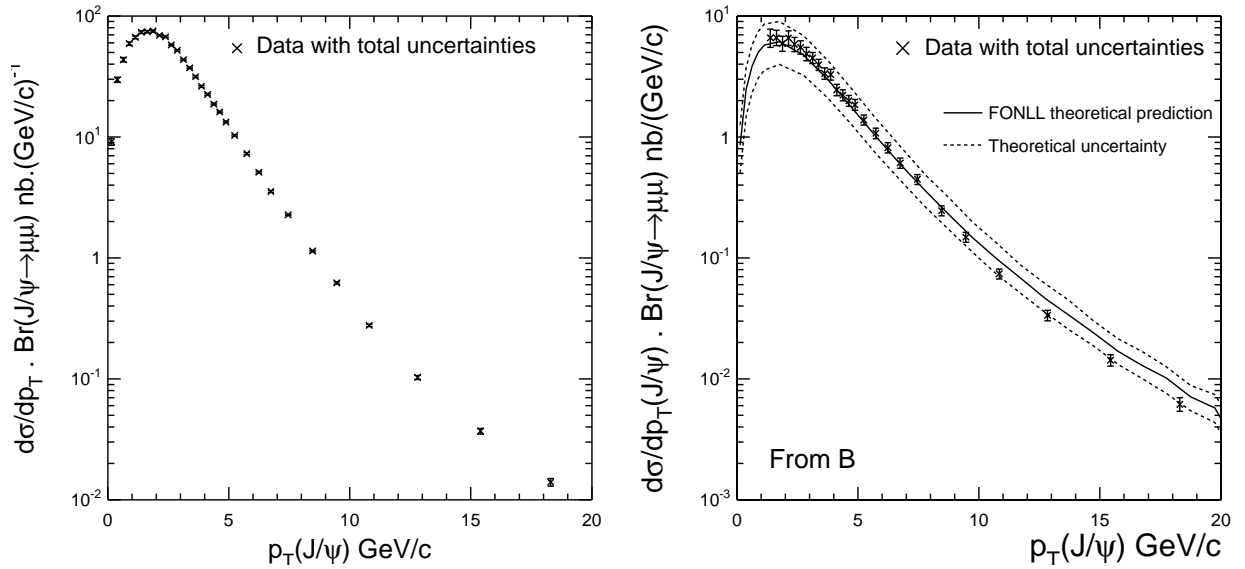| H	F_H (in %)
J/ψ	64 ± 6
$\psi(2S)$	7 ± 2 to 15 ± 5
$\chi_c(1P)$	29.7 ± 1.7(stat.) ± 5.7(sys.)

Fig. 5.3: Differential inclusive cross-section for $p\bar{p} \to J/\psi X$ (left). Differential cross-section distribution of J/ψ events from b-hadron decay (right). Both cross-sections are plotted as a function of the transverse momentum p_T of the J/ψ and are integrated over the rapidity range $|y(J/\psi)| < 0.6$.

for rapidity $|y| < 0.6$ has been obtained down to zero transverse momentum and is shown in the left panel of Fig. 5.3. The total integrated cross-section for inclusive J/ψ production in $p\bar{p}$ interactions at $\sqrt{s} = 1.96$ TeV is measured to be

$$\sigma[p\bar{p} \to J/\psi X, |y(J/\psi)| < 0.6] = 4.08 \pm 0.02(\text{stat}) \pm 0.36(\text{syst}) \; \mu\text{b}. \tag{5.19}$$

These new measurements await comparison with updated theoretical calculations in the low p_T region.

Using a sample of 4.7 pb^{-1} of Run II data, the D0 collaboration has verified that the J/ψ cross-section is independent of the rapidity of the J/ψ for a rapidity range $0 < |y| < 2$. This analysis has been performed for $p_T(J/\psi) > 5$ GeV and $p_T(J/\psi) > 8$ GeV [98]. The CDF and D0 collaborations have performed studies of forward differential J/ψ production cross-sections in the pseudo-rapidity regions $2.1 < |\eta(J/\psi)| < 2.6$ and $2.5 \leq |\eta(J/\psi)| \leq 3.7$, respectively, using their Run I data [99, 100].

Using 39.7 pb^{-1} of the Run II data, the CDF Collaboration has also measured the differential cross-section as a function of p_T and the cross-section integrated over p_T for the production of b-hadrons that decay in the channel $H_b \to J/\psi X$ [97]. The differential cross-section multiplied by the branching fraction for $J/\psi \to \mu^+\mu^-$ is shown in the right panel of Fig. 5.3. A recent QCD prediction that is based on a fixed order (FO) calculation plus a resummation of next-to-leading order logs (NLL) [101] is overlaid. The cross-section integrated over p_T was found to be

$$\sigma[p\bar{p} \to H_b X, p_T(J/\psi) > 1.25 \text{ GeV}, |y(J/\psi)| < 0.6] = 28.4 \pm 0.4(\text{stat})^{+4.0}_{-3.8}(\text{syst}) \; \mu\text{b}. \tag{5.20}$$

This measurement can be used to extract the total inclusive b-hadron cross-section.

2.2 Bottomonium cross-sections

Using Run I data, the CDF Collaboration has reported inclusive production cross-sections for the $\Upsilon(1S)$, $\Upsilon(2S)$ and $\Upsilon(3S)$ states in the region $0 < p_T < 20$ GeV [102]. The rates of inclusive production of the $\Upsilon(1S)$, $\Upsilon(2S)$ and $\Upsilon(3S)$ states for $p_T > 4$ GeV were found to be higher than the rates predicted by CSM calculations by a factor of about five. Inclusion of colour-octet production mechanisms within
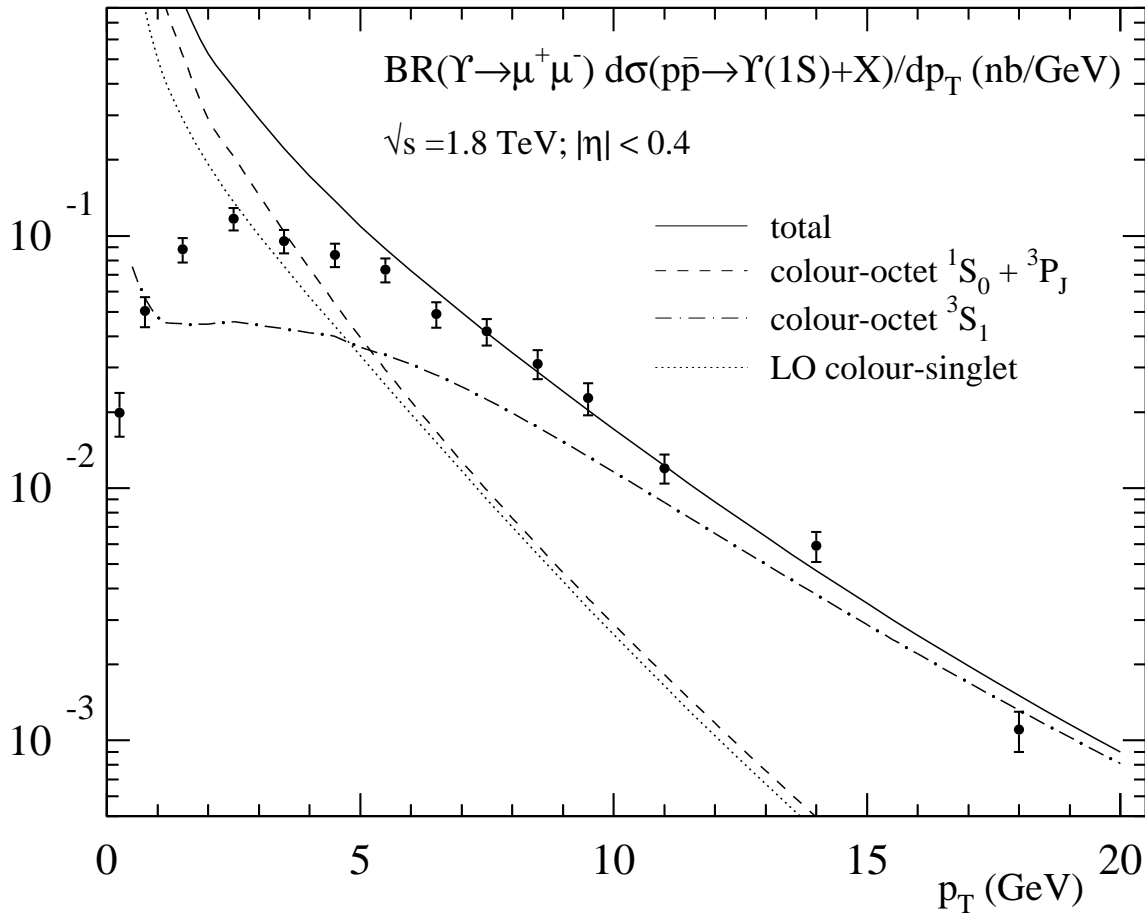
Fig. 5.4: Inclusive $\Upsilon(1S)$ cross-section at the Tevatron as a function of p_T. The data points are the CDF measurements [61]. The solid curve is the NRQCD factorization fit, and the other curves are individual contributions to the NRQCD factorization fit. From Ref. [64, 104].

the NRQCD framework can account for the observed cross-sections for $p_T > 8$ GeV [72, 73, 104, 105], as is shown for $\Upsilon(1S)$ production in Fig. 5.4. An accurate description of the Υ cross-section in the low-p_T region requires NLO corrections and a resummation of multiple gluon radiation. A fit to the CDF data using a parton shower Monte Carlo to model the effects of multiple gluon emission has given much smaller values of the colour-octet matrix elements that are compatible with zero [106].

The normalization and the shape of the bottomonium cross-sections at the Tevatron can also be described reasonably well by the colour-evaporation model (CEM). The CEM predictions are compared with the CDF data for $\Upsilon(1S)$, $\Upsilon(2S)$, and $\Upsilon(3S)$ in Fig. 5.5. Most of the relevant parameters can be fixed completely by fitting data from pN collisions and by using measured branching fractions for bottomonium decays. The predictions of the CEM at NLO that are shown in Fig. 5.5 have been calculated using the NLO parameter sets that are described in Section 3.3. The predicted cross-sections for $\Upsilon(1S)$ and $\Upsilon(3S)$ production are a little below the data; the normalizations can be improved by multiplying the cross-sections by a K-factor of 1.4. The shapes have been brought into good agreement with the data by including k_T smearing, with $\langle k_T^2 \rangle = 3.0$ GeV^2. This value of $\langle k_T^2 \rangle$ is a little larger than the value $\langle k_T^2 \rangle = 2.5$ GeV^2 that gives the best fit to the charmonium cross-sections.

A recent calculation of the production cross-sections for the $\Upsilon(1S)$, $\Upsilon(2S)$, and $\Upsilon(3S)$ at the Tevatron combines a resummation of logarithms of M_Υ^2/p_T^2 with a calculation at leading order in α_s in what is, in essence, the colour-evaporation model [41]. The resummation of the effects of multiple gluon
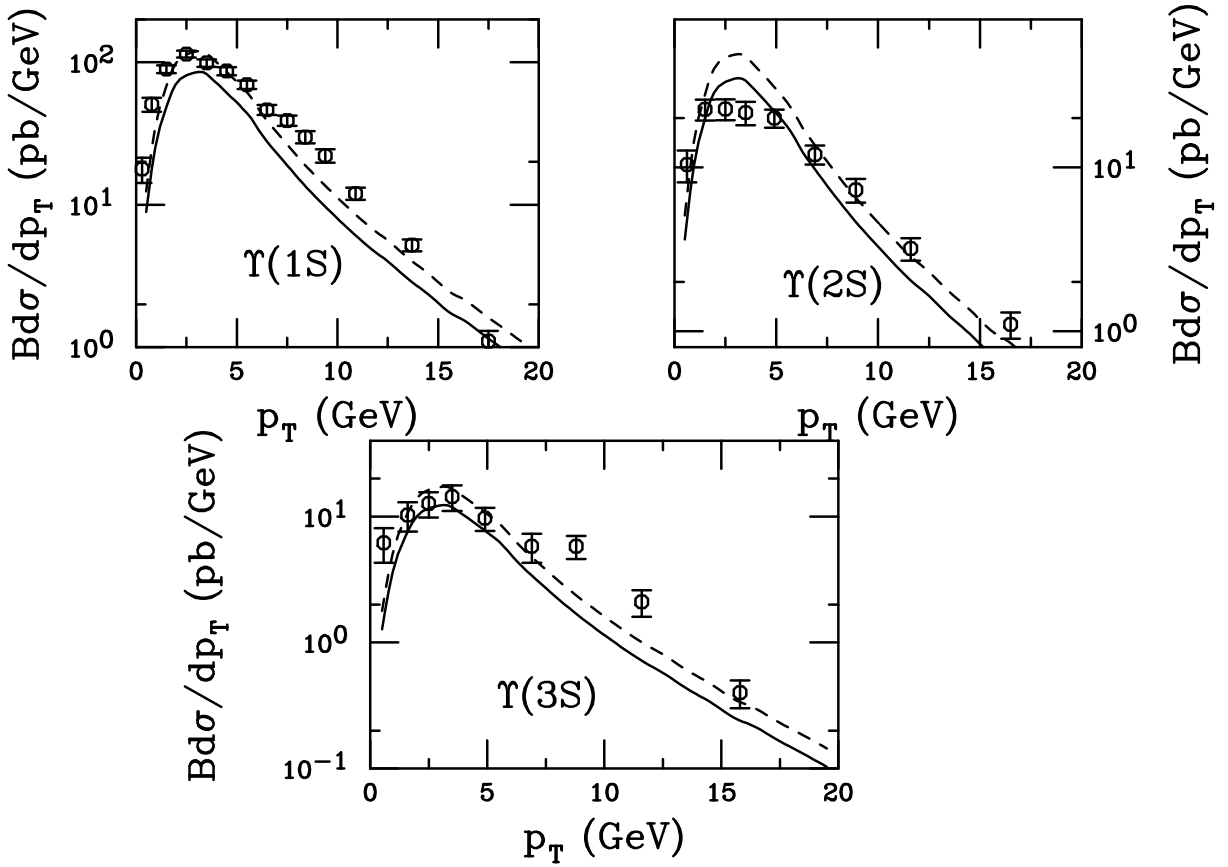
Fig. 5.5: Differential cross-sections for $\Upsilon(1S)$ (top left), $\Upsilon(2S)$ (top right), and $\Upsilon(3S)$ (bottom) at the Tevatron as a function of p_T. The data points are the CDF measurements [102]. The solid curves are the CEM predictions at NLO with $\langle k_T^2 \rangle = 3.0$ GeV^2, using the first bottomonium parameter set in Tables 5.8. The dashed curves are multiplied by a K-factor of 1.4.

emission in the CEM has some simplifications that do not occur in the NRQCD factorization approach. The results of the calculation of Ref. [41] are shown, along with CDF data, in Fig. 5.6. The resummation of logarithms of M_Υ^2/p_T^2 allows the calculation to reproduce the shape of the data at small p_T. The normalizations have been adjusted to obtain the best fit to the data. the best fit to the data.

The CDF Collaboration has also reported the fractions of $\Upsilon(1S)$ mesons, for $p_T > 8$ GeV, that come from decays of $\chi_b(1P)$, $\chi_b(2P)$, $\chi_b(3P)$, $\Upsilon(2S)$, and $\Upsilon(3S)$ and the fraction that originate from direct production [103]. The fractions from decays of $\Upsilon(nS)$ and for $\chi_b(nP)$ are defined by

$$F_{\Upsilon(nS)} = \mathrm{Br}[\Upsilon(nS) \to \Upsilon(1S) + X] \frac{\sigma[\Upsilon(nS)]}{\sigma[\Upsilon(1S)]}, \tag{5.21}$$

$$F_{\chi_b(nP)} = \sum_{J=0}^{3} \mathrm{Br}[\chi_{bJ}(nP) \to \Upsilon(1S) + X] \frac{\sigma[\chi_{bJ}(nP)]}{\sigma[\Upsilon(1S)]}. \tag{5.22}$$

The fraction of $\Upsilon(1S)$'s that are produced directly can be denoted by $F_{\Upsilon(1S)}$. The fractions are given in Table 5.4.

2.3   Polarization

The polarization of the quarkonium contains important information about the production mechanism. The polarization variable α for a 1^{--} state, such as J/ψ, $\psi(2S)$, or $\Upsilon(1S)$, is defined by Eq. (5.13),
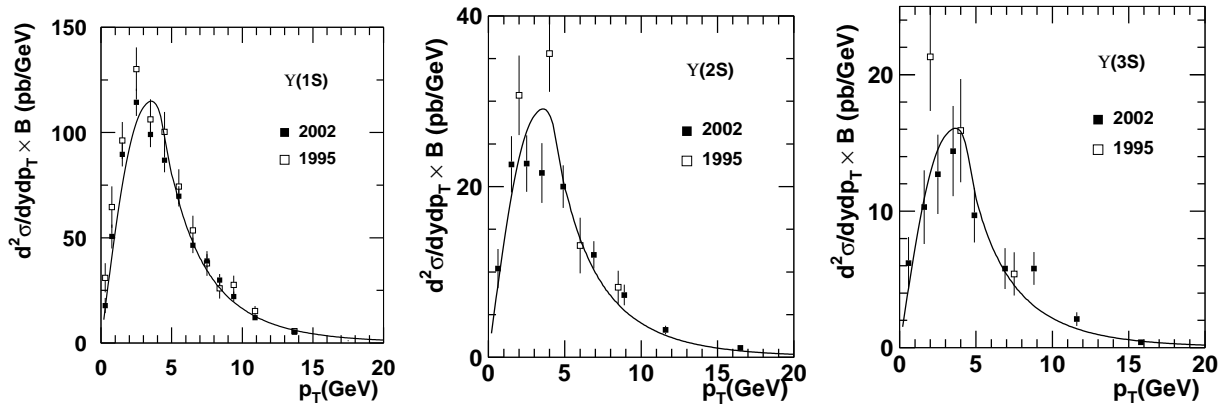
Fig. 5.6: Calculated differential cross-sections times leptonic branching fractions B, evaluated at $y = 0$, as functions of transverse momentum for hadronic production of (a) $\Upsilon(1S)$, (b) $\Upsilon(2S)$, and (c) $\Upsilon(3S)$ [41], along with CDF data [102, 107] at $\sqrt{S} = 1.8$ TeV. The solid lines show the result of the full calculation. The 1995 CDF cross-sections are multiplied a factor 0.88.

Table 5.4: The fractions F_H of $\Upsilon(1S)$ mesons that are produced by the decay of a higher bottomonium state H and the fraction $F_{\Upsilon(1S)}$ that are produced directly.

H	F_H (in %)
$\Upsilon(1S)$	$50.9 \pm 8.2(\text{stat.}) \pm 9.0(\text{sys.})$
$\Upsilon(2S)$	$10.7^{+7.7}_{-4.8}$
$\Upsilon(3S)$	$0.8^{+0.6}_{-0.4}$
$\chi_b(1P)$	$27.1 \pm 6.9(\text{stat.}) \pm 4.4(\text{sys.})$
$\chi_b(2P)$	$10.5 \pm 4.4(\text{stat.}) \pm 1.4(\text{sys.})$
$\chi_b(3P)$	< 6

where the angle θ is measured with respect to some polarization axis. At a hadron collider, a convenient choice of the polarization axis is the direction of the boost vector from the quarkonium rest frame to the centre-of-momentum frame of the colliding hadrons.

The NRQCD factorization approach gives a simple prediction for the polarization variable α at very large transverse momentum. The production of a quarkonium with p_T that is much larger than the quarkonium mass is dominated by gluon fragmentation — a process in which the quarkonium is formed in the hadronization of a gluon that is created with even larger transverse momentum. The NRQCD factorization approach predicts that the dominant gluon-fragmentation process is gluon fragmentation into a $Q\bar{Q}$ pair in a colour-octet $^3S_1$ state. The fragmentation probability for this process is of order α_s, while the fragmentation probabilities for all other processes are of order α_s^2 or higher. The NRQCD matrix element for this fragmentation process is $\langle \mathcal{O}_8^H(^3S_1) \rangle$. At large p_T, the fragmenting gluon is nearly on its mass shell, and, so, is transversely polarized. Furthermore, the velocity-scaling rules predict that the colour-octet $Q\bar{Q}$ state retains the transverse polarization as it evolves into an S-wave quarkonium state [108], up to corrections of relative order v^2. Radiative corrections and colour-singlet production dilute the quarkonium polarization somewhat [66, 89]. In the case of J/ψ production, feeddown from higher quarkonium states is also important [78]. Feeddown from χ_c states is about 30% of the J/ψ sample and dilutes the polarization. Feeddown from the $\psi(2S)$ is about 10% of the J/ψ sample and is largely transversely polarized. Despite these various diluting effects, a substantial polarization is
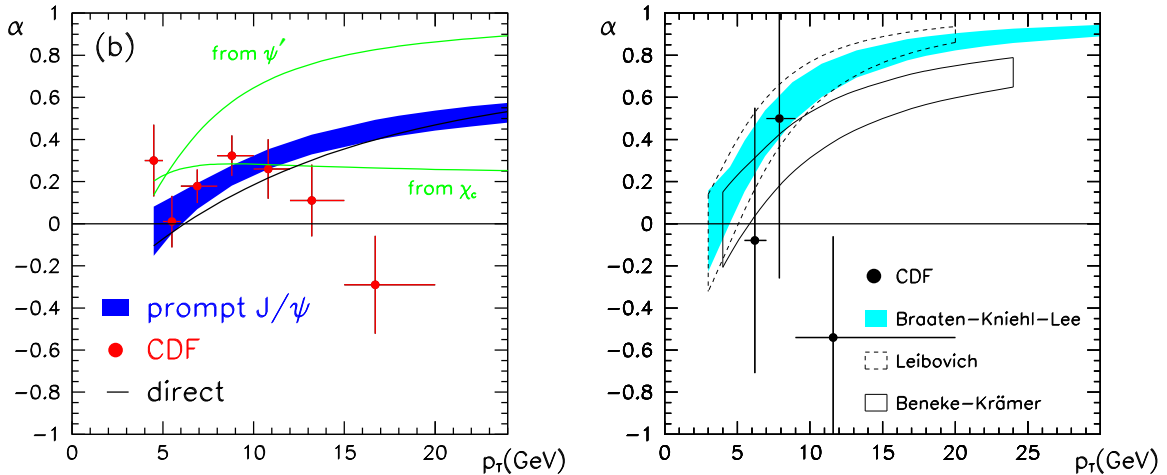
Fig. 5.7: Polarization variable α for prompt J/ψ (left) and for prompt $\psi(2S)$ (right) at the Tevatron as a function of p_T. The data points are the CDF measurements from Run I [103]. In the left panel (prompt J/ψ), the band is the NRQCD factorization prediction of Ref. [78], and the other curves are the values of α for individual components of the prompt J/ψ signal. In the right panel (prompt $\psi(2S)$), the bands are various NRQCD factorization predictions [66, 78, 109].

expected at large p_T, and its detection would be a "smoking gun" for the presence of the colour-octet production mechanism. In contrast, the colour-evaporation model predicts zero quarkonium polarization.

The CDF measurement of the J/ψ polarization as a function of p_T [103] is shown in the left panel of Fig. 5.7, along with the NRQCD factorization prediction [78]. The observed J/ψ polarization is in agreement with the prediction, except for the highest p_T bin. However, the prediction of increasing polarization with increasing p_T is not in evidence. The CDF data [103] and the NRQCD factorization prediction [66, 78, 109] for $\psi(2S)$ polarization are shown in the right panel of Fig. 5.7. The theoretical analysis of $\psi(2S)$ polarization is simpler than for the J/ψ, since feeddown does not play a rôle. However, the experimental statistics are not as good for the $\psi(2S)$ as for J/ψ. Again, the expectation of increasing polarization with increasing p_T is not confirmed.

Because the polarization depends on ratios of matrix elements, some of the theoretical uncertainties are reduced compared with those in the production cross-section. The polarization is probably not strongly affected by multiple gluon emission or K-factors. Uncertainties from contributions of higher-order in α_s could conceivably change the rates for the various spin states by a factor of two. Therefore, it is important to carry out the NLO calculation, but that calculation is very difficult technically and is computing intensive. order-v^2 corrections to parton fragmentation to quarkonium can be quite large. Bodwin and Lee [110] have found that the v^2 corrections to gluon fragmentation to J/ψ are about $+70\%$ for the colour-singlet channel and -50% for the colour-octet channel. The colour-singlet correction shifts α down by about 10% at the largest p_T. Since the colour-octet matrix element is fit to Tevatron data, the v^2 correction merely changes the size of the matrix element and has no immediate effect on the theoretical prediction. An additional theoretical uncertainty comes from the presence of order-v^2 spin-flip processes in the evolution of the $Q\bar{Q}$ pair into the quarkonium. It could turn out that spin-flip contributions are large, either because their velocity-scaling power laws happen to have large coefficients or because, as has been suggested in Refs. [111–115], the velocity scaling rules themselves need to be modified. Then spin-flip contributions could significantly dilute the J/ψ polarization. Nevertheless, it is is difficult to see how there could not be substantial polarization in J/ψ or $\psi(2S)$ production for $p_T > 4m_c$.[3]

---

[3] It has been argued that re-scattering interactions between the intermediate charm-quark pair and a co-moving colour field could yield unpolarized quarkonium [116, 117]. The theoretical analysis of these effects, however, relies on several simplifying
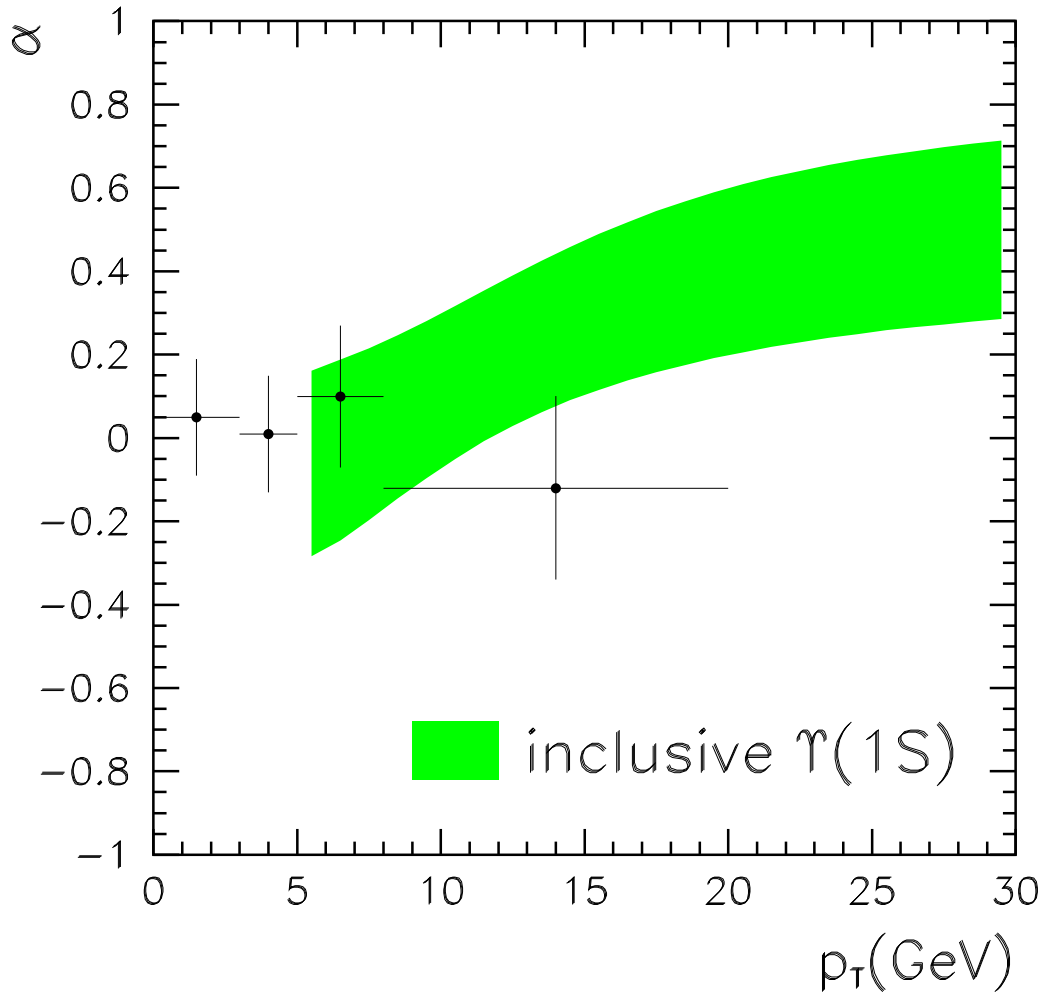
Fig. 5.8: Polarization variable α for inclusive $\Upsilon(1S)$ production at the Tevatron as a function of p_T. The data points are the CDF measurements from Run I [102]. The theoretical band represents the NRQCD factorization prediction [118].

The CDF data for Υ polarization is shown in Fig. 5.8, along with the NRQCD factorization prediction. Averaging over a range of p_T, the CDF Collaboration finds $\alpha = -0.06 \pm 0.20$ for 1 GeV $< p_T <$ 20 GeV [119, 120], which is consistent with the NRQCD factorization prediction [118]. In comparison with the prediction for J/ψ polarization, the prediction for Υ polarization has smaller v-expansion uncertainties. However, in the case of Υ production, the fragmentation mechanism does not dominate until relatively large values of p_T are reached, and, hence, the transverse polarization is predicted to be small for p_T below about 10 GeV. Unfortunately, the current Tevatron data sets run out of statistics in the high-p_T region.

2.4 Prospects for the Tevatron Run II

Run II at the Tevatron will provide a substantial increase in luminosity and will allow the collider experiments to determine the J/ψ, $\psi(2S)$ and χ_c cross-sections more precisely and at larger values of p_t. An accurate measurement of the J/ψ and $\psi(2S)$ polarization at large transverse momentum will be the most

assumptions, and further work is needed to establish the existence of re-scattering corrections in charmonium hadroproduction at large p_T.

crucial test of NRQCD factorization. In addition, improved data on the J/ψ and $\psi(2S)$ cross-sections will help to reduce some of the ambiguities in extracting the colour-octet matrix elements.

With increased statistics it might be possible to access other charmonium states such as the $\eta_c(nS)$ or the $h_c(nP)$. heavy-quark spin symmetry provides approximate relations between the nonperturbative matrix elements that describe spin-singlet and spin-triplet states. The matrix elements for $\eta_c(nS)$ are related to those for $\psi(nS)$, while the leading matrix elements for $h_c(nP)$ can be obtained from those for $\chi_c(nP)$. [See Eqs. (5.2–5.7).] Within NRQCD, the rates for $\eta(nS)$ and $h(nP)$ production can thus be predicted unambiguously in terms of the nonperturbative matrix elements that describe the J/ψ, $\psi(2S)$ and χ_c production cross-sections. A comparison of the various charmonium production rates would therefore provide a stringent test of NRQCD factorization and the heavy-quark spin symmetry. The cross-sections for producing the η_c and the h_c at Run II of the Tevatron are large [121,122], but the acceptances and efficiencies for observing the decay modes on which one can trigger are, in general, small, and detailed experimental studies are needed to quantify the prospects. Other charmonium processes that have been studied in the literature include the production of D-wave states [123], J/ψ production in association with photons [124, 125], and double gluon fragmentation to J/ψ pairs [126].

The larger statistics expected at Run II of the Tevatron will also allow the collider experiments to improve the measurements of the bottomonium cross-sections. As yet undiscovered states, such as the $\eta_b(1S)$, could be detected, for example, in the decay $\eta_b \to J/\psi + J/\psi$ [105] or in the decay $\eta_b \to D^* + D^{(*)}$ [127], and the associated production of Υ and electroweak bosons might be accessible [128]. If sufficient statistics can be accumulated, the onset of transverse $\Upsilon(nS)$ polarization may be visible at $p_{T,\Upsilon} \gtrsim 15$ GeV.

3   QUARKONIUM PRODUCTION IN FIXED-TARGET EXPERIMENTS

3.1   Cross-sections

Several collaborations have made predictions for fixed-target quarkonium production within the NRQCD factorization formalism [129–131]. The predictions of Ref. [129] for J/ψ and $\psi(2S)$ production in pN collisions are shown, along with the experimental data, in the left panels of Figs. 5.9 and 5.10. The calculation is at leading-order in α_s and uses the standard truncation in v that is described in Section 1.1. The data are from the compilation in Ref. [26], with additional results from Refs. [132–134]. In the case of pN production of J/ψ, the data clearly require a colour-octet contribution, in addition to a colour-singlet contribution. In the case of $\psi(2S)$ production, it is less clear that a colour-octet contribution is essential. One should keep in mind that the colour-singlet contribution is quite uncertain, owing to uncertainties in the values of m_c and the renormalization scale [111]. One can reduce these uncertainties by considering the ratio of the cross-sections for direct and inclusive J/ψ production, which is predicted to be approximately 0.6 in the NRQCD factorization approach and approximately 0.2 in the colour-singlet model [111]. Clearly, experiment favors the NRQCD factorization prediction. However, the prediction for the ratio depends on our knowledge of feed-down from χ_c states, and, as we shall see, NRQCD factorization predictions for χ_c production in fixed-target experiments are not in good agreement with the data.

In fixed-target production of J/ψ and $\psi(2S)$ at leading order in α_s (LO), the relevant production matrix elements are $\langle \mathcal{O}_8^H(^3S_1) \rangle$, $\langle \mathcal{O}_8^H(^1S_0) \rangle$, and $\langle \mathcal{O}_8^H(^3P_0) \rangle$, but the cross-section is sensitive only to the linear combination M_k^H defined in (5.8) with $k \approx 7$. The fits of the LO predictions for J/ψ and $\psi(2S)$ production in pN collisions [129] yield $M_7^{J/\psi} = 3.0 \times 10^{-2}$ GeV^3 and $M_7^{\psi(2S)} = 5.2 \times 10^{-3}$ GeV^3. The corrections at next-to-leading order in α_s (NLO) give a large K-factor in the colour-octet contributions [70]. A fit to the data using the NLO result for the colour-octet contributions gives $M_{6.4}^{J/\psi} = 1.8 \times 10^{-2}$ GeV^3 and $M_{6.4}^{\psi(2S)} = 2.6 \times 10^{-3}$ GeV^3 [71]. The NLO value of $M_{6.4}^{J/\psi}$ is about a factor 2 smaller than the LO value of $M_7^{J/\psi}$. Note that the NLO fit uses CTEQ4M [75] parton distributions, while the LO fit uses the CTEQ3L [140] parton distributions. The LO result for $M^{J/\psi}$ is somewhat smaller than the
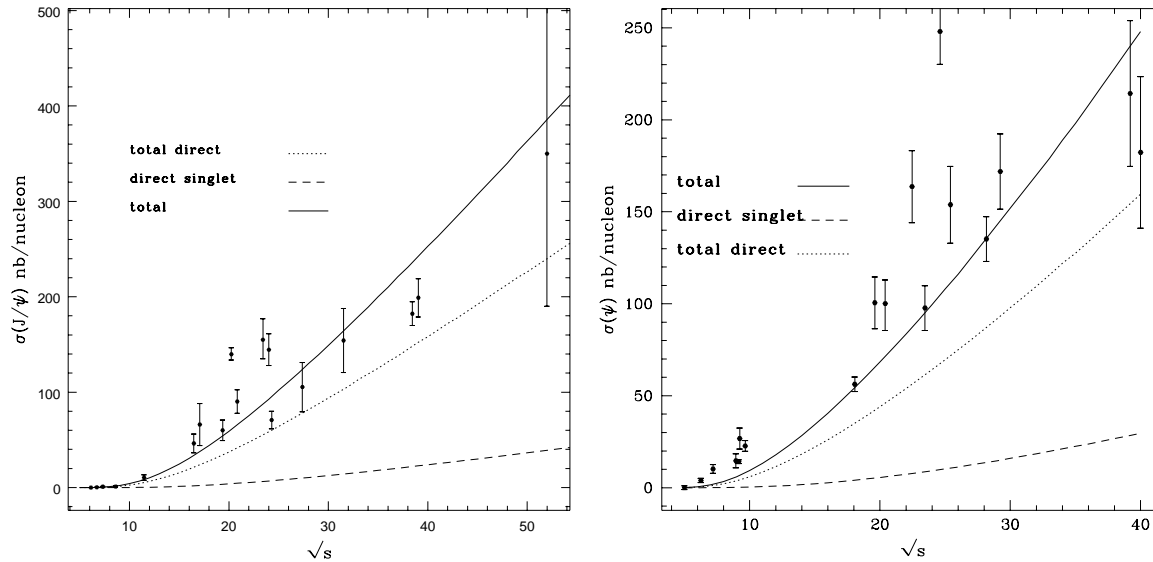
Fig. 5.9: Forward cross-section ($x_F > 0$) for J/ψ production in pN collisions (left) and πN collisions (right). The curves are the CSM predictions for direct J/ψ (dashed lines), the NRQCD factorization predictions for direct J/ψ with $M_7^{J/\psi} = 3.0 \times 10^{-2}$ GeV^3 (dotted lines), and the inclusive cross-sections for J/ψ including radiative feed-down from χ_{cJ} and $\psi(2S)$ (solid lines). From Ref. [129].

LO result from the Tevatron, and the NLO result for $M^{J/\psi}$ is somewhat larger than the parton-shower result from the Tevatron. However, given the large uncertainties in these quantities, the agreement is reasonable. It should also be remembered that the Tevatron cross-sections are sensitive to M_k^H with $k \approx 3$ rather than $k \approx 7$, and, so, comparisons are somewhat uncertain. Attempts to constrain this uncertainty are hampered by the fact that the $\overline{\text{MS}}$ matrix elements need not be positive. One can also question whether hard-scattering factorization holds for the total cross-section, which is dominated by small p_T-contributions. Furthermore, kinematic corrections from the difference between $2m$ and the quarkonium mass may be large.

The predictions of Ref. [129] for J/ψ and $\psi(2S)$ production in πN collisions are shown, along with the experimental data, in the right panels of Figs. 5.9 and 5.10. The calculation is at leading-order in α_s and uses the standard truncation in v that is described in Section 1.1. Again, the data are from the compilation in Ref. [26], with additional results from Refs. [132–134]. In the NRQCD predictions in Figs. 5.9 and 5.10, the values of M_7 that are used are the ones that were obtained from the fits to the pN production data. The πN production data clearly show an excess over these predictions that cannot be accounted for by the colour-octet contributions. This discrepancy has been discussed extensively in Ref. [26], and it may reflect our lack of knowledge of the gluon distribution in the pion or the presence of different higher-twist effects in the proton and the pion. Such higher-twist effects are not accounted for in the standard NRQCD factorization formulas, which are based on leading-twist hard-scattering factorization.

Some of the largest uncertainties in the predictions cancel out if we consider ratios of cross-sections. The uncertainties in the NRQCD factorization predictions can still be very large. They arise from uncertainties in the colour-octet matrix elements, uncalculated corrections of higher order in v and α_s, and uncertainties from the choices of renormalization and factorization scales. In addition, one can question whether hard-scattering factorization holds for the cross-section integrated over p_T.

The $\psi(2S)$ to J/ψ ratio R_ψ is defined in Eq. (5.11). The experimental results for R_ψ from fixed-target experiments are compiled in Table 5.5. The result from experiment E673 is obtained by dividing
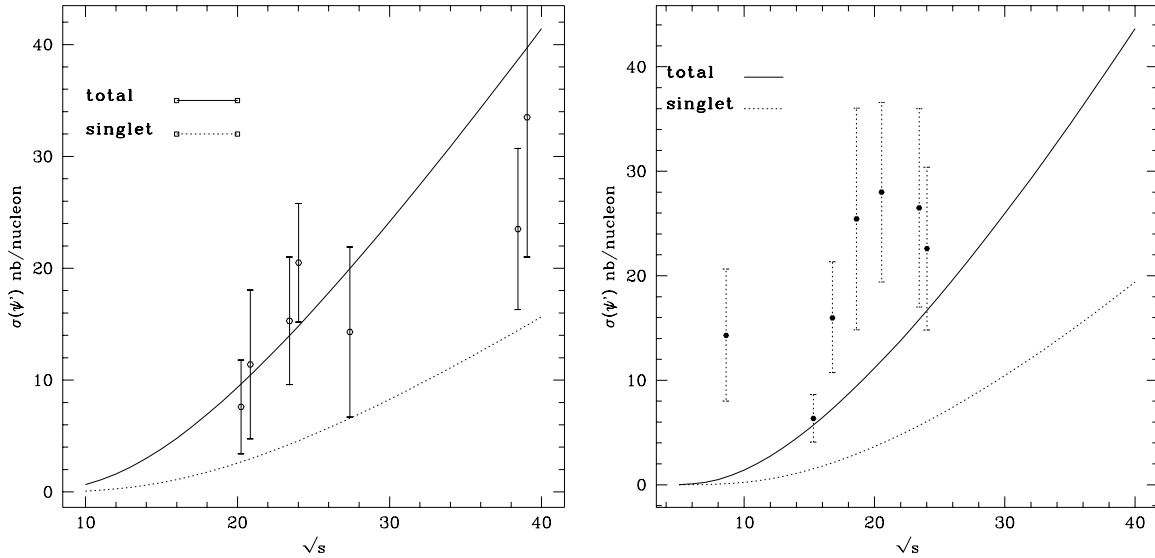
Fig. 5.10: Forward cross-section ($x_F > 0$) for $\psi(2S)$ production in pN collisions (left) and πN collisions (right). The curves are the CSM predictions (dotted lines) and the NRQCD factorization predictions with $M_7^{\psi(2S)} = 5.2 \times 10^{-3}$ GeV^3 (solid lines). From Ref. [129].

the observed fraction of J/ψ's from decays of $\psi(2S)$ by the branching fraction for $\psi(2S) \rightarrow J/\psi X$ given by the Particle Data Group [135]. The result from experiment E771 is obtained by dividing the observed ratio of the products of the cross-sections and the branching fractions into $\mu^+\mu^-$ by the ratio of the branching fractions into $\mu^+\mu^-$ given by the Particle Data Group [135]. The NRQCD factorization approach gives the values $R_\psi = 0.16$ for both pN collisions and π^-N collisions [129]. The colour-singlet model gives $R_\psi = 0.14$ for pN collisions and $R_\psi = 0.16$ for π^-N collisions [129]. In the colour-evaporation model, this ratio is simply an input. Thus the ratio R_ψ is not able to discriminate between any of these approaches.

The fraction F_{χ_c} of J/ψ's that come from χ_c decays is defined in Eq. (5.12). The experimental results for F_{χ_c} from fixed-target experiments are compiled in Table 5.6. The NRQCD factorization approach gives the values $F_{\chi_c} = 0.27$ for pN collisions and $F_{\chi_c} = 0.28$ for π^-N collisions [129]. The colour-singlet model gives $F_{\chi_c} = 0.68$ for pN collisions and $F_{\chi_c} = 0.66$ for π^-N collisions [129]. In the colour-evaporation model, this ratio is simply an input. Clearly, the experimental results favor the NRQCD factorization approach over the colour-singlet model. The most precise results from pN fixed target experiments are compatible with the Tevatron result in Table 5.3. The most precise results from πN fixed target experiments are somewhat larger.

The χ_{c1} to χ_{c2} ratio R_{χ_c} is defined in Eq. (5.10). There are substantial variations among the NRQCD factorization predictions for R_{χ_c} in fixed-target experiments. Beneke and Rothstein [129] give the values $R_{\chi_c} = 0.07$ for pN collisions and $R_{\chi_c} = 0.05$ for π^-N collisions. Their calculation is carried out at leading order in α_s and uses the standard truncation in v that is described in Section 1.1. Beneke and Rothstein [129] suggest that corrections to hard-scattering factorization may be large. Beneke [111] gives the estimate $R_{\chi_c} \approx 0.3$ for both pN and πN collisions. This estimate is based on the assumption that the $^3P_2$ and $^3P_0$ colour-octet matrix elements dominate the χ_{c1} production. It is consistent with the estimate in Ref. [136], once that estimate is modified to take into account the dominant colour-singlet channel in χ_{c2} production [111]. Maltoni [71] gives central values of R_{χ_c} for pN collisions that range from $R_{\chi_c} = 0.04$ to $R_{\chi_c} = 0.1$ as the beam energy ranges from 200 GeV to 800 GeV. Maltoni's calculation takes into account matrix elements at leading order in v, but contains corrections of next-to-leading order in α_s. His calculation displays a very large dependence on the renormalization scale. In

Table 5.5: Experimental results for the ratio R_ψ of the inclusive cross-sections for $\psi(2S)$ and J/ψ production.

Experiment	beam/target	$\sqrt{s}/\text{GeV}$	R_ψ
E537 [132]	$\bar{p}\text{W}$	15.3	0.185 ± 0.0925
E705 [141]	$p\text{Li}$	23.7	$0.14 \pm 0.02 \pm 0.004 \pm 0.02$
E705 [141]	$\bar{p}\text{Li}$	23.7	$0.25 \pm 0.22 \pm 0.007 \pm 0.04$
E771 [134]	$p\text{Si}$	38.8	0.14 ± 0.02
HERA-B [142]	p(C, W)	41.5	0.13 ± 0.02
E537 [132]	$\pi^-\text{W}$	15.3	0.2405 ± 0.0650
E673 [144]	πBe	20.6	0.20 ± 0.09
E705 [141]	$\pi^+\text{Li}$	23.7	$0.14 \pm 0.02 \pm 0.004 \pm 0.02$
E705 [141]	$\pi^-\text{Li}$	23.7	$0.12 \pm 0.03 \pm 0.03 \pm 0.02$
E672/706 [146]	$\pi^-\text{Be}$	31.1	$0.15 \pm 0.03 \pm 0.02$

summary, the existing predictions for R_χ based on NRQCD factorization are in the range 0.04–0.3 for both pN and πN collisions. The colour-singlet model predicts that $R_{\chi_c} \approx 0.05$–0.07 for both pN and πN collisions [111, 129]. The colour-evaporation model predicts that $R_{\chi_c} \simeq 3/5$ [34, 147].

The experimental results for R_{χ_c} are compiled in Table 5.6. As can be seen, the data are somewhat inconsistent with each other. The results from the most precise experiments are significantly smaller than the Tevatron result in Eq. (5.18). There seems to be a trend toward larger values of R_{χ_c} in πN experiments than in pN experiments. Such a dependence on the beam type is contrary to the predictions of the colour-evaporation model. It also would not be expected in the NRQCD factorization approach, unless there is an unusual enhancement in the $q\bar{q}$ production channel [111]. Both the pN and πN data yield results that are significantly larger than the predictions of the colour-singlet model. The pN experiments seem to favor the NRQCD factorization predictions, while the πN experiments seem to favor the colour-evaporation prediction. However, in light of the large theoretical and experimental uncertainties, no firm conclusions can be drawn.

3.2 Polarization

The polarization variable α for J/ψ production is defined by the angular distribution in Eq. (5.13). In fixed-target experiments, the most convenient choice of the polarization axis is the direction of the boost vector from the J/ψ rest frame to the lab frame. Experimental results for α are shown in Table 5.7. The prediction of the NRQCD factorization approach is $0.31 < \alpha < 0.63$ [129]. Both the theoretical prediction and the data include feeddown from χ_c states. The prediction is largely independent of the target and beam types. It was made specifically for the beam energy 117 GeV. However, the energy dependence of the prediction is quite mild, and the prediction would be expected to hold with little error even at a beam energy of 800 GeV. The colour-singlet model predicts a substantial transverse polarization [151]. The colour-evaporation model predicts that $\alpha = 0$ for all processes. There are also specific predictions for the HERA-B experiment in which the region of small p_T is excluded. The predictions for the range $p_T = 1.5$–4 GeV are $\alpha = 0$–0.1 in the NRQCD factorization approach and $\alpha = 0.2$–0.4 in the colour-singlet model [152]. Experimental results for the polarization variable α in J/ψ production are shown in Table 5.7. The data from the conventional fixed-target experiments are consistent with $\alpha = 0$ and favor the prediction of the colour-evaporation model over the predictions of NRQCD factorization or the colour-singlet model [129]. At the smaller values of p_T, one can question whether resummation

Table 5.6: Experimental results for the fraction of J/ψ's from χ_c decay, F_{χ_c}, and the χ_{c1} to χ_{c2} ratio, R_{χ_c}. In view of the experimental uncertainties, no attempt has been made to rescale older measurements to account for the latest χ_c branching fractions. Modified version of a table from Ref. [111].

Experiment	beam/target	$\sqrt{s}$/GeV	F_{χ_c}	R_{χ_c}
E673 [137]	pBe	19.4/21.7	0.47 ± 0.23	0.24 ± 0.28
E705 [138]	pLi	23.7	—	$0.08^{+0.25}_{-0.15}$
E705 [141]	pLi	23.7	0.30 ± 0.04	—
E771 [139]	pSi	38.8	—	$0.53 \pm 0.20 \pm 0.07$
HERA-B [142]	p(C, W)	41.5	$0.32 \pm 0.06 \pm 0.04$	—
WA11 [143]	πBe	18.6	0.305 ± 0.050	0.68 ± 0.28
E673 [137]	πBe	18.9	0.31 ± 0.10	0.96 ± 0.64
E673 [144]	πBe	20.6	0.37 ± 0.09	0.9 ± 0.4
E705 [138]	πLi	23.7	—	$0.52^{+0.57}_{-0.27}$
E705 [141]	π^+Li	23.7	0.40 ± 0.04	—
E705 [141]	π^-Li	23.7	0.37 ± 0.03	—
E672/706 [145]	π^-Be	31.1	$0.443 \pm 0.041 \pm 0.035$	$0.57 \pm 0.18 \pm 0.06$

of the perturbation series is needed and whether hard-scattering factorization would be expected to hold. The HERA-B data are also consistent with $\alpha = 0$ and favor the predictions of the NRQCD factorization approach and the colour-evaporation model over the prediction of the colour-singlet model.

There is also a measurement of the polarization of $\psi(2S)$ in a fixed-target experiment. The E615 experiment measured α for $\psi(2S)$ mesons produced in πN collisions at 253 GeV [153]. The data yield $-0.12 < \alpha < 0.16$, while the prediction of the NRQCD factorization approach is $0.15 < \alpha < 0.44$ [129].

The E866/NuSea experiment has studied the production of dimuons in the collision of 800 GeV protons with copper [154]. The experiment used the angular distributions of dimuons in the mass range 8.1–15.0 GeV to measure the polarization variable α for Drell–Yan pairs, for $\Upsilon(1S)$ mesons, and for a mixture of $\Upsilon(2S)$ and $\Upsilon(3S)$ mesons. The data cover the kinematic ranges $0.0 < x_F < 0.6$ and $p_T < 4.0$ GeV. The results for the polarization variable α as a function of p_T and x_F are shown in Fig. 5.11. The $\Upsilon(1S)$ data show almost no polarization at small x_F and p_T, but show nonzero transverse polarization at either large p_T or large x_F. A fit at the $\Upsilon(1S)$ mass for a polarization that is independent of x_F and p_T gives $\alpha = 0.07 \pm 0.04$. This observation is substantially smaller than a prediction that is based on the NRQCD factorization approach, which gives α in the range 0.28–0.31 [155,156]. However, it also disagrees with the prediction of the colour-evaporation model that the polarization should be zero [34]. The most remarkable result from this experiment is that the $\Upsilon(2S)$ and $\Upsilon(3S)$ were found to be strongly transversely polarized, with the polarization variable α close to its maximal value $\alpha = +1$ for all x_F and p_T, as in the case of Drell–Yan pairs. This result provides strong motivation for measuring the polarizations of the $\Upsilon(2S)$ and $\Upsilon(3S)$ at the Tevatron to see if these states are also produced with substantial polarizations in $p\bar{p}$ collisions.

It has been proposed that χ_2 production in hadron collisions at zero p_T may serve as a tool to measure the polarized gluon structure function of the proton [157]. This proposal relies on the assumption that χ_2 production at zero p_T is dominated by gluon fusion, and it requires that at least one of the colliding hadrons be polarized, as is the case, for example, in the RHIC polarized program.

Table 5.7: Experimental results for the polarization variable α in J/ψ production. Modified version of a table from Ref. [142].

Experiment	beam/target	Beam Energy/GeV	α
E537 [132]	(π, p)(Be, Cu, W)	125	0.024–0.032
E672/706 [148]	pBe	530	0.01 ± 0.15
E672/706 [148]	pBe	800	-0.11 ± 0.15
E771 [149]	pSi	800	-0.09 ± 0.12
E866 [150]	pCu	800	0.069 ± 0.08
HERA-B [142]	p(C, W)	920	$(-0.5, +0.1) \pm 0.1$

Table 5.8: Inclusive CEM parameters $F_{J/\psi}$ and $F_{\Upsilon(1S)}$ from Ref. [158] for various choices of PDF's, quark masses (in GeV), and scales.

PDF	m_c	μ/m_{cT}	$F_{J/\psi}$	PDF	m_b	μ/m_{bT}	$F_{\Upsilon(1S)}$
MRST HO	1.2	2	0.0144	MRST HO	4.75	1	0.0276
MRST HO	1.4	1	0.0248	MRST HO	4.5	2	0.0201
CTEQ 5M	1.2	2	0.0155	MRST HO	5.0	0.5	0.0508
GRV 98 HO	1.3	1	0.0229	GRV 98 HO	4.75	1	0.0225

Table 5.9: Ratios of the direct CEM parameters F_H^{dir} to the inclusive CEM parameter $F_{J/\psi}$ in the case of charmonium states and to the inclusive CEM parameter $F_{\Upsilon(1S)}$ in the case of bottomonium states. From Ref. [159].

H	J/ψ	$\psi(2S)$	χ_{c1}	χ_{c2}	
$F_H^{\mathrm{dir}}/F_{J/\psi}$	0.62	0.14	0.60	0.99	

H	$\Upsilon(1S)$	$\Upsilon(2S)$	$\Upsilon(3S)$	$\chi_b(1P)$	$\chi_b(2P)$
$F_H^{\mathrm{dir}}/F_{\Upsilon(1S)}$	0.52	0.33	0.20	1.08	0.84

3.3 Colour-evaporation-model parameters

Data from pp and pA collisions have been used to extract the parameters F_H of the colour-evaporation model. (The CEM parameter F_H should not be confused with the fraction of J/ψ's that come from decay of H.) The results of these extractions are given in Tables 5.8 and 5.9. The numerical values of the CEM parameters F_H that are obtained by fitting data depend on the choices of the parton densities (PDF's), the heavy quark mass m_Q, the renormalization/factorization scale μ, and the order in α_s of the calculation. The CEM parameters have been calculated using several sets of parton densities [69,79,160], quark masses, and scales [161,162] that reproduce the measured $Q\bar{Q}$ cross-section. In these calculations, the scale μ was set to a constant times $m_{QT} = (m_Q^2 + p_T^2)^{1/2}$, where p_T is the sum of the transverse momenta of the Q and the $\bar{Q}$.

We first describe the extraction of the CEM parameters F_H for charmonium states. The inclusive cross-section for J/ψ production has been measured in pp and pA collisions up to $\sqrt{s} = 63$ GeV. The data are of two types: the forward cross-section, $\sigma(x_F > 0)$, and the cross-section at zero rapidity, $d\sigma/dy|_{y=0}$. These cross-sections include the feeddown from decays of χ_{cJ} and $\psi(2S)$. The parameters
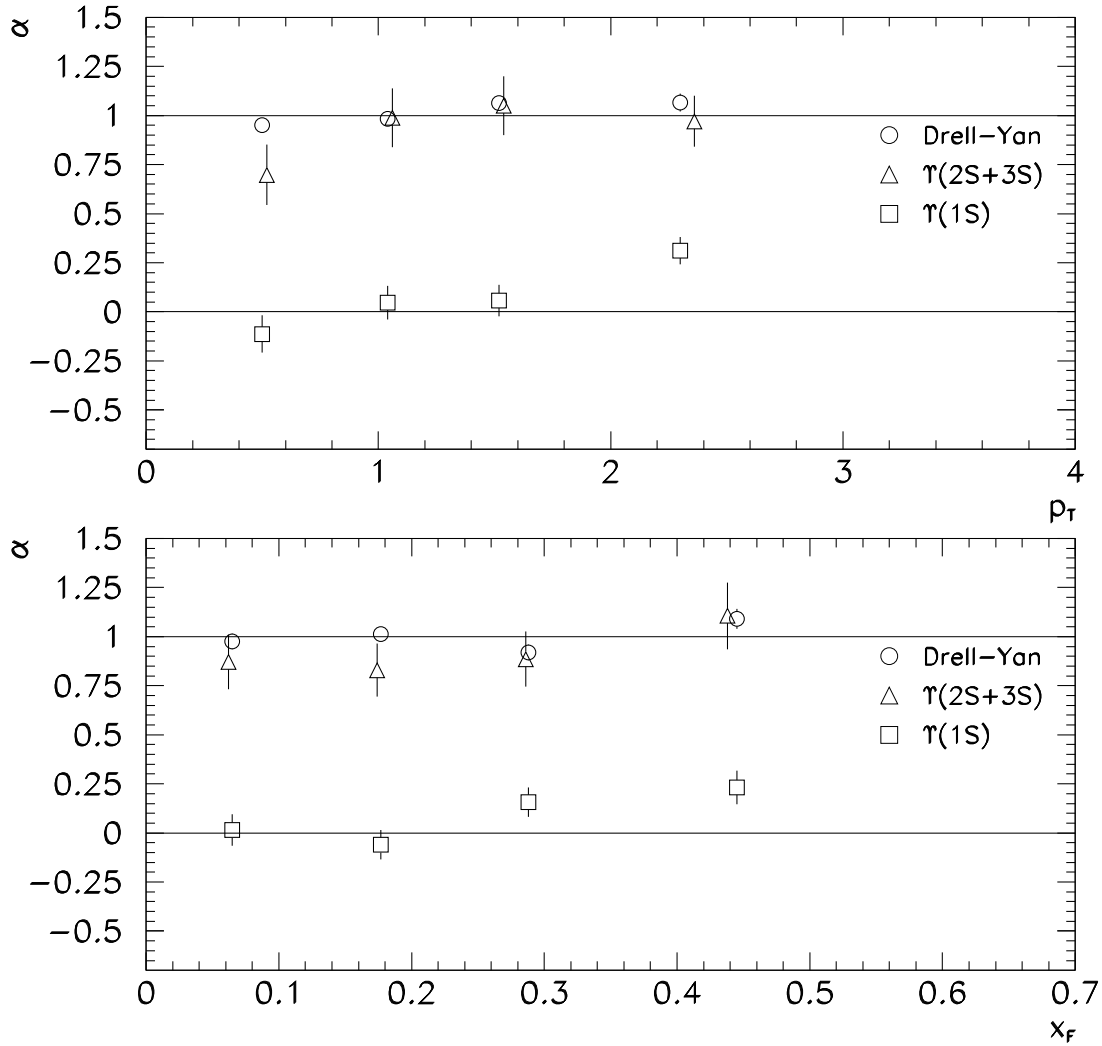
Fig. 5.11: Polarization of Υ mesons and Drell–Yan pairs as a function of p_T and x_F in p–Cu collisions in the E866 experiment. From Ref. [154].

$F_{J/\psi}$ that were obtained by fitting the inclusive J/ψ cross-sections measured in pp and pA collisions are given in Table 5.8 for four sets of PDF's and parameters. The ratio of the parameter F_H^{dir} for the direct production of a charmonium state H to the parameter $F_{J/\psi}$ for the inclusive production of J/ψ can be determined from the measured ratios of the inclusive cross-sections for H and J/ψ using the known branching fractions for the feeddown decays. These ratios are given in Table 5.9 for various charmonium states.

A similar procedure can be used to determine the CEM parameters F_H for bottomonium states. In most data on pp and pA collisions below $\sqrt{s} = 100$ GeV, only the sum of the $\Upsilon(1S)$, $\Upsilon(2S)$, and $\Upsilon(3S)$ cross-sections weighted by their branching fractions to decay into lepton pairs is reported. A fit to the lepton-pair cross-section in the Υ region at zero rapidity therefore gives a linear combination of the inclusive parameters $F_{\Upsilon(nS)}$ weighted by the branching fractions $B[\Upsilon(nS) \to \ell^+ \ell^-]$. The inclusive parameters $F_{\Upsilon(1S)}$ given in Table 5.8 were extracted by using the known branching fractions and the measured ratios of the inclusive cross-sections for $\Upsilon(nS)$ in $p\bar{p}$ collisions at the Tevatron [163]. The ratios of the parameters F_H^{dir} for the direct production of a bottomonium state H to the parameter $F_{\Upsilon(1S)}$ for the inclusive production of $\Upsilon(1S)$ that were obtained in Ref. [164] have been updated in Ref. [159] by using recent CDF data on χ_b production and are given in Table 5.9.
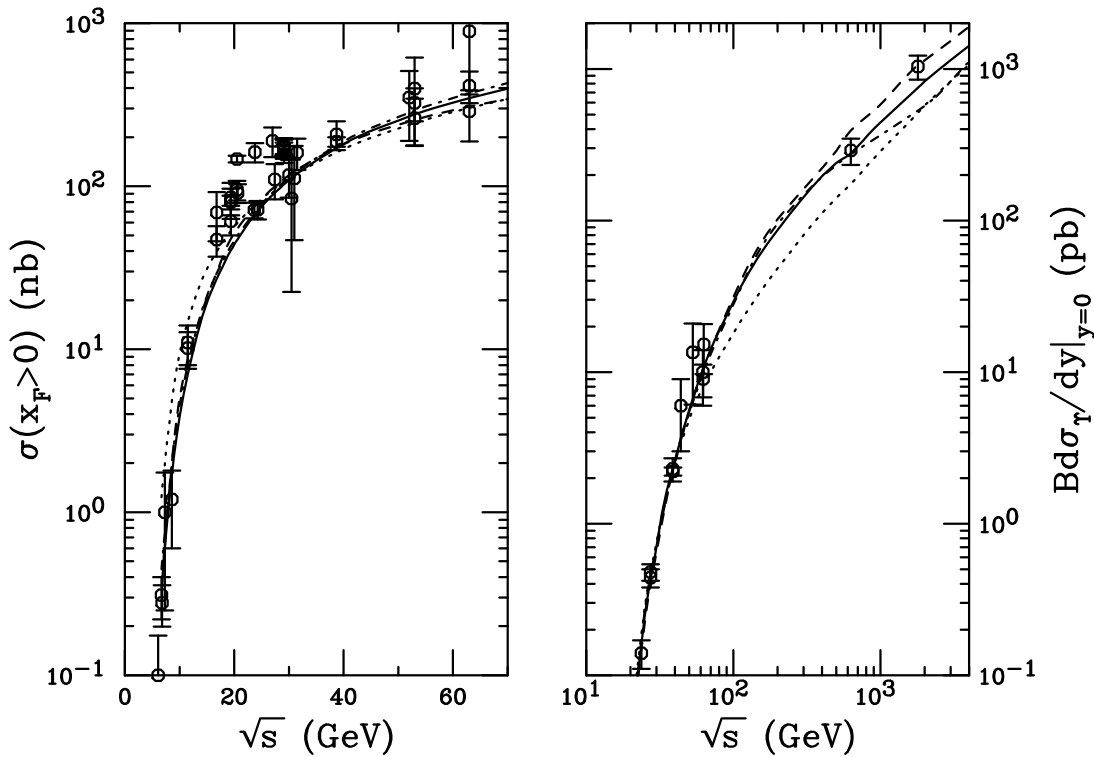
Fig. 5.12: Forward J/ψ production cross-section (left) and weighted average of the $\Upsilon(nS)$ production cross-sections at zero rapidity (right) as a function of the centre-of-mass energy $\sqrt{s}$. The J/ψ data are from pp experiments and from pA experiments with light targets $A \leq 12$. It has been assumed that the cross-sections scale as $A^{0.9}$. The low-energy Υ data are from pp and pA experiments. It has been assumed that the cross-sections are linear in A. The high-energy Υ data are from $p\bar{p}$ experiments. The curves are the cross-sections calculated to NLO in the CEM using the four charmonium parameter sets and the four bottomonium parameter sets in Table 5.8.

The forward cross-section for J/ψ and the weighted cross-section at zero rapidity for $\Upsilon(nS)$ are shown as a function of the centre-of-mass energy in Fig. 5.12. The energy dependence of both cross-sections is well reproduced by the CEM at NLO. All of the CEM parameter sets give good fits to the data for $\sqrt{s} \leq 63$ GeV, but their predictions for $\Upsilon(nS)$ differ by up to a factor of two when extrapolated to 2 TeV. The extrapolation of the forward J/ψ cross-section to 2 TeV cannot be compared with data from Run I of the Tevatron because the lepton-p_T cut excludes a measurement of the cross-section for J/ψ in the region $p_T < 5$ GeV that dominates the integrated cross-section.

4 QUARKONIUM PRODUCTION AT HERA

4.1 Inelastic photoproduction of charmonium

At the ep collider HERA, the inelastic charmonium production process is dominantly virtual-photon-gluon fusion: a photon emitted from the incoming electron or positron interacts with a gluon from the proton to produce a $c\bar{c}$ pair that subsequently forms a charmonium state. In photoproduction, the photon virtuality Q^2 is small and the photon is quasi-real. In this case, the photon can either couple to the c quark directly ("direct" processes, Fig. 5.13a or b) or it can interact via its hadronic component ("resolved" processes, Fig. 5.13c). Many models have been suggested to describe inelastic charmonium production in the framework of perturbative QCD, such as the colour-singlet model (CSM) [21–24] described in Section 1.2, the colour-evaporation model [28, 36] described in Section 1.3, and soft colour interactions [35].
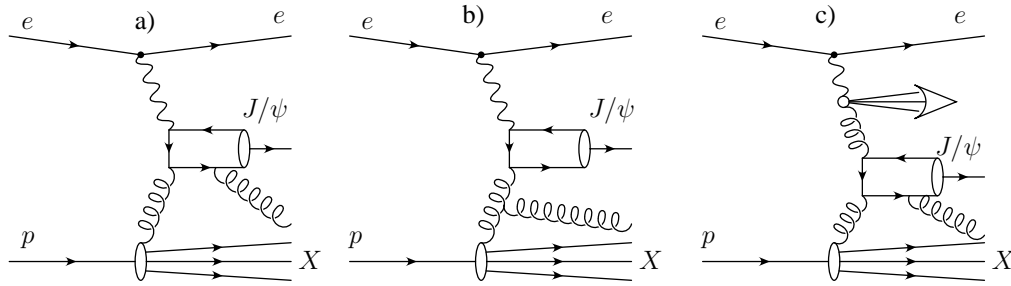
Fig. 5.13: Generic Feynman diagrams for inelastic J/ψ production. a,b) direct-photon processes; c) resolved-photon process. In diagrams a) and c), the $c\bar{c}$ pair leading to the formation of the J/ψ can be in a colour-singlet or a colour-octet state while in b) it can only be in a colour-octet state. Additional soft gluons emitted during the hadronization process are not shown.

For J/ψ and $\psi(2S)$ photoproduction, the CSM calculations are available to next-to-leading order [165, 166]. These are performed using standard hard-scattering factorization in which the gluon density depends only on the momentum fraction x. Alternatively, using the CSM, inelastic J/ψ production can be modeled in the k_T-factorization approach (see Section 1.4) using an unintegrated (k_T-dependent) gluon density in the proton.

Theoretical calculations based on the NRQCD factorization approach [1–3] are available in leading order. For J/ψ and $\psi(2S)$ photoproduction at HERA, these have been performed by Cacciari and Krämer [167], Beneke, Krämer, and Vänttinen [168], Amundson, Fleming, and Maksymyk [169], Ko, Lee, and Song [170], Godbole, Roy, and Sridhar [171], and Kniehl and G. Kramer [172, 173]. The theoretical calculations use the standard truncation in v, in which the independent NRQCD matrix elements are $\langle \mathcal{O}_1^{J/\psi}(^3S_1)\rangle$, $\langle \mathcal{O}_8^{J/\psi}(^1S_0)\rangle$, $\langle \mathcal{O}_8^{J/\psi}(^3S_1)\rangle$, and $\langle \mathcal{O}_8^{J/\psi}(^3P_0)\rangle$. The relative strength of the colour-octet contributions depends crucially on the size of the corresponding NRQCD matrix elements. Unfortunately the values of the matrix elements $\langle \mathcal{O}_8^{J/\psi}(^1S_0)\rangle$ and $\langle \mathcal{O}_8^{J/\psi}(^3P_0)\rangle$, which are most important in J/ψ and $\psi(2S)$ photoproduction at HERA, still show large uncertainties. (See Section 2.1 and Ref. [64].)

The theoretical predictions are sensitive to a number of input parameters, e.g., the parton distributions, the values of α_s, and the charm-quark mass m_c, as well as the choice of the renormalization and factorization scales. In the NRQCD factorization approach, the values of the colour-octet NRQCD matrix elements are additional parameters. The comparison with the data in the NRQCD approach also suffers from the uncertainties associated with LO calculations. Next-to-leading-order corrections might change the results substantially. Although the NLO terms have not been calculated in the NRQCD approach, effects that are similar to those in the CSM may be expected, in which the NLO terms lead to an increase in the cross-section of typically a factor two, with a strong $p_{T,\psi}$ dependence.

Figure 5.14 shows the measurements of the prompt J/ψ cross-section by the H1 collaboration [174] and the ZEUS collaboration [175], compared with the theoretical predictions given in Ref. [64]. The variable z denotes the fraction of the photon energy that is transferred to the J/ψ and is defined as

$$z = \frac{(E - p_z)_{J/\psi}}{(E - p_z)_{\text{hadrons}}}, \tag{5.23}$$

where E and p_z in the numerator are the energy and z-component of the momentum of the J/ψ and E and p_z in the denominator are the sums of the energies and z-components of the momenta of all the hadrons in the final state.
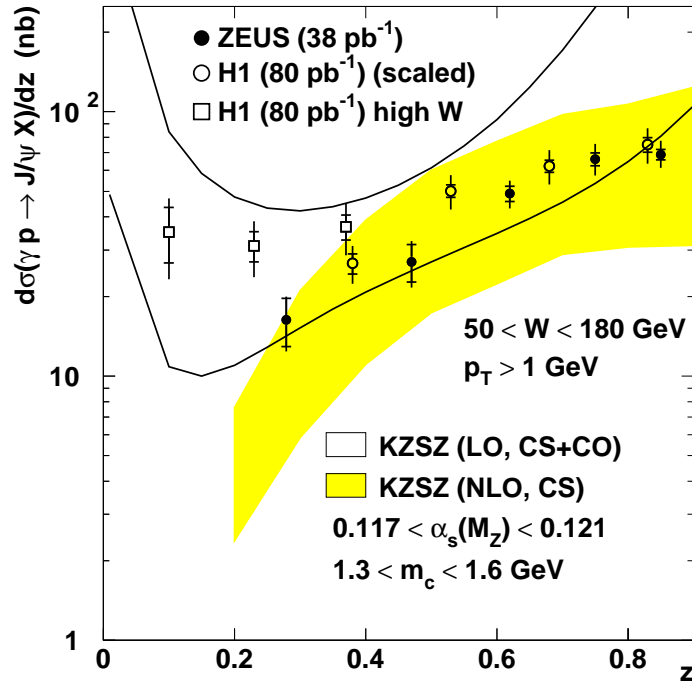
Fig. 5.14: The rate for inelastic J/ψ photoproduction at HERA as a function of z. The open band represents the LO NRQCD factorization prediction [64]. The solid band represents the NLO colour-singlet contribution [64,166]. The data points are from the H1 [174] and ZEUS [175] measurements.
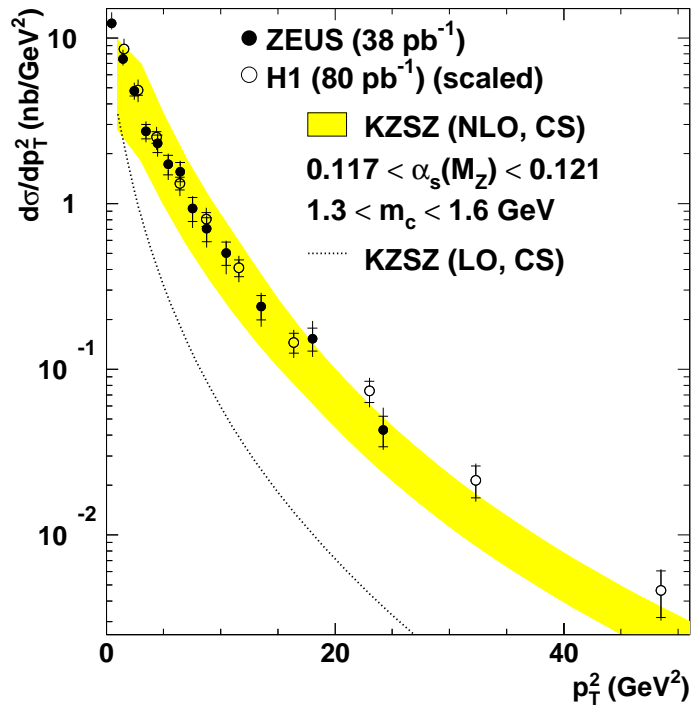

Fig. 5.15: The rate for inelastic J/ψ photoproduction at HERA as a function of $p_{T,\psi}$. The solid band represents the NLO colour-singlet contribution [64, 166]. The dotted line is the LO colour-singlet contribution. The data points are from the H1 [174] and ZEUS [175] measurements.
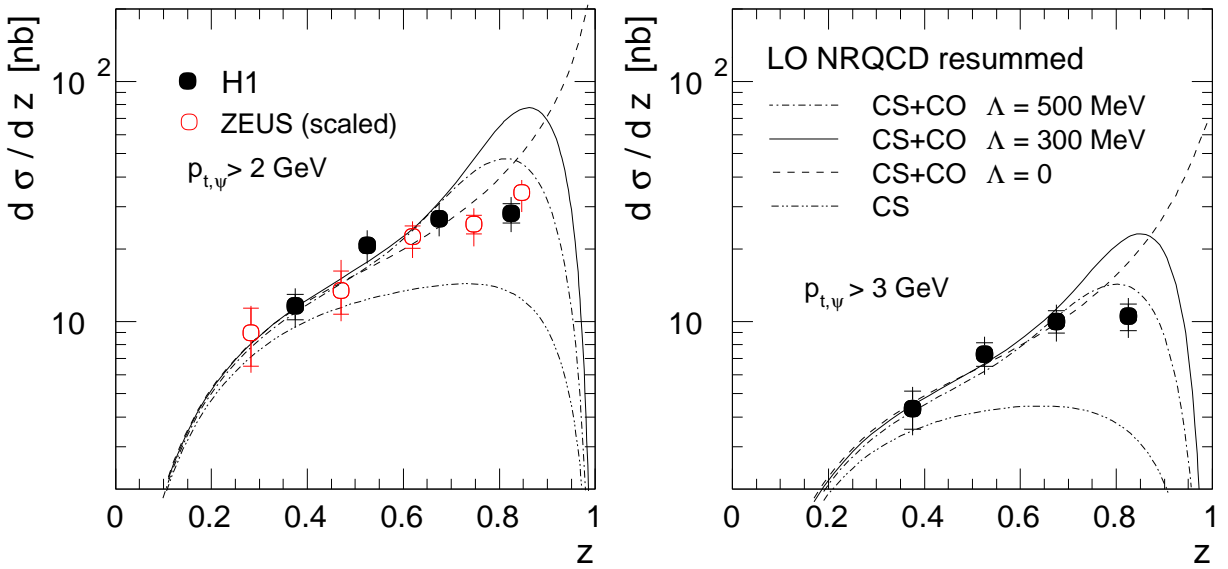
Fig. 5.16: Differential cross-sections $d\sigma/dz$ ($60 < W_{\gamma p} < 240\,\text{GeV}$) for $p_{T,\psi} > 2\,\text{GeV}$ (left panel) and $p_{T,\psi} > 3\,\text{GeV}$ (right panel) in comparison with NRQCD calculations that include colour-octet and colour-singlet contributions and resummations of soft contributions at high z [12]. The curves correspond to three values of the parameter Λ: $\Lambda = 0$, i.e., no resummation (dashed line), $\Lambda = 300$ MeV (solid line), and $\Lambda = 500$ MeV (dash–dotted line). The theoretical curves have been scaled with a common factor 2 in the left panel and 3 in the right panel.

The J/ψ data points shown in Fig. 5.14 are not corrected for feeddown processes, such as diffractive and inelastic production of $\psi(2S)$ mesons ($\approx 15\%$), the production of b hadrons with subsequent decays to J/ψ mesons, or feeddown from the production of χ_c states. The latter two contributions are estimated to contribute between 5% at medium z and 30% at the lowest values of z. The open band in Fig. 5.14 represents the sum of the colour-singlet and colour-octet contributions, calculated in leading order in QCD perturbation theory. The uncertainty is due to the uncertainty in the colour-octet NRQCD matrix elements. The NRQCD prediction deviates from the data near $z = 1$, owing to the large colour-octet contribution in that region. The shaded band shows the calculation of the colour-singlet contribution to next-to-leading order in α_s [165, 166]. The NLO corrections increase the colour-singlet contribution by about a factor of two, so that it accounts for the data quite well without the inclusion of a colour-octet contribution.

Uncertainties in m_c could lower the colour-singlet contribution by about a factor of two, leaving more room for colour-octet contributions. In the experimental data, the cut $p_{T,\psi} > 1\,\text{GeV}$ is employed. One can question whether hard-scattering factorization is valid at such small values of $p_{T,\psi}$. However, the data differential in $p_{T,\psi}$ are compatible with colour-singlet production alone at large $p_{T,\psi}$ (Fig. 5.15).

The next-to-leading-order QCD corrections are crucial in describing the shape of the transverse-momentum distribution of the J/ψ. The NLO colour-singlet cross-section includes processes such as $\gamma + g \rightarrow (c\bar{c}) + gg$, which are dominated by t-channel gluon exchange and scale as $\alpha_s^3 m_c^2/p_{T,\psi}^6$. At $p_{T,\psi} \gtrsim m_c$ their contribution is enhanced with respect to the leading-order cross-section, which scales as $\sim \alpha_s^2 m_c^4/p_{T,\psi}^8$. The comparison with the experimental data in Fig. 5.15 confirms the importance of the higher-order corrections.

At large z, the emission of soft gluons in the conversion of the $c\bar{c}$ pairs to J/ψ mesons is suppressed, owing to phase-space limitations. Furthermore, the velocity expansion of the NRQCD factorization approach is expected to break down [10]. These effects are not taken into account in the theoretical
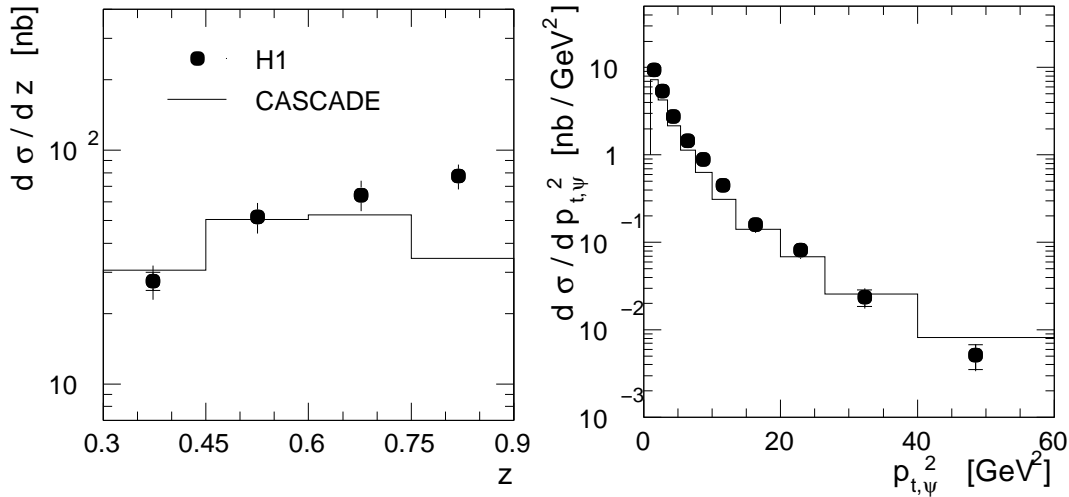
Fig. 5.17: Inelastic J/ψ production in the region $60 < W_{\gamma p} < 240$ GeV, $0.3 < z < 0.9$, and $p_{T,\psi}^2 > 1$ GeV^2, in comparison with a k_T-factorization model implemented in the Monte Carlo generator CASCADE [176, 177]. Left panel: differential cross-section $\mathrm{d}\sigma/\mathrm{d}z$; right panel: $d\sigma/dp_{T,\psi}^2$ in the range $0.3 < z < 0.9$.

calculation that is shown in Fig. 5.14. In Ref. [12], a resummation of the nonrelativistic expansion was carried out, leading to a decrease of the predicted cross-section at high z. The resummation involves a parameter Λ that describes the energy in the $c\bar{c}$ rest frame that is lost by the $c\bar{c}$ system in its conversion into the J/ψ meson. In Fig. 5.16, the measured cross-sections $d\sigma/dz$ for $p_{T,\psi} > 2$ GeV and for $p_{T,\psi} > 3$ GeV are compared with the results of these resummed calculations. The calculated curves have been roughly normalized to the data points at low z. The resummed calculation for $\Lambda = 500$ MeV gives an acceptable description of the data at $p_{T,\psi} > 3$ GeV, while the agreement between data and calculation is still poor for $p_{T,\psi} > 2$ GeV or for lower Λ values.

Effects from resummation of logarithms of $1 - z$ and model shape functions have also been calculated for the process $e^+ e^- \to J/\psi + X$ [11]. It may be possible to use this resummed theoretical prediction to extract the dominant shape function from the Belle and BaBar data for $e^+ e^- \to J/\psi + X$ and then use it to make predictions for J/ψ photoproduction near $z = 1$.

Measurements of the J/ψ production cross-section at large z are available from H1 [204] and from ZEUS [175]. In this region, the contribution from diffractively produced J/ψ mesons is expected to be large, as is discussed below in Section 4.3.

The ZEUS Collaboration has also measured the ψ' to J/ψ cross-section ratio [175] in the range $0.55 < z < 0.9$ and $50 < W < 180$ GeV. It is found to be consistent with being independent of the kinematic variables z, $p_{t,\psi}$ and W, as is expected if the underlying production mechanisms for the J/ψ and the ψ' are the same. An average value $\sigma(\psi')/\sigma(J/\psi) = 0.33 \pm 0.10(\text{stat.})^{+0.01}_{-0.02}(\text{syst.})$ is found which compares well with the prediction from the leading-order colour-singlet model [165].

The k_T-factorization approach (see Section 1.4) has recently been applied successfully to the description of a variety of processes [176–178]. In this approach, the J/ψ production process is factorized into a k_T-dependent gluon density and a matrix element for off-shell partons. A leading-order calculation within this approach is implemented in the Monte Carlo generator CASCADE [176, 177]. Figure 5.17 shows a comparison of the data with the predictions from the k_T-factorization approach. Good agreement is observed between data and predictions for $z \lesssim 0.8$. At high z values, the CASCADE calculation underestimates the cross-section. This may be due to missing higher-order effects, or missing relativistic corrections, which are not available for the off-shell matrix element. It could also indicate a possible missing colour-octet contribution. The CASCADE predictions for the the $p_{T,\psi}^2$ dependence of the cross-

section (Fig. 5.17c) fit the data considerably better than the collinear LO calculations. This improved fit is due to the transverse momentum of the gluons from the proton, which contributes to the transverse momentum of the J/ψ meson. Note, however, that the NLO colour-singlet calculation in collinear factorization [166] also describes the $p_{T,\psi}^2$ distribution.

The polarization of the J/ψ meson is expected to differ in the various theoretical approaches discussed here and could in principle be used to distinguish between them, independently of normalization uncertainties. The general decay angular distribution can be parametrized as

$$\frac{d\Gamma(J/\psi \to l^+ l^-)}{d\Omega} \propto 1 + \lambda \cos^2\theta + \mu \sin 2\theta \cos\phi + \frac{\nu}{2}\sin^2\theta \cos 2\phi, \tag{5.24}$$

where θ and ϕ refer to the polar and azimuthal angle of the l^+ three-momentum with respect to a coordinate system that is defined in the J/ψ rest frame. (See, for example, Ref. [168] for details.) The parameters λ, μ, ν can be calculated within NRQCD or the CSM as a function of the kinematic variables, such as z and $p_{T,\psi}$.

In Fig. 5.18, the data are shown, together with the results from two LO calculations: the NRQCD prediction, including colour-octet and colour-singlet contributions [168], and the colour-singlet contribution alone. A calculation that uses a k_T-factorization approach and off-shell gluons is also available [179]. In contrast to the predictions shown in the Fig. 5.18, in which λ is zero or positive, the prediction of the k_T-factorization approach is that λ should become increasingly negative toward larger values of $p_{t,J/\psi}$, reaching $\lambda \sim -0.5$ at $p_{T,\psi} = 6$ GeV. However, at present, the errors in the data preclude any firm conclusions. In this range of $p_{T,\psi}$ none of the calculations predicts a decrease in λ with increasing z. In order to distinguish between full NRQCD and the colour-singlet contribution alone, measurements at larger $p_{T,\psi}$ are required. The measured values of ν, for which no prediction is available from the k_T-factorization approach, favor the full NRQCD prediction.

4.2   Inelastic electroproduction of charmonium

As in photoproduction, inelastic leptoproduction of J/ψ mesons at HERA ($e+p \to e+J/\psi+X$) is dominated by virtual-photon-gluon fusion ($\gamma^* g \to c\bar{c}$). In leptoproduction, or deep inelastic ep-scattering (DIS), the exchanged photon has a nonzero virtuality $Q^2 = -q^2$, where q is the four-momentum of the virtual photon. For events with a photon virtuality of $Q^2 \gtrsim 1$ GeV^2, the electron scattering angle is large enough for the electron to be detected in the central detectors.

The analysis of leptoproduction at finite Q^2 has experimental and theoretical advantages in comparison with the analysis of photoproduction. At high Q^2, theoretical uncertainties in the models decrease and resolved-photon processes are expected to be negligible. Furthermore, the background from diffractive production of charmonia is expected to decrease faster with Q^2 than the inelastic process, and the distinct signature of the scattered lepton makes the inelastic process easier to detect.

A first comparison between data and NRQCD calculations was presented in Ref. [180]. The NRQCD calculations in Ref. [180] were performed by taking into account only "$2 \to 1$" diagrams (see the top left diagram of Fig.5.19) [181], and disagreement between data and theory was observed both in the absolute values of the cross-sections and in their shapes as functions of the variables that were studied.

More recently, the cross-section for J/ψ production in deep-inelastic ep scattering at HERA was calculated in the NRQCD factorization approach at leading order in α_s by Kniehl and Zwirner [182], taking into account diagrams of the type "$2 \to 2$", as are shown in the top right and bottom diagrams of Fig. 5.19. The calculation made use of the matrix elements of Ref. [78] and MRST98LO [79] and CTEQ5L [69] parton distributions.

In Fig. 5.20, the results of this calculation are plotted as a function of Q^2 and $p_{T,\psi}^2$, along with the H1 data [183]. The NRQCD results that are shown in Fig. 5.20 include the contributions from the
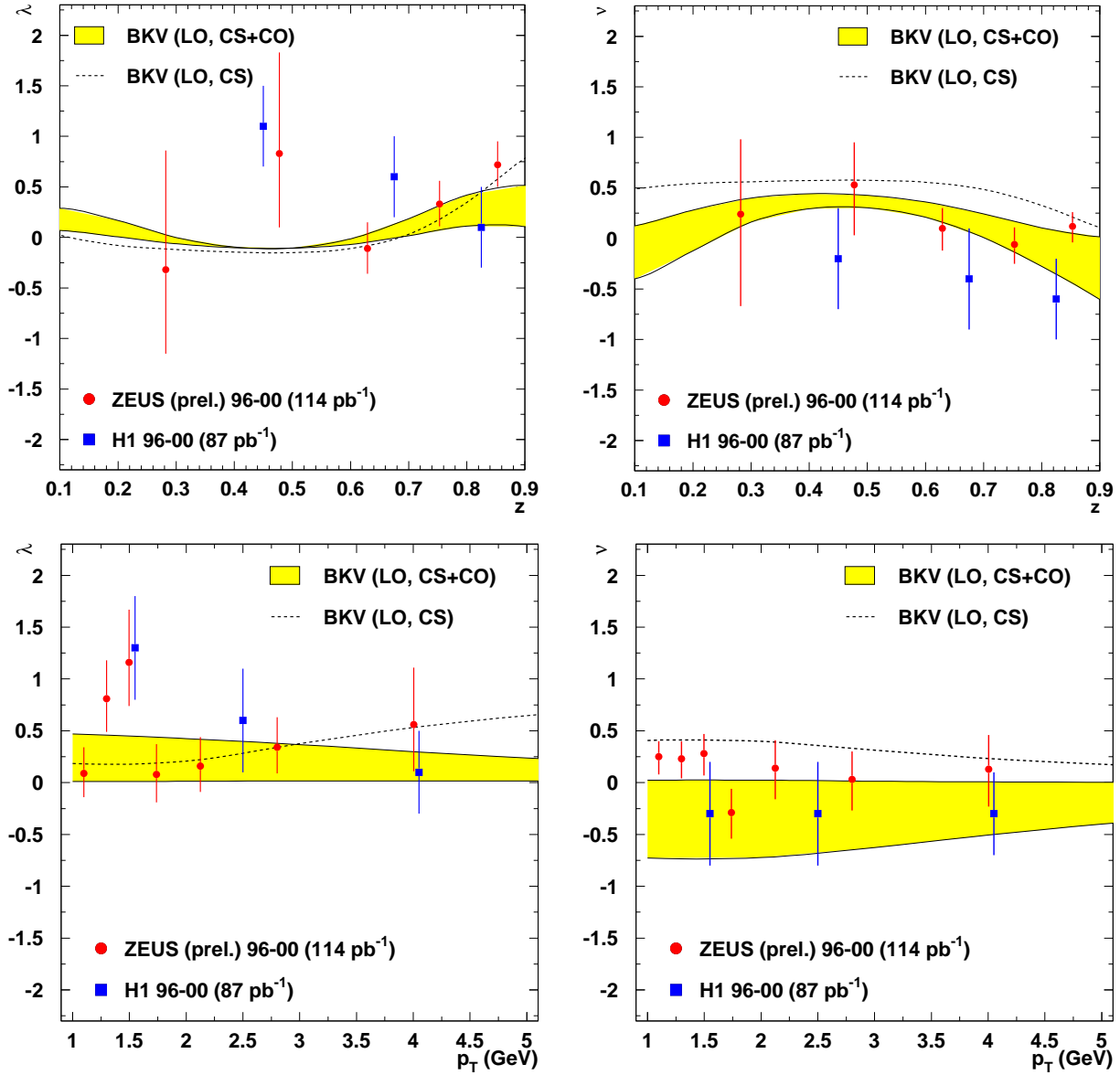
Fig. 5.18: Polarization parameters λ (left panels) and ν (right panels) in the target rest frame as functions of z (top panels) and $p_{T,\psi}$ (bottom panels). The error bars on the data points correspond to the total experimental error. The theoretical calculations shown are from the NRQCD approach [168] (shaded bands) with colour-octet and colour-singlet contributions, while the curves show the result from the colour-singlet contribution separately.
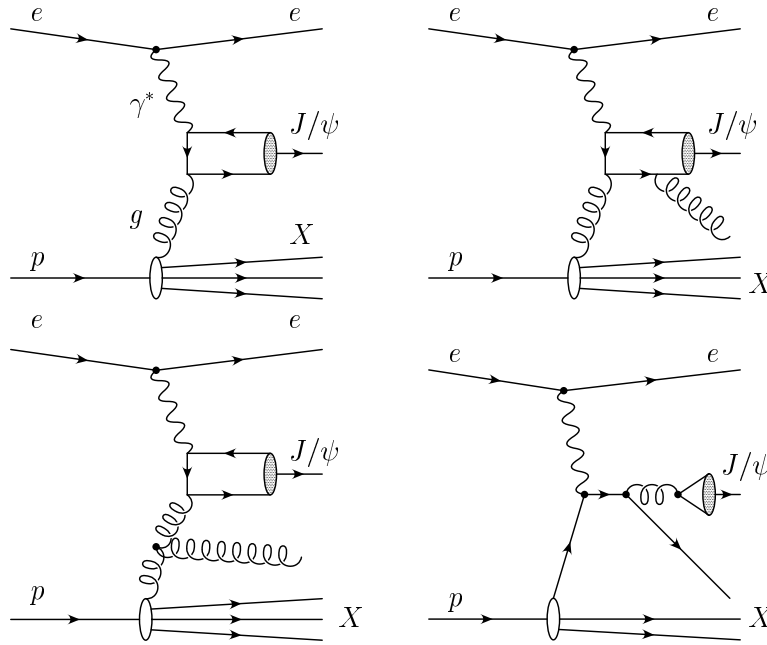
Fig. 5.19: Generic diagrams for charmonium production mechanisms: photon–gluon fusion via a "2 → 1" process (top left diagram) and "2 → 2" processes (remaining diagrams). All the diagrams contribute via colour-octet mechanisms, while the top right diagram can also contribute via the colour-singlet mechanism. Additional soft gluons emitted during the hadronization process are not shown.

Fig. 5.20: Differential cross-sections $d\sigma/dQ^2$ (top left panel) and $d\sigma/dp_{T,\psi}^{*2}$ (bottom left panel) and the corresponding ratios of data to theory (right panels). The data from H1 [183] are compared with the NRQCD calculation [182] (CO+CS, dark band) and the colour-singlet contribution [182] (CS, light band).

Fig. 5.21: Differential cross-sections $d\sigma/dQ^2$ (left) and $d\sigma/dz$ (right) and theory predictions. The data from ZEUS [184] are compared with the NRQCD calculation [182] (CO+CS, dark band), the colour-singlet contribution 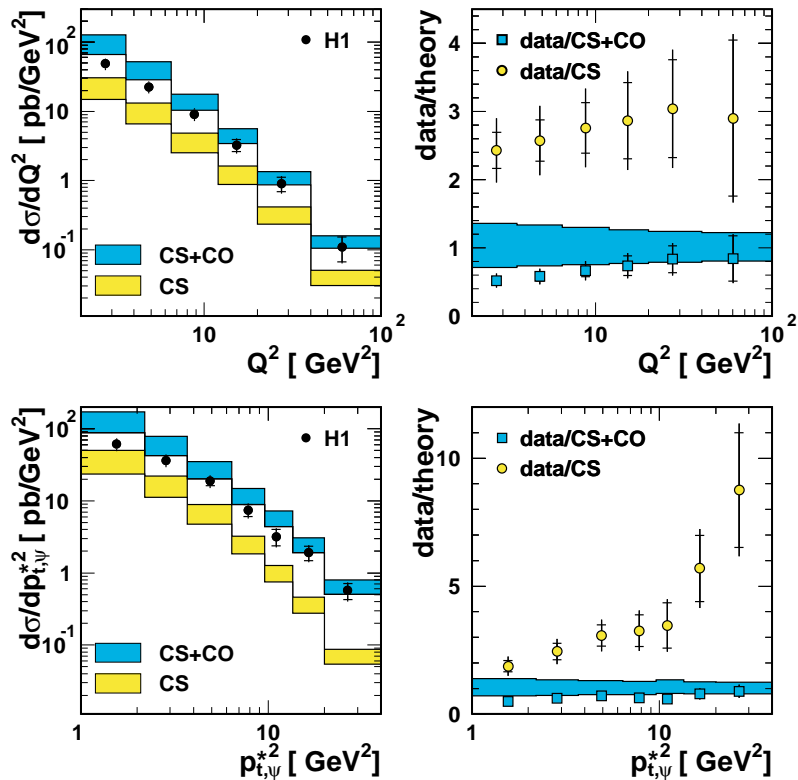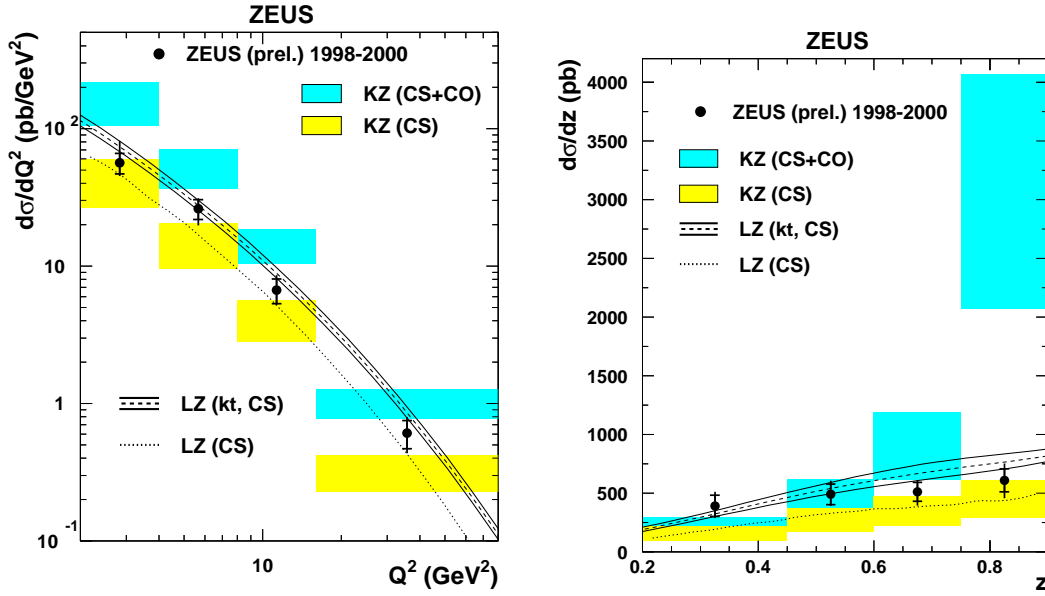(CS, light band), and with the prediction LZ(kt,CS) from the k_T-factorization approach within the CSM [185]. The solid lines delimit the uncertainties, and the dashed line show the central values. The CSM prediction LZ (CS) in the collinear-factorization approach, as given by the authors of Ref. [185], is also shown (dotted line).

colour-octet channels $^3S_1$, $^3P_{J=0,1,2}$, $^1S_0$, as well as from the colour-singlet channel $^3S_1$. The contribution of the colour-singlet channel is also shown separately. The values of the NRQCD matrix elements were determined from the distribution of transverse momenta of J/ψ mesons produced in $p\bar{p}$ collisions [78].[4] The bands include theoretical uncertainties, which originate from the uncertainty in the charm-quark mass $m_c = 1.5 \pm 0.1$ GeV, the variation of renormalization and factorization scales by factors $1/2$ and 2, and the uncertainties in the NRQCD matrix elements, all of which result mainly in normalization uncertainties that do not affect the shapes of the distributions.

Figure 5.21 shows the differential electroproduction cross-sections for J/ψ mesons as functions of Q^2 and z, as measured by the ZEUS collaboration [184]. The ZEUS data, which are consistent with the H1 results shown in Fig. 5.20, are compared with predictions in the framework of NRQCD (CS+CO) [182] and also with predictions in the k_T-factorization approach in which only the colour-singlet contribution (CS) is included [185]. As in Fig. 5.20, the uncertainties in the NRQCD calculations are indicated in Fig. 5.21 as shaded bands. For the prediction within the k_T-factorization approach (LZ(kt,CS)), only one of the sources of uncertainty is presented, namely the uncertainty in the pomeron intercept Δ, which controls the normalization of the unintegrated gluon density.

In Fig. 5.22, the normalization uncertainties of the theory, which are dominant, are removed by normalizing the differential cross-sections measured by H1 [183] and the theory predictions to the integrated cross-sections in the measured range for each distribution. The comparisons in Figs. 5.20–5.22 indicate that the colour-singlet contribution follows the shape of the data from H1 and ZEUS quite well. In general, the CSM predictions are below the H1 and ZEUS data, but are consistent with the data, given the uncertainties, both in shape and normalization. However, the differential cross-sections as a function of the transverse momentum squared of the J/ψ are too steep compared to the data (lower left plot in

---

[4] The extracted values for the NRQCD matrix elements depend on the parton distributions. For the set MRST98LO [79], the values are $\langle \mathcal{O}_1^{J/\psi}(^3S_1) \rangle = 1.3 \pm 0.1$ GeV^3, $\langle \mathcal{O}_8^{J/\psi}(^3S_1) \rangle = (4.4 \pm 0.7) \times 10^{-3}$ GeV^3 and $M_{3.4}^{J/\psi} = (8.7 \pm 0.9) \times 10^{-2}$ GeV^3, where $M_{3.4}^{J/\psi}$ is the linear combination of two NRQCD matrix elements that is defined in Eq. (5.8).
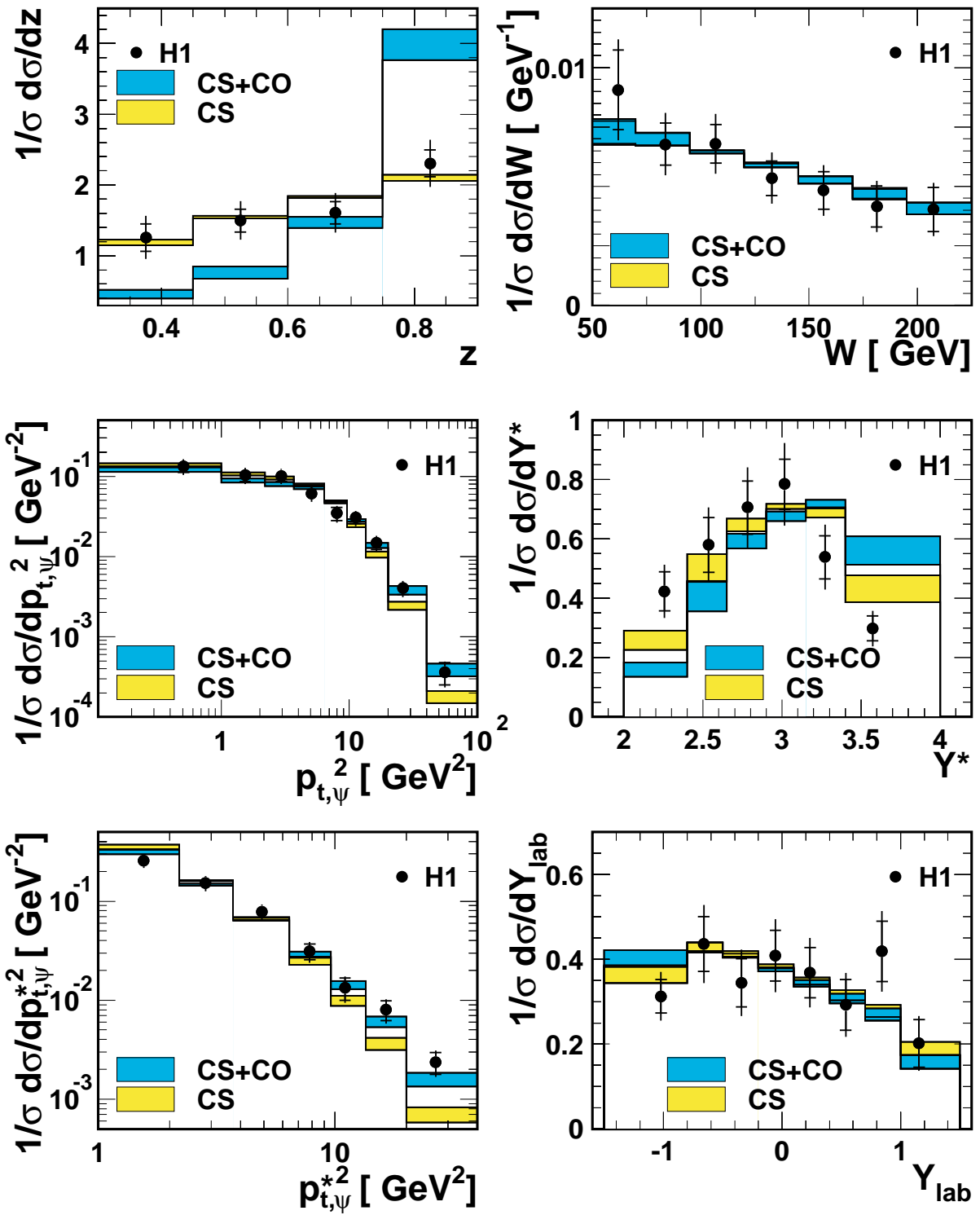
Fig. 5.22: Normalized differential cross-sections. $1/\sigma\, d\sigma/dz$ (top left panel), $1/\sigma\, d\sigma/dW$ (top right panel), $1/\sigma\, d\sigma/dp_{T,\psi}^2$ (middle left panel), $1/\sigma\, d\sigma/dY^*$ (middle right panel), $1/\sigma\, d\sigma/dp_{T,\psi}^{*2}$ (bottom left panel), and $1/\sigma\, d\sigma/dY_{lab}$ (bottom right panel). The histograms show calculations for inelastic J/ψ production within the NRQCD factorization approach [182], which have been normalized to the integrated cross-section. The dark band represents the sum of CS and CO contributions, and the light band represents the CSM contribution alone. These contributions are normalized separately. The error bands reflect the theoretical uncertainties.
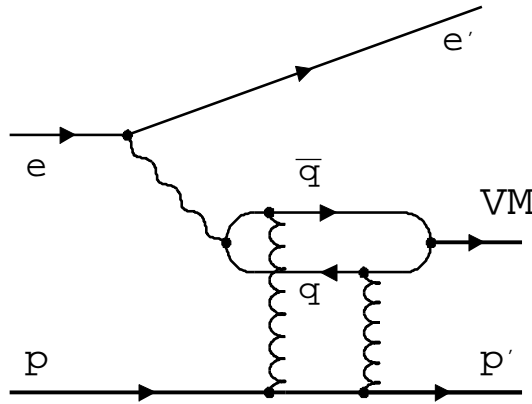
Fig. 5.23: Diagram for diffractive charmonium production via exchange of two gluons in a colour-singlet state.

Fig. 5.20). A similar observation was made for photoproduction (Section 4.1, Fig. 5.15), in which the LO CSM calculation is too steep and the NLO CSM calculation is found to describe the data well. The z distribution (Figs. 5.21 and 5.22) is very poorly described by the full calculation that includes colour-octet contributions, while the colour-singlet contribution alone reproduces the shape of the data rather well. The failure of the colour-octet calculations could be due to the fact that resummations of soft-gluons are not included here. It is worth noting that the calculation of Kniehl and Zwirner disagrees with a number of previous results [186–190], which themselves are not fully consistent.

4.3 Diffractive vector meson production

At HERA, the dominant production channel for quarkonia with quantum numbers of real photons (i.e., $J^{PC} = 1^{--}$) is through diffractive processes. In perturbative QCD, the diffractive production of vector mesons can be modeled in the proton rest frame by a process in which the photon fluctuates into a $q\bar{q}$ pair at a long distance from the proton target. The $q\bar{q}$ subsequently interacts with the proton via a colour-singlet exchange, i.e., in lowest order QCD via the exchange of a pair of gluons with opposite colour (see Fig. 5.23) [191–197]. At small $|t|$, where t is the momentum-transfer-squared at the proton vertex, the elastic process in which the proton stays intact dominates. Toward larger values of $|t|$, the dissociation of the proton into a small-invariant-mass state becomes dominant. Measurements of diffractive vector-meson production cross-sections and helicity structure from the H1 [180, 198–205] and ZEUS [206–211, 213, 214] collaborations are available for ρ^0, ω, ϕ, J/ψ, ψ', and Υ production, spanning the ranges of $0 \simeq Q^2 < 100$ GeV^2, $0 \simeq |t| < 20$ GeV^2, and $20 < W_{\gamma p} < 290$ GeV. ($W_{\gamma p}$ is the γp centre-of-mass energy.) In Fig. 5.24, the elastic photoproduction cross-sections are shown. Perturbative calculations in QCD are available for the kinematic regions in which at least one of the energy scales μ^2 (i.e., Q^2, M_V^2 or $|t|$) is large and the strong-coupling constant $\alpha_s(\mu^2)$ is small [215–221].

In the presence of such a 'hard' scale, QCD predicts a steep rise of the cross-section with $W_{\gamma p}$. At small Q^2, $|t|$ and meson masses M_V, vector-meson production is known to show a non-perturbative "soft" behavior that is described, for example, by Regge-type models [222–226]. Toward larger values of $|t|$, in the leading logarithmic approximation, diffractive J/ψ production can be described by the effective exchange of a gluonic ladder. At sufficiently low values of Bjorken x (i.e., large values of $W_{\gamma p}$), the gluon ladder is expected to include contributions from BFKL evolution [227–231], as well as from DGLAP evolution [232].

Experimentally, diffractive events are generally distinguishable from inelastic events, since, aside from meson-decay products, only a few final-state particles are produced in the central rapidity range in proton dissociation and no particles are produced in the central rapidity range in elastic diffraction. The elasticity variable z defined in Eq. (5.23) is often used to demark the boundary between the elastic
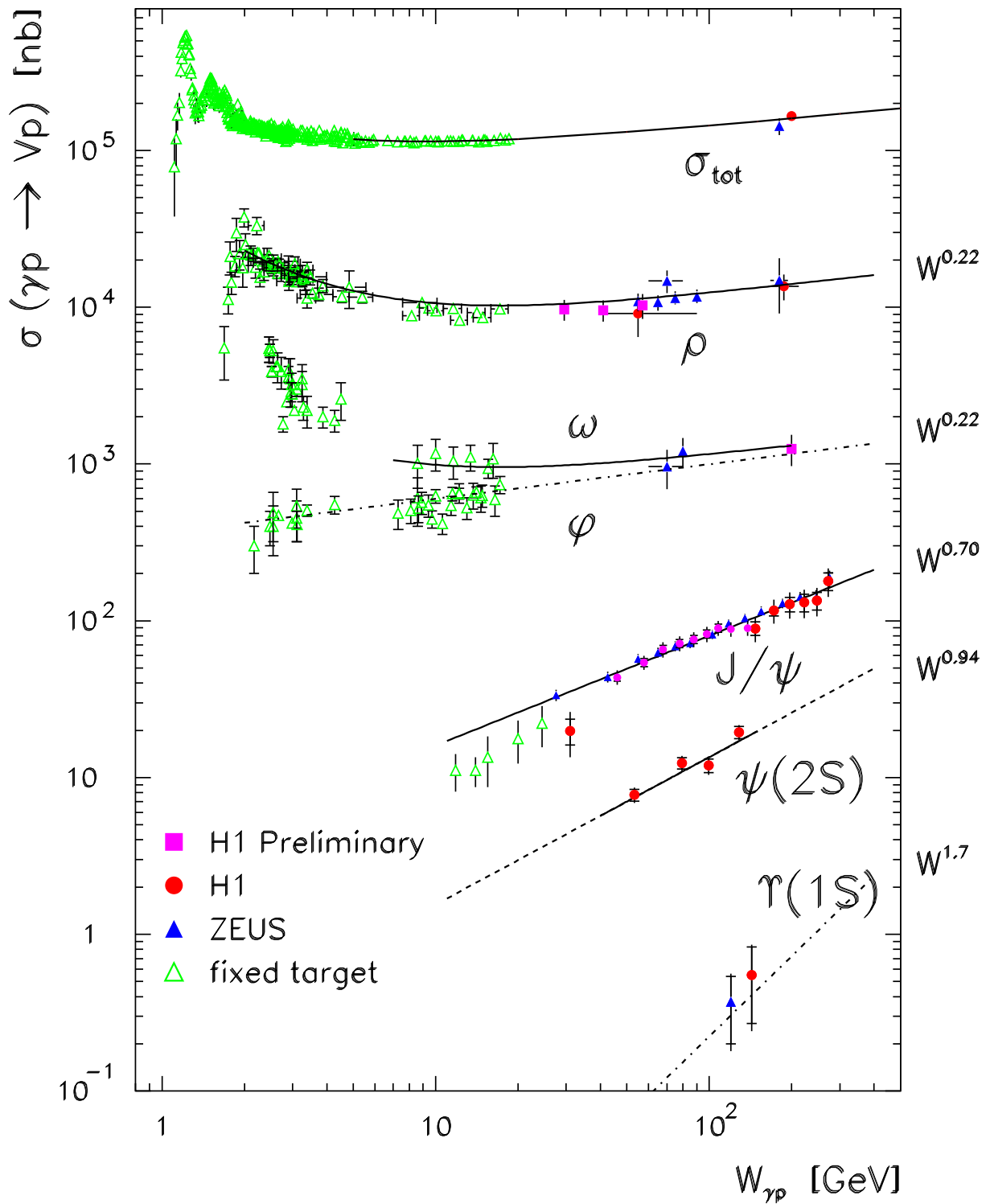
Fig. 5.24: Total cross-section and cross-sections for production of various vector mesons in γp collisions as a function of $W_{\gamma p}$, as measured at HERA and in fixed-target experiments.

and inelastic regions, with a typical demarcation for J/ψ production being $z > 0.95$ for the diffractive region and $z < 0.95$ for the inelastic region. However, at large z, there is actually no clear distinction between inelastic J/ψ production and diffractive J/ψ production in which the proton dissociates into a final state with large invariant mass, owing to the fact that the two processes can produce the same final-state particles. In the region of large z, both inelastic and diffractive processes are expected to contribute to the cross-section. In calculations that are based on the NRQCD factorization approach, the cross-section increases toward large z, owing to large contributions from colour-octet $c\bar{c}$ pairs, as is explained in Section 4.1. These contributions are, however, substantially reduced when one takes into account multiple soft gluon emission, e.g., in resummation calculations [12]. At the same time, calculations in perturbative QCD that assume a diffractive colour-singlet exchange are capable of describing the production cross-sections at large z [204, 211, 212]. A unified description in QCD of the large z region, taking into account both inelastic and diffractive contributions, has yet to be developed.

4.4 Prospects for the upgraded HERA collider

With the HERA luminosity upgrade, a wealth of new quarkonium data will become available. The existing J/ψ and $\psi(2S)$ measurements can be improved and extended into new kinematic regions, and other quarkonium final states may become accessible. The future analyses of quarkonium production at HERA offer unique possibilities to test the theoretical framework of NRQCD factorization. It should be noted here that calculations to next-to-leading order, which are not yet available in the framework of NRQCD factorization, could be an essential ingredient in a full quantitative understanding of charmonium production at HERA, and also at other experiments, such as those at the Tevatron. Some of the most interesting reactions will be discussed briefly below. See Refs. [64, 233] for more details.

The measurement of inelastic χ_c *photoproduction* is a particularly powerful way to discriminate between NRQCD and the colour-evaporation model. The assumption of a single, universal long-distance factor in the colour-evaporation model implies a universal $\sigma[\chi_c]/\sigma[J/\psi]$ ratio. A large χ_c cross-section is predicted for photon–proton collisions. The ratio of χ_c production to J/ψ production is expected to be similar to that at hadron colliders, for which $\sigma[\chi_c]/\sigma[J/\psi] \approx 0.5$ [62]. In NRQCD, on the other hand, the $\sigma[\chi_c]/\sigma[J/\psi]$ ratio is process-dependent and strongly suppressed in photoproduction. Up to corrections of $\mathcal{O}(\alpha_s, v^2)$ one finds that [64]

$$\frac{\sigma[\gamma p \to \chi_{cJ} X]}{\sigma[\gamma p \to J/\psi X]} \approx \frac{15}{8} (2J + 1) \frac{\langle \mathcal{O}_8^{\chi_{c0}}(^3S_1) \rangle}{\langle \mathcal{O}_1^{J/\psi}(^3S_1) \rangle} \approx (2J + 1) \, 0.005, \tag{5.25}$$

where the last approximation makes use of the NRQCD matrix elements that are listed in Table 5.1. A search for χ_c production at HERA that results in a cross-section measurement or an upper limit on the cross-section would probe directly the colour-octet matrix element $\langle \mathcal{O}_8^{\chi_J}(^3S_1) \rangle$ and would test the assumption of a single, universal long-distance factor that is implicit in the colour-evaporation model.

The inclusion of colour-octet processes is crucial in describing the photoproduction of the *spin-singlet states* $\eta_c(1S)$, $\eta_c(2S)$, and $h_c(1P)$. With regard to the P-wave state h_c, the colour-octet contribution is required to cancel the infrared divergence that is present in the colour-singlet cross-section [234]. The production of the η_c, on the other hand, is dominated by colour-octet processes, since the colour-singlet cross-section vanishes at leading-order, owing to charge-conjugation invariance [235, 236], as is the case for χ_c photoproduction. The cross-sections for $\eta_c(1S)$, $\eta_c(2S)$, and $h_c(1P)$ photoproduction are sizable [234, 235], but it is not obvious that these particles can be detected experimentally, even with high-statistics data.

The energy spectrum of J/ψ's *produced in association with a photon* via the process $\gamma p \to J/\psi + \gamma X$ is a distinctive probe of colour-octet processes [233, 237–239]. In the colour-singlet channel and at leading-order in α_s, $J/\psi + \gamma$ can be produced only through resolved-photon interactions. The corresponding energy distribution is therefore peaked at low values of z. The intermediate-z and large-z regions of the energy spectrum are expected to be dominated by the colour-octet process $\gamma g \to c\bar{c}_8(^3S_1)\, \gamma$.
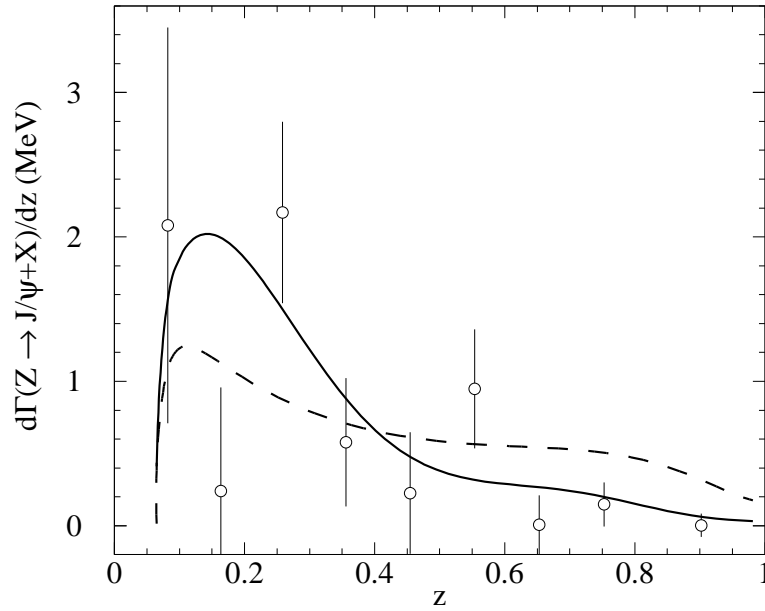
Fig. 5.25: Differential rate $d\Gamma/dz$ for inclusive decay of Z^0 into J/ψ. The data is from the ALEPH collaboration [240]. The dashed line is the sum of the tree-level colour-singlet and colour-octet terms. The solid line is an interpolation between resummed calculations in the small-z and large-z regions. From Ref. [244].

Observation of a substantial fraction of $J/\psi + \gamma$ events at $z \gtrsim 0.5$ would provide clear evidence for the presence of colour-octet processes in quarkonium photoproduction. Experimentally, this measurement is very difficult due to the large background from photons from π^0 decays which are produced in the final state.

With the significant increase in statistics at the upgraded HERA collider, it might be possible to study *inelastic photoproduction of bottomonium states* for the first time. The large value of the b-quark mass makes the perturbative QCD predictions more reliable than for charm production, and the application of NRQCD should be on safer ground for the bottomonium system, in which $v^2 \approx 0.1$. However, the production rates for Υ states are suppressed compared with those for J/ψ by more than two orders of magnitude at HERA — a consequence of the smaller b-quark electric charge and the phase-space reduction that follows from the larger b-quark mass.

5   QUARKONIUM PRODUCTION AT LEP

5.1 J/ψ production

The LEP collider was used to study e^+e^- collisions at the Z^0 resonance. Charmonium was produced at LEP through direct production in Z^0 decay, through the decays of b hadrons from Z^0 decay, and through $\gamma\gamma$ collisions. The contributions from the decays of b hadrons can be separated from those from direct production by using a vertex detector. Charmonium that is produced directly will be referred to as "prompt."

In Z^0 decay, the dominant mechanism for charmonium production is the decay of the Z^0 into $b\bar{b}$, followed by the fragmentation of the b or $\bar{b}$ into a heavy hadron and the subsequent decay of the heavy hadron into charmonium. The inclusive branching fraction of the Z^0 into a charmonium state H is to a good approximation the product of the branching fraction for $Z^0 \to b\bar{b}$, a weighted average of the inclusive branching fractions of b hadrons into H, and a factor of two to account for the b and the $\bar{b}$:

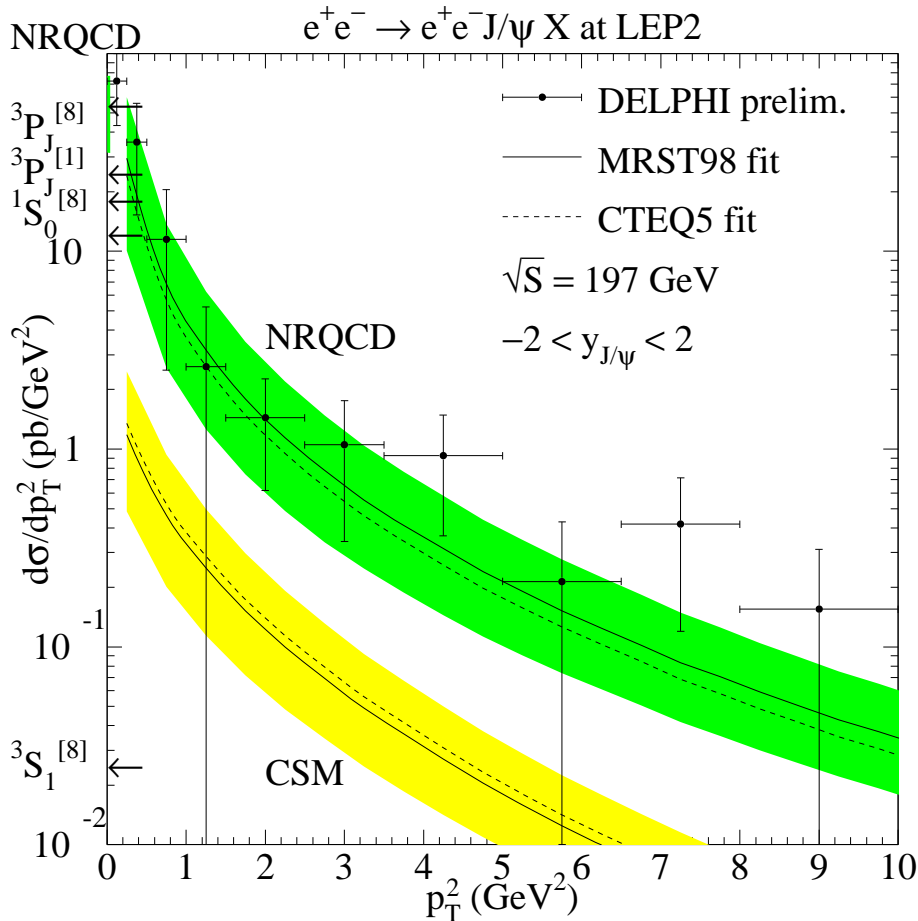$$\text{Br}[Z^0 \to HX] \approx 2\,\text{Br}[Z^0 \to b\bar{b}] \sum_B D_{b \to B}\,\text{Br}[B \to HX]. \tag{5.26}$$

Fig. 5.26: Differential cross-section for the process $\gamma\gamma \to J/\psi + X$ as a function of p_T^2. The data points are from the DELPHI Collaboration [245, 246]. The upper set of curves is the NRQCD factorization predictions, and the lower set of curves is the colour-singlet model prediction. The solid and dashed curves correspond to the MRST98LO [79] and CTEQ5L [69] parton distributions, respectively. The arrows indicate the relative contributions at $p_T = 0$ from parton processes $ij \to c\bar{c}$, which were ignored in the analysis. Here $ij = \gamma\gamma$, gg, or $q\bar{q}$. From Ref. [251].

The branching fraction for the b hadron B to decay into a state that includes H is weighted by the probability $D_{b \to B}$ for a 45 GeV b quark to fragment into B. The inclusive branching fractions for Z^0 decay into several charmonium states have been measured. Since these measurements have more to do with b-hadron decay than Z^0 decay, they are presented in Section 7.

The ALEPH, DELPHI, L3, and OPAL collaborations at LEP have measured the inclusive branching fraction of Z^0 into prompt J/ψ [240–243]. In the NRQCD factorization approach, there are two mechanisms that dominate direct J/ψ production. The first is Z^0 decay into $c\bar{c}$, followed by the fragmentation of the c or $\bar{c}$ into J/ψ via the colour-singlet channel $c\bar{c}_1(^3S_1)$. The second is Z^0 decay into $q\bar{q}gg$, followed by the fragmentation of the gluon into J/ψ via the colour-octet channel $c\bar{c}_8(^3S_1)$. Boyd, Leibovich, and Rothstein [244] have used the results from the four LEP collaborations to extract the colour-octet matrix element: $\langle \mathcal{O}_8^{J/\psi}(^3S_1) \rangle = (1.9 \pm 0.5_{stat} \pm 1.0_{theory}) \times 10^{-2}$ GeV^3. This is about a factor of two larger than the Tevatron value and has smaller theory errors, but feeddown from χ_c and $\psi(2S)$ states was not taken into account in the theoretical analysis. Boyd, Leibovich, and Rothstein [244] also carried out a resummation of the logarithms of M_Z^2/M_ψ^2 and z^2, where $z = 2E_{c\bar{c}}/m_Z$. Their result for the resummed z distribution for prompt J/ψ production is compared with data from the ALEPH

collaboration [240] in Fig. 5.25. Their analysis predicts an enhancement in the production rate near $z = 0.15$. The uncertainties in the data are too large to make a definitive statement about the presence or absence of this feature.

The inclusive cross-section for $\gamma\gamma \rightarrow J/\psi + X$ at LEP has been measured by the DELPHI Collaboration [245, 246]. The cross-section at nonzero p_T has been computed at leading order in α_s. The computation includes the direct-photon process $\gamma\gamma \rightarrow (c\bar{c}) + g$, which is of order $\alpha^2\alpha_s$, the single-resolved-photon process $i\gamma \rightarrow (c\bar{c}) + i$, which is of order $\alpha\alpha_s^2$, and the double-resolved-photon process $ij \rightarrow (c\bar{c}) + k$, which is of order α_s^3 [247–251]. (Here, $ij = gg$, gq, $g\bar{q}$, or $q\bar{q}$.) Note that all processes contribute formally at the same order in perturbation theory since the leading behavior of the parton distributions in the photon is $\propto \alpha/\alpha_s$. The contribution to the $\gamma\gamma \rightarrow J/\psi + X$ cross-section at LEP that is by far dominant numerically is that from single-resolved processes, i.e., photon–gluon fusion.

The results of the LO computation [251] are shown in Fig. 5.26. The computation uses the NRQCD matrix elements of Ref. [78]. Theoretical uncertainties were estimated by varying the renormalization and factorization scales by a factor two and by incorporating the effects of uncertainties in the values of the colour-octet matrix elements. As can be seen from Fig. 5.26, the comparison with the DELPHI data [245, 246] clearly favors the NRQCD factorization approach over the colour-singlet model. However, the comparison of Fig. 5.26 is based on a leading-order calculation. It is known from the related process of J/ψ photoproduction at HERA, which is also dominated by photon–gluon fusion, that the LO colour-singlet cross-section fails to describe the J/ψ data at nonzero p_T. Inclusion of the NLO correction, however, brings the colour-singlet prediction in line with experiment. Similarly large NLO corrections can be expected for $\gamma\gamma \rightarrow J/\psi + X$ production at LEP, and a complete NLO analysis is needed before firm conclusions on the importance of colour-octet contributions can be drawn. A first step in this direction has been taken recently in Ref. [252], where the NLO corrections to the direct process $\gamma\gamma \rightarrow (c\bar{c}) + g$ have been calculated.

5.2 $\Upsilon(1S)$ production

The OPAL collaboration has measured the inclusive branching fraction for the decay of Z^0 into $\Upsilon(1S)$ [253]. The NRQCD factorization prediction for $\mathrm{Br}[Z^0 \rightarrow \Upsilon(1S) + X]$ is 5.9×10^{-5} [254]. The colour-singlet-model prediction is 1.7×10^{-5} [254–259]. The experimental result from OPAL [253] is $[1.0\pm0.4(\mathrm{stat.})\pm0.1(\mathrm{sys.})\pm0.2(\mathrm{prod.\ mech.})]\times10^{-4}$. This is compatible with the NRQCD factorization prediction, but not with the colour-singlet-model prediction.

6 CHARMONIUM PRODUCTION IN e^+e^- ANNIHILATIONS AT 10.6 GeV

The B factories have proved to be a rich source of data on charmonium production in e^+e^- annihilation. The B factories operate near the peak of the $\Upsilon(4S)$ in order to maximize the production rate for B mesons, but about 75% of the events are continuum e^+e^- annihilation events. The enormous data samples that have been accumulated compensate for the relatively small cross-sections for e^+e^- annihilation into states that include charmonium.

6.1 J/ψ production

The Belle and BaBar Collaborations have measured the inclusive cross-section $\sigma[e^+e^- \rightarrow J/\psi X]$. The Belle Collaboration obtains $2.52 \pm 0.21 \pm 0.21$ pb [260], while the BaBar Collaboration obtains $1.47 \pm 0.10 \pm 0.13$ pb [261]. The leading-order parton process in the colour-singlet model is $e^+e^- \rightarrow (c\bar{c}) + gg$, which is of order $\alpha^2\alpha_s^2$. The leading colour-octet contributions in the NRQCD factorization approach come from e^+e^- annihilation into $(c\bar{c}) + g$, which is order $\alpha^2\alpha_s$, and into $(c\bar{c}) + q\bar{q}$ and $(c\bar{c}) + gg$, which are order $\alpha^2\alpha_s^2$. The prediction for the cross-section $\sigma[e^+e^- \rightarrow J/\psi X]$ in the colour-singlet model is $0.45 - 0.81$ pb [262–265], while the NRQCD factorization prediction is $1.1 - 1.6$ pb [263–265]. There is a 3σ discrepancy between the experiments, but the NRQCD factorization prediction seems to be favored.
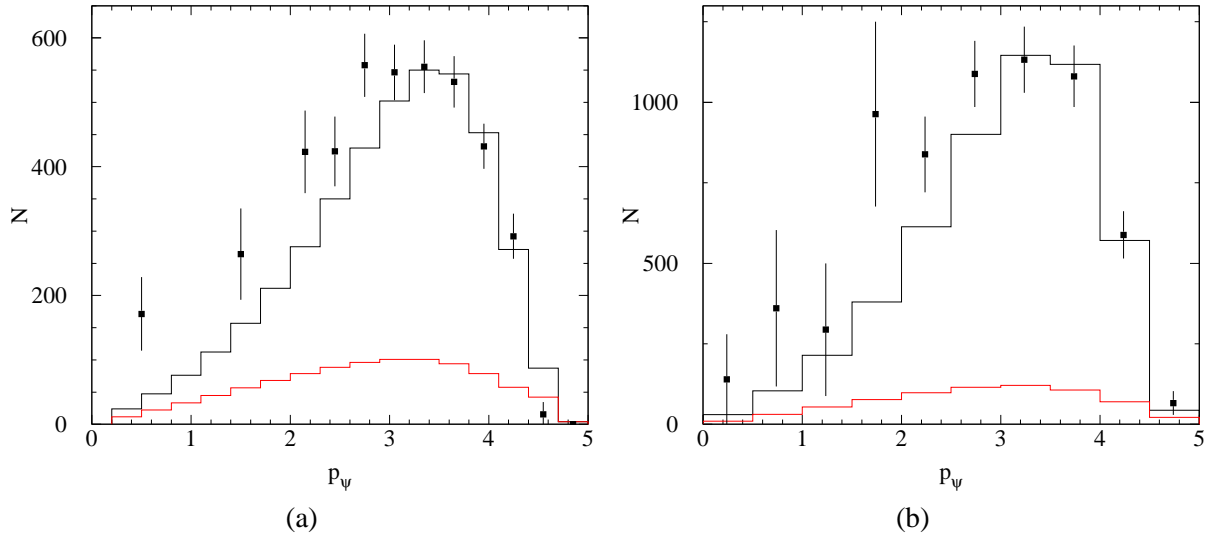
Fig. 5.27: J/ψ production rate in e^+e^- annihilation at 10.6 GeV as a function of $p^* = p_\psi$, the J/ψ momentum in the CM frame. The vertical axis is the number of J/ψ events per 0.5 GeV/c. The data points are from (a) the Belle Collaboration [260] and (b) the BaBar Collaboration [261]. The upper lines are the sum of the leading-order colour-singlet contribution and the colour-octet contribution, which includes a resummation of logarithms of $1 - z$ and a phenomenological shape function. The lower lines are the leading-order colour-singlet contribution alone. From Ref. [11].

The discrepancies between the two experiments in this and other measurements may be due partly to differences in cuts that were used to suppress contributions from processes in which the charmonium is not produced by annihilation of e^+ and e^- with a centre-of-mass energy of 10.6 GeV. These include radiative-return processes, in which the e^+ or e^- loses a substantial fraction of its momentum by radiating a collinear photon before the collision, virtual photon radiation, in which the e^+ or e^- radiates a virtual photon that becomes a J/ψ or $\psi(2S)$, and two-photon collisions, which produce η_c, χ_{c0}, and χ_{c2}.

The momentum distribution of the J/ψ provides information about the production mechanism. The momentum of the J/ψ in the CM frame can be characterized in terms of its magnitude p^* and its angle θ^* with respect to the beam direction. The Belle [260] and BaBar [261] measurements for the differential cross-section for J/ψ production as a function of p^* are shown in Fig. 5.27. The colour-singlet prediction, which is shown in the lower curves in Fig. 5.27, is far too small to describe the data. The measurements from Belle and BaBar do not show any enhancement at the maximum value of p^*, as might be expected from the colour-octet process $e^+e^- \to (c\bar{c}) + g$ that is of leading order in α_s. However, there are two effects that are expected to modify the leading-order result. The first effect is that the v expansion of NRQCD breaks down near the kinematic maximum value of p^*. Resummation of the expansion is required [10, 12], and it leads to a nonperturbative shape function [10], which smears out the peak in the leading-order result. A second effect near the maximum value of p^* is that there are large logarithms of $1 - z$, where $z = E_{c\bar{c}}/E_{c\bar{c}}^{\max}$, that must also be resummed. The effect of that resummation is again to smear out the peak in the leading-order result. A resummation of logarithms of $1 - z$ has been combined with a phenomenological shape function in Ref. [11]. The results of this calculation are shown in the upper curves in Fig. 5.27. The shape function has been chosen to fit the Belle and BaBar data. The normalization of the shape function is fixed by the colour-octet NRQCD matrix elements, which were taken to be $\langle \mathcal{O}_8^{J/\psi}({}^1S_0) \rangle = \langle \mathcal{O}_8^{J/\psi}({}^3P_0) \rangle = 6.6 \times 10^{-2}$ GeV. These values of the colour-octet matrix elements are consistent with data from photoproduction and hadroproduction [129, 169]. As can be seen, the resummations of the v expansion and the logarithms of $1 - z$ produce reasonable fits to the data. The resummation prediction is not expected to be valid at small values of p^*. It should also be kept in

mind that hard-scattering factorization may not hold unless $p^* \gg \Lambda_{\mathrm{QCD}}$. While the comparison of the resummed theory with experiment indicates that it is plausible that the NRQCD factorization approach can describe the experimental data, the theoretical results rely heavily on the phenomenological shape function, whose shape is tuned to fit the data. The resummed theory will receive a much more stringent test when a phenomenological shape function that has been extracted from the e^+e^- data is used to predict the J/ψ production cross-section in some other process, for example, photoproduction at HERA.

Table 5.10: Angular asymmetry variable A and polarization variable α for various ranges of the CM momentum p^* of the J/ψ in $e^+e^- \rightarrow J/\psi X$ at $\sqrt{s} = 10.6$ GeV, as measured by the Belle [260] and BaBar [261] Collaborations.

Belle			BaBar		
Range of p^* (GeV)	A	α	Range of p^* (GeV)	A	α
$2.0 < p^* < 2.6$	$0.82^{+0.95}_{-0.63}$	$-0.62^{+0.30}_{-0.24}$	$p^* < 3.5$	0.05 ± 0.22	-0.46 ± 0.21
$2.6 < p^* < 3.4$	$1.44^{+0.42}_{-0.38}$	$-0.34^{+0.18}_{-0.16}$			
$3.4 < p^* < 5.0$	$1.08^{+0.44}_{-0.33}$	$-0.32^{+0.20}_{-0.18}$	$3.5 < p^*$	1.5 ± 0.6	-0.80 ± 0.09

The other variable that characterizes the momentum of the J/ψ is its angle θ^* with respect to the beam direction in the CM frame. The angular distribution $d\sigma/d(\cos\theta^*)$ is proportional to $1 + A\cos^2\theta^*$, which defines an angular asymmetry variable A. The Belle [260] and BaBar [261] Collaborations have measured A in several bins of p^*. Their results are shown in Table 5.10. The NRQCD factorization approach predicts that $A \approx 0$ at small p^* and $0.6 < A < 1.0$ at large p^* [266] . The colour-singlet model predicts that $A \approx 0$ at small p_T and $A \approx -0.8$ at large p^* [266]. The Belle and BaBar results favor the NRQCD factorization prediction, but the uncertainties are large.

The polarization of the J/ψ provides further information about the production mechanism. The polarization variable α for J/ψ production is defined by the angular distribution in Eq. (5.13). In e^+e^- annihilation, the most convenient choice for the polarization axis is the boost vector from the quarkonium rest frame to the e^+e^- centre-of-momentum frame. The Belle and BaBar Collaborations have measured the polarization variable α in several bins of p^*. Their results are shown in Table 5.10. The polarization of J/ψ's from e^+e^- annihilation at the B factories has not yet been calculated within the NRQCD factorization approach. In contrast to the production of J/ψ's with large p_T at the Tevatron, where the dominance of gluon fragmentation into colour-octet $^3S_1$ $c\bar{c}$ states implies a large transverse polarization, production of J/ψ's at the B factories occurs at values of p^* for which there are no simple qualitative expectations for the polarization. A comparison between theory and experiment must await an actual calculation of the J/ψ polarization, including the effects of feeddown from higher charmonium states. It may be necessary to include in such a calculation resummations of the v expansion and logarithms of $1 - z$ in order to make precise quantitative statements. However, the effects of these resummations is mainly to re-distribute the J/ψ's that are produced via the colour-octet mechanism over a range in p^* without affecting the total number of such J/ψ's.

A surprising result from the Belle Collaboration is that most of the J/ψ's that are produced in e^+e^- annihilation at 10.6 GeV are accompanied by charmed hadrons. The presence of a charmed hadron indicates the creation of a second $c\bar{c}$ pair in addition to the pair that forms the J/ψ. A convenient measure of the probability for creating the second $c\bar{c}$ pair is the ratio

$$R_{\mathrm{double}} = \frac{\sigma[e^+e^- \rightarrow J/\psi + X_{c\bar{c}}]}{\sigma[e^+e^- \rightarrow J/\psi + X]} \ . \tag{5.27}$$

The Belle Collaboration finds that $R_{\mathrm{double}} = 0.82 \pm 0.15 \pm 0.14$ with $R_{\mathrm{double}} > 0.48$ at the 90% confidence level [267]. The NRQCD factorization approach leads to the prediction $R_{\mathrm{double}} \approx 0.1$ [262, 263,268], which disagrees with the Belle result by almost an order of magnitude. The discrepancy seems
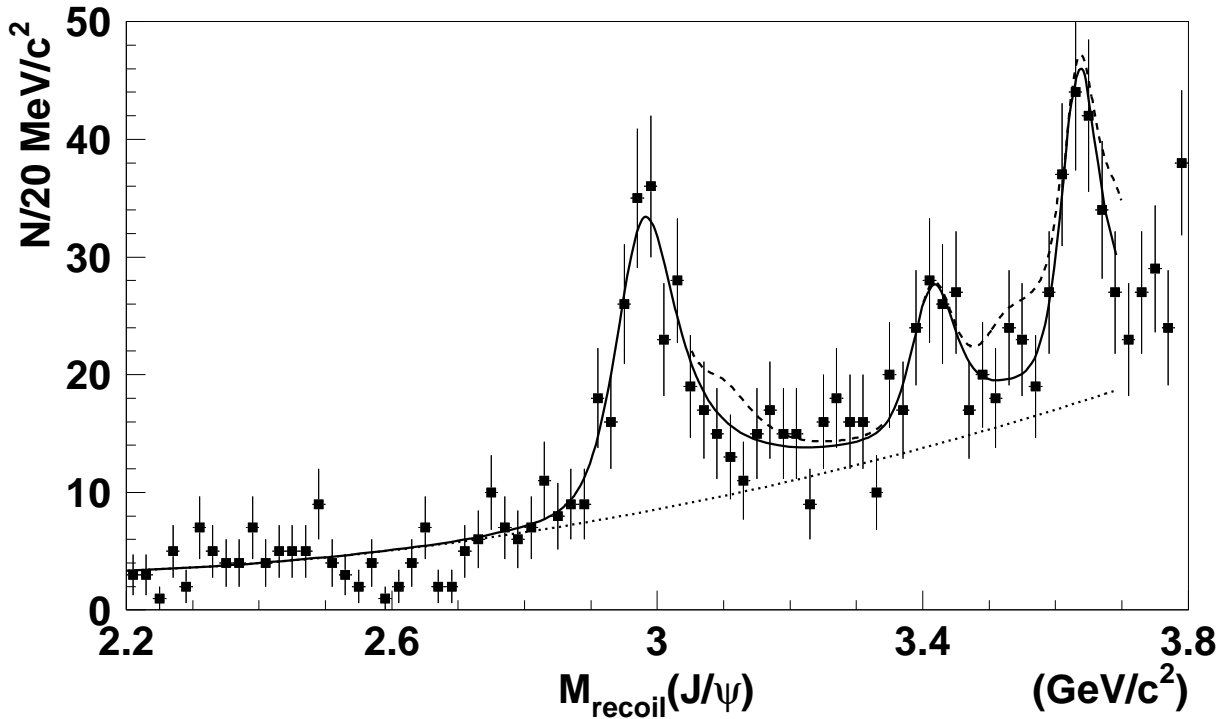
Fig. 5.28: Distribution of masses recoiling against the reconstructed J/ψ in inclusive $e^+e^- \to J/\psi X$ events at Belle [271]. The solid line is the best fit, including contributions from the η_c, $\chi_{c0}(1P)$, and $\eta_c(2S)$. The dotted line is a fit in which additional contributions from the J/ψ, $\chi_{c1}(1P)$, $\chi_{c2}(1P)$, and $\psi(2S)$ have been set at their largest possible values within the 90%-confidence-level limits.

to arise primarily from the cross-section in the numerator of (5.27). The Belle result for this cross-section is about 0.6–1.1 pb [269], while the prediction is about 0.10–0.15 pb [262, 263, 268, 270]. At leading order in α_s, which is α_s^2, the process of e^+e^- annihilation into $J/\psi + X_{c\bar{c}}$ proceeds through $(c\bar{c}) + c\bar{c}$. The contributions to this cross-section in which the J/ψ is formed from a colour-octet $c\bar{c}$ pair are suppressed by a factor $v^4 \approx 0.1$, and they have been found to yield only about 7% of the total cross-section [270]. Corrections of order α_s^3 and higher are also not expected to be particularly large. Thus, the source of the discrepancy between the Belle result for R_{double} and theory remains a mystery.

There is also a large discrepancy between theory and experiment in an exclusive double-$c\bar{c}$ cross-section. For the double-charmonium process $e^+e^- \to J/\psi + \eta_c$, the Belle Collaboration measures the product of the cross-section and the branching fraction for the η_c to decay into at least two charged tracks to be $25.6 \pm 2.8 \pm 3.4$ fb [271]. In contrast, leading-order calculations predict a cross-section of 2.31 ± 1.09 fb [272–274]. There are some uncertainties from uncalculated corrections of higher-order in α_s and v and from NRQCD matrix elements. However, because this is an exclusive process, only colour-singlet matrix elements enter, and these are fairly well determined from the decays $J/\psi \to e^+e^-$ and $\eta_c \to \gamma\gamma$.

Since the Belle mass resolution is 110 MeV but the J/ψ–η_c mass difference is only 120 MeV, it has been suggested that some of the $J/\psi + \eta_c$ data sample may consist of $J/\psi + J/\psi$ events [275, 276]. The state $J/\psi + J/\psi$ has charge-parity $C = +1$, and consequently, is produced in a two-photon process, whose rate is suppressed by a factor $(\alpha/\alpha_s)^2$ relative to the rate for $J/\psi + \eta_c$. However, as was pointed out in Refs. [275, 276], the two-photon process contains photon-fragmentation contributions that are enhanced by factors $(E_{\text{beam}}/2m_c)^4$ from photon propagators and $\log[8(E_{\text{beam}}/2m_c)^4]$ from a would-be collinear divergence. As a result, the predicted cross-section $\sigma[e^+e^- \to J/\psi + J/\psi] = 8.70 \pm 2.94$ fb is

larger than the predicted cross-section $\sigma[e^+e^-\rightarrow J/\psi + \eta_c] = 2.31 \pm 1.09$ fb [275, 276]. Corrections of higher order in α_s and v are likely to reduce the prediction for the $J/\psi + J/\psi$ cross-section by about a factor of three [276, 277]. These predictions spurred a re-analysis of the Belle data [278]. The invariant mass distribution of X in $e^+e^-\rightarrow J/\psi + X$ is shown in Fig. 5.28. No significant $J/\psi + J/\psi$ signal was observed. The upper limit on the cross-section times the branching fraction into at least two charged tracks [271] is $\sigma[e^+e^-\rightarrow J/\psi + J/\psi] < 9.1$ fb, which is consistent with the prediction of Refs. [275, 276].

6.2 Prospects at BaBar and Belle

The BaBar and Belle detectors are accumulating ever larger data samples of charmonium that is produced directly in e^+e^- annihilation. The simplicity of the initial state makes the theoretical analysis of this process particularly clean. These two factors make charmonium production in continuum e^+e^- annihilation a particularly attractive process in which to compare theoretical predictions with experiment. The experimental results that have already emerged from these detectors provide further motivation for understanding this process. There are significant discrepancies between previous measurements by BaBar and Belle. There are also surprising results from Belle on double $c\bar{c}$ production that differ dramatically from theoretical expectations. The resolution of these problems will inevitably lead to progress in our understanding of charmonium production.

The surprising double-$c\bar{c}$ results from Belle include an inclusive measurement, the ratio R_{double} defined in Eq. (5.27), and exclusive double-charmonium cross-sections, such as $\sigma[e^+e^-\rightarrow J/\psi + \eta_c]$. The discrepancies between theory and experiment in these measurements are among the largest in the standard model. Theory and experiment differ by about an order of magnitude — a discrepancy which is larger than any known QCD K-factor. It is important to recognize that these discrepancies are problems not just for NRQCD factorization, but for perturbative QCD in general. It is difficult to imagine how any perturbative calculation of R_{double} could give a value as large as 80%. With regard to the cross-section for $e^+e^-\rightarrow J/\psi + \eta_c$, the perturbative QCD formalism for exclusive processes [274] gives a result that reduces to that of NRQCD factorization [272, 273] in the nonrelativistic limit and is well-approximated by it if one uses realistic light-cone wave functions for J/ψ and η_c.[5] Clearly, it is very important to have independent checks of the Belle inclusive and exclusive double-$c\bar{c}$ results. If the Belle results are confirmed, then we would be forced to entertain some unorthodox possibilities: the inapplicability of perturbative QCD to double-$c\bar{c}$ production, new charmonium production mechanisms within the standard model, or perhaps even physics beyond the standard model.

The larger data samples that are now available should allow much more accurate measurements of the inclusive process $e^+e^-\rightarrow J/\psi X$, including the momentum distribution of the J/ψ and its polarization. The measurements of the J/ψ momentum distribution may allow the determination of all the relevant NRQCD matrix elements. A comparison with the NRQCD matrix elements measured at the Tevatron would then provide a test of their universality. Once the NRQCD matrix elements are determined, they can be used to predict the polarization of the J/ψ as a function of its momentum, which would provide a stringent test of the NRQCD predictions for spin. Instead of imposing cuts to suppress contributions from radiative return, virtual photon radiation, and two-photon collisions, it might be better to choose cuts in order to maximize the precision of the measurements, without any regard to the production mechanism. The contributions from other mechanisms could instead be taken into account in the theoretical analyses.

The large data samples of BaBar and Belle should also allow measurements of the inclusive production of other charmonium states, such as the $\psi(2S)$ and the $\chi_c(1P)$. Such measurements could be used to determine the NRQCD matrix elements for these charmonium states. They are also important because they provide constraints on the contributions to inclusive J/ψ production from decays of higher charmonium states.

---

[5]The Belle result can be accommodated by using asymptotic light-cone wave functions that are appropriate for light hadrons [279], but there is no justification for using such wave functions for charmonium.

There are some straightforward improvements that could be made in the theoretical predictions for inclusive charmonium production in e^+e^- annihilation. For example, there are only a few components missing from a complete calculation of all contributions through second order in α_s. In the contribution from the colour-octet $^3S_1$ channel, the virtual corrections at order α_s^2 have not been calculated. There are also colour-octet contributions to $e^+e^- \to c\bar{c}c\bar{c}$ at order α_s^2 that have not been calculated. The theoretical predictions for inclusive charmonium production could also be improved by treating more systematically the contributions from the feeddown from decays of higher charmonium states and from other mechanisms, such as radiative return, virtual photon radiation, and two-photon collisions.

7   CHARMONIUM PRODUCTION IN B-MESON DECAYS

B-meson decays are an excellent laboratory for studying charmonium production because B mesons decay into charmonium with branching fractions greater than a percent. At a B factory operating near the peak of the $\Upsilon(4S)$ resonance, about 25% of the events consist of a B^+B^- pair or a $B^0\bar{B}^0$ pair. The large sample of B mesons accumulated by the CLEO experiment allowed the measurements of many exclusive and inclusive branching fractions into final states that include charmonium. The Belle and BaBar experiments are accumulating even larger samples of B mesons, providing a new source of precise data on charmonium production in B decays.

The inclusive branching fractions of B mesons into charmonium states can be measured most accurately for the mixture of B^+, B^0, and their antiparticles that are produced in the decay of the $\Upsilon(4S)$ resonance [280, 281]. Those that have been measured are listed in Table 5.11. The fraction of J/ψ's that come from decay of χ_c's, which is defined in Eq. (5.12), is $F_{\chi_c} = (11 \pm 2)\%$. This is significantly smaller than the value that is measured at the Tevatron, which is given in Table 5.3. The χ_{c1} to χ_{c2} ratio, which is defined in Eq. (5.10), is $R_{\chi_c} = 5.1 \pm 3.0$. Although the error bar is large, this ratio seems to be substantially larger than the value that is measured at the Tevatron, which is given in Eq. (5.18), and the values measured in fixed-target experiments, which are given in Table 5.6. Such differences in R_{χ_c} and F_{χ_c} are contrary to the predictions of the colour-evaporation model.

Inclusive branching fractions into charmonium states have also been measured at LEP for the mixtures of B^+, B^0, B_s^0, b baryons, and their antiparticles that are produced in Z^0 decay [241, 282, 283]. This mixture of b hadrons can be interpreted as the one that arises from the fragmentation of a b quark that is produced with a momentum of 45 GeV. The branching fractions that have been measured are listed in Table 5.11. The branching fraction into $\chi_{c1}(1P)$ seems to be significantly larger than for the mixture from $\Upsilon(4S)$ decay. The difference could be due to the contribution from b baryons. It is often assumed that the mixture of b hadrons that is produced at high-energy hadron colliders, such as the Tevatron, is similar to that produced in Z^0 decay. This assumption could be tested by measuring ratios of inclusive cross-sections for charmonium states that come from the decays of b hadrons at the Tevatron.

Table 5.11: Inclusive branching fractions (in units of 10^{-3}) for mixtures of b hadrons to decay into charmonium states.

mixture	J/ψ	$\psi(2S)$	$\chi_{c1}(1P)$	$\chi_{c2}(1P)$
from $\Upsilon(4S)$ decay	11.5 ± 0.6	3.5 ± 0.5	3.6 ± 0.5	0.7 ± 0.4
from Z^0 decay	11.6 ± 1.0	4.8 ± 2.4	11.5 ± 4.0	

The observed inclusive branching fractions of B mesons into J/ψ and $\psi(2S)$ are larger than the predictions of the colour-singlet model by about a factor of three. Ko, Lee, and Song applied the NRQCD factorization approach to the production of J/ψ and $\psi(2S)$ in B decays [284]. The colour-octet $^3S_1$ term in the production rate is suppressed by a factor of v^4 that comes from the NRQCD matrix element. However, the production rate also involves Wilson coefficients that arise from evolving the effective weak

Hamiltonian from the scale M_W to the scale m_b. The Wilson coefficient for the colour-octet $^3S_1$ term is significantly larger than that for the colour-singlet term, although the smallness of the colour-singlet term may be the result of an accidental cancellation that occurs in the leading-order treatment of the evolution of the coefficients. Moreover, the colour-singlet contribution is decreased by the relativistic correction of order v^2. The inclusion of the colour-octet $^3S_1$ term allows one to explain the factor of three discrepancy between the data and the colour-singlet-model prediction.

The observed branching fraction for decays of B directly into J/ψ, which excludes the feeddown from decays of $\psi(2S)$ and χ_c, is much larger than the prediction of the colour-evaporation model. The CEM prediction for the direct branching fraction is $0.24 - 0.66$ [285], where the range comes from the uncertainty in the CEM parameters. The CLEO collaboration has made a precise measurement of the direct branching fraction of B into J/ψ [286]: $\mathrm{Br}_{\mathrm{dir}}[B{\rightarrow}J/\psi + X] = (0.813 \pm 0.041)\%$. The CEM prediction is significantly smaller than the data. As we have already mentioned, the data can be accommodated within the NRQCD factorization approach by including colour-octet terms.

Beneke, Maltoni, and Rothstein [287] have calculated the inclusive decay rates of B mesons into J/ψ and $\psi(2S)$ to next-to-leading order in α_s. They used their results to extract NRQCD matrix elements from the data. Their results for the linear combinations of NRQCD matrix elements defined in Eq. (5.8) are $M_{3.1}^{J/\psi} = (1.5_{-1.1}^{+0.8}) \times 10^{-2}$ GeV^3 and $M_{3.1}^{\psi(2S)} = (0.5 \pm 0.5) \times 10^{-2}$ GeV^3. The uncertainties arise from experiment and from imprecise of knowledge of the matrix elements $\langle \mathcal{O}_8^H(^3S_1) \rangle$ and $\langle \mathcal{O}_1^H(^3S_1) \rangle$. Ma, taking into account initial-state hadronic corrections, has extracted slightly different linear combinations of matrix elements [288]: $M_{3.4}^{J/\psi} = 2.4 \times 10^{-2}$ GeV^3 and $M_{3.4}^{\psi(2S)} = 1.0 \times 10^{-2}$ GeV^3. In both extractions, the colour-octet matrix elements are considerably smaller than those from the Tevatron fits, but the uncertainties are large.

The effects of colour-octet terms on the polarization of J/ψ in B decays were considered by Fleming, Hernandez, Maksymyk, and Nadeau [289] and by Ko, Lee, and Song [285]. The polarization variable α for J/ψ production is defined by the angular distribution in Eq. (5.13). In B meson decays, the most convenient choice of the polarization axis is the direction of the boost vector from the J/ψ rest frame to the rest frame of the B meson. The colour-evaporation model predicts no polarization. The predictions of NRQCD factorization and of the colour-singlet model depend on the mass of the b quark. For $m_b = 4.7 \pm 0.3$ GeV, the prediction of NRQCD factorization is $\alpha = -0.33 \pm 0.08$ [289] and the prediction of the colour-singlet model is $\alpha = -0.40 \pm 0.07$ [289]. The uncertainties that arise from m_b have been added in quadrature with other uncertainties. We note that the uncertainty in m_b that was used in this calculation is considerably larger than the uncertainty of 2.4% that is given in Chapter 6. Measurements of the polarization by the CLEO Collaboration have given the results $\alpha = -0.30 \pm 0.08$ for J/ψ and $\alpha = -0.45 \pm 0.30$ for $\psi(2S)$ [286]. The result for J/ψ strongly disfavors the colour-evaporation model and is consistent with the predictions of the NRQCD factorization approach and the colour-singlet model.

Bodwin, Braaten, Yuan, and Lepage have applied the NRQCD factorization approach to the production of the P-wave charmonium states χ_{cJ} in B decays [290]. For P-wave quarkonium production, there is a colour-octet NRQCD matrix element that is of the same order in v as the leading colour-singlet matrix element. Therefore, the factorization formula must include both the colour-singlet P-wave and the colour-octet S-wave contributions. The short-distance coefficient in the colour-singlet ^3P_J term for χ_{cJ} production vanishes at leading order in α_s for $J = 0, 2$ [18, 291]. The colour-octet $^3S_1$ term for χ_{cJ} production is proportional to the number of spin states $2J + 1$. Thus, the relative importance of the colour-singlet and colour-octet terms can vary dramatically among the three χ_{cJ} states. The prediction of the colour-singlet model at leading order in α_s that the direct production rate of χ_{c2} should vanish can be tested. The feeddown from $\psi(2S)$ decay contributes $(0.24 \pm 0.04) \times 10^{-3}$ to the inclusive branching fraction into χ_{c2} given in Table 5.11. The remainder $(0.5 \pm 0.4) \times 10^{-3}$ is consistent with zero, and hence it is compatible with the prediction of the colour-singlet model, but it is also compatible with a small colour-octet contribution.

8 B_c PRODUCTION

The B_c and B_c^* are the ground state and the first excited state of the $\bar{b}c$ quarkonium system. Their total angular momentum and parity quantum numbers are $J^P = 0^-$ and 1^+, and their dominant Fock states have the angular momentum quantum numbers $^1S_0$ and $^3S_1$, respectively. In the following discussion, we will refer to general $\bar{b}c$ quarkonium states as B_c mesons and use the terms B_c and B_c^* specifically for the ground state and the first excited state.

In contrast to charmonium and bottomonium states, which have "hidden flavour," B_c mesons contain two explicit flavours. As a consequence, the B_c decays only through the weak interactions, and the B_c^* decays through an electromagnetic transition into the B_c with almost 100% probability. The higher-mass B_c mesons below the BD threshold decay through hadronic and electromagnetic transitions into lower-mass B_c mesons with almost 100% probability. They cascade down through the $\bar{b}c$ spectrum, eventually producing a B_c or a B_c^*. Another consequence of the explicit flavours is that the most important production mechanisms for B_c mesons are completely different from those for hidden-flavour quarkonia. In the production of B_c mesons by strong or electromagnetic interactions, two additional heavy quarks $\bar{c}$ and b are always produced. The production cross-sections for B_c mesons are suppressed compared with the production cross-sections for hidden-flavour quarkonia because the leading-order diagrams are of higher order in the coupling constants and also because the phase-space is suppressed, owing to the presence of the additional heavy quarks.

The small cross-sections for producing B_c mesons make the prospects for observing the B_c at e^+e^- and ep colliders rather bleak. A possible exception to this assessment exists for the case of production at an e^+e^- collider with energy at the Z^0 peak, for which the production rate of the B_c is predicted to be marginal for observation [292]. The B_c was not discovered at LEP, despite careful searches [293–295]. It was finally discovered at the Tevatron by the CDF collaboration in 1998 [296, 297]. We restrict our attention in the remainder of this subsection to the production of B_c mesons at hadron colliders.

The production of B_c mesons was studied before the discovery of the B_c [292, 298–302, 307–309]. If one assumes that all nonperturbative effects in the production of the B_c in hadron–hadron collisions can be absorbed into the hadrons' parton distribution functions (PDF's), then the inclusive production cross-section can be written in the factorized form

$$d\sigma[h_A h_B \to B_c + X] \;\; = \;\; \sum_{ij} \int dx_1 dx_2 \; f_i^{h_A}(x_1, \mu) f_j^{h_B}(x_2, \mu) \; d\hat{\sigma}[ij \to B_c + X] \;. \quad (5.28)$$

The NRQCD factorization formula for the parton–parton cross-section is

$$d\hat{\sigma}[ij \to B_c + X] = \sum_n d\hat{\sigma}[ij \to (\bar{b}c)_n + X] \, \langle \mathcal{O}_n^{B_c} \rangle \;, \quad (5.29)$$

where the sum is over 4-fermion operators that create and annihilate $\bar{b}c$. At the leading order in α_s, which is α_s^4, the parton–parton process is $ij \to (\bar{b}c) + b\bar{c}$, where $ij = gg$ (gluon fusion) or $q\bar{q}$ (quark–antiquark annihilation). Since $m_{B_c} > m_b > m_c \gg \Lambda_{QCD}$, the leading-order parton–parton process involves only hard propagators, even at small p_T. Nevertheless, because of soft-gluon interactions, for example between the B_c and the recoiling b and $\bar{c}$ quarks, it is not clear that hard-scattering factorization holds at small p_T.

According to the velocity-scaling rules of NRQCD, the matrix element for B_c production that is of leading order in v is $\langle \mathcal{O}_1^{B_c}(^1S_0) \rangle$. The vacuum-saturation approximation can be used to show that it is proportional to $F_{B_c}^2$, where F_{B_c} is the decay constant of the B_c, up to corrections of order v^4. The leading matrix element for B_c^* production is $\langle \mathcal{O}_1^{B_c^*}(^3S_1) \rangle$. The vacuum-saturation approximation and heavy-quark spin symmetry can be used to show that this matrix element is also proportional to $F_{B_c}^2$, up to corrections of order v^3. The leading colour-octet matrix elements are suppressed as v^3 or v^4. The colour-octet terms in (5.29) are probably not as important for B_c mesons as they are for hidden-flavour

quarkonia. In the case of J/ψ production, the short-distance coefficients of the colour-octet matrix elements are enhanced relative to those for the colour-singlet matrix element by an inverse power of the QCD-coupling α_s, by factors of p_T/m_c at large p_T, by factors of m_c/p_T at small p_T, and by colour factors. The only one of these enhancement factors that may apply to the B_c is the colour factor. Because there are many Feynman diagrams that contribute to the parton process $ij\to(\bar{b}c) + b\bar{c}$ at order α_s^4, the colour correlations implied by individual Feynman diagrams tend to average out. We therefore expect a $\bar{b}c$ pair to be created in a colour-octet state roughly eight times as often as in a colour-singlet state. We will assume that, in spite of the enhancement from this colour factor, the colour-octet contributions to the production cross-sections for B_c and B_c^* are small compared with the leading colour-singlet contributions. This assumption is equivalent to using the colour-singlet model to calculate the production rate.

Two approaches have been used to compute the cross-sections for B_c mesons: the complete order-α_s^4 approach [299–302, 307, 308] and the fragmentation approach [298, 310]. In the complete order-α_s^4 approach, the parton cross-section in Eq. (5.29) is computed at leading order in α_s, where the only subprocesses are $ij\to(\bar{b}c) + b\bar{c}$:

$$d\hat{\sigma}[ij \to B_c + X] = d\hat{\sigma}[ij \to \bar{b}c_1(^1S_0) + b\bar{c}] \, \langle\mathcal{O}_1^{B_c}(^1S_0)\rangle \, . \tag{5.30}$$

The fragmentation approach is based on the fact that, for asymptotically large $p_T \gg M_{B_c}$, the cross-section (5.29) can be further factored into a cross-section for producing $\bar{b}$ and a fragmentation function $D_{\bar{b}\to B_c}(z,\mu)$ that gives the probability for the $\bar{b}$ to fragment into a B_c carrying a fraction z of the $\bar{b}$ momentum:

$$d\hat{\sigma}[ij \to B_c + X] \approx \int dz \, d\hat{\sigma}[ij \to \bar{b} + b] \, D_{\bar{b}\to B_c}(z,\mu) \, . \tag{5.31}$$

If both factors are calculated only at leading order in α_s, this is just an approximation to the complete order-α_s^4 cross-section in Eq. (5.29). One advantage of the fragmentation approach is that the expressions for the $\bar{b}$ production cross-section $d\hat{\sigma}$ and the fragmentation function $D_{\bar{b}\to B_c}$ in Eq. (5.31) can be written down in a few lines. For $p_T \gg m_{B_c}$, the fragmentation approach has another advantage in that the Altarelli–Parisi evolution equations can be used to sum the leading logarithms of p_T/m_c to all orders. Unfortunately, as was pointed out in Ref. [300–302], the fragmentation cross-section does not become an accurate approximation to the complete order-α_s^4 cross-section until surprisingly large values of p_T. For example, if the parton centre-of-mass energy is $\sqrt{\hat{s}} = 200$ GeV, the fragmentation cross-section is a good approximation only for $p_T \geq 40$ GeV. We will therefore not consider the fragmentation approach further.

The authors of Ref. [311] recently developed a Monte Carlo event generator for hadronic B_c and B_c^* production, using the complete order-α_s^4 approach and taking advantage of helicity amplitude techniques [312]. The generator is a Fortran package, and it is implemented in PYTHIA [313], which allows one to generate complete events. The complete order-α_s^4 cross-section includes contributions from gluon–gluon fusion and quark–antiquark annihilation. At the Tevatron, the gluon–gluon fusion mechanism is dominant over quark–antiquark annihilation, except in certain kinematics regions [299, 314]. At the LHC, the gluon–gluon fusion mechanism is always dominant. All the results below are obtained from the gluon–gluon fusion mechanism only.

The inputs that are required to calculate the complete order-α_s^4 cross-sections are the masses m_b, m_c, and m_{B_c}, the decay constant F_{B_c}, the PDF's, the QCD coupling constant α_s, and the factorization scale Q. The masses m_b and m_c are known with uncertainties of about 2.4% and 8%, respectively. In the NRQCD factorization approach, one sets $m_{B_c} = m_c + m_b$ and $m_{B_c^*} = m_c + m_b$ in the short-distance coefficients. Contributions from operators of higher order in v then account for the binding energy in m_{B_c} and $m_{B_c^*}$. This procedure is also required in order to preserve gauge invariance if one makes use of on-shell spin-projection operators for the B_c and B_c^* states [20, 315]. Since an experimental measurement of the decay constant F_{B_c} is not available, one has to use a value that is obtained from potential

Table 5.12: The cross-sections (in nb) for direct production of B_c and B_c^* at the Tevatron and at the LHC for various values of the charm-quark mass m_c. The gluon distribution function is CTEQ5L, the running of α_s is leading order, the scale is $\mu^2 = \hat{s}/4$, and the other parameters are $F_{B_c} = 480$ MeV, and $m_b = 4.9$ GeV.

	Tevatron ($\sqrt{s} = 2$ TeV)					LHC ($\sqrt{s} = 14$ TeV)				
m_c (GeV)	1.4	1.5	1.6	1.7	1.8	1.4	1.5	1.6	1.7	1.8
$\sigma[B_c]$ (nb)	3.87	3.12	2.56	2.12	1.76	61.0	49.8	41.4	34.7	28.9
$\sigma[B_c^*]$ (nb)	9.53	7.39	5.92	4.77	3.87	153.	121.	97.5	80.0	66.2

models [316–319] or from lattice gauge theory [320]. The uncertainty in the factor $F_{B_c}^2$ is about 6%. Since the order-α_s^4 cross-section is at leading order in perturbation theory, the running of α_s can be taken at leading order, and LO versions of the PDF's can be used.

The running coupling constant and the PDF's depend on the renormalization/factorization scale μ, and, so, a prescription for the scale μ is also required. There is no general rule for choosing the scale in an LO calculation, especially in the case of a 2→3 subprocess, such as $ij{\to}B_c + b\bar{c}$. The factorization formula (5.31) for asymptotically large p_T suggests that an appropriate choice for the scales in the fragmentation contribution to the cross-section might be to set $\mu = m_{bT} \equiv (m_b^2 + p_T^2)^{1/2}$ in the PDF's and $\alpha_s^4 = \alpha_s^2(m_{bT})\alpha_s^2(m_c)$ in the parton cross-section. However, the fragmentation term does not dominate until very large p_T, and there are important contributions to the cross-section that have nothing to do with fragmentation [300–302]. For example, there are contributions that involve the splitting of one of the colliding gluons into a $c\bar{c}$ pair, followed by the creation of a $b\bar{b}$ pair in the hard scattering of the c from the other gluon and then by the recombination of the $\bar{b}$ and c into a B_c. The sensitivity to the choice of μ could be decreased by carrying out a complete calculation of the production cross-section for the B_c at next-to-leading order in α_s, but this is, at present, prohibitively difficult. In the absence of such a calculation, we can use the variation in the complete order-α_s^4 cross-section for several reasonable choices for the scale as an estimate of the uncertainty that arises from the choice of scale.

The hadronic production cross-section for B_c mesons depends strongly on the collision energy. In Table 5.12, we give the direct cross-sections for B_c and B_c^* production at the Tevatron and the LHC for several values of the charm quark mass m_c and for typical values for the other parameters. The cross-section for B_c production at the LHC is larger than at the Tevatron by a factor of about 16. The cross-sections for B_c^* production are larger than those for B_c production by a factor of about 2.4. The cross-sections are fairly sensitive to the charm-quark mass, varying by more than a factor of two as m_c is varied from 1.4 to 1.8 GeV. In Fig. 5.29, we show the differential cross-sections for B_c production as a function of the B_c transverse momentum p_T and B_c rapidity y at the Tevatron and the LHC, using four different prescriptions for the scale μ. At central rapidity, the variations among the four choices of scale is about a factor of three at the Tevatron and a factor of two at the LHC. The differential cross-sections decrease more slowly with p_T and $|y|$ at the LHC than at the Tevatron. The total uncertainty from combining all of the uncertainties in the direct cross-section for B_c production is less than an order of magnitude. The uncertainty in the ratio of the direct-production cross-sections for the B_c^* and the B_c is much smaller because many of the uncertainties cancel in the ratio.

The results presented above are for the direct production of the B_c and the B_c^*. Experiments at the Tevatron and the LHC will measure the inclusive cross-sections, including the feeddown from all of the higher states of the $\bar{b}c$ system. The $\bar{b}c$ system has a rich spectrum of excited states below the BD threshold. They include an additional S-wave multiplet, one or two P-wave multiplets, and a D-wave multiplet. After being produced, these excited B_c mesons all cascade eventually down to the ground state B_c. Since the B_c^* decays into the B_c with a probability of almost 100%, the feeddown from directly-produced B_c^*'s increases the cross-section for the B_c by about a factor of 3.4. The complete
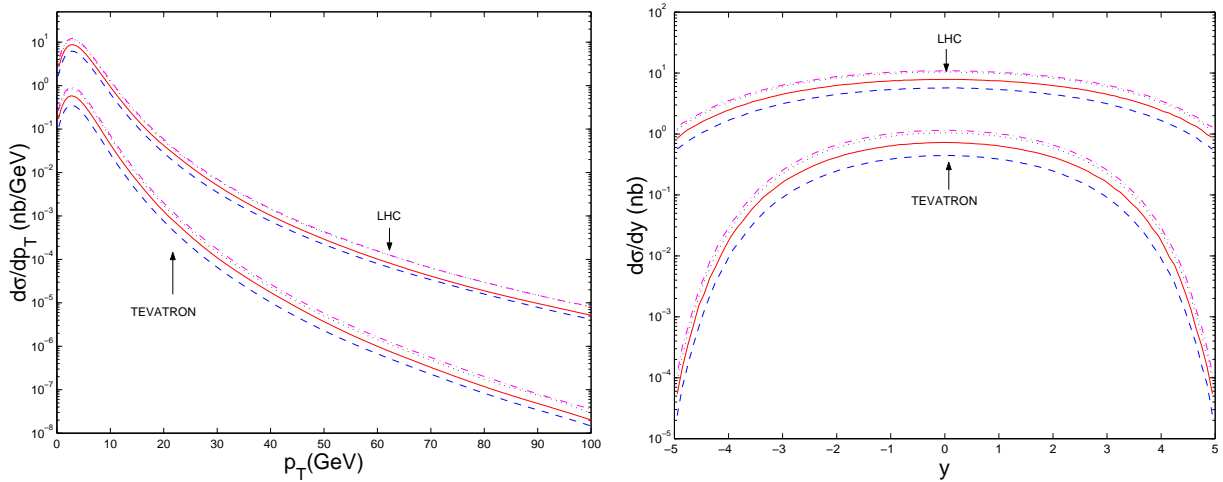
Fig. 5.29: The differential cross-sections for the direct production of the B_c as a function of its transverse momentum p_T and its rapidity y at the Tevatron ($\sqrt{s} = 2$ TeV) and at the LHC ($\sqrt{s} = 14$ TeV) for four choices of the scale: $\mu^2 = \hat{s}/4$ (solid line), $\mu^2 = p_T^2 + m_{B_c}^2$ (dotted line), $\mu^2 = \hat{s}$ (dashed line), and $\mu^2 = p_{Tb}^2 + m_b^2$ (dash–dot line). The gluon distribution is CTEQ5L, the running of α_s is leading order, and the other parameters are $F_{B_c} = 480$ MeV, $m_c = 1.5$ GeV, and $m_b = 4.9$ GeV.

order-α_s^4 cross-sections for B_c and B_c^* production can be applied equally well to the $2S$ multiplet. The direct-production cross-sections for these states are smaller than those for the $1S$ states by the ratio of the squares of the wave functions at the origin, which is about 0.6. Thus, the inclusive cross-section for B_c production, including the effect of feeddown from the direct production of all of the S-wave B_c states, is larger than the cross-section for direct B_c production, which is given in Table 5.12 and shown in Fig. 5.29, by a factor of about 5.4.

The production of B_c in $p\bar{p}$ collisons at $\sqrt{s} = 1.8$ TeV has been measured at the Tevatron by the CDF collaboration [296, 297]. CDF has measured the ratio

$$R[J/\psi l\nu] = \frac{\sigma[B_c]\mathrm{Br}[B_c^+ \to J/\psi l^+ \nu]}{\sigma[B^+]\mathrm{Br}[B^+ \to J/\psi K^+]} \tag{5.32}$$

for B_c^+ and B^+ with transverse momenta $p_T > 6.0$ GeV and with rapidities $|y| < 1.0$. Their result is $R[J/\psi l\nu] = 0.132^{+0.041}_{-0.037}(\text{stat.}) \pm 0.031(\text{syst.})^{+0.032}_{-0.020}(\text{lifetime})$. This result is consistent with results from previous searches [293–295]. Figure 5.30 compares the CDF measurements of $R[J/\psi l\nu]$ and the B_c lifetime with theoretical predictions from Refs. [303, 304] for two different values of the semileptonic width $\Gamma_{s.l.} = \Gamma[B_c \to J/\psi l\nu]$. The theoretical predictions use the values $|V_{cb}| = 0.041 \pm 0.005$ [305], $\sigma[B_c^+]/\sigma[\bar{b}] = 1.3 \times 10^{-3}$ [306], $\sigma[B^+]/\sigma[\bar{b}] = 0.378 \pm 0.022$ [305], and $\mathrm{Br}[B^+ \to J/\psi K^+] = (1.01 \pm 0.14) \times 10^{-3}$ [305]. The predictions and the measurement are consistent within experimental and theoretical uncertainties.

Quantitative predictions for the contribution to the inclusive B_c production cross-section from the feeddown from P-wave states would require complete knowledge of the order-α_s^4 cross-sections for the production of P-wave states. It is theoretically inconsistent to use the colour-singlet model to calculate these cross-sections for the P-wave states. There are colour-octet terms in the P-wave production cross-sections that are of the same order in both v and α_s as the colour-singlet terms, and they must be included. The colour-singlet production matrix elements for the P-wave states can be estimated from potential models or determined from lattice gauge theory. The colour-octet production matrix elements for the P-wave states can perhaps be estimated by interpolating between the corresponding matrix elements for charmonium and bottomonium states.
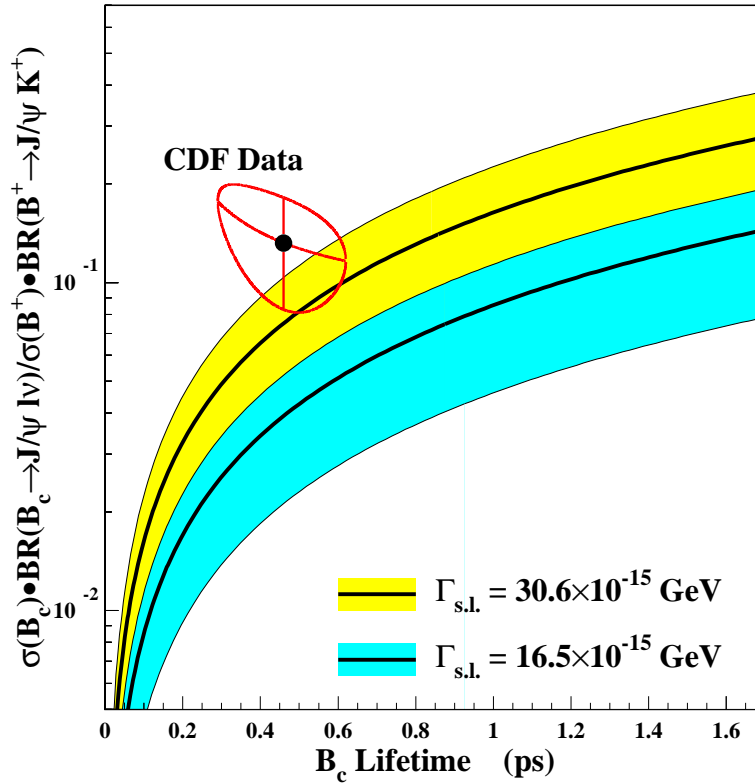
Fig. 5.30: The ratio $R[J/\psi l\nu]$, which is defined in Eq. (5.32), versus the B_c lifetime. The point, surrounded by a one-standard-deviation contour, shows the values of $R[J/\psi l\nu]$ and the B_c lifetime that were measured by CDF [296, 297]. The shaded region represents the theoretical predictions and their uncertainty bands from Refs. [303, 304] for two different values of the semileptonic width $\Gamma_{s.l.} = \Gamma[B_c \to J/\psi l\nu]$.

In summary, the order-α_s^4 colour-singlet production cross-section for S-wave $\bar{b}c$ mesons can be used to predict the B_c production cross-section, including feeddown from excited S-wave states. The uncertainty in the normalization of that prediction is less than an order of magnitude. If the inclusive cross-section for B_c production that is measured at the Tevatron or the LHC is much larger than that prediction, it could indicate that there is a large contribution from the feeddown from P-wave or higher-orbital-angular-momentum states. It could also indicate that the colour-octet contributions to the direct production of the B_c and the B_c^* are important.

9   SUMMARY AND OUTLOOK

NRQCD factorization, together with hard-scattering factorization, provides a systematic formalism for computing inclusive quarkonium production rates in QCD. Nonperturbative effects associated with the binding of a $Q\bar{Q}$ pair into a quarkonium are factored into NRQCD matrix elements that scale in a definite manner with the typical relative velocity v of the heavy quark in the quarkonium. The NRQCD matrix elements are predicted to be universal, i.e., independent of the process that creates the $Q\bar{Q}$ pair. The NRQCD factorization formula for inclusive cross-sections is believed to hold when $p_T \gg \Lambda_{QCD}$, where p_T is the transverse momentum of the quarkonium with respect to the colliding particles. It is well-motivated by the effective field theory NRQCD and by factorization theorems that have been proven for simpler hard-scattering processes. Explicit proofs of factorization for quarkonium production would be welcome, because they would help quantify the sizes of corrections to the factorization formula. It

is important to bear in mind that conventional proofs of hard-scattering factorization fail at small p_T. Consequently, NRQCD factorization formulas, even those that include soft-gluon resummation, may be unreliable in this region. It also follows that the NRQCD factorization approach may not be applicable to total cross-sections if they are dominated by contributions at small p_T.

The NRQCD factorization approach incorporates elements of both the colour-singlet model and the colour-evaporation model. It includes the colour-singlet model terms, for which the NRQCD matrix elements can be determined from annihilation decays. It also includes colour-octet production mechanisms, as in the colour-evaporation model. The NRQCD factorization approach extends these models into a systematically improvable framework. The colour-singlet model is emphatically ruled out by the observation of prompt J/ψ and $\psi(2S)$ production at the Tevatron at rates that are more than an order of magnitude larger than the colour-singlet-model predictions. The colour-evaporation model is ruled out by the observations of nonzero polarization of J/ψ's in B meson decays and in e^+e^- annihilation at 10.6 GeV and by the observation of nonzero polarization of $\Upsilon(2S)$'s and $\Upsilon(3S)$'s in fixed-target experiments. It is also ruled out by the fact that different values of the fraction of J/ψ's that come from χ_c decays are measured at the Tevatron and in B-meson decays. Despite having been ruled out, the colour-singlet model and the colour-evaporation model can still play useful roles as "straw men" with which to compare the predictions of NRQCD factorization. The colour-evaporation model has not yet been ruled out, for example, as a description of differential cross-sections at the Tevatron and in fixed-target experiments.

The NRQCD factorization approach provides a general phenomenological framework that cannot be ruled out easily. The factorization formula involves infinitely many NRQCD matrix elements, most of which are adjustable parameters. It is only the truncation in v that reduces those parameters to a finite set. The standard truncation has four independent NRQCD matrix elements for each S-wave multiplet and two independent NRQCD matrix elements for each P-wave multiplet. NRQCD factorization with the standard truncation in v remains a phenomenologically viable description of inclusive quarkonium production. As one tests NRQCD factorization at higher levels of precision, the standard truncation must ultimately fail. The NRQCD factorization approach itself may remain viable if one truncates at a higher order in v, but only at the cost of introducing many new adjustable parameters.

In the effort to make the predictions of the NRQCD factorization approach more quantitative, the most urgent need is to extend all calculations to next-to-leading order (NLO) in α_s. For hadron collisions at small p_T ($p_T \ll m$), the leading-order parton process is $ij \to Q\bar{Q}$. NLO calculations of that process are already available, but a resummation of multiple gluon emissions is required in order to tame large logarithms of m^2/p_T^2 and to turn the singular p_T distribution into a smooth distribution. For very large p_T ($p_T \gg m$), the production of quarkonium is dominated by gluon fragmentation. The leading-order fragmentation process is $g \to Q\bar{Q}_8(^3S_1)$, and the NLO calculation of the gluon fragmentation function into $Q\bar{Q}$ is available. What is still lacking is the NLO calculation at intermediate p_T, for which the leading-order parton process is $ij \to Q\bar{Q} + k$. By taking into account the NLO corrections in α_s, one should significantly decrease some of the uncertainties in the NRQCD factorization predictions.

One problematic source of uncertainties in the NRQCD factorization predictions is relativistic corrections. The first relativistic corrections of order v^2 in the channel that corresponds to the colour-singlet model have been calculated for many processes. In many cases, they have large coefficients that cast doubt on the validity of the expansion in powers of v for charmonium, and even for bottomonium. The success of lattice NRQCD in describing bottomonium spectroscopy ensures the applicability of the velocity expansion for this system in some form. It is possible that some reorganization or resummation of the velocity expansion might be necessary in order to make precise quantitative calculations of charmonium production.

The best individual experiments for determining the NRQCD production matrix elements for both charmonium and bottomonium are probably those at the Tevatron, because of the large range of p_T that is accessible. It will be important to take advantage of the measurements down to small p_T that were

achieved at the CDF detector for bottomonium in Run I and for charmonium in Run II. This will require taking into account the effects of multiple gluon emission in the theoretical analysis. Measurements of charmonium production in other experiments are also important because they provide tests of the universality of the production matrix elements. These experiments include those that measure charmonium production in ep collisions at HERA, in e^+e^- annihilation at the B factories, and in B meson decays at the B factories. One can use these experiments to extract values of the NRQCD matrix elements or, as has typically been the practice to date, one can use the matrix elements that have been extracted from the Tevatron data to make predictions for charmonium production in other experiments.

The ratios of the production cross-sections for different quarkonium states may also provide important tests of NRQCD factorization. (Here, particularly, one must keep in mind the *caveats* about the applicability of the NRQCD factorization approach to total cross-sections.) The uncertainties in the predictions for ratios of cross-sections are much smaller than those in the individual cross-sections because many of the uncertainties cancel in the ratio. The variations of the ratios from process to process and as functions of kinematic variables provide important information about the production mechanisms. The ratios of production rates of spin-triplet S-wave states, such as the $\psi(2S)$ to J/ψ ratio, do not seem to vary much. However, a significant variation has been observed in a ratio of the production rates of P-wave and S-wave states, namely the fraction of J/ψ's that come from decays of χ_c's. A substantial variation has also been observed in a ratio of production rates of P-wave states, namely the χ_{c1} to χ_{c2} ratio. More precise measurements of these and other ratios would be valuable. Of particular importance would be measurements of ratios of production rates of spin-singlet and spin-triplet quarkonium states, such as the η_c to J/ψ ratio. The absence of clean signatures for spin-singlet quarkonium states makes such measurements difficult.

The polarization of quarkonium is another important test of NRQCD factorization. The standard truncation in v leads to unambiguous predictions for the ratios of production rates of different spin states, without introducing any new parameters. The predictions are most easily tested for the quarkonium states with $J^{PC} = 1^{--}$, but they can also be tested for other states. It is extremely important to test the simple qualitative predictions that in hadron collisions the 1^{--} states should become transversely polarized at sufficiently large p_T. More careful quantitative estimates of the polarization of the J/ψ, the $\psi(2S)$, and the $\Upsilon(nS)$ as functions of p_T at the Tevatron and the LHC would be useful. More precise measurements of the polarization of the J/ψ and the $\psi(2S)$ in other production processes, such as ep collisions, e^+e^- annihilations, and B decay, would also be valuable.

The most puzzling experimental results in quarkonium production in recent years have been the double-$c\bar{c}$ results from e^+e^- annihilation at the B factories. The measurements by the Belle collaboration of the fraction of J/ψ's that are accompanied by charmed hadrons and of the exclusive cross-section for $J/\psi + \eta_c$ production are both much larger than expected. No satisfactory theoretical explanation of these results has emerged. It would be worthwhile to measure the fraction of J/ψ's accompanied by charm hadrons in other processes, such as $p\bar{p}$ annihilation at the Tevatron and ep collisions at HERA, to see if there are any surprises.

The outlook for progress in understanding quarkonium production is very bright. The NRQCD factorization approach provides a general framework for describing inclusive quarkonium production. Current experiments will provide severe tests of NRQCD factorization with the standard truncation of the velocity expansion. These tests will either provide a firm foundation for predictions of quarkonium production in future experiments or lead us to new insights into the physics of quarkonium production.

REFERENCES

[1] W. E. Caswell and G. P. Lepage, Phys. Lett. B **167** (1986) 437.

[2] B. A. Thacker and G. P. Lepage, Phys. Rev. D **43** (1991) 196.

[3] G. T. Bodwin, E. Braaten and G. P. Lepage, Phys. Rev. D **51** (1995) 1125 [Erratum-ibid. D **55** (1997) 5853] [hep-ph/9407339].

[4] G. T. Bodwin, S. Kim, and D. K. Sinclair, Nucl. Phys. B (Proc. Suppl.) **34** (1994) 434.

[5] G. T. Bodwin, S. Kim, and D. K. Sinclair, Nucl. Phys. Proc. Suppl. **42** (1995) 306 [hep-lat/9412011].

[6] G. T. Bodwin, D. K. Sinclair, and S. Kim, Phys. Rev. Lett. **77** (1996) 2376 [hep-lat/9605023].

[7] G. T. Bodwin, D. K. Sinclair, and S. Kim, Int. J. Mod. Phys. A **12** (1997) 4019 [hep-ph/9609371].

[8] G. T. Bodwin, D. K. Sinclair, and S. Kim, Phys. Rev. D **65** (2002) 054504 [hep-lat/0107011].

[9] J.-w. Qiu and G. Sterman (private communication).

[10] M. Beneke, I. Z. Rothstein, and M. B. Wise, Phys. Lett. B **408** (1997) 373 [hep-ph/9705286].

[11] S. Fleming, A. K. Leibovich and T. Mehen, Phys. Rev. D **68** (2003) 094011 [hep-ph/0306139].

[12] M. Beneke, G. A. Schuler, and S. Wolf, Phys. Rev. D **62** (2000) 034004 [hep-ph/0001062].

[13] M. B. Einhorn and S. D. Ellis, Phys. Rev. D **12** (1975) 2007.

[14] S. D. Ellis, M. B. Einhorn, and C. Quigg, Phys. Rev. Lett. **36** (1976) 1263.

[15] C. E. Carlson and R. Suaya, Phys. Rev. D **14** (1976) 3115.

[16] J. H. Kühn, Phys. Lett. B **89** (1980) 385.

[17] T. A. DeGrand and D. Toussaint, Phys. Lett. B **89** (1980) 256.

[18] J. H. Kühn, S. Nussinov, and R. Rückl, Z. Phys. C **5** (1980) 117.

[19] M. B. Wise, Phys. Lett. B **89** (1980) 229.

[20] C. H. Chang, Nucl. Phys. B **172** (1980) 425.

[21] R. Baier and R. Rückl, Nucl. Phys. B **201** (1982) 1.

[22] R. Baier and R. Rückl, Phys. Lett. B **102** (1981) 364.

[23] E. L. Berger and D. L. Jones, Phys. Rev. D **23** (1981) 1521.

[24] R. Baier and R. Rückl, Z. Phys. C **19** (1983) 251.

[25] W. Y. Keung, Print-81-0161 (BNL) *Presented at Z0 Physics Workshop, Ithaca, N.Y., Feb 6-8, 1981*.

[26] G. A. Schuler, hep-ph/9403387.

[27] H. Fritzsch, Phys. Lett. B **67** (1977) 217.

[28] F. Halzen, Phys. Lett. B **69** (1977) 105.

[29] M. Glück, J. F. Owens and E. Reya, Phys. Rev. D **17** (1978) 2324.

[30] V. D. Barger, W. Y. Keung and R. J. Phillips, Phys. Lett. B **91** (1980) 253.

[31] R. Gavai, D. Kharzeev, H. Satz, G. A. Schuler, K. Sridhar and R. Vogt, Int. J. Mod. Phys. A **10** (1995) 3043 [hep-ph/9502270].

[32] G. A. Schuler and R. Vogt, Phys. Lett. B **387** (1996) 181 [hep-ph/9606410].

[33] M. L. Mangano, P. Nason and G. Ridolfi, Nucl. Phys. B **405** (1993) 507.

[34] J. F. Amundson, O. J. P. Eboli, E. M. Gregores and F. Halzen, Phys. Lett. B **390** (1997) 323 [hep-ph/9605295].

[35] A. Edin, G. Ingelman and J. Rathsman, Phys. Rev. D **56** (1997) 7317 [hep-ph/9705311].

[36] O. J. P. Eboli, E. M. Gregores and F. Halzen, Phys. Lett. B **451** (1999) 241 [hep-ph/9802421].

[37] O. J. P. Eboli, E. M. Gregores and F. Halzen, Phys. Rev. D **67** (2003) 054002.

[38] O. J. P. Eboli, E. M. Gregores and J. K. Mizukoshi, Phys. Rev. D **68** (2003) 094009 [hep-ph/0308121].

[39] O. J. P. Eboli, E. M. Gregores and F. Halzen, Phys. Rev. D **64** (2001) 093015 [hep-ph/0107026].

[40] E. M. Gregores, F. Halzen and O. J. P. Eboli, Phys. Lett. B **395** (1997) 113 [hep-ph/9607324].

[41] E. L. Berger, J. w. Qiu, and Y. l. Wang, hep-ph/0404158.

[42] J. C. Collins, D. E. Soper and G. Sterman, Nucl. Phys. B **250** (1985) 199.

[43] H. Contopanagos, E. Laenen and G. Sterman, Nucl. Phys. B **484** (1997) 303 [hep-ph/9604313].

[44] see e.g., M. Cacciari, M. Greco, and P. Nason, JHEP **9805** (1998) 007 [hep-ph/9803400].

[45] F. E. Paige and S. D. Protopopescu, BNL-29777.

[46] F. E. Paige, S. D. Protopescu, H. Baer, and X. Tata, hep-ph/0312045.

[47] T. Sjöstrand, Comput. Phys. Commun. **39** (1986) 347.

[48] T. Sjöstrand and M. Bengtsson, Comput. Phys. Commun. **43** (1987) 367.

[49] G. Marchesini and B. R. Webber, Nucl. Phys. B **310** (1988) 461.

[50] G. Marchesini, B. R. Webber, G. Abbiendi, I. G. Knowles, M. H. Seymour, and L. Stanco, Comput. Phys. Commun. **67** (1992) 465.

[51] S. Frixione and B. R. Webber, JHEP **0206** (2002) 029 [hep-ph/0204244].

[52] S. Frixione and B. R. Webber, hep-ph/0207182.

[53] S. Frixione, P. Nason and B. R. Webber, JHEP **0308** (2003) 007 [hep-ph/0305252].

[54] S. Frixione and B. R. Webber, hep-ph/0402116.

[55] D. E. Soper, Phys. Rev. D **69** (2004) 054020 [hep-ph/0306268].

[56] M. Krämer and D. E. Soper, Phys. Rev. D **69** (2004) 054019 [hep-ph/0306222].

[57] G. T. Bodwin, S. J. Brodsky, and G. P. Lepage, Phys. Rev. D **39** (1989) 3287.

[58] J. w. Qiu and G. Sterman, Int. J. Mod. Phys. E **12** (2003) 149 [hep-ph/0111002].

[59] G. T. Bodwin, S. J. Brodsky, and G. P. Lepage, Phys. Rev. Lett. **47** (1981) 1799.

[60] G. T. Bodwin, Phys. Rev. D **31** (1985) 2616 [Erratum-ibid. D **34** (1986) 3932].

[61] F. Abe *et al.* [CDF Collaboration], Phys. Rev. Lett. **79** (1997) 572.

[62] F. Abe *et al.* [CDF Collaboration], Phys. Rev. Lett. **79** (1997) 578.

[63] S. R. Klein and J. Nystrand, Phys. Rev. Lett. **92** (2004) 142003 [hep-ph/0311164].

[64] M. Krämer, Prog. Part. Nucl. Phys. **47** (2001) 141 [hep-ph/0106120].

[65] E. Braaten and S. Fleming, Phys. Rev. Lett. **74** (1995) 3327 [hep-ph/9411365].

[66] M. Beneke and M. Krämer, Phys. Rev. D **55** (1997) 5269 [hep-ph/9611218].

[67] W. Buchmüller and S. H. Tye, Phys. Rev. D **24** (1981) 132.

[68] E. J. Eichten and C. Quigg, Phys. Rev. D **52** (1995) 1726 [hep-ph/9503356].

[69] H. L. Lai *et al.* [CTEQ Collaboration], Eur. Phys. J. C **12** (2000) 375 [hep-ph/9903282].

[70] A. Petrelli, M. Cacciari, M. Greco, F. Maltoni, and M. L. Mangano, Nucl. Phys. **B514** (1998) 245 [hep-ph/9707223].

[71] F. Maltoni, hep-ph/0007003.

[72] P. L. Cho and A. K. Leibovich, Phys. Rev. D **53** (1996) 150 [hep-ph/9505329].

[73] P. L. Cho and A. K. Leibovich, Phys. Rev. D **53** (1996) 6203 [hep-ph/9511315].

[74] A. D. Martin, W. J. Stirling, and R. G. Roberts, Phys. Lett. B **306** (1993) 145; **309** (1993) 492 (erratum).

[75] H. L. Lai *et al.*, Phys. Rev. D **55** (1997) 1280 [hep-ph/9606399].

[76] M. Glück, E. Reya and A. Vogt, Z. Phys. C **67** (1995) 433.

[77] A. D. Martin, R. G. Roberts and W. J. Stirling, Phys. Lett. B **387** (1996) 419 [hep-ph/9606345].

[78] E. Braaten, B. A. Kniehl and J. Lee, Phys. Rev. D **62** (2000) 094005 [hep-ph/9911436].

[79] A. D. Martin, R. G. Roberts, W. J. Stirling, and R. S. Thorne, Eur. Phys. J. C **4** (1998) 463 [hep-ph/9803445].

[80] M. A. Sanchis-Lozano, Nucl. Phys. Proc. Suppl. **86** (2000) 543 [hep-ph/9907497].

[81] W. K. Tung, *Prepared for International Workshop on Deep Inelastic Scattering and Related Subjects, Eilat, Israel, 6-11 Feb 1994.*

[82] B. A. Kniehl and G. Kramer, Eur. Phys. J. C **6** (1999) 493 [hep-ph/9803256].

[83] A. Petrelli, Nucl. Phys. Proc. Suppl. **86** (2000) 533 [hep-ph/9910274].

[84] K. Sridhar, A. D. Martin and W. J. Stirling, Phys. Lett. B **438** (1998) 211 [hep-ph/9806253].

[85] P. Hägler, R. Kirschner, A. Schäfer, L. Szymanowski and O. V. Teryaev, Phys. Rev. D **63** (2001) 077501 [hep-ph/0008316].

[86] J. Kwiecinski, A. D. Martin and A. M. Stasto, Phys. Rev. D **56** (1997) 3991 [hep-ph/9703445].

[87] F. Yuan and K. T. Chao, Phys. Rev. D **63** (2001) 034006 [hep-ph/0008302].

[88] F. Yuan and K. T. Chao, Phys. Rev. Lett. **87** (2001) 022002 [hep-ph/0009224].

[89] M. Beneke and I. Z. Rothstein, Phys. Lett. B **372** (1996) 157 [Erratum-ibid. B **389** (1996) 769] [hep-ph/9509375].

[90] J. P. Ma, Nucl. Phys. **B447** (1995) 405 [hep-ph/9503346].

[91] E. Braaten and J. Lee, Nucl. Phys. B **586** (2000) 427 [hep-ph/0004228].

[92] M. Cacciari and M. Greco, Phys. Rev. Lett. **73** (1994) 1586 [hep-ph/9405241].

[93] E. Braaten, M. A. Doncheski, S. Fleming, and M. L. Mangano, Phys. Lett. B **333** (1994) 548 [hep-ph/9405407].

[94] D. P. Roy and K. Sridhar, Phys. Lett. **B339** (1994) 141 [hep-ph/9406386].

[95] T. Affolder *et al.* [CDF Collaboration], Phys. Rev. Lett. **86** (2001) 3963.

[96] F. Maltoni (unpublished).

[97] http://www-cdf.fnal.gov/physics/new/bottom/030904.blessed-bxsec-jpsi/.

[98] http://www-d0.fnal.gov/Run2Physics/ckm/approved_results/approved_results.html; http://www-d0.fnal.gov/Run2Physics/ckm/Moriond_2003/index2.html.

[99] D. Acosta *et al.* [CDF Collaboration], Phys. Rev. D **66** (2002) 092001.

[100] B. Abbott *et al.* [D0 Collaboration], Phys. Rev. Lett. **82** (1999) 35.

[101] M. Cacciari, S. Frixione, M. L. Mangano, P. Nason and G. Ridolfi, JHEP **0407** (2004) 033 [hep-ph/0312132].

[102] D. Acosta *et al.* [CDF Collaboration], Phys. Rev. Lett. **88** (2002) 161802.

[103] T. Affolder *et al.* [CDF Collaboration], Phys. Rev. Lett. **85** (2000) 2886 [hep-ex/0004027].

[104] M. Krämer and F. Maltoni, in 'Bottom Production', P. Nason, G. Ridolfi, O. Schneider, G.F. Tartarelli, P. Vikas et al., [hep-ph/0003142], published in CERN-YR-2000/01, G. Altarelli and M.L. Mangano editors.

[105] E. Braaten, S. Fleming, and A. K. Leibovich, Phys. Rev. D **63** (2001) 094006 [hep-ph/0008091].

[106] J. L. Domenech and M. A. Sanchis-Lozano, Nucl. Phys. B **601** (2001) 395 [hep-ph/0012296].

[107] F. Abe *et al.* [CDF Collaboration], Phys. Rev. Lett. **75** (1995) 4358.

[108] P. L. Cho and M. B. Wise, Phys. Lett. B **346** (1995) 129 [hep-ph/9411303].

[109] A. K. Leibovich, Phys. Rev. D **56** (1997) 4412 [hep-ph/9610381].

[110] G. T. Bodwin and J. Lee, Phys. Rev. D **69** (2004) 054003 [hep-ph/0308016].

[111] M. Beneke, hep-ph/9703429.

[112] N. Brambilla, A. Pineda, J. Soto and A. Vairo, Nucl. Phys. B **566** (2000) 275 [hep-ph/9907240].

[113] S. Fleming, I. Z. Rothstein and A. K. Leibovich, Phys. Rev. D **64** (2001) 036002 [hep-ph/0012062].

[114] M. A. Sanchis-Lozano, Int. J. Mod. Phys. A **16** (2001) 4189 [hep-ph/0103140].

[115] N. Brambilla, D. Eiras, A. Pineda, J. Soto and A. Vairo, Phys. Rev. D **67** (2003) 034018 [hep-ph/0208019].

[116] N. Marchal, S. Peigne and P. Hoyer, Phys. Rev. D **62** (2000) 114001 [hep-ph/0004234].

[117] M. Maul, Nucl. Phys. B **594** (2001) 89 [hep-ph/0009279].

[118] E. Braaten and J. Lee, Phys. Rev. D **63** (2001) 071501 [hep-ph/0012244].

[119] R. Cropp [CDF collaboration], hep-ex/9910003.

[120] V. Papadimitriou [CDF Collaboration], Int. J. Mod. Phys. A **16S1A** (2001) 160.

[121] P. Mathews, P. Poulose and K. Sridhar, Phys. Lett. **B438** (1998) 336 [hep-ph/9803424].

[122] K. Sridhar, Phys. Rev. Lett. **77** (1996) 4880 [hep-ph/9609285].

[123] C. Qiao, F. Yuan and K. Chao, Phys. Rev. D **55** (1997) 5437 [hep-ph/9701249].

[124] C. S. Kim, J. Lee and H. S. Song, Phys. Rev. **D55** (1997) 5429 [hep-ph/9610294].

[125] P. Mathews, K. Sridhar and R. Basu, Phys. Rev. **D60** (1999) 014009 [hep-ph/9901276].

[126] V. Barger, S. Fleming and R. J. Phillips, Phys. Lett. B **371** (1996) 111 [hep-ph/9510457].

[127] F. Maltoni and A. D. Polosa, hep-ph/0405082.

[128] E. Braaten, J. Lee and S. Fleming, Phys. Rev. **D60** (1999) 091501 [hep-ph/9812505].

[129] M. Beneke and I. Z. Rothstein, Phys. Rev. D **54** (1996) 2005 [Erratum-ibid. D **54** (1996) 7082] [hep-ph/9603400].

[130] W. K. Tang and M. Vanttinen, Phys. Rev. D **54** (1996) 4349 [hep-ph/9603266].

[131] S. Gupta and K. Sridhar, Phys. Rev. D **54** (1996) 5545 [hep-ph/9601349].

[132] C. Akerlof *et al.*, Phys. Rev. D **48** (1993) 5067.

[133] M. H. Schub *et al.* [E789 Collaboration], Phys. Rev. D **52** (1995) 1307 [Erratum-ibid. D **53** (1996) 570].

[134] T. Alexopoulos *et al.* [E771 Collaboration], Phys. Lett. B **374** (1996) 271.

[135] S. Eidelman *et al.* [Particle Data Group Collaboration], Phys. Lett. B **592** (2004) 1.

[136] S. Gupta and P. Mathews, Phys. Rev. D **56** (1997) 3019 [hep-ph/9703370].

[137] D. A. Bauer *et al.*, Phys. Rev. Lett. **54** (1985) 753.

[138] L. Antoniazzi *et al.* [E705 Collaboration], Phys. Rev. D **49** (1994) 543.

[139] T. Alexopoulos *et al.* [E771 Collaboration], Phys. Rev. D **62** (2000) 032006 [hep-ex/9908010].

[140] H. L. Lai *et al.*, Phys. Rev. D **51** (1995) 4763 [hep-ph/9410404].

[141] M. Arenton [E705 Collaboration], Int. J. Mod. Phys. A **12** (1997) 3837.

[142] J. Spengler [HERA-B Collaboration], J. Phys. G **30**, S871 (2004) [arXiv:hep-ex/0403043].

[143] Y. Lemoigne *et al.*, Phys. Lett. B **113** (1982) 509 [Erratum-ibid. B **116** (1982) 470].

[144] S. R. Hahn *et al.*, Phys. Rev. D **30** (1984) 671.

[145] V. Koreshev *et al.* [E672-E706 Collaborations], Phys. Rev. Lett. **77** (1996) 4294.

[146] A. Gribushin *et al.* [E672 and E706 Collaborations], Phys. Rev. D **53** (1996) 4723.

[147] J. F. Amundson, O. J. Eboli, E. M. Gregores, and F. Halzen, Phys. Lett. B **372** (1996) 127 [hep-ph/9512248].

[148] A. Gribushin *et al.* [E672 Collaborations], Phys. Rev. D **62** (2000) 012001 [hep-ex/9910005].

[149] G. Introzzi [E771 Collaboration], Nucl. Phys. Proc. Suppl. **55A** (1997) 188.

[150] T. H. Chang *et al.* [FNAL E866/NuSea collaboration], Phys. Rev. Lett. **91** (2003) 211801 [hep-ex/0308001].

[151] M. Vanttinen, P. Hoyer, S. J. Brodsky and W. K. Tang, Phys. Rev. D **51** (1995) 3332 [hep-ph/9410237].

[152] Jungil Lee, presentation at the HERA-B Collaboration Meeting, December 7, 2000.

[153] J. G. Heinrich *et al.*, Phys. Rev. D **44** (1991) 1909.

[154] C. N. Brown *et al.* [FNAL E866 Collaboration], Phys. Rev. Lett. **86** (2001) 2529 [hep-

ex/0011030].

[155] A. Kharchilava, T. Lohse, A. Somov, and A. Tkabladze, Phys. Rev. D **59** (1999) 094023 [hep-ph/9811361].

[156] A. Tkabladze, Phys. Lett. B **462** (1999) 319.

[157] J. L. Cortes and B. Pire, Phys. Rev. D **38**, 3586 (1988).

[158] M. Bedjidian *et al.*, hep-ph/0311048.

[159] S. Digal, P. Petreczky and H. Satz, Phys. Rev. D **64** (2001) 094015 [hep-ph/0106017].

[160] M. Glück, E. Reya and A. Vogt, Eur. Phys. J. C **5** (1998) 461 [hep-ph/9806404].

[161] R. Vogt, in proceedings of the 18th Winter Workshop on Nuclear Dynamics, edited by R. Bellweid *et al.*, Debrecen, Hungary (2002) p. 253 [hep-ph/0203151].

[162] R. Vogt, Heavy Ion Phys. **18** (2003) 11 [hep-ph/0205330].

[163] T. Affolder *et al.* [CDF Collaboration], Phys. Rev. Lett. **84** (2000) 2094 [hep-ex/9910025].

[164] J. F. Gunion and R. Vogt, Nucl. Phys. B **492** (1997) 301 [hep-ph/9610420].

[165] M. Krämer, J. Zunft, J. Steegborn, and P. M. Zerwas, Phys. Lett. B **348** (1995) 657 [hep-ph/9411372].

[166] M. Krämer, Nucl. Phys. B **459** (1996) 3 [hep-ph/9508409].

[167] M. Cacciari and M. Krämer, Phys. Rev. Lett. **76** (1996) 4128 [hep-ph/9601276].

[168] M. Beneke, M. Krämer, and M. Vanttinen, Phys. Rev. D **57** (1998) 4258 [hep-ph/9709376].

[169] J. Amundson, S. Fleming and I. Maksymyk, Phys. Rev. D **56** (1997) 5844 [hep-ph/9601298].

[170] P. Ko, J. Lee and H. S. Song, Phys. Rev. D **54** (1996) 4312 [Erratum-ibid. D **60** (1999) 119902] [hep-ph/9602223].

[171] R. M. Godbole, D. P. Roy, and K. Sridhar, Phys. Lett. B **373** (1996) 328 [hep-ph/9511433].

[172] B. A. Kniehl and G. Kramer, Phys. Lett. B **413** (1997) 416 [hep-ph/9703280].

[173] B. A. Kniehl and G. Kramer, Phys. Rev. D **56** (1997) 5820 [hep-ph/9706369].

[174] C. Adloff *et al.* [H1 Collaboration], Eur. Phys. J. C **25** (2002) 25 [hep-ex/0205064].

[175] S. Chekanov *et al.* [ZEUS Collaboration], Eur. Phys. J. C **27** (2003) 173 [hep-ex/0211011].

[176] H. Jung and G. P. Salam, Eur. Phys. J. C **19** (2001) 351 [hep-ph/0012143].

[177] H. Jung, Comput. Phys. Commun. **143** (2002) 100 [hep-ph/0109102].

[178] V. A. Saleev and N. P. Zotov, Mod. Phys. Lett. A **9** (1994) 151 [Erratum-ibid. A **9** (1994) 1517].

[179] S. P. Baranov, Phys. Lett. B **428** (1998) 377.

[180] C. Adloff *et al.* [H1 Collaboration], Eur. Phys. J. C **10** (1999) 373 [hep-ex/9903008].

[181] S. Fleming and T. Mehen, Phys. Rev. D **57** (1998) 1846 [hep-ph/9707365].

[182] B. A. Kniehl and L. Zwirner, Nucl. Phys. **B621** (2002) 337 [hep-ph/0112199].

[183] C. Adloff *et al.* [H1 Collaboration], Eur. Phys. J. C **25** (2002) 41 [hep-ex/0205065].

[184] S. Chekanov *et al.* [ZEUS Collaboration], contributed paper 565, International Europhysics Conference on High Energy Physics (EPS 2003), Aachen, Germany, 2003.

[185] A. V. Lipatov and N. P. Zotov, Eur. Phys. J. C **27** (2003) 87 [hep-ph/0210310].

[186] J. G. Körner, J. Cleymans, M. Kuroda, and G. J. Gounaris, Phys. Lett. B **114** (1982) 195.

[187] J. P. Guillet, Z. Phys. C **39** (1988) 75.

[188] H. Merabet, J. F. Mathiot, and R. Mendez-Galain, Z. Phys. C **62** (1994) 639.

[189] D. Krücker, Ph.D. Thesis, RWTH Aachen, 1995.

[190] F. Yuan and K. T. Chao, Phys. Rev. D **63** (2001) 034017 [hep-ph/0008301].

[191] M. G. Ryskin, Z. Phys. C **57** (1993) 89.

[192] S. J. Brodsky, L. Frankfurt, J. F. Gunion, A. H. Mueller and M. Strikman, Phys. Rev. D **50** (1994)

3134 [hep-ph/9402283].

[193] J. C. Collins, L. Frankfurt and M. Strikman, Phys. Rev. D **56** (1997) 2982 [hep-ph/9611433].

[194] J. C. Collins, Phys. Rev. D **57** (1998) 3051 [Erratum-ibid. D **61** (2000) 019902] [hep-ph/9709499].

[195] T. Teubner, hep-ph/9910329.

[196] J. Bartels and H. Kowalski, Eur. Phys. J. C **19** (2001) 693 [hep-ph/0010345].

[197] A. Hayashigaki and K. Tanaka, hep-ph/0401053.

[198] S. Aid *et al.* [H1 Collaboration], Nucl. Phys. B **463** (1996) 3 [hep-ex/9601004].

[199] C. Adloff *et al.* [H1 Collaboration], Eur. Phys. J. C **13** (2000) 371 [hep-ex/9902019].

[200] C. Adloff *et al.* [H1 Collaboration], Phys. Lett. B **483** (2000) 23 [hep-ex/0003020].

[201] C. Adloff *et al.* [H1 Collaboration], Phys. Lett. B **483** (2000) 360 [hep-ex/0005010].

[202] C. Adloff *et al.* [H1 Collaboration], Phys. Lett. B **539** (2002) 25 [hep-ex/0203022].

[203] C. Adloff *et al.* [H1 Collaboration], Phys. Lett. B **541** (2002) 251 [hep-ex/0205107].

[204] A. Aktas *et al.* [H1 Collaboration], Phys. Lett. B **568** (2003) 205 [hep-ex/0306013].

[205] A. Aktas *et al.* [H1 Collaboration], contributed paper 6-0180, International Conference on High Energy Physics (ICHEP04), Beijing, China, 2004.

[206] J. Breitweg *et al.* [ZEUS Collaboration], Eur. Phys. J. C **6** (1999) 603 [hep-ex/9808020].

[207] J. Breitweg *et al.* [ZEUS Collaboration], Phys. Lett. B **437** (1998) 432 [hep-ex/9807020].

[208] J. Breitweg *et al.* [ZEUS Collaboration], Eur. Phys. J. C **14** (2000) 213 [hep-ex/9910038].

[209] J. Breitweg *et al.* [ZEUS Collaborations], Eur. Phys. J. C **12** (2000) 393 [hep-ex/9908026].

[210] J. Breitweg *et al.* [ZEUS Collaboration], Phys. Lett. B **487** (2000) 273 [hep-ex/0006013].

[211] S. Chekanov *et al.* [ZEUS Collaboration], Eur. Phys. J. C **26** (2003) 389 [hep-ex/0205081].

[212] S. Chekanov *et al.* [ZEUS Collaboration], contributed paper 549, International Europhysics Conference on High Energy Physics (EPS 2003), Aachen, Germany, 2003.

[213] S. Chekanov *et al.* [ZEUS Collaboration], Eur. Phys. J. C **24** (2002) 345 [hep-ex/0201043].

[214] S. Chekanov *et al.* [ZEUS Collaboration], Nucl. Phys. B **695** (2004) 3 [hep-ex/0404008].

[215] L. Frankfurt, W. Koepf and M. Strikman, Phys. Rev. D **57** (1998) 512 [hep-ph/9702216].

[216] M. McDermott, L. Frankfurt, V. Guzey and M. Strikman, Eur. Phys. J. C **16** (2000) 641 [hep-ph/9912547].

[217] L. Frankfurt, M. McDermott and M. Strikman, JHEP **0103** (2001) 045 [hep-ph/0009086].

[218] M. G. Ryskin, R. G. Roberts, A. D. Martin and E. M. Levin, Z. Phys. C **76** (1997) 231 [hep-ph/9511228].

[219] A. D. Martin and M. G. Ryskin, Phys. Rev. D **57** (1998) 6692 [hep-ph/9711371].

[220] A. D. Martin, M. G. Ryskin and T. Teubner, Phys. Rev. D **62** (2000) 014022 [hep-ph/9912551].

[221] D. Y. Ivanov, A. Schäfer, L. Szymanowski and G. Krasnikov, Eur. Phys. J. C **34** (2004) 297 [hep-ph/0401131].

[222] T. Regge, Nuovo Cim. **14** (1959) 951.

[223] T. Regge, Nuovo Cim. **18** (1960) 947.

[224] J. J. Sakurai, Phys. Rev. Lett. **22** (1969) 981.

[225] A. Donnachie and P. V. Landshoff, Phys. Lett. B **296** (1992) 227 [hep-ph/9209205].

[226] A. Donnachie and P. V. Landshoff, Phys. Lett. B **437** (1998) 408 [hep-ph/9806344].

[227] E. A. Kuraev, L. N. Lipatov and V. S. Fadin, Sov. Phys. JETP **44** (1976) 443 [Zh. Eksp. Teor. Fiz. **71** (1976) 840].

[228] E. A. Kuraev, L. N. Lipatov and V. S. Fadin, Sov. Phys. JETP **45** (1977) 199 [Zh. Eksp. Teor. Fiz. **72** (1977) 377].

[229] I. I. Balitsky and L. N. Lipatov, Sov. J. Nucl. Phys. **28** (1978) 822 [Yad. Fiz. **28** (1978) 1597].

[230] A. H. Mueller and B. Patel, Nucl. Phys. B **425** (1994) 471 [hep-ph/9403256].

[231] N. N. Nikolaev and B. G. Zakharov, Z. Phys. C **64** (1994) 631 [hep-ph/9306230].

[232] V. N. Gribov and L. N. Lipatov, Yad. Fiz. **15** (1972) 781 and 1218 [Sov. J. Nucl. Phys. **15** (1972) 438 and 675].

[233] M. Cacciari and M. Krämer, Talk given at the Workshop on Future Physics at HERA, Hamburg, Germany, 30-31 May 1996 [hep-ph/9609500].

[234] S. Fleming and T. Mehen, Phys. Rev. D **58** (1998) 037503 [hep-ph/9801328].

[235] L. Hao, F. Yuan and K. Chao, Phys. Rev. Lett. **83** (1999) 4490 [hep-ph/9902338].

[236] L. Hao, F. Yuan and K. Chao, Phys. Rev. D **62** (2000) 074023 [hep-ph/0004203].

[237] C. S. Kim and E. Reya, Phys. Lett. B **300** (1993) 298.

[238] T. Mehen, Phys. Rev. D **55** (1997) 4338 [hep-ph/9611321].

[239] M. Cacciari, M. Greco and M. Krämer, Phys. Rev. D **55** (1997) 7126 [hep-ph/9611324].

[240] [ALEPH Collaboration], CERN-OPEN-99-343 *Prepared for International Europhysics Conference on High-Energy Physics (HEP 97), Jerusalem, Israel, 19-26 Aug 1997.*

[241] P. Abreu *et al.* [DELPHI Collaboration], Phys. Lett. B **341** (1994) 109.

[242] M. Wadhwa [L3 Collaboration], Nucl. Phys. Proc. Suppl. **64** (1998) 441.

[243] G. Alexander *et al.* [OPAL Collaboration], Phys. Lett. B **384** (1996) 343.

[244] C. G. Boyd, A. K. Leibovich, and I. Z. Rothstein, Phys. Rev. D **59** (1999) 054016 [hep-ph/9810364].

[245] S. Todorova-Nova, hep-ph/0112050.

[246] J. Abdallah *et al.* [DELPHI Collaboration], Phys. Lett. B **565** (2003) 76 [hep-ex/0307049].

[247] J. P. Ma, B. H. J. McKellar and C. B. Paranavitane, Phys. Rev. D **57** (1998) 606 [hep-ph/9707480].

[248] G. Japaridze and A. Tkabladze, Phys. Lett. B **433** (1998) 139 [hep-ph/9803447].

[249] R. M. Godbole, D. Indumathi and M. Krämer, Phys. Rev. D **65** (2002) 074003 [hep-ph/0101333].

[250] M. Klasen, B. A. Kniehl, L. Mihaila and M. Steinhauser, Nucl. Phys. B **609** (2001) 518 [hep-ph/0104044].

[251] M. Klasen, B. A. Kniehl, L. N. Mihaila, and M. Steinhauser, Phys. Rev. Lett. **89** (2002) 032001 [hep-ph/0112259].

[252] M. Klasen, B. A. Kniehl, L. N. Mihaila and M. Steinhauser, [hep-ph/0407014].

[253] G. Alexander *et al.* [OPAL Collaboration], Phys. Lett. B **370** (1996) 185.

[254] P. L. Cho, Phys. Lett. B **368** (1996) 171 [hep-ph/9509355].

[255] W. Y. Keung, Phys. Rev. D **23** (1981) 2072.

[256] J. H. Kühn and H. Schneider, Z. Phys. C **11** (1981) 263.

[257] K. J. Abraham, Z. Phys. C **44** (1989) 467.

[258] K. Hagiwara, A. D. Martin and W. J. Stirling, Phys. Lett. B **267** (1991) 527 [Erratum-ibid. B **316** (1993) 631].

[259] E. Braaten, K. m. Cheung, and T. C. Yuan, Phys. Rev. D **48** (1993) 4230 [hep-ph/9302307].

[260] K. Abe *et al.* [BELLE Collaboration], Phys. Rev. Lett. **88** (2002) 052001 [hep-ex/0110012].

[261] B. Aubert *et al.* [BABAR Collaboration], Phys. Rev. Lett. **87** (2001) 162002 [hep-ex/0106044].

[262] P. L. Cho and A. K. Leibovich, Phys. Rev. D **54** (1996) 6690 [hep-ph/9606229].

[263] F. Yuan, C. F. Qiao, and K. T. Chao, Phys. Rev. D **56** (1997) 321 [hep-ph/9703438].

[264] F. Yuan, C. F. Qiao, and K. T. Chao, Phys. Rev. D **56** (1997) 1663 [hep-ph/9701361].

[265] G. A. Schuler, Eur. Phys. J. C **8** (1999) 273 [hep-ph/9804349].

[266] E. Braaten and Y. Q. Chen, Phys. Rev. Lett. **76** (1996) 730 [hep-ph/9508373].

[267] K. Abe *et al.* [Belle Collaboration], BELLE-CONF-0331, contributed paper, International Europhysics Conference on High Energy Physics (EPS 2003), Aachen, Germany, 2003.

[268] S. Baek, P. Ko, J. Lee, and H. S. Song, Phys. Lett. B **389** (1996) 609 [hep-ph/9607236].

[269] K. Abe *et al.* [Belle Collaboration], Phys. Rev. Lett. **89** (2002) 142001 [hep-ex/0205104].

[270] K. Y. Liu, Z. G. He and K. T. Chao, Phys. Rev. D **69** (2004) 094027.

[271] K. Abe *et al.* [Belle Collaboration], hep-ex/0407009.

[272] E. Braaten and J. Lee, Phys. Rev. D **67** (2003) 054007 [hep-ph/0211085].

[273] K. Y. Liu, Z. G. He, and K. T. Chao, Phys. Lett. B **557** (2003) 45 [hep-ph/0211181].

[274] S. J. Brodsky, C.-R. Ji, and J. Lee, private communication.

[275] G. T. Bodwin, J. Lee, and E. Braaten, Phys. Rev. Lett. **90** (2003) 162001 [hep-ph/0212181].

[276] G. T. Bodwin, J. Lee, and E. Braaten, Phys. Rev. D **67** (2003) 054023 [hep-ph/0212352].

[277] A. V. Luchinsky, hep-ph/0301190.

[278] K. Abe *et al.* [Belle Collaboration], hep-ex/0306015.

[279] J. P. Ma and Z. G. Si, hep-ph/0405111.

[280] R. Balest *et al.* [CLEO Collaboration], Phys. Rev. D **52** (1995) 2661.

[281] S. Chen *et al.* [CLEO Collaboration], Phys. Rev. D **63** (2001) 031102 [hep-ex/0009044].

[282] D. Buskulic *et al.* [ALEPH Collaboration], Phys. Lett. B **295** (1992) 396.

[283] O. Adriani *et al.* [L3 Collaboration], Phys. Lett. B **317** (1993) 467.

[284] P. Ko, J. Lee and H. S. Song, Phys. Rev. D **53** (1996) 1409 [hep-ph/9510202].

[285] P. Ko, J. Lee and H. S. Song, J. Korean Phys. Soc. **34** (1999) 301.

[286] S. Anderson *et al.* [CLEO Collaboration], Phys. Rev. Lett. **89** (2002) 282001.

[287] M. Beneke, F. Maltoni and I. Z. Rothstein, Phys. Rev. D **59** (1999) 054003 [hep-ph/9808360].

[288] J. P. Ma, Phys. Lett. B **488** (2000) 55 [hep-ph/0006060].

[289] S. Fleming, O. F. Hernandez, I. Maksymyk and H. Nadeau, Phys. Rev. D **55** (1997) 4098 [hep-ph/9608413].

[290] G. T. Bodwin, E. Braaten, T. C. Yuan and G. P. Lepage, Phys. Rev. D **46** (1992) 3703 [hep-ph/9208254].

[291] J. H. Kühn and R. Rückl, Phys. Lett. **135B** (1984) 477 [Erratum-ibid. B **258** (1991) 499].

[292] C. H. Chang and Y. Q. Chen, Phys. Rev. D **46** (1992) 3845 [Erratum-ibid. D **50** (1994) 6013].

[293] P. Abreu *et al.* [DELPHI Collaboration], Phys. Lett. B **398** (1997) 207.

[294] R. Barate *et al.* [ALEPH Collaboration], Phys. Lett. B **402** (1997) 213.

[295] K. Ackerstaff *et al.* [OPAL Collaboration], Phys. Lett. B **420** (1998) 157 [hep-ex/9801026].

[296] F. Abe *et al.* [CDF Collaboration], Phys. Rev. Lett. **81** (1998) 2432 [hep-ex/9805034].

[297] F. Abe *et al.* [CDF Collaboration], Phys. Rev. D **58** (1998) 112004 [hep-ex/9804014].

[298] E. Braaten, K. m. Cheung and T. C. Yuan, Phys. Rev. D **48** (1993) 5049 [hep-ph/9305206].

[299] C. H. Chang and Y. Q. Chen, Phys. Rev. D **48** (1993) 4086.

[300] C. H. Chang, Y. Q. Chen, G. P. Han and H. T. Jiang, Phys. Lett. B **364** (1995) 78 [hep-ph/9408242].

[301] C. H. Chang, Y. Q. Chen and R. J. Oakes, Phys. Rev. D **54** (1996) 4344 [hep-ph/9602411].

[302] K. Kolodziej, A. Leike and R. Rückl, Phys. Lett. B **355** (1995) 337 [hep-ph/9505298].

[303] M. Lusignoli and M. Masetti, Z. Phys. C **51** (1991) 546.

[304] D. Scora and N. Isgur, Phys. Rev. D **52** (1995) 2783.

[305] R. M. Barnett *et al.*, "Review of Particle Physics", Phys. Rev. D **54** (1996) 1.

[306] M. Lusignoli, M. Masetti and S. Petrarca, Phys. Lett. B **266** (1991) 142.

[307] A. V. Berezhnoy, V. V. Kiselev and A. K. Likhoded, Z. Phys. A **356** (1996) 89.

[308] S. P. Baranov, Phys. Rev. D **55** (1997) 2756.

[309] A. V. Berezhnoi, V. V. Kiselev, A. K. Likhoded and A. I. Onishchenko, Phys. Atom. Nucl. **60** (1997) 1729 [hep-ph/9703341].

[310] K. m. Cheung, Phys. Lett. B **472** (2000) 408 [hep-ph/9908405].

[311] C. H. Chang, C. Driouichi, P. Eerola and X. G. Wu, Comput. Phys. Commun. **159** (2004) 192 [hep-ph/0309120].

[312] M. L. Mangano and S. J. Parke, Phys. Rept. **200** (1991) 301, and references therein.

[313] T. Sjöstrand, Comput. Phys. Commun. **82** (1994) 74.

[314] C. H. Chang and X. G. Wu, hep-ph/0309121.

[315] B. Guberina, R. Meckbach, R. D. Peccei and R. Rückl, Nucl. Phys. B **184** (1981) 476.

[316] Y. Q. Chen and Y. P. Kuang, Phys. Rev. D **46** (1992) 1165 [Erratum-ibid. D **47** (1993) 350].

[317] E. J. Eichten and C. Quigg, Phys. Rev. D **49** (1994) 5845 [hep-ph/9402210].

[318] V. V. Kiselev, A. K. Likhoded and A. V. Tkabladze, Phys. Rev. D **51** (1995) 3613 [hep-ph/9406339].

[319] A. Abd El-Hady, J. H. Munoz and J. P. Vary, Phys. Rev. D **62** (2000) 014019 [hep-ph/9909406].

[320] C. T. H. Davies, K. Hornbostel, G. P. Lepage, A. J. Lidsey, J. Shigemitsu and J. H. Sloan, Phys. Lett. B **382** (1996) 131 [hep-lat/9602020].

Chapter 6

PRECISION DETERMINATIONS OF QCD PARAMETERS FROM QUARKONIA

Conveners: S. Eidelman, A.H. Hoang, M. Jamin

Authors: S. Boogert, C.T.H. Davies, S. Eidelman, A.H. Hoang, M. Jamin, A.S. Kronfeld, P.B. Macken-zie, A. Penin, A. Pineda, I.W. Stewart, T. Teubner

1 INTRODUCTION

The accurate knowledge of the parameters of the Standard Model (SM) is an important requirement in the indirect search for new physics based on observables that can be predicted with small theoretical uncertainties and that are measurable experimentally with high precision. Among the parameters of QCD, for example, the precise knowledge of the top quark mass plays a crucial role in the relation of the electroweak precision observables M_Z, M_W and the weak mixing angle, which is sensitive to the vacuum structure and to non-SM virtual particles. On the other hand, for the analysis of inclusive B-decay rates the bottom and charm quark masses are needed as an input.

Heavy quarkonium systems provide an ideal instrument to extract the heavy quark masses and to get constraints on the strong coupling using perturbative as well as non-perturbative methods. The perturbative methods rely on the fact that the heavy quark masses are larger than the hadronization scale Λ_{QCD} and that non-perturbative effects affecting the dynamics can be suppressed. Based on the concept of effective theories, on new techniques to compute higher order perturbative corrections and on an improved understanding of the higher order behaviour of perturbation theory, a number of powerful methods were developed in recent years that led to an improved understanding of the perturbative structure of heavy quarkonium systems and to more realistic estimates of the uncertainties. For the determination of the masses of the bottom and the charm quarks sum rules based on moments of the hadronic cross-section in e^+e^--annihilation are the most reliable tool. While theoretically one needs to predict the moments with high precision, dedicated experiments are needed to provide measurements of the hadronic cross-section with small uncertainties. A different method to determine the masses of the bottom and charm quarks employs the masses of the low lying bottomonium and charmonium resonances with the assumption that the perturbative contributions dominate.

An alternative method relies on lattice simulations of heavy quarkonium systems where theoretical predictions are made non-perturbatively. Here the main issues are the control of lattice artifacts, unquenching and the proper extrapolation to physical quark masses, and the matching to the continuum theory. Continuous improvements on this approach have been observed in recent years.

A heavy quarkonium system that can be studied at a future e^+e^- Linear Collider is the top–antitop threshold at a centre-of-mass energy of approximately twice the top quark mass. Although the top quark lifetime in the SM is predicted to be too small to allow the production of separated resonances, the top–antitop system is governed by bound-state-type non-relativistic dynamics. Moreover, the large top quark width provides a very effective protection against the influence of non-perturbative effects making the non-relativistic top–antitop systems almost entirely perturbative for predictions of inclusive quantities. A number of precise measurements of top quark properties can be carried out at the top–antitop threshold. Among them the measurement of the top quark mass with an uncertainty at the level of 100 MeV is the most prominent one, exceeding the capabilities of hadron colliders by an order of magnitude.

In this chapter an overview is given on the current status of precision determinations of QCD parameters from quarkonium systems. In Section 2 experimental aspects of measurements of the total cross-section $\sigma(e^+e^-\rightarrow\text{hadrons})$ in the charmonium and bottomonium energy regions are reviewed. These measurements are the basis for charm and bottom quark mass extractions using QCD sum rules. In Section 3 the theoretical aspects of charm and bottom mass determinations from QCD sum rules and from the quarkonium ground state masses are reviewed. The emphasis is placed on perturbative methods, but also the status of lattice simulations is summarised. Section 4 contains a brief review of determinations of the strong coupling from quarkonium properties using perturbative methods as well as lattice simulations of the quarkonium spectrum. Some conceptual aspects of Nonrelativistic QCD and, in particular, the issue of summing logarithms of the velocity in the theoretical description of the quarkonium dynamics in the framework of vNRQCD ("velocity NRQCD") are summarised in Section 5. Finally, in Section 6 the experimental and theoretical aspects of top quark pair production close to threshold at a future Linear Collider are reviewed. In particular, the prospects of measurements of the top quark mass, its width and its couplings to the Higgs boson and to gluons are discussed.

2 *R*-MEASUREMENTS IN HEAVY QUARKONIUM REGIONS

The so-called R-ratio is the total cross-section of producing hadrons in e^+e^- collisions corrected for initial state radiation and normalised to the lowest order QED cross-section of the reaction $e^+e^-\rightarrow\mu^+\mu^-$,

$$R(s) = \frac{\sigma(e^+e^-\rightarrow\text{hadrons})(s)}{\sigma^{(0)}(e^+e^-\rightarrow\mu^+\mu^-)(s)}, \qquad (6.1)$$

where $\sqrt{s}$ is the c.m. energy. Measurements of R or of the cross-section for hadrons containing a specific quark flavour such as charm or bottom can be used for a variety of fundamental tests of perturbative QCD using the assumption of duality and the operator product expansion (OPE) [1, 2]. For example, using QCD sum rules, which deal with moments of the hadronic cross-section, one can extract values for the quark masses, and for the quark and gluon condensates that parametrise non-perturbative effects in the OPE [1, 2]. Through dispersion relations R measurements give an important input to the calculations of the hadronic corrections to various fundamental quantities that are influenced by the photonic vacuum polarisation at low energies: the anomalous magnetic moment of the muon [3], the running fine structure constant $\alpha(s)$ [4], hyperfine splitting in muonium [5] etc. From the size of higher order QCD corrections it is also possible to get constraints on the strong coupling α_s [6]. Depending on the problem, different energy ranges are of importance.

In the c.m. energy range between 3 and 5 GeV, measurements of R were carried out by many experimental groups studying various states just above the charmonium threshold: PLUTO [7], DASP [8], MARK I [9, 10], Crystal Ball [11] and BES [12, 13]. In general, these measurements are consistent. Of all the analyses the results by BES are the most precise. In the first measurement R was measured at 6 energy points from 2.6 to 5.0 GeV with a systematic uncertainty between 5.9% and 8.4% [12] while in the second one the energy range from 2 to 5 GeV was scanned at 85 energy points with an average systematic uncertainty of about 7% [13]. Despite the rather detailed information on R collected by BES, no data on the cross-sections of exclusive channels or on the parameters of broad charmonia in this energy range are available yet from this experiment. As a result, the resonance properties of $\psi(4040), \psi(4160)$ and $\psi(4415)$ are still determined by the older DASP [8] and MARK I [9] measurements. A comparison of these experiments is presented in Table 6.1 whereas Fig. 6.1 shows the energy dependence of R between 3.6 and 5 GeV measured by PLUTO, Crystal Ball and BES.

A controversial situation exists between 5 and 7 GeV where R values measured by MARK I [10] are substantially higher than both those of Crystal Ball [14] and the prediction of perturbative QCD, see Fig. 6.2. The result of Crystal Ball is in fair agreement with the QCD prediction. Two groups, LENA [15] and MD-1 [16, 17], performed measurements in the broad energy range from 7.4 to 9.4 GeV and 7.2 to 10.34 GeV, respectively. Information on these experiments is summarised in Table 6.2.

Table 6.1: R Measurement at charmonium threshold

Group	PLUTO [7]	DASP [8]	MARK I [10]	Cr. Ball [11]	BES [12, 13]
Solid angle, $\Omega/4\pi$	0.86	0.6	0.65	0.93	0.80
Energy $\sqrt{s}$, GeV	$3.1 - 4.8$	$3.1 - 5.2$	$2.6 - 5.0$	$3.87 - 4.50$	$3.0 - 5.0$
$\int Ldt$, nb^{-1}	~ 3000	7500	~ 1500	~ 2000	~ 2500
Events	~ 20000	~ 40000	~ 7000	~ 22000	~ 35000
Av. efficiency, %	$70 - 80$	$35 - 40$	$30 - 60$	85	$70 - 80$
Syst. error, %	12	15	$10 - 20$	10	7

Table 6.2: R Measurements from 5 to 10 GeV

Group	MARK I [10]	Crystal Ball [14]	LENA [15]	MD-1 [17]
Solid angle, $\Omega/4\pi$	0.65	0.93	0.75	0.7
Energy $\sqrt{s}$, GeV	$5.0 - 7.8$	$5.0 - 7.4$	$7.4 - 9.4$	$7.80 - 10.45$
$\int Ldt$, nb^{-1}	~ 3300	~ 1500	1140	16000
Events	~ 20000	~ 11000	4050	48000
Av. efficiency, %	60	85	$82 - 90$	50
Syst. error, %	10	10	7	3.9

Various groups have measured the value of R in the narrow energy range in the vicinity of the Υ-family resonances [18–25]. The highest systematic accuracy of 1.9% was reached by CLEO [25]. We summarise the obtained values of R in Table 6.3. No energy dependence is observed within the experimental accuracy, which is not surprising taking into account that most of the measurements were made below the open beauty threshold.

In Fig. 6.2, we present the results of R Measurements below 10 GeV [4]. Only statistical errors are shown. The relative uncertainty assigned by the authors of Ref. [4] to their parameterisation, displayed as the solid line, is shown as a band and given with the numbers at the bottom.

The hadronic cross-section above the $B\bar{B}$ threshold (a centre-of-mass energy range from 10.60 to 11.25 GeV) was measured by the CUSB [26] and the CLEO [27] collaborations with an integrated luminosity of 123 pb^{-1} and 70 pb^{-1}, respectively. This energy range is of substantial interest since in quarkonium potential models two excited states are expected there [28]. Moreover the coupled-channel models also predict a rich structure in R due to the turn-on of various exclusive states [29]. Both groups observe similar structures and provide compatible parameters for the two highest states at 10.865 GeV and 11.019 GeV, tentatively referred to as $\Upsilon(5S)$ and $\Upsilon(6S)$. However, the values of these parameters are obtained under different assumptions, thus, their formal averaging presently applied by the PDG [30] hardly makes sense, as noted in Ref. [31]. There is also a visible step between the continuum points below the $\Upsilon(4S)$ and the average level above it. In Fig. 6.3(a) we show the results for the visible R ratio, R_{vis}, in this energy range obtained by CUSB [26]. Their results with an additional thrust cut to suppress the continuum are shown in Fig. 6.3(b).

It is important to note that for various applications, e.g., for extracting quark masses from spectral moments, it is necessary to know the component of R coming from a specific quark flavour, particularly in the threshold energy range. Experimentally, this is a rather complicated problem. One of the theory-driven possibilities can be illustrated by a method used in a recent charm mass determination [32]. For the energy range from 3.73 to 4.8 GeV the authors employ the data for the total R obtained by the
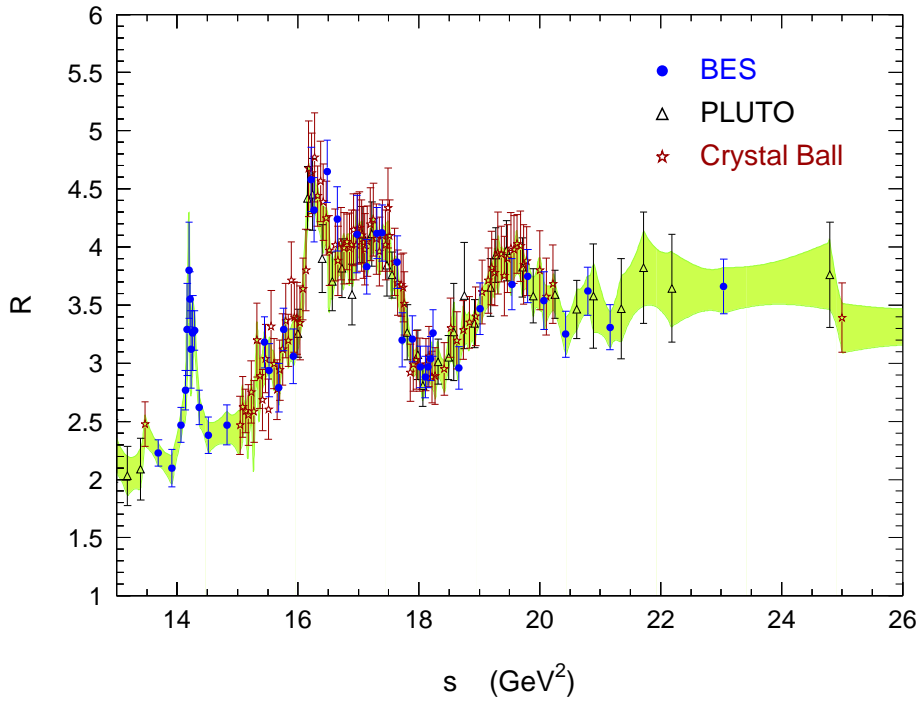
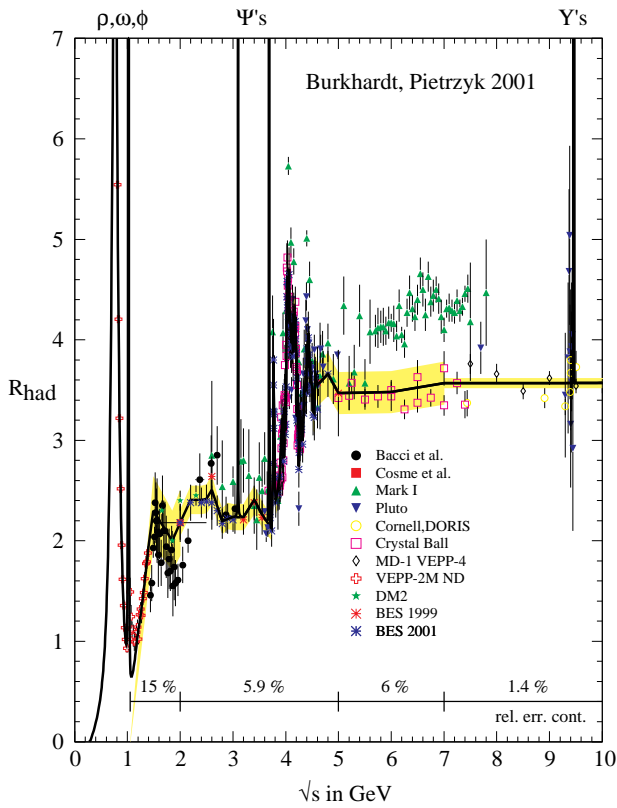Fig. 6.1: Results of R Measurements between 3.6 and 5 GeV

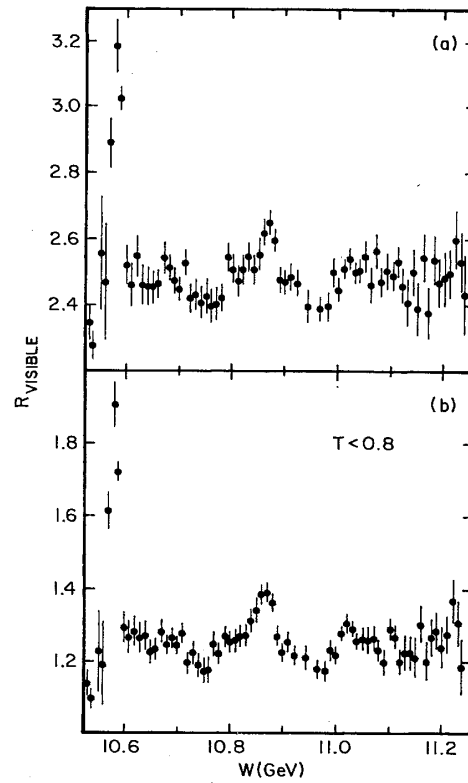Fig. 6.2: Results of R Measurements below 10 GeV

Fig. 6.3: (a) R_{vis} vs. total energy W measured by CUSB. (b) Same as (a) with a thrust cut to suppress continuum.

Table 6.3: Values of R in the Υ-family range

Group	Energy, $\sqrt{s}$, GeV	R
PLUTO [18]	9.4	$3.70 \pm 0.30 \pm 0.56$
DHHM [19]	9.4–9.5	$3.80 \pm 0.27 \pm 0.42$
	9.98–10.1	$3.60 \pm 0.36 \pm 0.54$
LENA [15]	7.4–9.4	$3.37 \pm 0.06 \pm 0.23$
ARGUS [20]	9.40–9.44,	$3.73 \pm 0.16 \pm 0.28$
	9.49–9.60	
CUSB [21]	10.34–10.52	$3.54 \pm 0.05 \pm 0.39$
CLEO [22]	10.49	$3.77 \pm 0.06 \pm 0.24$
Crystal Ball [23]	9.39	$3.48 \pm 0.04 \pm 0.16$
ARGUS [24]	9.36	$3.46 \pm 0.03 \pm 0.13$
MD-1 [17]	7.34–10.24	$3.58 \pm 0.02 \pm 0.14$
CLEO [25]	10.52	$3.56 \pm 0.01 \pm 0.07$

BES collaboration [13]. To obtain the charm component of R, R_{cc}, they first fit the non-charm R ratio, R_{nc}, assuming its energy independence and using the last four data points below 3.73 GeV. Finally, R_{cc} is obtained by subtracting the fitted values of R_{nc} from R_{tot}. Note that to estimate the final error of R_{cc} in this method a sophisticated analysis of various experimental uncertainties is needed. Another possibility is to reconstruct all exclusive final states containing particles with a corresponding quark flavour. For example, in the vicinity of the charm threshold one can assume that the corresponding R component, R_{cc}, is saturated by the contributions from the $D\bar{D}, D\bar{D}^*, D^*\bar{D}^*$ final states. Clearly, this method crucially depends on the assumptions made and requires reliable reconstruction of various final states. One should hope that an analysis of the already collected data samples as well as that of the new energy scan of the relevant energy range planned by BES will clarify the situation. In the future, substantial progress in the charmonium energy range can be expected from CLEOc and the $c - \tau$ factory. Prospects for the bottomonium energy range are less clear since both B-factories are running at the peak of the $\Upsilon(4S)$ only.

One should also take into account new possibilities suggested by the method of radiative return or initial state radiation (ISR) [33, 34]. Recently BaBar successfully applied this method to the detection of the $J/\psi \to \mu^+\mu^-$ decay [35]. The peak cross-section of this process was measured with a 2.2% systematic error and, using the world average values for the leptonic branching ratios, the total and leptonic width was obtained with an accuracy better than the world average. Also studied were various exclusive final states with pions and kaons. For example, the $2\pi^+2\pi^-$ final state with a hadronic mass from 900 to 3000 MeV was successfully studied and the corresponding cross-section already has better accuracy than all other experiments at fixed energy [36]. Also an inclusive approach was applied, where the hadronic mass is extracted from the ISR photon energy. However, in this method the resolution deteriorates rapidly for low recoil masses.

Now let us briefly discuss which accuracy seems ultimately feasible in future experiments under "ideal" detection and analysis conditions. The consideration of the experimental papers on R measurements, which claimed the smallest systematic uncertainty in the charmonium region (those of BES [12, 13]) and in the bottomonium region (those of MD-1 [17] and CLEO [25]) allows the following conclusions.

– The four main sources of systematic uncertainties are selection criteria, luminosity determination, detection efficiency and radiative corrections.

- The uncertainty caused by selection criteria is dominated by the knowledge of background. To large extent its level depends on the detector performance and ranges from 0.5% for CLEO to 2.0% for MD-1. We consider the value of 0.5% as a very aggressive one, which can hardly be improved and will further assume the value (0.5–1.0)%.

- The uncertainty due to the luminosity determination was 1% for CLEO after a very thorough analysis of the three normalisation processes Bhabha scattering, $e^+e^- \to \mu^+\mu^-$ and $e^+e^- \to \gamma\gamma$ [37]. One of the factors restricting the accuracy at that time was the knowledge of radiative corrections for the normalisation process, which was of the order of 1% [38]. Today the cross-section of the main QED processes is known to better than 0.2% [39]. Taking also into account the experience gained at LEP, it doesn't look impossible to achieve the level of 0.5 to 0.7%.

- The detection efficiency is usually obtained by Monte Carlo simulations of the experiment using the package JETSET [40] or its modification adapted to the charmonium energy range for the BES experiment [41]. The corresponding contribution to the uncertainty was 1% for CLEO and 2 to 3% for BES. Note that this contribution is very sensitive to the solid angle coverage. Therefore, a value of 1% for the future 4π detectors seems accessible.

- The modern approach to the calculation of the radiative corrections for the final hadronic state based on structure functions yields formulae with an intrinsic accuracy of about 0.5% [42]. Some uncertainty is induced by the calculational procedure itself, e.g., by the choice of the maximum allowed energy. This leads to an error of about 0.7 to 0.8%.

Finally, assuming that all four sources of the uncertainty are independent and adding the corresponding estimates in quadrature, one obtains that the ultimate systematic uncertainty could be as low as 1.4 to 1.8%. This is of course a very optimistic estimate. However, it should be possible to reach 3% in a dedicated R measurement.

3   BOTTOM AND CHARM QUARK MASS DETERMINATIONS

At the ongoing and future B-physics experiments the values of the bottom and charm quark masses and realistic estimates of their uncertainties will become increasingly important for the measurements of the CKM parameters and the search for new physics. However, due to confinement and the non-perturbative aspects of the strong interaction, the concept of quark masses cannot be tied to an intuitive picture of the weight or the rest mass of a particle, such as for leptons, which are to very good approximation insensitive to the strong interactions. Rather, analogous to the strong coupling α_s, quark masses should be considered as couplings of the Standard Model Lagrangian that have to be determined from processes that depend on them. As such, quark masses are quantities that depend on the renormalisation scheme that is used and in general also on the renormalisation scale. Although physical quantities do not depend on the renormalisation scheme, the question of which quark mass scheme should be employed can be relevant in order to avoid correlations to other unknown parameters or a badly converging perturbative expansion.

3.1   Quark mass definitions in perturbation theory

In principle, one is free to employ any renormalisation scheme, or definition for the quark masses. In the framework of QCD perturbation theory, the difference between two mass schemes can be expressed as a series in powers of the strong coupling α_s. Therefore, higher-order terms in the perturbative expansion of a quantity that depends on quark masses are affected by the renormalisation scheme that is employed. Moreover, certain schemes turn out to be more appropriate or more convenient for some purposes than others. In the following, we review some of the most common quark mass definitions, focusing for definiteness on the case of the bottom quark.

Pole mass

The bottom quark pole mass $m_{b,\text{pole}}$ is defined as the solution to the full inverse quark propagator,

$$\not{p} - m_{b,\text{pole}} - \Sigma(p, m_{b,\text{pole}})\Big|_{p^2 = m_{b,\text{pole}}^2} = 0\,, \tag{6.2}$$

where $\Sigma(p, m_b)$ is the bottom quark self energy. The pole mass definition is gauge-invariant and infrared-safe to all orders in perturbation theory [43,44] and has been used as the standard mass definition of many perturbative computations in the past. By construction, the pole mass is directly related to the concept of the mass of a free quark, which is, however, problematic because free quarks do not appear in nature. In practical applications the pole mass has the additional disadvantage that the perturbative series relating it to physical quantities are in general not well convergent, due to a strong sensitivity of the pole mass definition to small scales [45,46]. This property of the pole mass, often called the "pole-mass renormalon problem", is not related to any physical effect. The bad convergence of the perturbative expansion of quantities in the pole mass scheme indicates that the concept of the pole mass is ambiguous to an amount of order Λ_{QCD}. This issue is reviewed in more detail in Section 3.4.

Nevertheless, in low orders of perturbation theory, there is in principle nothing wrong to employ the pole mass as an intermediate quantity, as long as it is used in a consistent way. In particular, the presence of a renormalon ambiguity [45, 46] requires considering the numerical value of the pole mass as an order-dependent quantity. Because this makes estimates of uncertainties difficult, the pole mass definition should be avoided for analyses where quark mass uncertainties smaller than Λ_{QCD} are desired. The problems of the pole mass definition can be easily avoided if one uses quark mass definitions that are less sensitive to small momenta and do not have an ambiguity of order Λ_{QCD}. Such quark mass definitions are generically called "short-distance" masses. In contrast to the pole mass, short-distance masses have a parametric ambiguity of order $\Lambda_{\text{QCD}}^2/m_b$ or smaller.

$\overline{\text{MS}}$ *mass*

The most common short-distance quark mass parameter is the $\overline{\text{MS}}$ mass $\overline{m}_b(\mu)$, which is defined by regulating QCD with dimensional regularisation and subtracting only the $1/\epsilon$-divergences in the $\overline{\text{MS}}$ scheme [47]. Besides the renormalisation scheme, the $\overline{\text{MS}}$ mass also depends on the renormalisation scale μ. Since the subtractions do not contain any infrared sensitive terms, the bottom $\overline{\text{MS}}$ mass is only sensitive to scales of order or larger than m_b. The relation between the pole mass and the $\overline{\text{MS}}$ mass is known to $\mathcal{O}(\alpha_s^3)$ [48–50] and reads for massless light quarks ($\bar{\alpha}_s \equiv \alpha_s^{(n_l=4)}(\overline{m}_b(\overline{m}_b))$):

$$\frac{m_{b,\text{pole}}}{\overline{m}_b(\overline{m}_b)} = 1 + \frac{4}{3}\frac{\bar{\alpha}_s}{\pi} + \left(13.44 - 1.04\,n_l\right)\left(\frac{\bar{\alpha}_s}{\pi}\right)^2 + \left(190.6 - 26.7\,n_l + 0.65\,n_l^2\right)\left(\frac{\bar{\alpha}_s}{\pi}\right)^3 + \ldots\,. \tag{6.3}$$

The corrections coming from light quark masses at order α_s^2 are fully known [48], while at order α_s^3 only the dominant light quark mass corrections have been determined [51]. The bottom quark $\overline{\text{MS}}$ mass arises naturally in processes where the bottom quark is far off-shell. The scale μ in the $\overline{\text{MS}}$ mass is typically chosen of the order of the characteristic energy scale of the process under consideration since perturbation theory contains logarithmic terms $\sim \alpha_s(\mu)^n \ln(Q^2/\mu^2)$ that would be large otherwise. Using the renormalisation group equation for $\overline{m}_b(\mu)$, the values of the $\overline{\text{MS}}$ mass for different μ can be related to each other. The $\overline{\text{MS}}$ mass definition is less useful for processes in which the bottom quark is close to its mass-shell, which also includes when the bottom quark has non-relativistic energies.

Threshold masses

The shortcomings of the pole and the $\overline{\text{MS}}$ masses in describing non-relativistic bottom quarks can be resolved by so-called threshold masses [52]. The threshold masses do not possess the ambiguity of order Λ_{QCD} and, at the same time, are defined through subtractions that contain contributions that are universal

for the dynamics of non-relativistic quarks. Since the subtractions are not unique, an arbitrary number of threshold masses can be constructed. In the following some threshold mass definitions that appear in the literature are briefly reviewed.

Kinetic mass

The kinetic mass is defined as [53, 54]

$$m_{b,\text{kin}}(\mu_{\text{kin}}) = m_{b,\text{pole}} - \left[\bar{\Lambda}(\mu_{\text{kin}})\right]_{\text{pert}} - \left[\frac{\mu_\pi^2(\mu_{\text{kin}})}{2m_{b,\text{kin}}(\mu_{\text{kin}})}\right]_{\text{pert}} + \dots, \tag{6.4}$$

where $[\bar{\Lambda}(\mu_{\text{kin}})]_{\text{pert}}$ and $[\mu_\pi^2(\mu_{\text{kin}})]_{\text{pert}}$ are perturbative evaluations of HQET matrix elements that describe the difference between the pole mass and the B meson mass. The ellipses indicate matrix elements of operators with higher dimension, which have not been included in any analysis so far.

The relation between the kinetic mass and the $\overline{\text{MS}}$ mass is known to $\mathcal{O}(\alpha_s^2)$ and $\beta_0 \mathcal{O}(\alpha_s^3)$ [55, 56]. The formulae for $[\bar{\Lambda}(\mu_{\text{kin}})]_{\text{pert}}$ and $[\mu_\pi^2(\mu_{\text{kin}})]_{\text{pert}}$ at $\mathcal{O}(\alpha_s^2)$ read [56]

$$\left[\bar{\Lambda}(\mu_{\text{kin}})\right]_{\text{pert}} = \frac{4}{3} C_F \mu_{\text{kin}} \frac{\alpha_s(\overline{m})}{\pi} \left\{1 + \frac{\alpha_s}{\pi}\left[\left(\frac{4}{3} - \frac{1}{2}\ln\frac{2\mu_{\text{kin}}}{\overline{m}}\right)\beta_0 - C_A\left(\frac{\pi^2}{6} - \frac{13}{12}\right)\right]\right\}, \tag{6.5}$$

$$\left[\mu_\pi^2(\overline{m})\right]_{\text{pert}} = C_F \mu_{\text{kin}}^2 \frac{\alpha_s(\overline{m})}{\pi} \left\{1 + \frac{\alpha_s}{\pi}\left[\left(\frac{13}{12} - \frac{1}{2}\ln\frac{2\mu_{\text{kin}}}{\overline{m}}\right)\beta_0 - C_A\left(\frac{\pi^2}{6} - \frac{13}{12}\right)\right]\right\}, \tag{6.6}$$

where $\overline{m} \equiv \overline{m}_b(\overline{m}_b)$, $C_F = 4/3$, and $\beta_0 = 11 - 2n_f/3$ is the one-loop beta function. For $\mu_{\text{kin}} \to 0$ the kinetic mass reduces to the pole mass.

Potential-subtracted mass

The potential-subtracted (PS) mass is similar to the kinetic mass, but arises considering the static energy of a bottom–antibottom quark pair in NRQCD [57]. The PS mass is known to $\mathcal{O}(\alpha_s^3)$ and its relation to the pole mass reads

$$m_{b,\text{PS}}(\mu_{\text{PS}}) = m_{b,\text{pole}} - C_F \mu_{\text{PS}} \frac{\alpha_s(\mu)}{\pi} \left\{1 + \frac{\alpha_s(\mu)}{4\pi}\left[a_1 - \beta_0\left(\ln\frac{\mu_{\text{PS}}^2}{\mu^2} - 2\right)\right]\right. \tag{6.7}$$

$$\left. + \left(\frac{\alpha_s(\mu)}{4\pi}\right)^2\left[a_2 - (2a_1\beta_0 + \beta_1)\left(\ln\frac{\mu_{\text{PS}}^2}{\mu^2} - 2\right) + \beta_0^2\left(\ln^2\frac{\mu_{\text{PS}}^2}{\mu^2} - 4\ln\frac{\mu_{\text{PS}}^2}{\mu^2} + 8\right)\right]\right\},$$

where $\beta_1 = 102 - 38n_f/3$ is the coefficient of the two-loop beta function, and $a_1 = 31/3 - 10n_f/9$ as well as $a_2 = 456.749 - 66.354\,n_f + 1.235\,n_f^2$ [58, 59] are perturbative coefficients appearing in the static heavy $q\bar{q}$ potential. For $\mu_{\text{PS}} \to 0$ the PS mass also reduces to the pole mass.

1S mass

The kinetic and the potential-subtracted mass depend on an explicit subtraction scale to remove the universal infrared sensitive contributions associated with the non-relativistic heavy quark dynamics. The 1S mass [60–62] achieves the same task without a factorisation scale, since it is directly related to a physical quantity. The bottom 1S mass is defined as one half of the perturbative contribution to the mass of the $n = 1$, $^{2s+1}L_j = {}^3S_1$ quarkonium bound state in the formal limit $m_b \gg m_b v \gg m_b v^2 \gg \Lambda_{\text{QCD}}$. To three loop order (or NNLO in the non-relativistic expansion) the 1S-pole mass relation reads

$$\frac{m_{b,\text{1S}}}{m_{b,\text{pole}}} = 1 - \frac{1}{8}\left(C_F\alpha_s(\mu)\right)^2\left\{1 + \frac{\alpha_s(\mu)}{\pi}\left[\beta_0\left(L + 1\right) + \frac{a_1}{2}\right]\right.$$

$$+ \left(\frac{\alpha_{\rm s}(\mu)}{\pi} \right)^2 \left[\beta_0^2 \left(\frac{3}{4} L^2 + L + \frac{\zeta_3}{2} + \frac{\pi^2}{24} + \frac{1}{4} \right) + \beta_0 \frac{a_1}{2} \left(\frac{3}{2} L + 1 \right) \right. \tag{6.8}$$

$$\left. + \frac{\beta_1}{4} \left(L + 1 \right) + \frac{a_1^2}{16} + \frac{a_2}{8} + \left(C_A - \frac{C_F}{48} \right) C_F \pi^2 \right] \Bigg\},$$

where $L \equiv \ln(\mu/(C_F \alpha_{\rm s}(\mu)\, m_{b,{\rm pole}}))$ and $\zeta_3 = 1.20206$. The expression for the 1S mass is derived in the framework of the non-relativistic expansion, where powers of the bottom quark velocity arise as powers of $\alpha_{\rm s}$ in the 1S mass definition. Thus, to achieve the renormalon cancellation in the 1S mass scheme for quantities which are not defined in the non-relativistic power counting, such as for B decays, it is mandatory to treat terms of order $\alpha_{\rm s}^{n+1}$ in Eq. 6.8 as being of order $\alpha_{\rm s}^n$. This prescription is called "Upsilon expansion" [60, 61] (see also Ref. [63]) and arises because of the difference between the non-relativistic power counting and the usual counting in the numbers of loops (or in powers of $\alpha_{\rm s}$). In the upsilon expansion it is crucial that the renormalisation scale of all $\alpha_{\rm s}$ terms is chosen equal.

Renormalon-subtracted mass

The renormalon-subtracted mass [64] is formally defined as the perturbative series that results from subtracting all non-analytic pole terms from the Borel transform of the pole-$\overline{\rm MS}$ mass relation at $u = 1/2$ with a fixed choice for the renormalisation scale $\mu = \mu_{\rm RS}$. The scale $\mu_{\rm RS}$ is then kept independent from the renormalisation scale used for the computation of the quantities of interest. The expression for the relation between the RS and pole mass reads

$$m_{\rm RS(RS')}(\mu_{\rm RS}) = m_{\rm pole} - \sum_{n=0(1)}^{\infty} N_m\, \mu_{\rm RS} \left(\frac{\beta_0}{2\pi} \right)^n \alpha_{\rm s}^{n+1}(\mu_{\rm RS}) \sum_{k=0}^{\infty} c_k \frac{\Gamma(n+1+b-k)}{\Gamma(1+b-k)}, \tag{6.9}$$

where the coefficients c_1 and c_2 are known from Refs. [64, 65]. An approximation to the term N_m has been determined in Refs. [64, 66]. The values given in Table 6.4 refer to the RS' scheme.

In Table 6.4 b-quark threshold mass parameters are compared numerically taking the $\overline{\rm MS}$ mass $\overline{m}_b(\overline{m}_b)$ as a reference value for different values of the strong coupling. Each entry corresponds to the mass using the respective 1-loop/2-loop/3-loop relations.

3.2 Bottom quark mass from Upsilon sum rules

The spectral sum rules for $\sigma(e^+e^- \to b\bar{b})$ start from the correlator of two electromagnetic bottom quark currents

$$(q_\mu q_\nu - g_{\mu\nu} q^2)\, \Pi(q^2) = \int dx\, e^{i\, qx} \langle 0 | T\, j_\mu^b(x)\, j_\nu^b(0) | 0 \rangle, \tag{6.10}$$

where $j_\mu^b(x) \equiv \bar{b}(x)\gamma_\mu b(x)$. Using causality and the optical theorem one can relate theoretically calculable derivatives of $\Pi(q^2)$ at $q^2 = 0$ to moments of the total cross-section $\sigma(e^+e^- \to b\bar{b})$,

$$\mathcal{M}_n = \frac{12\,\pi^2\, Q_b^2}{n!} \left(\frac{d}{dq^2} \right)^n \Pi(q^2) \Bigg|_{q^2=0} = \int \frac{ds}{s^{n+1}}\, R_{bb}(s), \tag{6.11}$$

where $R_{bb} \equiv \sigma(e^+e^- \to b\bar{b})/\sigma(e^+e^- \to \mu^+\mu^-)$. From the comparison of the theoretical moments and those based on experimental data for R_{bb}, it is possible to determine the bottom quark mass [68]. Since the sum rules in Eq. (6.11) involve inclusive quantities referring only to global duality, they are believed to be one of the most reliable tools to extract QCD parameters. However, it is necessary to restrict the values of n to ensure that the moments are indeed sufficiently inclusive.

In general, one can distinguish between two regions in n, which require a different theoretical treatment. For low values of n the moments are dominated by relativistic dynamics and scales of order

Table 6.4: Numerical values for b-quark masses in units of GeV for a given $\overline{\text{MS}}$ mass $\overline{m}_b(\overline{m}_b)$, $n_l = 4$ and three values of $\alpha_s^{(5)}(m_Z)$. Flavour matching was carried out at $\mu = \overline{m}_b(\overline{m}_b)$. Numbers with a star are given in the large-β_0 approximation. The 1S and kinetic masses are frequently used in the theoretical description of inclusive B meson decays [67].

$\overline{m}_b(\overline{m}_b)$	$m_{b,\text{pole}}$	$m_{b,\text{kin}}(1\,\text{GeV})$	$m_{b,\text{PS}}(2\,\text{GeV})$	$m_{b,\text{1S}}$	$m_{b,\text{RS}'}(2\,\text{GeV})$
$\alpha_s^{(5)}(m_Z) = 0.116$					
4.10	4.48/4.66/4.80	4.36/4.42/4.45*	4.29/4.37/4.40	4.44/4.56/4.60	4.48/4.58/4.62
4.15	4.53/4.72/4.85	4.41/4.48/4.50*	4.35/4.42/4.45	4.49/4.61/4.65	4.53/4.64/4.67
4.20	4.59/4.77/4.90	4.46/4.53/4.56*	4.40/4.48/4.51	4.54/4.66/4.71	4.59/4.69/4.73
4.25	4.64/4.83/4.96	4.52/4.59/4.61*	4.46/4.53/4.56	4.60/4.72/4.76	4.64/4.75/4.78
4.30	4.69/4.88/5.01	4.57/4.64/4.67*	4.51/4.59/4.62	4.65/4.77/4.81	4.69/4.80/4.84
$\alpha_s^{(5)}(m_Z) = 0.118$					
4.10	4.49/4.69/4.84	4.37/4.44/4.46*	4.30/4.38/4.41	4.45/4.57/4.62	4.49/4.60/4.64
4.15	4.55/4.74/4.89	4.42/4.49/4.52*	4.36/4.43/4.47	4.50/4.63/4.67	4.55/4.66/4.70
4.20	4.60/4.80/4.94	4.47/4.55/4.57*	4.41/4.49/4.52	4.55/4.68/4.73	4.60/4.71/4.75
4.25	4.65/4.85/5.00	4.52/4.60/4.63*	4.46/4.54/4.58	4.61/4.73/4.78	4.65/4.77/4.81
4.30	4.71/4.91/5.05	4.58/4.66/4.69*	4.52/4.60/4.63	4.66/4.79/4.84	4.71/4.82/4.86
$\alpha_s^{(5)}(m_Z) = 0.120$					
4.10	4.51/4.72/4.88	4.37/4.45/4.48*	4.31/4.39/4.43	4.46/4.59/4.64	4.51/4.63/4.67
4.15	4.56/4.77/4.93	4.43/4.51/4.54*	4.36/4.45/4.48	4.51/4.64/4.70	4.56/4.68/4.72
4.20	4.61/4.83/4.99	4.48/4.56/4.59*	4.42/4.50/4.54	4.56/4.70/4.75	4.61/4.74/4.78
4.25	4.67/4.88/5.04	4.54/4.62/4.65*	4.47/4.56/4.59	4.62/4.75/4.80	4.67/4.79/4.83
4.30	4.72/4.94/5.10	4.59/4.67/4.71*	4.53/4.61/4.65	4.67/4.81/4.86	4.72/4.85/4.89

of the heavy quark mass m_b. This allows to apply the usual expansion in the number of loops for the theoretical computations, and the $\overline{\text{MS}}$ scheme is an appropriate choice for the heavy quark mass parameter. However, the lack of data for R_{bb} in the continuum regions above the quarkonium resonances introduces model-dependent errors. On the other hand, for large values of n the continuum regions are suppressed and the moments become dominated by the quarkonium resonance region where good sets of data have been obtained in the past. However, the theoretical predictions of moments for large values of n is more complicated since the usual loop expansion breaks down and the size of non-perturbative effects increases. Here, summations of higher order contributions proportional to powers of $(\alpha_s\sqrt{n})$ need to be carried out in order to capture the relevant non-relativistic perturbative information [69, 70], and the threshold masses discussed above are appropriate choices for the heavy quark mass parameter.

Moreover, there is an upper "duality" bound for the possible choices of n since the energy range contributing to the moments, which is of order m_q/n, needs to be larger than the typical hadronization scale Λ_{QCD} [70, 71]. In the case of R_{bb} and the determination of the bottom mass, this bound is around $n = 10$. The low-n and the large-n ranges are believed to be well separated with their boundary being approximately at $n = 4$. A good number of analyses exists for small and large values of n and respecting the cancellation of the $\mathcal{O}(\Lambda_{\text{QCD}})$ renormalon contributions associated to the choice of the quark mass definition. For low as well as for large values of n it is presently believed that non-perturbative effects are negligibly small, based on the size of the contributions from the non-perturbative gluon and quark condensates in the OPE [1]. Alternative views about the validity of the standard OPE (see e.g., Ref. [72]) have not been accounted for in any analysis so far. In the following the advantages and disadvantages of the two types of sum rules are reviewed. Results for bottom quark masses obtained in recent sum

Table 6.5: Collection in historical order of recent bottom quark mass determinations in units of GeV from spectral sum rules. The uncertainties quoted in the respective references have been added quadratically. All numbers have been taken from the respective publications.

Author		$\overline{m}_b(\overline{m}_b)$	other mass	comments, Ref.
spectral sum rules				
Voloshin	95		$m_{\mathrm{pole}} = 4.83 \pm 0.01$	$8 < n < 20$, NLO; no theo. uncert. [69]
Kühn	98		$m_{\mathrm{pole}} = 4.78 \pm 0.04$	$10 < n < 20$, NLO [73]
Hoang	98		$m_{\mathrm{pole}} = 4.88 \pm 0.09$	$4 < n < 10$, NNLO [70]
Melnikov	98	4.20 ± 0.10	$M_{\mathrm{kin}}^{\mathrm{1GeV}} = 4.56 \pm 0.06$	$x < n < x$, NNLO [56]
Penin	98	4.21 ± 0.11	$m_{\mathrm{pole}} = 4.80 \pm 0.06$	$8 < n < 12$, NNLO [74]
Jamin	98	4.19 ± 0.06		$7 < n < 15$ [75, 76]
Hoang	99	4.20 ± 0.06	$M_{\mathrm{1S}} = 4.71 \pm 0.03$	$4 < n < 10$, NNLO [77]
Beneke	99	4.26 ± 0.09	$M_{\mathrm{PS}}^{\mathrm{2GeV}} = 4.60 \pm 0.11$	$6 < n < 10$, NNLO [78]
Hoang	00	4.17 ± 0.05	$M_{\mathrm{1S}} = 4.69 \pm 0.03$	$4 < n < 10$, NNLO, $m_c \neq 0$ [51]
Kühn	01	4.21 ± 0.05		$1 < n < 4$, $\mathcal{O}(\alpha_{\mathrm{s}}^2)$ [6]
Erler	02	4.21 ± 0.03		$\mathcal{O}(\alpha_{\mathrm{s}}^2)$ [79]
Eidemüller	02	4.24 ± 0.10	$M_{\mathrm{PS}}^{\mathrm{2GeV}} = 4.56 \pm 0.11$	$3 < n < 12$ [80]
Bordes	02	4.19 ± 0.05		$\mathcal{O}(\alpha_{\mathrm{s}}^2)$ [81]
Corcella	02	4.20 ± 0.09		$1 < n < 3$, $\mathcal{O}(\alpha_{\mathrm{s}}^2)$ [31]
Ahmady	04	4.21 ± 0.01		$1 < n < 4$, $\mathcal{O}(\alpha_{\mathrm{s}}^2)$ only scale + mom. uncert. [82]

rule analyses have been collected in Table 6.5 and a graphical summary is presented as the red circles in Fig. 6.4.

Non-relativistic sum rules

The large-n sum rules have the advantage that the experimentally unknown parts of the $b\bar{b}$ continuum cross-section above the Υ resonance region are suppressed. A crude model for the continuum cross-section is sufficient and causes an uncertainty in the b-quark mass below the 10 MeV level. Depending on which moment is used the overall experimental uncertainties in the b-quark mass are between 15 and 20 MeV. Theoretically, large-n sum rules are characterised by the fact that the dynamics is non-relativistic. It can be shown that the average three-momentum and the average kinetic energies of the quarks scale like $m_b/\sqrt{n}$ and m_b/n, respectively. Thus for $n \leq 10$ the moments can be considered as being dominated by perturbation theory up to non-perturbative effects that can be described by the standard OPE [1] in terms of local condensates. The leading-order gluon condensate contributions to the large-n sum rules were determined in Refs. [69, 83] and shown to contribute at the level of permille for $n \leq 10$ [69]. None of the analyses discussed below therefore included any non-perturbative effects. It should be noted, however, that in practice a strong hierarchy of all relevant dynamical scales, $m_b \gg m_b/\sqrt{n} \gg m_b/n \gg \Lambda_{\mathrm{QCD}}$, is difficult to achieve numerically. So a successful application of the large-n sum rules is based on a balance between a good non-relativistic expansion and a good convergence of the OPE series. Over the past years there has been a revived interest in non-relativistic sum rules because new theoretical developments allowed for the systematic determination of $\mathcal{O}(v^2) \sim \mathcal{O}(1/n)$ (NNLO) corrections to the spectral moments [51, 56, 70, 74, 77, 78].
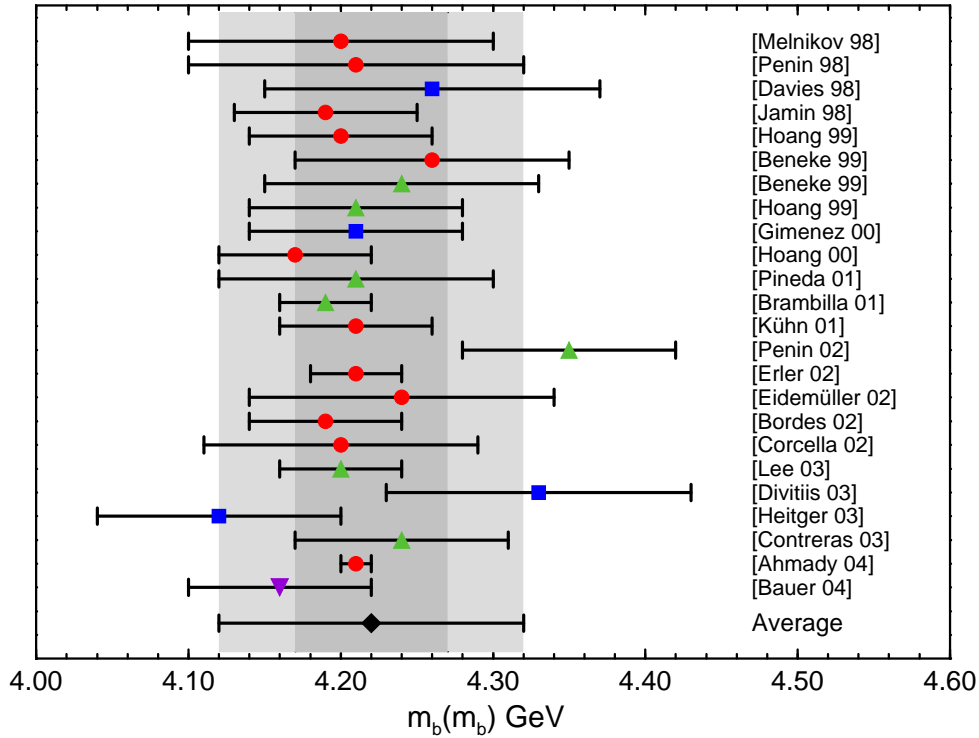
Fig. 6.4: Collection in historical order of recent bottom quark mass determinations. The red circles represent sum rule results, the green triangles Upsilon 1S determinations, the blue squares lattice QCD results and the purple upside down triangle a determination from semileptonic B decays. The full diamond gives our global average for $\overline{m}_b(\overline{m}_b)$. The darker and lighter shaded areas represent our subjective error estimates corresponding to a 1σ error and a range respectively. Our average and the related error estimates are further discussed in Section 3.6.

All analyses found that the NNLO corrections were as large or even larger than the NLO corrections and various different methods were devised to extract numerical values for the bottom quark mass. In Refs. [51, 56, 77, 78] threshold masses were implemented accounting for the renormalon problem. This removed one source of the bad perturbative behaviour, but it was found that a considerable theoretical uncertainty remained, coming from the theoretical description of the production and annihilation probability of the $b\bar{b}$ pair. In Refs. [56] and [78] the kinetic and the PS mass were determined from fits of individual moments. It was found that the NLO and NNLO results for the bottom mass differ by about 200 MeV. In Ref. [56] it was argued that the results form an alternating series and a value of $m_{b,\mathrm{kin}}(1\,\mathrm{GeV}) = 4.56 \pm 0.06(\mathrm{ex,th})$ GeV was determined. In Ref. [78] only the NNLO results were accounted based on consistency arguments with computations of the $\Upsilon(1\mathrm{S})$ mass and the result $m_{b,\mathrm{PS}}(2\,\mathrm{GeV}) = 4.60 \pm 0.02(\mathrm{ex}) \pm 0.10(\mathrm{th})$ GeV was obtained. In Ref. [77] the 1S mass was employed and a χ^2-fit based on four different moments was carried out. It was found that the large normalisation uncertainties drop out at NLO and NNLO and that the results for the mass at NLO and NNLO showed good convergence. The result was $m_{b,1\mathrm{S}} = 4.71 \pm 0.02(\mathrm{ex}) \pm 0.02(\mathrm{th})$ GeV. It was also shown that the sum rule analysis gives only very weak constraints on the value of the strong coupling and that sum rules are in fact not a very competitive tool to determine α_s with high precision. A subsequent analysis [51] which included the effects of the nonzero charm mass yielded $m_{b,1\mathrm{S}} = 4.69 \pm 0.02(\mathrm{ex}) \pm 0.02(\mathrm{th})$ GeV.

Relativistic sum rules

The small-n sum rules have the disadvantage that the unknown parts of the $b\bar{b}$ continuum cross-section above the Υ resonance region constitute a substantial contribution to the spectral moments. The advan-

tage is that the computation of the theoretical moments is less involved since usual perturbation theory in powers of α_s can be employed. In Ref. [6] the theoretical moments at order $\mathcal{O}(\alpha_s^2)$ were used and it was found that the perturbative behaviour of the theoretical moments is good if the $\overline{\text{MS}}$ mass scheme is used such that the pole mass ambiguity of order Λ_{QCD} is properly cancelled. For the bottom quark mass determination it was assumed that the unknown experimental continuum cross-section agrees with the perturbation theory prediction and subsequently the result $\overline{m}_b(\overline{m}_b) = 4.21 \pm 0.05$ GeV was determined. Compatible results were also obtained in an earlier analysis at larger n [75, 76] which employed the $\overline{\text{MS}}$ mass at a lower scale $\mu \approx 3$ GeV, in order to improve the stability of the sum rule. A more conservative $\mathcal{O}(\alpha_s^2)$ analysis in Ref. [31] using the same approach as employed in Ref. [6], but accounting also for finite charm mass effects, uncertainties coming from the experimental continuum region and for inconsistencies in the averages for the $\Upsilon(4S)$ and $\Upsilon(5S)$ data obtained the result $\overline{m}_b(\overline{m}_b) = 4.20 \pm 0.09$ GeV. In the same analysis non-perturbative effects in terms of the gluon condensate based on two-loop matching coefficients [84] were analysed and found to be negligible.

Alternative approaches

Besides the relativistic and non-relativistic sum rules discussed above, also alternative approaches employing other types of QCD sum rules have been investigated in the literature. These shall be briefly discussed in what follows. In Ref. [79], Erler and Luo performed an analysis based on the dispersion relation

$$12\pi^2 \left[\Pi(0) - \Pi(-t) \right] = t \int \frac{ds}{s} \frac{R_{bb}}{s+t} , \qquad (6.12)$$

in the limit $t \to \infty$, which is rather sensitive to the continuum contribution, together with low-n moments. The parameters of a certain ansatz for the shape of the continuum were constrained from the resulting sum rule, and a combined analysis led to $\overline{m}_b(\overline{m}_b) = 4.21 \pm 0.03$ GeV. In Ref. [80], on the other hand, besides the conventional moments of Eq. 6.11 which are evaluated at $q^2 = 0$, Eidemüller also studied moments being evaluated at $q^2 = -4m_b^2 \xi$ rather than at $q^2 = 0$. A variation of the parameter ξ then allows to modify the relative size of the various theoretical as well as phenomenological contributions, thus gaining further information on the system under investigation. Furthermore, for the theoretical spectral function at small velocities, a non-relativistic description was employed, whereas the relativistic description was chosen at large velocities. In addition, in the intermediate region, different choices for the matching of the two regions were studied. The resulting bottom quark mass then turned out to be $\overline{m}_b(\overline{m}_b) = 4.24 \pm 0.10$ GeV. Finally, in Ref. [81], Bordes, Penarrocha and Schilcher investigate finite energy sum rules similar to the analysis of the hadronic τ decay width. In the dispersion integral, a third degree polynomial was added, and the parameters were chosen such as to minimise the effect of the continuum contribution and the corresponding uncertainties. The final result for the bottom quark mass obtained from this analysis was $\overline{m}_b(\overline{m}_b) = 4.19 \pm 0.05$ GeV.

Recently, the analysis of inclusive semileptonic B decays has emerged as a new precise tool to determine the bottom mass taking advantage of the large amount of statistics accumulated at B-factories and the theoretical developments in heavy quark physics. In a global fit of various shape variables in semileptonic B→D decays the bottom 1S mass was determined as $m_{b,1S} = 4.68 \pm 0.04$ GeV [85] which is in very good agreement with the large-n sum rule analysis of Hoang [51] which also included the effects of a non-zero charm quark mass.

3.3 Charm quark mass from Charmonium sum rules

The determination of the charm quark mass from charmonium sum rules proceeds in principle in analogy to the bottom case. However, one needs to account for the fact that for R_{cc} and the determination of the charm mass, the distinction between large- and low-n moments is much more delicate because m_c is much smaller than m_b and in fact not much larger than Λ_{QCD}. Here, the upper duality bound for n is already around 3 or 4 and non-perturbative contributions need to be included numerically. The small

Table 6.6: Collection in historical order of recent charm quark mass determinations in units of GeV from spectral sum rules. The uncertainties quoted in the respective references have been added quadratically. All numbers have been taken from the respective publications.

Author	$\overline{m}_c(\overline{m}_c)$	other mass	comments, Ref.
spectral sum rules			
Eidemüller 00	1.23 ± 0.09	$M_{\mathrm{PS}}^{1\mathrm{GeV}} = 1.35 \pm 0.10$	$3 < n < 7$ [89]
Penarrocha 01	1.37 ± 0.09		FESR, $\mathcal{O}(\alpha_{\mathrm{s}}^2)$ [86]
Kühn 01	1.30 ± 0.03		$1 < n < 4$, $\mathcal{O}(\alpha_{\mathrm{s}}^2)$ [6]
Erler 02	1.29 ± 0.05		$\mathcal{O}(\alpha_{\mathrm{s}}^2)$ [79]
Ioffe 02	1.28 ± 0.02		$\mathcal{O}(\alpha_{\mathrm{s}}^2)$ [87]
Eidemüller 02	1.19 ± 0.11	$M_{\mathrm{PS}}^{1\mathrm{GeV}} = 1.30 \pm 0.12$	$4 < n < 7$ [80]
Hoang 04	1.29 ± 0.07		$n = 2, 3$, $\mathcal{O}(\alpha_{\mathrm{s}}^2)$ [32]

range of allowed values of n leaves basically no space at all to carry out the non-relativistic summations that can be applied in the bottom quark case because the corresponding techniques are only valid for large n and as long as m_q/n is larger than Λ_{QCD}. On the other hand, even for $n \leq 4$ the non-relativistic region close to the $c\bar{c}$ threshold can have a considerable contribution to the moments, while the model-dependences from the experimentally unknown continuum region can still be significant. Due to the recent BES data [13] for the e^+e^- total cross-section in the range up to 5 GeV a good part of the charm continuum region can be deduced using reasonable assumptions for the non-charm cross-section. For a reliable (error) analysis these issues need to be taken into account.

In Table 6.6, determinations of m_c from Charmonium sum rules within the last years have been summarised. A graphical representation of these results is also shown as the full circles in Fig. 6.5. A conservative investigation of the issues discussed above in the case of the relativistic sum rule was carried out in the very recent work [32], where also a discussion of the previous works [6,79,86,87] was given. In particular, it was found in Ref. [32] that different ways to compute the perturbative series for the moments appear to converge to different predictions if the standard methods to estimate theoretical errors are employed, a situation known also from predictions for hadronic τ decays [88]. non-relativistic sum rules for charmonium have been investigated in Refs. [80, 89]. Generally, m_c turns out to be somewhat lower in the non-relativistic case, but due to the low scale the resummation also introduces large uncertainties. To conclude, for the charm quark mass determinations relativistic sum rules appear to be more reliable than non-relativistic ones.

3.4 Bottom and charm quark mass from the 1S resonances

Compared to the sum rule methods described in the previous sections the heavy quarkonium masses are more exclusive quantities. However, since heavy quarkonia are colour singlet objects and their interactions with the QCD vacuum is suppressed at least by p^2/m^2, p being the average quark three-momentum, it is worth to consider also the heavy quarkonium masses as an alternative method to extract QCD parameters, and in particular the heavy quark masses. At this point it is instructive to mention that the momentum transferred between the heavy quark and antiquark is Euclidean. Therefore, computations of the spectrum do, at least to low orders in the perturbative expansion, not rely on local-duality and the crucial issue is whether perturbative calculations are applicable for the range of the relevant dynamical scales and whether the influence of the long-range parts of the potential is significant. It is obvious that for precise determinations of the heavy quark masses one has to be in a situation where the dynamics can be described to good approximation by a weak coupling analysis and that non-perturbative effects are subleading. While in the sum rules the average three-momentum and kinetic energy of the quarks can be
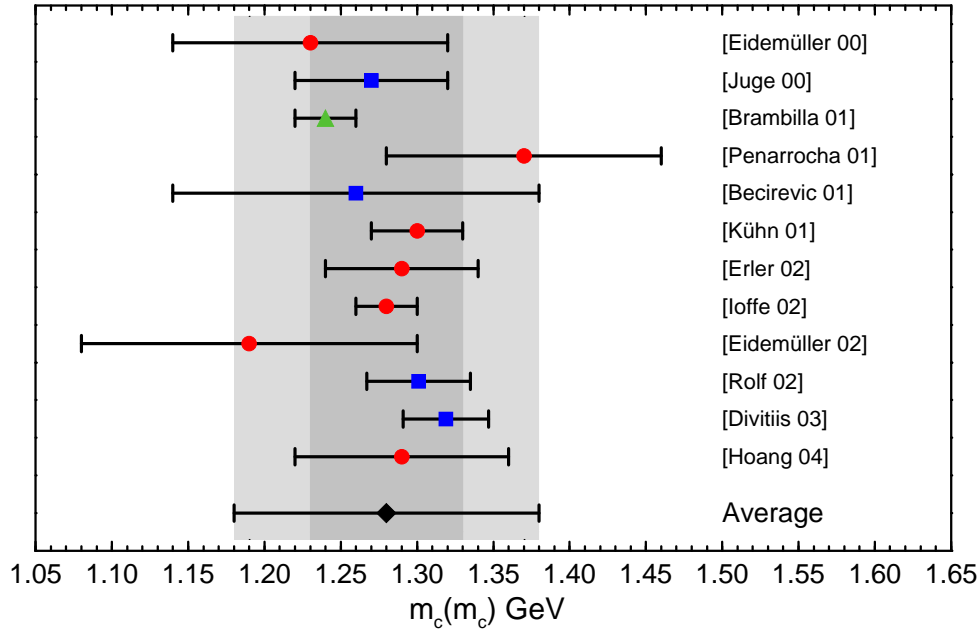
Fig. 6.5: Collection in historical order of recent charm quark mass determinations. The red circles represent sum rule results, the green triangles J/Ψ 1S determinations and the blue squares quenched lattice QCD results. The full diamond gives our global average for $\overline{m}_c(\overline{m}_c)$. The darker and lighter shaded areas represent our subjective error estimates corresponding to a 1σ error and a range respectively. Our average and the related error estimates are further discussed in Section 3.6.

influenced by adjusting the value of n, for the quarkonium states these scales are fixed by internal QCD dynamics. Thus some care has to be applied in the determination and the interpretation of the results obtained for the quarkonium masses. The average three-momentum transfer in the bottomonium is of order of or below 2 GeV whereas in the charmonium case is of order of or below 1 GeV. The corresponding average values of the quark kinetic energies are even lower. Thus it appears clear from the very beginning that only the ground states should be considered as tools for extractions of QCD parameters, cf. however Chapter 3, Section 2.3.1 for a perturbative calculation of the levels. In the following, recent work is reviewed where for the bottomonium and charmonium ground states is was assumed that a weak coupling analysis is possible.

Heavy Quarkonium Mass

It is convenient to work within an effective field theory framework. Since in the cases of bottomonium and charmonium the assumption $mv^2 \gg \Lambda_{\rm QCD}$ appears unrealistic, one might start with "optimistic" counting that $mv^2 \sim \Lambda_{\rm QCD}$. The effective theory pNRQCD has been applied to describe this situation [90–93]. (The effective theory vNRQCD has been constructed for the case $mv^2 \gg \Lambda_{\rm QCD}$ [94–96].) In the pole mass (OS) scheme the heavy quarkonium mass has the following structure,

$$M_{nlj} = 2m_{\rm pole} + \sum_{m=2}^{\infty} A_{nlj}^{m,\rm OS}(\nu_{us})\alpha_{\rm s}^m + \delta M_{nlj}^{\rm US}(\nu_{us}), \qquad (6.13)$$

where ν_{us} is a cutoff scale of order mv^2 that cancels in the sum (for the perturbative sum this dependence first appears in $A_{nlj}^{5,\rm OS}$) and

$$\delta M_{nlj}^{\rm US}(\nu_{us}) = \frac{T_F}{3N_c} \int_0^{\infty} dt \langle n,l|\mathbf{r}e^{-t(H_o^{\rm OS}-E_n^{\rm OS})}\mathbf{r}|n,l\rangle \langle g\mathbf{E}^a(t)\phi(t,0)_{ab}^{\rm adj}g\mathbf{E}^b(0)\rangle(\nu_{us}) \qquad (6.14)$$

The present status of the perturbative computations is as follows. The complete NNLO result has been computed in Refs. [74,97–99], the $\mathcal{O}(m\alpha_{\mathrm{s}}^5 \log \alpha_{\mathrm{s}})$ NNNLO terms in Refs. [100–104], the complete resummation of logs at NNLL in Refs. [96,105], the NNNLO large-β_0 result in Refs. [51,106], and some computations that complete the NNNLO result (up to the still missing three loop corrections to the static potential) in Refs. [107–109]. It should be noted that these NNNLO results were obtained assuming that $mv^2 \gg \Lambda_{\mathrm{QCD}}$, i.e., that the ultrasoft scale is perturbative. Nevertheless these computations are useful if one can identify the coefficient $A_{nlj}^{5,\mathrm{OS}}(\nu_{us})$ by separating, in a specific scheme, the contributions coming from the soft scale and those coming from the ultrasoft scale. The result obtained in Ref. [109] represents, up to the three-loop static potential coefficient, the sum

$$A_{nlj}^{5,\mathrm{OS}}(\nu_{us})\alpha_{\mathrm{s}}^5 + \delta M_{nlj}^{\mathrm{US}}(\nu_{us})|_{\mathcal{O}(\alpha_{\mathrm{s}}^5)\ \mathrm{pert.}}\,. \tag{6.15}$$

In principle, for the ground state of bottomonium, also finite mass charm effects have to be taken into account, since the soft scale is of the order of the charm mass. Estimates of finite charm mass effects are known up to NNLO [51, 110–112].

For the non-perturbative piece in Eq. 6.14, assuming $mv^2 \gg \Lambda_{\mathrm{QCD}}$, one can perform an expansion in local condensates. The leading and subleading terms are known [113–116]. An approach how to estimate the effect of even higher order condensates based on a delocalised expansion of short-distance effects was proposed in Ref. [117, 118]. However, as discussed above, in the more realistic situation where $mv^2 \sim \Lambda_{\mathrm{QCD}}$ the explicit functional form of the chromoelectric correlator is needed. On the other hand, in the situation $\Lambda_{\mathrm{QCD}} \gg mv^2$ the non-perturbative corrections to the potential scale as $\sim r^2$ (see [93, 119]) and new non-perturbative effects could exist [120]. Another point of concern relevant for the case $mv^2 \sim \Lambda_{\mathrm{QCD}}$ was pointed out in Ref. [96] using the vNRQCD framework. It was pointed out that there could be more non-perturbative effects than those encoded in Eq. (6.14) based on pNRQCD, since the soft and ultrasoft renormalisation scales are correlated and the running of the potential coefficients is affected by ultrasoft mixing effects for all scales below m. Therefore, once the ultrasoft scale approaches Λ_{QCD} also the coefficients of the potentials can become affected by non-perturbative effects.

Renormalons

If one applies the results above expressed in the pole mass scheme to heavy quarkonium ground states a quite bad convergence of the perturbative series, $A_{nlj}^{m,\mathrm{OS}} \sim m!$, is found. This situation is symptomatic for any quantity that has a strong dependence on the heavy quark mass and also exists for the sum rules reviewed in Section 3.2. Here, the bad convergence is coming from the perturbative corrections to the static potential [121], which renders the prediction of the binding energy ambiguous to an amount of order Λ_{QCD} although the left-hand side of Eq. 6.13 is an observable and ambiguity-free. This problem is directly related to the existence of the pole mass renormalon [45,46] mentioned before in Section 3.1 and represents a general feature of the pole mass scheme. It is related to an artificially strong sensitivity to small momenta in the pole mass scheme that renders the pole mass definition ambiguous to an amount of order Λ_{QCD}, but it is, to the present knowledge, not related to any physical effect. In fact, it can be shown in the Schrödinger equation that the ambiguities (and the dominant large corrections) cancel in the sum of twice the pole mass and the static potential [57, 122, 123]. Thus the resolution to the problem comes by obviating the pole mass and expressing it in terms of so-called threshold masses [45, 57, 60, 64] (see Section 3.1) so that the ambiguities cancel explicitly within the coefficients of the perturbative series; cf. also Chapter 3, Section 2.3.1 for a discussion about the renormalon subtraction in the spectrum.

One may also employ the $\overline{\mathrm{MS}}$ mass scheme using the upsilon expansion [60, 61]. Numerically the resulting series have been shown to converge well [63, 106] leading to reliable predictions. However, there are a few conceptual issues that should be mentioned. Employing the $\overline{\mathrm{MS}}$ mass scheme in the effective theory framework introduces a bilinear quark mass term of $\mathcal{O}(m\alpha_{\mathrm{s}})$ into the action, which formally breaks the non-relativistic power-counting since all leading order terms in threshold mass schemes are

Table 6.7: Collection in historical order of recent bottom and charm quark mass determinations in units of GeV from the $\Upsilon(1S)$ and $J/\Psi(1S)$ resonances. The uncertainties quoted in the respective references have been added quadratically. All numbers have been taken from the respective publications.

Author	$\overline{m}_b(\overline{m}_b)$	other mass	comments, Ref.
		$\Upsilon(1S)$ mass	
Beneke 99	4.24 ± 0.09	$M_{\mathrm{PS}}^{2\mathrm{GeV}} = 4.58 \pm 0.08$	NNLO [78]
Hoang 99	4.21 ± 0.07	$M_{1S} = 4.73 \pm 0.05$	NNLO [124]
Pineda 01	4.21 ± 0.09	$M_{\mathrm{RS}}^{2\mathrm{GeV}} = 4.39 \pm 0.11$	NNLO [64]
Brambilla 01	4.19 ± 0.03		NNLO, pert. th. only [125]
Penin 02	4.35 ± 0.07		NNNLO [109]
Lee 03	4.20 ± 0.04		NNNLO [66]
Contreras 03	4.24 ± 0.07		NNNLO [126]
	$\overline{m}_c(\overline{m}_c)$	$J/\Psi(1S)$	
Brambilla 01	1.24 ± 0.02		NNLO [127]

of order mv^2 [57, 124]. (In fact, the same happens in HQET.) Numerically this means the first order corrections in the $\overline{\mathrm{MS}}$ scheme are larger than in threshold mass schemes. The corresponding effect in $t\bar{t}$ physics has been demonstrated to be substantial [124] while for the bottom, the $\mathcal{O}(m\alpha_{\mathrm{s}})$ term does not seem to be that large numerically, being much smaller than the typical values of the soft scale in the $\Upsilon(1S)$. Conceptually this means the $\overline{\mathrm{MS}}$ mass extracted from the quarkonium mass has a smaller parametric precision than threshold masses. Another issue related to the use of the $\overline{\mathrm{MS}}$ mass is that it is impossible to avoid parametrically large logarithmic terms. If one uses a low scale $\sim m\alpha_{\mathrm{s}}$ one obtains logarithms of $m\alpha_{\mathrm{s}}/m$ from the series of the pole-$\overline{\mathrm{MS}}$ mass relation; if one uses the high scale $\sim m$, one obtains logarithms of $m\alpha_{\mathrm{s}}/m$ and $m\alpha_{\mathrm{s}}^2/m$ from the series in Eq. (6.13). For the bottomonium case these logarithms are, however, not numerically large and do not seem to spoil the perturbative expansion in practice. On the other hand, if one uses a prescription different from the upsilon expansion to avoid large logarithmic terms the cancellation of the renormalon ambiguity is incomplete.

Determination of the bottom and charm mass

In the following the different determinations of the bottom quark mass available in the literature are reviewed. The results are collected in Table 6.7. They have also been included as the full triangles in Figs. 6.4 and 6.5. In the following the main features of these analysis are summarised. In the first three references as well as in Ref. [109] no finite charm mass effects were included. In Ref. [78] a NNLO analysis was made in the PS mass scheme. The result obtained for the $\overline{\mathrm{MS}}$ mass was less precise as at the time of the analysis the conversion from the pole to the $\overline{\mathrm{MS}}$ scheme was not yet known with the required accuracy. Reference [124] contained a NNLO analysis in the 1S scheme, while in Ref. [64] the RS scheme was used at NNLO. The latter reference also contained an analysis at NNNLO including the logs at this order as well as the large β_0 result. In Ref. [125] a NNLO analysis was made including charm mass effects in the 1S scheme.[1] non-perturbative effects were not taken into account. In Ref. [109] a computation at NNNLO in the pole mass scheme was achieved, up to the still missing three-loop corrections to the static potential, which were taken from the Pade-estimates of Ref. [128].[2] The difference with the other results could be due to the presence of the renormalon as well as the fact that the ultrasoft contribution was computed within perturbation theory. Moreover, specific choices for renormalisation scale have been employed. In fact, using the upsilon expansion the authors of Ref. [109] also obtained

---

[1]The importance of the charm mass effects were first pointed out in Ref. [110].

[2]All NNNLO analyses mentioned below used the estimates of Ref. [128].

$\overline{m}_b(\overline{m}_b) = 4.274$ as the central value, which is consistent with the other results. In Ref. [66] a NNNLO analysis was made in a scheme similar to the RS one. In this reference the ultrasoft contribution was treated perturbatively. Reference [126] contains a very similar analysis but the ultrasoft contribution was treated in a different way than the soft contribution. Because the situation $mv^2 \gg \Lambda_{QCD}$ is not quite realistic, it is illustrative reanalysing these NNNLO results without the US contribution. In the results of Ref. [126] it is possible to eliminate the ultrasoft contribution in a scheme-dependent way, which shifts the $\overline{MS}$ bottom mass by around -50 MeV. There has also been a determination of the charm mass from the $J/\Psi(1S)$ mass [127]. The authors performed a NNLO analysis in the 1S scheme but did not account for non-perturbative contributions.

In the analyses discussed above, only the cancellation of the leading IR renormalon of the pole mass and the singlet static potential have been taken into account. But there are also subdominant renormalons that eventually could play a role and the following parametric consideration is useful (see also the discussion in Chapter 3, Section 2.3.1). On the singlet static potential side, one expects the first subleading ambiguities from a $\mathcal{O}(\Lambda_{QCD}^3 r^2)$ IR renormalon. From the pole mass in Eq. (6.13) there is a $\mathcal{O}(\Lambda_{QCD}^2/m)$ renormalon that is not cancelled in general in threshold mass schemes. It depends on the relative size of Λ_{QCD} and $m\alpha_s^2$ which of the ambiguities is parametrically larger. In the case $mv^2 \sim m\alpha_s^2 \gg \Lambda_{QCD}$, where a description in terms of local condensates is appropriate, the leading *genuine* non-perturbative corrections to the quarkonium mass scale like $m(\Lambda_{QCD}/m\alpha_s)^4$. However, this quantity is parametrically much smaller than the non-perturbative effects associated to the subleading renormalons, either from the pole mass or from the singlet static potential. In this case the leading remaining ambiguity comes from the subleading pole mass renormalon of $\mathcal{O}(\Lambda_{QCD}^2/m)$ and the actual accuracy of the result is set by the perturbative calculation and not by non-perturbative effects. In the more realistic situation where $m\alpha_s^2 \sim \Lambda_{QCD}$, on the other hand, the subleading renormalon ambiguities from the singlet static potential and the pole mass are of the same order as the *genuine* non-perturbative corrections.

3.5 Bottom and charm quark masses from lattice gauge theory

Lattice determinations of parameters of the QCD Lagrangian have two components. First, long-distance Monte Carlo calculations are used to fix the bare lattice quark masses m_{u0}, m_{d0}, etc. and the bare lattice coupling constant $\alpha_0(a)$ to make hadron masses and decays to match experiment. (a is the lattice spacing.) Second, short-distance calculations are used to ensure that short-distance physics with the lattice regulator is the same as short-distance physics with dimensional regularisation. The lattice parameters are converted to the $\overline{MS}$ parameters by calculating short distance quantities in both regulators and making them agree. For example, a perturbative relation between the lattice bare quark mass and the $\overline{MS}$ mass can be obtained by calculating the on-shell quark propagator with both regulators and requiring that they agree. The relation between QCD parameters in the two regulators may also be obtained from less usual quantities like the PCAC related quantity formed from the pseudoscalar density and the four-divergence of the axial vector current

$$m_{\text{PCAC}} = \frac{\langle S_1 | \partial \cdot A | S_2 \rangle}{\langle S_1 | P | S_2 \rangle}. \tag{6.16}$$

(S_1 and S_2 may be any states.) The lattice short-distance quantities may be calculated with perturbation theory as usual. They may also be calculated non-perturbatively, which makes possible robust lattice short distance calculations.

Through the 1990s, most lattice phenomenology had some degree of quantitative control over all sources of systematic error except one: the quenched approximation. In the last five years, unquenched calculations have have become more and more common, allowing more serious comparison of different lattice calculations. There are three main families of methods for including sea quarks in unquenched calculations (for more details see the lattice introduction in Chapter 1). Each has distinct advantages and complications. Wilson and clover fermions break chiral symmetry strongly at the lattice spacing, and

have practical complications in recovering it. In unquenched calculations, they have trouble reaching light quark masses much below $m_s/2$. Staggered and naive fermions can reach lightest quark masses with greatest precision and least computer time, but have theoretical complications due to fermion doubling. Domain wall and overlap fermions are theoretically the cleanest, but appear to be much more expensive in computer time.

To fix the parameters of the lattice QCD Lagrangian, including the heavy quark masses, we are free to use the hadronic quantities that are simplest for the lattice to calculate accurately. Stable particles, particularly mesons, require simpler lattice methods than unstable particles. Processes with a single hadron present at a time are simpler than multihadron processes. The numerous masses and mass splittings in the charmonium and bottomonium systems are especially suitable. Since the quarks are heavy, the difficult extrapolation of the valence quarks to the chiral limit is unnecessary. More importantly, the fact that the valence quarks are nonrelativistic means that one can apply nonrelativistic arguments, EFT and phenomenological potential models to gain a more solid understanding of systematic uncertainties than is possible with light hadrons. It implies that we have better than usual understanding of the importance of the various higher dimension correction operators that are used to improve the lattice Lagrangian. We expect in advance, for example, that some of the uncertainty arising from imprecise settings of correction operators like $\overline{\psi}\Sigma \cdot B\psi$ is cancelled in spin-averaged masses like $(3M_\psi + M_{\eta_c})/4$. On the other hand, the fact that quark momenta in quarkonia are larger than they are in light hadrons makes some discretisation errors larger. A meson like the D_s, which also has a tame chiral extrapolation, is also particularly simple to calculate on the lattice.

A variety of methods has been proposed to obtain $\overline{MS}$ masses from bare lattice quark masses (see [129] for a review of some of the methods). The standard perturbative way is to calculate the on-shell quark propagator on the lattice and in the $\overline{MS}$ scheme to a given order in perturbation theory and define renormalisation constants so that they are equal. Vector and axial vector Ward identities may be used to define a renormalised mass [130] which has been used in several ways to obtain the $\overline{MS}$ quark mass. Methods using Schrödinger functional and step-scaling functions have been developed [131].

Almost all existing unquenched lattice determinations of m_b use perturbation theory to relate the lattice quark mass to the $\overline{MS}$ mass. The best determination of the b quark mass from Bottomonium is the relatively old calculation of Davies et al. [132, 133], using NRQCD and two flavours of Wilson sea quarks. They used the mass of the Υ to set m_b. The $\overline{MS}$ mass was obtained with first-order perturbation theory from the bare lattice mass (or more precisely, from the energy shift between the meson mass and the lattice mass). They obtained for the $\overline{MS}$ mass $\overline{m}_b(\overline{m}_b) = 4.26(4)(3)(10)$ GeV. This agrees well with lattice determinations of the quark mass from the B meson mass. For example, Gimenez et al. [134, 135] use the static approximation for the b quark, and use two flavours of unquenched Wilson fermions. Incorporating a stochastic estimate of the third-order perturbative correction [136] they obtain $\overline{m}_b(\overline{m}_b) = 4.21(3)(5)(4)$ GeV. In the quenched approximation, Heitger and Sommer [137] use step-scaling methods with the static approximation for the b quark. They use non-perturbative Ward identity based methods to calculate the renormalisation constants, and obtain $\overline{m}_b(\overline{m}_b) = 4.12(7)(4)$ GeV. Divitiis et al. [138] use step-scaling methods with a relativistic formulation of both the heavy and light quarks, and non-perturbative Ward identity based determinations of the renormalisation constants. They obtain $\overline{m}_b(\overline{m}_b) = 4.33(10)$ GeV.

Unquenched determinations of m_c are just beginning to appear. A consistent lattice picture of the charm quark mass exists from quenched calculations from a few years ago. Using the charmonium spin-averaged 1S mass to set m_c and the 1P–1S splitting to fix the lattice spacing, Juge [139], following Kronfeld [140], obtained $\overline{m}_c(\overline{m}_c) = 1.27(5)$ GeV. For the charm quark action, he used the clover action with the Fermilab heavy quark interpretation. He used a second order perturbative expansion to relate the lattice and $\overline{MS}$ masses. The one-loop coefficient was obtained in the usual way. The two-loop coefficient was calculated by calculating the charm quark propagator at several very small values of α_s and fitting the results to a perturbative expansion.

This result is likewise compatible with results using the D_s meson to set the quark mass. For example, Becirevic, Lubicz, and Martinelli [141] related the quark masses of $\overline{\text{MS}}$ and the lattice using the vector and axial vector Ward identities. The lattice part of the calculation was done non-perturbatively. They obtained $\overline{m}_c(\overline{m}_c) = 1.26(3)(12)$ GeV. Rolf and Sint [131] have used the Schrödinger functional approach to calculate the renormalisation factors for the quark mass. They obtained $\overline{m}_c(\overline{m}_c) = 1.301(34)$ GeV when F_K was used to set the lattice spacing. Divitiis et al. [138], using the methods described previously, obtain $\overline{m}_c(\overline{m}_c) = 1.319(28)$ GeV. All of these quenched calculations contain an additional uncertainty comparable to their stated uncertainties from the quantity used to set the lattice spacing, arising from the quenched approximation. Preliminary unquenched results by Dougall, Maynard, and McNeile at Lattice 2004 [142, 143] are consistent with this picture. Other unquenched m_c determinations are in progress and will appear this year.

3.6 Final averages for m_b and m_c

In the previous sections we have presented the various bottom and charm quark mass determinations available in the literature and gave detailed discussions on the methods that were used to obtain the respective central values and uncertainties. A compilation of the individual numerical results from QCD sum rules, the 1S resonance and lattice QCD is displayed in Fig. 6.4 for the bottom quark mass and in Fig. 6.5 for the charm quark mass.

One of the general features of the analyses is that the theoretical component of the uncertainty is substantial, sometimes the dominant component. Some of the more precise results relied on additional assumptions and on specific prescriptions, and some of the more recent analyses obtained larger uncertainties than older ones because they considered new theoretical aspects. Therefore, the quoted errors are subjective and do not have any statistical meaning. Procedures such as taking a weighted average are meaningless a priori.

For this reason, first of all, the central values for bottom and charm quark masses are obtained by simply taking the mean value of all presented determinations with equal weights. Concerning our current knowledge of the corresponding uncertainties, we have decided to present two different approaches. For the first approach, we try to infer from Figs. 6.4 and 6.5 what a sensible 1σ deviation should be if the distribution of the various determinations could be interpreted statistically. In Figs. 6.4 and 6.5 this "one standard deviation" uncertainty has been displayed by the darker gray area which numerically corresponds to

$$\overline{m}_b(\overline{m}_b) = 4.22 \pm 0.05 \text{ GeV} \qquad \text{and} \qquad \overline{m}_c(\overline{m}_c) = 1.28 \pm 0.05 \text{ GeV}. \qquad (6.17)$$

Our second approach consists in presenting ranges for the quark mass values in which the respective $\overline{\text{MS}}$ masses are located to some high degree of probability. These "ranges" then read

$$\overline{m}_b(\overline{m}_b) = 4.12 - 4.32 \text{ GeV} \qquad \text{and} \qquad \overline{m}_c(\overline{m}_c) = 1.18 - 1.38 \text{ GeV}. \qquad (6.18)$$

and correspond to the lighter gray area in Figs. 6.4 and 6.5.

3.7 Future Opportunities

The determination of the bottom and charm quark masses from heavy quarkonium data represents a by now classic problem initiated by the early works on the QCD operator product expansion [1]. In recent years an impressive array of developments has led to a more refined understanding of the uncertainties inherent to the methods that can be applied and to a number of new higher order perturbative computations. Nevertheless, there are a number of issues that are still open.

So far all numerical analyses based on non-relativistic quantities relied on fixed-order perturbation theory. The renormalisation group improved computations already applied in the context of top

pair production at threshold could be applied here as well. In contrast to the top quark case, however, where the hierarchy of relevant scales is large and a renormalisation group improved treatment appears indispensable, the summation of logarithms for bottomonium and charmonium quantities will mainly serve as a cross-check for the fixed-order methods. Moreover, the proper renormalisation group treatment of the charmonium and the higher excited bottomonium states is not fully understood yet because for these systems the ultrasoft scale appears to be below the hadronic scale Λ_{QCD}. In any case, analyses based on renormalisation group improved perturbation theory would represent a valuable achievement toward a better understanding of the behaviour of perturbation theory to bottomonium and maybe also charmonium states.

A number of perturbative results at the NNNLO level exists for the quarkonium energy levels. As mentioned in the review, all these analyses determined the contributions coming from the ultrasoft scale perturbatively, which is, however, not realistic, particularly for higher radial bottomonium states and the charmonium states in general. Here, the systematic factorisation of the ultrasoft effects and a treatment based on non-perturbative methods could lead to a better understanding and more realistic estimate of the theoretical errors. In particular, the non-perturbative treatment of ultrasoft effects might also shed more light on the validity of the assumption that the leading order solution corresponds to a Coulomb-type bound state for quarkonium systems for which the ultrasoft scale is non-perturbative. Such an analysis might be even useful for quantities like the large-n moments used in bottom quark mass determinations and for the bottomonium ground state where there are good reasons for the assumption that the ultrasoft scale can be treated perturbatively.

A complementary approach toward a better understanding of non-perturbative effects, particularly for quarkonium systems where the ultrasoft scale is believed to be perturbative, would be the determination of quark and gluon condensate contributions beyond leading order. Here, first principles determinations of the quark and gluon condensates from lattice simulations would be quite important. At present the matching coefficients of the condensates are only known at leading-order in the non-relativistic expansion. Results at the next-to-leading order level would provide further tests for the approximation in terms of a series of local condensates. Likewise, effects of subleading condensates in the non-relativistic framework could be analysed more systematically.

Much programmatic work remains to be done combining the various ingredients that have been applied to heavy quark mass determinations on the lattice. All calculations need to be repeated with three flavours of unquenched light sea quarks. It should be possible to extend all the perturbative calculations to two-loop order at least. When this has been accomplished, an agreement between perturbative and non-perturbative determinations of m_b and m_c to around 30–50 MeV should be possible.

4 STRONG COUPLING CONSTANT FROM QUARKONIA

4.1 Strong coupling from Upsilon decays and sum rules

Heavy quarkonia leptonic and non-leptonic inclusive decay rates, in principle, provide means to determine the strong coupling α_{s} using perturbative QCD. Precise data are available from the decay widths of the 1^{--} $J/\psi(1S)$ and ψ states and the Υ resonances. Assuming that the hadronic and leptonic decay widths of the heavy quarkonium states can be factorised into a non-perturbative part, and a calculable perturbative part, ratios of partial decay widths can be predicted. The ratio of the total hadronic decay width of the $\Upsilon(1S)$ and its leptonic partial width is then given by [144–146]

$$
R_\mu(\Upsilon) = \frac{\Gamma(\Upsilon \to \mathrm{hadrons})}{\Gamma(\Upsilon \to \mu^+\mu^-)}
$$

$$
= \frac{10(\pi^2 - 9)\alpha_{\mathrm{s}}^3(M_b)}{9\pi\alpha_{\mathrm{em}}^2}\left[1 + \frac{\alpha_{\mathrm{s}}}{\pi}\left(-19.36 + \frac{3\beta_0}{2}\left(1.161 + \ln\frac{2M_b}{M_\Upsilon}\right)\right)\right]. \qquad (6.19)
$$

Theoretical corrections to Eq. 6.19 arise from two sources. Corrections of order v^2, due to the relativistic nature of the $Q\bar{Q}$ system have been analysed in [146]. Further corrections of non-perturbative nature, due to the annihilation from higher Fock states ("colour-octet" contribution), can only be estimated and have been discussed in [147, 148]. Both types of corrections are more severe for the charmonium and the higher Υ states. Thus for a determination of α_s the $\Upsilon(1S)$ state should be used.

Employing the experimental value $R_\mu(\Upsilon) = 39.11 \pm 0.4$ [30], the section on Quantum Chromodynamics in the Review of Particle Physics quotes $\alpha_s(M_b) = 0.177 \pm 0.010$ without reference, whereas the original work [147] obtains $\alpha_s(M_b) = 0.186 \pm 0.032$. The uncertainty is fully dominated by theory, and mainly originates from the above mentioned colour-octet contributions as well as the residual scale dependencies. Varying the renormalisation scale as well as the pole quark mass $M_b = 4.6 - 4.9$ GeV, the next-to-leading order α_s^4 correction in Eq. 6.19 is around 30–40%. Such a large NLO corrections entails that also the still unknown NNLO term could be sizeable. Altogether, the error estimate $\Delta\alpha_s(M_b) \approx 0.03$ appears realistic at the present stage, and it is unclear, how the result $\Delta\alpha_s(M_b) = 0.01$, quoted in the PDG, can be justified.[3]

In the past there have also been a number of analysis [70, 73, 75, 77, 149] attempting the determination of α_s from the large-n Upsilon sum rules described in Section 3.2 with realistic error estimates. The analyses were based on simultaneous fits for the bottom quark mass and α_s using several moments. In these analyses uncertainties $\Delta\alpha_s(M_b) \approx 0.03 - 0.05$ were found. In view of these remarks, the determination of α_s from heavy quarkonium properties does not appear to be a method that can compete with other more precise methods based on perturbation theory at higher scales or from the hadronic τ-decay rate [30, 150]. However, heavy quarkonium analyses may provide a useful cross-check for other methods.

4.2 Strong coupling constant from lattice QCD

Lattice determinations of the strong coupling constant have the same two components as lattice determinations of other standard model parameters: fixing bare lattice parameters from hadronic data, and conversion of lattice parameters into $\overline{\text{MS}}$ parameters. Spin-averaged splittings in charmonium and bottomonium are excellent quantities for determining the lattice spacing in GeV. Davies et al. [151] recently reported unquenched lattice calculations of the simplest heavy and light quark quantities with 2+1 (two light and one strange) flavours of unquenched staggered fermions. Unlike the previous unquenched calculation mentioned, these used the physical number of light quark flavours. In addition, the use of staggered fermions allowed the use of much lighter light quark masses, as low as $m_s/6$. The results, which were dominated by quarkonium splittings, showed good, few per cent agreement among lattice spacings obtained from the various quantities. In particular, the 1P–1S splitting in the ψ system and the 1P–1S, 2S–1S, etc. splittings in the Υ system all yielded the same lattice spacing to high accuracy.

The factor relating the bare lattice and $\overline{\text{MS}}$ couplings, however, is large, roughly a factor of two at typical lattice spacings, making the conversion demanding. Early lattice determinations of the physical coupling used a mean-field improved coupling constant, $\alpha_s = \alpha_0/\text{Tr}U_P$, to reduce the uncertainty due to the large tadpole contributions to the conversion which are responsible for much of the poor perturbative behaviour. ($\text{Tr}U_P$ is the trace of the plaquette operator on the lattice.) [152]. Subsequent work on perturbative methods proposed obtaining improved coupling constants from Monte Carlo measurements of small Wilson loops [153]. Lüscher and collaborators proposed non-perturbative methods for obtaining physical couplings via the Schrödinger functional [154].

Very recently, Mason et al. [155] have reported third-order perturbative results relating the couplings via many small Wilson loops and Creutz ratios. The many determinations agree with each other and agree with asymptotic freedom over a large range of q^2. Combined with the lattice spacings ob-

---

[3]The small uncertainty presented for α_s from quarkonia in the PDG [30], pulls down the global α_s average quite noticeably, as can also be seen from figure 9.1 in Ref. [30].

tained in [151], this work yields $\alpha_{\overline{\text{MS}}}(M_Z) = 0.117(1)$, in good agreement with the world average. Quark masses and other standard model parameters based on the calculations of Ref. [151] will soon appear.

Booth et al. [156] have used two-flavour simulations of the less physically transparent r_0 (defined from the heavy quark potential) to set the lattice spacing, and perturbation theory via the plaquette to obtain physical coupling constant. They obtain a result significantly lower than the above and than the world average. However, the perturbation theory resulting from Wilson sea quarks contains large, poorly convergent contributions from the fermionic graphs, and the calculation employs two rather than three light sea quarks.

The third-order perturbative determination of Mason et al. [155] is unlikely to be extended with perturbative methods in the near future. Future progress in α_s determinations from the lattice may await the fruition of unquenched non-perturbative methods for α_s determination.

5 NRQCD AND THE VELOCITY RENORMALISATION GROUP

In this section we discuss some of the more conceptual aspects involved in using effective theory methods for non-relativistic QCD. In particular we review issues regarding the power counting and renormalisation of these theories. For motivation it is useful to ask what properties we desire from an effective field theory of non-relativistic particles. The EFT should

1. have degrees of freedom that reproduce the IR divergences of the full theory in its entire region of validity and thus have no large logs in matching calculations,
2. have a well defined power counting in v so that the expansion is systematic,
3. exhibit all the expected symmetries of the physical problem, spin symmetries, gauge symmetries etc.,
4. start with a regulator independent Lagrangian, so that different choices of regulators and renormalisation schemes can be systematically implemented,
5. have a consistent renormalisation procedure so that UV divergences leave the theory well defined, and anomalous dimensions and renormalisation group evolution can be computed.

The original NRQCD [157–159] (see also Chapter 3 Sections 2.2 and 2.3) was formulated with the aim of separating the short distance physics at the scale m from the long distance physics at the non-relativistic momentum and energy scales, mv and mv^2. This effective theory has one distinct quantum field for each of the low energy quarks, antiquarks, and gluons. It succeeds at the majority of the above criteria but has well studied issues regarding item 2. In particular, the EFT matrix elements and diagrams do not have a unique scaling with v as emphasised in Refs. [160, 161].[4] From a modern viewpoint this is due to the fact that one gluon field is used to describe both soft and ultrasoft gluon effects, and the power counting for these two gluons differs [162–164]. In particular the soft gluons are responsible for binding while the ultrasoft gluons give real radiation and have couplings which need to be multipole expanded [165, 166]. A second complication is that, although a small $v \ll 1$ guarantees that the scales $m \gg mv \gg mv^2$ are well separated, the dispersion relation, $E = \mathbf{p}^2/(2m)$, couples the mv^2 energy and mv momentum scales together and affects the renormalisation group evolution [160].

One approach to resolving the power counting issue is to consider in sequence the mv and mv^2 scales and the soft and ultrasoft gluons. One first considers an NRQCD theory with soft gluons, and then "integrates out" the mv scale into nonlocal potential operators for the effective theory with ultrasoft gluons. This EFT is known as pNRQCD [90, 93]. While the soft NRQCD theory does not have a v power counting, the v power counting is obtained in the final pNRQCD theory. This construction has the advantage of avoiding the double counting gluon effects in a simply way, and also corresponds to the

---

[4]This version of NRQCD still satisfies the power counting in a weaker form since the subleading terms in the v expansion can in principle be obtained from higher order terms of the leading diagrams. This subtlety is therefore not important until calculations are done beyond leading order in v where both soft and ultrasoft effects become important.

Wilsonian picture of integrating out scales in step-wise fashion, $m{\to}mv{\to}mv^2$. Further details about the pNRQCD approach can be found in Chapter 3.

A second approach to resolving the power counting issue accounts for the correlation in energy and momentum scales from the start. In this case there is only one EFT below the scale m and it simultaneously contains soft and ultrasoft gluons. This EFT is known as vNRQCD [95, 96, 160, 167]. It has the advantage that power counting automatically induces the correct correlation between the ultrasoft μ_U and soft μ_S renormalisation scales, $\mu_U = \mu_S^2/m \equiv m\nu^2$, that preserves the dispersion relation. Renormalisation group evolution in ν is known as the velocity renormalisation group (vRGE), and incorporates the correspondence between μ_U and μ_S. In this section we give a brief review of the vNRQCD approach for the case $m \gg mv \gg mv^2 \gg \Lambda_{\rm QCD}$ relevant for QED and non-relativistic $t\bar{t}$ systems.[5]

The effective vNRQCD Lagrangian can be separated into ultrasoft, soft, and potential components, $\mathcal{L} = \mathcal{L}_u + \mathcal{L}_s + \mathcal{L}_p$. The presence of both soft and ultrasoft gluons immediately brings up the issue of double counting. To avoid double counting the effective theory is constructed such that the ultrasoft gluons reproduce only the physical gluon poles where $k^0 \sim \mathbf{k} \sim mv^2$, while soft gluons give only those with $k^0 \sim \mathbf{k} \sim mv$. The scales for the gluon momenta are influenced by the quark propagators, so the quark-gluon interactions must be constructed in such a way that we will not upset this scaling. In $\mathcal{L}_u$ this is achieved by the multipole expansion of interactions, which is enforced by a phase redefinition that separates label $\mathbf{p} \sim mv$ and residual $\sim mv^2$ momenta. This ensures that ultrasoft gluon momenta are always much smaller than the quark three-momenta. In $\mathcal{L}_s$ this is achieved by integrating out the intermediate static HQET like fermion propagators into the effective soft vertices [160] and by the pull-up mechanism [104]. The pull-up mechanism refers to the manner by which all soft loops in vNRQCD are made infrared finite while at the same time the ultraviolet divergences in ultrasoft loops are made to correspond directly to the hard scale m.

For example, the first few terms in the vNRQCD ultrasoft Lagrangian are

$$\mathcal{L}_u = \sum_{\mathbf{p}} \left\{ \psi_{\mathbf{p}}^\dagger \left[iD^0 - \frac{(\mathbf{p} - i\mathbf{D})^2}{2m} + \frac{\mathbf{p}^4}{8m^3} + \dots \right] \psi_{\mathbf{p}} + (\psi{\to}\chi) \right\} - \frac{1}{4} G_u^{\mu\nu} G_{\mu\nu}^u + \dots , \quad (6.20)$$

where $G_u^{\mu\nu}$ is the ultrasoft field strength and $\psi_{\mathbf{p}}$ is the quark field with label momentum $\mathbf{p}$, while χ is the field for antiquarks. In dimensional regularisation the covariant derivative has the form $D^\mu = \partial^\mu + i\mu_U^\epsilon g_u A^\mu$, where $\mu_U = m\nu^2$ and $g_u = g_u(\mu_U)$ is the renormalised ultrasoft QCD coupling. The soft Lagrangian $\mathcal{L}_s$ can be found in [95, 160, 167] and couples soft fields to the potential quarks with the soft QCD coupling $g_s = g_s(\mu_S)$ ($\mu_S = m\nu$). Finally the potential Lagrangian has terms like

$$\mathcal{L}_p = -\mu_S^{2\epsilon} V(\mathbf{p}, \mathbf{p}') \psi_{\mathbf{p}'}^\dagger \psi_{\mathbf{p}} \chi_{-\mathbf{p}'}^\dagger \chi_{-\mathbf{p}} + \dots , \quad (6.21)$$

where the coefficient function $V(\mathbf{p}, \mathbf{p}')$ acts like a potential (as do time ordered products of $\mathcal{L}_s$ vertices). For equal mass fermions in QCD perturbatively matching onto the first three orders in v gives terms

$$V(\mathbf{p}, \mathbf{p}') = (T^A \otimes \bar{T}^A) \left[\frac{\mathcal{V}_c^{(T)}}{\mathbf{k}^2} + \frac{\mathcal{V}_k^{(T)} \pi^2}{m|\mathbf{k}|} + \frac{\mathcal{V}_r^{(T)}(\mathbf{p}^2 + \mathbf{p}'^2)}{2m^2 \mathbf{k}^2} + \frac{\mathcal{V}_2^{(T)}}{m^2} + \frac{\mathcal{V}_s^{(T)}}{m^2} \mathbf{S}^2 \right.$$

$$\left. + \frac{\mathcal{V}_\Lambda^{(T)}}{m^2} \Lambda(\mathbf{p}', \mathbf{p}) + \frac{\mathcal{V}_t^{(T)}}{m^2} T(\mathbf{k}) + \dots \right] + (1 \otimes 1) \left[\frac{\mathcal{V}_c^{(1)}}{\mathbf{k}^2} + \frac{\mathcal{V}_k^{(1)} \pi^2}{m|\mathbf{k}|} + \frac{\mathcal{V}_2^{(1)}}{m^2} + \frac{\mathcal{V}_s^{(1)}}{m^2} \mathbf{S}^2 + \dots \right] ,$$

$$\mathbf{S} = \frac{\boldsymbol{\sigma}_1 + \boldsymbol{\sigma}_2}{2}, \quad \Lambda(\mathbf{p}', \mathbf{p}) = -i\frac{\mathbf{S} \cdot (\mathbf{p}' \times \mathbf{p})}{\mathbf{k}^2}, \quad T(\mathbf{k}) = \boldsymbol{\sigma}_1 \cdot \boldsymbol{\sigma}_2 - \frac{3\,\mathbf{k} \cdot \boldsymbol{\sigma}_1 \mathbf{k} \cdot \boldsymbol{\sigma}_2}{\mathbf{k}^2}, \quad (6.22)$$

---

[5] Up to NNLO this situation is basically equivalent to the case where $mv^2 \sim \Lambda_{\rm QCD}$, since the only obvious difference is that we must be careful to stop renormalisation group running before any coupling $\alpha_{\rm s}(\mu)$ becomes non-perturbative, so $\mu \geq$ few $\times \Lambda_{\rm QCD}$. The main difference at higher order is that in the latter scenario matrix elements involving ultrasoft gluons which are N^{3}LO become non-perturbative.

where $\mathbf{k} = \mathbf{p}' - \mathbf{p}$ is the momentum transfer and the colour and spin factors have the appropriate index contractions with the fields in Eq. (6.21). In Eqs. (6.20) and (6.21) the couplings are defined with dimensional regularisation and it is worth noting that the factors of μ_U^ϵ and μ_S^ϵ in $\mathcal{L}_{u,s,p}$ are uniquely determined by mass dimension and v power counting in $d = 4 - 2\epsilon$ dimensions [167] (see [96] for further detail). The renormalised couplings depend on the parameter ν, i.e., $\mathcal{V}_i = \mathcal{V}_i(\nu)$. In Section 6.3 additional Wilson coefficients are defined for the dominant current relevant for heavy quark pair production in e^+e^- annihilation, $c_1(\nu)$, as well as coefficients for subleading production currents, $c_{2,3}(\nu)$. Apart from the renormalisation scale for the couplings, the v power counting of an arbitrary diagram is universally determined by the powers of v assigned to operators, and therefore have no explicit dependence on the choice of regulator. Ambiguities regarding how multipole expanded interactions renormalise operator products were resolved in Ref. [96].

Since we are considering the case $mv^2 \gg \Lambda_{\mathrm{QCD}}$ the majority of computations are purely perturbative. In this case they can be performed in three stages,

i) matching QCD at $\mu_U = \mu_S = m$ ($\nu = 1$) onto vNRQCD,

ii) running with the velocity renormalisation group from $\nu = 1$ to $\nu = v_0$ where v_0 is a number of order the typical velocity in the non-relativistic bound state ($v_0 \simeq 0.15$ for $t\bar{t}$), and

iii) computing the EFT matrix elements at $\nu = v_0$.

From an EFT point of view the most novel aspect of these steps is the resummation of logarithms by running in ν. The correlation of energy and momentum cutoff scales in the evolution turns out to be crucial to the proper resummation of logarithms in many cases. In Ref. [168] it was shown for the first time that anomalous dimensions and the vRGE could be used to predict $\ln \alpha$ contributions in QED bound states like Hydrogen, positronium, and muonium. For positronium the $\alpha^7 \ln^2 \alpha$ hyperfine splitting corrections and $\alpha^3 \ln^2 \alpha$ corrections to decay rates were correctly reproduced, and the $\alpha^8 \ln^3 \alpha$ Lamb shift was predicted.[6] These results give a non-trivial consistency check on the vNRQCD approach to renormalisation. Further consistency checks from subdivergences are discussed in Refs. [170, 171]. In Ref. [172] it was shown that the correlation of energy and momentum scales is necessary to compute these QED corrections involving $\ln^k \alpha$ with $k \geq 2$. In QCD the correlation in energy and momentum cutoffs is also known to be crucial to resumming logs in the production current [160, 171, 173, 174].

The running of the nonrelativistic QCD potentials $\mathcal{V}_i$ in vNRQCD was worked out in [95, 104, 173] and for the c_i current coefficients in Refs. [94, 170, 173]. The running of the static potential due to ultrasoft effects in the pNRQCD formalism was determined in Ref. [175]. In Ref. [105] and also [96, 174] an error was corrected in some of the previous vNRQCD publications from a missing set of spin-independent operators.[7] All results for the vector current coefficient c_1 at NLL order and the running of the potentials $\mathcal{V}_{c,k,2,r,s,\Lambda,t}$ have now been checked by two independent groups. The renormalisation group improved results were applied to $t\bar{t}$ production near threshold in Refs. [170, 176], and significantly reduced the uncertainty in previous fixed order NNLO computations [52]. For renormalisation group improved $t\bar{t}$ production near threshold all the necessary components in steps i), ii), and iii) are known at NNLL order except for the full NNLL order computation for c_1, and are included in the state of the art $t\bar{t}$ analyses.

The necessary additional computations for c_1 at NNLL were discussed in Refs. [170, 171]. A partial result was obtained for the NNLL running of c_1 which fully incorporates the non-mixing part of the anomalous dimension [171]. This calculation required correctly associating the divergences in three-loop vertex graphs with renormalisation of operators in the effective theory.[8] At N^{3}LO the results are consistent with the fixed order computation in Ref. [177]. Updates for the changes due to a corrected operator basis and coming from the new results for the NNLL order running of the dominant vector current were made in Ref. [96] and [178] respectively. More details on the $t\bar{t}$ analyses are given in Section 6.3.2. Finally, computations of the running of the spin-dependent potentials beyond the leading logarithmic

---

[6]For Hydrogen the $\alpha^8 \ln^3 \alpha$ terms resolved a controversy in favour of Karshemboim's original result [169].

[7]Numerically, the change turned out to be insignificant for phenomenological $t\bar{t}$ applications as discussed in Section 6.3.2.

[8]The two-loop soft corrections to the $1/m|\mathbf{k}|$ potentials obtained in Ref. [107] were used as an input.

approximation order and some applications for $b\bar{b}$, $b\bar{c}$ and $c\bar{c}$ systems can be found in Refs. [179–181] for pNRQCD. In Ref. [181] also the spin-dependent part of the mixing contributions to c_1 at NNLL was determined. In these references the renormalisation group running is called the nonrelativistic renormalisation group.

6 TOP PAIR PRODUCTION AT THRESHOLD IN e^+e^- COLLISIONS

6.1 Physics of the top threshold

With a weight of around 175 GeV, the top quark is the heaviest known quark flavour and plays an important role in the understanding of the mass generation in the Standard Model and of electroweak symmetry breaking. Top–antitop quark pair production close to the threshold, i.e., for centre of mass (c.m.) energies $\sqrt{s} \approx 2m_t \approx 350$ GeV, will provide an integral part of the top quark physics program at the next e^+e^- Linear Collider, which is supposed to be the next major accelerator project after the LHC [182, 183]. In this kinetic regime the $t\bar{t}$ cross-section rises as soon as sufficient amount of energy is available to produce the top–antitop quark pair. Since almost all energy is spent on the top quark masses, the top quarks are non-relativistic and their velocities are small, $v \ll 1$. Due to the large top quark width,

$$\Gamma_t(t \rightarrow bW) \approx \frac{G_F}{\sqrt{2}} \frac{m_t^3}{8\pi} \approx 1.5 \text{ GeV} \gg \Lambda_{\text{QCD}}, \tag{6.23}$$

the would-be toponium resonances overlap and the total $t\bar{t}$ production cross-section line-shape is a smooth function of the energy. Theoretically this means that non-perturbative effects are strongly suppressed and can be neglected for studies of the total cross-section [184–186].

The total cross-section for $e^+e^- \rightarrow \gamma^*, Z^* \rightarrow t\bar{t}$ has the form

$$\sigma_{\text{tot}}^{\gamma,Z}(s) = \sigma_{\text{pt}} \left[F^v(s)\, R^v(s) + F^a(s) R^a(s) \right], \tag{6.24}$$

where $\sigma_{\text{pt}} = 4\pi\alpha^2/(3s)$ is the muon pair cross-section. The vector and axial-vector R-ratios are

$$R^v(s) = \frac{4\pi}{s} \text{Im} \left[-i \int d^4x\, e^{iq\cdot x} \left\langle 0 \left| T\, j_\mu^v(x)\, j^{v\mu}(0) \right| 0 \right\rangle \right],$$

$$R^a(s) = \frac{4\pi}{s} \text{Im} \left[-i \int d^4x\, e^{iq\cdot x} \left\langle 0 \left| T\, j_\mu^a(x)\, j^{a\mu}(0) \right| 0 \right\rangle \right], \tag{6.25}$$

where $q = (\sqrt{s}, 0)$ and j_μ^v (j_μ^a) is the vector (axial-vector) current in the Standard Model that produces a quark–antiquark pair. With both γ and Z exchange the prefactors in Eq. (6.24) are

$$F^v(s) = \left[Q_q^2 - \frac{2s\, v_e v_q Q_q}{s - m_Z^2} + \frac{s^2(v_e^2 + a_e^2)v_q^2}{(s - m_Z^2)^2} \right], \qquad F^a(s) = \frac{s^2\, (v_e^2 + a_e^2)a_q^2}{(s - m_Z^2)^2}, \tag{6.26}$$

where

$$v_f = \frac{T_3^f - 2Q_f \sin^2\theta_W}{2\sin\theta_W \cos\theta_W}, \qquad a_f = \frac{T_3^f}{2\sin\theta_W \cos\theta_W}. \tag{6.27}$$

Here, Q_f is the charge of fermion f, T_3^f is the third component of weak isospin, and θ_W is the weak mixing angle. In the threshold region the axial-vector contribution coming from the Z exchange is suppressed by order v^2 and, numerically, at the level of a few percent [62, 187].

The cross-section rises rapidly at the point where the remnant of a toponium 1S resonance can be formed. From the energy where this increase occurs, the top quark mass (in threshold mass schemes) can be determined with uncertainties at the level of 100 MeV, whereas shape and height of the cross-section near threshold can be used to determine Γ_t, the coupling strength of top quarks to gluons, α_s,
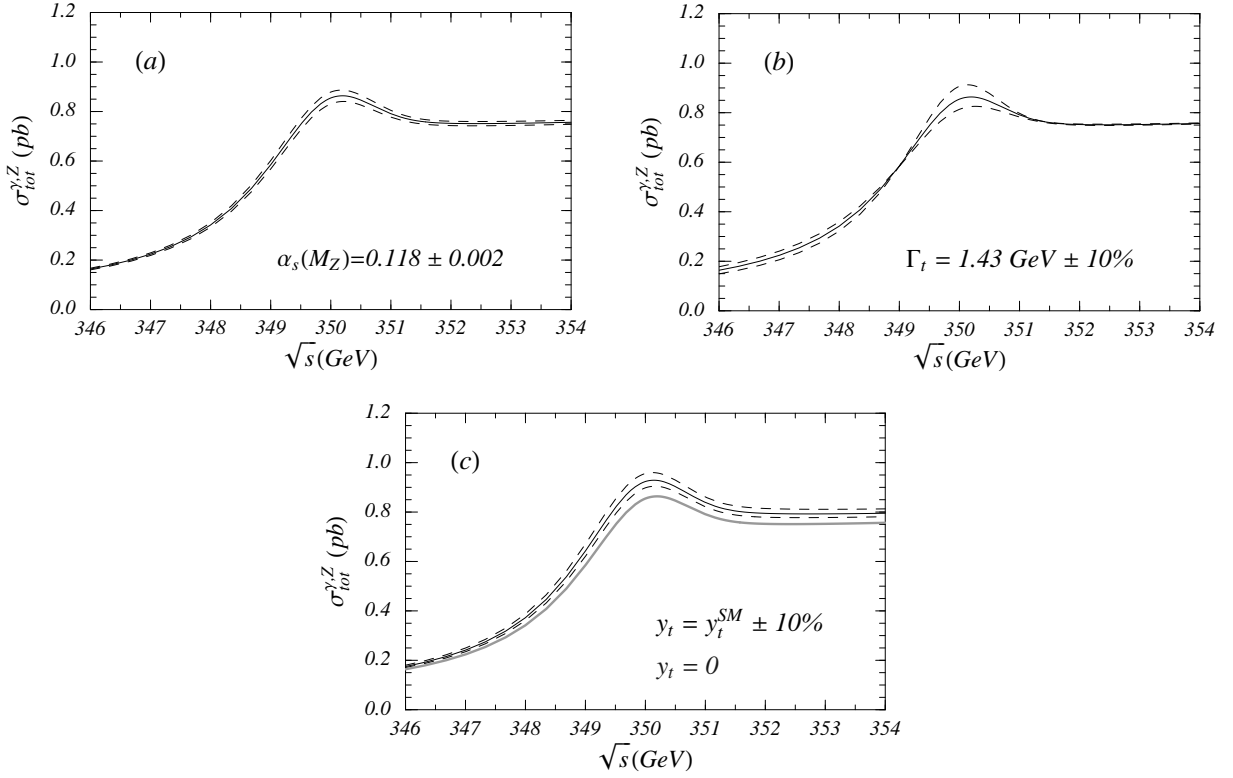
Fig. 6.6: Theoretical prediction for the top pair production cross-section without beam effects and its dependence on changes of a) the value of the strong coupling, b) the top quark width, and c) the inclusion of a Standard Model (SM) Higgs boson. Changes relative to the central value (solid lines) are shown by dashed red lines. In c) there are two solid lines, the lower black line is the decoupling limit for the Higgs boson ($m_H \to \infty$), and the upper blue line is for a SM Higgs with mass $m_H = 115$ GeV. The parameters $M_{1S} = 175$ GeV, $\Gamma_t = 1.43$ GeV, $\alpha_s(M_Z) = 0.118$, $y_t = 0$ and $\nu = 0.15$ have been used unless stated otherwise. The figures have been obtained in Ref. [170, 176] using vNRQCD at NNLL order.

and, if the Higgs boson is not heavy, the top Yukawa coupling $y_t = (2\sqrt{2}G_F m_t^2)^{1/2}$ [188, 189]. For the determination of the top quark width only very few other methods are known. In Fig. 6.6 the dependences of the prediction for the total $t\bar{t}$ cross-section at threshold on changes of α_s, Γ_t and y_t are displayed. The dependence of the cross-section on α_s and y_t comes to a good approximation from the potential between the top quark pair. The QCD Coulomb potential, which is responsible for the binding-effects at the $t\bar{t}$ threshold, has the form

$$V_{\mathrm{QCD}}(r) \quad = \quad -C_F \frac{\alpha_s(\mu)}{r} \tag{6.28}$$

at leading order and deepens when α_s is increased. This leads to an increase of the cross-section as the $t\bar{t}$ pair is bound together more strongly. Similarly, in the Standard Model the dominant effect of a light Higgs exchange can be understood from a Yukawa-type potential of the form

$$V_{tth}(r) \quad = \quad -\frac{y_t^2}{4\pi} \frac{e^{-m_H r}}{r}, \tag{6.29}$$

which also deepens for a stronger Yukawa coupling. In scenarios beyond the Standard Model such as Supersymmetry, the effects of Higgs exchanges can be larger than in the Standard Model due to modified couplings and due to the fact that Higgs mass limits are lower, Finally, the dependence on Γ_t can be easily understood from the fact that for smaller Γ_t the resonance structure becomes more
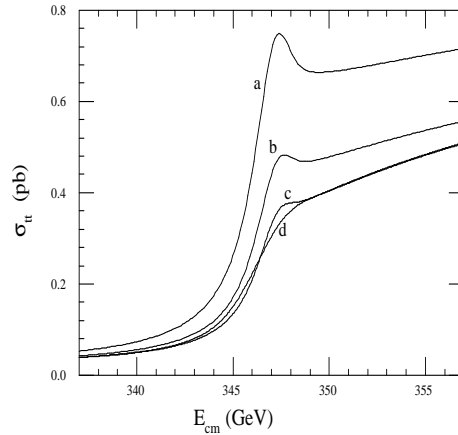
Fig. 6.7: Production cross-section for $t\bar{t}$ pairs at threshold for $m_t = 175$ GeV. The theoretical cross-section without beam effects is given by curve (a). The following energy redistribution and luminosity losing effects have been applied to the theory for the remaining curves: (b) initial-state radiation (ISR); (c) ISR and beamstrahlung; (d) ISR, beamstrahlung and single-beam energy spread. The figure has been taken from Ref. [203].

pronounced. The prediction in Fig. 6.6 have been made, exemplarily, in the 1S mass scheme. In threshold mass schemes the position of the 1S peak has, in general, only little dependence on α_s, y_t, Γ_t and other parameters such as the renormalisation scale. Therefore in threshold mass schemes the top mass measurement has only little correlation with other theoretical parameters. From differential quantities, such as the top momentum distribution, [190, 191] the forward–backward asymmetry or certain leptonic distributions, [192–195] one can obtain measurements of Γ_t, the top quark spin and possible anomalous couplings [196].

The top mass determination represents the most important task of a threshold line-shape measurement. In addition to the quite small expected error on the top quark mass, the $t\bar{t}$ line-shape measurement has the feature that the corresponding mass scheme is unambiguously defined since the location where the cross-section rises is a stable (and perturbatively calculable) function if threshold masses are employed. With respect to both aspects the top mass measurement from a threshold scan is superior to the reconstruction method as applied e.g., at hadron colliders. This is because the line-shape measurement relies on counting the number of colour singlet $t\bar{t}$ pairs, while reconstruction is based on the determination of a top four-momentum from the top decay products, which unavoidably leads to larger ambiguities since the top quark is coloured.

6.2 Experimental simulations for e^+e^- collisions

A considerable number of experimental studies were carried out in the past to assess the feasibility of top threshold measurements of the total cross-section and certain distributions [197–202]. Apart from the standard experimental issues related to the event selection and the identification of $t\bar{t}$ pairs, the treatment of background, efficiencies and detector effects, which need to be accounted for to measure the cross-section line-shape, a crucial role is played by the luminosity spectrum and the absolute energy scale of the e^+e^- beam. (For a recent experimental review see Ref. [203].) The luminosity spectrum arises from the effects of initial state radiation, beamstrahlung and the beam energy spread and leads to a loss of luminosity and a redistribution of collision energy down to lower energies. The latter effect is particularly important since it effectively smears out the resonance structure visible in Fig. 6.6. Likewise a precise knowledge of the absolute energy scale is crucial.

In Fig. 6.7 (taken from Ref. [203]) the effects of the three sources of the luminosity spectrum on the cross-section obtained for a fixed nominal c.m. energy are shown. The effects are substantial.
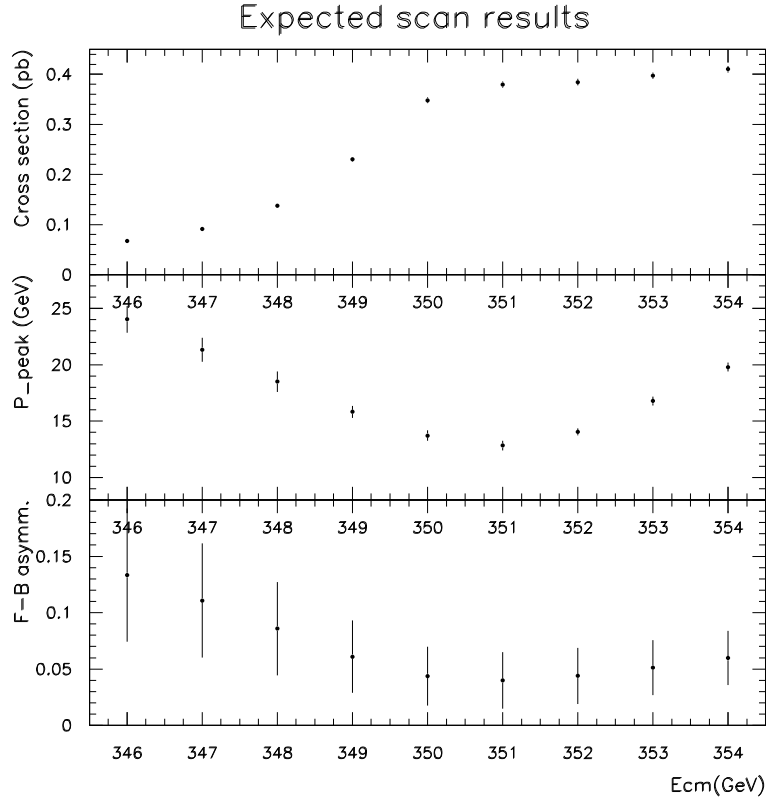
Fig. 6.8: The energy dependence of the three observables σ_{tot}, the peak position of the momentum distribution and A_{FB} as expected from a simulation of the threshold scan. For the top quark mass $M_{1S} = 175$ GeV is assumed (figure taken from Ref. [202].)

Thus the precise knowledge of the luminosity spectrum for any nominal c.m. energy of the e^+e^- beam is crucial for the measurement of the threshold line-shape. Since the luminosity spectrum is partially machine-dependent it has become standard for top threshold studies to account for the complete luminosity spectrum (including initial state radiation) during the experimental simulation. Thus it is the convention not to include the luminosity spectrum for the theoretical predictions. Since the luminosity spectrum cannot be fully predicted a priori in a machine-independent way it needs to be constantly measured while the top threshold scan is being performed. The luminosity spectrum can be deduced by using the acollinearity distribution of $e^+e^- \to e^+e^-$ Bhabha scattering which depends on the energy difference of the initial e^+ and e^- beams [204], while the absolute energy scale can be determined from spectrometers.

In a more recent simulation study by Martinez and Miquel [202] the size of the experimental uncertainties for simultaneous measurements of the 1S mass, $\alpha_s(M_Z)$, Γ_t and y_t in a top threshold run at an e^+e^- Linear Collider was examined, based on measurements of the total cross-section, the top three-momentum distribution and the forward–backward asymmetry for a 9+1 point threshold scan using a total integrated luminosity of 300 fb^{-1}, see Fig. 6.8. The analysis assumed perfect knowledge of the luminosity spectrum and the absolute energy scale and thus reflects the experimental uncertainties from other sources. Fixing y_t to the Standard Model (SM) value Martinez et al. obtained $\Delta M_{1S} = 19$ MeV, $\Delta\alpha_s(M_Z) = 0.0012$ and $\Delta\Gamma_t = 32$ MeV from a three-parameter fit. In a one parameter fit, fixing all other parameters, they obtained $\delta y_t/y_t = ^{+0.18}_{-0.25}$. In a fit where Γ_t is fixed to the SM value and α_s is constrained to $\alpha_s(M_Z) = 0.120 \pm 0.001$ they obtained $\delta M_{1S} = 27$ MeV and $\delta y_t/y_t = ^{+0.33}_{-0.54}$. In a fit where only α_s is constrained to $\alpha_s(M_Z) = 0.120 \pm 0.001$ they obtained $\delta M_{1S} = 31$ MeV, $\delta\Gamma_t = 34$ MeV

and $\delta y_t / y_t = {}^{+0.35}_{-0.65}$ for a Higgs mass of $m_h = 120$ GeV. Note that the sensitivity on the top Yukawa coupling strongly decreases for increasing Higgs mass. It is therefore likely that only weak constraints on the Yukawa coupling can be obtained if the Higgs is considerably larger than the current LEP limit.

Recently, a first study of the uncertainties in the measurements of the luminosity spectrum (excluding the effect of linac energy spread) has been carried out by Boogert [205]. The luminosity spectrum is typically expressed in terms of the scaled c.m. energy $x = \sqrt{s'}/\sqrt{s}$, where $\sqrt{s'}$ is the event c.m. energy after beamstrahlung, ISR and beam spread and $\sqrt{s}$ is the nominal pre-collision energy. The cross-section after the inclusion of the luminosity spectrum is

$$\sigma'_{tot}(s) = \int_0^1 dx \, L(x)\sigma_{tot}(x^2 s) \tag{6.30}$$

where $L(x)$ is a probability distribution representing the luminosity spectrum. Unlike the analysis performed by Martinez and Miquel, a near perfect detector was considered with a constant detector efficiency for all scan points and only the cross-section information was used. The theoretical cross-section smeared with the luminosity spectrum was fitted with the same theoretical cross-section smeared by the corresponding reconstructed luminosity spectrum. This fit was performed for an 11 point threshold scan with a integrated luminosity per scan point of 30 fb^{-1}, with M_{1S} and $\alpha_s(M_Z)$ as free parameters, while Γ_t is fixed. Systematic shifts of $\delta M_{1S} = M_{1S}^{\text{fit}} - M_{1S} = -44$ MeV and $\delta(\alpha_s) = \alpha_s^{\text{fit}} - \alpha_s = -0.0016$, were observed, significantly larger than the statistical errors obtained in the three parameter fit of Ref. [202].

The results of Boogert and similar studies must be taken with caution as the luminosity spectrum and its reconstruction varies significantly between different linear collider designs and the detail in which the particle acceleration, focusing and collision dynamics are simulated. The development of linked accelerator, collision dynamics, hard scattering and detector reconstruction simulations will enable more realistic determination of the expected systematic errors on the top mass.

Finally, other observables such as the forward–backward asymmetry and top three-momentum distribution, discussed in Section 6.4, must also be modified due to the effects of the luminosity spectrum and included into a complete analysis of the top threshold with realistic luminosity spectra.

6.3 Theoretical status for e^+e^- collisions

With the excellent experimental prospect in view it is obvious that a careful analysis and assessment of theoretical uncertainties in the prediction of the total cross-section and various distributions is mandatory. Initially, a number of leading order [206] and next-order computations, [188, 190–195, 207] were carried out. The latter relied basically on QCD-inspired potential models that used phenomenological input from Υ and charmonium data. As such they did not represent true first-principles QCD calculations and there was no systematic way how the computations could be consistently improved to include higher order radiative or relativistic corrections. Moreover it was not clear, at a level of precision of order 100 MeV, how the top quark mass appearing in these computations relates to a Lagrangian mass in QCD.

6.3.1 Fixed order approach

The fixed order expansion of the non-relativistic heavy quark pair production cross-section has the schematic form

$$R = \frac{\sigma_{t\bar{t}}}{\sigma_{\mu^+\mu^-}} = v \sum_k \left(\frac{\alpha_s}{v}\right)^k \left\{ 1\,(\text{LO}); \alpha_s, v\,(\text{NLO}); \alpha_s^2, \alpha_s v, v^2\,(\text{NNLO}) \right\}, \tag{6.31}$$

where v is the top velocity and where the indicated terms are of leading (LO), next-to-leading (NLO), and next-to-next-to-leading order (NNLO). The LO terms proportional to $(\alpha_s/v)^n$ are the well-known Coulomb singularities and arise from the iteration of the interaction between the $t\bar{t}$ pair created by the

QCD Coulomb potential. Parametrically, one counts α_s/v of order 1 for the entire threshold regime. The systematic computation of the expansion in this scheme became possible after adopting the concepts of effective theories in the framework of NRQCD [146, 208]. Consistent fixed order computations up to NNLO were then worked out in Refs. [62, 99, 209–220]. The expansion in the fixed order scheme is obtained by identifying the corresponding contributions in the cross-section from the various momentum regions. Since the contribution from each region has an unambiguous scaling in the top velocity the expansion can be carried out systematically. The contributions of the same order can then be summed by using the Schrödinger equation and time-independent perturbation theory.

The results obtained in this scheme were not just some new higher order corrections, but led to a number of surprising and important insights. Although the methods and techniques used to perform the computations differed among the groups, it was generally found that the NNLO corrections to the location where the cross-section rises and to the height of the cross-section were found to be much larger than expected from the results at NLO. The large corrections to the location of the rise obtained initially [99, 214, 215] were found to be an artifact of the use of the on-shell pole mass definition and it was realized that the top pole mass cannot be extracted with an uncertainty smaller than $\mathcal{O}(\Lambda_{\mathrm{QCD}})$ from non-relativistic heavy quark–antiquark systems [57, 121, 123]. (See Section 3.4.) Subsequently, carefully designed threshold mass definitions (Section 3.1) were proposed to allow for a stable extraction of the top quark mass parameter [57, 60–62, 220].

In Ref. [52] the results for the normalised total photon-induced cross-section $Q_t^2 R^v$ of a number of groups were compiled and compared numerically in detail using an equivalent set of parameters to analyse the scheme-dependence of the fixed order approach. Since the axial-vector current contributions are only a small correction at the percent level it is justified to consider only the photon-induced cross-section. Figure 6.9 shows the results obtained in Ref. [52] in different threshold mass schemes where the respective values of the threshold masses were obtained from the top $\overline{\mathrm{MS}}$ mass value $\overline{m}_t(\overline{m}_t) = 165$ GeV as a reference point. It was concluded that the perturbative uncertainty in the determination of threshold masses from the peak position (i..e when beam smearing effects are neglected), is between 50 and 80 MeV. It was also pointed out that the $\overline{\mathrm{MS}}$ mass can be determined with a comparable perturbative precision, only if $\alpha_s(M_Z)$ is known with an uncertainty of around 0.001. This restriction arises from the relatively large order α_s correction in the relation between threshold masses and $\overline{\mathrm{MS}}$ mass. For example, for a given measurement of the 1S mass, let's say $M_{1S} = 175$ GeV $\pm \delta M_{1S}$, and $\alpha_s(M_Z) = 0.118 \pm x\, 0.001$ the result for $\overline{m}_t(\overline{m}_t)$ reads [62]

$$\overline{m}_t(\overline{m}_t) \;=\; \left[175 - 7.58 - 0.96 - 0.23 \;\pm\; \delta M_{1S} \;\pm\; x\, 0.07 \right] \mathrm{GeV} \qquad (6.32)$$

where the first four numbers represent the perturbative series up to NNLO (three-loops). For a discussion of the behaviour of perturbative corrections at the next order see Refs. [63, 109]. The results in Fig. 6.9 also show a large uncertainty in the normalisation of the cross-section. This uncertainty is particularly puzzling, because there is no obvious physical reason for its existence. At present it does not seem to be related to renormalon-type higher order corrections, although it has also been speculated that the large size of the corrections could have some infrared origin that might be cured by accounting for off-shell effects of the toponium dynamics [221]. On the other hand, it has been shown in Ref. [103, 177] that the dominant N³LO logarithmic corrections to the cross-section of (relative) order $\alpha_s^3 \ln^2 v$ and $\alpha_s^3 \ln v$ are not small. It was estimated in Ref. [52] that the present theoretical relative uncertainty in the normalisation of the cross-section in the fixed order approach is at least at the level of 20%. This seems to jeopardise precise measurements of the top width, the top quark coupling to gluons and the Higgs boson. At present the only way to possibly improve the situation in the fixed order approach seems to be the determination of N³LO or even higher order corrections in order to learn more about the structure of the perturbative series.
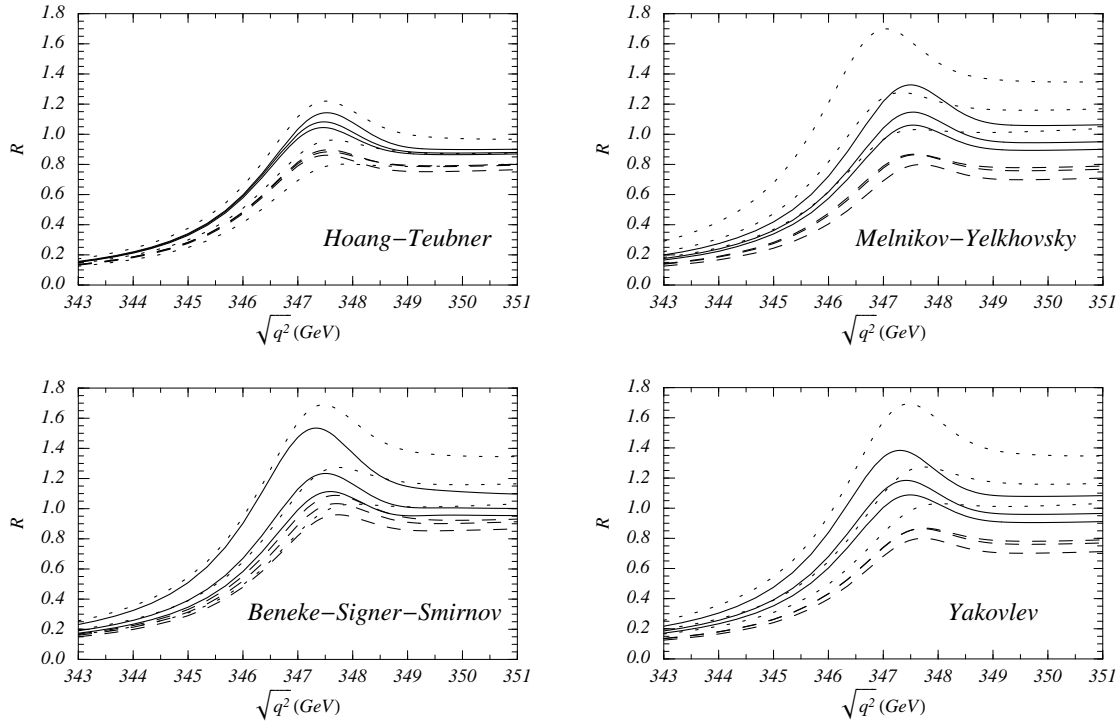
Fig. 6.9: The total normalised photon-induced $t\bar{t}$ cross-section R at the Linear Collider versus the c.m. energy in the threshold regime at LO (dotted curves), NLO (dashed) and NNLO (solid) for $\alpha_s(M_Z) = 0.119$, $\Gamma_t = 1.43$ GeV and $\mu = 15$, 30, 60 GeV. Hoang–Teubner used the 1S mass $M_{1S} = 173.68$ GeV, Melnikov–Yelkhovsky the kinetic $M_{\mathrm{kin}}(15\,\mathrm{GeV}) = 173.10$ GeV, and Beneke–Signer–Smirnov and Yakovlev the PS mass $M_{\mathrm{PS}}(20\,\mathrm{GeV}) = 173.30$ GeV. The plots were given in Ref. [52] from results provided by Hoang–Teubner, Melnikov–Yelkhovsky, Beneke–Signer–Smirnov and Yakovlev. The effects of the luminosity spectrum are not taken into account.

6.3.2 Renormalisation group improved approach

Apart from the Coulomb singularities proportional to powers of α_s/v, which have to be summed according to the scheme shown in Eq. (6.31) there is one additional source of potentially large higher corrections coming from logarithms of the top mass $m_t = 175$ GeV, the average top three-momentum $\mathbf{p}_t \sim 25$ GeV and the average kinetic energy $E_t \sim 4$ GeV. Terms such as $\alpha_s(m_t) \ln(m_t^2/E_t^2) \sim 0.8$ can spoil the fixed order expansion, as discussed before, and should to be summed to all orders. The scheme where all such logarithmic terms are summed consistently has the form

$$R = \frac{\sigma_{t\bar{t}}}{\sigma_{\mu^+\mu^-}} = v \sum_k \left(\frac{\alpha_s}{v}\right)^k \sum_i (\alpha_s \ln v)^i \times$$

$$\times \left\{ 1\,(\mathrm{LL}); \alpha_s, v\,(\mathrm{NLL}); \alpha_s^2, \alpha_s v, v^2\,(\mathrm{NNLL}) \right\}, \tag{6.33}$$

where the indicated terms are of leading-logarithmic (LL), next-to-leading-logarithmic (NLL), and next-to-next-to-leading-logarithmic order (NNLL). The expansion in Eq. (6.33) is called "renormalisation group improved" perturbation theory. Since the fixed-order approach relies on the identification of the contributions from the hard, soft, potential and ultra soft momentum regions in full QCD diagrams, it only accounts for the anomalous dimension associated with the running of the strong coupling and cannot be used to carry out renormalisation group improved computations for the top threshold cross-section. Moreover, in fixed order expansions it is not clear a priori which scale to use for the couplings in the highest computed order.

To achieve the expansion scheme in Eq. (6.33) one needs to apply a full effective theory description where all resonating degrees of freedom responsible for the $t\bar{t}$ low energy dynamics are implemented as fields of an effective theory and where all contributions from off-shell effects are integrated out. The logarithmic terms mentioned above are associated with UV-divergences in the effective theory and can be summed up after renormalisation of the effective theory operators and solution of the resulting renormalisation group equations. In this formulation all logarithmic terms are contained in the Wilson coefficients of the effective theory operators after they have been run to the low energy scale. On the other hand, all matrix elements are free of any large logarithmic contributions. Since the logarithmic terms mentioned above involve only perturbative scales much larger than Λ_{QCD}, the effective field theory description for the $t\bar{t}$ total cross-section at threshold allows for purely perturbative computations of the Wilson coefficients as well as of the low-energy matrix elements.

Renormalisation group improved computations that can be applied to the total top threshold cross-section have been carried out in pNRQCD and vNRQCD. In addition to the operators in the respective effective Lagrangians also external currents need to be defined that describe the production of the top quark pair for non-relativistic momenta through the electroweak interactions. The vector ($^3S_1$) currents relevant at NNLL order have the form $\mathbf{J}_{\boldsymbol{p}}^v = c_1\boldsymbol{O}_{\mathbf{p},1} + c_2\boldsymbol{O}_{\mathbf{p},2}$, where [170]

$$\boldsymbol{O}_{\mathbf{p},1} = \psi_{\mathbf{p}}^\dagger\,\boldsymbol{\sigma}(i\sigma_2)\,\chi_{-\mathbf{p}}^*\,, \tag{6.34}$$

$$\boldsymbol{O}_{\mathbf{p},2} = \frac{1}{m^2}\,\psi_{\mathbf{p}}^\dagger\,\mathbf{p}^2\boldsymbol{\sigma}(i\sigma_2)\,\chi_{-\mathbf{p}}^*\,,$$

and the relevant axial-vector ($^3P_1$) current is $\mathbf{J}_{\boldsymbol{p}}^a = c_3\boldsymbol{O}_{\mathbf{p},3}$, where

$$\boldsymbol{O}_{\mathbf{p},3} = \frac{-i}{2m}\,\psi_{\mathbf{p}}^\dagger\,[\,\boldsymbol{\sigma},\boldsymbol{\sigma}\cdot\mathbf{p}\,]\,(i\sigma_2)\,\chi_{-\mathbf{p}}^*\,. \tag{6.35}$$

The corresponding annihilation currents $\boldsymbol{O}_{\mathbf{p},i}^\dagger$ are obtained by complex conjugation. The currents $\boldsymbol{O}_{\mathbf{p},2,3}$ contribute only at the NNLL level. The NNLL total cross-section is then written in the form

$$\sigma_{t\bar{t}} = c_1^2\,\mathrm{Im}[\,\mathcal{A}_{11}(\sqrt{s})\,] + c_1 c_2\,\mathrm{Im}[\,\mathcal{A}_{12}(\sqrt{s}) + \mathrm{h.c.}\,] + c_3^2\,\mathrm{Im}[\,\mathcal{A}_{33}(\sqrt{s})\,]\,, \tag{6.36}$$

where the c_i are the Wilson coefficients of the currents and the $\mathcal{A}_{ij}$ are the Fourier transforms of time ordered products of the currents $\boldsymbol{O}_{\mathbf{p},i}$ and $\boldsymbol{O}_{\mathbf{p},i}^\dagger$. The first term contributes at the LL level, while the second and third terms contribute at NNLL order only. The $\mathcal{A}_{ij}$ are obtained from the zero-distance Green function $G(\mathbf{r}=0,\mathbf{r}'=0,\sqrt{s}-2m_t)$ of a two-body Schrödinger equation. At present, analyses of the total top pair cross-section at threshold at NNLL order within renormalisation group improved perturbation theory have only been presented in the framework of vNRQCD [170, 176] (see Section 5). The Wilson coefficients of the potentials in the Schrödinger equation and of the v^2-suppressed currents are known at NNLL order for the cross-section [95, 96, 104, 105, 167, 173–175], whereas the Wilson coefficient c_1 of the leading order vector current is only fully known at NLL order [94, 96, 173, 174]. Recently, the NNLL order non-mixing contributions to the anomalous dimension of c_1 coming from genuine three-loop vertex diagrams in vNRQCD were computed in Ref. [171]. These corrections were found to be comparable to the NLL contributions. The NNLL order corrections associated to the higher order running of the couplings that mix into the NLL order anomalous dimension of c_1 are still unknown. Figure 6.10 shows the photon-induced total cross-section in renormalisation group improved perturbation theory obtained in Ref. [178]. The curves show the LL (dotted blue lines), NLL (dashed green lines) and NNLL (solid red lines) cross-section for the vNRQCD scaling parameter $\nu = 0.15, 0.2$ and 0.3, $\alpha_{\mathrm{s}}(M_z) = 0.118$, $\Gamma_t = 1.43$ and $m_{1\mathrm{S}} = 175$ GeV. Compared to the fixed order results discussed above there is an improvement in the convergence and the remaining scale variation, but the NNLL order curves are still shifted by a positive correction similar to the fixed order predictions (see Fig. 6.9). In Ref. [178] the present theoretical uncertainty in the normalisation of the NNLL order cross-section was estimated
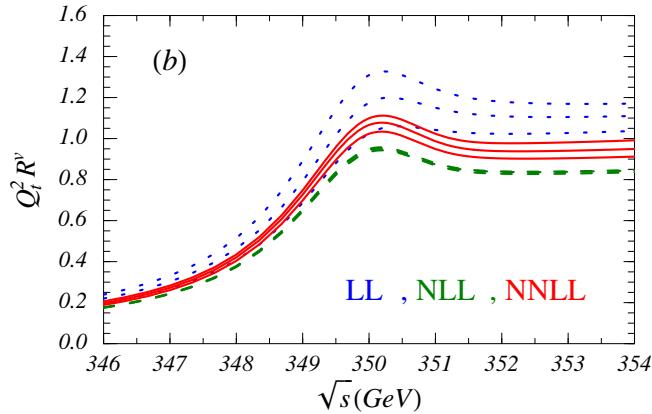
Fig. 6.10: The photon-induced top pair threshold cross-section for $M^{1S} = 175\,\text{GeV}$, $\alpha_s(M_z) = 0.118$ and $\Gamma_t = 1.43\,\text{GeV}$ in renormalisation group improved perturbation theory in vNRQCD at LL (dotted lines), NLL (dashed lines) and NNLL (solid lines) order. For each order curves are plotted for the renormalisation parameter $\nu = 0.15$, 0.20, and 0.3. The effects of the luminosity spectrum are not included.

as $\delta\sigma_{t\bar{t}}/\sigma_{t\bar{t}} = 6\%$. Here, the determination of the still missing mixing contributions to the NNLL anomalous dimension of c_1 is needed to get a more complete picture on the theoretical uncertainties. The spin-dependent mixing contributions have been determined in Ref. [181]

6.3.3   Treatment of unstable particles

For the theoretical description of the top threshold dynamics it is not possible to treat the top quark as a stable particle because within the Standard Model the top quark is expected to have a width of approximately $\Gamma_t \approx 1.5$ GeV, which is comparable to the average kinetic energy of the produced top quarks. For the total cross-section, as long as one is not interested in any differential information of the decay process, the finite width effects can be implemented as modifications of the effective theory Wilson coefficients that arise when the effective theory is matched to the Standard Model. These modifications lead to additional real and imaginary contributions. Such imaginary contributions are a well known concept in quantum mechanics of inelastic processes where particle decay and absorption are described by potentials and coefficients carrying complex coefficients. Due to the unitarity of the Standard Model the optical theorem used in Eq. (6.25) still holds in the effective theory.

At leading order in the non-relativistic expansion, due to gauge invariance, the only modification in the effective theory matching conditions caused by electroweak effects are related to an additional imaginary mass term proportional to the total on-shell top width [186],

$$\delta\mathcal{L} \;=\; \sum_{\mathbf{P}} \psi_{\mathbf{P}}^{\dagger} i\,\frac{\Gamma_t}{2}\,\psi_{\mathbf{P}} + \sum_{\mathbf{P}} \chi_{\mathbf{P}}^{\dagger} i\,\frac{\Gamma_t}{2}\,\chi_{\mathbf{P}}\,. \tag{6.37}$$

Since one has to apply the counting rule $\Gamma_t/m_t \sim \alpha_s^2 \sim v^2$ [62] this leads to

$$\frac{i}{k^0 - \frac{\mathbf{p}^2}{2m_t} + \delta m_t + \frac{i}{2}\Gamma_t} \tag{6.38}$$

for the form of the top quark propagator, where δm_t is related to the top mass scheme that is used for the computations. For the total cross-section this is equivalent to a shift of the c.m. energy into the positive complex plane, $\sqrt{s} \rightarrow \sqrt{s} + i\Gamma_t$. [186] For the total cross-section the results of Refs. [186, 222–224] show that this prescription remains valid even at next-to-leading order due to cancellation of QCD non-factorisable corrections connecting the top quark production and decay. The full set of

electroweak corrections to the effective theory matching conditions at next-to-next-to-leading order is currently unknown, although some contributions have been identified at this order. [62, 225–230] These results indicate that these corrections are at the level of a few percent.

For differential observables a number of leading order analyses have been made in the past in order to assess their physics impact (see Section 6.4). However, a systematic description of electroweak effects in differential observables, which would require a consistent theory describing unstable top and antitop quarks, does not exist at this time. First steps towards such a theory have been undertaken in Ref. [231, 232].

6.3.4 Non-perturbative effects

As discussed above, all scales in the effective field theory calculation are large compared to Λ_{QCD}, and $t\bar{t}$ production can be calculated in perturbative QCD. Nevertheless, as we are aiming at a very high accuracy, the question about the size of possible residual non-perturbative effects is legitimate. Such effects can be estimated through the interaction of the non-relativistic $t\bar{t}$ system with long-range fluctuations of the gluon field, see Chapter 3, Section 2.3. In the approximation of a constant (w.r.t. the size and lifetime of the $t\bar{t}$ state) chromoelectric field these corrections can be parametrised in form of the gluon condensate $\langle 0|\alpha_{\mathrm{s}}G_{\mu\nu}G^{\mu\nu}|0\rangle$. In Ref. [233] an explicit formula was derived, and it was found that the corrections due to the gluon-condensate are strongly energy dependent but small and decreasing with increasing m_t, Γ_t. For a realistic top mass and width they are completely negligible (of the order 10^{-4} for the cross-section) compared to the uncertainties from the perturbative treatment, see also [234]. This result also agrees with studies of the influence of the long-distance part of phenomenological QCD potentials. [188, 235] There, the effect from a linearly rising potential (or even more drastic deviations from the coulombic form) was shown to be irrelevant, a reflection of the extremely short lifetime of the $t\bar{t}$ system.

6.4 Studies of distributions and polarised beams

With the expected high luminosity at TESLA it is clear that, apart from the scan of the total cross-section through the threshold regime, detailed measurements of distributions will become feasible. Such distributions will help to disentangle correlations between m_t and α_{s} and improve the accuracy of the determination of the top quark mass. Even more important, the measurement of distributions will allow for detailed studies of the top quark's couplings (and possible deviations from SM expectations) in production and decay of $t\bar{t}$. Detailed analyses have been carried out by the European and Asian Linear Collider study groups in the past years, partly before the NNLO (and NNLL) improved calculations for the total cross-section became available. However, important information may be gained from those leading order (partly higher order improved) analyses, and, eventually, higher order corrections should be calculated also for observables beyond the total inclusive cross-section.

In the following we will discuss the momentum distribution of top quarks, measurements of the forward–backward asymmetry A_{FB} and the issue of top quark polarisation and polarised e^- (and possibly e^+) beams.

6.4.1 Momentum distribution of top quarks

As is clear from the picture of non-relativistic, quasi-bound top quarks having a sizeable decay width, even at fixed c.m. energy $\sqrt{s}$, t and $\bar{t}$ are not produced with a well defined momentum but with a broad distribution. In the picture of non-relativistic Quantum Mechanics this momentum distribution is proportional to the square of the (momentum-space) wave function and can be measured by reconstruction of the top decays. Figure 6.11 shows theoretical predictions for typical momentum distributions for two different values of m_t but the same fixed c.m. energy. The shaded bands come from the variation of $\alpha_{\mathrm{s}} = 0.118 \pm 0.003$. It is clear from Fig. 6.11 that the peak position of the momentum distribution is much more sensitive to m_t than to α_{s} which mainly influences the normalisation.
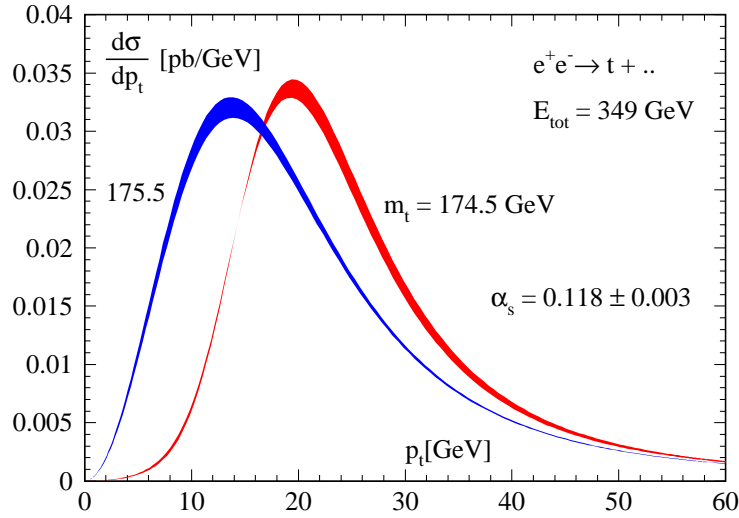
Fig. 6.11: Momentum distribution of the top quark for two different values of m_t at the same fixed c.m. energy $E_{\text{tot}} = 349$ GeV. The bands arise from variation of α_s as indicated (figure taken from Ref. [236].)

6.4.2 The forward–backward asymmetry A_{FB}

Top pair production through a virtual Z boson leads to a small P wave in addition to the dominant S-wave contribution. Interference of S and P-wave results in a forward–backward asymmetry defined as

$$A_{\text{FB}} = \frac{1}{\sigma_{\text{tot}}} \left(\int_0^1 \mathrm{d} \cos \Theta - \int_{-1}^0 \mathrm{d} \cos \Theta \right) \frac{\mathrm{d}\sigma}{\mathrm{d} \cos \Theta} \tag{6.39}$$

which is of order 10% but energy dependent with a minimum of about 5% close to the energy of the $1S$ peak (see Fig. 6.8 in Section 6.2). As A_{FB} comes from the *overlap* of the (smeared out) $1S$ and $1P$ would-be resonances, it is sensitive to the top quark width Γ_t and, to a lesser extent, to α_s.

In experimental simulations, the momentum distribution and the forward–backward asymmetry have been used in addition to the total cross-section in order to add valuable information and to increase the accuracy of the determination of m_t, α_s, Γ_t and possibly even the top Yukawa coupling y_t, see the discussion in Section 6.2 above.

6.4.3 Polarisation

Near threshold, S-wave production dominates, and the spins of $t, \bar{t}$ are aligned with the electron beam direction. Therefore, even for unpolarised incoming e^+, e^- beams the longitudinal top quark polarisation is still $\sim 40\%$. With polarised beams one can obtain a sample of highly polarised top quarks near threshold, and with a tunable polarisation of the e^- beam the top quark polarisation could be selected. Quantitatively, for a realistic longitudinal e^- polarisation, $P_{e^-} = +80\% \ (-80\%)$, and unpolarised positrons, $P_{e^+} = 0$, one would arrive at $+60\% \ (-90\%)$ polarised top quarks! This level would be further enhanced if the e^+ beam would be polarised as well.

Because of the large top quark width this polarisation is transferred to the top decay products practically without hadronization effects. As in addition the top spin can be well measured through the angular distribution of W decay leptons, $t\bar{t}$ production near threshold is also a very interesting field for spin physics.

While the top quarks are mainly polarised longitudinally, polarisation transverse and normal to the production plane is induced through S–P wave interference effects and the QCD threshold dynamics, see [193–195] for details. It is interesting to note that normal polarisation is sensitive to the (electric, weak and strong) EDM of the top quark and could, if measured to be larger than predicted, signal CP

violation beyond the SM. With tunable $e^{\pm}$ polarisations and measurements at several c.m. energies, the different effects from the top quarks couplings to γ, Z and g could be disentangled [196]. Such analyses in the threshold region would complement top coupling measurements in the continuum at larger c.m. energies and can have an unexpectedly high sensitivity due to the tunable polarisation.

6.4.4 *Rescattering corrections*

Since the typical energy transfer at threshold is comparable to the top quark width there is in general no factorisation between production and decay of t and $\bar{t}$. In principle one would have to calculate $e^+e^- \rightarrow W^+\,b\,W^-\,\bar{b}$, including non-resonant backgrounds. However, the non-factorisable corrections due to gluonic cross-talk between $t \leftrightarrow \bar{b}$, $\bar{t} \leftrightarrow b$ and $b \leftrightarrow \bar{b}$ are suppressed in the total cross-section as mentioned above [186, 194, 195, 222–224]. The situation is different for exclusive observables which are in general affected by final state corrections at NLO. For the momentum distribution, A_{FB} and the top quark polarisation there exist results for these rescattering corrections in the non-relativistic approximation, see [194, 195]. They are of the expected parametric size (order α_{s}) and slightly reduce the momentum of the top quarks. Depending on the c.m. energy and the $e^{\pm}$ polarisation, they also lead to a sizeable change of A_{FB}. Similarly, the different components of the top quark polarisation can be strongly affected. Therefore, realistic experimental studies should take the rescattering corrections into account. Nevertheless, observables have been constructed which are independent of the $t\bar{t}$ production dynamics and rescattering corrections and only probe the decay of the polarised t, $\bar{t}$, even in the presence of anomalous decay vertices [194, 195, 237, 238].

6.5 Future Opportunities

The study of the problem of top quark pair production at threshold has, starting with the first pioneering works about 15 years ago, led to impressive results, including the recent development of effective field theories for heavy quarkonia. Nevertheless, many problems remain to be solved. Among them are, as discussed above, the complete computation of the NNLL corrections (renormalisation group improvement) for the total cross-section. Complementary information about the behaviour of the perturbative expansion and independent cross-checks will also be gained through further advances in fixed-order calculations beyond NNLO. Such results would also contribute to the matching conditions of a NNNLL renormalisation group improved computation of the cross-section. Some of the N^{3}LO contributions are already known [103, 177], and more is to be expected as the technology to carry out such computations is in principle available.

On the conceptual side, a consistent treatment of electroweak corrections including the instability of the top quark and interferences with non-resonant final states is still missing. These effects should be more important for differential cross-sections, but a relevant impact on the total cross-section cannot be excluded. Closely connected to this issue is the problem of rescattering corrections. NLO calculations have shown their relevance for distributions, but a consistent treatment within the effective field theory context will require further breakthroughs in the treatment of unstable particles.

With the Tevatron Run II and at the future LHC, hadroproduction of $t\bar{t}$ is growing out of the discovery era and entering the phase of precision measurements. Consequently top threshold dynamics may also play a role there. Similarly, the production process $\gamma\gamma \rightarrow t\bar{t}$ (e.g., through the option of laser backscattering at a future e^+e^- collider) is not explored with the same accuracy as the production in e^+e^- annihilation [219, 239]. The formulation of the threshold dynamics in the framework of effective field theories may also be suitable to calculate the threshold production of coloured particles in extended models, like e.g., squark pairs in supersymmetry, systematically and with higher precision.

Hopefully, in a not too far future from now, a future e^+e^- Linear Collider will be in operation. To make best use of the anticipated $t\bar{t}$ threshold data, fully realistic simulations including experimental cuts are needed. This requires the theoretical treatment of differential distributions, width and rescattering ef-

fects as discussed above, but also the simulation of detector and beam effects as discussed in Section 6.2. In this respect further collaboration between experiment and theory will be crucial to extend the existing simulations which were performed within the regional study groups preparing for the next e^+e^- Linear Collider.

REFERENCES

[1] M.A. Shifman, A.I. Vainshtein and V.I. Zakharov, Nucl. Phys. B **147** (1979) 385, 448.

[2] L.J. Reinders, H. Rubinstein and S. Yazaki, Phys. Rept. **127** (1985) 1.

[3] M. Davier, S. Eidelman, A. Höcker and Z. Zhang, Eur. Phys. J. C **31** (2003) 503, hep-ph/0308213.

[4] H. Burkhardt and B. Pietrzyk, Phys. Lett. B **513** (2001) 46.

[5] A. Czarnecki, S.I. Eidelman and S.G. Karshenboim, Phys. Rev. D **65** (2002) 053004, hep-ph/0107327.

[6] J.H. Kühn and M. Steinhauser, Nucl. Phys. B **619** (2001) 588, hep-ph/0109084.

[7] PLUTO Collaboration, J. Burmester *et al.*, Phys. Lett. B **66** (1977) 395.

[8] DASP Collaboration, R. Brandelik *et al.*, Phys. Lett. B **76** (1978) 361.

[9] J. Siegrist *et al.*, Phys. Rev. Lett. **36** (1976) 700.

[10] J. Siegrist *et al.*, Phys. Rev. D **26** (1982) 969.

[11] A. Osterheld *et al.*, SLAC-PUB-4160.

[12] BES Collaboration, J.Z. Bai *et al.*, Phys. Rev. Lett. **84** (2000) 594, hep-ex/9908046.

[13] BES Collaboration, J.Z. Bai *et al.*, Phys. Rev. Lett. **88** (2002) 101802, hep-ex/0102003.

[14] Crystal Ball Collaboration, C. Edwards *et al.* (1990), SLAC-PUB-5160.

[15] LENA Collaboration, B. Niczyporuk *et al.*, Zeit. Phys. C **15** (1982) 299.

[16] A.E. Blinov *et al.*, Z. Phys. C **49** (1991) 239.

[17] A.E. Blinov *et al.*, Z. Phys. C **70** (1996) 31.

[18] PLUTO Collaboration, C. Berger *et al.*, Phys. Lett. B **81** (1979) 410.

[19] DESY-Hamburg-Heidelberg-Munich Collaboration, P. Bock *et al.*, Zeit. Phys. C **6** (1980) 125.

[20] H. Albrecht *et al.*, Phys. Lett. B **116** (1982) 383.

[21] E. Rice *et al.*, Phys. Rev. Lett. **48** (1982) 906.

[22] CLEO Collaboration, R. Giles *et al.*, Phys. Rev. D **29** (1984) 1285.

[23] Crystal Ball Collaboration, Z. Jakubowski *et al.*, Z. Phys. C **40** (1988) 49.

[24] ARGUS Collaboration, H. Albrecht *et al.*, Z. Phys. C **54** (1992) 13.

[25] CLEO Collaboration, R. Ammar *et al.*, Phys. Rev. D **57** (1998) 1350, hep-ex/9707018.

[26] D.M.J. Lovelock *et al.*, Phys. Rev. Lett. **54** (1985) 377.

[27] CLEO Collaboration, D. Besson *et al.*, Phys. Rev. Lett. **54** (1985) 381.

[28] E. Eichten *et al.*, Phys. Rev. D **17** (1978) 3090.

[29] N.A. Tornqvist, Phys. Rev. Lett. **53** (1984) 878.

[30] Particle Data Group Collaboration, S. Eidelman *et al.*, Phys. Lett. B **592** (2004) 1.

[31] G. Corcella and A.H. Hoang, Phys. Lett. B **554** (2003) 133, hep-ph/0212297.

[32] A.H. Hoang and M. Jamin, Phys. Lett. B **594** (2004) 127, hep-ph/0403083.

[33] S. Binner, J.H. Kühn and K. Melnikov, Phys. Lett. B **459** (1999) 279, hep-ph/9902399.

[34] M. Benayoun, S.I. Eidelman, V.N. Ivanchenko and Z.K. Silagadze, Mod. Phys. Lett. A **14** (1999) 2605, hep-ph/9910523.

[35] BABAR Collaboration, B. Aubert *et al.*, Phys. Rev. D **69** (2004) 011103, hep-ex/0310027.

[36] M. Davier (2003), hep-ex/0312063.

[37] CLEO Collaboration, G.D. Crawford *et al.*, Nucl. Instrum. Meth. A **345** (1994) 429.

[38] F.A. Berends and R. Kleiss, Nucl. Phys. B **178** (1981) 141.

[39] A.B. Arbuzov *et al.*, JHEP **10** (1997) 001, hep-ph/9702262.

[40] T. Sjostrand, Comput. Phys. Commun. **82** (1994) 74.

[41] B. Andersson and H. Hu (1999), hep-ph/9910285.

[42] E.A. Kuraev and V.S. Fadin, Sov. J. Nucl. Phys. **41** (1985) 466.

[43] R. Tarrach, Nucl. Phys. B **183** (1981) 384.

[44] A.S. Kronfeld, Phys. Rev. D **58** (1998) 051501, hep-ph/9805215.

[45] I.I.Y. Bigi, M.A. Shifman, N.G. Uraltsev and A.I. Vainshtein, Phys. Rev. D **50** (1994) 2234, hep-ph/9402360.

[46] M. Beneke and V.M. Braun, Nucl. Phys. B **426** (1994) 301, hep-ph/9402364.

[47] W.A. Bardeen, A.J. Buras, D.W. Duke and T. Muta, Phys. Rev. D **18** (1978) 3998.

[48] N. Gray, D.J. Broadhurst, W. Grafe and K. Schilcher, Z. Phys. C **48** (1990) 673.

[49] K.G. Chetyrkin and M. Steinhauser, Nucl. Phys. B **573** (2000) 617, hep-ph/9911434.

[50] K. Melnikov and T.v. Ritbergen, Phys. Lett. B **482** (2000) 99, hep-ph/9912391.

[51] A.H. Hoang (2000), hep-ph/0008102.

[52] A.H. Hoang *et al.*, Eur. Phys. J. direct C **2** (2000) 3, hep-ph/0001286.

[53] I.I. Bigi, M.A. Shifman, N.G. Uraltsev and A.I. Vainshtein, Phys. Rev. D **52** (1995) 196, hep-ph/9405410.

[54] I.I.Y. Bigi, M.A. Shifman, N. Uraltsev and A.I. Vainshtein, Phys. Rev. D **56** (1997) 4017, hep-ph/9704245.

[55] A. Czarnecki, K. Melnikov and N. Uraltsev, Phys. Rev. Lett. **80** (1998) 3189, hep-ph/9708372.

[56] K. Melnikov and A. Yelkhovsky, Phys. Rev. D **59** (1999) 114009, hep-ph/9805270.

[57] M. Beneke, Phys. Lett. B **434** (1998) 115, hep-ph/9804241.

[58] Y. Schröder, Phys. Lett. B **447** (1999) 321, hep-ph/9812205.

[59] M. Peter, Phys. Rev. Lett. **78** (1997) 602, hep-ph/9610209.

[60] A.H. Hoang, Z. Ligeti and A.V. Manohar, Phys. Rev. Lett. **82** (1999) 277, hep-ph/9809423.

[61] A.H. Hoang, Z. Ligeti and A.V. Manohar, Phys. Rev. D **59** (1999) 074017, hep-ph/9811239.

[62] A.H. Hoang and T. Teubner, Phys. Rev. D **60** (1999) 114027, hep-ph/9904468.

[63] Y. Kiyo and Y. Sumino, Phys. Rev. D **67** (2003) 071501, hep-ph/0211299.

[64] A. Pineda, JHEP **06** (2001) 022, hep-ph/0105008.

[65] M. Beneke, Phys. Rept. **317** (1999) 1, hep-ph/9807443.

[66] T. Lee, JHEP **10** (2003) 044, hep-ph/0304185.

[67] M. Battaglia *et al.* (2003), hep-ph/0304132. CERN-YR: The CKM matrix and the unitarity triangle.

[68] V. A. Novikov *et al.*, Phys. Rev. Lett. **38** (1977) 626. [Erratum-ibid. **38** (1977) 791].

[69] M.B. Voloshin, Int. J. Mod. Phys. A **10** (1995) 2865, hep-ph/9502224.

[70] A.H. Hoang, Phys. Rev. D **59** (1999) 014039, hep-ph/9803454.

[71] E.C. Poggio, H.R. Quinn and S. Weinberg, Phys. Rev. D **13** (1976) 1958.

[72] M.N. Chernodub, F.V. Gubarev, M.I. Polikarpov and V.I. Zakharov, Phys. Lett. B **475** (2000) 303, hep-ph/0003006.

[73] J.H. Kühn, A.A. Penin and A.A. Pivovarov, Nucl. Phys. B **534** (1998) 356, hep-ph/9801356.

[74] A.A. Penin and A.A. Pivovarov, Nucl. Phys. B **549** (1999) 217, hep-ph/9807421.

[75] M. Jamin and A. Pich, Nucl. Phys. B **507** (1997) 334, hep-ph/9702276.

[76] M. Jamin and A. Pich, Nucl. Phys. Proc. Suppl. **74** (1999) 300, hep-ph/9810259.

[77] A.H. Hoang, Phys. Rev. D **61** (2000) 034005, hep-ph/9905550.

[78] M. Beneke and A. Signer, Phys. Lett. B **471** (1999) 233, hep-ph/9906475.

[79] J. Erler and M. x. Luo, Phys. Lett. B **558** (2003) 125, hep-ph/0207114.

[80] M. Eidemüller, Phys. Rev. D **67** (2003) 113002, hep-ph/0207237.

[81] J. Bordes, J. Penarrocha and K. Schilcher, Phys. Lett. B **562** (2003) 81, hep-ph/0212083.

[82] M.R. Ahmady *et al.* (2004), hep-ph/0401036, hep-ph/0401036.

[83] A.I. Onishchenko (2000), hep-ph/0005127.

[84] D.J. Broadhurst *et al.*, Phys. Lett. B **329** (1994) 103, hep-ph/9403274.

[85] C. W. Bauer, Z. Ligeti, M. Luke, A. V. Manohar and M. Trott, Phys. Rev. D **70** (2004) 094017 [arXiv:hep-ph/0408002].

[86] J. Penarrocha and K. Schilcher, Phys. Lett. B **515** (2001) 291, hep-ph/0105222.

[87] B.L. Ioffe and K.N. Zyablyuk, Eur. Phys. J. C **27** (2003) 229, hep-ph/0207183.

[88] F. Le Diberder and A. Pich, Phys. Lett. B **286** (1992) 147.

[89] M. Eidemüller and M. Jamin, Phys. Lett. B **498** (2001) 203, hep-ph/0010334.

[90] A. Pineda and J. Soto, Nucl. Phys. Proc. Suppl. **64** (1998) 428, hep-ph/9707481.

[91] A. Pineda and J. Soto, Phys. Lett. B **420** (1998) 391, hep-ph/9711292.

[92] A. Pineda and J. Soto, Phys. Rev. D **59** (1999) 016005, hep-ph/9805424.

[93] N. Brambilla, A. Pineda, J. Soto and A. Vairo, Nucl. Phys. B **566** (2000) 275, hep-ph/9907240.

[94] M.E. Luke, A.V. Manohar and I.Z. Rothstein, Phys. Rev. D **61** (2000) 074025, hep-ph/9910209.

[95] A.V. Manohar and I.W. Stewart, Phys. Rev. D **62** (2000) 014033, hep-ph/9912226.

[96] A.H. Hoang and I.W. Stewart, Phys. Rev. D **67** (2003) 114020, hep-ph/0209340.

[97] A. Pineda and F.J. Yndurain, Phys. Rev. D **58** (1998) 094022, hep-ph/9711287.

[98] A. Pineda and F.J. Yndurain, Phys. Rev. D **61** (2000) 077505, hep-ph/9812371.

[99] K. Melnikov and A. Yelkhovsky, Nucl. Phys. B **528** (1998) 59, hep-ph/9802379.

[100] N. Brambilla, A. Pineda, J. Soto and A. Vairo, Phys. Rev. D **60** (1999) 091502, hep-ph/9903355.

[101] N. Brambilla, A. Pineda, J. Soto and A. Vairo, Phys. Lett. B **470** (1999) 215, hep-ph/9910238.

[102] B.A. Kniehl and A.A. Penin, Nucl. Phys. B **563** (1999) 200, hep-ph/9907489.

[103] B.A. Kniehl and A.A. Penin, Nucl. Phys. B **577** (2000) 197, hep-ph/9911414.

[104] A.H. Hoang, A.V. Manohar and I.W. Stewart, Phys. Rev. D **64** (2001) 014033, hep-ph/0102257.

[105] A. Pineda, Phys. Rev. D **65** (2002) 074007, hep-ph/0109117.

[106] Y. Kiyo and Y. Sumino, Phys. Lett. B **496** (2000) 83, hep-ph/0007251.

[107] B.A. Kniehl, A.A. Penin, M. Steinhauser and V.A. Smirnov, Phys. Rev. D **65** (2002) 091503, hep-ph/0106135.

[108] B.A. Kniehl, A.A. Penin, M. Steinhauser and V.A. Smirnov, Nucl. Phys. B **635** (2002) 357, hep-ph/0203166.

[109] A.A. Penin and M. Steinhauser, Phys. Lett. B **538** (2002) 335, hep-ph/0204290.

[110] A.H. Hoang and A.V. Manohar, Phys. Lett. B **483** (2000) 94, hep-ph/9911461.

[111] M. Melles, Phys. Rev. D **58** (1998) 114004, hep-ph/9805216.

[112] D. Eiras and J. Soto, Phys. Lett. B **491** (2000) 101, hep-ph/0005066.

[113] M.B. Voloshin, Nucl. Phys. B **154** (1979) 365.

[114] H. Leutwyler, Phys. Lett. B **98** (1981) 447.

[115] M.B. Voloshin, Sov. J. Nucl. Phys. **36** (1982) 143.

[116] A. Pineda, Nucl. Phys. B **494** (1997) 213, hep-ph/9611388.

[117] A.H. Hoang and R. Hofmann, Phys. Rev. D **67** (2003) 054024, hep-ph/0206201.

[118] A.H. Hoang, Nucl. Phys. Proc. Suppl. **116** (2003) 274, hep-ph/0210440.

[119] I.I. Balitsky, Nucl. Phys. B **254** (1985) 166.

[120] N. Brambilla, A. Pineda, J. Soto and A. Vairo, Phys. Lett. B **580** (2004) 60, hep-ph/0307159.

[121] U. Aglietti and Z. Ligeti, Phys. Lett. B **364** (1995) 75, hep-ph/9503209.

[122] A. Pineda, Ph.D. thesis, University of Barcelona (1998).

[123] A.H. Hoang, M.C. Smith, T. Stelzer and S. Willenbrock, Phys. Rev. D **59** (1999) 114014, hep-ph/9804227.

[124] A.H. Hoang, Nucl. Phys. Proc. Suppl. **86** (2000) 512, hep-ph/9909356.

[125] N. Brambilla, Y. Sumino and A. Vairo, Phys. Rev. D **65** (2002) 034001, hep-ph/0108084.

[126] C. Contreras, G. Cvetic and P. Gaete, Phys. Rev. D **70** (2004) 034008, hep-ph/0311202.

[127] N. Brambilla, Y. Sumino and A. Vairo, Phys. Lett. B **513** (2001) 381, hep-ph/0101305.

[128] F.A. Chishtie and V. Elias, Phys. Lett. B **521** (2001) 434, hep-ph/0107052.

[129] V. Lubicz, Nucl. Phys. Proc. Suppl. **94** (2001) 116, hep-lat/0012003.

[130] M. Bochicchio *et al.*, Nucl. Phys. B **262** (1985) 331.

[131] J. Rolf, S. Sint and A. Collaboration], JHEP **0212** (2002) 007, hep-ph/0209255.

[132] C.T.H. Davies *et al.*, Phys. Rev. Lett. **73** (1994) 2654, hep-lat/9404012.

[133] K.H.N. Collaboration], Nucl. Phys. Proc. Suppl. **73** (1999) 339, hep-lat/9809177.

[134] V. Gimenez, L. Giusti, G. Martinelli and F. Rapuano To appear in the proceedings of 22nd International Symposium on Lattice Field Theory (LATTICE 2004), Fermilab, June 21-26, 2004.

[135] V. Gimenez, L. Giusti, G. Martinelli and F. Rapuano, JHEP **03** (2000) 018, hep-lat/0002007.

[136] F. di Renzo To appear in the proceedings of 22nd International Symposium on Lattice Field Theory (LATTICE 2004), Fermilab, June 21-26, 2004.

[137] J. Heitger, R. Sommer and A. Collaboration], JHEP **0402** (2004) 022, hep-lat/0310035.

[138] G.M. de Divitiis et al., Nucl. Phys. B **675** (2003) 309, hep-lat/0305018.

[139] K.J. Juge, Nucl. Phys. Proc. Suppl. **94** (2001) 584, hep-lat/0011021.

[140] A.S. Kronfeld, Nucl. Phys. Proc. Suppl. **63** (1998) 311, hep-lat/9710007.

[141] D. Becirevic, V. Lubicz and G. Martinelli, Phys. Lett. B **524** (2002) 115, hep-ph/0107124.

[142] A. Dougal, C.M. Maynard and C. McNeille, to appear in the proceedings of 22nd International Symposium on Lattice Field Theory (LATTICE 2004), Fermilab, June 21-26, 2004.

[143] A. Dougall, C.M. Maynard and C.M.U. Collaboration], Nucl. Phys. Proc. Suppl. **129** (2004) 170, hep-lat/0309081.

[144] R. Barbieri, M. Caffo, R. Gatto and E. Remiddi, Phys. Lett. B **95** (1980) 93.

[145] P.B. Mackenzie and G.P. Lepage, Phys. Rev. Lett. **47** (1981) 1244.

[146] G.T. Bodwin, E. Braaten and G.P. Lepage, Phys. Rev. D **51** (1995) 1125, hep-ph/9407339.

[147] M. Gremm and A. Kapustin, Phys. Lett. B **407** (1997) 323, hep-ph/9701353.

[148] N. Brambilla *et al.*, Phys. Rev. D **67** (2003) 034018, hep-ph/0208019.

[149] A.A. Penin and A.A. Pivovarov, Phys. Lett. B **435** (1998) 413, hep-ph/9803363.

[150] S. Bethke, Nucl. Phys. Proc. Suppl. **121** (2003) 74, hep-ex/0211012.

[151] HPQCD Collaboration, C.T.H. Davies *et al.*, Phys. Rev. Lett. **92** (2004) 022001, hep-lat/0304004.

[152] A.X. El-Khadra, G. Hockney, A.S. Kronfeld and P.B. Mackenzie, Phys. Rev. Lett. **69** (1992) 729.

[153] G.P. Lepage and P.B. Mackenzie, Phys. Rev. D **48** (1993) 2250, hep-lat/9209022.

[154] M. Lüscher, R. Narayanan, P. Weisz and U. Wolff, Nucl. Phys. B **384** (1992) 168, hep-lat/9207009.

[155] Q. Mason *et al.*, to appear in the proceedings of 22nd International Symposium on Lattice Field

Theory (LATTICE 2004), Fermilab, June 21-26, 2004.

[156] QCDSF-UKQCD Collaboration, S. Booth *et al.*, Phys. Lett. B **519** (2001) 229, hep-lat/0103023.

[157] W.E. Caswell and G.P. Lepage, Phys. Lett. B **167** (1986) 437.

[158] B.A. Thacker and G.P. Lepage, Phys. Rev. D **43** (1991) 196.

[159] G.T. Bodwin, E. Braaten and G.P. Lepage, Phys. Rev. D **51** (1995) 1125, hep-ph/9407339.

[160] M.E. Luke and A.V. Manohar, Phys. Rev. D **55** (1997) 4129, hep-ph/9610534.

[161] A.V. Manohar, Phys. Rev. D **56** (1997) 230, hep-ph/9701294.

[162] M.E. Luke and M.J. Savage, Phys. Rev. D **57** (1998) 413, hep-ph/9707313.

[163] M. Beneke and V.A. Smirnov, Nucl. Phys. B **522** (1998) 321, hep-ph/9711391.

[164] H.W. Griesshammer, Phys. Rev. D **58** (1998) 094027, hep-ph/9712467.

[165] P. Labelle, Phys. Rev. D **58** (1998) 093013, hep-ph/9608491.

[166] B. Grinstein and I.Z. Rothstein, Phys. Rev. D **57** (1998) 78, hep-ph/9703298.

[167] A.V. Manohar and I.W. Stewart, Phys. Rev. D **62** (2000) 074015, hep-ph/0003032.

[168] A.V. Manohar and I.W. Stewart, Phys. Rev. Lett. **85** (2000) 2248, hep-ph/0004018.

[169] S. Karshenboim, Sov. Phys. JETP **76** (1993).

[170] A.H. Hoang, A.V. Manohar, I.W. Stewart and T. Teubner, Phys. Rev. D **65** (2002) 014014, hep-ph/0107144.

[171] A.H. Hoang, Phys. Rev. D **69** (2004) 034009, hep-ph/0307376.

[172] A.V. Manohar, J. Soto and I.W. Stewart, Phys. Lett. B **486** (2000) 400, hep-ph/0006096.

[173] A.V. Manohar and I.W. Stewart, Phys. Rev. D **63** (2001) 054004, hep-ph/0003107.

[174] A. Pineda, Phys. Rev. D **66** (2002) 054022, hep-ph/0110216.

[175] A. Pineda and J. Soto, Phys. Lett. B **495** (2000) 323, hep-ph/0007197.

[176] A.H. Hoang, A.V. Manohar, I.W. Stewart and T. Teubner, Phys. Rev. Lett. **86** (2001) 1951, hep-ph/0011254.

[177] B.A. Kniehl, A.A. Penin, M. Steinhauser and V.A. Smirnov, Phys. Rev. Lett. **90** (2003) 212001, hep-ph/0210161.

[178] A.H. Hoang, Acta Phys. Polon. B **34** (2003) 4491, hep-ph/0310301.

[179] B.A. Kniehl *et al.*, Phys. Rev. Lett. **92** (2004) 242001, hep-ph/0312086.

[180] A.A. Penin, A. Pineda, V.A. Smirnov and M. Steinhauser, Phys. Lett. B **593** (2004) 124, hep-ph/0403080.

[181] A.A. Penin, A. Pineda, V.A. Smirnov and M. Steinhauser, Nucl. Phys. B **699** (2004) 183, hep-ph/0406175.

[182] ECFA/DESY LC Physics Working Group Collaboration, J.A. Aguilar-Saavedra *et al.* (2001), hep-ph/0106315.

[183] American Linear Collider Working Group Collaboration, T. Abe *et al.* (2001), hep-ex/0106057.

[184] J.H. Kühn, Acta Phys. Polon. B **12** (1981) 347.

[185] I.I.Y. Bigi *et al.*, Phys. Lett. B **181** (1986) 157.

[186] V.S. Fadin and V.A. Khoze, JETP Lett. **46** (1987) 525.

[187] J.H. Kühn and T. Teubner, Eur. Phys. J. C **9** (1999) 221, hep-ph/9903322.

[188] M.J. Strassler and M.E. Peskin, Phys. Rev. D **43** (1991) 1500.

[189] R. Harlander, M. Jeżabek and J.H. Kühn, Acta Phys. Polon. **27** (1996) 1781, hep-ph/9506292.

[190] M. Jeżabek, J.H. Kühn and T. Teubner, Z. Phys. C **56** (1992) 653.

[191] Y. Sumino *et al.*, Phys. Rev. D **47** (1993) 56.

[192] H. Murayama and Y. Sumino, Phys. Rev. D **47** (1993) 82.

[193] R. Harlander, M. Jeżabek, J.H. Kühn and T. Teubner, Phys. Lett. B **346** (1995) 137, hep-ph/9411395.

[194] R. Harlander, M. Jeżabek, J.H. Kühn and M. Peter, Z. Phys. C **73** (1997) 477, hep-ph/9604328.

[195] M. Peter and Y. Sumino, Phys. Rev. D **57** (1998) 6912, hep-ph/9708223.

[196] M. Jeżabek, T. Nagano and Y. Sumino, Phys. Rev. D **62** (2000) 014034, hep-ph/0001322.

[197] G. Bagliesi *et al.*, prepared for Workshops on Future e^+e^- Linear Colliders, Hamburg, Germany and Saariselka, Finland, Sep 2-3 and Sep 9-11, 1991.

[198] K. Fujii, T. Matsui and Y. Sumino, Phys. Rev. D **50** (1994) 4341.

[199] P. Comas, R. Miquel, M. Martinez and S. Orteu, talk given at Physics with e^+e^- Linear Colliders (The European Working Groups 4 Feb - 1 Sep 1995: Session 1 (Session 2: 2-3 Jun 1995 in Assergi, Italy: Session 3: 30 Aug - 1 Sep 1995 in Hamburg, Germany), Annecy, France, 4 Feb 1995.

[200] D. Cinabro, talk given at 4th International Workshop on Linear Colliders (LCWS 99), Sitges, Barcelona, Spain, 28 Apr - 5 May 1999, hep-ex/0005015.

[201] D. Peralta, M. Martinez and R. Miquel, talk presented at the 4th International Workshop on Linear Colliders, Sitges, Barcelona, Spain, April 28 - May 5 1999.

[202] M. Martinez and R. Miquel, Eur. Phys. J. C **27** (2003) 49, hep-ph/0207315.

[203] R. Frey *et al.*, ECONF C **960625** (1996) STC119, hep-ph/9704243.

[204] M.N. Frary and D.J. Miller In 'Munich/Annecy/Hamburg 1991, Proceedings, e^+e^- collisions at 500 GeV', pp. 379-391.

[205] S.T. Boogert, talk presented at the International Conference on 1523: Linear Colliders (LCWS 2004), Paris, France, April 19-23, 2004.

[206] V.S. Fadin and V.A. Khoze, Sov. J. Nucl. Phys. **48** (1988) 309.

[207] W.k. Kwong, Phys. Rev. D **43** (1991) 1488.

[208] W.E. Caswell and G.P. Lepage, Phys. Lett. B **167** (1986) 437.

[209] A.H. Hoang, Phys. Rev. D **56** (1997) 7276, hep-ph/9703404.

[210] A.H. Hoang, Phys. Rev. D **56** (1997) 5851, hep-ph/9704325.

[211] A. Czarnecki and K. Melnikov, Phys. Rev. lett. **80** (1998) 2531, hep-ph/9712222.

[212] M. Beneke, A. Signer and V.A. Smirnov, Phys. Rev. lett. **80** (1998) 2535, hep-ph/9712302.

[213] A.H. Hoang, Phys. Rev. D **57** (1998) 1615, hep-ph/9702331.

[214] A.H. Hoang and T. Teubner, Phys. Rev. D **58** (1998) 114023, hep-ph/9801397.

[215] O.I. Yakovlev, Phys. Lett. B **457** (1999) 170, hep-ph/9808463.

[216] M. Beneke, A. Signer and V.A. Smirnov, Phys. Lett. B **454** (1999) 137, hep-ph/9903260.

[217] T. Nagano, A. Ota and Y. Sumino, Phys. Rev. D **60** (1999) 114014, hep-ph/9903498.

[218] A.A. Penin and A.A. Pivovarov, Nucl. Phys. B **550** (1999) 375, hep-ph/9810496.

[219] A.A. Penin and A.A. Pivovarov, Phys. Atom. Nucl. **64** (2001) 275, hep-ph/9904278.

[220] O.I. Yakovlev and S. Groote, Phys. Rev. D **63** (2001) 074012, hep-ph/0008156.

[221] Y. Kiyo and Y. Sumino, Phys. Lett. B **535** (2002) 145, hep-ph/0110277.

[222] K. Melnikov and O.I. Yakovlev, Phys. Lett. B **324** (1994) 217, hep-ph/9302311.

[223] V.S. Fadin, V.A. Khoze and A.D. Martin, Phys. Rev. D **49** (1994) 2247.

[224] W. Beenakker, F.A. Berends and A.P. Chapovsky, Phys. Lett. B **454** (1999) 129, hep-ph/9902304.

[225] R.J. Guth and J.H. Kühn, Nucl. Phys. B **368** (1992) 38.

[226] W. Mödritsch and W. Kummer, Nucl. Phys. B **430** (1994) 3.

[227] W. Kummer and W. Mödritsch, Phys. Lett. B **349** (1995) 525, hep-ph/9501406.

[228] W. Hollik and C. Schappacher, Nucl. Phys. B **545** (1999) 98, hep-ph/9807427.

[229] K. Kolodziej, Eur. Phys. J. C **23** (2002) 471, hep-ph/0110063.

[230] A. Biernacik and K. Kolodziej, Nucl. Phys. Proc. Suppl. **116** (2003) 33, hep-ph/0210405.

[231] M. Beneke, A.P. Chapovsky, A. Signer and G. Zanderighi (2003), hep-ph/0312331.

[232] M. Beneke, A.P. Chapovsky, A. Signer and G. Zanderighi, Nucl. Phys. B **686** (2004) 205, hep-ph/0401002.

[233] V.S. Fadin and O.I. Yakovlev, Sov. J. Nucl. Phys. **53** (1991) 688.

[234] A.H. Hoang (2002), hep-ph/0204299.

[235] T. Teubner, Production and decay of heavy quarks near threshold, Diploma thesis (in German), University of Karlsruhe (1993), unpublished.

[236] ECFA/DESY LC Physics Working Group Collaboration, E. Accomando *et al.*, Phys. Rept. **299** (1998) 1, hep-ph/9705442.

[237] Y. Sumino, Acta Phys. Polon. B **28** (1997) 2461, hep-ph/9711233.

[238] Y. Sumino and M. Jeżabek, Acta Phys. Polon. B **29** (1998) 1443.

[239] A. Czarnecki and K. Melnikov, Phys. Rev. D **65** (2002) 051501, hep-ph/0108233.

Chapter 7

CHARM AND BEAUTY IN MEDIA

Conveners: D. Kharzeev, M. P. Lombardo, C. Lourenço, M. Rosati, H. Satz

Authors: S. Datta, O. Kaczmarek, F. Karsch, D. Kharzeev, S. R. Klein, V. Laporta, M. P. Lombardo, C. Lourenço, L. Maiani, P. Petreczky, F. Piccinini, A. D. Polosa, L. Ramello, R. Rapp, V. Riquer, M. Rosati, H. Satz, E. Scomparin, R. Vogt, F. Zantow

1 INTRODUCTION[1]

Quarkonium in media is a topic which is central to the ultrarelativistic heavy ion program. In recent years this subject has been among the focal points of discussion at meetings such as "Quark Matter". ("The Quark Matter" series is traditionally the main forum of the high energy heavy ion community). Indeed, in these collisions — "little bangs" — one hopes to recreate matter as it was at the very beginning of the universe: a hot system with deconfined quarks and gluons and no chiral symmetry breaking.

This fascinating possibility calls for a number of theoretical and phenomenological studies. The QCD phase diagram and the mechanisms of chiral symmetry restoration, screening, and deconfinement at high temperature and baryon density need to be understood. A theory of the initial conditions must be developed and the equilibration of the plasma, if any, must be assessed in real experiments. It is also necessary to identify the thermodynamical region which is being explored and to study nonequilibrium effects. Finally, observables must be defined which provide physical signatures in real experiments.

Quarkonium plays a very important role in these phenomena. Indeed, quarkonium suppression was long ago suggested as a signal of deconfinement [1]. Due to their small size, quarkonia can, in principle, survive the deconfinement phase transition. However, because of colour screening, no bound state can exist at temperatures $T > T_D$ when the screening radius, $1/\mu_D(T)$, becomes smaller than the typical bound-state size [1]. Later it was realized that dramatic changes in the gluon momentum distributions at the deconfinement phase transition result in a sharp increase in the quarkonium dissociation rates [2–4]. Both the magnitude [5] and the energy dependence [6] of charmonium dissociation by gluons result in significant suppression of the $c\bar{c}$ states even for $T < T_D$ but higher than the deconfinement transition temperature, T_c. Moreover, close to T_D the thermal activation mechanism is expected to dominate [7,8]. The relative importance of gluon dissociation and thermal activation is governed by the ratio of the quarkonium binding energy $\epsilon(T)$ and the temperature T, $X(T) \equiv \epsilon(T)/T$ [9]. At $X(T) \ll 1$ thermal activation dominates while for $X(T) \gg 1$ the dominant mechanism is "ionization" by gluons.

Dissociation due to colour screening was studied using potential models with different parameterizations of the heavy quark potential [10–13] to determine T_D. All these studies predicted that excited charmonium states (χ_c, ψ') will essentially dissolve at T_c while the ground state J/ψ will dissociate at 1.1–1.3 T_c. Some potential models also predicted a strong change in the binding energy, see e.g., Ref. [12]. Recently, charmonium properties were investigated using lattice calculations [14,15] which indicate that the ground states exist with essentially unchanged properties at temperatures around $1.5T_c$.

Lattice investigations suggest that at low temperatures, $T < 1.5T_c$, screening is not efficient and therefore gluon dissociation may be the appropriate source of quarkonium suppression. One should also keep in mind that non-equilibrium effects in the very early stages of a heavy-ion collision, when the energy density is highest, should be considered for quarkonium suppression. Not much is known about

---

[1]Authors: D. Kharzeev, M. P. Lombardo, C. Lourenço, M. Rosati, H. Satz

these effects. However, they may be an even more important source of quarkonium suppression than a thermalized system, see e.g., Ref. [16].

To use heavy quarkonium as an effective probe of the state of matter in QCD, we should also have good theoretical control over the scattering amplitudes in a hadronic gas.

While addressing the issues outlined above, we will face questions familiar to the heavy quark and the thermodynamics communities. To fully understand the behaviour of quarkonium in media, these two communities should communicate and interact. For further background material and a review of the results as of Summer 2003, see Ref. [17].

The behavior of quarkonium in cold nuclear matter can be used to better understand the nuclear medium. For example, quarkonium can also be used to study nuclear parton distributions, particularly that of the gluon. In addition to hadroproduction studies, quarkonium photoproduction is directly sensitive to the nuclear gluon distribution.

2   QCD IN MEDIA, AND THE LATTICE APPROACH[2]

This section introduces strong interactions 'in media' using the field theory of QCD as the basic theoretical framework. We build on work presented in the 'Introduction to QCD' and 'General Tools' sections of this Yellow Report and briefly discuss basic aspects which are not covered there but are used in the rest of this Chapter.

We first discuss the phases of QCD, i.e., the fate of chiral symmetry and confinement at high temperature and density. We then introduce lattice thermodynamics, the main theoretical tool for studying equilibrium characteristics of the phase diagram. In doing so, deconfinement, screening, and spectral modifications, which are discussed at length later, will be briefly touched upon.

Our main interest is in heavy ion colliders experiments where the baryon density is relatively small. Lattice high density calculations are far less mature then those at high temperature. In particular, no results for heavy quarks have been obtained in the high density regime. Hence we will focus on the physics of QCD at high temperature.

Let us first consider the fate of confinement at high temperature. A sketchy view of the screening mechanism, already at work at $T = 0$, is the recombination of a (heavy) quark and antiquark with pairs generated by the vacuum, $Q\overline{Q} \rightarrow \overline{q}Q + q\overline{Q}$. At high temperature it becomes easier to produce light $q\overline{q}$ pairs from the vacuum. Hence it is easier to 'break' the colour string between a (heavy) quark, Q, and antiquark $\overline{Q}$. In other words, we expect colour screening to increase (sharply) at a phase boundary, eventually leading to quark and gluon liberation, the quark gluon plasma. Lattice simulations indicate that enhanced screening occurs at about $T \sim 200$ MeV, in a range accessible to collider experiments (see e.g., [18] for a recent review).

Consider now the fate of chiral symmetry at high temperature obtained by following the behaviour of the chiral condensate $\langle \overline{\psi}\psi \rangle$. One picture of the high T QCD transition can be drawn by using the ferromagnetic analogy of the chiral transition where $\overline{\psi}\psi$ can be thought of as a spin field taking values in real space, but oriented in the chiral sphere. Chiral symmetry breaking occurs when $\langle \overline{\psi}\psi \rangle \neq 0$, corresponding to the ordered phase. By increasing T, disorder increases, and $\langle \overline{\psi}\psi \rangle \rightarrow 0$, restoring chiral symmetry. Lattice simulations suggest that chiral symmetry restoration and enhanced screening happen at the same temperature within the numerical accuracy.

These seemingly simple pictures of chiral symmetry restoration and deconfinement at high temperature are complicated by a number of considerations. A finite quark mass breaks the chiral symmetry of the Lagrangian while screening can be rigorously related to deconfinement only at infinite quark mass. Rigorously speaking, the two mechanisms we are concerned with are defined in two opposite limits: zero
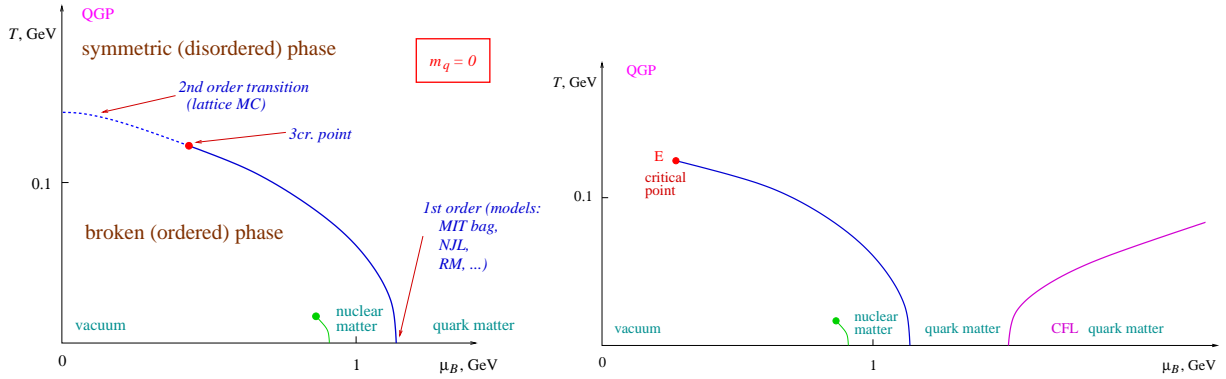
[2]Author: M. P. Lombardo

Fig. 7.1: The phase diagram of QCD for two massless flavours (left) and what is expected for realistic values of the quark masses (right). From M. Stephanov [19].

mass for chiral symmetry and infinite mass for confinement. For two (massless) flavours the transition seems to be of second order while the transition with three (massless) flavour turns out to be first order. We have to find out how the two flavour picture morphs with the three flavour one. In addition, it may well be that the $U_A(1)$ symmetry, broken at zero temperature, is effectively restored at high temperature, further complicating the patterns of chiral symmetry. It is also worth mentioning in this brief introduction that, even if the string 'breaks', bound states might well survive, giving rise to complicated, nonperturbative dynamics above the critical temperature, characterising the strongly-interacting quark gluon plasma. In addition to these conceptual difficulties, there are calculational problems since the phenomena we are concerned with are well outside the reach of perturbative calculations.

One goal of our subgroup is to understand how all of these phenomena affect the heavy quark spectrum when the phase boundary in Fig. 7.1 is crossed. Here, we show the phase diagram of QCD in the temperature and chemical potential plane. The diagrams for 'light QCD' (two massless quarks), and for realistic values of the u, d and s masses, were built using symmetry arguments and model calculations. The informal discussion presented here should already suggest that the physics of heavy quark bound states in media is driven by a rich and complex admixture of chiral symmetry restoration and enhanced screening, requiring both lattice and analytic studies. Recent advances will be presented in the next sections.

As a last introductory remark, we review a few basic facts about finite temperature field theory [20] and its formulation on the lattice [21]. In equilibrium field theory, the grand canonical partition function, $Z(V, T, \mu)$ completely determines the thermodynamic state of a system according to:

$$P = T\frac{\partial \ln Z}{\partial V} \tag{7.1}$$

$$N = T\frac{\partial \ln Z}{\partial \mu} \tag{7.2}$$

$$S = \frac{\partial[T \ln Z]}{\partial T} \tag{7.3}$$

$$E = -PV + TS + \mu N \tag{7.4}$$

while the physical observables $\langle O \rangle$ can be computed as

$$\langle O \rangle = \frac{\text{Tr}(O\hat{\rho})}{Z} . \tag{7.5}$$

In short, the problem is to represent Z for QCD at finite temperature and design a calculational scheme to describe it.

The partition function, Z, is the trace of the density matrix of the system, $\hat{\rho}$, so that

$$Z = \text{Tr}\,\hat{\rho} \tag{7.6}$$

$$\hat{\rho} = \exp[(-H - \mu\hat{N})/T] \tag{7.7}$$

where H is the Hamiltonian, T is the temperature and $\hat{N}$ is any conserved number operator. Introducing the integral, $S(\phi, \psi)$, of the Lagrangian density where Te is the temporal extent in Euclidean space,

$$S(\phi, \psi) = \int_0^{Te} dt \int d^3x \mathcal{L}(\phi, \psi) , \tag{7.8}$$

and Z is defined as

$$Z = \int d\phi\, d\psi\, \exp[-S(\phi, \psi)] . \tag{7.9}$$

Comparing the path integral representation of the partition function, Eq. (7.9), with the statistical mechanics representation, Eq. (7.7), we can identify the finite temporal extent of the Euclidean space, Te, with the reciprocal of the system temperature [20]. The only missing ingredients are the boundary conditions for the fields in Eq. (7.9) which follow from the (anti)commuting properties of the (fermi)bose fields, implying

$$\hat{\phi}(\vec{x}, 0) = \hat{\phi}(\vec{x}, \beta) \tag{7.10}$$

for bosons and

$$\hat{\psi}(\vec{x}, 0) = -\hat{\psi}(\vec{x}, \beta) \tag{7.11}$$

for fermions. Fermions and bosons obey antiperiodic and periodic boundary conditions, respectively, in the time direction.

Finite temperature lattice field theory is then straightforward since temperature comes for free. Because the lattice has a finite extent, $N_t a$, temperature is given by $T = 1/N_t a$. The discretization procedure is the same as at zero temperature and most of the standard lattice techniques, reviewed in the introductory Sections above, carry over to finite temperature. Such a field theoretic approach to finite temperature QCD allows us to put thermodynamics and spectral calculations on the same footing.

3 QCD AT FINITE TEMPERATURE: COLOUR SCREENING AND QUARKONIUM SUPPRESSION[3]

On quite general grounds, it is expected and, in fact, confirmed by lattice simulations that strongly interacting matter undergoes a transition to quark gluon plasma at high temperature and density. One of the most prominent properties of this state of matter is the screening of colour forces between static quarks. The associated screening length (often referred to as the chromoelectric or non-Abelian Debye length) is inversely proportional to the temperature.

Heavy quarkonia, unlike usual (light) hadrons, may exist in the quark gluon plasma due to their relative small sizes. However, above some temperature the screening radius eventually becomes smaller than the typical quarkonia radii, leading to their dissolution. This physical picture was used by Matsui and Satz to propose quarkonium suppression as a signal for deconfinement in heavy ion collisions [1]. In fact, it was found that the J/ψ dissolves above but close to the deconfinement temperature T_c. Estimates of the dissociation temperature based on the screening picture have some shortcomings. It is not clear to what extent many body effects present in the strongly coupled quark gluon plasma can be approximated by modification of the interaction between the two heavy quarks. Unfortunately, it is also not trivial to define the screening radius.

Although a detailed understanding of screening phenomena at large distances is still missing, it is evident that in this regime the temperature is the dominant scale and consequently will control the

---

[3]Section coordinator: P. Petreczky; Authors: S. Datta, O. Kaczmarek, D. Kharzeev, F. Karsch, M. P. Lombardo, P. Petreczky, H. Satz, F. Zantow

running of the QCD coupling, i.e., $g \simeq g(T)$ for $(rT \gg 1, T \gg T_c)$[4]. However, at short distances, $r \cdot \max(T, T_c) \ll 1$, hard processes dominate the physics of the quark gluon plasma even at high temperature and it is expected that a scale appropriate for this short distance regime will control the running of the QCD coupling, i.e., $g \simeq g(r)$. The interplay between short and large distance length scales plays a crucial role for a quantitative understanding of hard as well as soft processes in dense matter. It will, for instance, determine the range of applicability of perturbative calculations for thermal dilepton rates or the production of jets as well as the analysis of processes that can lead to thermalization of the dense matter produced in heavy ion collisions. Moreover, the short and intermediate distance regime also is most relevant for the discussion of in-medium modifications of heavy quark bound states which are sensitive to thermal modifications of the heavy quark potential as well as the role of quasi-particle excitations in the quark–gluon plasma.

Another powerful tool to study the dissolution of quarkonia states in the plasma is the corresponding meson spectral functions.

The first subsection will be devoted to a general discussion of screening in hot matter and the running coupling and its observable implications. Next, we discuss direct lattice calculations of the spectral functions. These simulations grow extremely expensive at larger quark mass, which require a fine spacing, and b quark physics seems to be out of reach within this approach. It is then natural to consider NRQCD thermodynamics, a new theoretical tool. We will comment on this new possibility at the end.

3.1 Colour screening and running coupling

The simplest way to understand the screening phenomenon is to consider the potential between an arbitrarily heavy (but not static) quark and antiquark in perturbation theory. At zero temperature the potential can be calculated from the Born heavy quark–antiquark scattering amplitude in the non-relativistic limit. In the Born approximation, the potential in momentum space is just the scattering amplitude which, at lowest order in the non-relativistic expansion, is

$$-\frac{4}{3}g^2 D_{00}(k) \tag{7.12}$$

where $D_{00}(k)$ is the propagator in the Coulomb gauge [22]. Using the leading order perturbative form, $D_{00}(k) = 1/k^2$, we recover the Coulomb potential in coordinate space.

Now consider the high temperature plasma phase. Assuming that the heavy quark and antiquark are well defined quasi-particles, the scattering amplitude is

$$-\frac{4}{3}g^2 \frac{1}{k^2 + \Pi_{00}(k)} \ , \tag{7.13}$$

where $\Pi_{00}(k)$ is the medium induced gluon self-energy. At leading order and small momenta, $\Pi_{00}(k)$ is gauge independent and leads to a non-zero mass term in the gluon propagator, $m_D^2 \equiv \lim_{k \to 0} \Pi_{00}(k) = \frac{1}{3}g^2 T^2 (N + \frac{1}{3}N_f)$. Thus we obtain the screened Coulomb potential

$$-\frac{4}{3}\frac{g^2}{4\pi r}\exp(-m_D r) \tag{7.14}$$

as a function of distance r.

Another way to discuss colour screening which is also suitable for nonperturbative (lattice) study, is to consider the partition function in the presence of a static quark–antiquark pair normalized by the

---

[4]We use the deconfinement temperature T_c as a characteristic energy scale rather than a more conventionally used Λ-parameter.

partition function $Z(T)$ of the system without static charges which can be written as [23]

$$
\begin{aligned}
\frac{Z_{q\bar{q}}(r,T)}{Z(T)} &= \frac{1}{Z(T)} \int DA_\mu D\overline{\psi} D\psi e^{-\int_0^{1/T} d\tau \int d^3x \mathcal{L}_{QCD}(\tau,\vec{x})} W(\vec{r}) W^\dagger(0) \\
&= \langle W(\vec{r}) W^\dagger(0) \rangle
\end{aligned}
$$

where the Wilson line or Polyakov loop is defined as

$$
W(\vec{x}) = P e^{ig \int_0^{1/T} d\tau A_0(\tau,\vec{x})} \ .
$$

The above partition function contains all colour orientations of the static $Q\overline{Q}$ pair. Using projection operators one can formally define the partition function for colour singlet (1), colour octet (8), and colour average (av) channels as [24, 25]

$$
\frac{Z_{q\bar{q}}^{(1)}(r,T)}{Z(T)} = \frac{1}{3} \mathrm{Tr} \langle W(\vec{r}) W^\dagger(0) \rangle \tag{7.15}
$$

$$
\frac{Z_{q\bar{q}}^{(8)}(r,T)}{Z(T)} = \frac{1}{8} \langle \mathrm{Tr} W(r) \mathrm{Tr} W^\dagger(0) \rangle - \frac{1}{24} \mathrm{Tr} \langle W(r) W^\dagger(0) \rangle \tag{7.16}
$$

$$
\frac{Z_{q\bar{q}}^{(\mathrm{av})}(r,T)}{Z(T)} = \frac{1}{9} \langle \mathrm{Tr} W(r) \mathrm{Tr} W^\dagger(0) \rangle \ . \tag{7.17}
$$

Only the colour average partition function is manifestly gauge invariant. To define the singlet and octet partition functions one may replace the Wilson line by dressed gauge invariant Wilson lines [26] or one may fix the Coulomb gauge in Eq. (7.15). These two definitions were shown to be equivalent [26] (see also [27]). Having defined the partition function in the presence of a static quark–antiquark pair, the change in the free energy, F_i, the internal energy, V_i, and the entropy, S_i, of the static quark–antiquark pair relative to a system with no static charges are calculated as

$$
F_i(r,T) = -T \ln\left(\frac{Z_{q\bar{q}}^{(i)}(r,T)}{Z(T)}\right) = V_i(r,T) - T S_i(r,T) \tag{7.18}
$$

$$
V_i(r,T) = T^2 \frac{\partial}{\partial T} \ln\left(\frac{Z_{q\bar{q}}^{(i)}(r,T)}{Z(T)}\right) = -T^2 \frac{\partial[F_i(r,T)/T]}{\partial T} \tag{7.19}
$$

$$
S_i(r,T) = -\frac{\partial F_i(r,T)}{\partial T} \quad i = 1, 8, \mathrm{av} \ . \tag{7.20}
$$

We concentrate on the colour singlet case in the following. In leading order perturbation theory, F_1 is dominated by 1-gluon exchange and is therefore also given by Eq. (7.14) [23]. For this reason the free energies were (mis)interpreted as potentials. However, F_1 generally contains an r-dependent entropy contribution which starts at order g^3 in perturbation theory so that $V_1 = F_1$ only at leading order.

Recently the colour singlet free and internal energies of static quark antiquark pair have been studied in lattice simulations of SU(3) gauge theory [28, 29]. Below the deconfinement transition temperature, $T < T_c$, $F_1(r,T)$ shows a linear rise with r, as expected in the confined phase. In the plasma phase ($T > T_c$) both $F_1(r,T)$ and $V_1(r,T)$ approach a finite value for $r \to \infty$, indicating the presence of colour screening. The numerical results for F_1 and V_1 in the plasma phase are shown in Fig. 7.2. For small distances, $r < 0.2$ fm, and temperatures close to T_c both F_1 and V_1 coincide with the $T = 0$ potential, as expected since, at small distances, medium effects are negligible and the free energy of the static $Q\overline{Q}$ pair is simply the interaction energy, i.e., the heavy quark potential at zero temperature. In general, however, the free energy and the internal energy show quite different T- and r-dependences.
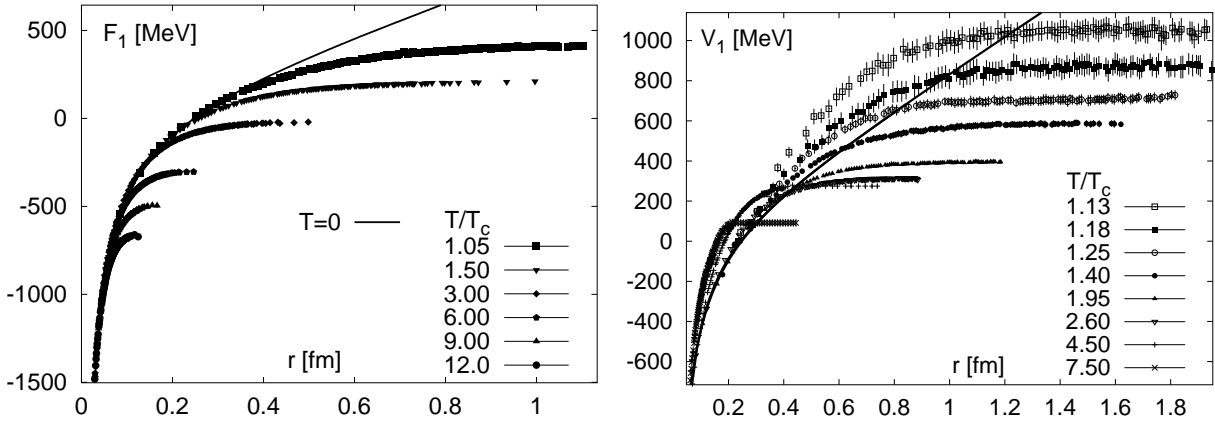
Fig. 7.2: The free energy (left) and the internal energy (right) of static $Q\overline{Q}$ pair in the plasma phase.

The perturbative short and large distance relations for the singlet free energy have recently been used to define a running coupling at finite temperature [30],

$$\alpha_{\mathrm{qq}}(r, T) = \frac{3r^2}{4} \frac{\mathrm{d}F_1(r, T)}{\mathrm{d}r} \quad . \tag{7.21}$$

In general, however, the definition of a running coupling in QCD is not unique beyond the validity range of 2-loop perturbation theory; aside from the scheme dependence of higher order coefficients in the QCD β-functions it will strongly depend on non-perturbative contributions to the observable used for its definition.

We compare the finite temperature results (symbols) to calculations performed at zero temperature (lines) [31–34] in Fig. 7.3. These numerical results on α_{qq} at distances smaller than 0.1 fm cover also distances substantially smaller than those analyzed so far at $T = 0$. They clearly show the running of the coupling with the dominant length scale r also in the QCD plasma phase. For temperatures below $3T_c$ one finds that α_{qq} agrees with the zero temperature perturbative result in its entire regime of validity, i.e., for $r \lesssim 0.1$ fm. At these temperatures thermal effects only become visible at larger distances and lead, as expected, to a decrease of the coupling relative to its zero temperature value; at distances larger than $r \simeq 0.1$ fm non-perturbative effects clearly dominate the properties of α_{qq}. It thus is to be expected (and found) that the properties of a running coupling will strongly depend on the physical observable used to define it [30].

3.2 Real time properties of finite temperature QCD, spectral functions

Most of the dynamic properties of the finite temperature system are incorporated in the spectral functions. The spectral function, $\sigma_H(p_0, \vec{p})$, for a given mesonic channel H in a system at temperature T can be defined through the Fourier transform of the real time two point functions $D^>$ and $D^<$ or equivalently as the imaginary part of the Fourier-transformed retarded correlation function [35],

$$
\begin{aligned}
\sigma_H(p_0, \vec{p}) &= \frac{1}{2\pi}(D_H^>(p_0, \vec{p}) - D^>(p_0, \vec{p})) \\
&= \frac{1}{\pi}\mathrm{Im}D_H^R(p_0, \vec{p}) \\
D_H^{>(<)}(p_0, \vec{p}) &= \int \frac{d^4p}{(2\pi)^4} e^{ip.x} D_H^{>(<)}(x_0, \vec{x}) \\
D_H^>(x_0, \vec{x}) &= \langle J_H(x_0, \vec{x}), J_H(0, \vec{0})\rangle \\
D_H^<(x_0, \vec{x}) &= \langle\langle J_H(0, \vec{0}), J_H(x_0, \vec{x})\rangle , x_0 > 0 .
\end{aligned}
$$

(7.22)

(7.23)
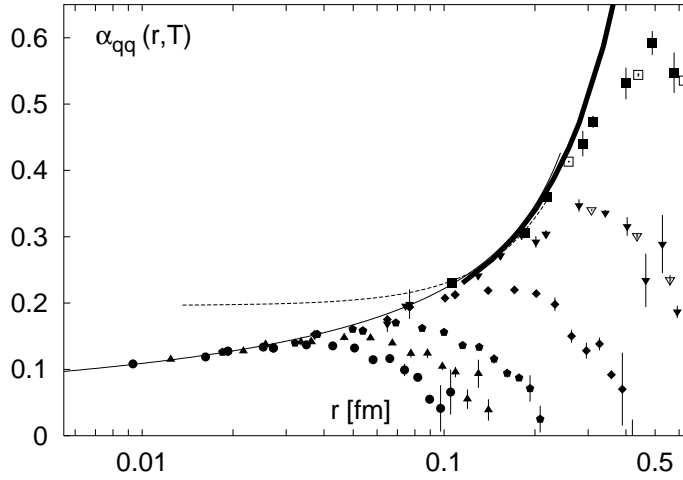
Fig. 7.3: The running coupling in the qq-scheme determined on lattices of size $32^3 \times N_\tau$ with $N_\tau = 4$ (open symbols) and 8 (filled symbols) from derivatives the short distance part of the singlet free energy ($T = 0$: from the force) at different temperatures. The relation of different symbols to the values of the temperature are as in the previous figure (left). The various lines correspond to the string picture (dashed), perturbative (thin) and numerical (thick) studies at zero temperature.

The correlators $D_H^{>(<)}(x_0, \vec{x})$ satisfy the well-known Kubo–Martin–Schwinger (KMS) condition [35]

$$D_H^>(x_0, \vec{x}) = D^<(x_0 + i/T, \vec{x}) . \tag{7.24}$$

Inserting a complete set of states and using Eq. (7.24), one gets the expansion

$$\sigma_H(p_0, \vec{p}) = \frac{(2\pi)^2}{Z} \sum_{m,n} \quad (e^{-E_n/T} \pm e^{-E_m/T}) |\langle n|J_H(0)|m\rangle|^2$$
$$\times \quad \delta^4(p_\mu - k_\mu^n + k_\mu^m) \tag{7.25}$$

where e.g., k^n refers to the four-momenta of the state $|n\rangle$.

A stable mesonic state contributes a δ function-like peak to the spectral function,

$$\sigma_H(p_0, \vec{p}) = |\langle 0|J_H|H\rangle|^2 \epsilon(p_0) \delta(p^2 - m_H^2) , \tag{7.26}$$

where m_H is the mass of the state. For an unstable particle, a smoother peak is obtained with a width related to the decay width. For sufficiently small decay widths, a Breit–Wigner form is commonly used. As the temperature increases, the contributions from states in the spectral function changes due to collision broadening, and, at sufficiently high temperatures, these states may be too broad to contribute to the resonance any longer. Such a change in the contributions to the resonance states and eventual 'disappearance of resonances' in the thermal spectral function has been studied analytically, for example, in the Nambu–Jona–Lasinio model in Ref. [36]. The spectral function as defined in Eq. (7.25) is directly accessible in high energy heavy ion experiments. For example, the spectral function for the vector current is directly related to the differential thermal cross-section for the production of lepton pairs [37]

$$\frac{dW}{dp_0 d^3 p} = \frac{5\alpha^2}{27\pi^2} \frac{1}{p_0^2(e^{p_0/T} - 1)} \sigma(p_0, \vec{p}) . \tag{7.27}$$

Then presence or absence of a bound state in the spectral function will manifest itself in the peak structure of the differential dilepton rate.

In finite temperature lattice calculations, one calculates Euclidean time propagators, usually projected to a given spatial momentum

$$G_H(\tau, \vec{p}) = \int d^3 x e^{i\vec{p}.\vec{x}} \langle T_\tau J_H(\tau, \vec{x}) J_H(0, \vec{0}) \rangle_T \tag{7.28}$$

where $\langle ... \rangle_T$ indicates a thermal trace, as in Eq. (7.22), and T_τ refers to ordering in Euclidean time τ. This quantity is the analytical continuation of $D^>(x_0, \vec{p})$

$$G_H(\tau, \vec{p}) = D^>(-i\tau, \vec{p}) . \tag{7.29}$$

Using this equation and the KMS condition one can easily show that $G_H(\tau, \vec{p})$ is related to the spectral function, Eq. (7.22), by an integral equation

$$G_H(\tau, \vec{p}) = \int_0^\infty d\omega \sigma(\omega, \vec{p}) K(\omega, \tau) \tag{7.30}$$

$$K(\omega, \tau) = \frac{\cosh(\omega(\tau - 1/2T))}{\sinh(\omega/2T)} . \tag{7.31}$$

Equation (7.30) lies at the heart of attempts to extract spectral functions and properties of hadrons from correlators calculated in lattice QCD. In what follows, we use Eq. (7.30) to extract the behavior of degenerate heavy meson systems in a thermal medium from finite temperature mesonic correlators. Equation (7.31) is valid only in the continuum. It is not clear in general whether the $G_H(\tau, \vec{p})$ measured on the lattice will satisfy the same spectral representation but it was shown in Ref. [38] that this is the case for the free theory.

3.3 Charmonium at finite temperature: recent results on correlators and spectral functions

Direct investigations of the charmonia temperature modifications, using the Matsubara correlators of suitable operators, have been available over the past 3–4 years. All such studies available at present are based on quenched lattices, that is, they do not include any quark loops, even thermal quark loops (which indicates scattering of thermal quarks off the medium). Excluding such loops may result in exclusion of important physics below T_c since the thermal excitation of pions and meson resonances is considered to be one of the main driving mechanisms of the QCD phase transition. Above the transition, at least for J/ψ dissociation, the existing wisdom is that the thermal gluons are the more relevant degrees of freedom. Therefore, the description of quenched lattices should be at least qualitatively correct.

In the following, the current status of the direct lattice studies on charmonia are summarized. Only the main results are described here. For detailed analysis of the systematics and other effects, please refer to the original papers [39–41]. As already mentioned in the previous section, detailed information about the hadronic properties are contained in the spectral function. In order to study thermal modifications of hadrons, ideally Eq. (7.30) should be inverted to extract $\sigma(\omega, T)$ from the thermal correlators. (In the following, we will only be interested in mesonic states at rest in the heat-bath frame, i.e., $\vec{p} = 0$ in Eq. (7.30), and will omit the $\vec{p}$ index altogether.) However, such an inversion is a notoriously ill-defined problem, since the continuous function, $\sigma(\omega, T)$ must be extracted from the correlators at a discrete number of points. Progress in solving this problem became possible with the introduction of Bayesian techniques in lattice data analysis [42]. In the Maximum Entropy Method (MEM), one can determine the most probable spectral function which describes the data, subject to known constraints like positivity, asymptotic behavior, etc. [43]. At temperatures a few times T_c or higher, however, as we will see below, it is tricky to extract the spectral function even with these techniques.

We begin with the low temperature phase where the larger extent of the temporal direction makes it easier to extract the spectral functions. In Fig. 7.4 we show the spectral functions in the hadronic phase for the currents J_H in different representations. Figure 7.4(a) shows the spectral functions obtained at
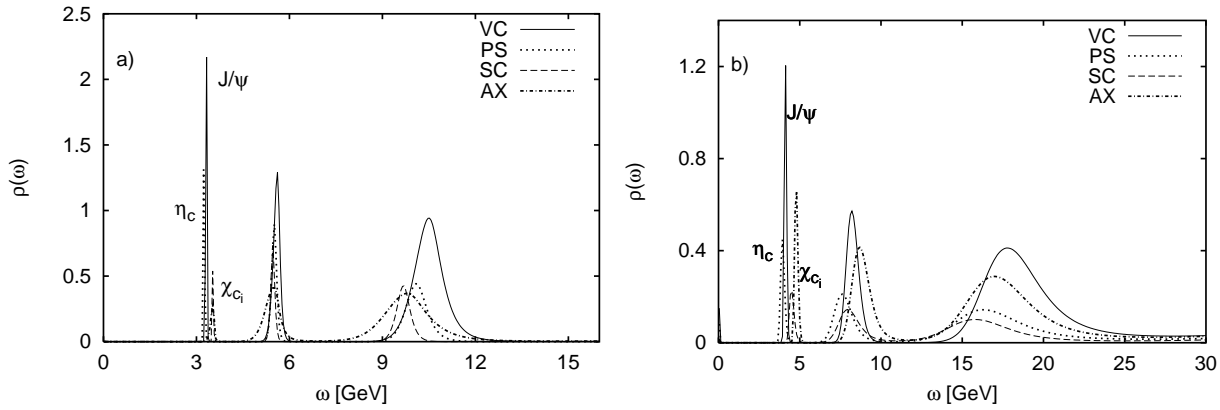
Fig. 7.4: Spectral functions for the vector, pseudos-calar, scalar and axial vector operators [39]. (a) Lattices at 0.75 T_c with $a = 0.04$ fm spacing and (b) at 0.9 T_c and $a = 0.02$ fm. The ground state peaks correspond to J/ψ, η_c, χ_{c_0} and χ_{c_1}, respectively. The label χ_{c_i} is used because the χ_{c_0} and χ_{c_1} are difficult to resolve on the figure.

0.75 T_c on lattices with 0.04 fm spacing. The peaks at low ω correspond to the ground state J/ψ (VC), η_c (PS), χ_{c_0} (SC) and χ_{c_1} (AX) respectively. Note that we do not discuss the $2S$ and $2P$ states because these are indistinguishable from lattice artifacts. The properties of the lowest states are reproduced quite well by Fig. 7.4 since the peak position and the integrated width of the peak are in reasonable agreement with the mass and residue obtained from a fit. Figure 7.4(b) shows spectral functions obtained from lattices with 0.02 fm spacing at $T = 0.9T_c$. A comparison of the two figures helps explain the nature of the peaks at higher ω, since they can be seen to scale approximately as the inverse lattice spacing and therefore are probably dominated by lattice artifacts [39, 44]. It is interesting to note that even at very high ω the structure of the spectral function is quite different from the free theory.

It is possible to get a first idea of the temperature modification of the charmonia above T_c by looking at the Matsubara correlators measured at these temperatures. To factor out the trivial temperature dependence of the kernel (see Eq. (7.31)), one can construct 'model correlators' by using the spectral function from the hadron phase (Fig. 7.4). The measured correlators, $G(\tau, T)$, are then compared with these reconstructed correlators using Eq. (7.31):

$$G_{\text{recon}}(\tau, T) = \int_0^\infty d\omega \sigma(\omega, T^*) \frac{\cosh(\omega(\tau - 1/2T))}{\sinh(\omega/2T)}. \tag{7.32}$$

Here T^* refers to a temperature below T_c. Figure 7.5 shows such a comparison for the $1S$ and $1P$ channels in two figures from Ref. [39]. While the comparison at 1.1 T_c uses the spectral function constructed at $T^* = 0.75T_c$, Fig. 7.4(a), the other temperatures use the spectral functions shown in Fig. 7.4(b), i.e., $T^* = 0.9T_c$. The figure clearly shows that the $1S$ states are not strongly affected by the deconfinement transition. For the η_c we see no statistically significant change up to temperatures of 1.5 T_c and only very modest changes at 2.25 T_c. For the J/ψ, the ratio $G(\tau, T)/G_{\text{recon}}(\tau, T)$ shows no significant deviations from unity at short Euclidean time, τ, a little above T_c, while some small but significant deviations are seen as one goes to higher temperatures. For the $1P$ channels, large temperature modifications of the correlator relative to the reconstructed correlator are seen when crossing T_c, indicating that the $1S$ states undergo only very modest modifications up to 1.5–2 T_c while the $1P$ states suffer more serious modifications.

In order to further understand the nature of thermal modifications of the states, it is necessary to extract the spectral function directly from the correlators. Three groups have presented results for spectral functions for the pseudo-scalar and vector charmonium states using the MEM. Since the extraction becomes tricky at high temperatures and there are some differences in the results, it is useful to keep in
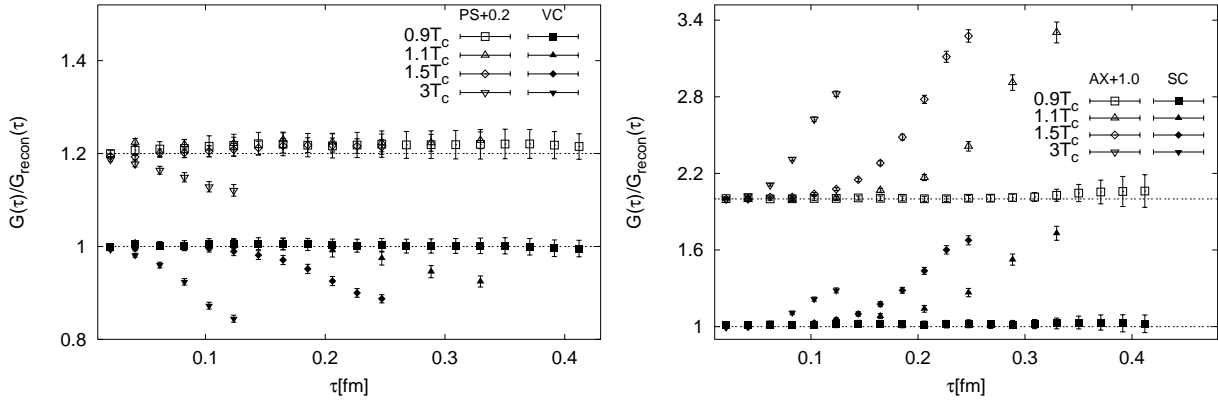
Fig. 7.5: G/G_{recon} as a function of Euclidean time for different temperatures for vector and pseudo-scalar channels (top) and in the scalar and axial vector channels (bottom). The figures above mix two sets of data in Ref. [39] with different lattice spacings and slightly different quark masses, with the data at $1.1\,T_c$ using $T^* = 0.75\,T_c$ and the others using $T^* = 0.9\,T_c$. The data for the pseudo-scalar and axial vector channels have been shifted by a constant for better visualization.

mind the initial differences between them. While all three work within the quenched approximation and use Wilson-type valence fermions, some differences exist in their approaches. The Bielefeld group uses very fine isotropic lattices with the nonperturbatively improved clover action for the valence fermions. Asakawa and Hatsuda use space–time anisotropic lattices, to allow more data points in the temporal direction and use the unimproved Wilson action for the fermions. Umeda *et al.* also use anisotropic lattices but use the tadpole-improved Fermilab action. They also use smeared operators while the others use point operators.

As Fig. 7.4 reveals, the structure of the spectral function at high ω, for the interacting theory on lattice, is considerably different from the free spectral function [44]. The Bielefeld group uses this high energy structure as part of the prior information when extracting the spectral function. The default spectral function above T_c, in their analysis, uses the high energy part of Fig. 7.4, continuously matched to $m_1\omega^2$ at lower ω where m_1 is defined to match the spectral functions at temperatures below T_c. The spectral functions for the $1S$ states, obtained with this default model and the MEM analysis of Bryan [45], are shown in Fig. 7.6. The error bars shown in the figure are standard deviations of the spectral functions averaged over the ω interval indicated by the horizontal error band (see [43], Eq. (5.13)). We see that, up to $1.5\,T_c$ the $1S$ states persist as bound states with no significant weakening. There is also no significant change in mass on crossing T_c. At $2.25\,T_c$, while the peak position is still not significantly changed, a depletion of the peak strength, i.e., the area under the peak, is seen. Finally, at $3\,T_c$ no statistically significant peak is seen.

Figure 7.6 suggests that in a gluonic plasma the $1S$ charmonia survive as bound states till $\geq 2T_c$, with no significant weakening up to $\approx 1.5\,T_c$ and then a gradual weakening, perhaps due to collision broadening. Since these results are for point operators, the results for the vector current, Fig. 7.6(b), will be directly connected to the thermal dilepton rate. Further results for point operators come from Asakawa and Hatsuda who use the free continuum asymptotic form of the spectral function, $\approx m_1\omega^2$, as their default model. Their latest results [46] are shown in Fig. 7.7. They find a sharp bound state, with little significant thermal modification, up to $1.62\,T_c$, in complete agreement with Fig. 7.4 up to 1.5 T_c. On going to higher temperatures, however, their results seem to suggest a sharp disappearance of the bound states at some temperature, with no statistically significant peak being seen at $1.9\,T_c$ [40] and, in preliminary results, already at $1.7\,T_c$ [46]. While the exact dissolution temperature is probably not expected to match the Bielefeld group, since the Bielefeld group uses a quark mass somewhat heavier than
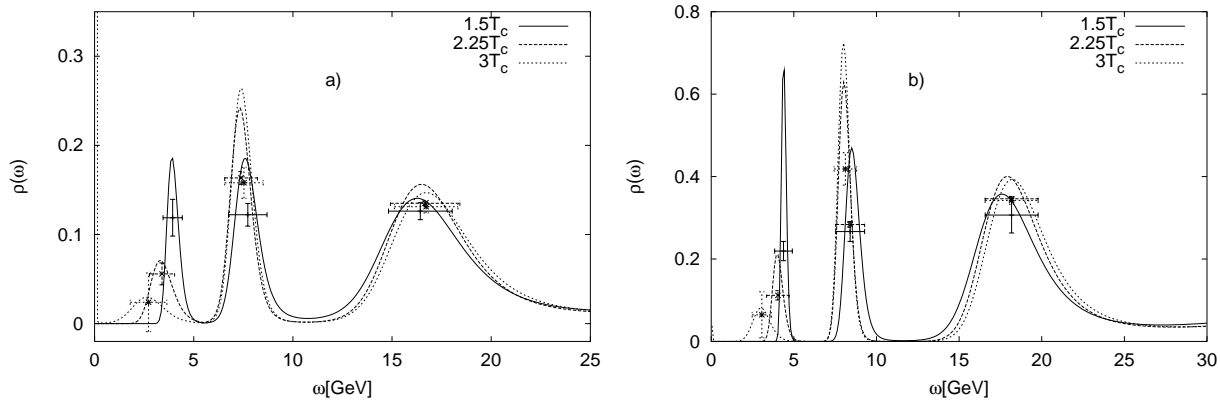
Fig. 7.6: Spectral functions above deconfinement for (a) pseudo-scalar and (b) vector channels [39]. Here lattice spacing $a \approx 0.02$ fm and $m_{J/\psi} \approx 3.6$ GeV.

the charm, if further analysis supports the dissolution at 1.7 T_c then it will clearly suggest a qualitatively different picture from the gradual dissolution shown in Fig. 7.6, and possibly suggest a drastic change in the properties of the plasma between 1.6 and 1.7 T_c.

Unlike the two previous groups, Umeda *et al.* use smeared operators with a smearing function of the form $w(\vec{x}) = \exp(-a|\vec{x}|^b)$ where the parameters a and b are chosen to optimize the overlap with the ground state. While use of a smeared operator has the advantage of a good overlap with the ground state, so that it may be possible to extract the properties of J/ψ and η_c more reliably, it has two disadvantages. First, bound state dissolution must be carefully handled since smearing always mimics a bound state. Second, the direct connection of the vector current correlator to the dilepton rate, Eq. (7.27, is lost. The first problem can be dealt with by comparing results using a different level of smearing [41].

Figure 7.8 shows their results for the $1S$ spectral functions. Evidence for the existence of a bound state above T_c is found for the $1S$ states, in agreement with results of other groups using point operators. No dramatic change between 1.4 T_c and 1.75 T_c is indicated in the properties of the peak. In addition, Umeda *et al.* [41, 46] attempted a constrained fit of the correlators to obtain more accurate information on the ground state properties such as thermal modifications of the mass and width. This analysis with extended operators indicate that the masses of ground state charmonia do not change significantly up to temperatures 1.7 T_c. These studies also indicate a non-zero thermal width which increases with temperature. The precise determination of the width, however, appears to be difficult.

We now summarize what direct lattice studies have told us about the properties of the $1S$ states in equilibrium with a plasma. The studies all agree that the J/ψ and the η_c survive the deconfinement transition with little significant change in their properties. At least up to temperatures ≈ 1.5 T_c such states exist as bound states in the equilibrated plasma without significant weakening of the state. Here, it may be worthwhile to also mention earlier results from Umeda *et al.* for these states [47]. In this study, where they looked at the fall-off of the $c\bar{c}$ spatial correlation, Umeda *et al.* previously concluded that the $1S$ states survive as bound states, up to temperatures of 1.5 T_c, in a gluonic plasma. Another important fact revealed by the recent studies is that no significant $1S$ state mass reduction is seen above T_c. If, as was the prevailing wisdom, these states become Coulombic above T_c, one may have expected a significant mass reduction which is not seen by any of the groups. Beyond 1.5 T_c there seems to be some disagreement between the different groups: while Ref. [39] and preliminary results from Umeda *et al.* suggest a gradual disappearance of the state, perhaps due to collision broadening, preliminary results from Asakawa and Hatsuda suggest a sharp cutoff temperature below 1.7 T_c, beyond which the gluonic plasma cannot support these bound states.

Results for the orbitally excited χ_c states are available so far only from the Bielefeld group. As was
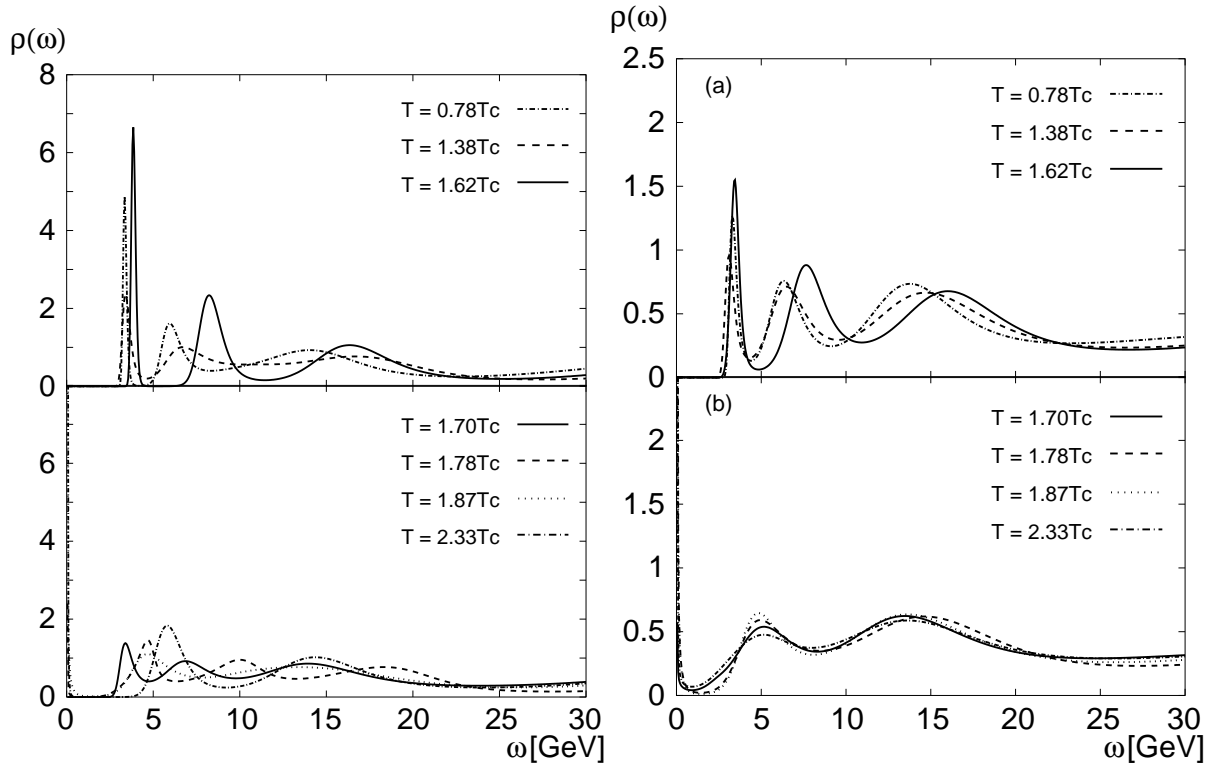
Fig. 7.7: Spectral functions above and below deconfinement for pseudo-scalar (left) and vector (right) channels, for anisotropic lattices with $a_\tau \approx 0.0125$ fm, as found by Asakawa & Hatsuda [40, 46]. (a) Temperatures ≤ 1.62 T_c, where a statistically significant ground state is seen. (b) Temperatures $\geq 1.70\,T_c$ where the ground state of (a) is not seen any more. The peak at a slightly higher temperature is not statistically significant.

shown in Fig. 7.5, the behavior of these states is considerably different from that of the $1S$ states since the correlators above T_c differ substantially from the ones reconstructed from the spectral function below T_c, suggesting serious modification of these states due to deconfinement. The spectral functions can be extracted from the correlators even though they are more noisy, making such an extraction somewhat more difficult [39]. Figure 7.9(a) shows the spectral functions for the scalar channel. As before, as part of the prior guess we provided the high ω structure of the lattice spectral function in the interacting theory, as obtained below T_c. The figure shows that the χ_{c_0} peak below T_c is not present already at 1.1 T_c. Figure 7.9(b) shows a similar result for the axial vector channel, indicating these states suffer serious system modification, possibly dissolution, already just above T_c.

3.4 Theory perspectives: NRQCD at $T > 0$

All studies of the charmonium spectral functions mentioned above were done either using relativistic Wilson fermions or Fermilab fermions. In both formulations the so-called Wilson term is introduced to remove the doublers. This, however, strongly distorts the quark dispersion relation on the lattice leading to the artifact peaks in the lattice spectral function. For heavy quarks an additional large discretization error of order $m_q a$ appears where m_q is the heavy quark mass, making bottomonium studies with relativistic actions very difficult although the Fermilab formalism can help to a certain extent. A useful alternative, at least close to T_c, where the condition $m_q \gg T$ necessary for the approach to be valid is satisfied, could be to employ NRQCD at $T > 0$. In this formulation, the scale related to m_q is integrated out so that this formulation has the advantage of being doubler free. Furthermore, since the spectral functions scale as $\sqrt{\omega}$ instead of the ω^2 behavior of the relativistic formulation, the high energy part of the spectral functions contribute less to the meson correlator. This can simplify the reconstruction of meson
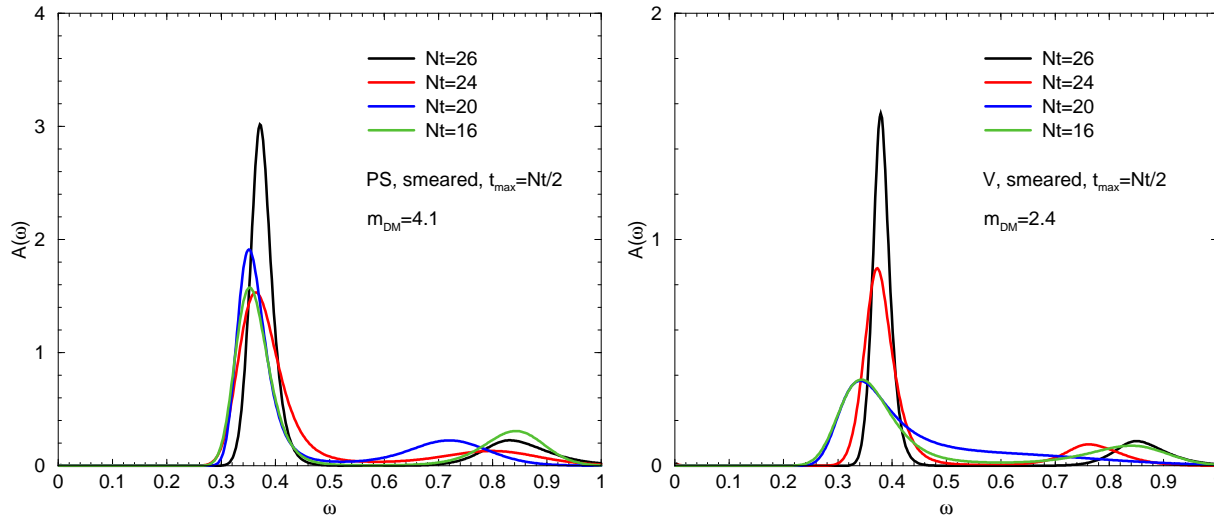
Fig. 7.8: Spectral functions above deconfinement for pseudo-scalar (left) and vector (right) channels, for anisotropic lattices with $a_\tau \approx 0.025$ fm and smeared operators (Umeda *et al.* [41, 46]). The decreasing Nt correspond to $T/T_c \approx 1.08$, 1.17, 1.4 and 1.75, respectively.

properties, related to the low energy part of the vector spectral function. Some preliminary studies of the charmonium spectral function in NRQCD at zero temperature were presented in Ref. [48].

4 J/ψ ABSORPTION IN HEAVY-ION COLLISIONS AT FINITE TEMPERATURE[5]

4.1 Cross-section calculations

Since the original paper by Matsui and Satz [1] on J/ψ suppression in heavy-ion collisions, a number of studies on J/ψ absorption in nuclear matter have been proposed to suggest other mechanisms than the quark gluon plasma screening of the $c\bar{c}$ potential. We will use the words "suppression" and "absorption" to distinguish between the plasma and non-plasma mechanisms responsible for the observed reduced yield of J/ψ particles in heavy ions collisions.

According to Ref. [1], one should observe very few J/ψ in heavy-ion collisions because plasma formation could weaken the effectiveness of the quarkonium potential and prevent J/ψ formation. But what if no plasma phase is generated? The J/ψ can be produced in the early stages of the collision since the energy is high enough to produce them. Their destiny is then related to the interactions they will experience with the nuclear medium (the nuclear thickness the J/ψ must traverse during the intepenetration of the two colliding nuclei) and with the hadron gas (a possible state excited from vacuum left behind in the collision region by the two receding nuclei, assuming zero baryon number).

The $J/\psi N$ cross-section, σ_{abs}, extracted from data is $\sigma_{abs} = 4.3 \pm 0.6$ mb [49]. The exponential absorption factor for the J/ψ in nuclear matter is $\propto \exp(-x/\lambda)$, where x is the distance traveled and λ is the mean free path, given by

$$\lambda \approx 1/(\rho_A \sigma_{abs}), \tag{7.33}$$

where ρ_A is the nuclear density. Nuclear absorption alone cannot explain the anomalous J/ψ suppression described as a function of length in Ref. [50]. This argument has been used in favor of a plasma interpretation. On the other hand, nuclear absorption does not take into account interactions with all hadrons ($\pi, \eta, K, \rho, \omega, K^*, \phi$...) that can be excited from vacuum when very high energy densities are reached, as in heavy-ion collisions. Each of these particles is presumably able to interact with the J/ψ,

---

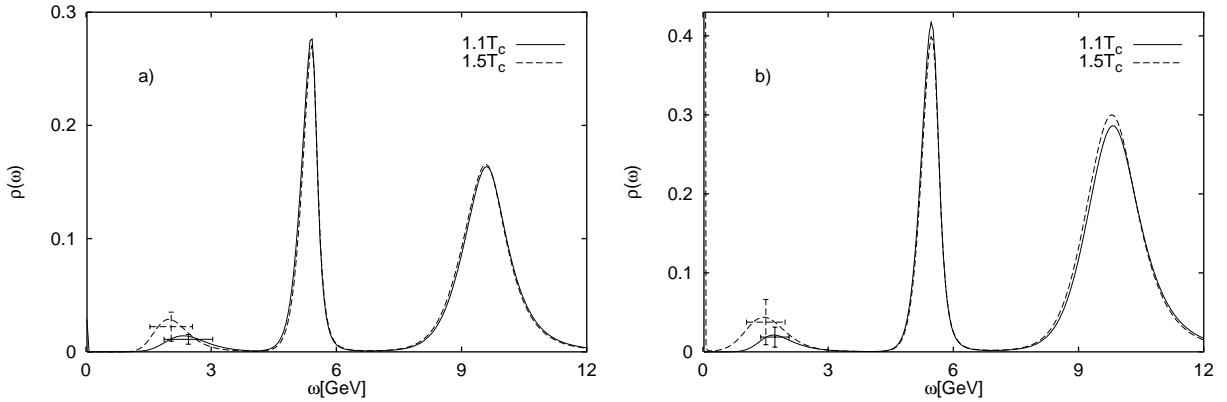[5]Section coordinator: A. D. Polosa; Authors: V. Laporta, L. Maiani, F. Piccinini, A. D. Polosa, V. Riquer

Fig. 7.9: Spectral functions for (a) scalar and (b) axial vector states above deconfinement, reconstructed from Matsubara correlators measured on lattices of ≈ 0.04 fm spacing [39].

reshuffling its $c\bar{c}$ content into an open charm final state such as $D^{(*)}_{(s)}D^{(*)}_{(s)}$. Can such interactions provide an explanation of the anomalous suppression?

The description of these interactions is difficult because they cannot be derived from first principles or extracted from independent experimental information. One has to resort to models of their dynamics [51–58].

Dissociation of the J/ψ by hadrons has been considered in several approaches, with rather different predictions for energy dependence and magnitude of the cross-sections near threshold. Basically, earlier calculations in the literature can be grouped into four classes:

– perturbative QCD based calculations (pQCD);
– quark interchange models;
– QCD sum rule calculations;
– meson exchange models.

The idea behind the pQCD method is that the interaction between heavy quark bound states and light hadrons can be described perturbatively when the heavy quark mass is sufficiently large. The small size of the heavy quark bound state allows for a multipole expansion of its interaction with external gluons where the colour-dipole interaction dominates at long range. Using pQCD, Peskin and Bhanot and later Kharzeev and Satz [52] estimated the scattering cross-sections of J/ψ with light hadrons, finding very low values, less than 0.1 mb at about $\sqrt{s} = 5$ GeV. The pQCD result was further improved by including finite target mass corrections and relativistic phase space corrections [53]. However, the collisions between mesons and the J/ψ in heavy-ion reactions occur at low energy where the application of pQCD is questionable.

In the case of quark interchange models, the J/ψ dissociation cross-section is calculated in terms of non-perturbative quark exchanges between the J/ψ and light hadrons using explicit non-relativistic quark model wave functions for the initial and final hadrons. The largest contributions to the cross-section come from the energy region just a few hundred MeV above threshold since the overlap integrals are damped by the external meson wave functions at higher momenta. The first calculation in this framework was performed by Martins, Blaschke and Quack [54], finding a J/ψ dissociation cross-section by pions of ≈ 7 mb at about 1 GeV above threshold. Subsequently, similar calculations have been carried out with different treatments of the confining interaction, obtaining lower cross-sections (of the order of 1.5 mb at $\sqrt{s} \approx 4$ GeV) and have been extended to $\rho J/\psi$ and $N J/\psi$ interactions [55].

Another independent approach is given by the QCD sum rules [56]. This method relates the scattering amplitude to a sum of operator vacuum-expectation-values (VEVs). It gives a model independent
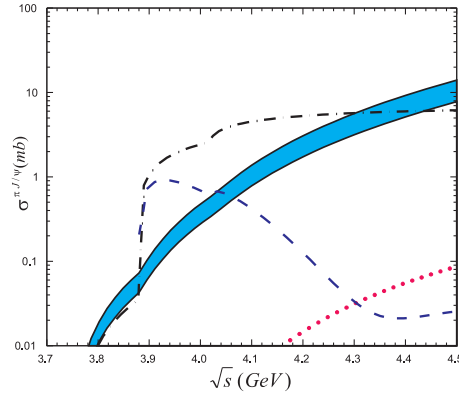
Fig. 7.10: The J/ψ-hadron cross-sections calculated with QCD sum rules (band), short-distance QCD (dotted line), meson-exchange models (dot–dashed lines) and the non-relativistic constituent quark model (dashed line) [60].

result provided that the set of selected operators dominates the scattering amplitude in the chosen kinematic regime and that their VEVs are known experimentally. QCD sum rule calculations for the reaction $\pi + J/\psi \to D^{(*)}\overline{D}^{(*)}$ give cross-sections at the mb level in the near-threshold region.

Finally, the meson-exchange model [57], is based on hadronic effective Lagrangians. Vector mesons are treated as gauge bosons mediating the interactions between pseudoscalar mesons. An SU(4)-invariant effective meson Lagrangian is assumed. One starts from a free Lagrangian of the form $\mathcal{L}_0 = \text{Tr}(\partial_\mu P^\dagger \partial^\mu P) - 1/2\text{Tr}(F^\dagger_{\mu\nu} F^{\mu\nu})$ and derives the couplings between pseudoscalar and vector mesons with the minimal substitution

$$\partial_\mu P \to \partial_\mu P - i/2g[V_\mu, P]$$
$$F_{\mu\nu} \to \partial_\mu V_\nu - \partial_\nu V_\mu - i/2g[V_\mu, V_\nu] \ , \tag{7.34}$$

giving rise to three-vector meson couplings and four-point couplings. The values of the couplings are obtained from experimental results via Vector Meson Dominance and SU(4) relations, although the assumption of SU(4) symmetry is rather questionable. The most studied channels are: $\pi J/\psi$, $\rho J/\psi$, $K J/\psi$ and $K^* J/\psi$ where quite large cross-sections, of the order of $1 - 10$ mb, have been obtained [58]. Since the exchanged mesons are not pointlike, several studies have introduced form factors at the interaction vertices at the price of introducing additional unknown or poorly known parameters. A strong dependence on the shape and cutoff values of the form factors is found. Some authors calculate the interaction vertices and form factors with the help of sum rules [59]. The state of the art of these calculations, including an uncertainty band, is summarized in Fig. 7.10 [60]. For a nice review of these topics see Ref. [61].

With the exception of pQCD, these approaches, each subject to different limitations, give cross-sections on the order of mb, in particular for initial π's and ρ's. This is a clear indication that the picture of J/ψ absorption by nuclear matter as the only alternative mechanism to plasma suppression is incomplete and that interactions with *comoving particles* in the hadron gas have to be taken into account. We will not attempt to further review existing approaches. We instead focus on some more recent calculations which do not fall in the four classes described above. The $(\pi, \eta, K, \rho, \omega, K^*, \phi)J/\psi \to D^{(*)}_{(s)} D^{(*)}_{(s)}$ cross-sections have recently been evaluated [63], based on the Constituent Quark Model (CQM). The CQM was originally devised to compute exclusive heavy-light meson decays and was tested on a large number of such processes [65]. The CQM is based on an effective Lagrangian which incorporates the heavy quark spin-flavour symmetries and chiral symmetry in the light sector. In particular, it contains effective vertices between a heavy meson and its constituent quarks, as shown on the left-hand side of Fig. 7.11, which occur when applying bosonization techniques to the Nambu–Jona–Lasinio interaction terms of
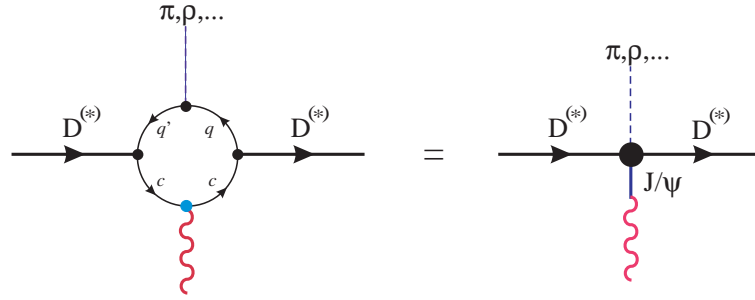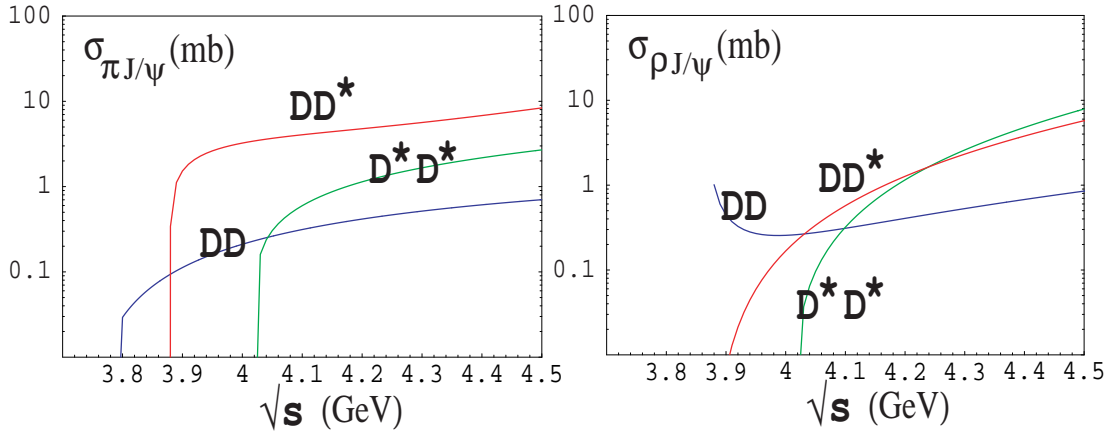
Fig. 7.11: Basic diagrammatic equation to compute the couplings g_3 and g_4.

Fig. 7.12: Cross-sections in CQM model. On the left-hand side, the cross-sections $\pi J/\psi \to D^{(*)}D^{(*)}$ modulated by a form factor (ff) directly derived from the model [67] are shown. The case of $\rho J/\psi$ interactions is technically more complicated and it does not seem feasible to extract the dependency on E_ρ of these cross-sections in the form of a polar ff. If we compute physical quantities such as the mean free paths determined by the inverse of thermal averages, $\langle \rho^{(\rho)}\sigma \rangle_T$, where $\rho^{(\rho)}$ is the ρ number density, the Boltzmann factor will serve as an exponential ff cutting high energy tails faster than any polar ff.

heavy and light quark fields [66]. On this basis, we believe that the CQM is a more solid approach than effective Lagrangian methods, often based on SU(4) symmetry.

We compute the effective trilinear, $g_3 = (\pi, \eta, K, \rho, ...)D^{(*)}_{(s)}D^{(*)}_{(s)}$, or $g_3 = J/\psi D^{(*)}_{(s)}D^{(*)}_{(s)}$ and quadrilinear, $g_4 = (\pi, \eta, K, \rho, ...)J/\psi D^{(*)}_{(s)}D^{(*)}_{(s)}$, couplings. In Fig. 7.11 we show the diagrammatic equation which has to be solved in order to obtain $g_4(g_3)$ in the various cases. The right-hand side represents the effective four-linear coupling to be used in the cross-section calculation. To obtain the trilinear couplings we suppress either the J/ψ or one of the dashed lines representing the light resonances. The effective interaction at the meson level (right-hand side) is modeled as an interaction at the quark-meson level (left-hand side of Fig. 7.11).

The J/ψ is introduced using a Vector Meson Dominance (VMD) ansatz. In the effective loop on the left-hand side of Fig. 7.11 we have a vector current insertion on the heavy quark line c while on the right-hand side the J/ψ is assumed to dominate the tower of $J^{PC} = 1^{--}$ $c\bar{c}$ states mixing with the vector current, for more details see Refs. [17, 67]. Similarly, vector particles coupled to the light quark component of heavy mesons such as ρ and ω when $q = (u, d)$ and K^*, ϕ, when one or both light quarks are strange, are also taken into account using VMD arguments. The pion and other pseudoscalar fields have a derivative coupling to the light quarks of the Georgi–Manohar kind [68]. The final results for $\sigma_{\pi J/\psi}$ and $\sigma_{\rho J/\psi}$ are displayed in Fig. 7.12.
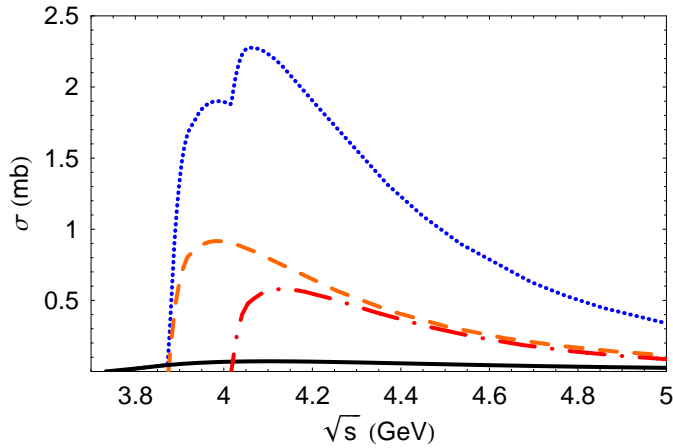
Fig. 7.13: The total cross-section (dotted line) together with the contributions coming from the $J/\psi + \pi \rightarrow D + \overline{D}$ (solid line), $J/\psi + \pi \rightarrow D^* + \overline{D}$ (dashed line) and $J/\psi + \pi \rightarrow D^* + \overline{D^*}$ (dot–dashed line) processes are shown.

The authors of Ref. [69] employ a relativistic quark model [70] to calculate amplitudes and cross-sections for the same processes discussed above with only pions in the initial state. Their model is based on an effective Lagrangian which describes the coupling of hadrons H to their constituent quarks, q_1 and $\overline{q}_2$, given by:

$$\mathcal{L}_{\text{int}}(x) = g_H H(x) \int dx_1 \int dx_2 F_H(x, x_1, x_2) \overline{q}_2(x_2) \Gamma_H \lambda_H q_1(x_1) + \text{h.c.}. \qquad (7.35)$$

Here, λ_H and Γ_H are the Gell-Mann and Dirac matrices which describe the flavour and spin quantum numbers of the meson field $H(x)$. The vertex function F_H is given by:

$$F_H(x, x_1, x_2) = \delta\left(x - \frac{m_1}{m_1 + m_2} x_1 - \frac{m_2}{m_1 + m_2} x_2\right) \Phi_H\left((x_1 - x_2)^2\right), \qquad (7.36)$$

where Φ_H is the correlation function of two constituent quarks of mass m_1 and m_2. Moreover, for Φ_H, in momentum space, they chose the form $\tilde{\Phi}_H(k_E^2) \doteq \exp(-k_E^2/\Lambda_H^2)$, where k_E is a Euclidean momentum [71]. The coupling g_H is determined by the compositeness condition discussed in Ref. [69]. By using the corresponding Feynman rules, the S-matrix elements describing hadronic interactions are obtained in terms of a set of quark diagrams.

In this approach, the dissociation processes are described by box and resonance diagrams. The details of the cross-section calculations can be found in Ref. [69]; here we show the numerical results for the cross-sections as a function of $\sqrt{s}$.

In Fig. 7.13 the continuous line represents the $J/\psi + \pi \rightarrow D + \overline{D}$ cross-section while the dashed and the dot–dashed lines are for $J/\psi + \pi \rightarrow D^* + \overline{D}$ and $J/\psi + \pi \rightarrow D^* + \overline{D^*}$, respectively. The dotted line shows the total cross-section as a function of $\sqrt{s}$. One can see that the maximum is about 2.3 mb at $\sqrt{s} \approx 4.1$ GeV. This value turns out to be smaller than the previous one, but still in the millibarn range.

To make a realistic computation of the effect of the interactions with the hadronic gas, several things have to be considered.

1. There is a temperature dependence of absorption in the hadron gas due to the energy dependence of the cross-sections and to the fact that, as the temperature varies, the particle content and the characteristics of the hadron gas change. One should calculate thermal averages $\langle \rho \sigma \rangle_T \approx 1/\lambda$. This can be done, e.g., by simply using the Bose distribution with zero chemical potential in an ideal gas approximation [62, 63].

2. There is a problem of convergence. Including heavier resonances, on one hand, is disfavored because of the Boltzmann factor $\exp(-M/T)$. On the other hand, heavier resonances, h, integrate more cross-section at low momentum in the $hJ/\psi{\rightarrow}D\overline{D}$ channel and have large spin multiplicities. The lowest lying vector meson nonet, for instance, has a charge-spin multiplicity 9 times larger than that of pions. It is difficult to asses a priori the relative weight of these two effects.

3. Some arguments indicate that there may be a limiting temperature of hadronic matter: the Hagedorn temperature, $T_H \simeq 177$ MeV, [64]. To be credible, a purely hadronic interpretation of J/ψ absorption should be for temperatures $T \leq T_H$.

4. The SPS collaboration NA50 studies the J/ψ yield as a function of the collision centrality. At a certain centrality there is some evidence of a discontinuous breakdown in the J/ψ yield [73–75]. Can such a discontinuity be explained by some hadronic absorption mechanism where cross-sections are expected to be mainly smooth polynomials?

Studying absorption versus suppression is like estimating the background to a weak signal. The shape and size of the background can be crucial in assessing the reliability of the signal.

4.2 Comparison with data

As stated earlier, nuclear absorption can be taken into account by the factor $\exp(-\rho_A\sigma_{\mathrm{abs}}L)$, where ρ_A is the nuclear density and L the path length the J/ψ's traverse during the intepenetration of the two colliding nuclei.

To compute the effect of the hadron gas also requires modeling the fireball produced by the two receding nuclei. We will briefly describe the working hypotheses adopted in two recent papers [62, 63].

1. The fireball is a zero baryon density region of approximately spherical shape which the J/ψ has to escape to be detected.

2. The fireball thermalizes as a hadron gas at temperature T soon after its formation. Primary collisions give rise mostly to pions with an average energy of about 300 MeV and a density of few/(fm^3) and interaction cross-sections of about 10 mb. These parameters lead [72] to mean free paths of a fraction of a fermi, much shorter than the linear dimensions of the fireball, $\approx 5 - 10$ fm.

3. The hadron gas is at zero chemical potential. This is an especially reasonable hypothesis for pions.

4. We calculate the thermal averages $\langle\rho\sigma\rangle_T$ using an ideal gas at temperature T. Interactions can be taken into account by allowing higher and higher resonances in the gas.

5. The NA50 data [73–75] can be plotted as a function of collision centrality. The more central the collision, the larger the average size of the fireball and the higher the energy density.

We take both nuclear and hadronic absorption into account by the convolution of two exponentials, $\exp[-L(l)/\lambda]\exp[-l/\lambda(T)]$ where $\lambda(T)$ is the mean free path of the J/ψ through the hadron gas, $l = 2R_A - b$, R_A is the nuclear radius and b is the impact parameter. The first exponential is for nuclear absorption while the second takes the thermal mean free path through a hadron gas into account. One can introduce such a dependence on l by assuming that the energy density, ϵ, depends on the number of nucleons divided by the effective surface area of the nuclear interaction as a function of b [72]. Using the energy–temperature relation appropriate to the hadron gas, one can determine the temperature profile as function of centrality and the corresponding absorption profile.

In Fig. 7.14 (a) and (b) we show the calculated absorption (nuclear + hadron gas) superimposed on the NA50 data [73–75]. The boxes show the Pb+Pb data while the stars give the S+U data. The temperatures indicated on the curves are the temperatures at low centrality (the first three points from the left). The hadron gas picture is more reliable in more peripheral collisions.

It is very interesting to note that the estimated temperatures are in the same region as the temperature expected for the phase transition and close to the temperatures measured at freeze-out from various hadron abundances. The curve labeled with $T = 175$ MeV, where T varies from 175 to about 195 MeV,
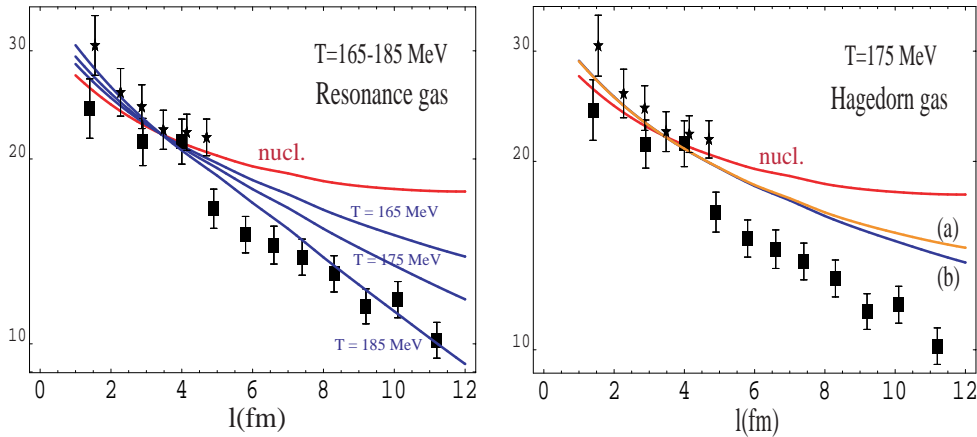
Fig. 7.14: Left-hand side: The exponential attenuation model compared to Pb+Pb (boxes) and S+U (stars) J/ψ normalized to Drell–Yan for three different values of the initial temperature in the hadron gas. The curve labeled as "nucl." includes only nuclear absorption effects. The other curves include both hadron gas and nuclear attenuation. Right-hand side: Same but for a Hagedorn gas. The curves labeled (a) and (b) show that there is no significant centrality dependence of the temperature since (one of the two curves shown has the geometrical effect switched off)

fits the data for low centrality but still falls short of reproducing the observed drop in J/ψ production above $l = 5$ fm. The curve with $T = 185$ MeV fits the low centrality data and agrees relatively well with the data in central collisions. However the temperature rises to 200 MeV at $l \simeq 11$ fm, likely too high for a hadron gas (see below).

The increase in temperature due to the increase in energy density that we find for the resonance gas is less pronounced than in the case of a pure pion gas in Ref. [62] because the number of degrees of freedom in the resonance gas increases appreciably with temperature. The extra energy density has to be shared among more and more degrees of freedom and the temperature increases less than with a fixed $\epsilon = CT^4$ power law. This behaviour begins to reproduce that expected from a Hagedorn gas with an exponentially increasing resonance density per unit mass interval [64, 76, 77].

The extrapolation to increasing centrality using the energy–temperature relation of the Hagedorn gas is shown in Fig. 7.14 (b) with $T = 175$ MeV. The result is quite spectacular. The sharp rise of the degrees of freedom due to the vicinity of the Hagedorn temperature makes the temperature of the gas nearly constant so that the dissociation curve cannot become harder and the prediction falls far short of explaining the drop observed by NA50. The simplest interpretation of Fig. 7.14 (b) is that with increasing centrality, more energy goes into the excitation of more and more thermodynamical degrees of freedom, leading to the final transition to the quark–gluon plasma. The curve shown represents the limiting absorption from the Hadron gas so that anything harder would be due to the dissociation of the J/ψ in the quark–gluon plasma.

Some words of caution are in order. In the framework of our calculation, it is certainly reasonable to expect the relevant insertions in the quark loop of Fig. 7.11 to correspond to the Dirac matrices S, P, A, V, and T where the latter are dominated by the lowest $q\bar{q}$, S-wave states we have been considering. On the other hand, we cannot exclude that decreasing couplings of the higher resonances may eventually resum up to a significant effect which would change the picture obtained by truncating the cross-section to include only the lowest states.

However, in all cases where this happens, such as in deep inelastic lepton–hadron scattering, the final result reproduces what happens for free quarks and gluons. In our case, this would mean going above the Hagedorn temperature into the quark and gluon gas, precisely what Fig. 7.14 (b) seems to tell us.

5   SHADOWING AND ABSORPTION EFFECTS ON J/ψ PRODUCTION IN D+AU COLLISIONS[6]

The nuclear quark and antiquark distributions have been probed through deep inelastic scattering (DIS) of leptons and neutrinos from nuclei. These experiments showed that parton densities in free protons are modified when bound in the nucleus [78]. This modification, referred to collectively as shadowing, depends on the parton momentum fraction x and the square of the momentum transfer, Q^2. Thus, in addition to the already aforementioned nuclear absorption and secondary hadronic scattering effects, initial state shadowing can also play a role, especially as the energy increases, simultaneously decreasing the values of parton momentum fraction, x, probed in the collision.

Most models of shadowing predict that the modification should vary depending on position within the nucleus [79] but DIS experiments are typically insensitive to this position dependence. However, some spatial inhomogeneity has been observed in νN scattering [80]. Here we discuss the combined effects of shadowing and absorption both in minimum bias d+Au collisions at RHIC and as a function of centrality.

Our calculations employ the colour evaporation model (CEM) which treats all charmonium production identically to $c\bar{c}$ production below the $D\overline{D}$ threshold, neglecting colour and spin. The leading order (LO) rapidity distributions of J/ψ's produced in dA collisions at impact parameter b is

$$\frac{d\sigma_{\mathrm{d}A}}{dyd^2bd^2r} = 2F_{J/\psi}K_{\mathrm{th}} \int dz\,dz' \int_{2m_c}^{2m_D} M dM \left\{ F_g^d(x_1,Q^2,\vec{r},z)F_g^A(x_2,Q^2,\vec{b}-\vec{r},z')\frac{\sigma_{gg}(Q^2)}{M^2} \right. \quad (7.37)$$

$$+ \sum_{q=u,d,s} [F_q^d(x_1,Q^2,\vec{r},z)F_{\bar{q}}^A(x_2,Q^2,\vec{b}-\vec{r},z') + F_{\bar{q}}^d(x_1,Q^2,\vec{r},z)F_q^A(x_2,Q^2,\vec{b}-\vec{r},z')]\frac{\sigma_{q\bar{q}}(Q^2)}{M^2} \left. \right\} .$$

The partonic cross-sections are given in Ref. [81], $M^2 = x_1 x_2 S_{NN}$ and $x_{1,2} = (M/\sqrt{S_{NN}})\exp(\pm y) \approx (m_{J/\psi}/\sqrt{S_{NN}})\exp(\pm y)$ where $m_{J/\psi}$ is the J/ψ mass. The fraction of $c\bar{c}$ pairs below the $D\overline{D}$ threshold that become J/ψ's, $F_{J/\psi}$, is fixed at next-to-leading order (NLO) [82]. Both this fraction and the theoretical K factor, K_{th}, drop out of the ratios. We use $m_c = 1.2$ GeV and $Q = 2m_c$ [82].

We assume that the nuclear parton densities, F_i^A, are the product of the nucleon density in the nucleus, $\rho_A(s)$, the nucleon parton density, $f_i^N(x,Q^2)$, and a shadowing ratio, $S_{\mathrm{P,S}}^j(A,x,Q^2,\vec{r},z)$, where $\vec{r}$ and z are the transverse and longitudinal location of the parton in position space. The first subscript, P, refers to the choice of shadowing parameterization, while the second, S, refers to the spatial dependence. Most available shadowing parameterizations ignore effects in deuterium. However, we take the proton and neutron numbers of both nuclei into account. Thus,

$$F_i^d(x,Q^2,\vec{r},z) = \rho_d(s)f_i^N(x,Q^2) \quad (7.38)$$
$$F_j^A(x,Q^2,\vec{b}-\vec{r},z') = \rho_A(s')S_{\mathrm{P,S}}^j(A,x,Q^2,\vec{b}-\vec{r},z')f_j^N(x,Q^2) , \quad (7.39)$$

where $s = \sqrt{r^2+z^2}$ and $s' = \sqrt{|\vec{b}-\vec{r}|^2+z'^2}$. With no nuclear modifications, $S_{\mathrm{P,S}}^j(A,x,Q^2,\vec{r},z) \equiv 1$. The nucleon densities of the heavy nucleus are assumed to be Woods–Saxon distributions with $R_{\mathrm{Au}} = 6.38$ fm and $R_{\mathrm{Pb}} = 6.62$ fm [83]. We use the Hulthen wave function [84] to calculate the deuteron density distribution. The densities are normalized so that $\int d^2r dz \rho_A(s) = A$. We employ the MRST LO parton densities [85] for the free nucleon.

We have chosen shadowing parameterizations developed by two groups which cover extremes of gluon shadowing at low x. The Eskola $et\ al.$ parameterization, EKS98, is based on the GRV LO [86] parton densities. Valence quark shadowing is identical for u and d quarks. Likewise, the shadowing of $\bar{u}$, $\bar{d}$ and $\bar{s}$ quarks are identical at Q_0^2. Shadowing of the heavier flavour sea, $\bar{s}$ and higher, is, however, calculated and evolved separately at $Q^2 > Q_0^2$. The shadowing ratios for each parton type are evolved to
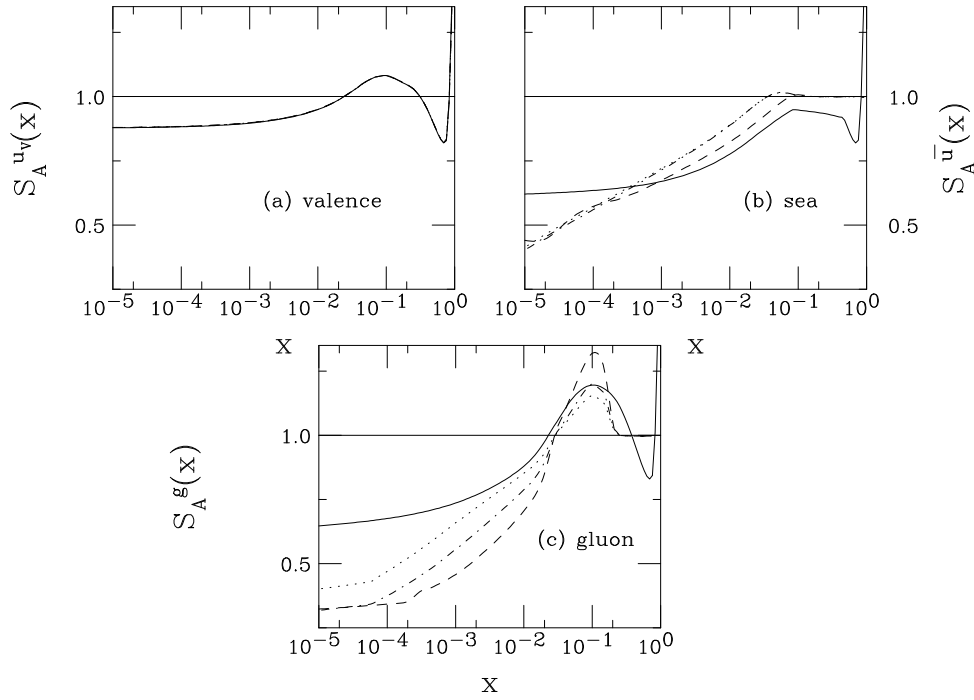
---

[6]Author: R. Vogt

Fig. 7.15: The shadowing parameterizations are compared at the scale $\mu = 2m_c = 2.4$ GeV. The solid curves are EKS98, the dashed, FGSo, dot–dashed, FGSh, and dotted, FGSl.

LO for $1.5 < Q < 100$ GeV and are valid for $x \geq 10^{-6}$ [87, 88]. Interpolation in nuclear mass number allows results to be obtained for any input A. The parameterizations by Frankfurt, Guzey and Strikman (FGSo, the original parameterization, along with FGSh and FGSl for high and low gluon shadowing) combine Gribov theory with hard diffraction [89]. They are based on the CTEQ5M [90] parton densities and evolve each parton species separately to NLO for $4 < Q^2 < 10^4$ GeV. Although the x range is $10^{-5} < x < 0.95$, the sea quark and gluon ratios are unity for $x > 0.2$. The EKS98 valence quark shadowing ratios are used as input since Gribov theory does not predict valence shadowing. The FGSo parameterization is available for four different values of A: 16, 40, 110 and 206 while FGSh and FGSl also include $A = 197$. We use $A = 206$ for the gold nucleus with FGSo and $A = 197$ for the other parameterizations.

Figure 7.15 compares the four homogeneous ratios, S_{EKS98} and S_{FGS} for $Q = 2m_c$. The FGSo calculation predicts far more shadowing at small x and larger antishadowing at $x \sim 0.1$. The difference is especially large for gluons. At very low x, the gluon ratios for FGSo and FGSh are quite similar but, in the intermediate x regime, the FGSh parameterization drops off more smoothly. On the other hand, the FGSl parameterization levels off at a higher value of S_P^i than the other two FGS parameterizations. In the antishadowing regime, FGSh and FGSl are rather similar to the EKS98 result.

We now turn to the spatial dependence of the shadowing. We show results for a parameterization proportional to the parton path length through the nucleus [91],

$$S_\rho^j(A, x, Q^2, \vec{r}, z) = 1 + N_\rho(S^j(A, x, Q^2) - 1)\frac{\int dz \rho_A(\vec{r}, z)}{\int dz \rho_A(0, z)} . \tag{7.40}$$

where N_ρ is chosen so that $(1/A) \int d^2 r dz \rho_A(s) S_\rho^j(A, x, \mu^2, \vec{b}, z) = S^j(A, x, \mu^2)$. When $s \gg R_A$, the nucleons behave as free particles while in the centre of the nucleus, the modifications are larger than the average value S^j. The normalization requires $(1/A) \int d^2 r dz \rho_A(s) S_{\text{P},\rho}^j = S_\text{P}^j$. While there are three homogeneous FGS parameterizations, only two inhomogeneous parameterizations are provided. No spa-

tial dependence is given for FGSo, the case with the strongest gluon shadowing. We have checked the available dependencies against those calculated using $S^j_{\mathrm{FGSo,WS}}$ and $S^j_{\mathrm{FGSo},\rho}$ and found that, at similar values of the homogeneous shadowing ratios, $S^j_{\mathrm{FGSo},\rho}$ is quite compatible with the available FGS inhomogeneous parameterizations. Therefore, to characterize the spatial dependence of FGSo and EKS98, we use $S^j_{\mathrm{P},\rho}$ while the given inhomogeneous parameterizations are used for FGSh and FGSl.

To implement nuclear absorption on J/ψ production in dA collisions, the production cross-section in Eq. (7.37) is weighted by the survival probability, S^{abs}, so that

$$S^{\mathrm{abs}}(\vec{b} - \vec{s}, z') = \exp\left\{-\int_{z'}^{\infty} dz'' \rho_A(\vec{b} - \vec{s}, z'') \sigma_{\mathrm{abs}}(z'' - z')\right\} . \tag{7.41}$$

where z' is the longitudinal production point, as in Eq. (7.39), and z'' is the point at which the state is absorbed. If shadowing is not considered and $S^{\mathrm{abs}} = 1$, $\sigma_{\mathrm{d}A} = 2A\sigma_{pN}$. For $S^{\mathrm{abs}} \neq 1$, $\sigma_{\mathrm{d}A} = 2A^{\alpha}\sigma_{pN}$. The nucleon absorption cross-section, σ_{abs}, depends on where the state is produced and how far it travels through nuclear matter. The effective A dependence is obtained from Eqs. (7.37) and (7.41) by integrating over z', z, and b. The contribution to the full A dependence in $\alpha(x_F)$ from absorption alone is only constant if σ_{abs} is constant and independent of the production mechanism [92]. The observed J/ψ yield includes feed down from χ_{cJ} and ψ' decays, giving

$$S^{\mathrm{abs}}_{J/\psi}(\vec{b} - \vec{s}, z') = 0.58 S^{\mathrm{abs}}_{J/\psi, \mathrm{dir}}(\vec{b} - \vec{s}, z') + 0.3 S^{\mathrm{abs}}_{\chi_{cJ}}(\vec{b} - \vec{s}, z') + 0.12 S^{\mathrm{abs}}_{\psi'}(\vec{b} - \vec{s}, z') . \tag{7.42}$$

In colour singlet production, the final state absorption cross-section depends on the size of the $c\bar{c}$ pair as it traverses the nucleus, allowing absorption to be effective only while the cross-section is growing toward its asymptotic size inside the target. On the other hand, if the $c\bar{c}$ is only produced as a colour octet, hadronization will occur only after the pair has traversed the target except at very backward rapidity. We have considered a constant octet cross-section, as well as one that reverts to a colour singlet at backward rapidities. For singlets, $S^{\mathrm{abs}}_{J/\psi, \mathrm{dir}} \neq S^{\mathrm{abs}}_{\chi_{cJ}} \neq S^{\mathrm{abs}}_{\psi'}$ but, with octets, one assumes that $S^{\mathrm{abs}}_{J/\psi, \mathrm{dir}} = S^{\mathrm{abs}}_{\chi_{cJ}} = S^{\mathrm{abs}}_{\psi'}$. As can be seen in Fig. 7.16, the difference between the constant and growing octet assumptions is quite small at large $\sqrt{S}$ with only a small singlet effect at $y < -2$. Singlet absorption is also important only at similar rapidities and is otherwise not different from shadowing alone. Finally, we have also considered a combination of octet and singlet absorption in the context of the NRQCD model, see Ref. [92] for more details. The combination of nonperturbative singlet and octet parameters changes the shape of the shadowing ratio slightly. The results are shown integrated over impact parameter for the EKS98 shadowing parameterization since it gives good agreement with the trend of the PHENIX data shown later in this chapter.

Several values of the asymptotic absorption cross-section, $\sigma_{\mathrm{abs}} = 1$, 3 and 5 mb, corresponding to $\alpha = 0.98$, 0.95 and 0.92 respectively for absorption alone in e.g., beryllium and tungsten targets are shown in Fig. 7.16. These values of σ_{abs} are somewhat smaller than those obtained for the sharp sphere approximation where the relation between σ_{abs} and α can be calculated analytically: $\sigma_{\mathrm{abs}} = 16\pi r_0^2(1 - \alpha)/9$. The diffuse surface of a real nucleus and the longer range of the density distribution results in a smaller value of σ_{abs} than that found for a sharp sphere nucleus.

The right-hand side of Fig. 7.16 compares the EKS98 parameterization and $\sigma_{\mathrm{abs}} = 3$ mb with the FGS parameterizations at the same value of σ_{abs}. In the region that PHENIX can measure, the EKS98 and FGSl results are essentially indistinguishable. The FGSh result lies between the FGSo and EKS98 results at forward rapidity but is also quite similar to FGSh at negative rapidity.

In central collisions, the inhomogeneous shadowing is stronger than the homogeneous result. The stronger the homogeneous shadowing, the larger the inhomogeneity. In peripheral collisions, the inhomogenous effects are somewhat weaker than the homogenous results but some shadowing is still present. Shadowing persists in part because the density in a heavy nucleus is large and approximately constant except close to the surface and partly because the deuteron wave function has a long tail. We also expect
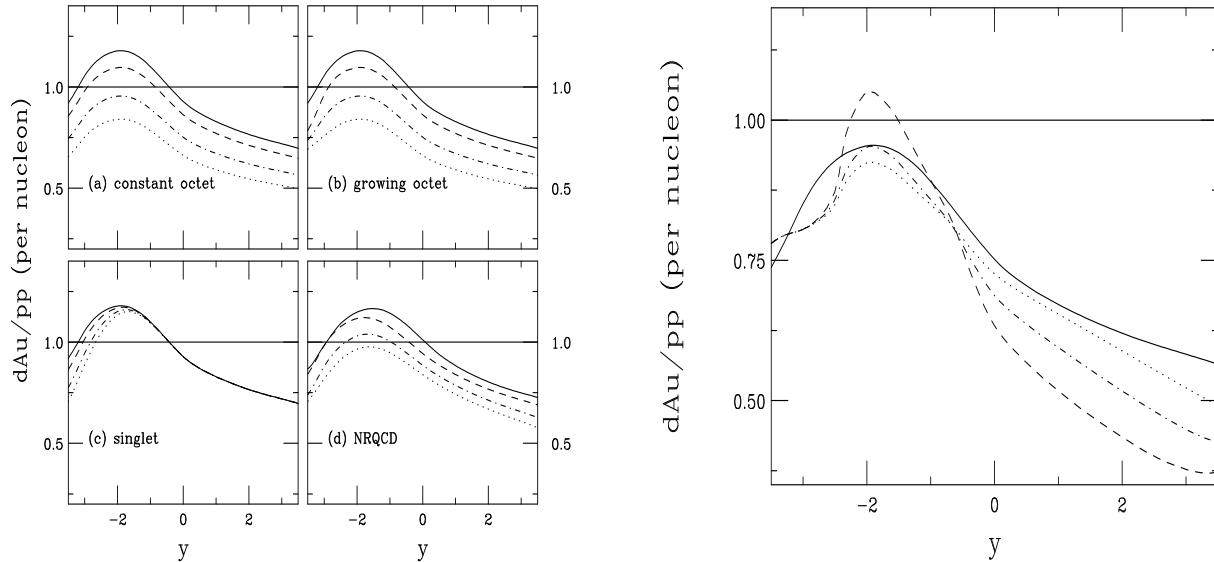
Fig. 7.16: Left-hand side: The J/ψ dAu/pp ratio with EKS98 at 200 GeV as a function of rapidity for (a) constant octet, (b) growing octet, (c) singlet, all calculated in the CEM and (d) NRQCD. For (a)–(c), the curves are no absorption (solid), $\sigma_{abs} = 1$ (dashed), 3 (dot–dashed) and 5 mb (dotted). For (d), we show no absorption (solid), 1 mb octet/1 mb singlet (dashed), 3 mb octet/3 mb singlet (dot–dashed), and 5 mb octet/3 mb singlet (dotted). Right-hand side: The J/ψ dAu/pp ratio at 200 GeV for a growing octet with $\sigma_{abs} = 3$ mb is compared for four shadowing parameterizations. We show the EKS98 (solid), FGSo (dashed), FGSh (dot–dashed) and FGSl (dotted) results as a function of rapidity.

absorption to be a stronger effect in central collisions. In Fig. 7.17, we show the inhomogeneous shadowing and absorption results for EKS98 and $\sigma_{abs} = 3$ mb as a function of b/R_A for the dAu/pp ratio as a function of b relative to the minimum bias ratio on the left-hand side and the ratio dAu/pp as a function of the number of binary collisions, N_{coll}, on the right-hand side. The ratios are shown for several values of rapidity to represent the behavior in the anti-shadowing (large negative y), shadowing (large positive y) and transition regions (midrapidity).

The (dAu(b)/pp)/(dAu/pp) ratios, denoted dAu(b)/dAu(ave) on the y-axis of the left-hand figure, are all less than unity for $b/R_A < 0.7$, with stronger than average shadowing and absorption, and rise above unity for large b/R_A, weaker than average shadowing and absorption. The right-hand side shows the dAu/pp ratios for the same rapidity values as a function of the number of collisions, N_{coll}. The dependence of the ratios on N_{coll} is almost linear. We do not show results for $N_{coll} < 1$, corresponding to $b/R_A > 1.3$ on the left-hand side, the point where those ratios begin to flatten out. The weakest N_{coll} dependence occurs where the shadowing effect itself is weakest, at $y = -2$ at RHIC, in the antishadowing region, as expected. The trends of the ratios as a function of N_{coll} are consistent with the PHENIX data from the north muon arm ($y = 2$) and the electron arms ($y = 0$) but the PHENIX results from the south arm ($y = -2$) are much stronger than our predictions.

Thus the combination of shadowing and absorption seems to be in good agreement with the PHENIX data from RHIC. It is more difficult to make predictions of shadowing for the CERN SPS since the average values of x at which the J/ψ is produced are much higher, $x \sim 0.16$ at $\sqrt{S_{NN}} = 20$ GeV. In this x region, the nuclear gluon shadowing ratio is either nearly crossing unity into the EMC region (EKS98) or assumed to be unity (FGS), see Fig. 7.15. Therefore we have only shown results for RHIC. At the LHC, the x values probed are significantly lower, leading to a stronger shadowing effect over all rapidity, see Ref. [91]. Combining J/ψ and Υ production results in dA collisions at RHIC and the LHC could help map out the nuclear gluon distribution in x and Q^2, both in minimum bias collisions and as a function of centrality.
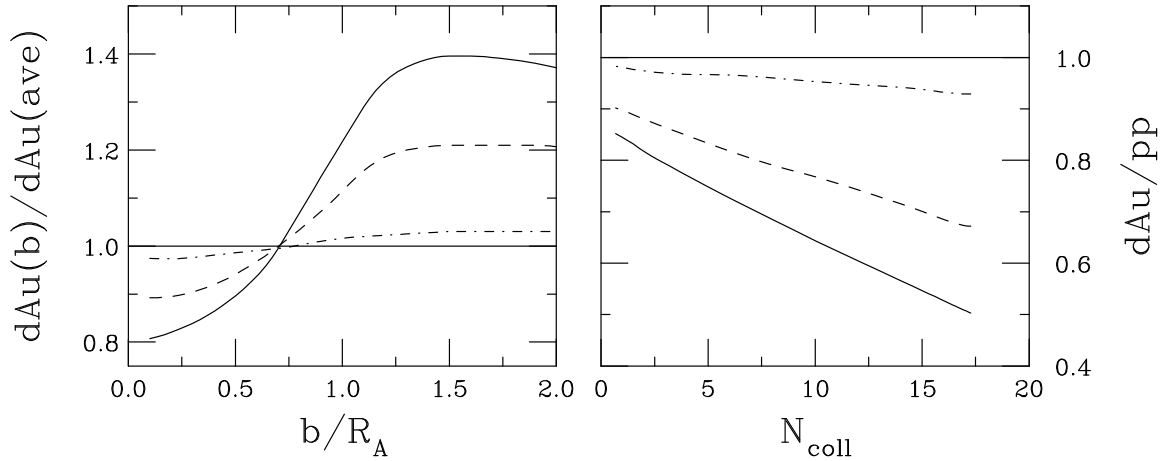
Fig. 7.17: Left-hand side: The J/ψ (dAu(b)/pp)/(dAu(ave)/pp) ratio as a function of b/R_A. Right-hand side: The ratio dAu/pp as a function of N_{coll}. Results are shown for $y = -2$ (dot–dashed), $y = 0$ (dashed) and $y = 2$ (solid) at 200 GeV for a growing octet with $\sigma_{\mathrm{abs}} = 3$ mb and the EKS98 parameterization.

6 QUARKONIUM DISSOCIATION IN HOT QCD MATTER[7]

The use of heavy quarkonium suppression as a signature of deconfinement [1] requires understanding dissociation mechanisms in the confined and deconfined phases of QCD matter. In this section, we comment on the current calculations of quarkonium dissociation rates and possible ways to improve them.

In the confined hadron gas, the interactions of quarkonium are traditionally treated in a low-density approximation to the kinetic approach, where the survival probability is expressed through the quarkonium–hadron dissociation cross-sections. An overview of different approaches to calculating these cross-sections has been given previously. As discussed there, all of these approaches rely on certain assumptions and approximations, the accuracy of which is often difficult to assess *a priori*. Nonperturbative interactions of light hadrons are still beyond the reach of reliable theroetical calculations, so the hope is that the large heavy quark mass forming the quarkonium bound state can lead to simplifications.

Among the approaches discussed before, the short-distance QCD approach [2, 6] is based on the assumption that the heavy quark mass is sufficiently large, $m_q \gg \Lambda_{\mathrm{QCD}}$, and the corresponding bound state size, $R \sim 1/(m_q \alpha_s)$, is sufficiently small for interactions with light hadrons of size $\sim 1/\Lambda_{\mathrm{QCD}}$ can be treated by using the multipole, or operator product, expansion. In leading twist (or, in the more intuitive language of the QCD multipole expansion, in the leading electric dipole approximation), the cross-section is expressed through Wilson coefficients (for the leading electric dipole operator, they describe the electric polarizability of heavy quarkonium), and the gluon structure functions of light hadrons at the scale determined by the size of the $Q\overline{Q}$ state.

There are two main caveats to this approach. An analysis of the applicability of the multipole expansion shows that not only the quarkonium size should be small, $R \sim 1/(m_q \alpha_s) \ll \Lambda_{\mathrm{QCD}}$, but also the binding energy (which determines, by the uncertainty principle, the characteristic interaction time) has to be large, $\epsilon \sim m_q \alpha_s^2 \gg \Lambda_{\mathrm{QCD}}$. The latter inequality is only marginally justified for charmonium, at the borderline between the perturbative and nonperturbative regimes. The second caveat is the knowledge of the gluon structure function at large Bjorken x, corresponding to low energies and relatively small virtuality, $\sim \epsilon$. For the J/ψ, the binding energy is $\epsilon = 2M_D - M_{J/\psi} \simeq 0.64$ GeV. The gluon structure function is not well determined at such low scales. Nevertheless, at large x the gluon structure functions have to be relatively suppressed by quark counting rules which dictate at least a $\sim (1-x)^4$ suppression at $x \to 1$ since the valence quarks dominate the light hadron structure functions at large x.

---

[7]Author: D. Kharzeev

This naturally brings us to the possibility that the light quark exchanges, despite being suppressed in the heavy quark limit, become important in the dissociation of charmonium states — in fact, most of the approaches reviewed previously model such exchanges in different ways. At least in principle the picture can be clarified by a lattice calculation of the quarkonium matrix elements involving quark and gluon operators of different dimension. Such a calculation could establish a hierarchy of different mechanisms of quarkonium dissociation. It would also be important for understanding the dynamics of quarkonium production and decay. On the phenomenological side, many of the approaches can be tested in quarkonium decays, e.g., $\psi' \to \psi X$ (see e.g., Ref. [93] and references therein).

Apart from the magnitude of the quarkonium dissociation cross-section, one should also examine the validity of the low-density approximation in the kinetic approach. This approach leads to the quarkonium dissociation rate, $R = \sum_i v_i \sigma_i \rho_i$, where the sum runs over different hadron species with densities ρ_i and dissociation cross-sections σ_i and v_i are the corresponding relative quarkonium–hadron velocities. The survival probability of heavy quarkonium is then obtained by integrating over the time history of the hadron gas. For example, an isentropic longitudinal expansion yields (see e.g., Ref. [94])

$$S \sim \exp\left(-\sum_i v_i \sigma_i \rho_i \ln\left(\frac{\rho_i}{\rho_f}\right)\right),\tag{7.43}$$

where ρ_f^i is a "freeze-out" density at which the system falls apart and ρ_i corresponds to the initial densities of the different hadron species.

Such treatment assumes the dominance of two-body interactions of the quarkonium and thus applies only at sufficiently low temperature. The dissociation process, by the uncertainty principle, takes place over a time inversely proportional to the binding energy, $\sim 1/\epsilon$. The typical time between subsequent thermal interactions at temperature T is $\sim 1/T$. The condition for the applicability of the low-density approximation is thus $\epsilon(T)/T \gg 1$. The binding energy can be modified in a thermal system and is thus a function of temperature. Lattice results presented in the previous sections, especially Section 3.3, indicate no substantial modification of the binding energy below T_c so that up to $T_c \sim 200$ MeV the ratio $\epsilon(T)/T \simeq 3$ is likely to be large enough to justify the kinetic approach.

In the deconfined phase, the original screening scenario can be seen to correspond to the opposite "weak coupling" limit of $\epsilon(T)/T \ll 1$. Indeed, the heavy quarkonium state binding energy vanishes when it is screened out of existence. The lattice results presented in Section 3 indicate that this does not happen for the J/ψ until $T \approx 1.5\,T_c$. Moreover, the previous lattice results indicate no significant change in the J/ψ mass up to these temperatures, suggesting that the weak coupling approach is not appropriate even for $T_c \leq T \leq 1.5\,T_c$. However, this does not mean that the quarkonia are not dissociated at temperatures below $1.5\,T_c$ since "ionization" of heavy quarkonia by gluons [2, 5] is still possible. An estimate of the dissociation rate in this regime was given in Ref. [7],

$$R_{\text{act}} = \frac{(LT)^2}{6\pi}\, m_q\, \exp(-\epsilon/T)\;.\tag{7.44}$$

Here L is the size of the $q\bar{q}$ system which is generally temperature dependent and can, in principle, exceed the typical hadronic size, $\sim 1/\Lambda_{\text{QCD}}$, in the deconfined phase. While this rate is moderate (at $T = 300$ MeV and $L = 1$ fm, we find $R_{\text{act}} \simeq 0.05$ fm^{-1}), a medium with a lifetime of ≈ 10 fm can reduce the survival probability by factor of two. Thus, one cannot presently conclude from the lattice results that there is no J/ψ suppression in the deconfined phase below $1.5T_c$. A conclusive answer can be given by lattice calculations once a reliable extraction of the J/ψ width becomes possible.

Once the weak coupling limit of $\epsilon(T)/T \ll 1$ is reached, dissociation occurs very rapidly with a rate [7]

$$R_{\text{act}} = \frac{4}{L}\sqrt{\frac{T}{\pi m_q}}\;.\tag{7.45}$$

This expression is easy to understand once we recall that the thermal velocity of a free particle in three dimensions is $v_{\text{th}}(T) = 4\sqrt{T/\pi m_q}$ where we recover the classical high-temperature limit for the thermal activation rate

$$R_{\text{act}} = \frac{v_{\text{th}}(T)}{L} \ .$$ (7.46)

An estimate of Eq. (7.45) gives a large rate, $R_{\text{act}} \sim 1/\text{fm}$ suggesting that once the binding energy of quarkonium becomes small compared to the temperature, dissociation occurs very rapidly and should lead to strong suppression, as envisioned in the original scenario [1].

7 SECONDARY CHARMONIUM PRODUCTION AND CHARM–QUARK COALESCENCE[8]

In recent years, a new element has been added to charmonium production in heavy-ion collisions with the realization that $c\bar{c}$ bound states might be recreated in later stages of the reaction. In Refs. [95–99] secondary charmonium production was evaluated in the statistical model for hadron production, motivated by the success of this framework in the description of light hadron species [100]. Whereas in Ref. [95] the J/ψ abundance was calculated simply in terms of its thermal density at the hadronization temperature, T_c, yielding fair agreement with NA50 data [101, 102] at the SPS, Refs. [96–99] included the notion that the (rather heavy) charm quarks are exclusively produced in primordial (hard) nucleon–nucleon (NN) collisions. This constraint is implemented by introducing a charm–quark fugacity, $\gamma_c \equiv \gamma_{\bar{c}}$, to match the primordial number of $c\bar{c}$ pairs, $N_{c\bar{c}}$, to the total (hadronic) charm content in the fireball at hadronization,

$$N_{c\bar{c}} = \frac{1}{2} N_{\text{op}} \ \frac{I_1(N_{\text{op}})}{I_0(N_{\text{op}})} \ + \ V_{FB}(T) \ \gamma_c(T)^2 \sum_\Psi n_\psi(T) \ .$$ (7.47)

Here $N_{\text{op}} = V_{FB}(T) \ \gamma_c \ \sum_C n_C(T, \mu_B)$ and $C = D, \overline{D}, D^*, \overline{D}^*, \Lambda_c \ldots$, runs over all known open charm hadrons, V_{FB} denotes the (centrality-dependent) hadronic fireball volume covering an appropriate range in rapidity and $I_{0,1}$ are modified Bessel functions. The number of charmonium states ($\Psi = \eta_c$, J/ψ, $\psi' \ldots$) produced by "statistical coalescence" then follows as

$$N_\Psi^{\text{eq}}(T, \gamma_c) = V_{FB}(T) \ d_\Psi \ \gamma_c^2 \ \int \frac{d^3q}{(2\pi)^3} f^\psi(m_\psi; T)$$ (7.48)

where d_Ψ is the spin-degeneracy. The statistical approach correctly reproduces the ψ' to J/ψ ratio [103] for sufficiently central Pb+Pb collisions ($N_{\text{part}} \geq 200$) at the SPS. However, to describe the absolute J/ψ and ψ' numbers in terms of statistical coalescence alone (implying that all primordially produced charmonium states are suppressed), an enhancement of total charm production over the standard expectation from NN collision-scaled pp cross-sections by a factor of ~ 3 is necessary. This requirement, as well as the assumption of complete suppression of primordial charmonia, has been relaxed in the "two-component model" of Refs. [104, 105] where statistical charmonium production has been combined with a primordial component subject to suppression in both Quark–Gluon Plasma (QGP) and hadron gas phases. As a result, it has been found that the (moderately) suppressed primordial J/ψ component prevails as the major yield at SPS energies, whereas statistical recombination is the dominant source in central Au+Au collisions at RHIC, with interesting consequences for the excitation function, cf. the left-hand side of Fig. 7.18.

As discussed in Section 3, an important new insight from QCD lattice calculations is that low-lying charmonium states survive as resonance/bound states with finite width in the QGP up to temperatures of about $1.5 - 2 \, T_c$. This implies that these charmonium states can be formed not only at the hadronization transition, but also in the QGP. Of course, at the same time, dissociation reactions are operative, and the evolution of the J/ψ number should be described by kinetic theory within a Boltzmann equation. In
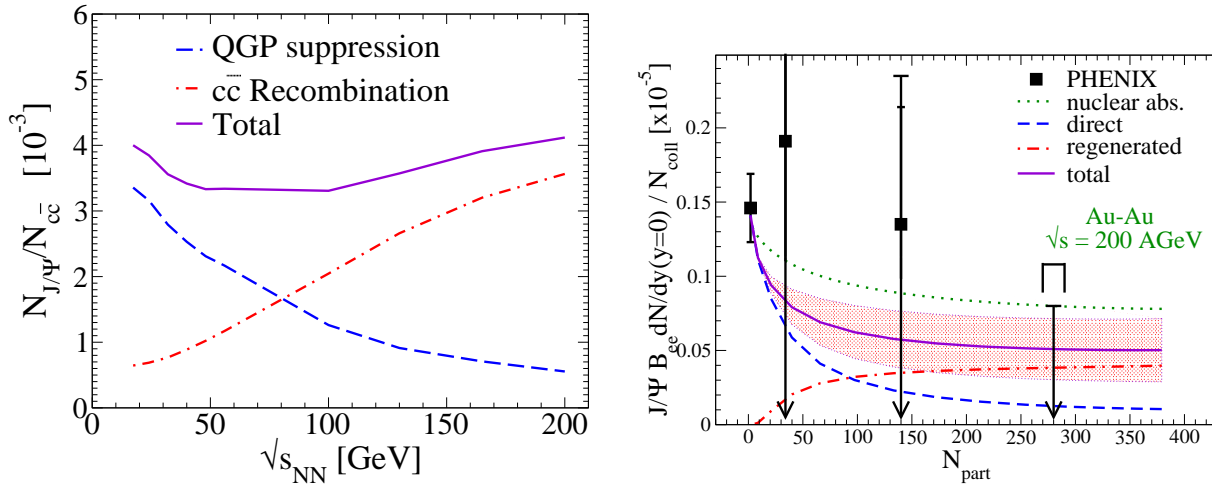
---

[8]Author: R. Rapp

Fig. 7.18: Left-hand side: excitation function of the ratio of J/ψ's over $c\bar{c}$ pairs in central heavy-ion collisions ($N_{\text{part}} = 360$) from SPS to RHIC energies [104, 105] for the J/ψ yield from quark gluon plasma suppressed primordial production (dashed), secondary J/ψ production from $c\bar{c}$ coalescence (dot–dashed) and the sum (solid). Right-hand side: Centrality dependence of the J/ψ yield, normalized to the number of primordial NN collisions, in Au+Au collisions at RHIC within a kinetic theory framework including in-medium effects on both open and hidden charm states [108]. We show J/ψ suppression with only the loss term in Eq. (7.50) (dashed), secondary J/ψ production (dot–dashed), primordial J/ψ's subject to nuclear absorption only (dotted) while the band around the solid line, representing the full solution of the rate equation, indicates the uncertainty induced by varying the in-medium masses of open-charm hadrons.

simplified form, the latter can be written as

$$\frac{dN_\Psi}{d\tau} = -\hat{\Gamma}_D\, N_\Psi + \hat{\Gamma}_F\, N_c\, N_{\bar{c}} \tag{7.49}$$

where $\hat{\Gamma}_D$ and $\hat{\Gamma}_F$ are the charmonium dissociation and formation rates respectively. The inclusion of the backward reaction in inelastic charmonium interactions such as, $J/\psi + X_1 \leftrightharpoons X_2 + c + \bar{c}\,(D + \overline{D})$, is, in fact, mandated by the principle of detailed balance. A key question is then under which conditions regeneration becomes quantitatively relevant. First, the equilibrium number of J/ψ mesons should be comparable to initial production (after nuclear absorption). While at the SPS, where $N_{c\bar{c}} \simeq 0.2$ in central Pb+Pb collisions (based on binary NN collision scaling), this is not the case, the situation is more favorable at RHIC, where, according to current measurements [106, 107], $N_{c\bar{c}} \simeq 15 - 30$ in central Au+Au collisions. Also note that the higher QGP temperatures at RHIC presumably lead to stronger suppression of the primordial component. Second, the amount of regeneration depends on the momentum distributions of charm quarks. Thus, if the latter are in thermal equilibrium (along with gluons and light quarks) and as long as a well-defined J/ψ (resonance) state persists, Eq. (7.49) takes a particularly simple and instructive form,

$$\frac{dN_\Psi}{d\tau} = -\Gamma_\Psi(T) \left[N_\Psi - N_\Psi^{\text{eq}}(T, \gamma_c) \right] \;. \tag{7.50}$$

An important point here is that the key ingredients to Eq. (7.50) are rather directly related to equilibrium in-medium properties of charm(onium) states, i.e., quantities which can be extracted from lattice QCD: (i) the reaction rate $\Gamma_\Psi(T)$ is the (inelastic) width of the Ψ spectral function; (ii) the equilibrium charmonium abundance, N_Ψ^{eq}, given by Eq. (7.48), depends on the in-medium charmonium mass and, via γ_c in Eq. (7.47), on the spectrum of open-charm states (including their in-medium masses). A recent

calculation including current knowledge from lattice QCD has been performed in Ref. [108]; results for RHIC are shown on the right-hand side of Fig. 7.18, indicating appreciable sensitivity to the in-medium open-charm threshold, mostly due to its impact on N_Ψ^{eq}. This investigation has also shown that most of the secondary J/ψ production occurs through resonance formation in the QGP. At full RHIC energy, relative chemical equilibrium is reached close to the hadronization temperature and frozen thereafter due to small reaction rates in hadronic matter, implying approximate agreement with the limiting case of statistical coalescence models applied at T_c, as discussed above.

The sensitivity of secondary production to the charm quark momentum distributions (i.e., deviations from thermal equilibrium) has been addressed in Refs. [109, 110], as well as in recent transport simulations [111, 112]: although the use of, e.g., primordial (perturbative QCD) charm quark distributions reduces the regenerated yield appreciably, it still remains significantly larger than expectations based on suppression scenarios alone. Measurements of elliptic flow of D-mesons at RHIC, testing their (early) thermalization, will therefore impose important constraints on models for charmonium regeneration. Similarly, since in coalescence approaches $N_\Psi^{\text{eq}} \propto N_{c\bar{c}}^2$ (cf. Eqs. (7.47) and (7.48)), an accurate measurement of open-charm production will be essential for reliable predictions of charmonium yields and spectra. Finally, it will be of great interest to extend both experimental and theoretical investigations to the bottomonium sector.

8 QUARKONIUM PRODUCTION IN NUCLEAR COLLISIONS[9]

8.1 Charmonium suppression at the CERN SPS

The experimental study of charmonium production in collisions of light and heavy ions at ultrarelativistic energies was carried out at the CERN SPS over 15 years (1986–2000) by experiments NA38 (see Refs. [113, 114] for initial results and [115, 116] for the most recent ones) and NA50 (see Refs. [50, 117–120]). It is continuing with experiment NA60, taking data in 2003 and 2004.

In addition, NA51 provided a reference measurement of charmonium production in pp and pd collisions [121] while proton–nucleus, pA, reference data were collected by NA38 [116, 122] and, with higher statistics, by NA50 [123, 124].

The SPS energies, between 158 and 450 GeV per nucleon in a fixed target configuration, are well suited for charmonium studies since the J/ψ production cross-section in the forward hemisphere ($x_F > 0$) in proton–proton interactions is between 50 and 100 nb/nucleon (see e.g., Ref. [125]), well above threshold. The high intensity experimental area at the SPS provides beam rates of about 10^7 Pb ions/s and 10^9 protons/s which, with a branching ratio $J/\psi \to \mu^+\mu^-$ of about 6% and a typical acceptance of 15%, resulted in samples of several tens of thousand of J/ψ collected for a given system. The statistics collected (see Tables 7.1 and 7.2) made it possible to perform detailed studies of J/ψ and ψ' production as a function of centrality in ion–ion collisions. The centrality was evaluated via the transverse energy, E_T, by NA38, as well as via the forward energy in the zero degree calorimeter, E_{ZDC}, and the charged multiplicity, N_{ch} by NA50.

The experimental program at the CERN SPS was developed in successive phases. At first, the pioneering experiment NA38 [113] collected data with light ions (oxygen and sulphur) at 200 GeV/nucleon and with proton beams at 450 GeV, using the NA10 dimuon spectrometer and an electromagnetic calorimeter as a centrality detector. Then, the second generation experiment NA50 [117] studied J/ψ production in lead–lead collisions at 158 GeV/nucleon with new or improved centrality detectors, and in proton–nucleus collisions with much higher statistics relative to NA38. Finally, experiment NA60 collected data with indium–indium collisions at 158 GeV/nucleon and proton–nucleus collisions at 400 GeV with a new silicon vertex spectrometer and a beam tracker (see next section).

In order to compare the hard production of charmonium states in different collisions ranging from pp to Pb+Pb, it is appropriate to define the cross-section per nucleon–nucleon collision, obtained by

---

[9]Section coordinator: M. Rosati; Authors: C. Lourenço, L. Ramello, M. Rosati, E. Scomparin

Table 7.1: Summary of proton–nucleus data collected by NA50.

Years	1996–1998	1998–2000	2000
Energy (GeV/nucleon)	450	450	400
Target thickness L/λ_I	26–39%	26–39%	26–39%
Targets	Be, Al, Cu, Ag, W	Be, Al, Cu, Ag, W	Be, Al, Cu, Ag, W, Pb
Beam intensity (p/s)	$(4-13) \times 10^8$	$(0.8-2.5) \times 10^8$	$(9-13) \times 10^8$
J/ψ ($\times 10^3$)	350–800	80–180	38–68

Table 7.2: Summary of S+U data and Pb+Pb data collected by NA38 and NA50.

Year	1992	1995	1996	1998	2000
Energy (GeV/nucleon)	200	158	158	158	158
Target thickness L/λ_I	20.5%	17%	30%	7%	9.3%
Beam–Target	S+U	Pb+Pb	Pb+Pb	Pb+Pb	Pb+Pb
Beam intensity (ions/5 s)	8×10^7	3×10^7	5×10^7	5.5×10^7	7×10^7
J/ψ ($\times 10^3$)	113	50	190	49	129

dividing the measured cross-section by the product of the mass numbers, AB, of the colliding nuclei. In the study of centrality, the measured Drell–Yan cross-section can replace AB since it has been verified experimentally (see e.g., Refs. [74, 118]) that the Drell–Yan cross-section is proportional to the number of nucleon–nucleon collisions.

The nuclear dependence of the charmonium cross-section is often parametrized as $\sigma_{pA} = \sigma_{pp}A^\alpha$, where $\alpha = 1$ is expected for a hard process in the absence of nuclear absorption effects. A more accurate description, valid also for light targets, is provided by the Glauber formalism [126]. A detailed description of such formalism applied to both pA and nucleus–nucleus collisions is given in Ref. [94]. The distribution of matter inside nuclei is described by 2-parameter or 3-parameter Woods–Saxon distributions from a compilation of electron scattering measurements [127]. When comparing the centrality evolution of different systems, a useful variable is the average path of the $c\bar{c}$ pair through nuclear matter, denoted by L.

The first NA38 results, obtained with 200 GeV/nucleon oxygen and sulphur beams, revealed [113, 114] that J/ψ production is suppressed in ion collisions, both relative to pU and as a function of the transverse energy, E_T. However, it was later found that the suppression pattern observed in S+U collisions was compatible with the extrapolation of the trend observed in pA collisions. NA38 then collected a significantly larger sample of S+U events (see Table 7.2), obtaining [115] absolute cross-sections for J/ψ, $B\sigma_\psi = 7.78 \pm 0.04 \pm 0.62$ μb, ψ', $B\sigma_{\psi'} = 59.1 \pm 6.2 \pm 4.7$ nb, and Drell–Yan in the mass window $2.9 < M < 4.5$ GeV, $\sigma_{\rm DY} = 310 \pm 10 \pm 25$ nb. Comparing the suppression pattern of the two resonances it was found that the ψ' is more suppressed than the J/ψ by at least a factor of two, even more so for central collisions. A global study of this result together with pp and pd results from NA51 [121] and pA results from NA38 [122] revealed (see Ref. [116], in particular Fig. 5) that J/ψ production exhibits a continuous decreasing pattern from pp to S+U reactions (including the centrality dependence observed in S+U interactions) which can be accounted for by normal nuclear absorption. On the other hand, the ψ' showed extra suppression in S+U interactions. Since the ψ' state is very loosely bound, it can be broken into a pair of open charm mesons by purely hadronic interactions, independent of whether the produced matter is confined or deconfined.
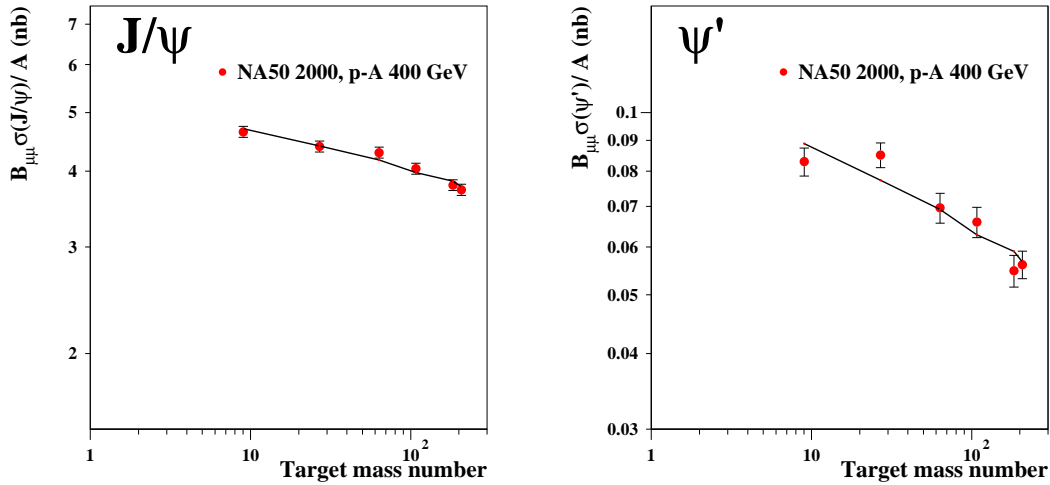
Fig. 7.19: The J/ψ (left) and ψ' (right) cross-sections in proton–nucleus collisions with six different targets at 400 GeV, measured by NA50, together with the result of the Glauber fits.

The understanding of the reference proton–nucleus data improved dramatically thanks to recent high statistics measurements by NA50, see Table 7.1. Figure 7.19 (see Ref. [74]) shows the absolute J/ψ and ψ' cross-sections, multiplied by the branching ratio to dimuons and divided by the target mass number A for the most recent pA data collected at 400 GeV. A fit using the Glauber formalism [94, 126], more accurate than the usual A^α parametrization, leads to absorption cross-sections $\sigma_{\rm abs}^\psi = 4.2 \pm 0.5$ mb and $\sigma_{\rm abs}^{\psi'} = 9.6 \pm 1.6$ mb. A difference between the J/ψ and ψ' absorption cross-sections is observed already in proton–nucleus collisions, thanks to higher statistics and improved systematics relative to NA38.

A more precise picture of normal nuclear absorption is obtained by combining the absolute cross-sections with the (J/ψ)/Drell–Yan ratios at all available beam energies. Using, in addition to the 400 GeV p–A data, also the NA50 data collected with a 450 GeV proton beam [123, 124] and the NA51 pp and pd results [121], a simultaneous Glauber fit gives [74] $\sigma_{\rm abs}^\psi = 4.3 \pm 0.3$ mb. The NA38 S+U data at 200 GeV/nucleon have been reanalysed with the most recent techniques. By fitting the reanalyzed data to a centrality-dependent Glauber calculation for six different centrality regions (see Fig. 7.20 left), $\sigma_{\rm abs}^\psi = 7.3 \pm 3.3$ mb is obtained, statistically compatible with the pA cross-section. A global fit to pp, pd, pA and S+U data, with separate normalizations for the three different (energy and rapidity) kinematical conditions, leads to $\sigma_{\rm abs}^\psi = 4.3 \pm 0.3$ mb (see Fig. 7.20 right). An extrapolation from the 200 GeV/nucleon S+U to the 158 GeV/nucleon Pb+Pb kinematical conditions is then made in order to obtain the normal absorption curve against which the Pb+Pb results are compared.

The analysis of the Pb+Pb data collected in 1995, 1996 and 1998 (see Table 7.2) showed [117, 118] that J/ψ production, relative to Drell–Yan, is anomalously suppressed with respect to the normal nuclear absorption pattern. This integrated result was complemented by detailed studies of the J/ψ suppression pattern as a function of collision centrality [50, 119, 120], determined from E_T and $E_{\rm ZDC}$, which suggests that this extra suppression sets in for semi-central collisions, with the transition occurring over a rather small range of centrality values. The suppression pattern, showing a departure from normal absorption and then no saturation at high E_T, is currently interpreted in the quark–gluon plasma scenario as the sequential suppression of two $c\bar{c}$ states, first the χ_c and then the J/ψ.

A more detailed analysis of Pb+Pb data revealed that the peripheral centrality data was affected by a considerable admixture of Pb–air interactions, especially in the multi-target configuration used in
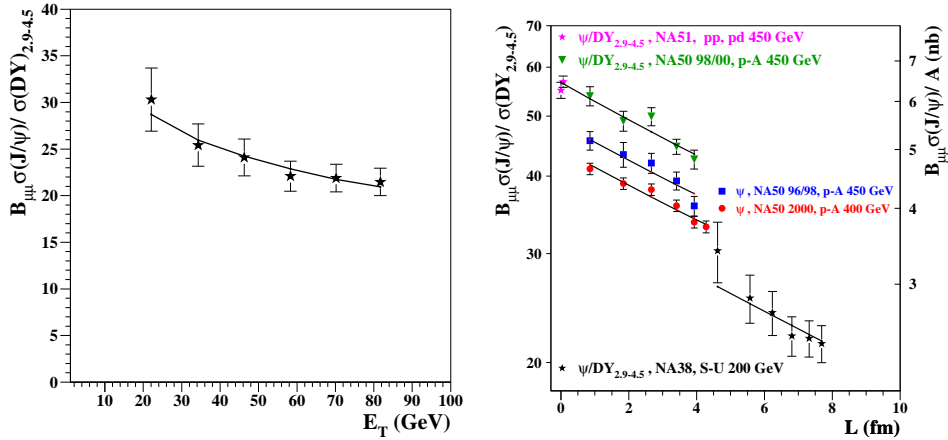
Fig. 7.20: Left-hand side: the (J/ψ)/Drell–Yan ratio as a function of centrality (determined by E_T) in S+U collisions. Right-hand side: the (J/ψ)/Drell–Yan as a function of L for several systems.

1996. Therefore, more data were collected by NA50 in 2000 with a single target under vacuum. The 2000 Pb+Pb J/ψ result is shown on the left-hand side of Fig. 7.21 together with the absorption curve derived from the analysis presented in Fig. 7.20. The departure from the ordinary nuclear absorption is still, in the new data set, a striking feature. The Pb+Pb data are compared to other systems on the right-hand side of Fig. 7.21.

A new result on ψ' production, recently obtained [75] from the 1998 and 2000 Pb+Pb data samples, analysed with the most recent procedures, is presented in Fig. 7.22. The left-hand side shows the relative suppression of the two $c\bar{c}$ bound states for several systems ranging from pBe to Pb+Pb, as a function of the product AB. As indicated above, the ψ' is more absorbed than the J/ψ already in pA collisions. Furthermore, a stronger ψ' suppression relative to the J/ψ is observed for the heavier S+U and Pb+Pb systems. On the right-hand side, ψ' suppression relative to Drell–Yan is presented as a function of centrality, expressed by the path length L. The ψ' suppression is the same in S+U and Pb+Pb interactions as a function of centrality and about three times stronger than in pA interactions.

In conclusion, experiments NA38, NA50 and NA51 provided valuable information on J/ψ and ψ' production with proton and ion beams at the SPS fixed target energies. A synthesis of the main result, the different suppression patterns of the two $c\bar{c}$ states, is presented in Fig. 7.23.

8.2 Recent studies of charmonium production in heavy-ion collisions at the SPS

Charmonium physics in ultrarelativistic nucleus–nucleus collisions is now being studied at the SPS by NA60. The experimental apparatus includes the muon spectrometer already used by NA50 and a vertex spectrometer, based on silicon pixel detectors, that allows an accurate determination of primary and secondary interaction vertices with a resolution better than 50 μm. By matching the muons measured in the muon spectrometer to tracks in the pixel telescope, simultaneously using coordinate and momentum information, it is possible to overcome the uncertainties introduced by the multiple scattering and energy loss fluctuations induced by the 5.5 m long hadron absorber positioned in front of the muon spectrometer. The consequent improvement in dimuon mass resolution is extremely impressive, and reaches a factor ~ 4 for low mass dimuons ($M < 1$ GeV), where multiple scattering is quantitatively more important. In the charmonia mass region, NA60 reaches a mass resolution of ≈ 70 MeV as opposed to ≈ 105 MeV in NA50, particularly important for ψ' studies.

In 2003, NA60 collected more than 230 million dimuon triggers in In+In collisions at 158 GeV/nucleon. The choice of Indium, an intermediate mass nucleus, is particularly interesting for the study of
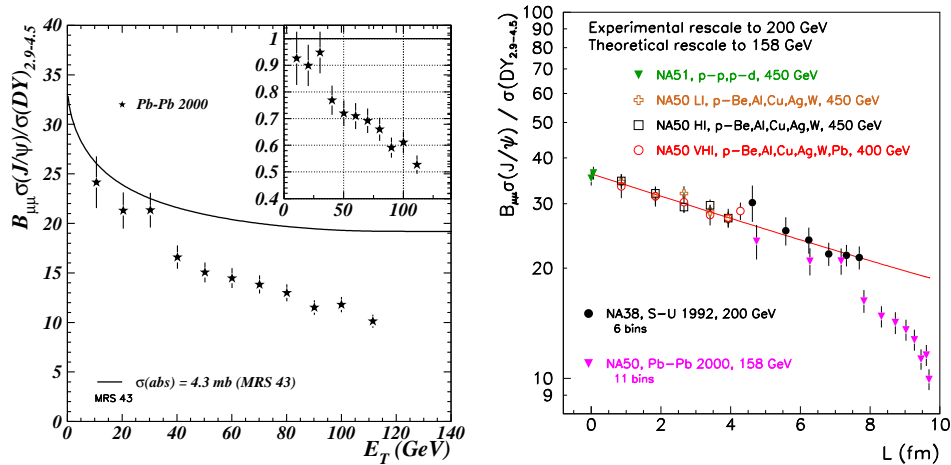
Fig. 7.21: Left-hand side: the (J/ψ)/Drell–Yan ratio as a function of centrality in Pb+Pb collisions at 158 GeV/nucleon. Right-hand side: the (J/ψ)/Drell–Yan ratio for several systems, from pp to Pb+Pb, as a function of L.

the anomalous J/ψ suppression observed by NA50 in Pb+Pb collisions. The onset of the anomalous J/ψ suppression occurs in semiperipheral Pb+Pb events, a region with potentially important systematic uncertainties due to the presence of out-of-target events. For the lighter In+In system, the anomaly should show up for comparatively more central events, thereby confirming this effect in a region where systematics are easier to control.

Furthermore, other useful insights into the suppression mechanisms can be obtained by studying the J/ψ yield as a function of centrality for both In+In and Pb+Pb, plotting the results as a function of centrality using several variables such as L, the thickness of nuclear matter traversed by the charmonium state, the number of participant nucleons, N_{part}, and the energy density, ϵ. In this way it may become possible to precisely identify the centrality variable that governs the anomalous suppression and, therefore, its origin. In particular, one could distinguish between the thermal (QGP) and geometrical (percolation) phase transitions, both resulting in the suppression of J/ψ production but as a function of different variables and with different thresholds in collision centrality.

Figure 7.24 shows the ratio between the J/ψ and the Drell–Yan production cross-sections measured in In–In collisions, in three centrality bins, either as a function of L (the distance of nuclear matter crossed by the J/ψ mesons after production) or N_{part}. On the right panel the J/ψ suppression pattern is divided by the normal nuclear absorption curve, defined by p–nucleus data. The J/ψ and Drell–Yan cross-sections are evaluated in the phase space window $2.92 < y_{\mathrm{lab}} < 3.92$ and $-0.5 < \cos\theta_{\mathrm{CS}} < 0.5$, where θ_{CS} is the polar decay angle of the muons in the Collins–Soper reference system. The Drell–Yan value is given in the 2.9–4.5 GeV/c^2 mass window. We see that, unlike what happens in the S–U collisions studied by NA38, the J/ψ production is suppressed in indium–indium collisions beyond the normal nuclear absorption. When the J/ψ over Drell–Yan ratio is plotted as a function of N_{part} the indium data points seem to agree with the suppression pattern measured in Pb–Pb. The two sets of data points *do not* overlap as a function of L. To clarify the origin of the anomalous J/ψ suppression, the statistical significance of the results must be increased and reference processes alternative to Drell–Yan are presently under study in NA60. Also the study as a function of the energy density is in progress.

8.3 Charmonium production in proton–nucleus collisions at 158 GeV

The NA60 experiment was proposed to clarify several physics questions resulting from specific experimental measurements made by previous SPS experiments, including the observation that J/ψ production
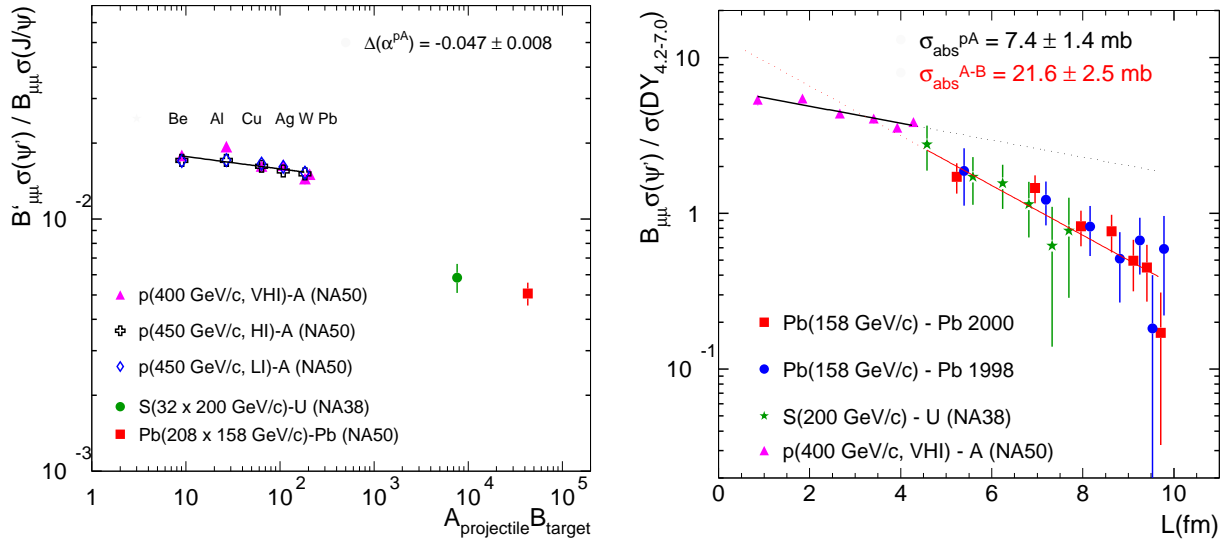
Fig. 7.22: Left-hand side: the ratio of ψ' to J/ψ in different collision systems as a function of AB. Right-hand side: the (ψ')/Drell–Yan ratio as a function of L.

is suppressed in heavy-ion collisions with respect to the yields extrapolated from proton–nucleus data. The NA60 In+In measurements have been made at the same energy as Pb+Pb to minimize systematic uncertainties in their comparison. However, to fully interpret the J/ψ production patterns observed in nuclear collisions as a function centrality, it is crucial to have a proper "reference baseline", to extract any "anomalous behaviour" specific to heavy ion collisions. Only with such a "normal nuclear absorption" curve we can look for signatures of quark–gluon plasma formation in the heavy-ion data. However, this reference has so far been based on proton–nucleus data collected at a rather different beam energies, 450 GeV (and a small data sample at 400 GeV). Figure 7.25 summarizes those results.

The NA50 collaboration has also made use of the S+U data set collected by NA38 at 200 GeV. While it is certainly true that the rescaling from 200 to 158 GeV is much more robust than from 450 GeV, this data set has been used making the extra assumption that there is nothing new happening between the proton–nucleus reference and the S+U collision system. We know, however, that the ψ' resonance is considerably suppressed in S+U collisions with respect to its "normal nuclear absorption" pattern, established by exclusively studying proton–nucleus interactions. Therefore, even though this assumption is based on the compatibility of the results obtained from p, O and S induced reactions, it remains nevertheless a questionable assumption which must be verified with a precise measurement. This problem does not prevent us from directly comparing the In and Pb data since both sets were taken at exactly the same energy, 158 GeV. However, the interpretation of the measured pattern in terms of "new physics" requires the comparison to an "expected" pattern, based on a purely conventional "normal nuclear absorption". Presently, this comparison is mostly limited by the accuracy with which we can rescale the measured proton–nucleus points to the energy and kinematical domain of the heavy-ion measurements.

In 2004 the NA60 experiment has collected three days of data to study J/ψ production in proton–nucleus collisions with a high intensity 158 GeV primary proton beam. This data sample will allow us to directly establish a normal nuclear absorption reference based on proton induced interactions, minimizing systematic uncertainties and model-dependent assumptions.

The normal nuclear absorption pattern can be determined by comparing the measured J/ψ production cross-sections (or production yield with respect to high mass Drell–Yan) in proton–nucleus collisions for several target nuclei with a calculation based on the Glauber scattering formalism. It can be approximately expressed as an exponential function of the average length of nuclear matter the produced
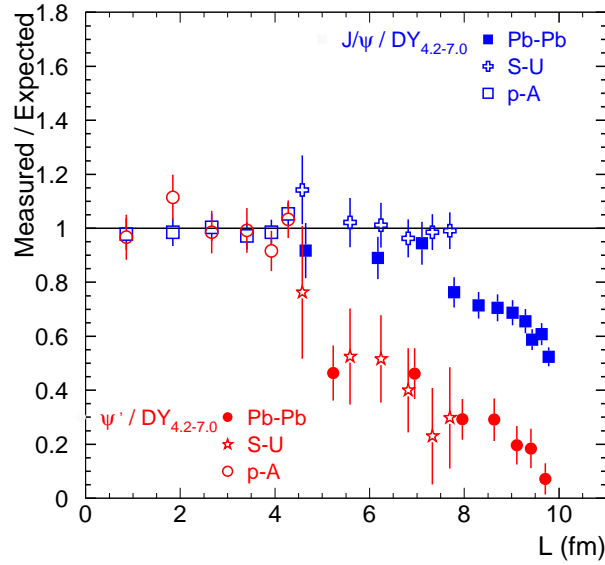
Fig. 7.23: The Measured/Expected ratio for J/ψ and ψ' in pA, S+U and Pb+Pb collisions at the CERN SPS.

charmonium state needs to traverse to get out of the nucleus, $\sigma_{pA}(L) = \sigma_{pp}\exp(-\rho_A L \sigma_{abs})$. This calculation uses the Woods–Saxon nuclear density profiles. We can describe the measured data points by adjusting a normalization coefficient and the absorption cross-section, σ_{abs}, to get the absorption rate.

A priori, it may very well happen that the absorption cross-section depends on the energy of the interactions. In fact, it is well known that the NA50 experiment measured stronger J/ψ absorption than E866, for the same x_F range (close to 0). The main difference is the proton beam energy: 800 GeV in E866 and 450 GeV in NA50. Expressed in terms of the simple A^α parameterization, E866 gives values of α around 0.95 while NA50 gives values closer to 0.92. If the difference is due to the change in energy, we can easily imagine that at 158 GeV, the energy of the In and Pb beams, the value of α would be even smaller, equivalent to having a higher normal nuclear absorption cross-section. Unfortunately, the energy is not the only difference between NA50 and E866 and the change of α is not understood well enough to extrapolate to lower energy. For instance, the J/ψ mesons produced at 800 GeV have, on average, higher values of p_T and the value of α increases with p_T (Cronin effect).

Figure 7.26 shows the ratio between the J/ψ and Drell–Yan (in the mass range $2.9 < M < 4.5$ GeV) production cross-sections, as a function of L, for the proton–nucleus and S+U data, collected either at 450 or 200 GeV. The fit of the 400 and 450 GeV data points leads to $\sigma_{abs} = 4.3 \pm 0.5$ mb. On the left-hand side, we show what happens if we impose this σ_{abs} when fitting the 200 GeV data points, leaving the normalization of the curve free. On the right-hand side the 200 GeV data were independently fitted, resulting in $\sigma_{abs} = 6.8 \pm 1.8$ mb. The dotted lines indicate the uncertainty band, including both the errors on σ_{abs} and on the normalization. These values indicate that the absorption cross-section seems to increase when the collision energy decreases, a tendency that would match the 800 GeV data collected by E866.

Besides the possible change of σ_{abs} from 450 to 158 GeV, another very important unknown is the normalization of the absorption curve at 158 GeV, needed to compare the In and Pb data. In principle, the energy dependence of the J/ψ production cross-section should be calculable so that it would be possible to estimate the normalization at 158 GeV from the 450 GeV data. In practice, however, such calculations are not unique and are severely limited by nonperturbative contributions. The accuracy we need can only be obtained from a measurement made at the same energy and in the same experiment that measured the nuclear data.
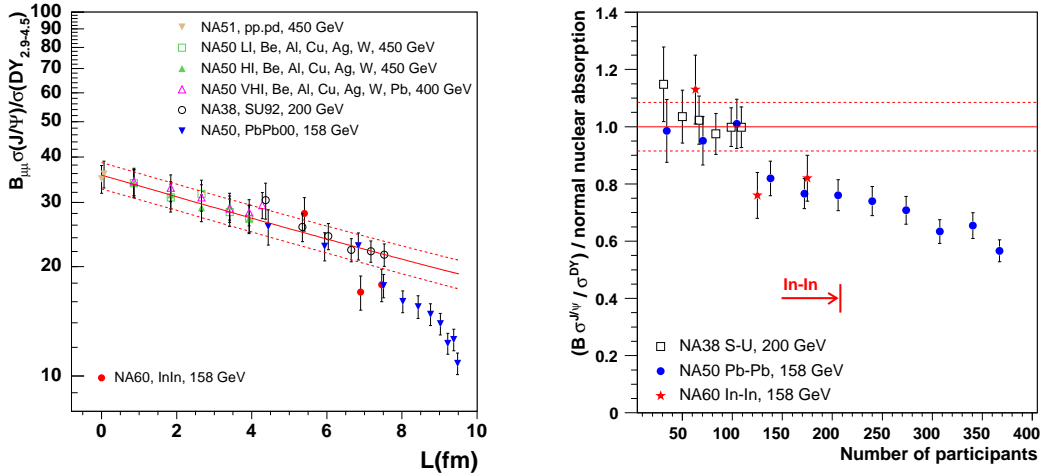
Fig. 7.24: The J/ψ suppression pattern versus L (left) and, after dividing by the normal nuclear absorption curve, versus N_{part} (right), including the NA60 indium–indium measurements.

Even if we assume that σ_{abs} is not energy dependent and use the value determined at 400 and 450 GeV, $\sigma_{\mathrm{abs}} = 4.3 \pm 0.5$ mb, to build the nuclear absorption curve at 158 GeV, we still need to determine its normalization. The NA50 collaboration has taken the normalization value determined at 200 GeV, assuming that the S+U and pA data share the same σ_{abs} value, obtain the normalization at 158 GeV using the so-called "Schuler parameterization". This procedure has the big advantage that the energy difference is very small, thereby reducing the importance of the uncertainties on the energy dependence. However, it has the disadvantage of imposing the extra assumption that the σ_{abs} value is the same in proton–nucleus and S+U collisions (besides ignoring any energy dependence of σ_{abs}). If we accept that the S+U data does not need to be described by the σ_{abs} value derived from the pA data, we must start from the 450 GeV normalization and scale it down to 158 GeV, requiring accurate knowledge of the energy dependence of J/ψ production.

Since we are comparing data expressed as the ratio between the J/ψ and Drell–Yan cross-sections, the energy dependence of the Drell–Yan process also needs to be accurately known in the same phase space window to evaluate the scaling factor needed to normalize the 158 GeV data from 450 GeV. Different parton distribution functions may give somewhat different energy dependences although the calculations are more robust. Unfortunately, the statistics collected in a few days will not allow us to verify the energy dependence of the Drell–Yan production cross-section.

It should be clear by now that it is crucial to measure the J/ψ absolute production cross-section in proton–nucleus collisions at 158 GeV, if we want to fully understand J/ψ suppression. Such measurements started in 2004 but should be repeated in the near future, with much higher statistics, to ensure a proper baseline for ψ' and Drell–Yan production in heavy-ion collisions. We conclude by summarizing the issue:

– The 450 GeV data points alone are not enough to determine the normal nuclear absorption at 158 GeV since the energy rescaling factors are too uncertain.

– The existing 200 GeV data points are also not enough because of their poor precision.

– The 450 and 200 GeV data sets, used together, would solve the problem if the absorption cross-section is the same for the two sets, an assumption presently without solid experimental evidence.

Thus proton data at 158 GeV must be collected in order to establish a robust reference baseline with respect to which the In+In and Pb+Pb J/ψ suppression patterns can be directly compared to place the existence of "anomalous" effects in the heavy-ion data on more solid ground. The present systematic
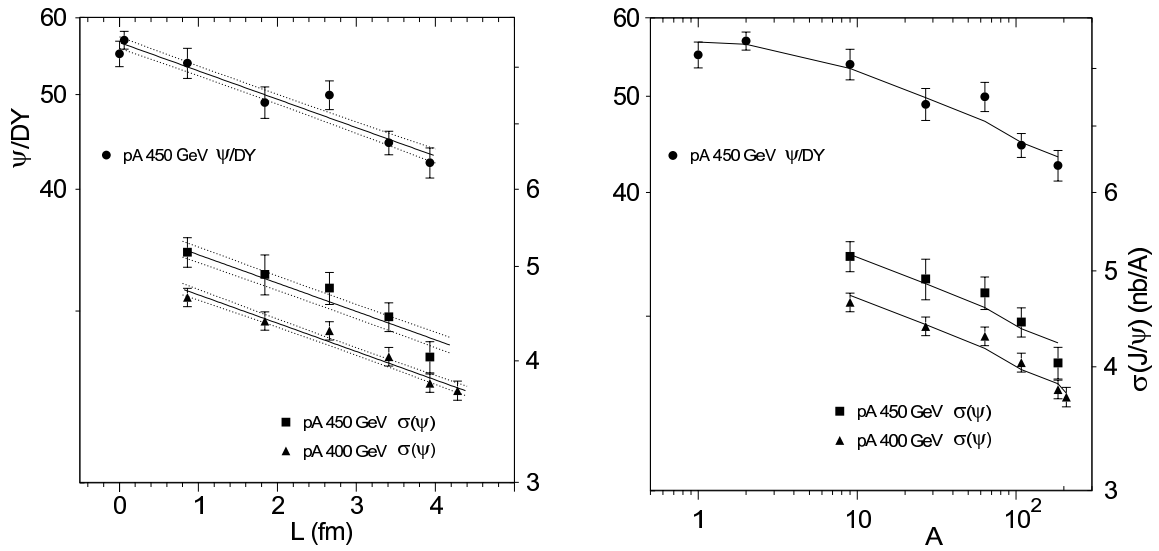
Fig. 7.25: The J/ψ production cross-sections in pA collisions at 400 and 450 GeV times the branching ratio to dimuons, in the phase space window of the measurements (right axis), or with respect to the yield of Drell–Yan dimuons in the mass range $2.9 < M < 4.5$ GeV (left axis). The data are plotted as a function of L (left-hand side) and of the mass number of the nuclei (right-hand side). The lines represent a fit in the framework of the Glauber nuclear absorption model, and result in a common absorption cross-section $\sigma_{\mathrm{abs}} = 4.3 \pm 0.3$ mb. The uncertainties on the result of the fit are represented by the dotted lines on the left-hand side.
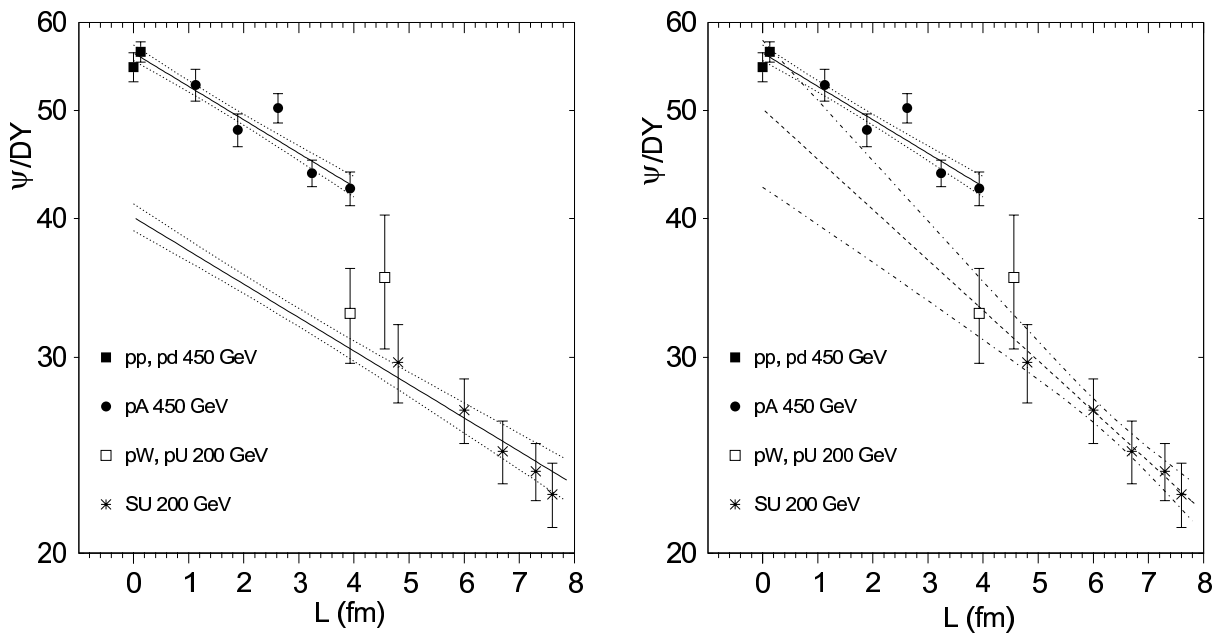
Fig. 7.26: Ratio of the J/ψ and Drell–Yan yields measured in pA and S+U collisions, as a function of L.

errors due to the energy (and phase space) corrections and to the absence of solid evidence that the absorption cross-section remains the same from 450 to 158 GeV, are the main sources of uncertainty in the interpretation of the data collected in nuclear collisions.

8.4 Charmonium production at RHIC

We review here the first results on charmonia produced in nuclear collisions at the Relativistic Heavy Ion Collider (RHIC). PHENIX is specifically designed to make use of high luminosity ion–ion, proton–ion, and proton–proton collisions at the RHIC to sample rare physics probes including the J/ψ and other heavy quarkonium states. The PHENIX experiment reported on J/ψ production in p–p, d–Au and Au–Au reactions at $\sqrt{s_{NN}} = 200$ GeV [128–130].

The PHENIX experiment is able to measure J/ψ's through their dilepton decay in four spectrometers: two central arms covering the mid-rapidity region of $|\eta| < 0.35$ and twice $\pi/2$ in azimuth and two forward muon arms covering the full azimuth and $1.2 < |\eta| < 2.4$ in pseudorapidity. The central spectrometers are comprised, from the inner radius outward, of a Multiplicity and Vertex Detector (MVD), Drift Chambers (DC), Pixel Pad Chambers (PC), Ring Imaging Cerenkov Counters (RICH), a Time-of-Flight Scintillator Wall (TOF), Time Expansion Chambers (TEC), and two types of Electromagnetic Calorimeters (EMC). This combination of detectors allows for the clean electron identification over a broad range of transverse momentum. Each forward spectrometer consists of a precision muon tracker (MuTr) comprised of three stations of cathode-strip readout chambers followed by a muon identifier (MuID) comprised of multiple layers of steel absorbers instrumented with low resolution planar drift tubes. Muons at the vertex must have a mean energy of at least 1.9 GeV to reach the MuID system. Further details of the detector design and performance are given in Ref. [131].

The data were recorded during the 2001/2002 and 2003 runs at $\sqrt{s} = 200$ GeV with 150 nb^{-1} and 350 nb^{-1} p–p collisions. Event samples were selected using online triggers and offline reconstruction criteria as described in Ref. [128]. Unlike-sign pairs and, for background estimation, like-sign pairs were combined to form invariant mass spectra. In Fig. 7.27, unlike-sign and like-sign invariant mass spectra from the entire Run2 pp data set are shown together. For electrons, the net yield in the mass region 2.8–3.4 GeV is 46, for muons in the range 2.71–3.67 GeV is 65.

The J/ψ cross-sections were determined from the measured yields using

$$B_{ll} \frac{d^2 \sigma_{J/\psi}}{dy \, dp_T} = \frac{N_{J/\psi}}{(\int \mathcal{L} dt) \, \Delta y \, \Delta p_T} \frac{1}{A \, \epsilon} \tag{7.51}$$

where $N_{J/\psi}$ is the measured J/ψ yield, $\int \mathcal{L} dt$ is the integrated luminosity, B_{ll} is the branching fraction for the J/ψ to either $e^+ e^-$ or $\mu^+ \mu^-$ pairs (PDG average value 5.9% [132]), and $A \, \epsilon$ is the acceptance times efficiency for detecting a J/ψ. The J/ψ rapidity distribution obtained by combining the dielectron and dimuon measurements is shown in Fig. 7.28 with the muon arm data divided into two rapidity bins. A fit to a shape generated with PYTHIA using the GRV94HO parton distribution functions is performed and gives a total cross-section, multiplied by the dilepton branching ratio, equal to:

$$\mathrm{BR} \times \sigma_{pp}^{J/\psi} = 159 \text{ nb} \pm 8.5\% \, (\text{fit}) \pm 12.3\% \, (\text{abs}) \tag{7.52}$$

where the first uncertainty comes from the fit and thus includes both the statistical and point-to-point systematics. The second uncertainty accounts for normalization systematic errors.

Preliminary analysis is now available of the data recorded during the 2003 run at $\sqrt{s} = 200$ GeV with 2.74 nb^{-1} d–Au collisions. In d–Au collisions, PHENIX is able to measure J/ψ production at forward, backward and central rapidity probing moderate to low x regions of the Au nucleus. The covered rapidity region spans the expected shadowing, antishadowing and no shadowing regions. The ratio between the J/ψ yields observed in d–Au and p–p collisions divided by 2×197 is shown in Fig. 7.29. Solid error bars represent statistical and point to point systematic uncertainties. The dashed
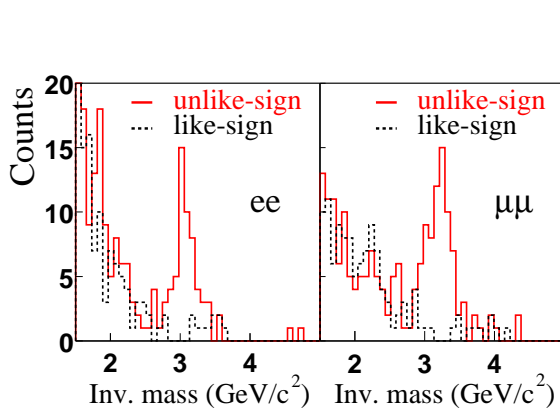
Fig. 7.27: The invariant mass spectra for dielectron and dimuon pairs in the Run 2 data sample. Unlike-sign pairs are shown as solid lines, like-sign pairs as dashed lines.
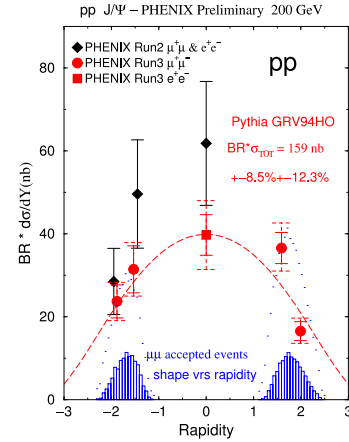

Fig. 7.28: J/ψ differential cross-section, multiplied by the dilepton branching ratio, versus rapidity as measured by the central and muon spectrometers.
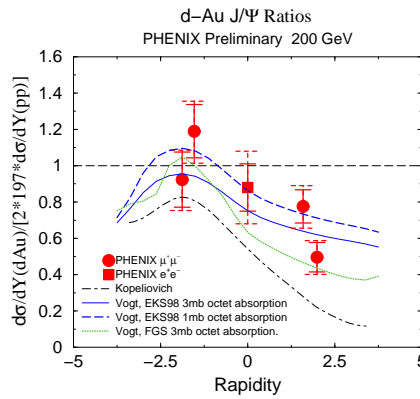

Fig. 7.29: Ratio between d–Au and p–p J/ψ differential cross-sections, divided by 2×197, versus rapidity.

error bars stand for the systematic uncertainties common to one spectrometer. An additional 13.4% global error bar is not displayed.

While this ratio is close to unity at backward rapidity, it is significantly lower at forward rapidity, where parton distributions are expected to be shadowed in a heavy nucleus. Theoretical predictions [133, 134] are displayed on the figure for comparison. The shape is consistent with shadowing at low x and less shadowing at larger x. Unfortunately, the statistical and systematic error bars make it difficult to distinguish among various shadowing models and models with various amounts of nuclear absorption.

The Au–Au data at $\sqrt{s_{NN}} = 200$ GeV used in this analysis were recorded during Run 2 at RHIC in the fall of 2001. For three exclusive centrality bins, 0–20%, 20–40%, and 40–90% of the total Au–Au cross-section, we determined the branching fraction of $J/\psi \to e^+e^-$ (B=5.93 $\pm$ 0.10 $\times 10^{-2}$ [132]) times the invariant yield at mid-rapidity $dN/dy|_{y=0}$.

In Fig. 7.30 we show the results from the three Au–Au centrality bins and the proton–proton data normalized per binary nucleon–nucleon collision as a function of the number of participating nucleons. Note that for proton–proton reactions, there are two participating nucleons and one binary collision. Despite the limited statistical significance of these first J/ψ results, we can address some important physics questions raised by the numerous theoretical frameworks in which J/ψ rates are calculated. The binary scaling expectations are also shown as a gray band. We also show a calculation of the suppression

expected from "normal" nuclear absorption using a $\sigma_{\text{abs}} = 4.4$ mb [123] and 7.1 mb [94]. We show the NA50 suppression pattern relative to binary scaling [119, 120], normalized to match our proton–proton data point at 200 GeV. The data disfavor binary scaling while they are consistent with "normal" nuclear absorption alone and also the NA50 suppression pattern measured at lower energies, within the large statistical errors.

One model calculation [104, 105] including just the "normal" nuclear and plasma absorption components at RHIC energies is shown in Fig. 7.31. The higher temperature (T) and longer time duration of the system at RHIC lead to a predicted larger suppression of J/ψ relative to binary collision scaling.

Many recent theoretical calculations also include the possibility for additional late stage re-creation or coalescence of J/ψ states. In Ref. [104,105], both break-up and creation reactions $D + \overline{D} \leftrightarrow J/\psi + X$ are included. At the lower fixed target CERN energies, this represents a very small contribution due to the small charm production cross-section. However, at RHIC energies, where in central Au–Au collisions around 10 $c\bar{c}$ pairs are produced, the contribution is significant.

The sum of the initial production, absorption, and re-creation is shown in Fig. 7.31.

A different calculation [135] assumes the formation of a quark–gluon plasma in which the mobility of heavy quarks in the deconfined region leads to increased $c\bar{c}$ coalescence. This leads to a very large enhancement of J/ψ production at RHIC energies for the most central reactions. The model considers the plasma temperature (T) and the rapidity width (Δy) of charm quark production as input parameters. Shown in Fig. 7.31 are the calculation results for $T = 400$ MeV and $\Delta y = 1, 2, 3$, and 4. The narrower the rapidity window in which all charm quarks reside, the larger the probability for J/ψ formation. All of these parameters within this model predict a J/ψ enhancement relative to binary collisions scaling, disfavored by our data.

Another framework for determining quarkonia yields is to assume a statistical distribution of charm quarks that may then form quarkonia. A calculation assuming thermal, but not chemical equilibration [99], is shown in Fig. 7.31.

Significantly larger data sets are required to address the various models that are still consistent with our first measurement. Key tests will be the p_T and x_F dependence of the J/ψ yield, and how these compare with other quarkonium states such as the ψ'.

9 QUARKONIUM PRODUCTION IN NUCLEAR COLLISIONS[10]

Quarkonium may be produced via photoproduction at hadron colliders. The electromagnetic field of a proton or ion projectile acts as a field of virtual photons. These photons may collide with an oncoming target nucleus to produce quarkonium. The photon flux is high enough to allow detailed studies of charmonium photoproduction. The cross-section is sensitive to the gluon content of the target. Photoproduction at the LHC reaches an order of magnitude higher energies than are possible at HERA. For ions, the advance beyond existing data is even larger which may allow the first real low-x measurements of gluon shadowing.

Photoproduction has traditionally been studied with fixed target photon beams and at electron–proton colliders. However, energetic hadrons also have significant electromagnetic fields and high energy pp, $\overline{p}p$ and AA colliders can be used to study photoproduction at photon energies higher than those currently accessible. These photoproduction reactions are of interest as a way to measure the gluon distribution in protons at low Feynman x. The Fermilab Tevatron, RHIC and the LHC (with both proton and ion beams) all produce significant quantities of heavy quarkonium. Indeed, J/ψ photoproduction may have already been seen by the CDF collaboration.

One unique aspect of photoproduction at hadron colliders is that the initial system is symmetric so that photoproduction can occur from either ion. Since these two possibilities are indistinguishable,
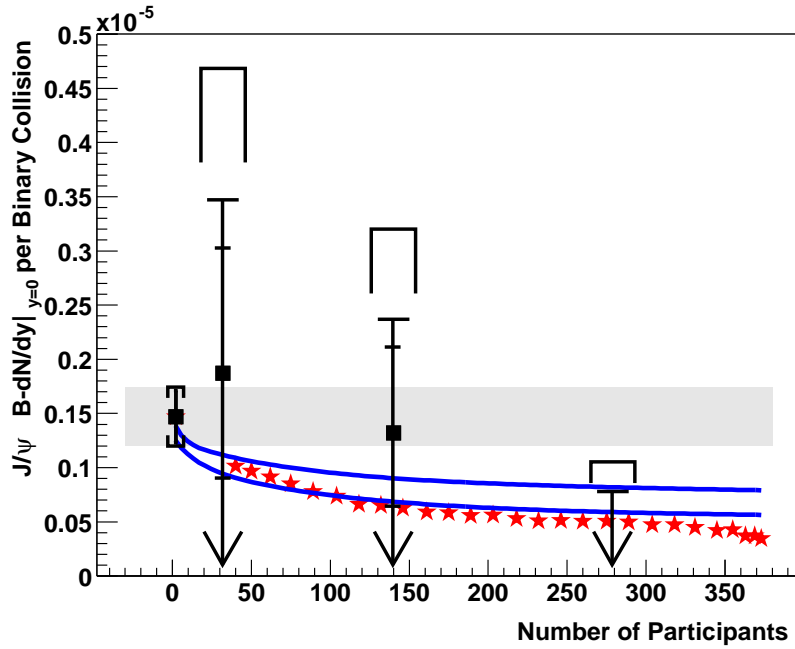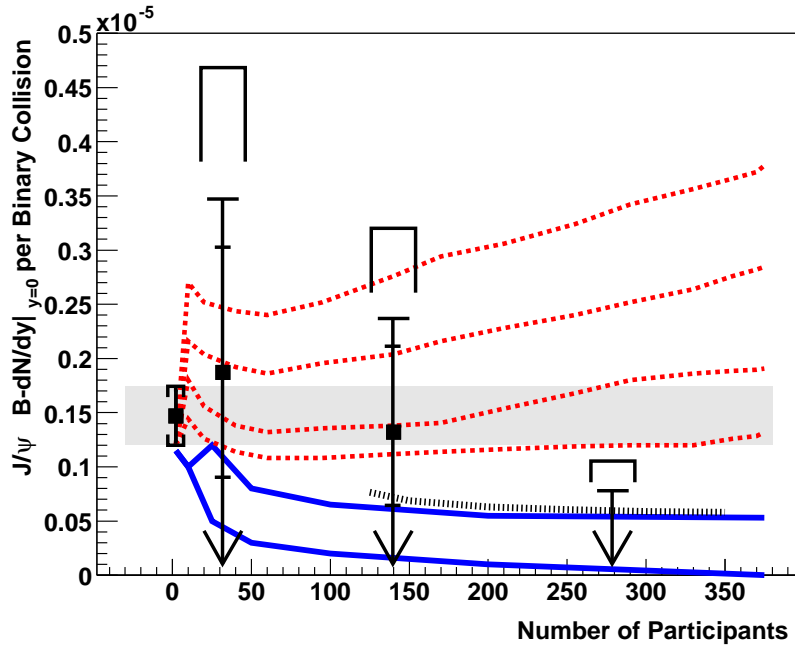
---

[10]Author: S. R. Klein

Fig. 7.30: The J/ψ yield per binary collision is shown from proton–proton reactions and three exclusive centrality ranges of Au–Au reactions all at $\sqrt{s_{NN}} = 200$ GeV. The solid line is the theoretical expectation from "normal" nuclear absorption with $\sigma_{c\bar{c}-N} = 4.4$ mb (upper curve) and 7.1 mb (lower curve) cross-section. The stars are the J/ψ per binary collision measured by the NA50 experiment at lower collision energy. In order to compare the shapes of the distribution, we have normalized the NA50 data to match the central value for our proton–proton results.

Fig. 7.31: The J/ψ yield per binary collision is shown from proton–proton reactions and three exclusive centrality ranges of Au–Au reactions all at $\sqrt{s_{NN}} = 200$ GeV. The lowest curve is a calculation including "normal" nuclear absorption in addition to substantial absorption in a high temperature quark–gluon plasma [104, 105]. The curve above this is including backward reactions that recreate J/ψ. The statistical model [99] result is shown as a dotted curve for mid-central to central collisions just above that. The four highest dashed curves are from the plasma coalescence model [135] for a temperature parameter of $T = 400$ MeV and different charm rapidity widths.

the amplitudes must be added. This interference significantly affects the p_T spectrum of the produced quarkonium. The relative sign of the two amplitudes depends on the symmetry of the system. The symmetry is different for $p\bar{p}$ than pp and AA colliders, leading to significantly different p_T spectra for particle–particle and particle–antiparticle colliders.

9.1 Cross-section calculation

The cross-section for vector meson production is the convolution of the photon flux dn/dk for photon energy k with the photon–proton or photon–nucleus cross-sections $\sigma_{\gamma A}$ [136, 137]:

$$\sigma(A + A \rightarrow A + A + V) = 2 \int_0^\infty \frac{dn}{dk} \sigma_{\gamma A}(k) \, dk \ . \tag{7.53}$$

Here, A refers to any ion, including protons. The '2' is because either nucleus can emit the photon or be the target. Interference between the two possibilities alters the p_T distribution but does not significantly affect the total cross-section.

The rapidity, y, of a produced state with mass M_V is related to the photon energy through $y = \ln(2k/M_V)$. Using this relation in Eq. (7.53) and differentiating gives

$$\frac{d\sigma}{dy} = k \frac{dn}{dk} \sigma_{\gamma A \rightarrow VA}(k) \ . \tag{7.54}$$

At mid-rapidity, $y = 0$, the photon energies for the two possibilities (as to which nucleus emitted the photon) are equal. However, away from mid-rapidity, the photon energies are different,

$$k_{1,2} = \frac{M_V}{2} \exp(\pm y) \tag{7.55}$$

so that the amplitudes for the two possibilities are also different.

We now consider the ingredients in the cross-section in turn. The photon flux from a relativistic hadron is given by the Weizsäcker–Williams formalism. One important detail is the form factor of the emitter.

For protons, the form factor was considered by Drees and Zeppenfield. They use a dipole form factor $F(Q^2) = 1/(1 + Q^2/(0.71 \, \text{GeV}^2))^2$ for the proton, and found [138]:

$$\frac{dn}{dk} = \frac{\alpha}{2\pi k} \left[1 + (1 - z)^2 \right] \left(\ln I - \frac{11}{6} + \frac{3}{I} - \frac{3}{2I^2} + \frac{1}{3I^3} \right) \tag{7.56}$$

where $z = W_{\gamma p}^2/s$, $A = 1 + (0.71 \, \text{GeV}^2)/Q_{\min}^2$ and $Q_{\min}^2 \approx (k/\gamma)^2$. Here, $W_{\gamma p}$ is the γp centre of mass energy, and $\sqrt{s}$ is the proton–proton centre of mass energy. This photon spectrum is similar to that of a point charge with a minimum impact parameter of $b_{\min} = 0.7$ fm.

Drees and Zeppenfeld neglected the magnetic form factor of the proton which is important only at very high energies [139]. They also required that the proton remain intact. If the proton is allowed to be excited, the effective flux increases considerably [140]. However, in this case, one or both protons dissociate, producing hadronic debris. We will ignore this possibility here since the debris considerably complicates event selection.

For ion–ion collisions, the cutoff conditions are somewhat different. For a vector meson to be observable, the two nuclei must miss each other, with $b_{\min} = 2R_A$, where R_A is the nuclear radius. The effective photon flux from a charge Z nucleus is the flux striking an incoming nucleus subject to that constraint. This is within 15% of the flux integrated over the requirement $r > 2R_A$, given analytically by [141]

$$\frac{dn}{dk} = \frac{2Z^2\alpha}{\pi k} \left(X K_0(X) K_1(X) - \frac{X^2}{2} \left[K_1^2(X) - K_0^2(X) \right] \right) \tag{7.57}$$

where $X = kr/\gamma\hbar$. More detailed calculations find the photon flux numerically by determing the photon flux from one nucleus that interacts in another, subject to the criteria that the two nuclei do not interact hadronically.

As a check of the photon flux rates, we consider an alternate calculation that replaces the proton form factor with a hard cutoff, $b_{\min} = 1.0$ fm. This stricter requirement slightly decreases the effective photon flux.

The leading-order vector meson photoproduction cross-section for a vector meson with mass M_V is [142]

$$\left.\frac{d\sigma(\gamma p \to V p)}{dt}\right|_{t=0} = \frac{\alpha_s^2 \Gamma_{ee}}{3\alpha M_V^5} 16\pi^3 \left[xg(x, M_V^2/4)\right]^2 . \tag{7.58}$$

More recent and more sophisticated calculations have considered the use of relativistic wave functions, off-diagonal parton distributions, and NLO contributions [143, 144]. Parton–hadron duality has also been used to study quarkonium production. Calculations give cross-sections $\sim$30–50% larger than the pQCD results, depending on $W_{\gamma p}$ [144]. The QCD calculations are in reasonable agreement with data on J/ψ [145] and Υ [146] [147] production at HERA. The Υ data has limited statistics, and, consequently, significant uncertainties.

To assess the viability of photoproduction at hadron colliders, we use simple cross-section parameterizations to estimate the rates:

$$\sigma_{\gamma p}(W_{\gamma p}) = 1.5 W_{\gamma p}^{0.8} \text{ pb} \tag{7.59}$$

for J/ψ, and

$$\sigma_{\gamma p}(W_{\gamma p}) = 0.06 W_{\gamma p}^{1.7} \text{ pb} \tag{7.60}$$

for $\Upsilon(1S)$ where $W_{\gamma p}$ is in GeV. Both H1 and ZEUS estimate that roughly 70% of the signal is from the $\Upsilon(1S)$ state. The cross-section for the ψ' is expected to be about 15% of that for the J/ψ.

One drawback for this parameterization is that there is a significant discontinuity at threshold, $W_{\gamma p} = m_p + m_{J/\Psi}$. In this region, either better data or a more sophisticated calculation is needed.

For heavy mesons, the cross-section $\gamma A \to V A$ is not well measured. There is little data for the J/ψ and none on the Υ. The ion-target cross-sections depends on the square of the gluon density. Thus vector meson photoproduction can provide a sensitive measurement of gluon shadowing. At LHC, mid-rapidity production of the J/ψ and Υ corresponds to $x \approx 5 \times 10^{-4}$ and 1.7×10^{-3} respectively. In this region, shadowing will likely reduce the cross-sections by 30–50% for Pb+Pb collisions at the LHC.

Neglecting shadowing, the cross-section for vector meson photoproduction in a nucleus, $\gamma A \to V A$, may be determined using data on photoproduction off a proton target as input to a Glauber calculaton. However, because the cross-section for a $c\bar{c}$ or $b\bar{b}$ pair to interact in a nucleus is relatively small, multiple interactions are unlikely and the calculation simplifies so that the forward scattering cross-section scales with A^2 [137, 148]

$$\left.\frac{d\sigma(\gamma A \to \Upsilon A)}{dt} = A^2 \frac{d\sigma(\gamma p \to \Upsilon p)}{dt}\right|_{t=0} |F(t)|^2 . \tag{7.61}$$

A Woods–Saxon distribution can be used for the nuclear form factor $F(t)$. The total photonuclear cross-section is the integral of Eq. (7.61) over all momentum transfers, $t > t_{\min} = [M_\Upsilon^2/4k\gamma]^2$. For protons, $d\sigma/dt|_{t=0}$ is determined from HERA data. For the Υ, an exponential t-dependence is assumed with the same slope, 4 GeV^{-2}, as for J/ψ production, leading to a forward scattering amplitude about 5% lower than if the proton form factor had been used. With these ingredients, the ion–ion photoproduction cross-section may be calculated from Eq. (7.53).

This A^2 scaling applies for coherent production with $p_T < \hbar/R_A$. At significantly larger p_T, the scattering is incoherent and the cross-section should scale as A. The coherence leads to a large peak in the production at small p_T, providing a clean experimental signature which greatly simplifies the data analysis.

Table 7.3: Cross-sections and rates for production of the J/ψ and the Υ. The rates are for 10^7 s of running at the Tevatron, pp at the LHC and AA at RHIC, and 10^6 s of running with AA at the LHC and pp at RHIC.

Collider	Species	$\sqrt{s_{NN}}$ (GeV)	Luminosity (cm^{-2}s^{-1})	J/ψ		Υ	
				σ (μb)	Rate	σ (nb)	Rate
RHIC	pp	500	10^{31}	0.007	7.0×10^4	0.012	120
RHIC	Au+Au	200	2×10^{26}	290	5.8×10^5	–	–
Tevatron	$p\overline{p}$	1960	2×10^{32}	0.023	4.6×10^7	0.12	2.4×10^5
LHC	pp	14000	10^{34}	0.120	1.2×10^{10}	3.5	3.5×10^8
LHC	Pb+Pb	5500	10^{27}	32000	3.2×10^6	170000	1.7×10^5

For lighter mesons, the interaction cross-section is larger and the Glauber calculation is required to determine the A scaling. The STAR collaboration has studied ρ photoproduction in Au+Au collisions [149] and has found that the cross-sections agree with a calculation based on Eq. (7.53) and a Glauber calculation.

Exclusive J/ψ photoproduction in pp interactions was also considered by Khoze *et al.* [150]. They use a very different approach, based on the proton energy lost.

9.2 Experimental prospects

We consider pp and AA collisions at RHIC, $p\overline{p}$ at the Tevatron, and pp and Pb+Pb the LHC. The cross-sections and rates, as well as the assumed energies and luminosities, are shown in Table 7.3. Since the LHC is primarily a pp collider, assume 10^7 s of pp and 10^6s of AA running per year. Because RHIC is primarily an ion collider, we reverse the two durations. We assume 10^7 s of Tevatron operation per year. Although it is interesting, we do not consider dA collisions at RHIC or pA or dA collisions at the LHC.

Figure 7.32 shows the rapidity distribution for vector meson production in pp and $\overline{p}p$ collisions. The solid histogram is with the dipole form factor discussed above. For the Υ, the shaded bands show the uncertainty in the production rates, based on the uncertainties in the HERA cross-sections but neglecting extrapolation uncertainties. The dashed line is an alternative calculation, with $b_{\min} = 1.0$ fm replacing the form factor. For the J/ψ, the abrupt dropoff at large $|y|$ is due to the discontinuity at threshold.

Figure 7.33 shows the rapidity distribution for Υ production in Si+Si collisions at RHIC (the Υ is below the effective threshold in Au+Au), and Pb+Pb collisions at the LHC. The solid histogram is for the dipole form factor, and the shaded bands show the uncertainty due to the uncertainties in the HERA cross-sections, but neglecting uncertainties due to the extrapolation.

Coherent Υ production at the LHC was also studied by Frankfurt *et al.* [151]. The result (solid curve in Fig. 7.33) is about 10% higher than their result for the impulse approximation (no shadowing). The difference may be due to the slightly different photon spectrum and slope of $d\sigma/dt$ in photon–proton interactions.

At the LHC, the cross-sections are very large for both pp and AA collisions, and obtaining good event samples should be relatively straightforward. For the Υ in pp collisions, production tends to be at large $|y|$. The rapid rise in cross-section, $\sigma \propto W^{1.7}$ outweighs the $dn/dk \propto 1/k$ photon spectrum. For the J/ψ, the $W_{\gamma p}$ dependence is smaller and nearly 'cancels' the photon spectrum, leading to a rather flat $d\sigma/dy$. In both cases, it should be easy to obtain good statistics, even with only a central detector.

At the Tevatron, the cross-sections are smaller. However, the CDF collaboration has already observed an apparent exclusive J/ψ signal which appears consistent with photoproduction [152]. With an appropriate trigger and more data, the Υ should be within reach.

Very roughly, the photoproduction cross-section is about 1/1000 of the equivalent hadroproduction cross-sections [153] with moderate variation depending on species and beam energy. Despite the small
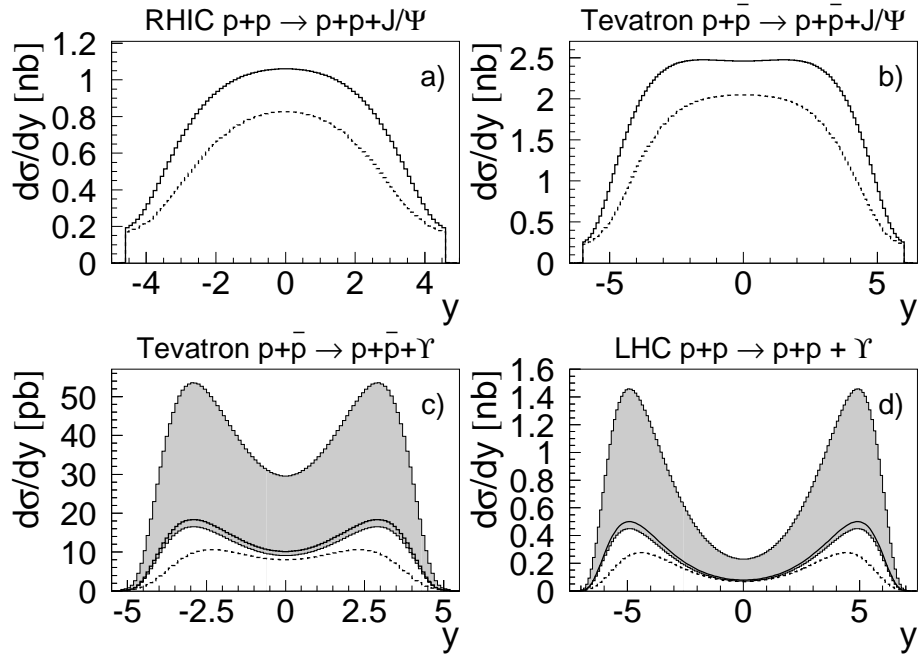
Fig. 7.32: Rapidity distributions for photoproduction of J/ψ and $\Upsilon(1S)$ mesons in pp and $p\overline{p}$ interactions at RHIC, the Tevatron, and the LHC [136]. The curves are explained in the text.

fraction, because of the very different event characteristics, clean separation of photoproduction seems possible.

Hadronically produced vector mesons have $p_T \sim M_V$. In contrast, almost all photoproduced mesons have $p_T < 1$ GeV (cf. Fig. 7.34). Such a cut eliminates about 94% of the hadroproduced Υ at the Tevatron [154] while retaining almost all of the photoproduction.

As long as both protons remain intact, the vector meson will not be accompanied by any other particles in the same event. In contrast, in hadronic events, additional particles are distributed over the available phase space. A moderate requirement for two rapidity gaps around the vector meson should remove most of the remaining hadronic background [153], even at RHIC energies. The Fermilab results on exclusive J/ψ production appear to bear this out.

For heavy-ion collisions, the situation is even simpler since most of the coherent vector meson production is at $p_T < 100$ MeV/c. In addition, the ions can be required to remain intact and/or rapidity gaps can be required. These techniques were effective in isolating the ρ^0 in STAR [149]. In 2004, the RHIC experiments collected a large data sample of Au+Au collisions at $\sqrt{s_{NN}} = 200$ GeV. Thus large experiments should be able to observe J/ψ photoproduction and measure gluon shadowing in the region $x \approx 0.015$.

9.3   Interference and the p_T spectrum

Photoproduction in pp and $p\overline{p}$ collisions differs from production in ep or eA collisions in that either projectile can act as photon source or target. For small meson p_T, the two possibilities are indistinguishable so that the amplitudes add [155]. The vector meson production is well localized to in or near (within 1 fm of) the two sources, giving a cross-section of

$$\sigma = \left| A_1(y) \mp A_2(y) \exp i(\vec{p}_T \cdot \vec{b}) \right|^2 \tag{7.62}$$

where $A_1(y)$ and $A_2(y)$ are the amplitudes for photoproduction at the two sources and the propagator, $\exp i(\vec{p}_T \cdot \vec{b})$, accounts for the ion–ion separation. The relative sign of the two amplitudes depends
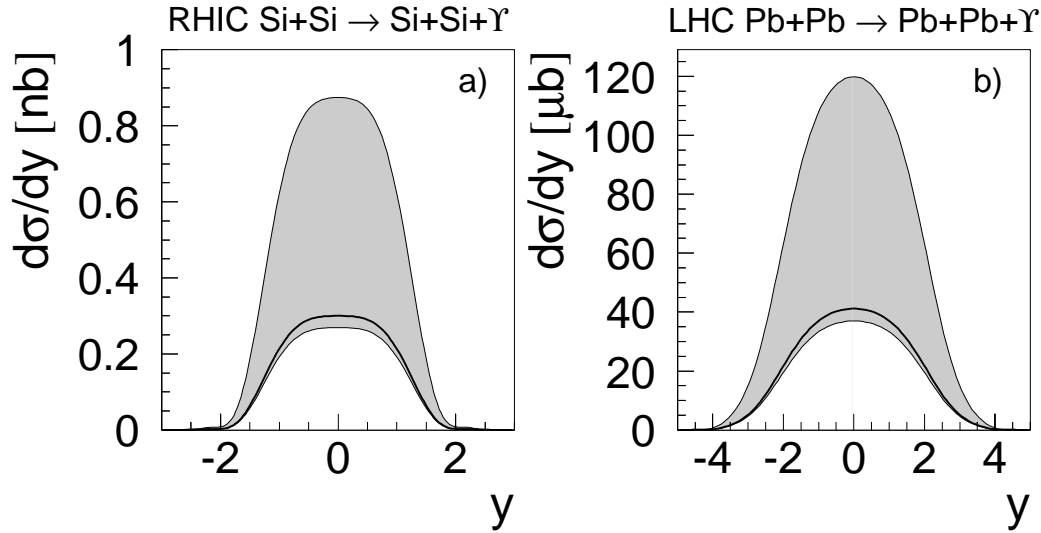
Fig. 7.33: Rapidity distributions of Υ mesons produced in coherent photonuclear interactions at RHIC and the LHC [136]. The solid curves correspond to the parameterization $\sigma_{\gamma p}(W_{\gamma p}) = 0.06 W_{\gamma p}^{1.7}$ (pb) and the grey bands show the uncertainty in $\sigma_{\gamma p}$

on the symmetry of the system. For pp and AA collisions, transforming from nucleus 1 emitting a photon which interacts with nucleus 2, to nucleus 2 emitting a photon which interacts with nucleus 1 is a parity transformation. Vector mesons are negative parity, so the sign is negative. For $p\overline{p}$ collisions, the transformation is CP, positive for vector mesons, giving a positive sign.

At mid-rapidity, $A_1 = A_2$ and

$$\sigma = \sigma_0 \left(1 \mp \cos\left(\vec{p}_T \cdot \vec{b} \right) \right) \tag{7.63}$$

where σ_0 is the cross-section without interference. The interference depends on the unknown impact parameter which must be integrated over.

Without interference, the p_T spectrum is that for production off a single (anti)proton. This spectrum is the convolution of the photon transverse momentum spectrum with the spectrum of transverse momentum transfers from the target [155]. For $p_T > \hbar/\langle b \rangle$, $\cos(\vec{p}_T \cdot \vec{b})$ oscillates rapidly as b varies, giving a zero net contribution to the integral. For small transverse momenta, however, $\vec{p} \cdot \vec{b} < \hbar$ for all relevant impact parameters and interference alters the spectrum. This alteration has been observed in ρ^0 production at RHIC [156].

Figure 7.34 compares $d^2\sigma/dydt$ with and without interference at RHIC and the Tevatron. Figure 7.34 includes a $b_{min} = 1.0$ fm cut which has a small effect on the spectrum. The interference is large for $t < 0.05$ GeV$^2/c^2$. The different sign of the interference in pp and $p\overline{p}$ is clearly visible.

Photoproduction of other final states should also be accessible at existing and future $p\overline{p}$ and pp colliders. Open charm, bottom and even top quark production should be accessible [157] in ion–ion and deuterium–ion collisions and could be used to measure the charge of the top quark as well as determine the nuclear gluon distributions. These events would have only a single rapidity gap but the experimental techniques should be similar. Because of the large rates, at least for ion–ion collisions, the signal to noise ratios should be high.

To summarize, we have calculated the heavy vector meson photoproduction cross-sections in pp and $p\overline{p}$ collisions. The cross-sections are large enough for this reaction channel to be observed experimentally. The $d\sigma/dt$ distribution is distinctly different in pp and $p\overline{p}$ collisions because of the interference between the production sources. The cross-section for producing Υ mesons in coherent photonuclear
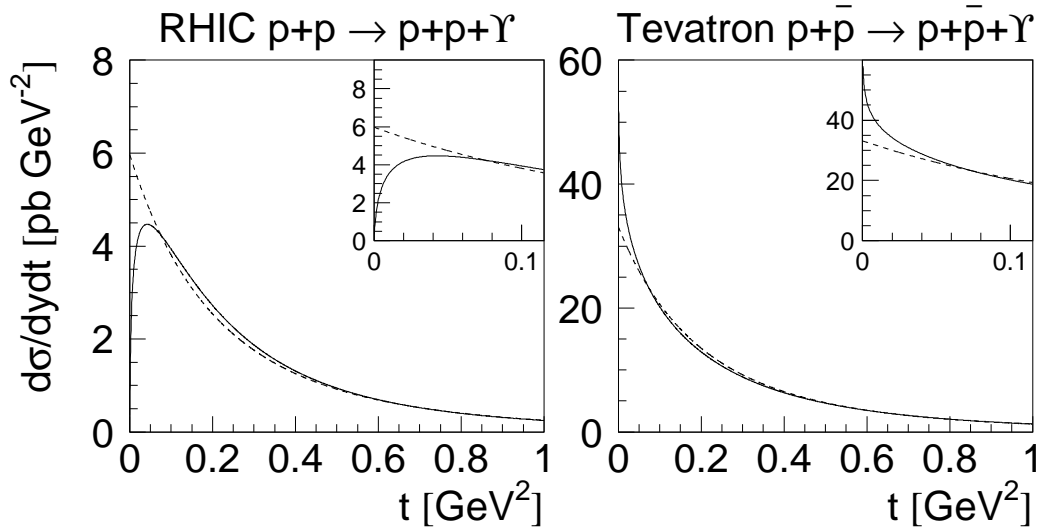
Fig. 7.34: The $\Upsilon(1S)$ photoproduction cross-section, $d\sigma/dydt$, at mid-rapidity in pp and $p\bar{p}$ collisions at RHIC and the Tevatron [136]. The inset has an expanded t scale.

Pb+Pb interactions at the LHC is large. Because of the distinctive experimental signature, these reactions should be easy to detect.

10 OUTLOOK[11]

Recent advances in lattice and analytical calculations described in this Chapter have significantly improved the theoretical understanding of heavy quarkonium dynamics in hot QCD matter. In fact, since many of the recent results came as a surprise, they still need to be analyzed, improved upon, and clarified.

The list of open issues which can be addressed by theory and experiment in the near future includes:

– Lattice QCD at finite temperature:
   What is the critical temperature at which different quarkonium states dissociate? What is the influence of temperature on the masses, dispersion relations, and widths of quarkonia? How big is the influence of light quarks? What are the properties of strongly interacting matter in the vicinity of the deconfining transition and how do they compare with phenomenological models?
– Lattice QCD at zero temperature:
   What are the matrix elements of different gluon and quark operators of various dimension which are related to quarkonium dissociation?
– Analytic theoretical calculations at zero temperature:
   Analyze the expressions for quarkonium dissociation amplitudes, and relate them to the matrix elements which can be computed on the lattice. Apply and test theoretical approaches developed for the studies of quarkonium dissociation to exclusive quarkonium decays and quarkonium production; understand the range of validity of various approaches.
– Analytic theoretical calculations at finite temperature:
   Understand the properties of Quark–Gluon Plasma in the vicinity of the deconfinement phase transition; identify the dynamical degrees of freedom and apply this knowledge to understanding the lattice results at finite T. Try to develop a quantitative theory of quarkonium interactions with hot QCD matter.

– Experiment:
Collect data on the nuclear dependence of the production of different quarkonium states, including the χ family, in pA collisions in a broad range of x_F (rapidity), and different energies. Refine the data on quarkonium suppression in nucleus–nucleus collisions at SPS energy; improve statistics on quarkonium suppression in Au+Au (and some other, lighter, AA system) collisions at RHIC; prepare for the LHC. Measure photoproduction cross-sections to determine the nuclear gluon density.

To summarize, impressive progress in the physics of quarkonium interactions with QCD media has been made in recent years. It has already become clear that the physics of heavy quark bound states in QCD media is a rich and promising field of theoretical and experimental studies. Nevertheless, even a brief examination of the list above shows that a lot more has to be done before one can claim an understanding of quarkonium interactions in media.

REFERENCES

[1] T. Matsui and H. Satz, Phys. Lett. B **178** (1986) 416.

[2] D. Kharzeev and H. Satz, Phys. Lett. B **334** (1994) 155

[3] D. Kharzeev and H. Satz, arXiv:hep-ph/9505345.

[4] X. M. Xu, D. Kharzeev, H. Satz and X. N. Wang, Phys. Rev. C **53** (1996) 3051

[5] E. V. Shuryak, Phys. Lett. B **78** (1978) 150

[6] G. Bhanot and M. E. Peskin, Nucl. Phys. B **156** (1979) 391.

[7] D. Kharzeev, L. D. McLerran and H. Satz, Phys. Lett. B **356** (1995) 349

[8] C. Y. Wong, Phys. Rev. C **65** (2002) 034902

[9] D. Kharzeev, Nucl. Phys. A **610** (1996) 418c

[10] S. Digal, P. Petreczky and H. Satz, Phys. Rev. D **64**, 094015 (2001)

[11] G. Röpke, D. Blaschke and H. Schulz, Phys. Rev. D **38** (1988) 3589.

[12] F. Karsch, M. T. Mehr and H. Satz, Z. Phys. C **37** (1988) 617.

[13] T. Hashimoto, K. Hirose, T. Kanki and O. Miyamura, Z. Phys. C **38** (1988) 251.

[14] T. Umeda, K. Nomura and H. Matsufuru, arXiv:hep-lat/0211003.

[15] S. Datta, F. Karsch, P. Petreczky and I. Wetzorke, arXiv:hep-lat/0208012.

[16] S. Digal, S. Fortunato, P. Petreczky and H. Satz, Phys Lett. B **549**, 101 (2002); J. P. Blaizot, M. Dinh and J. Y. Ollitrault, Phys. Rev. Lett. **85**, 4012 (2000).

[17] M. Bedjidian *et al.*, in *Hard Probes in Heavy Ion Collisions at the LHC*, CERN-2004-009, p. 247.

[18] F. Karsch and E. Laermann, in Hwa, R.C. (ed.) *et al.*:*Quark gluon plasma* pag. 1, arXiv:hep-lat/0305025

[19] M. A. Stephanov, Prog. Theor. Phys. Suppl. **153** (2004) 139

[20] J. Kapusta, *Finite Temperature Field Theory*, Cambridge University Press, 1994.

[21] F. Karsch, Lect. Notes Phys. **583**, 209 (2002) [arXiv:hep-lat/0106019].

[22] For pedagogical presentation in QED see Landau and Lifshitz, *Quantum Electrodynamics*; for QCD see e.g., W. Lucha, F. F. Schoberl and D. Gromes, Phys. Rept. **200** (1991) 127.

[23] L. McLerran, B. Svetitsky, Phys. Rev D **24** (1981) 450

[24] J. Brown, E. Weisberger, Phys. Rev. D **20** (1979) 3239

[25] S. Nadkarni, Phys. Rev. D **34** (86) 3904

[26] O. Philipsen, Phys. Lett. B **535** (2002) 138

[27] O. Jahn, O. Philipsen, Phys. Rev. D **70** (2004) 074504

[28] O. Kaczmarek *et al.*, Phys.Lett. B **543** (2002) 41

[29] O. Kaczmarek *et al.*, Nucl.Phys. B (Proc. Suppl.) **129** (2004) 560

[30] O. Kaczmarek *et al.*, Phys. Rev. D **70** (2004) 074505

[31] S. Necco, R. Sommer, Phys. Lett. B **523** (2001) 135

[32] S. Necco, R. Sommer, Nucl. Phys. B **622** (2002) 328

[33] M. Peter, Nucl. Phys. B **501** (1997) 471

[34] Y. Schröder, Phys. Lett. B **447** (1999) 321

[35] M. Le Bellac, *Thermal Field Theory*, Cambridge, 1996

[36] T. Hatsuda and T. Kunihiro, Phys. Rev. Lett. **55**, 158 (1985); Phys. Rept. **247**, 221 (1994).

[37] E. Braaten,, R. D. Pisarski and T. C. Yuan, Phys. Rev. Lett. **64** (1990) 2242.

[38] F. Karsch, E. Laermann, P. Petreczky and S. Stickan, Phys. Rev. D **68**, 014504 (2003)

[39] S. Datta, F. Karsch, P. Petreczky and I. Wetzorke, Phys. Rev. D **69** (2004) 094507

[40] M. Asakawa and T. Hatsuda, Phys. Rev. Lett. **92** (2004) 012001

[41] T. Umeda et al, Eur. Phys. J. C **39S1** (2005) 9.

[42] M. Asakawa, T. Hatsuda and Y. Nakahara, Prog. Part. Nucl. Phys. **46** (2001) 459

[43] M. Jarrel and J.E. Gubernatis, Phys. Rep. **269**, 133 (1996).

[44] T. Yamazaki et al (CP-PACS), Phys. Rev. D **65**, 014501 (2002).

[45] R. K. Bryan, Eur. Biophys. J. **18**, 165 (1990)

[46] Talks by M. Asakawa, S. Datta and H. Matsufuru in the RIKEN BNL workshop on "Lattice QCD ar Finite Temperature and Density", Feb 8-12, 2004; see proceedings.

[47] T. Umeda *etal*., Int. J. Mod. Phys. A **16**, 2215 (2001).

[48] M. Oevers, C. Davies and J. Shigemitsu, Nucl. Phys. Proc. Suppl. **94** (2001) 423

[49] B. Alessandro *et al.* (NA50 Coll.), Nucl. Phys. **A715**, 679c (2003).

[50] M.C. Abreu *et al.* (NA50 Collaboration), Phys. Lett. B 450 (1999) 456.

[51] J.W. Chen and M.J. Savage, Phys. Rev. D **57** (1998) 2837; E. Shuryak and D. Teaney, Phys. Lett. B **430** (1998) 37; K.L. Haglin and C. Gale, Phys. Rev. C **63** (2001) 065201; nucl-th/0002029; C.Y. Wong, E.S Swanson and T. Barnes, nucl-th/0002034; K.L. Haglin, nucl-th/0205049; C.Y. Wong, T. Barnes, E.S. Swanson and H.W. Crater, nucl-th/0112023; S.H. Lee and Y. Oh, J. Phys. G **28** (2002) 1903; R.S. Azevedo and M. Nielsen, nucl-th/0407080; Y. Oh, T. Song, S.H. Lee and C.Y. Wong, J. Korean Phys. Soc. **43** (2003) 1003; Y. Oh, T. Song, S.H. Lee, Phys. Rev. C **63** (2001) 034901.

[52] M. Peskin, Nucl. Phys. B **156** (1979) 365; G. Bhanot and M. Peskin, Nucl. Phys. B **156** (1979) 391; D. Kharzeev and H. Satz, Phys. Lett. B **334** (1994) 155.

[53] D. Kharzeev, H. Satz and G. Zinovjev, Phys. Lett. B **389** (1996) 595; S.H. Lee and Y. Oh, J. Phys. G **28** (2002) 1903; F. Arleo, P.B. Gossiaux, T. Gousset and J. Aichelin, Phys. Rev. D **65** (2002) 014005; Y. Oh, S. Kim and S.H. Lee, Phys. Rev. C **65** (2002) 067901.

[54] K. Martins, D. Blaschke and E. Quack, Phys. Rev. C **51** (1995) 2723.

[55] C.Y. Wong, E.S. Swanson and T. Barnes, Phys. Rev. C **62** (2000) 045201; Phys. Rev. C **65** (2002) 014903, Erratum C **66** (2002) 029901; C.Y. Wong, Phys. Rev. C **65** (2002) 034902; G.R.G. Burau, D.B. Blaschke and Y.L. Kalinovsky, Phys. Lett. B **506** (2001) 297; V.V. Ivanov, Y.L. Kalinovsky, D.B. Blaschke and G.R.G. Burau, hep-ph/0112354.

[56] F.S. Navarra, M. Nielsen, R.S. Marques de Carvalho and G. Krein, Phys. Lett. B **529** (2002) 87; F.O. Duraes, S.H. Lee, F.S. Navarra and M. Nielsen, Phys. Lett. B **564** (2003) 97; F.O. Duraes, H. Kim, S.H. Lee, F.S. Navarra and M. Nielsen, Phys. Rev. C **68** (2003) 035208.

[57] S.G. Matinyan and B. Müller, Phys. Rev. C **58** (1998) 2994.

[58] K.L. Haglin, Phys. Rev. C **61** (2000) 031902; Z. Lin and C.M Ko, Phys. Rev. C **62** (2000) 034903; Z. Lin and C.M. Ko, Nucl. Phys. A **715** (2003) 533; Y. Oh, T. Song and S.H. Lee, Phys. Rev. C

63 (2001) 034901; H. Kim and S.H. Lee, Eur. Phys. J. C **22** (2002) 707; W. Liu, C.M. Ko and Z. Lin, Phys. Rev. C **65** (2002) 015203; A. Sibirtsev, K. Tsushima and A.W. Thomas, Phys. Rev. **63** (2001) 044906; F.S. Navarra, M. Nielsen and M.R. Robilotta, Phys. Rev. C **64** (2001) 021901; K.L. Haglin and C. Gale, J. Phys. G **30** (2004) S375; R.S. Azevedo and M. Nielsen, Braz. J. Phys. **34** (2004) 272; R.S. Azevedo and M. Nielsen, Phys. Rev. C **69** (2004) 035201; R.S. Azevedo and M. Nielsen, nucl-th/0407080.

[59] F.S. Navarra, M. Nielsen, M.E. Bracco, M. Chiapparini and C.L. Schat, Phys. Lett. B **489** (2000) 319; F.S. Navarra, M. Nielsen, M.E. Bracco, Phys. Rev. D **65** (2002) 037502; R.D. Matheus, F.S. Navarra, M. Nielsen and R. Rodrigues da Silva, Phys. Lett. B **541** (2002) 265; M.E. Bracco, M. Chiapparini, A. Lozea, F.S. Navarra and M. Nielsen, Phys. Lett. B **521** (2001) 1; R.D. Matheus, F.S. Navarra, M. Nielsen and R. Rodrigues da Silva, hep-ph/0310280.

[60] F.O. Duraes, H. Kim, S.H. Lee, F.S. Navarra and M. Nielsen, Phys. Rev. C **68** (2003) 035208.

[61] T. Barnes, nucl-th/0306031.

[62] L. Maiani, F. Piccinini, A.D. Polosa, V. Riquer, Nucl. Phys. A **741** (2004) 273.

[63] L. Maiani, F. Piccinini, A.D. Polosa, V. Riquer, hep-ph/0408150.

[64] R. Hagedorn, Nuovo Cim. Suppl. **3** (1965) 147.

[65] A. Deandrea, N. Di Bartolomeo, R. Gatto, G. Nardulli and A.D. Polosa, Phys. Rev. D **58**, 034004 (1998); See also A.D. Polosa, "The CQM Model", Riv. Nuovo Cim. Vol. **23**, N. 11 (2000).

[66] D. Ebert, T. Feldmann, R. Friedrich and H. Reinhardt, Nucl. Phys. B **434** (1995) 619; D. Ebert, T. Feldmann and H. Reinhardt, Phys. Lett. B **388** (1996) 154.

[67] A. Deandrea, G. Nardulli and A.D. Polosa, Phys. Rev. D **68** (2003) 034002

[68] A. Manohar and H. Georgi, Nucl. Phys. B **234** (1984) 189.

[69] M.A. Ivanov, J.G. Korner and P. Santorelli, Phys. Rev. D **70** (2004) 014005.

[70] M.A. Ivanov, M.P. Locher and V.E. Lyubovitskij, Few Body Syst. **21** (1996) 131; M.A. Ivanov and V.E. Lyubovitskij, Phys. Lett. B **408** (1997) 435.

[71] M.A. Ivanov and P. Santorelli, Phys. Lett. B **456** (1999) 248; M.A. Ivanov, J.G. Körner and P. Santorelli, Phys. Rev. D **63** (2001) 074010; A. Faessler, T. Gutsche, M.A. Ivanov, J.G. Körner and V.E. Lyubovitskij, Eur. Phys. J. **C4** (2002) 18; A. Faessler, T. Gutsche, M.A. Ivanov, V.E. Lyubovitskij and P. Wang, Phys. Rev. D **68** (2003) 014011.

[72] J. Bjorken, Phys. Rev. D **27** (1983) 140.

[73] http://na50.web.cern.ch/NA50/

[74] G. Borges *et al.* (NA50 Collaboration), J. Phys. G: Nucl. Part. Phys. **30** (2004) S1351.

[75] H. Santos *et al.* (NA50 Collaboration), J. Phys. G: Nucl. Part. Phys. **30** (2004) S1175.

[76] J. Letessier and J. Rafelski, "*Hadrons and Quark Gluon Plasma*", Cambridge Monogr. Part. Phys. Nucl. Phys. Cosmol. **18** (2002).

[77] N. Cabibbo and G. Parisi, Phys. Lett. **59B** (1975) 67.

[78] J.J. Aubert *et al.*, Nucl. Phys. B **293** (1987) 740; M. Arneodo, Phys. Rep. **240** (1994) 301.

[79] V. Emel'yanov, A. Khodinov, S.R. Klein and R. Vogt, Phys. Rev. C **61** (2000) 044904.

[80] T. Kitagaki *et al.*, Phys. Lett. B **214** (1988) 281.

[81] B.L. Combridge, Nucl. Phys. B **151** (1979) 429.

[82] R.V. Gavai, D. Kharzeev, H. Satz, G. Schuler, K. Sridhar and R. Vogt, Int. J. Mod. Phys. A **10** (1995) 3043; G.A. Schuler and R. Vogt, Phys. Lett. B **387** (1996) 181.

[83] C.W. deJager, H. deVries, and C. deVries, Atomic Data and Nuclear Data Tables **14** (1974) 485.

[84] D. Kharzeev, E.M. Levin and M. Nardi, hep-ph/0212316; L. Hulthen and M. Sagawara, in *Handbüch der Physik*, **39** (1957).

[85] A.D. Martin, R.G. Roberts, and W.J. Stirling, and R.S. Thorne, Phys. Lett. B **443** (1998) 301.

[86] M. Glück, E. Reya, and A. Vogt, Z. Phys. C **53** (1992) 127.

[87] K.J. Eskola, V.J. Kolhinen and P.V. Ruuskanen, Nucl. Phys. B **535** (1998) 351.

[88] K.J. Eskola, V.J. Kolhinen and C.A. Salgado, Eur. Phys. J. C **9** (1999) 61.

[89] L. Frankfurt, V. Guzey and M. Strikman, arXiv:hep-ph/0303022.

[90] H.L. Lai *et al.*, Eur. Phys. J. C **12** (2000) 375.

[91] S.R. Klein and R. Vogt, Phys. Rev. Lett. **91** (2003) 142301.

[92] R. Vogt, Nucl. Phys. A **700** (2002) 539.

[93] H. Fujii and D. Kharzeev, Phys. Rev. D **60**, 114039 (1999)

[94] D. Kharzeev, C. Lourenço, M. Nardi and H. Satz, Z. Phys. C **74**, 307 (1997)

[95] M. Gazdzicki and M. I. Gorenstein, Phys. Rev. Lett. **83**, 4009 (1999) [arXiv:hep-ph/9905515].

[96] P. Braun-Munzinger and J. Stachel, Phys. Lett. B **490**, 196 (2000) [arXiv:nucl-th/0007059].

[97] M. I. Gorenstein, A. P. Kostyuk, H. Stöcker and W. Greiner, Phys. Lett. B **509**, 277 (2001) [arXiv:hep-ph/0010148].

[98] A. P. Kostyuk, M. I. Gorenstein, H. Stocker and W. Greiner, Phys. Lett. B **531**, 195 (2002) [arXiv:hep-ph/0110269].

[99] A. Andronic, P. Braun-Munzinger, K. Redlich and J. Stachel, Phys. Lett. B **571**, 36 (2003) [arXiv:nucl-th/0303036].

[100] P. Braun-Munzinger, K. Redlich and J. Stachel, arXiv:nucl-th/0304013.

[101] M. C. Abreu *et al.* [NA50 Collaboration], Phys. Lett. B **450**, 456 (1999).

[102] M. C. Abreu *et al.* [NA50 Collaboration], Phys. Lett. B **477**, 28 (2000).

[103] H. Santos *et al.* [NA50 Collaboration], J. Phys. G **30**, S1175 (2004) [arXiv:hep-ex/0405056].

[104] L. Grandchamp and R. Rapp, Phys. Lett. B **523**, 60 (2001) [arXiv:hep-ph/0103124].

[105] L. Grandchamp and R. Rapp, Nucl. Phys. A **709**, 415 (2002) [arXiv:hep-ph/0205305].

[106] J. Adams *et al.* [STAR Collaboration], arXiv:nucl-ex/0407006.

[107] S. S. Adler *et al.* [PHENIX Collaboration], arXiv:nucl-ex/0409028.

[108] L. Grandchamp, R. Rapp and G. E. Brown, Phys. Rev. Lett. **92**, 212301 (2004) [arXiv:hep-ph/0306077].

[109] R. L. Thews, arXiv:hep-ph/0206179.

[110] V. Greco, C. M. Ko and R. Rapp, Phys. Lett. B **595**, 202 (2004) [arXiv:nucl-th/0312100].

[111] B. Zhang, C. M. Ko, B. A. Li, Z. W. Lin and S. Pal, Phys. Rev. C **65**, 054909 (2002) [arXiv:nucl-th/0201038].

[112] E. L. Bratkovskaya, W. Cassing and H. Stocker, Phys. Rev. C **67**, 054905 (2003) [arXiv:nucl-th/0301083].

[113] C. Baglin *et al.* (NA38 Collaboration), Phys. Lett. B **220** (1989)471.

[114] C. Baglin *et al.* (NA38 Collaboration), Phys. Lett. B **255** (1991)459.

[115] M.C. Abreu *et al.* (NA38 Collaboration), Phys. Lett. B **449** (1999) 128.

[116] M.C. Abreu *et al.* (NA38 Collaboration), Phys. Lett. B **466** (1999) 408.

[117] M.C. Abreu *et al.* (NA50 Collaboration), Phys. Lett. B **410** (1997) 327.

[118] M.C. Abreu *et al.* (NA50 Collaboration), Phys. Lett. B **410** (1997) 337.

[119] M.C. Abreu *et al.* (NA50 Collaboration), Phys. Lett. B **477** (2000) 28.

[120] M.C. Abreu *et al.* (NA50 Collaboration), Phys. Lett. B **521** (2001) 195.

[121] M.C. Abreu *et al.* (NA51 Collaboration), Phys. Lett. B **438** (1998) 35.

[122] M.C. Abreu *et al.* (NA38 Collaboration), Phys. Lett. B **444** (1998) 516.

[123] M.C. Abreu *et al.* (NA50 Collaboration), Phys. Lett. B **553** (2003) 167.

[124] B. Alessandro *et al.* (NA50 Collaboration), Eur. Phys. J. C **33** (2004) 31.

[125] R. Vogt, Phys. Rep. **310** (1999) 197.

[126] R.J. Glauber, *Lectures in Theoretical Physics*, NY, 1959, Vol. 1, 315.

[127] C.W. de Jager *et al.*, Atomic Data and Nuclear Data Tables 14(1974) 479.

[128] S. S. Adler *et al.* [PHENIX Collaboration], Phys. Rev. Lett. **92**, 051802 (2004)

[129] R. G. de Cassagnac [PHENIX Collaboration], J. Phys. G **30**, S1341 (2004)

[130] S. S. Adler *et al.* [PHENIX Collaboration], Phys. Rev. C **69**, 014901 (2004)

[131] K. Adcox *et al.* [PHENIX Collaboration], Nucl. Instrum. Meth. A **499**, 469 (2003).

[132] Particle Data Group, Phys. Rev. D **66**, 010001 (2002)

[133] S. R. Klein and R. Vogt, Phys. Rev. Lett. **91**, 142301 (2003)

[134] B. Kopeliovich, A. Tarasov and J. Hufner, Nucl. Phys. A **696**, 669 (2001)

[135] R. L. Thews, M. Schroedter and J. Rafelski, Phys. Rev. C **63**, 054905 (2001)

[136] S. Klein and J. Nystrand, Phys. Rev. Lett. **92**, 142003 (2004)

[137] S. Klein and J. Nystrand, Phys. Rev. C **60**, 014903 (1999); A. J. Baltz, S. R. Klein and J. Nystrand, Phys. Rev. Lett. **89**, 012301 (2002)

[138] M. Drees and D. Zeppenfeld, Phys. Rev. D **39**, 2536 (1989).

[139] B. A. Kniehl, Phys. Lett. B **254**, 267 (1991).

[140] J. Ohnemus, T. F. Walsh and P. M. Zerwas, Phys. Lett. B **328**, 369 (1994).

[141] G. Baur *et al.*, Phys. Rep. **364**, 359 (2002).

[142] M. G. Ryskin, Z. Phys. C **57**, 89 (1993).

[143] L. L. Frankfurt, M. F. McDermott and M. Strikman, JHEP **9902**, 002 (1999).

[144] A. D. Martin, M. G. Ryskin and T. Teubner, Phys. Lett. B **454**, 339 (1999).

[145] J. A. Crittenden, *Exclusive Production of Neutral Vector Mesons at the Electron-Proton Collider HERA*, Springer-Verlag, 1997.

[146] C. Adloff *et al.* [H1 Collaboration], Phys. Lett. B **483**, 23 (2000).

[147] J. Breitweg *et al.* [ZEUS Collaboration], Phys. Lett. B **437**, 432 (1998).

[148] L. Frankfurt, M. Strikman and M.Zhalov, Phys. Lett. **B540**, 220 (2002).

[149] C. Adler *et al.* [STAR Collaboration], Phys. Rev. Lett. **89**, 272302 (2002).

[150] V. A. Khoze, A. D. Martin and M. G. Ryskin, Eur. Phys. J. C **24**, 459 (2002).

[151] L. Frankfurt, V. Guzey, M. Strikman and M. Zhalov, JHEP **0308**, 043 (2003).

[152] Angela Wyatt, presented at "Small-x and Diffraction 2003," Sept. 17-20, 2003, Fermilab, IL. Transparencies are available at http://conferences.fnal.gov/smallx/new_program.htm.

[153] S. Klein and J. Nystrand, hep-ph/0310223, presented at "Small-x and Diffraction 2003," Sept. 17-20, 2003, Fermilab, IL.

[154] F. Abe *et al.* [CDF Collaboration], Phys. Rev. Lett. **75**, 4358 (1995).

[155] S. R. Klein and J. Nystrand, Phys. Rev. Lett. **84**, 2330 (2000); Phys. Lett. A **308**, 323 (2003).

[156] S. Klein (STAR Collaboration), nucl-ex/0310020.

[157] N. Baron and G. Baur, Phys. Rev. C **48**, 1999 (1993); M. Greiner *et al.*, Phys. Rev. C **51**, 911 (1995); S. Klein, J. Nystrand and R. Vogt, Phys. Rev. C **60**, 044906; S. R. Klein, J. Nystrand and R. Vogt, Eur. Phys. J. C **21**, 563 (2001).

Chapter 8

BEYOND THE STANDARD MODEL

Convener: M. Sanchis-Lozano
Authors: J. P. Ma, M. Sanchis-Lozano

1 GENERAL OVERVIEW

During the last years, a large amount of new data on charmonium and bottomonium production and decays have been collected in B-factories, Tevatron, HERA and BEPC, greatly improving the accuracy of the measured widths and branching fractions. Such measurements, together with the soundness of the theoretical background based on effective field theories, could show up possible deviations from SM expectations, thereby pointing out the existence of NP. Lepton flavour and CP violation in heavy quarkonia decays are good examples of such precision physics. Moreover, in the past radiative decays of heavy quarkonium were employed in the search for axions and Higgs particles according to the Wilczek mechanism [1]. Recently, the possibility of relatively light non-standard Higgs bosons (which might have evaded LEP searches) has been pointed out in different scenarios beyond the SM [2–4]. Therefore, discovery strategies should be conducted to detect possible signals of new physics from heavy quarkonia decays.

2 PROSPECTS TO DETECT NEW PHYSICS

Heavy quarkonium offers an interesting place where probing NP which would manifest experimentally in different ways: a) slight but observable modifications of decay rates and branching fractions; b) unexpected topologies in decays; c) CP and lepton flavour violation, etc. Along this chapter we will discuss in some detail three proposals to search for new physics and the prospects to detect non-standard light particles based on decays of heavy quarkonium:

– CP test with J/ψ decays, probing the electric and chromo-dipole moments of charm quarks
– Lepton flavour violation in J/ψ's two-body decays
– non-standard Higgs-mediated leptonic decays of Upsilon resonances

Moreover, let us mention other possibilities (not developed further in this chapter) to seek NP:

– Inspired by string-like scenarios, field theories formulated in noncommutative spaces should be explored. In particular, noncommutative QCD corrections to the gluonic decays of heavy quarkonia have been analyzed in [5]. Despite proving the consistency of perturbative calculations in this model, the inclusion of such corrections does not change substantially the magnitudes of the hadronic widths, thereby making difficult the experimental test.

– A relatively light bottom squark and gluino sector in supersymmetry was put forward some time ago [6] to explain the longstanding discrepancy on the bottom hadroproduction cross-section between theory and experiment found at Tevatron [7, 8]. Under this hypothesis, interesting consequences could show up in bottomonium phenomenology [9–11], e.g., the decay modes

$$\Upsilon \to \tilde{b}\tilde{b}^* \quad ; \quad \chi_b \to \tilde{b}\tilde{b}^*, \quad \Upsilon \to \gamma\,\tilde{S} \quad ; \quad \Upsilon \to \gamma\,\eta_{\tilde{g}}$$

If the bottom squark was relatively "stable" it might yield a $\tilde{B}^-$ or a $\tilde{B}^0$ "mesino" (the superpartner of the B meson) by picking up a $\bar{u}$ or a $\bar{d}$ quark, respectively. Such a meson has baryon number zero but would act like a heavy $\bar{p}$ (of mass $\sim 3-7$ GeV). In fact at LHC experiments it could fake a heavy muon in muon chambers but leaving some activity in the hadron calorimeter; ionization,

445

time-of-flight and Cherenkov measurements would be consistent with a particle whose mass is heavier than a proton. However, recently a more accurate description of the b-quark fragmentation function has substantially reduced the difference between theoretical expectations and experimental results in bottom hadroproduction [12, 13]. Although the situation is not definitely settled, now the claim for a new physics contribution in bottom production is not compelling at all. Besides, a throughout analysis of the $e^+e^- \to hadrons$ cross-section from PEP, PETRA, TRISTAN, SLC and LEP allows the 95% C.L. exclusion of sbottom with mass below 7.5 GeV [14]. Also a light gluino mass less than 6.3 GeV has been excluded [15].

3   PRECISION TESTS USING J/ψ DECAYS

Huge amount of data (to be) collected in e^+e^- factories like BEPC (and the upgraded BEPCII) and CLEO should allow to test some aspects of the SM to an unprecedented accurracy. In the following sections we describe two research lines based on J/ψ rare decays.

3.1   CP test with J/ψ decays[1]

We open this review on searches for new physics by remarking that a nonzero electrical dipole moment (EDM) of a quark or a lepton implies that CP symmetry is violated. Actually, EDM's of quarks and leptons are very small from the SM (see [16–18] and references therein). If the EDM of a quark is found to be nonzero, it is likely an indication of new physics.

Since the operator for EDM does not converse helicities of quarks, its effect is suppressed in a high energy process by a factor m_q/E, where m_q is the quark mass and E is a large energy scale. For light quarks, useful information can be obtained through measurement of the EDM of the neutron [16]. So far there is no experimental information about EDM's of heavy quarks, like charm- and bottom-quark. J/ψ decays can provide information of EDM of charm quark and has the advantage that the effect of EDM will be not suppressed, because the large energy scale is around m_c. Since in radiative decays a $c\bar{c}$ pair is annihilated into a photon and gluons, it also provides a way to detecting the chromodipole moment of the charm quark. These moments are defined by the effective Lagrangian:

$$L_{CP} = -i\frac{d_c}{2}\bar{c}\gamma_5\sigma_{\mu\nu}F^{\mu\nu}c - i\frac{\tilde{d}_c}{2}\bar{c}\gamma_5\sigma_{\mu\nu}G^{\mu\nu}c, \tag{8.1}$$

where d_c is the electric dipole moment, $\tilde{d}_c$ is the chromodipole moment.

In general a CP symmetry test requires a large data sample because the effect of its possible violation is expected to be very small. In the following we focus on J/ψ decays [19] as large data samples already exist or will be collected at BEPC and CLEO-c. Indeed, such huge data samples (with $10^7 \sim 10^{10}$ J/ψ's) are very suited for CP tests. However, not every decay mode of J/ψ can be used for this purpose. For a J/ψ decay into a particle and its antiparticle, a CP test is not possible if these particles are spinless or their polarizations are not observed [18, 20]. It is only possible if polarizations of decay products are measured. The decay $J/\psi \to \Lambda\bar{\Lambda}$ is an example, where the polarizations can be determined through subsequential decays of Λ and $\bar{\Lambda}$ [21].

On the other hand, a CP test can be carried out for three-body decays, even without knowing the polarizations of the decay products. This is the case of the $J/\psi \to \gamma\phi\phi$ decay mode, which can provide useful information about the charm quark EDM. The reason for choosing this channel is because ϕ is a very narrow resonance, just above $K\bar{K}$ threshold, and can be clearly identified by its K^+K^- decay mode in experiment. In principle $J/\psi \to \gamma\rho\rho$ could also serve for the purpose, but experimentally the broad width of ρ meson makes it impossible to get a clean sample from this channel. Therefore, let us consider the decay in the rest-frame of J/ψ produced at a e^+e^- collider:

$$e^+(k_+) + e^-(k_-) \to J/\psi(P) \to \gamma(k) + \phi(p_1) + \phi(p_2), \tag{8.2}$$

---

[1]Author: Jian-Ping Ma

where momenta are given in brackets. Because the two ϕ mesons are identical particles, we require $p_1^0 > p_2^0$ to distinguish them in experiment. In our case two CP-odd observables can be constructed:

$$O_1 = \hat{\mathbf{k}}_+ \cdot \hat{\mathbf{p}}_1 \hat{\mathbf{k}}_+ \cdot (\hat{\mathbf{p}}_1 \times \hat{\mathbf{p}}_2), \ \ O_2 = \hat{\mathbf{k}}_+ \cdot \hat{\mathbf{p}}_2 \hat{\mathbf{k}}_+ \cdot (\hat{\mathbf{p}}_1 \times \hat{\mathbf{p}}_2), \tag{8.3}$$

where momenta with a hat denote their directions. From these oberservables, one can define the CP-asymmetry as

$$B_i = \langle \theta(O_i) - \theta(-O_i) \rangle \ \ (i = 1, 2), \tag{8.4}$$

where $\theta(x) = 1$ if $x > 0$ and is zero if $x < 0$. If these asymmetries are not zero, CP symmetry is violated.

In calculating these asymmetries, we will use nonrelativistic wave-functions for J/ψ and also for ϕ mesons. It should be noted that reliable predictions for various distributions can not be obtained with this approximation. Neverthesless, one may expect that for integrated asymmetries it could become a good approximation, especially because the integrated asymmetries will not depend on the wave functions at the origin.

The following CP asymmetries are obtained:

$$
\begin{aligned}
B_1 &= 4.2 \left[\frac{d_c}{10^{-10}e \text{ cm}} \right] - 1.2 \left[\frac{\tilde{d}_c}{10^{-10}e \text{ cm}} \right], \\
B_2 &= -3.9 \left[\frac{d_c}{10^{-10}e \text{ cm}} \right] + 1.3 \left[\frac{\tilde{d}_c}{10^{-10}e \text{ cm}} \right].
\end{aligned}
\tag{8.5}
$$

A statistic sensitivity to d_c and $\tilde{d}_c$ can be determined from these results by requiring that the asymmetry generated by these dipole moments should be larger than the statistical error. With the 5.8×10^7 J/ψ data sample at BES, the sensitivities of such CP asymmetries to these dipole moments are

$$d_c \sim 1.4 \times 10^{-13}e \text{ cm}, \quad \tilde{d}_c \sim 4.5 \times 10^{-13}e \text{ cm}. \tag{8.6}$$

With a 10^{10} data sample which will be collected in the near future, the sensitivities are:

$$d_c \sim 1.2 \times 10^{-14}e \text{ cm}, \quad \tilde{d}_c \sim 3.6 \times 10^{-14}e \text{ cm}. \tag{8.7}$$

To conclude this section: With large date samples of J/ψ, which are collected at BES and will be collected with BES III and CLEO-c program, a CP test is possible with J/ψ decays. By using the decay mode $J/\psi \to \gamma\phi\phi$, the electric- and chromo-dipole moment can be probed at order of $10^{-13}e$ cm $\sim 10^{-14}e$ cm.

3.2 Lepton flavour violation

In the SM, lepton flavour number is independently conserved provided that neutrinos are massless, although (being a global symmetry) there is no fundamental dynamical principle requiring its conservation. Actually, lepton flavour is violated in many extensions of the SM, such as grand unified theories [22], supersymmetric models [23], left-right symmetric models [24] and models where the electroweak symmetry is dynamically broken [25]. Recent results [26, 27] indicate that neutrinos indeed have nonzero masses and can mix with each other; therefore, lepton flavour is a broken symmetry in nature. Here, we focus on lepton flavour violation (LFV) via the two-body J/ψ decay (which conserves total lepton number):

$$J/\psi \to \ell\ell'$$

with ℓ and ℓ' denoting charged leptons of different species. This process could occur at tree-level induced by leptoquarks, sleptons (both in the t-channel) or mediated by Z' bosons (in the s-channel) [28, 29] in correspondence with the aforementioned scenarios.

The large sample (5.8×10^7 events) collected in leptonic decays of J/ψ resonances at BEPC and analized by BES up to now makes this search especially interesting; in fact, upper limits for different lepton combinations have already been set at 90% C.L. [30, 31]:

$$\mathcal{B}(J/\psi \to \mu\tau) < 2.0 \times 10^{-6}$$
$$\mathcal{B}(J/\psi \to e\tau) < 8.3 \times 10^{-6}$$
$$\mathcal{B}(J/\psi \to e\mu) < 1.1 \times 10^{-6}$$

In the future, larger samples collected at BEPC(II) should allow to test LFV at a higher precision, severely constraing new physics models. Similarly, estimates of the LFV Upsilon decay $\Upsilon \to \ell\ell'$ can be found in [29].

4   SEARCHES FOR LIGHT PSEUDOSCALARS IN Υ DECAYS

In many extensions of the SM, new scalar and pseudoscalar states appear in the physical spectrum. Admittedly, the masses of these particles are typically of the same order as the weak scale and, in principle, a fine-tuning is required to make them much lighter. Nevertheless, if the theory possesses a global symmetry, its spontaneous breakdown gives rise to a massless Goldstone boson, the "axion". The original axion [32] was introduced in the framework of a two-Higgs doublet model (2HDM) to solve the strong CP problem. However, such an axial U(1) symmetry is anomalous and the pseudoscalar acquires a (quite low) mass which has been ruled out experimentally. Thus, theorists have looked for other models (by relaxing model parameter constraints) and axion-like particles, not running into conflict with present terrestrial experiments and astrophysical limits (see [33] and references therein).

On the other hand, if the global symmetry is explicitly (but slightly) broken, one expects a pseudo-Nambu–Goldstone boson in the theory which, for a range of model parameters, still can be significantly lighter than the other scalars. A good example is the so-called next to minimal supersymmetric standard model (NMSSM) where a new gauge-singlet superfield is added to the Higgs sector [34]. The mass of the lightest CP-odd Higgs can be naturally small due to a global symmetry of the Higgs potential only softly broken by trillinear terms [2]. Moreover, the smallness of the mass is protected from renormalization group effects in the large $\tan\beta$ limit. Actually, there are other scenarios containing a light[2] pseudoscalar Higgs boson which could have escaped detection in the searches at LEP-II, e.g., a MSSM Higgs sector with explicit CP violation [4]. Another example is a minimal composite Higgs scenario [3] where the lower bound on the CP-odd scalar mass is quite loose, as low as ~ 100 MeV (from astrophysical constaints).

Thus we conclude that the existence of a relatively light pseudoscalar Higgs (to be denoted as A^0 hereafter) is not in contradiction with current experimental data and could be accomodated within well motivated extensions of the SM. Therefore, it is worth to revisit some of the "old" techniques to search for non-standard particles in quarkonia decays, also exploring new possibilities like a possible breakdown of lepton universality in Υ decays.

4.1 $\Upsilon(J/\psi) \to \gamma + X^0$

Heavy resonances have been helpful so far putting limits in the searches for extensions of the SM through the radiative decay channel

$$\Upsilon(J/\psi) \to \gamma + X^0$$

where X^0 stands for a weakly interacting (experimentally unseen) particle. This decay mode represents, in essence, the Wilczek mechanism [1] for the real emission of either a Higgs boson or an axion from quarkonium. The experimental signature would be very clean: the observation of a single photon with

---

[2]By "light" we consider here a broad interval which might reach a $\simeq 10$ GeV mass value
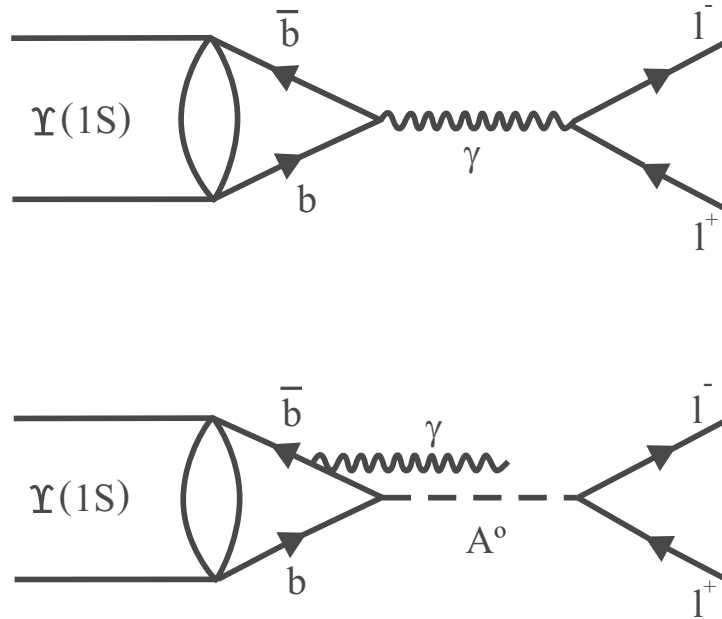
Fig. 8.1: $\Upsilon(1S)$ resonance into a charged lepton pair through a virtual photon; (b)[lower panel]: Hypothetical annihilation of an intermediate η_b^* state (subsequent to a M1 structural transition yielding a final-state soft photon) into a charged lepton pair through a CP-odd Higgs-like particle denoted by A^0.

a considerable missing energy in the event. Let us observe that this would be so if the X^0 is sufficiently stable, i.e., the probability to decay inside the detector (of typical size $r \sim 10$ m) is quite small, $\Gamma_{X^0} << E_{X^0}/m_{X^0}r$, where E_{X^0} and m_{X^0} denote the (laboratory) energy and mass of the unseen particle, respectively. Notice, however, that the chances to leave unseen the detector decrease for values of m_{X^0} close to E_{X^0} as the Lorentz dilation factor approaches unity. To date, no evidence has been found and limits have been set as a function of the mass of the X^0 particle [35]. Note that such limits in Υ decays only exclude particles below $5-7$ GeV! [36] Thus, in view of the renewed interest in pseudoscalars whose mass may lie around 10 GeV, an open mind should be kept in those and related searches.

4.2 Non-standard Higgs-mediated leptonic decays of Υ resonances

In the previous section we considered the possibility of emission by heavy quarkonium of a real, long-lived but unseen particle. However, if the emitted particle width is large enough, the particle would promptly decay and its products could make possible its observation by the detector. On the other hand, virtual poduction of (off-shell) particles should be also analized. In this section we examine the possible existence of a CP-odd Higgs mediating the annihilation of the $b\bar{b}$ pair (subsequent to a magnetic dipole transition of the Upsilon resonance) into a final-state dilepton (see Fig. 8.1). This channel would constitute a rare decay mode of the Υ resonance, observable however if the Higgs mass is not too far from the Υ mass and the couplings are not small. In fact, rare decays have been traditionally employed for seeking new physics, in particular looking for extensions of the Higgs sector of the SM. Let us mention, as a significant example, the (flavor-changing neutral current) decays of B mesons into lepton pairs (e.g., $B^0_{s,d} \to \mu^+\mu-$), where a non-standard Higgs-mediated contribution could modify (enhancing) the SM decay rates [37].

As pointed out in a series of recent papers [38–40], bottomonium also offers the possibility of testing extensions of the SM by looking at possible non-standard Higgs-mediated leptonic decay channels of Upsilon resonances below the $B\bar{B}$ threshold, in addition to the dominating electromagnetic mode

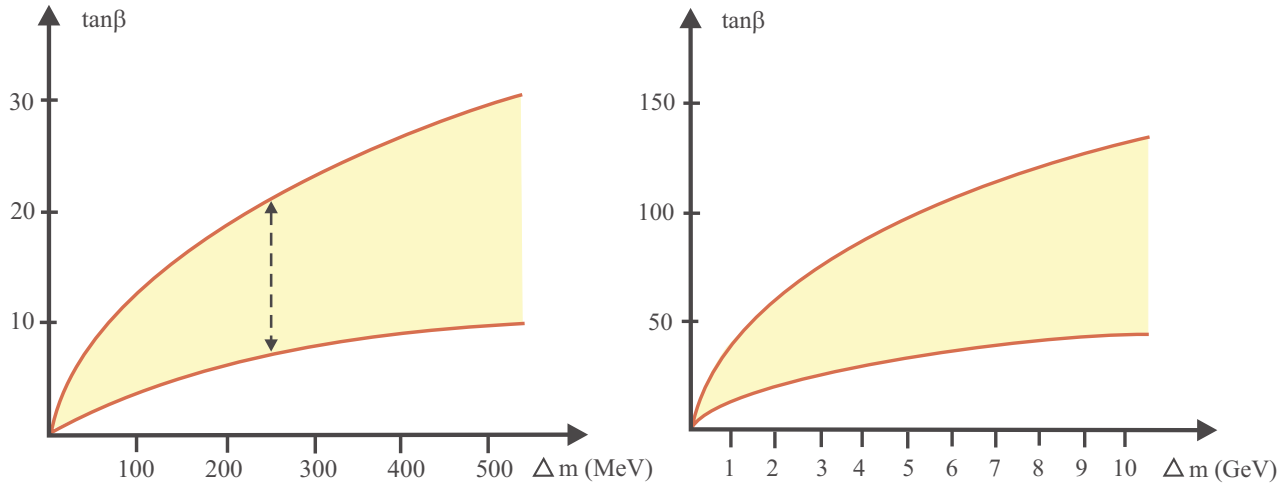$$\Upsilon(nS) \to \gamma^* \to \ell^+\ell^- \quad (\ell = e, \mu, \tau, \; n = 1, 2, 3)$$

Fig. 8.2: Required $\tan\beta$ values (shaded area) as a function of Δm needed to account for a $\sim 10\%$ breakdown of lepton universality in Υ decays according to a 2HDM(II). The vertical dotted line shows the range of $\tan\beta$ for $\Delta m = 250$ MeV used in [39] as a reference value.

We shall focus as a theoretical background on a general 2DHM of the type II [34] where down fermions couple to the Higgs boson proportionally to the ratio $(\tan\beta)$ of the two Higgs vacuum expectation values. Nevertheless, the main conclusions can be extended to different scenarios predicting other Higgs-like particles with analogous phenomenological features.

Let us assume that a prior magnetic dipole (M1) direct transition from the initial-state Υ can take place yielding a pseudoscalar $b\bar{b}$ intermediate state as shown in Fig. 8.1, subsequently annihilating into a lepton pair via a non-standard CP-odd Higgs boson A^0:

$$\Upsilon(nS) \;\rightarrow\; \gamma_s\,\eta_b^*(\rightarrow A^0 \rightarrow \ell^+\ell^-) \quad (\ell = e, \mu, \tau, \; n = 1, 2, 3)$$

where γ_s stands for an undetected soft photon with energy in the range 35–150 MeV, depending on the still unknown $\Upsilon - \eta_b$ hyperfine splitting. As the photon is quite soft, the M1-transition probability $\mathcal{P}^\Upsilon(\eta_b^*\gamma_s)$ was roughly obtained in [39, 40] from a textbook expression relating on-shell states. A consequence of the existence of this kind of NP would be the "apparent"[3] breaking of lepton universality based on the two following keypoints:

– In the experimental determinations of the leptonic BF of the Upsilon resonances, the Higgs contribution would be unwittingly ascribed to the leptonic decay mode as the radiated photon would remain undetected. This would be especially the case for the $\tau^\pm$ channel[4]
– The leptonic (squared) mass dependence in the width from the Higgs contribution would introduce a dependence on the leptonic species in the leptonic BF. The effect would only be noticeable in the tauonic decay mode as the electron and muon masses are much smaller than the tau mass.

Current experimental data (see Table 8.1) may indeed hint that there is a difference of order 10% in the BFs between the tauonic channel on the one side, and the electronic and muonic modes on the other side [39]. The range of the $\tan\beta$ needed to account for such an effect is shown in Fig. 8.2 as a function of the mass difference (Δm) between the non-standard Higgs and the $\eta_b(1S)$ resonance, applying the

---

[3]In the sense that once the Higgs contribution were taken into account, lepton universality would be restored

[4]The leptonic mass squared with a final-state photon is given by $m_{\ell\ell}^2 = m_\Upsilon^2(1 - 2E_\gamma/m_\Upsilon)$. Hence E_γ is much more limited by invariant mass reconstruction of either final-state electrons or muons than for tau's where such constraint is not applicable.

Table 8.1: Measured leptonic BF's and error bars in % of $\Upsilon(1S)$ and $\Upsilon(2S)$ (from [36]).

channel:	e^+e^-	$\mu^+\mu^-$	$\tau^+\tau^-$
$\Upsilon(1S)$	2.38 ± 0.11	2.48 ± 0.06	2.67 ± 0.16
$\Upsilon(2S)$	1.34 ± 0.20	1.31 ± 0.21	1.7 ± 1.6

factorization of the decay width used in [39]. The upper and lower curves correspond to the maximal and mimimal estimates of the M1-transition probability $\mathcal{P}^{\Upsilon}(\eta_b^*\gamma_s)$, respectively. For the large values of Δm, only the lower values of the shaded region would be acceptable, corresponding to the higher estimates of $\mathcal{P}^{\Upsilon}(\eta_b^*\gamma_s)$.

In addition to the postulated breaking of lepton universality, other experimental signatures which would eventually support the conjecture on a CP-odd Higgs boson showing up in bottomonium spectroscopy and decays are:

– A $\Upsilon - \eta_b$ hyperfine splitting larger than expected from quark potential models, caused by $A^0 - \eta_b$ mixing. A mass splitting significantly larger than 100 MeV could be hardly accomodated within the SM

– A rather large full width of the η_b resonances due to the NP channel (especially for high values of $\tan\beta$)

– If, instead, the η_b state is not too broad (as this would be the case for the lowest values of $\tan\beta$ in Fig. 8.2), one could look for monoenergetic photons with energy of order 100 MeV (hence above detection threshold) in those events mediated by the CP-odd Higgs boson (estimated to be about 10% of all Υ tauonic decays)

4.2.1 *Spectroscopic consequences for bottomonium states*

In view of our previous considerations, one can speculate about a quite broad η_b resonance (e.g., $\Gamma_{\eta_b} \gtrsim 30$ MeV)[5] which might partially explain why there was no observed signal from the hindered radiative decays of higher Upsilon resonances in the search performed by CLEO [41, 42]. Indeed the signal peak (which should appear in the photon energy spectrum) could be considerably smoothed — in addition to the spreading by the experimental measurement — and thereby might not be significantly distinguished from the background (arising primarily from π^0's decays). Of course, the matrix elements for the hindered M1 transitions are expected to be small and difficult to predict as they are generated by relativistic and finite size corrections. Nevertheless, most of the theoretical calculations are ruled out by CLEO results (at least) at a 90% CL (see a compilation in [43]), though substancially lower rates are obtained in [44] where exchange currents play an essential role and currently cannot be excluded. Notice finally that a large full width of the η_b resonance would bring negative effects on the prospects for its detection at the Tevatron through the double-J/ψ decay: $\eta_b \to J/\psi + J/\psi$. Indeed, the expected BF would drop by about one order of magnitude with respect to the range between 7×10^{-5} and 7×10^{-3} assumed in [45].

Furthermore, another interesting possibility is linked to a $A^0 - \eta_b$ mixing [46] which could sizeably lower the mass of the mixed (physical) η_b state, especially for high $\tan\beta$ values starting from similar masses of the unmixed states [39]. Then the signal peak in the photon energy plot could be (partially) shifted off the search window used by CLEO [41, 42] towards higher γ energies (corresponding to a smaller η_b mass[6] perhaps contributing additionally to the failure to find evidence about the existence of the η_b resonances to date.

---

[5]One expects $\Gamma_{\eta_b(1S)} \simeq 4\,\mathrm{MeV}$ using the asymptotic expression $\Gamma_{\eta_b} \simeq m_b/m_c \times [\alpha_s(m_b)/\alpha_s(m_c)]^5 \times \Gamma_{\eta_c}$ and setting the measured $\Gamma_{\eta_c(1S)} = 16 \pm 3\,\mathrm{MeV}$ [36]

[6]This would be the case if the (unmixed) CP-odd Higgs boson had a mass greater than the (unmixed) η_b resonance [46]

The mass formula for the physical A^0 and η_b states in terms of the unmixed states (denoted as A_0^0 and η_{b0} respectively), and the off-diagonal mass matrix element $\delta m^2 \simeq 0.146 \times \tan\beta$ GeV^2, for quite narrow resonances (i.e., $\Gamma_{\eta_{b0}}$, $\Gamma_{A_0^0} \ll m_{\eta_{b0}}$, $m_{A_0^0}$) reads [39]:

$$m^2_{\eta_b, A^0} \simeq \frac{1}{2}(m^2_{A_0^0} + m^2_{\eta_{b0}}) \mp \frac{1}{2}\left[(m^2_{A_0^0} - m^2_{\eta_{b0}})^2 + 4(\delta m^2)^2\right]^{1/2}$$

which yields in the case of the physical η_b and A^0 particles for different mass intervals:

$$m_{\eta_b, A^0} \simeq m_{\eta_{b0}} \mp \frac{\delta m^2}{2m_{\eta_{b0}}} \; ; \;\; 0 < m^2_{A_0^0} - m^2_{\eta_{b0}} << 2\,\delta m^2$$

$$m_{\eta_b, A^0} \simeq m_{\eta_{b0}, A_0^0} \mp \frac{(\delta m^2)^2}{2m_{\eta_{b0}}(m^2_{A_0^0} - m^2_{\eta_{b0}})} \; ; \;\; m^2_{A_0^0} - m^2_{\eta_{b0}} >> 2\,\delta m^2$$

As a particular but significant example, assuming for the masses of the unmixed states $m_{\eta_{b0}} \simeq m_{A_0^0} = 9.4$ GeV and the moderate $\tan\beta = 12$ value, one gets for the physical states $m_{A^0} \simeq 9.5$ GeV and $m_{\eta_b} \simeq 9.3$ GeV respectively, which corresponds to a mass difference $m_{\Upsilon(1S)} - m_{\eta_b(1S)} \simeq 160$ MeV. Higher $\tan\beta$ values would, in principle, lead to larger mass shifts. However a caveat is in order: the hyperfine splitting (enhanced by the mixing) cannot raise unlimitedly, since the dependence on the third power of the photon energy in $\mathcal{P}^\Upsilon(\eta_b^* \gamma_s)$ (corresponding to a magnetic dipole transition) would eventually push up the new physics contribution for the tauonic BF beyond the postulated $\mathcal{O}(10\%)$ effect.

To end this section, let us point out that CLEO has completed detailed scans of the $\Upsilon(nS)$ ($n = 1, 2, 3$) resonances and we want to stress the relevance of these measurements (aside other applications) for testing more accurately the possible existence of NP by a more precise determination of the electronic, muonic and tauonic BFs of *all three* resonances below open bottom threshold. In case no lepton universality breaking is definitely found, some windows in the $\tan\beta$–m_{A^0} plane for such a non-standard CP-odd light Higgs boson would be closed.

5 SUMMARY

Quarkonium phenomenology should play an important role to explore new physics as it did in the past to develop the SM. Annihilation and radiative decays of resonances are well suited for testing symmetry conservation laws, as well as searching for (relatively) light particles arising in diverse scenarios beyond the SM, in addition to a much heavier sector.

The expected large statistics of J/ψ and Υ resonances, to be collected at e^+e^- and hadronic colliders along the next few years, makes heavy quarkonium physics especially convenient to conduct high precision studies and the quest for new particles and new phenomena. In this chapter, we have particularly developed three issues concerning CP and lepton-flavour violation in J/ψ decays, and a possible lepton universality breaking in Υ decays indicating the existence of a non-standard light Higgs boson. An open mind should be kept regarding those and other possible phenomena beyond the SM in heavy quarkonium physics.

REFERENCES

[1] F. Wilczek, Phys. Rev. Lett. **39**, 1304 (1977).

[2] G. Hiller, arXiv:hep-ph/0404220.

[3] B. A. Dobrescu and K. T. Matchev, JHEP **0009**, 031 (2000) [arXiv:hep-ph/0008192].

[4] M. Carena, J. R. Ellis, S. Mrenna, A. Pilaftsis and C. E. M. Wagner, Nucl. Phys. B **659**, 145 (2003) [arXiv:hep-ph/0211467].

[5] A. Devoto, S. Di Chiara and W. W. Repko, Phys. Lett. B **588**, 85 (2004) [arXiv:hep-ph/0401071].

[6] E. L. Berger, B. W. Harris, D. E. Kaplan, Z. Sullivan, T. M. P. Tait and C. E. M. Wagner, Phys. Rev. Lett. **86**, 4231 (2001) [arXiv:hep-ph/0012001].

[7] B. Abbott *et al.* [D0 Collaboration], Phys. Lett. B **487**, 264 (2000) [arXiv:hep-ex/9905024].

[8] F. Abe *et al.* [CDF Collaboration], Phys. Rev. D **55**, 2546 (1997).

[9] E. L. Berger and L. Clavelli, Phys. Lett. B **512**, 115 (2001) [arXiv:hep-ph/0105147].

[10] E. L. Berger and J. Lee, Phys. Rev. D **65**, 114003 (2002) [arXiv:hep-ph/0203092].

[11] E. L. Berger, G. T. Bodwin and J. Lee, Phys. Lett. B **552**, 223 (2003) [arXiv:hep-ph/0206115].

[12] M. Cacciari and P. Nason, Phys. Rev. Lett. **89**, 122003 (2002) [arXiv:hep-ph/0204025].

[13] M. Cacciari, S. Frixione, M. L. Mangano, P. Nason and G. Ridolfi, arXiv:hep-ph/0312132.

[14] P. Janot, arXiv:hep-ph/0403157.

[15] P. Janot, Phys. Lett. B **564**, 183 (2003) [arXiv:hep-ph/0302076].

[16] X. G. He, B. H. J. McKellar and S. Pakvasa, Int. J. Mod. Phys. A **4**, 5011 (1989) [Erratum-ibid. A **6**, 1063 (1991)].

[17] W. Bernreuther and M. Suzuki, Rev. Mod. Phys. **63**, 313 (1991) [Erratum-ibid. **64**, 633 (1992)].

[18] J. G. Korner, J. P. Ma, R. Munch, O. Nachtmann and R. Schopf, Z. Phys. C **49**, 447 (1991).

[19] J. P. Ma, R. G. Ping and B. S. Zou, Phys. Lett. B **580**, 163 (2004) [arXiv:hep-ph/0311012].

[20] W. Bernreuther, U. Low, J. P. Ma and O. Nachtmann, Z. Phys. C **43**, 117 (1989).

[21] X. G. He, J. P. Ma and B. McKellar, Phys. Rev. D **47**, 1744 (1993) [arXiv:hep-ph/9211276].

[22] J. C. Pati and A. Salam, arXiv:hep-ph/0010105.

[23] H. E. Haber and G. L. Kane, Phys. Rept. **117**, 75 (1985).

[24] R. N. Mohapatra and J. C. Pati, Phys. Rev. D **11**, 566 (1975).

[25] C. T. Hill and E. H. Simmons, Phys. Rept. **381**, 235 (2003) [Erratum-ibid. **390**, 553 (2004)] [arXiv:hep-ph/0203079].

[26] Y. Fukuda *et al.* [Super-Kamiokande Collaboration], Phys. Rev. Lett. **81**, 1562 (1998) [arXiv:hep-ex/9807003].

[27] K. Eguchi *et al.* [KamLAND Collaboration], Phys. Rev. Lett. **90**, 021802 (2003) [arXiv:hep-ex/0212021].

[28] X. m. Zhang, arXiv:hep-ph/0010105.

[29] W. J. Huo, T. F. Feng and C. x. Yue, Phys. Rev. D **67**, 114001 (2003) [arXiv:hep-ph/0212211].

[30] J. Z. Bai *et al.* [BES Collaboration], Phys. Lett. B **561**, 49 (2003) [arXiv:hep-ex/0303005].

[31] [BES Collaboration], arXiv:hep-ex/0406018.

[32] R. D. Peccei and H. R. Quinn, Phys. Rev. D **16**, 1791 (1977).

[33] E. Masso, Nucl. Phys. Proc. Suppl. **114**, 67 (2003) [arXiv:hep-ph/0209132].

[34] J. Gunion et al., *The Higgs Hunter's Guide* (Addison-Wesley, 1990).

[35] R. Balest *et al.* [CLEO Collaboration], Phys. Rev. D **51**, 2053 (1995).

[36] K. Hagiwara *et al.* [Particle Data Group Collaboration], Phys. Rev. D **66**, 010001 (2002).

[37] A. Dedes, J. R. Ellis and M. Raidal, Phys. Lett. B **549**, 159 (2002) [arXiv:hep-ph/0209207].

[38] M. A. Sanchis-Lozano, Mod. Phys. Lett. A **17**, 2265 (2002) [arXiv:hep-ph/0206156].

[39] Int. J. Mod. Phys. A **19**, 2183 (2004) [arXiv:hep-ph/0307313].

[40] M. A. Sanchis-Lozano, arXiv:hep-ph/0401031.

[41] A. H. Mahmood *et al.* [CLEO Collaboration], arXiv:hep-ex/0207057.

[42] T. E. Coan, arXiv:hep-ex/0305045.

[43] S. Godfrey and J. L. Rosner, Phys. Rev. D **64**, 074011 (2001) [Erratum-ibid. D **65**, 039901 (2002)] [arXiv:hep-ph/0104253].

[44] T. A. Lahde, C. J. Nyfalt and D. O. Riska, Nucl. Phys. A **645**, 587 (1999) [arXiv:hep-ph/9808438].

[45] E. Braaten, S. Fleming and A. K. Leibovich, Phys. Rev. D **63**, 094006 (2001) [arXiv:hep-ph/0008091].

[46] M. Drees and K. i. Hikasa, Phys. Rev. D **41**, 1547 (1990).

Chapter 9

FUTURE EXPERIMENTAL FACILITIES

Conveners: S. Godfrey, M. A. Sanchis-Lozano

Authors: D. Bettoni, P. Crochet, S. Godfrey, F. A. Harris, A. Hoang, O. Iouchtchenko, A. Nairz, J. Napolitano, S. Olsen, P. Petreczki, M. A. Sanchis-Lozano, O. Schneider, A. Zieminski

Opportunities for quarkonium physics abound from a broad range of complementary facilities; CESR-c/CLEO-c, BECP II/BES III, B-factories, CDF and D0 (and BTEV) at the Tevatron, RHIC, GSI, and the LHC. In this chapter we look at these future facilities reviewing and suggesting experimental measurements that can be used as a roadmap for future directions in quarkonium physics.

1 TEVATRON

The Tevatron is an existing facility offering an exciting programme on future opportunities for heavy quarkonium physics in the short, medium and long terms (e.g., BTeV, with data taking foreseen in 2009). By August 2004 shutdown, each experiment (CDF and D0) had collected approximately 500 pb^{-1} of data on tape. The number of reconstructed quarkonium states is quite impressive: 2.5 million and 4 million J/ψ candidates collected by D0 and CDF, respectively. D0 reported over 50 000 $\Upsilon(1S)$ events in the data sample corresponding to 200 pb^{-1}.

Run II at the Tevatron will provide a substantial increase in luminosity (about 1.4 fb^{-1} delivered to CDF and D0 by the end of 2005 and 8.5 fb^{-1} by 2009) and will allow the collider experiments to determine the J/ψ, $\psi(2S)$ and χ_c cross-sections more precisely and at a larger p_T range. An accurate measurement of the J/ψ and $\psi(2S)$ polarization at large transverse momentum will be the most crucial test of NRQCD factorization. In addition, improved data on the J/ψ and $\psi(2S)$ cross-sections will help to reduce some of the ambiguities in extracting the colour-octet matrix elements.

With increased statistics it might be possible to access charmonium states such as the $\eta_c(nS)$ or the $h_c(nP)$. Heavy-quark spin symmetry provides approximate relations between the non-perturbative matrix elements that describe spin-singlet and spin-triplet states. The matrix elements for $\eta_c(nS)$ are related to those for $\psi(nS)$, while the leading matrix elements for $h_c(nP)$ can be obtained from those for $\chi_c(nP)$. Within NRQCD, the rates for $\eta_c(nS)$ and $h_c(nP)$ production can thus be predicted unambiguously in terms of the non-perturbative matrix elements that describe the J/ψ, $\psi(2S)$ and χ_c production cross-sections. A comparison of the various charmonium production rates would therefore provide a stringent test of NRQCD factorization and the heavy-quark spin symmetry. The cross-sections for producing the η_c and the h_c at Run II of the Tevatron are large [1, 2], but the acceptances and efficiencies for observing the decay modes on which one can trigger are, in general, small, and detailed experimental studies are needed to quantify the prospects. Other charmonium processes that have been studied in the literature include the production of D-wave states [3], J/ψ production in association with photons [4, 5], and double gluon fragmentation to J/ψ pairs [6].

On the other hand, Run II of the Tevatron will also allow the collider experiments to improve the measurement of the bottomonium cross-sections. As-yet-undiscovered states, such as the $\eta_b(1S)$, could be detected, for example, in the decay $\eta_b \to J/\psi + J/\psi$ [7] or in the decay $\eta_b \to D^* + D^{(*)}$ [8], and the associated production of Υ and electroweak bosons might be accessible [9]. If sufficient statistics can be accumulated, the onset of transverse $\Upsilon(nS)$ polarization may be visible at $p_T(\Upsilon) > 15$ GeV.

In sum, the future large statistics data will be used for:

Production studies

- Detailed differential cross-section measurements covering the transverse momentum range up to at least 30 GeV and rapidity range up to probably 1.1 (CDF) and 2 (D0), respectively.
- Determination of fractions of quarkonium states produced through the radiative χ decays. The $\gamma \rightarrow ee$ conversions provide a mass resolution sufficient to separate contributions from individual χ states (both for the χ_c and χ_b case). Both experiments have already demonstrated their potential to do such studies.
- Establishment of cross-sections for direct production of quarkonium states (J/ψ, $\psi(2S)$, and $\Upsilon(1S)$).
- Measurement of polarization of J/ψ, $\psi(2S)$ and Υ states.
- Associated production of quarkonium states, e.g., double J/ψ production.
- Associated production of quarkonium states and heavy quarks, e.g., J/ψ production in association with $c\bar{c}$ pairs.

Quarkonium decays

A large sample of $\psi(2S) \rightarrow J/\psi\pi^+\pi^-$ decays can be used for a better determination of the dependence of the decay matrix element on the invariant di-pion mass. The observed event accumulation rate is over 5000/fb^{-1} (D0) and 25 000/fb^{-1} (CDF). However, BES accumulated statistics for this channel will be difficult to beat.

$X(3872)$ state properties

The two experiments collected approximately 500 (D0) and 750 (CDF) $X(3872) \rightarrow J/\psi\pi\pi$ decays per 230 pb^{-1} of data. Studies of the $X(3872)$ properties will continue as the statistics increase. The quantities to measure include the fractions of $X(3872)$ states produced via b-quark decays as a function of the production transverse momentum, the decay matrix element dependence on the invariant mass of two final-state pions, $m(\pi\pi)$, and the di-pion resonance contribution to the decay process.

Searches for exotics decaying into final states involving quarkonia

CDF searches for strange and charmed pentaquarks have been widely publicized. CDF is also looking for the ($u\, d\, u\, s\, \bar{b}$) pentaquarks decaying into the $J/\psi p$ final state.

Hadron decays into charmonia

Exclusive B hadron decays into final states involving a J/ψ have been used for the world's best determination of the B$_s$ and Λ_b masses and their lifetimes. The B$\rightarrow$VV decays (where one of the vector decay products is a J/ψ) are being used for time-dependent polarization amplitude studies. These studies have led to the determination of lifetime differences of the CP-odd and CP-even B$_s$ mass eigenstates. They also provide tests of factorization, i.e., representing the weak decay matrix element as a product of two independent hadronic currents.

B$_c$ studies

Both collaborations are advancing their analyses of the B$_c$ mass and lifetime with Run II data. The yield of observed events in the B$_c \rightarrow$ J/$\psi\mu$ + X semileptonic decay channel is approximately 250 events/250 pb^{-1} (D0). These studies require large statistics and a good understanding of the fake muon background in order to reduce systematic uncertainties. A search for exclusive B$_c \rightarrow$ J/$\psi\pi$ decays is also under way in both experiments.
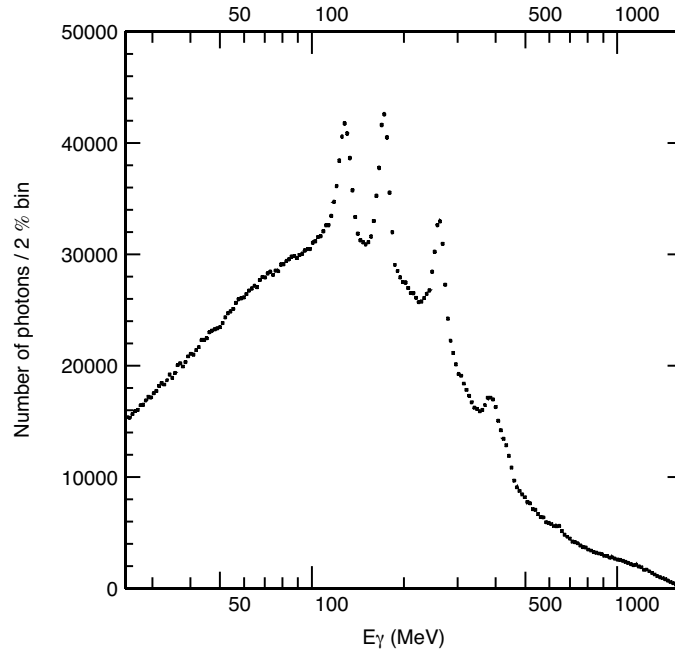
Fig. 9.1: The inclusive photon spectrum from $\psi(2S)$ decay. The data were taken with the CLEO III detector, prior to the CLEO-c upgrade. The peaks from single photon transitions between charmonium states are evident. This already exceeds the data volume acquired by the Crystal Ball at SLAC.

2 CLEO-c

CLEO-c is an experiment that makes use of the upgraded CLEO III detector, at the upgraded CESR storage ring. The storage ring (dubbed CESR-c) will use 12 wiggler magnet systems to give increased luminosity at low energies. This section reviews the CLEO-c experimental programme with particular emphasis on charmonium physics. The full details of CLEO-c and CESR-c are available in Ref. [10].

2.1 Charmonium physics with the $\psi(2S)$

CLEO-c has already begun taking data on the $\psi(2S)$. The inclusive photon spectrum from the first data set is shown in Fig. 9.1.

More running, with an upgraded CESR and higher instantaneous luminosity, is in the planning stages for the $\psi(2S)$. (In fact, at the time of writing, more data has already been taken.) Depending on running conditions and the will of the collaboration (see Section 2.4), a very large $\psi(2S)$ data set may eventually be accumulated. It is possible that this running may be traded for integrated luminosity on the J/ψ (see Section 2.3).

Potential physics opportunities with the $\psi(2S)$ include the following:

– Inclusive photons. Absolute branching fractions for $\psi(2S) \to \gamma \eta_c$ and $\psi(2S) \to \gamma \eta_c(2S)$ will be measured, although no signal for the former is evident (yet). Note that the mass of the $\eta_c(2S)$ is now accurately known from B-meson decay at Belle [11] and from $\gamma\gamma$ fusion at CLEO [12].

– Detailed studies of χ_{c0}, χ_{c1}, and χ_{c2}. High-statistics single-photon tags of the intermediate χ_c states will allow various measurements of their decay branching fractions.

– Hadronic decays of $\psi(2S)$. A prime goal is to search for the h_c in $\psi(2S) \to \pi^0 h_c$. The decay $\psi(2S) \to \rho\pi$ will also be searched for, a branching ratio which is anomalously small.

– Exotica from $\psi(2S)$ decay. Radiative decay of high mass vectors is expected to be a prime source for glue-rich final states. (See the discussion in Section 2.3.) Although one expects the majority
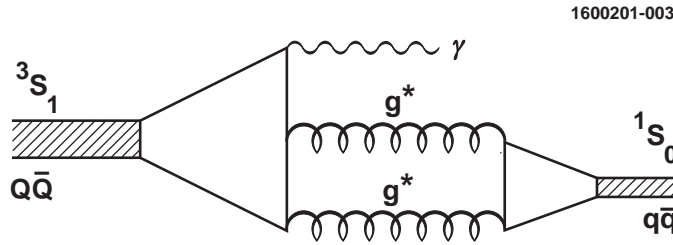
Fig. 9.2: Radiative decay of vector mesons, such as J/ψ, to a photon and two gluons. This process is expected to be a copious source of glueballs X via $J/\psi \rightarrow \gamma X$.

of this data to come from J/ψ running, $\psi(2S)$ decay would also allow flavour tagging through the hadronic decays where a low-mass vector meson (i.e., ρ, ω, ϕ) replaces the radiative photon. The possibility of studying J/ψ decay using $\psi(2S)$ running and tagging the J/ψ from $\psi(2S) \rightarrow \pi\pi J/\psi$ is also being investigated.

2.2 Physics at the $\psi(3770)$

CLEO-c has already begun taking a large data sample (eventually 3 fb^{-1}) at the $\psi(3770)$. The main goal of this running is to acquire a large sample of tagged D$\bar{\text{D}}$ events, but the opportunity presents itself for charmonium studies as well.

Measurements include searches for (presumably) rare decays of the $\psi(3770)$. Examples are $\psi(3770) \rightarrow \pi^+\pi^- J/\psi$; inclusive photons from $\psi(3770) \rightarrow \gamma X$, where one would expect to detect transitions to $X = \chi_{cJ}$ if the branching ratio is greater than about 10^{-3}; and the double cascade decay $\psi(3770) \rightarrow \gamma\chi_{c1,c2} \rightarrow \gamma\gamma J/\psi \rightarrow \gamma\gamma\ell^+\ell^-$ in which one might detect some ten events or so if there is no background and the branching ratio for $\psi(3770) \rightarrow \gamma\chi_{c1,c2}$ is more than $\approx 3 \times 10^{-4}$. These results would provide information on $1D_1/2S_1$ mixing.

2.3 Decays of the J/ψ

An important goal for CLEO-c and CESR-c is to acquire $\approx 10^9$ events at the J/ψ peak. In addition to various rare decay processes, a prime focus will be to study gluonic excitations through radiative decay, i.e., $J/\psi \rightarrow \gamma X$. The basic idea is shown in Fig. 9.2. A vector resonance can decay to three (but not two) vector particles. If one of these decay products is a photon, then there is a fair probability that the remaining two are gluons. Hence, this process is expected to give rise to final-state glueballs X [13].

2.4 Summary: the CLEO-c schedule

CLEO-c began taking data in October 2003, and has been running smoothly. An upgrade of CESR-c, adding more wigglers for higher luminosity, is on track for spring and summer 2004. The facility will run for approximately three years.

The values of the actual beam energies are decided upon dynamically by the collaboration, and will depend on technical issues as well as emerging physics cases. The original plan [10] is as follows:

  – Act I: Obtain 3 fb^{-1} at the $\psi(3770)$, yielding $\sim 1.5 \times 10^6$ D$\bar{\text{D}}$ events.
  – Act II: Obtain 3 fb^{-1} at $\sqrt{s} \approx 4.1$ GeV, yielding $\sim 3 \times 10^5$ tagged D$_\text{s}$ decays.
  – Act III: Obtain 10^9 J/ψ.

CLEO-c was encouraged by the QWG to consider running at the $\psi(2S)$ for a long period of time, making use of $\psi(2S) \rightarrow \pi\pi J/\psi$ to tag J/ψ. This prospect is being studied, including determination of the final-state polarization of the J/ψ and detector acceptance issues, as they relate to the ability to carry out a partial wave analysis.

Table 9.1: Main parameters of BEPCII in comparison with BEPC

Parameters	Unit	BEPCII	BEPC
Operation energy (E)	GeV	1.0–2.1	1.0–2.5
Injection energy (E_{inj})	GeV	Up to 1.89	1.3
Circumference (C)	m	237.5	240.4
Revolution frequency (f_r)	MHz	1.262	1.247
Lattice type		FODO + micro-β	FODO + low-β
β^*–function at IP (β_x^*/β_y^*)	cm	100/1.5	120/5
Natural energy spread (σ_e)		2. 73E$\times 10^{-4}$	2.64E$\times 10^{-4}$
Damping time ($\tau_x/\tau_y/\tau_e$)		25/25/12.5 at 1.89 GeV	28/28/14 at 1.89 GeV
RF frequency (f_{rf})	MHz	499.8	199.533
Harmonic number (h)		396	160
RF voltage per ring (V_{rf})	MV	1.5	0.6–1.6
Bunch number (N_b)		93	2$\times$1
Bunch spacing	m	2.4	240.4
Bunch current (I_b)	mA	9.8 at 1.89 GeV	35 at 1.89 GeV
Beam current (colliding)	mA	910 at 1.89 GeV	2$\times$35 at 1.89 GeV
Bunch length (σ_l)	cm	$\sim$1.5	$\sim$5
Impedance ($|Z/n|_0$)	Ω	$\sim$0.2	$\sim$4
Crossing angle	mrad	$\pm$11	0
Vert. beam–beam param. (ξ_y)		0.04	0.04
Beam lifetime	hrs	$\sim$2.7	6–8
Luminosity at 1.89 GeV	10^{31} cm^{-2}s^{-1}	100	1

3   THE BEPCII/BES III PROJECT

The Beijing Electron–Positron Collider (BEPC) is going to have a major upgrade, called the BEPCII project. The BEPCII feasibility report has been officially approved by the Chinese government.

The main physics goals of BEPCII are precision measurements and searches for new particles and new phenomena, mainly in the energy region from the J/ψ to the $\psi(3770)$. For example, precision measurements of D and D_s meson decays will be essential to allow the CKM matrix parameters, V_{cs} and V_{cd}, to be determined with a precision of a few per cent. Studies of light hadron spectroscopy and glueball candidates with very high statistics will be necessary to test QCD, in particular lattice QCD calculations, which should reach precisions of a few per cent in the coming years. Searches for $D_0\bar{D}_0$ mixing are important to look for physics beyond the Standard Model. The number of important physics topics in the τ-charm energy region is very large.

Our physics goals require major upgrades of the BEPC to increase its luminosity by two orders of magnitude and the BES detector to reduce its systematic errors, as well as to adapt to the small bunch spacing and high event rates. The large-scale upgrade will enable BEPC to approach the specifications of a factory-type machine, whose main parameters are listed in Table 9.1, along with a comparison to those of the current BEPC.

BEPCII will be a double-ring collider with superconducting micro-β magnets, a 500 MHz RF system with superconducting cavities, and a low-impedance antechamber beam pipe. The second ring can be accommodated in the existing BEPC tunnel. BEPCII will have a large horizontal crossing angle of 11 mrad at the southern interaction region. There will be 93 bunches per ring with a total current of 910 mA in each ring. The peak luminosity of BEPCII will be 10^{33}cm^{-2} s^{-1} at the beam energy of 1.89 GeV, which is about 100 times higher than that of the BEPC. The peak luminosity at the J/ψ and at

4.1 GeV c.m. energy will be about $0.6 \times 10^{33} \mathrm{cm}^{-2}\,\mathrm{s}^{-1}$. The upgrade of the linac will provide full energy injection up to 1.89 GeV for 'topping off' the beam. The positron injection rate will reach 50 mA/min compared to the present rate of about 5 mA/min. The number of events expected for one year of running for various physics topics is given in Table 9.2.

Table 9.2: Number of events expected in one year of running

Physics channel	CM energy (GeV)	Peak luminosity $(10^{33}\mathrm{cm}^{-2}\mathrm{s}^{-1})$	Physics cross-section (nb)	Number of events per year
J/ψ	3.097	0.6	$\sim$3400	10×10^9
τ	3.67	1.0	$\sim$2.4	12×10^6
$\psi(2S)$	3.686	1.0	$\sim$640	3.0×10^9
D	3.770	1.0	$\sim$5	25×10^6
D_s	4.030	0.6	$\sim$0.32	1.0×10^6
D_s	4.140	0.6	$\sim$0.67	2.0×10^6

Most of the existing utility facilities of the BEPC, after some upgrading, will be used for BEPCII. A cryogenics system of 1000 W at 4.2 K will be installed for the three different superconducting devices. The design of BEPCII will keep the electron beam in the outer ring during the dedicated synchrotron radiation running, and all synchrotron radiation beam lines and the experimental stations will be unchanged, but the beam current will be increased from 140 mA at 2.2 GeV to 250 mA at 2.5 GeV.

BEPCII is a high luminosity, multi-bunch collider, which requires a comparable high quality detector with modern technology. The main features of the detector are as follows (a schematic view of the BES III detector is shown in Fig. 9.3):

– Main draft chamber (MDC): the design features small cell structure, aluminium filled wires, and He-based gas, with expected performances of $\sigma_{xy} = 130$ μm, $\Delta p/p = 0.5\%$ at 1 GeV, and dE/dx = 6–7%. The stepped end plates provide space for the superconducting micro-β magnets;
– Electromagnetic calorimeter (EMCAL): CsI crystals of 15 radiation length (28 cm), with expected performances of $\Delta E/E = 2.5$ % at 1 GeV and $\sigma_{pos} = 0.5$ cm/$\sqrt{E}$;
– TOF: plastic scintillators with $\Delta T = 90$ ps for the barrel part and $\Delta T = 100$ ps for the end caps;
– 1 tesla superconducting solenoidal magnet;
– Resistive Plate Chambers (RPC) for muon identification: nine layers interleaved with the iron plates of the return yoke;
– Trigger: largely based on FPGA technology and using information of the MDC tracks and EMCAL showers, pipelined with a time latency of 6.4 μs.

The total estimated budget for the BEPCII will be around 640 million Chinese Yuan (about $77 million). The Chinese government will provide funding to cover the costs of the machine and the major part of the detector. Part of the detector cost is expected to be provided by international contributions. International cooperation is already helping IHEP with the design and R&D of BEPCII, as well as the production of some key devices, e.g., Brookhaven National laboratory is helping with the superconducting micro-β magnets; KEK is helping with the superconducting RF cavities and the superconducting solenoid magnet.

The preliminary design of BEPCII has been finished. The engineering design is under way and most parts are finalized. Contracts are already signed for many important items. The project is expected to be completed by the end of 2006, and physics running is scheduled in 2007.
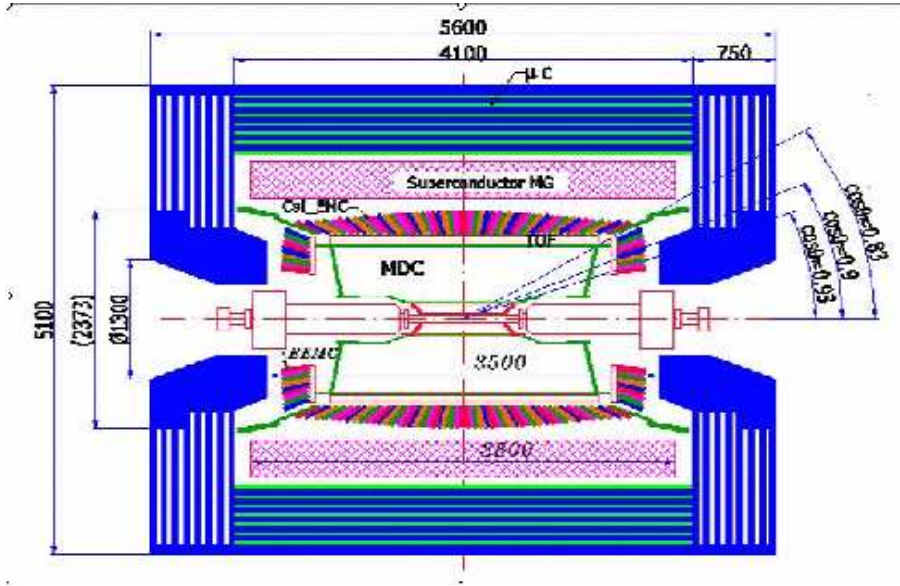
Fig. 9.3: Schematic view of the BES III detector

The great physics potential of BEPCII/BES III will attract the interest of many physicists who are warmly welcomed to join the BEPC/BES upgrade and its physics programme. The completion of the BEPC II will add a new machine of 'factory class' to the fabric of high-energy physics, thus adding new momentum to the research efforts in τ-charm physics.

4 B-FACTORIES

One of the goals of a Super B-factory is the search for new physics in B-meson decays. In addition, a very interesting programme on quarkonium physics can be undertaken since b decays are good sources of $c\bar{c}$ states. In this section we shall focus on the KEKB facility, although similar expectations and physical potential apply equally to the SLAC PEPIII project. In particular, there is a proposal to upgrade KEKB to a Super KEKB with a design luminosity of 5×10^{35} cm^{-2}s^{-1} which is 50 times the peak luminosity achieved by KEKB. The target annual integrated luminosity is 5 ab^{-1}.

Along with the luminosity upgrade the Belle detector would be upgraded. The largest challenge will be the very harsh background environment due to the high beam current. Another challenge is the background level in the end-cap and an upgrade to another advanced technology is necessary. Among the candidates, pure CsI crystals with photo tetrode readout is the most promising for the end-cap electromagnetic calorimeter (EECL) and tiles of plastic scintillator with silicon photomultipliers (SiPM) is a good candidate for the end-cap K_L^0 muon system (EKLM). The trigger and data acquisition systems should be upgraded to handle the 20 times higher occupancy level from the higher beam current. Computing is another technological challenge with online data having to be recorded at a speed of 250 MB/s after online reconstruction and reduction amounting to the data size of 5 PB/year. Including Monte Carlo simulations, a storage system holding 10–20 PB is needed at the beginning which should be expandable to several tens of PB.

In B-meson decays the $b\rightarrow c\bar{c}s$ subprocess is CKM-favoured so that final states containing charmonium particles are common. A super-B factory would provide superb opportunities for high-sensitivity measurements of the charmonium system and the discovery of missing charmonium states such as the h_c, or the D-wave states:

  – in the continuum: $e^+e^-\rightarrow\chi_{c1}$ $(c\bar{c})$; η_c $(c\bar{c})$; search for $C = -1$ states (h_c, etc.) in the χ_{c1}, η_c recoil spectra;

461

– in B decays, either with exclusive channels like B→K 1^3D_2 (how big is the suppression factor?) or with inclusive channels like B→1^3D_2→$\pi^+\pi^-$J/ψ at the $\Upsilon(4S)$.

Another exciting possibility is the discovery of one or more charmonium hybrid states. B-factories can also shed light on the possibility of D$\bar{\text{D}}$ molecules. The discovery of the $X(3872)$ just above D$^0\bar{\text{D}}^{*0}$ threshold by the Belle Collaboration has led to speculation that the $X(3872)$ is a D$\bar{\text{D}}^*$ molecule or some other 4-quark object. The high statistics available at a super B-factory would allow detailed studies of the $X(3872)$ and other new states, including D$\bar{\text{D}}$ molecules if they exist.

5 GSI

5.1 Introduction

The charmonium spectroscopy physics programme of the PANDA ($\bar{\text{P}}$ ANnihilations at DArmstadt) experiment using $\bar{\text{p}}$p annihilations at GSI [14] is an extension of successful experiments performed recently at the Fermilab antiproton accumulator. Advanced $\bar{p}$ cooling techniques and a more versatile detector setup will be employed, allowing for the first time the measurement of both electromagnetic and hadronic decays. The goal is to make comprehensive measurements of the spectroscopy of the charmonium system and hence provide a detailed experimental study of the QCD confining forces in the charm region to complement theoretical investigation.

Unlike e^+e^-, where only states with the quantum numbers of the photon ($J^{PC} = 1^{--}$) can be formed directly, all quantum numbers are directly accessible in $\bar{\text{p}}$p annihilation. Charmonium states are studied by accelerating the $\bar{\text{p}}$ beam to the energy of the resonance, which is then scanned by changing the beam momentum in small steps.

The experimental programme of PANDA also includes the study of gluonic excitations (glueballs and hybrids) in the charmonium sector, as well as the study of charmonium in nuclei.

5.2 Experimental apparatus

The PANDA experiment will be installed at the High Energy Storage Ring (HESR), a major component of the recently approved new accelerator facility at GSI in Darmstadt, Germany [14]. The antiproton beam will be produced by a primary proton beam from the planned fast cycling, superconducting 100 T·m synchrotron ring. The antiprotons will be produced with a rate of approximately 2×10^7/s and then stochastically cooled; after 5×10^{10} $\bar{\text{p}}$ have been stored, they will be transferred to the HESR where internal experiments in the momentum range from 1 to 15 GeV can be performed. Two modes of operation are foreseen: a high-luminosity mode, where peak luminosities of 2×10^{32} cm^{-2}s^{-1} will be reached with a beam momentum spread $\delta p/p \approx 10^{-4}$, achieved by means of stochastic cooling in the HESR ring, and a high-resolution mode, where for beam momenta below 8 GeV electron cooling will yield a smaller beam momentum spread $\delta p/p \approx 10^{-5}$ at a reduced luminosity of 10^{31}cm^{-2}s^{-1}.

The proposed PANDA detector is being designed to study the structure of hadrons in the charmonium mass range as well as the spectroscopy of double hypernuclei. The detector must provide (nearly) full solid-angle coverage, it must be able to handle high rates (2×10^7 annihilations/s) with good particle identification and momentum resolution for γ, e, μ, π, K and p. Additional requirements include vertex reconstruction capability and, for charmonium, a pointlike interaction region, efficient lepton identification, and excellent calorimetry (both resolution and sensitivity to low-energy photons).

A schematic view of the present detector concept is shown in Fig. 9.4. The antiprotons circulating in the HESR hit an internal hydrogen pellet (or jet) target, while for the nuclear target part of the experimental programme wire or fibre targets will be used. The detector consists of a Target Spectrometer (TS) and a Forward Spectrometer (FS).

The TS, for the measurement of particles emitted at laboratory polar angles larger than 5°, is located inside a solenoidal magnet, 2.5 m in length and 0.8 m in inner radius. Its main components are four
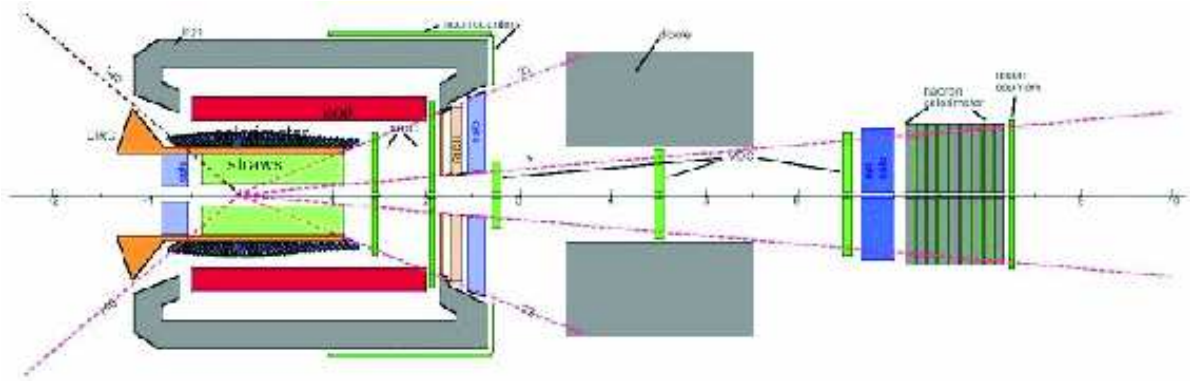
Fig. 9.4: Schematic view of the PANDA detector (side view)

diamond or silicon start detectors surrounding the interaction region followed by a 5-layer silicon microvertex detector; 15 layers of crossed straw tubes, for the measurement of charged-particle trajectories; a cylindrical DIRC and a forward aerogel Čerenkov detector for particle identification; an electromagnetic calorimeter consisting of $PbWO_4$ crystals with Avalanche Photo Diode (APD) readout. The region between the calorimeter and the end-cap will be instrumented with two sets of mini drift chambers; scintillator strips used for muon identification will be located behind the return yoke of the magnet.

The FS will measure particles emitted at polar angles below $10°$ in the horizontal and $5°$ in the vertical direction. It will consist of a dipole magnet with a 1 m gap, with MDCs before and after for charged-particle tracking. Particle identification will be achieved by means of a TOF stop and a dual-radiator RICH detector. Other components of the FS are an electromagnetic and a hadronic calorimeter followed by a set of muon chambers.

Detailed simulations of the detector concept presented here show its ability to measure electrons, muons, pions, kaons and photons over a large phase space region. Combining a momentum resolution of 1–2% with a high discriminating power for particle identification and a nearly 4π solid angle coverage allows the application of strong kinematical constraints, which will serve to achieve an excellent level of final-state identification and background suppression.

The PANDA project is part of the recently approved new accelerator facility at GSI. An international collaboration is currently forming to develop a detailed technical proposal for the design and construction of the detector system.

5.3 Physics programme

5.3.1 *The ground state of charmonium,* $\eta_c(1^1S_0)$

Despite the abundance of experimental measurements, it is disappointing how little is known about the ground state of charmonium, $\eta_c(1^1S_0)$. Five new measurements of its mass were reported in 2002 and 2003, disagreeing by more than 5 MeV [15]. The fit to all existing measurements of the η_c mass yields an error of 1 MeV (adequate to the accuracy of present theoretical model calculations), but the consistency between the various measurements is fairly poor (CL = 0.5%). In addition to that, as the accuracy of theoretical calculation increases it will be mandatory to measure its mass with a precision better than 1 MeV. The width of the η_c is even more uncertain. Four new measurements were reported in 2002 and 2003, and the fit to all data yields a width value of (25.0 ± 3.3) MeV, with a CL of 0.05%. It is important to know the width of the η_c because a width value as large as 25 MeV is difficult to reconcile with simple quark models, and it has been suggested that instanton effects may be responsible [16].

It must be stressed that unlike the E760/E835 experiments [17,18], which were obliged to identify η_c formation in the extremely weak two-photon decay channel $(BR(\eta_c \to \gamma\gamma) \simeq 3 \times 10^{-4})$, the PANDA

detector at the new facility at GSI is being designed to detect both electromagnetic and hadronic final states. This will make it possible to study the η_c in several decay channels, which have hundred times larger branching ratios: $\eta_c \rightarrow 2(K^+K^-), K\overline{K}\pi, 2(\pi^+\pi^-), \eta\pi\pi$, etc.

5.3.2   *The radial excitation of charmonium, $\eta_c(2S)$*

The $\eta_c(2S)$ was discovered by the Belle experiment in the hadronic decays of the B meson [19], with a mass of $(3654 \pm 6 \pm 8)$ MeV, incompatible with the Crystall Ball observation [20]. The $\eta_c(2S)$ was then seen also by BaBar [21] and Cleo [22] in $\gamma\gamma$ collisions. The mass measurements of the three experiments are consistent [15] and yield a value of (3637.7 ± 4.4) MeV (CL = 14%); this value is only marginally consistent with most model calculations and it has been suggested that coupled channels effects may shift the $\eta_c(2S)$ mass [23]. The present accuracy on the $\eta_c(2S)$ width is only 50%, the measured value being (19 ± 10) MeV. More precise measurements of the mass and width are clearly needed.

A search for the $\eta_c(2S)$ was performed by the experiments E760 and E835 at Fermilab in the process $\overline{p}p \rightarrow \eta_c(2S) \rightarrow \gamma\gamma$ [17, 24]. No signal was observed by either experiment. The technique employed by E760/E835 suffered from the severe limitations due to the relatively high background from $\pi^0\pi^0$ and $\pi^0\gamma$ compared to the small $\gamma\gamma$ signal [25]. Further measurements using this channel will require increased statistics and a substantial reduction of the background. The real significant improvement of PANDA with respect to the Fermilab experiments will be the ability to detect the hadronic decay modes, such as $\eta_c(2S) \rightarrow K^*\overline{K}^*$ or $\eta_c(2S) \rightarrow \phi\phi$, which will allow a clean identification of this state.

5.3.3   *The $h_c(^1P_1)$ resonance of charmonium*

The singlet P resonance of charmonium $h_c(^1P_1)$ is of extreme importance in determining the spin-dependent component of the $q\overline{q}$ confinement potential.

If the recent observation of h_c, described in Chapter 3, is confirmed during this decade, the precise measurement of its width will have to wait for the high statistics to be accumulated by the PANDA experiment. By comparing the total width with the probably dominant radiative width to $\eta_c\gamma$, it will be possible to measure its partial width to light hadrons, relevant for NRQCD calculations. It must be pointed out that owing to its very narrow width (≤ 1 MeV) and expected low yields, only a $\overline{p}p$ formation experiment like PANDA will be able to perform this measurement and to carry out a systematic study of its decay modes. The study of the h_c constitutes a central part of the PANDA charmonium physics programme.

5.3.4   *Radiative transitions of the $\chi_J(^3P_{0,1,2})$ charmonium states*

The measurement of the angular distributions in the radiative decay of the χ_1 and χ_2 states formed in $\overline{p}p$ annihilations provides insight into the dynamics of the formation process, the multipole structure of the radiative decay, and the properties of the $c\overline{c}$ bound state. A comparison of the E760 result at the χ_{c2} [26] with the Crystal Ball result at the χ_{c1} [27] is not consistent with theory, and may suggest the existence of additional contributions to the theoretical predictions for the M2 amplitudes. The simultaneous measurement of both angular distributions has been recently performed by E835 [28]. They too observed a discrepancy with respect to theoretical predictions, which could indicate the presence of competing mechanisms, leading to the cancellation of the M2 amplitude at the χ_{c1}. The effect seen by E835 is at the 2.5σ level, therefore further high-statistics measurements are clearly needed to increase the significance of this result.

5.3.5   *Charmonium states above the $D\overline{D}$ threshold*

The energy region above the $D\overline{D}$ threshold at 3.73 GeV will be object of many studies during this decade. This is the region in which narrow $^1D_2$, $^3D_2$ states (which are narrow because they cannot decay to $D\overline{D}$) and the first radial excitations of the singlet and triplet P states are expected to exist, as shown in Chapter 3. The discovery of X(3872) has raised further interest in this energy region: the nature of this

new, narrow state is not yet clear, and speculation ranges from a $D^0\overline{D}^{0*}$ molecule to a $^3D_2$ state. There are theoretical problems with all these interpretations, and further, more accurate measurements of its width and particularly of its decay modes are needed to shed light on this state [23]. This kind of study is ideally suited for a $\overline{p}p$ formation experiment. The study of the energy region above the $D\overline{D}$ threshold is a central part of the charmonium physics programme of PANDA. It will require high-statistics, small-step scans of the entire energy region accessible at GSI.

5.3.6 Charmonium hybrids

Predictions for hybrids come mainly from calculations based on the bag model, flux tube model, constituent gluon model and recently, with increasing precision, from lattice QCD (LQCD) [31]. For these calculations the parameters are fixed according to the properties of the known $Q\overline{Q}$ states. All model predictions and LQCD calculations agree that the masses of the lowest-lying charmonium hybrids are between 3.9 and 4.5 GeV and that the state with the lowest mass has $J^{PC} = 1^{-+}$ [32]. Some of the charmonium hybrids have spin exotic quantum numbers, so mixing effects with nearby $c\overline{c}$ states are excluded for them, thus making their experimental identification easier. Predictions for the widths of these states range from a few MeV to several tens of MeV. Cross-sections for the formation and production of charmonium hybrids are estimated to be similar to those of normal charmonium states.

In PANDA two kinds of experiments can be done: formation and production. Formation experiments would generate non-exotic charmonium hybrids, while production experiments would yield a charmonium hybrid together with another particle, such as a π or an η. In $\overline{p}p$ annihilation, production experiments are the only way to obtain exotic quantum numbers. This distinction is a very powerful tool from the experimental point of view: the detection of a state in production and its non-detection in formation is a clear, unique signature for exotic behaviour.

5.3.7 Charmonium in nuclei

The proposed experimental programme of PANDA will address open problems of in-medium modifications of hadrons with charmed quarks in nuclei and the interaction of these hadrons with nuclei. This is, on the one hand, an extension of the present chiral dynamics studies with partial restoration of chiral symmetry in the hadronic environment, from the light quark to the open charm quark sector. On the other hand, this programme is focused on the first experimental studies of the charmonium–nucleon and charmonium–nucleus interaction, which is also of basic importance for ultra-relativistic heavy-ion collisions.

6 JEFFERSON LAB 12 GEV UPGRADE

The Jefferson Laboratory has plans to upgrade the Continuous Electron Beam Accelerator Facility (CEBAF) to 12 GeV [33]. The 12 GeV electron beam will be used to produce 9 GeV photons in the new Hall D. Photon fluxes of up to 10^8 photons/s with 50% linear polarization are achievable. In Hall D, a tagged coherent bremsstrahlung beam and solenoidal detector will be constructed in support of a programme of gluonic spectroscopy. The detector has been optimized to provide nearly hermetic acceptance for both charged particles and photons. In addition, a combination of particle identification systems will allow very good K–π separation. Optimization will allow the detector to fully reconstruct exclusive many-body final states. In conjunction with high statistics, this will allow excellent partial wave analyses of many final states. The 4π acceptance of the Hall D detector and the energy resolution of its tagged beam could help to reduce the background considerably.

The threshold production of charmonium and open charm production open up a new window into QCD dynamics; in particular, these reactions are sensitive to multiquark, gluonic, and so-called 'hidden colour' correlations in nucleons and nuclei. In contrast to diffractive charm production at high energy, which tests the behaviour of the gluon structure functions at small x, charm production near threshold

tests the structure of the target near $x = 1$ and its short-range behaviour. This difference results from the kinematics of the reaction products. For J/ψ production off the nucleon, the threshold energy is $E_\gamma = 8.2$ GeV and because of the large mass of the charmed quark the $c\bar{c}$ fluctuation of the photon travels over a short coherence length. Charm production near threshold implies a small impact parameter so that all five valence quarks must be in the same small interaction volume and all the quarks must be involved in the reaction mechanism. For nucleon targets this implies that three-gluon exchange may dominate two-gluon and one-gluon exchange.

Even though the $c\bar{c}$ pair is created with rather high momentum at threshold, it may be possible to observe reactions where the pair is captured by the target nucleus forming 'nuclear-bound quarkonium'. The discovery of such qualitatively new states of matter would be significant.

7   LHC (ATLAS/CMS)

The Large Hadron Collider (LHC) is a proton–proton collider currently being built at CERN and scheduled to start in the second half of 2007. It will provide many opportunities for studying heavy quarkonia, which will be produced at unprecedented rates and energies. Significant contributions may be expected in the fields of heavy quarkonia production and decays, whereas high background rates will make dedicated studies on heavy quarkonia spectroscopy difficult (as at other hadron machines).

This section concentrates on future opportunities at the two multipurpose LHC experiments ATLAS and CMS. Aspects related to the dedicated B-physics experiment LHCb and to studies 'in media' are covered in separate sections.

Heavy quarkonia production issues at the LHC in general are discussed in Section 7.1, and therefore apply to both ATLAS and CMS. Section 7.2 presents selected topics from current, heavy-quarkonia-related ATLAS studies. Results from CMS were not available at the time of writing. The selected topics are by no means comprehensive and are intended to serve as illustrative examples only.

7.1   Heavy quarkonia production at the LHC

Thanks to its high collision energy (design centre-of-mass energy 14 TeV) and high luminosity (design luminosity $\mathcal{L} = 10^{34}$ cm^{-2}s^{-1}), the LHC will be able to explore a new high-energy frontier at the TeV scale. It is expected, however, that the LHC will not operate at its design luminosity from the beginning, but rather at an initial luminosity of $\mathcal{L} = 2 \times 10^{33}$ cm^{-2}s^{-1}. This initial period will be best suited for dedicated studies on heavy quarkonia at the LHC, both in view of affordable trigger rates, modest pile-up (i.e., minimum-bias events superimposed on interesting signal), event reconstruction, etc.

The production rates for heavy quark flavours at the LHC will be huge. The total cross-section at the LHC is about 100 mb; the expected total cross-section for charm production is 7.8 mb, for bottom production 0.5 mb, and for top production 0.8 nb, respectively [34]. Thus, for an integrated luminosity of only 1 fb^{-1}(i.e., about one week of running at initial luminosity), as many as 7.8×10^{12} charm events, 0.5×10^{12} bottom events, and 0.8×10^{6} top events will be produced.

Figure 9.5 shows the differential cross-section for heavy-quark pair production at the LHC as a function of the transverse momentum of the heavy quark [34]. Up to next-to-leading-order (NLO) perturbative QCD, the c and b cross-sections are identical for high $p_{\rm T}$; differences due to mass effects show up only for very small $p_{\rm T}$ values ($p_{\rm T} < 20$ GeV). For orders higher than NLO, the spectrum for c quarks is expected to become softer, and differences might become visible even for high $p_{\rm T}$.

In order to predict the production rates for heavy quarkonia at the LHC, the available models (including Monte Carlo generators) are tuned with Tevatron data and extrapolated to LHC energies; see [35] for a detailed description. Fig. 9.6 illustrates the results of this procedure applied to the prediction of the J/ψ production cross-section. An eventual measurement of heavy quarkonia production rates at the LHC will help in understanding, for high energies and $p_{\rm T}$, the roles and importance of individual production mechanisms (e.g., colour-singlet vs. colour-octet) and the applicability of concepts used so
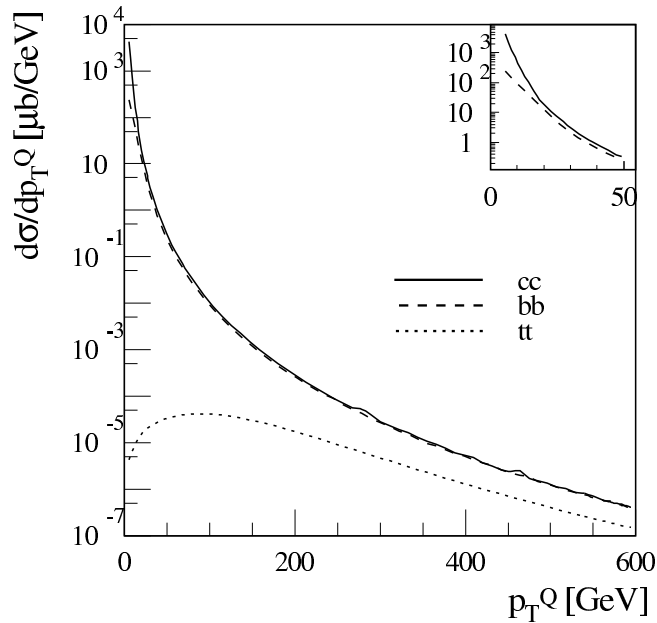
Fig. 9.5: Differential cross-section for heavy-quark-pair production as a function of the transverse momentum p_T^Q of the heavy quark. The smaller figure shows the region $p_\mathrm{T}^Q < 50$ GeV for charm and bottom production [34].

far in the calculations (e.g., factorisation in NRQCD). It might also be possible to probe the gluon density in the proton [36].

The fact that the LHC will produce heavy quarkonia with high transverse momentum in large numbers will also allow for a better discrimination between different models of heavy quarkonia polarization, like NRQCD and the colour-evaporation model; see Ref. [35]. For example, NRQCD predicts transversely polarized J/ψ and $\psi(2S)$ (see Fig. 9.7) at high p_T. This seems not to be supported by CDF data [42], although the statistics is too low to draw definitive conclusions. Measurements at the LHC will help in resolving the issue of quarkonium polarization.

7.2 Heavy quarkonia studies with ATLAS: selected topics

The ATLAS experiment has been designed both to maximize the discovery potential for new physics and to enable high-accuracy measurements. ATLAS also accommodates features which make it possible to incorporate an ambitious B-physics programme, in particular in the first years of running at low luminosity. Most of the foreseen studies on heavy quarkonia will be performed in the context of the B-physics programme. For a full review of the ATLAS detector and physics performance, see Ref. [34].

7.2.1 ATLAS B-Physics Trigger Issues

ATLAS will have a flexible and efficient multi-level trigger system. The ATLAS trigger will consist of three levels, reducing the trigger rates from 40 MHz to $\mathcal{O}(20)$ kHz at level 1, to $\mathcal{O}(1\text{–}5)$ kHz at level 2, and to $\mathcal{O}(200)$ Hz at level 3 ('Event Filter', EF).

The classical B-physics trigger scenario [43] foresees to trigger for a muon with $p_\mathrm{T} > 6$ GeV and pseudo-rapidity $|\eta| < 2.4$ at level 1; to confirm this muon with better resolution and efficiency at level 2, together with performing a full scan of the Inner Detector (ID) to search for interesting signatures; and to refine the search at the EF level, where offline algorithms will be used and calibration and alignment data will be available.

In view of tight funding constraints, changes in detector geometry, the possible usage of a reduced detector at start-up, and a changed luminosity target at start-up ($1\rightarrow2 \times 10^{33}$ cm^{-2}s^{-1}), the classical
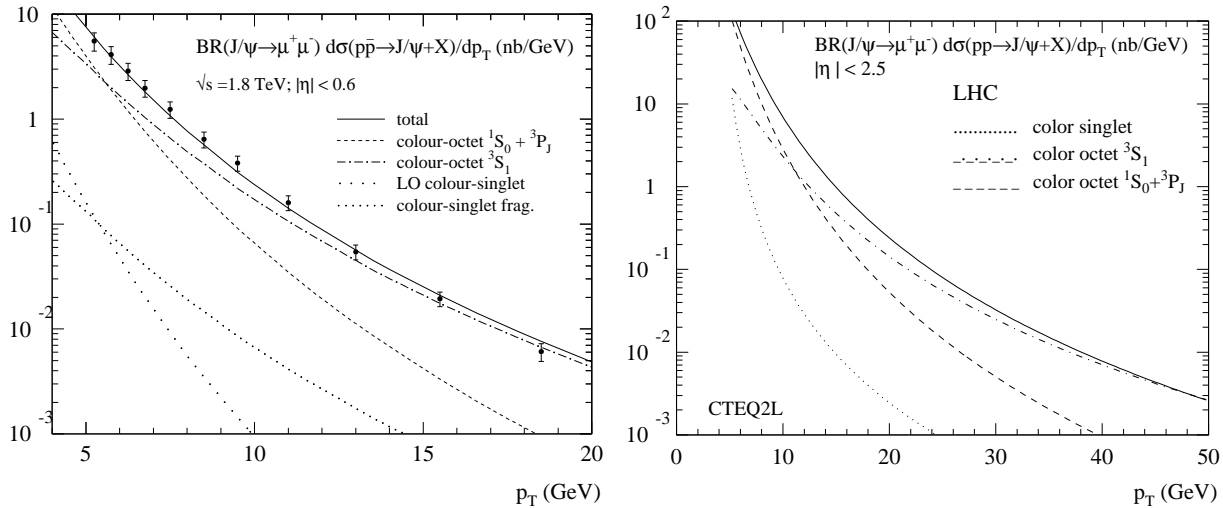
Fig. 9.6: Left: Colour-singlet and colour-octet contributions to direct J/ψ production in $p\bar{p}{\to}J/\psi + X$ at the Tevatron, together with experimental data from CDF [38]. Right: cross-sections for J/ψ production in $pp{\to}J/\psi+X$ at the LHC, as obtained with the Monte arlo generator PYTHIA supplemented by leading order colour-octet processes [39, 40]. Plots are taken from Refs. [35, 37].

scenario had to be revised; see Ref. [44] for details. In addition to more flexibility with respect to varying luminosity conditions, the revised scenario foresees additional trigger objects at level 1 (e.g., muon, 'Regions-of-Interest'/RoIs from calorimeter jet or electromagnetic triggers), and the RoI-guided search for tracks in the ID, in order to avoid the resource-intensive ID full scan. Studies are still ongoing, but first results look promising.

In the context of heavy quarkonia studies, the di-muon trigger will be the most important one. Fig. 9.8 shows the expected rates at a luminosity of $\mathcal{L} = 10^{33}$ cm^{-2}s^{-1} [44]. The di-muon trigger will allow for an effective selection of channels with $J/\psi(\mu^+\mu^-)$, rare decays like B${\to}\mu^+\mu^-$(X), etc. Minimum possible thresholds in the level 1 muon trigger are $p_T > 5$ GeV (barrel) and $p_T > 3$ GeV (end-cap), but the actual thresholds will be determined by the (yet incompletely known) level 1 muon rate. At higher trigger levels (level 2, EF), the muons from level 1 will be confirmed using the ID and Muon Detector precision chambers. Preliminary studies yield modest di-muon trigger rates of ∼200 Hz after level 2, and of ∼10 Hz after the EF, for the initial luminosity scenario of $\mathcal{L} = 2 \times 10^{33}$ cm^{-2}s^{-1}.

7.2.2 Recent ATLAS Studies on J/ψ

The main emphasis in ongoing ATLAS physics-related studies lies on technical issues like validation and optimization of the architecture of trigger and offline software, performance, etc., not on doing full-fledged, detailed physics analyses. The results presented here are taken from a study on measuring the direct J/ψ production cross-section, carried out in a wider context of studies on the performance of a staged (i.e., incomplete) detector in an initial commissioning period of 1 fb^{-1} (corresponding to one year at 5% of the planned start-up luminosity).

The determination of the direct J/ψ production cross-section will be one of the first B-physics measurements in ATLAS. There will be a large J/ψ rate after the level 1 trigger, whose direct J/ψ contribution will not be known. The measurement of the direct J/ψ production cross-section is, among other things, important in order to find the best strategy for selecting b-events, e.g., to optimize the interplay between p_T and vertexing cuts.

Events of the type $pp{\to}J/\psi(\mu^+\mu^-)+X$ were generated with a version of PYTHIA which includes colour-octet processes [39–41]. One of the muons coming from J/ψ was required to have $p_T > 6$ GeV, the second to have $p_T > 3$ GeV. For this purpose, functionality to enable filtering at generation time [45]
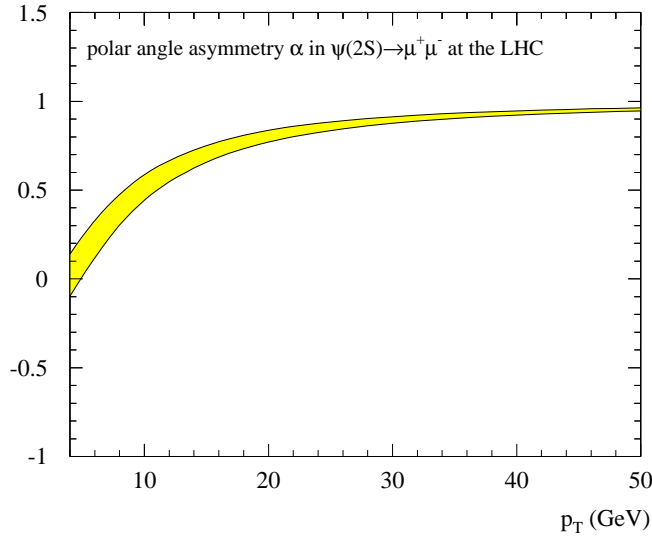
Fig. 9.7: Polar angle asymmetry $\alpha = (\sigma_T - 2\sigma_L)/(\sigma_T + 2\sigma_L)$ for $\psi(2S)$ production in $pp \to \psi(2S)(\to \mu^+\mu^-) + X$ at the LHC as a function of p_T [37].

was implemented into PYTHIA. Taking muons with p_T as low as 3 GeV is only possible when information from the hadronic calorimeter (Tile Calorimeter) is additionally taken into account, to allow for muon/hadron separation [34].

As a result, one obtains a cross-section for direct J/ψ production of about 5 nb [45]. Typical values for relevant resolutions are primary vertex resolution $\sigma_{PV} < 15 \ \mu$m (given by the LHC beam cross-section); secondary vertex resolution $\sigma_{xy}(\text{core}) \simeq 70 \ \mu$m and $\sigma_{xy}(\text{tail}) \simeq 150 \ \mu$m; mass resolution $\sigma_{J/\psi} \simeq 40$ MeV. Preliminary studies suggest that, based on those performance parameters, a good separation of direct J/ψ's and J/ψ's from B-decays will be feasible. For a qualitative illustration, see Fig. 9.9.

7.2.3 Recent ATLAS Studies on B_c

The expected large production rates at the LHC will also allow for precision measurements of B_c properties. Assuming a branching ratio $f(b \to B_c) \simeq 10^{-3}$, an integrated luminosity of 20 fb^{-1} (i.e., one year at initial luminosity), and requiring a level 1 muon with $p_T > 6$ GeV and $|\eta| < 2.4$, recent estimates show that ATLAS will be able to record about 5600 events of the type $B_c \to J/\psi \, \pi$, and about 100 events of the type $B_c \to B_s \, \pi$.

The channels studied so far in ATLAS are $B_c \to J/\psi \, \pi$ for B_c mass measurement, and $B_c \to J/\psi \, \mu\nu$, since it provides a clean signature and can be used as an ingredient for determination of the CKM matrix element $|V_{cb}|$ [34]. Examples of older studies can be found in Ref. [46].

Since the production of B_c is suppressed by the hard production of an additional $c\bar{c}$ pair, Monte Carlo generation of B_c events using standard tools (e.g., PYTHIA) is CPU intensive. As an example, out of 100 000 PYTHIA pp events, one obtains about one B_c event, which in turn does not necessarily survive the ATLAS level 1 trigger selection. Recent developments in ATLAS have therefore concentrated on implementing dedicated B_c generators into PYTHIA. One approach is via the so-called 'Fragmentation Approximation Model', the other the so-called 'Full Matrix Element' (FME) approach [47].

The FME approach is based on the concept of extended helicity, i.e., the grouping of Feynman diagrams into gauge-invariant sub-groups to simplify the calculations, an approach never before followed in $gg \to QQ$ processes. It takes into account matrix elements from PQCD up to $\mathcal{O}(\alpha_s^4)$ (36 diagrams). Results obtained with the FME generator (subroutine BCVEGPY) in PYTHIA are shown in Figs. 9.10
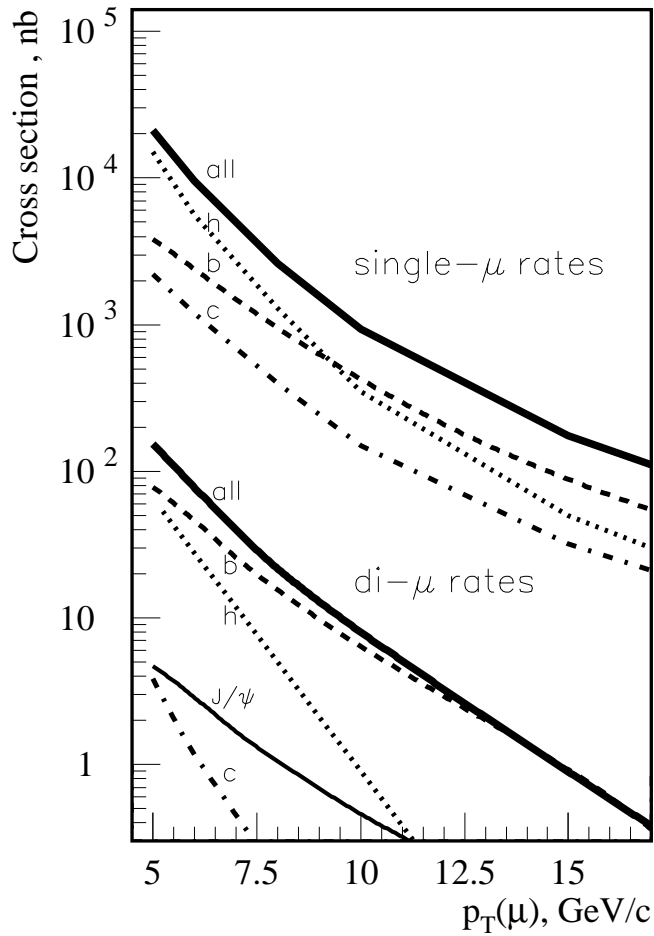
Fig. 9.8: Single-muon and di-muon cross-sections. Curves are shown for muons from K and π in-flight decays (labelled 'h'), b and c decays, and for the sum of all sources ('all'). Muons are considered within $|\eta| < 2.5$. For di-muons, the horizontal axis shows the p_T of the lower-p_T muon. At least one muon must have $p_T > 6$ GeV and $|\eta| < 2.4$ according to level 1 trigger conditions [44].

(total cross-sections of B_c and B_c^* productions) and 9.11 (B_c pseudo-rapidity distribution). In terms of CPU performance, BCVEGPY is six times faster than other Monte Carlo generators available.

Studies on B_c physics performance in ATLAS are ongoing, where events generated by BCVEGPY /PYTHIA are passed through a full GEANT3 detector simulation and are subsequently reconstructed. As a preliminary result, a mass resolution of $\sigma_{B_c} = 74$ MeV was obtained in the channel $B_c \rightarrow J/\psi\,\pi$ for a staged-detector scenario.

7.3 Conclusions and outlook

The LHC will be a heavy quarkonia factory, producing them in high statistics up to large transverse momenta. Measurements of heavy quarkonia production rates at the LHC will be valuable for a deepened understanding of the production mechanisms involved and the applicability of the present theoretical approaches.

The multi-purpose experiments ATLAS (and CMS) at the LHC have the potential to play important roles in exploring the properties of heavy quarkonia. A deeper knowledge of heavy quarkonia properties is not only interesting as such, but also of vital interest for other physics fields, e.g., to understand the backgrounds occurring there.
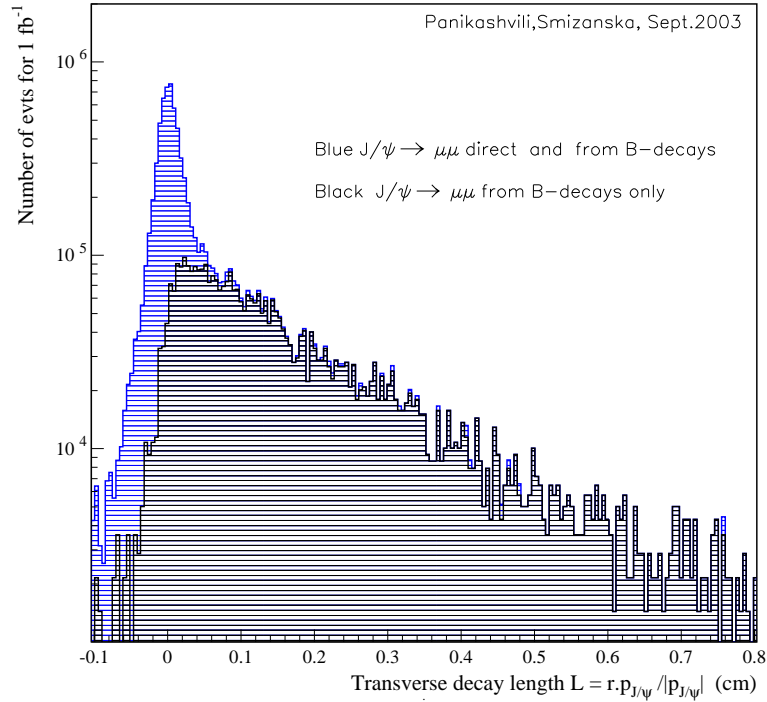
Fig. 9.9: The expected ATLAS potential for separating direct J/ψ's and J/ψ's from B-decays [45]. As discriminating variable, $L = \vec{r} \cdot \vec{p}_{J/\psi}/|\vec{p}_{J/\psi}|$ is used, where $\vec{r}$ and $\vec{p}_{J/\psi}$ denote the vectors of transverse J/ψ decay radius and transverse J/ψ momentum, respectively.

ATLAS is planning to continue the studies on heavy quarkonia in the future, including topics not covered until now like cross-section measurements for $\psi(2S)$ or for the process $\chi_c \rightarrow J/\psi\,\gamma$, polarization measurements, and studies on Υ states.

8   LHCB

8.1   The LHCb detector

The LHCb detector is designed to exploit the large number of b-hadrons produced at the LHC in order to make precision studies of CP asymmetries and of rare decays in the B-meson systems. It has a high-performance trigger which is robust and optimized to collect B mesons efficiently, based on particles with large transverse momentum and displaced decay vertices.

The detector can reconstruct a B-decay vertex with very good resolution and provide excellent particle identification for charged particles. Excellent vertex resolution is essential for studying the rapidly oscillating B_s mesons and in particular their CP asymmetries. It also helps to reduce combinatoric background when reconstructing rare decays.

The LHCb experiment plans to operate with an average luminosity of 2×10^{32} cm^{-2} s^{-1}, which should be obtained from the beginning of the LHC operation. Running at this luminosity has further advantages. The detector occupancy remains low, and radiation damage is reduced. Events are dominated by single pp interactions that are easy to analyse. The luminosity at the LHCb interaction point can be kept at its nominal value while the luminosities at the other interaction points are being progressively increased to their design values. This will allow the experiment to collect data for many years under constant conditions. About 10^{12} b$\bar{\text{b}}$ pairs are expected to be produced in one year of data taking.

In addition to investigating CP violation in B-meson decays, the physics programme of the LHCb experiment will include studies of rare B and τ decays, D–$\overline{\text{D}}$ oscillations and B_c-meson decays.
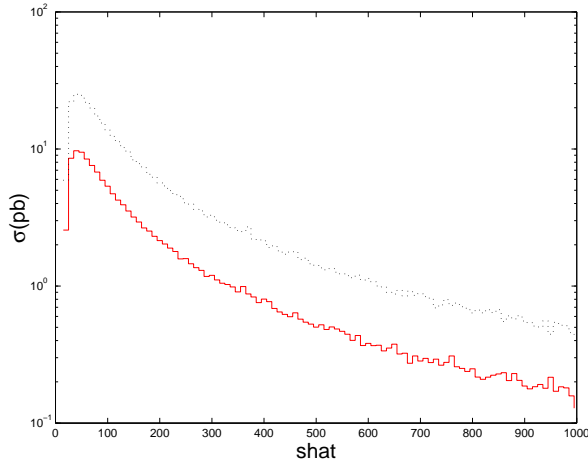
Fig. 9.10: Integrated cross-sections for the sub-process $gg{\to}B_c(B_c^*) + b + \bar{c}$ as obtained with the BCVEGPY Monte Carlo generator [47]. The solid (dotted) line corresponds to B_c (B_c^*) production. 'shat' denotes $\sqrt{\hat{s}}$, the centre-of-mass energy of the sub-process.
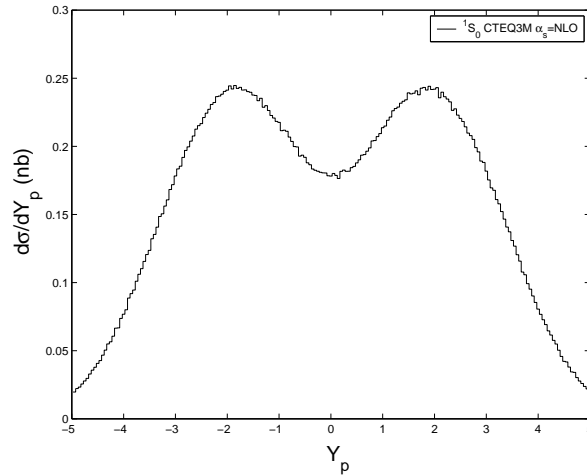
Fig. 9.11: The B_c pseudo-rapidity distribution obtained with the parton distribution function CTEQ3M. For details see Ref. [47].

Fig. 9.12 shows the layout of the LHCb detector. It consists of the beam pipe, VELO (VErtex LOcator), dipole magnet, tracking system, two Ring Imaging Cherenkov detectors with three radiators (RICH1 and RICH2), calorimeter system and muon system.

The trigger system is designed to suppress the initial rate of about 40 MHz to approximately 200 Hz by selecting the events with high-p_T hadrons, leptons and photons, requiring secondary vertices, and performing partial event online reconstruction to select the desired b-hadron decays. The trigger system is designed to be flexible, robust and efficient. Events are selected by various criteria that can be easily adjusted according to the experimental conditions. For a full review of the LHCb detector and physics performance, see Refs. [48, 49].

8.2 Recent LHCb studies on B_c

The B_c meson is the ground state of the $\bar{b}c$ system which in many respects is an intermediate between charmonium and bottomonium systems. However, since the B_c mesons carry flavour, they provide a window for studying heavy-quark dynamics very different from that of by $c\bar{c}$- and $b\bar{b}$-quarkonia.

The $\bar{b}c$ system exhibits a rich spectroscopy of orbital and angular-momentum excitations, radiative and weak decays. In addition, the B_c also provides a good place for extracting the Cabibbo–Kobayashi–Maskawa (CKM) matrix elements V_{cb} and V_{ub}. Two-body hadronic decays of B_c mesons can play an important role for the exploration of CP violation. For a recent review of the B_c physics issues, see Ref. [50].

The production of B_c states at high p_T is well described by b-quark fragmentation, while the complete $O(\alpha_s^4)$ calculations show the dominance of the recombination mechanism in the low-p_T region (see Fig. 9.13 where the p_T dependence of B_c and B_c^* production is shown).

The low-p_T region is dominated by high-momentum B_c (see Fig. 9.14) that gives additional advantages for the LHCb detector where B_c meson decays will produce secondary vertices well separated from the primary one. This fact ensures that B_c decays will satisfy the LHCb trigger conditions and provides the possibility of strong background suppression.

The exclusive decay channel $B_c^{\pm}{\to}J/\psi\pi^{\pm}$, $J/\psi{\to}\mu^+\mu^-$ has been studied in Ref. [51]. B_c mesons with $m = 6.4$ GeV and $\tau = 0.47$ ps were used for the signal Monte Carlo. The main background
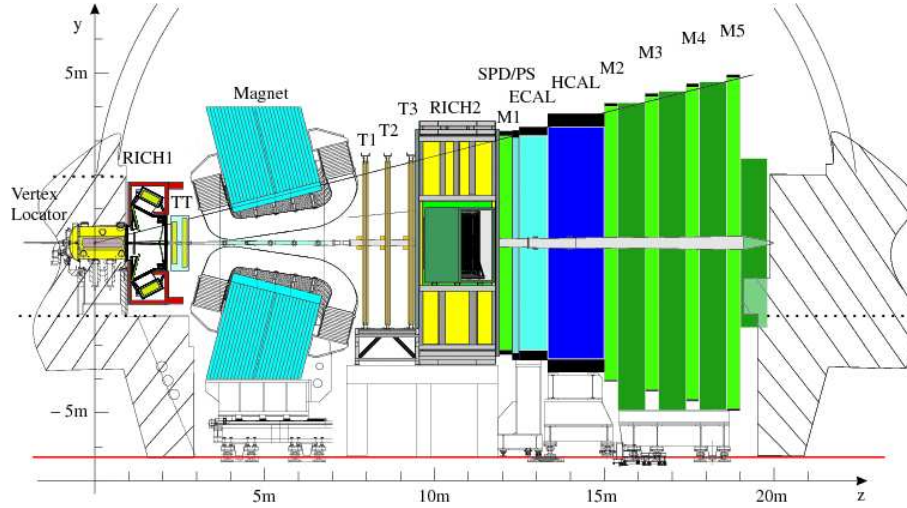
Fig. 9.12: LHCb detector layout

comes from the prompt J/ψ production (~ 0.8 mb) and B$\rightarrow$J/ψX decays. The complete GEANT simulation of the signal and background events (including minimum-bias background) has been performed with the detailed description of the detector response. Trigger algorithms have been applied, B$_c\rightarrow$J/$\psi\pi$ candidates have been reconstructed using full pattern recognition, and specific offline cuts have been applied to reject background.

The mass resolution is shown in Fig. 9.15 with the shaded area representing the surviving background. A clean and narrow signal is observable, with an expectation of about 14 k B$_c\rightarrow$J/$\psi\pi$ decays reconstructed per year with a B/S ratio estimated to be < 0.8.

The reconstructed events were used to determine the B$_c$ lifetime as well. The difference between true and reconstructed lifetime is shown in Fig. 9.16. The proper time resolution is about 0.04 ps and can be improved using high-momentum B$_c$ mesons.

LHCb is planning to study B$_c$ mesons production including radiative B$_c^*$ decays as well as other ground-state decay channels.

9 ALICE

ALICE is the dedicated heavy-ion experiment at the LHC. The apparatus will investigate the properties of strongly interacting matter at extreme energy density where the formation of quark–gluon plasma (QGP) is expected [52]. For this purpose, heavy quarkonium states are especially relevant since they provide, via their leptonic decays, an essential probe of the medium produced in the collision. A lot of effort has been devoted to the subject (for reviews see Refs. [53, 54]) since the early predictions of charmonium suppression by Debye screening in a deconfined medium [55]. The LHC energy is unique for such studies since it allows, for the first time, the spectroscopy of charmonium and bottomonium resonances in heavy-ion collisions. In particular, because the $\Upsilon(1S)$ is expected to dissolve only significantly above the critical temperature [56,57], the spectroscopy of the Υ family at LHC energies should reveal unique information on the characteristics of the QGP [58]. On the other hand, the study of heavy-quark resonances in heavy-ion collisions at the LHC is subject to significant differences with respect to lower energies. First, in addition to prompt charmonia produced directly via hard scattering, secondary charmonia can be produced from bottom decay [59], D$\bar{\text{D}}$ annihilation [60], and by coalescence mechanisms which could result in enhancement rather than suppression [61]. Then, in the environment of a heavy-ion reaction, in-medium effects such as shadowing and heavy-quark energy loss may substantially modify the final yields and spectra [61]. Open charm and open beauty production is another important issue addressed
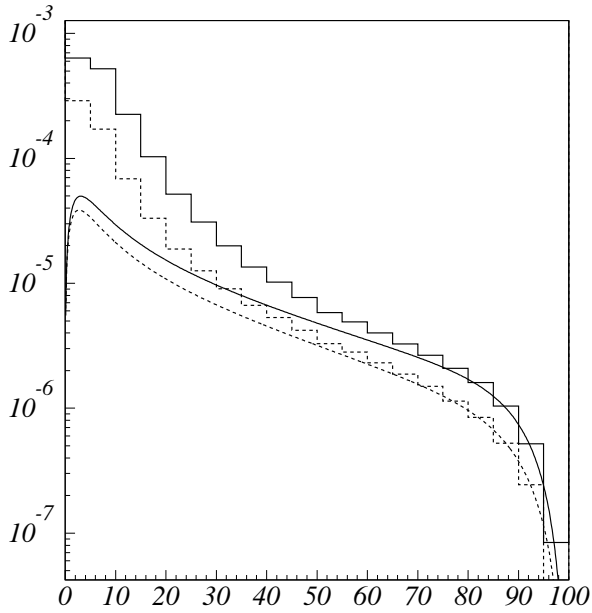
Fig. 9.13: $O(\alpha_s^4)$ calculations (histograms) and fragmentation model (curves) for vector (solid) and pseudo-scalar (dashed) B_c mesons production at $\hat{s} = 200$ GeV. The horizontal axis denotes the B_c transverse momentum.
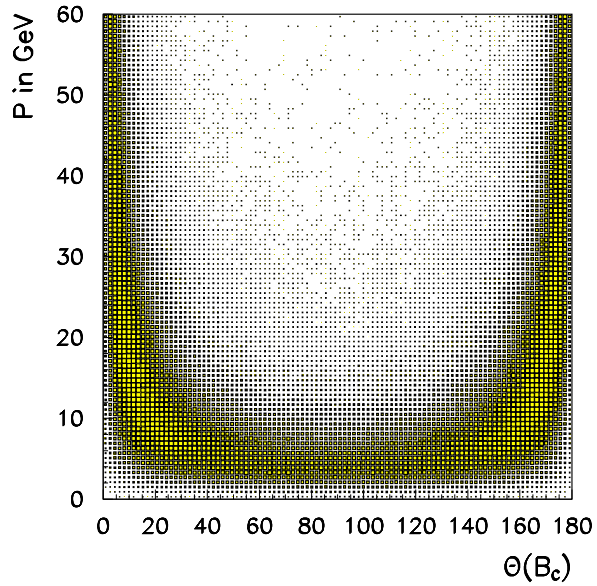
Fig. 9.14: The momentum $P(B_c)$ vs. the angle between the momentum of the B_c and the z-axis in the laboratory system at LHC energies.

by ALICE since they provide the most natural normalization to quarkonia suppression/enhancement. On the other hand, in a QGP, an additional source of charm quarks may arise from secondary parton scattering [62, 63] and information on the properties of the deconfined medium could be revealed by the kinematical properties of heavy mesons.

ALICE will allow measurements of heavy flavours in both the muon and the electron channels as well as full reconstruction of D mesons in the hadronic channel. Although the apparatus is dedicated to heavy-ion collisions, proton–proton and proton–nucleus collisions are also an important part of the ALICE physics programme in order to unravel initial and final-state medium effects.

9.1 ALICE detector

The ALICE detector [64] is designed to cope with large particle multiplicities which, in central Pb–Pb collisions, are expected to be between 2000 and 8000 per unit rapidity at mid rapidity. It consists of a central part, a forward muon spectrometer, and forward/backward small acceptance detectors. The central part of ALICE consists of four layers of detectors placed in the solenoidal field ($B < 0.5$ T) provided by the LEP L3 magnet. From the inner side to the outer side, these detectors are the Inner Tracker System (ITS), the large Time Projection Chamber (TPC), the Transition Radiation Detector (TRD) and the Time of Flight system (TOF). They provide charged-particle reconstruction and identification in the pseudo-rapidity range $|\eta| < 0.9$, with full azimuthal coverage and a broad p_T acceptance. These large-area devices are complemented by smaller acceptance detectors: the High-Momentum Particle Identification (HMPID), the PHOton Spectrometer (PHOS) and the Photon Multiplicity Detector (PMD). In the forward/backward region, the charged multiplicity and the zero degree energy will be measured by additional detectors (T0, V0, FMD, ZDC) which will allow fast characterization and selection of the events. Finally, a forward muon spectrometer covering the pseudo rapidity range $2.5 < \eta < 4$ is placed on the right side of the central part. It consists of a front absorber, a dipole magnet, ten high-granularity tracking chambers, a muon filter, and four large-area trigger chambers.
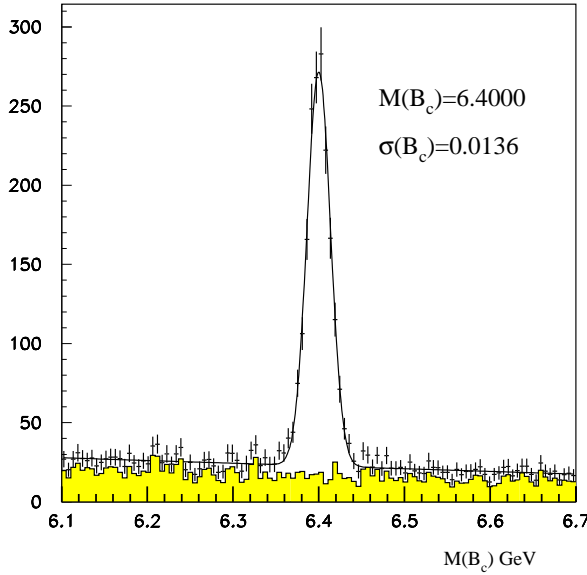
Fig. 9.15: The reconstructed B_c mass with background. The curve is a Gaussian plus polynomial fit.
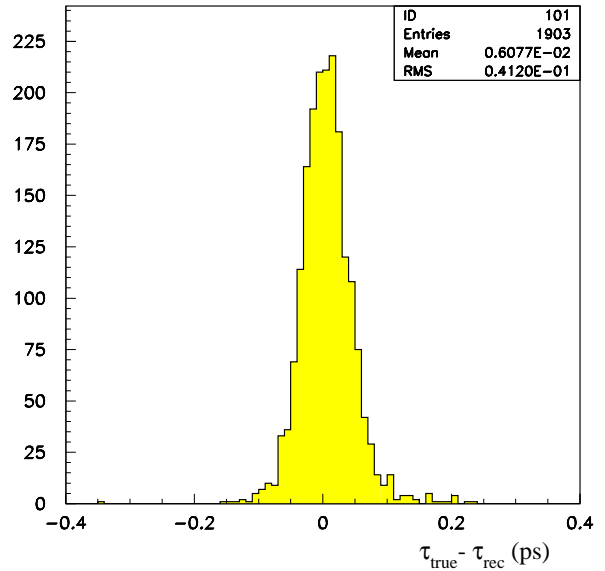

Fig. 9.16: Comparison of the reconstructed and generated B_c lifetime

9.2   Muons

The goal of the forward muon spectrometer [65] is to measure the full set of onium resonances from the ϕ to the Υ, with high statistics, a low background, and a high resolution. The spectrometer is equipped with a dimuon trigger based on the selection of pairs of muons with large transverse momentum. An important specification of the spectrometer is its mass resolution which has to be about 100 MeV at 10 GeV to allow the separation of the Υ substates. Detailed simulations have shown that this goal should be reached, even in the worst scenario of background environment that could be foreseen. The acceptance for J/ψ and Υ is fairly uniform in p_T and allows both J/ψ and Υ to be detected down to $p_T = 0$. The statistics expected in a 10^6 s run, roughly corresponding to one month of data taking, is of $\sim 500 \times 10^3$ J/ψ and ~ 10000 Υ in minimum-bias Pb–Pb collisions. For J/ψ, the rate and signal-over-background (S/B) are very good and permit a high-precision measurement of the differential cross-section. The $\psi(2S)$ can be measured at best with an accuracy of the order of 10% because of less favourable S/B. For the Υ family, the S/B is larger than unity and the significance is 70, 31 and 22 for $\Upsilon(1S)$, $\Upsilon(2S)$ and $\Upsilon(3S)$. In addition to quarkonia measurements, the spectrometer will allow measurements of the differential open bottom cross-section. This will be achieved both in the single muon and the dimuon channels.

9.3   Electrons

The measurement of dielectrons in the central barrel of ALICE is complementary to the dimuon channel. It extends quarkonia measurements from the forward rapidity region to mid-rapidity and allows one to measure secondary J/ψ from bottom decay thanks to the vertex capabilities of the ITS. This will permit the distinction between primary and secondary J/ψ and also lead to a direct measurement of the B-meson production cross-section. Furthermore, single high-p_T electrons with displaced vertex give access to the inclusive open charm and open bottom cross-sections. The centrepiece for dielectron physics is the TRD which provides an electron trigger and identification [66]. Its acceptance is identical to that of the ITS/TPC ($|\eta| < 0.9$ with full azimuthal coverage). Its expected pion rejection factor in a high-multiplicity environment has been investigated by means of detailed simulations. These simulations were adjusted to test beam data for well isolated tracks and then performed for various track multiplicities. Going from well isolated tracks to a full multiplicity event (8000 charged particles per unit of rapidity at mid-rapidity), a worsening of the pion rejection by a factor 6–7 is observed. For an electron efficiency

of 90% the pion rejection factor is still better than 50. On the other hand, the track reconstruction using information from the ITS, TPC and TRD leads to a Υ mass resolution good enough for the separation of the Υ substates.

9.4 Hadrons

In the central part of ALICE, heavy mesons can be fully reconstructed from their charged-particle decay products in the ITS, TPC and TOF. Thus, not only their integrated yields, but also their p_T distributions can be measured. The most promising decay channel for open charm detection is the $D^0 \rightarrow K^- \pi^+$ decay (and its charge conjugate) which has a branching ratio of about 3.8% and $c\tau = 124~\mu m$. The expected rates (per unit of rapidity at mid rapidity) for D^0 (and $\bar{D}^0$) mesons, decaying in a $K^\mp \pi^\pm$ pair, in central (5%) Pb–Pb at $\sqrt{s} = 5.5$ TeV and in pp collisions at $\sqrt{s} = 14$ TeV are 5.3×10^{-1} and 7.5×10^{-4} per event, respectively. The selection of this decay channel allows the direct identification of the D^0 particles by computing the invariant mass of fully-reconstructed topologies originating from displaced secondary vertices. The expected statistics are $\simeq 13\,000$ reconstructed D^0 in 10^7 central Pb–Pb events and $\simeq 20\,000$ in 10^9 pp events. The significance is larger than 10 for up to about $p_T = 10$ GeV both in Pb–Pb and in pp. The cross-section can be measured down to $p_T \simeq 1$ GeV in Pb–Pb collisions and down to almost $p_T = 0$ in pp collisions.

REFERENCES

[1] P. Mathews, P. Poulose and K. Sridhar, Phys. Lett. B **438**, 336 (1998) [arXiv:hep-ph/9803424].

[2] K. Sridhar, Phys. Rev. Lett. **77**, 4880 (1996) [arXiv:hep-ph/9609285].

[3] C. Qiao, F. Yuan and K. Chao, Phys. Rev. D **55**, 5437 (1997) [arXiv:hep-ph/9701249].

[4] C. S. Kim, J. Lee and H. S. Song, Phys. Rev. D **55**, 5429 (1997) [arXiv:hep-ph/9610294].

[5] P. Mathews, K. Sridhar and R. Basu, Phys. Rev. D **60**, 014009 (1999) [arXiv:hep-ph/9901276].

[6] V. Barger, S. Fleming and R. J. Phillips, Phys. Lett. B **371**, 111 (1996) [arXiv:hep-ph/9510457].

[7] E. Braaten, S. Fleming, and A. K. Leibovich, Phys. Rev. D **63**, 094006 (2001) [arXiv:hep-ph/0008091].

[8] F. Maltoni and A. D. Polosa, Phys. Rev. D **70**, 054014 (2004) [arXiv:hep-ph/0405082].

[9] E. Braaten, J. Lee and S. Fleming, Phys. Rev. D **60**, 091501 (1999) [arXiv:hep-ph/9812505].

[10] R. A. Briere *et al.*, CLNS-01-1742.

[11] S. K. Choi *et al.* [BELLE collaboration], Phys. Rev. Lett. **89**, 102001 (2002) [Erratum-ibid. **89**, 129901 (2002)] [arXiv:hep-ex/0206002].

[12] D. M. Asner *et al.* [CLEO Collaboration], Phys. Rev. Lett. **92**, 142001 (2004) [arXiv:hep-ex/0312058].

[13] F. E. Close, G. R. Farrar and Z. p. Li, Phys. Rev. D **55**, 5749 (1997) [arXiv:hep-ph/9610280].

[14] *An International Accelerator Facility for Beams of Ions and Antiprotons*; Conceptual Design Report, November 2001. http://www.gsi.de/GSI-Future/cdr .

[15] T. Swkarnicki, *Heavy Quarkonia*, Proceedings of XXI International Symposium on Lepton and Photon Interactions at High Energies, Fermilab, August 2003, To be published.

[16] M. B. Voloshin, private communication.

[17] E760 Collaboration, T.A. Armstrong *et al.*, Phys. Rev. D **52**, 4839 (1995).

[18] E835 Collaboration, M. Ambrogiani *et al.*, Phys. Lett. B **566**, 45 (2003).

[19] Belle Collaboration, S.K. Choi *et al.*, Phys. Rev. Lett. **89**, 102001 (2002);
Belle Collaboration, K. Abe *et al.*, Phys. Rev. Lett. **89**, 142001 (2002).

[20] Crystal Ball Collaboration, C. Edwards *et al.*, Phys. Rev. Lett. **48**, 70 (1982).

[21] B. Aubert *et al.* [BABAR Collaboration], Phys. Rev. Lett. **92**, 142002 (2004) [arXiv:hep-ex/0311038].

[22] CLEO Collaboration, T. Ferguson, *Observation of η_c in two-photon collisions at CLEO*, presentation given at the Second QWG Workshop on Heavy Quarkonia,
http://www.qwg.to.infn.it/WS-sep03/WS2talks/spectr/ferguson.pdf .

[23] S. Godfrey, *Quarkonium spectroscopy*, presentation given at the Second QWG Workshop on Heavy Quarkonia,
http://www.qwg.to.infn.it/WS-sep03/WS2talks/spectr/godfrey_pot.pdf.

[24] E835 Collaboration, M. Ambrogiani *et al.*, Phys. Rev. D **64**, 052003 (2001).

[25] E760 Collaboration, T.A. Armstrong *et al.*, Phys. Rev. D **56**, 2509 (1997).

[26] E760 Collaboration, T.A. Armstrong *et al.*, Phys. Rev. D **48**, 3037 (1993).

[27] Crystal Ball Collaboration, M. Oreglia *et al.*, Phys. Rev. D **25**, 2259 (1982).

[28] E835 Collaboration, M. Ambrogiani *et al.*, Phys. Rev. D **65**, 052002 (2002).

[29] Belle Collaboration, S.K. Choi *et al.*, Phys. Rev. Lett. **91**, 262001 (2003) [arXiv:hep-ex/0309032].

[30] CDF Collaboration, G. Bauer, *Observation of a Narrow State Decaying to $J/\psi \pi^+ \pi^-$ in CDF*, presentation given at the Second QWG Workshop on Heavy Quarkonia,
http://www.qwg.to.infn.it/WS-sep03/WS2talks/spectr/plenary/bauer.ps.gz.

[31] P. Chen, X. Liao and T. Manke, Nucl. Phys. Proc. Suppl. **94**, 342 (2001);
C. Michael, Proceedings of Heavy Flavours 8, Southampton, UK, 1999.

[32] T. Barnes, F.E. Close and E.S. Swanson, Phys. Rev. D **52**, 5242 (1995).

[33] The Science Driving the 12 GeV Upgrade of CEBAF, Jefferson Lab, 2001.

[34] ATLAS Collaboration, *ATLAS Detector and Physics Performance Technical Design Report Vol. I*, CERN/LHCC/99-14; *Vol. II*, CERN/LHCC/99-15 (May 1999).

[35] P. Nason *et al.*, hep-ph/0003142 (2000);
published in M. Mangano, G. Altarelli (ed.), *1999 CERN Workshop on Standard Model Physics (and More) at the LHC*, CERN-2000-004 (2000).

[36] J. L. Domenech-Garret, M. A. Sanchis-Lozano and S. Wolf, J. Phys. G **28**, 687 (2002) [arXiv:hep-ph/0110085].

[37] M. Krämer, Prog. Part. Nucl. Phys. **47**, 141 (2001) [arXiv:hep-ph/0106120].

[38] F. Abe *et al.*, CDF Collaboration, Phys. Rev. Lett. **79**, 572 (1997).

[39] M. A. Sanchis-Lozano, Nucl. Phys. Proc. Suppl. **86**, 543 (2000) [arXiv:hep-ph/9907497].

[40] M. A. Sanchis-Lozano, Nucl. Phys. Proc. Suppl. B **75**, 191 (1999) [arXiv:hep-ph/9810547].

[41] B. Cano-Coloma and M. A. Sanchis-Lozano, Nucl. Phys. B **508**, 753 (1997) [arXiv:hep-ph/9706270].

[42] T. Affolder *et al.*, CDF Collaboration, Phys. Rev. Lett. **85**, 2886 (2000).

[43] ATLAS Collaboration, *ATLAS High-Level Triggers, DAQ and DCS Technical Proposal*, CERN/LHCC/2000-017 (March 2000).

[44] ATLAS Collaboration, *ATLAS High-Level Trigger, Data Acquisition and Controls Technical Design Report*, CERN/LHCC/2003-022 (June 2003).

[45] N. Panikashvili, private communication; write-up as ATLAS Internal Note ATL-COM-PHYS-2003-048 (2003).

[46] F. Albiol, R. Pérez Ochoa, M. A. Sanchis-Lozano and J. A. Valls, hep-ph/9506306 (1995);
M. Galdón, R. Pérez Ochoa, M. A. Sanchis-Lozano and J. A. Valls, hep-ph/9510450 (1995).

[47] C. H. Chang, C. Driouichi, P. Eerola and X. G. Wu, Comput. Phys. Commun. **159**, 192 (2004) [arXiv:hep-ph/0309120].

[48] LHCb Collaboration, S. Amato *et al*, Technical Proposal, CERN-LHCC/98-4.

[49] LHCb Collaboration, R. Antunes Nobrega *et al*, Technical Design Report. Reoptimized Detector Design and Performance, CERN/LHCC 2003-030.

[50] I.P. Gouz, V.V. Kiselev, A.K. Likhoded, V.I. Romanovski and O.P. Yushchenko, Phys. Atom. Nucl. **67**, 1559 (2004) and hep-ph/0211432 (2002).

[51] O.P. Yushchenko, Search for the $B_c^+ \to J/\psi(\mu^+\mu-)\pi^+$ decay with the LHCb spectrometer, LHCb-note 2003-113.

[52] ALICE Collaboration, ALICE Physics Performance Report, in preparation; ALICE Collaboration internal note, ALICE-INT-2002-25.

[53] H. Satz, Rep. Prog. Phys. **63**, 1511 (2000) [arXiv:hep-ph/0007069].

[54] R. Vogt, Phys. Rep. **310**, 197 (1999) .

[55] T. Matsui and H. Satz, Phys. Lett. B **178**, 416 (1986).

[56] S. Digal, P. Petreczky and H. Satz, Phys. Rev. D **64**, 094015 (2001) [arXiv:hep-ph/0106017].

[57] C. Y. Wong, Phys. Rev. C **65**, 034902 (2002) [nucl-th/0110004].

[58] J. F. Gunion and R. Vogt, Nucl. Phys. B **492**, 301 (1997) [arXiv:hep-ph/9610420].

[59] S. Eidelman *et al.* [Particle Data Group Collaboration], Phys. Lett. B **592**, 1 (2004).

[60] P. Braun-Munzinger and K. Redlich, Eur. Phys. J. C **16**, 519 (2000) [arXiv:hep-ph/0001008].

[61] M. Bedjidian *et al.*, Workshop on Hard Probes in Heavy–Ion Collisions at the LHC, CERN–2004–009, [arXiv:hep-ph/0311048].

[62] B. Müller and X.N. Wang, Phys. Rev. Lett. **68**, 2437 (1992).

[63] K. Geiger, Phys. Rev. D **48**, 4129 (1993).

[64] http://alice.web.cern.ch/Alice/AliceNew/ .

[65] ALICE Collaboration, TDR of the muon Spectrometer, CERN/LHCC 99-22 (1999); Addendum 1 to the TDR of the muon Spectrometer, CERN/LHCC 2000-046 (2000).

[66] ALICE Collaboration, TDR of the TRD, CERN/LHCC 2001-021 (2001).

Chapter 10

OUTLOOK

Conveners: S. Godfrey, M. A. Sanchis-Lozano

Authors: G. Bodwin, E. Braaten, N. Brambilla, A. Deandrea, E. Eichten, S. Godfrey, A. Hoang, M. Krämer, R. Mussa, P. Petreczki, M. A. Sanchis-Lozano, A. Vairo

1 THE RENAISSANCE OF HEAVY QUARKONIUM PHYSICS

Quarkonium physics has played a fundamental role in the development of quantum chromodynamics. It may play an even more relevant role now for QCD, the Standard Model, and physics beyond the Standard Model. Heavy quarkonium, being a multiscale system, offers a precious window into the transition region between high-energy and low-energy QCD and thus a way to study the behaviour of the perturbative series and the nontrivial vacuum structure. The existence of energy levels below, close to and above threshold, as well as the several production mechanisms, allows one to test the population of the QCD Fock space in different regimes and eventually to search for novel states with nontrivial glue content (hybrids, glueballs). Precise determinations of Standard Model parameters from quarkonium systems have become possible because of the level of precision reached by the experimental data and by the most recent developments in effective field theories and lattice QCD. Moreover, the clean signature of heavy quarkonium in heavy-ion collisions provides a perfect probe of in-media phenomena, and eventually of quark–gluon plasma formation and the confinement–deconfinement transition in QCD. The expected large statistics of ψ and Υ resonances to be collected in the next few years at e^+e^- and hadronic colliders makes heavy quarkonium physics also suitable for searches for new particles and new phenomena. A number of new physics scenarios can be constrained or discovered in the near future, ranging from the contribution of supersymmetric particles or extended Higgs sectors in quarkonium decay, to lepton flavour violation tests, CP tests and chromo-dipole moments of quarks. All these studies will play a major role in the test of extensions of the Standard Model, and will be complementary to direct searches at colliders like the LHC or a future linear collider.

2 OPPORTUNITIES IN THEORY AND EXPERIMENT

The future relevance of quarkonium physics will be proportional to the number of observables that can be rigorously described in terms of the Standard Model and its parameters and well measured by experiments. The enormous progress made in this direction in recent years is the reason for the quarkonium renaissance that we are witnessing today and that has been documented in this report. It comes mainly from QCD effective field theories in either their continuum or in their lattice versions, while phenomenological models have played (and will still play in the future) a crucial role in suggesting experimental search strategies and interpreting new results. In order to achieve further progress it will be important to complete the following general programme.

(1) Adopt a common, model-independent, EFT-based, language to describe all aspects of heavy quarkonium physics. This has not been achieved yet for all observables, and, noteworthily, not for observables sensitive to threshold effects, where phenomenological models still provide the only available theoretical tool.

(2) Improve the determination of the nonperturbative parameters that describe the low-energy dynamics either by experimental data or by lattice calculations. In an EFT context the number of these parameters is finite. Therefore, precise quarkonium data are important today more than ever.

They may check factorization, allow for precise extractions of the Standard Model parameters, and severely constrain theoretical determinations and predictions.

We note that the more progress there is in (1), the more importance that experimental data will acquire for (2).

In the following we discuss progress expected or invoked for some specific set of observables.

2.1 Quarkonium ground and lower states

Ground-state observables and to a lesser extent low lying quarkonium-state observables may be studied in the framework of perturbative QCD. These studies are relevant because they may allow, in principle, the precise extraction of some of the fundamental parameters of the Standard Model, such as the heavy quark masses and the strong coupling constant (see Chapter 6). B_c will be copiously produced at future hadron colliders and will allow the determination of the electroweak parameters of the Standard Model, such as the CKM matrix elements and CP violating parameters (see Chapter 4). However, the accuracy with which the fundamental parameters can be measured is at present limited by nonperturbative contributions whose form is in many cases known, but whose size is not known with sufficient precision. Therefore the main theoretical challenge is the precise determination of these nonperturbative contributions (see Chapters 3 and 4). On the other hand we could take the opposite approach and use the lower quarkonium states as a theoretically clean environment to study the interplay of perturbative and nonperturbative effects in QCD and extract nonperturbative contributions by comparison with data. A few examples are:

– The η_b has been intensively searched for at the Tevatron and CLEO. Theoretically several observables related to the production mechanism (Chapter 5), spectroscopy (Chapter 3), and decay (Chapter 4) have been studied. Most likely, the η_b discovery will come from the Tevatron experiments CDF and D0. NRQCD predictions suggest ($\sigma_{\eta_b+X} \approx 2.5\ \mu b$ at 1.96 TeV), so that η_b should be found during Run II. However, as the decay rates are expected to be very low, reliable theory estimates for the decays into $J/\psi J/\psi$, $D\bar{D}\pi$, $K\bar{K}\pi$ are important. Indications can also come from the efforts made to detect its charmonium analogue, the η_c, in hadronic collisions. An eventual discovery will put severe constraints on the size of the nonperturbative corrections and confirm or disprove our current understanding of the bottomonium ground state. In case this system, as expected, turns out to be mainly perturbative, it will provide, combined with the $\Upsilon(1S)$, a very precise measurement of α_s.

– The perturbative $\Upsilon(1S)$ mass is used for a competitive determination of m_b. However, at present accuracy, perturbation theory has difficulty reproducing the measured width $\Upsilon(1S) \to e^+e^-$. Given the importance of this quantity, the origin of these difficulties should be clarified. Furthermore, the experimental determination of the $\Upsilon(1S)$ polarization at the Tevatron is roughly consistent with the NRQCD prediction, and fixed-target experiments find an almost transverse polarization for the $\Upsilon(2S)$ and $\Upsilon(3S)$ (although the experimental result disagrees with NRQCD for the $\Upsilon(1S)$). This provides a strong motivation for measuring the polarization of all three resonances at the Tevatron. However, because of the large bottom mass, the fragmentation mechanism does not dominate until relatively high values of p_T are reached ($p_T > 10$ GeV). LHC experiments will likely play a decisive role in settling this issue because of the broader p_T range.

– The B_c mass determined by experiments is affected at present by about 400 MeV uncertainty, while theoretical calculations based on perturbative QCD are affected by errors which are not larger than 30 MeV (see Chapter 3). Again a precise determination of the B_c mass will strongly constrain the size of the nonperturbative contributions and confirm or disprove our understanding of this system in terms of perturbative QCD. An analogous argument holds for the yet undiscovered B_c^*.

– Baryons with two or three heavy quarks and in particular the yet undiscovered baryons with two bottom quarks will offer a completely new system to test our understanding of low-lying heavy

quarkonium resonances (see Chapter 3). The study of these systems from QCD is just beginning with lattice simulations just starting to analyse these systems. Further progress is expected in the future, in particular if driven by new experimental findings.

– As the $\eta_c(2S)$ and h_c complete the low-mass charmonium multiplets, the theoretical understanding of fine and hyperfine splittings is far from the precision reached by experiments (see Chapter 3). Further progress in unquenched lattice calculations is needed. The plans to produce very large ($> 10^9$) samples of J/ψ's and $\psi(2S)$'s can open the era of 1–2% precision measurements on many radiative transitions, allowing access to the suppressed (M1, M2 and E2) amplitudes, which are mostly dependent on higher-order corrections and better test different theoretical approaches. Runs at the $\psi(2S)$ energy will also provide a very large sample of tagged J/ψ decays (as more than half of these mesons decay to J/ψ), but are also an excellent source of χ_c's, and, as recently shown, of h_c's.

– At last, B factories will allow us to reach accuracies better than 10% on the $\gamma\gamma$ widths of the $\eta_c(1,2S)$ and $\chi_{c0,2}$, by the proper combination of their data with measurements from p$\bar{\text{p}}$ and τ-charm factories. Electromagnetic and hadronic decay widths, whose experimental accuracy is already sensitive to NLO corrections (see Chapter 4), may in perspective provide a competitive measurement of α_{s} at charmonium energies.

– In the LHC era, very large samples ($>10^{10}$ events) of J/ψ and $\psi(2S)$ mesons will allow the high-precision test of lepton flavour violation, severely constraining new physics models. Lepton flavour violation can be tested via two-body decay, $J/\psi \rightarrow \ell\ell'$ (which conserves total lepton number), with ℓ and ℓ' denoting charged leptons of different species. This process (discussed in Chapter 8) could occur at tree-level induced by leptoquarks, sleptons (both in the t channel) or mediated by Z' bosons (in the s channel).

2.2   Higher quarkonium states

The rigorous study of higher quarkonium states, including exotic states like hybrids, will mostly rely on lattice calculations. However, at the moment, phenomenological models still play a major role in describing states above the open flavour threshold. In the framework of nonrelativistic EFTs on the lattice, further progress will need:

– the calculation in lattice perturbation theory of the Wilson coefficient of the EFT at least at NLO (see Chapters 1 and 3);

– the lattice implementation of lower-energy EFTs like pNRQCD. In this framework the lattice data would provide the form of the potentials and the states would be determined by solving the corresponding Schrödinger-like equation.

The observation of the $X(3872)$ is the start of challenging searches for non-vector states across the open flavour threshold. This is probably the richest experimental field of research on heavy quarkonia at present. As mentioned above, phenomenological models have played a particularly important role in predicting which states are likely to be narrow enough to be observed and suggesting the most promising channels for their observation.

– Studies on the nature of the $X(3872)$, described in Chapters 3, 4, and 5 can benefit from data taking at B factories, Tevatron, and even τ-charm factories: these should have high priority, as emphasized throughout the report.

– Given the excellent momentum resolution of the B factories and the unexpected double charm process, J/ψ recoil techniques also have good discovery potential. More conventional methods, like the study of the production of pairs of open charm mesons near threshold (in B decays and hadronic collisions) are now reaching the statistics necessary to allow the discovery of new resonances in the $c\bar{c}$ system with quantum numbers other than 1^{--}. In particular, the remaining

$1D$ states, some of the $2P$ states and the 3^1S_0 are likely to be observable in this way. Observation of new states with different quantum numbers is also beneficial for the understanding of the mechanism of charmonium production.

– The current CLEO-c run at $\psi(3770)$ energy, presently measuring f_D from $\bar{D}D$ decays, can also look for rare radiative and hadronic decays to lower $c\bar{c}$ states. This study can give a unique insight into the S–D mixing and coupling to decay channel effects. It may also give clues to the understanding of the ρ–π puzzle.

2.3 Production

If measurements of quarkonium production are to be exploited fully to test theoretical models, then the precision of the theoretical predictions should be improved. Several theoretical tools that are, by now, standard could be applied to increase the precision of theoretical predictions for charmonium and bottomonium production rates. These tools include calculations at NLO in α_s and v, resummation of logarithms of m^2/p_T^2 or $m^2/(p^*)^2$, resummation of logarithms of p_T^2/m^2 or $(p*)^2/m^2$, resummation of logarithms of s/m^2, resummation of logarithms of $1-z$, and lattice calculations of quarkonium matrix elements.

– Calculations of cross-sections at NLO in α_s already exist for total cross-sections and for some quarkonium fragmentation functions. NLO calculations of quarkonium differential cross-sections in the colour-singlet model also exist. However, full NLO calculations in the NRQCD factorization approach are lacking, in general, for quarkonium differential cross-sections and, in particular, for the important cases of quarkonium cross-sections that are differential in p_T.

– Some calculations of corrections of higher order in the heavy-quark velocity v have already been carried out and have yielded large corrections. It is important to investigate such higher-order corrections for all quarkonium production processes and to develop a phenomenology of the higher-order NRQCD matrix elements. It is also important to understand the origins of large corrections of higher order in v, with the aim of controlling them to all orders in the v expansion.

– Logarithms of m^2/p_T^2 are important at small p_T. Their resummation involves the introduction of non-perturbative k_T-dependent parton distributions. The effects of these distributions are small for bottomonium, but are important for charmonium. It may be possible to work out a phenomenology of such distributions by exploiting their universality properties to extract them from processes other than quarkonium production, such as Drell–Yan production of lepton pairs.

– Logarithms of p_T^2/m^2 are important at large p_T. They may have a large effect on, for example, extractions of the $^3S_1$ colour-octet matrix elements that dominate J/ψ and Υ production at large p_T.

– Logarithms of s/m^2 may play an important rôle in diffractive quarkonium production and quarkonium production in which sub-processes involve small momentum transfer. They are often resummed in existing calculations in the k_T-factorization approach by making use of the BFKL equation. Large corrections that occur at NLO in the BFKL equation cast some doubt on the accuracy of such resummed calculations.

– The quantity $1-z$ generally measures the departure of a quarkonium production process from a kinematic endpoint. Examples of z are the quarkonium energy fraction and the quarkonium longitudinal-momentum fraction. It follows that logarithms of $1-z$ are important near the kinematic limits of cross-sections. Their resummation involves nonperturbative shape functions. It would be useful to develop a phenomenology of these shape functions so that information from, say, quarkonium production in e^+e^- collisions could be used to make predictions for other quarkonium production processes, such as photoproduction at HERA.

– Lattice techniques can be used to compute colour-singlet NRQCD production matrix elements in the vacuum-saturation approximation, and, hence, to supplement information on the values of

these matrix elements that can be obtained from the phenomenology of quarkonium decay and production. Unfortunately, it is not yet known, except within the vacuum-saturation approximation, how to formulate the problem of the calculation of production matrix elements in lattice field theory. In particular, no lattice method exists for the computation of colour-octet production matrix elements.

In addition to the logarithmic contributions that we have already mentioned, large non-logarithmic contributions appear in some calculations of production cross-sections at NLO in α_s. Examples of large corrections also exist in NLO calculations of quarkonium decay rates. It is important to understand the origins of such large corrections and to bring them under control to all orders in α_s.

A significant theoretical issue is the correctness of the NRQCD factorization formula for production. An all-orders perturbative proof of the factorization formula would be an important step forward. Such a proof might establish that there is a range of validity of the factorization formula. For example, the formula might hold at large p_T, but not at small p_T or for total cross-sections. Most of the experimental data are at small p_T. Experiments at small p_T are important to fix the values of certain NRQCD matrix elements and, hence, to test matrix-element universality. However, theoretical confidence in NRQCD factorization is highest at values of p_T that are significantly larger than the heavy-quark mass. Therefore, it is also important for experiments to obtain data points with the highest possible statistics at the largest accessible values of p_T. Such high-p_T measurements are particularly important in testing the key prediction that, owing to the colour-octet mechanism, there should be a large transverse polarization in spin-triplet quarkonium produced at large p_T.

The results from the Belle Collaboration on inclusive and exclusive double $c\bar{c}$ production in e^+e^- collisions are strongly at odds with current theoretical calculations. These calculations are carried out, essentially, within the colour-singlet model. However, colour-octet corrections are absent at leading twist in the exclusive case and are expected to be small in the inclusive case. An independent check of the Belle Collaboration results would be welcome. If these results are confirmed, they would pose a severe challenge to the current theoretical thinking about double $c\bar{c}$ production in e^+e^- collisions. A measurement of the double $c\bar{c}$ production cross-section in $p\bar{p}$ collisions at the Tevatron might give some additional clues as to the nature of the production mechanisms.

Polarized beams are available at RHIC and may be available at the LHC. Polarized-beam measurements of quarkonium production rates might be useful in discriminating between various models for quarkonium production and between various production mechanisms within the NRQCD factorization approach. Exploratory theoretical work on quarkonium production cross-sections for polarized beams is needed in order to understand the potential of such measurements.

2.4 In media

The study of quarkonia in media is relevant because one may use the media as a filter to study the time and length scale associated with quarkonia production and thus learn more about the production mechanism. Moreover, one may use quarkonia as a test of the medium to find out its properties (e.g., whether it is hadronic or deconfined). It has been suggested that production and suppression of quarkonia in heavy-ion collisions could signal deconfinement and quark–gluon plasma formation and eventually estimate its temperature (see Chapter 7). To use quarkonium to study the quark–gluon plasma one needs to understand its properties inside the plasma using lattice QCD and understand its formation in a high density environment. A list of future challenges related to these issues may consist of the following.

– Several lattice QCD studies show that ground-state charmonia survive in the plasma at temperatures as high as $1.5\,T_c$. At the same time all these studies show strong lattice artefacts in the charmonium spectral functions. Better lattice actions are needed to reduce these artefacts (e.g., lattice NRQCD, perfect actions).

– It would be important to understand what governs the quarkonium suppression in the plasma. In this respect it would be extremely interesting to study the bottomonium system and see whether or

not the $1P$ bottomonium states (χ_b), which are expected to have the same size as the J/ψ, melt at the same temperature.

- It is expected that the medium created in heavy-ion collisions is not fully equilibrated. Thus it would be very important to determine the thermal width of different quarkonium states on the lattice to make contact with experiments.

- In heavy-ion collisions at very high energy, the initial state is given by coherent gluon fields, the so-called colour glass condensate with typical momentum scale (saturation scale) $Q_s \simeq 1$–2 GeV. In the presence of colour glass condensate, heavy-quark and quarkonium production may be quite different from superposition of proton–proton production at the same energy. A detailed proton–nucleus study is needed together with nucleus–nucleus experiments to study this issue.

- Hydrodynamic models suggest a fast equilibrization in heavy-ion collisions at RHIC which will be even faster at LHC. The time scale of quark–gluon plasma formation $\tau \simeq 0.6$ fm is comparable to the time scale of the quarkonium formation. In order to disentangle between possible effects in quarkonium yield due to in-medium production from true medium effects, e.g., screening, a detailed analysis of quarkonium yields versus rapidity, energy, and p_T is required.

2.5 Top–antitop production

Top–antitop quark-pair production will provide an integral part of the top-quark physics programme at the International Linear Collider (ILC), which after the decision for cold, superconducting technology, is now becoming an inter-regional endeavour. A precise measurement of the threshold cross-section can provide a top-quark mass determination with uncertainties at the level of 100 MeV, a measurement of the total top decay rate Γ_t, the coupling strength of top quarks to gluons, α_s, and, if the Higgs boson is light, the top Yukawa coupling. For more details see Chapter 6.

On the theoretical side there are a number of problems that need to be solved. Among them are the still missing NNLL corrections to the top-pair production current, which affect the theoretical uncertainties of the cross-section normalization. Also, a complete fixed-order prediction at NNNLO of the total cross-section would be desirable as a cross-check of the importance of the summation of logarithms and as a starting point to renormalization group improved calculations beyond the NNLL level. An important conceptual issue to be solved is a consistent treatment of the interplay of electroweak and QCD effects. Since the top quark decay is a leading order effect in the threshold region, this problem includes the consistent treatment of interference effects of top quark production and decay, of factorizable and non-factorizable corrections and also of non-resonant final states. Closely related is also the problem of rescattering corrections.

Top quark threshold dynamics may also play a role in other processes at high energy. For example, the process $\gamma\gamma \to t\bar{t}$, accessible through the option of laser backscattering at the ILC, should be explored with the same accuracy as the production in e^+e^- annihilation. Likewise, top threshold dynamics also governs associated top-pair production processes in specific kinematic end-point regions, such as $e^+e^- \to t\bar{t}H$ in the limit of large Higgs energy. The importance of the top threshold region might also be systematically explored in the framework of hadron collisions. These threshold effects are not important at the present level of accuracy, but they could become relevant at the LHC where top pairs will be produced with very high statistics.

From the beginning of Linear Collider studies more than 10 years ago, a number of experimental studies analysing the principle feasibility of top threshold measurements have been carried out. But only recently were machine-specific and more subtle effects such as the influence of uncertainties in measurements of the luminosity spectrum considered and found to be very important. After the recent technology decision for the ILC, such design-dependent studies need to be driven further to fully explore the potential of threshold measurements and to derive the optimal scan strategy. The most important

missing tool, however, is a fully implemented top threshold event generator. This endeavour will be enormous, since such a generator will have to describe production, propagation, and the decay of quasi-bound top quarks in one single consistent framework. A close collaboration between experiment and theory will be crucial.

3 THE SUPERLAB

In recent years, the field of experimental high-energy physics has experienced a substantial reduction in the number of running experiments, together with the growth of large, expensive facilities used by an increasing number of physicists. In this respect, quarkonium physics is only one of the many physics studies competing for manpower and resources. In any of the experiments: CLEO-c, BES III, PANDA, Belle and BaBar at the B factories, and CDF and D0 at the Tevatron, the physics potential for quarkonia is many times larger than the analyses that are likely to actually be made. Because of this, many physics opportunities are lost. Heavy quarkonium studies will probably be a high-priority topic for BES III and possibly for PANDA. The currently running experiments, together with the BES III and LHC experiments, are likely to yield in the next five years an increase by one to two orders of magnitude of the number of reconstructed heavy quarkonia.

Initiatives involving transversally the different experiments are needed, to sort priorities between the different analyses to be done on the datasets, and to provide, whenever needed, a guideline for the best possible usage of available luminosity. By thinking of future studies on heavy quarkonia as an ideal 'Quarkonium Superlab', the QWG aims at merging theoretical and experimental efforts in this subject in a more effective and constructive way.

Recently, heavy quarkonium discoveries and confirmations in different production mechanisms have been blossoming in a concerted way at all the accelerator facilities. The observation of the $\eta_c(2S)$ and the $X(3872)$ are cases in point. While the $\eta_c(2S)$ was first observed by Belle in B decay and double charm production, it was subsequently confirmed by CLEO and BaBar in $\gamma\gamma$ collisions. Similarly, the $X(3872)$ was discovered by Belle in B decay and subsequently confirmed by both CDF and D0 in high-energy $p\bar{p}$ collisions at the Tevatron. Discoveries of the same state with different production mechanisms are very important in order to gain information on the nature of the state. The study of quarkonia production in high-energy, heavy-ion collisions, as a signature of the production of a deconfined state of QCD matter, started at CERN in 1986, and gave rise to one of the most exciting observations made in the field of experimental QCD thermodynamics. Here again, the comparison of heavy quarkonium production results in pp, $p\bar{p}$, pA and AA collisions is crucial to have full control of the underlying physics mechanisms.

Future expectations on heavy quarkonium experiments may be grouped as follows:

– In the short term (2004–2006), dedicated measurements on charmonium systems, mainly above the open charm threshold will be performed by CLEO-c, by running at $\psi(3770)$ between 4 and 4.4 GeV. At the same time, the two asymmetric B factories are poised to reach a total ~ 1000 fb^{-1} of data at the $\Upsilon(4S)$ resonance, yielding record samples of $\eta_c(1,2S)$, $X(3872)$ mesons with probably a few new surprises. The collider experiments CDF and D0 will likely accumulate about 20 times the data samples taken during Run I, and will hopefully shed new light on the issue of heavy quarkonium production and polarization. A precise determination of the mass of the B_c meson, done using exclusive $J/\psi\,\pi$ decays, will be available soon (see *Fermilab Today*, December 3, 2004). Results from the NA60 experiment at CERN and the STAR and PHENIX experiments at RHIC are expected to provide further evidence of QGP. With the expected significant increase in statistics of the upgraded HERA collider, it might be possible to study inelastic photoproduction of bottomonium states for the first time, with the caveat that production rates of Υ resonances are suppressed by more than two orders of magnitude compared with the J/ψ.

– In the mid term (2007–2009), high-precision results are expected from the CLEO-c run at the J/ψ, and hopefully at the $\psi(2S)$, as recommended by the QWG. In the meantime, the fully upgraded BES III detector will take over the precision studies of charmonium started by CLEO-c. BES III could run on higher ψ resonances, high above the $D\bar{D}$ threshold and with high enough statistics to produce the higher P, D states via transitions from the ψ's. While the two running Tevatron experiments will complete their period of data taking, reaching total final samples of about $16\,\text{fb}^{-1}$, CERN will return to the scene in 2008, when the first beams are expected to circulate in the LHC accelerator. The first period of data taking, at low luminosity, will be very important to establish the physics potential of the ATLAS, CMS and LHCb experiments on heavy quarkonium production and B_c studies. Later, three experiments will be able to study quarkonia production in heavy-ion collisions at the LHC: ALICE, CMS and ATLAS. ALICE will measure the charmonia states through their decay into electron and muon pairs. Before the LHC start-up, the CERN experiment COMPASS also has the possiblility of obtaining new information on the doubly charmed baryons discovered by SELEX at FNAL. At CEBAF, high-intensity 9 GeV photon beams will allow the study of the J/ψ photoproduction mechanism at low energy.

The future of the asymmetric B factories is unclear at present. If at least one of the two facilities increases its luminosity to become a super B factory, a large number of charmonium measurements will be within reach, and even the simple ISR production mechanism will yield record samples of $\Upsilon(1,2,3S)$ decays. A promising opportunity, recommended by the QWG, is to turn one of the two asymmetric B factories into an $\Upsilon(1,2,3S)$ factory during the last fraction of its running period. There is considerable $b\bar{b}$ physics that remains to be done. A few examples are: $\eta_b(n^1S_0)$ searches using M1 radiative transitions from the $\Upsilon(n^3S_1)$ states, h_b searches via hadronic transitions $\Upsilon(3S){\to}h_b+\pi^0{\to}\eta_b+\gamma+\pi^0$ or $\Upsilon(3S){\to}h_b+\pi\pi{\to}\eta_b+\gamma+\pi\pi$, and measuring radiative and hadronic transitions in the $b\bar{b}$ system.

– In the long term (2010 and beyond), PANDA at GSI offers the opportunity to study many charmonium states with non 1^{--} quantum numbers and can challenge BES III on high-statistic studies of the narrow charmonium states. Given the huge yields of heavy quarkonia expected from LHC experiments when running at full luminosity, the main problem will be the choice of high-priority physics cases and the main challenge will come from the need to keep trigger rates under control. At the same time the BTeV experiment at Tevatron will challenge LHCb on B_c physics in the forward region. Finally, the ILC, in the next decade, will test NRQCD at $t\bar{t}$ threshold, as well as a number of still unpredicted future hot issues in heavy quarkonium physics.

Acknowledgements